

AGARD

ADVISORY GROUP FOR AEROSPACE RESEARCH & DEVELOPMENT

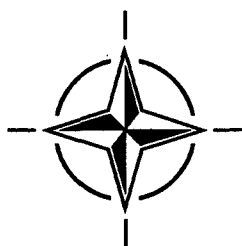
7 RUE ANCELLE, 92200 NEUILLY-SUR-SEINE, FRANCE

AGARD CONFERENCE PROCEEDINGS NO. 552

Aerodynamics and Aeroacoustics of Rotorcraft

(l'Aérodynamique et l'aéroacoustique des aéronefs
à voilure tournante)

*Papers presented and discussions recorded at the 75th Fluid Dynamics Symposium held in Berlin,
Germany, 10-13 October 1994.*



NORTH ATLANTIC TREATY ORGANIZATION

Published August 1995

Distribution and Availability on Back Cover

19950927 049

AGARD

ADVISORY GROUP FOR AEROSPACE RESEARCH & DEVELOPMENT

7 RUE ANCELLE, 92200 NEUILLY-SUR-SEINE, FRANCE

AGARD CONFERENCE PROCEEDINGS NO. 552

Aerodynamics and Aeroacoustics of Rotorcraft

(l'Aérodynamique et l'aéroacoustique des aéronefs
à voilure tournante)

Papers presented and discussions recorded at the 75th Fluid Dynamics Symposium held in
Berlin, Germany, 10-13 October 1994.



North Atlantic Treaty Organization
Organisation du Traité de l'Atlantique Nord

The Mission of AGARD

According to its Charter, the mission of AGARD is to bring together the leading personalities of the NATO nations in the fields of science and technology relating to aerospace for the following purposes:

- Recommending effective ways for the member nations to use their research and development capabilities for the common benefit of the NATO community;
- Providing scientific and technical advice and assistance to the Military Committee in the field of aerospace research and development (with particular regard to its military application);
- Continuously stimulating advances in the aerospace sciences relevant to strengthening the common defence posture;
- Improving the co-operation among member nations in aerospace research and development;
- Exchange of scientific and technical information;
- Providing assistance to member nations for the purpose of increasing their scientific and technical potential;
- Rendering scientific and technical assistance, as requested, to other NATO bodies and to member nations in connection with research and development problems in the aerospace field.

The highest authority within AGARD is the National Delegates Board consisting of officially appointed senior representatives from each member nation. The mission of AGARD is carried out through the Panels which are composed of experts appointed by the National Delegates, the Consultant and Exchange Programme and the Aerospace Applications Studies Programme. The results of AGARD work are reported to the member nations and the NATO Authorities through the AGARD series of publications of which this is one.

Participation in AGARD activities is by invitation only and is normally limited to citizens of the NATO nations.

The content of this publication has been reproduced
directly from material supplied by AGARD or the authors.

Published August 1995

Copyright © AGARD 1995
All Rights Reserved

ISBN 92-836-0015-0



*Printed by Canada Communication Group
45 Sacré-Cœur Blvd., Hull (Québec), Canada K1A 0S7*

Recent Publications of the Fluid Dynamics Panel

AGARDOGRAPHS (AG)

Computational Aerodynamics Based on the Euler Equations

AGARD AG-325, September 1994

Scale Effects on Aircraft and Weapon Aerodynamics

AGARD AG-323, July 1994

Design and Testing of High-Performance Parachutes

AGARD AG-319, November 1991

Experimental Techniques in the Field of Low Density Aerodynamics

AGARD AG-318 (E), April 1991

Techniques expérimentales liées à l'aérodynamique à basse densité

AGARD AG-318 (FR), April 1990

A Survey of Measurements and Measuring Techniques in Rapidly Distorted Compressible Turbulent Boundary Layers

AGARD AG-315, May 1989

Reynolds Number Effects in Transonic Flows

AGARD AG-303, December 1988

REPORTS (R)

Optimum Design Methods for Aerodynamics

AGARD R-803, Special Course Notes, November 1994

Missile Aerodynamics

AGARD R-804, Special Course Notes, May 1994

Progress in Transition Modelling

AGARD R-793, Special Course Notes, April 1994

Shock-Wave/Boundary-Layer Interactions in Supersonic and Hypersonic Flows

AGARD R-792, Special Course Notes, August 1993

Unstructured Grid Methods for Advection Dominated Flows

AGARD R-787, Special Course Notes, May 1992

Skin Friction Drag Reduction

AGARD R-786, Special Course Notes, March 1992

Engineering Methods in Aerodynamic Analysis and Design of Aircraft

AGARD R-783, Special Course Notes, January 1992

Aircraft Dynamics at High Angles of Attack: Experiments and Modelling

AGARD R-776, Special Course Notes, March 1991

ADVISORY REPORTS (AR)

A Selection of Experimental Test Cases for the Validation of CFD Codes

AGARD AR-303, Vols I and II, Report of WG-14, August 1994

Quality Assessment for Wind Tunnel Testing

AGARD AR-304, Report of WG-15, July 1994

Air Intakes of High Speed Vehicles

AGARD AR-270, Report of WG13, September 1991

Appraisal of the Suitability of Turbulence Models in Flow Calculations
AGARD AR-291, Technical Status Review, July 1991

Rotary-Balance Testing for Aircraft Dynamics
AGARD AR-265, Report of WG11, December 1990

Calculation of 3D Separated Turbulent Flows in Boundary Layer Limit
AGARD AR-255, Report of WG10, May 1990

Adaptive Wind Tunnel Walls: Technology and Applications
AGARD AR-269, Report of WG12, April 1990

CONFERENCE PROCEEDINGS (CP)

Application of Direct and Large Eddy Simulation to Transition and Turbulence
AGARD CP-551, December 1994

Wall Interference, Support Interference and Flow Field Measurements
AGARD CP-535, July 1994

Computational and Experimental Assessment of Jets in Cross Flow
AGARD CP-534, November 1993

High-Lift System Aerodynamics
AGARD CP-515, September 1993

Theoretical and Experimental Methods in Hypersonic Flows
AGARD CP-514, April 1993

Aerodynamic Engine/Airframe Integration for High Performance Aircraft and Missiles
AGARD CP-498, September 1992

Effects of Adverse Weather on Aerodynamics
AGARD CP-496, December 1991

Manoeuvring Aerodynamics
AGARD CP-497, November 1991

Vortex Flow Aerodynamics
AGARD CP-494, July 1991

Missile Aerodynamics
AGARD CP-493, October 1990

Aerodynamics of Combat Aircraft Controls and of Ground Effects
AGARD CP-465, April 1990

Computational Methods for Aerodynamic Design (Inverse) and Optimization
AGARD CP-463, March 1990

Applications of Mesh Generation to Complex 3-D Configurations
AGARD CP-464, March 1990

Fluid Dynamics of Three-Dimensional Turbulent Shear Flows and Transition
AGARD CP-438, April 1989

Validation of Computational Fluid Dynamics
AGARD CP-437, December 1988

Aerodynamic Data Accuracy and Quality: Requirements and Capabilities in Wind Tunnel Testing
AGARD CP-429, July 1988

Aerodynamics of Hypersonic Lifting Vehicles
AGARD CP-428, November 1987

Aerodynamic and Related Hydrodynamic Studies Using Water Facilities
AGARD CP-413, June 1987

Applications of Computational Fluid Dynamics in Aeronautics
AGARD CP-412, November 1986

Foreword

A wide range of complex phenomena contribute to the aerodynamic and acoustic characteristics of rotorcraft. The AGARD Fluid Dynamics Panel's Specialists' Meeting on "Prediction of Aerodynamic Loads on Rotorcraft" in 1982 and its Special Course on "Aerodynamics of Rotorcraft" in 1990 provided valuable assessments of the predictive capability for helicopter aerodynamics. The present Symposium recognized not only the continuing importance of understanding and accurately predicting both aerodynamic and acoustic characteristics of military and civil rotary-wing aircraft, but also the need for improved phenomenological insight, more detailed experiments using modern test equipment, and more precise and efficient numerical methods.

The aim of the Symposium was to bring together scientists in different fields of aerodynamics and aeroacoustics to review and discuss their recent results in the field of rotary-wing aircraft and to foster their future development. The program included 35 papers from North America, Western Europe, and Russia, organized in the following technical sessions:

- Dynamic Stall
- Wind Turbines
- Aerodynamic 3D Prediction Methods
- Experimental Investigations of Helicopter Rotors
- Acoustic Prediction Methods
- Interference Problems
- Round Table Discussion and Invited Commentaries

Although significant limitations remain, the Symposium showed that considerable progress has been made in many technological fields in the last decade. New test facilities and test stands have been constructed and major new multi-national test campaigns have been completed. Improvements in aerodynamic theory and tools have led to a better understanding of noise generation phenomena, and Computational Fluid Dynamics (CFD) and Computational Aeroacoustics (CAA) have evolved into powerful and useful techniques for designers. The Symposium provided a unique forum to publicize these important new developments.

The Program Committee would like to thank Dr. Karl Kienapple and his colleagues for hosting the Symposium so successfully in Berlin.

Dr.-Ing. Horst Körner and Dr. W.J. McCroskey
Program Committee Co-Chairmen

Avant-propos

Les caractéristiques aérodynamiques et aéroacoustiques des aéronefs à voilure tournante sont tributaires d'un large éventail de phénomènes complexes. La réunion de spécialistes du Panel AGARD de la dynamique des fluides sur «La prédiction des charges aérodynamiques des aéronefs à voilure tournante» organisée en 1982, ainsi que le Cours sur «L'aérodynamique des aéronefs à voilure tournante» donné en 1990, ont fourni des éléments d'évaluation appréciables pour la prédiction de l'aérodynamique des hélicoptères.

Le présent symposium a reconnu l'importance : de la continuité de la compréhension et de la prédiction exacte des caractéristiques acoustiques et aérodynamiques des aéronefs à voilure tournante civils et militaires, de la nécessité d'une meilleure approche phénoménologique, de l'accroissement d'expérimentations poussées, réalisées à l'aide de matériel d'essais moderne, ainsi que de méthodes numériques plus précises et plus efficaces.

Le symposium a eu pour objectif de rassembler des scientifiques travaillant dans différents secteurs de l'aérodynamique et de l'aéroacoustique, afin de leur permettre d'examiner et de discuter des derniers résultats obtenus dans le domaine des aéronefs à voilure tournante et d'encourager leur développement futur. Le programme comprenait 35 communications présentées par des scientifiques de l'Amérique du Nord, de l'Europe occidentale et de la Russie. Il était organisé en sessions techniques comme suit :

- le décrochage dynamique
- les éoliennes
- les méthodes de prédiction de l'aérodynamique en trois dimensions
- la recherche expérimentale dans le domaine des rotors d'hélicoptères
- les méthodes de prédiction acoustiques
- les problèmes d'interférence
- une table ronde et commentaires

Bien que des limitations considérables subsistent, le symposium a confirmé les progrès importants qui ont été réalisés dans un grand nombre de domaines technologiques au cours de la dernière décennie. De nouvelles installations d'essais ont été montées et de nouveaux bancs d'essai ont été fabriqués. De nouvelles campagnes d'essais multinationales de grande envergure ont également été conduites. Les améliorations apportées au niveau de la théorie et des outils aérodynamiques ont permis une meilleure compréhension des phénomènes de génération de bruit et, en même temps, l'aérodynamique numérique (CFD) et l'aéroacoustique numérique (CAA) sont devenues des techniques puissantes qui intéressent les concepteurs. Le symposium a servi de forum pour la promotion de ces développements importants.

Le comité du programme tient à remercier le Dr Karl Kienapple et ses collègues pour l'organisation très réussie de ce symposium à Berlin.

FLUID DYNAMICS PANEL

Chairman: M.C. DUJARRIC
Future Launchers Office
ESA Headquarters
8-10 rue Mario Nikis
75015 Paris - France

Deputy Chairman: Professor C. CIRAY
Aeronautical Eng. Department
Middle East Technical Univ.
Inonnu Bulvari PK: 06531
Ankara - Turkey

PROGRAMME COMMITTEE

Dr. Ing. H. KORNER (Co-Chairman)
Direktor-Institut für
Entwurfsaerodynamik der DLR
LilienthalPlatz 7
D-38108 Braunschweig - Germany

Dr. W.J. McCROSKEY (Co-Chairman)
Senior Research Scientist
US Army Aeroflightdynamics Directorate
Mail Stop N258-1
NASA Ames Research Center
Moffett Field, CA 94035-1000 - USA

Prof. R. DECUYPERE
Ecole Royale Militaire
Ave de la Renaissance 30
B-1040 Brussels - Belgium

Dr. L. CHAN
Institute for Aerospace Research
NRC Canada - Montreal Road
Ottawa
Ontario K1A 0R6 - Canada

Ing. General B. MONNERIE
Directeur de l'Aérodynamique
ONERA - BP72
92322 Châtillon Cedex - France

Prof. F. SABETTA
Universita di Roma "La Sapienza"
Via Eudossiana 18
00184 Roma - Italy

Prof. Dr. Ir. J.A. STEKETEE
Rotterdamseweg 195
262g HD Delft - Netherlands

Dr. L.P. RUIZ CALAVERA
INTA
Carretera de Ajalvir KM. 4.5
28850 Torrejon de Ardoz (Madrid) - Spain

Prof. Dr. C. CIRAY
Middle East Technical University
Inonu Bulvari PK: 06531
Ankara - Turkey

Mr. C.D.S. CLARKSON
British Aerospace Defence Ltd
Military Aircraft Division
Brough
North Humberside HU15 1EQ - U.K.

Prof. W.S. SARIC
Arizona State University
Mechanical & Aerospace Engineering
Tempe, AZ 85287-6106 - U.S.A.

Mr. L.J. WILLIAMS
Office of Aeronautics
NASA Headquarters (Code RH)
Washington, DC 20546 - U.S.A.

PANEL EXECUTIVE

Mr. J.K. MOLLOY

Mail from Europe
AGARD-OTAN
Attn: FDP Executive
7 rue Ancelle
92200 Neuilly-sur-Seine
France

Mail from USA and Canada
AGARD-NATO
Attn: FDP Executive
Unit 21551
APO AE 09777

Tel: 33 (1) 4738 5775

Contents

	Page
Recent Publications of the Fluid Dynamics Panel	iii
Foreword	v
Avant-propos	vi
Fluid Dynamics Panel	vii
Technical Evaluation Report by L.U. Dadone	TER
KEYNOTE SPEECH	
Chairman: H. Korner	
New Directions in Rotorcraft Computational Aerodynamics Research in the U.S. by A.J. Landgrebe (Invited)	1
SESSION I — DYNAMIC STALL	
Chairman: H. Korner	
Present Capabilities of Predicting Two-Dimensional Dynamic Stall by J.A. Ekaterinaris, G.R. Srinivasan, and W.J. McCroskey	2
Compressibility Effects on Dynamic Stall of Oscillating Airfoils by M.S. Chandrasekhara and L.W. Carr	3
Effect of Turbulence Modeling on Dynamic Stall Computations by M. Dindar and Ü. Kaynak	4
*Investigation Into Effect Produced by Blade Airfoil Unsteady Airflow on Helicopter Main Rotor Power Required by V.A. Ivchinn	5
Dynamic Stall Control by Variable Airfoil Camber by W. Geissler and H. Sobieczky	6
SESSION II — WIND TURBINES	
Chairman: L.J. Williams	
Review of Recent Aerodynamic Research on Wind Turbines with relevance to Rotorcraft by H. Snel and Th. van Holten	7
Dynamic Stall Simulation Applied to Vertical-Axis Wind Turbines by K.F. Tchon, S. Hallé and I. Paraschivoiu	8
Stall Hysteresis and 3D Effects on Stall Regulated Wind Turbines: Experiment and Modelling by H.A. Madsen and F. Rasmussen	9
A Viscous-Inviscid Interaction Model for Rotor Aerodynamics by A. Filippone and J.N. Sørensen	10
Investigation of the Yawed Operation of Wind Turbines by means of a Vortex Particle Method by S.G. Voutsinas, M.A. Belessis and K.G. Rados	11

* Contribution through the AGARD Technology Cooperation Program

SESSION III — 3D-AERODYNAMIC PREDICTION METHODS I

Chairman: B. Monnerie

- Méthodes de calcul aérodynamique appliquées aux rotors d'hélicoptères à l'ONERA** 12
by M. Costes, P. Beaumier, P. Gardarein and J. Zibi
- 3D Euler Calculations of Multibladed Rotors in Hover: Investigation of the Wake Capturing Properties** 13
by J. Raddatz and K. Pahlke
- Forward Flight Rotor Airloads Predictions using a Coupled Navier-Stokes/Full-Potential Analysis** 14
by C. Berezin and L.N. Sankar
- Computational Fluid Dynamics Development and Validation at Bell Helicopter** 15
by J.C. Narramore
- Cost Efficient Calculation of Compressible Potential Flow Around a Helicopter Rotor Including Free Vortex Sheet by a Field Panel Method** 16
by A. Röttgermann and S. Wagner
- **Évaluation de modèles aérodynamiques et dynamiques des rotors d'hélicoptères par confrontation à l'expérience** 17
by J. Bessone and D. Petot

SESSION IV — EXPERIMENTAL INVESTIGATIONS ON HELICOPTER ROTORS I

Chairman: C.D.S. Clarkson

- ***Rotorcraft System Identification — An Overview of AGARD FVP Working Group 18** 18
by P. Hamel and J. Kaletka (Invited)
- Effect of Individual Blade Control on Noise Radiation** 19
by G. Niesl, S.M. Swanson, S.A. Jacklin, A. Blaas and R. Kube
- A Study of Blade-Vortex Interaction Aeroacoustics Utilizing an Independently Generated Vortex** 20
by C. Kitaplioglu and F.X. Caradonna
- External Noise of Single Rotor Helicopters** 21
by V.F. Samokhin and M.G. Rozhdestvensky

SESSION V — EXPERIMENTAL INVESTIGATIONS ON HELICOPTER ROTORS II

Chairman: G. Reichert

- In Flight Research with Instrumented Main and Tail Rotor Blades Using the DRA Bedford AeroMechanics Research Lynx Helicopter** 22
by P.C. Tarttelin and A.W. Martyn
- Flow Field Investigation of a Rotating Helicopter Blade by Three-Component Laser-Doppler-Velocimetry** 23
by U. Seelhorst, B.M.J. Beesten and K.A. Bütetisch
- Détermination des charges aérodynamiques du rotor en vol stationnaire, à l'aide d'une technique de vélocimétrie laser** 24
by E. Berton, D. Favier, C. Maersca and M. Nsi Mba
- Initial Results from the Higher Harmonic Control Aeroacoustic Rotor Test (HART) in the German-Dutch Wind Tunnel** 25
by R. Kube, W.R. Splettstoesser, W. Wagner, U. Seelhorst, Y.H. Yu, A. Boutier, F. Micheli and E. Mercker

** Contribution from SMP

*** Contribution from FVP

SESSION VI — ACOUSTIC PREDICTIONS METHODS I

Chairman: C. Ciray

Effect of Higher Harmonic Control on Helicopter Rotor Blade-Vortex Interaction Noise: Prediction and Initial Validation	26
by P. Beaumier, J. Prieur, G. Rahier, P. Spiegel, A. Demargne, C. Tung, J.M. Gallman, Y.H. Yu, R. Kube, B.G. Van der Wall, K.J. Schultz, W.R. Spletstoesser, T.F. Brooks, C.L. Burley, D.D. Boyd Jr.	
Calculation of High-Speed Noise from Helicopter Rotor Using Different Descriptions of Quadrupole Source	27
by S. Ianniello and E. De Bernardis	
A Boundary Integral Method for United Transonic Aerodynamic and Aeroacoustic Analysis of Hovering Rotors	28
by M. Gennaretti, U. Iemma and L. Morino	
Aeroacoustic Calculation of Helicopter Rotors at DLR	29
by K.-J. Schultz, D. Lohmann, J.A. Lieser and K.D. Pahlke	
Prévision du bruit externe des hélicoptères: les méthodes numériques vues par un industriel	30
by F. Toulmay, D. Falchero and G. Arnaud	

SESSION VII — INTERFERENCE PROBLEMS

Chairman: R. Decuyper

Analysis of Rotor Forces in a Ship Airwake	31
by G. Syms and S.J. Zan	
A Theoretical and Experimental Investigation into the Rotor Blade Aeroelastic Behaviour of a Shipborne Helicopter during Rotor Engagement and Braking	32
by S.J. Newman	

SESSION VIII — ACOUSTIC PREDICTIONS METHODS II

Chairman: L. Chan

The Role and Status of Euler Solvers in Impulsive Rotor Noise Computations	33
by J.D. Baeder	
The Use of Kirchhoff's Method in Rotorcraft Aeroacoustics	34
by A.S. Lyrintzis	
Acoustic Design of Rotor Blades Using a Genetic Algorithm	35
by V.L. Wells, A.Y. Han and W.A. Crossley	
GENERAL DISCUSSION	GD

TECHNICAL EVALUATION REPORT

AGARD Fluid Dynamics Panel Symposium on AERODYNAMICS AND AEROACOUSTICS OF ROTORCRAFT

L. Dadone
Boeing Defense and Space Group
Helicopter Division
Philadelphia, Pennsylvania 19142
USA

ABSTRACT

The Fluid Dynamics Panel of AGARD held a Symposium on the Aerodynamics and Aeroacoustics of Rotorcraft in Berlin, Germany, on October 10-14, 1994. The Symposium addressed recent analytical and experimental developments relevant to the aerodynamic and acoustic design of advanced rotorcraft. Most notable and promising is the current emphasis on computational fluid dynamics, computational aeroacoustics and advanced testing methods. Several recent experimental programs, unprecedented in scope and depth, have been possible because of the cooperation among a number of AGARD member countries. The thirty four papers presented at this Symposium have been published in Conference Proceedings AGARD-CP-552, and are listed in the Appendix of this report. This evaluation report provides a summary of each paper, followed by general comments and a few specific recommendations.

1. INTRODUCTION

The 75th Meeting of the AGARD Fluid Dynamics Panel (FDP) was held from the 10th to the 14th of October, 1994, in Berlin, Germany. The following theme was set by the Organizing Committee:

"The aim of the symposium is to review and discuss recent developments in aerodynamics and aeroacoustics as they apply to the rotary-wing aircraft, and to foster the future development of this class of flight vehicles. The Symposium recognizes the importance of understanding and accurately predicting the aerodynamic and acoustic characteristics of military and civil rotorcraft; and the need for improved phenomenological insight, better math models, adequate test equipment, and more precise and efficient numerical methods. Despite current limitations, considerable progress has been made in many technological fields in the last decade. New test facilities and test stands have been constructed, improvements in aerodynamic theory and tools have led to a better understanding of noise generation phenomena, and Computational Fluid Dynamics (CFD) and Computational AeroAcoustics (CAA) have evolved into useful techniques for designers."

The agenda of the Symposium was as follows:

- Opening Remarks
- Keynote Speech
- Keynote Paper
- Session 1, Dynamic Stall
- Session 2, Wind Turbines
- Session 3, Three-Dimensional Aerodynamic Prediction Methods
- Session 4 and 5, Experimental Investigations on Helicopter Rotors
- Session 6 and 8, Acoustic Prediction Methods
- Session 7, Interference Problems
- Closing Remarks
- Discussion

Thirty four of thirty six papers originally planned for the Symposium were presented. Regrettably, two were withdrawn. Appendix A lists the papers in the order of their presentation. Approxi-

mately one hundred twenty (120) delegates were in attendance. The Symposium dealt with helicopter and helicopter-related windmill topics. Tiltrotor issues were not addressed. The large number of co-authors in some of the papers is the result of cooperation among organizations from the AGARD member countries. The first participation by Russia, with two papers, is a very promising and encouraging development.

The Russian presence results from recent, and potentially most positive, changes in the world's political arena. The end of the Cold War, however, has created new challenges for this industry which has, traditionally, relied on military procurement for a significant share of its business.

We often witness the perception that research in rotorcraft Aerodynamics and Aeroacoustics is far too removed from practical applications. At times that may be true, and we need to focus our research on useful near-term goals and bold long-term challenges. But it is also true that to support the development of advanced rotorcraft we must address very complex and interdependent phenomena which cannot be quantified only by intuition and improved empirical models.

The complexity of the rotorcraft flow environment and the interdisciplinary aspects of rotorcraft design require an effective use both of advanced analytical modeling and highly accurate and comprehensive experimental techniques. The papers presented during this Symposium prove that truly impressive progress has taken place both in analysis and test.

2. OVERVIEW OF THE PAPERS

During his opening remarks, Dr. Körner pointed out that since the 1982 Rotor Airloads Conference in London, Reference (1), the following new, major developments have taken place: 1) Computational Fluid Dynamics (CFD) has become a reality. Advanced computers and a new generation of computer experts have made the development of CFD possible. 2) New, major, wind tunnel and flight test programs have taken place. 3) New rotor test hardware is now available. 4) We have new measurement techniques, ranging from Laser Doppler Velocimetry to Particle Velocimetry, and 5) Improved noise prediction and measurement methods have been developed. The papers selected for this Symposium address all significant current developments.

2.1 Keynote Paper

In his invited paper (2), A. J. Landgrebe presented an overview of Computational Fluid Dynamics developments in the United States of America, specifically as directed to rotorcraft applications. Landgrebe's presentation covered all the key challenges: grid generation, numerical diffusion, computational efficiency and turbulence modeling. The paper reviewed all recent developments and key codes, and showed examples of state-of-the-art calculations. A major rotorcraft challenge that remains is the modeling of the complete interactional problem. That challenge will not be met until rotor wake modeling can overcome present numerical diffusion problems. While it is clear that Navier-Stokes methods are not yet accurate and practical enough for routine, comprehensive helicopter computations, many of the CFD codes, and particularly the Euler and Full-Potential solutions, are starting to yield practical results in selected rotorcraft aerodynamics and aeroacoustics problems.

2.2 Session 1 - Dynamic Stall

In the first paper (3) in the Dynamic Stall session, by Ekaterinaris, Srinivasan and McCroskey, reviewed present CFD capabilities in the prediction of two-dimensional dynamic stall. Dynamic stall is a very difficult challenge in advanced helicopter rotor design, so difficult in fact, that until now the only reliable source of dynamic stall information has been wind tunnel testing. As with all CFD applications the issues remain: a) accuracy, b) robustness and c) computing costs. In the absence of stall, good agreement with test was obtained at $M = 0.3$, with the $k-\omega$ turbulence model. At higher angles of attack lift stall was predicted fairly accurately, while drag and pitching

moments remained more difficult to predict. The prediction of reattachment from stall remains a problem, which is not surprising since experiments have shown that stall reattachment is highly non-repetitive. Transition modeling is very important, and to date it remains unresolved. The present results are very encouraging because they show that analysis can be used to examine local flow details at useful Mach numbers (i.e., at $0.3 \leq M \leq 0.4$). Analysis may be soon available to identify details which can explain unresolved 2-D testing issues.

Chandrasekhara and Carr (4) described two-dimensional wind tunnel tests to investigate compressibility effects on dynamic stall. The NACA 0012 airfoil was employed over models with 3 and 6 inch chords. The test revealed multiple shocks at the Leading Edge during stall. In addition to valuable preliminary data on LE flow details, the present investigation, and future 2-D tests employing the same setup, can be a source of much needed data on the effect of compressibility on dynamic stall at model rotor Reynolds Numbers.

Regrettably, the third paper in the Dynamic Stall session was withdrawn.

Next, Ivchin (5) addressed unsteady aerodynamic effects on the profile drag in the assessment of rotor performance. The method is based on an unsteady aerodynamic formulation by V. E. Baskin, and it is backed by extensive test evidence. While a significant body of oscillating airfoil data is available to document dynamic stall effects on the sectional lift and pitching moment, there is relatively little data on instantaneous unsteady drag measurements. Ivchin's paper was particularly interesting because it offered an insight into Russian helicopter research, which included 2-D oscillating airfoil tests and rotor blade airload measurements by means of blade mounted balances. Test / theory correlation examples involving Mi-26 performance were also presented.

Geissler's and Sobieczky's paper (6) presented the results of an analytical investigation, carried out by CFD, of "dynamically deforming" airfoils as the means to reduce the severity of dynamic stall effects. Prior work had shown that variations in airfoil thickness can have a beneficial effect of dynamic stall. Variations in LE camber, however, hold an even greater potential for the alleviation of deep stall airloads. Analysis was used to investigate leading edge camber changes over 10% of a NACA 23012 airfoil. The calculations showed that it should be possible to prevent the bursting of a supersonic LE "bubble" at high angles of attack, and also to alter pitching moment stall hysteresis in a way which reduces negative aerodynamic damping. The variable camber schedules examined in the paper were prescribed, and not yet optimized for specific rotor flow regimes.

2.3 Session 2 - Wind Turbines

Snel and van Holten (7) reviewed recent wind turbine aerodynamics research of relevance to rotorcraft. Wind turbines experience many of the flow problems encountered on rotor blades, and particularly on tiltrotor blades: the wake is close to the rotor disc, airloads and performance are influenced by dynamic stall effects, the flow turbulence environments are comparable, as are the diameters. The methods developed for windmills closely resemble the rotor analysis methods, in both the areas of comprehensive analysis and blade CFD. Interesting developments include the representation of free wakes by vortex particles floating freely with the stream, in addition to the better known vortex lattice and vortex tube models. Momentum theory and dynamic inflow methods have also been examined as they offer computational advantages when high frequency airload fidelity is not required. Rotating boundary layer calculations have included Coriolis force effects resulting from spanwise flow. Root end flows have been examined in detail. The lessons learned in windmills merit close scrutiny as they may be very relevant to rotor blade design.

Tchon, Hallé and Paraschivoiu (8) reported on CFD calculations carried out to investigate dynamic stall effects on a NACA 0015 airfoil section employed on a vertical axis (Darrieus) windmill. Navier-Stokes solvers were used with both laminar and turbulent flow assumptions. All Darrieus motions were included. The computation grid was of the hybrid type, involving structured and unstructured meshes. The laminar calculations displayed alternating LE and TE stall vortices, which did not agree with the test evidence. The turbulent solution, using a $k-\omega$ turbulence model, accurately modeled stall events and key local flow features associated with stall. As the authors cor-

rectly concluded, "the results stress the need for turbulence modeling to realistically simulate dynamic stall."

Madsen and Rasmussen (9) examined differences in dynamic stall between the 2-D oscillating airfoil environment, and the environment of a horizontal axis wind turbine. This research was motivated by the need to design wind turbines in which maximum power and loads are "self-regulating" by appropriate use of dynamic stall effects. The 2-D oscillating airfoil tests produce airload trends which are not in agreement with the windmill test evidence. Particularly significant are the discrepancies between 2-D and 3-D data at the root end of blades. The dynamic stall characteristics on windmill blades have a "chaotic content that is not well represented by semi-empirical models developed for helicopters." The investigation included examples of preliminary CFD modeling of a segment of windmill blade, with both laminar and turbulent flow assumptions

Filippone and Sørensen (10) described rotor CFD research aimed at both accuracy and efficiency, achieved by breaking up the computational domain into viscous regions close to the blade surface, and inviscid regions away from the surface. The method addresses both steady and unsteady flow regimes for blade "strip" elements experiencing three-dimensional induced velocities. While problems remain with the coupling of the outer inviscid region with the inner viscous solution, the method was correlated with measured windmill blade pressures with very encouraging results.

Voutsinas, Belessis, and Rados (11) developed a three-dimensional, non-linear aeroelastic numerical analysis to investigate the response of a horizontal wind axis turbine during yawed flow operation. Blade structural effects and tower interference effects were also included. The aerodynamic solution was based on a time marching scheme and an unsteady free-wake employing vortex particles. The vortex particle approach is of significant interest for helicopter rotor applications. Correlation with measured blade bending moments was satisfactory, but showed that further improvements in the modeling should be implemented for more accurate results.

2.4 Session 3 - Three-Dimensional Aerodynamic Prediction Methods

Costes, Beaumier, Gardarein, and Zibi (12) presented a survey of ONERA methods for the aerodynamic analysis of helicopter rotors in hover and forward flight. All areas of interest were covered, including transonic flow over the advancing blades, retreating blade stall, hover and forward flight flow field characteristics, rotor trim, aeroelastic coupling, interactional aerodynamics, blade CFD, design optimization methods, and test / theory correlation with data from advanced experimental investigations. All main analysis codes are described. While the ONERA codes are similar in approach to codes developed by other European and American organizations, the ONERA researchers have carried out an impressive amount of test-theory correlation with data acquired by means of state-of-art methods. The paper is of great interest also because it describes comprehensive and multi-disciplinary computation procedures which are well understood in principle, but quite difficult in their application to actual helicopter rotor designs.

Raddatz and Pahlke (13) carried out an investigation of the hover "wake capturing properties" of an Euler solver applied to multi-bladed rotors. The investigation addressed grid resolution and single vs two- block grids, including the effects of chimera boundaries. Calculated wake geometry features and pressure distributions were compared to test results by Caradonna and Tung. The study showed that refining the wake grid does improve the accuracy of the calculated hover wake features, although the improved wake details do not necessarily result in improved blade surface pressure predictions. At present, rotor design is carried out by means of codes relying on "vortex element" wake models, which are closely coupled with the blade loading and may have free-wake features but are not modeled by CFD. The results of this Euler investigation showed that multi-block computation schemes hold significant promise in the modeling of both hover and forward flight rotor wakes. However, the assessment of still more accurate blade airloads and performance will eventually require the introduction of viscosity.

Berezin, and Sankar (14) approached the CFD modeling of the UH-60 rotor in forward flight by a hybrid approach. The computational domain was split into two regions. A Navier-Stokes formulation was used near the blade surface, and a Full-Potential solution elsewhere. The two regions were coupled through boundary conditions on the interface surface separating them. Splitting the computational domain was shown again to be very promising: the hybrid approach resulted in an approximately 50% reduction in CPU time, compared with a stand-alone Navier Stokes solver, although some problems remain in the prediction of separated flow regions. Examples of test/theory correlation were shown in the presentation.

Narramore (15) reviewed how CFD has been put to use in industry (at BHT) in support of rotorcraft design. Excellent qualitative and quantitative results have been obtained with the more "mature" CFD applications, e.g., 2-D airfoil design, by direct and inverse solutions. With more complex 3-D models, for which Narramore used state-of-art computers such as the NAS, CFD may not necessarily produce quantitative answers, but it yields an extremely useful insight into the phenomena involved. Narramore also illustrated and emphasized how computer graphics and work-stations facilitate the utilization of CFD in the engineering design environment.

Röttgermann and Wagner (16) described the coupling of a vortex lattice wake model with a Cartesian computation mesh (not body fitted) to capture blade flow details by means of a full-potential solver. The emphasis is on "Cost Efficient Calculations" As illustrated by comparison with blade pressure data, the method yields satisfactory results up to flow conditions including weak shocks. The simplified computation grid around the blades and the use of a pre-defined (non CFD) rotor wake model lead to significant improvements in numerical convergence, and a significant reduction in data storage requirements. The method can and eventually will be coupled with a boundary layer analysis to calculate profile drag.

Finally, Bessone and Petot (17) presented the results of the systematic evaluation of a comprehensive rotor analysis code (ROTOR) combining current aerodynamics and dynamics models, different advanced rotor wake options (METAR) and blade CFD (FP3D). The results of the analysis were compared with data from rotor tests at Modane of the 7A and ROSOH rotors. The correlation with test data points out that unsteady tip effects cannot be captured by methods based on 2-D information, and that the accuracy of the aerodynamic solution is dominated by elastic blade torsion effects. The use of CFD improves the modeling of tip flow effects, but presently, the value of CFD is more qualitative than quantitative. A new stall model, including swept tip effects, is being developed at ONERA. The ROTOR predictions are satisfactory for the lower harmonic airloads, but for the moment problems remain with the higher harmonic airloads. The great long-term advantage of the ROTOR code is the modularity of its elements.

2.5 Session 4 - Experimental Investigations on Helicopter Rotors

Hamel and Kaletka's invited overview paper (18), presented by Dr. Hamel, summarized the findings of Flight Vehicle Panel's (FVP) Working Group 18 in Rotorcraft System Identification. System identification involves the definition of mathematical models of aircraft, or rotorcraft, response and the determination of empirical coefficients which are adjusted to improve the agreement between the models and test evidence. The paper presented a detailed discussion of Maneuvers, Measurements, Models and Methods, drawn from flight test evidence for the AH-64, SA-330 and BO-105 helicopters. The Working Group's Final Report and Lecture Series have been published, respectively, in References (36) and (37). Key conclusions were that while industry acceptance of System Identification methodology is growing, and significant progress has been made, today's methods permit a correlation of Wind Tunnel, Flight Test, Analysis and CFD on a "rudimentary" level only. The accurate modeling of complete helicopter characteristics from design through production is still a major challenge.

Niesl, Swanson, Jacklin, Blaas and Kube (19) summarized the results of a full scale MBB BO-105 rotor test to investigate the effects of Individual Blade Control (IBC) on noise radiation. The test was carried out in the 40x80 ft Wind Tunnel at the NASA Ames Research Center as a cooperative research program involving NASA, ZF Luftfahrttechnik, DLR and EUROCOPTER Deutschland.

The test established the feasibility of reducing BVI noise by reducing blade lift both where the vortex is generated and where the blade encounters the vortex. BVI noise reductions of up to 7 dB were measured with different higher harmonic input modes. While the IBC inputs as tested were not optimized, and caused some performance or vibration penalties, the results of the test imply that there are no fundamental obstacles to the use of feedback-controlled IBC inputs to reduce BVI noise with minimized performance and vibration penalties. For that purpose, a feedback controller could be linked with blade pressure or other key measurements. The results of this test will be very useful in guiding the development of other advanced blade control system, as, for instance, devices employing smart structures.

Kataplioglu and Caradonna (20) reported on a Blade Vortex Interaction test conducted to quantify key aeroacoustic effects and to generate the detailed test data necessary to validate the CFD methodology necessary to assess BVI pressures and noise. The test was carried out in the 40 by 80 ft Wind Tunnel at the NASA Ames Research Center, and it involved a 7 ft diameter model rotor with pressure instrumented blades, installed downstream of a vortex generating wing. The two-bladed teetering rotor had rectangular untwisted blades, with a NACA 0012 airfoil section, and 6 inch chord. Acoustic data were obtained with fixed near-field microphones and movable array far-field microphones. Flow visualization was used to verify the position of the vortex involved in BVI. The test quantified the effect of variations in blade-vortex separation, vortex strength and direction, and blade lift at BVI encounter. "Miss" distance between blade and vortex was found to be a major parameter in reducing BVI noise.

Samokhin's and Rozhdestvensky's paper (21) presented an overview of the results of acoustic studies carried out by means of flight test for three multi-bladed single-rotor helicopters. The three helicopters, the MI-8, MI-24 and MI-28, are currently produced and operated in Russia. Far field noise level measurements were carried out by ground-based microphone arrays. A helicopter's far-field noise includes main and tail rotor contributions, and contributions from the engine, gearboxes and transmission. The examples of measured noise spectra display discrete component frequencies attributable to the main and tail rotors, and broadband components. An X-tail rotor configuration, with same diameter and chord as the baseline, was tested on the MI-28. The X-tail rotor reduced the noise by 3 to 5 PNdb in level flight.

2.6 Session 5 - Experimental Investigations on Helicopter Rotors

Tartelin and Martyn (22) described key results from an in-flight research program carried out by the Defence Research Agency (DRA), Bedford, UK, on the Aeromechanics Lynx Control and Agility Testbed (ALYCAT). The Lynx helicopter used in this program was equipped with pressure gage instrumented main and tail rotor blades. The main rotor blades were also instrumented with strain gages. The blade instrumentation and the codes used in analyzing the ALYCAT data were based on prior experience with the Puma helicopter. Tail rotor blade loads were obtained empirically from LE and TE pressure measurements. Blade pressure distributions were compared to 2-D wind tunnel test data for the RAE9617 and RAE9615 airfoil sections. The objective of the test program was to obtain a large data base for advanced flight simulation, and therefore the flight conditions ranged from hover and level flight to maneuver and transition, climb / descent and control input response. The analysis of the data is only in the early stages, but the data contain a large volume of very interesting information, including main and tail rotor interaction effects.

In paper (23), Seelhorst, Beesten and Bütefisch showed examples of rotor flow field measurements obtained by three-component Laser Doppler Velocimetry in both hover and forward flight. Blade Vortex Interaction (BVI) conditions were also examined. The tests were carried out for two four-blade model rotors, one with rectangular tips and the other with swept tip winglets. The NACA 0015 airfoil was employed on both rotors. The hover tests were carried out at DLR Göttingen, and the rest in the open test section of the ILR Aachen low-speed wind tunnel. Objective of the test was an improved understanding of the mechanism of tip vortex rollup as a function of tip geometry, and the documentation of vortex strength, core size and tip vortex kinematics. Excellent examples of vorticity contours were shown for the two tip configurations.

The vortex trailed by the square tip rolled up very rapidly. The vortex trailed by the winglet rolled up at a considerably slower rate. The data deserve further close scrutiny.

Berton, Favier, Maresca and Nsi Mba presented the results of airload measurements obtained over rotor blades in hover by Laser Doppler Velocimetry. The velocity measurements were carried out over a path taking into consideration the Kutta condition at the trailing edge (Equations de bilan de quantité de Mouvement et de Kutta - KME method). Besides determining the local lift, the LDV data also allowed an assessment of the local profile drag. The tests were carried out in IMFM's S1-Luminy wind tunnel with 1.5 m diameter model rotors having -8.3° of twist, the OA209 airfoil section, and four different blade tips outboard or 0.95R. The trajectory of the trailed vortices was determined by smoke visualization and hot wire anemometry. In the examples shown, there was excellent agreement between blade measurements by LVD and hub balance measurements, both in terms of thrust and torque. A significant point was also raised about the choice of integration path: while in a two-dimensional environment the determination of the local circulation is independent of path, in the rotor environment the same integration can be significantly influenced by nearby rotor wake elements.

Kube, Splettstoesser, Wagner, Seelhorst, Yu, Boutier, Micheli, and Mercker presented a status report (25) about the Higher Harmonic Control Aeroacoustic Rotor Test (HART). The HART program was conducted jointly by AFDD, NASA, ONERA and DLR in the German Dutch Wind Tunnel (DNW). The objective of the test was to investigate the effect of Higher Harmonic Control (HHC) on Blade Vortex Interaction (BVI) noise and vibration by both theoretical and experimental methods. The tests were conducted on an DLR test rig, ROTEST II, with a 2 m Mach scaled model of the hingeless MBB BO-105 rotor. The rotor balance measured both static and dynamic forces and moments. The blades were instrumented with 132 pressure transducers and 32 strain gages. Noise measurements were carried out by means of fourteen microphones (eleven movable, and three fixed). Extensive flow visualization and Laser Doppler Velocimetry (LDV) measurements were also made. Two different LDV techniques were employed for advancing and retreating side blade vortex interaction events. Two different systems were also used to measure in-flight elastic blade deflections. The test conditions included descent flight with a variation in velocity from low to high speed, but emphasis was placed on a low speed descent condition simulating landing approach at $\mu = 0.15$. A very large volume of data has been acquired. HHC was shown to be effective in reducing BVI noise (5 db) at some cost in loading noise, but loading noise is not as bothersome to human beings as BVI. The reduction in vibration, and, possibly performance improvements require different HHC schedules. Differences in vortex structure were observed as a result of HHC.

2.7 Session 6 - Acoustic Prediction Methods

Paper (26), by Beaumier, Prieur, Rahier, Spiegel, Demargne, Tung, Gallman, Yu, Kube, Van der Wall, Schultz, Splettstoesser, Brooks, Burley and Boyd summarized the theoretical predictions carried out in preparation of the HART test, and subsequent initial validation efforts. Predictions were carried out by different teams using state-of-art European and US codes. The analysis addressed blade deformations, wake/vortex geometry, sectional loads and noise and provided a first insight into the mechanisms by which Higher Harmonic Control (HHC) may affect BVI noise. Initial conclusions are that free wakes and accurate aeroelastic blade analyses are necessary to understand the conditions leading to BVI. Generally, the methods for BVI analysis still need improvement, and the authors conclude that, at this time, it is premature to propose, from pure theoretical studies, a complete explanation of the mechanisms by which HHC may affect BVI noise. The data, however, will be extremely valuable in identifying key effects which might be exploited in future HHC investigations or in the definition of other advanced rotor blade control concepts.

Ianniello and De Bernardis (27) addressed quadrupole noise prediction methods and its treatment through the acoustic analogy approach, comparing different forms of solution of the non-linear term in the Ffowcs Williams and Hawkings equation. The authors recommend a three-dimensional integration through a prescribed volume around a blade. The proposed method

requires a significant investment in computer resources, but it is quite accurate. An example is shown for a non-lifting rotor in hover, with tip Mach numbers up to 0.8 and an in-plane microphone location, for which excellent results were obtained by integration of the aerodynamic data from a full-potential solver. A comparison between solutions on a Convex C3860 and the Cray YMP showed the latter to be approximately four times faster.

Gennaretti, Iemma and Morino (28) proposed a Boundary Integral Method (BEM) for the unified aerodynamic and aeroacoustic analysis of rotors hovering at transonic tip speeds. The BEM approach is recommended as it can be computationally more efficient than current CFD techniques in addressing complex flow fields, such as a rotor wake in the presence of a helicopter fuselage. The method is still under development, but a few examples are shown to illustrate the excellent agreement between BEM, test evidence and existing numerical results based on the solution of the Ffowcs Williams and Hawkings equation. While only non-lifting hover conditions have been modeled so far, the calculated aerodynamic solutions are comparable to results obtained by CFD methods.

Schultz, Lohmann, Lieser, and Pahlke (29) presented an overview of helicopter aeroacoustic calculations carried out at DLR. Primary emphasis has been on blade vortex interaction noise (BVI) and high speed compressibility impulsive noise. First the paper discusses low speed BVI noise predictions with aerodynamic inputs from a Lifting Body Surface method (originally developed for propellers) and the linear terms from the Ffowcs Williams and Hawkings equation. Next high speed hover and forward flight noise is addressed, by a combination of 3-D Euler solvers and the FW-H equation. Comparisons are made with UH-1H and BO-105 model test data from DNW. The aerodynamic results are not always in good agreement with the test evidence, and that is at least in part due to inaccuracies in the wake model. The acoustic results, however, are in fairly good agreement with the experimental data. Four different approaches to solve the quadrupole volume integral are compared for a hover case. While some methodology improvements are still necessary, both the BVI and the high speed noise prediction methods yield useful results.

Toulmay, Falchero and Arnaud (30) described the methods available to predict exterior noise, from the French helicopter manufacturer's point of view. They divided their requirements into four different noise assessment categories: 1) Overall rotor noise, 2) Blade-Vortex Interaction, 3) Fan-in-fin, and 4) Complete helicopter in flight. The presentation included a tape recording of noise at various flight conditions. Foremost, the blade airloads must be correct, since airloads are the first step in the chain of calculations. The paper discusses in detail the different methods of analysis and shows several examples of test/theory correlation with wind tunnel and flight test data. Fenestron noise in hover and main rotor rotational noise can be predicted fairly accurately, but problems remain with computations involving aerodynamic interactions. Strut interference, causing fan-in-fin turbulence ingestion, will be investigated experimentally in the near future. In some instances, as with engine noise and complete helicopter configurations, there is no substitute for test.

2.8 Session 7 - Interference Problems

Syms and Zan (31) discussed experimental and numerical methods to assess interference effects during helicopter operation from non-aviation ships, such as frigates. Data on the wake of a representative ship superstructure were acquired by means of a small (1/300) scale wind tunnel model for various head-on speeds. The measurement methods included hot-film anemometers, and "flying" and stationary probes. The ship wake data were then imposed on a simulated UH-60 Black Hawk to evaluate wake effects on helicopter force and moment variations in the presence of different large scale separated flow features. As could be expected, the most dangerous conditions are in the presence of a reverse flow region behind a frigate's hangar and above the flight deck. The simulation also showed that the measured vertical velocity fluctuations had a greater effect on rotor loads than any streamwise variations.

In paper (32), Newman described a recent investigation of rotor blade flapping motions during engagement and breaking aboard ships. The uncontrolled motions of the rotor blades during startup and shutdown in the presence of strong winds are referred to as "blade sailing", and can

be quite dangerous. The experimental investigation involved testing a small scale model of a rotor, similar to the Westland Lynx rotor, on a structure representative of a ship's flight deck, aligned at right angles to the incident wind direction. The assembly was tested in the settling chamber of a wind tunnel up to speeds corresponding to full scale 47 knot winds. Records were made of the flow environment and of the flapping behavior of the rotor at various rotational speed and wind conditions. Subsequent analysis showed that the driving force behind blade sailing is the vertical component of the wind and its variation over the rotor disc. Maximum flapping amplitudes occur at rotor speeds approximately 10% to 15 % of the normal operating value.

2.9 Session 8 - Acoustic Prediction Methods

Baeder's presentation (33) reviewed the role and status of Euler solvers in the assessment of the impulsive noise of helicopter rotors. While not yet usable routinely, Euler solvers can be considered "fairly mature" in providing the aerodynamic data necessary as input to Kirchhoff and acoustic analogy methods for the prediction of far-field noise. While Euler solvers are not yet sufficiently mature to allow the prediction of Blade Vortex Interaction noise under the complex three-dimensional environment of the rotor flow field, they can be used to investigate promising phenomena on a two-dimensional basis. Examples shown in the paper include the effect of introducing a fast airfoil pitching motion, during BVI, to cause the blade-vortex encounter to occur at a lower lift level. This airfoil pitch change reduces the pressure gradients in comparison to the unmodified encounter. The entire encounter, and any consequences of the additional pitching motion on the sectional forces and moments, can be modeled by means of CFD codes such as TURNS.

Lyrintzis (34) presented a comprehensive review of the use of Kirchhoff's method in rotorcraft aeroacoustics, starting from its the early applications to fields other than acoustics and a description of the development of typical formulations. The use of Kirchhoff's method in the prediction of high speed helicopter noise has increased over the past 5 to 10 years because of the development of CFD methods that can be used to evaluate the near-field aerodynamics. Several examples are shown comparing various methods of impulsive pressure predictions and test data. In concluding, the author points out that simple portable Kirchhoff subroutines can be developed to calculate the far-field noise from the near- and mid-field CFD solutions for rotor blades in high speed flight.

In paper (35), Wells, Han and Crossley discussed the possible use of genetic algorithms in the design of low-noise rotor blades. Optimization by genetic algorithm methods allows the investigation of designs combining highly diverse objective functions and under rules which avoid the local maxima, or minima, that limit other more conventional methods. Without claiming that the acoustic prediction methodologies involved are totally reliable, the paper presents the results of optimization calculations addressing thickness noise only, loading noise only, and a combination of the two under constraints which allow variations in airfoil, planform taper, tip speed and number of blades, without any constraint on performance. While the methods described are not sufficiently mature for detailed design, it would be a mistake to overlook their potential applications to preliminary design.

Again regrettably, the very last paper in the Symposium was withdrawn.

3. DISCUSSION

The Symposium covered a variety of technical subjects in considerable depth, but this discussion will be generally limited to broad issues, and will try to emphasize the applicability of current research from a rotorcraft manufacturer's point of view.

Are there significant trends in our research? A survey of the thirty four (34) papers presented shows that:

- o Seventeen (17) dealt with Computational Fluid Dynamics (CFD),
- o Twelve (12) addressed rotor noise,
- o Twelve (12) addressed experimental investigations,
- o Eleven (11) were survey papers.

This distribution reflects today's concerns with the complexity of the rotor flow environment, and with the difficulty in understanding and quantifying some of the most important phenomena. We can see that significant progress has been made, and we have good reasons to be proud of our accomplishments, but in looking to the future we must seek the answer to difficult questions, such as:

- o Are we addressing the essential problems?
- o Do we have a good mix of near-term and long-term research goals?
- o What are, or should be, our priorities?

The subjects covered during the Symposium include most of today's concerns, including the resolution of fundamental problems in Computational Fluid Dynamics, the contents and validity of comprehensive rotor analysis codes, the coupling of comprehensive codes with rotor CFD, the complexity and value of rotor wake modeling, and the results of extensive analytical and experimental investigations. The subject of rotorcraft acoustics was addressed very extensively from both points of view of noise prediction and measurement. Relatively limited attention was paid to interactional aerodynamics and optimization, but that was not because of any "maturity" in the methods involved, but rather because both represent challenges which cannot yet be met. A discussion of the major subjects and points of interest follows.

Computational Fluid Dynamics - J. Landgrebe's survey paper (2) set the stage for all the detailed presentations that followed. In one way or the other, all papers concurred with Landgrebe's message that CFD still has to overcome problems with:

- o The efficiency of the flow solvers,
- o Grid generation,
- o Turbulence modeling,
- o Numerical diffusion.

At present, we envision a significant role for CFD in almost all aspects of rotor and windmill analysis because CFD offers a unique insight, even when the quantitative results do not fully meet our expectations. The range of CFD applications covers the entire spectrum of advanced rotor concepts and key phenomena. We have seen CFD used to quantify:

- o Rotor blade flow environments, from effects due to advanced blade shapes to local 3-D conditions, and transonic flow and blade-vortex interaction information needed to evaluate rotor noise,
- o Windmill flows, with emphasis on blade root-end effects and stall control,
- o Rotor wakes - very promising, but not yet useful because of numerical dissipation problems,
- o Fuselage design issues, primarily aimed at the reduction of flow separation and interactional aerodynamic effects,
- o Airfoil design,
- o Dynamic stall modeling, which remains a difficult challenge until transition and turbulence modeling problems are resolved,
- o Variable camber concepts, particularly necessary to quantify unsteady aerodynamic effects associated with the motions of deployable blade surfaces.

The most promising CFD developments addressed during the Symposium include:

- o Hybrid grids,
- o Split computation domains,
- o Multi-block grids and Chimera type boundaries,
- o Wake / vorticity capturing schemes,
- o The coupling of rotor CFD with comprehensive rotor analysis codes.

While CFD needs to be improved to represent better the physics involved, it was recognized that "cost effectiveness" is a very important issue in the application of CFD to actual problems. Moreover, "cost effectiveness" encompasses "accuracy" as well as "computational efficiency" and ease in processing input and output information. The proper utilization of CFD has been of great concern to the fixed-wing aircraft industry, long before it was seen as a viable alternative to supporting rotorcraft design. Recently, Paul Rubbert (38) presented an excellent overview of the situation in his AIAA Wright Brothers Lecture on the role of CFD in airplane design. In airplane design a key element is time. The reduction in time needed to develop a new airplane is the best contribution CFD can make to the process. Rubbert advocates the use of CFD in tackling only a few of the most critical (and challenging) flight regimes, and not the computation of trends which could be obtained by other means.

In supporting rotorcraft design, the use of CFD is not "mature" (i.e., both common and successful), partly because CFD is a relatively new tool for us, and partly because the rotor flow environment is significantly more complex than the flow over fixed wing aircraft. While we have to continue pursuing difficult CFD challenges, such as rotor wake modeling, BVI and dynamic stall, very useful data can be obtained today by more limited and better understood applications, as described, for instance, in References (15) and (39).

Dynamic Stall - Coping with dynamic stall remains an open research challenge, although over 20 years have passed since the start of systematic oscillating airfoil tests, e.g., references (40) and (41). While tests are still necessary, we now expect Computational Fluid Dynamics to provide some of the insight, if not the actual data, necessary to address dynamic stall and unsteady effects in rotor design. Fundamental modeling issues will have to be resolved before CFD can be used for detailed design support in unsteady aerodynamics. Having participated in a number of oscillating airfoil tests, I would alert the code developers to the extreme lack of repeatability, from cycle to cycle, often observed in the recovery from dynamic stall.

It should be also noted that the test setup reported in paper (4) may provide dynamic stall data at model rotor scale Reynolds numbers and at full Mach numbers. Oscillating airfoil data for the correct combination of scale and compressibility effects have not been available to date.

Windmills - Windmill research continues to be a source of data and methodology for rotor and prop rotor applications. Of particular interest are: 1) The developments in wake-vortex particle methods, which could contribute significantly to the definition of efficient free-wake models, and 2) The research on blade root-end boundary layer and separation modeling, which could prove to be valuable in the definition of inboard blade contours on future tiltrotor blades. The research in windmill blade stall should provide additional insight into dynamic stall effects.

Comprehensive Codes - It was interesting to observe the variety of comprehensive rotor analysis codes available today, and the great commonality among them, as they all employ similar approaches in the modeling of blade aerodynamics and dynamics. Today's comprehensive methods of rotor analysis are either "modular" in their structure, or consist of separate codes which can be linked by the user. All can be coupled with blade CFD codes, and all are starting to take advantage of computer assisted graphics in displaying results. And, finally, all the codes suffer from decidedly uneven success when correlated with test data.

A specific problem that remains to be addressed before the CFD and comprehensive codes can be fully coupled (without "correction" factors) is the overprediction of sectional lift-curve slopes by the CFD codes. This is a well known consequence of ignoring viscosity, in the potential and Euler

solvers, and the applicable examples presented during the Symposium confirm this trend. In the longer term, when viscosity effects can be routinely accounted for, prediction errors due to the absence of boundary layer effects should no longer be a problem. Examples of successful two-dimensional Navier-Stokes calculations have already been reported (42), but comparable Navier-Stokes solutions for rotor blades have not yet been practical. While many code developers recognize that the sectional (or local) lift-curve slope values calculated by their CFD codes may be high, most of them do not appreciate the consequences of a 10% or 20% error in rotor blade loading calculations when coupled with blade motions and elastic deflections.

Flight and Rotor Tests - Together, the test programs described during the Symposium provide a staggering amount of experimental data, and probably hold answers to many, if not most, of the problems we presently encounter in the development of advanced rotors. Only one major program was mentioned and not described in detail, and that was the Flight Test of the Heavily Instrumented UH-60 Helicopter (43). The data acquired during recent wind tunnel tests and flight tests include:

- o Blade surface pressures and strain gage data,
- o Acoustic data,
- o Higher Harmonic and Individual Blade Control (HHC and IBC),
- o Main and tail rotor airloads,
- o Results from advanced flow measurement techniques, documenting rotor wake velocities, wake rollup, blade circulation and details of blade vortex interaction (BVI),
- o Special purpose BVI tests.

Although it is an exciting development to have acquired such high quality and comprehensive data, funding problems have typically beset all large test programs and have too often compromised the adequate reduction, analysis, documentation and dissemination of test results. One can only hope that the cooperative nature of most of the test programs reported at this time will assure the support necessary to compile useful records of the most critical information.

Acoustics - Progress has taken place on three fronts: CFD, test, and aeroacoustics methodology. The evaluation of rotor noise depends on an accurate knowledge of the time derivatives of blade surface pressures, which will eventually be predicted by CFD. Very encouraging results have been obtained in the evaluation of high speed quadrupole noise by various integration methods. While high speed noise prediction by CFD methods was considered "mature" by some of the speakers, the prediction of BVI noise was recognized to be a challenge not yet within reach.

Independently of the relatively slow progress in Computational Fluid Dynamics and Computational Aeroacoustics, many of the advanced rotor tests reported during the Symposium will provide direct physical evidence quantifying the flow field phenomena, the time derivatives of relevant pressures, and the associated rotor noise. The same tests should provide guidelines (not clouded by computational difficulties) on the means to reduce rotor noise.

Interference - The two papers on interference (31) and (32) addressed ship flow environments and their effects on helicopter operation and safety. Both dealt with difficult problems which cannot be approached by conventional rotor analysis methods because of the complexity of the flow environment (aerodynamic interference effects from ship structures), the lack of periodicity in the events being modeled, and the wide excursions in blade airloads and motions. Both papers described methods which introduce measured flow field data into special purpose blade aerodynamics and dynamics analysis codes, with very revealing results.

Optimization - The last paper (35) dealt with acoustics, but it introduced genetic optimization as a non-intuitive method to determine which combinations of blade properties result in reduced noise within given flight conditions. While the algorithms used to relate blade geometry and noise were not necessarily valid throughout the design space, the approach generated interesting results, significant interest, and a great deal of discussion. Genetic algorithms require a large investment in computer resources, but are a promising development in advanced optimization methods.

New Horizons - The Russian papers on unsteady drag (5) and acoustic measurements (21) presented only a small sample of the experimental data, and analytical and empirical methods developed over decades in the former Soviet Union. Contacts with the Russian scientific community are steadily increasing. The proceedings of the First Forum of the Russian Helicopter Society (44), held in Moscow during September 1994, offer the first up-to-date overview of Russian research and technology in the area of rotorcraft.

In Summary

The most significant developments addressed during the Symposium were:

- o Computational Fluid Dynamics applications dominate all analysis developments. CFD has not yet fulfilled its promise, but it will eventually be the single most powerful tool available to support advanced rotorcraft design.
- o Computational Aero Acoustics (CAA) does not lag far behind CFD in its development, but it is not yet ready to support routinely the development of quiet rotors.
- o Testing techniques have evolved to yield an unprecedented amount of flow field, airloads and acoustic details.
- o In Rotorcraft System Identification, today's methods and procedures permit only a rudimentary level of correlation among Wind Tunnel, Flight Test, Analysis and CFD.
- o Windmill research continues to complement rotor research.
- o Our comprehensive rotor analysis codes are very similar. We have similar success in test-theory correlation. The coupling with CFD codes will eventually make a significant difference.

Are we after the right problems?

Generally, yes, in my opinion. Progress is being made in all relevant technologies, but many challenges remain. Among them:

- o The definition of advanced tiltrotor analysis methodology.
- o An emphasis on usable CFD, which starts with "application friendly" grid generation and post-processing methods. Also, CFD methods should be routinely correlated with test evidence, preferably for some generally accepted benchmark conditions, before being extended to complex flows. Adaptive grids were mentioned but not explicitly addressed.
- o The overprediction of 2-D lift curve slopes by rotor CFD codes, in the coupling of CFD and comprehensive rotor analysis, has been largely ignored. CFD and rotor analysis cannot be meaningfully coupled until this and related difficulties are resolved.
- o A n understanding of how aeromechanics and aeroacoustics should interface with design and manufacturing technologies to reduce rotorcraft development costs.
- o The resolution of the numerical dissipation of CFD wakes.
- o Better means to separate numerical problems from the physics modeling problems.

The definition of maneuver and transition rotor analysis methods.

Do we have a good mix of near- and long-term research goals?

For the near-term, the mix appears to be reasonably good. And in judging some of the research we have to remember that the primary charter of Universities is educating students. Even more than in the past, however, we have to make a continuing effort to remain aware of on-going developments, and will have to adjust the direction of research as necessary. A steady dialogue among Industry, Government Research Centers and Universities is absolutely necessary because our products, and the way we design and manufacture them, are changing faster than ever. From the researcher's and educator's points of view, what is at stake is not just the timely support of emerging technology requirements, but also the career prospects of future engineering graduates.

For the longer term, i.e., during the next decade, I can only suggest that the following developments are probable:

- o Tiltrotor aircraft, including high-speed civil tiltrotors will become a reality.
- o Low noise features will be essential for civil helicopter and tiltrotor designs. Acceptance by the public of future civil rotorcraft depends on low noise (primarily low BVI noise) during descent and approach to vertiports. We need practical solutions as soon as possible, and will have to rely on test as long as analysis remains inadequate.
- o Smart structure materials will be employed on rotor blades and other rotorcraft components. The initial implementation of smart structure devices on rotor blades will probably benefit from the experiences with Higher Harmonic Control (HHC) and Individual Blade Control (IBC).
- o Transition and maneuver flight modeling by comprehensive rotor analysis methods has not been practical to date. Eventually, improved methods and faster computers will make maneuver and transition analysis possible. Timing depends on funding priorities. The comprehensive rotor analysis codes will have to be extended to non-periodic solutions.
- o Advanced computers (parallel and distributed) are starting to have an impact on both accuracy and efficiency (i.e., "wall clock time") of large calculations. The cost of computing hardware continues to drop. Difficulties remain, however, with the "user friendliness" and robustness of large, multidisciplinary computation methods.
- o Comprehensive, advanced aerodynamics/dynamics modeling will be employed to an increasing extent in rotorcraft flight simulation. Real-time comprehensive rotor analysis calculations are not yet possible, and may not be desirable, but better algorithms and faster computers will make it possible to introduce more accurate models in the flight simulation codes.
- o There is an increased interest in Remotely Piloted and Unmanned rotorcraft. While fixed wing RPVs have been in use for some time, most recently, helicopter and non-helicopter rotorcraft concepts have been investigated for their military and agricultural applications.

What should be our priorities?

Clearly, tiltrotor aircraft have not yet been recognized as a long-term opportunity by a significant portion of the rotorcraft community. That will change, and new specific methods of analysis will prove necessary to support the design of advanced tiltrotors. Fortunately, most current helicopter methodology will be applicable, although additional development efforts will be necessary to address a variety of interactional flow environments involving wings and tail surfaces, large variations in rotor orientation, blade tip-fuselage proximity airloads, and all propeller design issues ranging from whirl-flutter stability to high speed performance and vibration.

A recent assessment of priorities in the development of tiltrotor technologies is described by H. Alexander, et al., in reference (45). Not surprisingly, Alexander's study concluded that "Safety" is always the first priority. It is followed by concerns with "Community Noise Outside Vertiports." Passenger confidence, operating costs, fares etc. all play important but diminishing roles. To a great extent, these conclusions also apply to helicopter operation in a civil transportation environment. "Safety" can be related to the reduction in vibratory airloads and is an aspect of the aeromechanics and aeroacoustics technologies we are concerned with, but it is not a clearly quantifiable challenge. Community noise, on the other hand, is easily quantifiable (if not predictable) as a goal, and it is a challenge that we can and should take personally. Therefore, for the near term, I believe that we should place a high priority on the investigation of the means to reduce Blade-Vortex Interaction noise during descent flight, in helicopter regimes. The reduction of BVI effects is likely to reduce vibration as well as noise.

BVI noise is the most difficult of the technical challenges addressed during this Symposium, and it is "multi-disciplinary," because it requires virtually all aspects of rotor analysis to be combined into one accurate prediction procedure.

4. CONCLUSIONS

- o The Symposium was very valuable. It summarized key developments in rotorcraft aerodynamics and aeroacoustics technologies over the past decade.
- o Analytical tools are becoming more accurate, and more difficult to use. The experimental programs are providing an ever greater insight into the rotor flow field and the detailed aerodynamic behavior of rotor blades.
- o More information is becoming available on the interdependence of rotor aerodynamics, dynamics and acoustics. Valuable aerodynamic modeling techniques are being pursued in conjunction with windmill research.
- o The reduction of rotor noise does not rank as high as Safety, but it appears to be the second highest priority problem. It ranks much higher than passenger confidence and other qualifiers. Safety is related to vibration, but through other disciplines.
- o Computational Fluid Dynamics demonstrates great promise, but has been very difficult to utilize in the support of rotor design. The unresolved issues that limit the application of CFD in fix wing aircraft are even more of an obstacle in rotorcraft applications (grid generation, turbulence modeling, lack of transition models, numerical dissipation of vorticity, separated flow modeling, etc.). In the longer term rotor CFD will become more usable, and will be fully coupled first with comprehensive rotor analysis codes and then with blade Finite Element structural models. In the near term useful results will have to be obtained from limited coupling.
- o A significant body of test data is now available to document rotor flow field and blade aerodynamics. The data include blade dynamics, elastic effects, and acoustic measurements. The investigation of higher harmonic control applications, and the measurement of flow field velocities, blade pressures and rotor acoustics provide the basis for a better understanding of the mechanism of noise generation and reduction. Reviewing and documenting the data is likely to be a costly effort and will require an long term commitment by the sponsoring organizations.

5. RECOMMENDATIONS

- o Place high priority on the prediction and reduction of rotor noise. This challenge includes all analytical and experimental methods.
- o Use the CFD and comprehensive codes to produce and document key trends.
- o Pursue vortex particle methods in modeling rotor wakes for use in rotor analysis codes.
- o Pursue oscillating airfoil data at model rotor scale conditions.
- o Lift-curve slope problems with CFD code predictions must be resolved before rotor CFD and comprehensive rotor analysis codes can be truly coupled, i.e., without "fudge factors". Otherwise all aerodynamic effects, elastic blade deflections, induced power, pressure gradients, etc., will continue to be quantitatively incorrect. Accurate pitching moment and drag predictions by means of rotor CFD will also be, eventually, needed.
- o We must try to obtain "interim" useful results from analysis. We cannot and should not wait for all code features to be validated. Preliminary trends are often very valuable in guiding design.
- o Researchers involved in the development of advanced computation methods (CFD, CAA, comprehensive codes, etc.) should keep in mind that while the eventual user of their codes has to understand all the underlying physics, that user is not likely to tolerate really unfriendly computer procedures or any significant lack of "robustness" in the codes. Instances in which a complex and unreliable computer code must be used for the sake of the competitive edge are few and far between. When the advanced methods of analysis fail to produce results, industry has to resort to simpler analysis, and testing.
- o Development costs, manufacturing costs, maintenance issues and regulations are receiving greater and greater attention. Increasingly, traditional aeromechanics is justified only as it can address product oriented issues.

6. ACKNOWLEDGMENT

The reviewer gratefully acknowledges Dr. W. J. McCroskey's advice and assistance in the preparation of these notes.

7. PROGRAM COMMITTEE MEMBERS

Dr. Ing. H. Dr. Körner (Co-Chairman), DLR, Braunschweig - Germany

Dr. W. J. McCroskey (Co-Chairman), US Army Aeroflightdynamics Directorate, Moffett Field, California - U.S.A.

Prof. R. Decuyper, Ecole Royale Militaire, Brussels - Belgium

Dr. L. Chan, NRC Canada, Ottawa, Ontario - Canada

Ing. General B. Monnerie, ONERA, Châtillon Cedex - France

Prof. F. Sabetta, Università di Roma "La Sapienza", Roma - Italy

Prof. Dr. Ir. J. A. Steketee, Delft - Netherlands

Dr. L. P. Ruiz Calavera, INTA, Madrid - Spain

Prof. Dr. C. Ciray, Middle East Technical University, Ankara - Turkey

Mr. C. D. S. Clarkson, British Aerospace Defence Ltd, North Humberside - U.K.

Prof. W. S. Saric, Arizona State University, Tempe, Arizona - U.S.A.

Mr. L. J. Williams, NASA Headquarters, Washington, D.C. - U.S.A.

8. REFERENCES

(1) "Prediction of Aerodynamic Loads on Rotorcraft," AGARD Conference Proceedings No. 334. Fluid Dynamics Panel Specialists' Meeting held at Church House, London, United Kingdom, 17-18 May, 1982.

References (2) through (35) list the Symposium papers in order of presentation.

2) Landgrebe, A. J., "New Directions in Rotorcraft Computational Aerodynamics Research in the U.S."

3) Ekaterinaris, J. A., Srinivasan, G.R., and McCroskey, W. J., "Present Capabilities of Predicting Two-Dimensional Dynamic Stall"

4) Chandrasekhara, M. S., and Carr, L. W., "Compressibility Effects on Dynamic Stall of Oscillating Airfoils"

5) Ivitchin, V. A., "Investigation into Effect Produced by Blade Airfoil Unsteady Airflow on Helicopter Main Rotor Power Required"

6) Geissler, W. and Sobieczky, H., "Dynamic Stall Control by Variable Airfoil Camber"

7) Snel, H. and van Holten, Th., "Review of Recent Aerodynamic Research on Wind Turbines with Relevance to Rotorcraft"

8) Tchou, K.-F., Hallé, S. and Paraschivoiu, I., "Dynamic Stall Simulation Applied to Vertical-Axis Wind Turbines"

9) Madsen, H. A. and Rasmussen, F., "Stall Hysteresis and 3D Effects on Stall Regulated Wind Turbines: Experiment and Modelling"

10) Filippone, A. and Sørensen, J. N., "A Viscous-Inviscid Interaction Model for Rotor Aerodynamics"

11) Voutsinas, S. G., Belessis, M. A. and Rados, K. G., "Investigation of the Yawed Operation of Wind Turbines by Means of a Vortex Particle Method"

12) Costes, M., Beaumier, P., Gardarein, P. and Zibi, J., "Méthodes de Calcul Aérodynamique Appliquées aux Rotors d'Hélicoptères à l'ONERA"

13) Raddatz, J. and Pahlke, K., "3D Euler Calculations of Multibladed Rotors in Hover: Investigation of the Wake Capturing Properties"

14) Berezin, C. and Sankar, L., "Forward Flight Rotor Airloads Predictions Using a Coupled Navier-Stokes / Full-Potential Analysis"

15) Narramore, J. C., "Computational Fluid Dynamics Development and Validation at Bell Helicopter"

- 16) Röttgermann, A. and Wagner, S., "Cost Efficient Calculation of Compressible Potential Flow around a Helicopter Rotor Including Free Vortex Sheet by a Field Panel Method"
- 17) Bessone, J. and Petot, D., "Evaluation de Modèles Aérodynamiques et Dynamiques des Rotors d'Hélicoptères par Confrontation à l'Expérience"
- 18) Hamel, P. G. and Kaletka, J., "Rotorcraft System Identification - An Overview of AGARD FVP Working Group 18"
- 19) Niesl, G., Swanson, S. M., Jacklin, S. A., Blaas, A. and Kube, R., "Effect of Individual Blade Control on Noise Radiation"
- 20) Kataploglu, C. and Caradonna, F. X., "A Study of Blade-Vortex Interaction Aeroacoustics Utilizing an Independently Generated Vortex",
- 21) Samokhin, V. F. and Rozhdestvensky, M. G., "External Noise of Single Rotor Helicopters"
- 22) Tartelin, P. C. and Martyn, A. W., "In Flight Research with Instrumented Main and Tail Rotor Blades Using the DRA Bedford Aeromechanics Research Lynx Helicopter"
- 23) Seelhorst, U., Beesten, B. M. J. and Bütefisch, K. A., "Flow Field Investigation of a Rotating Helicopter Rotor Blade by Three-Component Laser-Doppler-Velocimetry"
- 24) Berton, E., Favier, D., Maresca, C., Nsi Mba, M., "Détermination des Charges Aérodynamiques du Rotor en Vol Stationnaire, à l'Aide d'une Technique de Vélométrie Laser"
- 25) Kube, R., Splettstoesser, W. R., Wagner, W., Seelhorst, U., Yu, Y. H., Boutier, A., Micheli, F. and Mercker, M., "Initial Results from the Higher Harmonic Control Aeroacoustic Rotor Test (HART) in the German-Dutch Wind Tunnel"
- 26) Beaumier, P., Prieur, J., Rahier, G., Spiegel, P., Demargne, A., Tung, C., Gallman, J. M., Yu, Y. H., Kube, R., Van der Wall, B. G., Schultz, K. J., Splettstoesser, W. R., Brooks, T. F., Burley, C. L. and Boyd, D. D., Jr., "Effect of Higher Harmonic Control on Helicopter Rotor Blade-Vortex Interaction Noise: Prediction and Initial Validation"
- 27) Ianniello, S. and De Bernardis, E., "Calculation of High-Speed Noise from Helicopter Rotor Using Different Descriptions of Quadrupole Source"
- 28) Gennaretti, M., Iemma, U. and Morino, L., "A Boundary Integral Method for Unified Transonic Aerodynamic and Aeroacoustic Analysis of Hovering Rotors"
- 29) Schultz, K. -J., Lohmann, D., Lieser, J. A. and Pahlke, K. D., "Aeroacoustic Calculation of Helicopter Rotors at DLR"
- 30) Toulmay, F., Falchero, D. and Arnaud, G., "Prévision du Bruit Externe des Hélicoptères: Les Méthodes Numériques Vues par un Industriel"
- 31) Syms, G. and Zan, S. J., "Analysis of Rotor Forces in a Ship Airwake",
- 32) Newman, S. J., "A Theoretical and Experimental Investigation into the Rotor Blade Aeroelastic Behaviour of a Shipborne Helicopter during Rotor Engagement and Braking"
- 33) Baeder, J. D., "The Role and Status of Euler Solvers in Impulsive Rotor Noise Computations"
- 34) Lyrintzis, A. S., "The Use of Kirchhoff's Method in Rotorcraft Aeracoustics"

- (35) Wells, V. L., Han, A.Y. and Crossley, W. A., "Acoustic Design of Rotor Blades Using a Genetic Algorithm"
- (36) Hamel, P.G. (editor), "Rotorcraft System Identification." AGARD AR-280, 1991
- (37) Hamel, P.G. (editor), "Rotorcraft System Identification." AGARD LS-178, 1991
- (38) Rubbert, P.E., "CFD and the Changing World of Airplane Design." AIAA Wright Brothers Lecture, Anaheim, California, September 18-23, 1994
- (39) Dadone, L., Liu, J., Wilkerson, J. and Acree, C.W.: "Proprotor Design Issues for High Speed Tiltrotors." Presented at the 50th Annual Forum of the American Helicopter Society, Washington, DC, May 1994.
- (40) Liiva, J., Davenport, F.J., Gray, L. and Walton, I.D.: "Two-Dimensional Tests of Airfoils Oscillating near Stall," U.S. Army AVLABS TR 68-13, 1968.
- (41) McCroskey, W.J., Carr, L.W. and McAlister, K.W.: "Dynamic Stall Experiments on Oscillating Airfoils," AIAA paper 75-125, presented at the AIAA 13th Aerospace Sciences Meeting, Pasadena, CA, January 20-22, 1975.
- (42) McCroskey, W.J., Baeder, J.D. and Bridgeman, J.O., "Calculation of Helicopter Airfoil Characteristics for High Tip-Speed Applications," Journal of the American Helicopter Society, Volume 31, Number 2, April 1986, pp. 3-9.
- (43) Kufeld, R., Balough, D. L., Cross, J. L., Studebaker, K. F., Jennison, C. D. and Bousman, W. G., "Flight Testing of the UH-60A Airloads Aircraft." Presented at the 50th Annual Forum of the American Helicopter Society, Washington, D.C., May 11-13, 1994
- (43) Proceedings of the First Forum of the Russian Helicopter Society, Volumes 1 and 2, Moscow, September 20-21, 1994
- (45) Alexander, H.R., Biggers, J., Forman, E. and Schleicher, D., "Prioritization of Civil Tiltrotor Technologies Using the Analytic Hierarchy Process." Presented at the Third International Symposium on the Analytic Hierarchy Process, George Washington University, Washington, D.C., July 11-13, 1994

NEW DIRECTIONS IN ROTORCRAFT COMPUTATIONAL AERODYNAMICS RESEARCH IN THE U.S.

Anton J. Landgrebe

Division Program Leader, Sikorsky Program
United Technologies Research Center
United Technologies Corporation
411 Silver Lane
East Hartford, Connecticut, USA 06108

SUMMARY

Recent research activities in the United States are presented that are representative of the directions of research for computational aerodynamics for rotorcraft. Emphasis is given to Navier-Stokes methodology for airflow and airload prediction, and specifically the fundamental technical challenges associated with grid systems and achieving wake generation without numerical diffusion.

Although the current rotorcraft CFD methods have not yet generally demonstrated sufficient accuracy for the helicopter industry, the recent rate of progress is encouraging.

1. INTRODUCTION

As stated in the theme for this 75th AGARD Fluid Dynamics Panel Symposium, the importance of understanding and accurately predicting the aerodynamic characteristics of rotorcraft is recognized, as well as the need for improved phenomenological insight, better math models, adequate test equipment, and more precise and efficient numerical methods. This requires improvements in Computational Fluid Dynamics (CFD) and computers.

The accurate prediction of helicopter airloads and airflow remains an elusive challenge. Despite the recent advances in rotorcraft aerodynamic methodology through improved technology and high speed computers, limitations in payload, range, forward speed, flight dynamics, aeroelastic stability, and structural loads, along with excessive noise and vibration, still exist because of the inability to perform aerodynamic associated design with sufficient accuracy. This is due to the complex interactive flow field of the helicopter which encompasses all of the aerodynamic challenges shown in the frequently used Figure 1.

The ultimate computational aerodynamics goal is to represent the entire rotorcraft (rotors, fuselage, etc.) and its flow field, by the Navier-Stokes equations with a sufficiently detailed grid, time interval, and turbulence model to obtain accurate solutions. However, this is awaiting the super-computer of the future with vastly greater memory and speed capacity. In the interim, aerodynamicists have relied on innovative assumptions to simplify the problem to the extent required by the computer power available. The selections of assumptions for a particular method or computer code have been tailored to the immediate objective, recognizing the limitations and constraints of the methodology.

Limited computer power has led to many different types of aerodynamic methods with features determined by levels of complexity. The primary types of methods are listed below:

Simple Momentum
Blade-Element Momentum
Potential -Lifting Line, Vortex Lattice, Lifting Surface
Full Potential
Euler
Navier-Stokes

Some features characterizing the levels of increasing complexity or operating regime are:

Hover/Steady Forward Flight/Maneuvers
Airfoil/Blade/Rotor/Fuselage/Complete Rotorcraft
Two Dimensional/Three Dimensional
Incompressible/Compressible
Inviscid/Viscous

2. BACKGROUND

Accurate representation of the rotor wake and inflow is necessary to improve blade airload prediction. Much progress has been made since the author of this paper presented the need for rotor wake research at the AGARD Fluid Dynamics Panel Meeting in 1972 [1] and an "Overview of Helicopter Wake and Airloads Technology" [2] at the European Rotorcraft Forum in 1986 and the International Conference on Basic Research in 1988. Modeling of the wake by hundreds and then thousands of vortex elements was made possible by the rapid progress of large main-frame computers. Classical undistorted wake models were supplemented with more rigorous prescribed wake and free wake methods. Induced velocities at the blades and in the wake were calculated using the Biot-Savart law in a coupled iterative manner with the blade airload solution based on potential theory. Examples of forward flight wake geometry predictions by Egolf of UTRC are shown in Figure 2.

In the 1980's, the use of modern computational fluid dynamics (CFD) techniques to predict airloads over the blade surface was initiated. The wake methods initially used a lifting line representation for each blade. To predict the blade chordwise as well as spanwise airloading, higher level methods (vortex lattice, full potential, Euler, Navier-Stokes) are required. To directly predict the wake, Navier-Stokes methodology is required. The complex airloads

predicted at UTRC (B. E. Wake) with a Navier-Stokes analysis, for a low speed forward flight condition, are shown in Figure 3. Like other methods, the general agreement with experimental data is not at the level of accuracy required by the helicopter industry.

Considerable progress has recently been made in developing CFD methodology for rotorcraft. To name all of the numerous contributors is beyond the scope allotted here, and thus only representative names will be cited. By organization, key contributions in the U.S. have been made at each of the major helicopter manufacturers, the NASA Ames and Langley Research Centers (Ames is the designated lead Center for rotorcraft CFD) and universities (e.g., Ga. Tech., U. of Md., RPI, Iowa St., etc.), and corporate and independent research organizations (e.g. UTRC, AMI, CDI).

Rotorcraft CFD methodology development has continued to proceed at a complexity level consistent with the rapid progress of computers. With the advent of supercomputers, methods for computer codes have advanced to full potential and more recently Euler and Navier-Stokes research codes. In simplified terms, these three methods can be distinguished as follows. The Navier-Stokes method is the ultimate method consisting of equations containing fluid viscosity, momentum, and energy considerations. The inclusion of viscosity is needed to rigorously compute boundary layer influence on skin-friction drag, tip vortex formation, and stall (b.l. separation). The Euler and full potential equations do not include viscosity, and thus Euler and full potential codes either ignore or approximate it. In the full potential equations, fluid entropy is assumed constant and vorticity is not convected. It is thus necessary to couple a wake model. Although this is not ultimately necessary for Navier-Stokes methodology, current numerical diffusion due to insufficient grid density and turbulence models prevent accurate computation of the rotor wake and its influence on airflow and airloads.

Advanced rotorcraft CFD methods are currently being assessed and used where feasible and sufficiently accurate. The following is a list of some of the applications of current interest that are being explored:

Hover and cruise performance	Tip design
Interactional aerodynamics	Airfoil design
Aeroacoustics	Flaps, slats
Blade vortex interaction	Higher harmonic control
Tip vortex formation	Individual blade control
Fuselage drag (separation)	Tilt rotor
Dynamic stall	Aeroelastic coupling

Navier-Stokes analyses (e.g., TURNS) and Strawn's adaptive Euler solver have been developed which attempt to capture the wake and predict hover performance. A major technical hurdle for hover performance prediction is to adequately resolve the tip vortex to at least the first blade

passage. The TURNS analysis has also been applied to rotors for acoustic predictions.

Navier-Stokes methods are beginning to be used for fuselage configurations. Narramore has applied ENS3D to Bell Helicopter fuselages using a single-block grid. Berry has demonstrated CFL3D, INS3D, and OVERFLOW for a basic fuselage configuration. Detailed calculations of the Comanche fuselage airloads were made by Duque and Dimanlig using OVERFLOW. OVERFLOW has been applied to the tilt-rotor and a tilt-rotor with wing and body. The rotor/body results will not be useful until the wake is adequately captured.

Concurrently with aerodynamic code development, comprehensive multi-disciplinary codes (CAMRAD, 2GCHAS, RDYNE, COPTER, B-60 Series, etc.) have been developed. The integration and expansion of these codes to incorporate the wake, airflow, and/or airload predictions from the CFD codes is a major future activity.

Another forthcoming challenge is the development of a first generation Numerical Rotor Test Facility. A CFD code will harness parallel computing technology for the numerical simulation of the interactional aerodynamics of rotorcraft.

The challenge for the future in aerodynamics is to achieve advanced rotorcraft designs that take into account the accurate prediction of airloads and the many aerodynamic interaction effects that may influence the performance and dynamic loading of the total vehicle. Aerodynamic interactions among the rotors, airframe, fixed control surfaces in the rotor wake, auxiliary propulsion systems operating in and out of the rotor wake in proximity to the ground, and variations in these interactions with forward speed have been difficult to model during the design process. With the enormous capacity of modern computers, however, these aerodynamic interactions are being addressed with increasing success. In the future, theoretical approaches to rotorcraft design will benefit tremendously from the rapid growth in the capabilities of Computational Fluid Dynamics (CFD). The supercomputers envisioned for the twenty-first century will have the capacity and speed to deal adequately with the complex aerodynamic flow of an entire vehicle.

In this paper, recent advances and new directions in rotorcraft CFD are presented. Emphasis is on CFD where the current fundamental challenges are grid methodology, wake generation without numerical diffusion, turbulence modelling and aeroelastic and aeroacoustic coupling.

Considering the numerous research programs that have been conducted on the subject, only representative activities in the United States have been selected for inclusion in this paper. Considering the extensive research activities by NASA and the Army at the Ames Research Center, under the leadership of W. L. McCroskey and Y. Yu (with R. Strawn, E. Duque, F. Caradonna et al.), and the author's

direct knowledge of the UTRC/Sikorsky activities (T. A. Egolf, B. E. Wake, C. Berezin, et al.), most of the representative activities are from these sources.

The intent of this paper is to show that the new directions for rotorcraft CFD (coupled with the anticipated advances in computers) have positioned rotorcraft aerodynamic technology at the forefront of major advances in the determination of rotorcraft airloads and airflow in the next decade.

3. COMPUTATIONAL FLUID DYNAMICS

In order to accurately predict the complex flows associated with the rotor wake, shocks, and blade and body-vortex interaction, and separated flow, Navier-Stokes methodology must be applied. The Euler form of the Navier-Stokes equations can be used for relatively inviscid regions. With advanced computers and computer networks, the current direction for rotorcraft Computational Fluid Dynamics (CFD) is the solution of the Navier-Stokes equations in complete or Euler form, depending on the operating condition and region of interest. However, major technical challenges persist such as achieving proper grid modeling for the different complex flow regions and alleviation of the numerical diffusion of vorticity.

3.1 Grid Systems

Grid methodology development has taken two paths based on structured and unstructured grids. Structured grid methods work well for flow regions near bodies. They use implicit solution methods that allow for larger time steps. The grid can cluster near surface boundaries without severe time step limits. However, current structural grid methods are not well suited for three dimensional grid adaption to capture a vortex wake. Unstructured grids are adaptive and can refine around flow features more readily than structured grids. As stated by Duque [3], three-dimensional dynamically adaptive structured grids have not yet shown an ability to adequately capture flow features in a true unsteady manner. In contrast, dynamic unsteady remeshing and grid adaptation on unstructured grids, with the ability to freely remove and add points within regions of interest, is a major advantage of unstructured grids, although they have higher computer requirements. Unstructured grid methods are particularly applicable for the wake of the helicopter blade where the solution methodology needs to resolve the connecting tip vortex and the vortex sheet.

3.1.1 Structured Grids

Significant progress has been made in the development of structured grid systems for rotorcraft since the first rotor Navier-Stokes code (NSR3D) was developed by Wake and Sankar [4] in the late 1980's. An early Navier-Stokes code for the hovering rotor is TURNS by Srinivasan et al. [5-7]. These codes use single-block grids with clustering near the blade. Duque and Srinivasan [8] modified TURNS to use

a multi-block method based on a system of embedded structured grids. This Chimera grid approach uses interconnected sub-domains with grids that are selected for the rotor blade (1 grid) and the wake (2 grids). The blade grid shown in Figure 4 clusters points toward the airfoil surface to capture the boundary layer flows, while the wake grid places additional points in the wake's vicinity. This approach was recently extended by Ahmad and Duque to the forward flight regime for which the dynamic motion of the helicopter rotor blades was included through relative grid motion [9]. The Chimera embedded grid scheme greatly simplifies the representation for arbitrary blade motions which is important in achieving trimmed flight conditions. The unsteady forward flight airloads and flow field of the AH-IG helicopter were computed using this thin-layer Navier-Stokes code with moving embedded grids. The computed flow visualization using unsteady streakline particles emitted from the inboard and outboard blade tips is shown in Figure 5. The time history of tip airloading is shown in Figure 6. Differences in airloads at the tip and inboard on the blade, as well as a significant over prediction of power required, is attributed mainly to the need to improve the trim solution through a tighter airload/aeroelastic blade dynamics coupling and the need to reduce numerical diffusion in the wake.

Simulation of the flow about the V-22 tilt rotor aircraft has been conducted by Meakin [10] using a 3-D unsteady multizone implicit Navier-Stokes code. Dynamic "Chimera" overset grids were used to simulate the unsteady viscous airflow. A connectivity algorithm was included to dynamically establish domain connectivity among the system of fixed and overset rotating grids. The V-22 geometry was decomposed into a system of overset grids, using novel body-fitted grid topologies for the nose, wing/fuselage intersections, wing tip and rotor tips. In all, 25 component grids were used, totalling more than 1.3 million grid points. Particle trace simulation of the rotor wake structure is shown in Figure 7 for a 75 kt condition. The instantaneous surface pressure on the fuselage and wing at one time step is shown in Figure 8. The pressure waves on the fuselage and wing due the blade and wake passages were simulated. Validation of this code with experimental data remains to be conducted. Improved resolution of the vortical wakes and associated body interactions will be pursued with solution adaptive overset grids for which the software is being developed.

Duque and Dimanlig [11] have used the Navier-Stokes code OVERFLOW to compute the airloads on the AH-66 Comanche fuselage as shown in Figure 9. Actuator disks were used to model the influence of the main rotor and fan-tail on the fuselage. Berry et al. [12] compared four Navier-Stokes methods (CFL3D, INS3D, OVERFLOW, and VSAERO) for the prediction of the isolated fuselage airloads.

3.1.2 Unstructured Grids

The unstructured grid solver permits adaptive grid refinement in order to improve the resolution of flow features such as shocks, rotor wakes, and acoustic waves. The unstructured mesh generally allows for faster and efficient grid generation around highly complex geometries. Appropriate unstructured grid data structures facilitate the insertion and deletion of points and enable the computational mesh to locally adapt to the flow field solution. In the wake of a helicopter blade, unstructured grid methods permit the addition and deletion of points to resolve the convecting tip vortex and vortex sheet.

Strawn and Barth [13] developed the first unstructured grid solver for predicting the aerodynamics of rotor blades. This unsteady Euler flow solver is a finite volume scheme that computes flow quantities at the vertices of the mesh. The code was applied to a hovering model rotor for which surface pressure data was available. The grid was adapted from 63,000 nodes to 260,000 nodes with 1.4 million tetrahedral elements. Approximately 10 hours of CPU time and 32 MW of memory were required on the NAS CRAY YMP computer at the NASA Ames Research Center. A cross section of the subdivided grid is shown in Figure 10. The resulting contours of vertical flow velocity are shown in Figure 11. The tip vortex was found to diffuse rapidly after 270 degrees of vortex age where a change in the level of grid subdivision was located. Discrepancies in the predicted blade airloading were attributed mainly to inadequate grid resolution of the rotor wake system.

In order to reduce the numerical dissipation that artificially diffuses rotor wakes and acoustic signals, Biswas and Strawn recently developed a new procedure for the simultaneous coarsening and refinement of the unstructured tetrahedral meshes [14]. An innovative data structure allows the mesh connectivity to be rapidly reconstructed after mesh points are added and/or deleted. These local grid modifications enhance the resolution of rotor wakes and acoustic signals and reduce numerical dissipation in the solutions. The method has been applied to the high-speed impulsive rotor noise problem [15]. The final mesh and computed pressure contours are shown in Figure 12. Grid refinement is shown at the shock, near the blade tip, and along the acoustic wave that propagates into the farfield. The corresponding pressure contours show large gradients in these regions. Using a Kirchhoff formulation to propagate the acoustic pressures to the farfield, this dynamic adaptive unstructured grid method achieved generally good agreement with the experimental acoustic pressures of a hovering model rotor with tip Mach numbers as high as 0.95. For this hover application, excellent agreement was shown with the structured grid Euler TURNS code calculations of Baeder et al. [16], and thus the demonstration of the advantages of the unstructured grid approach awaits a forward flight application.

3.1.3 Structured/Unstructured Grids

In order to utilize the advantages of both structured and unstructured grid methods, they have recently been combined by Duque [3] in a structured/unstructured grid solver for helicopter rotor flows. A schematic of a 2-D structured/unstructured grid system with an unstructured background grid and a structured airfoil grid is shown in Figure 13. Embedded structured grids are used with an implicit finite-difference Navier-Stokes solver for regions close to the rotor blade to capture the boundary layer flow field and vortex formation. The structured grids lie within an unstructured grid that uses an explicit finite-volume Euler solver to convect the wake of a hovering rotor. In this hybrid code, the two grid systems overlap and interpolate flow quantities at their boundaries (Fig. 13). Since the unstructured grid does not have to resolve the boundary layer, its inherent explicit flow solver does not inhibit convergence. Although this first application demonstrated the general feasibility of the method, the predicted blade pressures and resulting airloads exhibited some discrepancies that were attributed to the coarse wake grid used and the resulting poorly resolved tip vortex. For future investigation, improved grid resolution at tip vortex locations and grid interface boundaries is recommended along with dynamic grid adaption of the unstructured mesh and application to forward flight.

3.2 Wake Prediction and Numerical Diffusion

Accurate wake prediction using a Navier-Stokes method is currently inaccurate due to numerical diffusion and associated dissipation (hereafter referred to as numerical diffusion). It has been observed that the calculated tip vortex excessively expands and loses vorticity with increasing distance from wing and blade tips. This is generally attributed to insufficiencies in the grid resolution, order of accuracy of the Navier-Stokes solver, and turbulence model.

Srinivasan et al. [5] noted in their application of TURNS to hovering UH-60 and BERP rotors that "the structure of the captured tip vortex is diffused by numerical viscosity." Wake and Baeder [17], in their application of TURNS to UH-60 and 3:1 tapered tip model rotors in hover, found that numerical diffusion produced significant discrepancies in tip vortex location and structure near the following blade, even with 950,000 grid points. Duque [3], with his structured/unstructured grid solver found that the grid system "does not adequately resolve the tip vortex core." He cited maintaining grid resolution at the grid interface boundaries, and the need for unstructured grid adaption to convect the wake, as areas for future attention.

The numerical diffusion problem has been addressed for the less complex tip vortex of the fixed wing. Strawn [18] developed an Euler adaptive grid method for computing tip vortex flow fields of rectangular wings. He concluded that an Euler solver is insufficient to predict the structure of the

tip vortex close to the wing and that viscous effects play an important role in the vortex roll-up process. An inviscid model should be able to convect the vortex once it has formed, but it is very difficult to obtain a grid independent simulation of vortex formation with an Euler solver. The Euler model predicted too large a rotational core. An accurate viscous-flow solution is required to resolve the tip vortex. Mariani, Zilliac et al. [19] applied a Navier-Stokes code to a rectangular wing. They found that a higher order accurate differencing scheme is needed for the convective terms. For their selected grid with at least 230,000 grid points, fifth order accurate differencing for the convective terms was shown to be essential in reducing numerical diffusion and achieving reasonable agreement with measured vortex flow velocities.

B. Wake and D. Choi have recently confirmed at UTRC the need for combining higher order accuracy with an appropriate grid and number of grid points to reduce vortex numerical diffusion. The NASA CFL3D Navier-Stokes code was applied to a rectangular wing, and the resulting tip vortex prediction is shown in Figures 14 and 15. Contours of flow velocity in Figure 15 show the excessive vortex diffusion which increases from the trailing edge ($x = 1$) to 0.8 of a chord length ($x = 1.8$) behind the trailing edge for a third order solution. The benefit of using a higher order differencing solution for the convective terms was studied by using a model problem. In Figure 16 cross flow contours are shown. The tip vortex diffusion has been reduced significantly by using 5th order accuracy.

Hariharan and Sankar [20] recently extended a Navier-Stokes solver from third to fifth order spatial accuracy and applied it to a hovering rotor. They concluded that "the higher order schemes can capture complex flow fields better." However, it remains to use the higher order scheme, in combination with a finer grid than the 60,000 grid points used, to accurately convect the vorticity.

Turbulence modeling is recognized as another major challenge for accurate wake prediction. At this time, none of the turbulence models are considered sufficient for tip vortex prediction. The models are currently believed to be overly dissipative.

While the grid, numerical diffusion and turbulence problems with Navier-Stokes codes await solution, rotor wake methods with vortex modeling are continuing to be developed. Free wake methods, such as those of Egolf [21], Ramachandran [22], and Quackenbush [23] are being refined and applied to current rotors. The Navier-Stokes NSR3D code of B. E. Wake [4] was combined with the FREEWAKE code of T. A. Egolf [24]. Steinhoff's "vortex confinement" method has been applied with the TURNS code by Wang et al. [25] to rotor blades and simple body airflow. Berezin [26] has developed a hybrid Navier-Stokes/full potential code NSFPE, and applied it to a UH-60 A rotor in forward flight. The insertion of the

blade's Navier-Stokes domain within a full-potential domain allows use of a potential wake model for the far-field, and results in a 50 percent reduction in computer time requirement relative to a complete Navier-Stokes code.

3.3 Parallel Processing

To provide the computational power needed to routinely apply these advanced CFD codes to rotorcraft problems, the use of parallel processing will become more prevalent. Most of the advanced CFD work with parallel processing has been performed by Government Labs and Universities for non-rotorcraft problems. UTRC has been a pioneering corporate entity for rotorcraft problems, demonstrating the use of massively parallel processing for a wide variety of disciplines, including the development of two massively parallel rotorcraft CFD codes [27, 28]. Due to the current economic environment and the difficulties, real or perceived, of using parallel computers, the near term future of parallel processing has changed direction. For many corporations, the purchase and use of dedicated massively parallel large-scale systems is being replaced by the use of small coarse-grained systems based on networks of existing workstations, allowing industry to capitalize on unused compute cycles.

4. CONCLUDING REMARKS

Recent research activities in the U.S. have been presented that are representative of the directions of research for rotorcraft CFD, with emphasis on Navier-Stokes methodology. Various types of grid systems are being evaluated including a new hybrid structured/unstructured grid solver for helicopter rotor flows. The latter combines the advantages of a structured grid for the boundary layers of blade and body surfaces and an unstructured grid for complex flow regions. However, like all methods, it suffers from numerical diffusion for vortex convection. The numerical diffusion problem is being addressed by grid resolution and higher order solutions.

Although the current rotorcraft CFD methods have not yet generally demonstrated sufficient accuracy for the helicopter industry, the rate of progress is encouraging. With this rate of progress and forthcoming computers, rotorcraft CFD technology appears to be on the forefront of the capability for inclusion in the helicopter design process.

5. ACKNOWLEDGEMENTS

The author would like to acknowledge the help of W. J. McCroskey, T. A. Egolf, and B. E. Wake in the preparation of this paper.

6. REFERENCES

1. Landgrebe, A. J., "Rotor Wakes - Key to Performance Prediction", Specialist's Meeting on the Aerodynamics of Rotary Wings, AGARD Fluid Dynamics Panel, AGARD Conference Proceedings No. III, September 1972; also Symposium on Status

- of Testing and Modeling Techniques for V/STOL Aircraft, Mideast Region of the American Helicopter Society, October 1972 (coauthor).
2. Landgrebe, A. J., "Overview of Helicopter Wake and Airloads Technology", Proceedings of the International Conference on Basic Rotorcraft Research, American Helicopter Society/University of Maryland, February 1988; Proceedings of the 12th European Rotorcraft Forum, Paper No. 18, Garmisch-Partenkirchen, Federal Republic of Germany, September 1986.
 3. Duque, E. P. N., "A Structured/Unstructured Embedded Grid Solver for Helicopter Rotor Flows", 50th AHS Annual Forum Proceedings, Washington, May 1994.
 4. Wake, B. E. and Sankar, L. N., "Solution of the Navier-Stokes Equations for the Flow about a Rotor Blade", American Helicopter Society Journal, April 1989.
 5. Srinivasan, G. R., Baeder, J. D., Obayashi, S., and McCroskey, W. J. "Flowfield of a Lifting Rotor in Hover: A Navier-Stokes Simulation," Proceedings of the 16th European Rotorcraft Forum, Vol. 1, September 1990. Also, *AIAA Journal*, Vol. 30, No. 10, October 1992.
 6. Srinivasan, G. R. and Baeder, J. D., "TURNS: A Free-Wake Euler/Navier-Stokes Numerical Method for Helicopter Rotors", *AIAA Journal*, Vol. 31, No. 5, May 1993. (Presented at the Fourth International Symposium on Computational Fluid Dynamics, Davis, CA, September 1991.)
 7. Srinivasan, G. R., Raghavan, V., Duque, E. P. N., and McCroskey, W. J. "Flow Field Analysis of Modern Helicopter Rotors in Hover by Navier-Stokes Method", *AHS Journal*, Vol. 38, No. 4, July 1993. (presented at the AHS International Technical Specialists' Meeting on Rotorcraft Acoustics and Fluid Dynamics, Philadelphia, PA, October 1991).
 8. Duque, E. P. N., and Srinivasan, G. R., "Numerical Simulation of a Hovering Rotor Using Embedded Grids", AHS 48th Annual Forum, Washington, June 1992.
 9. Ahmad, J., and Duque, E. P. N., "Helicopter Rotor Blade Computation in Unsteady Flow Using Moving Embedded Grids", AIAA Paper 94-1928, 12th Applied Aerodynamics Conference, Colorado Springs, June 1994.
 10. Meakin, R. L., "Moving Body Overset Grid Methods for Complete Aircraft Tiltrotor Simulations", AIAA Paper 93-3350-CP, AIAA 11th Computational Fluid Dynamics Conference, Orlando, FL, July, 1993.
 11. Duque, E. P. N., and Dimanlig, A. C. B., "Navier-Stokes Simulation of the AH-66 (Comanche) Helicopter", AHS Aeromechanics Specialists' Conference, San Francisco, January 1994.
 12. Berry, J. D., Chaffin, M. S. and Duque, E. P., "Helicopter Fuselage Aerodynamic Predictions: Navier-Stokes and Panel Method Solutions and Comparison with Experiment", American Helicopter Society Aeromechanics Specialists Conference, San Francisco, January 1994.
 13. Strawn, R. C. and Barth, T. J., "A Finite-Volume Euler Solver for Computing Rotary-Wing Aerodynamics on Unstructured Meshes", *AHS Journal*, vol. 38, No. 2, April 1993. (Presented at the AHS 48th Annual Forum, Washington, DC, June 3-5, 1992.)
 14. Biswas, R. and Strawn, R. C., "A New Procedure for Dynamic Adaption of Three-Dimensional Unstructured Grids," *Applied Numerical Mathematics*, Vol. 13, 1994, pp. 437-452.
 15. Strawn, R., Garceau, M. and Biswas, R., "Unstructured Adaptive Mesh Computations of Rotorcraft High Speed Impulsive Noise", AIAA Paper 93-4359, AIAA 15th Aeroacoustics Conference, Long Beach, CA, October 1993. To be published in *AIAA Journal of Aircraft*.
 16. Baeder, J. D., Galiman, J. M. and Yu, Y. H., "Computational Study of the Aeroacoustics of Rotors in Hover", 49th Annual American Helicopter Society Forum Proceedings, St. Louis, MO, May 1993.
 17. Wake, B. E. and Baeder, J. D., "Evaluation of the TURNS Analysis for Hover Performance Prediction", American Helicopter Society Aeromechanics Specialists Conference, San Francisco, January 1994.
 18. Strawn, R. C., "Wing Tip Vortex Calculations with an Unstructured Adaptive-Grid Euler Solver", 47th American Helicopter Society Forum, May 1991.
 19. Mariani, J. D., Rogers, S. Kwak, D., Zilliac, G. and Chow, J., "A Computational Study of Wingtip Vortex Flow Field", AIAA Paper 93-3010, 29th AIAA Fluid Dynamics Conference, July 1993.
 20. Hariharan, N. and Sankar, L. N., "Higher Order Numerical Simulation of Rotor Flow Field", 50th American Helicopter Society Forum Proceedings, May 1994.

21. Egolf, T. A., Helicopter Free Wake Prediction of Complex Wake Structures Under Blade-Vortex Interaction Operating Conditions, Proceedings of the 44th AHS Forum, June 1988.
22. Ramachandran, K., Owen, S. J., Caradonna, F. X., and Moffitt, R. C., "Hover Performance Prediction Using CFD", 50th American Helicopter Society Forum Proceedings, May 1994.
23. Quackenbush, T. R., Lam, C., Wachpress, D. and Bliss, D., "Analysis of High Resolution Unsteady Airloads for Helicopter Rotor Blades", 50th American Helicopter Society Forum, May 1994.
24. Wake, B. E. and Egolf, T. A., "Initial Validation of an Unsteady Euler/Navier-Stokes Flow Solver for Helicopter Airloads in Forward Flight", AHS International Technical Specialists Meeting on Rotorcraft Basic Research, Atlanta, March 1991.
25. Wang, C., Bridgemen, J. O., Steinhoff, J. S. and Wearen, Y., "The Application of Computational Vorticity Confinement to Helicopter Rotor and Body Flows", 49th American Helicopter Society Forum Proceedings, May 1993.
26. Berezin, C., "Forward Flight Rotor Airloads Prediction Using a Coupled Navier-Stokes/Full Potential Analysis", 75th AGARD Fluid Dynamics Panel Meeting on Aerodynamics and Aeroacoustics of Rotorcraft, Berlin, October 1994.
27. Wake B. E., and Egolf, T. A., "Implementation of a Rotary Wing Navier-Stokes Solver on a Massively Parallel Computer, AIAA Journal, Vol. 29, No. 1, January 1991.
28. Egolf, T. A., "Helicopter Free-Wake Analysis on a Massively Parallel Computer", Presented at the International Symposium on Boundary Element Methods, ISBEM 89, held at UTRC, October 2-4, 1989.

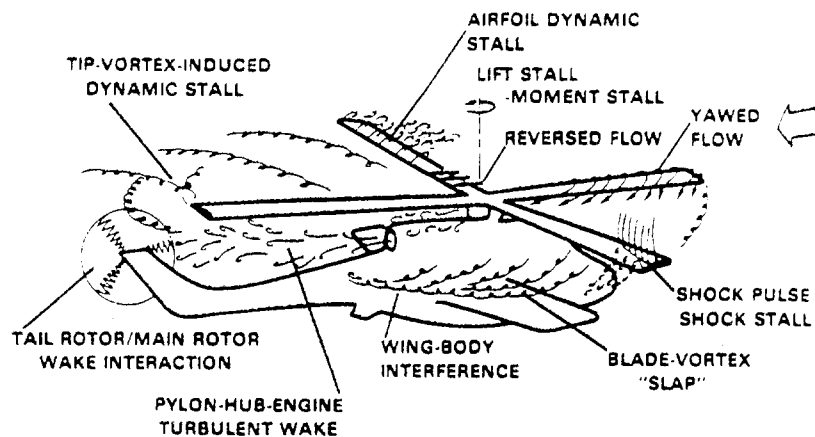


Fig. 1 Complex Rotorcraft Aerodynamics

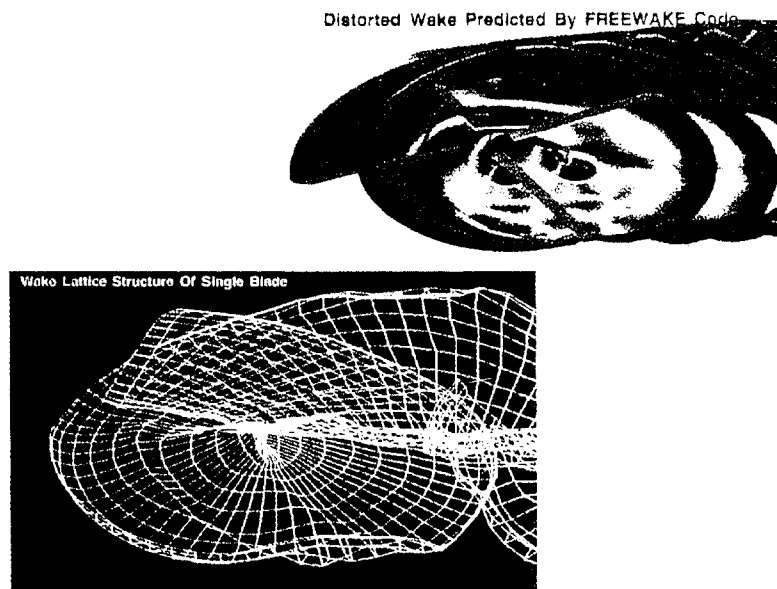


Fig. 2 Predicted Rotor Wake

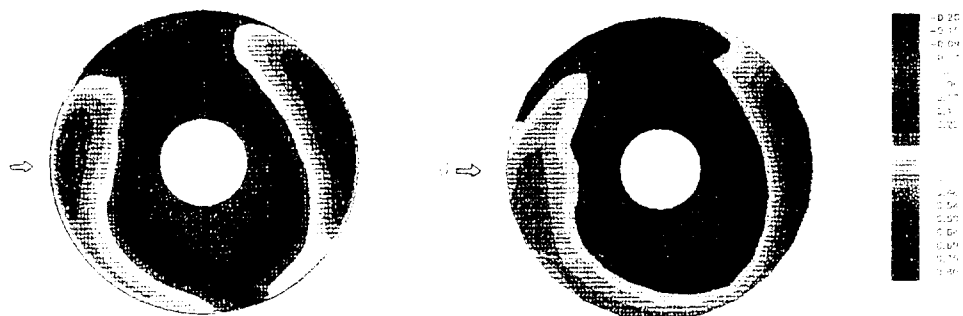


Fig. 3 Predicted (left) and Experimental (right) Blade Airloading

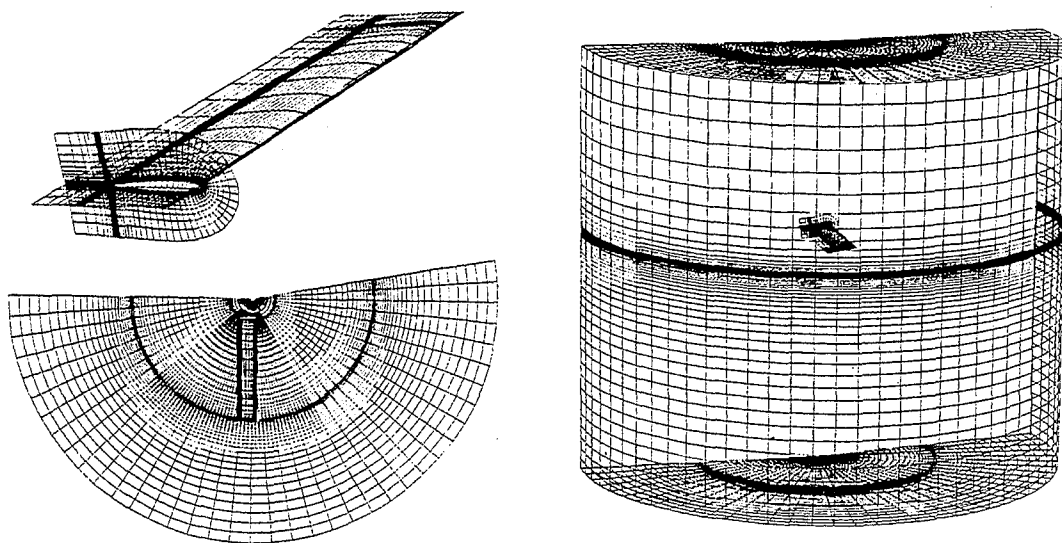


Fig. 4 Structured Embedded Grids for Blade and Wake

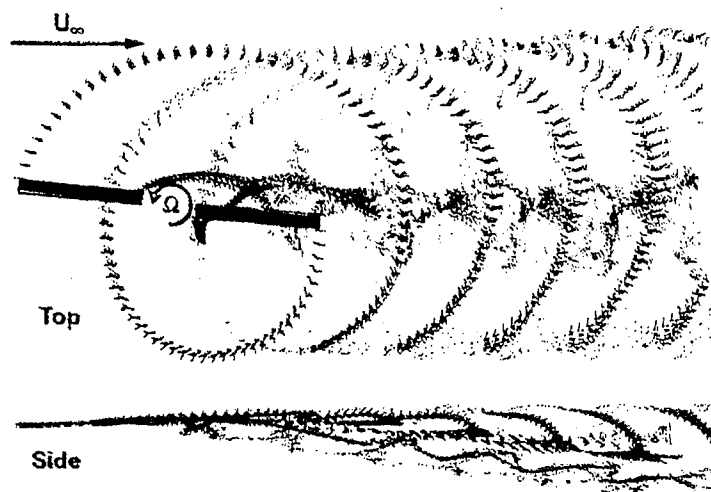


Fig. 5 Predicted Particle Traces Showing the Outer and Inner Wake

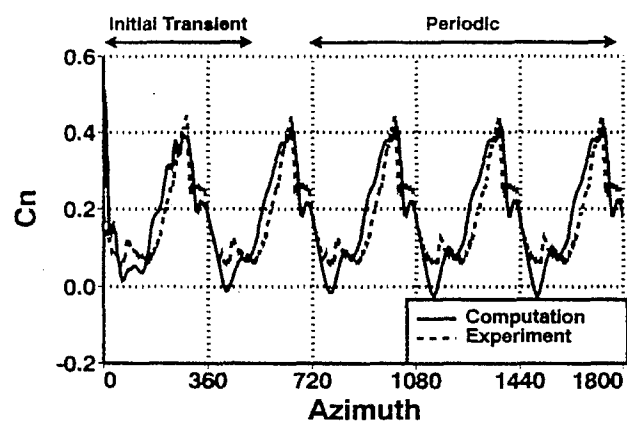


Fig. 6 Airload Time History Near Blade Tip ($r/R = 0.97$)



Fig. 7 Predicted Particle Traces Showing The Tilt Rotor Wake

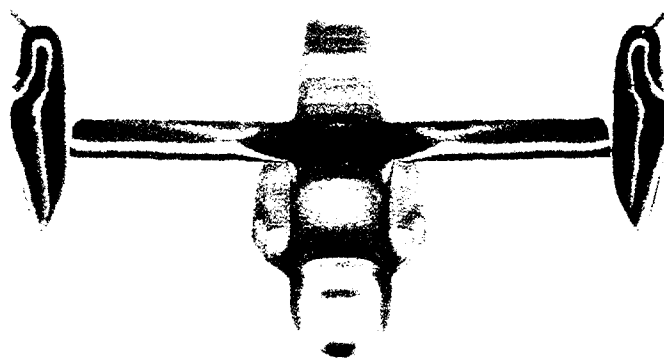


Fig. 8 Predicted Instantaneous Surface Pressure

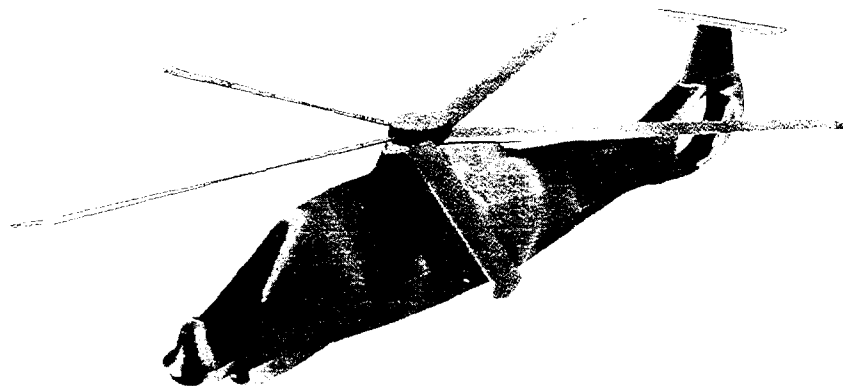


Fig. 9 Predicted Comanche Surface Pressure

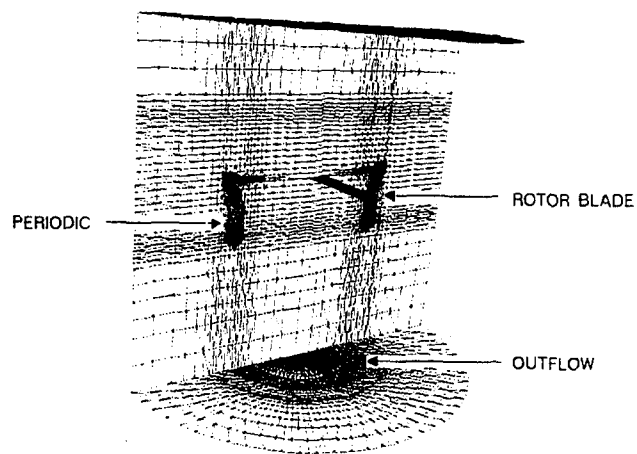


Fig. 10 Unstructured Grid

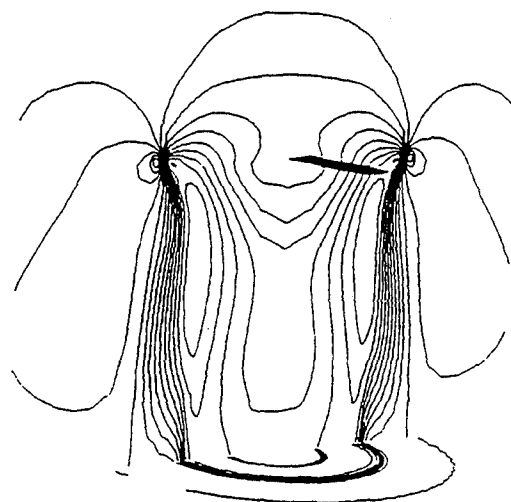


Fig. 11 Contours of Vertical Flow Velocity

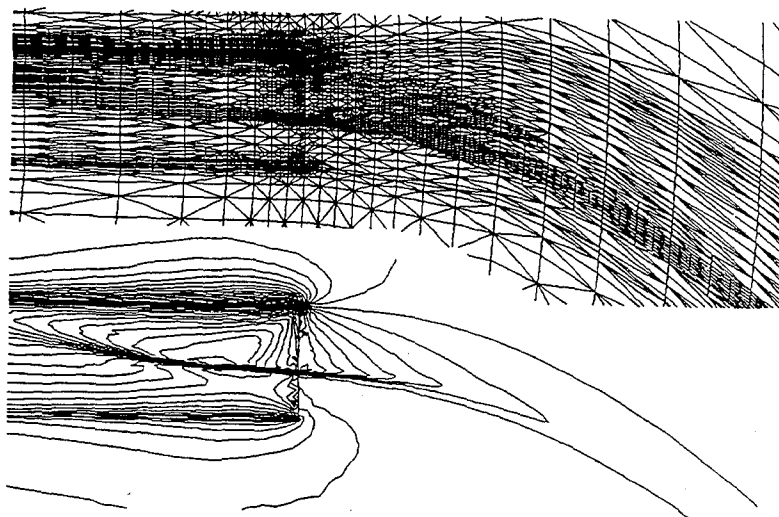


Fig. 12 Unstructured Adaptive Grid and Computed Pressure Contours

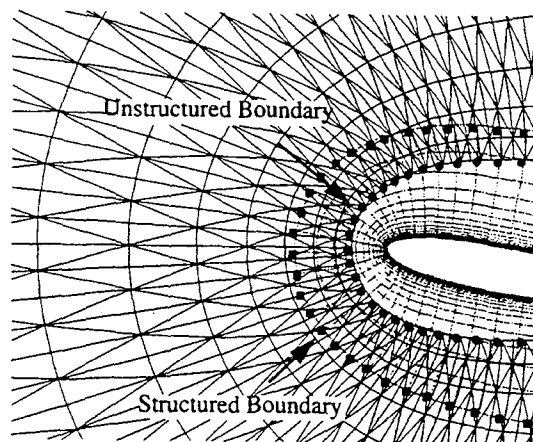


Fig. 13 Schematic 2-D Embedded Structured-Unstructured Grid

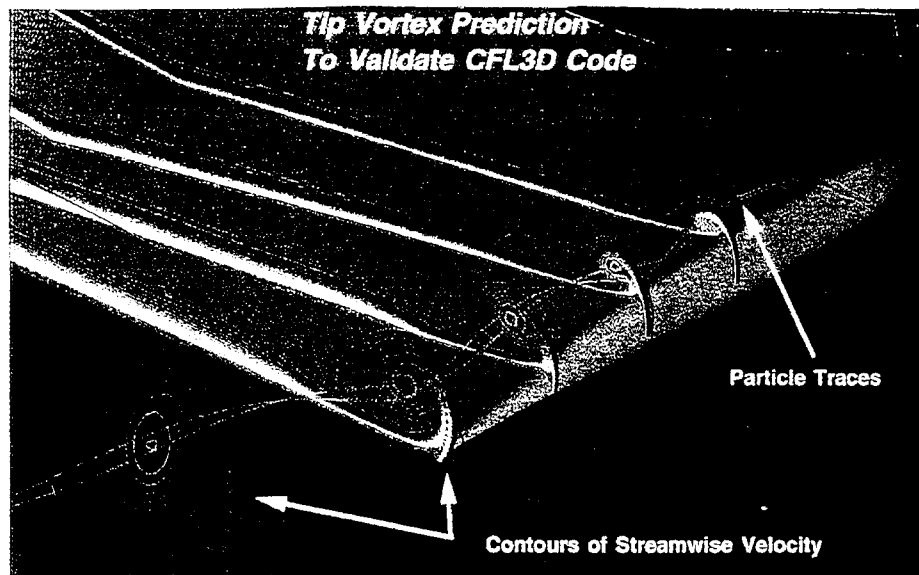


Fig. 14 Tip Vortex Prediction

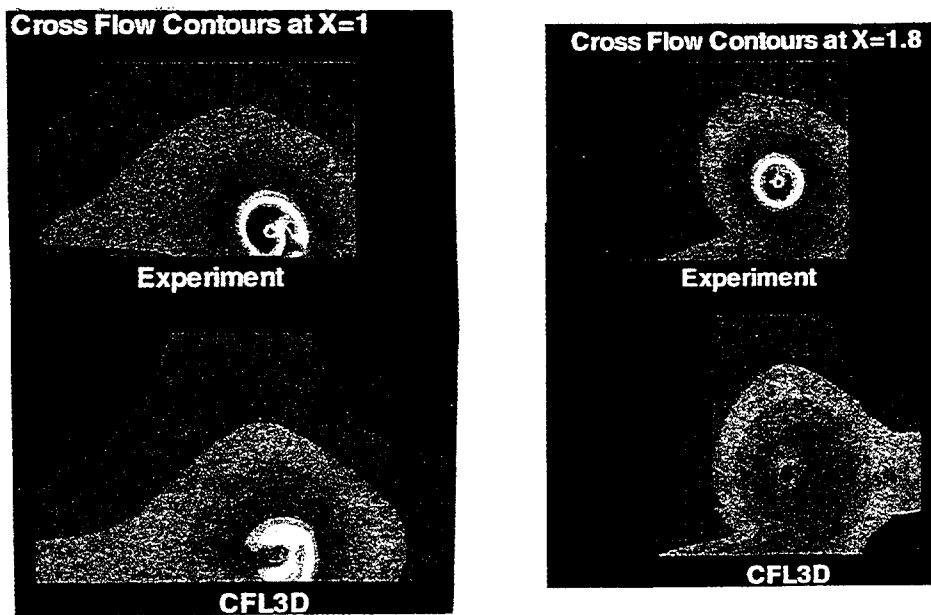


Fig. 15 Predicted Cross Flow Velocities Showing Tip Vortex Numerical Diffusion



Fig. 16 Higher Order Solution to Reduce Vortex Numerical Diffusion

Present Capabilities of Predicting Two-Dimensional Dynamic Stall

J. A. Ekaterinaris
Navy-NASA Joint Institute of Aeronautics
Naval Postgraduate School
Monterey, California 93943-5000, U. S. A.

G. R. Srinivasan
Sterling Software
NASA Ames Research Center
Moffett Field, California 94035-1000, U. S. A.

W. J. McCroskey
U.S. Army Aeroflightdynamics Directorate-ATCOM
NASA Ames Research Center
Moffett Field, California 94035-1000, U. S. A.

Abstract

The current status of computational methods in predicting dynamic stall is summarized. Computed results for unsteady, attached and separated, turbulent flows over airfoils undergoing oscillatory motion are presented. The compressible form of the Reynolds-averaged Navier-Stokes equations is used. Numerical integration of the governing equations is performed with an approximately factorized algorithm. The inviscid fluxes are evaluated using both central differences and an upwind-biased method. The ability of several turbulence models, widely used for the prediction of steady flows, is tested for the unsteady flows. Solutions computed with algebraic, one-equation, and two-equation turbulence models are compared with experimental data. For the fully turbulent flows with tripped boundary layer most turbulence models predict lift hysteresis reasonably well. Some turbulence models give good qualitative agreement with the measured drag and pitching moment hysteresis loops. The computed results for untripped flows, where a small transitional region at the leading edge exist, show that the key to the accurate prediction of the unsteady loads at stall conditions is the modeling of this transition region at the leading edge. A simplified criterion for the transition onset is used, and the transitional flow region is computed with a modified form of the turbulence model. The computed solutions, where the transitional flow region is included, show that the small laminar/transitional separation bubble formed during the pitch-up motion has a decisive effect on the near wall flow and the development of the unsteady loads. Finally, the numerical solutions show some sensitivity to the kind of numerical algorithm used despite the reasonably fine grids used.

Introduction

The term "dynamic stall" usually refers to the unsteady separation and stall phenomena of aerodynamic bodies or lifting surfaces that are forced to execute time-dependent (unsteady) ramp or oscillatory motion. It is a complex fluid dynamic phenomenon of practical importance and occurs on retreating blades of helicopter rotors, maneuvering aircraft wings, wind turbine blades, and compressor cascades. As summarized in extensive reviews by McCroskey (Refs. 1-2) and Carr (Ref. 3), the majority of the work on this fundamental fluid dynamic problem is devoted to the case of airfoils oscillating with moderate amplitude in a uniform freestream. Quantitative information for dynamic stall of airfoils and wings in the form of unsteady surface pressure coefficients and integrated loads exists in the experimental investigations of Refs. 4-11. The experiments of Ref. 4 are for a wide variety of two-dimensional oscillating airfoils spanning the wind tunnel walls, at a low Mach number compressible flow regime $0.1 \leq M_\infty \leq 0.3$, and various reduced frequencies. These measurements have been used by many investigators as a test case to validate numerical results. In Ref. 5 two- and three-dimensional dynamic stall measurements over a wing with NACA 0015 cross sections have been obtained for $M_\infty = 0.3$. In Ref. 6 measurements on a pitching and oscillating NACA 0012 have been reported for a wide range of free stream speeds. In Ref. 7 unsteady measurements for an oscillating and pitching Sikorsky SC-1095 airfoil have been reported. Three-dimensional dynamic stall measurements for swept and upswept wings have been reported in Refs. 8 and 9. Measurements for pitching airfoils and wings have been also reported in Refs. 10 and 11, respectively.

The physics of dynamic stall has also been investigated by flow visualization studies. Freymuth¹² performed smoke visualization studies for pitching airfoils in low speed incompressible flow. Recent experimental investigations^{13,14} for $0.2 \leq M_\infty \leq 0.4$ provide unsteady schlieren and Particle Diffraction Interferometry (PDI) flowfield visualization, as well as unsteady field pressures and Laser Doppler Velocimetry (LDV) measurements.

The distinctive feature of dynamic stall is that when the airfoil reaches fairly high angles of attack during a ramp motion or an oscillatory cycle, past the static stall angle limit, the generated unsteady flowfield is characterized by massive unsteady separation and formation of large-scale vortical structures. One important difference between this flowfield structure and that generated by the static stall is the large hysteresis in the unsteady separation and reattachment. As a result, the maximum values of lift, drag, and pitching-moment coefficients can greatly exceed their static counterparts, and not even the qualitative behavior of these can be reproduced by neglecting the unsteady motion of the body surface (airfoil or wing). Usually, dynamic stall is manifest by a steep decrease of the pitching moment and increase of the drag coefficients. This feature of dynamic stall often leads to the initiation of stall flutter. Stall flutter of helicopter blades, propellers and turbomachinery blades is an important problem in the design and development of modern helicopter and propulsion systems. Carta and Lorber¹⁵ performed an experimental study of the aerodynamics of incipient torsional stall flutter of propeller blades and found that small amplitude oscillations near stall may be extremely unstable.

Two different physical mechanisms that may initiate dynamic stall are leading edge separation and trailing edge separation. In both cases the occurrence and progression of dynamic stall depends on a large number of parameters. The important ones are reduced frequency or pitch rate, the airfoil shape, the Mach number, amplitude of oscillations, type of motion (ramp or oscillatory), Reynolds number, three-dimensional effects, and wind tunnel effects. To date most of the research in this area has been performed for the simpler model problems of two-dimensional oscillating airfoils. As a result most of what is understood about the characteristics and various regimes of dynamic stall has essentially come from experimental observations, which are mostly two-dimensional. Attempts to calculate the quantitative effects of dynamic stall abound in the literature (Refs. 16-28). The purely laminar case seems to have been solved (Refs. 16-18), although recent studies (Ref. 18) show small-scale details of possible importance. However, the laminar calculations have not been validated with experiments, because purely laminar data are unavailable. The flows with turbulent boundary layers have not yet been successfully predicted.

In this paper turbulent and transitional flows over oscillating airfoils are computed. Numerical solutions

are obtained with both a central difference method with added artificial dissipation and an upwind-biased numerical method based on Osher (Ref. 29) upwind scheme. Time integration is performed with a factored iterative algorithm. The weak link in the computational methods for an accurate simulation of these unsteady flowfields is the turbulence modeling. Of course, the transitional nature of the boundary layer has always been neglected; instead the flow is approximated to be either completely laminar or completely turbulent on the airfoil surface. It was found in Ref. 40 that such an approximation is not correct if the flowfield is dominated by leading-edge separation. In any case, a reasonably good turbulence model must be used to accurately calculate the nonequilibrium nature of the separated turbulent boundary layer and the associated unsteady time-lag features. Simple algebraic eddy viscosity models, such as the Cebeci-Smith model³⁰ or the Baldwin-Lomax model,³¹ have been found to be inadequate. The objective here is to identify a reasonably accurate and robust turbulence model. Several turbulence models that are in use in most Computational Fluid Dynamics (CFD) codes are considered for evaluation. It should be noted that other studies²²⁻²⁷ have also considered a similar exercise.

The following turbulence models are considered in the present study. The Baldwin-Lomax (B-L) algebraic model,³¹ the Renormalization Group (RNG) based algebraic model,³² the half-equation Johnson-King (J-K) model,^{33,34} which has been very successful in computing steady separated flows, the recently developed one-equation Baldwin-Barth (B-B) model,³⁵ and the one-equation Spalart-Allmaras (S-A) model.³⁶ In addition the two-equation $k - \epsilon$ ³⁷ and $k - \omega$ ³⁸ models, with the modification proposed by Menter³⁹ in order to overcome free stream dependency inherent in the original $k - \omega$ model, are also tested. The performance of all these models is evaluated for accuracy and robustness by using them to calculate the unsteady, two-dimensional, viscous, flowfields of an oscillating NACA 0015 wing. The accuracy of the calculated results is determined by comparison with the oscillating-wing experimental data (Ref. 5) measured at the U. S. Army Aeroflightdynamics Directorate at NASA Ames Research Center. The eventual objective is to use the turbulence model that calculates the unsteady boundary layer and flow physics accurately to simulate the three-dimensional dynamic stall of oscillating wing and the retreating blade stall of a helicopter rotor blade.

Recent experimental (Ref. 14) and numerical studies (Ref. 40) of airfoil flows, for a range of Reynolds number from 0.5×10^5 to 1.0×10^6 , have shown that the effect of the leading edge transitional flow region is of primary importance to the overall development of the suction side viscous flow region. Laminar/transitional separation bubbles form near the airfoil leading edge for angles of incidence as low as six degrees and alter significantly the suction side

pressure distribution and the boundary layer formation. These observations of the low Reynolds number flow behavior stimulated our interest to investigate the effect of transitional flow on dynamic stall at a higher Reynolds number of $Re_c = 4.0 \times 10^6$.

Initially, the flow over an oscillating NACA 0012 airfoil of Ref. 4 was computed with the upwind-biased scheme as fully turbulent. The solution showed poor agreement with the measured loads, especially for the downstroke where not even qualitative agreement was obtained. Similar observations and drag coefficients were obtained. Similar observations were made in Refs. 25 and 26 where only algebraic and half-equation models have been used. In these references the computations were performed at a slightly larger amplitude of oscillation than the experiment. In these investigations the larger oscillation amplitude was employed in order to force the flow to separate enough and to obtain a hysteresis loop. Numerical experiments (Ref. 28) have also demonstrated that certain turbulence models may reproduce the lift and pitching moment hysteresis loops quite closely when the amplitude of the oscillation is increased. However, the predicted drag hysteresis does not agree with the experiment and the surface pressure history during the downstroke has large deviations from the experimental values.

In this paper it is demonstrated that it is important to take into account the leading edge transitional flow not only for the lower Reynolds number regime but also for the high Reynolds number. Solutions are computed where the leading edge transitional region is modeled. For the high Reynolds number regime, transition is expected to occur very close to the leading edge immediately after the adverse pressure gradient region is encountered. The extent of the transition region and the separation bubble is also expected to be very small. For the low Reynolds number regime $Re = 0.1 \times 10^6$ to 1.0×10^6 experimental investigations (Ref. 41) have shown that transition occurs downstream of the leading edge suction peak, sometimes in the vicinity of the midchord or close to the trailing edge depending on the airfoil shape and the Reynolds number. Reliable prediction of the location of transition onset for these cases requires more sophisticated analysis which is still in the development stage, even for steady flows. Modeling of the transitional region for these cases presents a difficult problem because the extent of the transitional region is large. On the other hand, predictions of the transitional region for complex geometries with Navier-Stokes methods requires enormous computational effort. Application of the recently developed Parabolized Stability Equation (PSE) method (Refs. 42-43) is more promising for these cases. Therefore, the high Reynolds number case was chosen in the present study to demonstrate the effect of transition on the prediction of dynamic stall.

A simplified criterion for the onset of transitional region is used. Furthermore, an effective eddy viscosity for the transitional flow region is obtained from the

same turbulence model which is used for the computation of the turbulent flow. The computed results for an oscillating airfoil show that modeling of the transitional flow near the leading edge decisively changes the character of the pitching moment hysteresis loop. The results show that the initial part of the downstroke of the oscillatory cycle is in close agreement with the experiment for the lift, pitching moment, and drag hysteresis loops. However, the prediction of the development of the flow during the remainder of the downstroke still shows substantial deviations from the experiments.

GOVERNING EQUATIONS

The governing equations are the Reynolds-averaged, two-dimensional, Navier-Stokes equations considered in strong conservation-law form. These can be written in a generalized body-conforming curvilinear coordinate system (ξ, η, τ) as follows:

$$\partial_\tau \hat{Q} + \partial_\xi \hat{F} + \partial_\eta \hat{G} = \frac{1}{Re} \partial_\eta \hat{S} \quad (1)$$

where $\xi = \xi(x, y, t)$, $\eta = \eta(x, y, t)$, $\hat{Q} = Q/J$, and $Q = (\rho, \rho u, \rho v, e)^T$ is the vector of conserved variables, and \hat{F} , \hat{G} are the inviscid flux vectors given by

$$\hat{F} = \frac{1}{J} \begin{pmatrix} \rho U \\ \rho u U + \xi_x p \\ \rho v U + \xi_y p \\ (e + p)U - \xi_t p \end{pmatrix}, \quad \hat{G} = \frac{1}{J} \begin{pmatrix} \rho V \\ \rho u V + \eta_x p \\ \rho v V + \eta_y p \\ (e + p)V - \eta_t p \end{pmatrix}$$

The vector \hat{S} is the viscous stress vector in the η direction and is considered in the thin layer approximation. It is written as

$$\hat{S} = \frac{1}{J} \begin{pmatrix} 0 \\ \mu m_1 u_\eta + (\mu/3) m_2 \eta_x \\ \mu m_1 v_\eta + (\mu/3) m_2 \eta_y \\ \mu m_1 m_3 + (\mu/3) m_2 m_4 \end{pmatrix}$$

where

$$\begin{aligned} m_1 &= \eta_x^2 + \eta_y^2 \\ m_2 &= \eta_x u_\eta + \eta_y v_\eta \\ m_3 &= \left(\frac{1}{2}\right) \frac{\partial}{\partial \eta} (u^2 + v^2) + \frac{1}{Pr(\gamma - 1)} \left(\frac{\partial a^2}{\partial \eta}\right) \\ m_4 &= \eta_x u + \eta_y v \end{aligned}$$

where U and V are the contravariant velocity components and ξ_x , ξ_y , η_x , η_y , ξ_t , and η_t are the coordinate transformation matrices.

In the above equations all geometrical dimensions are normalized with the airfoil chord length, c , the Cartesian velocity components, u and v are scaled by

the freestream sound speed a_∞ , and the time t is normalized as tc/a_∞ ; p is the static pressure normalized by $\rho_\infty a_\infty^2$; ρ is the density normalized by free-stream density ρ_∞ ; e is the total energy per unit volume normalized by $\rho_\infty a_\infty^2$; a is the speed of sound; Re is the Reynolds number; Pr is the Prandtl number; γ is the ratio of specific heats; and μ is the viscosity coefficient normalized by its free-stream value. The pressure is related to the density and total energy through the equation of state for an ideal gas,

$$p = (\gamma - 1)[e - \rho(u^2 + v^2)/2] \quad (2)$$

The rotational speed ω is obtained from the type of motion prescribed as $\omega = d\alpha/dt$. The reduced frequency parameter is defined as either $k = \dot{\alpha}c/2U_\infty$ or $\pi fc/U_\infty$, where f is the frequency of oscillation and U_∞ is the free-stream velocity. Then $\omega = \alpha_1(2kU_\infty/c)\cos[(2kU_\infty/c)t]$ for $\alpha(t) = \alpha_0 + \alpha_1\sin(Kt)$ where α_0 is the mean angle of oscillation, and α_1 is the amplitude of the pitch.

NUMERICAL SCHEME

Central Difference Scheme

The finite-difference, implicit, approximately factorized Beam-Warming algorithm is used to integrate the governing equations. Central differences are used to compute the inviscid fluxes. The viscous terms are treated implicitly. The approximately factored algorithm is given by

$$\begin{aligned} & \left\{ I + h[\delta_\xi \hat{A}_{i,j}^n + (D_{imp})_i] \right\}^p \times \\ & \left\{ I + h[\delta_\eta \hat{B}_{i,j}^n - Re^{-1}\delta_\eta \hat{M}_{i,j}^n + (D_{imp})_j] \right\}^p \Delta \hat{Q}_{i,j}^p \\ & = - \left\{ \hat{Q}_{i,j}^p - \hat{Q}_{i,j}^n + \Delta t[\delta_\xi \hat{E}_{i,j}^n + \delta_\eta \hat{F}_{i,j}^n - \delta_\eta \hat{S}_{i,j}^n] \right. \\ & \quad \left. + \epsilon_e D_{i,j}^n \right\} \end{aligned} \quad (3)$$

Here δ is the central difference operator and h is the time-step factor that determines whether the algorithm is first- or second-order time accurate. The time index is denoted by n and $\Delta \hat{Q}_{i,j}^n = (\hat{Q}_{i,j}^{n+1} - \hat{Q}_{i,j}^n)$. The explicit inviscid fluxes are given by $\hat{E}_{i,j}$, $\hat{F}_{i,j}$ and $\hat{S}_{i,j}$ is the viscous flux. The quantities \hat{A} , \hat{B} , and \hat{M} in Eq. (3) are flux Jacobian matrices obtained from the linearization of the left hand side and D_{imp} and $\epsilon_e D$ denotes the implicit and explicit dissipation terms, respectively. A Jameson-type⁴⁴, blended second- and fourth-order numerical dissipation, based on the computed pressure field, is used to suppress high frequency numerical oscillations. For subsonic shock free solutions only the fourth-order dissipation is used, while for transonic solutions the second-order dissipation is activated in the vicinity of

shocks where the pressure jump has steep gradients. Both the implicit and explicit dissipation are scaled by the spectral radius. For the accuracy of calculated solutions, the added dissipation coefficients are kept as small as possible.

Upwind-Biased Scheme

The following upwind-biased, factorized, iterative, implicit numerical scheme is used to compute the Reynolds-averaged flow.

$$\begin{aligned} & [I + h_\xi(\nabla_\xi^b \tilde{A}_{i,k}^+ + \Delta_\xi^f \tilde{A}_{i,k}^-)]^p \\ & \times [I + h_\eta(\nabla_\eta^b \tilde{B}_{i,k}^+ + \Delta_\eta^f \tilde{B}_{i,k}^- \\ & - Re^{-1}\delta_\eta \tilde{M}_{i,k})]^p \times (\tilde{Q}_{i,k}^{p+1} - \tilde{Q}_{i,k}^p) \\ & = -[(\tilde{Q}_{i,k}^p - Q_{i,k}^n) + h_\xi(\hat{F}_{i+1/2,k}^p - \hat{F}_{i-1/2,k}^p) \\ & + h_\eta(\hat{G}_{i,k+1/2}^p - \hat{G}_{i,k-1/2}^p) \\ & - Re^{-1}h_\eta(\hat{S}_{i,k+1/2}^p - \hat{S}_{i,k-1/2}^p)] \end{aligned} \quad (4)$$

In this equation, $h_\xi = \Delta\tau/\Delta\xi$, etc., $\Delta\xi$, $\Delta\eta$, etc., are equal to unity, $\tilde{A}^\pm = (\partial\tilde{F}/\partial\tilde{Q})$, etc., are the flux Jacobian matrices, and Δ , ∇ , and δ are the forward, backward and central difference operators, respectively. The quantities $\tilde{F}_{i+1/2,k}$, $\tilde{G}_{i,k+1/2}$, and $\tilde{S}_{i,k+1/2}$ are numerical fluxes.

The inviscid fluxes \hat{F} and \hat{G} are evaluated using Osher's²⁹ upwinding scheme. The numerical fluxes for a third-order accurate upwind-biased scheme are given by

$$\begin{aligned} \tilde{F}_{i+1/2,k} &= \tilde{F}_{i+1/2,k} + \frac{1}{6} \left[\Delta F_{i-1/2,k}^+ + 2\Delta F_{1+1/2,k}^+ \right] \\ & - \frac{1}{6} \left[\Delta F_{i+3/2,k}^- + 2\Delta F_{1+1/2,k}^- \right] \\ & = \tilde{F}(Q_{i,k}, Q_{i+1,k}) + \frac{1}{6} \left[\Delta F^+(Q_{i+1,k}, Q_{i,k}) \right. \\ & \quad \left. + 2\Delta F^+(Q_{i,k}, Q_{i+1,k}) \right] \\ & - \frac{1}{6} \left[\Delta F^-(Q_{i,k}, Q_{i+1,k}) \right. \\ & \quad \left. + 2\Delta F^-(Q_{i+1,k}, Q_{i,k}) \right] \end{aligned} \quad (5)$$

Here, \tilde{F} is the first-order accurate numerical flux evaluated by Osher's scheme²⁹ as follows:

$$\tilde{F}_{i+1/2,k} = \frac{1}{2} \left[F_{i,k} + F_{i+1,k} - \int_{Q_i}^{Q_{i+1}} \{F_q^+ - F_q^-\} dQ \right] \quad (6)$$

where $F_q = F_q^+ + F_q^-$, $F_q^\pm = (\partial F/\partial Q)^\pm$, and ΔF^\pm are the corrections to obtain high-order accuracy. For

the linearization of the left-hand side terms, the flux Jacobian matrices A , B are evaluated by the Steger-Warming⁴⁵ flux-vector splitting. The viscous fluxes $S_{i,k+1/2}$ are computed with central differences.

For both schemes, the errors introduced by the linearization and approximate factorization of the left hand side of the numerical algorithm may be minimized by performing Newton subiterations at each time-step during the unsteady calculations. The approximation to \tilde{Q}^{n+1} at each subiteration is the quantity \tilde{Q}^p . When $p \geq 2$, during a given level of subiteration to convergence, $\tilde{Q}^p = \tilde{Q}^{n+1}$, but when $p = 1$ and no subiterations are performed, then $\tilde{Q}^p = \tilde{Q}^n$, and $\tilde{Q}^{p+1} = \tilde{Q}^{n+1}$. In the present study, the numerical experiments have demonstrated that because of the small time-steps used, the Newton subiterations are not required. It was also found that the two time-level numerical scheme does not increase the accuracy of the unsteady calculations.

In the normal practice of the thin layer approximation for viscous terms, only the terms in the normal direction (\hat{S}) are retained because of the large flow gradients in that direction. Calculations performed retaining the viscous terms for the η direction alone and keeping terms for both the ξ and η directions showed very little difference between the solutions. Therefore, all calculations are performed by retaining the viscous terms only in the η direction. The computational cost was not significantly increased for keeping explicit viscous terms in both directions. However, numerical experiments have demonstrated that implicit treatment of the viscous term, \hat{M} of Eq. 3, does not contribute to the accuracy of the solution but results in increased computational cost.

Body-fitted C-type computational grids are used in all calculations. These are generated using a hyperbolic grid generator. The grids are clustered at the body surface in the normal direction, leading edge, and trailing edge regions. The spacing of the first grid point at the surface in the normal direction varied from 0.00002 to 0.000005 chord length and the grid boundaries are located at 15 chords in all directions. The orientation of the moving frame with respect to the fixed frame is changing at each instant of time. Therefore, after the grid is moved to the new location at each time step all metrics are recomputed.

Boundary conditions are updated explicitly. For subsonic inflow-outflow, the flow variables at the boundaries are evaluated using one-dimensional Riemann invariant extrapolation. For the density, a simple first-order extrapolation is used. On the body surface a nonslip condition is applied for the velocities, viz., the contravariant velocities in the body-fixed coordinates are set to zero. It should be noted that the surface velocity is non-zero in inertial coordinates because of the body motion. For C-type grids used in

this study averaging of the flow variables at the wake cut is used.

TURBULENCE MODELS

All flows computed in this part of the study are assumed to have fully turbulent boundary layers on both the upper and lower surfaces of the airfoil, by neglecting the laminar and transitional boundary layer. In the experiments of Piziali,⁵ with which these calculations are compared, the boundary layer is tripped in the leading-edge region. For turbulent viscous flows, the non-dimensional viscosity μ in the viscous flux vectors is calculated as the sum total of the laminar and turbulent viscosity. It is the determination of this turbulent viscosity that is of special significance and the focal point of this present study. Two algebraic turbulence models, the Johnson-King^{33,34} model, the Baldwin-Barth³⁵ and the Spalart-Allmaras³⁶ one equation models, as well as, two-equation turbulence models are used for calculating turbulent eddy viscosity and the unsteady flowfield of an oscillating NACA 0015 airfoil. The results are used to evaluate their performance. The details of how these models are developed are described elsewhere.³¹⁻³⁹ The following paragraphs describe briefly the salient features of these models and the specific versions used in the present investigation.

Algebraic models

Baldwin-Lomax (B-L) model

This is a two-layer, zero-equation model. It is patterned after Cebeci-Smith model³⁰ and introduces a modification that eliminates the need to search for the edge of the boundary layer to determine length scale. It is the most commonly used turbulence model available in most of the CFD codes. Its strength and weakness are well known in CFD community; it predicts accurately the steady flows with little or no separation and fares poorly if there is large separation, either shock-induced or otherwise. It uses an inner and outer layer formulation for determining the turbulent viscosity with a smooth transition that spreads over the two regions. It uses a classical mixing-length hypothesis for the inner layer with a van Driest damping function to force the eddy viscosity at the wall to zero. In the outer layer, the length scale is fixed by the location where the product of distance from the solid wall and vorticity reaches a maximum in the boundary layer. The Klebanoff intermittency factor is used to drive the eddy viscosity to zero in the outer flow away from the wall. Some of the constants of the theory are determined by correlating with experimental data. The details of the theory are described in Ref. 31.

RNG model

This is another algebraic eddy viscosity model, proposed recently for the closure of the Reynolds averaged Navier-Stokes equations. It is based on the Renormalization Group (RNG) theory of turbulence³². The model, although free from uncertainties related to the experimental determination of empirical modeling constants, still requires specification of an integral length-scale of turbulence, similar to the B-L model, which reduces the generality of the model. In this model the integral scale is assumed to be proportional to the boundary layer thickness δ , and the kinematic eddy viscosity is obtained by

$$\nu = \nu_l \left[1 + H \left\{ \frac{\hat{a}}{\nu_l^3} \phi \left(\frac{1}{y} + \frac{1}{0.225\delta} \right)^{-4} - C_c \right\} \right]^{\frac{1}{3}} \quad (7)$$

where $\nu = \nu_t + \nu_l$, the subscripts t and l refer to the turbulent and laminar components, respectively and δ is the boundary layer thickness. It is determined as $\delta = 1.2 y_{1/2}$ where $y_{1/2}$ is the normal distance from the wall at which the vorticity function $F(y)$ (see Ref. 34) attains its half amplitude. H is the Heaviside step function and ϕ is the dissipation rate, which is determined by assuming production equals dissipation for equilibrium flows. The parameter $\hat{a} = 0.0192$ corresponding to the von Karman constant $\kappa = 0.372$ and the parameter $C_c = 75$. The turbulent eddy viscosity is then obtained by solving Eq. (7) at every point in the computational domain. In estimating the eddy viscosity with this model in this study, the model is applied only to the suction side of the airfoil (upper surface) while the pressure side (having attached flow) and wake regions are computed with the B-L model. Application of the model to both the upper and lower surfaces essentially gave the same results as the one obtained by applying for only upper surface; so the latter was used.

Half-equation Johnson-King (J-K) model

The above two models, viz., the B-L and RNG models, are termed equilibrium models, meaning that the eddy viscosity instantaneously adjusts to the local flow without any history effects. The next three models presented are called non-equilibrium models in which the calculated eddy viscosity accounts for the upstream history of the flow.

Since Johnson and King first introduced their half-equation turbulence model³³, there have been several modifications and/or enhancements to improve their original model for separated flows. In the present application to unsteady flows, the original version of this model is used and is briefly described in the following paragraphs.

The Johnson-King model takes into account the convection and diffusion effects on the Reynolds shear

stress $-\overline{u'w'}$ in the streamwise direction. The eddy viscosity is given by

$$\nu_t = \nu_{t_o} \left[1 - \exp\left(-\frac{\nu_{t_i}}{\nu_{t_o}}\right) \right] \quad (8)$$

where ν_{t_i}, ν_{t_o} describe the eddy viscosity variation in the inner and outer part of the boundary layer. The inner eddy viscosity is computed as

$$\begin{aligned} \nu_{t_i} &= D^2 \kappa y \sqrt{(-u'w')_{max}} \\ D &= 1 - e^{-(y/A^+)} \end{aligned} \quad (9)$$

where the constant $A^+ = 15$. The outer eddy viscosity is given by

$$\nu_{t_o} = \sigma(x) [0.0168 U_e \delta^* \gamma] \quad (10)$$

where δ^* is the boundary layer displacement thickness, γ is the Klebanoff intermittency function given by $\gamma = [1 + 5.5(\frac{y}{\delta})^6]^{-1}$, and $\sigma(x)$ is obtained from the solution of an ordinary differential equation which describes the development of $-\overline{u'w'}|_{max}$ along the path of the maximum shear stress. It should be noted that the Johnson-King model reduces to the Cebeci-Smith model³⁰ when $\sigma(x)$ is identically equal to one, except $A^+ = 15$ not 26.

The effects of convection and diffusion on the Reynolds shear stress development are accounted from the solution of the following ordinary differential equation

$$\begin{aligned} \frac{dg}{dx} &= \frac{a_1}{2\bar{u}_m L_m} \left\{ \left(1 - \frac{g}{g_{eq}} \right) + \right. \\ &\quad \left. \frac{C_{dif} L_m}{a_1 \delta [0.7 - (\frac{y}{\delta})_m]} \left[1 - \sqrt{\frac{\nu_{t_o}}{\nu_{t_o,eq}}} \right] \right\} \end{aligned} \quad (11)$$

Here C_{dif} and a_1 are modeling constants, \bar{u}_m is the maximum average mean velocity,

$$\begin{aligned} g &= [-\overline{u'w'}_m]^{-1/2}, \\ g_{eq} &= [-\overline{u'w'}_{m,eq}]^{-1/2} \end{aligned}$$

where L_m is the dissipation length evaluated as follows:

$$\begin{aligned} L_m &= 0.40y \quad \text{for} \quad y_m/\delta \leq 0.225 \\ L_m &= 0.09\delta \quad \text{for} \quad y_m/\delta \geq 0.225 \end{aligned} \quad (12)$$

The boundary layer thickness δ is determined in the same way³⁴ as explained in the discussion of RNG model. The equilibrium shear stress g_{eq} in Eq. 8 is determined from the following equilibrium eddy viscosity distribution

$$\begin{aligned} \nu_{t,eq} &= \nu_{t_o,eq} \left[1 - \exp\left(-\frac{\nu_{t_i,eq}}{\nu_{t_o,eq}}\right) \right] \\ \nu_{t_i,eq} &= D^2 \kappa y \sqrt{(-u'w')_{m,eq}} \\ \nu_{t_o,eq} &= 0.0168 U_e \delta^* \gamma \end{aligned} \quad (13)$$

where U_e is the velocity at the edge of the boundary layer.

An implicit Euler method is used for the numerical solution of Eq. 11, and the maximum shear stress at each iteration level is updated using

$$\sigma(x)^{n+1} = \sigma(x)^n \frac{\nu_{t_o}^{n+1}}{\nu_{t_o}^n} \quad (14)$$

It should be noted that the unsteady term is neglected in the above formulation. Solutions with the Johnson-King turbulence model are obtained as follows. First a convergent solution using the Baldwin-Lomax turbulence model for the entire flowfield is obtained. Then the Johnson-King model is applied only to the upper surface of the airfoil as using it for both the surfaces did not change the results. To initiate the solution $\sigma(x)$ in Eq. 10 is set unity and it is allowed to change according to Eq. 11. It should be noted that the Johnson-King model reduces to the Cebeci-Smith model²² when $\sigma(x)$ is identically equal to one.

One-Equation models

An attractive feature of one- and two-equation models is that they can be utilized in a more straightforward manner compared to algebraic models in either structured or unstructured flow solvers. However, the accuracy and the numerical robustness of these models needs to be further demonstrated. Among the most widely used one-equation models are the Baldwin-Barth³⁵ (B-B) and the Spalart-Allmaras³⁶ (S-A) models. The first model was derived from the two-equation $k - \epsilon$ model by introducing some simplifying assumptions. The Spalart-Allmaras model was developed based on dimensional analysis and empirical criteria. An advantage of these field-equation turbulence models compared to the algebraic and half-equation models is that they do not require evaluation of ambiguous length scales. On the other hand, one-equation models require numerical solution of only one partial differential equation; therefore, they are less computationally intensive compared to two-equation models. In this paper the standard versions of the Baldwin-Barth and Spalart-Allmaras models are used to compute steady and unsteady separated flows.

Baldwin-Barth (B-B) model

The eddy viscosity of the Baldwin-Barth one-equation model³⁵ is given by $\nu_t = \nu c_\mu f_\mu R_T = \nu c_\mu f_3 \tilde{R}_T$, where $R_T = k^2/\nu\epsilon$ is the turbulent Reynolds number and \tilde{R}_T is the modified turbulent Reynolds number. The quantity \tilde{R}_T is the solution of the following field equation

$$\begin{aligned} \frac{D(\nu \tilde{R}_T)}{Dt} &= (c_{\epsilon_2} f_2 - c_{\epsilon_1}) \sqrt{\nu \tilde{R}_T} P \\ &+ (\nu + \frac{\nu_t}{\sigma_\epsilon}) \nabla^2 (\nu \tilde{R}_T) \\ &- \frac{1}{\sigma_\epsilon} (\nabla \nu_t) \cdot \nabla (\nu \tilde{R}_T) \end{aligned}$$

This is a partial differential equation for the field quantity $R_T = \tilde{R}_T f_3(\tilde{R}_T)$, and

$$\begin{aligned} \frac{1}{\sigma_\epsilon} &= (c_{\epsilon_2} - c_{\epsilon_1}) \sqrt{c_\mu} / \kappa^2 \\ \nu_t &= c_\mu (\nu \tilde{R}_T) D_1 D_2 \\ \mu_t &= \rho \nu_t \\ f_\mu &= D_1 D_2 \\ D_1 &= 1 - \exp(-y^+ / A^+) \\ D_2 &= 1 - \exp(-y^+ / A_2^+) \\ P &= \nu_t \left(\frac{\partial U_i}{\partial x_j} + \frac{\partial U_j}{\partial x_i} \right) \frac{\partial U_i}{\partial x_j} - \frac{2}{3} \nu_t \left(\frac{\partial U_i}{\partial x_j} \right) \\ f_2(y^+) &= \frac{c_{\epsilon_1}}{c_{\epsilon_2}} + (1 - \frac{c_{\epsilon_1}}{c_{\epsilon_2}}) \left(\frac{1}{\kappa y^+} + D_1 D_2 \right) \\ &\quad \left\{ \sqrt{D_1 D_2} + \frac{y^+}{\sqrt{D_1 D_2}} \left(\frac{1}{A^+} \exp(-y^+ / A^+) D_2 \right. \right. \\ &\quad \left. \left. + \frac{1}{A_2^+} \exp(-y^+ / A_2^+) D_1 \right) \right\} \end{aligned}$$

where $y^+ = u_\tau y / \nu$ and u_τ is the skin friction velocity. The constants of the model are:

$$\begin{aligned} \kappa &= 0.41, \quad c_{\epsilon_1} = 1.2, \quad c_{\epsilon_2} = 2.0 \\ c_\mu &= 0.09, \quad A^+ = 26., \quad A_2^+ = 10. \end{aligned}$$

This model is applied to the entire flowfield to compute the eddy viscosity.

Spalart-Allmaras (S-A) model

The second one-equation model used is the Spalart-Allmaras (S-A) model³⁶. The eddy viscosity is obtained from the solution of the partial differential equation for $\tilde{\nu}$ given below.

$$\begin{aligned} \frac{D\tilde{\nu}}{Dt} &= c_{b1}(1 - f_{t2})\tilde{S}\tilde{\nu} \\ &+ \frac{1}{\sigma} \left[\nabla \cdot ((\nu + \tilde{\nu})\nabla \tilde{\nu}) + c_{b2}(\nabla \tilde{\nu})^2 \right] \\ &- \left[c_{w1}f_w - \frac{c_{b1}}{\kappa^2}f_{t2} \right] \left[\frac{\tilde{\nu}}{d} \right]^2 + f_{t1}\Delta U^2 \end{aligned}$$

here S is the vorticity magnitude and $\tilde{S} = S + \frac{\tilde{\nu}}{\kappa^2 d^2} f_{v2}$, $f_{v2} = 1 - \frac{\chi}{1 + \chi f_{v1}}$, $f_{v1} = 1 - \frac{\chi^3}{1 + \chi^3 + c_{v1}}$, $c_{v1} = 7.1$ and d is the distance to the closest wall. The other functions of the model are:

$$\begin{aligned} f_{t1} &= c_{t1} g_t \exp \left(-c_{t2} \frac{\omega_{tr}^2}{\Delta U^2} [d^2 + g_t^2 d_t^2] \right) \\ f_{t2} &= c_{t3} \exp(-c_{t4} \chi^2) \\ g_t &= \min(0.1, \Delta U / \omega_{tr} \Delta x) \end{aligned}$$

where $\chi = \bar{\nu}/\nu$ and ω_{tr} is used here to denote the vorticity at the wall at the boundary layer trip point. The constants of this model have been chosen the same as in the original reference³⁶. The constants of the model are:

$$\begin{aligned} c_{b1} &= 0.1355, \quad c_{b2} = 0.622, \quad \sigma = 2/3 \\ c_{w1} &= \frac{c_{b1}}{\kappa^2} + \frac{1 + c_{b2}}{\sigma}, \quad c_{w2} = 2.0, \quad c_{w3} = 0.3 \\ \kappa &= 0.41, \quad f_w = g \left(\frac{1 + c_{w3}}{g^6 + c_{w3}^6} \right)^{1/6} \\ g &= r + c_{w2}(r^6 - r), \quad r = \frac{\nu_t}{S\kappa^2 d^2} \\ c_{t1} &= 1.0, \quad c_{t2} = 2.0, \quad c_{t3} = 1.1, \quad c_{t4} = 2.0 \end{aligned}$$

The turbulent kinematic eddy viscosity is given as

$$\nu_t = \bar{\nu} f_{v1}$$

and the Reynolds shear stresses are given by $-\bar{u}_i \bar{u}_j = 2\nu_t \sigma_{ij}$.

Two-Equation models

The most popular non-algebraic turbulence models are two-equation eddy-viscosity models. These models solve two transport equations, one for the turbulent kinetic energy k and another one related to the turbulent length- (or time-) scale. Among the two-equation models, the $k - \epsilon$ model is the most widely used today. The original Jones and Launder $k - \epsilon$ model³⁷ and its variations have been very successful in a large variety of different flow situations, but it also has a number of well known shortcomings. From the standpoint of aerodynamics, the most disturbing is the lack of sensitivity to adverse pressure-gradients. Another shortcoming of the $k - \epsilon$ model is associated with the numerical stiffness of the equations when integrated through the viscous sublayer.

The $k - \omega$ model has been developed by Wilcox³⁸ to overcome the shortcomings of the $k - \epsilon$ model. This model solves one equation for the turbulent kinetic energy k and a second equation for the specific turbulent dissipation rate (or turbulence frequency) ω . The $k - \omega$ model performs significantly better under mild adverse pressure-gradient conditions than the $k - \epsilon$ model. Another strong point of the model is the simplicity of its formulation in the viscous sublayer. The model does not employ damping functions and has straightforward boundary conditions. This leads to significant advantages in numerical stability. The $k - \omega$ model has been validated extensively^{39,46} for many flow cases with and without adverse pressure gradient. For all cases it was found to perform equally well or better than the $k - \epsilon$ model. The major shortcoming of the $k - \omega$ model is that the results of the model depend strongly on the freestream values, ω_f , that are specified outside the shear-layer.

The free stream dependency of the original Wilcox $k - \omega$ model has been investigated in detail in Ref. 39, and it has been shown that the magnitude of the eddy viscosity can be changed by more than 100% just by using different values for ω_f . This is clearly unacceptable and corrections are necessary to ensure unambiguous solutions. The standard $k - \omega$ model developed by Wilcox has been modified in Ref. 39 so that the computed solutions are insensitive to the freestream values of ω_f . This modified model is called Baseline (BSL) $k - \omega$ model. The BSL $k - \omega$ model was further modified⁴⁷ in order to improve the predictions of strong adverse pressure gradient separated flows, this model is called Shear Stress Transport (SST) $k - \omega$ model. In this paper, the SST $k - \omega$ turbulence model will be extensively tested for unsteady flows. This model has been tested in Ref. 47 for a wide class of steady separated flows and has shown good agreement with experiments.

Original $k - \omega$ model

The original $k - \omega$ model is given by

$$\begin{aligned} \frac{D\rho k}{Dt} &= \tau_{ij} \frac{\partial u_i}{\partial x_j} - \beta^* \rho \omega k + \frac{\partial}{\partial x_j} \left[(\mu + \sigma_k^W \mu_t) \frac{\partial k}{\partial x_j} \right] \\ \frac{D\rho \omega}{Dt} &= \frac{\gamma^W}{\nu_t} \tau_{ij} \frac{\partial u_i}{\partial x_j} - \beta \rho \omega^2 + \frac{\partial}{\partial x_j} \left[(\mu + \sigma_\omega^W \mu_t) \frac{\partial \omega}{\partial x_j} \right] \end{aligned}$$

The constants of the original Wilcox model are

$$\begin{aligned} \sigma_k^W &= 0.5, \quad \sigma_\omega^W = 0.5, \quad \beta^W = 0.0750, \\ \beta^* &= 0.09, \quad \kappa = 0.41, \quad \gamma^W = \beta^W / \beta^* - \sigma_\omega^W \kappa^2 / \sqrt{\beta^*} \end{aligned}$$

BSL $k - \omega$ model

The BSL model is identical to the $k - \omega$ model of Wilcox³⁸ for the inner region of a boundary layer (up to approximately $\delta/2$) and gradually changes to the standard $k - \epsilon$ model in the outer wake region. In order to enable computations with one set of equations, the $k - \epsilon$ model was first transformed into a $k - \omega$ formulation. The blending between the two regions is performed by a blending function that gradually changes from one to zero in the desired region. No a priori knowledge of the flowfield is necessary to perform the blending. The function also ensures that the $k - \epsilon$ formulation is selected for free shear layers. The performance of the new (BSL) model is very similar to that of the Wilcox $k - \omega$ model for adverse pressure gradient boundary-layer flows (and therefore better than that of the $k - \epsilon$ model), but without the undesirable freestream dependency. For free shear layers the new model is basically identical to the $k - \epsilon$ model, which predicts spreading rates more accurately than the $k - \omega$ model. The Baseline $k - \omega$ model is

$$\begin{aligned}\frac{D\rho k}{Dt} &= \tau_{ij} \frac{\partial u_i}{\partial x_j} - \beta^* \rho \omega k + \frac{\partial}{\partial x_j} \left[(\mu + \sigma_k \mu_t) \frac{\partial k}{\partial x_j} \right] \\ \frac{D\rho \omega}{Dt} &= \frac{\gamma}{\nu_t} \tau_{ij} \frac{\partial u_i}{\partial x_j} - \beta \rho \omega^2 + \frac{\partial}{\partial x_j} \left[(\mu + \sigma_\omega \mu_t) \frac{\partial \omega}{\partial x_j} \right] \\ &\quad + 2(1 - F_1) \rho \sigma_\omega \frac{1}{\omega} \frac{\partial k}{\partial x_j} \frac{\partial \omega}{\partial x_j}\end{aligned}$$

where the constants of the model are computed as $\phi = F_1 \phi^W + (1 - F_1) \phi^K$ where F_1 is a blending function as defined in Ref. 39 and ϕ^W and ϕ^K the constants for the original $k - \omega$ and the $k - \epsilon$ model, respectively. The following standard values for the $k - \epsilon$ model are used,

$$\begin{aligned}\sigma_k^K &= 1.0, \quad \sigma_\omega^K = 0.856, \quad \beta^K = 0.0828, \\ \beta^* &= 0.09, \quad \kappa = 0.41, \quad \gamma^K = \beta^K / \beta^* - \sigma_\omega^K \kappa^2 / \sqrt{\beta^*}\end{aligned}$$

corresponding to the constants $C_{\epsilon 1} = 1.4$, $C_{\epsilon 2} = 1.92$ of the $k - \epsilon$ model.

$k - \epsilon$ model

The $k - \epsilon$ model implemented here is based on the same formulation as the BSL model, except that the switch from the Wilcox model, constants ϕ^W , to the $k - \epsilon$ model, constants ϕ^K , takes place not in the wake region of the boundary layer but just outside the viscous sublayer. With this formulation, the Wilcox model is only used as a sublayer model and the model is referred to as a two-layer $k - \epsilon$ model.

SST $k - \omega$ model

Although the original and the new BSL $k - \omega$ model perform better in adverse pressure gradient flows than the $k - \epsilon$ model, they still underpredict the amount of separation for severe adverse pressure gradient flows.⁴⁶ In an attempt to improve matters, the eddy-viscosity formulation of the BSL model is modified to account for the transport effects of the principal turbulent shear stress. The motivation for this modification comes from the Johnson-King (J-K) model³³ which has proven to be highly successful for adverse pressure gradient flows. The J-K model is based on the assumption that the turbulent shear stress is proportional to the turbulent kinetic energy in the logarithmic and wake regions of a turbulent boundary layer. Johnson and King solve an equation for the maximum turbulent shear stress at each downstream station and limit the eddy viscosity in order to satisfy this proportionality. In the framework of two-equation models, the turbulent kinetic energy is already known and it is therefore only necessary to limit the eddy viscosity to account for the same effect. The resulting model is called Shear Stress Transport (SST) model. For the SST $k - \omega$ model, the constants ϕ^W of the BSL model are replaced by the constants ϕ^S as follows:

$$\begin{aligned}\sigma_k^S &= 0.85, \quad \sigma_\omega^S = 0.5, \quad \beta^S = 0.0750, \quad \alpha = 0.31 \\ \beta^* &= 0.09, \quad \kappa = 0.41, \quad \gamma^S = \beta^S / \beta^* - \sigma_\omega^S \kappa^2 / \sqrt{\beta^*}\end{aligned}$$

The same convention of $\phi = F_1 \phi^S + (1 - F_1) \phi^K$ is used here. The eddy viscosity is given by

$$\nu_t = \frac{a_1 k}{\max(\alpha \omega; \Omega F_2)}$$

where Ω is the vorticity magnitude and $F_2 = \tanh(\arg_2^2)$ with $\arg_2 = \max(2 \frac{\sqrt{k}}{0.09 \omega y}, \frac{500 \nu}{y^2 \omega})$

RESULTS AND DISCUSSION

Fully Turbulent Tripped Unsteady Flows

For validation of unsteady, fully turbulent solutions, the experimental measurements of Ref. 5 for a NACA 0015 airfoil are used, because in this experiment, as opposed to that of Ref. 13, the boundary layer was tripped at the leading edge to ensure a fully turbulent boundary layer for attached, light stall and deep stall cases. Oscillatory motions at sufficiently high angles of incidence include both flow separation during the upstroke and flow reattachment during the downstroke and they serve as a good test case for validation of turbulence models. The free stream Mach number is $M_\infty = 0.3$ and the Reynolds number, based on the airfoil chord length is, $Re_c = 2 \times 10^6$.

The airfoil oscillates as $\alpha(t) = \alpha_0 + \alpha_1 \sin(\omega t)$ with a reduced frequency $k = 0.1$. The oscillation amplitude remains fixed at $\alpha_1 = 4.2^\circ$ and variation of the mean angle α_0 leads to different flow regimes. Attached flow corresponds to $\alpha_0 = 4^\circ$. The light and deep stall regimes are obtained for $\alpha_0 = 11^\circ$, and $\alpha_0 = 15^\circ$, respectively. The discussion of unsteady results is divided into these three flow regimes. After calculating the quasi-steady solution at the lowest angle of the pitch cycle for each of the conditions, the airfoil is made to execute pitching oscillations rotating about its quarter-chord point. The unsteady flow evolution is monitored. Generally two oscillatory cycles are computed for every case because the results from the third cycle was found to be nearly the same as the second cycle.

The results obtained with the central-difference scheme were calculated using a 361×71 point C-grid. The first point off the surface is located at 0.00002 chord lengths. A complete oscillation cycle is normally computed with 10,000 constant time-steps. This number of time-steps per cycle corresponds to a nondimensional time-step of $\Delta t = 0.0108$, based on c and a_∞ . An explicit dissipation coefficient of $\epsilon_e = 0.05$ was used as the standard value. A parametric study of the grid size, the value of ϵ_e , and number of time-steps per cycle has also been done for one turbulence model, for the light-stall case, to

identify optimum values to be used for all calculations and this discussion is presented in the section on the light-stall. Solutions are computed with the B-L, algebraic RNG, J-K, B-B, and S-A models for all of these cases.

Solutions are computed with the upwind-biased scheme on a baseline 311×91 point C-grid where the first point off the surface is located 0.00001 chord lengths. A grid refinement study was performed using a 421×151 point grid where the distance of the first point from the surface is 0.000005 chord lengths. Different number of time steps for a cycle was tested, and it was found that solutions for the light stall obtained with 10000, 16000 and 40000 time steps gave nearly identical load predictions. The results presented here are obtained using 16000 time steps, which correspond to a nondimensional time step $\Delta t \approx 0.0065$ or a Courant number $Cu \approx 700$.

It should be noted that in spite of using reasonably fine grids for evaluating the turbulence models, the numerical results presented here show some sensitivity to the type of numerical algorithm used. But the results themselves are essentially grid independent for a given numerical algorithm, central-difference or upwind scheme.

$$\alpha(t) = 4^\circ + 4.2^\circ \sin(t)$$

This flow is essentially attached and very little separation is found at the peak of the cycle and during the initial part of the downstroke. Solutions with the B-L, RNG, J-K, B-B, and S-A models obtained with the central-difference scheme are presented in Fig. 1. This case is also computed with the upwind-biased scheme using the B-B and SST $k-\omega$ models, and the hysteresis loops are compared with the experiment in Fig. 2. The loads computed with the SST $k-\omega$ model are in better agreement with experiments than others. The lift computed with the B-B model overpredicts the experimental values and the pitching moment hysteresis does not agree with the experiment in either figure. The computed pressure drag, however, is in good agreement with experiment. Comparison of unsteady surface pressures at two different times of $\alpha = 4^\circ$ and $\alpha = 8^\circ$ during the upstroke, computed by the two models, shows that the lift and pitching moment disagreements are not caused by large differences of the computed unsteady surface pressures, as shown in Fig. 3. Rather the variation in the pitching-moment and the drag coefficients is due to a small trailing edge separation. The magnitudes of the drag and pitching-moment for this case is an order of magnitude smaller than deep stall cases.

$$\alpha(t) = 11^\circ + 4.2^\circ \sin(t)$$

The computed solutions show that this flow is characterized by moderate trailing edge separation

which develops at the peak of the cycle. The flow remains separated for a large portion of the downstroke and a recirculatory region of about half a chord length is observed. As a result, more significant hysteresis effects than the previous case are obtained. The hysteresis loops obtained from solutions using the central-difference scheme with the RNG, J-K, B-B, and the S-A, turbulence models are compared with the experimental data in Fig. 4. The hysteresis loops obtained from solutions using upwind-biased scheme and the baseline grid with the B-B, the S-A, and SST $k-\omega$ turbulence models are compared with the experimental data in Fig. 5. The B-B model predicted the most separation and yields a lower lift during reattachment but it gives good predictions for pressure drag and pitching moment coefficients. The S-A model predicts the least separation and shows earlier flow reattachment. Even though the SST $k-\omega$ model with upwind algorithm predicts a closer agreement for lift with experiment during the initial part of the downstroke, it shows a very rapid lift recovery similar to the S-A model used with central-difference algorithm. To verify if the solution is grid sensitive, a solution computed on the refined 421×151 point grid with the SST $k-\omega$ turbulence model is compared with the baseline grid solution in Fig. 6. As seen, the two are nearly identical demonstrating that the solution is not grid sensitive.

$$\alpha(t) = 15^\circ + 4.2^\circ \sin(t)$$

The computed solutions show that this unsteady flowfield is characterized by massive flow separation which develops before the peak angle of incidence. At peak incidence and before the downstroke the dynamic stall vortex is shed and a trailing edge vortex forms. Shedding of the dynamic stall vortex causes decrease in lift and pitching-moment. The flow remains separated for a large part of the downstroke and significant hysteresis effects are obtained. It is a challenge for turbulence models to be able to capture flow separation and reattachment and yield good quantitative predictions for these kinds of flows.

The lift, drag, and pitching moment hysteresis loops obtained from computations with the B-B and S-A one-equation turbulence models with the central-difference scheme are compared with the experiment in Fig. 7. The lift hysteresis is overpredicted by all models. The drag and pitching moment hysteresis loops indicate that only the solution computed with the B-B model is in quantitative agreement with the experiment. The lift, drag, and pitching moment hysteresis loops obtained from computations with the B-B and S-A one-equation turbulence models and the upwind-biased scheme are compared with the experiment in Fig. 8. The lift hysteresis is predicted reasonably well by both models. The drag and pitching moment hysteresis loops indicate that both models delay the onset of separation. The loads computed with the B-B model show oscillatory behavior at the

downstroke. Again, the B-B model predictions are in closer agreement with the experiment. A smaller extent of separated flow is obtained with the S-A model, resulting in smaller extreme values of drag and pitching moment. A more rapid flow reattachment was also observed.

Predictions of hysteresis loops obtained from solutions with the two-equation turbulence models using upwind algorithm are compared with the experiment in Fig. 9. The $k-\epsilon$, the original $k-\omega$, and the BSL $k-\omega$ (where the free stream dependency is removed) did not yield enough separation. Therefore, the loads computed with these models significantly deviated from the experimentally measured values. The solution obtained with the SST $k-\omega$ model shows large flow separation and the predictions agree about as well with the experiment as the B-B calculations. However, at large angles of incidence and during the downstroke the loads show again oscillatory behavior.

Solutions computed with the B-B and SST $k-\omega$ models show development of a trailing edge vortex at the end of the pitch-up motion. During the downstroke this vortex convects in the wake and another trailing edge vortex forms. The second vortex initially grows in size and then convects in the wake and the vortex shedding repeats. This vortical activity and the suction side separated flowfield is shown by a series of snapshots during the downstroke in Fig. 10. In this figure the flowfield is illustrated with particles which are released continuously from certain locations and they are convected with the local computed velocity. The UFAT program⁴⁸ is used to convect particles over time, using as input the computed velocity fields and grid locations over 200 equally spaced time instants during the oscillation cycle. During the downstroke the trailing edge vortex shedding causes oscillations in the air loads. The computed solutions for this part of the cycle are sensitive to grid distribution at the trailing edge and the wake region.

The unsteady solutions presented for different flow conditions show the following overall trends. The B-B and SST $k-\omega$ models overpredict the extent of separation with B-B model in the lead. The S-A model tends to underpredict the extent of separation but not nearly to the degree of the standard $k-\omega$ and $k-\epsilon$ models. To better put the results in perspective, the experimental pitching-moment data for all three oscillatory cases are plotted to the same scale in Fig. 11 and compared to the B-B and SST $k-\omega$ model solutions. As seen in Fig. 11, the discrepancies between experiment and computation for the attached and light stall cases are very small in relation to those for the deep stall case. It should be noted that the drag and pitching-moment coefficients for the deep stall case is an order of magnitude larger compared to the light stall and the attached flow cases.

The various turbulence models produce different sizes of dynamic stall vortex and separated flow. An examination of the loci of the flow reversal point (x_s) on the upper surface of the airfoil (Fig. 12) shows that at any given instant of time, the extent of reversed flow varies widely. The B-L model produces the smallest extent of reversed flow over most of the cycle whereas the B-B model produces the largest extent of reversed flow. The position indicating 0° phase denotes the mean angle of oscillation. It is apparent from this figure that the B-B model completes the recovery process on the upstroke only when it reaches approximately the mean angle. For the large part of the cycle, from 15° upstroke to 15° downstroke, the RNG, B-B, and S-A models predict nearly the same extent of reversed flow. The massive reversed flow regions clearly increase the unsteady-lag effects.

The effect of transition

A light stall case from the experimental results reported in Ref. 4 is chosen to demonstrate the effect that leading edge transition can have on the development of the unsteady flowfield. In Ref. 4, measurements in the form of integrated aerodynamic loads (C_l, C_d, C_m) have been reported for a wide range of flow conditions and airfoil shapes. In addition, unsteady surface pressure coefficients are given. In contrast to the NACA 0015 experiment of Ref. 5, in Ref. 4 boundary layer trips were used only for limited number of deep stall cases. Unsteady solutions are obtained for a NACA 0012 airfoil executing harmonic motion $\alpha(t) = 10^\circ + 5^\circ \sin(\omega t)$, with a reduced frequency $k = 0.1$, $M_\infty = 0.3$ with untripped flow for a Reynolds number $Re_c = 4.0 \times 10^6$. The same case was also considered in Refs. 25 and 26. However, because significant hysteresis effects were not obtained for the experimental maximum angle of incidence, the amplitude of the oscillation or the mean angle were slightly increased for the computation. As a result, in both investigations a maximum angle of attack larger than $\alpha_{max} = 15^\circ$ reported by the experiment was reached. Experimental uncertainties and tunnel wall interference effects were cited to justify this alteration of the experimental conditions. Another reason why the maximum angle of incidence had been increased was to promote separation predicted by the turbulence models. Hysteresis effects were obtained at these larger angles of incidence, and it was concluded that massive flow separation at the trailing edge alone was responsible for stall.

Fully turbulent flow simulations of the previous section have demonstrated that the B-B model produces the most separation. The S-A model produces less separation compared to the B-B and the SST $k-\omega$ models. The B-B and the SST $k-\omega$ models yield similar predictions, but the B-B model is more computationally efficient. Therefore, this case is

solved only with one-equation models. A solution obtained with the B-B model, which produces the most separation for the same oscillation amplitude as the experiment⁴, still did not yield significant hysteresis effects. In addition, a counterclockwise loop for the pitching moment, as opposed to the clockwise loop shown in the experiment, was obtained. The same procedure of Refs. 25 and 26 was followed again, and the oscillation amplitude was "arbitrarily" increased. A solution with the B-B model was obtained with an oscillation amplitude of 5.3° . For the S-A model, which yields less separation, the oscillation amplitude was further increased to 5.5° .

The loads obtained with the B-B and the S-A models are compared with the experiment in Fig. 13. The lift and pitching moment hysteresis reasonably agree with the experiment. The computed pressure drag, even though it follows the experimental trends, underpredicts the extreme measured drag values. Also the phase angle where the computed drag and nose down pitching moment increases lags the experimental values by approximately one degree. Comparison of the measured unsteady surface pressure measurements with the computed surface pressure indicates that large discrepancies occur on the suction side, and that the agreement of the lift and the pitching moment with the experiment is coincidental.

Careful observation of the experimental surface pressure measurements shows that the lift drop, the increases in drag, and nose-down pitching moment are associated with a drop in the leading edge suction peak. This suction pressure drop occurs because of leading edge flow separation. The two physical mechanisms that can force the flow to separate at the leading edge are either a shock or laminar/transitional flow behavior. The progressive drop of the suction peak shown in the experiment does not support the shock separated flow assumption. Therefore, there is an indication that, even though the Reynolds number is large, the leading edge flow could be transitional. Therefore, a rough approximation of the transitional flow behavior at the leading edge was performed with the following procedure. The transition onset is specified to occur immediately downstream of the suction peak location. The flow from the stagnation point up to the transition onset is computed as laminar. The production term of the one-equation B-B model is set equal to zero for the laminar region. As a result, the model yields an eddy viscosity of almost zero for the laminar region. Beyond the transition point, the full production term is utilized and the computed eddy viscosity rapidly increases downstream from the transition point until a fully turbulent value is reached.

A 351×91 point C-grid with 170 points on the suction side was used for the numerical solution. This grid has refined resolution at the leading edge region. In the computed solutions the transitional

flow region extends only over a few streamwise computational cells. A leading edge separation bubble forms at approximately 14 degrees during the upstroke and increases significantly in size before the peak of the cycle. The loads obtained from the laminar/transitional/turbulent flow solutions are compared with the experiment in Fig. 14. For comparison, the loads obtained from a fully turbulent solution are shown in the same figure. The lift hysteresis loop (Fig. 14a) shows good qualitative agreement with the experiment. Good quantitative agreement is obtained for the upstroke but a more rapid lift recovery during part of the downstroke is observed. Similar trends are shown for the drag and pitching moment. It appears that the transitional solution predicts a more rapid flow reattachment. However, there is good agreement with the experiment for the computed nose down pitching moment and drag increase attributed to the massively separated flow during the initial part of the downstroke. It is also significant that the extreme values of the drag and pitching moment are closely predicted and the computed loads do not lag the experiment. Discrepancies obtained for the downstroke are caused by uncertainties in transition modeling and deficiencies of the turbulence model.

The surface pressure coefficient distributions for three angles during the upstroke, $\alpha = 14.0^\circ$, $\alpha = 14.5^\circ$ and $\alpha = 14.9^\circ$, obtained from the fully turbulent and the transitional computations are compared with the measured values in Fig. 15. At $\alpha = 14.0^\circ$ (Fig. 15a) both the fully turbulent and the transitional solutions are in agreement with the experiment. The fully turbulent solution, however, slightly overpredicts the suction peak. The surface pressure distribution obtained from the transitional solution is in closer agreement with the experiment and shows the development of a leading edge separation bubble. A very small region of transitional flow is found. As the angle of attack increases to $\alpha = 14.5^\circ$, the experiment shows a large drop in the suction peak caused by flow separation. Visualization of the computed velocity fields shows that only trailing edge separation was obtained for the fully turbulent computation. The transitional solution, on the other hand, yields more separated flow and shows formation of a vortex-like structure. At $\alpha = 14.9^\circ$, which is the peak angle of attack of the experiment, the suction peak is further diminished and the vortical structure generated at the leading edge is convected downstream. At this angle the fully turbulent solution does not agree with the experiment and shows further increase of the suction peak. It appears that the transitional solution properly captures the physical mechanism observed in the experiment and shows development of a leading edge, vortical, dynamic-stall-like structure, as the computed surface pressure coefficient demonstrates.

The values of lift and pitching moment obtained from the turbulent solution with an increased oscillation amplitude (Fig. 13) are coincidentally close to the measured values. The computed drag coefficient, however, disagrees with the experiment. Therefore, it is necessary to always compare lift, drag and pitching moment coefficients, when surface pressure measurements are not available. The fully turbulent solution predicts attached leading edge flow and trailing edge separation. The transitional solution predicts a leading edge vortex-like structure and larger overall separation, compared to the fully turbulent solution. This leading edge flow development affects significantly the suction surface flowfield and results in larger overall separation. However, this leading edge vortical structure is not the same as a classical dynamic stall vortex, which is clearly observed in both experiments and computations for larger oscillation amplitudes or different pitch rates. This structure forms at about 14 degrees during the upstroke and bursts in the boundary layer. Around the peak angle of the cycle a rapid progression of the trailing edge separation towards the leading edge is also observed.

In Ref. 49, solutions were computed for a NACA 0012 airfoil oscillating with a smaller mean angle of incidence $\alpha_m = 9^\circ$ and with the same amplitude $\alpha_a = 5^\circ$ and reduced frequency. The leading edge transition was modeled in the same way described before and a significant improvement compared to a fully turbulent solution was obtained for the unsteady loads and the surface pressure distributions. In order to confirm that the leading edge transitional flow behavior is also independent of airfoil shape and reduced frequency parameter, a solution for a Sikorsky SC-1095 airfoil of Ref. 4 oscillating with a reduced frequency $k = 0.2$ is computed. The airfoil oscillates as $\alpha(t) = 14^\circ + 2^\circ \sin(\omega t)$ and the same transition model is applied. The computed unsteady loads are compared with the experiment in Fig. 16. Hysteresis loops for a fully turbulent solution are shown in the same figure. For this case, leading edge stall is predicted by both the fully turbulent and transitional solution. The transitional solution closely predicts the dynamic stall onset, while the fully turbulent solution lags the experiment by half degree and the downstroke does not follow the experimental trends.

As an approximate location for the transition onset, the maximum suction pressure point is used. For high Reynolds number flow, the transitional region is small. It appears that this approximate transition-onset location and the use of a simple transition model that yields an "effective" eddy viscosity for the transitional region, do not significantly degrade the solution for the pitch-up part of the cycle. It is not expected that these rough approximations allow accurate modeling of the complex physical mechanisms of transition, bubble formation and reattachment. But it is demonstrated that transition plays a significant

role in the development of the unsteady separated flowfield. Also, it was found to be necessary to include transition for most of the downstroke to approximately 10 degrees where the flow reattaches. If the fully turbulent solution is switched on at an earlier part of the cycle, the flow rapidly reattaches and the loads converge to the fully turbulent values.

Conclusions

An evaluation of the ability of one- and two-equation turbulence models in predicting hysteresis effects of unsteady fully turbulent flow over oscillating airfoils in the light and deep stall regime was conducted. It can be concluded that none of the models considered in this investigation is capable of accurately predicting the deep stall case. However, the B-B, the S-A, and the SST $k - \omega$ models show a significant improvement over the standard two-equation models. For the light stall case the S-A model did not yield sufficient separation and underpredicted the extreme values of the unsteady loads. The B-B model shows slow recovery of lift hysteresis during the pitch-down part of the cycle for the light stall and the attached flow cases. The standard $k - \epsilon$ and the $k - \omega$ models did not predict separation even for the deep stall case. The SST $k - \omega$ model gave good predictions for the attached and the light stall cases.

It was found that the leading edge transitional flow is of primary importance to the overall development of the unsteady flowfield, if the flow is not tripped at the leading edge. A laminar/transitional leading-edge separation bubble developing during the pitch-up motion produces a dynamic-stall-like vortical structure. It was shown that a simple transition model significantly improves the predictions. However, accurate methods for transition modeling and prediction are still required. Finally, the numerical results show some sensitivity to the numerical algorithm in spite of using reasonably fine grids.

References

- 1 McCroskey, W. J., "Some Current Research in Unsteady Fluid Dynamics - 1976 Freeman Scholar Lecture," *Journal of Fluids Engineering*, Vol. 99, March 1977, pp. 8-38.
- 2 McCroskey, W. J., "Unsteady Airfoils," *Annual Reviews of Fluid Mechanics*, Vol. 14, Van Dyke et al. Eds., Annual Reviews, Inc., Palo Alto, Calif., 1982, pp. 285-311.
- 3 Carr, L. W., "Progress in Analysis and Prediction of Dynamic Stall," *Journal of Aircraft*, Vol. 25, No. 1, January 1988, pp. 6-17.
- 4 McCroskey, W. J. and Pucci, S. L., "Viscous Inviscid Interaction on Oscillating Airfoils in Subsonic Flow," *AIAA Journal*, Vol. 20, No. 2, Feb. 1982, pp. 167-174.

- 5 Piziali, R. A., "An Experimental Investigation of 2D and 3D Oscillating Wing Aerodynamics for a Range of Angle of Attack Including Stall," NASA Technical Memorandum, 1994 (To be published).
- 6 Landon, R. H., "NACA 0012 Oscillatory and Transient Pitching," AGARD Report No. 702, 1981.
- 7 Lorber, P. F., and Carta, F. O., "Airfoil Dynamic stall at Constant Pitch rate and High Reynolds Number," AIAA Paper 87-1329, Jan. 1987.
- 8 Lorber, P. F., Covino, A. F., Jr., and Carta, F. O., "Dynamic Stall Experiments on a Swept Three Dimensional Wing in Compressible Flow," AIAA Paper 91-1795, Jan. 1991.
- 9 Lorber, P. F., "Compressibility Effects on the Dynamic Stall of a Three-Dimensional Wing," AIAA Paper 92-0191, Jan. 1992.
- 10 Walker, J. M., Helin, H. E., and Strickland, J. H., "An Experimental Investigation of an Airfoil Undergoing Large Amplitude Pitching Motions," AIAA journal, Vol. 23, No. 8, 1985, pp. 1141-1142.
- 11 Schreck, S. J. and Helin, H. E., "Unsteady Vortex Dynamics and Surface Pressure Topologies on a Pitching Wing," AIAA Paper 93-0435, Jan. 1993.
- 12 Freymuth, P., "Propulsive Vortical Signature of plunging and Pitching Airfoils," AIAA Journal, Vol. 26, 1988, pp. 881-883.
- 13 Chandrasekhara, M. S. and Carr, L. W., "Flow Visualization Studies of the Mach Number Effects on the Dynamic Stall of Oscillating Airfoils," Journal of Aircraft, Vol. 27, No. 6, June 1990, pp. 516-522.
- 14 Wilder, M. C., Chandrasekhara, M. S. and Carr, L. W., "Transition Effects on Compressible Dynamic Stall of Transiently Pitching Airfoils," AIAA Paper 93-2978, Orlando FL, July 1993.
- 15 Carta, F. O. and Lorber, P. F., "Experimental Study of the Aerodynamics of Incipient Torsional Stall Flutter," Journal of Propulsion, Vol. 3, No. 2, 1987, pp. 164-170.
- 16 Ghia, K. N., Yang, Y., Oswald, G. A., and Ghia, U., "Study of the Role of Unsteady Separation in the Formation of Dynamic Stall Vortex," AIAA Paper 92-0196, Jan. 1992.
- 17 Visbal, M. R. and Shang, J. S., "Investigation of the Flow Structure Around a Rapidly Pitching Airfoil," AIAA Journal, Vol. 27, No. 8, Aug. 1989, pp. 1044-1055.
- 18 Choudhuri, P. G., Knight, D. D., and Visbal, M. R., "Two-Dimensional Unsteady Leading-Edge Separation on a Pitching Airfoil," AIAA Journal, Vol. 32, No. 4, 1994, pp. 673-681.
- 19 Geissler, W. and Vollmers, H., "Unsteady Separated Flows on Rotor-Airfoils-Analysis and Visualization of Numerical Data," Proceedings of the Eighteenth European Rotorcraft Forum, Paper No. 79, Sept. 1992, Avignon, France.
- 20 Jang, H. M., Ekaterinaris, J. A., Platzer, M. F., and Cebeci, T., "Essential Ingredients for the Computation of Steady and Unsteady Boundary Layers," Journal of Turbomachinery, Vol. 13, Oct. 1991, pp. 608-616.
- 21 Ekaterinaris, J. A., Cricelli, A. S., and Platzer, M. F., "A zonal Method for Unsteady, Viscous, Compressible Airfoil Flows," Journal of Fluid and Structures, Vol. 8, Jan. 1994.
- 22 Wu, J.-C., Huff, D. L., and Sankar, L. N., "Evaluation of Three Turbulence Models in Static Air Loads and Dynamic Stall Predictions," Journal of Aircraft, Vol. 27, No. 4, April 1990, pp. 382-384.
- 23 Rizetta, D. P. and Visbal, M. R., "Comparative Numerical Study of Two Turbulence Models for Airfoil Static and Dynamic Stall," AIAA Journal, Vol. 31, No. 4, April 1993, pp. 784-786.
- 24 Rumsey, C. L. and Vatsa, V. N., "A Comparison of the Predictive Capabilities of Several Turbulence Models Using Upwind and Central-Difference Computer Codes," AIAA Paper 93-0192, Jan. 1993.
- 25 Clarkson, J. D., Ekaterinaris, J. A. and Platzer, M. F., "Computational Investigation of Airfoil Stall Flutter," Unsteady Aerodynamics, Aeroacoustics and Aeroelasticity of Turbomachines and Propellers, Editor H. M. Atassi, Springer-Verlag, 1993, pp. 415-432.
- 26 Dindar, M. and Kaynak, U., "Effect of Turbulence Modeling on Dynamic Stall of a NACA 0012 Airfoil," AIAA Paper 92-0027, Jan. 1992.
- 27 Srinivasan, G. R., Ekaterinaris, J. A. and McCroskey, W. J., "Dynamic Stall of an Oscillating Wing, Part 1: Evaluation of Turbulence Models," AIAA Paper 93-3403, Aug. 1993.
- 28 Ekaterinaris, J. A. and Menter, F. R., "Computation of Separated and Unsteady Flows with One and Two Equation Turbulence Models," AIAA Paper 94-0190, Jan. 1994.
- 29 Osher, S., Solomon, F., "Upwind Difference Schemes for Hyperbolic Systems of Conservation Laws," Mathematics of Computation, Vol. 38, 1982, No. 158, 339-374.
- 30 Cebeci, T. and Smith, A. M., Analysis of Turbulent Boundary Layers, Academic Press, New York, 1974.
- 31 Baldwin, B. S. and Lomax, H., "Thin Layer Approximation and Algebraic Model for Separated Turbulent Flows," AIAA Paper 78-257, Jan. 1978.
- 32 Yakhot, V., and Orzag, S. A., "Renormalization Group Analysis of Turbulence. 1-Basic Theory," Journal of Scientific Computing, Vol. 1, 1986.
- 33 Johnson, D. A. and King, L. S., "A Mathematically Simple Turbulence Closure Model for Attached and Separated Turbulent Boundary Layers," AIAA Journal, Vol. 23, Nov. 1985, pp. 1684-1692.

- 34 Johnson, D. A., "Nonequilibrium Algebraic Turbulence Model Considerations for Transonic Airfoils and Wings," AIAA Paper 92-0439, Jan. 1992.
- 35 Baldwin, B. S. and Barth, T. J., "A One-Equation Turbulence Transport Model for High Reynolds Number Wall-Bounded Flows," NASA TM 102847, 1990.
- 36 Spalart P. R. and Allmaras, S. R., "A One-Equation Turbulence Model for Aerodynamic Flows," AIAA Paper 92-0439, Jan. 1992.
- 37 Jones, W. P. and Launder B. E., "The Calculation of Low-Reynolds-Number-Phenomena with a Two-Equation Model of Turbulence," *International Journal of Heat and Mass Transfer*, Vol. 16, 1973, pp. 1119-1130.
- 38 Wilcox, D. C., "Reassessment of the Scale-Determining Equation for Advanced Turbulence Models," *AIAA Journal*, Vol. 26, Nov. 1988, pp. 1299-1310.
- 39 Menter, F. R., "Influence of Freestream Values on $k - \omega$ Turbulence Model Predictions," *AIAA Journal*, Vol. 30, No. 6, 1992.
- 40 Ekaterinaris, J. A., Chandrasekhara, M. S. and Platzter, M. F., "Analysis of Low Reynolds Number Airfoils," AIAA Paper 94-0534, Jan 1994.
- 41 Hoheisel, H., "A Comparison of Laser-Doppler Anemometry and Probe Measurements within the Boundary Layer of an Airfoil in Subsonic Flow," *Laser Doppler Anemometry in Fluid Mechanics*, Second International Symposium on Applications of Laser Anemometry to Fluid Mechanics, Lisbon, Portugal, July 1984, pp. 143-157.
- 42 Herbert, Th., "Boundary Layer Transition Analysis and Prediction Revisited," AIAA Paper 91-0737, Jan. 1991.
- 43 Bertolotti, F. P., "Compressible Boundary Layer Stability Analyzed with the PSE Equations," AIAA Paper 91-1637, June 1991.
- 44 Jameson, A., Schmidt, W., and Turkel, E., "Numerical Solutions of the Euler Equations by Finite Volume Methods Using Runge-Kutta Time Stepping Schemes," AIAA Paper 81-1259, June 1981.
- 45 Steger, J. L., Warming, R. F. "Flux Vector Splitting of the Inviscid Gas Dynamic Equations with Applications to Finite-Difference Methods," *Journal of Computational Physics*, Vol. 40, 1981, pp. 263-293.
- 46 Menter, F. R., "Performance of Popular Turbulence Models for Attached and Separated Adverse Pressure Gradient Flows," *AIAA Journal*, Vol. 30, Aug. 1992, pp. 2066-2072.
- 47 Menter, F. R., "Zonal Two Equation $k - \omega$ Turbulence Models for Aerodynamic Flows," AIAA Paper 93-2906, July 1993.
- 48 Lane, D. A., "Unsteady Flow Analysis Kit - UFAT," Report RND-93-009, NASA Ames Research Center, May 1993.
- 49 Ekaterinaris, J. A., and Platzter, M. F., "Numerical Investigation of Stall Flutter," International Gas Turbine and Aeroengine Congress, ASME Paper 94-GT-206, 1994.

Table 1: CASES COMPUTED

Turbulence Model	Case 1 NACA 0015 $\alpha = 4^\circ \pm 4^\circ$	Case 2 NACA 0015 $\alpha = 11^\circ \pm 4^\circ$	Case 3 NACA 0015 $\alpha = 15^\circ \pm 4^\circ$	Case 4 NACA 0012 $\alpha = 10^\circ \pm 5^\circ$	Case 5 SC-1095 $\alpha = 14^\circ \pm 2^\circ$
B-L	CD – Fig. 1		CD – Figs. 7, 12		
RNG	CD – Fig. 1	CD – Fig. 4	CD – Figs. 7, 12		
J-K	CD – Fig. 1	CD – Fig. 4	CD – Figs. 7, 12		
B-B	CD – Fig. 1 Up – Figs. 2, 3	CD – Fig. 4 Up – Figs. 5, 6	CD – Figs. 7, 12 Up – Figs. 8, 10, 11		Up – Fig. 16
S-A	CD – Fig. 1	CD – Fig. 4 Up – Fig. 5	CD – Figs. 7, 12 Up – Fig. 8	Up – Fig. 13, 14, 15	
K – ε			Up – Fig. 9	Up – Fig. 13	
K – ω			Up – Fig. 9		
BSL			Up – Fig. 9		
SST	Up – Figs. 2, 3	Up – Figs. 5, 6	Up – Figs. 9, 11		

CD = Central Difference scheme

Up = Upwind scheme

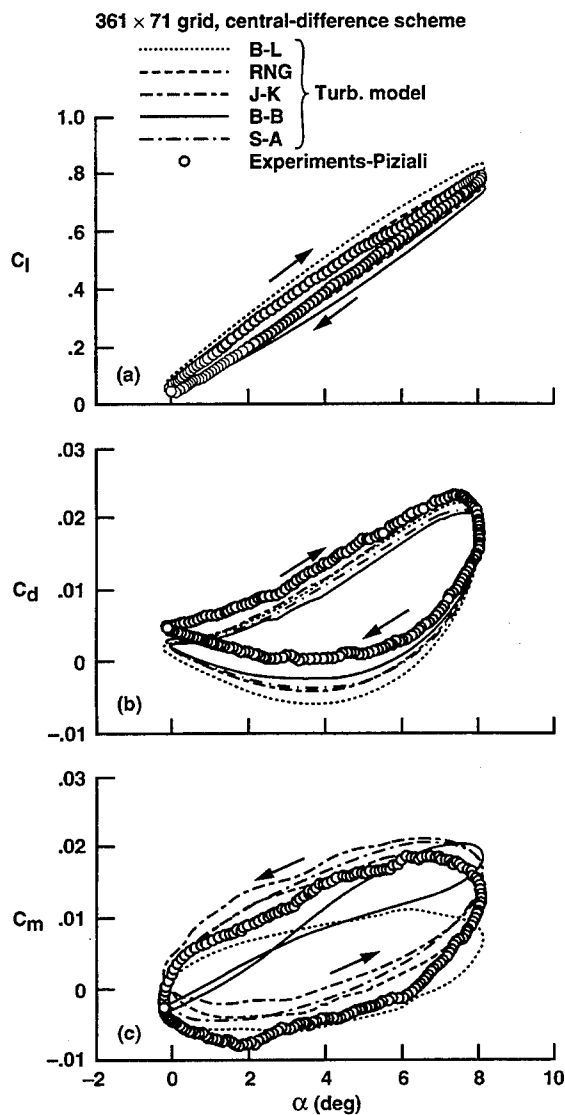


Fig. 1 Hysteresis effects for attached flow computed with the central-difference scheme; $M = 0.3$, $\alpha(t) = 4^\circ + 4.2^\circ \sin(t)$, $k = 0.1$, $Re = 2 \times 10^6$.

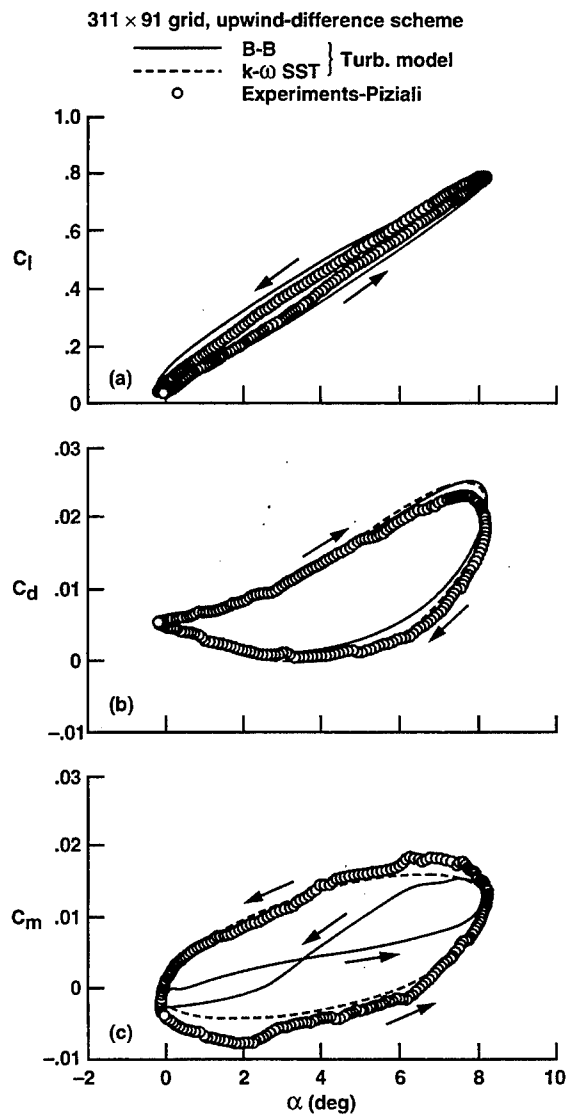


Fig. 2 Hysteresis effects for attached flow computed with the upwind scheme; $M = 0.3$, $\alpha(t) = 4^\circ + 4.2^\circ \sin(t)$, $k = 0.1$, $Re = 2 \times 10^6$.

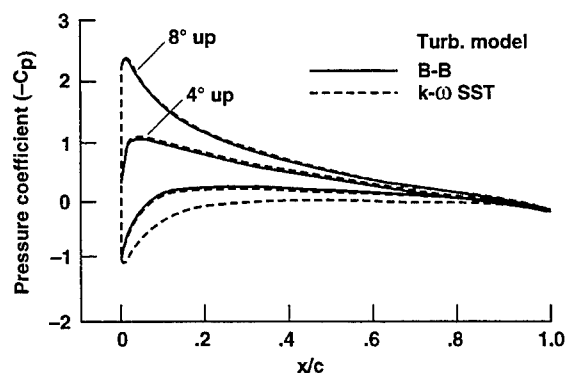


Fig. 3 Comparison of the surface pressure coefficient at $\alpha = 4^\circ$ up and $\alpha = 8^\circ$ up computed with the B-B and the SST $k - \omega$ models.

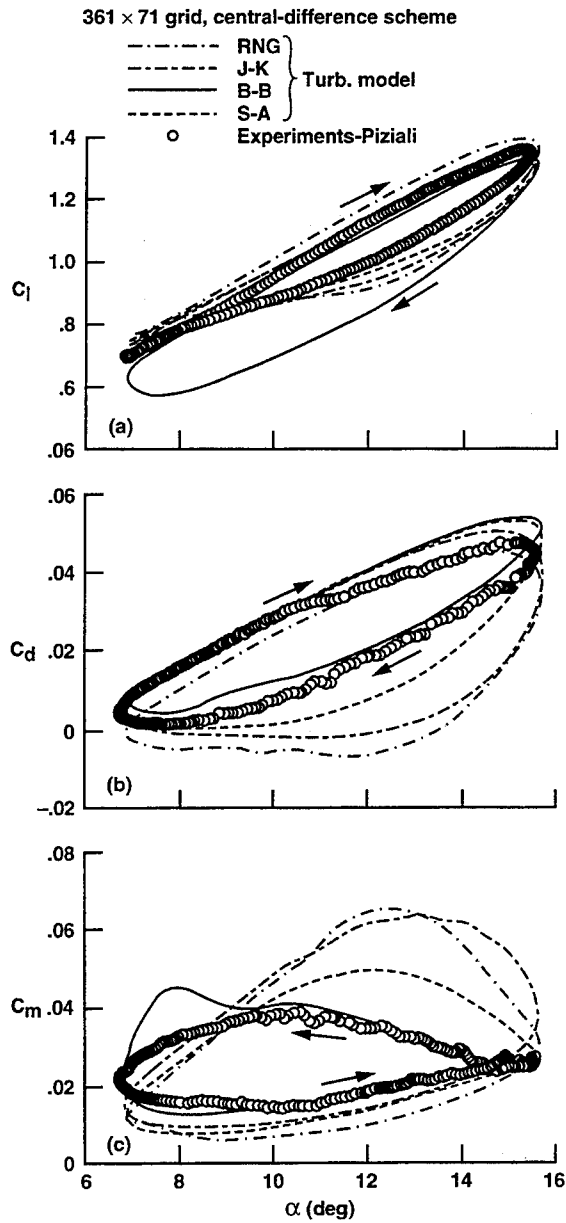


Fig. 4 Hysteresis effects for light stall flow computed with the central-difference scheme; $M = 0.3$, $\alpha(t) = 11^\circ + 4.2^\circ \sin(t)$, $k = 0.1$, $Re = 2 \times 10^6$.

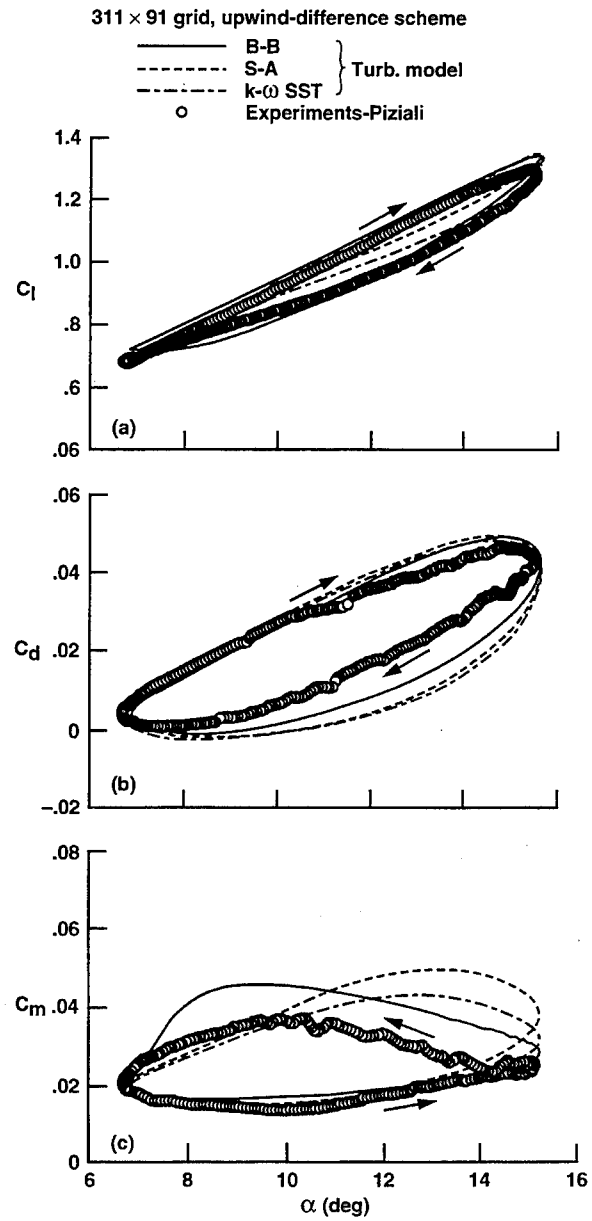


Fig. 5 Hysteresis effects for light stall flow computed with the upwind scheme; $M = 0.3$, $\alpha(t) = 11^\circ + 4.2^\circ \sin(t)$, $k = 0.1$, $Re = 2 \times 10^6$.

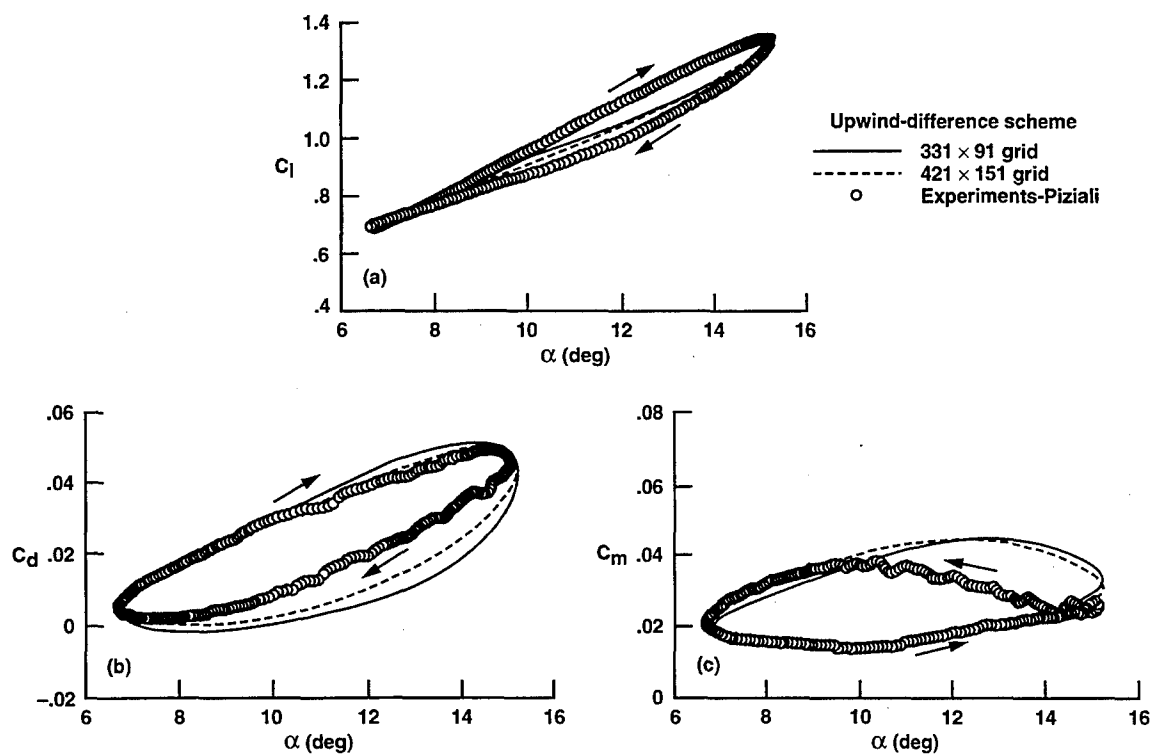


Fig. 6 Effect of grid refinement on the unsteady airloads hysteresis computed with the upwind scheme and the B-B model; $M = 0.3$, $\alpha(t) = 11^\circ + 4.2^\circ \sin(t)$, $k = 0.1$, $Re = 2 \times 10^6$.

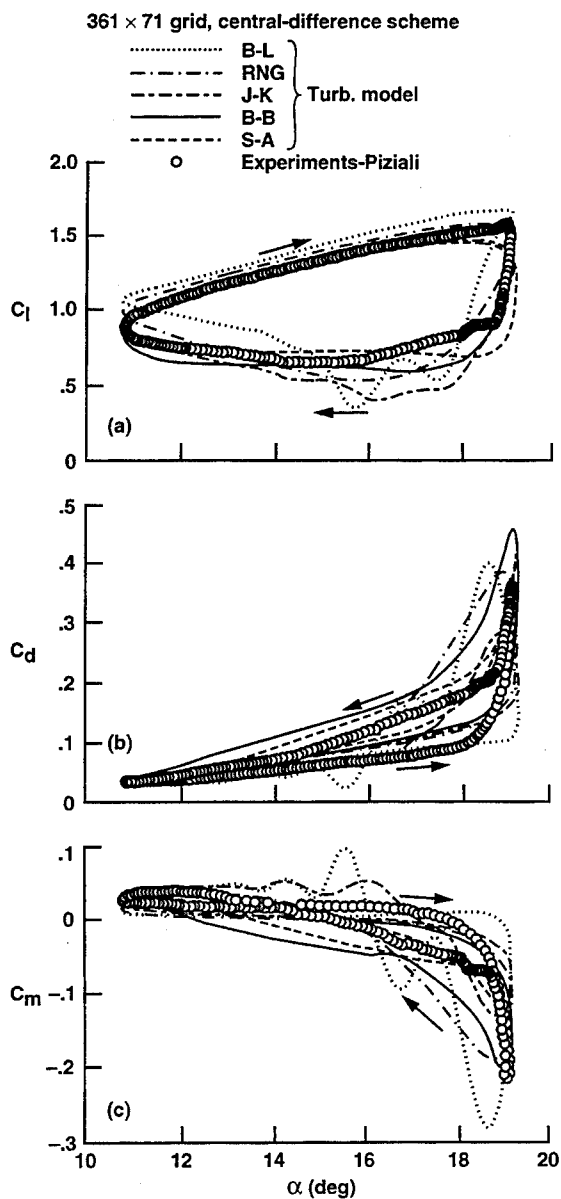


Fig. 7 Hysteresis effects for deep stall obtained with algebraic, half- and one-equation models and computed with the central-difference scheme; $M = 0.3$, $\alpha(t) = 15^\circ + 4.2^\circ \sin(t)$, $k = 0.1$, $Re = 2 \times 10^6$.

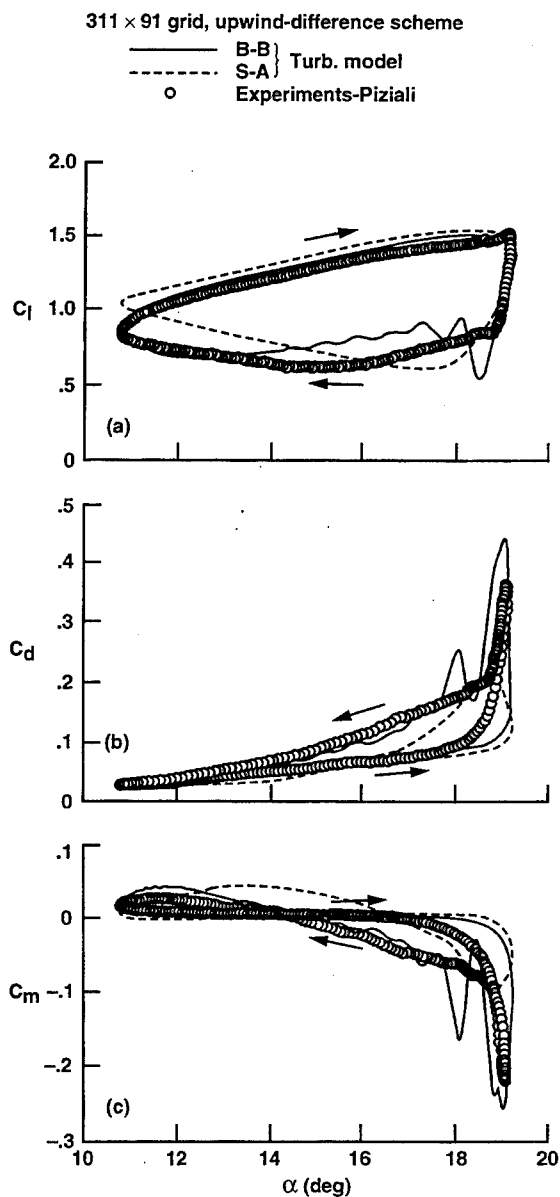


Fig. 8 Hysteresis effects for deep stall obtained with one-equation models and computed with the upwind scheme; $M = 0.3$, $\alpha(t) = 15^\circ + 4.2^\circ \sin(t)$, $k = 0.1$, $Re = 2 \times 10^6$.

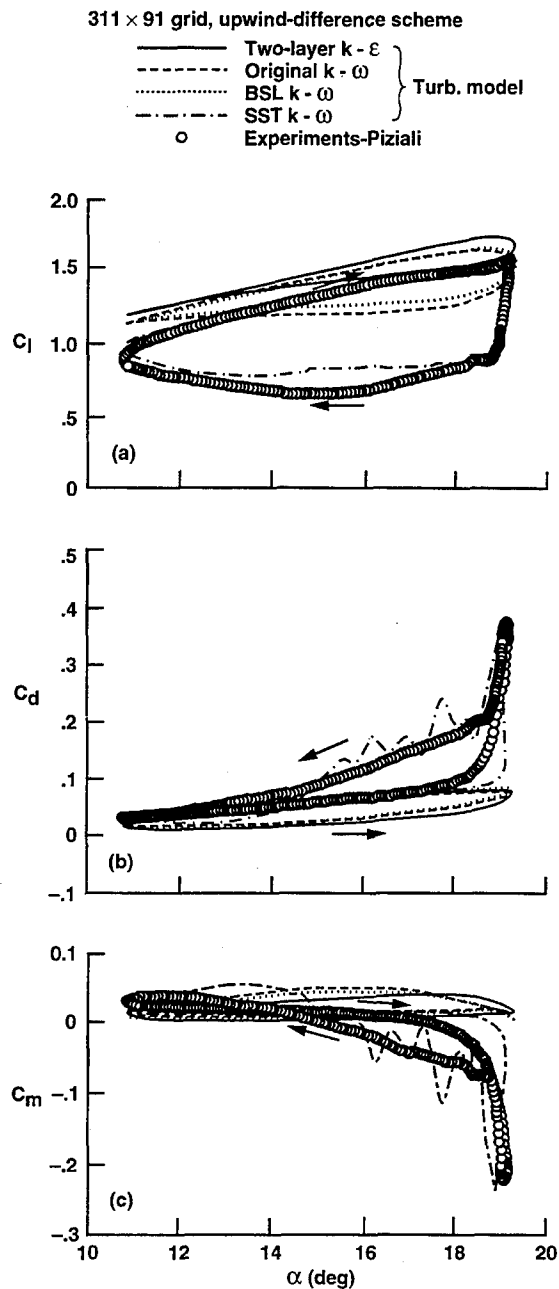


Fig. 9 Hysteresis effects for deep stall obtained with two-equation models and the upwind scheme; $M = 0.3$, $\alpha(t) = 15^\circ + 4.2^\circ \sin(t)$, $k = 0.1$, $Re = 2 \times 10^6$.

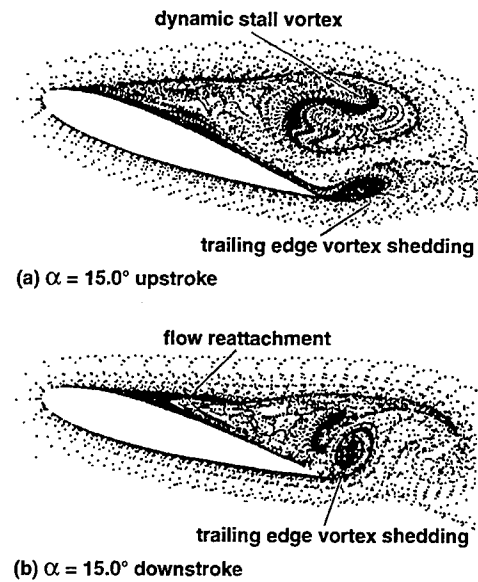


Fig. 10 Vortical flowfield development with B-B model; $M = 0.3$, $\alpha(t) = 15^\circ + 4.2^\circ \sin(t)$, $k = 0.1$, $Re = 2 \times 10^6$.

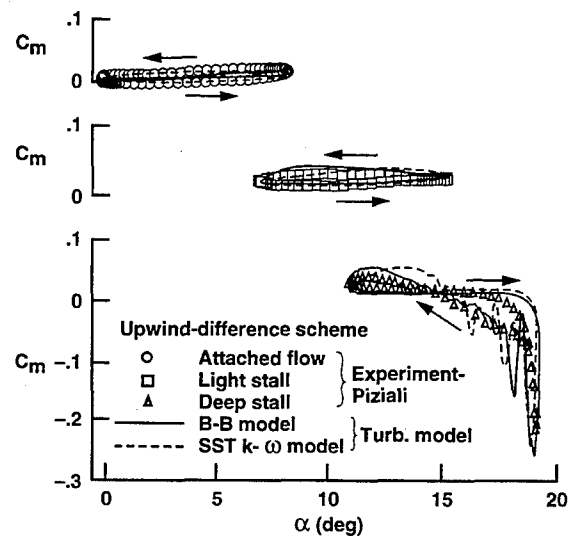


Fig. 11 Effect of increased mean angle on pitching moment.

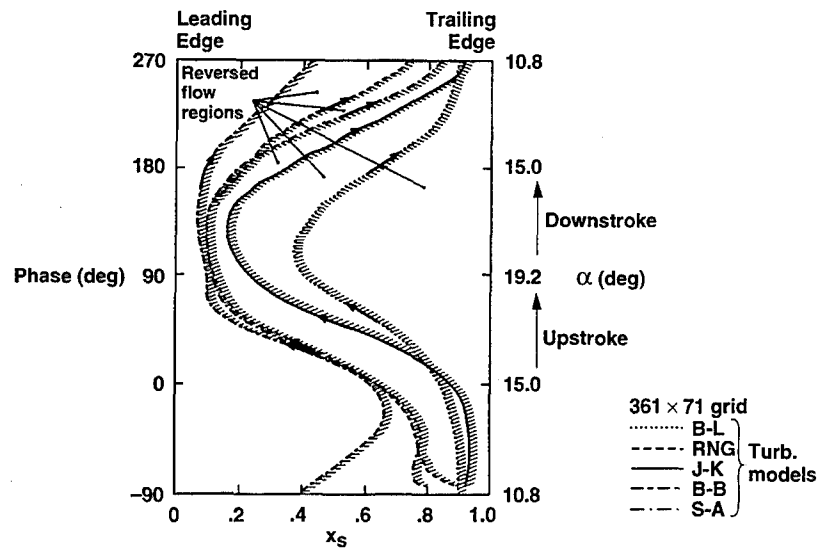


Fig. 12 Locus of flow reversal point during the oscillatory cycle for different turbulence models computed with central-difference scheme; $M = 0.3$, $\alpha(t) = 15^\circ + 4.2^\circ \sin(t)$, $k = 0.1$, $Re = 2 \times 10^6$.

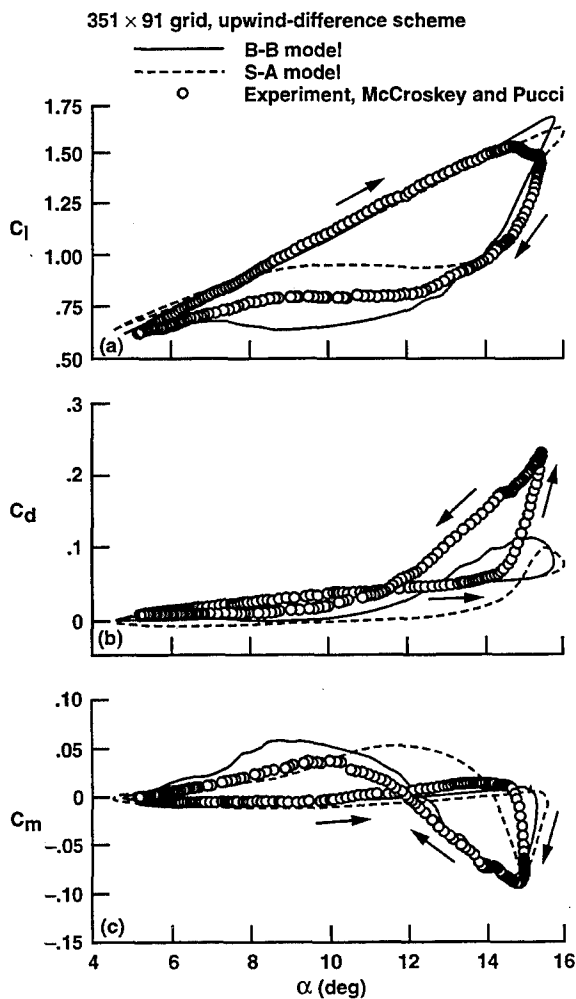


Fig. 13 Effect of increased oscillation amplitude on airloads hysteresis for NACA 0012 airfoil; $M = 0.3$, $\alpha(t) = 10^\circ + 5^\circ \sin(t)$, $k = 0.1$, $Re = 4 \times 10^6$.

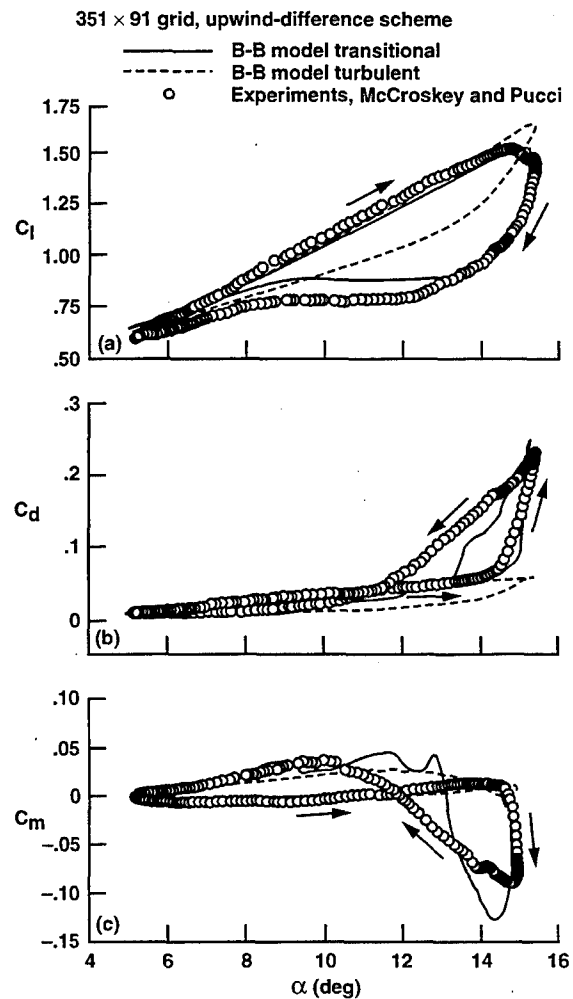


Fig. 14 Effect of leading edge transition on airloads hysteresis for NACA 0012 airfoil; $M = 0.3$, $\alpha(t) = 10^\circ + 5^\circ \sin(t)$, $k = 0.1$, $Re = 4 \times 10^6$.

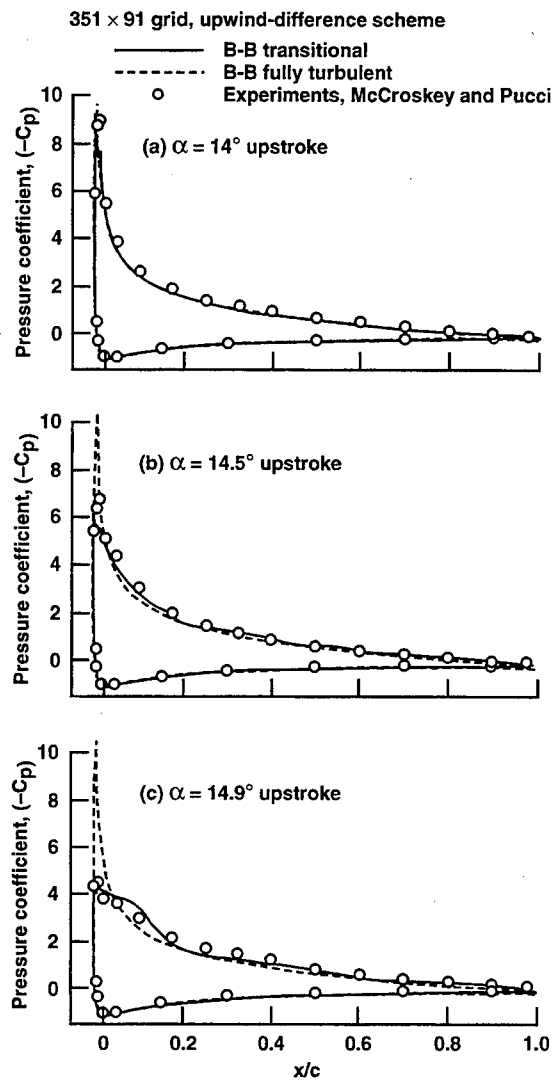


Fig. 15 Effect of transition on the computed surface pressure coefficient for a NACA 0012 airfoil; $M = 0.3$, $\alpha(t) = 10^\circ + 5^\circ \sin(t)$, $k = 0.1$, $Re = 4 \times 10^6$.

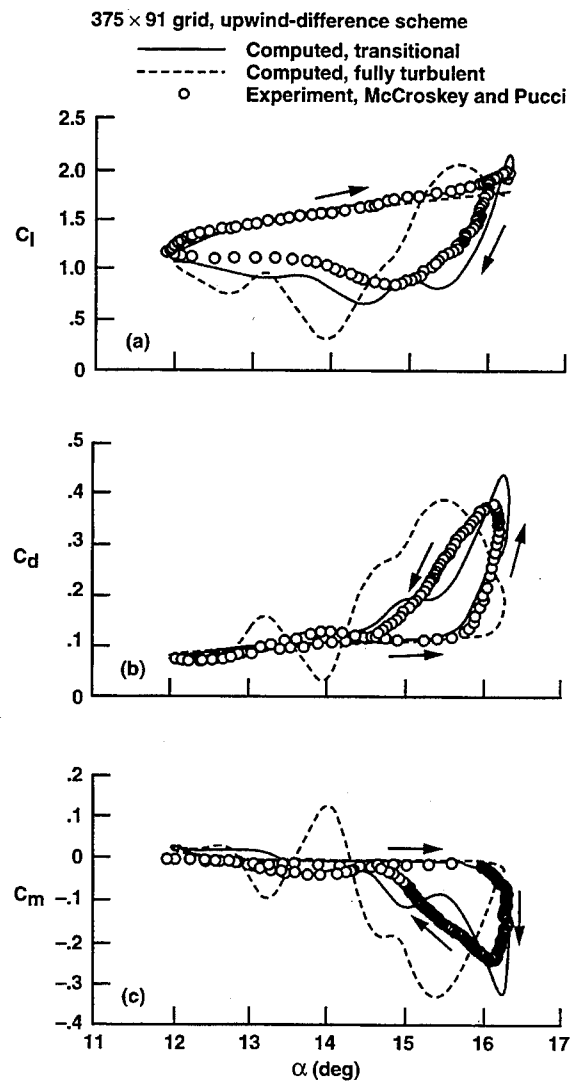


Fig. 16 Effect of leading edge transition on loads hysteresis for Sikorsky SC-1095 airfoil; $M = 0.3$, $\alpha(t) = 14^\circ + 2^\circ \sin(t)$, $k = 0.2$, $Re = 4 \times 10^6$.

Compressibility Effects on Dynamic Stall of Oscillating Airfoils

M.S. Chandrasekhara¹

Associate Director and Research Associate Professor
Navy-NASA Joint Institute of Aeronautics
Department of Aeronautics and Astronautics
Naval Postgraduate School, Monterey, CA 93943

and

L.W. Carr

Research Scientist and Group Leader, Unsteady Viscous Flows
Aeroflightdynamics Directorate, U.S. Army ATCOM and,
Fluid Mechanics Laboratory Branch
NASA Ames Research Center, Moffett Field, CA 94035-1000, U.S.A.

1. SUMMARY

A review of experimental results from an ongoing study of the effects of compressibility on dynamic stall of an oscillating NACA 0012 airfoil is presented. The study shows that compressibility effects become significant at a free stream Mach number of 0.3. Dynamic stall is accelerated above this Mach number, but increasing unsteadiness delays onset of stall even under compressible flow conditions. Interferometric images of the flow show that process of dynamic stall occurs rapidly over a small angle of attack range. For certain flow conditions, multiple shocks form in the flow near the airfoil leading edge. The delay of stall has been shown to be due to delayed development combined with modification of the adverse pressure gradient in the flow. Transition has been shown to significantly modify the observed flow behavior, and thus is a very important factor to be considered, especially since it occurs near the vortex formation location. Proper modelling of its effects is critical in dynamic stall flow computations.

LIST OF SYMBOLS

C_p	pressure coefficient
C_{pmin}	peak suction pressure coefficient
c	airfoil chord
f	frequency of oscillation, Hz
k	reduced frequency = $\frac{\pi f c}{U_\infty}$
M	free stream Mach number
U_∞	free stream velocity
x, y	chordwise and vertical distance
α	angle of attack
α_0	mean angle of attack
α_m	amplitude of oscillation
ω	circular frequency, radians/sec

2. INTRODUCTION

The performance of a helicopter is severely restricted by the occurrence of dynamic stall on its retreating blade; it is critical to avoid the consequent concomitant strong pitching moment variations that are destructive to the vehicle. The retreating blade operates in a strongly compressible environment at a high Reynolds number and its stall is a clear case of forced, large amplitude, unsteady, flow separation. A characteristic feature of the flow is the formation of the

dynamic stall vortex due to the coalescence of the vorticity input by the unsteady pitching motion. The leading edge favorable pressure gradient in the flow is $O(10^2 - 10^3)$ and thus, the fluid encounters a region of strong adverse pressure gradient immediately following the suction peak, which could by itself cause flow separation. The large flow acceleration can induce supersonic velocities near the leading edge. In fact, it has been shown (Ref. 1) that compressibility effects appear in the flow at a very low free stream Mach number of 0.2. Many airfoils show a dramatic change in the stall behavior under this condition, as the normal trailing-edge stall becomes leading-edge stall. The dynamic stall vortex still forms, now in the presence of strongly compressible flow. Shocks can form in the flow and interact with the airfoil boundary layer, possibly inducing premature flow separation, and leading to early formation of a dynamic stall vortex. Thus, dynamic stall onset can occur from a completely different mechanism than that observed from low speed experiments. The complexity of the fluid mechanics issues of dynamic stall flow have defied a proper and thorough understanding of the fundamental aspects of the process (Ref. 2 and 3). To this series of issues needs to be added factors like the effects of transition of the boundary layer (or shear layer), and the effects of Reynolds number on the state of turbulence in the boundary layer under compressible flow conditions. In almost all cases, dynamic stall occurs as leading edge stall near the location where the flow undergoes transition, even when the chord based Reynolds number is in the turbulent regime. The transition point moves upstream with increasing angle of attack, and the transition length decreases with the increasing adverse pressure gradient (Ref. 4) as the airfoil is pitched up. This ever changing transition behavior immensely complicates the flow physics, and its proper physical modelling is a major requirement for the study. Much of the disagreement between experimental data and computational results can be attributed to improper physical modelling of the effects of transition, and the role transition plays in the dynamic stall process. However, since the relevant physics still eludes researchers, one is forced to make poor approximations to represent the flow, such as turbulence models based on equilibrium turbulent flow.

¹ Mailing Address: M.S. 260-1, NASA Ames Research Center, Moffett Field, CA 94035-1000, U.S.A.

An important connection between laboratory experiments and full scale testing occurs through model rotor testing. Laboratory tests are generally performed in 2-D flow due to their lesser degree of complexity and questions have arisen concerning the applicability of 2-D tests to the complex helicopter flow environment. But, it is worth noting that in a recent workshop on three dimensional oscillatory dynamic stall (Ref. 5), it was concluded that two dimensional dynamic stall tests gave acceptable lift, drag and moment distributions for calibrating three dimensional computational codes, except very near the wing tip. The consensus of the participants was that the critical difficulty was in fact in accurately predicting two dimensional dynamic stall. In a recent attempt to extend model rotor test data to full scale rotors, the boundary layer was tripped and tests were conducted (Ref. 6). However, tripping an airfoil is a formidable task (Ref. 7) especially since the trip location nearly coincides with the vortex origination point and the consequences of the presence of a trip in this sensitive compressible flow region are not easy to separate.

The present studies are specifically aimed at understanding the underlying processes of dynamic stall, under compressible transitional flow conditions; the previous studies (Ref. 8 and 9) mainly concerned with establishing the various loads and moment loops for different airfoil shapes at high Reynolds numbers. The goal of this research is to eventually develop dynamic stall control concepts that are applicable to a practical helicopter. This paper reviews the results of the research investigation being conducted in the Navy-NASA Joint Institute of Aeronautics at NASA Ames Research Center.

3. EXPERIMENTAL FACILITY AND FACILITY

The experiments were conducted in the *Compressible Dynamic Stall Facility* (CDSF) which is a 25cm x 35cm test section wind tunnel with a specially designed (Ref. 10) airfoil oscillating drive system. The airfoil is supported between two optical glass windows in the CDSF. The uniqueness of the model support system provides unobstructed optical access to the complete airfoil contour, which is critical since dynamic stall events originate from the surface near the airfoil leading edge. The operating envelope of the CDSF is wider than the flight envelope of the present day helicopter. Also, the results are directly applicable to that of a $\frac{1}{2}$ th scale model rotor. Fig. 1 shows the details of the facility. The airfoil angle of attack can be arbitrarily set between 0 - 15 deg., with the amplitude and frequency of oscillation continuously variable from 2 - 10 deg. and 0 - 100 Hz respectively. The tunnel Mach number can be varied from 0 - 0.5 by a choked downstream throat. The airfoil used in the tests is NACA 0012 with 7.62cm chord. The test Reynolds number ranged from 0.36×10^6 - 0.81×10^6 for Mach numbers from 0.2 to 0.45.

In addition to stroboscopic schlieren flow visualization pictures, quantitative experimental data was obtained using the recently developed (Ref. 11) real time

technique of point diffraction interferometry, (PDI). PDI uses an expanded laser beam to fill the entire field of view in a standard Z-type schlieren configuration, with the optics aligned to minimize astigmatism. A pre-developed, partially transmitting photographic plate replaces the knife edge. In operation, a pin-hole is created *in situ* in the photographic plate with no flow in the test section. This pin-hole serves as a point diffractor. During the wind tunnel test, the light beam passing through the flow is deflected due to density changes in the flow field and thus focuses to a bigger spot around the pin-hole. The portion of this distorted light beam passing through the pin-hole then becomes the reference beam and interferes with the portion passing around it (signal beam) to create fringes in real-time, which are captured on Polaroid film. A schematic of the PDI system is illustrated in Fig. 2. A large number of flow interferograms have been obtained and analyzed to provide a quantitative flow description. A custom interferogram image processing package has been developed for the purpose.

The experiments were performed at Mach numbers of 0.2, 0.25, 0.3, 0.35, 0.4 and 0.45. The reduced frequencies were 0 (steady), 0.025, 0.05, 0.075 and 0.1. The angle of attack variation was $\alpha = 10^\circ + 10^\circ \sin \omega t$. Some of the important results from this experimental data base will be discussed in the next section.

4. RESULTS AND DISCUSSION

4.1. Qualitative Flow Description

4.1.1. Effect of Mach Number

Figure 3 (Ref. 12) shows stroboscopic schlieren pictures of the flow over an oscillating airfoil at different Mach numbers. These pictures obtained over an exposure time of $1.5 \mu\text{sec}$ represent the instantaneous density gradient field without any history effects present, unlike most other flow visualization images. The dynamic stall vortex can be seen as a dark circular structure at approximately 50% chord location in all images with lighter shades of gray towards the leading edge (due to the orientation of the knife edge); the streaks seen slightly downstream of the vortex at $x/c = 0.7$ are cracks in the glass. It is interesting that the angle of attack at which the vortex reaches this location is 15.1 deg. up to $M = 0.25$, but as the Mach number increases, the corresponding angle decreases monotonically; for example, it is 13.8 deg. at $M = 0.35$, 12.7 deg. at $M = 0.4$ and 12.3 deg. at $M = 0.45$. This is photographic evidence that the angle of attack at which the dynamic stall process is initiated is independent of Mach number up to $M = 0.3$ and decreases with increasing Mach number beyond this value. Thus, it can be said that compressibility effects set in at $M = 0.3$ and premature dynamic stall occurs at higher Mach numbers.

Quantitative support to the above statement can be found in the data presented in Fig. 4, (Ref. 12). Stroboscopic schlieren pictures were obtained for a wide range of different conditions. The pictures were analyzed by following the movement of the vortex center along the airfoil upper surface. It can be seen that (within experimental scatter) up to $M = 0.3$, the vor-

tex trajectory as a function of the angle of attack is nearly identical. However, for $M \geq 0.3$, the curves depart considerably, moving to progressively lower angles of attack as the Mach number is increased. This supports the conclusion that the threshold for significant compressibility effects is at $M = 0.3$. As M is increased above 0.3, the vortex originates at lower angles of attack and is also shed at correspondingly lower angles of attack. Thus, compressibility accelerates the initiation of the dynamic stall vortex and hence, occurrence of deep stall.

4.1.2. Effect of Unsteadiness

Figure 5 (Ref. 13) is a plot of the dynamic stall angle of attack vs. reduced frequency for different Mach numbers. The results discussed above can be seen in this figure as well. It should be noted that for any given Mach number, as the reduced frequency is increased, the dynamic stall angle also increases. Thus, even though dynamic stall occurs at lower angles of attack at higher values of M , dynamic stall can be delayed by increasing the reduced frequency in the compressible flow regime as well. Thus, increasing unsteadiness always delays occurrence of stall. The reason for this is believed to be the way in which unsteadiness alters the airfoil leading edge pressure distribution (see Sec. 4.2.3) and thus, the vorticity production there.

Other noteworthy results include the fact that the vortex convection velocity was 30% of the free stream velocity for all cases studied. No shocks could be detected in the images obtained in the schlieren studies for these conditions (see Sec. 4.2.4), but a small shock was observed for the case of $\alpha = 10^\circ + 2^\circ \sin \omega t$ at $M = 0.45$ and $k = 0.075$, (Ref. 14).

Having identified the features of the flow after the vortex has formed, attention will now be focused on the finer details of the flow. It is worth noting that for control purposes, the game is already 'lost' once the vortex has formed.

4.2. Flow Description from PDI Studies

4.2.1. Dynamic Stall Flow Development

Figure 6 (Ref. 15) shows a sequence of interferograms obtained over the oscillating airfoil for $M = 0.35$ and $k = 0.05$. The fringes seen in it are constant density contours of the flow. The stagnation point is on the airfoil lower surface, near the leading edge and the fringes are seen to converge here. At $\alpha = 10.65^\circ$, (Fig. 6a) a moderately thick boundary layer is seen near the trailing edge. The fringes indicate that there is a slight local trailing edge separation; however, it appears to have no measurable effect on the overall flow. The fringes at $\alpha = 12.11^\circ$ (seen in Fig. 6b), after radiating from around the leading edge, turn towards the airfoil upper surface downstream of the suction peak. But, when they encounter the local boundary layer, they turn sharply again towards the trailing edge. A closer examination reveals that there is a small region on the upper surface near the leading edge which is enclosed by the fringes that physically appears like a bubble. Pressure distributions (see Ref. 16) deduced

from the interferograms confirm that a laminar separation bubble is present under these conditions. As the angle of attack is increased, the bubble breaks down and a vortical structure appears at $\alpha = 12.83^\circ$. The static stall angle for $M = 0.35$ is 11.6° , and thus, the first indication that the dynamic stall delay has ended and the dynamic stall process *itself* has begun is seen in Fig. 6d, 1.2 degrees beyond static stall. The events that lead to the formation of dynamic stall vortex occur very rapidly from this angle of attack, in a very small angle of attack range, (less than one degree, shown in Fig. 6b - 6d). Thus, the complete details of the changes are not easy to capture; the rapidity of the process and possible cycle-to-cycle variations make it a very challenging measurement problem. The earlier schlieren data showed that the deep dynamic stall angle for this case was 15.2° ; thus, by $\alpha = 16.02^\circ$, deep dynamic stall has already occurred. However, the number of fringes on the lower surface near the trailing edge shows that sharp gradients are still present there. The subsequent trailing edge flow evolution (such as vortex shedding, the occasional propagation of the vortex upstream over the airfoil upper surface (Ref. 17), etc.) influences the other details aspects of the separated flow like reattachment, hysteresis loops, etc.

4.2.2 Effect of Mach Number

Figure 7 presents interferograms for $M = 0.3, 0.35, 0.4$ and 0.45 , obtained at $k = 0.05$ and $\alpha = 12.06^\circ$. Fig. 7a at $M = 0.3$, shows a laminar separation bubble is about to break-down at this angle of attack. However, the effect is not detectable in the outer flow. Fig. 7b, at $M = 0.35$, shows the formation of vertical fringes from $x/c = 0.04$ to $x/c = 0.15$. It has been shown in Ref. 17 that this state represents the onset of dynamic stall and that the vortex is in its primitive stages of formation. The outer flow still is not affected by the major changes in the flow field close to the airfoil. At $M = 0.4$, (Fig. 7c) the dynamic stall vortex has fully developed and has convected over the airfoil surface; it should be pointed out that the imprint of the dynamic stall vortical region in compressible flow is not circular, but some what oval in shape. The outer edge of the vortex has reached about 30% chord; further downstream, the boundary layer has grown considerably in size. In contrast, Fig. 7d shows that at $M = 0.45$, the dynamic stall process has progressed to an extent where the vortex has already convected beyond $x/c = 0.5$. In fact, deep dynamic stall occurred for $M = 0.45$ and $k = 0.05$ at $\alpha = 14.2^\circ$, but for $M = 0.3$, the corresponding angle was 15.9° . These quantitative results support the schlieren flow visualization discussed earlier. The corresponding global pressure distributions are shown in Fig. 7e to 7h. These were derived by using isentropic flow assumptions, even when a dynamic stall vortex was present, (it is believed that the errors introduced do not result in a different interpretation of the results at these Mach numbers). The dramatic influence of the vortical flow on the outer inviscid flow is clearly seen in Fig. 7g and Fig. 7h.

4.2.3. Delay of Stall Due to Unsteadiness

Figure 8 shows the peak suction pressure coefficient,

$C_{p_{min}}$ plotted as a function of angle of attack for $M = 0.3$, for steady flow ($k = 0$) and the unsteady flow cases of $k = 0.05$ and 0.1 . The distribution for steady flow shows abrupt leading edge stall that is typical of NACA 0012 airfoil. The curves for the unsteady cases show a delay of stall from that of steady flow, which increases with k . This clearly points out that the airfoil develops less suction at comparable angles of attack and thus, the airfoil experiences a lesser adverse pressure gradient with increasing unsteadiness. The peak suction eventually reaches a value higher than that in steady flow, although the resultant adverse pressure gradient may not be much higher (see Fig. 10). It has been shown in Ref. 17 that for a transiently pitching airfoil, the suction pressure coefficient remains at the maximum value during the time when the dynamic stall vortex forms and organizes, and then drops as the vortex convects down the airfoil; the same result is seen for the oscillating airfoil also. The organization time seems to depend on the reduced frequency, since the amount of coherent vorticity introduced by the airfoil motion also depends on k . So, it can be expected that at higher reduced frequencies, the plateau seen in the $C_{p_{min}}$ distributions lengthens, leading to a longer stall delay; this effect can be seen in Fig. 8. The peak suction drops gradually once vortex convection begins.

Figure 9 compares the pressure distributions at $M = 0.3$ between the steady flow at $\alpha = 11.0$ deg and unsteady flow at $k = 0.05$ at $\alpha = 10.0$ deg. It is evident that the two compare very well, with only a slight deviation in the bubble region. The agreement indicates that the unsteady flow at a higher angle of attack is similar to steady flow at a lower angle of attack, prior to stall onset, pointing to a general lag of flow development in the unsteady flow. In this case for $M = 0.3$, and $k = 0.05$, this lag is one degree. The plateau seen in the distributions points to the existence of a laminar separation bubble, since the pressure everywhere along the bubble is constant. The pressure rises normally after the bubble closes. The bubble forms over the airfoil since the Reynolds number (360,000 - 840,000) of the flow was in the transitional regime. The other small differences are within the one fringe the uncertainty of the PDI technique.

Figure 10 presents the pressure distributions for $0 \leq x/c \leq 0.05$ for $k = 0, 0.05$ and 0.1 at $\alpha = 10.0$ deg. at $M = 0.3$. The plots show that the suction develops over an oscillating airfoil at a reduced rate as the frequency of oscillation is increased and in fact does not reach the steady state level at the angle compared. Past the suction peak, the pressure rises more slowly in the unsteady cases. This delay of the airfoil flow development, with corresponding delay in the development of the adverse pressure gradients can be seen to be one of the causes of dynamic stall delay that is observed. It should be noted that each symbol in Fig. 10 corresponds to a quantitative measure of the instantaneous pressure as obtained from the interferogram. This is the first set of data to show the lessening of the local adverse pressure gradient by unsteadiness in such detail and offers a reasonable explanation for the delay for stall.

4.2.4. Formation of Multiple Shocks

For certain compressible flow conditions, (e.g. $M = 0.45$, $k = 0.05$, $\alpha = 10^\circ$) a shock or a series of shocks formed near the airfoil leading edge as shown in Fig. 11. The *lambda* shocks seen are characteristic of laminar flow behavior. Interestingly, the flow does not separate immediately once a shock forms. It seems to be able to withstand the local adverse pressure gradient caused by the shock for a small range of angle of attack before separating. A series of pictures for these experimental flow conditions showed that flow separation at the foot of the last shock eventually resulted in the dynamic stall vortex. At this time, the cause of the multiple shocks is still under investigation. It is believed that the first shock interacts with the laminar leading edge boundary layer introducing a waviness in the boundary layer thickness which seems to be sufficient for producing the expansion waves and compression waves necessary for the system to sustain itself during a small angle of attack sweep of the airfoil.

A map of the pressure coefficient distribution in the vicinity of the multiple shocks for the case shown above is presented in Fig. 12. The leading edge region has been magnified so that the flow variations due to the shocks can be analyzed. This unique quantitative evaluation of the *outer flow* was made possible by the fringe tracing/analysis algorithm developed specifically for this task. It is clear that the flow becomes supersonic near the surface and that a region of $M > 1$ (the sonic line corresponds to $C_p = -2.76$) which is significantly wider than previously thought exists in the flow. In this region, 5 shocks are present. The shocks terminate in the sonic line. The outer flow, however, is subsonic; this is one of the key differences in compressible dynamic stall flow that cannot be reproduced at low speeds. As the angle of attack is increased, the shock pattern changes since the interaction with the boundary layer changes. Eventually, a dynamic stall vortex appears at the foot of the last shock. The x/c location at which this happens is about $0.05 - 0.08$, indicating that the dynamic stall vortex does not form at the leading edge. This figure attests to both the presence of the fine scale details in the flow as well as the ability of the measurement technique used in this research to capture them.

4.3. Role of Transition

As stated earlier, the dynamic stall vortex forms near the point where the separating shear layer undergoes transition. Thus, it can be expected that factors affecting transition also affect the processes of dynamic stall onset and vortex formation. Applicability of low Reynolds number testing methods and test data to model rotors and eventually to flight Reynolds numbers thus becomes a formidable challenge and suffers from several limitations. Whereas this situation is not new, it is nevertheless a major issue in model rotor testing, since the process of flow separation is particularly sensitive to the state of the boundary layer. A standard approach to simulate high Reynolds number

results in the laboratory is to conduct tests by tripping the airfoil boundary layer with the intent that the flow subsequently develops as a fully turbulent flow. It is important to recognize that despite the vast number of previous experimental studies on tripping in steady flow and the recommendations on the right kind of trips that have resulted, these schemes are not directly applicable to dynamic stall flow; and the use of steady flow tripping schemes for dynamic stall flow studies has not been satisfactory.

4.3.1 Description of the Trips

The airfoil boundary layer at the vortex formation location on the present model was $O(50\mu\text{m})$; hence, the trip height that was needed was much smaller than this. Also, the trip used could radically change the stall behavior of the airfoil, Ref. 7. Thus, it was imperative that tests be conducted with a series of trips and that selection be based on which trip provided "turbulent" flow-like information. As part of this study, five different trips were studied in the CDSF. Randomly distributed roughness elements (aluminum oxide particles or grit) were glued on to the airfoil surface by a thin lacquer or adhesive, depending upon the trip material. The trip height ranged from $170\mu\text{m}$ to about the height of the boundary layer, $\approx 50\mu\text{m}$. The length was either 3% chord, starting at 1% chord location (near the leading edge) to 4% chord; or from stagnation point on the lower surface to 4% chord point on the upper surface. PDI data was obtained for the flow over an oscillating with the different trips installed, at several Mach numbers and reduced frequencies. The trips were evaluated based on the criteria of elimination of the laminar separation bubble, delay of dynamic stall and the production of higher suction levels than the untripped airfoil. The trip that satisfied these conditions was accepted as the "right" trip. This optimum trip was made from 22-36 μm aluminium oxide particles deposited over a thin lacquer coating installed with a total height of about $43\mu\text{m}$ from $0.005 \leq x/c \leq 0.03$.

4.3.2 Qualitative Analysis

Figure 13a and 13b compare interferograms over the airfoil with and without the optimum trip at $M = 0.3$ and $k = 0.05$ and $\alpha = 10.0^\circ$. The presence of the laminar bubble (described in Sec. 4.2.2, Fig. 6) can be clearly found in Fig. 13a by studying the fringe pattern. In Fig. 13b, the fringe very near the airfoil leading edge shows a closed loop pattern, which corresponds to a well defined suction peak. The fringes slightly downstream of the suction peak meet the upper surface over a small length of the airfoil region rather than near a point as seen in Fig. 13a. This fringe pattern indicates the absence of the bubble; the corresponding pressure distributions confirmed this interpretation (Ref. 7). Fig. 13c shows the flow field at $\alpha = 13.99^\circ$, when the dynamic stall vortex has fully formed and has convected past the $x/c = 0.25$ point for the untripped airfoil, whereas in Fig. 13d, at the same angle of attack, the vertical fringes which precede the dynamic stall vortex have just appeared, pointing very definitely to delay of stall that was achieved due to the presence of the trip, (it is worth pointing that if improper trips were used, the

stall process could even be accelerated, as was demonstrated in Ref. 18).

4.3.3. Quantitative Analysis

Figure 14 presents the variation of the airfoil peak suction in the presence of the trip at $M = 0.45$ and $k = 0.05$. The significantly increased suction levels are proof that the airfoil was tripped successfully and a flow more representative of turbulent flow dynamic stall was achieved in the wind tunnel. It is interesting to note that the $C_{p_{min}}$ values for both the untripped and tripped airfoil exceed the critical value of -2.76; thus, the flow in both cases becomes supersonic. The larger C_p values of the tripped airfoil flow suggest that the local Mach numbers in this flow are higher. It is interesting to note that despite the larger Mach number, the shock system that results over the airfoil is much less dramatic (see Fig. 15 compared to Fig. 12), once again attributable to the turbulent flow over it. The corresponding pressure distribution obtained from a PDI image is shown in Fig. 15 for $M = 0.45$, $k = 0.05$ and $\alpha = 10.0^\circ$. In comparison with Fig. 12, (multiple shocks flow field over the untripped airfoil at the same conditions) it is seen that the local C_p values are higher and that the sonic line is much broader. Its shape is also different, with a bulging front and a longer tail extending to $x/c = 0.15$. Despite the larger Mach numbers, only two shocks (represented by the dotted lines nearly normal to the surface) are seen in it. Further, there is no flow separation seen in this case. This pair of figures graphically demonstrates the importance of proper tripping of the boundary layer, especially in unsteady compressible flow. It is interesting that there is qualitative similarity of this result to the turbulent computational dynamic stall studies of Ref. 19 and 20.

4.4. Role of Adverse Pressure Gradient

Analysis of the adverse pressure gradient near the untripped airfoil leading edge at $M = 0.3$ showed that dynamic stall was caused by the *failure of the laminar shear layer to reattach* (Ref. 18) due to the levels of this gradient. At higher Mach numbers dynamic stall occurred either from the above reason or from a shock-induced separation. It has been shown in Ref. 18 that dynamic stall is initiated over a transiently pitching airfoil when the leading edge adverse pressure gradient ($\frac{dC_p}{d(x/c)}$) reaches a critical value that depends upon Mach number and pitch rate. Fig. 16 (Ref. 18) shows that the critical value of the adverse pressure gradient decreases with increasing Mach number, once again indicating the strong influence of compressibility on the process. It appears that compressibility weakens the ability of the boundary layer to withstand the adverse pressure gradient, even though the adverse pressure gradient value is smaller. Increasing the pitch rate seems to enable the boundary layer to withstand higher levels of adverse pressure gradients, (Fig. 10, Ref. 18). The results seem to be true for both the untripped and tripped airfoil, leading to the conclusion that unsteadiness introduces certain changes to the leading edge vorticity layer and makes it behave differently.

Figure 17 presents the adverse pressure gradient development over the oscillating airfoil at $M = 0.3$ at $k = 0.05$. For the untripped airfoil, the pressure gradient immediately following the suction peak is plotted. It was found that the value of the pressure gradient at the formation of the laminar separation bubble is about 40, at an angle of attack of about 7 deg. Dynamic stall is seen to occur at a pressure gradient of 125 at $\alpha = 12.5$ deg. As the dynamic stall vortex begins to convect, the pressure gradient drops. In case of the tripped airfoil, the dynamic stall process begins at $\alpha = 13.5$ deg., when the pressure gradient is about 150. Thus, there is a slight delay of stall, attributable to an improvement in the ability of the boundary layer to withstand the forces inducing flow separation. The trends at other reduced frequencies were nearly the same, although at times the pressure gradients at the angle of attack of dynamic stall vortex formation were slightly less for the tripped airfoil when compared to the untripped flow. But, the values were *always* higher than that at which the laminar separation bubble formed in the untripped flow. Some of the differences seen can be attributed to the noise inherent in the process of numerical differentiation of the pressure distribution to recover the pressure gradient information. Also, any trip, however small it is, still increases the momentum thickness of the boundary layer and hence, introduces additional drag, which has the equivalent effect of reducing the total adverse pressure gradient that can be attained before stall occurs. This points to the difficulty of conducting laboratory tests by tripping to simulate the higher Reynolds number flow, a fact of critical importance to model rotor testing.

5. CONCLUSIONS

A review of results from an ongoing study of the effects of compressibility on dynamic stall of oscillating airfoils has been presented. A unique compressible dynamic stall facility was designed and developed for this purpose. The flow was studied using stroboscopic schlieren and stroboscopic point diffraction interferometry (PDI) techniques. The latter was developed for use in unsteady separated flows to provide a quantitative description of the instantaneous surface and global pressure distributions of the flow. The experimental conditions were chosen to be directly relevant to that encountered by the retreating blade of a helicopter model rotor. The results show that the process of dynamic stall vortex formation occurs rapidly in a very small (half-a-degree) angle of attack range. Compressibility effects become critical at a free stream Mach number of 0.3. Compressibility promotes dynamic stall onset by decreasing the angle of attack at which the flow separates with increase in Mach number. The strongly compressible local flow can produce multiple shocks in the leading edge region, and at times can also induce flow separation leading to dynamic stall. Increasing the reduced frequency delays stall onset, even under compressible conditions. As much as two degrees of stall onset delay was observed at $M = 0.3$ when compared to steady flow. The PDI results also revealed that dynamic stall occurred as the laminar separation bubble that formed over the airfoil broke down. Evidence points to the failure of the laminar shear layer to reattach as the cause of stall

onset. This premature stall at higher Mach numbers could be attributed to the inability of the compressible boundary layer to withstand the adverse pressure gradient in the flow. Increasing unsteadiness has a beneficial effect in this regard, even in compressible flow. Tests conducted to simulate higher Reynolds number flow situations by tripping the leading edge boundary layer have revealed some of the issues and concerns of tripping leading-edge-stalling flows.

The various fluid flow physics issues that have been uncovered by this investigation include formation of multiple shocks, effects of leading edge pressure gradient in unsteady flow separation as affected by the degree of unsteadiness, the delay of the leading edge pressure development with increase in pitch rate, and the effects of boundary layer transition. The quantitative flow field data base that has been developed will be of significant value to researchers involved in flow modelling and in validating CFD codes developed to represent this complex and challenging flow phenomenon.

ACKNOWLEDGEMENTS

The project was supported by ARO-MIPR-114-91, 132-92, and 125-93 to the Naval Postgraduate School and was monitored by Dr. T.L. Doligalski. Additional support was received from the U.S. AFOSR, which was monitored by Maj. D.B. Fant. The work was carried out in the Fluid Mechanics Laboratory Branch of NASA Ames Research Center. The steady encouragement of Dr. S.S. Davis, Chief, FML Branch, the able assistance of Dr. M.C. Wilder while performing the experiments, the support of Mr. J.D. Loomis in the conduct of experiments and the interferogram image processing support of Ms. S.Nado are greatly appreciated.

6. REFERENCES

1. W.J., McAlister, K.W., Carr, L.W., Pucci, S.L., Lambert, O. and Indergrand, R.F., "Dynamic Stall on Advanced Airfoil Sections," *AHS Journal*, 26,3, July 1981, pp. 40-50.
2. Carr, L.W., "Progress in Analysis and Prediction of Dynamic Stall," *J. Aircraft*, 25,1, Jan. 1988, pp. 6-17.
3. McCroskey, W.J., "The Phenomenon of Dynamic Stall," NASA TM 81264, March 1981.
4. Gostelow, J.P., Blunden, A.R. and Walker, G.J., "Effects of Free-Stream Turbulence and Adverse Pressure Gradients on Boundary Layer Transition", *ASME Paper No. 92-GT-380*, IGTE, Cologne, Germany, June 1-4, 1992.
5. Tan, C.M., and Carr, L.W., A Report on the 1992 AFDD International Dynamic Stall Workshop on "Correlation of Dynamic Stall Models with 3-D Dynamic Stall Data" NASA TM in preparation, 1994.
6. Lorber, P.F., Strauer, R.C., Haas, R.J., Anderson, T.J., Torok, M.S. and Kohlhepp, F.W., "Techniques for Comprehensive Measurement of Model Helicopter Rotor Aerodynamics", *AHS Forum 50*, Washington, D.C., May 11-14, 1994.

7. Chandrasekhara, M.S., Wilder, M.C. and Carr, L.W., "Boundary Layer Tripping Studies of Compressible Dynamic Stall Flow", *AIAA Paper No. 94-2340*, 25th Fluid Dynamics Conference. Colorado Springs, Co, June 20-23, 1994.
8. Carr, L.W., McAlister, K.W. and McCroskey, W.J., "Analysis of Development of Dynamic Stall Based on Oscillating Airfoil Experiments", NASA TN D-8382, 1977.
9. Liiva, J., "Unsteady Aerodynamic and Stall Effects on Helicopter Rotor Blade Airfoil Sections", *J. Aircraft*, 5,1, Jan-Feb. 1969, pp. 46-51.
10. Carr, L.W. and Chandrasekhara, M.S., "Design and Development of a Compressible Dynamic Stall Facility", *J. Aircraft*, 29,3, May-June 1992, pp. 314-318.
11. Brock, N., Chandrasekhara, M.S. and Carr, L.W., "A Real Time Interferometry System for Unsteady Flow Measurements", in "ICIASF'91 RECORD", IEEE Publication 91CH3028-8, pp. 423-430.
12. Chandrasekhara, M.S. and Carr, L.W., "Flow Visualization Studies of the Mach Number Effects on the Dynamic Stall of Oscillating Airfoils", *J. Aircraft*, 27,6, June 1990, pp. 516-522.
13. Platzer, M.F., Chandrasekhara, M.S., Ekaterinaris, J.A. and Carr, L.W., "Dynamic Airfoil Stall Investigations", in "Proc. 5th Symposium on Numerical and Physical Aspects of Aerodynamic Flows", Long Beach, CA, January 13-15, 1992.
14. Chandrasekhara, M.S. and Brydges, B.E., "Amplitude Effects on Dynamic Stall of an Oscillating Airfoil", *AIAA Paper 90-0575*, 28th Aerospace Sciences Meeting, Reno, NV, January 1990.
15. Carr, L.W., Chandrasekhara, M.S., Ahmed, S., and Brock, N.J., "A Study of Dynamic Stall Using Real Time Interferometry", *AIAA Paper 91-0007*, To appear in *J. Aircraft*.
16. Carr, L.W., Chandrasekhara, M.S. and Brock, N.J., "A Quantitative Visual Study of Unsteady Compressible Flow on an Oscillating Airfoil", *AIAA Paper 91-1683*, To appear in *J. Aircraft*.
17. Chandrasekhara, M.S., Carr, L.W. and Wilder, M.C., "Interferometric Investigations of Compressible Dynamic Stall Over a Transiently Pitching Airfoil", *AIAA Journal*, 32, 3, Mar. 1994, pp. 586-593.
18. Wilder, M.C., Chandrasekhara, M.S., and Carr, L.W., "Transition Effects on the Compressible Dynamic Stall of Transiently Pitching Airfoil", *AIAA Paper No. 93-2978*, 24th Fluid Dynamics Conference, Orlando, FL, July 6-9, 1993.
19. Visbal, M.R., "Effect of Compressibility on Dynamic Stall of a Pitching Airfoil", *AIAA Paper 88-0132*, Jan. 1988.
20. Ekaterinaris, J.A., "Compressible Studies of Dynamic Stall", *AIAA Paper 89-0024*, Jan., 1989.

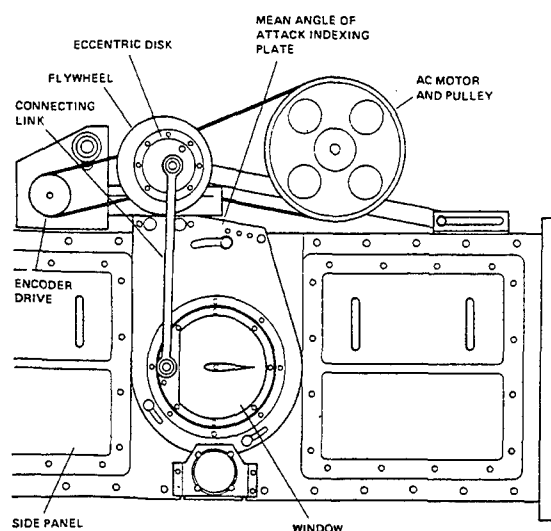


Fig. 1. Schematic of the Compressible Dynamic Stall Facility

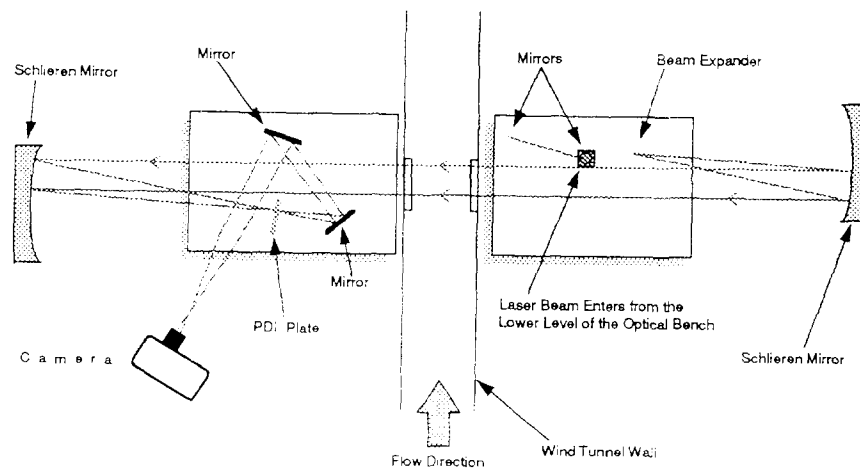


Fig. 2. Schematic of the Point Diffraction Interferometry System.

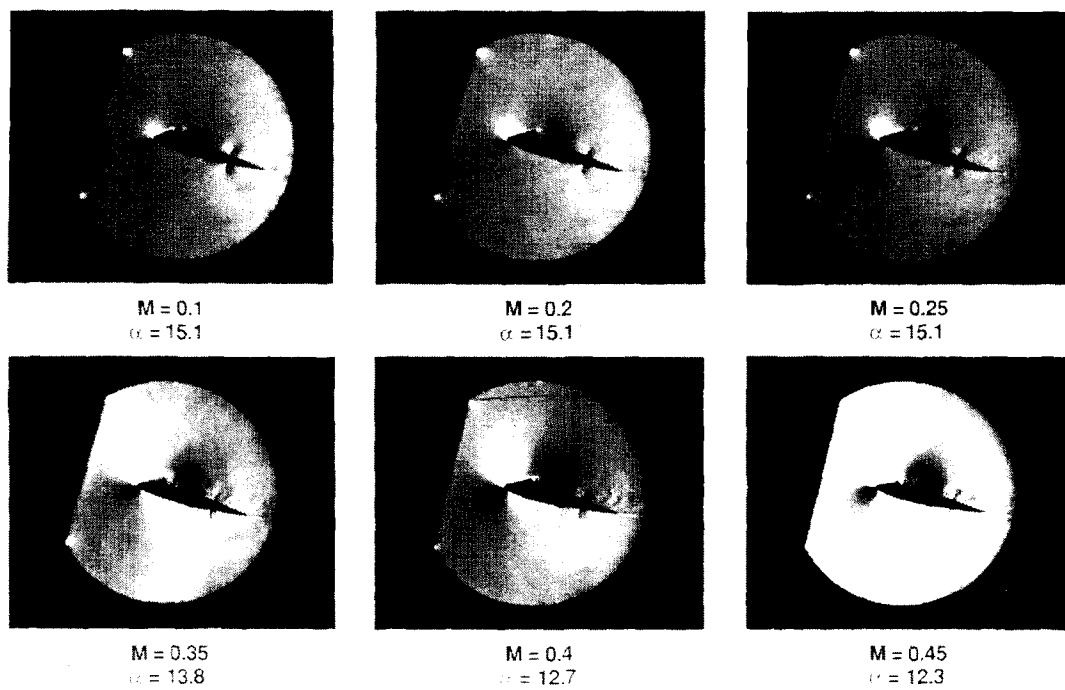


Fig. 3. Effect of Compressibility on Dynamic Stall of an Oscillating Airfoil; $k = 0.05$.

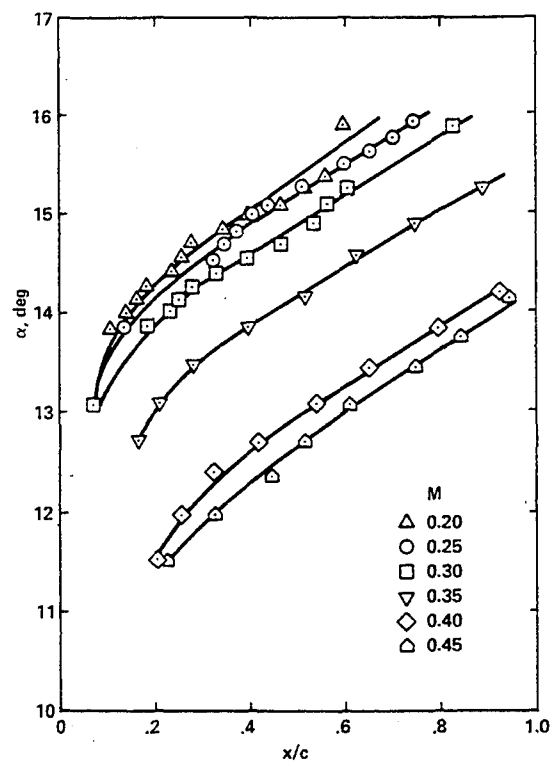


Fig. 4. Quantitative Effects of Mach Number on Dynamic Stall Process; $k = 0.05$.

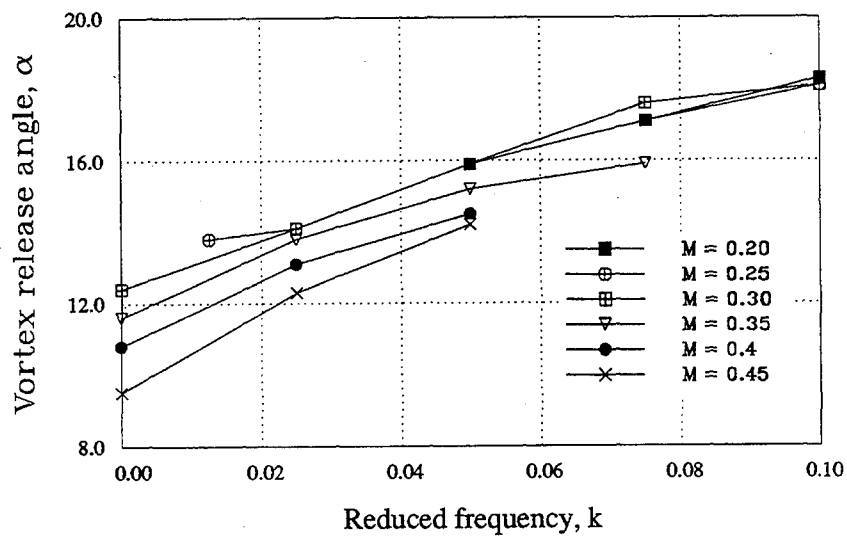


Fig. 5. Quantitative Effects of Reduced Frequency on Dynamic Stall Process.

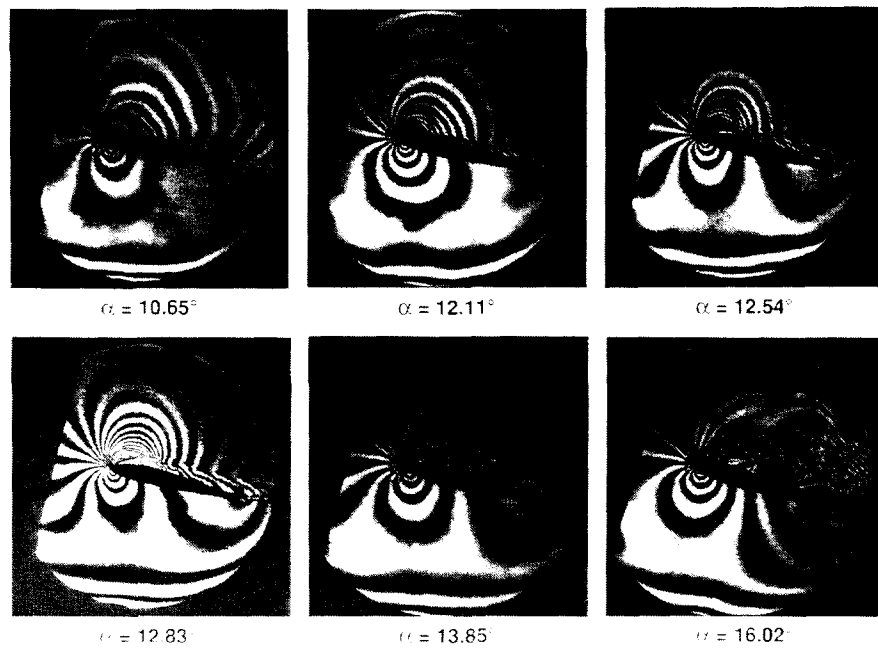


Fig. 6. Sequence of Interferograms Showing Dynamic Stall Development Over an Oscillating Airfoil; $M = 0.35$, $k = 0.05$.

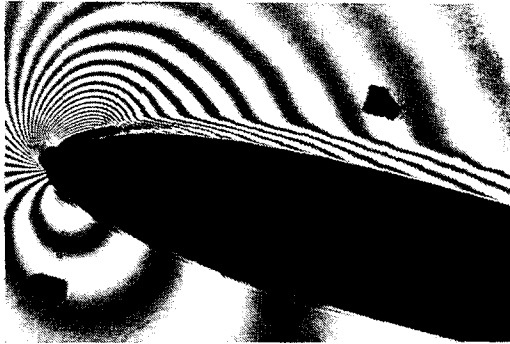
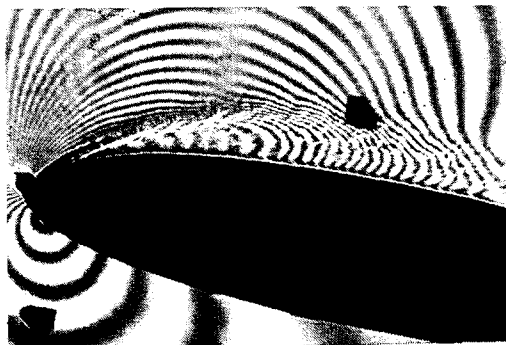
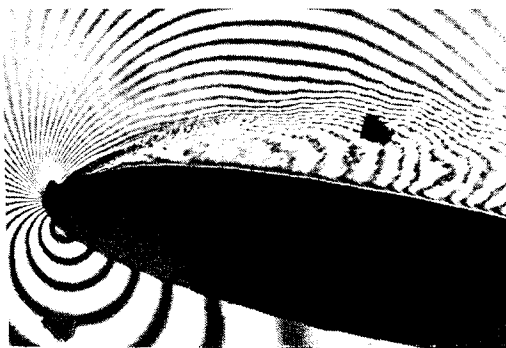
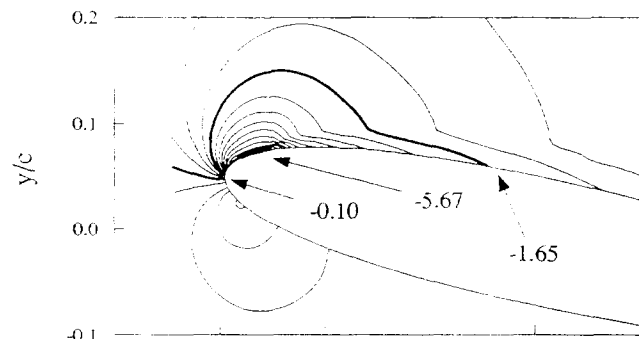
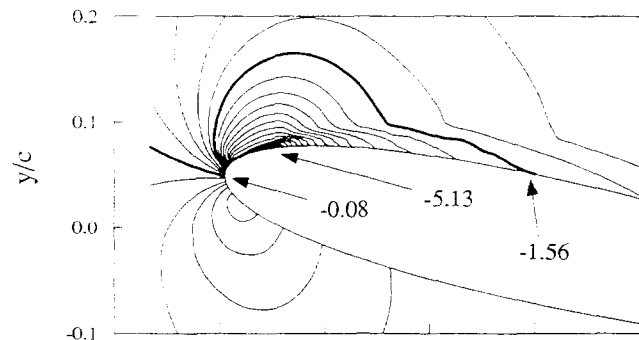
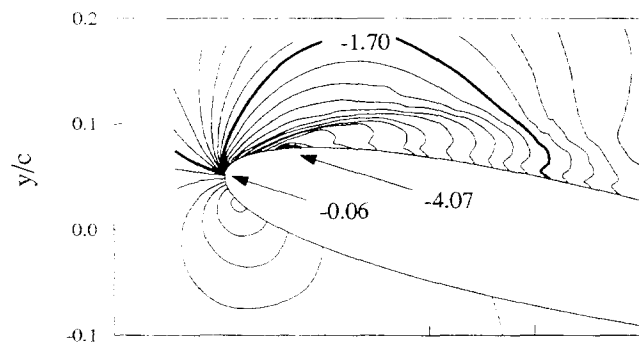
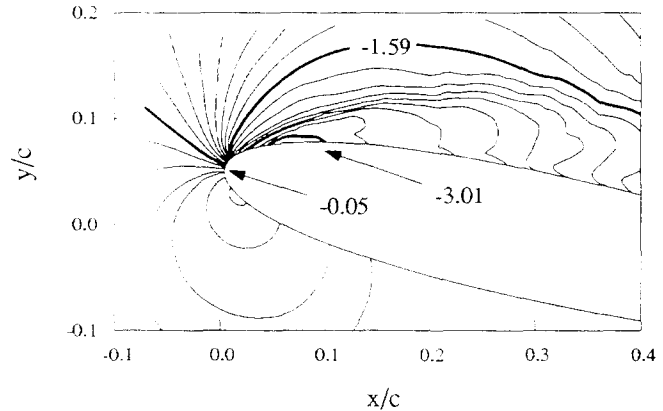
(a) $M = 0.3$ (b) $M = 0.35$ (c) $M = 0.4$ (d) $M = 0.45$ (e) $M = 0.3$ (f) $M = 0.35$ (g) $M = 0.4$ (h) $M = 0.45$ 

Fig. 7. Effect of Compressibility on Dynamic Stall: (a–d) PDI Images; (e–h) Global Pressure Fields.

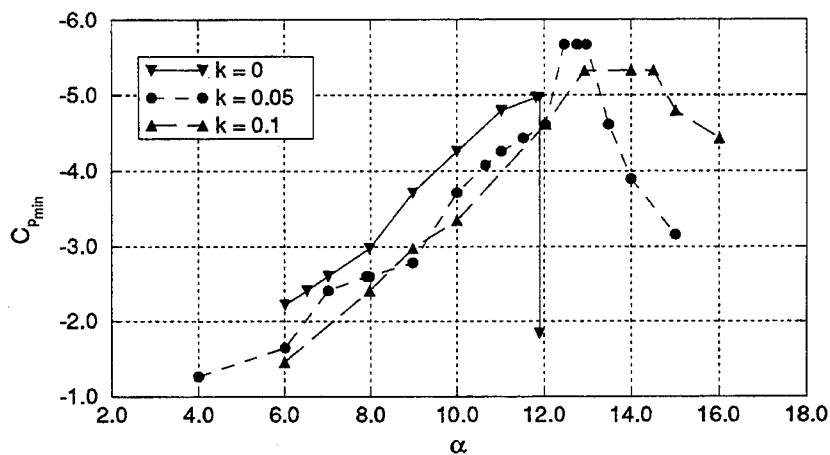


Fig. 8. Effect of Unsteadiness on Airfoil Peak Suction Development; $M = 0.3$.

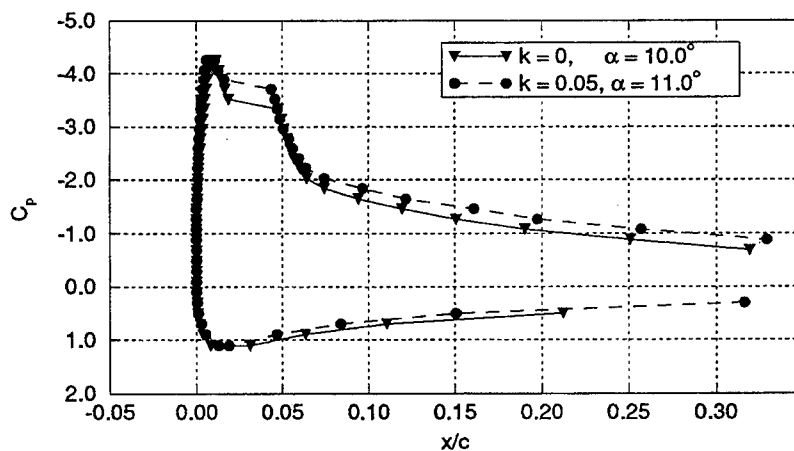


Fig. 9. Comparison of Steady and Unsteady Airfoil Pressure Distributions; $M = 0.3$.

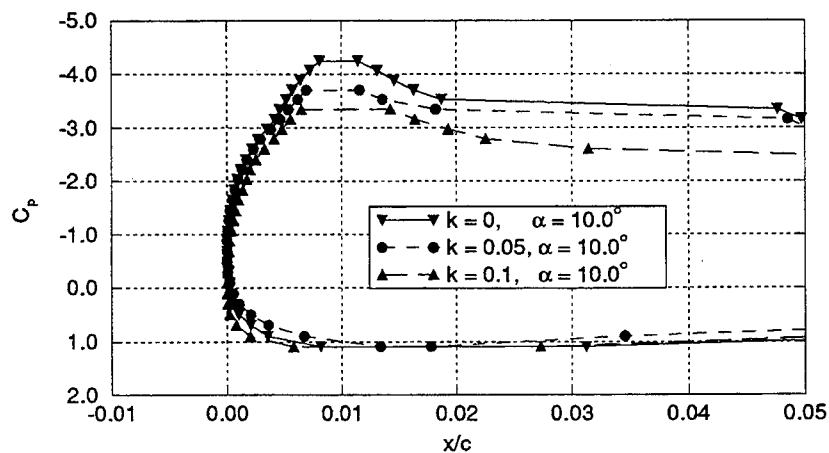


Fig. 10. Effect of Unsteadiness on Airfoil Leading-Edge Pressure Distribution; $M = 0.3$.

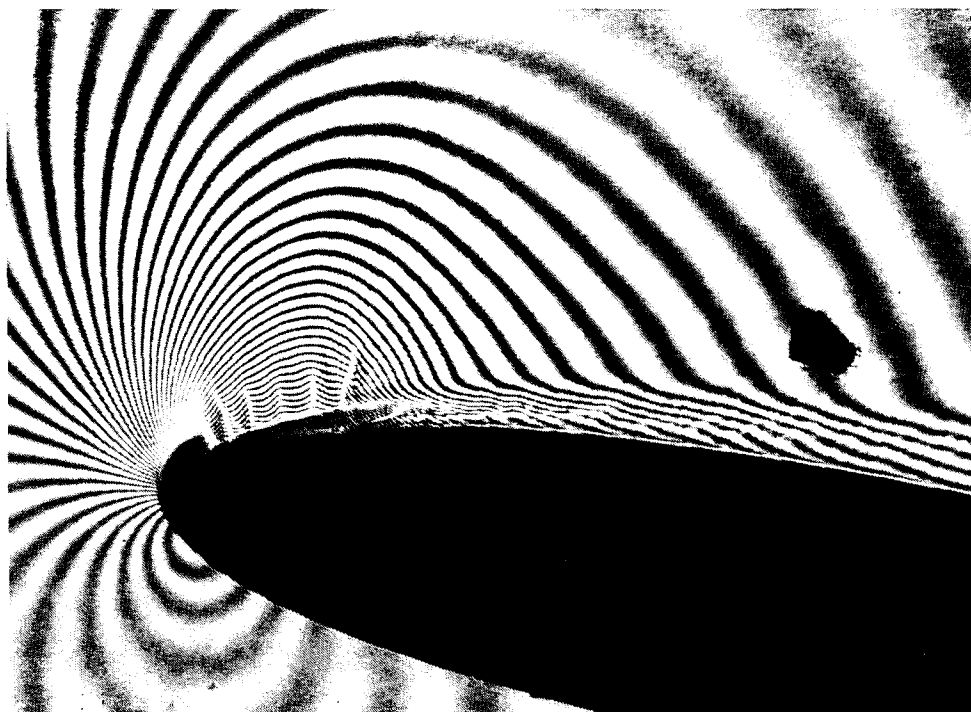


Fig. 11. PDI Image of Multiple Shocks Over Untripped Oscillating Airfoil; $M = 0.45$, $k = 0.05$, $\alpha = 10.0^\circ$.

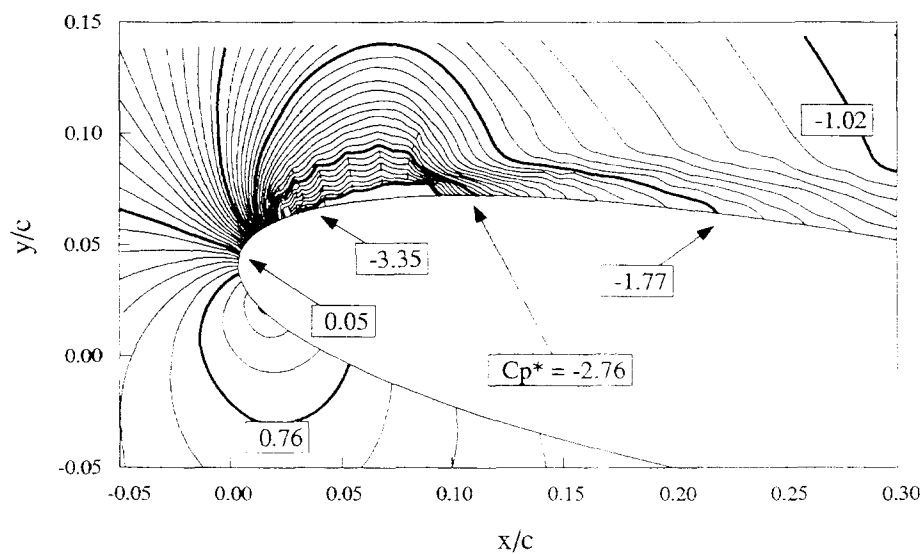


Fig. 12. Global Pressure Field Over Untripped Airfoil; $M = 0.45$, $k = 0.05$, $\alpha = 10.0^\circ$.

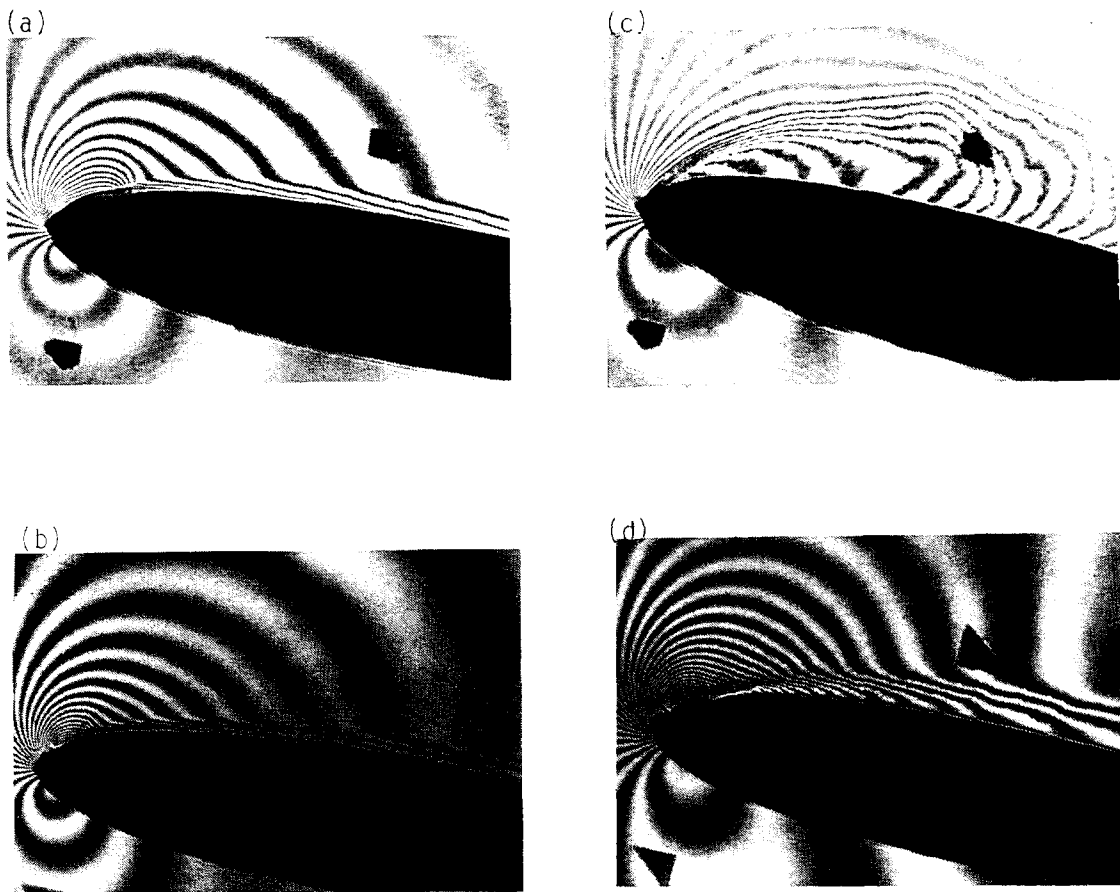


Fig. 13. Comparison of PDI Images of Untripped and Tripped Flow Fields; $M = 0.3$, $k = 0.05$.
Top Row: Untripped Airfoil, Bottom Row: Tripped Airfoil, (a, b) $\alpha = 10.0^\circ$, (c, d) $\alpha = 13.99^\circ$.

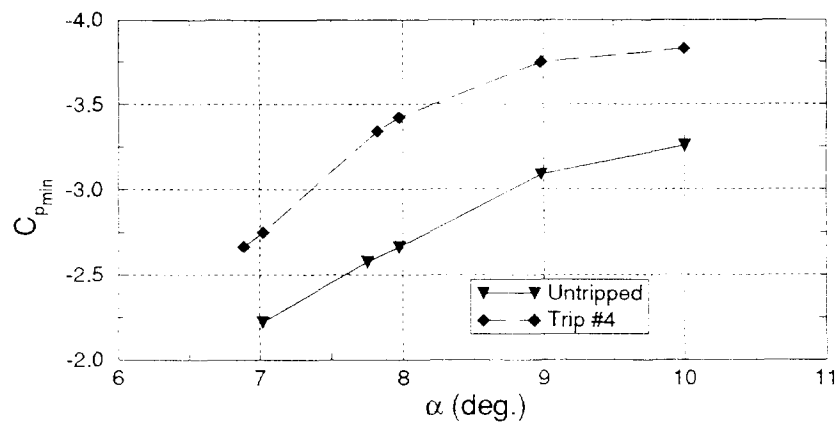


Fig. 14. Effect of Tripping on Airfoil Peak Suction Development; $M = 0.45$, $k = 0.05$.

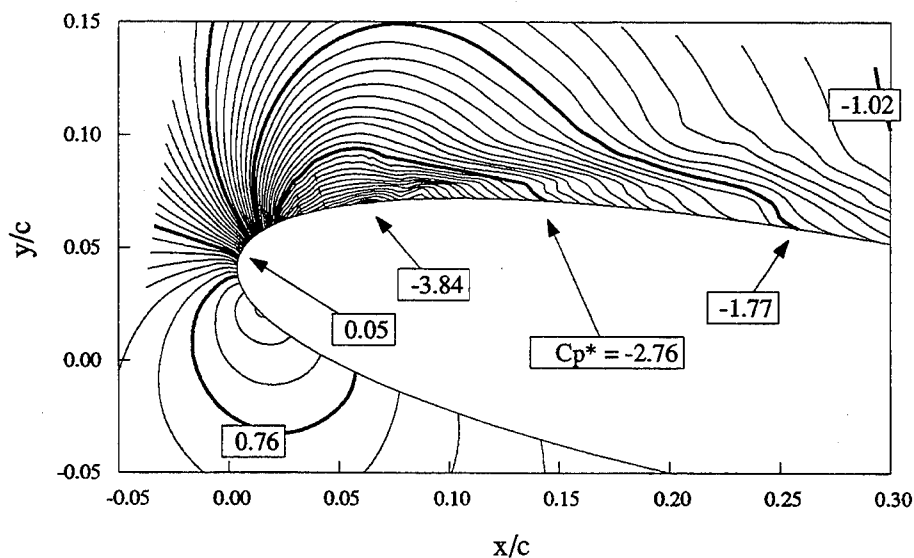


Fig. 15. Global Pressure Coefficient Field Over Tripped Airfoil; $M = 0.45$, $k = 0.05$, $\alpha = 10.0^\circ$.

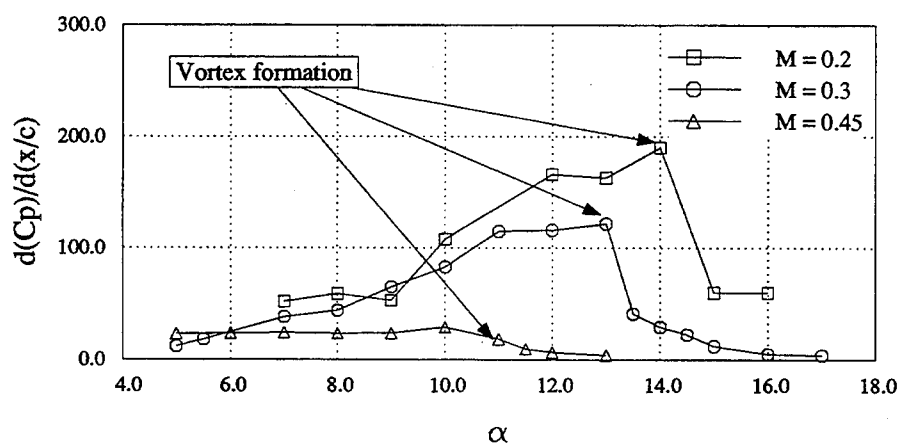


Fig. 16. Mach Number Effect on Leading-Edge Adverse Pressure Gradient Development on Tripped Airfoil; $\alpha^+ = 0.03$.

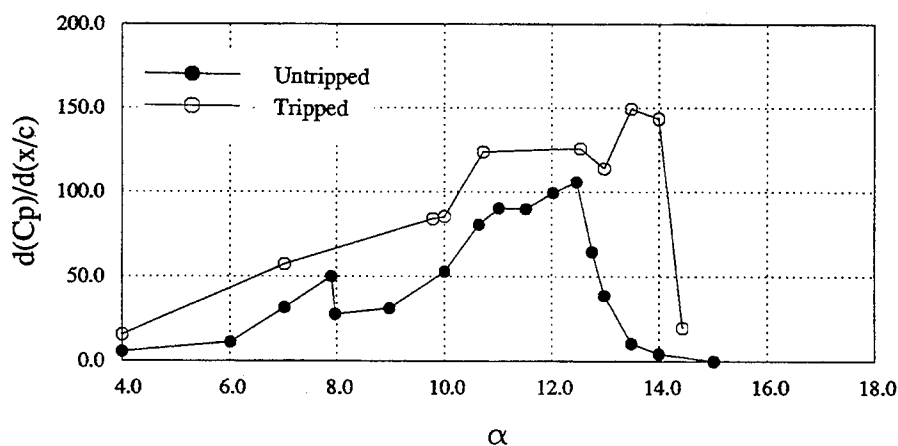


Fig. 17. Leading-Edge Adverse Pressure Gradient Development; $M = 0.3$, $k = 0.05$.

EFFECT OF TURBULENCE MODELING ON DYNAMIC STALL COMPUTATIONS

Mustafa Dindar*, Ünver Kaynak†

Turkish Aerospace Industries, Advanced Design Department
P.O. Box 18, 06692 Kavaklıdere/Ankara TURKEY

Abstract

Dynamic stall phenomenon was studied numerically to investigate effects of turbulence modeling. An unsteady Navier-Stokes code capable of solving flow field around an airfoil undergoing unsteady harmonic motion was used for this purpose. A comparative study conducted between equilibrium and nonequilibrium turbulence models. It was found that, nonequilibrium effects play an important role in determining the separation and vortex shedding mechanisms of dynamic stall. First of all, in light stall, inadequacy of equilibrium models defeated by including nonequilibrium effects, and only Johnson-King model could be able to produce light stall hysteresis loop that is similar to experiment. Secondly, in the deep stall regime, vortex shedding mechanism was found to be greatly influenced by turbulence model.

Introduction

Ever increasing demand in understanding the complicated nature of the problems in Applied Aerodynamics has compelled researcher's motivation for many years. Through the progressive stages of refined theories and approximations, primary emphasis was to understand viscous-inviscid interactions and their relations to flow separation, vortical flows and unsteadiness. Major operational difficulties that are faced in today's fixed and rotary wing aircraft, are due to our inadequate knowledge of complex unsteady flows and lack of its projection to design parameters. For instance, a helicopter often operates under severe conditions of flow separation and its own turbulent wake, which indeed introduce most of the undesirable effects to the vehicle's flight envelope. Apparently, tomorrow's most effective aeronautical devices will be built, once we expand our knowhow on viscous, turbulent unsteady flows. Within this broad flow category, one notices dynamic stall phenomenon which has always been addressed and studied due to its importance in fluid dynamic devices. Our knowledge of dynamic stall has expanded through theoretical, experimental and numerical efforts of numerous researchers^{1,2,3,4}. In Ref. 5 dynamic stall is defined as the break down of the flow field around an oscillat-

ing slender lifting surface beyond its critical angle of attack. Also, various experiments established that either trailing edge oriented unsteady separation or burst of a leading edge separation bubble yields vortex-like disturbances which entirely effect the forces and moments acting on the surface. Besides its practical utilization as a lift enhancement mechanism, control of post-dynamic stall effects, which differ from their static counterparts, persist on overall practical importance of this phenomenon. We also note that, the reason for delay of stall onset in a dynamic system stem from the formation of a vortex close to surface of the airfoil which continues to provide lift above the static stall angle.

The features of dynamic stall are characterized by degree of viscous-inviscid interactions taking place in the flow field. The intensity of a viscous-inviscid interaction in a shear flow depends on extend of the viscous layer. An interaction is said to be weak if various phenomena can be studied separately and combined to give total effect. Flows with shear layers can have weak interaction if these layers are either of $O(5.3Re^{-1}L)$ for laminar flow or $O([\ln Re]^{-1}L)$ for turbulent flows⁶. When viscous layers rapidly thicken and become larger than this magnitude, interaction is classified as a strong viscous-inviscid interaction. McCroskey and Pucci⁷ collected dynamic stall regimes into four groups depending on their viscous-inviscid interaction regions. They are:

- I) No Stall - Weak Interactions,
- II) Stall Onset - Mild Interactions,
- III) Light Stall - Strong Interactions,
- IV) Deep Stall - Viscous Dominant.

Among the four, the most challenging and difficult ones are the light and deep dynamic stall regimes. Light stall, for instance, shows general features of static stall, but unsteady separation and the extend of strong viscous-inviscid interaction are the primary features in classifying this regime. Aerodynamic damping is the strongest and boundary layer thickness is of the order of airfoil thickness during the stall. Deep stall, on the other hand, is characterized by highly nonlinear pressure fluctuations and large passage of vortical structures over the lifting surface. During the deep stall, boundary layer thickness can be of the order of airfoil chord length. The similar qualitative picture of these

* Research Assistant

† Research Scientist

two regimes is that both light and deep dynamic stall poses difficulties, such as resolution of temporal and spatial scales and effect of turbulence, when prediction methods are under consideration.

Principal developments in Computational Aerodynamics were made with increasing computer power and improved numerical algorithms. Solution of unsteady interactive flows have taken their share from this development as much as the computer time was available. Consequently, various aspects of dynamic stall problem were studied in different flow field conditions and appeared in technical publications. In Ref. 8 deep dynamic stall was studied in incompressible, laminar and turbulent flows. There, it was concluded that numerical analysis lacked certain accuracy to indicate some of the important features of dynamic stall observed in experiment. Ref. 9 wrote Navier-Stokes equations in terms of vorticity and stream function for incompressible, laminar flows. Impressive similarity between numerical simulation and experiment stressed the ability of computational tools in unsteady flows. To cover more practical applications of dynamic stall, compressibility effects were studied in Refs. 10 and 11. For Mach numbers above 0.2, where assumption of incompressible flow vanishes, it was found that compressibility has predominant effect on formation and growth of the leading edge vortex. Spatial and temporal accuracy of a compressible Navier-Stokes solver was studied in Ref. 12 for a deep dynamic stall case (which is also a case of this paper) with laminar flow assumption. Another deep stall case in Ref. 13 was used to study turbulence effects. Surprisingly it was concluded that effect of a higher-order turbulence model ($k - \epsilon$) was minimal in their particular case of study. In Ref. 14 incompressible full Navier-Stokes equations were used to study deep dynamic stall at low Mach numbers. Qualitative agreement between experiment and computation were reported.

The purpose of this paper is to present some of the recent results obtained with different turbulence models, in two important regimes of the dynamic stall phenomenon. In the light of these results^{15,16}, it is further desirable to pursue comparison studies, along with the recent developments in turbulence modeling, in order to point out a robust methodology for the unsteady problems of rotorcraft aerodynamics, such as dynamic stall.

Computational Method

Reynolds-Averaged Navier Stokes equations are written in inertial frame of reference using general time-dependent coordinate transformation.

$$\partial_t \hat{Q} + \partial_\xi \hat{E} + \partial_\eta \hat{F} = Re^{-1}(\partial_\xi \hat{E}_v + \partial_\eta \hat{F}_v) \quad (1)$$

where $\hat{Q} = J^{-1}[\rho, \rho u, \rho v, e]$ is the vector of dependent variables. Inviscid and viscous flux vectors (\hat{E} , \hat{F} , \hat{E}_v and \hat{F}_v) are not repeated here and can be found in Ref. 17

Numerical boundary conditions are applied on the airfoil surface and outer boundaries. On the airfoil surface adiabatic, no-slip wall boundary conditions are imposed by setting contravariant velocity components to zero ($U = 0, V = 0$). Then, Cartesian velocity components are found from,

$$u = J^{-1}(-\eta_y \xi_t + \xi_y \eta_t), \quad v = J^{-1}(\eta_x \xi_t - \xi_x \eta_t) \quad (2)$$

Pressure on the airfoil surface is obtained by solving the normal momentum equation

$$\begin{aligned} \rho(\partial_t \eta_t + u \partial_\tau \eta_x + v \partial_\tau \eta_y) - \rho U(\eta u_\xi + \eta v_\xi) = \\ (\eta \xi_x + \xi_y \eta_y) p_\xi + (\eta_x^2 + \eta_y^2) p_\eta = \\ J^{-1} \sqrt{\eta_x^2 + \eta_y^2} p_n. \end{aligned} \quad (3)$$

Density is extrapolated from the field and the total energy is found using the perfect gas relations. At the external boundaries locally one dimensional flow assumption is made to describe the incoming and outgoing characteristics. Therefore, at the inflow boundary, all the conservative variables are fixed at their freestream values, and at the outflow boundary zero-order extrapolation is used for conservative variables except pressure which is held fixed.

In order to eliminate the need for generating a new grid at each time step, a fixed grid is rotated with the airfoil (Fig. 1).

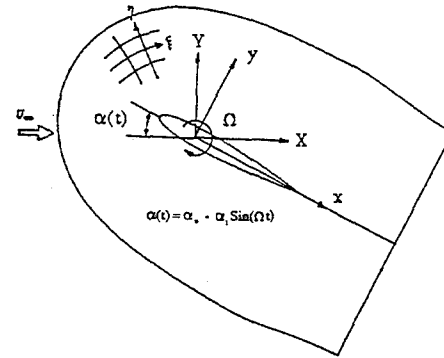


Figure 1: Unsteady airfoil motion

New points at each time step are found by using rotational transformation matrix, and the metric of coordinate transformation are computed from

$$\xi_t = -\xi_x x_t - \xi_y y_t, \quad \eta_t = -\eta_x x_t - \eta_y y_t \quad (4)$$

Grid speeds are computed at each time step from $x_t = \dot{\alpha}y$ and $y_t = -\dot{\alpha}x$, where $\dot{\alpha}$ is the instantaneous angular speed of the sinusoidal oscillation of angle of attack given by $\alpha(t) = \alpha_0 + \alpha_1 \sin(\omega t)$. Here, α_0 is the mean angle of attack, α_1 is the amplitude and ω is the circular frequency.

Governing equations are solved using approximate factorization algorithms of LU-ADI due to Obayashi and Kuwahara¹⁸ and diagonal algorithm due to Pulliam and Chaussee¹⁷. The algorithms are first order accurate in time and second order in space. In order to control numerical stability implicit smoothing terms are added to the basic algorithm. Details of these algorithms can be found in their original papers.

Turbulence Modeling

Accurate predictions of airfoil performance up to and beyond stall require that the turbulent boundary layers and wake be correctly defined. For high Reynolds number flows the accuracy of results depends on the validity of the closure model that is used to describe the turbulent shear stresses. When unsteady turbulent flows are considered, it is the minimum requirement for Reynolds-averaged equations that the averaging time interval must be long enough to resolve characteristic time of the principal eddies and short enough for the characteristic time of the unsteady mean flow¹⁹. Usually, experiments provide some quantitative information which permits the identification of these time-scales in certain cases²⁰. Another point that should be carefully examined is the safety margins of steady-flow turbulence models in unsteady flow predictions. When the turbulence structure is unaffected by externally induced unsteadiness, there is a critical frequency below which steady-flow turbulence models can also be used to predict unsteady turbulent flows¹⁹. Such critical frequency ranges for zero-, and adverse pressure gradient flows are given in terms of turbulent burst frequency based on outer scales²¹. Apparently, detailed analysis of these factors are beyond the coverage of this paper and additional information can be obtained from their original review papers.

The so-called first-order approach turbulence models, in which the Reynolds stress tensor is defined in terms of the mean flow quantities, have formed the basis of the various zero-, one- and higher-equation models. Mostly, zero-equation models found wide range of application areas due to their simplicity. For instance, Cebeci-Smith²² and Baldwin-Lomax²³ models were used in Reynolds-averaged two- and three-dimensional steady and unsteady Navier-Stokes solvers. The weakness of the zero-equation or "equilibrium" models is that they are not suitable for flows with massive separation, and

it is in fact dangerous to use these models, for instance, in airfoil design²⁴. Recently, an algebraic turbulence model, namely Johnson-King model, was formulated to capture important "nonequilibrium" effects of the separated flows^{24,25} by solving a differential equation of the streamwise development of the Reynolds shear stress. The performance of Johnson-King model relative to "equilibrium" models was illustrated for the three airfoil cases of the 1987 AIAA Viscous Transonic Airfoil Workshop, Reno, Nevada. Since then, model is further improved to account for some of the deficiencies arising in weak shock/boundary-layer interactions²⁶. Three dimensional extensions of Johnson-King model is reported by Abid et al.²⁷ using p.d.e approach and Kaynak²⁸ using streamwise o.d.e approach for vortical flows about delta wings. A brief outline of the these models (i.e, Baldwin-Lomax, Cebeci-Smith and Johnson-King models) will be given in the following subsections of the paper.

Cebeci-Smith and Baldwin-Lomax Models

Both in Cebeci-Smith and Baldwin-Lomax models, the boundary layer is a composite two-layer structure consisting of inner and outer layers. In the inner layer, they assume the eddy viscosity distribution as

$$\nu_{ti} = (D\kappa y)^2 \left| \frac{\partial q}{\partial y} \right| \quad (3a)$$

where y is the normal distance from the wall and $\kappa=0.41$ is the Karman's constant. The near-wall damping term D is given by

$$D = 1 - \exp[-yu_\tau/\nu_w A^+] \quad (3b)$$

with $A^+=26$, and the wall-friction velocity $u_\tau = (\tau_w/\rho_w)^{1/2}$. The difference between these two models is in their definition of outer eddy viscosity. Cebeci-Smith model uses the Clauser formulation

$$\nu_{to} = \alpha q_e \delta_i^* \gamma_{CS} \quad (3c)$$

where q_e is the magnitude of the boundary layer edge velocity, δ_i^* is the incompressible displacement thickness given by

$$\delta_i^* = \int_0^\delta \left(1 - \frac{q}{q_e}\right) dy \quad (3d)$$

here, the magnitude of the mean velocity is $q = (u^2 + v^2)^{1/2}$.

Baldwin-Lomax model, on the other hand, in an attempt to eliminate determination of δ^* as the length scale, uses an alternative expression

$$\nu_{to} = \alpha y_{max} C_{BL} \min \left(F_{max}, \frac{(q_{F_{max}} - q_{min})}{4F_{max}} \right) \gamma_{BL} \quad (3e)$$

here function $F(y)$ is the moment of vorticity defined as

$$F(y) = y|\omega| \left[1 - \exp\left(-\frac{y^+}{26}\right) \right] \quad (3f)$$

where ω is the vorticity and the quantity y_{max} is evaluated at the normal distance where function $F(y)$ takes on its maximum. The values of C_{BL} and α are 1.6 and 0.0168, respectively. Finally, Klebanoff intermittency factors are given by

$$\gamma_{CS} = \left[1 + 5.5 \left(\frac{y}{\delta} \right)^6 \right]^{-1}$$

$$\gamma_{BL} = \left[1 + 5.5 \left(\frac{0.3y}{y_{max}} \right)^6 \right]^{-1} \quad (3g)$$

Johnson-King Model

The Johnson-King model accounts for the convection and diffusion effects by solving a differential equation governing the development of the maximum shear stress derived from the turbulent kinetic energy (t.k.e.). An eddy viscosity distribution is assumed across the boundary layer that is functionally dependent on the maximum Reynolds shear stress. Using an isotropic turbulence assumption, the total Reynolds shear stress at a point may be assumed to be in the following form:

$$\tau = \nu_t \omega \quad (3h)$$

Here, ν_t and ω are the eddy viscosity and vorticity at a point. Note that the total Reynolds shear stress τ as defined above is in fact τ/ρ , but the above definition is used here for convenience. The following blending formula for inner and outer layer eddy viscosity formulations is used to set the eddy viscosity:

$$\nu_t = \nu_{to} [1 - \exp(-\nu_{ti}/\nu_{to})] \quad (3i)$$

which behaves like the inner and outer formulas for small and large y values respectively, and smoothly blends the inner and outer regions. It also makes ν_t functionally dependent on ν_{to} across the boundary layer. The inner formula is given by

$$\nu_{ti} = D^2 \kappa y \overline{u'v'}_m^{1/2} \quad (3j)$$

where D is given by

$$D = 1 - \exp[-\overline{y-u'v'}_m/\nu_m A^+] \quad (3k)$$

However, the constant A^+ is taken as 15 as opposed to 26, to account for the different y dependencies of the two formulations.

The Johnson-King model²⁴ uses Clauser's outer eddy viscosity formulation similar to Cebeci-Smith model,

$$\nu_{to} = \sigma(s) \alpha q_e \delta_i^* \gamma \quad (3l)$$

Recently, Johnson²⁹ devised a straightforward way of estimating Clauser's outer eddy viscosity without determining δ^* as length scale. Based on the observation of moment of vorticity distribution, $F(y)$, in Navier-Stokes solutions, he suggests the following outer formula for eddy viscosity,

$$\nu_{to} = \sigma(s) \alpha C_1 \left[\frac{1 + \Pi}{1 + C_o \Pi} \right] \delta F_{max} \quad (3m)$$

where Π is the Coles wake parameter given by

$$\Pi = \frac{1}{C_o} \left[\frac{\kappa F_{max}}{|u_\tau|} - \frac{u_\tau}{|u_\tau|} \right] \quad (3n)$$

and C_o is 1.82 for cosine wake function and C_1 is the tuning parameter which is reported to be 0.9 for current computations³⁰. Determination of length scales for outer formulations will be explained in the next subsection. The parameter $\sigma(s)$ provides the link between the assumed eddy viscosity distribution, and rate equation for the streamwise development of the maximum Reynolds stress. An equation for $-\overline{u'v'}$ can be obtained from the turbulent kinetic energy equation by making the assumption that the ratio of maximum shear stress, $\tau_m = -\overline{u'v'}_m$, to maximum t.k.e, $k_m = \frac{1}{2}(\overline{u'^2} + \overline{v'^2})$, is constant. Therefore, along a path s in the streamwise direction, turbulent kinetic energy equation for an incompressible boundary layer reads

$$\frac{\partial \tau_m}{\partial t} + q_m \frac{\partial \tau_m}{\partial s} = \frac{a_1}{L_m} (\tau_{m,eq}^{1/2} - \tau_m^{1/2}) - a_1 D_m \quad (3o)$$

Furthermore, if steady flow assumption is applicable then above p.d.e reduces to only directional derivative of τ_m , which is indeed an o.d.e of the form

$$q_m \frac{d\tau_m}{ds} = \frac{a_1}{L_m} (\tau_{m,eq}^{1/2} - \tau_m^{1/2}) - a_1 D_m \quad (3p)$$

Here, the subscript "eq" denotes the equilibrium value corresponding to $\sigma(s)=1$, q_m is the magnitude of the mean velocity at $\tau = \tau_m$, and D_m is the diffusion term (see Johnson and King²⁴ for its modeling). Furthermore, the modeling constant a_1 and the dissipation length scale L_m are given by

$$a_1 = \frac{\tau_m}{k_m}, \quad L_m = \frac{\tau_m^{3/2}}{\epsilon_m} \quad (3q)$$

where a_1 is taken as 0.25, and ϵ_m is the dissipation. The dissipation length scale L_m is assumed to scale with y in the inner part of the boundary layer, and with the boundary layer thickness δ in the outer part. The diffusion term is modeled as

$$D_m = \frac{C_{dif} \tau_m^{3/2}}{a_1 \delta [0.7 - (y/\delta)_m]} [1 - \sigma(s)^{1/2}] \quad (3r)$$

where C_{dif} is modeling constant taken as 0.5.

Once the above rate equation (Eq. (3o) or (3p)) is solved, the link parameter $\sigma(s)$ is determined at a specific location by iteratively satisfying the following relation:

$$\nu_{tm} = \tau_m / \left| \frac{\partial q}{\partial n} \right| \quad (3s)$$

where ν_t is given by Eq.(3i). Having satisfied the above relation, $\sigma(s)$ is found from

$$\sigma(s) = \frac{\nu_{to,n}}{\nu_{to,eq}} \quad (3t)$$

Here, $\nu_{to,eq}$ denotes the outer eddy viscosity as determined from Eq.(3l) or Eq.(3m) by setting $\sigma(s)=1$, and $\nu_{to,n}$ is determined while iteratively satisfying Eq.(3t).

Determination of Turbulent Length Scale

It is apparent from the given outer eddy viscosity formulations that the extend of the viscous layer will mainly be determined by the turbulent length scale. This, in turn, poses certain problems to which it can be predicted in terms of mean flows parameters in Navier-Stokes applications. Baldwin-Lomax model tries to eliminate this problem by using quantity y_{max} in place of δ_i^* . Despite its convenience in practical problems, the well-known two-maxima problem of function $F(y)$ avoids accurate computations of y_{max} . Although a correction method is suggested in Ref. 31, for this problem, its applicability and generality to different flow problems is uncertain.

Recently Stock and Hasee³² developed a method for predicting the boundary-layer thickness using Coles velocity profiles. In this method, the boundary-layer edge is found from the relation that reads

$$\delta = 1.936 y_{max} \quad (3u)$$

thus, δ_i^* can be obtained from Eq. (3d) using numerical integration. A further extension of this technique is made by Johnson²⁹. Based on the observation that streamwise distribution of function $F(y)$, in Navier-Stokes solutions, a collapse of data $F(y)/F_{max}$ can be obtained if $y_{1/2}$, which is the normal distance at which $F(y)$ attains its half amplitude, is used for scaling the normal distance y (i.e, $y/y_{1/2}$). This, in correlation to same behavior of data when δ is used in place of $y_{1/2}$ (i.e, y/δ) permits the method to compute boundary layer thickness from

$$\delta = 1.2 y_{1/2} \quad (3v)$$

The factor 1.2 is a calibration constant found by numerical experimentation. The advantage of this technique is twofold if it is used in the outer eddy viscosity formula given in Eq. 3l, where δ_i^* is eliminated. Further details of this method can be found in Ref. 29.

Results and Discussion

In this paper, computations were performed for the NACA0012 airfoil with C-type grid of dimensions 157×57 in static stall and light stall computations, and 215×60 for a deep stall computation (Fig. 2). A min-

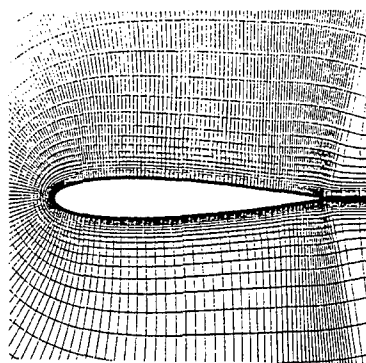


Figure 2: C-type hyperbolic grid around NACA0012 airfoil

imum normal spacing of $0.00001c$ at the airfoil surface was chosen to guarantee at least one or two grid points in the viscous sublayer. Outer boundary extend of the grid was exponentially stretched to 20 chord lengths from the airfoil surface to avoid reflection of boundary conditions. Although, much finer grid resolutions will enhance the solutions, current computational cost of the study confines us to use a rather medium grid. Computational experiments with the code revealed that a particular solution can be resolved in time if a sufficiently small time step ($O(0.001)$) is chosen. Also, before unsteady computations code has been validated for steady state (see Ref. 16).

Static Stall

Relative differences of dynamic stall phenomenon could be best understood, if they are compared with their static counterparts. Therefore, here a static stall case of NACA0012 airfoil will be investigated. The flow case is, $M_\infty=0.3$ and $Re = 4 \times 10^6$. Experimental data with wind tunnel corrections available from McCroskey et al.⁷. Fig. 3 shows the comparison of $C_l - \alpha$ curve for Baldwin-Lomax and Johnson-King turbulence models with experiment. Although results of Baldwin-Lomax are in agreement with experiment up to 13° , onset of static stall is delayed and the resulting C_l values are above the experimental limits. Also, in Fig. 4 pitching moment coefficients resulted from Baldwin-Lomax model unable predict negative damping portion of the static stall. On the other hand, Johnson-King model

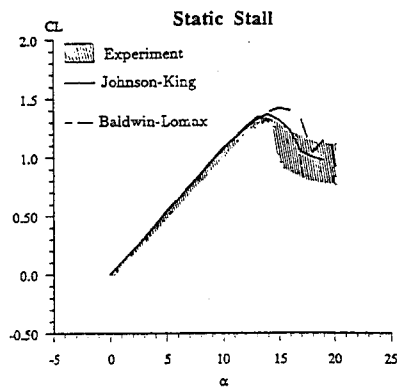


Figure 3: Comparison of predicted and experimental static $C_L - \alpha$ curve, $M_\infty = 0.3$, $Re_\infty = 4 \times 10^6$

produced quite accurate $C_L - \alpha$ curve compared to experiment before and after the stall (Fig. 3). Furthermore, qualitative nature of the $C_m - \alpha$ curve obtained with Johnson-King model is similar to those of experiment (Fig. 4). Here, inadequacy of equilibrium model highlights the importance of nonequilibrium effects in predicting flows with relatively large separation region.

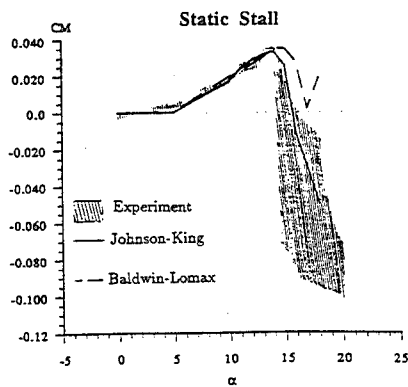


Figure 4: Comparison of predicted and experimental static $C_m - \alpha$ curve, $M_\infty = 0.3$, $Re_\infty = 4 \times 10^6$

Light Stall

Case-7 of Ref. 7 for the light stall of the NACA0012 airfoil was chosen as the test case. The flow conditions for this case were $M_\infty = 0.3$, $Re = 4 \times 10^6$. The airfoil is oscillated according to the formula $\alpha(t) = \alpha_0 + \alpha_1 \sin(2M_\infty kt)$ where $k = \omega c/2U_\infty$ is the reduced frequency, ω is the circular frequency, and α_0 and α_1 are the mean angle and the amplitude of the oscillation. The parameters of the harmonic motion for this case are $k = 0.1$, $\alpha_0 = 10^\circ$ and $\alpha_1 = 5^\circ$. Effects of turbu-

lent diffusion have been shown to be very important¹⁶ in order to obtain reasonable solution to dynamic stall problem. Similar results were independently obtained in Ref. 12 for a deep stall case. Therefore no attempt has been made to use laminar flow assumption in either light or deep stall computations.

Turbulent flow calculations for this case using Baldwin-Lomax and Cebeci-Smith models are shown in Fig. 5. During the upstroke motion of the airfoil

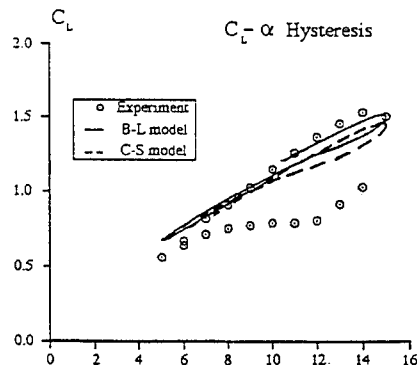


Figure 5: Comparison of predicted and experimental $C_L - \alpha$ hysteresis for light dynamic stall of NACA0012 airfoil, B-L and C-S models

both models give similar trends lying close to experiment. The difference between the two models during the upstroke motion comes from using different initial conditions. This is for numerical experimentation, and results would have shown similar trends, had they been started from the same initial conditions. Also, one cycle was completed because of the computer time limitations. Although the upstroke motion was captured, the downstroke motion and the overall hysteresis loop are very inaccurate in both models.

In all these calculations, the similar features of the flow is that around the maximum angle of attack a very tiny region of separation was forming at the trailing edge but due to inadequately modeled viscous and turbulent interaction, the light stall hysteresis loop could not be obtained. One may tend to conclude that this is because of the inadequacy of the turbulence models, but use of free air grid without corrections on the experimental data could also be a restricting point. To check this aspect of the problem it was decided to increase the mean angle of attack of the harmonic motion by 1° so that some kind of wall corrections are included. A result of such a computation using Baldwin-Lomax model for a mean angle of attack α_0 of 16° is shown in Fig. 6. The solution is basically the same as its counterpart in Fig. 5. At this point, it was concluded that the prob-

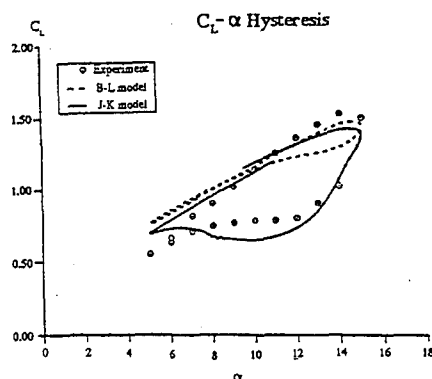


Figure 6: $C_l - \alpha$ hysteresis for light dynamic stall of NACA0012 airfoil, B-L, J-K models

ably the equilibrium turbulence model was inadequate and nonequilibrium effects might be important. Use of Johnson-King model this point as shown in Fig. 6. The hysteresis loop produced by this model is quite similar to the experiment demonstrating the need to include nonequilibrium behavior of the Reynolds shear stress in the calculations. The moment hysteresis curves for the B-L and J-K models are given in Fig. 7. Whereas the B-

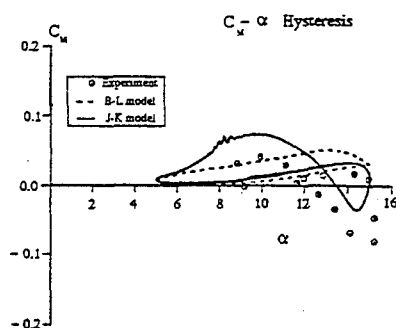


Figure 7: $C_m - \alpha$ hysteresis for light dynamic stall of NACA0012 airfoil, B-L, J-K models

L model gives a very inaccurate prediction, J-K model produces the correct shape of the curve including the negative pitch damping. In Fig. 8, a time history of C_l and C_m coefficients for Baldwin-Lomax and Johnson-King models are compared with experiment. To further illuminate this point, the link parameter $\sigma(s)$ (Eq. (3t)) is given in Fig. 9 that shows the $\sigma(s) - \alpha$ sequence in the turbulent boundary layer during the harmonic motion. The change in $\sigma(s)$ in the downstroke is particularly interesting. It is seen that after the midchord and around the trailing edge of the airfoil strong nonequilibrium

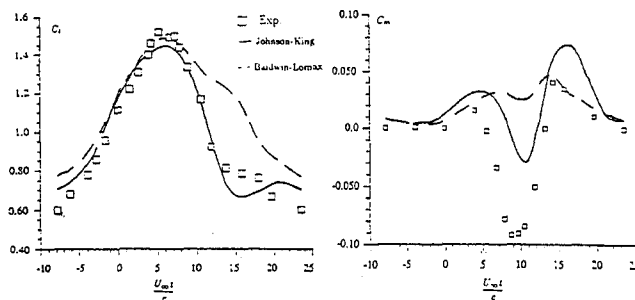


Figure 8: History of force and moment coefficients for light stall of NACA0012, B-L, J-K models

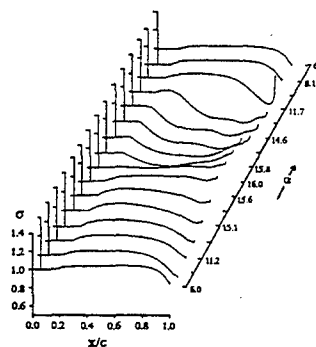


Figure 9: Computed $\sigma - \alpha$ variation during the light stall

effects take place that alter the level of the maximum eddy viscosity. Probably this helps to set up the strength and location of the stall vortex more realistically. Finally, the particle traces on the airfoil showing the stall vortex is presented in Fig. 10. Here, the location of the vortex indicates this to be a trailing edge stall and its interaction region, which is in the order of the airfoil thickness, is a typical of the light stall regime.

Deep Stall

To complete the discussion of dynamic stall, it is further desirable to go one more step and analyze the deep dynamic stall. Behavior of this regime is known to be the large vortex-like disturbance from the leading edge region and the shedding of this vortex over the upper

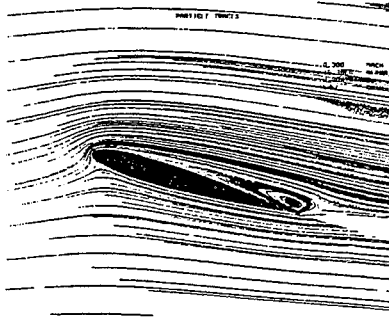


Figure 10: Instantaneous particle traces showing the location of light stall vortex

surface of the airfoil⁷. Also, overshoots in suction pressure and large amounts of hysteresis loops of force coefficients are the remarkable qualitative features.

The model problem in this part was chosen as the Case-8 of Ref. 7. The flow conditions are $M_\infty=0.3$, $Re=4 \times 10^6$, $k=0.1$, $\alpha_0 = 10^\circ$, $\alpha_1 = 10^\circ$. Fig. 11 shows the $C_l - \alpha$ hysteresis curves for Baldwin-Lomax and Johnson-King models compared with experiment. Performance of two models shows very similar trends

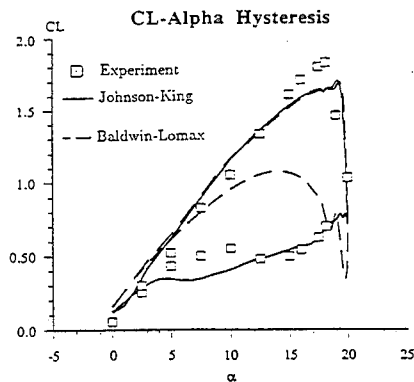


Figure 11: $C_l - \alpha$ hysteresis for deep dynamic stall of NACA0012 airfoil, B-L, J-K model

during the upstroke motion but predict lower C_l values at the maximum angle of attack. Behavior of two models for the downstroke motion is completely different from each other. Baldwin-Lomax model, for instance, shows steep decrease in C_l at $\alpha = 20^\circ$ exceeding the experimental data. Although C_l values around $\alpha = 18^\circ$

recovered back to experimental limits with a sharp increase, further trajectory the $C_l - \alpha$ curve diverges from the experiment and as a result predicts totally inaccurate hysteresis loop of the deep stall. Johnson-King model, on the other hand, throughout the downstroke stays close to experiment and produce highly accurate results compared to Baldwin-Lomax model. This in comparison to light stall case studied in previous section, shows that nonequilibrium turbulence effects not only help the formation of the stall vortex but also predict its proper shedding form the lifting surface. The moment hysteresis curves are given in Fig. 12. Here,

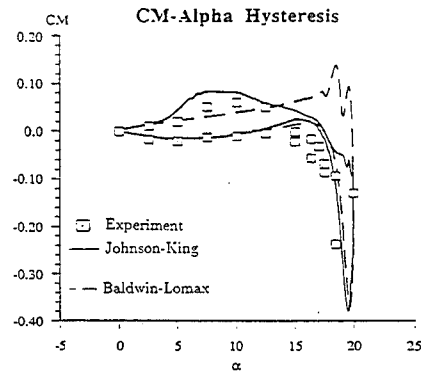


Figure 12: $C_m - \alpha$ hysteresis for deep dynamic stall of NACA0012 airfoil, B-L, J-K model

the results are comparable to experiment only in terms of qualitative nature of the problem. History of C_l and C_m coefficients are also given in Fig. 13. One should

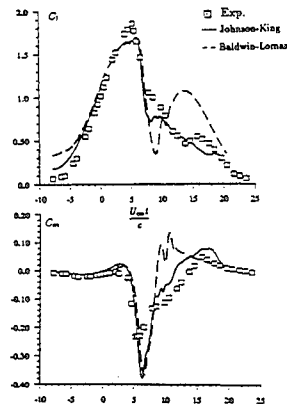


Figure 13: History of force and moment coefficients for deep stall of NACA0012, B-L, J-K model

be aware of the fact that the experimental data⁷ are

phased-averaged over a large number of cycles whereas computations reflects only the results of the first cycle. Had the computations continued over a few cycles more, a more reasonable quantitative comparison could be obtained.

Fig. 14 shows the variation of computed and experimental pressure coefficient on the upper surface of the airfoil. As seen, a leading edge vortex around $\alpha = 16^\circ$

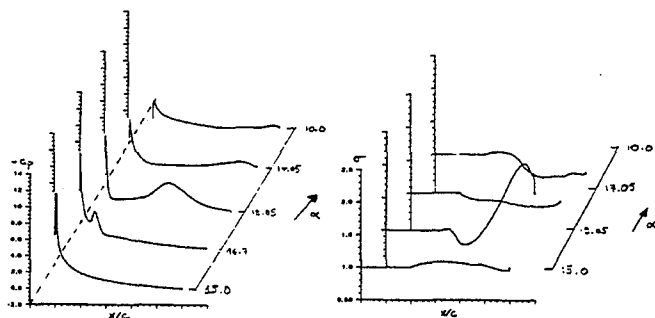


Figure 14: Coefficient of pressure and σ variation during deep stall

forms and manifest itself as the angle of attack increases. During the stall, at $\alpha \geq 19.5^\circ$ leading edge suction pressure collapses abruptly resulting a steep decrease in force coefficients. Furthermore, as in the light stall case the nonequilibrium state of the problem is emphasized by plotting the variation of link parameter $\sigma(s)$ versus angle of attack. Finally, the formation and development of dynamic stall vortex in Baldwin-Lomax and Johnson-King turbulence models is summarized by particle traces taken at several locations of the deep stall hysteresis loop (Fig. 15).

Conclusion

An unsteady Navier-Stokes program developed in Ref. 16 is used to compute the effects of turbulence modeling on the dynamic stall of a NACA0012 airfoil. Important differences were found between the performance of equilibrium and nonequilibrium turbulence models in light and deep dynamic stall regimes. For light stall, it was found that the equilibrium models were incapable of producing the stall vortex. Use of a nonequilibrium model together with a correction to the mean angle of attack produced qualitatively similar results to those of experiment. For the deep stall, the vortex shedding was found to be greatly influenced by the nonequilibrium turbulence effects. As a result, it was

concluded that enhancements in predicting flows with large regions of unsteady separation, as in the case of dynamic stall, is achievable through better turbulence modeling.

References

- Johnson, W., and Ham, N.D., "On the Mechanism of Dynamic Stall," *Journal of American Helicopter Society*, Vol. 17, OCT 1972, pp. 36-45.
- Martin, J.M., Empey, R.W., McCroskey, W.J., and Caradonna, F.X., "An Experimental Analysis of Dynamic Stall on an Oscillating Airfoil," *Journal of American Helicopter Society*, Vol. 19, No. 1, JAN 1974, pp. 26-32.
- McCroskey, W.J., "Some Current Research in Unsteady Fluid Dynamics," *Journal of Fluids in Engineering*, Vol. 99, JAN 1979, pp. 8-39.
- McCroskey, W.J., Carr, L.W., McAlister "Dynamic Stall Experiments on Oscillating Airfoils," *AIAA Journal*, Vol. 14, No. 1, JAN 1976.
- McCroskey, W.J. "The Phenomenon of Dynamic Stall," NASA TM 81-264, MAR 1981.
- Cebeci, T., and Bradshaw, P., "Momentum Transfer in Boundary Layers," Hemisphere Publishing.
- McCroskey, W.J., Pucci, L.S "Viscous-Inviscid Interaction on Oscillating Airfoils in Subsonic Flow," *AIAA Journal*, Vol. 20, No. 2, FEB 1982, pp. 167-174.
- McCroskey, W.J., Philippe, J.J., "Unsteady Viscous Flows on Oscillating Airfoils," *AIAA Journal*, Vol. 13, No. 1, JAN 1975, pp. 71-79.
- Mehta, U.B., "Dynamic Stall of an Oscillating Airfoil," AGARD CP-227, Paper No. 23, Symposium on Unsteady Aerodynamics, Ottawa, CAN, 1977.
- Sankar, N.L, and Tassa, Y., "Compressibility Effects on Dynamic Stall of a NACA0012 Airfoil," *AIAA Journal*, Vol. 19, No. 5, pp. 557-568.
- Ekatrinaris, J.A., "Compressible Studies on Dynamic Stall," AIAA Paper 89-0024, 1986.
- Shida, Y., Takami, H., Kuwahara, K. and Ono, K., "Computation of Dynamic Stall of a NACA0012 Airfoil by Block Pentadiagonal Matrix Scheme," AIAA Paper 86-0116, 1986.
- Wu, J.C., Huff, D.L., Sankar, L.N., "Evaluation of Three turbulence Models in Static Air Loads and Dynamic Stall Predictions," *AIAA Journal of Aircraft*, Vol. 27, No. 4, APR 1990, pp. 382-384.

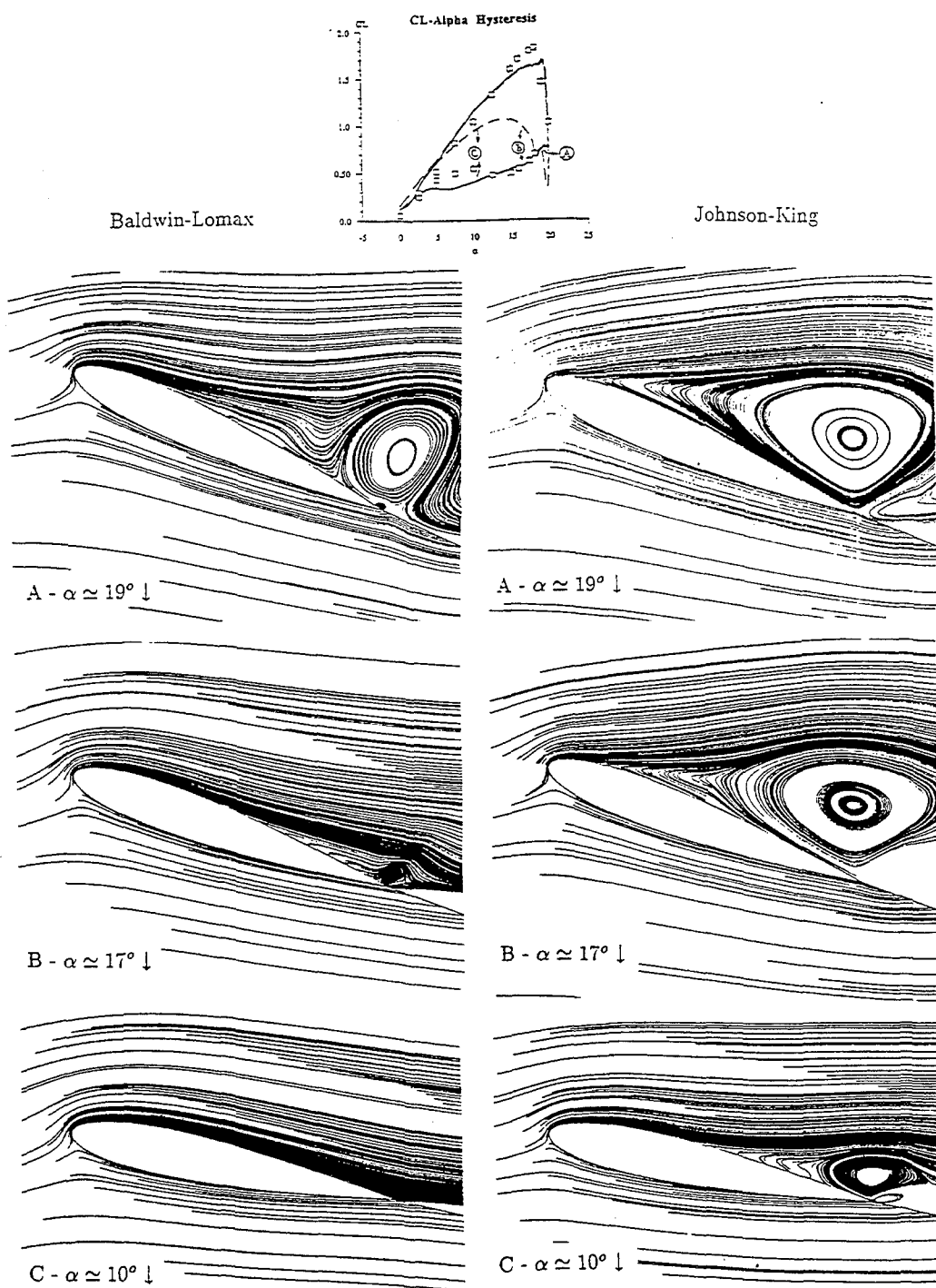


Figure 15: Particle traces showing the behavior of deep stall vortex for B-L and J-k turbulence models

- ¹⁴ Tuncer, I.H., Wu, J.C., Wang, C.M., "Theoretical and Numerical Studies of Oscillating Airfoils," *AIAA Journal* Vol. 28, No. 9, SEPT 1990, pp. 1615-1624.
- ¹⁵ Dindar, M., Kaynak, Ü., and Fujii, K., "Nonequilibrium Turbulence Modeling Studies on Light Dynamic Stall of A NACA0012 Airfoil," *AIAA Journal Aircraft*, Vol.30, No:3, pp. 304-308, 1993.
- ¹⁶ Dindar, M., Kaynak, Ü., "Effect of Turbulence Modeling on Dyanamic Stall of a NACA0012 Airfoil," *AIAA Paper* 92-0027, Reno, NV 1992.
- ¹⁷ Pulliam, and T.H., Chaussee, D.S., "A Diagonal Form of an Implicit Factorization Algorithm," *Journal of Computational Physics*, Vol. 39, 1981, pp. 347-363.
- ¹⁸ Obayashi, S., and Kuwahara, K., "Lu Factorization of an Implicit Scheme for the Compressible Navier-Stokes Equations," *AIAA Paper* 84-1670, 1984.
- ¹⁹ Lomax, H., and Mehta, U.B., "Some Physical and Numerical Aspects of Computing the Effects of Viscosity on Fluid Flow," *Computational Methods in Viscous Flows*, Vol. 3, Pineridge Press.
- ²⁰ Chapman, D.R., "Computational Aerodynamics Development and Outlook," *AIAA Journal*, Vol. 17, No. 12, DEC 1979, pp. 1293-1313.
- ²¹ Cousteix, J., Houdeville, R., Raynaud, M., "Oscillating Turbulent Boundary Layer with Strong Mean Pressure Gradient," *Turbulent Shear Flows*, Vol. 2, Springer-Verlag.
- ²² Cebeci, T., and Smith, A.M.O., "Analysis of Turbulent Boundary Layers," Academic Press.
- ²³ Baldwin, B.S., and Lomax, H., "Thin-Layer Approximation and Algebraic Model for Separated Turbulent Flows," *AIAA Paper* 78-257, 1978.
- ²⁴ Johnson, D.A., and King, L.S., "A Mathematically Simple Turbulence Closure Model for Attached and Separated Turbulent Boundary Layers," *AIAA Journal*, Vol. 23, No. 11, NOV 1985, pp. 1684-1692.
- ²⁵ Johnson, D.A., "Transonic Separated Flow Predictions with an Eddy Viscosity/Reynolds Shear Stress Closure Model," *AIAA Journal*, Vol. 25, No. 2, FEB 1987, pp. 252-259.
- ²⁶ Johnson, D.A., and Coakley, T.J., "Improvements to a Nonequilibrium Algebraic Turbulence Model," *AIAA Journal*, Vol. 28, No. 11, NOV 1990, pp. 2000-2003.
- ²⁷ Abid, R., "Extension of the Johnson-King Turbulence Model to 3-D Flows," *AIAA Paper* 88-0223, JAN 1988.
- ²⁸ Kaynak, Ü., Tu, E., Dindar, M., and Barlas, R., "Nonequilibrium Turbulence Modeling Effects on Transonic Vortical Flows About Delta Wings," *AGARD Paper*, FDP Symposium, The Netherlands 1990.
- ²⁹ Johnson, D.A., "Nonequilibrium Algebraic Turbulence Modeling Considerations for Transonic Airfoils and Wings," *AIAA Paper* 92-0026, 1992.
- ³⁰ Johnson, D.A., Personal Communication, 1991.
- ³¹ Degani, D., and Schiff, L.B., "Computation of Turbulent Supersonic Flows Around Pointed Bodies Having Crossflow Separation," *Journal of Computational Physics*, Vol. 66, 1986, pp. 173-196.
- ³² Stock, H.W., and Haase, W., "The Determination of Turbulent Length Scales in Algebraic Turbulence Models for Attached and Slightly Separated Flows Using Navier-Stokes Methods," *AIAA Paper* 87-1302, 1987.

Investigation into Effect Produced by Blade Airfoil Unsteady Airflow on Helicopter Main Rotor Power Required.

V. A. Ivchin

Head of Aerodynamics Section
Mil Moscow Helicopter Plant
2, Sokolnichesky Val
Moscow, 107113
Russia

1. SUMMARY

The paper presents the results obtained from the analysis of experimental data on the profile drag for pitch oscillating airfoils, as well as the technique developed for application of these data in calculations of helicopter main and tail rotors. The effect of the unsteady airflow on the profile drag was not taken into account. The reason is that it is very difficult to obtain experimental data. The existing analytical techniques of obtaining unsteady airfoil aerodynamic characteristics in a drained wing section allowed to determine only an average per cycle value of the profile drag. The problem of defining the profile drag of pitch oscillating airfoils has been more completely solved by V.E. Baskin. He has developed and successfully applied his unique method of defining aerodynamic characteristics of airfoils oscillating in the airflow. This approach has allowed to determine not only the pitch moment and lift values, but the instantaneous value of the profile drag as well. The data obtained from the experiments has been used to develop a method capable of calculating rotor shaft horsepower with due account of the profile drag characteristics. The analysis for forward flight conditions has been made by using the main rotor disc vortex theory. It has taken due account of the values of the pitch oscillating airfoil lift coefficient as well. The paper presents comparison of the instantaneous profile drag values versus the angle of attack data obtained from calculations and experiments.

2. LIST OF SYMBOLS

M Mach number,
Re Reynolds number,
 C_{lmax} maximum value of airfoil steady lift coefficient
 α_s airfoil steady flow stall angle of attack
 α_{os} airfoil steady zero lift angle of attack
 $dC_y / d\alpha$ airfoil steady lift coefficient derivative with respect to angle of attack
 $dC_m / d\alpha$ airfoil steady longitudinal moment coefficient derivative with respect to angle of attack
 $\Delta\alpha_i$ induced wash at central cross section measuring section
 C_{di} induced drag at central cross section measuring section
 α angle of attack

C_l profile lift coefficient
 C_d profile drag coefficient
 C_m profile moment coefficient
 ΔC_l unsteady increment amplitude profile lift coefficient
 ΔC_d unsteady increment amplitude profile drag coefficient
 ΔC_m unsteady increment amplitude profile moment coefficient
 \bar{C}_{li} nondimensional unsteady increment i-harmonic amplitude profile lift coefficient
 \bar{C}_{di} nondimensional unsteady increment i-harmonic amplitude profile drag coefficient
 \bar{C}_{mi} nondimensional unsteady increment i-harmonic amplitude profile moment coefficients
 C_{II} inertia force coefficient, affecting on the measuring section
 C_{dI} inertia force coefficient, affecting on the measuring section
 C_{mI} inertia moment coefficient, affecting on the measuring section
 $C_{l\Sigma}$ total force coefficient, affecting on the measuring section
 $C_{d\Sigma}$ total force coefficient, affecting on the measuring section
 $C_{m\Sigma}$ total moment coefficient, affecting on the measuring section
 C_{do} profile drag coefficient by averaged angle of attack in steady flow
 φ_0 average value of the airfoil pitch
 $\Delta\varphi$ amplitude of pitch oscillation
 $k = c\omega/W$ adjusted frequency
W instantaneous airfoil velocity on the current blade section
 ω angular frequency of harmonic angle of attack of the current blade section
c airfoil chord
 $\theta = \omega t$ airfoil movement rate
t time
n number of aerodynamic coefficient unsteady increment harmonics, used in calculations
 α_0 dimensionless averaged per rotor revolution current blade section angle of attack

$\bar{\alpha}_0$	nondimensional averaged per rotor revolution current blade section angle of attack
m	number of azimuth subintervals per one rotor revolution
Φ_i	phase shift of aerodynamic coefficient unsteady increment i- harmonic
K_{Mi}	coefficient, reflecting the effect of Mach number on the aerodynamic coefficient unsteady increment i-harmonic amplitude
K_{ki}	coefficient, reflecting the effect of adjusted frequency on the aerodynamic coefficient unsteady increment i-harmonic amplitude
α_T	main rotor angle of attack
μ	rotor advance ratio
C_t	rotor thrust coefficients
C_p	rotor power coefficients
σ	rotor solidity ratio
V_y	climb rate
N_e	helicopter engines power

3. INTRODUCTION

Helicopter main and tail rotors are characterized by blade cross section operation in substantially unsteady conditions in forward flight. There are many papers [1,2,3,4], in which the methods, for calculating of the effect produced by unsteady airflow on airfoil lift and pitch moment are presented. The free-wake analysis used for rotor calculations are the best now for solving the problem. However, calculations of unsteady blade section profile drag with accuracy sufficient for practical use can not be carried out now using any theory. On the other hand, the experimental data for two-dimensional harmonic oscillating wing sections profile drag [6,7] may show its essential change. For example VR230-10-1.58 airfoil profile drag measurement data in direct and reverse flows are shown on figure 1.

The profile drag was obtained using the flow impulse losses measuring method, which makes it possible to estimate only the change of average values of the drag. According to the plot the unsteady unseparated flow increases profile drag by 30-50 percent in direct and reverse flows. In separated flow changes in profile drag in unsteady conditions increase even more. This fact makes it possible to make a very rough estimation of unsteady effect on profile drag. The experimental investigation carried out by V.E. Baskin and V.R. Lapatov in TsAGI has made it possible to define these data much more accurately. The new method of measuring has made it possible to obtain not only average data, but instantaneous values of profile drag as well. The experimental data obtained has been used to develop the semi-empirical method for calculating unsteady airfoil data, including the profile drag. Combining of this method with the methods of helicopter main and tail rotors calculating has allowed to investigate the effect produced by the blade section unsteady profile drag on the helicopter required power.

4. DETERMINATION OF INSTANTANEOUS UNSTEADY DRAG OF PITCH-OSCILLATING PROFILE USING EXPERIMENTAL DATA.

The method of pressure distribution measuring on the pitch oscillating or reciprocating infinite-wing section has been until quite recently the best one for calculating unsteady airfoil data [6,7]. This approach enabled to define the lift and the pitch moment of the airfoil, but the unsteady profile drag has not been measured. In the method the average value of the profile drag has been obtained by measuring the changes of the flow impulse values, caused by oscillating wing.

In the experiment, aimed to define unsteady pitch oscillating airfoil data, that was formulated and carried out by V.E. Baskin and V.R. Lapatov there was used the method of defining the finite - wing central measuring section lift, pitching moment and drag (fig.2). The width

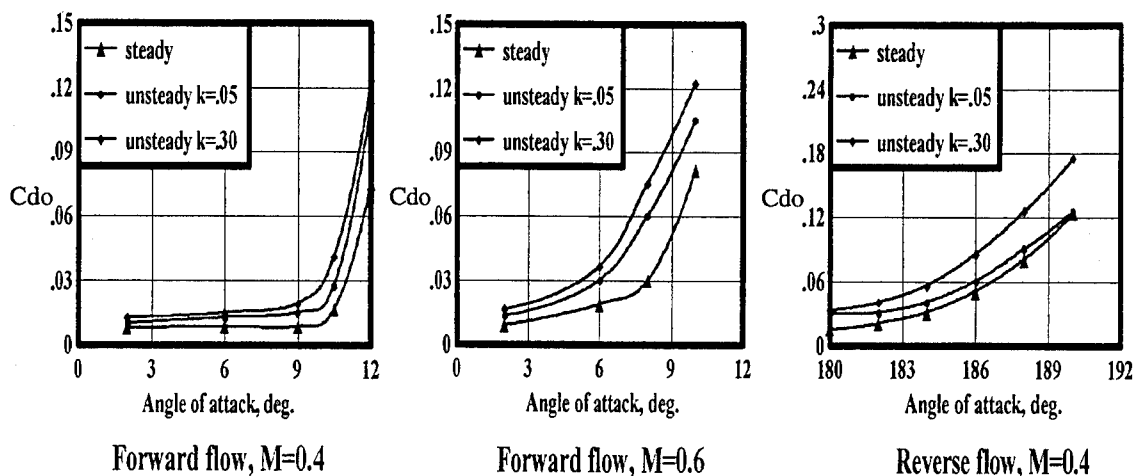


Figure 1 Average per cycle profile drag of the pitch oscillating airfoil V-230-10-1.5 versus its angle of attack

of the central section was equal to ten percent of the wing span, and aspect ratio was equal to five. The approach made it possible to measure both the average value of the drag and instantaneous drag values of the wing measuring section. With the use of a special device, driven by hydraulics, the wing under investigation performed harmonic pitch oscillations with variable amplitude and angular velocity at various mean pitch values. The strain gauges built into the measuring section balance were used for measuring of forces and moments.

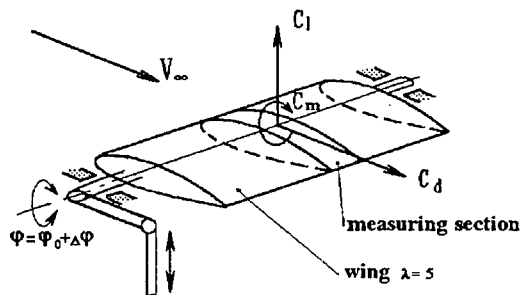


Figure 2 The schema of the device for finite-wing central measuring section lift, pitching moment and drag definition

In order to take into account inertia forces and moments, arising on the oscillating wing the investigation was carried out in two steps. During the first step a sealed casing was put into the measuring section to isolate it from the flow. Thus inertia forces and moment affecting the measuring section were measured and recorded on the storage medium. In the second stage the hermetic casing was taken off and the measures were repeated in the same operational conditions. The values of total forces and moments, affecting the section were recorded again. After synchronizing of the two records aerodynamic forces and moment affecting the measuring section were picked out.

$$\begin{aligned} C_l(\theta, k, \varphi_0, \Delta\varphi) &= C_{l\Sigma}(\theta, k, \varphi_0, \Delta\varphi) - C_{lI}(\theta, k, \varphi_0, \Delta\varphi) \\ C_d(\theta, k, \varphi_0, \Delta\varphi) &= C_{d\Sigma}(\theta, k, \varphi_0, \Delta\varphi) - C_{dI}(\theta, k, \varphi_0, \Delta\varphi) \end{aligned} \quad (1)$$

$$C_m(\theta, k, \varphi_0, \Delta\varphi) = C_{m\Sigma}(\theta, k, \varphi_0, \Delta\varphi) - C_{mI}(\theta, k, \varphi_0, \Delta\varphi)$$

In processing of experimental data obtained by the method the aerodynamic force and moment coefficients acting on the measuring section should be transformed into airfoil data as a function of central cross-section angle of attack and the profile drag should be determined. For this purpose the author has used non-linear unsteady finite-wing computation method developed by S.M. Belotserkovsky on the basis of vortex theory [9].

Basing on the parametric calculations there were determined the functions connecting wing geometric pitch and angle of attack of measuring section centre section. Using these functions the measuring section induced wash

and induced drag C_{di} were obtained at each experimental mode and aerodynamic airfoil data were determined:

$$\begin{aligned} \Delta\alpha_i &= f(\theta, k, \varphi_0, \Delta\varphi) \\ C_{di} &= f(\theta, k, \varphi_0, \Delta\varphi) \end{aligned} \quad (2)$$

Using the calculated functions and after transformation of experimental data, the author has determined the unsteady airfoil data in the form of aerodynamic coefficients versus instantaneous angle of attack, adjusted frequency and oscillation amplitude for the fixed values of Mach number:

$$\begin{aligned} C_l &= f(\alpha, k, \Delta\varphi) \\ C_d &= f(\alpha, k, \Delta\varphi) \\ C_m &= f(\alpha, k, \Delta\varphi) \end{aligned} \quad (3)$$

5. EXPERIMENTAL UNSTEADY AIRFOIL DATA DEFINITION FOR HELICOPTER ROTOR CALCULATION

On the basis of experimental study [8] and papers [6,7], for helicopter rotor aerodynamic calculation purpose the author has developed the method of experimental unsteady airfoil data definition including the profile drag. The method developed was reported at the Branch Conference on Rotorcraft Aerodynamics and Dynamics, that was held in 1987 in TsAGI. It was used for the main and tail rotor aerodynamic data definition and control system loads calculations for helicopter simulation purposes[10].

The essence of the developed method is the following:

1. The rotor blade section aerodynamic data are defined by summing up of its steady values, determined for an instantaneous angle of attack and Mach number, and the unsteady increments of these coefficients determined for the current values of adjusted frequency, pitch oscillation amplitude and flow velocity derivative.
2. The aerodynamic coefficient unsteady increments are determined in the form of amplitudes and phases of Fourier series expansion, from which constant the component and two first harmonics are retained.
3. In order to extend a limited experimental data to the majority of airfoils used in helicopter rotors the harmonic amplitudes of aerodynamic coefficient unsteady increments are connected by a formula with the steady values of the data characterizing airfoil at a current value of Mach number: $C_{lmax}, \alpha_s, \alpha_{os}, dC_y/d\alpha, dC_m/d\alpha$
4. While calculating lift and pitch moment coefficients pitch oscillating and airfoil vertical motion unsteady effects are taken into account separately.
5. The unsteady flow velocity changes are taken into account by using Y. Johnson formulas showing that the unsteady flow velocity changes can be approximated

into account by defining the Theodorsen function for the instantaneous adjusted frequency values in the current blade section.

The stated principals have been realized in the form of the following mathematical relations:

$$\begin{aligned} C_l(\alpha, M, k, \Delta\varphi) &= C_l(\alpha, M) + \Delta C_l(\alpha_0, M, k, \Delta\varphi) \\ C_d(\alpha, M, k, \Delta\varphi) &= C_d(\alpha, M) + \Delta C_d(\alpha_0, M, k, \Delta\varphi) \quad (4) \\ C_m(\alpha, M, k, \Delta\varphi) &= C_m(\alpha, M) + \Delta C_m(\alpha_0, M, k, \Delta\varphi) \end{aligned}$$

Aerodynamic coefficient unsteady increment values ΔC_l , ΔC_d , ΔC_m are defined from the expressions:

$$\begin{aligned} \Delta C_m(\alpha_0, M, k, \Delta\varphi) &= [\bar{C}_{mo} + \sum_{i=1}^n \bar{C}_{mi} \times \\ &\times \sin(\omega t + \Phi_{mi})] \times C_{lmax} \times \frac{dC_m}{d\alpha} \times K_{Mm} \times K_{km} \end{aligned}$$

$$\begin{aligned} \Delta C_d(\alpha_0, M, k, \Delta\varphi) &= [\bar{C}_{do} + \sum_{i=1}^n \bar{C}_{di} \times \\ &\times \sin(\omega t + \Phi_{di})] \times K_{Md} \times K_{kd} \times C_{do} \end{aligned}$$

$$\begin{aligned} \Delta C_m(\alpha_0, M, k, \Delta\varphi) &= [\bar{C}_{mo} + \sum_{i=1}^n \bar{C}_{mi} \times \\ &\times \sin(\omega t + \Phi_{mi})] \times C_{lmax} \times \frac{dC_m}{d\alpha} \times K_{Mm} \times K_{km} \end{aligned}$$

where:

$$\bar{\alpha}_0 = \frac{1}{2\pi} \int_0^{2\pi} \alpha_i \times d\theta$$

$$\bar{C}_{li}(\bar{\alpha}_0, \Delta\varphi) = \frac{C_{li}}{C_{lmax} \times \frac{dC_l}{d\alpha}}$$

$$\bar{C}_{di}(\bar{\alpha}_0, \Delta\varphi) = \frac{C_{di}}{C_d(\alpha_0, M)}$$

$$\bar{C}_{mi}(\bar{\alpha}_0, \Delta\varphi) = \frac{C_{mi}}{C_{lmax} \times \frac{dC_m}{d\alpha}}$$

$$C_{ln} = \frac{1}{\pi} \int_0^{2\pi} C_l \times \sin(\theta \times n + \Phi_{ln}) d\theta$$

$$C_{dn} = \frac{1}{\pi} \int_0^{2\pi} C_d \times \sin(\theta \times n + \Phi_{dn}) d\theta$$

$$C_{mn} = \frac{1}{\pi} \int_0^{2\pi} C_m \times \sin(\theta \times n + \Phi_{mn}) d\theta$$

This methodology was adjusted and tested thorough comparison with the results of experimental investigation presented in papers [6,7,8]. In the paper [10] there is a detailed comparison of unsteady airfoil calculations data for all typical helicopter rotor blade section flow operational conditions including stall, reverse flow and variable flow velocity versus blade azimuth. As the present paper is devoted to investigation of the unsteady profile drag variations, the figures 3 and 4 show some results comparing calculated instantaneous profile drag values with their experimental data.

Figure 3 shows the effect of adjusted frequency on the profile drag for the average angle of attack equal to 9.5 degrees and variable pitch amplitude equal to 4.5 degrees. Figure 4 shows the effect of adjusted frequency on the profile drag for the average angle of attack equal to 24.5 degrees and variable pitch amplitude equal to 4.5 degrees. The data are given for two adjusted frequency values : $k=0.09$ and $k=0.47$. The figure shows, that the proposed method of unsteady profile drag determination gives satisfactory results for the use in helicopter rotor calculations.

The presented results have been obtained by using the zero and the two first harmonics of aerodynamic coefficient unsteady decrements in Furie series expansion. This limitation is connected with the running speed and operational memory values of used computer.

Let us estimate the unsteady effect on profile drag. The figure 5 shows the diagrams of aerodynamic coefficient unsteady increment harmonics of Furie series expansion for the operating conditions. Unsteady profile drag increments are calculated by dividing the corresponding harmonic value by steady profile drag value obtained for the average angle of attack. The first bar of the diagram shows the maximum difference between unsteady profile drag and its steady value calculated for the average angle of attack. Evidently, the two first profile drag unsteady increment harmonic have the highest value. That is why the assumed calculating limitation consisting of two harmonic is quite reasonable. It is also evident, that the profile drag average value increase versus steady profile drag determined for the average angle of attack makes up to 27... 33% in unseparated flow conditions and 7...22% for stall in the range of adjusted frequency 0.09...0.47. The profile drag unsteady increment first harmonic makes up to 11...18% for unseparated flow conditions and 7...33% for stall conditions (depending on the adjusted frequency) compared to its steady value calculated for instant-

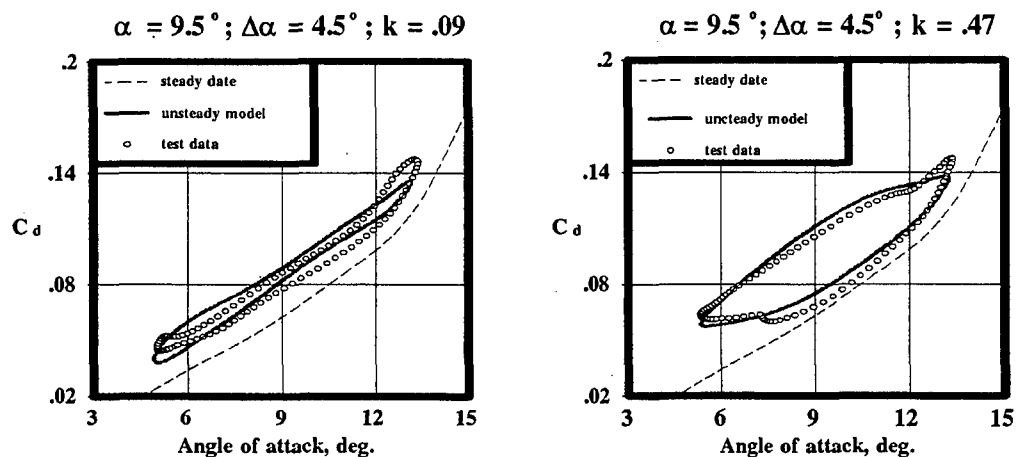


Figure 3 Adjusted frequency effect on pitch oscillating airfoil profile drag $\alpha_0 = 9.5^\circ$

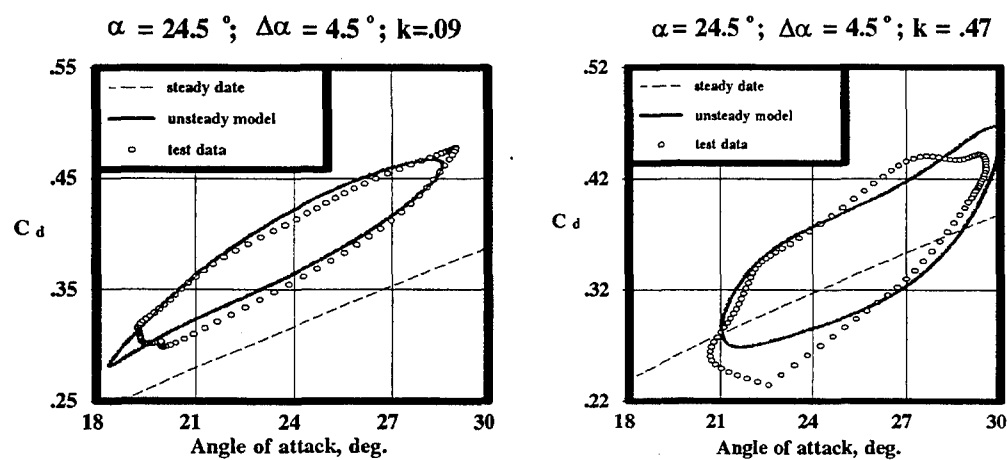


Figure 4 Adjusted frequency effect on pitch oscillating airfoil profile drag $\alpha_0 = 24.5^\circ$

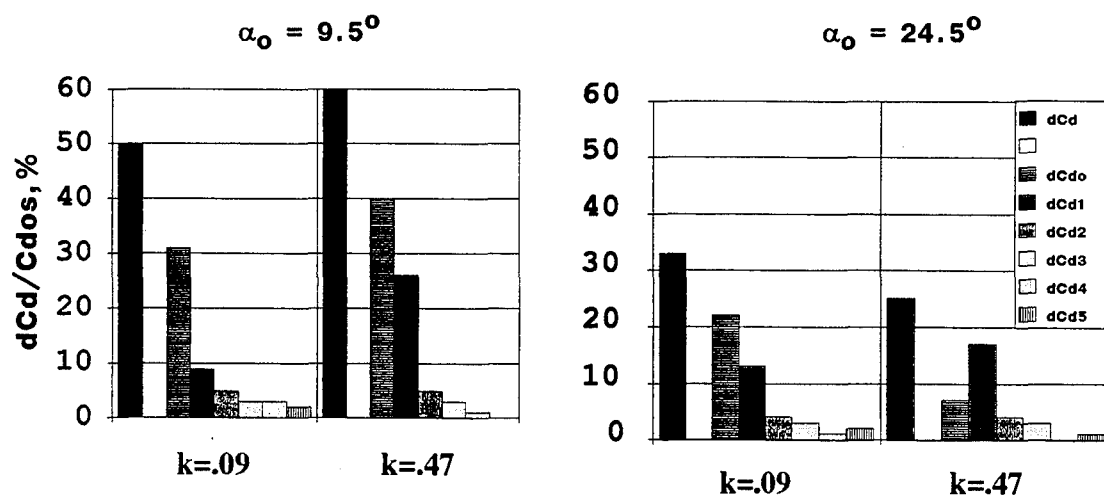


Figure 5 Harmonics of profile drag unsteady increment for the pitch oscillating airfoil

neous angle of attack values in stall conditions. The second harmonic value changes from 11 to 17% depending on the adjusted frequency average angle values. The maximum difference between unsteady profile drag and its steady value, obtained for the average angle of attack, as it is shown in the diagram, makes up 50% for unseparated flow and 25...33% for stall conditions. Comparison of unsteady profile drag with its steady value, defined for the instantaneous angle of attack, as presented on the figures 3 and 4, shows that the difference between them may change in wide range: 82...104% for the unseparated flow and 23...30% for stall conditions.

6. THE UNSTEADY PROFILE DRAG EFFECT ON THE ROTOR REQUIRED POWER VALUE.

Basing on the method of the unsteady airfoil data definition and using the formulas presented in papers [10,12], which take into account the airfoil aerodynamic characteristics changes in the yawed flow conditions, the forward flight helicopter performance were calculated.

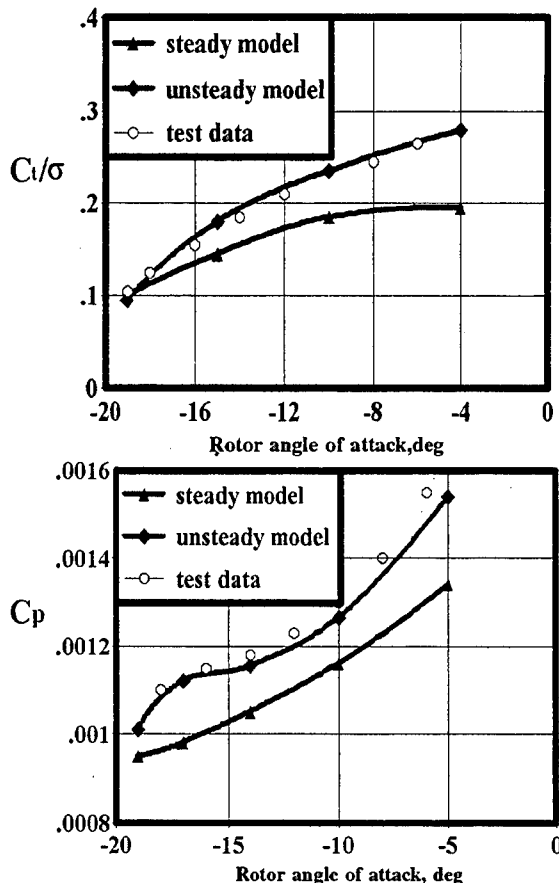


Figure 6 Comparison of calculated data with the model main rotor experimental characteristics.

The most accurate blade unsteady flow effect estimation may be carried out by comparing the results of

calculations with model rotor experimental data obtained in a wind tunnel. However, there are problems explained by the fact that in model experiments Re number similarity with both full-scale rotors and airfoil experimental characteristics used in rotor calculations usually cannot be achieved. In order to approach to full-scale blade dimensions the experiments for airfoil data measuring are carried out with Re number approaching to those of the full-scale rotor. At the same time the model blade Re number is much smaller. The adjustment of these experimental data to small Re numbers was made using the procedure, suggested in paper [12] on the basis of experimental investigation of Re number effect on airfoil characteristics.

Figure 6 shows the comparison of model rotor calculations with experimental data [14] for the hinged rotor with 4 meter diameter, pitch-flap coupling and no cyclic pitch control. Using test results the thrust and torque moment coefficient curves versus angle of attack were obtained for advance ratio $\mu = 0.35$. In order to evaluate the unsteady effect, the calculations were carried out using both steady airfoil data and unsteady ones.

The rotor thrust coefficient curve shows its typical increase in flow separation area for angle of attack values higher than -15 degrees, when unsteady effect is taken into account. In deep stall conditions ($\alpha_r = -6^\circ$) the account of unsteady effect gives the 41% increase of lift coefficient compared to the steady airfoil data. In unseparated flow conditions the unsteady effect account gives a slight rotor thrust coefficient decrease of 6.5%, as a result of airfoil lift coefficient average value decrease.

Interesting results were obtained while evaluating the unsteady effect on the rotor torque moment, shown on the same figure. The curve shows that the unsteady effect account in unseparated flow conditions leads to the 5% rotor torque moment increase, improving agreement between the results of calculations and the experimental data. In the stall flow conditions ($\alpha_r = -6^\circ$) the torque moment due to unsteady effect increases by 16%.

Let us consider the agreement between calculations and flight tests results. Figure 7 presents the Mi-26 helicopter forward flight required power in standard conditions at 0 and 6000 m altitude. The figure shows, that the calculations with unsteady effect account have good agreement with flight test data. On the same figure the required power calculated for rotor blade airfoil steady characteristics is also presented for comparison. The comparison shows, that in low flight conditions (the lift coefficient value of .15) the best endurance required power value with unsteady effects account is 19% higher than the one calculated for the steady airfoil data. As flight speed increases, unsteady effect becomes less, decreasing the difference in power to 10%. In high altitude flight conditions (the lift coefficient value of 0.235) unsteady

flow effect account gives 8...9% difference at the best endurance and maximum flight speed.

Figure 8 compares flight test and calculated vertical climb rate value around the best endurance flight speed in OEI conditions for the Mi-26 helicopter with low AUV[15]. The figure shows that calculations with the account of profile drag unsteady changes provides good agreement with flight test data, while those calculations using the steady airfoil data give an increase of vertical climb rate by 2 m/s because of underestimation of forward flight required power.

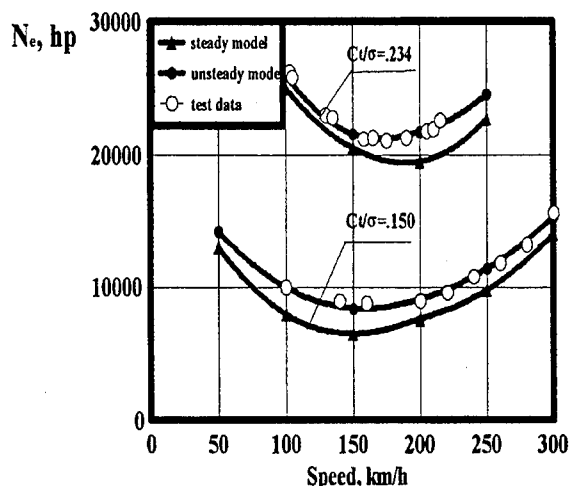


Figure 7 Unsteady airflow effect on the rotor required power for the heavy transport helicopter Mi-26

Figure 9 compares flight test and calculated data, for the Mi-26 helicopter pitch pull-up landing in case of one engine failure. Calculations were carried out using methodology developed by the author and presented

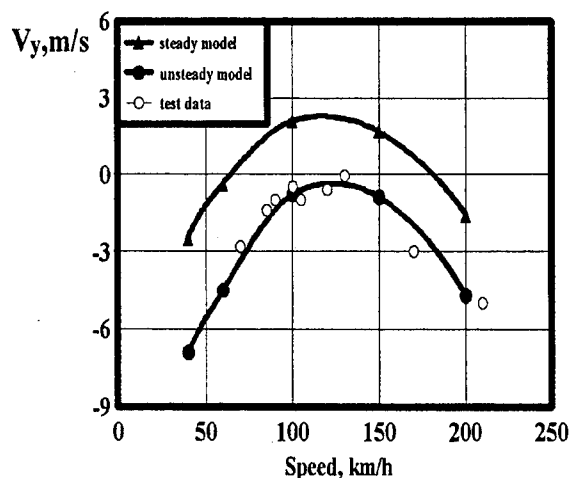


Figure 8 Unsteady airflow effect on climb ratio after engine failure for the heavy transport helicopter Mi-26

at the industrial conferences held in TsAGI in 1983 and 1987. Combined operation of the main and tail rotor and helicopter powerplant was taken into account in calculations. The curves presented show that the account of unsteady flow effect allows to improve the agreement of the computed and flight test data. In contingency engine power rating the calculated power reaches

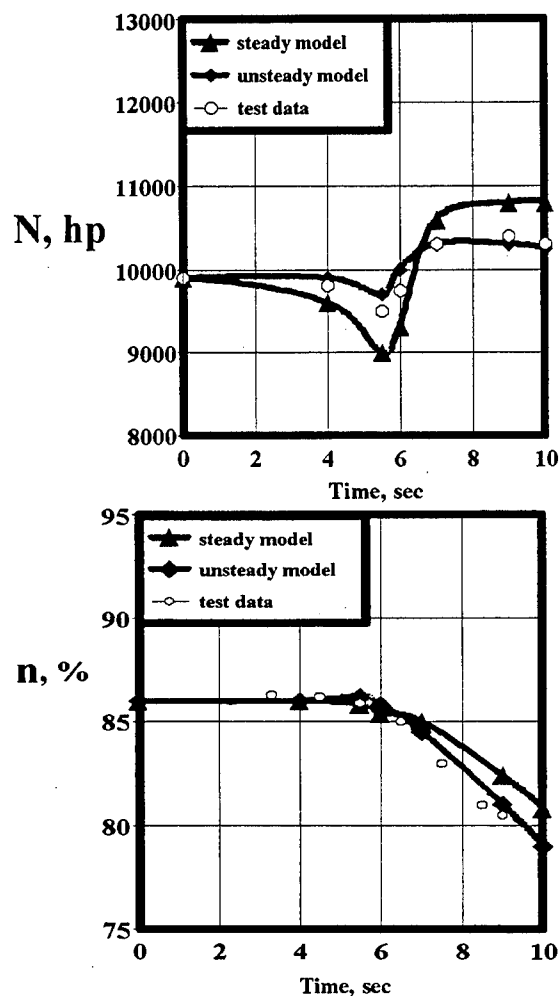


Figure 9 Changes in required powerplant and main rotor rotational speed of the heavy helicopter Mi-26 in landing with an engine failure determined by calculations and in flight tests.

the value of 10450 hp, which correspond to statistically average engine. Some discrepancy of the engine power curve character is caused by the fact that helicopter c.g. position has not been maintained and the trajectory data were taken directly from flight tests. Nevertheless, the curves show, that calculations without unsteady profile drag account give 1% lower than actual main rotor r.p.m. value in pitch pull-up landing and the engine spool up to maximum power is delayed by 0.5 seconds.

7. CONCLUSIONS

Basing on the investigations done the following conclusions may be drawn:

1. Unsteady effect account resulted in the profile drag average increase by 27...33% in unseparated flow conditions and by 7...22% in stall conditions in the range of adjusted frequency values of 0.09...0.4 with respect to the steady profile drag, determined for the average angle of attack. The unsteady profile drag first harmonic increment value was 11...18% in unseparated flow condition and 13...17% in stall conditions. The second harmonic value changes from 11% to 17% depending on the adjusted frequency and average angle of attack. The oscillating airfoil unsteady profile drag value may increase by 23...104% depending on operating conditions with respect to its steady value determined for the instantaneous angle of attack value.

2. The oscillating airfoil unsteady drag account causes the main rotor power profile drag increase by 5...20% depending on flight conditions.

8. REFERENCES

1. Myagkov Y.A., Rozhdestvensky M.G. Investigation of the Helicopter Tail Rotor Stall Flutter. Mil Helicopter plant Papers, N.11. Moscow, 1979.
2. Baskin V.E., Lapatov V.R. Representation of the Main Rotor Blade Section Experimental Unsteady Lift, Using the Generalized Parameters. TsAGI Technical Report, 1975.
3. Ericson L.E., Reding J.P. Dynamic Stall Analysis in Light Efficient Dynamic Stall Experimental Results, Journal of Aircraft, v.13, April, 1976.
4. Beddoes T.S. Practical Computation of Unsteady Lift, Vertica, v.8, N.1, 1984.
5. Belotserkovsky S.M., Vasin V.A., Loktev B.E. To the Main Rotor Unsteady Inflow Mathematical Nonlinear Simulation. The A.S. of the USSR Reports, t.240, N.6, 1978.
6. Liiva J., Davenport F.J. Dynamic Stall of Airfoil Section for High-Speed Rotors, Prog. of The 24Th. Forum of AHS, 1968.
7. Grey L., Dadone L., Gross D., Child R. Wind Tunnel Investigation of Inverse Flow Oscillating Airfoils. TsAGI Technical Translation, Moscow, 1975.
8. Lapatov V.R., Koroleva K.K., Peneetsa I.M. Experimental Investigation of P5-1, 21-50-23, 5-33-11x Helicopter Airfoil Unsteady Aerodynamic Data. TsAGI Technical Report, 1982.
9. Belotserkovsky S.M., Nisht M.I. Ideal Fluid Separated and Unseparated Flow over Thin Wings, M., Nauka, 1978.
10. Braverman A.S., Ivchine V.A. The Helicopter Simulation. Mil Helicopter Plant, Technical Report, 1989.
11. Johnson W. Helicopter Theory, Princeton University Press, 1980.
12. Harris F.D., Preliminary Study of Radial Flow Effects on Rotor Blades. Journal of AHS, v.11, July, 1966.
13. Ivchine V.A., Przhebel'sky V.V. The Reynolds Number Effect on the Helicopter Main Rotor Blade Airfoil Aerodynamic Characteristics. B.N. Uriev Memorial Conference Proceedings.
14. Pavlov A.S. Flow Stall Investigation of the Hinged Main Rotor Model Blades. TsAGI Technical Report N.4447, 1980.
15. Litvinov B.A., Tsygankov G.M. Fuel Consumption And Minimum Flight Speed Investigation Results for the Mi-26 Helicopter in High Altitude Flights LII Technical Report, N 378-87P, 1987.

Dynamic Stall Control by Variable Airfoil Camber

W. Geissler

H. Sobieczky

DLR, Institute of Fluid Mechanics

Bunsenstr.10

37073 Göttingen

Germany

1. SUMMARY

In the present numerical investigations the unsteady flow about a helicopter airfoil section under deep dynamic stall conditions has been influenced by dynamic airfoil deformation. First attempts with a dynamic variation of the airfoil *thickness* have already shown the favorable effects on the dynamic stall phenomenon: the dynamic stall onset could be shifted to considerably higher incidences within the oscillatory loop. In the present paper the extension of this method to more arbitrary types of dynamic deformations is discussed and the influence of a dynamic change of the airfoil leading edge curvature (*nose droop*) is investigated in detail. Special emphasis is placed on the variation of the Machnumber. It is shown that for incompressible flow ($Ma_\infty = 0.1$) the shedding of a dynamic stall vortex can be avoided at all. At a slightly higher Machnumber ($Ma_\infty = 0.3$) however the complete suppression of the dynamic stall vortex is a much more difficult task. The present results show the way how to proceed successfully also in the compressible flow cases.

Further it is obvious that the concept of deforming airfoils has considerable potential in other areas of helicopter aerodynamics, i.e. reduce or even avoid shock motion on the advancing side and therefore reduce the problem of compressibility noise radiation.

2. INTRODUCTION

Helicopter blades in high speed forward flight encounter extremely complicated unsteady flow phenomena, i.e. rapidly moving shock waves up to shock induced separation on the advancing side and cyclic separation and reattachment (dynamic stall) on the retreating side due to very high incidences during this part of the cycle.

The design of rigid airfoils for these different flow environments can therefore only be a compromise. Furtheron the design of helicopter airfoils is mainly based on quasi-steady assumptions.

In the past several attempts have been made to influence the flow about wings and blades by both active and passive control devices:

- With nose drooping on fixed wings [1],[2] high-speed stalling was influenced favourably.
- With a leading edge slat [3] the dynamic stall vortex could almost be avoided.

- With blowing and suction [4] the negative effects of the dynamic stall process could be reduced.
- With a pneumatic pulsating airfoil device [5] the onset of dynamic stall could be delayed and the poststall characteristics of the flow could be smoothed.

More recently various methods including airfoil leading edge deformation have been investigated to calculate and measure the effects on dynamic stall [6]. In this case the investigations have been done in incompressible flow.

In the present paper numerical investigations are carried out on the basis of a 2d-Navier-Stokes code using structured and deformable grids. This method has been proven successfully for rigid airfoils under deep dynamic stall conditions [7]. In DLR-Göttingen a design tool has been developed to calculate the surface of arbitrary bodies and wings [8]. This tool is also very suitable to be applied for arbitrary *time-dependent* airfoil deformations. A variation of the leading edge of a NACA 23012 airfoil with respect to time has been developed with this method. The deforming and oscillating airfoil has then been investigated under deep dynamic stall conditions. The results are compared with rigid airfoil data.

For the representation of the highly unsteady flow quantities like vorticity-, Mach- and pressure-distributions a video movie has been developed [9] which is shown during the presentation. The paper does include only a selection of the most important results of the calculation procedure.

3. TIME-ACCURATE NAVIER-STOKES CODE

For the calculations a time-accurate 2d-Navier-Stokes code has been used and further developed to be applicable for flow cases with unsteady flow separation and vortex shedding [10]. The algorithm of this code has the following main features:

- approximate factorization implicit (Beam/Warming-type)
- central differencing
- structured and deformable grid
- improved farfield conditions (vortex correction)
- eigenvalue-scaled numerical damping

- algebraic turbulence model (Baldwin/Lomax)
- fixed transition

To start the unsteady calculations numerical data in all grid points have first to be determined on the basis of a corresponding steady Navier-Stokes code. These steady data are obtained at the minimum incidence within the oscillatory loop. The present results have been obtained with as much as 50 000 time steps per cycle. One and a half cycle were sufficient for a converged cyclic result.

4. VARIABLE CAMBER AIRFOIL DESIGN

Recently a new geometry preprocessor (E88) has been developed in DLR-Göttingen as a purely mathematically explicit function generator to create solid 3D modelling with emphasis on airplane and other aerospace vehicle boundary definition [8]. This software allows to provide data of single or combined solid surfaces for whole aircraft or its components, with special surface metrics as required by grid generators for flow simulation. Many studies have been performed using this tool and aerospace industry has expanded it to create very complex configurations. The advantage over standard CAD tools is the availability of phenomena-motivated parameters to vary the shapes in optimization cycles, these parameters being developed within aerodynamic research and therefore carrying aerodynamic knowledge base in such fields like transonic fluid mechanics or hypersonic aero/thermodynamics. Because of explicit function evaluation without any iteration or interpolation, this method is extremely fast. A full aircraft solid surface can usually be defined within a few seconds on a workstation.

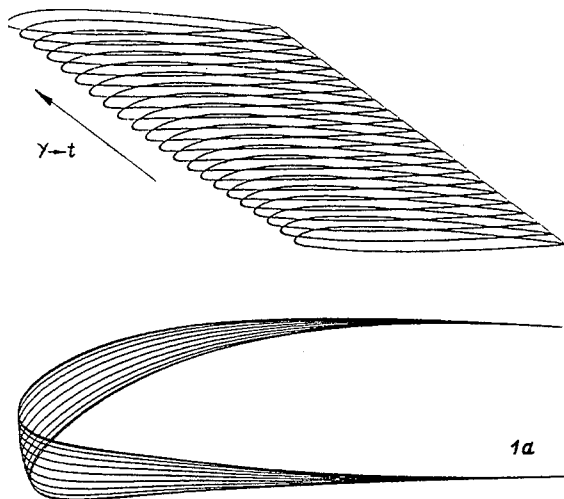


Fig. 1: 3D-wing design.
Variation of NACA 23012 section for nose droop (Fig. 1a).

Presently the code is being extended to the 4th dimension: Variation of certain selected parameters with time allows to create moving or pulsating surfaces, with direct applications in unsteady aerodynamics. In the present study the tool has been applied to create airfoils with dynamically changing shapes. For this task only the 3D version of the code is necessary. Fig. 1 shows a 3D wing design with a variation of the airfoil leading

edge (nose droop) in spanwise direction. The wing has an NACA 23012 airfoil section at both edges and a smooth variation to a nose droop configuration in the wing midsection. The wing is defined by a total of 21 airfoil sections which are equally spaced in spanwise direction. Details of the airfoil shapes are displayed in Fig. 1a.

It is very straightforward to apply such a wing design for the problem of a dynamically deforming airfoil: Assuming the spanwise wing axis (y) is replaced by the time-axis (t). Then the constant spacing in spanwise direction is replaced by a constant time step: The 3D wing surface is changing to a time-dependent deforming airfoil.

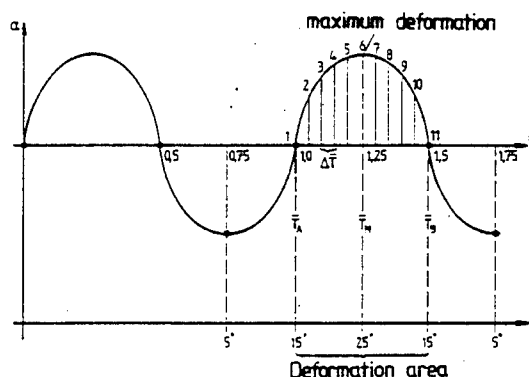


Fig. 2: Dynamic airfoil deformation with respect to time.

5. DYNAMIC DEFORMATION STRATEGIES

With the strategy described in the previous section a considerable number of additional parameters exists which are free to be varied. Fig. 2 shows the sinusoidal incidence variation of a helicopter blade section as function of time:

$$\alpha = \alpha_0 + \alpha_1 \sin 2 \cdot \pi \cdot \bar{T}$$

with

$$T = \frac{t \cdot U_\infty}{c} ; \quad \bar{T} = \frac{\omega^*}{2 \cdot \pi} \cdot T ; \quad \omega^* = \frac{2 \cdot \pi \cdot f \cdot c}{U_\infty}$$

as the dimensionless time \bar{T} , reduced frequency ω^* and normalized time T respectively.

In the following investigations the deep dynamic stall case with:

$$\alpha_0 = 15^\circ, \alpha_1 = 10^\circ \text{ has been verified.}$$

The deformation of the airfoil can now be placed within a prescribed time window of the oscillatory cycle (deformation area in Fig. 2). The extension of this time-window has been chosen to be $\Delta \bar{T} = 0.5$. A second parameter is the location of the time-window within the oscillatory cycle. In the present case this window has been placed symmetrically to $\bar{T} = 1.25$ i.e. to the maximum incidence $\alpha = 25^\circ$.

The global calculation procedure is then as follows:

- start the calculation with the determination of steady initial data at $\bar{T} = 0.75 \hat{=} \alpha = 5^\circ$ with the NACA 23012 airfoil section.

- start the unsteady calculation with the rigid airfoil up to the beginning of the deformation area, i.e. $\bar{T} = 1.0, \alpha = 15^\circ \uparrow$
- continue the unsteady calculation with a variable airfoil to the maximum deformation which is coincident with the maximum incidence $\alpha = 25^\circ$.
- continue the calculation further from the maximum deformation back to the basis airfoil at $\bar{T} = 1.5, \alpha = 15^\circ \downarrow$
- complete the cycle from $\bar{T} = 1.5$ to $\bar{T} = 1.75$ with the rigid airfoil.

In the deformation area the deforming airfoil is defined by 11 sections, which are located after constant time-steps corresponding to constant spanwise steps along span of the 3D wing section (Fig. 1). With the corresponding 11 sections the airfoil is changing its shape back from the maximum deformation at $\alpha = 25^\circ$ to the basis airfoil at $\alpha = 15^\circ \downarrow$. For the time-steps between the defining airfoil sections the grid is recalculated by a linear interpolation procedure between adjacent sections.

6. GRID-GENERATION PROCEDURE

For the calculations a curvilinear coordinate mesh has been used. The mesh is fixed to the moving airfoil surface and to the outer boundary in a space fixed frame of reference, i.e. the mesh is allowed to deform with respect to time. To calculate the mesh for each time-step would be very time consuming. A simple linear interpolation procedure has therefore been developed to determine the mesh at arbitrary time-points: In areas of rigid airfoil motion (Fig. 2) the mesh about the NACA 23012 airfoil at the extreme incidences $\alpha = 5^\circ$ and $\alpha = 15^\circ \uparrow$ is interpolated. Progressing in time into the deforming area of Fig. 2 the mesh is interpolated lineary between adjacent deformed airfoil sections at the instantaneous incidence. After the deformation area has been left the interpolation is again done for the rigid airfoil at the corresponding incidence. Fig. 3 shows the calculated meshes at the extreme incidences: $\alpha = 5^\circ$ (NACA 23012 rigid) and $\alpha = 25^\circ$ (maximum nose droop).

7. DYNAMIC STALL CALCULATIONS, RESULTS FOR RIGID VERSUS DEFORMING AIRFOIL

The following discussion of results concentrates on four different cases:

1. rigid NACA 23012 airfoil at $Ma_\infty = 0.1$
2. Deforming airfoil at $Ma_\infty = 0.1$
3. rigid NACA 23012 airfoil at $Ma_\infty = 0.3$
4. Deforming airfoil at $Ma_\infty = 0.3$

The deformation strategy is described in Fig. 2, the nose droop variation is displayed in Fig. 1.

7.1 Vorticity Distribution

Fig. 4 shows sequences of vorticity distributions just before, at and after the maximum incidence which corresponds to the maximum nose droop deformation

in the airfoil deforming case. Fig. 4a displays vorticity distributions for a small Machnumber $Ma_\infty = 0.1$ and Fig. 4b for a higher Machnumber $Ma_\infty = 0.3$. The lefthand sequence of figures shows results for the rigid airfoil, the righthand sequence shows results for the deforming airfoil.

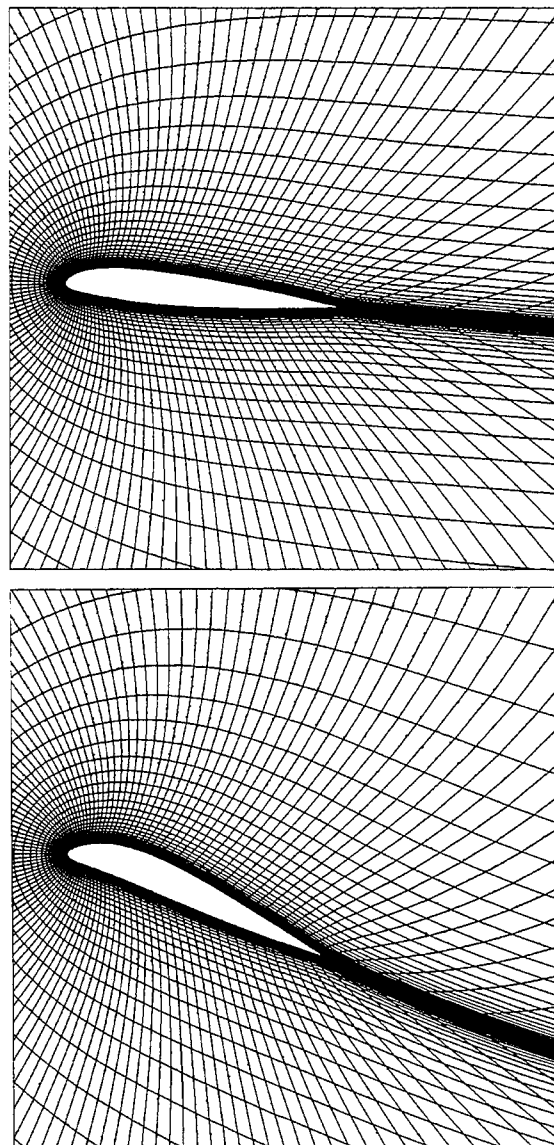


Fig. 3: Calculated meshes in extreme incidence positions:
upper figure: NACA 23012 rigid: $\alpha = 5^\circ$
lower figure: Nose droop: $\alpha = 25^\circ$.

In the incompressible rigid case (Fig. 4a) the dynamic stall vortex develops shortly before the maximum incidence ($\alpha = 25^\circ$) and is lifting off from the airfoil surface already at the beginning of the downstroke motion. This vortex lift-off is coincident with a breakdown of the lift in the oscillatory cycle as will be demonstrated in section 7.3. The deforming airfoil, right sequence of figures in Fig. 4a, does not show any sign of a concentrated vortex even during the high incidence part of the cycle. Only a thickening of the vorticity layer can be detected on the upper surface.

In the higher Machnumber case of Fig. 4b considerable differences can be observed compared to Fig. 4a. The dynamic stall vortex is now developing at a considerably lower incidence in the rigid case and it is already lifted off the airfoil surface before the maximum inci-

dence is reached. At the beginning of the downstroke a counter-rotating vortex is created at the trailing edge (dashed curves) separating the primary vortex completely from the airfoil.

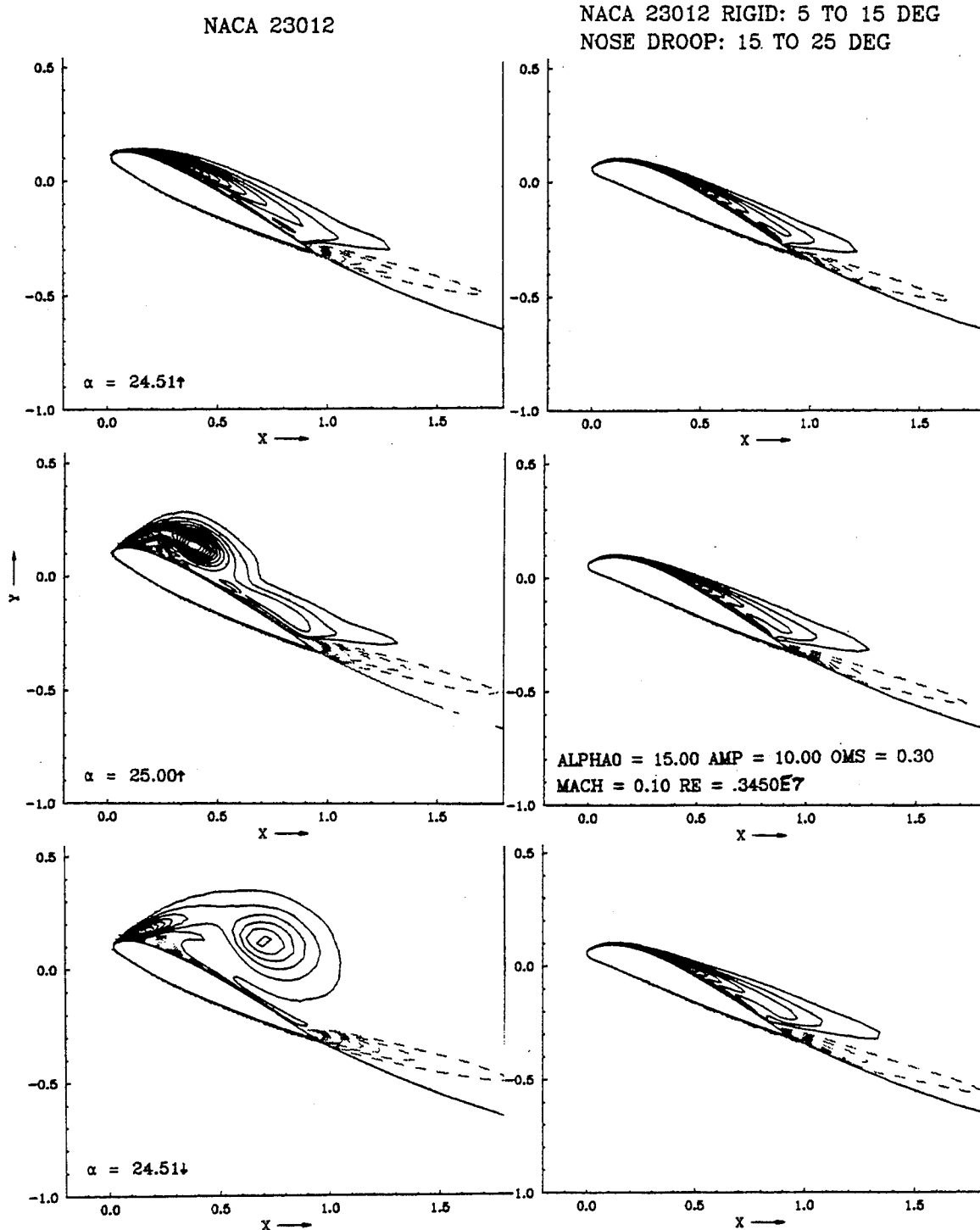


Fig. 4a: Vorticity-distributions at high incidence motion.
left: rigid NACA 23012 airfoil, right: nose droop,
 $Ma_\infty = 0.1$

In the deforming case however the development of a concentrated vortex is delayed considerably within the loop and starts beyond α_{max} . But in this case the vortex is weaker and stays nearly completely attached to the

airfoil surface. So a much less negative effect on forces and moment can be expected for this case as will be outlined in section 7.3.

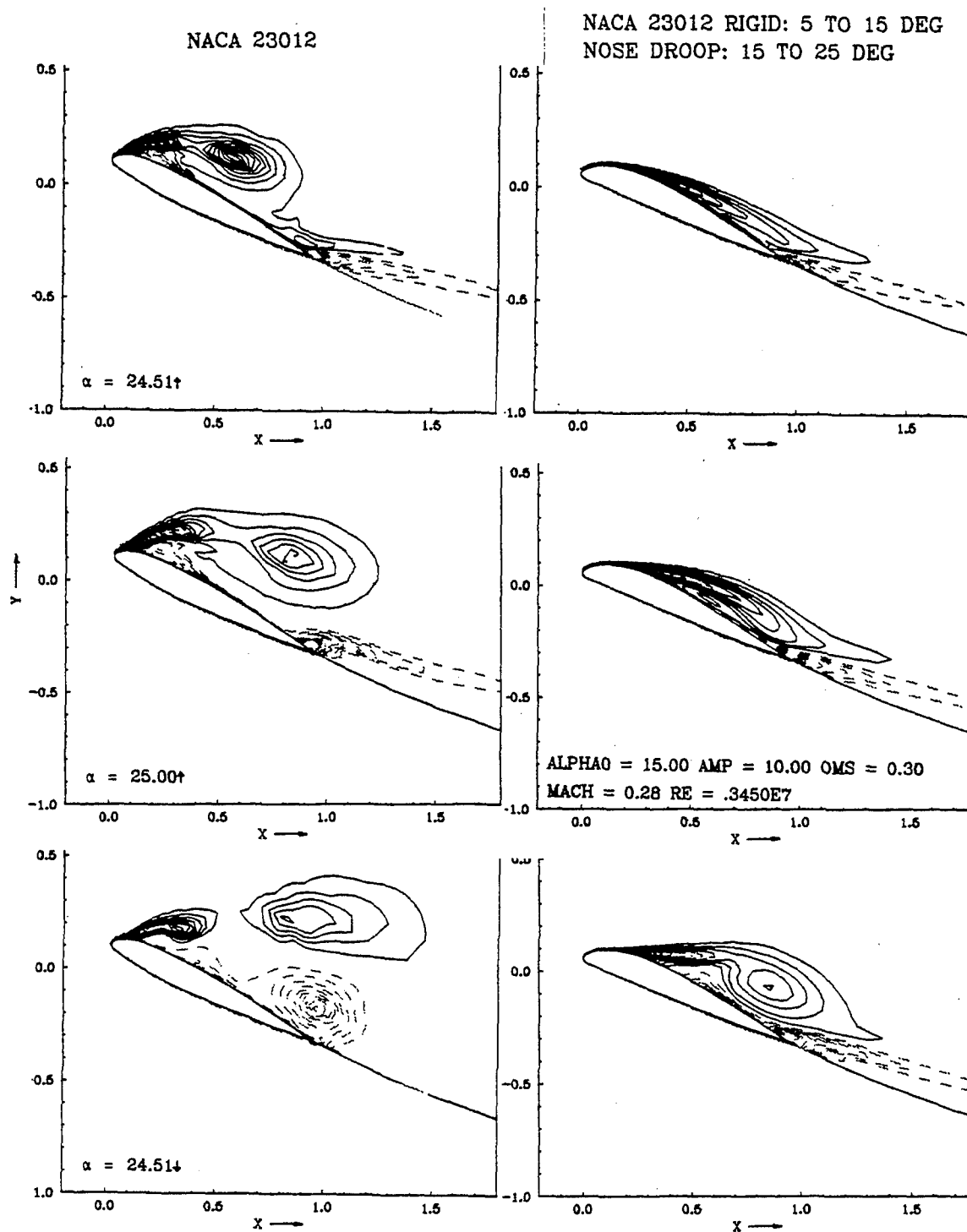


Fig. 4b: Vorticity-distributions at high incidence motion.
left: rigid NACA 23012 airfoil, right: nose droop,
 $Ma_\infty = 0.3$

The reason why such severe differences occur between the two Machnumber cases $Ma_\infty = 0.1/0.3$ is on the first view not quite obvious. Looking into the details of the flow at the airfoil leading edge a small supersonic bubble has been found in the higher Machnumber case which is completely avoided at $Ma_\infty = 0.1$ (see section 8).

The results given so far show already the strong potential of a dynamically deforming airfoil compared to the rigid case. At least in the incompressible case a concentrated vortex could be avoided completely. And also in the higher Machnumber case the flow is much smoother and the vortex stays attached to the airfoil surface during the entire motion.

7.2 Pressure Distributions

In the next sequence of figures the surface pressure distributions are shown for both rigid and nose droop airfoils. Again the two Machnumber cases ($Ma_\infty = 0.1/0.3$) are compared. Fig. 5a displays results for the low Machnumber and Fig. 5b for the higher Machnumber respectively.

In all figures the pressure distributions have been plotted for some selected normalized times in correspondence to instantaneous incidences in the high upstroke and downstroke regions.

Fig. 5a(left) shows first of all the typical development of pressures during the formation and initial movement of the dynamic stall vortex. The adverse pressure gradient at the leading edge is increasing prior to separation. Then between $\alpha = 24.5^\circ \uparrow$ and 25° the leading edge pressure peak is broken down and a smooth pressure maximum ($\alpha = 25^\circ$) is formed. This pressure peak is the effect of the dynamic stall vortex which is

then moving downstream during the continuation of the cyclic motion until it is shedded into the wake. At $\alpha = 23.1^\circ \downarrow$ the vortex has reached the trailing edge.

Fig. 5a(right) shows the corresponding plots for the deformable airfoil case. All pressure distributions do not show any sign of severe separation or vortex shedding. Looking at the details in the leading edge area shows, that the adverse pressure gradients remain nearly unchanged during the incidence variation and simultaneous nose drooping of the airfoil.

Results obtained for the higher Machnumber case displayed in Fig. 5b show similar tendencies but also some remarkable differences in the details. Fig. 5b(left) displays again the pressure distributions for the rigid airfoil. The development of a dynamic stall vortex is now initiated earlier within the cycle. The movement of the vortex takes place in a similar way as in the incompressible case. With airfoil deformation, Fig. 5b(right) a strong effect of a dynamic stall vortex is not visible in the pressure distributions. However compared to Fig. 5a the adverse pressure gradient at the leading edge is still steepening with increasing incidence and nose drooping. This is a compressibility effect which is caused by the development of a small supersonic bubble sitting at the airfoil leading edge and which can not be avoided by the present dynamic deformation of the airfoil leading edge. Details of this leading edge flow situation will be discussed in section 8.

Only in the trailing edge region and beyond the maximum incidence i.e. at the beginning of the downstroke motion the effect of a dynamic stall vortex is visible in the pressure distribution (see Fig. 4b).

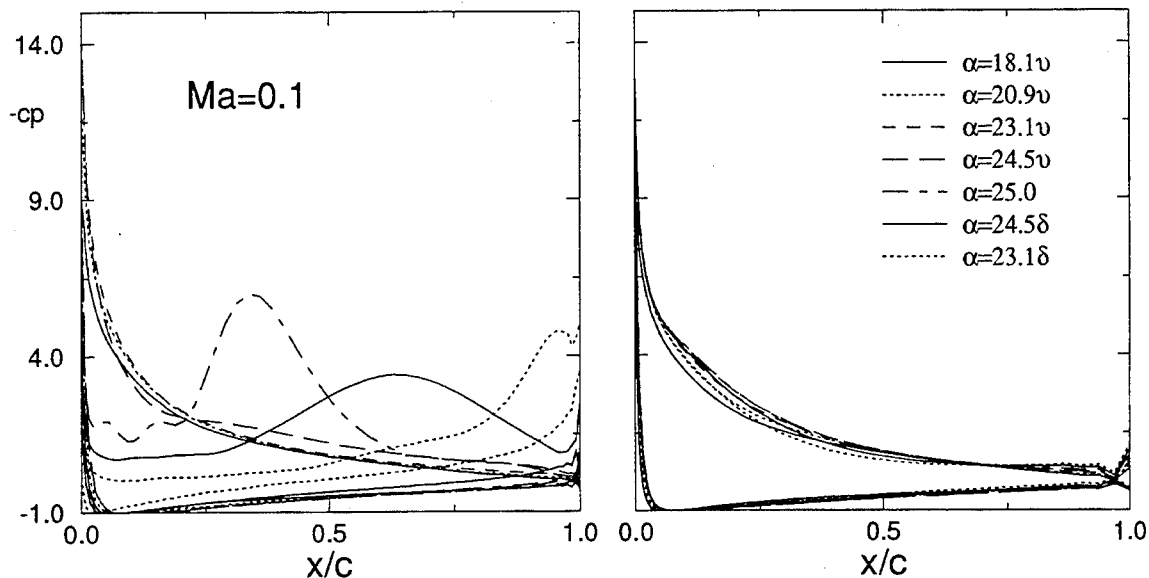


Fig. 5a: Surface pressure distributions at $Ma_\infty = 0.1$.
left figure: rigid NACA 23012 airfoil.
right figure: nose droop.

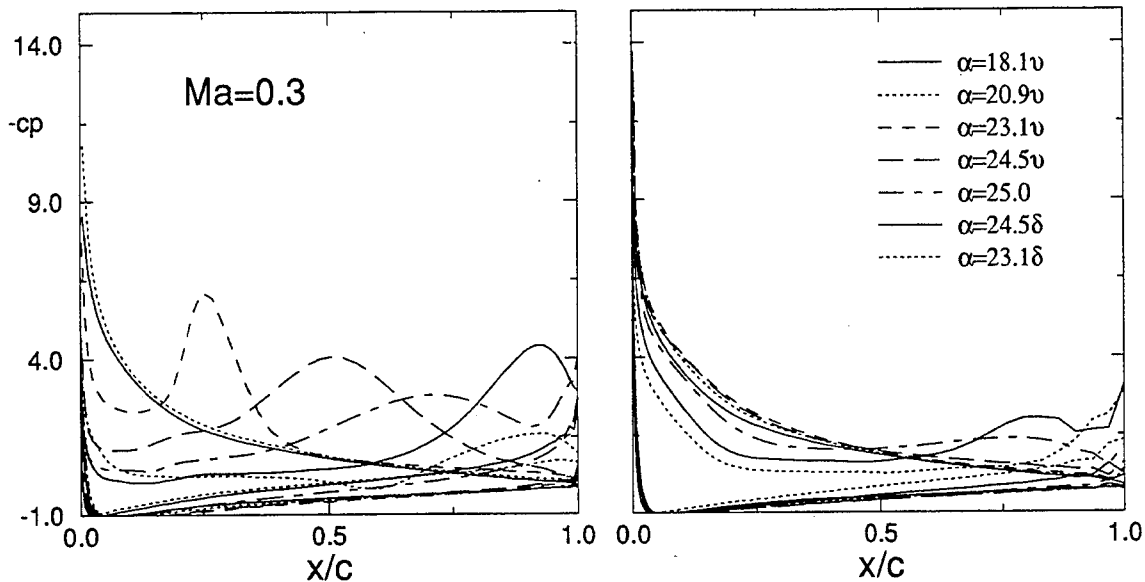


Fig. 5b: Surface pressure distributions at $Ma_\infty = 0.3$.
left figure: rigid NACA 23012 airfoil,
right figure: nose droop.

7.3 Force and Moment Distributions

Of practical importance is the influence of the dynamic airfoil deformation on force and moment loops. Fig. 6 shows lift-, drag- and pitching moment-distributions versus incidence for both incompressible (Fig. 6a) and compressible (Fig. 6b) cases. The results for the deformable airfoil are compared with the rigid airfoil case (dashed curves in Fig. 6). In the incompressible case the reduction of the hysteresis curves to flat loops is very remarkable: this kind of behavior is known from inviscid flows and is therefore the indicator that strong viscous effects due to the development and shedding of a dynamic stall vortex is completely avoided.

In detail one can figure out the following features:

1. the maximum lift is nearly unchanged in the deformable airfoil case. The benefit due to the dynamic incidence variation of the airfoil is kept.
2. the severe increase of drag in the rigid airfoil case is completely avoided.
3. the pitching moment does not show any negative peak as in the rigid case. This negative peak which is occurring within a very short time range has strong negative effects on the blade structure. Furtheron if the moment curve is traversed in a clockwise cycle, which is the case for the rigid airfoil, negative aerodynamic damping may lead to a dangerous stall flutter situation during this part of the cyclic loop.

Fig. 6b shows the corresponding results for the compressible flow-case. The effects come out to be similar as in the previous case, but the hysteresis loops still

remain large. Also in this case the maximum lift is reached with the nose drooping airfoil. The peaks in the drag and pitching moment loops are reduced considerable. But the negative peak in the c_m -curve including a small area of negative aerodynamic damping could not be completely avoided.

A number of additional calculations have been carried out to minimize the negative c_m -peak by shifting the deformation area either more into the upstroke or into the downstroke region respectively. But in both cases the results could not be improved, i.e. the negative c_m -peak was again increased and the area of negative damping was enlarged.

8. INFLUENCE OF COMPRESSIBILITY

All the results discussed so far have clearly shown that the dynamic deformation of the airfoil leading edge has large benefits for the incompressible very low Mach-number flow case. For helicopter rotor blades this means, that the benefits are large for very high advance ratios where the uncoming flow velocity is reduced to very small values. For higher Machnumbers the benefit of a dynamic nose drooping is still remarkable but emphasis should be placed on a further improvement of the results also for compressible cases.

It has already been mentioned in the previous section that during the upstroke motion of the airfoil a small supersonic bubble develops very close to the airfoil leading edge. Fig. 7 shows Iso-Machcontours at the airfoil leading edge ($Ma_\infty = 0.3$) at $\alpha = 21^\circ$ (Fig. 7a) and at a slightly later time at $\alpha = 23^\circ$ (Fig. 7b).

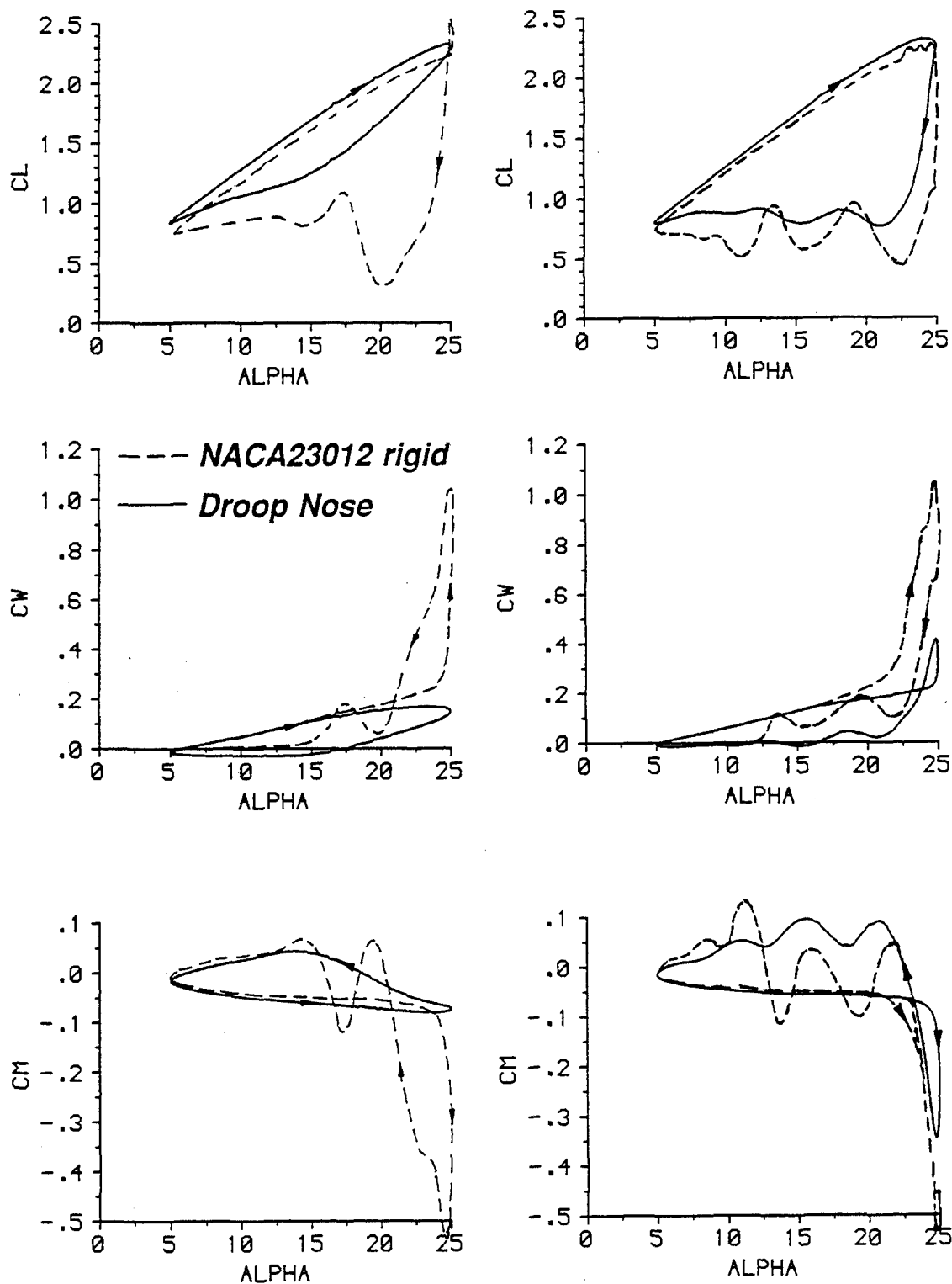


Fig. 6: Lift-, drag- and pitching moment-loops.

Fig. 6a (left): $Ma_\infty = 0.1$ Fig. 6b (right): $Ma_\infty = 0.3$

At the lower incidence (Fig. 7a) in both rigid and deforming cases a supersonic bubble is visible (white spot in the figure) which is sitting at almost the same leading edge position. At the higher incidence, Fig. 7b, the bubble has disappeared in the rigid airfoil case and the flow is separated directly downstream from the

position where the bubble was located. In the deforming case however the supersonic bubble is still existent and is even enlarged. Later in the cycle (at the downstroke motion) a breakdown of the bubble accompanied by flow separation does occur also in the

deforming case. The separation is much smoother as for the rigid airfoil.

The compressibility effects in form of a small supersonic bubble obviously lead to the reduced efficiency of the airfoil deformation in the compressible compared to the incompressible case. To improve the effect of deformation it therefore must be tried to suppress the

bubble completely and therefore try to avoid separation over the entire cycle of airfoil oscillation. A strategy towards this goal could be to reduce the curvature of the airfoil in the region where the bubble is located. This should be possible since as can be seen in Figs. 7 the bubble is nearly stationary located and does not change its size.

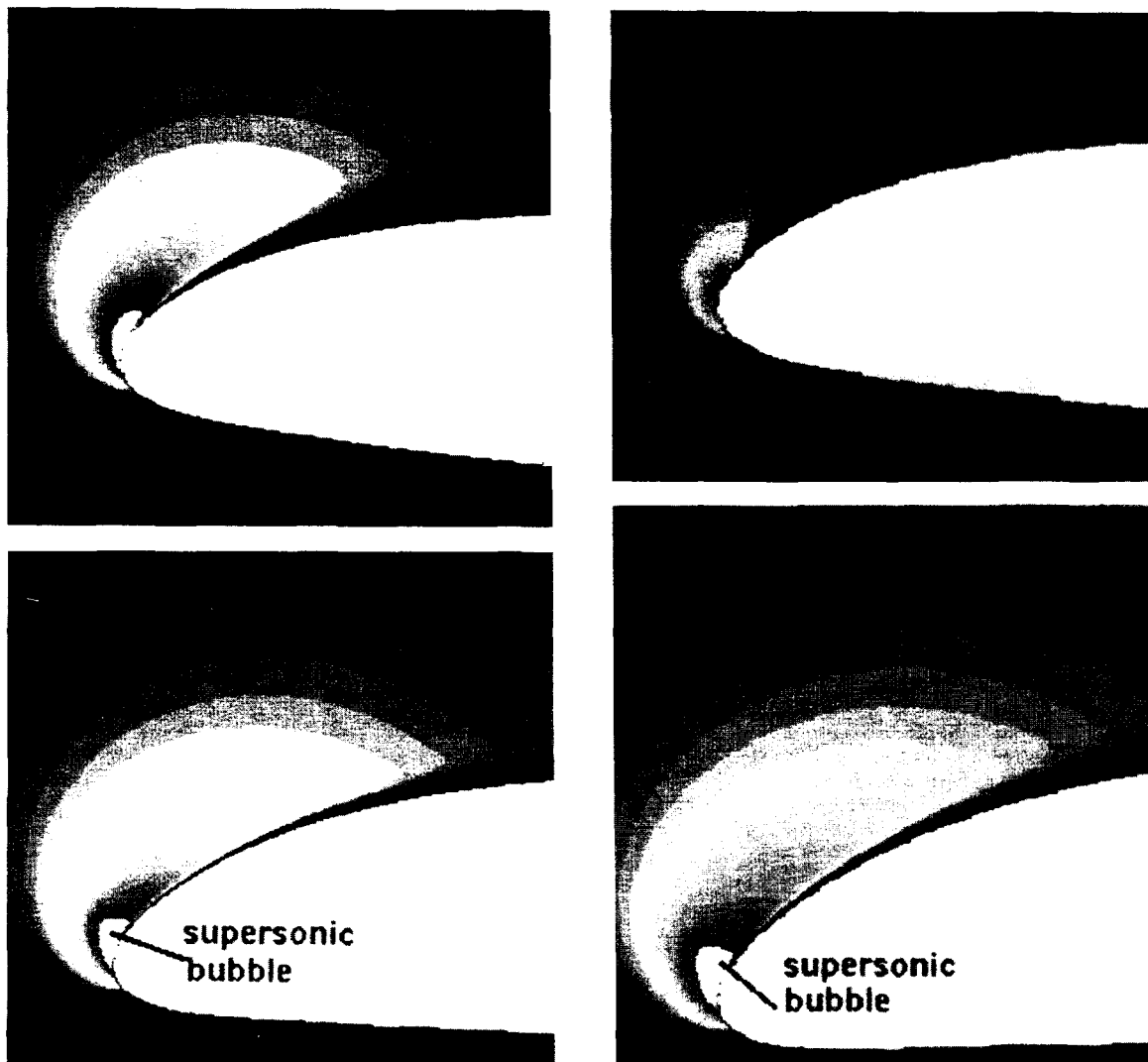


Fig. 7: Machnumber contours at airfoil leading edge during upstroke:
upper figures: rigid airfoil, lower figures: nose droop.

Fig.7a (left): $\alpha = 21^\circ$

Fig.7b (right): $\alpha = 23^\circ$

9. CONCLUSIONS, FUTURE ACTIVITIES

With numerical calculations the flow about dynamically deforming airfoils under deep dynamic stall conditions has been investigated. It was shown that with a nose drooping of the airfoil very good results can be achieved in reducing or even completely avoiding the development and shedding of a dynamic stall vortex. These effects have severe impact on the force and moment hysteresis loops: The maximum lift is nearly unchanged but the negative peak in the pitching moment

loop is reduced, negative aerodynamic damping and the tendency to dangerous stall flutter is diminished.

Comparisons between incompressible flow and a low Machnumber case show influences of a small supersonic bubble emanating at the airfoil leading edge during the upstroke motion. This bubble could not be avoided by the nose drooping and seems to be the reason for the slightly reduced effectiveness of the drooping procedure in compressible flow. In future investigations some emphasis will be placed on avoiding the bubble

completely. This may be accomplished by a reduction of the airfoil curvature at its location.

Future work will also be concentrated on the development of measures to realize deformation strategies on blade models. A 2D model could be a first candidate to check the predicted data in real flow. Different design tools are envisaged to realize a deforming airfoil leading edge either by conventional means [2] on the basis of hydraulic actuators or by more sophisticated means on the basis of smart structures and/or smart materials technologies. The latter tools are of great interest if one wants to finally apply the deformation strategies on a real helicopter rotor blade.

In addition to the influence of the dynamic stall process at the retreating side of the rotor one can also think about influencing the advancing side of the cycle. In highspeed forward flight the rotorblade encounters transonic flow at the blade tip. Moving shock waves are present at this part of the cycle which are responsible for compressibility noise radiation. A suppression or at least reduction of the shock wave by local airfoil deformation could have considerable benefit in noise reduction.

10. REFERENCES

1. Küchemann, D., F.R.S.
The Aerodynamic Design of Aircraft.
Pergamon Press, Oxford (1978).
2. Moss, G.F.; Haines, A.B.; Jordan, R.
The Effect of Leading-edge Geometry on High Speed Stalling.
AGARD CP-102 (1972), pp.13-1,13-6.
3. Carr, L.W.; McAllister, K.W.
The Effect of a Leading Edge Slat on the Dynamic Stall of an Oscillating Airfoil.
AIAA-paper 83-2533, Oct.1983.
4. McCloud, J.L.; Hall, L.P.; Bready, J.A.
Full-Scale Windtunnel Tests of Blowing Boundary Layer Control Applied to a Helicopter Rotor.
NASA TN D-335, Sept.1960.
5. Geissler, W.; Raffel, M.
Dynamic Stall Control By Airfoil Deformation
Proceedings of the 19th European Rotorcraft Forum, Paper No. C2
Sept.14-16, 1993, Cernobbio(Como), Italy
6. Yu, Y.H.; Lee, S.; McAllister, K.W.; Tung, C.
High Lift Concepts for Rotorcraft Applications
Paper at the 49th American Helicopter Society Annual Forum,
St.Louis, MO, May 19-21, 1993
7. Geissler, W.; Vollmers, H.
Unsteady Separated Flows on Rotor-Airfoils - Analysis and Visualization of Numerical Data -
Proceedings of the 18th European Rotorcraft Forum, Paper No. 79
Sept. 15-18, 1992, Avignon, France
8. Sobieczky, H.
Multiblock Grid Generation
Notes on Num. Fluid Mechanics, Vol.44, pp.71-76
ed. N. Weatherhill et al. (Vieweg, 1993)
9. Geissler, W.; Ehrenfried, K.
Dynamic Airfoil Deformation on a NACA 23012 Airfoil
- Influence of Compressibility -
Video-Movie, VHS-PAL
DLR-Göttingen, 1994
10. Geissler, W.
Instationäres Navier-Stokes Verfahren für beschleunigt bewegte Profile mit Ablösung.
DLR-FB 92-02 (1992)

REVIEW of RECENT AERODYNAMIC RESEARCH on WIND TURBINES with relevance to ROTORCRAFT

Data (and riddles) on DYNAMIC INFLOW, FLOW FIELD OF YAWED ROTORS, and ROTATING 3-D STALL

H. Snel¹⁾ and Th. van Holten²⁾

¹⁾ Netherlands Energy Research Foundation ECN
Westerduinweg 3, P.O.Box 1, 1755 ZG Petten, Netherlands

²⁾ Delft University of Technology, Faculty Aerospace Engin.
Kluyverweg 1, 2629 HS Delft, Netherlands

1. SUMMARY

A review is given of recent research on the aerodynamics of wind turbine rotors. The following subjects are covered in extenso:

- The induced velocity field of rotors, including dynamic inflow and yawed flow effects.

- Stall delay on rotating blades. A new boundary layer formulation is outlined applicable to this phenomenon.

Without any further discussion, also some references have been given concerning recent wind turbine research on:

- simulation methods of atmospheric turbulence,
- dynamic stall effects, comparisons between theory and experiments,
- Effect of several types of blade tips on radiated noise.

2. NOTATIONS

a induction factor v_i / U
 $C_{D,ax}$ drag coefficient of entire rotor
 C_y axial force coefficient of blade section
R rotor radius
r local radius
t time
U free stream velocity
V total resulting velocity at blade section
 v_i induced velocity in disc plane
 σ solidity
 τ time constant, or shear stress

other notations explained in figures

3. INTRODUCTION

This paper presents a review of recent aerodynamic research related to wind turbine rotors, which may not be very well known outside the "wind community" but may nevertheless have relevance for rotorcraft as well.

The requirements for a long, maintenance-free life and low first cost of wind turbines have stimulated the development of accurate prediction methods of extreme aerodynamic loads and fatigue spectra. Furthermore, a considerable amount of research has been done in order to reduce aerodynamic loads by proper control systems and by flexible rotor systems which employ the same principles as hingeless

helicopters.

Apart from the obvious similarities between the rotors and aerodynamics of wind turbines and rotorcraft, there are also typical differences. The disc loading of wind turbines is high, so that normal operation is often close to the turbulent wake state, with values of the induction factor $a = v_i/U$ around 1/3. This implies close proximity of the free vortex sheets to the disc, and large self-induced deformations of the wake configuration. Linearization applied in helicopter aerodynamics must often be questioned for wind turbine applications. In the case of a hovering rotor the loading is also high in an aerodynamic sense (i.e. there is a large influence of self-induction on the wake configuration). In the case of the helicopter this results in a contracting wake, whereas the high loading on a wind turbine rotor results in wake expansion.

A high blade loading of turbine rotors is another typical feature. In fact, stalling is often used as a means of limiting the power absorbed from the flow. Stalled flow is thus effectively part of the operational envelope of the turbine.

Finally, the rotor dimensions of a turbine are generally larger than those of rotorcraft. The scale of the turbulence experienced by wind turbines, operating close to the ground, is for that reason more comparable to the radius. A strong "rotational sampling effect" (in rotorcraft literature sometimes referred to as "rotating frame turbulence") is therefore always present.

During the "pioneering phase" of modern wind turbines - roughly from 1970 until 1980 - much aerodynamic knowledge was borrowed from aeronautics, in particular from the field of helicopters. In a later phase, dedicated R&D programs have emerged, directed at the specific aerodynamic problems of wind turbines where the need was felt to improve upon the available rotorcraft knowledge.

For the "helicopter community" the results of this work may be interesting, since well known theoretical models have in this way have been verified in flow regions outside the usual range of parameters. Some unexpected discrepancies between models and experiments have indeed shown up.

4. SOME REFERENCES TO RELEVANT RESEARCH WHICH IS NOT FURTHER DETAILED IN THE PAPER
 Apart from the projects discussed in the paper in some detail, other relatively large scale research projects on windturbines have recently been completed. For lack of space they could not be included in the present review. It may nevertheless be useful to give here some relevant references, without pretending to be exhaustive. These research subjects were:

- Modeling of inflow turbulence, as "felt" by rotating blades: ref.1, based on the earlier work of ref.2.

- Experiments on dynamic stall and comparisons with theory: ref.3.

- Noise research, in particular the influence of several types of tip shape: refs.4 and 5.

5. DYNAMIC INFLOW EFFECTS IN AXIAL FLOW

5.1. Background of CEC-research on dynamic inflow

Research on dynamic inflow effects of wind turbines was initiated after it had been observed that sometimes large, unpredicted blade loads occur during fast braking of wind turbines by blade feathering. The phenomenon was qualitatively explained as a "dynamic inflow" effect.

Apart from the effect of dynamic inflow, blade forces during transient operating conditions may also be influenced by unsteady profile characteristics. However, the typical time scales of dynamic inflow effects and of unsteady section aerodynamics are well separated. The possible influence of unsteady profile aerodynamics may be estimated, e.g. using the ONERA-model (ref.6). From such exercises it can be concluded that during typical pitching steps of wind turbines the unsteady profile characteristics play a minor role.

There is a long history of inflow modeling in helicopter aerodynamics, see Chen (ref.7). One of the most successful methods for the estimation of dynamic inflow effects for helicopters is based on the work of Pitt and Peters (with a large and ever growing number of associates, see i.a. ref.8, based on the earlier ref.9).

However, in view of the above mentioned differences between the helicopter rotor and the highly loaded turbinerotor, research was initiated by the CEC, within the Joule-program, on dynamic inflow effects in the case of wind turbine rotors. The aim of this research program was to generate an experimental database of typical dynamical inflow effects as encountered by highly loaded turbinerotors, and compare this with the predictions obtained by several theoretical methods.

5.2. Brief description of experiments and theoretical models

1) Experiments.

Although several wind turbines and

windtunnel models were used, the most important experiments were performed on the Tjaereborg 2 MW turbine (60 meters diameter) in Denmark.

Data were measured under the following conditions:

- fast pitching steps
- emergency stops by feathering
- yawed operation

The most interesting results were found for the case of small pitching steps. For this reason we will concentrate on this case in the following. Complete results of the project will be published in the final report on the project, not yet available.

2) Theoretical methods.

The theoretical methods covered a wide range of different approaches:

I. Free-wake models. Three different models were investigated, based on either vortex lattices, vortex particles or on a description in terms of the acceleration potential.

II. Comparisons were made with a simple prescribed-wake model, where the wake was modeled as a vortex tube with varying vortex strength.

III. Several engineering models were investigated as well. These were based on blade element - momentum theory, modified by formulating them as first-order differential equations to simulate the time lag. Three different models were investigated, where the time constants were derived from three different theoretical analyses.

Before results of the comparisons are shown, a brief description of these models will be given.

Free-wake, lifting surface model using vortex particles (National Technical University of Athens)

The computercode GENUVP of NTUA is a time-marching code based on a consistent combination of the boundary element method and the vortex particle method. The boundary elements consist of distributed dipoles on the solid surfaces of the flow. The boundary conditions of non-penetration determine the intensities of these distributions. The vortex particles are used to simulate the generation and evolution of the free vorticity. The vorticity shed along the edges of the blades is locally integrated and assigned to point vortices (or equivalently, to fluid particles carrying vorticity). Next the evolution of these vortex particles is followed by integrating the vorticity transport equations in Lagrangian coordinates. For further details, see ref.10.

Free-wake, lifting surface model using vortex filaments (University of Stuttgart, IAG)

In this free wake code (ROVLM) the blade is covered with panels on which a constant dipole strength is assumed. The induced

velocities are calculated with the Biot and Savart law using the vortex strength corresponding to the differences of the dipole strengths on adjacent panels. Due to the external flow field and the induced velocities at the blade, points from the separation edges move downstream and build up the panels of the free wake which are deformed in such a way that the forces on the wake vanish. The kinematic boundary condition on the blade is fulfilled in the model. For further details, see ref.11.

Free-wake, lifting line model using the acceleration potential (Delft University of Technology, Inst. Wind Energy)

This code (PREDICAT) is based on an unsteady lifting line theory which was originally developed for helicopter rotors (ref.12). In order to modify classical lifting line theory in such a way that it becomes usable and consistent under unsteady and yawed flow conditions, a rigorous matched asymptotic expansion method was applied to derive lifting line theory from first principles. This was facilitated by using the acceleration potential for a description of the flow field. When this theory is applied to rotors, analytical expressions are derived for the complete, time varying pressure field associated with the rotor blades. As a next step the corresponding velocity field is found by numerically integrating the acceleration of fluid particles coming from far upstream and finally reaching the near field of the rotor. Although the Laplace equation for the pressure field is derived by linearizing the flow equations, in the present code PREDICAT the most important non-linear effects are taken into account. This is achieved by letting the path followed by the particles completely free, which simulates the free-wake effects. The method is computationally very efficient, because use is made of closed form solutions for the pressure field. It is a free-wake method which may be run conveniently on a normal PC. For further details, see ref.13.

Simple prescribed wake model (Energy Research Foundation Netherlands ECN)

The induced velocities in both axial and tangential direction are calculated with a cylindrical vortex sheet model. The vortex distribution on the cylindrical wake is obtained by the time history of the shed tip-vorticity which is related to the axial force on the blade. With the Biot-Savart law the induced velocities can then be found. It is assumed that the wake extends up to four rotor diameters downstream. Inputs that may be semi-empirically adjusted are the axial convection velocity and the effective diameter of the cylindrical wake. For further details see ref.14.

Differential equation model, with time constant based on the simple prescribed wake method (Energy Research Foundation Netherlands ECN)

The induced velocity in axial direction within an annulus of the rotor disc is

equation with the addition of a time derivative of the induced velocity:

$$4 R f(r/R) \frac{dv_i}{dt} = C_{p,ax} U^2 - 4 v_i (U - v_i)$$

The value of the time constant $f(r/R)$ is deduced from the equations for the cylindrical wake mentioned above (ECN, simple prescribed wake model):

$$f(r/R) = 2\pi \int_0^{2\pi} \frac{[1 - (r/R) \cos\phi] d\phi}{[1 + (r/R)^2 - 2(r/R) \cos\phi]^{3/2}}$$

The function $f(r/R)$ equals 1 for $r/R=0$ (the rotor centre) and 0 for $r/R=1$, the rotor edge. Hence the time constant for the rotor centre position equals $4R/U$, while at the rotor edge the time constant equals zero, so that the equilibrium relations always hold there. This can be seen to be a natural consequence of the cylindrical vortex wake model. In fact, the only vorticity inducing axial velocity at the tip is the vortex in the process of being released, while at the rotor centre a large portion of the wake, and hence of the time history, causes axial induced velocity.

For large induced velocities, particularly for $v_i/U > .5$, the blade element momentum theory is not valid, the turbine operates in the so-called turbulent wake state. In the actual implementation a model for the latter effect is used for $a > .38$, where the right hand side of the above differential equation is replaced by:

$$r.h.s. = C_{p,ax} U - 0.96 v_i + 0.5776 U$$

Differential equation model based on Pitt & Peters time constants (Garraad, Hassan & Partners, UK)

This model is based on the same ideas as the previous model. The time constant, however, is taken from the method of Pitt and Peters (ref.8). The original method is on a global disc level. For a disc of radius R the apparent mass is given approximately by potential theory (Tuckerman, ref.15) as $8/3 \rho R^3$, but is in the present method applied on blade element level. This results in a differential equation for the axial induction factor a :

$$\frac{16 (r_2^3 - r_1^3) da}{3\pi U (r_2^2 - r_1^2) dt} = \frac{\sigma V^2}{U^2} C_y - 4a(1-a)$$

In contrast to the earlier described differential equation model by ECN, in this case the time constant grows linearly with r (together with the area of the respective annuli).

Differential equation model with two different time constants (Technical University of Denmark)

The induced velocities in axial direction are calculated with the blade element-momentum equations with the addition of a time derivative of the induced velocity. This is similar to the models given above. TUDK however uses two differential equations. These have the following form:

$$y + \tau_1 \frac{dy}{dt} = x + k \cdot \tau_1 \frac{dx}{dt}$$

$$z + \tau_2 \frac{dz}{dt} = y$$

with $k = 0.6$ and:

$$\tau_1 = \frac{1.1}{(1 - 1.3 a) U} R$$

$$\tau_2 = \{0.39 - 0.26 (r/R)^2\} \cdot \tau_1$$

This amounts to one short and one longer time scale for the decay. The time constants weakly depend on the radius of the blade element. The time constants are derived from an actuator disc - vortex ring program which includes the effect of wake expansion.

5.3. Results

Typical results of the comparisons between the experiments and the theoretical models are shown in the figures 1 and 2.

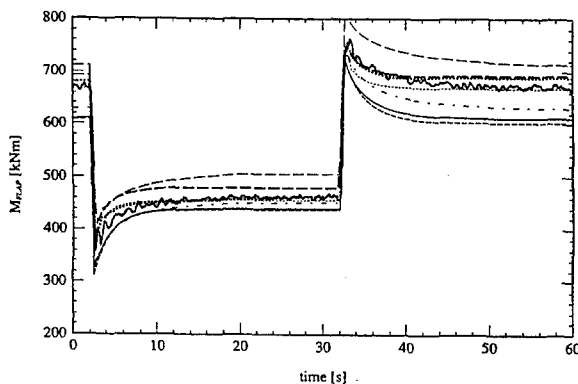


Fig.1: Measured and predicted flapping moments at blade root. Measured data: irregular full line.

What is shown here is the effect of pitching steps on several forces and moments measured on the Tjaereborg windturbine. During these transients, after an initial period the blade pitch angle is first increased at a fast rate of approx. $3.5^\circ/\text{s}$, next maintained constant for about 30 seconds and then decreased to its initial value at the same fast rate. The measurement period extends over a total of 60 seconds. Measured values for blade and shaft loads have been averaged over a number of realizations, and over the three blades in order to filter out stochastic wind influences and deterministic effects such as (average) windshear and tower shadow.

For the case discussed here the average windspeed was 8.7 m/s. The value of the calculated equilibrium induction factor $a = v_i/U$ may serve as an indication of the loading situation. This factor was $a = 0.34$ before the pitching steps were applied, whereas $a = 0.23$ was calculated after the first transient.

Fig.1 shows the flapping moments at the blade root. The irregular full line shows the measured values. It must be realized that the response shown by the experimental line includes flapping motions due to

flexibility of the blades. The bundle of other lines gives an impression of the levels found from the computational results.

Similar results are shown in fig.2 for the rotorshaft torque.

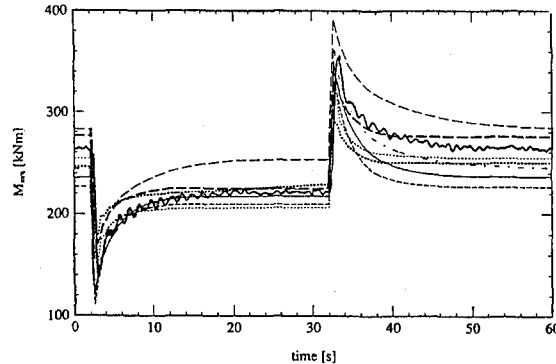


Fig.2. Measured and predicted rotorshaft torque. Measured data: irregular full line.

Both the measured and the calculated curves show that there is indeed a large overshoot of the forces and moments due to the dynamic inflow effect. The overshoot damps out in approximately 10 seconds which, as would be expected, corresponds very roughly to convection of the wake vorticity over a distance of between 1 and 2 diameters.

Closer examination of these and other results reveals the following:

- the equilibrium ranges (i.e. the difference between the equilibrium values) predicted with the differential equation models are consistently lower than those of the measurements, while those of the wake models compare very well with the measurements.
- In contrast to this, it appears that the dynamic ranges calculated by the engineering models (the differential equation models) are in good agreement with the measured values, whereas the dynamic ranges calculated with the free wake models are consistently lower.
- The differential equation models differed mainly in the value of the time constants chosen, and the variation of the time constants with radius. These differences do not really show up in the comparisons with the measured blade loads.

5.4. Discussion

5.4.1. One of the striking results is, that the differential equation methods show a relatively poor performance as far as the equilibrium predictions are concerned. This problem has no relation with the way in which the dynamic effects have been modeled. In fact, the straight-forward application of very classical blade element-momentum theory appears to be the weak point !

This observation is found in the literature more often (e.g. Viterna and Corrigan, ref.16). At present it is sometimes suspected that such problems might be of a rather more fundamental nature than just the incorrect "tuning" of for instance a tip-correction factor.

For instance, Van Kuik (ref.17) doubts the internal consistency of any disc-type model of the flow, when no attention is paid to the edges of the disc, where singularities might occur (similar to the "nose suction" of aerofoils or "edge suction" on wingtips).

Apart from this there may be other inconsistencies, inherent in the way these inflow models are coupled to blade-element theory. The momentum models as well as Pitt and Peters's theory try to predict the so-called "induced velocities" which, in combination with a blade-element consideration, will yield the forces on the blade. "Induced velocity" as used in this sense is a typical lifting-line concept. It is not a measurable physical quantity, but rather a theoretical concept, originating from Prandtl's classical lifting concepts for the straight wing in steady flow.

It is well known that lifting line theory as classically formulated breaks down in the case of swept wings and in unsteady flow, among other reasons due to singularities occurring along the lifting line if analyzed correctly. In rotating flow, where the streamlines relative to the blade are curved, no singularities occur, but nevertheless lifting line theory is neither strictly valid.

By Van Holten (ref.12, 18) the lifting line theory for swept wings and for unsteady flow was investigated in a more rigorous way, using a matched asymptotic expansion technique. It was found that in classical lifting line theory a term is neglected which is not important for the straight wing in steady flow, but which is essential in more complicated situations.

From the asymptotic theory it appears that the complete flow field in lifting line theory (the "composite field") should be considered as a sum of three contributions:

- 1) The "far field", corresponding to the contribution of the free trailing and shed vorticity in the wake.
- 2) The "near field", corresponding to the velocity field of a two-dimensional unsteady profile, including its wake of shed vorticity,
- 3) The "common field", to be subtracted from the far field, which cancels the singularities in unsteady flow, and at the same time prevents a double count of the shed vorticity near the wing.

The situation is schematically depicted in fig.3 for the unsteady case. "Induced velocity" in Prandtl's sense is the difference between 1) and 3).

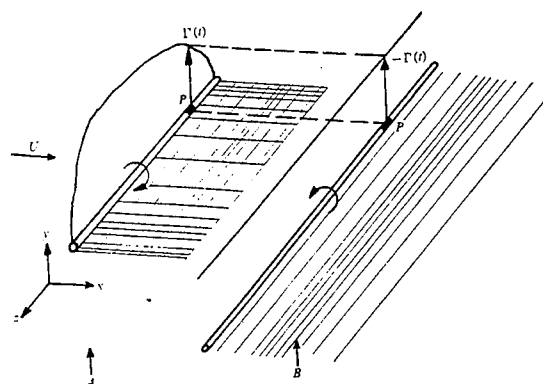


Fig.3: Definition of induced velocity at P; sum of contributions of vortex systems A and B.

In the case of a swept wing analogous effects, mathematically resembling the above unsteady effects, occur. Although not analyzed in ref.12 and 18, from the theory it is clear that a wing relative to which the streamlines are curved must in principle experience similar phenomena, making the classical lifting line concepts less valid.

From this brief summary it will be clear that in unsteady, yawed or circular flows the concept of "induced velocity" is more of a theoretical notion - though mathematically well defined - than a physical quantity that can be measured at some place in the field.

At present it is thought that the above considerations deserve more attention and caution when inflow models of rotors are used such as Pitt and Peters' or vortex-tube models and conceptually comparable ones. What is to be determined by such models (if the calculated velocity is consequently used in a blade-element method) is the "induced velocity" in the lifting line sense, and not a real, physical velocity.

Other models used during the above described dynamic inflow calculations do not suffer from these conceptual difficulties. The free-wake models using flow field descriptions in terms of either vortex lattices or vortex particles (refs.10 and 11) are both essentially based on lifting surface theory, where concepts like "induced velocity" (in Prandtl's sense) and "two-dimensional section characteristics" do not play a role, and do not even have a meaningful definition. The third free wake method (ref.13) using the acceleration potential for the field description is based on an unsteady lifting line theory where all the three earlier mentioned field components are correctly taken into account.

5.4.2. Also disappointing is the relatively poor performance of the elaborate free-wake methods, as far as the dynamic effects are concerned. This has led to an in-depth discussion about questions of stability, convergence and accuracy of these methods.

The free vortex wake models are based on an exact formulation of the inviscid flow equations. However, the numerical discretization procedure into either vortex lattices or vortex particles warrants special attention. An exception to this is the free-wake lifting line method based on acceleration potential theory, where no discretizations of this type are necessary.

Such a discretization artificially introduces singularities in the description of the flowfield. Nevertheless, in a case where the position of the singularities is fixed in space (linearized theory) or is prescribed beforehand as a function of time on the basis of experiments ("prescribed wake methods"), it can be shown that the correct inviscid limit is approached when the number of discrete vortex elements is increased indefinitely.

In the case of freely convecting vortex elements ("free wake") there may occur a computational stability problem due to the very irregular flow field associated with the discretized singularities. For this reason artificial desingularization (or: "regularization") is used in both the free-wake vortex methods by the introduction of a "cut-off" length: close to the singular points a regular flow field is substituted in place of the almost singular flow field near the discrete singularities. In principle there is no guarantee that the convergence characteristics are still maintained under these circumstances.

A simple test case has been used to obtain some insight in this question. The test case consisted of a two-dimensional strip on which vorticity is continuously distributed in such a way that the self-induction is constant along the strip. Although the test case is mathematically very simple and possesses an exact solution in closed form, in some respects it is very demanding for the numerical solution methods. What is in fact tested is, how accurately a numerical calculation will predict the free convection of vorticity in the edge region of the vortex sheets.

It was concluded that a free wake analysis will be stable as well as convergent if care is taken that, when the grid size and time steps are decreased, at the same time the cut-off lengths are reduced such that a specific ratio between all these quantities is maintained.

The finally remaining question is then, how accurate the numerical free wake analyses are in the case of a practical choice of grid size and time step. This proves to be the weak point. The problem is not of a fundamental nature, but is associated with the speed and capacity of the presently available computers. In conclusion it can be said that in those flow regions where the deformations of the free vortex sheets are large the grid size would probably have to be made much smaller than is practically feasible at present.

6. VELOCITIES AND FORCES IN YAWED FLOW

6.1. Theoretical models and experiments

For wind turbines yawed operation may strongly affect load spectra of the blades and shaft. The same Joule-program as described above on dynamic inflow also covered an investigation of load prediction methods associated with yawed flow situations.

Again measurements were performed using the Tjaereborg windturbine (60 meter, 2 MW). Additional measurements were performed on windtunnel models, at Delft University of Technology, Institute for Windenergy.

The more elaborate free-wake vortex models were the same as used during the "dynamic inflow" research. These free-wake models do not require any essential changes in order to analyse yawed flow.

Simpler engineering models were essentially implementations of the "Pitt and Peters" method (ref.8). The Pitt & Peters model is a description in terms of first and higher harmonics of the relation between dynamic disc loads and inflow, based on an expansion solution of the (yawed) flow across an actuator disc.

6.2. Results

A comparison between measurements and the prediction by "Pitt and Peter" type models is shown in fig.4. The figure shows the contribution of the blade bending moments to the restoring yaw moment of the Tjaereborg turbine at 32° and -51° yaw angle respectively. The comparison shows fair agreement, but certainly not very good. Although not shown in the same figure, the results of the free wake calculations show the same general behaviour.

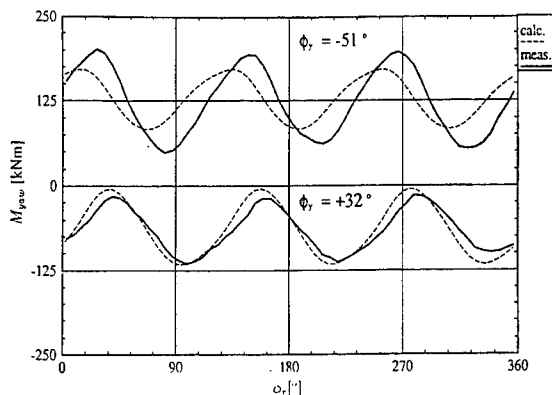


Fig.4: Contribution of blade bending moments to restoring yaw moment at 32° and -51° yaw angle. Comparison of measurements and calculations. Definition azimuth angle: see fig.5.

Windtunnel experiments (ref.19) made it possible to do measurements of the inflow itself, at different positions directly behind the rotor plane. Information at this level is very important to improve the modeling. Some data of the tunnel, the model and the measurement setup are shown in fig.5.

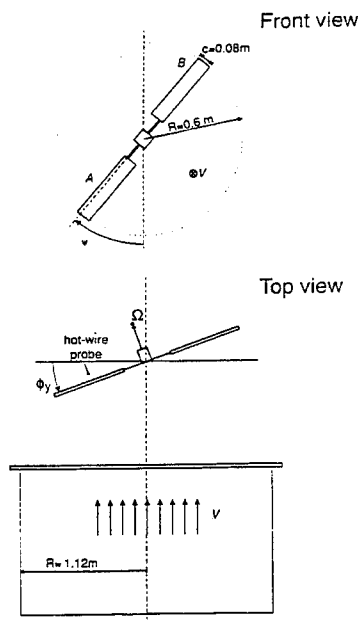


Fig. 5: Windtunnel setup and notations.

Fig. 6 shows the measured axial velocity at a number of radial stations, as functions of the azimuth, for a yaw angle of 30° . The measurements have been averaged over one revolution of the rotor. Apart from the tip sections (90% and 95% radial position) the induced velocity appears to have a maximum in the "upstream" region of the disc, contrary to theoretical predictions!

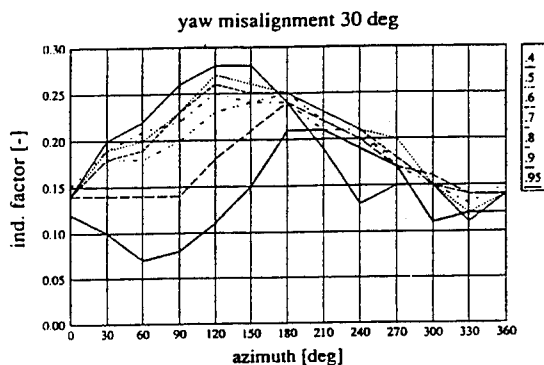


Fig. 6: Measured axial induction distribution, wind tunnel.

6.3. Discussion of the discrepancies between theoretical and experimental results.

A number of intriguing questions thus remain for further research. Several hypotheses have been put forward to explain the qualitative disagreement between the windtunnel measurements and calculations of the field of inflow, so far in vain however. Nevertheless, the search for an explanation has been very fruitful, because it was instrumental to uncover several effects that appear to have been overlooked often in the literature on rotor flow calculations.

1) The hot wires used for the flow measurements were placed in a vertical position, so that the resulting velocity in a horizontal plane was measured. Simple skewed vortex tube models show that in-plane induction velocities will occur, apart from the perpendicular induction velocity which is being sought primarily. These additional in-plane velocities are often neglected in blade-element analyses, although they will definitely influence the advancing-retreating blade effect. An order of magnitude estimate showed however, that the influence of the in-plane induction on the hot-wire measurements cannot explain the noted discrepancy between windtunnel and prediction.

2) The situation of a wind turbine rotor is, as already stated in the introduction, somewhat different from a helicopter rotor. In the case of the mentioned windtunnel tests, there was no flapping motion of the blades so that the "rolling" and "pitching" moments of the rotor were much larger than usual for a rotor with flapping freedom. Also, the shed vorticity associated with the advancing-retreating blade effects will be much stronger. Especially the latter phenomenon is not considered in the Pitt/Peters model. At present a further investigation of these effects by comparison with detailed free-wake calculations is being done.

7. THREE-DIMENSIONAL SECTION CHARACTERISTICS, AS INFLUENCED BY BLADE ROTATION

7.1. Background of research into stall characteristics

It is well known that the influence of rotation on the profile characteristics of rotorblades may be appreciable, especially near stall. In particular the inboard parts of a rotating blade may show a much larger $C_{l,max}$ than would be expected on the basis of two-dimensional section characteristics. In the case of wind turbines the phenomenon is very important for the prediction of performance and loads, because blade loadings are generally high. Operational conditions often occur where the inboard part of the blades is on the verge of stalling or is indeed stalled, for instance when stall-regulated rotors are employed.

It was recently pointed out by Corrigan (ref. 20) that stall delay due to rotation is also important for the performance and load prediction of highly loaded lifting rotors such as used in tiltrotors and highly maneuverable helicopters.

A theoretical and experimental investigation of the phenomenon was done in the Netherlands, by ECN, NLR and TUD under a contract by NOVEM.

7.2. A boundary layer theory for rotating blades

The essential core of the research was a new formulation by Snel (ref. 21) of the boundary layer equations on a high aspect ratio rotating surface similar to a rotorblade (for notations, see fig. 7). An order of magnitude analysis of the terms occurring in the boundary layer equations

leads to the conclusion that in attached flow the usual two-dimensional boundary layer equations are recovered, exact up to terms of the order $O(c/r)$:

$$\frac{\partial u}{\partial s} + \frac{\partial w}{\partial z} = 0 + O(c/r)^2 \quad (\text{continuity equ.})$$

$$u \frac{\partial u}{\partial s} + w \frac{\partial u}{\partial z} = -\frac{1}{\rho} \frac{\partial p}{\partial s} + \frac{1}{\rho} \frac{\partial \tau_1}{\partial z} + O(c/r)^2 \quad (\text{chordwise momentum})$$

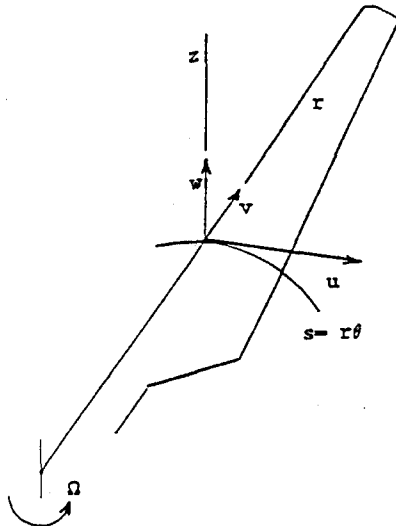


Fig.7: Rotating boundary layer analysis, notations.

If desired, one can also set up a spanwise momentum equation for the velocity component v in radial direction. One can see from the equations above however that to first order the chordwise flow is not coupled with the radial flow component v , and the situation is essentially two-dimensional.

Furthermore, it appears that all the terms in the spanwise momentum equation are of order $O(c/r)$ or smaller compared with the chordwise momentum equation. Hence, the boundary layer effects associated with the radial flow are weak.

In the case of separated flow, the situation is different, however. Now the fluid is essentially transported with the blade. Physically one may reason that the chordwise pressure gradient is small compared to its value in attached flow. Under these assumptions an order of magnitude consideration leads to the conclusion that, neglecting terms of $O(c/r)^{2/3}$, the relevant boundary layer equations become as follows:

$$\frac{\partial u}{\partial s} + \frac{\partial w}{\partial z} = 0 \quad (\text{continuity equ.})$$

$$u \frac{\partial u}{\partial s} + w \frac{\partial u}{\partial z} = -\frac{1}{\rho} \frac{\partial p}{\partial s} + \frac{1}{\rho} \frac{\partial \tau_1}{\partial z} + 2 \Omega v \quad (\text{chordwise momentum})$$

$$u \frac{\partial v}{\partial s} + w \frac{\partial v}{\partial z} = -\frac{1}{\rho} \frac{\partial p}{\partial r} + \frac{1}{\rho} \frac{\partial \tau_2}{\partial z} + \frac{(u - \Omega r)^2}{r} \quad (\text{spanwise momentum})$$

We see that in the chordwise momentum equation a Coriolis force has appeared, which couples this equation with the radial flow. Furthermore, it appears that the radial flow terms are no longer smaller in magnitude than the terms in the chordwise momentum equation, and may therefore no longer be neglected. The radial flow is clearly driven by centrifugal forces in the case that $u \ll \Omega r$, and by the radial pressure gradient.

In the equations as they are shown, a few terms have been kept which are of a smaller order than in fact would be relevant in the present order of approximation. Strictly speaking, in separated flow the centrifugal term in the spanwise equation might be approximated by $\Omega^2 r^2$. The advantage of the above given formulation is, that it covers both attached flow as well as separated flow, and gives a smooth transition in between.

Looking at the resulting expressions, the physical explanation of the differences between 2D stall and 3D separation on rotating blades can now be understood as follows. Significant radial flow can only develop in regions of strongly retarded flow (with respect to the blade) such as separation regions. Flow towards the tip develops at the suction side of the blade and results in a Coriolis force in the main flow direction, which acts as a favourable pressure gradient. This decreases the displacement thickness of the separated boundary layer, leading to less decambering and higher lift coefficients.

Apart from the physical insight provided by the above given equations, there is also a mathematical advantage in this formulation. In all the equations the advection operator (i.e. the non-linear left hand sides of the momentum equations) remains two-dimensional. The system of equations can be simultaneously solved in a way which is similar to the usual two-dimensional boundary layer calculations, along chordwise strips. In the boundary layer equations, the chordwise momentum equation is coupled with the spanwise equation through the Coriolis acceleration. In the computational procedure, this coupling term can be handled in a way analogous to the term expressing the chordwise pressure gradient.

The above boundary layer equations were implemented in a 2D viscous-inviscid strong interaction code, meaning that the chordwise pressure gradient is derived from the inviscid outer flow, while taking into account that the outer flow is strongly influenced by the development of the boundary layer. The code in question was the ULTRAN-V code, developed at NLR for the prediction of unsteady viscous transonic

flow about oscillating aerofoils (refs.22 and 23).

7.3. Experimental verification and results
Computational results were compared with experimental data, derived from ref.24. A few results are depicted in fig.8 and 9.

computations were performed for an 18 % thickness section, at an assumed Reynolds number of $Re = 0.5 \cdot 10^6$ and natural transition with a downstream limit of 50 % chord.

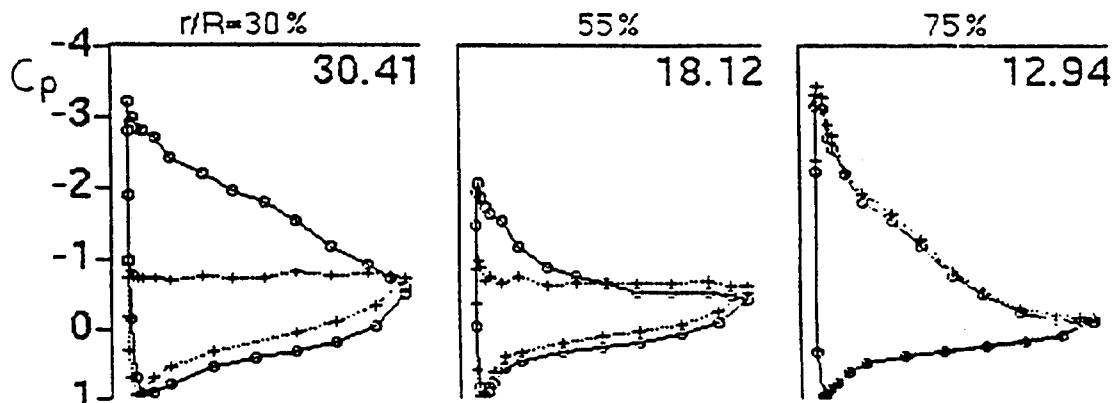


Fig.8: Experimental pressure distributions for the rotating blade (circle) and the non-rotating blade (cross).

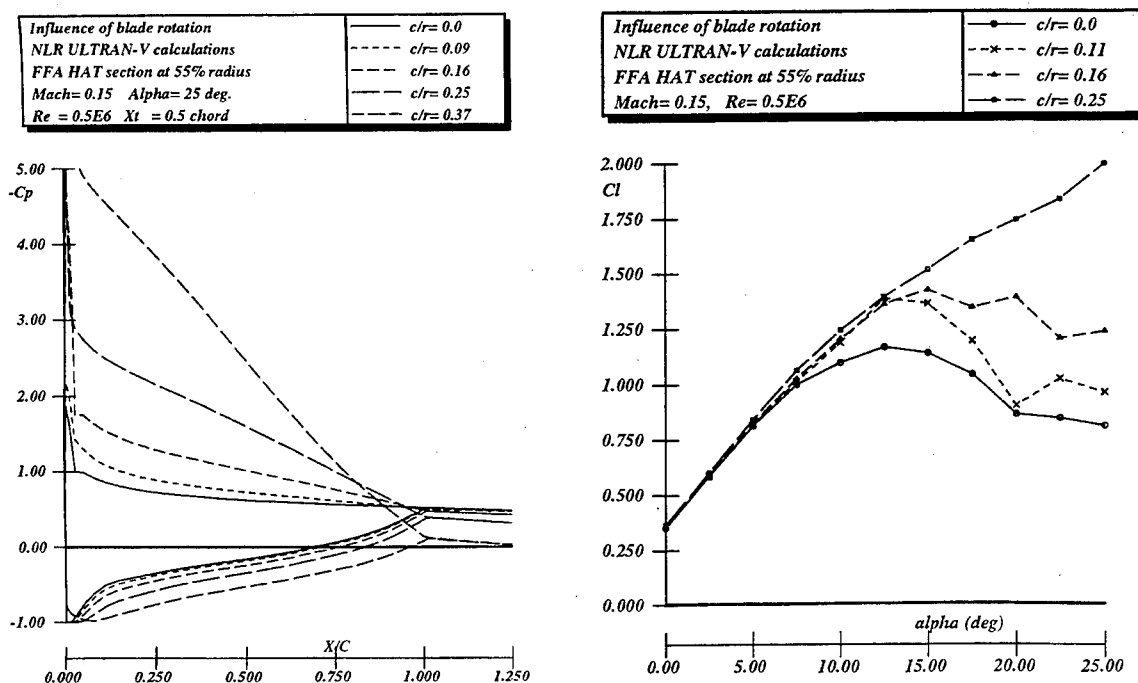


Fig.9: Calculated pressure distributions for rotating blade, geometry of fig.8.

Fig.8 shows measured pressure distributions at several radii of a wind turbine blade, for the rotating as well as the non-rotating case. The measurements were performed in the 12 * 16 m windtunnel of the China Aerodynamic Research and Development Centre (CARD), using a blade of approx. 2 m length (ref.24). Especially at small values of c/r it is very clear that separation may be suppressed almost completely by the 3-D rotational effects. Calculated results of the effect of rotation are shown in fig.9. The

It appears that the agreement is qualitatively good. Quantitatively however, there is a discrepancy, because in the computation a smaller value of c/r had to be taken in order to reproduce the measured pressure distributions.

In future it is, among other possible refinements, intended to better represent the three-dimensional environment. For the determination of the radial pressure gradient, it was until now assumed that the spanwise pressure gradient is proportional

to $\Omega^2 r^2$. This assumption is certainly unjustified near the root and near the tip, where rapid changes in the bound circulation will occur.

Another possible improvement will be, to make a formal asymptotic expansion of the boundary layer equations in terms of c/r , and include the next higher order terms.

For the time being, the results of the investigations were synthesized into a simple engineering formula. For this purpose several calculations were made with the ULTRAN-V code for a test rotor built and tested by the Delft University of Technology equipped with a NLF(1)-0416 aerofoil, as described in ref.25. The computations were made for a Reynolds number of one million at a "corrected" spanwise position to account for the earlier mentioned discrepancies between test and theory. In the resulting formula, similar to engineering formulae for unsteady aerodynamics or dynamic stall, a correction is expressed in terms of the difference between the 2D measured liftcoefficient and the inviscid lift coefficient, by multiplying this difference with a factor and adding to the 2D value:

$$C_{l,3D} = C_{l,2D} + f \cdot (C_{l,inv} - C_{l,2D})$$

The multiplication factor f is for the time being only a function of c/r :

$$f = \tanh(3 \cdot (c/r)^2)$$

Typical results obtained by this engineering formula are shown in fig.10.

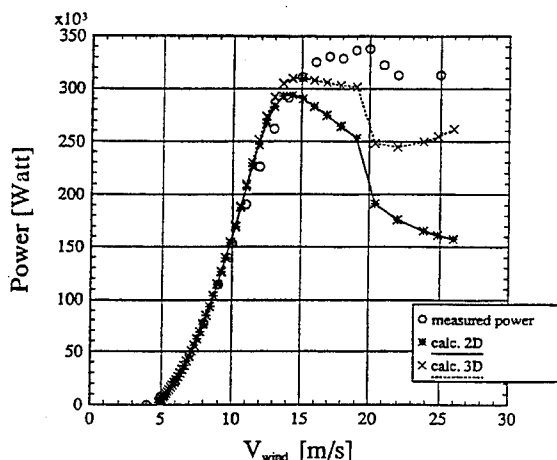


Fig.10: Calculated and measured power curves Nordtank 350 kW wind turbine.

8. CONCLUSIONS

A review has been given of recent research on the aerodynamics of wind turbine rotors. The following subjects were covered in extenso:

- The induced velocity field of rotors, including dynamic inflow and yawed flow effects.

- Stall delay on rotating blades. A new boundary layer formulation was outlined applicable to this phenomenon.

Without any further discussion, also some references have been given concerning recent wind turbine research on:

- simulation methods of atmospheric turbulence,
- dynamic stall effects, comparisons between theory and experiments,
- Effect of several types of blade tips on radiated noise.

As far as dynamic and yawed inflow is concerned, it is concluded that qualitative understanding is reasonable. "Engineering models" as well as very sophisticated computer methods are now available, and the prediction tools have been subjected to a fair amount of experimental validation. The models are in general capable of providing useful engineering estimates.

At the same time, the comparison with experiments has revealed that there are also a few fundamental problems to be solved yet:

- Even the most classical blade-element analyses are not always reliable, perhaps due to more basic, conceptual problems. These problems might be related to the way in which blade element considerations are usually combined with inflow models like momentum theory, "Pitt & Peters", or "vortex tube" models.

- The hope that sophisticated computer methods for free-wake analyses already have improved this situation is not yet fulfilled.

Thanks to recent theoretical work on rotating boundary layers, a good qualitative understanding now exists of stall delay. For reliable calculations to be made, higher order terms will probably have to be added.

9. REFERENCES

- 1) D.Winkelaar: SWIFT program for three-dimensional wind simulation, ECN-R-92-013, 1992
- 2) P.S.Veers: Three-dimensional wind simulation. Tech. Rep. SAND 88-0152, Sandia National Laboratories, Albuquerque, 1988.
- 3) F.Rasmussen, J.T.Petersen, D.Winkelaar, R.Rawlinson-Smith: Response of stall Regulated Wind Turbines - Stall induced vibrations, Risø National Lab., report R-691(EN), 1993.
- 4) J.Jakobsen, B. Andersen: Aerodynamical noise from wind turbine generators, experiments with modification of full scale rotors, Danish Acoustical Institute, report EFP 1363/89-5
- 5) N.J.C.M. van der Borg, P.W.Vink: Tip noise measurements on the Uniwex wind turbine, ECN-C-94-002, 1994.
- 6) C.T.Tran, D.Petot: Semi-empirical model for the dynamic stall of airfoils in view of the application to the calculation of responses of a helicopter blade in forward flight. Vertica 5, 1981.

- 7) R.T.N. Chen: A survey of nonuniform inflow models for rotorcraft flight dynamics and control applications, paper no.64, 15th European Rotorcraft Forum, Amsterdam 1989.
- 8) G.H.Gaonkar and D.A.Peters: Review of dynamic inflow modeling for rotorcraft flight mechanics, Vertica, vol.12, no.3, pp.213-242. 1988
- 9) D.M.Pitt, D.A.Peters: Theoretical prediction of dynamic inflow derivatives, Vertica, vol.5, no.1, pp. 21-34, 1983.
- 10) A.Zervos, S.Huberson, A.Hermon: Three-dimensional free wake calculation of wind turbine wakes, J. Wind Eng. and Ind. Aerod., vol.27, 1988, pp.65-76.
- 11) Ch.Schöttl and S.Wagner: Aerodynamic model for application within aeroelastic simulation programs. Presented at CEC-conf. New Energies 1988, Saarbrücken 1988.
- 12) Th. van Holten: On the validity of lifting line concepts in rotor analysis, Vertica, vol.1, pp.239-254, 1977.
- 13) G.J.W. van Bussel: PREDICAT, First order performance calculations of windturbine rotors using the method of the acceleration potential, Techn.Univ.Delft, Inst.for Windenergy, report IW-93069R, 1993.
- 14) H.Snel, J.G.Schepers: Engineering models for dynamic inflow phenomena, Journal of Wind Eng. and Industr. Aerodyn., 39 (1992), pp.267-281
- 15) L.B.Tuckerman: Inertia factors of ellipoids for use in airship design, NACA Report 210, 1925.
- 16) L.A.Viterna, R.D.Corrigan: Fixed pitch rotor performance of large horzional axis windturbines, paper presented at the DOE/NASA Workshop on large horizontal axis windturbines, July 1981.
- 17) G.A.M. van Kuik: Experimental verification of an improved actuator disc concept, paper no.18, 15th European Rotorcraft Forum, Amsterdam 1989.
- 18) Th. van Holten: Some notes on lifting line theory, J. Fluid Mech., vol.77, part 2, pp.561-579, 1976.
- 19) L.J.Vermeer: Contribution of windtunnel Experiments to the EC-Joule project "dynamic inflow", Part I: Rotor in Yaw, Delft Univ. of Technol., Inst.for Windenergy report IW-92060R, 1994.
- 20) J.J.Corrigan: Empirical model for stall delay due to rotation, paper presented at Am. Hel. Soc. Aeromechanics Specialists Conf., San Francisco, jan. 1994.
- 21) H.Snel, R.Houwink, J.Bosschers: Sectional prediction of lift coefficients on rotating wind turbine blades in stall, ECN-C-93-052, 1993.
- 22) R.Houwink, A.E.P.Veldman: steady and unsteady separated flow computations for transonic airfoils, AIAA paper 84-1618, 1984.
- 23) R.Houwink: Computation of unsteady turbulent boundary layer effects on unsteady flow about airfoils, NLR TP 89003 L, 1989
- 24) G.Ronsten: Static pressure measurements on a rotating and a non-rotating 2.375 m wind turbine blade. Comparison with 2D calculations. Paper presented at the European Wind Energy Conf. Amsterdam, 1991.
- 25) A.Bruining: Pressure measurements on a rotating wind turbine blade on the open air rotor research facility of the Delft Univ. of Technology, Proc. 1993 ECWEC Conf., Travemünde, march 1993.

Dynamic Stall Simulation Applied to Vertical-Axis Wind Turbines

K. F. Tchon

Arrow Research, 6111 Ave. du Boise, Suite 4J
Montreal (Quebec) H3S 2V8, Canada

S. Hallé and I. Paraschivoiu

J.A. Bombardier Aeronautical Chair Group, Ecole Polytechnique de Montreal
C.P. 6079, Succursale Centre-Ville, Montreal (Quebec) H3C 3A7, Canada

1. SUMMARY

The dynamic stall on a NACA 0015 airfoil performing a rotation motion characteristic of Darrieus vertical-axis wind turbines is simulated using laminar and turbulent Navier-Stokes solvers. The numerical results are compared with experimental data and show the importance of an adequate turbulence model to realistically simulate such a phenomenon. The differences between a Darrieus rotation motion and a pure pitching motion are also discussed.

2. INTRODUCTION

Environmental concerns combined with advanced technology have made wind turbines a viable commercial option for large-scale power production. Those modern turbines either use a horizontal-axis of rotation, like the traditional farm wind pump, or a vertical-axis, like the curved-blade Darrieus wind turbine (Fig. 1). Although horizontal-axis turbines are the most common presently, the vertical-axis design offers an advantageous alternative due to its independence from wind direction and its mechanical simplicity. However, this simplicity does not extend to the rotor aerodynamics and its blades can operate in a dynamic stall regime. The dynamic stall term refers here to the stalling behavior of an airfoil when its angle of attack is changing rapidly with time. This

unsteady phenomenon is characterized by dynamic delay of stall to angles significantly beyond the static stall angle and by massive recirculating regions moving downstream over the airfoil surface, leading to lift overshoot, force and moment hysteresis as well as loss of aerodynamic damping as described by McCroskey (Ref. 1). It is encountered in the Darrieus wind turbine context when the maximum operational speed is approached and that all the blade sections exceed the static stall angle. The whole blade operates then under dynamic stall conditions causing structural fatigue, and even stall flutter leading to catastrophic failure. This phenomenon can thus become the primary limiting factor of such a turbine and must be accounted for to accurately predict aerodynamic performances and provide aerodynamic loading information to structural dynamic codes.

An adequate numerical model cannot consider the flow evolution as a succession of steady states, as in classical quasi-steady methods, and must be able to capture the unsteady aerodynamics of a vertical-axis rotor blade, and more particularly the dynamic stall phenomenon. Semi-empirical models developed for helicopter aerodynamics, such as the Gormont, MIT, and indicial models, can

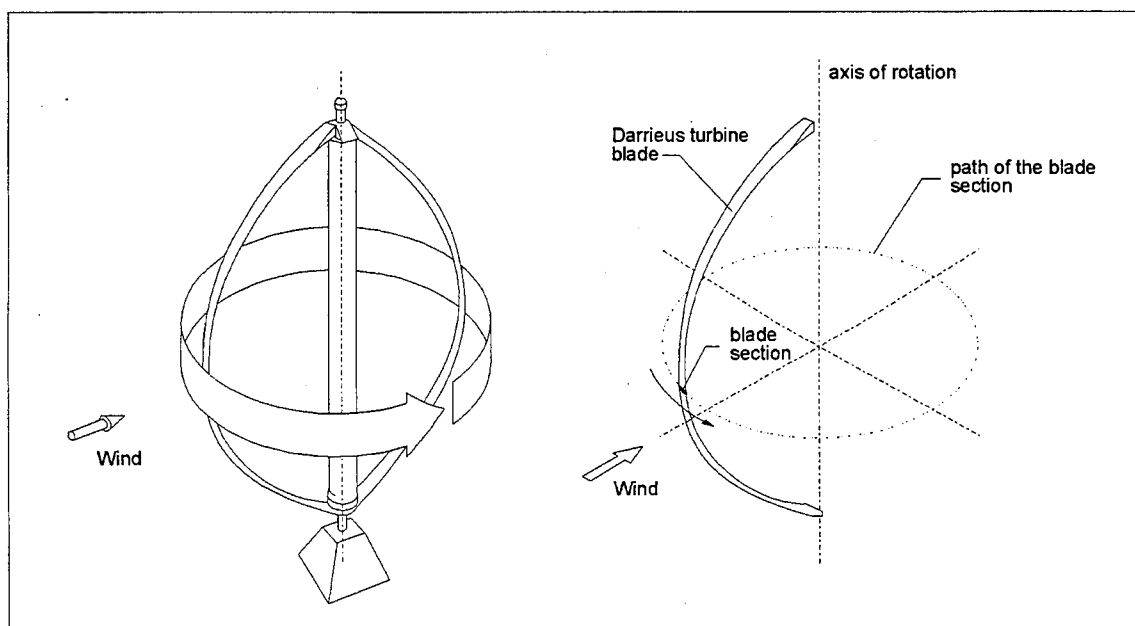


Fig. 1 Darrieus type vertical-axis wind turbine.

significantly improve the prediction of global aerodynamic loads in dynamic stall conditions. Although their application range is essentially limited to the type of airfoil and motion used in the experiments from which they were derived, these models were successively modified to predict the aerodynamic performances of a Darrieus wind turbine (Ref. 2). However, these models cannot predict local aerodynamics such as the pressure distribution and help us understand the physics of the dynamic stall phenomenon. For such tasks, the computational fluid dynamics (CFD) approach is growing more and more popular with the increasing power of computers. Several Navier-Stokes solvers have been used to simulate dynamic stall, but most of the studies were concerned with helicopter retreating-blade stall or agile fighter aircraft and have thus considered pitching airfoils (Refs. 3 to 7, among others). However, the physics of the flow around a wind turbine blade is significantly different and should also be investigated.

That is why a research project was initiated at Ecole Polytechnique de Montreal to develop a Navier-Stokes solver able to simulate the flow around an airfoil in Darrieus motion, i.e., the combined translation and rotation motion corresponding to the path of a Darrieus rotor blade cross section as shown in Fig. 1. The present paper describes the numerical simulation of the dynamic stall on a NACA 0015 airfoil in Darrieus motion using both laminar and turbulent solvers.

3. SIMULATION METHODS

The governing equations of the laminar and turbulent solvers, along with a brief description of the corresponding algorithms, are presented in this section.

3.1 Laminar solver

The laminar simulation was performed by a finite element solver developed by the J.A. Bombardier Aeronautical Chair Group at Ecole Polytechnique de Montreal (Ref. 8). This solver is based on the two-dimensional incompressible Navier-Stokes equations expressed in a stream function-vorticity formulation and a non-inertial frame of reference rotating with the airfoil. This formulation is composed of the stream function compatibility equation

$$\nabla^2 \psi + \omega = 0 \quad (1)$$

and the vorticity transport equation

$$\frac{\partial \omega}{\partial t} + \nabla \cdot (\omega \mathbf{u} - \nu \nabla \omega) = 0 \quad (2)$$

where t is the time, ν is the kinematic viscosity and \mathbf{u} is the flow velocity vector. The perturbation stream function ψ and vorticity ω are defined respectively by

$$-\mathbf{k} \times \nabla \psi \equiv \mathbf{u} - \mathbf{u}_\infty + \Omega \mathbf{k} \times \mathbf{x} \quad (3)$$

$$\omega \equiv \mathbf{k} \cdot \nabla \times \mathbf{u} + 2\Omega \quad (4)$$

where \mathbf{k} is the unit vector orthogonal to the plane, \mathbf{x} is the position vector, \mathbf{u}_∞ is the free stream velocity vector and Ω is the angular rotation speed of the non-inertial frame of reference. Initially, the vorticity has to be imposed and the stream function is determined by the compatibility equation. On solid walls, both Dirichlet and Neumann conditions, corresponding to the no-slip requirement, are imposed on the stream function

$$\psi = \psi_b - \mathbf{k} \times \mathbf{u}_\infty \cdot \mathbf{x} - \frac{1}{2} \Omega x^2 \quad (5)$$

$$\nabla \psi \cdot \mathbf{n} = (\Omega \mathbf{k} \times \mathbf{x} - \mathbf{u}_\infty) \cdot \mathbf{s} \quad (6)$$

where ψ_b is a constant while \mathbf{s} and \mathbf{n} are respectively the unit vectors tangent and normal to the wall. The compatibility equation and the vorticity transport equation are solved simultaneously in order to use the redundant information on the stream function to determine the vorticity on solid walls (Refs. 9 and 10). For multiply connected domains, an additional condition has to be imposed on each internal boundary to determine the constant ψ_b

$$\oint (\omega \mathbf{u} - \nu \nabla \omega) \cdot \mathbf{n} dC = 2A_b \frac{d\Omega}{dt} \quad (7)$$

where A_b is the area enclosed by the internal boundary. This condition is deduced by integrating the momentum equation along the internal boundary and by requiring that the pressure be a single-valued function (Ref. 10). In order to avoid second order derivatives of the stream function and simplify boundary conditions for the pressure equation, the field pressure is computed using a modified pressure, which can be related to the total pressure head (Ref. 8).

Spatial discretization is achieved by the streamline upwind Petrov-Galerkin finite element method (Ref. 11). To have a better control over the node distribution, the mesh is composed of a structured region of quadrilateral elements only in the vicinity of solid boundaries and an unstructured region of triangular elements everywhere else. A layer of infinite elements surrounds the domain to project the external boundary to infinity (Ref. 12) and simple Dirichlet conditions, i.e., $\psi = \omega = 0$, are imposed on this boundary. Temporal discretization is achieved by second order accurate finite differences in conjunction with an implicit iterative scheme. The resulting discrete system is non-linear and is solved iteratively for each time step using a Newton method. The linearized Newton systems are solved by the GMRES minimum residual method (Ref. 13) with an incomplete triangular factorization preconditioning. The resulting solver has been validated on rotating cylinders. Full details of the algorithm and its validation are given in Ref. 8.

3.2 Turbulent solver

The J.A. Bombardier Aeronautical Chair Group is presently working on the implementation of turbulence modeling in the stream function-vorticity solver. For the present paper, however, a new finite volume solver developed independently by the first author (Refs. 14 and 15) was used for the turbulent simulation. This solver is based on the two-dimensional time-dependent compressible Navier-Stokes equations expressed in a conservative form on arbitrary moving grids. These equations can be written in the following non-dimensional form

$$\frac{\partial \mathbf{Q}}{\partial t} + \nabla \cdot (\mathbf{F} - \mathbf{G}) = 0 \quad (8)$$

where \mathbf{Q} is the conservative state vector, while \mathbf{F} and \mathbf{G} are the convective and diffusive flux tensors respectively

$$\mathbf{Q} = \begin{bmatrix} \rho \\ \rho \mathbf{u} \\ \rho E \end{bmatrix}, \quad \mathbf{F} = \begin{bmatrix} \rho(\mathbf{u} - \mathbf{v}) \\ \rho \mathbf{u}(\mathbf{u} - \mathbf{v}) + p\mathbf{i} \\ \rho E(\mathbf{u} - \mathbf{v}) + p\mathbf{u} \end{bmatrix}, \quad \mathbf{G} = \begin{bmatrix} 0 \\ \tau \\ \mathbf{u} \cdot \tau - \theta \end{bmatrix} \quad (9)$$

where \mathbf{i} is the unit tensor, \mathbf{u} is the flow velocity vector, \mathbf{v} is the grid velocity vector, ρ is the density and E is the total energy. The pressure p is given by the equation of state for a perfect gas

$$p = (\gamma - 1)\rho \left[E - \frac{1}{2} \mathbf{u}^2 \right] = (\gamma - 1)\rho T \quad (10)$$

where T is the temperature. The shear stress tensor τ and the heat conduction vector θ are given by

$$\tau = (\mu + \mu_t) \left[\nabla \mathbf{u} + (\nabla \mathbf{u})^T - \frac{2}{3} \mathbf{i} \nabla \cdot \mathbf{u} \right] \quad (11)$$

$$\theta = -\gamma \left(\frac{\mu}{Pr} + \frac{\mu_t}{Pr_t} \right) \nabla T \quad (12)$$

where γ is the ratio of specific heats taken as 1.4 while Pr and Pr_t are the laminar and turbulent Prandtl numbers and are set to 0.72 and 0.9 respectively. The molecular or laminar viscosity μ is determined through Sutherland's law while the turbulent viscosity μ_t is determined using the k - w model of Wilcox (Ref. 16). This model was chosen because it seems to give better results for adverse pressure gradient flows than other two-equation turbulence models. This model is also mathematically simpler and computationally more robust because its local formulation does not require damping functions to integrate the transport equations through the viscous sublayer. Initially, the flow is considered uniform and isentropic. On solid walls, no-slip conditions, $\mathbf{u} - \mathbf{v} = 0$, and adiabatic conditions, $\nabla T \cdot \mathbf{n} = \nabla p \cdot \mathbf{n} = 0$, are imposed. At the exterior boundary, non-reflective conditions are constructed from local one-dimensional Riemann invariants as described by Jameson and Baker (Ref. 17).

Spatial discretization is performed by an upwind cell-centered finite volume scheme on the same type of hybrid mesh as the stream function-vorticity solver. Quadrilateral cells are used wherever steep one-dimensional gradients are expected, such as in boundary layers, because they are better suited for high stretching ratios. Elsewhere, triangular cells are used to efficiently control the mesh density, particularly on complex geometries. The upwind scheme is an extension to moving grids of Roe's method that intrinsically satisfies the geometric conservation laws (Ref. 18). Temporal discretization is performed by backward Euler differencing and the solution is advanced in time using an explicit scheme. The major disadvantage of such a scheme is that the maximum allowable time step is limited by a CFL-like stability condition. For each cell, the maximum allowable local time step Δt^{CFL} is computed by taking into account the characteristic wave propagation speed as well as the characteristic diffusion speed. The maximum allowable global time step is then taken as the minimum value of the local time steps Δt_{min}^{CFL} . It is thus controlled by the smallest cells of the computational mesh and can become excessively small for high Reynolds flows that require severe node clustering near solid walls. One way to alleviate this problem is to march the solution in each cell at the maximum allowable local time step. However, this procedure is not time accurate and is only used to accelerate the convergence to a steady state. To simulate an intrinsically unsteady phenomenon such as dynamic stall, a time accurate local stepping has to be used. In the present solver, we use such a procedure recently introduced by Kleb et al. (Ref. 19) and called temporal adaptation because of its similarity to spatial adaptation by grid embedding. In this procedure, each cell is assigned a local time step equal to the closest power-of-two

multiple of Δt_{min}^{CFL} . The cells are then marched at their own local time steps, but they all, ultimately, reach the same time level at given intervals. The temporal accuracy is maintained by interpolating the necessary intermediate states for connected cells marching at different time steps.

The resulting solver was implemented using object-oriented concepts and the C++ programming language. Object-orientation facilitates the implementation of complex algorithms by introducing a degree of self-awareness to the elementary programming modules. For the present solver, these modules, called objects, are the nodes, the faces and the volumes of the computational mesh. Full details of the algorithm and its validation are given by Tchon in Refs. 14 and 15.

4. RESULTS AND DISCUSSION

In the present paper, the laminar and turbulent solvers are used to numerically simulate the flow around a NACA 0015 airfoil in Darrieus motion (Fig. 2). The parameters of the experimental study of Oler et al. (Ref. 20) were used, i.e., a tip speed ratio $\lambda = \Omega R / u_\infty$ of 2.5 and a chord to radius of rotation ratio c/R of 0.25. The experimental blade Reynolds number $Re_b = \rho_\infty \Omega R c / \mu_\infty$ of 67000 was used for the turbulent computations but a reduced value of 6700 was used for the laminar computations. To have a better understanding of such a motion, it is interesting to consider an equivalent pitching motion characterized by an effective flow velocity vector that is the resultant of the blade velocity vector and the wind velocity vector (Fig. 2)

$$\mathbf{u}_e = \mathbf{u}_\infty - \Omega \mathbf{k} \times \mathbf{R} \quad (13)$$

Fig. 3 presents the evolution of the effective flow velocity modulus u_e and angle of attack α_e in function of the azimuth θ , as well as the evolution of the corresponding effective Reynolds number $Re_e = \rho_\infty u_e c / \mu_\infty$ seen by the airfoil. As shown on this figure, the airfoil spends a substantial fraction of the period at an effective angle of attack much superior to the static stall angle and is thus undergoing deep dynamic stall. Note also that the effective Reynolds number has a maximum value of 93800 when the blade Reynolds number is set to 67000. Such a Reynolds number, combined with the rapid motion of the airfoil, leads to non-negligible turbulence, particularly in the wake, and justifies the use of a turbulent solver.

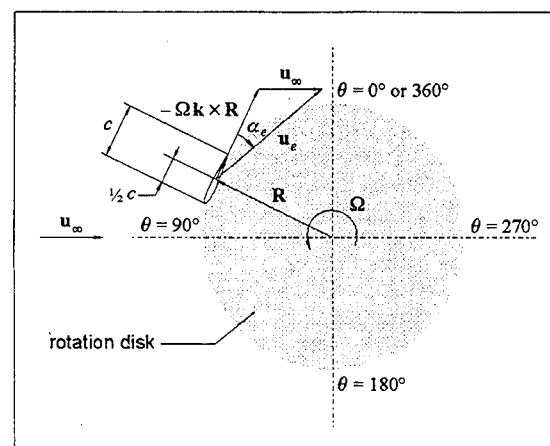


Fig. 2 Darrieus rotation motion.

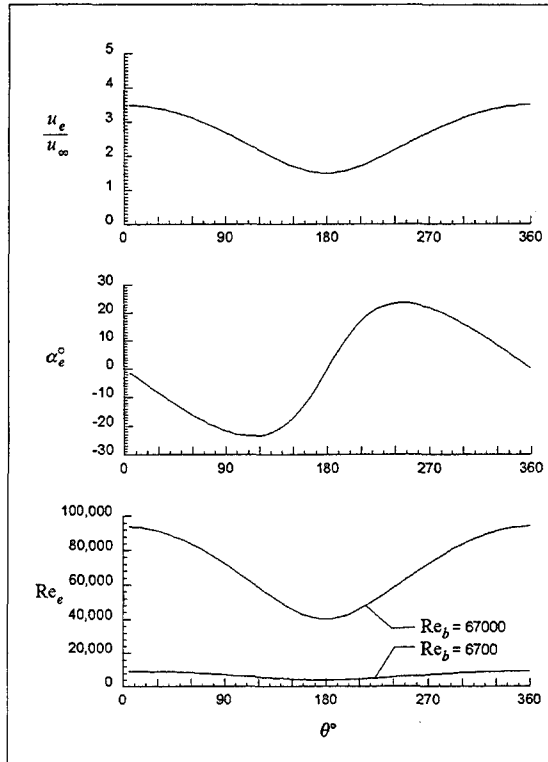


Fig. 3 Evolution of the effective velocity, angle of attack and Reynolds number for $\lambda = 2.5$.

The computational mesh for the laminar case was composed of a structured region of 3120 quadrilateral elements around the airfoil, an unstructured region of 10308 triangular elements elsewhere and a layer of 20 infinite elements located at 80 chords from the mesh center (Fig. 4). The airfoil surface was covered by 260 elements with a minimum thickness and length of $0.0002c$ and $0.0003c$ respectively. Note that the square trailing-edge of the NACA 0015 airfoil has been rounded in order to avoid sharp gradients at this location. For the turbulent case, the mesh was essentially the same except for the location of the first nodes off the wall. In order to guarantee a good mesh resolution in the viscous sublayer, these nodes were placed at an average $y^+ = y(\rho\tau_{wall})^{1/2} / \mu$ of 1.0, where y is the normal distance from the wall and τ_{wall} is the wall shear stress. The Darrieus motion was simulated by decentering the airfoil from the center of the mesh by a distance R and simply performing a rigid body rotation of the mesh about its center at an angular speed Ω . The laminar stream function-vorticity solver computes the solution in the non-inertial frame of reference rotating with the mesh while the turbulent solver computes the solution in the fixed inertial frame of reference.

4.1 Laminar flow

Using the laminar stream function-vorticity solver and a blade Reynolds number of 6700, the flow was computed from rest up to a non-dimensional time $t u_\infty / c$ of 10.08, corresponding to one complete rotation. The implicit time step was fixed at 0.0014 to be able to follow the flow evolution correctly. A detailed description of the results can be found in Ref. 8 and only the features relevant to the comparison with the turbulent case are presented here. The

evolution of the normal and tangential force coefficients, $C_N = 2F_N / \rho_\infty u_\infty^2 c$ and $C_T = 2F_T / \rho_\infty u_\infty^2 c$ respectively, is presented in Fig. 5. Note that a positive normal force F_N acts radially outward and a positive tangential force F_T acts in the direction of motion of the airfoil. During the first or upwind half rotation, dynamic stall occurs in the interval $25^\circ \leq \theta \leq 195^\circ$, corresponding to $\alpha_e = -7^\circ \rightarrow -23^\circ \rightarrow 9^\circ$, on the inner surface, i.e., the surface located inside the rotation disk. During the second or downwind half rotation, dynamic stall occurs in the interval $230^\circ \leq \theta \leq 360^\circ$, corresponding to $\alpha_e = 22^\circ \rightarrow 23^\circ \rightarrow 0^\circ$, on the outer surface, i.e., the surface located outside the rotation disk. This dynamic stall generates multiple alternating leading-edge and trailing-edge vortices, causing the peaks in Fig. 5, and stalling conditions prevail over most of the rotation. Since the flow velocity relative to the airfoil varies not only in direction but also in magnitude, there is a significant variation of the vortex strength and velocity. The unusually great number of shed vortices is simply a direct consequence of the duration of the stall phenomenon and the variation of the vortex velocity.

For reference only, we also plotted in Fig. 5 the experimental data of Oler et al. (Ref. 20) obtained for a blade Reynolds number of 67000, i.e., 10 times higher than the computational one and for which the turbulence effects are no longer negligible. Curves obtained from both pressure and strain gage measurements are presented, giving thereby a bound on the experimental error caused by an insufficient number of pressure sensors, play in the drive train and slight twisting of the blade. The computed normal force seems to loosely follow these experimental curves but its evolution presents multiple peaks caused by stall vortices that do not appear in the experiments. This discrepancy is typical of

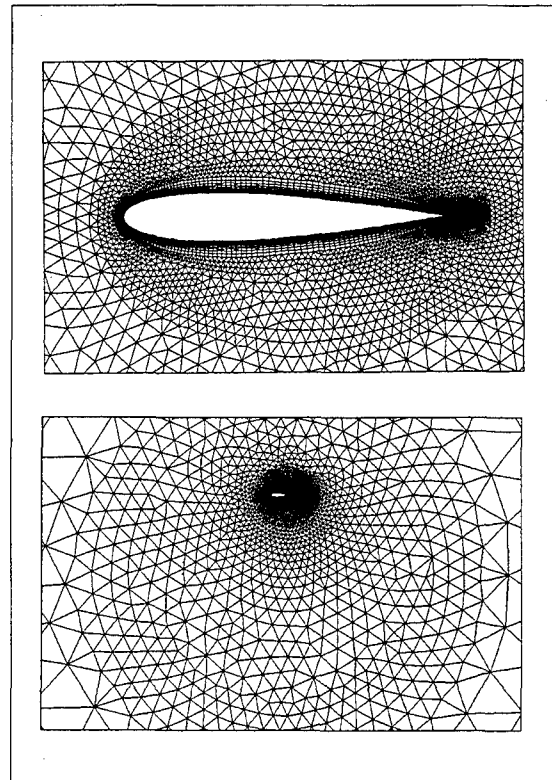


Fig. 4 Computational mesh.

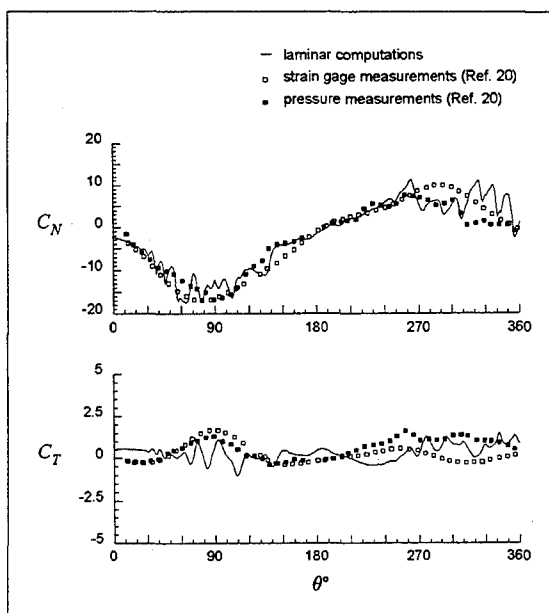


Fig. 5 Laminar case — Evolution of the normal and tangential forces.

comparisons between laminar computations and turbulent experiments and was also observed in Refs. 3 and 7. In laminar computations, the boundary layer has less energy and separates at lower angles of attack. The vorticity is then shed in a succession of small vortices over a long period of time instead of a big vortex over a small period of time as in the turbulent experiments. This qualitative comparison confirms that turbulence changes the flow structure and stresses the need for turbulence modeling.

4.2 Turbulent flow

The turbulent simulation was performed at the same blade Reynolds number of 67000 than the experiments. Since these experiments were conducted in water, the free stream Mach number had to be limited to 0.1 to minimize compressibility effects in the turbulent solver computations. Due to the rotation motion, the corresponding Mach number on the airfoil surface is around 0.25. The resulting flow stays subsonic during the whole rotation with a maximum Mach number around 0.7 near the leading edge. Starting from rest, the flow was computed up to a non-dimensional time of 20.16, corresponding to two complete rotations, but the results are presented only for the second rotation. The explicit time step was limited to an average value of 4.45×10^{-6} by a CFL-like condition. To illustrate the flow structure, the evolution of the computed non-dimensional vorticity $\mathbf{k} \cdot \nabla \times \mathbf{u} c / u_\infty$ is presented in Fig. 6. The evolution of the wall pressure $C_p = 2(p_{\text{wall}} - p_\infty) / \rho_\infty u_\infty^2$ and friction $C_f = 2\tau_{\text{wall}} / \rho_\infty u_\infty^2$ distributions, presented in Figs. 7 and 8, shows the formation of the stall vortices and their trajectory on the airfoil surface. From the analysis of Fig. 7, the history of the dynamic stall on the inner surface of the airfoil during the upwind half rotation can be decomposed in the following stages:

- A reverse flow at the trailing-edge starts to progress upwind at $\theta \approx 30^\circ$.
- A leading-edge reverse flow bubble appears at $\theta \approx 60^\circ$.

- The bubble bursts and generates a leading-edge vortex at $\theta \approx 80^\circ$ while the trailing-edge reverse flow has only progressed up to mid-chord.
- The leading-edge vortex reaches mid-chord at $\theta \approx 100^\circ$ and passes over the trailing-edge at $\theta \approx 120^\circ$, generating thereby a trailing-edge vortex. A secondary leading-edge vortex can also be spotted as the main leading-edge vortex progresses downwind but it is much smaller in intensity.
- The reattachment of the boundary layer starts at $\theta \approx 140^\circ$ and is completed at $\theta \approx 170^\circ$.

Similarly, from the analysis of Fig. 8, the history of the dynamic stall on the outer surface of the airfoil during the downwind half rotation can be decomposed in the following stages:

- A very mild reverse flow at the trailing-edge starts to progress upwind and a leading-edge reverse flow bubble appears at $\theta \approx 200^\circ$.
- The bubble bursts and generates a leading-edge vortex at $\theta \approx 210^\circ$ while the reverse flow has progressed upwind only 10% of chord from the trailing-edge.
- The leading-edge vortex reaches mid-chord at $\theta \approx 250^\circ$ and passes over the trailing-edge at $\theta \approx 270^\circ$, generating thereby a trailing edge-vortex.
- The reattachment of the boundary layer starts at $\theta \approx 280^\circ$ and is completed at $\theta \approx 350^\circ$.

Note in Figs. 7 and 8 that two peaks can be spotted at the trailing-edge in the wall pressure and friction distributions outside the separation regions, i.e., at $\theta \approx 270^\circ$ on the inner surface and at $\theta \approx 120^\circ$ on the outer surface. These peaks correspond to the acceleration of the boundary layer caused by the formation of the trailing-edge vortices during the separation on the opposite surface.

Thus, although the k - w model was designed for fully turbulent flows and not for combined laminar, transitory and turbulent flows as in the present case, it, nonetheless, significantly improves the results by comparison with the laminar computations. More precisely, the separation starts later and the flow stays separated for a shorter period of time, resulting in the generation of only one pair of contrarotating leading-edge trailing-edge vortices during each half rotation, as observed in the experiments (Ref. 20). This improvement can also be seen in Fig. 9 that compares the computed normal and tangential forces with experimental data. The maximum absolute values of the computed normal force are reached when the leading-edge vortices pass mid-chord, at $\theta \approx 100^\circ$ and $\theta \approx 250^\circ$, and these values match the experimental peaks of 16.0 and 10.0 respectively. The stall following each of these peaks seems more severe than in the experiments but its duration matches overall the experimental stall intervals of $100^\circ \leq \theta \leq 140^\circ$, corresponding to $\alpha_e = -20^\circ \rightarrow -23^\circ$, on the inner surface and $265^\circ \leq \theta \leq 290^\circ$, corresponding to $\alpha_e = 18^\circ \rightarrow 23^\circ$, on the outer surface. The comparison of the computed and experimental tangential forces is, however, less conclusive because, as indicated in the experimental study (Ref. 20), the measurements of this component are much less accurate.

Finally, it is interesting to point out the differences between the dynamic stall on an airfoil in Darrieus motion and the dynamic stall on an airfoil performing an equivalent pitching motion based only on the variation of the effective angle of

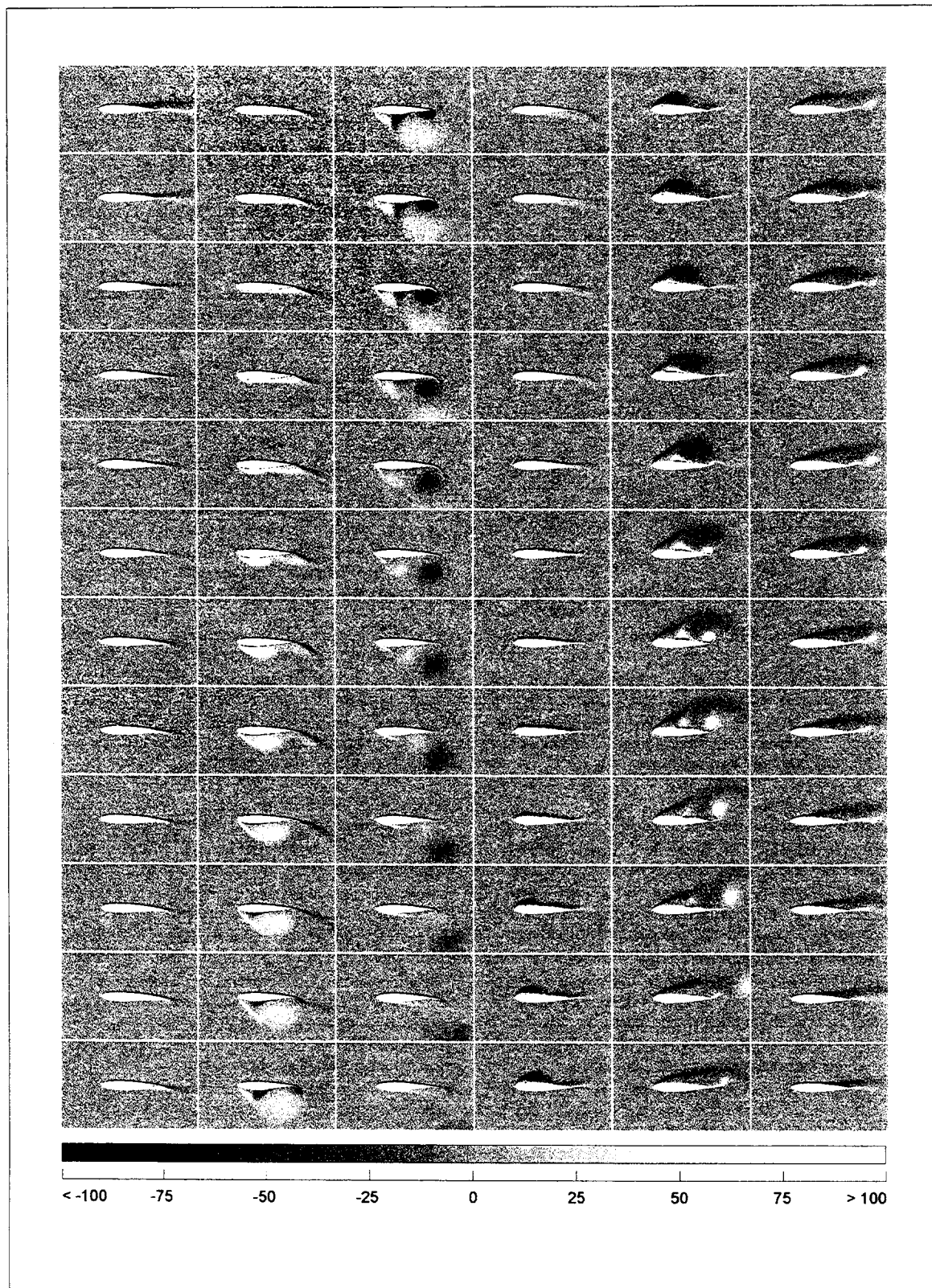


Fig. 6 Turbulent case – Evolution of the vorticity field from $\theta = 5^\circ$ to 360° (from top to bottom and from left to right with 5° between each frame).

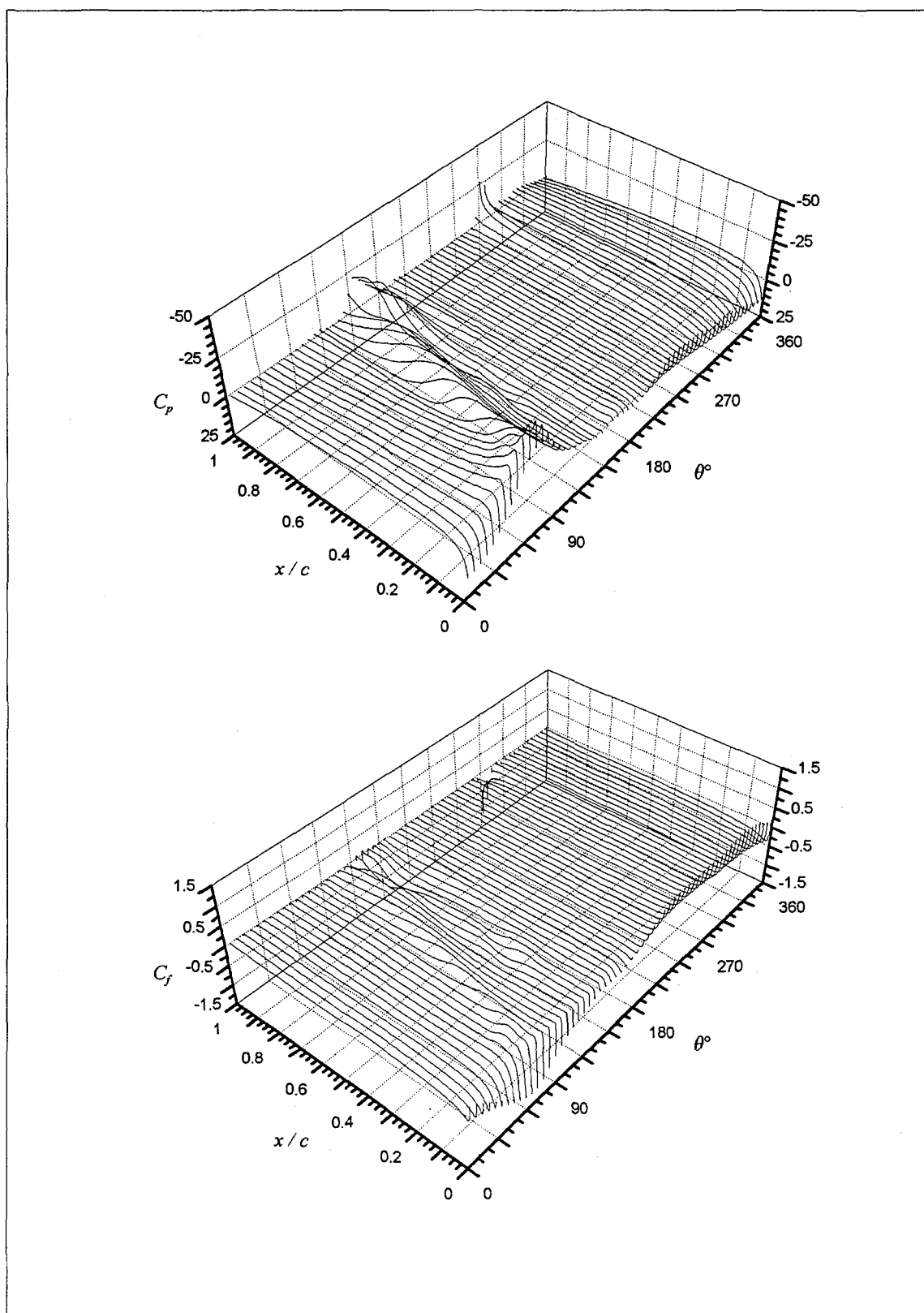


Fig. 7 Turbulent case – Evolution of the wall pressure and friction distributions on the inner surface.

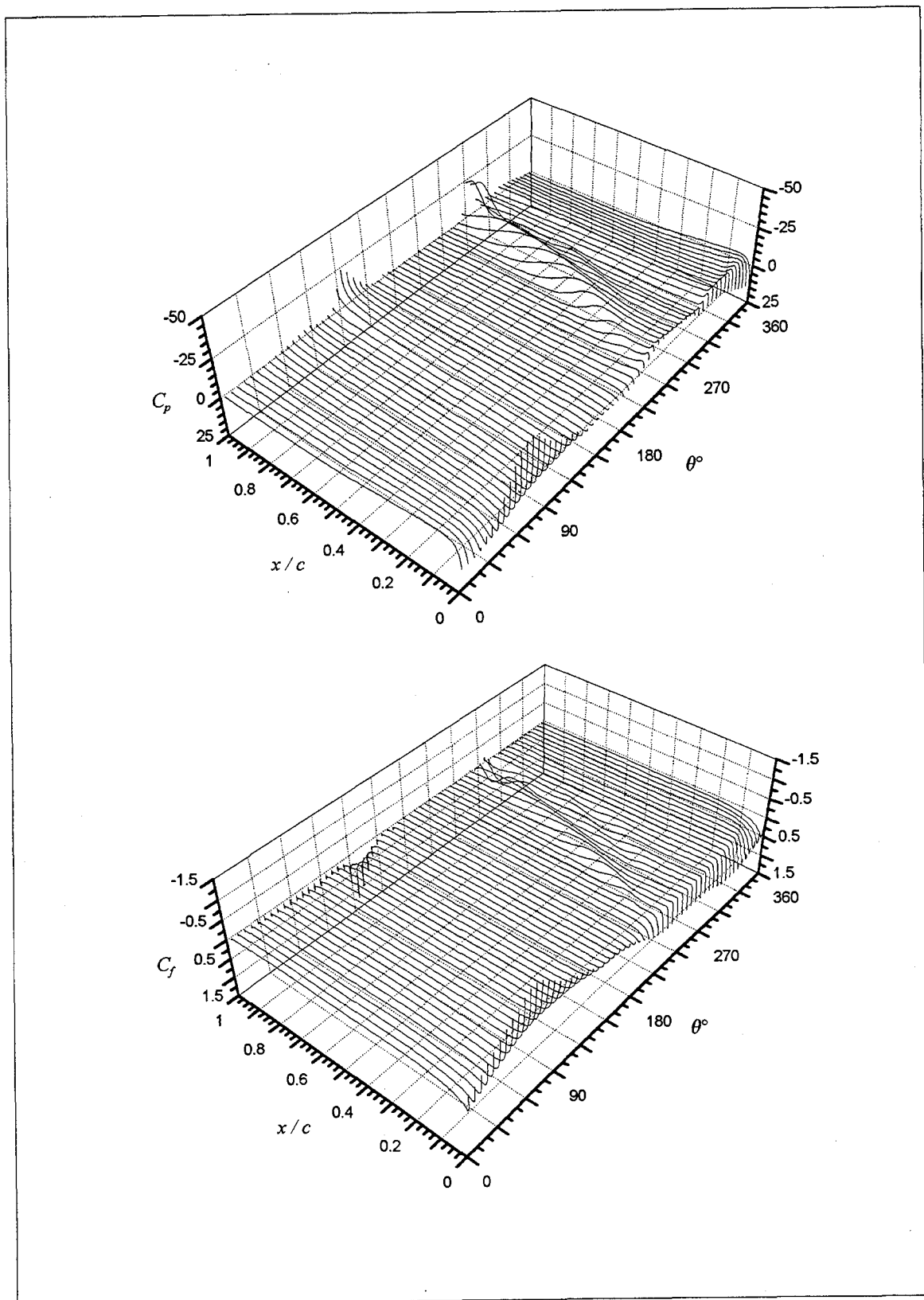


Fig. 8 Turbulent case — Evolution of the wall pressure and friction distributions on the outer surface.

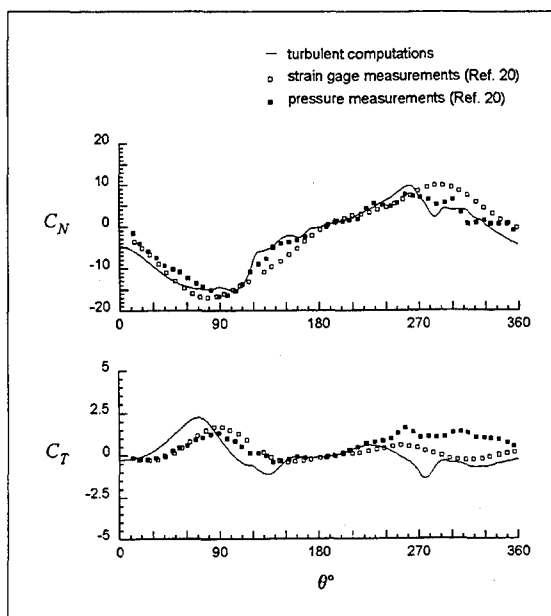


Fig. 9 Turbulent case — Evolution of the normal and tangential forces.

attack α_e . Firstly, such a pure pitching motion is not able to take into account the variation of the effective flow velocity and Reynolds number that results in a much higher peak in the normal force, indicating a stronger stall vortex, during the upwind half rotation than during the downwind half. Secondly, the flow structure generated by a rotation motion is different from the flow structure resulting from a pure pitching motion or even a combined pitching and fore-and-aft motion that would take into account the velocity variation. This is best illustrated by the asymmetrical convection of the stall vortices during the two halves of the rotation (Fig. 10). During the upwind half, the wind tends to convect the wake towards the airfoil: the vortices stay near the airfoil and the stall lasts longer. During the downwind half, the wind tends

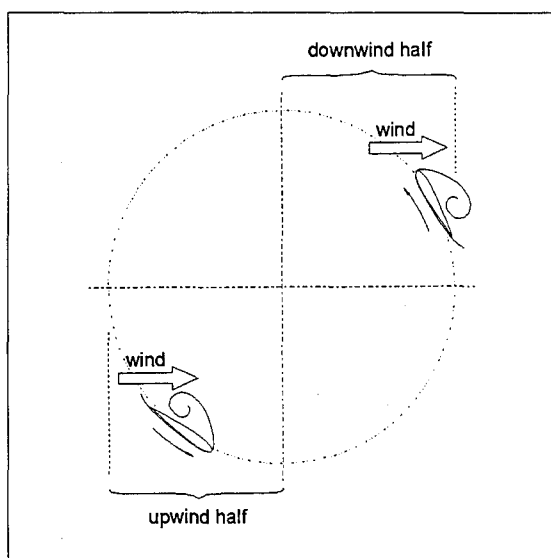


Fig. 10 Asymmetric wake convection.

to convect the wake away from the airfoil: the vortices move away faster and the stall is shorter. That is why the complex flow around a Darrieus vertical-axis wind turbine blade should be simulated by an airfoil performing a full rotation motion and not a pure or combined pitching motion.

5. CONCLUSIONS

The dynamic stall on a NACA 0015 airfoil in Darrieus rotation motion has been numerically simulated using two Navier-Stokes solvers and the results were compared with experimental data. The first solver assumed laminar flow and predicted a premature boundary layer separation and the generation of a succession of alternating leading-edge trailing-edge dynamic stall vortices that were not observed in the experiments. This discrepancy is typical of comparisons between laminar computations and experiments conducted in turbulent conditions, stressing the need for turbulence modeling to realistically simulate dynamic stall. The second solver used a $k-\omega$ turbulence model and fared much better. The dynamic stall occurred much later than in the laminar case and was initiated by a reverse flow progressing upwind from the trailing edge followed by a burst of a reverse flow bubble at the leading edge. This stall generates only one pair of contrarotating leading-edge trailing-edge vortices during each half rotation as in the experiments and the computed normal force fairly matched the experimental data.

The analysis of the results also showed the distinct features of the Darrieus motion compared to a pitching motion, i.e., the variation of the effective flow velocity and Reynolds number seen by the airfoil and the asymmetry of the wake convection during the upwind and downwind halves of the rotation.

Finally, although the flow conditions considered in the present study are not typical of actual turbines, the chord to radius ratio being too high and the Reynolds number being too low, the turbulent solver showed its potential for the prediction of the dynamic stall phenomenon. The next step in the development of this solver will be the automatic spatial adaptation of the computational mesh.

ACKNOWLEDGMENTS

The development of the laminar stream function-vorticity solver was supported by Energy, Mines and Resources Canada under contract No. 23440-0-9457/01-SS.

REFERENCES

1. McCroskey, W. J., "Some Current Research in Unsteady Fluid Dynamics - The 1976 Freeman Scholar Lecture," *Journal of Fluids Engineering*, Vol. 99, March 1977, pp. 8-39.
2. Paraschivoiu, I., "Double-Multiple Streamtube Model for Studying Vertical-Axis Wind Turbines," *AIAA Journal of Propulsion and Power*, Vol. 4, No. 4, July-August 1988, pp. 370-378.
3. Shida, Y., Kuwahara, K., Ono, K., and Takami, H., "Computation of Dynamic Stall of a NACA-0012 Airfoil," *AIAA Journal*, Vol. 25, No. 3, March 1987, pp. 408-413.
4. Daube, O., Ta Phuoc, L., Dulieu, A., Coutanceau, M., Ohmi, K., and Textier, A., "Numerical Simulation and

- Hydrodynamic Visualization of Transient Viscous Flow Around an Oscillating Aerofoil," *International Journal for Numerical Methods in Fluids*, Vol. 9, 1989, pp. 891-920.
5. Visbal, M. R., "Dynamic Stall of a Constant-Rate Pitching Airfoil," *Journal of Aircraft*, Vol. 27, No. 5, May 1990, pp. 400-407.
 6. Tuncer, I. H., Wu, J. C., and Wang, C. M., "Theoretical and Numerical Studies of Oscillating Airfoils," *AIAA Journal*, Vol. 28, No. 9, September 1990, pp. 1615-1624.
 7. Dindar, M., Kaynak, U., and Fujii, K., "Nonequilibrium Turbulence Modeling Study on Light Dynamic Stall of a NACA0012 Airfoil," *Journal of Aircraft*, Vol. 30, No. 3, May-June 1993, pp. 304-308.
 8. Tchon, K. F., and Paraschivoiu, I., "Navier-Stokes Simulation of the Flow Around an Airfoil in Darrieus Motion," SED-Vol. 14, *Wind Energy ASME* 1993, pp. 11-18. Also to be published in the *ASME Journal of Fluids Engineering*.
 9. Peeters, M. F., Habashi, W. G., and Dueck, E. G., "Finite Element Stream Function-Vorticity Solutions of the Incompressible Navier-Stokes Equations," *International Journal for Numerical Methods in Fluids*, Vol. 7, 1987, pp. 17-27.
 10. Gunzburger, M. D., and Peterson, J. S., "On Finite Element Approximations of the Streamfunction-Vorticity and Velocity-Vorticity Equations," *International Journal for Numerical Methods in Fluids*, Vol. 8, 1988, pp. 1229-1240.
 11. Tezduyar, T. E., Glowinsky, R., and Liou, J., "Petrov-Galerkin Methods on Multiply Connected Domains for the Vorticity-Stream Function Formulation of the Incompressible Navier-Stokes Equations," *International Journal for Numerical Methods in Fluids*, Vol. 8, 1988, pp. 1269-1290.
 12. Zienkiewicz, O. C., Emson, C., and Bettess, P., "A Novel Boundary Infinite Element," *International Journal for Numerical Methods in Engineering*, Vol. 19, 1983, pp. 393-404.
 13. Saad, Y., and Schultz, M., "GMRES: A Generalized Minimum Residual Algorithm for Solving Nonsymmetric Linear Systems," *Research Report YALEU/DCS/RR-254*, 1983.
 14. Tchon, K. F., "Dynamic Stall Simulation Using a Temporal Adaptive Navier-Stokes Solver and a k-w Turbulence Model," *AIAA Paper 95-0186*, to be presented at the *AIAA 33rd Aerospace Sciences Meeting*, Reno, NV, on January 9-12, 1995.
 15. Tchon, K. F., "Object-Oriented Programming for a Temporal Adaptive Navier-Stokes Solver," *AIAA Paper 95-0574*, to be presented at the *AIAA 33rd Aerospace Sciences Meeting*, Reno, NV, on January 9-12, 1995.
 16. Wilcox, D. C., "Reassessment of the Scale-Determining Equation for Advanced Turbulence Models," *AIAA Journal*, Vol. 26, No. 11, November 1988, pp. 1299-1310.
 17. Jameson, A., and Baker, T. J., "Solution of the Euler Equations for Complex Configurations," *AIAA Paper 83-1929*, 1983.
 18. Trépanier, J. Y., Reggio, M., Zhang, H., and Camarero, R., "A Finite-Volume Method for the Euler Equations on Arbitrary Lagrangian-Eulerian Grids," *Computers Fluids*, Vol. 20, No. 4, 1991, pp. 399-409.
 19. Kleb, W. L., Batina, J. T., and Williams, M. H., "Temporal Adaptive Euler/Navier-Stokes Algorithm Involving Unstructured Dynamic Meshes," *AIAA Journal*, Vol. 30, No. 8, August 1992, pp. 1980-1985.
 20. Oler, J. W., Strickland, J. H., Im, B. J., and Graham, G. H., "Dynamic Stall Regulation of the Darrieus Turbine," *SANDIA Report SAND83-7029*, 1983.

STALL HYSTERESIS AND 3D EFFECTS ON STALL REGULATED WIND TURBINES: EXPERIMENT AND MODELLING

H.A. Madsen, F. Rasmussen
The Test Station for Wind Turbines
Risø National Laboratory
Roskilde, DK-4000
Denmark

1. SUMMARY

The stall regulation is used for control of maximum power and loads on a major part of wind turbines today of sizes up to 50-60 m in diameter. Operation with the blades partially or fully stalled is for this type of machines a part of their normal operating regime. Aeroelastic calculations below stall using 2D airfoil data give satisfactory results but in stall and above stall the calculations indicate self excited flapwise vibrations. Fortunately, they are not in general confirmed by measurements. This discrepancy seems to be due to dynamic stall effects and the 3D airfoil characteristics for the rotating blade. Such airfoil characteristics have been measured on a 19 m stall regulated rotor and the deviations from 2D data are considerable. High normal force coefficients are measured at the root end and the lift curve has no negative slope up to 25-30 deg. angle of attack. Considerable stall hysteresis has been measured in normal operation and in particular during yawed operation. Measurements in a 4x4 m wind tunnel on the same blade has been carried out in order to determine the airfoil characteristics without the influence of rotation. This comparison indicates that rotational effects are of some importance for the discrepancy between 2D and 3D data. A CFD calculation on a simplified model of a rotating blade and at a low Reynolds number indicates that rotation does reduce the thickness of the separated boundary layer, resulting in an increased lift. Although the use of a stall hysteresis model in aeroelastic calculations generates damping and eliminates the self-excited vibrations, the problem still is to predict dynamic stall events, which have the correct power spectral characteristics.

2. BACKGROUND/INTRODUCTION

From the beginning of the development of modern wind turbines in the late seventies, two different development paths for the regulation of maximum power and blade loads have been followed. The first one is the pitch regulation principle, where the incidence on the blade at high wind is controlled by pitching the blade towards feather.

Stall regulation is the other main principle and the maximum rotor power and blade loads are here limited by a proper stall along the blade.

However, during the past there has been considerable concern about the applicability of the stall regulation principle due to the fear for self excited blade vibrations during operation in stall. This concern has had a clear impact on the development in the way that stall regulation has been

implemented stepwise, from small 15-30 Kw machines in the beginning and till today's prototype machines in the range of 700-1500 kW rotor power and a rotor diameter from 50-60 m.

So far, the general experience has been that the dynamic loads do not increase dramatically during operation in stall and that a properly designed stall regulated rotor can limit the power output effectively above the design wind speed for maximum power. On the other hand, aerodynamic performance predictions and aeroelastic loads predictions are generally quite uncertain for operating conditions in stall and post stall. Shortly, it seems that the use of two-dimensional (2D), steady airfoil sectional data which are based on wind tunnel measurements are not adequate for use in calculations in stall and post stall.

One of the first experimental evidences of the deviation between on-rotor three-dimensional (3D) airfoil data and 2D data was presented by Rasmussen [1]. On the basis of measurements of the flapwise blade bending moment at different radial positions along the blade span and measurement of the total rotor thrust, a 3D airfoil data set was derived for the blade. A considerable variation of the airfoil characteristics along the blade was found with high normal force coefficients C_N at the root.

These observations initiated in 1987 a more detailed experimental investigation of the local airfoil characteristics on a full scale stall regulated rotor Madsen [2] and key results from this work will be presented in the present paper. In the same period experimental programs with the same main subject "study of the on-rotor airfoil characteristics" were initiated in different countries, Butterfield [3], Ronsten [4], Hales [5] and Bruining [6]. So, a number of sources with experimental data on 3D airfoil characteristics are available today and it should be mentioned that presently a project is ongoing within the International Energy Agency (IEA) which aims at collecting some of these data in a common data base.

The present paper will focus on the characteristics of the 3D data and stall hysteresis, and ongoing research at Risø on exploring these phenomena will be presented.

3. STALL REGULATION

The typical design layout of a stall regulated wind turbine is a three-bladed rotor with a fixed hub and connected to an induction generator through a gearbox. This gives an almost constant rotational speed and for increasing wind speed the effective angle of attack at the blade will increase with highest slope at the inner part of the blade due to the

relative low tangential velocity of the blade in this region, Figure 1. At a certain wind speed the stall angle for the airfoil will be reached and the blade will be stalled progressively over a wider part for an increased wind speed.

The optimal characteristics of the power curve for a stall regulated rotor is a steep slope before stall and a constant power for increasing wind speed above stall. The measured power curve for a 37 m diameter rotor depicted in Figure 2 has such good characteristics. The blade planform and twist are important parameters for the stalling characteristics, but the airfoil type and its characteristics is the most crucial factor. Typical airfoil families used are: NACA 44XX, NACA 63_n-2nn, NACA63_n-4nn and more recently airfoils, designed specifically for wind turbines; the SERI airfoils Tangler [7] and the FFA airfoils Björck [8].

Contrary to the limited rotor power, the blade flapwise mean loads will continue to increase as function of wind speed after stall, however with a lower slope than before stall. Also the stochastic part of the flapwise loads will increase by operation in stall and deep stall but in most cases not dramatically. As mentioned in the introduction, concern has been on the possibility of high stochastic loads during operation in stall and deep stall, emerging as stall induced vibrations.

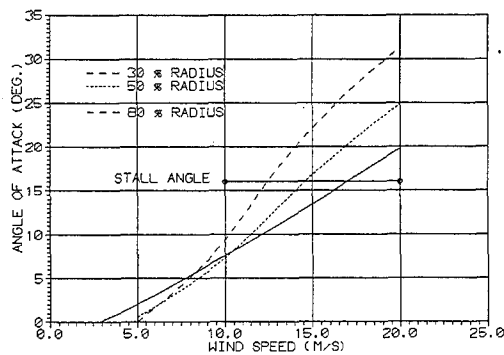


Figure 1. The variation of the effective angle of attack on a stall regulated rotor.

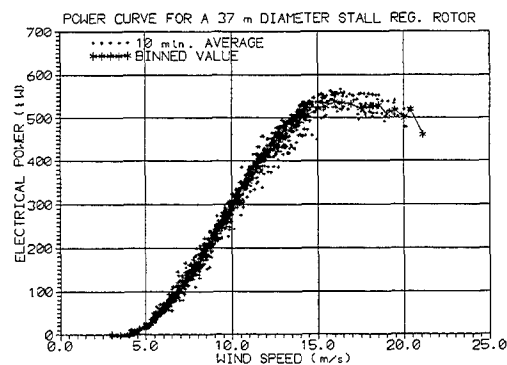


Figure 2. Measured power curve of a stall regulated rotor.

3.1 Stall Induced Vibrations

The result of a short time series aeroelastic simulation of a stall regulated rotor operating at a wind speed between 15 - 20 m/s is presented in Figure 3.

The parameter shown is the blade root flapwise bending

moment and the simulation is based on a state-of-the-art aeroelastic code developed by Petersen [9].

It is clearly seen that the blade is going into self excited high flapwise vibrations (stall induced vibrations) causing high blade bending moments when compared with normal operation in the beginning of the time series. The reason for the stall induced vibrations is found by looking at the instantaneous C_L as function of the angle of attack (α) during the simulated time interval, shown in Figure 4.

It is seen that during the simulated time interval the C_L (shown for the mid part of the blade) is in a region where the slope of the C_L vs. α curve is negative. This results in a negative aerodynamic damping for the flapwise vibrations of the blade and the amplitude will increase gradually unless the structural damping is high enough to limit the vibrations at some stage.

However, with a few exceptions the stall induced vibrations are not confirmed by measurements on stall regulated rotors. This fundamental question has initiated much research effort on the aerodynamics of the stall regulated rotor.

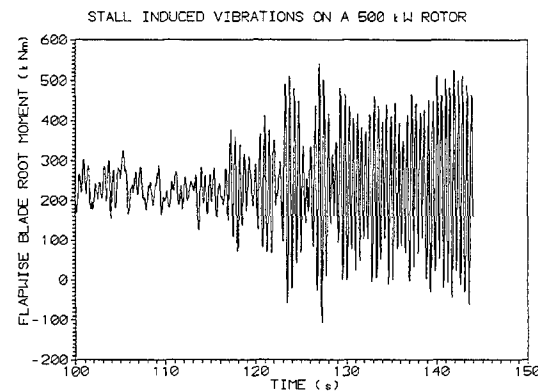


Figure 3. Simulated flapwise blade root moment during operation in stall. Wind speed 15 - 20 m/s, 2D airfoil data, no stall hysteresis.

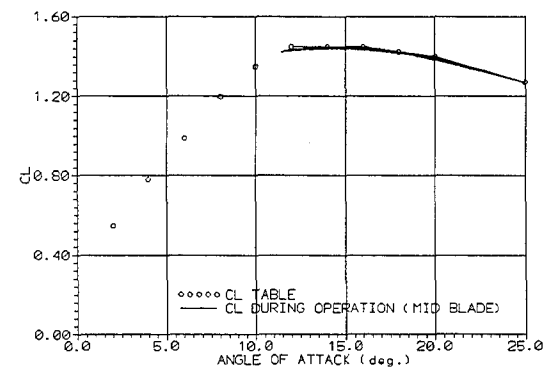


Figure 4. The C_L as function of angle of attack for the time series shown in Figure 3. The two parameters are for the mid span of the blade.

4. OBSERVATIONS ON ROTOR AERODYNAMICS

A number of experimental programs with the main objective to get insight into rotational airfoil characteristics, have been carried out in various countries during the last 5-8 years. Surface pressure measurements on a rotor have been made by Butterfield [3], Ronsten [4], Hales [5] and Bruining [6]. Integration of the pressure data has provided the basis for deriving the lift and drag characteristics at different spanwise stations on the blade.

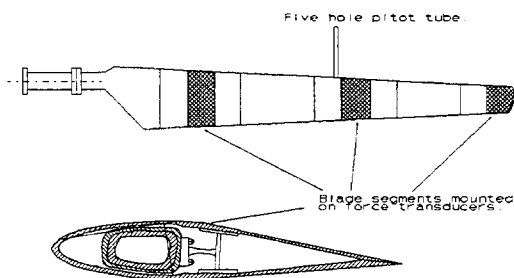


Figure 5. The principal layout of the test blade.

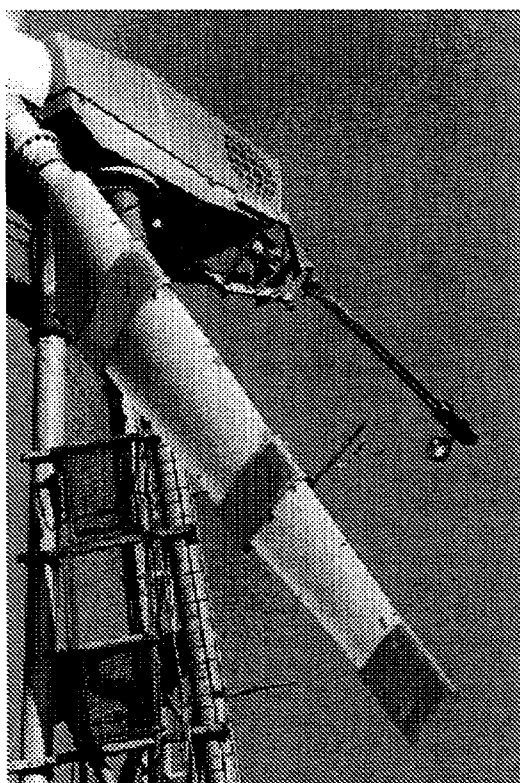


Figure 6. The test blade installed on the 19 m diameter wind turbine.

At Risoe, a different technique has been used for a full scale 19 m diameter stall regulated rotor, Madsen [2]. One of the blades has been rebuild so that three blade segments could

be mounted on balances, attached to the main spar in the blade as shown in Figure 5. The segments, each 0.5 m in spanwise width and with NACA 63_n-2nn airfoils, are located close to the root of the blade, at the mid span and at the tip, respectively, as illustrated in Figure 6. Accelerometers mounted at the base of the balances are used for subtracting the inertia force component of the total force signal from the balance.

For measurement of the inflow relative velocity vector \mathbf{W} , a five hole pitot tube is mounted on a pipe about one chord length in front of the leading edge of the blade section, immediately outboard of the actual segment, Figure 6. Finally it should be mentioned that the turbine can be run at two different rotational speeds, 36 rpm and 47 rpm.

4.1 3D Airfoil Characteristics

3D airfoil data is in this paper defined as airfoil data on a rotor contrary to 2D data which could either be measured as sectional data in a wind tunnel or computed on basis of an airfoil code.

The measured C_L C_D curves as function of local angle of attack α_1 are shown in Figures 7 and 8 for the mid and root segment, respectively.

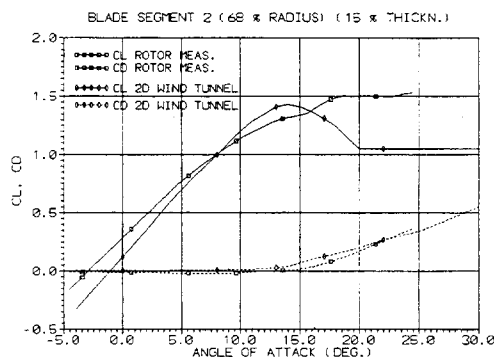


Figure 7. Measured C_L C_D vs. local angle of attack α_1 curves on the mid span of the blade.

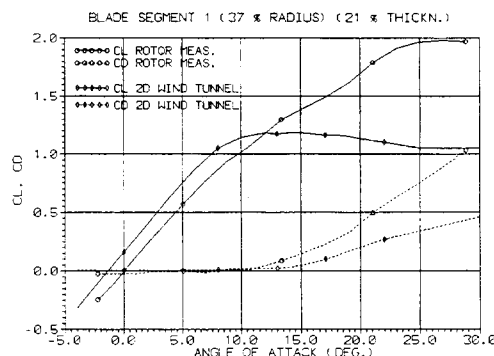


Figure 8. Measured C_L C_D vs. local angle of attack α_1 curves at the root of the blade.

A discussion of the angle of attack measurement with a pitot tube and its interpretation is included in the main report on these measurements, Madsen [10]. Several possible correc-

tions of the measured local angle of attack α_i can be argued. At this point is just noted that the only correction introduced to the measured α_i is the addition of a constant α_0 . The constant was determined from comparison of a computed rotor power curve as function of effective angle of attack α_e at the pitot tube, using a blade element momentum code, with the corresponding measured power vs. α_i curve. To get coincidence between these curves below stall a value of α_0 equal to -1° was determined.

The measured C_L C_D curves are compared with 2D wind tunnel data of Abott and Doenhoff [11] for similar airfoils, NACA 63₂-215 in Figure 7 and NACA 63₄-221 in Figure 8. The wind tunnel data are for a Reynolds number (Re. no.) equal to 3 million while the Re. no. of the rotor data is 1.3 million for the mid blade segment and 1.1 million for the root segment (operation at the low rotational speed of 36 rpm).

Considerable deviations are seen when comparing the 2D and 3D data. The type of stall is quite different in the two data sets as the 3D lift curves have no negative slope up to α_i about 30° . The post stall values are much higher for the 3D data, in particular for the root section. However, for this section the drag values are also much higher than the 2D values in the post stall region. The deviations below stall are expected mainly to be due to the interpretation of the measured α_i . For example, the lower slope of the 3D C_L curve in Fig. 7 could be due to some influence from the upwash of the bound circulation on the blade. Of course, the same uncertainty due to the interpretation of α_i must be expected in the stall and post stall region, but if it is assumed of the same magnitude as below stall it would not change the general tendency in the deviations between the 2D and 3D data.

4.2 Unsteadiness of the inflow

A part of the basis for understanding the aerodynamics of a rotor operating in turbulent wind conditions is the knowledge about the unsteadiness of the inflow seen by the rotating blade. The axial component u of the turbulent wind will mainly give variations in α on the blade. On the other

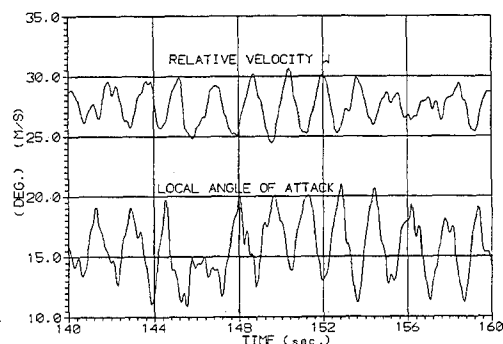


Figure 9. Variations in angle of attack and the relative velocity during normal operation.

hand, the horizontal component v causes variations in both α and the relative velocity W because the rotor cannot follow the rapid changes in the wind direction. This means that the rotor in most of the time operates with a yaw error ranging from a few degrees and momentarily up to $20-30^\circ$. The measurements with the pitot tube on the rotating blade have provided detailed insight into this unsteadiness. In

Figure 9 is shown a time trace of the measured angle of attack and relative velocity on the mid part of the blade for the turbine in normal operation. Considerable variations in both parameters are seen and this is due to an instantaneous yaw error, wind shear, tower shadow and rotational sampled turbulence. It can also be seen that α_i and W_i typically are in counter phase.

In Figure 10 is shown the power spectrum of the measured stochastic part of α_i during normal operation at 10.9 m/s. Most of the energy is centered around 0.8 Hz which corresponds to the 1p for the rotor (operating at the high rotational speed, 47 rpm.). However, smaller peaks are also seen at frequencies corresponding to 2p, 3p and 4p of the rotor. The reason for the energy of the spectrum being centered around 1p, 2p etc. is the so-called rotational sampling of the turbulence Kristensen and Frandsen [12] which is an important phenomenon for the stochastic loading of the rotor. For comparison is also shown the spectrum derived on the basis of a simulated three-dimensional turbulence wind field using the model of Mann [13]. A good correlation is found between the measured and simulated spectrum of α and this also holds for the spectra of the relative velocity, Kretz et al. [14].

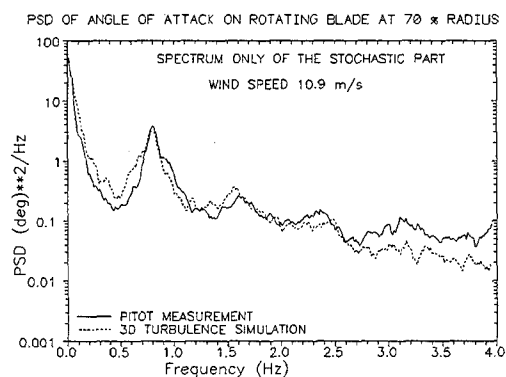


Figure 10. Power spectral density of the stochastic part of the angle of attack for operation at 10.9 m/s.

4.3 Stall Hysteresis

The unsteadiness of the inflow as described above will influence the aerodynamics of the rotor and unsteady effects such as dynamic stall must be expected to be important for the dynamic loading of the rotor. Typical values for the reduced frequency, $k = \omega c / 2V$ are 0.05 - 0.2.

Stall hysteresis measured on the mid segment of the blade during normal operation and in 30° yawed operation, respectively, measured on the mid segment of the blade is shown in the Figures 11 and 12. The figures reflect that even for normal operation, considerable stall hysteresis can occur. For yawed operation, the loops become more regular, and this is because the variations in α and W then are more harmonic.

5. ANALYSIS OF THE PHENOMENA

Two main conclusions on the observations described above in Section 4 can be made; 1) the 3D data measured on a rotor operating in real turbulent wind conditions deviate

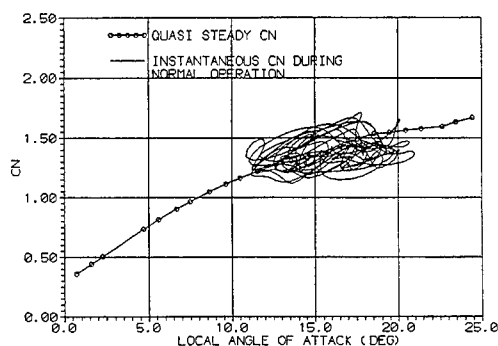


Figure 11. Measured stall hysteresis on the mid segment of the blade during normal operation. (The same time interval as in Figure 9)

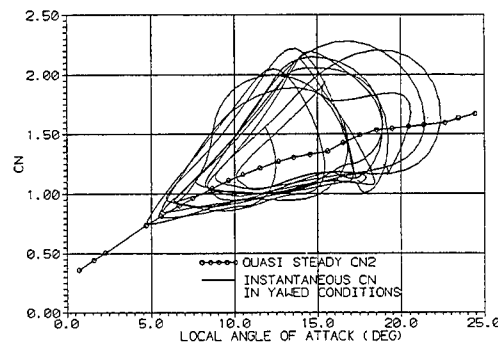


Figure 12. Measured stall hysteresis on the mid segment on the blade during yawed operation.

considerably from 2D data measured under steady conditions and 2) the unsteadiness of the inflow is high enough to trigger unsteady effects such as stall hysteresis. Concerning the deviations between 3D and 2D data they can be summarized as; 1) an increasing 3D C_{Lmax} towards the root of the blade; 2) the 3D post-stall C_L values are higher than the 2D data and 3) the character of the C_L vs. α curve in stall and post stall is different in the 3D data as almost no intervals with negative slope is found. General speaking, it seems that the different measurement programs [3] - [6] mentioned above give results which can confirm these main findings. The issue that naturally follows is then to analyze and explore the phenomena behind the 3D data and stall hysteresis. Then to use this knowledge to derive simple, engineering models that can describe the phenomena satisfactorily and can be coupled to aeroelastic models. At the present stage aeroelastic computations on wind turbines can be carried out with satisfactory accuracy below stall whereas above stall the results are uncertain. This is mainly related to the lack of proper models for dynamic stall and 3D aerodynamic effects.

A state-of-the-art aeroelastic code for wind turbines such as the one developed by Petersen [9] has three main elements; 1) an aerodynamic part based on strip theory or blade

element/momentum theory and coupled with a stall hysteresis model; 2) a multi-degree-of-freedom structural dynamics model and 3) a three component turbulent wind field simulation model as e.g. Mann [13].

5.1 The Phenomena

The characteristics of the 3D on-rotor data are both due to 3D effects and unsteadiness of the inflow. Harris [14] lists the following five parameters that should be considered when studying 3D effects (equivalent to spanwise or radial flow effects):

- the outer potential flow
- chordwise pressure distribution
- spanwise pressure distribution
- the centrifugal force field
- the coriolis force field

For the stall regulated wind turbine rotor the following parameter is assumed also to be important:

- interaction between stalled and attached flow regions

In the on-going research at Risø to analyze and explore these phenomena, different tools are used comprising the described on-rotor measurements, wind tunnel experiments and CFD.

5.2 Wind Tunnel Measurements

To get insight into the influence of rotation on the aerofoil data, the blade with the three separate blade segments as described in section 4 has been tested in a wind tunnel. The wind tunnel is of the return type and has a $10 \times 7.5 \times 7.5$ m test section with a jet of 4×4 m blowing through. The blade was mounted horizontally on a rig outside the test section with the segment mid on the blade centered in the jet. Measurements were carried out at a tunnel speed around 30 m/s corresponding to a Re. no. of 1.6 million. This is a little above the field test Re. no of 1.3 million. The blade was instrumented as during the field tests and with the five hole pitot tube. A measurement of the blade pitch was carried out in parallel in order to validate the pitot angle measurement.

Both static and dynamic pitch tests were carried out. In the static tests, α was held constant in a time interval of 5 - 10 seconds before change to the next step. Other static tests were carried out with a very slow continuous change of α . A comparison of the C_N curves measured in the wind tunnel with the 3D C_N curve measured on the rotor is shown in Fig. 13. Two C_N curves from the wind tunnel measurements are presented, the one as function of α from the pitot tube and the other as function of α from the blade pitch angle measurement. It is seen that there is a rather good correlation between the two methods of measuring the angle of attack.

Comparing the wind tunnel data with the rotor data the main deviations are found in the post stall region where the 3D C_N curve exceeds the wind tunnel data with 10 - 20 %. Also the form of the curves are somewhat different in this region.

The main parameter causing this deviation is assumed to be the influence from the rotation (centrifugal- and coriolis forces) although differences in flow unsteadiness and the

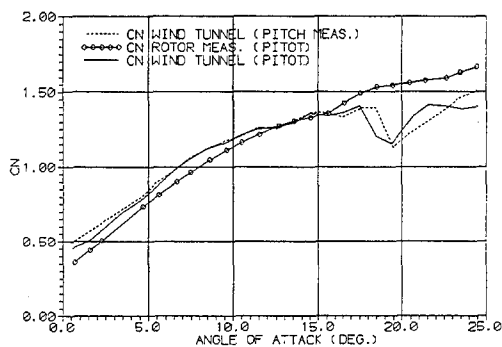


Figure 13. Comparison of C_N curves for the mid segment of the blade. Wind tunnel measurements and rotor measurements, respectively.

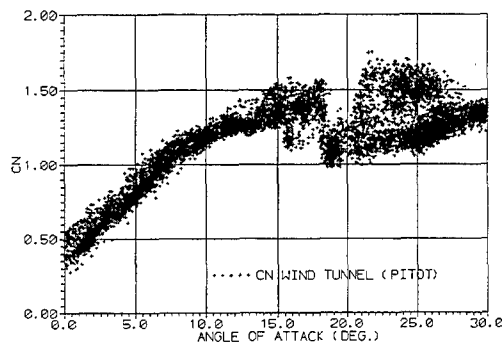


Figure 14. The data from the wind tunnel tests binned over a short time interval.

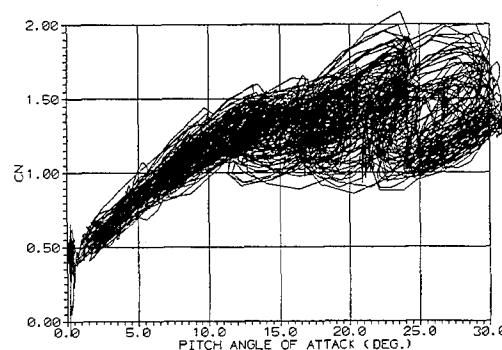


Figure 15. Stall hysteresis loops measured during 1 Hz pitch oscillations in the wind tunnel. Amplitude ± 5 deg at 5,10,15,20,25 mean angle of attack and a reduced frequency $k = 0.07$.

spanwise pressure gradient between the wind tunnel and the rotor measurements can have some influence. The unsteadiness in the wind tunnel experiments were mainly due to flapwise vibrations of the blade which was supported at both ends. The influence from the spanwise pressure gradient is

probably small because the particular section is mid on the blade where the blade twist is small. To get more detailed insight into the stall and post stall region of the wind tunnel measurements, the data are shown in Figure 14 as binned values over a short time. Two distinct levels for C_N in the post stall region are clearly seen, with the high level closer to the values from the rotor measurements. The high level is probably a stage where a suction peak still exists at the leading edge whereas the lower level corresponds to leading edge separation. The parameter(s) which trigger the jump between the two levels have not been identified uniquely but it could be due to a laminar separation bubble very close to the leading edge. During the rotor measurements there are indications of the two levels but over a much shorter α interval. The general experience with rotors having these airfoils is that different levels are often found both in the power curve and in the flapwise blade root bending moment curves.

Oscillating pitch experiments were carried out in order to study the stall hysteresis. The pitch activation was done by hand and thus neither pure sinusoidal, nor completely constant in amplitude. Data from a run with a 1 Hz oscillation corresponding to $k=0.07$ and with an amplitude of approximately ± 5 deg at 5,10,15,20,25 average pitch angle is shown in Figure 15.

5.3 CFD

Presently, three different CFD codes at Risø are used to analyze and explore the wind turbine aerodynamics. The first one is a 2D code based on the vorticity/streamfunction approach, Christensen [15], the second is a 2D/3D finite volume code, Sørensen [16], and the third one is the commercial code FIDAP which uses the finite element discretization principle.

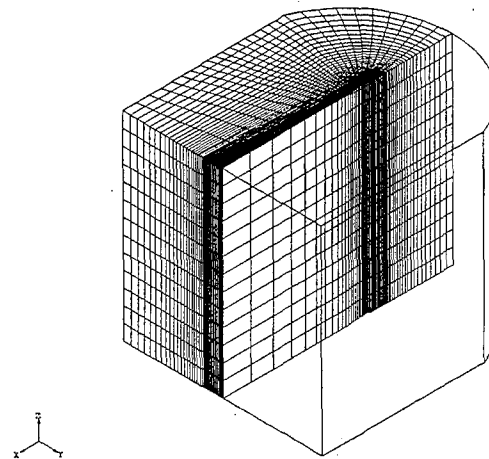


Figure 16. The grid used for the computations. The chord length is 1.0 and the spanwise length is 10.0. Axis of rotation is the y axis.

CFD calculations have been applied both on the overall rotor flow as well as on the flow over a single blade/airfoil, Madsen [17].

In principle two types of calculations are carried out; 1) turbulent flow computations at the full-scale Re. no. which typically is 1-4 million.; 2) laminar flow calculations with Re.

no. in the range from 1000-50000.

The first type of calculations have so far been used only on 2D problems to calculate stall and post stall characteristics of different airfoils. The accuracy of these computations are still not satisfactory, mainly due to an inadequate turbulence modelling for massive separation. 2D calculations are also performed on dynamic stall problems and such analyses seem to give valuable information for example when a measured time series of α , W on the rotor is used as input. The second type of calculations are used on more complex problems, typically 3D, where the real calculations of type one are too time consuming and require too much computer capacity. Although the results of the second type of calculations cannot be used directly, it seems that they can provide some insight into the different phenomena. Presently such calculations are used to study the interaction between stalled and attached flow regions along a blade and to study the influence of rotation.

As an example, the results of a calculation of type two is shown in the Figures 16, 17 and 18. The simulation is intended to show the mechanism of the influence of spanwise flow in combination with massive separation.

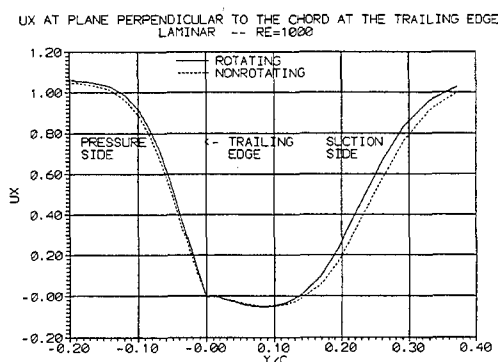


Figure 17. The u_x (chordwise direction) profile at a line through the trailing edge and perpendicular to the chord plane of the airfoil.

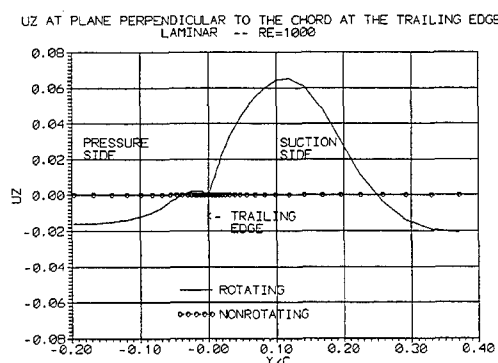


Figure 18. The u_z (spanwise direction) profile at a line through the trailing edge and perpendicular to the chord plane of the airfoil.

The problem is a rotating, straight, non-twisted blade at a constant geometrical angle of attack equal to 8 deg. along the blade, constant inflow velocity boundary conditions along the blade and zero spanwise velocities v_z at both ends, Figure

16. The computations were carried out, respectively, with and without the influence from the coriolis force field and in both cases without the centrifugal forces.

The velocity profile for the chordwise component u_x and for the spanwise component u_z at a line perpendicular to the chord plane and through the trailing edge, mid span on the blade, is shown in Figure 17 and Figure 18. A flow towards the tip is seen in the boundary layer, Figure 18, when the coriolis forces are included. The effect of this spanwise flow seems to be that the corresponding u_x profiles are slightly more steep. In other words, the thickness of the recirculating boundary layer decreases and an increase in lift must be expected. One of the problems by such simplified models is that the boundary conditions, which do not correspond to the real problem can distort the results. In the present case, the fixed u_z velocities at both ends of the model are non physical and will influence the spanwise pressure gradient.

6. STATUS ON ENGINEERING MODELS FOR 3D EFFECTS AND DYNAMIC STALL

The research on analyzing and exploring the phenomena behind 3D effects and dynamic stall has as one of the targets to end up with engineering models for inclusion in aeroelastic models. This is also the objective of a comprehensive EU-funded JOULE 2 project "Dynamic Stall and 3D effects" which is being conducted by several European research organizations in common.

The present status on these effects is that there is still a long way to go before reliable models based on thorough understanding of the phenomena have been developed although many aspects of dynamic stall have been described, McCroskey [18].

Concerning steady rotational 3D effects the first correction formula for conversion from 2D to 3D data have been presented, e.g. by Snell [19].

Dynamic stall models developed for use on helicopters on the basis of oscillating 2D airfoil measurements have been the starting point for wind turbine analysis including unsteady aerodynamics, Rasmussen et al. [20]. The blade of a helicopter in forward flight is undergoing large cyclic variations in flow conditions during each revolution, from fully attached flow to fully separated, followed by reattachment.

The semi-empirical dynamic stall models aims at describing by engineering methods the associated flow phenomena. As described by Ericsson and Reading [21] this is the dynamic delay of flow separation and the upstream movement of the separation point followed by the formation and downstream travel of the leading edge vortex. The rate of change of angle of attack is an important parameter for most of the corresponding events in this description of dynamic stall.

The engineering methods seem to give an accurate representation of the consecutive events obtained during such tests in wind tunnel (even for wind turbine airfoils), however the flow condition for a wind turbine blade is somewhat different. It does not undergo repeated cyclic variations including reattachment for each cycle, but rather operates around a partly stalled condition, as it was illustrated in Fig. 11. This modification of the series of events for the airfoil being part of a wind turbine blade might be an important issue. It is easily shown that the occurrence of stall induced vibrations in the simulation example in Fig. 3 is eliminated by inclusion of a simple time lag dynamic stall model, Øye [22] and/or assumptions on measured airfoil data corresponding

to those in Section 4.1, which reduces the problem of stall induced vibrations to a representation of dynamic stall and 3D effects. However, it is not in general possible to predict in details correct response characteristics by using such a simple model, Rasmussen et al. [20].

The open air field test and the wind tunnel tests described in the preceding sections offers an excellent opportunity to test the dynamic stall models separately, by running the model with the measured flow characteristics as input. Such a test is illustrated in Fig. 19, from where it is obvious that the measured dynamic stall loops are not well represented by the simulations. The deviation is further illustrated in Fig. 20, which gives the power spectral density of measured and simulated signals. The important difference is at the higher frequencies, where the energy is underestimated. Changing the time delay factor changes the shape of the hysteresis loops and the energy at 1p, but has little influence on the higher frequencies. As the output from the dynamic stall model "activates" the wind turbine structural dynamics, the correct energy at all frequencies is important in order to get correct overall turbine response.

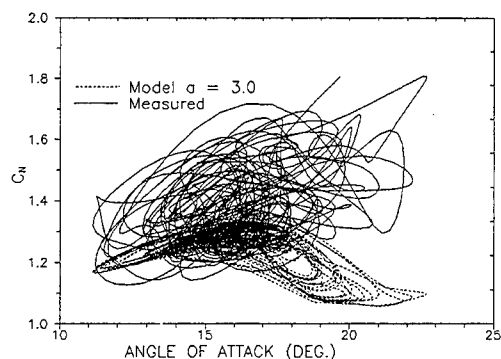


Figure 19. Comparison of the C_N vs. α_i curve simulated with a time delay stall hysteresis model and compared with experiment.

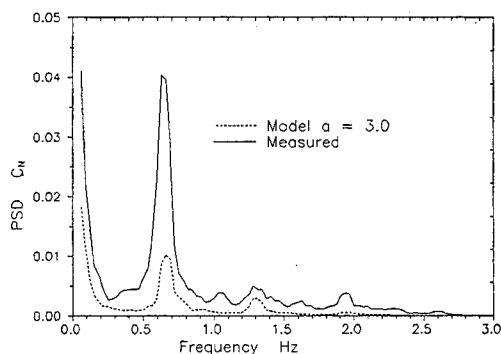


Figure 20. Comparison of the power spectra of C_N simulated with a time delay stall hysteresis model and compared with experiment.

Further analysis of the measured data have revealed that the rate of change of angle of attack indeed is an important parameter, and that the synthesized airfoil data method like the UTRC α, A, B method by Bielawa [23] or Gangwani [24], which uses the instantaneous incidence, angular velocity and

angular acceleration parameters to essentially curve fit measured data, can be tuned to reasonably match both hysteresis loops and power spectral densities. However, as these methods are based upon experiments and aiming at extrapolating these to real operational conditions, this suggests the application of Neural Networks to perform an equivalent procedure. This method has been applied by Kretz [25] to both the wind tunnel measurements from Section 5.2 and the rotating blade measurements in Section 4.1. The work until now seems to indicate that the reproduction of measured dynamic stall characteristics is quite good down to reasonable details and that the application of routines "learned" from wind tunnel experiments on the rotating blade measurements works with less accuracy, which on the other hand should reflect the rotational effects.

CONCLUSIONS

The analysis performed within this paper reveals that dynamic stall and three-dimensional aerodynamic effects are of major importance for wind turbine flow characteristics, and the prediction of loads in stall. Rotational blade airfoil section measurements correlated with measurements of local inflow conditions have given a unique opportunity for direct test of dynamic stall models, models for rotational sampling of turbulence and for investigations of the 3D aerodynamic effects. The rotor tests have been supported by corresponding stationary measurements with the blade in wind tunnel. The general tendency is that lift coefficients are increased in the 3D rotational case in particular at the inboard stations. The measured dynamic stall characteristics has a chaotic content that is not very well represented by semi-empirical models developed for helicopters. This could be due to differences in characteristics of the unsteadiness of the inflow where it has been shown that the stochastic part of the unsteadiness is high for a wind turbine.

ACKNOWLEDGEMENTS

The present research work has been funded by The Danish Ministry of Energy.

REFERENCES

- [1] Rasmussen, F. et. al.: "Investigations of Aerodynamics, Structural Dynamics and Fatigue on Danwin 180 kW". Risø National Laboratory, June 1988, Risø-M-2727.
- [2] Madsen, H.A.: "Measured Airfoil Characteristics of Three Blade Segments on a 19 m HAWT Rotor". Proceedings of the Ninth ASME Wind Energy Symposium, New Orleans, Louisiana, January 14-18 1990. pp. 55-62.
- [3] Butterfield, C.P.: "Three-Dimensional Airfoil Performance Measurements on a Rotating Wing. Proc. European Wind Energy Conference, Glasgow 10 - 13 July 1989. pp. 90-94.
- [4] Ronsten, G.: "Static Pressure Measurements on a Rotating and Non-Rotating 2.375 m Wind Turbine Blade - Comparison with 2D Calculations". FFA TN 1991-36, Stockholm 1991.

- [5] Hales, R.L.: "Dynamic Stall on Horizontal-axis Wind Turbines". Proc. European Wind Energy Conf., EWEC 91, Amsterdam. pp 34-39.
- [6] Bruining, A.: "Pressure Measurements on a Rotating Wind Turbine Blade on the en Air Rotor Research Facility of the Delft University of Technology". Proc. 1993 European Community Wind Energy Conference, Lübeck-Travemünde 8 - 12 March 1993. pp. 376-379.
- [7] Tangler, J.: "Status of the Special-Purpose Airfoil Families". Proceedings of the 2. IEA Symposium on Aerodynamics of Wind Turbines, Lyngby 21 -22 November 1988, Denmark. pp. 179-185.
- [8] Björck, A.: "Airfoil Design for Horizontal Axis Wind Turbines". Proceedings of the 2. IEA Symposium on Aerodynamics of Wind Turbines, Lyngby 21 -22 November 1988, Denmark. pp. 204-230.
- [9] Petersen, J.T.: "Kinematically Nonlinear Finite Element Model of a Horizontal Axis Wind Turbine". PhD thesis, Risø National Laboratory, DK- 400 Roskilde, July 1990.
- [10] Madsen, H.A.: "Aerodynamics of a Horizontal-axis Wind Turbine in Natural Conditions". Risø National Laboratory, September 1991, Risø-M-2903.
- [11] Abbott, H. and Doenhoff A.E.: "Theory of Wing Sections". Dover Publications 1959, New York.
- [12] Kristensen, L. and Frandsen S.: "Model for Power Spectra of the Blade of a Wind Turbine Measured from the Moving Frame of Reference". Journal of Wind Engineering and Industrial Aerodynamics, Vol. 10, 1982. pp 249-262.
- [13] Mann J. Krenk S.: "Fourier Simulation of a Non-Isotropic Wind Field Model". Paper no. 117/3/27. In proceedings of the 6th International Conference on Structural Safety and Reliability, ICOSSAR', Innsbruck, Austria, 9-13 August, 1993. Layer Turbulence
- [14] Kretz A., Madsen H.A. and Petersen J.T.: "Measured and Simulated Turbulence Compared at a Section of a Rotating Wind Turbine Blade". Risø-R-671, Risø National Laboratory, DK-4000 Roskilde, Denmark. March 94.
- [15] Christensen, H.F.: "AVorticity-Streamfunction Formulation for Turbulent Airfoil Flows". PhD Thesis, Risø-R-740. Risø National Laboratory, Roskilde, Denmark. December 1993.
- [16] Sørensen, N.: Private Communication. Risø National Laboratory, August 1994.
- [17] Madsen, H.A. and Rasmussen F.: "Application of a General Purpose Navier Stokes Code to Wind Turbine Flow Problems". Proc. 1993 European Community Wind Energy Conference, Lübeck-Travemünde 8 - 12 March 1993. pp. 387-390.
- [18] McCroskey, W.J.: "The Phenomenon of Dynamic Stall". NASA Technical Memorandum 81264.
- [19] Snel, H. et al. "Sectional Prediction of 3D-Effects for Stalled Flow on Rotating Blades and Comparison with Measurements". Proc. 1993 European Community Wind Energy Conference, Lübeck-Travemünde 8 - 12 March 1993. pp. 395-399.
- [20] Rasmussen et al.: "Response of Stall Regulated Wind Turbines - Stall Induced Vibrations". Final Report on JOULE 1 Contract No. JOUR-0076 for the Commission of the European Communities, Directorate General XII for Science, Research and Development. Risø-R-691. Risø National Laboratory, Roskilde, Denmark, June 1993.
- [21] Ericsson, L.E. and Reding, J.P.: "Fluid Mechanics of Dynamic Stall Part I. Unsteady Flow Concepts". Journal of Fluids and Structures, 1988, pp. 1-33.
- [22] Øye, Stig: "Dynamic Stall Simulated as a Time Lag of Separation". Proceedings of the Fourth IEA Symposium on The Aerodynamics of Wind Turbines. Edited by K.F. McAnulty. January 1991.
- [23] Bielawa, R. E.: "Synthesized Unsteady Data with Applications to Stall Flutter Calculations". Presented at the 31st Annual National Forum of The American Helicopter Society, Washington DC, May 1975
- [24] Gangwani, S.T.: "Synthesized Airfoil Data Method for Prediction of Dynamic Stall and Unsteady Airloads". Vertica Vol 8 No2 pp. 93-118, 1984
- [25] Kretz, A.: "Application of Neural Networks for the Representation of Dynamic Stall". In Danish. Internal Risø Report. February 1994.

A Viscous-Inviscid Interaction Model for Rotor Aerodynamics

A. Filippone, J.N. Sørensen
Department of Fluid Mechanics,
Technical University of Denmark
 DK-2800 Lyngby, Denmark

e-mail: afb@afm.dtu.dk
 jns@afm.dtu.dk

Abstract

This paper presents a numerical model for viscous-inviscid interactive computations of rotor flows. The model presented is fairly general, as it allows for both steady and unsteady calculations. The basic methodology for deriving the outer inviscid solution is a fully three-dimensional boundary element method. The inner viscous domain, i.e. the boundary layer, is described by the two-dimensional Navier-Stokes equations. For the interactive procedure a blade strip approach is used. The outer inviscid solution provides the distribution of induced velocities to be used as boundary condition for the Navier-Stokes solver. The outer solution is then updated with new boundary conditions, arising from the viscous effects. For unsteady flow calculations a time marching procedure is used. Some preliminary results are presented for the rotor blade of a wind turbine.

1 Introduction

The most used model for aerodynamic performance predictions of rotors and propellers is the combined blade-element/momentum theory which has undergone a long period of development since it was formulated by Glauert [1]. The advantage of this model is that it is easy to implement on a computer, it contains most of the physics of rotary aerodynamics, and it has proven to be accurate for the most common flow conditions and rotor configurations. The main drawback of the model is that it needs measured airfoil data, and that it is based on the assumption of axisymmetric flow conditions in which blade elements are assumed not to interact on each other. The problems of the model are most pronounced at operating situations far from the design point. For a wind turbine such a situation may e.g. occur when the wind changes direction. This causes periodic variations in the angle of attack and invalidates the assumption of axisymmetric flow conditions. Thus, both the airfoil characteristics and the wake are subject to complex 3-dimensional and unsteady flow behaviour.

In this respect the ultimate goal is to perform a full rotor calculation by using the 3-dimensional Navier-Stokes (NS) equations. Although such models are under development, a complete mesh-independent NS solution including both the boundary layer and the far-field wake demands prohibitive computing costs.

To achieve an affordable compromise between accuracy and computing costs we here present a model based on viscous-inviscid interaction. In the model the flow field is divided into an inviscid domain, represented by a Boundary Element Method (BEM), and a boundary layer region, modelled by a set of 2-dimensional Navier-Stokes equations, each representing a strip of the blade. The interaction is carried out through a coupling in which the Navier-Stokes solver, through the displacement thickness, provides an injection velocity for the BEM. The BEM, in turn, determines a velocity distribution on the edge of the viscous domain which is employed as boundary condition for the Navier-Stokes solver. In this respect the coupling is weak, but since the Navier-Stokes algorithm in itself represents both the viscous domain and a part of the inviscid near-field, the interaction mainly serves to provide induced velocities, arising from the

3-dimensionality of the inviscid far field, at the outer edge of the viscous domain. Therefore, a converged solution is expected to be obtained in a few iterative cycles. The main advantage of the interactive model is that the BEM and the Navier-Stokes algorithms are kept separate, such that existing codes (provided they are correctly validated) can be used straightforwardly, with only minor modifications on the boundary conditions.

This paper is organized as follows. In § 2 the boundary element model for the inviscid flow is presented. The Navier-Stokes equations for the viscous flow are derived in § 3 and the interaction technique discussed in § 4. In § 5 some results for the flow past the rotor of a wind turbine will be presented and compared to the experiments.

2 The Boundary Element Method

Consider a rotor blade subject to a rotational speed Ω and an uniform inflow \mathbf{q}_∞ with respect to an absolute (inertial) reference system. The flow around the blade can be analyzed in a blade-fixed reference system (Fig. 1). The time dependent inflow relative to the blade at a distance \mathbf{r} from the axis of rotation is given as

$$\mathbf{q}_{in} = \mathbf{q}_\infty + \Omega \times \mathbf{r}. \quad (1)$$

The time-dependent flow around the blade in the blade-fixed reference system is described in terms of the perturbation potential $\phi(\mathbf{x}, t)$

$$\mathbf{q}(\mathbf{x}, t) = \mathbf{q}_{in}(\mathbf{x}, t) + \nabla\phi(\mathbf{x}, t), \quad (2)$$

The perturbation potential satisfies the Laplace equation, due to the hypothesis of incompressible and initially irrotational aerodynamic flows

$$\nabla^2\phi = 0. \quad (3)$$

The domain of definition of the above equation is an open space, the exception being the vortex layers shedding from the blades trailing edges. From Green's second identity Eq. 3 can be transformed into

$$\phi^* = - \oint_{S_B} \left[\phi \frac{\partial G}{\partial n} - G \frac{\partial \phi}{\partial n} \right] dS - \oint_{S_w} \Delta\phi \frac{\partial G}{\partial n} dS, \quad (4)$$

with the Green's function G satisfying $\nabla^2 G = \delta(\mathbf{x} - \mathbf{x}^*)$, where $\delta(\mathbf{x} - \mathbf{x}^*)$ is the vector Dirac delta. The solution of this equation is the point source potential in unbounded space: $G = 1/4\pi \|\mathbf{x} - \mathbf{x}^*\|$. The boundary condition in Eq. 4 is assigned through the normal derivative of the potential, i.e. the tangential velocity at the blade surface.

Eq. 4 is the basis for constructing our numerical solutions. Further modelling is needed, though. This is related to the flow conditions at the trailing edge line. For incompressible flows the conservation of mass and the momentum across the wake yield, respectively,

$$\Delta \left[\frac{\partial \phi}{\partial n} \right] = 0, \quad (5)$$

$$\Delta p = 0. \quad (6)$$

Eqs. 5 and 6 are independent of the wake point and assumed to hold in the limit of the wake point approaching the trailing edge. In the original model, Morino [2] employed the following trailing edge condition

$$\Delta\phi_{te} = \Delta\phi_w, \quad (7)$$

which is an implicit assumption of Eq. 6 at the trailing edge. The condition of zero loading at the trailing edge is probably the best candidate to set a numerical Kutta condition.

2.1 Numerical Solution

The body surface is divided into quadrilateral panels. The collocation points are located at the centroids of the quadrilaterals. The potential is assumed to be constant over each panel and equal to its value at the collocation point.

A straightforward discretization of Eq. 4 leads to an implicit form of the potential discontinuity in which the potential is determined at each time-step, whereas the potential discontinuity at the trailing edge is taken from the previous time-step and treated with appropriate delays. The set of equations is assembled into the system

$$\mathbf{Y}\phi(t_n) = \mathbf{R}(t_n) + \mathbf{F}\Delta\phi(t_{n-1}), \quad (8)$$

where \mathbf{R} is the known term and \mathbf{Y} the influence matrix. The matrix \mathbf{F} provides the influence of the wake panels. A different discretization technique in which the potential discontinuity at each blade strip is treated explicitly, is presently under investigation.

For stationary solid bodies, the influence matrix \mathbf{Y} is constant and the matrix \mathbf{F} , which depends on the wake geometry, has to be computed at each time step (free wake analysis). By using a *wake-relaxation* method, the wake points are updated with the following Euler scheme

$$\mathbf{x}_w(t_n + \Delta t) = \mathbf{x}_w(t_n) + \mathbf{q}_w(t_n)\Delta t. \quad (9)$$

The calculation is started with a prescribed wake. Calculation of the influence coefficients and the solution of the system of equations are the two major computational tasks of this procedure.

2.2 A Trailing Edge Condition

The analytical condition of Eq. 7 can only be applied, strictly speaking, in a limiting case and takes a different form when a finite number of panels is used.

Preliminary calculations have shown that Eq. 7 does not work in rotating environments, since it leads to a *non-unique* pressure at the trailing edge line. This result is somewhat independent of the grid refinement. The inaccuracy is believed to be due to the effect of the numerical discretization, the prescribed wake panels, and the large radial velocities induced by the blade tip vortices. This anomaly can be observed better by sweeping and twisting the blade, while reducing its aspect-ratio. Other examples can be found in the literature, e.g. in Ref. [3] for marine propellers and in Ref [4] and [5] for helicopter rotors.

In a time-true solution $\Delta\phi$ can be updated from the previous time-steps by using the concept that the doublet strength is convected downstream.

The values of the doublet at the first row of wake panels can be found by requiring the following relationship at the generic blade strip i

$$\Delta\phi_i(t_n) = \Gamma_i(t_{n-1}), \quad (10)$$

where Γ_i is the section circulation. Since Eq. 10 does not assure that Eq. 6 is satisfied at the trailing edge, a Newton-Raphson scheme based on the iterative correction of the potential discontinuity is used. At each time-step a correction is introduced as

$$\Delta\phi^{k+1} = \Delta\phi^k + \mathbf{J}_k^{-1} \Delta P^k, \quad (11)$$

with

$$J_k = \left[\frac{\partial \Delta p}{\partial \Delta \phi} \right]^k, \quad (12)$$

leading to

$$\phi^{k+1}(t_n) = Y^{-1} \left[R(t_n) + F \Delta \phi^{k+1}(t_{n-1}) \right], \quad (13)$$

where k is the iteration count. The derivatives are approximated numerically by first-order finite differences. In general, one needs to know the trailing edge pressure P^{k-1} corresponding to the solution $\Delta \phi^{k-1}$. At the start of the procedure Morino's solution is assumed, e.g. a trailing edge pressure P^0 corresponding to $\Delta \phi^0$.

Since the above correction not always proved to converge, a different numerical treatment of the integral equation is under investigation. The iterative correction is time consuming.

2.3 Off-Body Analysis

The interaction model, as well as the free wake analysis, requires the calculation of a velocity distribution on specified grid points in order to provide appropriate outer boundary condition to the inner viscous flow solver. The calculation of grid-point velocities can be accomplished by taking the gradient of Eq. 4 with respect to the coordinates of point x^*

$$q^* = - \oint_{S_B} \left[\phi \frac{\partial}{\partial n} (\nabla G) - \nabla G \frac{\partial \phi}{\partial n} \right] dS + \oint_{S_w} \Delta \phi \frac{\partial}{\partial n} (\nabla G) dS. \quad (14)$$

In discrete form Eq. 14 can be written as

$$q(t) = b\chi + c\phi(t) + f\Delta\phi(t), \quad (15)$$

where the matrices b , c and f are influence coefficients depending only upon the geometry and the configuration of the wake.

2.4 Calculation of Surface Pressure

With the solution of the vector system (Eq. 8) the surface velocity potential is known at the panel control points. Derivation of the potential yields the surface velocity and hence the surface pressure. The surface velocity comes from the numerical solution of Eq. 4, whereas the pressure coefficient is deduced from the Bernoulli equation. For incompressible flows the pressure difference in the inertial reference system is determined from the following expression

$$\frac{p - p_\infty}{\rho} = \frac{1}{2} \left[(\nabla \phi)^2 + (\Omega \times r) \cdot \nabla \phi + \frac{\partial \phi}{\partial t} \right] \quad (16)$$

3 The Navier-Stokes Model

To handle separated boundary layers, which is the typical situation for e.g. stall-regulated wind turbines operating at high wind velocities, the Navier-Stokes equations are employed to describe the viscous flow field. Furthermore, to reduce computing costs, the computations will be carried out as a coupling between the 2-dimensional Navier-Stokes equations, with a later extension to a quasi 3-dimensional formulation, and the BEM algorithm. In order not to involve the pressure explicitly and to facilitate the implementation of boundary conditions in the interactive process the vorticity/stream-function form of the Navier-Stokes equations is employed. In Cartesian coordinates (x, y) the vorticity transport equation is written as

$$\frac{\partial \omega}{\partial t} - \frac{\partial}{\partial x} \left(\frac{\partial \psi}{\partial y} \omega \right) + \frac{\partial}{\partial y} \left(\frac{\partial \psi}{\partial x} \omega \right)$$

$$= \nu \frac{\partial^2}{\partial x^2} \left[\left(1 + \frac{\nu_t}{\nu} \right) \omega \right] + \nu \frac{\partial^2}{\partial y^2} \left[\left(1 + \frac{\nu_t}{\nu} \right) \omega \right], \quad (17)$$

where t is time, ν is the kinematic viscosity, and the Reynolds stresses are modelled by the eddy-viscosity ν_t . Denoting the velocity components in the x - and y -direction as u and v , respectively, the vorticity, ω , is defined as

$$\omega = \frac{\partial v}{\partial x} - \frac{\partial u}{\partial y}, \quad (18)$$

and the stream-function, ψ , is given by

$$u = -\frac{\partial \psi}{\partial y}, \quad v = \frac{\partial \psi}{\partial x}. \quad (19)$$

Combining Eqs. 18 and 19 a Poisson equations is obtained for ψ as follows

$$\frac{\partial^2 \psi}{\partial x^2} + \frac{\partial^2 \psi}{\partial y^2} = \omega. \quad (20)$$

A transformation from the Cartesian coordinates, (x, y) , to a boundary-fitted curvilinear mesh is carried out by introducing the general transformation

$$\xi = \xi(x, y), \quad \eta = \eta(x, y),$$

where (ξ, η) denotes the coordinates in the curvilinear system.

Applying the chain-rule of differentiation and making the variables dimensionless by the chord length, c , and the local freestream velocity, U_o , the governing equations 17 and 20 are formulated in strong conservative form as follows

$$\begin{aligned} & J^{-1} \frac{\partial \omega}{\partial t} - \frac{\partial}{\partial \xi} \left(\frac{\partial \psi}{\partial \eta} \omega \right) + \frac{\partial}{\partial \eta} \left(\frac{\partial \psi}{\partial \xi} \omega \right) \\ &= \frac{1}{Re} \left[\frac{\partial}{\partial \xi} \left(\alpha \frac{\partial(\epsilon \omega)}{\partial \xi} + \gamma \frac{\partial(\epsilon \omega)}{\partial \eta} \right) + \frac{\partial}{\partial \eta} \left(\beta \frac{\partial(\epsilon \omega)}{\partial \eta} + \gamma \frac{\partial(\epsilon \omega)}{\partial \xi} \right) \right], \end{aligned} \quad (21)$$

$$\frac{\partial}{\partial \xi} \left[\alpha \frac{\partial \psi}{\partial \xi} + \gamma \frac{\partial \psi}{\partial \eta} \right] + \frac{\partial}{\partial \eta} \left[\beta \frac{\partial \psi}{\partial \eta} + \gamma \frac{\partial \psi}{\partial \xi} \right] = J^{-1} \omega, \quad (22)$$

where $Re = U_o c / \nu$ is the Reynolds number, $\epsilon = 1 + \nu_t / \nu$, and J^{-1} is the transformation jacobian. The metric coefficients are defined as follows

$$\alpha = \frac{1}{J^{-1}} (x_\eta^2 + y_\eta^2), \quad \beta = \frac{1}{J^{-1}} (x_\xi^2 + y_\xi^2), \quad \gamma = -\frac{1}{J^{-1}} (y_\eta y_\xi + x_\eta x_\xi). \quad (23)$$

The streamfunction is now defined as

$$\frac{\partial \psi}{\partial \xi} = v^c, \quad \frac{\partial \psi}{\partial \eta} = -u^c, \quad (24)$$

where superscript c denotes contra-variant components

$$u^c = y_\eta u - x_\eta v, \quad v^c = -y_\xi u + x_\xi v. \quad (25)$$

The airfoil is embedded in a single-block C-grid, with ξ -coordinates defining the airfoil and the outer contour of the mesh. The transformation to the boundary-fitted mesh is performed such that $\Delta\xi = \Delta\eta = 1$. At the airfoil the usual no-slip condition is assumed, with the corresponding boundary conditions for ω and ψ obtained from their definition equations. At the outer boundary of the viscous domain the boundary conditions are provided from the inviscid BEM computation. Denoting by $\mathbf{U}_{Ie} = (U_{Ie}, V_{Ie})$ the inviscid velocity vector at the edge of the viscous domain the boundary conditions for the stream-function is determined from the following Neumann condition

$$\frac{\partial\psi_e}{\partial\eta} = -(y_\eta U_{Ie} - x_\eta V_{Ie}). \quad (26)$$

This condition is applied also at the outflow boundary. The vorticity is by definition zero at the edge of the viscous domain and at the outflow boundary the vorticity is assumed to be convected out by the local velocity field.

The eddy-viscosity is modelled by the Baldwin-Lomax turbulence model [6]. This model is a two-layer algebraic eddy-viscosity model, patterned after that of Cebeci-Smith, which avoids the need of finding the edge of the boundary layer and the displacement thickness.

The governing equations 21 and 22 are discretized by employing central difference expressions for the Laplacians and either simple upwinding or a so-called plus/minus upwinding for the convective terms [7]. The latter upwinding technique assures the solution to be second order accurate when a steady solution is obtained and formally first order accurate during the time-stepping. The discretization is carried out on a semi-staggered grid, with the vorticity located on cell-centers and the streamfunction on cell-vertices. The time-stepping is performed by an ADI technique. The coupling between Eqs 21 and 22 is performed as a predictor-corrector scheme, where the momentum equation is employed as the predictor and the Poisson equation for the streamfunction acts as the corrector.

In the present work the interaction has only been carried out between the BEM and the described 2-dimensional Navier-Stokes algorithm. To take into account rotational effects and spanwise flow in the boundary layer, a quasi 3-dimensional model will be implemented later. This model is based on approximating the 3-dimensional Navier-Stokes equations by the following expressions (see [8])

$$\frac{\partial}{\partial z}\left(\frac{u}{\Omega z}\right) \simeq 0, \quad \frac{\partial}{\partial z}\left(\frac{v}{\Omega z}\right) \simeq 0, \quad \frac{\partial w}{\partial z} \simeq 0, \quad (27)$$

where z denotes the spanwise distance, measured from the axis of rotation, Ω is the rotational speed, and w is the spanwise velocity component. As the model not yet has been employed in combination with the BEM, no further details will be given here.

4 The Viscous-Inviscid Interaction

The fully three-dimensional geometry is divided into strips (blade elements) along the span. The blade tips are excluded from the interaction. At each blade-element the flow field is split into two overlapping domains. The inner domain is extended to include all possible viscous effects. In general, there is no problem in capturing the boundary layer, but if the inner domain is large, it might include one or more wake spirals. This may happen in the case of a hovering rotor or a wind turbine operating at high tip speed ratios, in which case a blade vortex interaction must be taken into account. The two domains of the blade strip are sketched in Fig. 2.

Assume that a complete three dimensional solution of the BEM has been computed. A velocity distribution \mathbf{U}_{Ie} (outer boundary condition for the viscous flow) is then computed from Eq. 14. For each blade-element we next perform a Navier-Stokes calculation with the outer boundary condition given and the the boundary conditions on the blade surface determined from the no-slip condition.

The Navier-Stokes equations are solved by a time stepping method and yield a surface injection velocity distribution. The convergence of the method is ensured by the time-marching procedure. Note that the viscous and inviscid velocities are the same at the matching surface and that the displacement thickness and the updated injection velocity are determined from the Navier-Stokes algorithm. The

injection velocity, which is the proper inner boundary condition for the BEM at the next iteration, is given as follows

$$V_b = \frac{1}{\rho} \frac{d}{ds} (\rho U_{Iw} \delta^*), \quad (28)$$

where δ^* is the displacement thickness and the index 'w' denotes that the velocity is evaluated at the wall.

The advantages of the interactive procedure can be summarized as follows:

1. The BEM solves for a fully three-dimensional flow and accounts for the main rotational effects at a lower cost than a full three-dimensional Navier-Stokes calculation on the entire domain.
2. The BEM and Navier-Stokes codes are kept separate, thus interaction only occurs from the point of view of the boundary conditions.

5 Preliminary Results

The test case is the experimental wind turbine rotor blade described in Ref. [9]. The blade is untapered, untwisted, with constant chord $c = 0.5$ m, radius $r = 5.0$ m; it has constant cross section given by the airfoil NLF(1)-416. The blade length is 4.4 m from the root to the tip. In the experimental case the blade was rotating at 80 rpm. We have considered a uniform wind speed of $W = 8$ m/s. The Reynolds number for the NS solver has been taken equal to 10^6 . Fig. 4 shows the result at the spanwise section $0.7r$. The results of our viscous-inviscid interaction are compared with the experimental three-dimensional field data, and the pure inviscid solution taken from the boundary element method.

The BEM has been run with a grid 25×15 (750 panels) and two wake spirals (300 panels on the wake). The Navier-Stokes grid is 206×45 (9270 grid points). The outer boundary condition on the NS is given on the external C-contour (296 points). The mesh is based on a first-guess angle of attack (Fig.3). The result presented is a double sweep BEM + NS.

6 Conclusions and Perspectives

It has been shown how in principle the interaction between a BEM solver and a Navier-Stokes solver can be performed on a rotating blade. The progress in the development of this methodology has been hampered by some fundamental difficulties in the BEM. The circulation computed by the BEM with the Kutta condition of Eq. 7 is not enough to provide the correct lifting characteristics to the blade strip, whereas the iterative condition has not been fully validated (the result shown in Fig. 5 is less accurate than a pure 2-D inviscid calculation). Some difficulties in performing the VII have been identified when reducing the grid size. Problems of convergence may also occur. As the Navier-Stokes solver requires the appropriate circulatory flow, the interaction seems to be of increasing difficulty with the decreasing grid size. However, a small grid size is strategic in order to assess the validity of such a procedure over a pure two-dimensional calculation. The Kutta condition has to be solved efficiently in presence of the blowing velocity. Once this problem has been overcome, the next step is to perform a strong interaction, by sweeping between BEM and NS until convergence. The use of a quasi-three-dimensional Navier-Stokes model is the final goal.

Acknowledgements

The authors wish to thank J.H. Walther, Dept. of Fluid Mechanics, TUDenmark, for providing the grid generator used for the Navier-Stokes solver. This research has been partially supported by CIRA spa, Italy. Dr. P. Renzoni and A. Visingardi are gratefully acknowledged for the many useful discussions.

References

- [1] H. Glauert. *Propeller Theory*. in Durand, Aerodynamic Theory, 1936.
- [2] L. Morino and C.C. Kuo. Subsonic Potential Aerodynamics for Complex Configurations: A General Theory. *AIAA J.*, Vol. 12(2):pp. 191-197, Feb 1974.
- [3] J.E. Kerwin, S.A. Kinnas, J.T. Lee, and W.Z. Shih. A Surface Panel Method for the Hydrodynamic Analysis of Ducted Propellers. *ASME Transactions*, Vol. 95:pp. 93-122, 1987.
- [4] Y.J. Lee and J.K. Yang. A Panel Method for Arbitrary Moving Boundaries Problems. *AIAA J.*, Vol. 28(3):pp. 432-438, 1990.
- [5] L. Morino, M. Gennaretti, U. Iemma, and F Mastroddi. Boundary Integral Transonics for Wings and Rotors. *Aerotecnica Missili e Spazio*, pages pp. 52-61, Jun 1992.
- [6] Baldwin B. S. and H. Lomax. Thin Layer Approximation and Algebraic Model for Separated Turbulent Flows. *AIAA Paper*, 78-257, 1978.
- [7] J. N. Sørensen and Ta Phuoc Loc. High-order Axisymmetric Navier-Stokes Code: Description and Evaluation of Boundary Conditions. *Int. J. for Num. Meth. in Fluids*, Vol. 9:1517-1537, 1989.
- [8] J. N. Sørensen and D. N. Sørensen. A quasi 3-dimensional Airfoil Model. In *Proc. of the Seventh IEA Symp. on the Aerodynamics of Wind Turbines*, DTU, Lyngby, 1994.
- [9] A. Bruining, G.J.W. van Bussel, G.P. Corten, and W.A. Timmer. Pressure Distributions from a Wind Turbine Blade; Field Measurements Compared to 2-Dimensional Wind Tunnel Data. Technical report, Institute for Wind Energy, Technical University of Delft, The Netherlands, Aug 1993. IW-93065R.

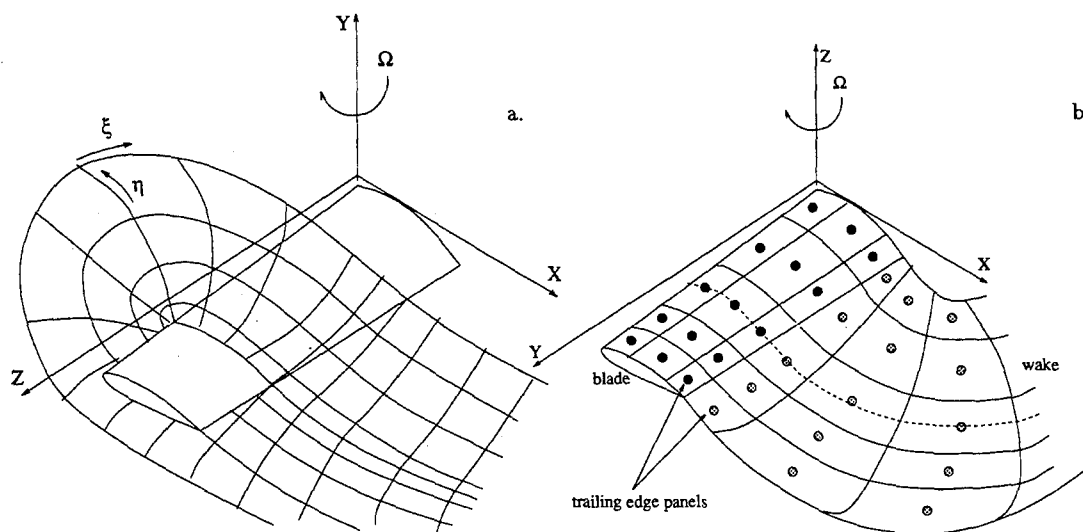


Figure 1: Reference systems .a.) and panel arrangement for the BEM b.)

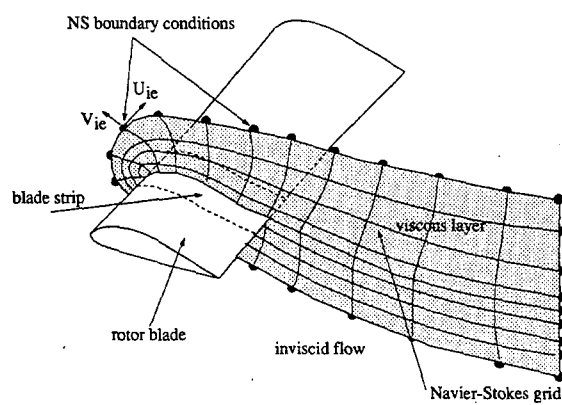


Figure 2: The Viscous and Inviscid Overlapping domains.

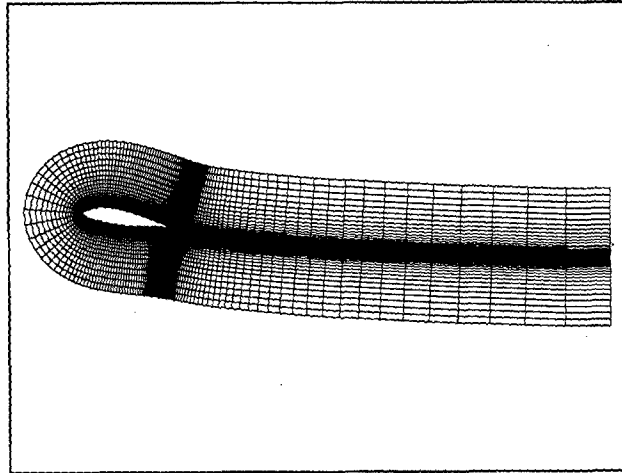


Figure 3: The Navier-Stokes Grid.

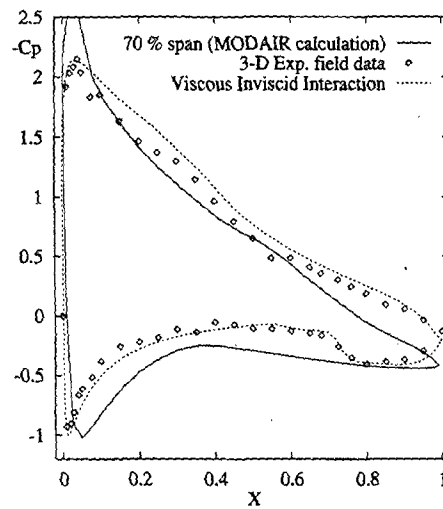


Figure 4: Surface pressure distribution for the NLF rotor blade at 70% span. The VII is compared with the inviscid solution (obtained by using an iterative Kutta condition and the experimental 3-D field data).

Investigation of the Yawed Operation of Wind Turbines by means of a Vortex Particle Method

S.G.Voutsinas, M.A.Belessis and K.G.Rados
National Technical University of Athens,
Department of Mechanical Engineering, Fluids Section,
P.O. Box 64070, 15710 Zografou, Athens, Greece

1. SUMMARY

A fully three-dimensional non-linear aeroelastic numerical investigation of the response of horizontal axis wind turbines during yawed operation was carried out. The numerical tool used, consists of a time-marching method based on the coupling of an unsteady free-wake vortex particle model and a 3D beam-type structural model. The investigation led to a complete data base of numerical results concerning the Tjaereborg wind turbine for which extensive full scale measurements of very good quality exist. Among the points that were given particular attention are: the effect of the root vortex, the coupling with the shear of the inflow and the tower effect on the dynamics of the blades. Herein the most significant results are presented and discussed.

2. DYNAMICS OF WIND TURBINES IN YAW AND MODELLING

The operation of wind turbines in yaw constitutes a special case of dynamic excitation that consists of a combination of different mechanisms. As a whole this combination leads to a non-linear response that is not fully understood basically because of its close connection to three-dimensional effects on one hand and dynamic stall on the other. Due to its frequent appearance especially in cases of non-flat terrain applications, yawed operation is of particular importance from the design point of view. It certainly affects the performance (energy production) as well as the availability of the wind turbines.

As in all physical problems, the most appropriate methodology for a better understanding, is a combination of measurements and theoretical calculations. Because the corresponding experiments are difficult to realize, the number of available complete data bases is small. Even smaller is the number of campaigns that someone could rely on during his theoretical/numerical investigations. Fortunately, in Denmark an extensive campaign of high quality full scale measurements taken from the 2MW wind turbine at Tjaereborg. This campaign covered a wide range of cases with dynamic inflow effects. Some of them were made available to us. Based on these data, we carried out our numerical study (Ref 1).

In most cases the existing theoretical work on the subject, concerned mainly the evaluation and improvement of engineering tools of rather simplified structure such as the blade element model (Ref 2). The reason is clear: In practice only aeroelastic calculations leading to load spectra of wide range make sense. This type of calculations are extremely time consuming so any complication in the modelling would render the work more a research than a design procedure. More elaborate theoretical models however do exist (Ref 3-7). They were developed rather recently as tools for applied research. In their basic features, they are all variants of the panel or boundary element method, differing the one from the other in

what concerns the modelling of the wakes of the blades. Following closely the developments made in the past for helicopters in forward flight, the aerodynamic models for wind turbines are classified into prescribed and free-wake models. No doubt that free-wake models are more suitable to give a detailed understanding of the different excitation mechanisms related to yaw. This is due to the complexity of the case of yawed operation. In particular, as the blade rotates fluctuations of the local angle will result load vibrations, that can be significant especially if the incidence enters the stalling envelope of the corresponding airfoil. These fluctuations of the incidence are due to: (a) the lateral component of the inflow velocity which has an alternating effect on the magnitude of the relative with respect to the blade velocity, (b) the shear of the inflow that acts on the axial velocity component, (c) the tower that decreases furthermore the axial velocity relative to the blade when it passes in front of it and (d) the structural flexibility that contributes to the velocity diagram the rate of deformation as an additional velocity term. These fluctuations of the velocity result a time variation of the circulation around the airfoil considered. In its turn this variation will lead to extra vortex emission in the wake that will feed back to the velocity diagram different induced velocity. Moreover if the amount of the shed vorticity varies, also the velocity field in the wake will vary which means that geometry of the wake becomes important. Several important cases could be mentioned: (a) Case of uniform inflow, no tower effects, no flexibility effects, (b) Case of sheared inflow, no tower effects, no flexibility effects, (c) Case of uniform inflow, with tower effects, no flexibility effects, (d) Case of sheared inflow, tower effects included, no flexibility effects, and (e) Case of sheared inflow, tower effects and flexibility effects included.

Based on the above remarks, it is easy to see that during yawed operation strong aerodynamic and aeroelastic interactions take place that justify the choice of elaborate models and in particular free-wake models. In this sub-class of free-wake models, we can distinguish the potential approach that considers the wake as a surface of discontinuity (Ref 6), the vortex-filament models that represent the wake by a set of thin vortex filaments (Ref 4,5) and the vortex particle model that represents the wake as an ensemble of blobs that carry vorticity (Ref 7). The model that was used in the present work is a later version of the GENUVP code also used and outlined in Ref 7. The difference consists of the aeroelastic coupling with a beam type structural model and a three-dimensional wind simulator. It corresponds to a computational environment that supports the research carried out on Aerodynamics at NTUA.

In brief GENUVP is defined along the following guidelines:

According to Helmholtz's decomposition theorem (Ref 8) the velocity field is made up of an irrotational part

representing the disturbance due to the presence of the solid boundaries and a rotational part representing the disturbance due to the wakes. In order to determine the irrotational part a Neumann boundary value problem for the Laplace equation is solved. On the other hand the rotational part of the velocity field is determined directly as convolution of the vorticity contained in the wakes. As the fluid is assumed inviscid, there is no link between the irrotational and the rotational part of the velocity field. In order to bring these parts into contact, a link can be defined that models the vorticity emission process observed in real flows. Mathematically this link is based on the Kutta condition (more exactly on an appropriate formulation of Kelvin's theorem). The fulfilment of the Kutta condition, permits to define quantitatively the conversion of the bound-vorticity into free-vorticity. This mechanism constitutes the inviscid analog of the vorticity production process already existing in all the conventional aerodynamic models.

In the discrete formulation, singularity distributions are defined on all solid boundaries (sources on the nacelle and tower, dipoles on the blades) in order to generate the potential part of the flow, whereas the wakes of the blades are approximated by vortex particles that are continuously generated along the edges of the blades. Next these vortex particles are convected downstream by the flow. This is performed by solving the vorticity transport equations by means of a Lagrangian procedure.

In the sequel, the most important findings of this campaign are presented together with a concise presentation of the model. As a general conclusion one could say that the comparisons between predictions and measurements on one hand showed the robustness of the model and on the other hand its ability to reproduce in a consistent way the reality.

3. THE NUMERICAL METHOD

3.1 GENUVP: A Free-Wake Aerodynamic Model Based on Vortex Particle Approximations

GENUVP consists of a GENeralized Unsteady Vortex Particle computational tool that can perform unsteady calculations around a configuration consisted of N_B three-dimensional bodies B_k , $k=1...N_B$ that move independently the one from the other. Each component B_k , can be either *non-lifting* (as the nacelle and the tower) or *lifting* (as the blades), according to its operational characteristics. For the purposes of the present work the configuration of a wind turbine is formed by the tower and the blades as shown in Fig 1. Also in the same figure the convention regarding the basic operational characteristics such as the rotation speed of the turbine $\bar{\omega}$, the position of zero azimuthal angle and the inflow velocity.

Let D denote the flow field and S its boundary. According to Helmholtz's decomposition theorem, the velocity field $\bar{u}(\cdot; t)$ can be given the form (Ref 9):

$$(1) \quad \bar{u}(\bar{x}; t) = \bar{U}_\infty(\bar{x}; t) + \bar{U}_\omega(\bar{x}; t) + \nabla\phi(\bar{x}; t), \quad \bar{x} \in D, \quad t \geq 0$$

where $\nabla\phi(\cdot; t)$ represents the irrotational part of the flow, $\bar{U}_\infty(\cdot; t)$ is the inflow velocity and $\bar{U}_\omega(\cdot; t)$ is a div-free field induced by the free vorticity. For an incompressible fluid, $\nabla\phi(\cdot; t)$ is included basically to account for the non-entry boundary conditions. Because $\phi(\cdot; t)$ is harmonic, it can be represented by source and/or dipole distributions defined on S (Ref 10). Dipole distributions are used to generate lift on solid

boundaries and surface vorticity on vortex sheets whereas sources are used in order to give the displacement generated by the thickness of the bodies. In order to reduce the computational cost, the blades are considered to be lifting surfaces, i.e. of zero thickness. Therefore they are represented solely by dipole distributions. Source distributions were used only for the non-lifting tower.

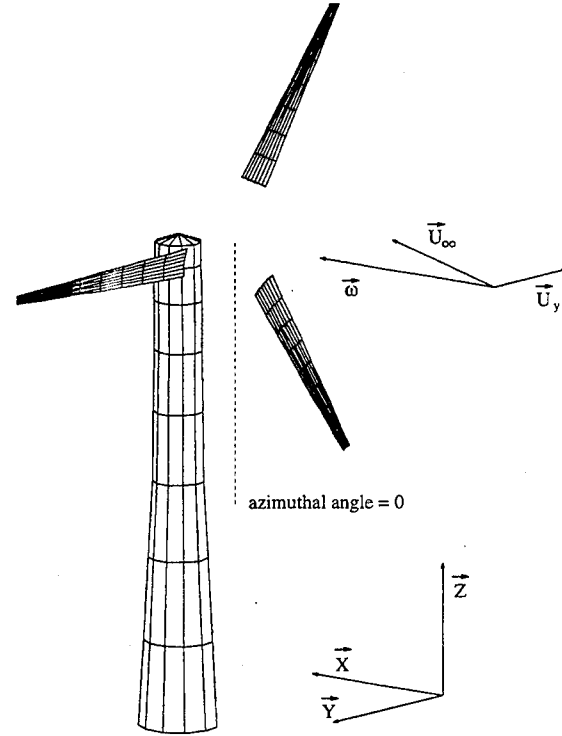


Figure 1: The configuration of a Horizontal Axis Wind Turbine

In the case of a wind turbine, S will comprise the solid boundaries S_k , $k=1...N_B$ of the different components as well as the wakes S_{wk} , $k=1...N_B-1$ shed by the N_B-1 blades (The tower is set last in the list of components. Moreover index w is used to designate quantities defined on the wakes). Thus,

$$(2) \quad \partial D \equiv S = \bigcup_{k=1}^{N_B} S_k + \bigcup_{k=1}^{N_B-1} S_{wk}$$

For an inviscid fluid, a wake can be represented either by means of a dipole distribution, and thus included in the irrotational part of the flow field, or as a vorticity carrying (vortex) sheet in which case it will appear in $\bar{U}_\omega(\cdot; t)$ (Ref 11, 8). This dual interpretation of a wake permits us to have the following hybrid formulation:

The numerical model is defined as a time marching algorithm. In fact the computations follow the gradual generation of the wakes, as part of the response of the wind turbine to all the different external excitations. During a time step of the scheme, first the wakes that were generated up to that time, i.e the *old* or *far parts* S_{wk}^* , $k=1...N_B-1$, are convected downstream leaving a gap in the near vicinity of the shedding body. Next this gap is filled by the *new* or *near part* of the wakes S_{wk}

(Fig 2). In GENUVP the near-wakes are represented as strips on which dipole distributions are defined. On the contrary the far-wakes are represented as spatial distributions of vorticity. This means that as time passes, the model treats the wakes within different physical contexts. In particular, at the end of each time step as the near wake is convected it becomes part of the far-wake. In other words the dipoles of the near-wakes are transformed into vorticity. That is why the whole scheme is termed hybrid. The passage from the "potential" interpretation to the "vortical" can be reasoned qualitatively, as being part of the deformation process that the wakes will undergo. A more rigorous justification is given below.

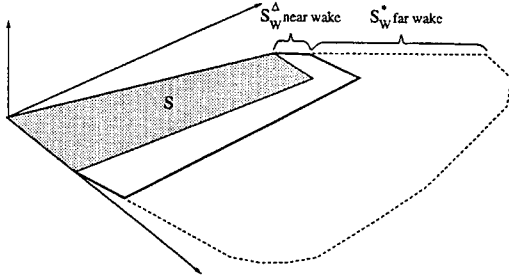


Figure 2: The hybrid modeling of a wake

The potential interpretation considers a wake $\Sigma(t)$ to be a moving surface on which the potential of the flow and the tangential to $\Sigma(t)$ velocity component are discontinuous (for incompressible fluids the normal to $\Sigma(t)$ velocity remains continuous).

This means that $\Sigma(t)$ can be represented by a dipole distribution $\mu(\cdot; t)$. Let $\vec{x} = \vec{x}_\Sigma(\xi; t)$, $\xi = (\xi^1, \xi^2) \in A \subset \mathbb{R}^2$, $t \geq 0$ denote the Lagrangian representation of $\Sigma(t)$. Then: $\mu(\xi; t) = -[[\Phi]](\xi; t)$ and $[[\vec{u}_\mu]](\xi; t) = \nabla_\Sigma \mu(\xi; t)$ where $[[\cdot]](\cdot; t)$ denotes jump on $\Sigma(t)$ (Fig 3). The evolution of $\Sigma(t)$ is determined by its equation of motion as defined by the mean velocity $\vec{U}_m(\cdot; t)$ on $\Sigma(t)$ and the zero pressure jump condition obtained by applying Bernoulli's equation to the two faces of $\Sigma(t)$:

$$(3a) \quad \frac{d\vec{x}_\Sigma(\xi; t)}{dt} = \vec{U}_m(\vec{x}_\Sigma; t)$$

$$(3b) \quad \frac{\partial [[\Phi]]}{\partial t}(\vec{x}_\Sigma; t) + U_m(\vec{x}_\Sigma; t) \cdot [[\vec{u}_\mu]](\vec{x}_\Sigma; t) = 0$$

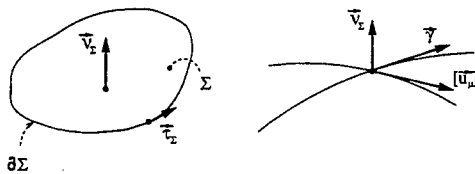


Figure 3: Definition of surface vorticity on a vortex sheet

Condition (3b) can be recast in Lagrangian form to give the

material conservation of $\mu(\cdot; t)$, equivalent to Kelvin's theorem:

$$(4) \quad \frac{d_m [[\Phi]](\xi; t)}{dt} = \left[\frac{\partial}{\partial t} + (\vec{U}_m(\vec{x}_\Sigma; t) \cdot \nabla_\Sigma) \right] [[\Phi]](\xi; t) = 0$$

Note that the superficial material time derivative is defined with respect to the mean velocity $\vec{U}_m(\cdot; t)$. (3b) also yields an evolution equation for the intrinsic surface vorticity $\vec{g} = N\vec{\gamma}$ where $\vec{\gamma} = \vec{\nabla}_\Sigma \wedge [[\vec{u}_\mu]]$, $\vec{\nabla}_\Sigma$ is the unit normal to Σ and N its metric. Because this equation is similar to the well known Helmholtz evolution equation for the vorticity, $\vec{g}(\cdot; t)$ is identified as part of the spatially distributed vorticity $\vec{\omega}(\cdot; t)$ (Ref 12). In case Σ is open, in addition to $\vec{g}(\cdot; t)$, there is also a line term defined along the boundary $\partial\Sigma$ of Σ . Summarizing, for a vortex sheet $\Sigma(t)$, the generalized vorticity is defined as follows:

$$(5) \quad \vec{\omega}_\Sigma(\vec{x}; t) = \nabla \wedge \vec{u}_\mu(\vec{x}; t) = \underbrace{\delta_\Sigma(\vec{x} - \vec{x}_\Sigma) \cdot \nabla \mu(\vec{x}_\Sigma; t) \wedge \vec{\nabla}(\vec{x}_\Sigma; t)}_{\text{surface vorticity}} + \underbrace{\delta_{\partial\Sigma}(\vec{x} - \vec{x}_{\partial\Sigma}) \mu(\vec{x}_{\partial\Sigma}; t) \vec{\tau}(\vec{x}_{\partial\Sigma}; t)}_{\text{line vorticity}}$$

where $\delta_\Sigma(\cdot)$ and $\delta_{\partial\Sigma}(\cdot)$ denote the surface and line Dirac functions defined on the interior and the boundary of $\Sigma(t)$ respectively and $\vec{\tau}(\cdot, t)$ denotes the unit tangential to $\partial\Sigma$ vector (Fig 3). Note that if $\mu(\cdot; t)$ is constant then there is no surface term and the line vorticity is reduced to a closed vortex filament along $\partial\Sigma$. This situation appears in the case of piecewise constant dipole distributions which is in fact the choice made in GENUVP for thin lifting surfaces.

According to the above analysis, $\Phi(\cdot; t)$ will be represented by means of: a source distribution $\sigma(\cdot; t)$ defined on the tower, bound dipole distributions $\mu_k(\cdot; t)$ defined on the blades and free dipole distributions $\mu_{wk}(\cdot; t)$ defined on the near-wakes of the blades S_{wk}^Δ . As explained in the sequel $\sigma(\cdot; t)$, $\mu_k(\cdot; t)$ and $\mu_{wk}(\cdot; t)$ constitute the unknown degrees of freedom at every time step. It is noted that also unknown is the exact geometry of the near-wakes S_{wk}^Δ .

In order to determine the unknown fields of the problem there are two types of conditions available:

- the kinematic conditions and more specifically the non-entry conditions on all the solid surfaces, and the conditions of material motion of the near-wakes S_{wk}^Δ (as in (3a))
- the dynamic conditions, i.e. the requirement of zero pressure jump throughout the vortex sheets S_{wk} (as in (3b) or (4)).

Let $\vec{U}_{Bk}(\cdot; t)$ denote the rigid body velocity distribution defined on S_k and \vec{v} the unit normal to S_k . Then the non-entry condition for $\vec{x} \in S_k$ and $k=1 \dots N_B$ takes the form:

$$(6) \quad \frac{\partial \Phi}{\partial \nu}(\vec{x}; t) = \vec{v}(\vec{x}; t) \cdot \left[\vec{U}_{Bk}(\vec{x}; t) - \vec{U}_m(\vec{x}; t) - \vec{U}_\omega(\vec{x}; t) \right]$$

In the discrete formulation, $\sigma(\cdot; t)$, $\mu_k(\cdot; t)$ and $\mu_{wk}(\cdot; t)$ are defined with reference to surface grids of boundary elements. Let S_k^e , $e=1 \dots E_k$ and S_{wk}^e , $e=1 \dots E_{wk}$ denote the elements of S_k and S_{wk}^Δ respectively (E_k and E_{wk} are the number of elements that form S_k and S_{wk}^Δ). The boundaries of these elements will be denoted by ∂S_k^e and ∂S_{wk}^e (Fig 4). Assuming that $\sigma(\cdot; t)$,

$\mu_k(\cdot; t)$ and $\mu_{wk}(\cdot; t)$ are piecewise constant, the aerodynamic discrete degrees of freedom will be their intensities at the boundary elements $\sigma_e(t)$, $\mu_k^e(t)$ and $\mu_{wk}^e(t)$ respectively.

The application of (6) to the centers \bar{x}_{cp}^e of the elements covering the solid boundaries S_k , gives the discrete equations

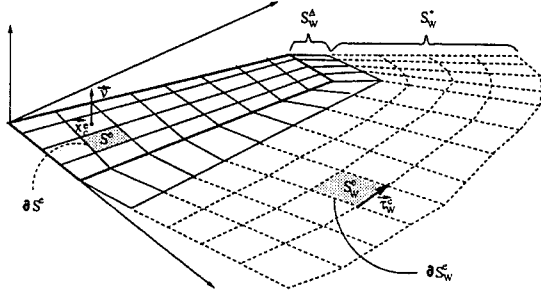


Figure 4: The notations of the boundary element grids

wherefrom $\sigma_e(t)$ and $\mu_k^e(t)$, $e=1 \dots E_k$ are determined. As regards $\mu_{wk}^e(t)$, they are determined by applying (4) along the so called *emission lines*, i.e. the parts of the border of the blades wherefrom the wakes originate. These lines usually include the trailing edge, the tip and the root of the blades. The leading edge is also included in the case of stall. This option was left apart throughout the work presented herein. By interpreting (4) as a Kutta condition, it results that at all boundary elements S_{wk}^e of the near-wakes, $\mu_{wk}^e(t)$ must be set equal to the corresponding bound dipole intensity, i.e. the dipole intensity of the element on S_k that is adjacent to S_{wk}^e . As regards the geometry of the near-wakes S_{wk}^A , this is defined by the Lagrangian kinematics. According to (3a), S_{wk}^A will be convected by the local velocity.

The last point to be considered, concerns the rotational part of the flow $\bar{U}_\omega(\cdot; t)$ and in particular the process of transforming the dipole distribution of the near-wake into vorticity. Let, $\bar{\omega}_w(\cdot; t)$ denote the vorticity contained in the far-wakes of all blades. Then

$$(7) \quad \bar{U}_\omega(\bar{x}_0; t) = \int_{D_\omega(t)} \frac{\bar{\omega}_w(\bar{x}; t) \wedge (\bar{x}_0 - \bar{x})}{4\pi |\bar{x}_0 - \bar{x}|^3} dD(\bar{x})$$

where $D_\omega(t)$ denotes the support of the free vorticity

$$(8) \quad \bar{\omega}_w(\bar{x}; t) = \nabla \wedge \bar{U}_\omega(\bar{x}; t) = \sum_{k=1}^{N_B-1} \sum_{e=1}^{E_{wk}} \sum_{n=1}^{NT-1} \delta_{\sigma_{wk}^{(n)}(\bar{x} - \bar{x}_{wk}^{(n)})} \mu_{wk}^{(n)e} \bar{\tau}_w^{(n)e}(\bar{x}_{wk}^{(n)})$$

according to (5). In (8), the three summations run respectively the blades, the elements on each near-wake strip and the time steps already passed. Also note that only line-vorticity terms are included. This is due to the piecewise approximation of the dipole distributions $\mu_{wk}(\cdot; t)$. Although it is not strictly said, (8) suggests that the wakes are interpreted as a collection of panels that formed all the near-wake strips throughout the time interval $[0, NT \cdot \Delta t]$ (where NT is the current number of

time steps). There is enough evidence both theoretical and experimental, showing that the evolution of a vortex sheet is unstable in time. This is due to the singular character of the velocity field that it requires the calculation of Cauchy type integrals. Consequently some kind of smoothing is required. A method to accomplish stable and consistent calculations is to introduce particle approximations for the vorticity (Ref 13,14,15). In this case,

$$(9) \quad \bar{\omega}_w(\bar{x}; t) = \sum_{j \in J(t)} \bar{\Omega}_j(t) \cdot \zeta_e(\bar{x} - \bar{Z}_j(t))$$

where $\bar{\Omega}_j(t)$ and $\bar{Z}_j(t)$ denote the intensities and positions of the vortex particles, $J(t)$ the index set for the vortex particles and $\zeta_e(t)$ the cut-off function that ensure the necessary smoothing. By selecting (Ref 16):

$$(10) \quad \zeta_e(r) = \frac{1}{\epsilon^3} e^{-\left(\frac{r}{\epsilon}\right)^3}$$

$\bar{U}_\omega(\cdot; t)$ takes the form:

$$(11) \quad \bar{U}_\omega(\bar{x}; t) = \sum_{j \in J(t)} \frac{\bar{\Omega}_j(t) \wedge [\bar{x} - \bar{Z}_j(t)]}{4\pi |\bar{x} - \bar{Z}_j(t)|^3} f_e(\bar{x} - \bar{Z}_j(t))$$

where

$$(12) \quad f_e(r) = 1 - e^{-\left(\frac{r}{\epsilon}\right)^3}$$

Thus instead of calculating the geometry of the vortex sheets and the dipole distributions they carry, we follow the evolution of the vortex particles defined by the following dynamic equations:

$$(13) \quad \begin{cases} \frac{d\bar{Z}_j(t)}{dt} = \bar{u}(\bar{Z}_j; t) \\ \frac{d\bar{\Omega}_j(t)}{dt} = (\bar{\Omega}_j(t) \cdot \nabla) \bar{u}(\bar{Z}_j; t) \end{cases} \quad j \in J(t)$$

Equations (13) concern the evolution of the far-wakes. As the near parts still retain their character as vortex sheets their determination is different. Let \bar{U}_{em} denote the mean velocity at a point \bar{X}_{em} along the vorticity emission line of a lifting body. The geometry of the near part of the corresponding wake S_{wk}^A is determined kinematically through the following relation:

$$(14) \quad \bar{X}^A = \bar{X}_{em} + \Delta t \cdot \bar{U}_{em}$$

where $\bar{X}^A - \bar{X}_{em}$ denotes the width of S_{wk}^A in vectorial form (Fig 5). Finally the intensity of the dipole distribution of S_{wk}^A is determined by means of the dynamic condition (4). According to (4) and because the model uses piecewise constant dipole distributions, $\mu_{wk}^e(t)$ must be set equal to the bound dipole intensity of the element adjacent to the e_{wk} near-wake element.

Due to the time dependent character of the problem, the wakes as well as the vortex particles they include in their far parts, will be constructed gradually. This means that vortex particles will be created as the near parts of the wakes evolve. In order to make this approach compatible with the dynamics of vortex

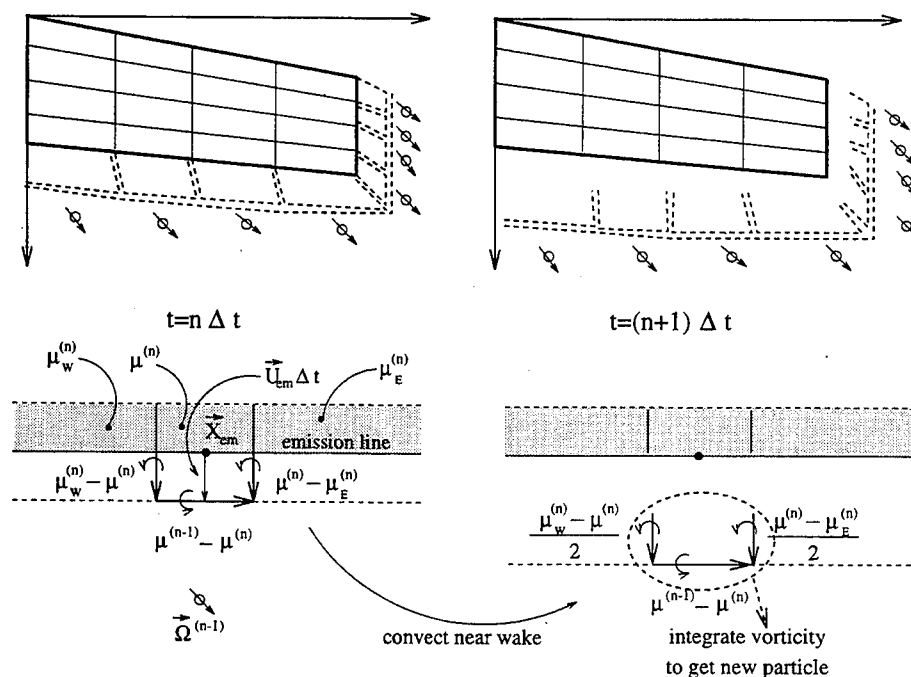


Figure 5: The mechanism of vortex particles generation

sheets, $\bar{\Omega}_j(t)$ and $\bar{Z}_j(t)$ are defined as follows:

$$(15) \quad \bar{\Omega}_j = \int \bar{\omega}_w dS \quad \bar{Z}_j = \int \bar{\omega}_w \wedge \bar{x} dS$$

In the above relations, the integration covers for every vortex particle the surface of an element of the near part of the wake considered.

THE FLOW CHART OF THE GENUVP MODEL

For every time step ($t = n \cdot \Delta t$)

A. POTENTIAL CALCULATIONS

$$\bar{u} = \bar{U}_\infty + \nabla \Phi + \nabla \Phi_w^\Delta + \bar{U}_w$$

0. Initialize S_w^Δ and Φ_w^Δ (through the values of μ_w along the emission lines of the lifting bodies)

Iterative schemes for the near wake:

1. Calculate Φ (H-fulfilment of non-entry boundary conditions)
2. Calculate the emission velocities \bar{U}_{em} along the emission lines
- 3.1 Correct S_w^Δ
- 3.2 Correct $[\Phi]_w^\Delta$ (H-fulfilment of the Kutta condition)
4. Check for convergence: $\delta[\Phi]^\Delta < \epsilon$
5. FIRST OUTPUT: Force and velocity calculations

B. VORTICITY CALCULATIONS

1. Create new vortex particles
2. SECOND OUTPUT: Wake structure and velocity profiles in the wake
3. Move and deform all the Vortex Particles
- 3.1 Calculate the velocities and deformations induced at the Vortex Particle locations
- 3.2 Check for Vortex-Solid surface interaction and correct accordingly
- 3.3 Produce the new far-wake

The calculations of loads. The calculation of the unsteady loads on the rotor blades was based on Bernoulli's equation. For a thin lifting surface this equation takes the form:

$$(16) \quad \frac{\partial[\Phi]}{\partial t}(\bar{x}, t) + \bar{U}_m(\bar{x}, t) \cdot [\bar{u}](\bar{x}, t) = - \frac{[p](\bar{x}, t)}{\rho}$$

where $-[\Phi] (= \mu)$ denotes the surface dipole distribution, $\bar{U}_m(\bar{x}, t)$ denotes the mean velocity, $[\Phi](\bar{x}, t) = \nabla[\Phi]$ denotes the tangential velocity discontinuity and $[p](\bar{x}, t)$ the pressure jump. In the discrete problem equation (16) is applied to the control points. Due to the piecewise approximations used for the dipole distributions, $[\bar{u}]$ is calculated through a zero-order difference scheme (Ref 12). Let $[p]_k^e, e=1(1)E_k, k=1(1)N_B$, denote the calculated values of the pressure jump. Integrating over the corresponding elements, the calculation of the loads is obtained as follows:

$$\text{for every element, } \bar{F}_k^e(t) = \bar{v}_k^e \cdot [p]_k^e \cdot |S_k^e|$$

$$\text{for every body, } \bar{F}_k(t) = \sum_{e=1}^{N_B} \bar{v}_k^e \cdot [p]_k^e \cdot |S_k^e|$$

where $|S_k^e|$ denotes the area of S_k^e . In addition to these loads and because of the thin-wing approximation that was made for the blades, the suction force is also added.

Due to the essentially inviscid character of the modelling adopted, it can only predict the "inviscid" part of the loading. The rest, i.e. the loads due to viscous effects must be superimposed. In this connection an approximate a-posteriori scheme, similar to the one used by the classical strip theory was applied. This scheme is based on the calculation of the radial distribution of the effective angle of attack. Next the drag coefficient C_D is estimated from given airfoil data. Finally the drag forces are integrated over radial strips and thus an account of viscous effects is obtained.

3.2 The Aeroelastic Coupling

Measurements as well as prior numerical investigations, clearly showed that flexibility effects are important in the case of yawed operation. In order to take them into account GENUVP was coupled with the structural dynamics of the rotor. To this end, the beam approximation was used to give the flexibility characteristics of the blades. The coupling between the structural and the aerodynamic part of the problem was realised in the time domain by performing consecutively aerodynamic and structural time steps. Two coupling interfaces were defined: the first communicates to the structure the loads as calculated by the aerodynamic model, and the second communicates the blade deformations together with their rates, to the aerodynamic. Because of the different character that the aerodynamic and structural part have, the stability restrictions for the two parts are not the same. In fact the structural part is much stiffer demanding a time step smaller than that used for the aerodynamic calculations. Consequently, in order to cover the time interval corresponding to one aerodynamic time step, several structural steps must be performed. In all cases reported herein, the calculations were realised by repeating the sequence: one aerodynamic step followed by several structural steps. Such a marching scheme signifies the choice of an explicit time integration for the aeroelastic problem. More elaborate and in particular implicit schemes can be easily defined. They will require an iterative exchange of information between the aerodynamic and structural part that should converge before the calculations proceed in time. There is no doubt that such a scheme would increase the computational cost a fact we took seriously into account because of the number of runs that had to be made (Further details can be found in Ref 17).

4. RESULTS

The main body of the tests concerns the Tjaereborg wind turbine for which extensive full scale measurements exist of very good quality. The machine is upwind oriented and pitch regulated. The diameter of the 3-bladed rotor is 60 meters, rotating at 22RPM. In order to have a clear idea of the different effects, the following simulations of yawed operation were performed: (a) uniform inflow, no tower effects, no flexibility effects, (b) sheared inflow, no tower effects, no flexibility effects, (c) uniform inflow, with tower effects, no flexibility effects, (d) sheared inflow, tower effects included, no flexibility effects, and (e) sheared inflow, tower effects and flexibility effects included. In the sequel a representative part of the results obtained, is given.

As an introduction to the presentation of the results we thought useful to start with a brief discussion on the basics of the yawed operation of wind turbines. Let us assume that the rotation is clockwise and the yaw angle positive. This corresponds exactly to what Fig 1 shows. The first and most critical point is the role of the lateral component \vec{U}_y of the inflow velocity. Fig 6 shows two typical velocity diagrams for azimuthal angles 0° and 180° , in the case of uniform inflow. These two azimuth positions constitutes the positions where the effect of the lateral velocity due to yaw reaches its peaks. The difference is clear. At 0° azimuthal angle \vec{U}_y is added to the circumferential component of the effective velocity \vec{U}_ϕ . On the contrary at 180° azimuthal angle \vec{U}_y is subtracted. In fact this additive/subtractive role is conserved respectively throughout the lower/upper half of the rotation of the blade. As a result, \vec{U}_ϕ will exhibit a periodic variation that results in an increase of the axial force in most of the lower part and a decrease in most of the upper part of the rotation. Fig 7

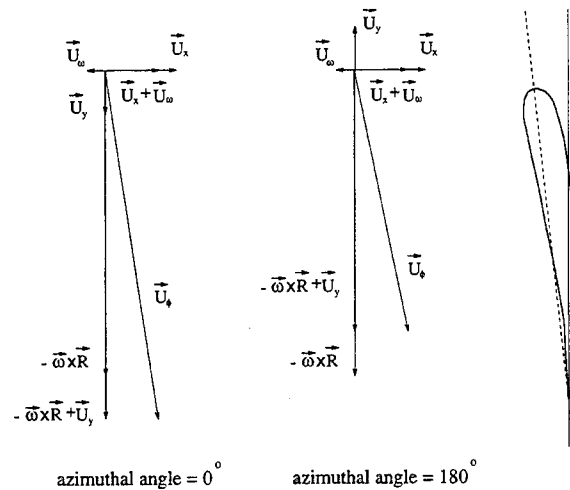


Figure 6: Typical velocity diagrams for 0° and 180° azimuthal angles

and 8 clearly show this effect. As expected, there is a phase shift so that the two peaks do not appear at azimuthal angles 0° and 180° . The phase shift is about 45° and is due to the fact that the wake of the turbine is inclined with respect to its axis. In fact there are two interacting mechanisms of excitation with 90° lag the one from the other. The first is due to the lateral velocity with peaks at azimuthal angles 0° and 180° and the second is due to the wake with peaks at azimuthal angles 90° and 270° . The fine tuning of the 45° phase shift is determined by the details of the configuration (e.g. the pitch, the twist distribution e.t.c). In Fig 8 the dependence on the value of the yaw angle is shown. As expected for larger yaw angles the amplitude of the fluctuation increases. For larger yaw angles, a second local fluctuation is seen around the azimuthal angle 270° as a result of a more intense interaction with the wake. In particular, most of the local fluctuation is due to the root vortex as shown in Fig 9. The effect of the root vortex is moderate and has to do with the fact that the design point of the turbine corresponds to inflow velocity equal to 9m/s. At higher velocity the intensity of the root vortex is expected to equally increase together with its influence on the axial forces. Because of the special significance of the root vortex, its placement is given in Fig 10b. Compared to the configuration of the wake in the case of zero yaw, a deviation with respect to the direction of the inflow velocity is remarked. In what concerns the calculations, this deviation is a direct consequence of the velocity deficit that changes the pitch angles along which the shedding of vorticity takes place. In our calculations, this is ensured by the freedom we give to the wake to deform in shape. It is noted that flow visualizations carried out by FFA revealed similar wake shapes.

Having the above remarks in mind we proceed with the discussion on the influence of the other parameters of the problem. A summary of results is given in Fig 11, where for different operational conditions, the variation of the flapping moment at root due to aerodynamic forces is given for yaw angles 0° , $+32^\circ$ and -32° . In Fig 11a, the ideal case with no-shear, no-tower and no-flexibility effects is shown giving a simple 180° phase shift in the azimuthal angle. In Fig 11b, the blades are treated as deformable beams. As seen in the figure, the result of the flexibility is the decrease of the amplitudes. In Fig 11c the effect of shear is examined. As expected for zero yaw, there is a peak at 180° azimuthal angle because the

inflow in the upper part of the rotation is larger in comparison to the inflow in the lower part. When this effect is coupled with yaw then the peak is shifted, of course differently for positive and negative yaw angles respectively. Again we have the superposition of two excitation mechanisms with phase lag of 180° . As a result not only a phase shift of the peak takes place but also a modification of the amplitude. More specifically, in the case of negative yaw, the sheared inflow acts as an amplifier for the peak whereas in the case of positive yaw it decreases it. In Fig 11d the flexibility effects are added. Again there is no significant remark to make. In Fig 11e the effect of the tower is examined. For a more clear vision of the tower effect in Fig 12 the azimuthal variation of the induced velocity in the axial direction is given for the whole span of one of the blades. As expected the tower will induce extra deficit around the zero azimuthal angle. Compared to the calculations without tower effects, it can be remarked that this effect is significant for a range of about 90° . Due to the rotation of the blades even at zero yaw, the tower effect is non-symmetric. This asymmetry becomes more pronounced when yaw is imposed. For positive yaw the minimum is shifted at an azimuthal angle of about 15° whereas for negative yaw, there is no real shift of the minimum but a distributed decrease for about 30° before the zero azimuthal angle. When flexibility effects are added to this case (Fig 11f), a distortion of the shape of the curves is noticed especially after the blade has passed the zero azimuthal angle. Fig 11g and 11h complete the results by adding shear to the inflow. There is no special comment to make except that the curves represent the result of the superposition of more than two excitation mechanisms on the rotor of the wind turbine.

In Fig 13 the predictions are compared against full scale measurements for four different yaw angles. The quantity considered is the flapping moment, which is important as regards the assessment of the structural robustness of wind turbines. In all cases the model reproduces accurately the form of the corresponding experimental curve. Also in terms of absolute values, there is a level difference which could be attributed to the difference between the processing followed for obtaining the series compared in the figure. More specifically, the inflow velocity used in the calculations is the result of averaging over 1min out of a 10min time series. No spatial variations were input at the inflow plane of the turbine as happens in reality. Also approximate is the estimation of the shear. Nevertheless there are some discrepancies that need further investigation. In the three cases of positive yaw, experiments have a bump just after 270° azimuthal angle. The code predicts only the bump in the case of the extreme yaw of 54° . This could be due to the pronounced influence of the root vortex, which according to Fig 8, should be small for much smaller yaw angles. This could mean that the bumps for the two smaller yaw angles are of different origin. Indeed the appearance of the bump for yaw angle 3° justifies such a possibility.

As regards the effect of the tower, it can be noticed that in the case of positive yaw, the low peak just after the 0° azimuthal angle, is predicted satisfactorily, even though there is a phase shift. On the contrary, at negative yaw the code fails to predict the peak as if the tower and yaw effects cancel each other.

5. CONCLUSIONS

During the investigation carried out on the yawed operation of wind turbines:

- a) an advanced prediction methodology was established,
- b) a detailed data-base was produced regarding the behaviour of a specific wind turbine.

According to the evaluation performed the following conclusions can be made:

- a) In general the predictions can be considered satisfactory both in quantitative and qualitative sense: the model gives values comparable to measurements and the behaviour of the wind turbine as revealed by the model is similar to the experimental one.
- b) However difference between measurements and calculations does exist giving hints for possible improvements. In this respect the following points are of interest:
 - The time-integration scheme used for the aeroelastic coupling could be made implicit.
 - The blades of the rotor should be turned to thick wings so as to get a better flow field and also to prepare the necessary input for viscous corrections.
 - In the case of thick blades, the coupling of the outer-inviscid region with an inner viscous layer could improve the flow predictions on the blades and consequently the prediction of the loads. This is true especially when stall occurs.

Acknowledgements

The present work was partially financed by the DG XII of the Commission of the European Union under the contract JOU2-CT92-0186 and JOU2-CT92-0113. The authors would like to thank Professor A.Panaras and Professor S.Tsaggaris for their assistance in diffusing the present work. Special thanks are addressed to Captain K.Giannopoulos and Lieutenant A.Petropoulos of the Greek Air Force for the help they provided to K.Rados.

References

1. Oye, S., "Tjaereborg wind turbine, First Dynamic Inflow Measurements", AFM Notak Vb-189, April 1991
2. Snel, H. and J.G., Schepers, "Investigation and Modelling of Dynamic Inflow Effects", in "European Wind Energy Conference Proceedings", March 1993, Paper H3, pp 371-375
3. Bussel, G.J.W., "The Use of the Asymptotic Acceleration Potential Method for Horizontal Axis Wind Turbine Rotor Aerodynamics", in "Wind Energy: Technology and Implementation", Proceedings of Amsterdam EWEC '91, Part I, October 1991, pp18-23
4. Gould, J. and Fiddes, S.P., "Computational Methods for the Performance Prediction of HAWTs", in "Wind Energy: Technology and Implementation", Proceedings of Amsterdam EWEC '91, Part I, October 1991, pp29-33
5. Pesmajoglou, S. and Graham, J.M.R., "Prediction of Yaw Loads on a Horizontal Axis Wind Turbine", in "European Wind Energy Conference Proceedings", March 1993, Paper H17, pp 420-423
6. Bereiss, S. and Wagner, S., "The Free Wake / Hybrid Wake Code ROVLM - A Tool for Aerodynamic Analysis of Wind Turbines", in "European Wind Energy Conference Proceedings", March 1993, Paper H18, pp

424-427

7. Voutsinas, S.G., Belessis, M.A. and Huberson, S., "Dynamic Inflow Effects and Vortex Particle Methods", in "European Wind Energy Conference Proceedings", March 1993, Paper H19, pp 428-431
8. Richardson, S.M. and Conrith, A.R.H., "Solution of three-dimensional incompressible flow problems", J. Fluid Mech., 82, 2, 1977, pp. 309-319
9. Batchelor, G.K., "An introduction to fluid dynamics", Cambridge University Press, 1967
10. Hunt, B., "The Panel Method for Subsonic Aerodynamic Flows: A Survey of Mathematical Formulations and Numerical Models and an Outline of the New British Aerospace Scheme", VKI Lecture Notes, 1980
11. Hess, J.L., "Calculation of Potential Flow about Arbitrary 3D Lifting Bodies", McDonnell Douglas Report, MDC J567901, 1973
12. Voutsinas, S.G., "Numerical Simulation of Three Dimensional Vortical Flows", NTUA report, 1994
13. Leonard, A., "Computing Three-Dimensional Incompressible Flows with Vortex Filaments", Ann. Rev. Fluid Mech., 17, 1985, pp. 523-559
14. Hoeijmakers, "Numerical Simulation of Vortical Flows, Introduction to Vortex Dynamics", VKI Lecture Notes, 1986
15. Smith, J.H.B., "Vortex flows in Aerodynamics", Ann. Rev. Fluid Mech., 18, 1986, pp. 221-242 (See also: Smith, J.H.B., "Modelling 3D Vortex Flows in Aerodynamics, Introduction to Vortex Dynamics", VKI Lecture).
16. Beale, J.T. and Majda, A., "Higher Order Accurate Vortex Methods with Explicit Velocity Kernels", J. Computational Physics, 58, 1985, pp.188-208
17. Belessis, M.A., Kouroussis, D.A., Voutsinas, S.G., "Development, Testing and Evaluation of an Advanced Aeroelastic Numerical Tool for Horizontal Axis Wind Turbines", NTUA report, 1994

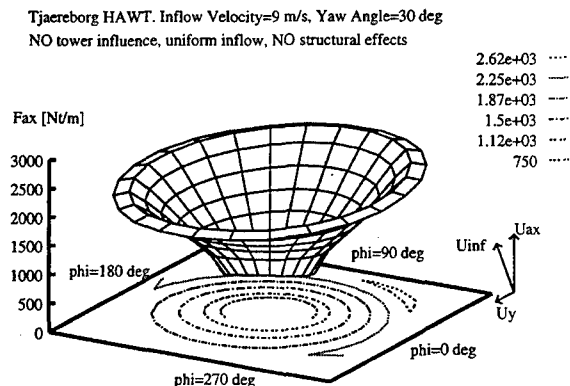


Figure 7: Radial distribution of the axial loading on the blade at several azimuthal positions ($\phi=0$: blade oriented to the ground)

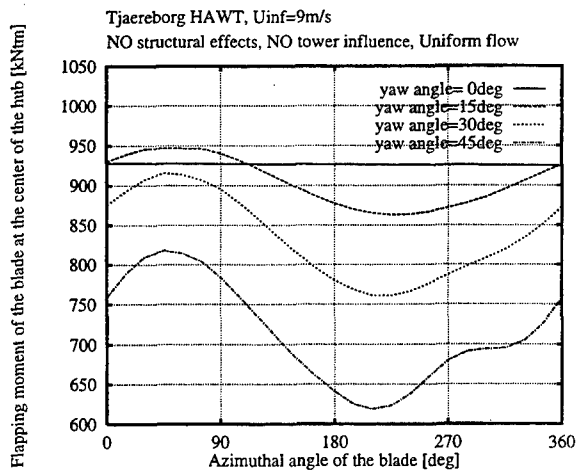


Figure 8: The effect of yaw angle in flapping moment variation

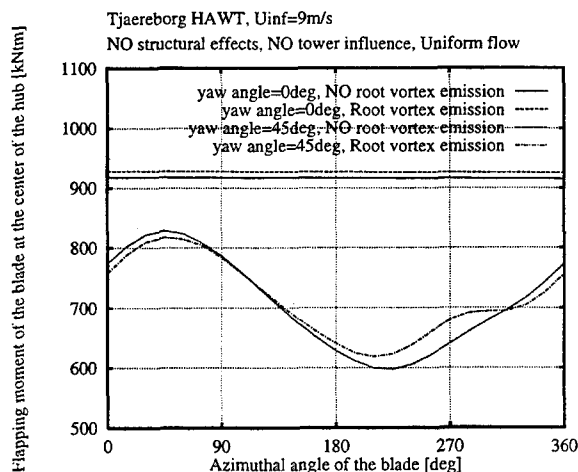


Figure 9: The influence of root vorticity emission

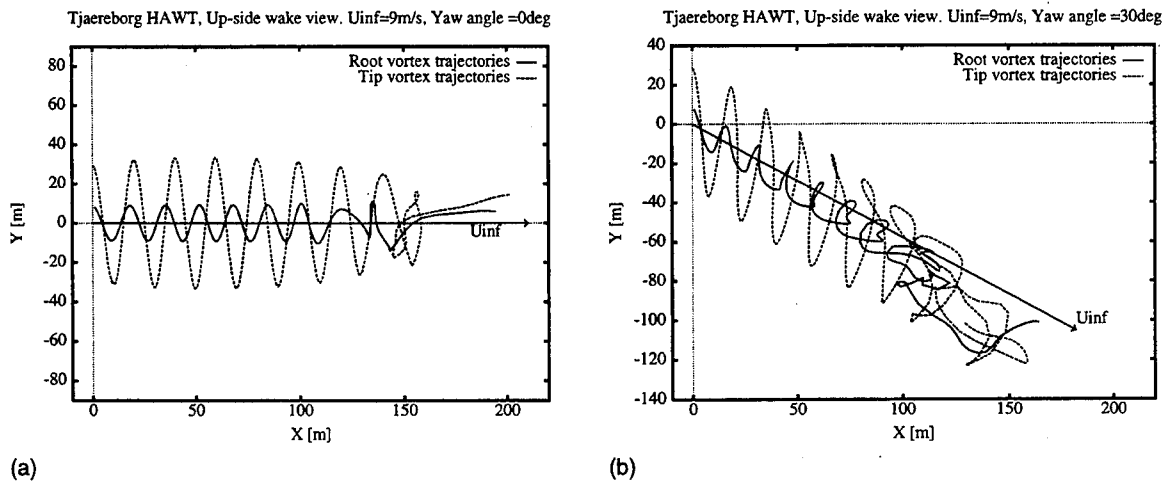
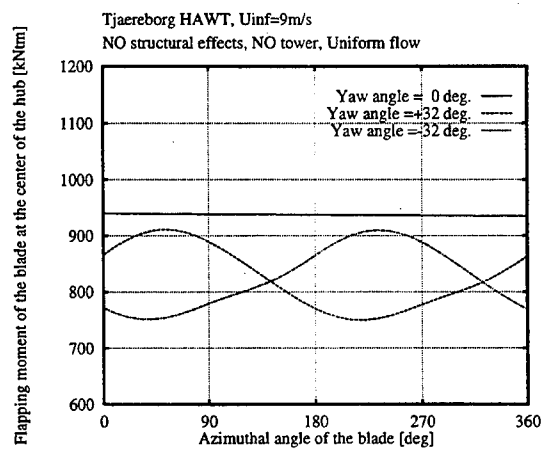
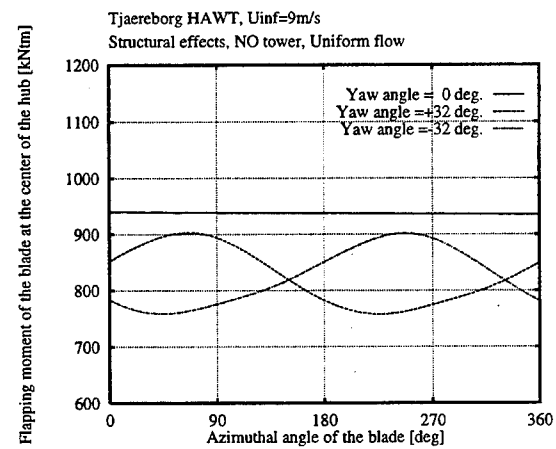


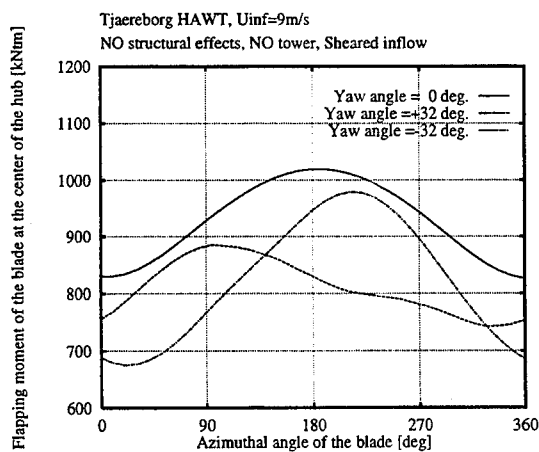
Figure 10: Influence of the yaw angle in the geometry of the wake



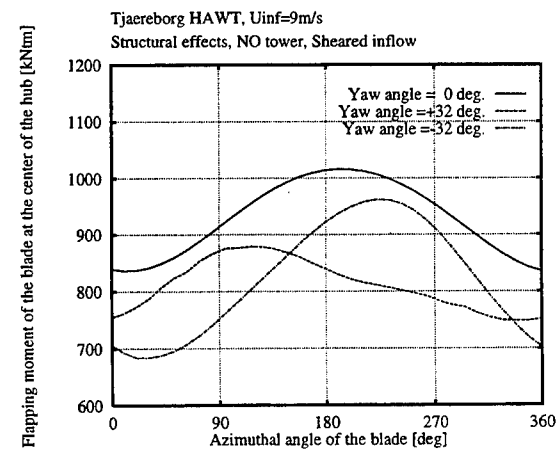
(a)



(b)

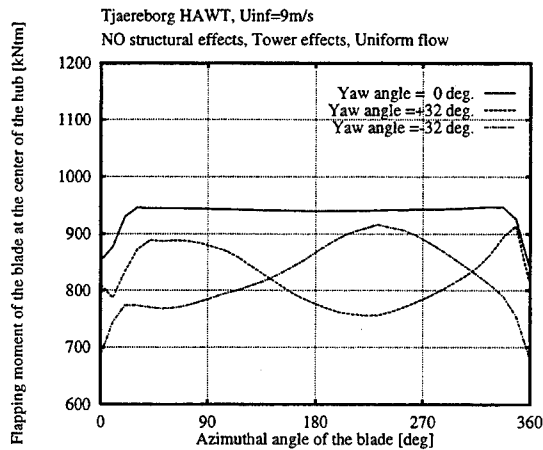


(c)

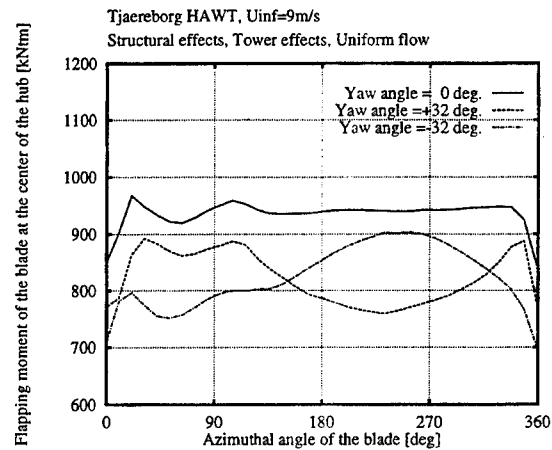


(d)

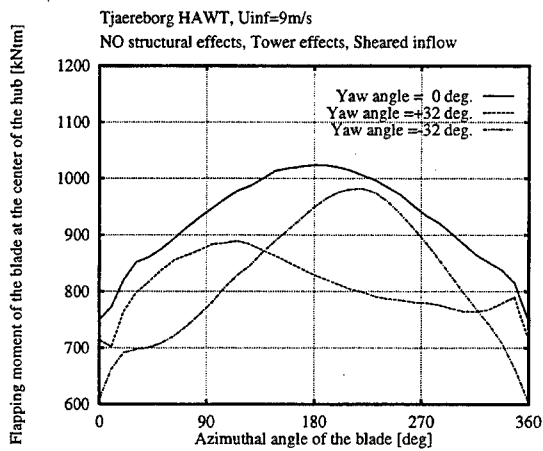
(for caption see next page)



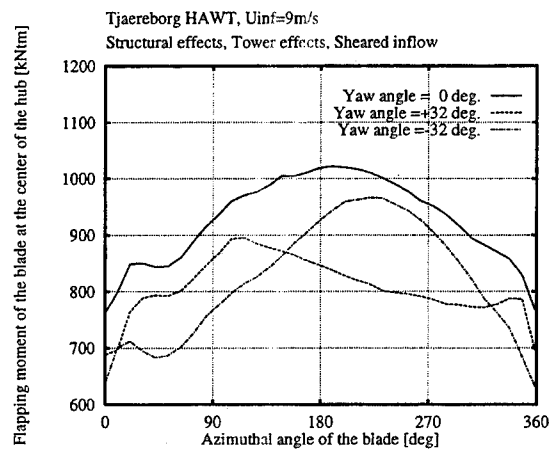
(e)



(f)

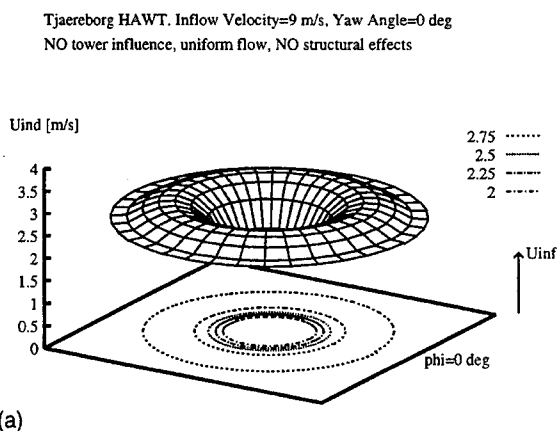


(g)

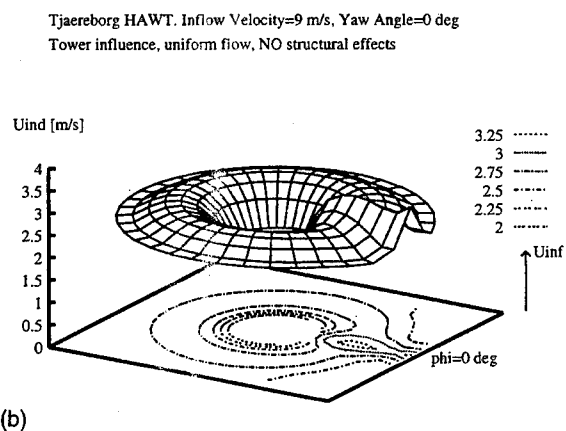


(h)

Figure 11: Effects of sheared inflow, tower existence and elastodynamic deformation on the loadings in yawed operation

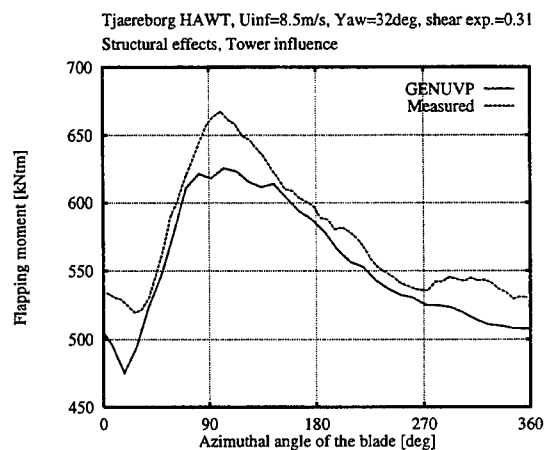


(a)

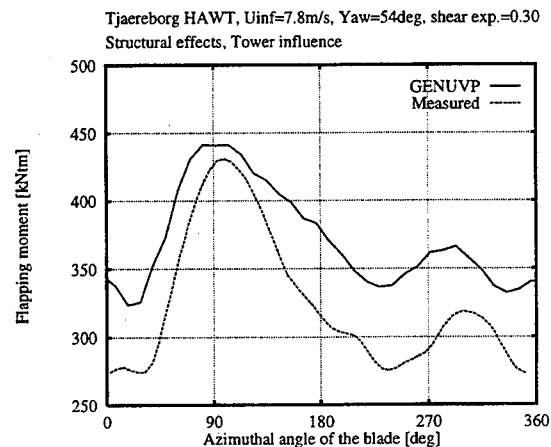


(b)

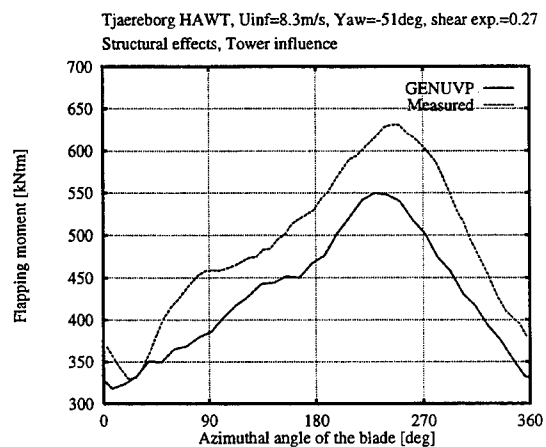
Figure 12: Radial distribution of the induced velocities on the blade at several azimuthal positions with and without tower influence. (phi=0: blade oriented to the ground)



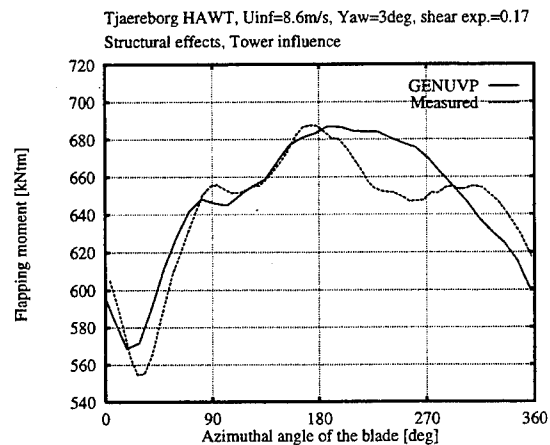
(a)



(b)



(c)



(d)

Figure 13: Loadings calculations for real cases of yawed operation

Méthodes de calcul aérodynamique appliquées aux rotors d'hélicoptères à l'ONERA

M. Costes, P. Beaumier, P. Gardarein, J. Zibi

ONERA, BP72, 92322 Châtillon Cedex, France

1 SUMMARY

This paper presents the aerodynamic methods which are used currently at the Applied Aerodynamics Department of ONERA for the computation of helicopter rotors in hover and forward flight. They cover a wide range of algorithms, from classical blade element theory to more complex unsteady three-dimensional methods, each of them being well adapted to deal with a particular problem related to the helicopter main rotor. Typical applications for blade loads and dynamics, wake geometry, pressure distribution, performance prediction and parametric optimisation are shown. Finally, the future trends in terms of CFD applications in the field of helicopter rotors at ONERA are given.

2 PRINCIPALES NOTATIONS

$\mu = \frac{V_\infty}{R\omega}$ paramètre d'avancement de l'hélicoptère

$FM = \frac{F_N}{P} \sqrt{\frac{F_N}{2\rho S}}$ figure de mérite du rotor

$\bar{Z} = \frac{100 F_z}{1/2 \rho S_p (R\omega)^2}$ coefficient de portance du rotor

$\bar{C} = \frac{100 C}{1/2 \rho S_p R(R\omega)^2}$ coefficient de couple du rotor

3 INTRODUCTION

La configuration particulière de l'hélicoptère, avec sa voilure tournante sustentatrice et propulsive, en fait un cas unique réunissant presque toutes les difficultés connues en aéronautique, aussi bien dans le domaine de l'aérodynamique subsonique et transsonique, que de la mécanique des structures et la mécanique du vol de l'appareil. Ceci explique pourquoi ce type d'appareil n'a véritablement connu son développement et son essor que près d'un demi siècle après l'avion à voilure fixe. Cette configuration est également la cause des limitations

principales de l'appareil (coût élevé, restriction du domaine de vol aux vitesses modérées, ...). En contrepartie, l'hélicoptère a une capacité unique de vol vertical et à très basse vitesse, ce qui explique son succès dans l'accomplissement de missions difficiles telles que la desserte des plateformes pétrolières, le travail aérien, l'évacuation sanitaire, ...

La complexité de l'hélicoptère se traduit naturellement par des difficultés au niveau de sa simulation numérique, et les méthodes de calcul aérodynamique utilisées dans les applications hélicoptère sont généralement en retard, au niveau de la complexité des équations résolues, par rapport aux modèles numériques utilisés pour les avions à voilure fixe ou les turbomachines. Cependant, l'un des caractères propres à la simulation de l'hélicoptère est la nécessité de maîtriser simultanément plusieurs disciplines scientifiques en raison de l'étroite interaction qui existe entre elles, si bien qu'il est nécessaire d'utiliser des algorithmes de calcul bien éprouvés pour effectuer un couplage entre ces modèles et représenter au mieux les phénomènes qui apparaissent sur l'appareil.

L'objectif principal de cette communication est de présenter les méthodes de calcul aérodynamique opérationnelles à l'ONERA dans les applications aux rotors d'hélicoptères. Dans une première partie, les particularités de l'écoulement sur l'hélicoptère sont présentées, en insistant davantage sur le rotor principal. La deuxième partie traite du rotor d'hélicoptère en vol d'avancement, pour lequel différentes méthodes de calcul sont utilisées suivant l'application visée. Ce sont une méthode de type élément de pale, capable de fournir une estimation des performances du rotor et de la cinématique de la pale, une méthode de calcul du sillage discrétisé par un réseau de segments tourbillonnaires, et une méthode de calcul tridimensionnel instationnaire par résolution de l'équation du potentiel complet des vitesses. La troisième partie traite du rotor d'hélicoptère en vol stationnaire, pour lequel on dispose soit d'une méthode élément de pale, soit d'une méthode de résolution de l'équation du potentiel avec représentation Lagrangienne des nappes tourbillonnaires. Dans une quatrième partie, l'application d'une méthode d'optimisation numérique à la définition de nouveaux rotors est présentée, illustrant ainsi l'utilisation d'une méthode de calcul hélicoptère à ce problème. Enfin, la cinquième et dernière partie conclut cette communication en présentant les perspectives

1 This work is supported by the French Ministry of Defence (STPA, DRET)

d'évolution de ces différentes méthodes et les nouvelles méthodes en cours de validation, dressant ainsi une perspective des possibilités d'utilisation des méthodes de calcul aérodynamique pour la définition et l'étude des rotors d'hélicoptères.

4 GENERALITES SUR LES HELICOPTERES

4.1 Introduction

La cellule de l'hélicoptère peut généralement être décomposée en trois éléments principaux : le fuselage, le rotor principal et le rotor arrière. Les rotors principal et arrière fournissent l'essentiel des forces aérodynamiques nécessaires à la sustentation de l'appareil. Le rotor principal en assure également la propulsion, par orientation de la force normale développée par le disque rotor, permettant aussi le pilotage en tangage et roulis de l'hélicoptère. Le rotor arrière, ou tout autre dispositif équivalent (fenestron, NOTAR, ...), est destiné à contrer le couple du moteur qui s'exerce sur le fuselage par réaction, et permet également le pilotage de l'appareil en lacet.

4.2 Mécanique du rotor principal

Le rotor principal est la partie aéromécanique la plus complexe de l'hélicoptère. En raison de la rotation des pales, les efforts aérodynamiques croissent de façon quadratique du centre à la frontière externe du disque rotor. Il en résulte l'apparition de contraintes mécaniques importantes au niveau des attaches de pale. L'introduction d'un vrillage négatif permet d'uniformiser la distribution des efforts en envergure. Cependant, la tenue mécanique des pales n'est rendue possible que par l'introduction d'articulations ou d'une souplesse concentrée entre le moyeu et les pales, afin d'atténuer ces efforts. L'introduction de l'articulation de battement a été une étape décisive dans le développement des hélicoptères. Elle permet à la pale de battre librement dans le plan formé par sa ligne quart de corde et l'axe de rotation du rotor principal. La combinaison du battement et de la rotation de la pale introduit alors un effort dans le plan de la pale (accélération de Coriolis), qui est annulé par l'introduction d'une articulation de traînée dans ce plan du disque rotor. En vol d'avancement, la dissymétrie de vitesse entre la pale avançante et la pale reculante crée une dissymétrie latérale de portance. Celle-ci est partiellement compensée par l'articulation de battement par effet gyroscopique (la pale monte du côté de la pale avançante et descend du côté de la pale reculante, diminuant ainsi les incidences locales en pale avançante et les augmentant en pale reculante). Une variation cyclique de la commande de pas permet alors d'équilibrer le disque rotor en roulis et de piloter l'hélicoptère par inclinaison du disque rotor. Ce

fonctionnement complexe du rotor principal fait que, pour des conditions de vol données de l'hélicoptère, la cinématique des pales est une inconnue supplémentaire, déterminée par l'équilibre des pales au niveau des articulations de battement et de traînée sous l'effet des efforts aérodynamiques et des efforts d'inertie, et par l'ajustement de la loi de commande de pas pour assurer les conditions de vol désirées. La tendance actuelle à remplacer des moyeux articulés, très complexes, par des moyeux de type "hingeless" ou "bearingless" où les articulations sont remplacées par une souplesse concentrée, complique encore le problème. Enfin, les pales se déforment sous l'effet des charges aérodynamiques et des efforts d'inertie, phénomène d'autant plus important que l'utilisation de matériaux composites se généralise. Les interactions entre l'aérodynamique et la dynamique de la pale peuvent donc avoir une importance prépondérante pour certaines conditions de vol, et dans ce cas il est indispensable de prendre en compte ce couplage aéroélastique de façon précise dans les calculs.

4.3 Aérodynamique du rotor principal

Les problèmes purement aérodynamiques qui apparaissent sur le rotor principal sont eux-mêmes très complexes. En premier lieu, les pales en rotation peuvent recouper leur propre sillage, avec notamment un tourbillon d'extrémité très intense dû à la concentration de circulation en extrémité de pale. Ceci perturbe fortement l'écoulement incident et peut induire des interactions pale-tourbillon, sources de bruit impulsif. Ce phénomène apparaît essentiellement à basse vitesse et en vol de descente, et est donc fortement pénalisant en approche et à l'atterrissage. L'influence du sillage du rotor est également très importante en vol stationnaire, car, n'étant convecté que sous l'effet de ses propres vitesses induites dans cette configuration de vol, il reste proche du disque rotor et conditionne fortement l'écoulement incident sur les pales. Ceci montre que, pour ces conditions de vol, une représentation très réaliste du sillage tourbillonnaire des pales doit être obtenue pour évaluer correctement les performances du rotor. En vol d'avancement, l'écoulement est instationnaire et transsonique en extrémité de pale avançante et des ondes de choc apparaissent. Celles-ci limitent la vitesse de l'hélicoptère, car leur apparition augmente fortement le niveau vibratoire du rotor, la puissance consommée et le bruit rayonné par le rotor (en particulier lorsque la vitesse d'avancement est suffisante pour que la délocalisation des ondes de choc apparaisse, correspondant à un mouvement supersonique de l'onde de choc attachée à la pale). En pale reculante, les vitesses d'attaque sont faibles, et même négatives dans le cercle d'inversion où les sections de pale sont attaquées par leur bord de fuite. Au contraire de la pale avançante, les incidences sont élevées en raison de l'équilibre du rotor en roulis, les sections de pale pouvant même fonctionner au-delà de leur incidence de portance maximale ; des phénomènes complexes de décrochage dynamique apparaissent alors, avec un effet de

surportance tourbillonnaire qui permet aux profils de la pale de fonctionner au-delà de leur portance maximale stationnaire.

4.4 L'appareil complet

L'appareil complet introduit un degré de complexité supplémentaire qui doit être pris en compte dans une modélisation réaliste du rotor [1]. Le fuselage présente des régions d'écoulement décollé difficiles à simuler, notamment en aval du mât rotor. Il modifie la géométrie du sillage du rotor, et plus particulièrement à basse vitesse, perturbant ainsi l'écoulement incident sur les pales. De même, le sillage du rotor est en interaction avec le fuselage, venant même heurter ses parois, en particulier au niveau des empennages, ce qui a un effet important pour le contrôle de l'hélicoptère en vol. Le passage du sillage du rotor principal à proximité du rotor arrière crée également des perturbations impulsives de l'écoulement incident, créant ainsi un bruit d'interaction rotor principal-rotor arrière.

4.5 Conséquences

La complexité aérodynamique de l'hélicoptère rend sa simulation numérique complète coûteuse et difficile. Celle-ci nécessite la maîtrise de techniques numériques évoluées, notamment en raison de la cinématique complexe des pales en mouvement relatif par rapport au fuselage mais également les unes par rapport aux autres. Un calcul de l'hélicoptère complet avec prise en compte de tous les phénomènes par même méthode n'est donc pas réaliste à l'heure actuelle, en particulier pour les applications. Une approche indirecte divise le problème global en plusieurs problèmes plus simples, pour lesquels des méthodes de calcul spécialisées sont développées, la simulation de l'hélicoptère complet (ou même de son rotor principal) étant obtenue en couplant ces méthodes entre elles. A l'heure actuelle, seule cette approche est viable au niveau des applications industrielles pour fournir des résultats de calcul du champ aérodynamique autour de l'hélicoptère.

5 LE ROTOR D'HELICOPTERE EN VOL D'AVANCEMENT

5.1 Le code de calcul R85

5.1.1 Introduction

Le code de calcul R85 a été développé par Eurocopter France pour disposer d'un outil rapide d'analyse et de définition des rotors d'hélicoptères [2], [3]. La Direction de l'Aérodynamique de l'ONERA coopère avec ECF pour l'évaluation et l'amélioration de ce code, afin d'étendre son domaine de validité et d'améliorer sa précision et son efficacité.

Cette méthode de type élément de pale calcule la position d'équilibre de la pale en prenant en compte sa souplesse de façon à assurer les conditions de vol désirées (efforts globaux ou commandes imposées), à partir d'une description simple des pales et du moyeu du rotor. Elle fournit à la fois une estimation de la cinématique de la pale et de ses déformations, ainsi que les performances du rotor.

5.1.2 Description de la méthode

En supposant le mouvement des pales périodique, R85 décompose les diverses inconnues du problème (angles rigides et déformations) en série de Fourier. De façon à diminuer le nombre d'inconnues, chaque degré de liberté est décomposé sur une base modale de déformation préalablement calculée, qui comprend en pratique les N premiers modes propres de la pale en rotation (N pouvant aller de 5 à 8 selon les cas). L'équilibre du rotor est obtenu par résolution des équations de Lagrange :

$$\frac{d}{dt} \left(\frac{\partial T}{\partial \dot{q}_i} \right) - \frac{\partial T}{\partial q_i} + \frac{\partial U}{\partial q_i} = Q_i \quad (1)$$

où l'on a :

- l'énergie cinétique T directement exprimée en fonction des inconnues du problème,
- l'énergie élastique U qui s'exprime à l'aide des formules de la résistance des matériaux en assimilant la pale à une poutre se déformant en flexion et en torsion,
- les coordonnées généralisées q_i décrivant la pale en rotation, et qui sont en pratique les contributions temporelles (décomposées en série de Fourier) des N modes de déformation,
- les efforts généralisés Q_i relatifs à chaque coordonnée généralisée q_i , qui sont calculés à partir des efforts aérodynamiques s'exerçant sur la pale.

Le système non linéaire formé par les équations de Lagrange est résolu par une méthode itérative (méthode de la sécante).

Du point de vue aérodynamique, la pale est assimilée à une ligne portante, et les coefficients aérodynamiques C_z , C_x et C_m sont lus dans des fichiers de polaires de profils obtenues à partir d'essais en soufflerie. Diverses corrections peuvent être apportées à ces coefficients aérodynamiques afin de mieux simuler l'écoulement réel sur l'hélicoptère, fortement tridimensionnel en extrémité de pale. Par exemple, des corrections d'attaque en flèche sont effectuées de façon à pouvoir traiter des pales de géométrie non rectangulaire. Deux modèles de sillage sont disponibles dans le code pour simuler l'écoulement induit à travers le disque rotor. Le premier est le modèle linéaire semi-empirique de Meijer-Drees. Un modèle plus réaliste de sillage a été introduit par le couplage du code R85 avec le code METAR (§5.2).

5.1.3 Résultats de calcul

Un important effort de validation du code R85 a été effectué au cours des dernières années [4], en utilisant plus particulièrement les résultats obtenus au cours des essais ROSOH à S2Ch [5] et au cours de la 11^{ème} campagne d'essais à S1MA. La puissance consommée par le rotor est en général assez bien estimée par le calcul utilisant le modèle de sillage le plus sophistiqué, donnant un écart moyen avec l'expérience inférieur à 5%, sauf aux frontières du domaine de vol (Fig. 1).

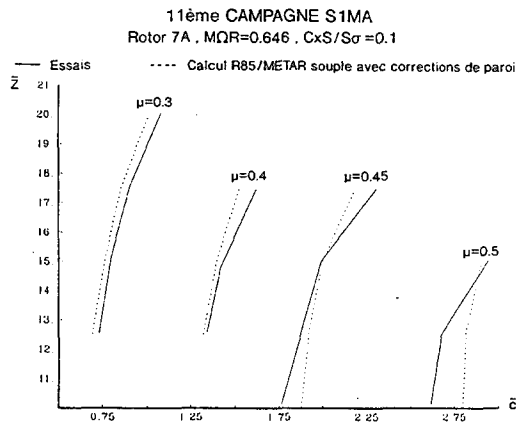


Fig. 1 Puissance calculée par R85

Les efforts aérodynamiques locaux sur les pales sont également assez proches des mesures expérimentales pour les sections allant du pied de pale à 95% du rayon (Fig. 2). Au delà, des écarts plus importants apparaissent : ces écarts sont attribués à la conjugaison des efforts tridimensionnels partiellement modélisés par l'approche ligne portante et des déformations de pale qui peuvent être importantes, notamment en torsion.

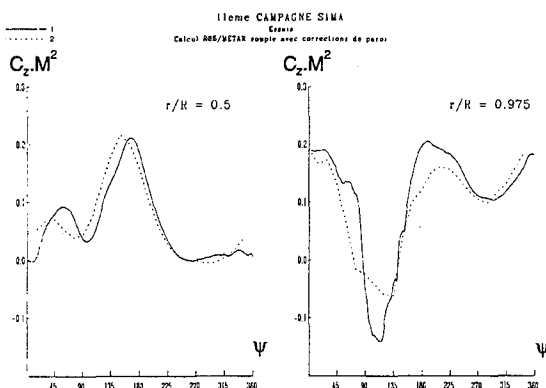


Fig. 2 Calcul des efforts aérodynamiques par R85

De fait, l'amplitude des déformations de torsion en extrémité de pale est en général sous-estimée par rapport à l'expérience (Fig. 3), montrant les faiblesses actuelles de la méthode de calcul.

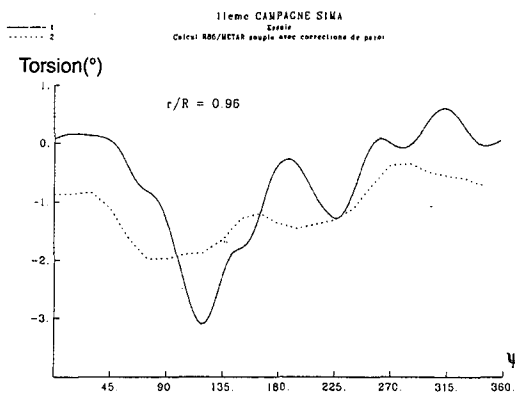


Fig. 3 Calcul des déformations de torsion par R85

5.2 Les codes de calcul METAR/MESIR

5.2.1 Introduction

L'importance particulière du sillage tourbillonnaire des pales a déjà été soulignée, en raison notamment de son influence importante sur l'écoulement incident sur les pales. En particulier, le tourbillon d'extrémité de pale, très intense, est convecté beaucoup plus lentement que le reste de la nappe sous le disque rotor, et son influence est prépondérante. De plus, le système tourbillonnaire permet une première prise en compte des effets tridimensionnels qui apparaissent en extrémité de pale, et notamment de simuler la chute de portance en extrémité de pale.

Deux modèles de simulation du sillage tourbillonnaire du rotor principal de l'hélicoptère sont présentés dans cette partie, les codes METAR et MESIR. Ce dernier est une évolution du premier dans lequel la géométrie du sillage est mise en équilibre. Ceci signifie que METAR, qui impose a priori la géométrie du sillage rotor, est adapté au calcul de l'hélicoptère en croisière (paramètres d'avancement supérieurs à 0,25), tandis que MESIR permet de traiter les problèmes du vol à basse vitesse ou en descente, pour lesquels des interactions pale-tourbillon apparaissent.

5.2.2 Le modèle METAR

Ce code de calcul a été développé par Eurocopter France. La pale est toujours représentée par une ligne portante, utilisant les polaires de profils bidimensionnels des sections de pale pour évaluer les efforts aérodynamiques. Le sillage émis par chaque pale est représenté par des lanières tourbillonnaires (Fig. 4), ces lanières pouvant être radiales (pour modéliser les variations de circulation le long de la pale) ou tangentielles (pour modéliser les variations temporelles de circulation).

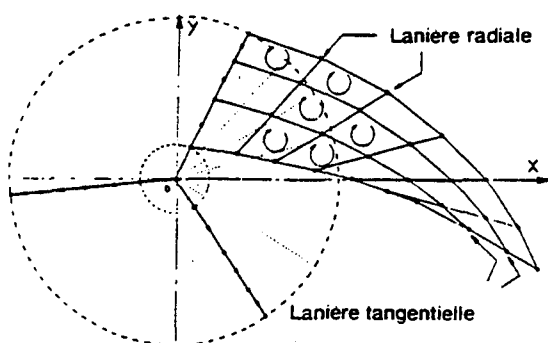


Fig. 4 Modélisation du sillage par METAR

La géométrie de cet ensemble de lanières est figée et supposée connue a priori, de forme hélicoïdale, de sorte que chaque tourbillon est convecté vers l'aval à la vitesse de l'hélicoptère augmentée d'une vitesse induite moyenne, donnée par la formule de Meijer-Drees. En écoulement incompressible, l'influence de ces lanières de géométrie connue, en chaque point de la pale et pour chaque azimut, est entièrement définie par une matrice d'influence M_i , obtenue en appliquant la loi de Biot et Savart en chaque point de discrétisation de la pale. La vitesse induite par le sillage V_i sur les points de la pale est alors donnée par :

$$V_i = M_i \cdot \Gamma \quad (2)$$

où Γ est le vecteur qui définit la répartition de circulation sur la pale pour l'ensemble des points de discrétisation du disque rotor, en envergure et en azimut.

Dans le code METAR, le mouvement de la pale est supposé connu (à partir d'un calcul R85 ou de résultats expérimentaux). Le programme effectue des itérations de façon à trouver la répartition de circulation permettant de converger sur les vitesses induites. Le modèle METAR a également été couplé au code R85 afin de prendre en compte de façon plus réaliste l'influence du sillage du rotor sur l'équilibre de la pale.

5.2.3 Le modèle MESIR

Afin de simuler les interactions pale-tourbillon, l'ONERA a développé une méthode de mise en équilibre du sillage construite à partir du modèle METAR et baptisée MESIR [6], [7]. En effet, ce type de problème ne peut être traité sérieusement en imposant une géométrie de sillage figée, car il s'agit de configurations de vol à basse vitesse où le sillage passe très près des pales, les variations locales de vitesses induites ne pouvant alors plus être négligées.

La mise en équilibre du sillage est effectuée de façon itérative jusqu'à la convergence du processus, en démarrant avec un sillage figé calculé par METAR. Ainsi, pour un azimut de calcul donné, la vitesse induite par l'ensemble du sillage et des pales est calculée en tout point du sillage en utilisant la formule de Biot et Savart. Chaque point du sillage est alors convecté à la vitesse

totale en ce point, égale à la somme de la vitesse induite et de la vitesse d'avancement de l'hélicoptère, contrairement à METAR où cette vitesse de convection, uniforme, est la somme de la vitesse d'avancement de l'hélicoptère et de la vitesse induite moyenne à travers le disque rotor. Le processus de mise en équilibre est poursuivi pendant trois révolutions de pale afin de permettre à la déformation du sillage de s'étendre de façon consistante sur les trois tours de rotor pris en compte dans le calcul. La matrice d'influence est alors calculée pour cette nouvelle géométrie de sillage, et il est nécessaire de converger à nouveau sur les valeurs de la circulation sur la pale. Ceci termine la description d'une itération complète de mise en équilibre du sillage, et le processus est poursuivi jusqu'à convergence sur la géométrie du sillage, pour laquelle la vitesse locale est tangente en tout point de la nappe.

La méthode MESIR a été appliquée à l'hélicoptère SA349 Gazelle en vol de palier basse vitesse. La géométrie du sillage (Fig. 5) montre nettement les déformations locales de la nappe, avec en particulier l'enroulement en extrémité, conforme aux observations expérimentales.

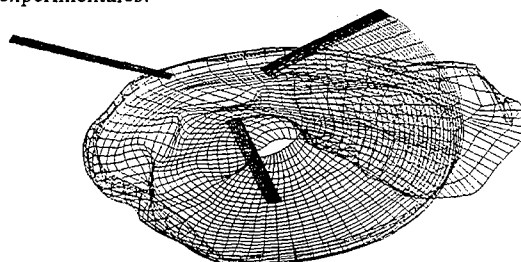


Fig. 5 Sillage de la Gazelle calculé par MESIR

Cette amélioration de la représentation du sillage par rapport à une géométrie figée se traduit naturellement par une meilleure évaluation de l'évolution azimutale des charges dans une section de pale (Fig. 6). En particulier, les forts gradients de portance autour des azimuts 90° et 270° , dus à des interactions entre la pale et le sillage, sont beaucoup mieux calculés par MESIR que par METAR.

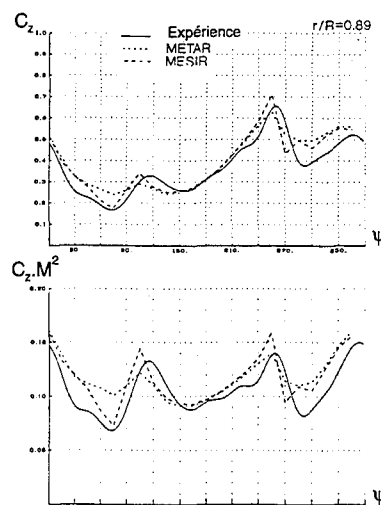


Fig. 6 Comparaison de la portance en $r/R=0,89$ pour la Gazelle

La méthode MESIR, par sa capacité à calculer la géométrie des nappes tourbillonnaires, est un outil précieux pour le calcul des interactions pale-tourbillon. Cependant, elle ne permet pas le calcul des pressions sur les pales, indispensable pour une estimation correcte du bruit d'interaction pale-tourbillon. Un couplage avec une méthode potentiel, ARHIS [8] ou FP3D par exemple (§5.3), permet d'atteindre cet objectif.

5.3 Le code de calcul FP3D

5.3.1 Introduction

Le code de calcul FP3D a été initialement développé pour simuler les écoulements transsoniques qui apparaissent en extrémité de pale avançante [9]. De nombreuses applications [7], [10], [11], [12], montrent la généralité du modèle potentiel pour simuler une grande partie des phénomènes non visqueux qui apparaissent sur un rotor d'hélicoptère.

En effet, les écoulements transsoniques sur un rotor d'hélicoptère restent modérés, même pour le vol de croisière rapide, le nombre de Mach maximum excédant rarement 1,3. Dans ces conditions, l'écoulement peut être considéré comme isentropique. En dehors du sillage, l'écoulement est alors irrotationnel, en première approximation. Sous ces conditions d'isentropie et d'irrotationnalité, le champ de vitesse dérive d'un potentiel, et la résolution des équations de la dynamique des fluides se simplifie considérablement, puisqu'elles ne dépendent plus que d'une variable, le potentiel des vitesses ϕ , tout en gardant le comportement non linéaire des phénomènes. Le principal inconvénient du modèle potentiel est son incapacité à capturer les nappes tourbillonnaires, dont l'influence est fondamentale pour certaines applications hélicoptère. Il est alors nécessaire d'introduire une influence du sillage dans les conditions aux limites du calcul [13]. Une modélisation du sillage directement dans le champ potentiel est cependant possible par l'intermédiaire d'un potentiel de Clebsch [14]. Dans le cas contraire, l'équation du potentiel est résolue sur un maillage entourant une pale isolée, l'influence des autres pales et du sillage étant prises en compte dans les conditions aux limites de l'équation.

5.3.2 Equations

Les équations de conservation de la dynamique des fluides, masse, quantité de mouvement et énergie, sont écrites dans un référentiel Galiléen. Leur expression dans un repère non Galiléen nécessite l'introduction de termes supplémentaires dans les équations, termes qui peuvent être assez complexes pour un référentiel lié à une pale d'hélicoptère. Il est donc beaucoup plus simple d'écrire les équations dans le référentiel Galiléen lié à l'air au repos. Un changement de coordonnées est alors nécessaire pour exprimer ces équations dans un système de coordonnées lié à la pale, ce qui revient à introduire

implicitement les accélérations d'entraînement et de Coriolis dans les équations. Après passage aux coordonnées de calcul, les équations s'écrivent :

$$\frac{\partial(\sqrt{g} \rho)}{\partial \tau} + \frac{\partial}{\partial \xi^j} (\sqrt{g} \rho U^j) = 0 \quad (3)$$

$$\rho^{\gamma-1} = 1 - \frac{\gamma-1}{2} \left[2 \frac{\partial \phi}{\partial \tau} + (\xi_T^j + U^j) \frac{\partial \phi}{\partial \xi^j} \right] \quad (4)$$

Dans les nouvelles coordonnées de calcul définies par le maillage sur lequel est discrétisé le problème, l'équation de conservation de la masse (3) est sous sa forme conservative. Ceci est obtenu grâce à une identité non triviale, [15], assimilable à une relation de conservation géométrique [16]. Dans ces équations (3) et (4), les termes U^j sont les composantes contravariantes de la vitesse dans le repère de calcul, exprimées par :

$$U^j = \xi_T^j + g^{ji} \frac{\partial \phi}{\partial \xi^i} \quad (5)$$

où ξ_T^j sont les composantes de la vitesse de déplacement du maillage dans le repère de calcul et g^{ji} le tenseur métrique fondamental.

5.3.3 Discrétisation de l'équation

Discrétisation temporelle

L'algorithme de calcul utilisé a été initialement développé par Steger et Caradonna [17], [18], et une première application aux rotors d'hélicoptère effectuée par Strawn et Caradonna [19]. L'équation de conservation de la masse est discrétisée sous forme implicite, en utilisant une différence décentrée du premier ordre en temps. Afin de résoudre une équation pour le potentiel comme seule inconnue, les termes de densité et de flux sont linéarisés au premier ordre en fonction du potentiel, les opérateurs de linéarisation étant obtenus à partir de l'équation de Bernoulli. Le système linéarisé s'écrit alors :

$$\begin{aligned} & \left[1 + h^{n+1} U^j \partial_{\xi^j} - \frac{h^{n+1} h^{n+1}}{\hat{\rho}_n^{2-\gamma}} \partial_{\xi^j} \hat{\rho}_n^{n+1} g^{jj} \partial_{\xi^j} \right] (\phi^{n+1} - \phi^n) \\ &= \frac{h^{n+1} h^{n+1}}{\hat{\rho}_n^{2-\gamma}} \left[\frac{\hat{\rho}_n^n - \hat{\rho}_n^{n-1}}{h^{n+1}} + \left(\hat{\rho}_n U^j \right)_{\xi^j}^n \right] + \\ & \quad \frac{h^{n+1}}{h^n} (\phi^n - \phi^{n-1}) + \end{aligned} \quad (6)$$

$$h^{n+1} \frac{\hat{\rho}_n^{2-\gamma}}{\hat{\rho}_n^{2-\gamma}} \left[\left(\frac{\phi^n - \phi^{n-1}}{h^n} - \frac{(\phi^{n-1} - \phi^{n-2})}{h^{n-1}} \right) + U^{j^{n-1}} \partial_{\xi^j} (\phi^n - \phi^{n-1}) \right]$$

Au second membre de l'équation, apparaît l'équation de conservation de la masse sous sa forme explicite, ainsi que les termes explicites de linéarisation de la densité. Dans cette formulation, les deux termes de densité sont

linéarisés afin d'avoir une solution consistante en temps. Ce système peut être inversé à l'aide d'une factorisation approchée, donnant la solution du problème à chaque pas de temps, pourvu que ce dernier soit suffisamment petit. Une amélioration peut être apportée à la méthode, en convergeant les linéarisations effectuées par une méthode de Newton. A convergence la valeur du potentiel obtenue est la solution exacte de l'équation de conservation de la masse sous sa forme implicite. Le système linéaire à résoudre a un second membre simplifié par rapport à (6), puisque seule la forme explicite de l'équation de conservation de la masse pour le dernier "prédicteur" connu y apparaît. Ceci est obtenu par linéarisation du seul premier terme de densité et des termes de flux par rapport au dernier "prédicteur" connu. Pour démarrer le processus, un premier "prédicteur" est nécessaire, et une équation sensiblement différente doit être résolue. Pour cela, on utilise généralement (6).

Discretisation spatiale

La discrétisation spatiale de l'équation est obtenue à l'aide de différences finies centrées, exactes au second ordre. Pour les zones supersoniques de l'écoulement, cette discrétisation centrée est inadaptée en raison du caractère hyperbolique en espace de l'écoulement dans ces régions. Il est alors nécessaire d'introduire dans le schéma cette influence amont par un décentrement de la densité, obtenu à l'aide du schéma d'Engquist-Osher [20], [21]. En pratique, on utilise une version "monodimensionnelle" de ce schéma suivant chaque direction de ligne de maillage, ce qui donne suffisamment de dissipation numérique pour obtenir une solution stable avec choc.

Calcul des métriques

Plusieurs approches peuvent être utilisées pour le calcul des termes métriques. La plus simple consiste à inverser la matrice des dérivées des coordonnées du maillage par rapport aux coordonnées de calcul. L'autre approche, moins commune, se déduit d'une interprétation "volumes finis" de l'équation (3), qui donne la signification suivante aux termes de l'équation :

- le terme \sqrt{g} , inverse du Jacobien du changement de variables, est égal au volume de la cellule élémentaire sur laquelle l'équation discrétisée est résolue,
- les termes $U^i \sqrt{g} \Delta \xi^j \Delta \xi^k$ représentent les termes de flux à travers les frontières des cellules élémentaires où le problème discrétisé est résolu, c'est-à-dire le produit scalaire du vecteur vitesse avec la surface orientée délimitant la frontière de la cellule.

On en déduit alors que le calcul des termes métriques peut également être effectué uniquement à partir des composantes de la surface normale aux facettes des cellules de calcul, divisées par le volume de la cellule de calcul.

Le calcul des termes métriques conditionne la qualité de la solution obtenue. En particulier, la méthode discrétisée doit être capable de donner la solution exacte pour un écoulement non perturbé. Ceci impose des conditions de consistance que doivent vérifier les métriques discrétisées [22]. Au contraire du bidimensionnel, ces conditions sont difficiles à satisfaire en tridimensionnel. C'est pourquoi un terme correctif, correspondant à l'erreur de la solution pour un écoulement non perturbé, est soustrait du second membre de l'équation. Une approche purement volumes finis est également possible en appliquant le théorème de la divergence de Gauss au potentiel des vitesses. Ceci permet de s'affranchir totalement du calcul des termes métriques.

Conditions aux limites

A la surface de la pale, une condition de transpiration est introduite, permettant soit d'assurer la tangence de l'écoulement à la pale, soit d'imposer la composante de vitesse normale à la pale afin de simuler les modifications de l'écoulement incident induites par le sillage tourbillonnaire et les autres pales du rotor.

Dans la première section de calcul, une condition d'écoulement de perturbation bidimensionnel est introduite.

Pour un écoulement potentiel, l'égalité des pressions extrados et intrados au bord de fuite fait apparaître une discontinuité du potentiel en ce point (condition de Joukowski). Le sillage apparaît comme une surface de glissement, à travers laquelle la vitesse tangentielle et le potentiel sont discontinus. Dans le sillage, une équation de convection de la circulation est appliquée afin de transporter cette discontinuité de potentiel vers l'aval et corriger ainsi les dérivées du potentiel à la traversée du sillage. Cette équation de convection est obtenue à partir de l'équation de Bernoulli en exprimant la continuité de pression à la traversée de la coupure représentant la nappe.

Une analyse des valeurs propres du système différentiel construit à partir de l'équation montre que celle-ci est hyperbolique, et sa solution est donc dominée par les phénomènes propagatifs, la vitesse des ondes dans un plan normal à la surface $\xi^i = \text{cte}$ étant égale à $U^i \pm a \sqrt{g^{ii}}$. A la frontière externe du maillage, des conditions de non réflexion sont donc appliquées afin d'éviter que la réflexion des ondes ne viennent perturber la solution. Elles sont obtenues à partir d'une linéarisation de l'équation du potentiel pour une onde se propageant dans une direction donnée et sont de la forme:

$$\phi_{\xi} + (U \pm a \sqrt{g^{11}}) \phi_{\xi} + v \phi_{\eta} + w \phi_{\zeta} = 0 \quad (7)$$

Corrections d'entropie

Des corrections d'entropie ont été introduites dans le code FP3D afin de capturer des conditions de saut plus

proches des relations de Rankine-Hugoniot au niveau des ondes de choc. Cette correction très simple est semblable à celles décrites dans [23] et [24] :

$$\rho^{\gamma-1} = \rho_{\text{isen}}^{\gamma-1} e^{-\Delta S / c_v} \quad (8)$$

Correction de couche limite

Une correction de couche limite a également été appliquée au calcul FP3D, en utilisant une technique simple de couplage faible. Le calcul de couche limite est effectué avec le code CCLT développé par Cousteix et Houdeville au CERT/DERAT [25], qui simule une couche limite turbulente et instationnaire par une méthode intégrale. Le calcul FP3D fournit les conditions aux limites pour le calcul visqueux, et l'effet de déplacement de la couche limite est introduit dans les conditions de transpiration du calcul potentiel de façon explicite en temps.

5.3.4 Applications de la méthode

La 11^{ème} campagne d'essais réalisée par l'ONERA et ECF à S1MA, sur les rotors 7A et 7AD munis chacun de plus de 100 capteurs instationnaires distribués sur 5 sections de mesure, a fourni des résultats expérimentaux très complets et d'excellente qualité pour les configurations de vol du rotor à grande vitesse : elle a donc été utilisée de façon extensive pour valider la méthode FP3D [13]. Un des buts de la validation est de vérifier que la méthode de calcul est capable de reproduire correctement l'effet d'une variation de géométrie de la pale sur les caractéristiques de l'écoulement ; ceci constitue une condition préalable à l'utilisation d'un tel outil pour la définition de nouveaux rotors.

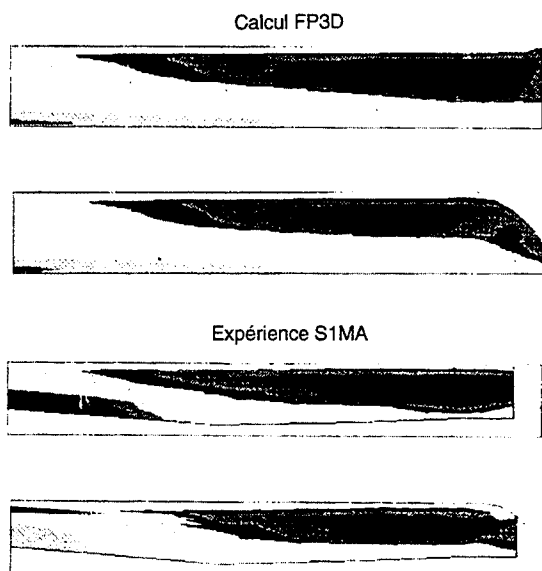


Fig. 7 Comparaison des lignes iso-Mach calculées et mesurées sur les rotors 7A et 7AD ($V=320$ km/h, $\psi=90^\circ$)

La Fig. 7 montre la répartition de lignes iso-Mach instantanées calculées et mesurées à l'azimut 90° , pour un paramètre d'avancement $\mu=0,4$. Un bon accord entre le calcul et l'expérience peut être observé. En particulier, la diminution de l'intensité des écoulements transsoniques apportée par la forme parabolique en flèche de l'extrémité SPP8 apparaît clairement sur l'expérience et sur le calcul.

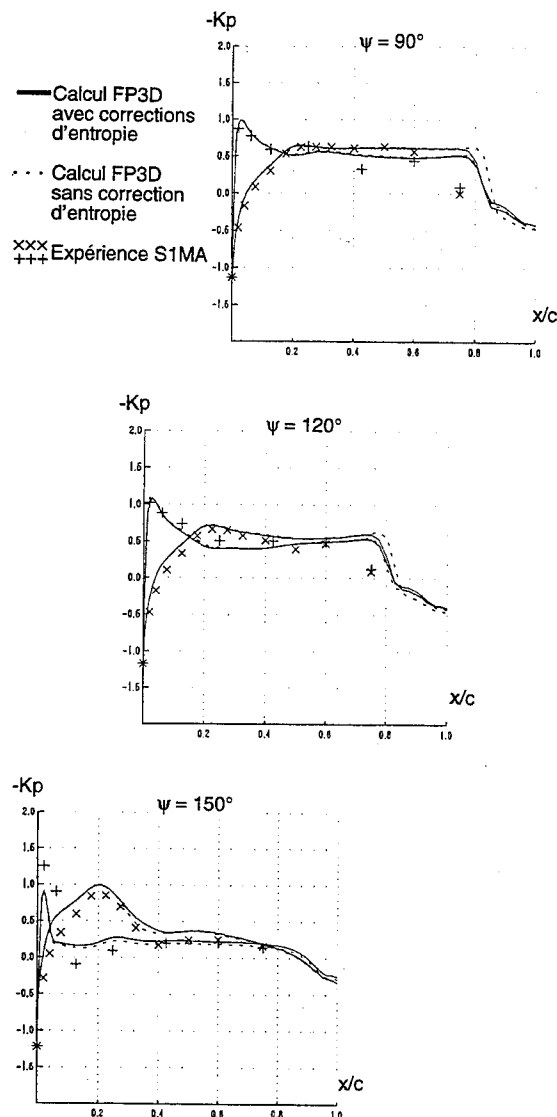


Fig. 8 Coefficient de pression calculé et mesuré sur le rotor 7A ($M_{\infty}=0,646$ $\mu=0,45$ $r/R=0,975$)

La Fig. 8 montre une comparaison calcul-expérience du coefficient de pression en extrémité de pale avançante, qui peut être considéré comme satisfaisant à l'exception d'une surestimation de l'intensité des chocs, ceux-ci se trouvant positionnés trop en aval vis-à-vis de l'expérience sur la corde du profil. Malgré l'incertitude apportée par le modèle de sillage utilisé, ceci illustre les limitations de la formulation isentropique et non visqueuse. Un calcul avec corrections d'entropie est également présenté sur cette même figure, montrant une légère amélioration dans le calcul de la position des chocs.

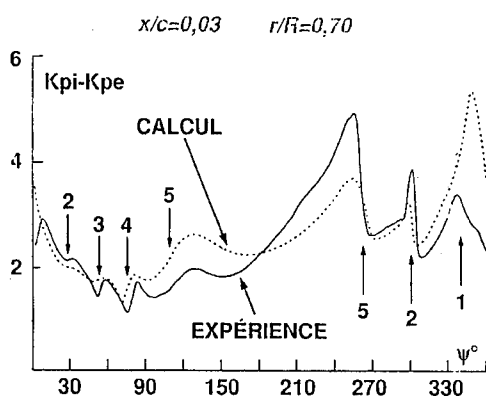


Fig. 9 Coefficient de pression différentielle pour le rotor OLS en vol de descente ($x/c=3\%$ $r/R=70\%$)

L'application du code FP3D à des interactions pale-tourbillon nécessite un calcul de l'écoulement incident par le code MESIR. De plus, un traitement plus précis de ces interactions est nécessaire, avec calcul des vitesses induites par les tourbillons en interaction en tous les points de la pale, alors que l'influence du reste du sillage est prise en compte de façon simplifiée par un calcul d'incidence au point "quart de corde". L'application de la méthode au rotor OLS de l'US Army (Fig. 9), montre un assez bon accord avec les résultats expérimentaux obtenus dans la soufflerie du DNW. En particulier, les oscillations de pression différentielle caractéristiques de l'interaction pale-tourbillon (dues à une brusque modification de l'écoulement incident induite par le passage proche d'un tourbillon) sont capturées en phase avec l'expérience par le calcul ; toutefois, certaines d'entre elles ont leur amplitude amortie par rapport à l'expérience, indiquant que la distance d'interaction ou l'intensité du tourbillon ne sont pas suffisamment bien calculées. Ceci illustre la difficulté de ce type de calcul qui est fortement dépendant du modèle de sillage utilisé, pour lequel des paramètres empiriques tels que le choix du rayon de régularisation, de la discrétisation, ... peuvent avoir une influence importante sur les résultats obtenus. Aucun ajustement de ces paramètres de façon à reproduire au mieux les résultats expérimentaux n'est effectué dans notre approche, leur choix dépendant uniquement de considérations purement numériques.

Un des objectifs principaux du développement des méthodes numériques est la prévision de grandeurs facilement utilisables dans un processus de définition. En particulier, la puissance à fournir au rotor est le critère principal qui intéresse les bureaux d'études. Une première application de la méthode FP3D avec corrections de couche limite a été effectuée dans ce cadre pour le cas simple d'un rotor non portant. En effet, le calcul de traînée est un problème extrêmement difficile. L'avantage d'un cas non portant est de

supprimer le terme de traînée induite du calcul, ce qui permet d'avoir une estimation de l'erreur due à l'intégration des pressions sur la traînée à partir d'un calcul à bas paramètre d'avancement où la traînée en fluide parfait est nulle (absence de choc). La contribution de la traînée visqueuse dans le calcul du couple est obtenue par la formule de Squire et Young à partir des résultats du calcul de couche limite. La contribution du frottement à ce terme de traînée visqueuse peut également être obtenue par intégration du terme de frottement. Le couple calculé (Fig. 10) est légèrement plus faible que celui mesuré en soufflerie. La non prise en compte de la partie interne de la pale (jusqu'à 60% du rayon) peut expliquer cela. Par contre, l'augmentation du couple nécessaire au rotor avec le paramètre d'avancement est bien reproduit, car ce terme provient essentiellement des ondes de choc en extrémité de pale.

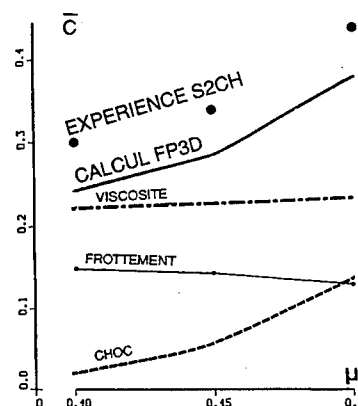


Fig. 10 Evolution du couple en fonction de la vitesse (Rotor S2Ch non portant, pales droites)

5.4 Couplage Dynamique-Aérodynamique

Les méthodes exposées jusqu'à présent ne permettent pas de traiter simultanément le problème de la dynamique des pales souples et celui de l'aérodynamique 3D, c'est-à-dire d'évaluer les effets de l'aérodynamique 3D sur les déformations des pales. C'est dans cette optique qu'est menée une étude concernant le couplage itératif entre le code de dynamique R85 et le code d'aérodynamique FP3D.

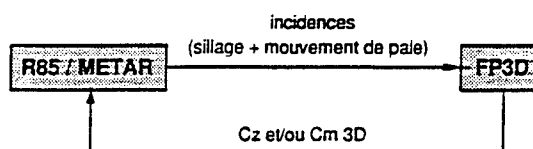


Fig. 11 Schéma du couplage R85/FP3D

Le schéma de principe de cette méthode (Fig. 11) est assez simple : le code R85 fournit à FP3D les informations sur le mouvement de la pale souple et sur le sillage tourbillonnaire. Le code FP3D fournit en retour les corrections à apporter sur les coefficients C_z (et/ou

C_m) lus dans les fichiers polaires de profil. De telles itérations sont effectuées jusqu'à ce que les C_z (et/ou les C_m) de R85 et FP3D soient égaux. Une relaxation est effectuée sur les corrections apportées par l'aérodynamique 3D de façon à converger rapidement, généralement 3 à 4 itérations. Des premiers résultats obtenus par cette méthode ont permis d'améliorer la répartition des efforts de portance et de mieux calculer l'amplitude des déformations de torsion en extrémité de pale (Fig. 12).

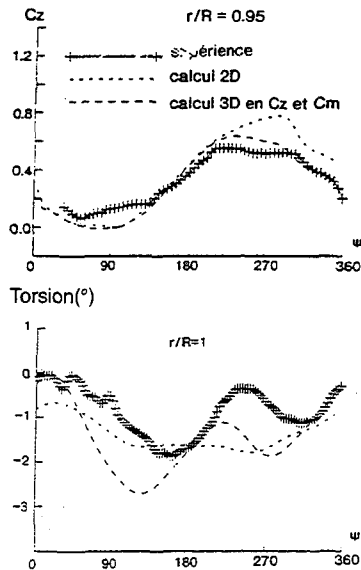


Fig. 12 Effet du couplage R85/FP3D

6 LE ROTOR D'HELICOPTERE EN VOL STATIONNAIRE

6.1 Les méthodes élément de pale

En dépit de la simplification du problème due à un écoulement permanent dans un repère lié à la pale, le vol stationnaire est très complexe à modéliser à cause de l'influence prépondérante du sillage des pales. Cette configuration de vol servant au dimensionnement de l'hélicoptère, il est important de disposer de méthodes de calcul simples et rapides, capables de fournir une estimation des performances du rotor dans ce cas.

Eurocopter France a ainsi inclus une modélisation du rotor en vol stationnaire par la méthode des anneaux dans le code R85. Le disque rotor y est divisé en couronnes élémentaires sur lesquelles les caractéristiques de l'écoulement ne dépendent que de la position radiale. Un bilan de quantité de mouvement couplé à une condition de conservation du débit sur chaque couronne élémentaire fournit alors une description simple du problème, les efforts sur la pale étant obtenus à partir des polaires des profils qui l'équipent et des incidences qui se déduisent des vitesses induites. Des raffinements permettant de mieux rendre compte des effets de courbure sur les pales ou de

contraction du sillage peuvent être utilisés. Cette méthode, extrêmement rapide, fournit une estimation correcte des grandeurs globales sur le rotor (Fig. 13).

Figure de mérite

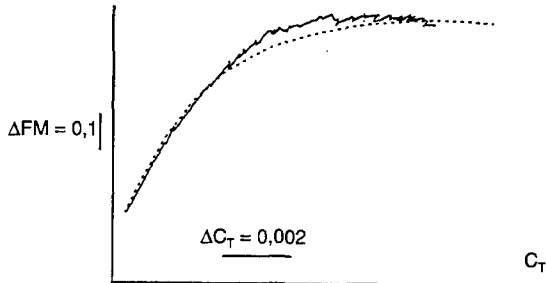


Fig. 13 Figure de mérite du rotor 7AD (calcul R85-méthode des anneaux)

Une méthode ligne portante, en principe similaire à METAR, a été développée à l'ONERA pour le calcul des rotors en vol stationnaire. La pale et son sillage sont décrits par un réseau de segments tourbillonnaires pour lesquels la vitesse induite est calculée par la loi de Biot et Savart. La géométrie de la nappe est figée et décrite par les lois empiriques de Landgrebe [26] et Kokurek [27], et un calcul itératif sur la distribution de vitesse induite doit être effectué. Cette méthode permet une estimation assez réaliste de la distribution de circulation, et donc de vitesse induite, sur la pale (Fig. 14) en comparaison des résultats expérimentaux obtenus à l'IMFM [28].

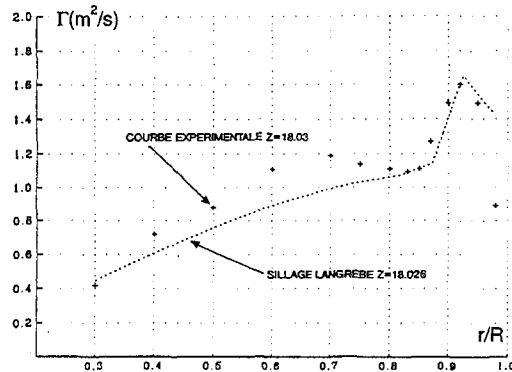


Fig. 14 Répartition de circulation sur le rotor 7 de l'IMFM (calcul ligne portante)

6.2 Le code de calcul PHOENIX 2

Les méthodes décrites ci-dessus, simples et peu coûteuses, permettent d'obtenir une évaluation rapide des performances du rotor en vol stationnaire. Cependant, elles ne donnent pas accès aux caractéristiques locales de l'écoulement tridimensionnel, et leur validité peut être remise en question pour des pales de géométrie avancée. Au contraire, la méthode PHOENIX 2 calcule l'écoulement tridimensionnel autour d'une pale d'hélicoptère en vol stationnaire par résolution de l'équation du potentiel complet des vitesses couplée à une représentation Lagrangienne du sillage tourbillonnaire. Elle a été mise au point par Steinhoff et Ramachandran à l'UTSI ([29], [30]).

La méthode de résolution de l'équation du potentiel est proche de celle décrite au § 5.2, les différences principales étant une simplification de la discrétisation en temps due à la forme stationnaire de l'équation, et le schéma de discrétisation d'espace de type "volumes finis". L'originalité de cette méthode est sa représentation du sillage, dans laquelle on remplace la saut de potentiel habituellement utilisé par une distribution équivalente de vitesse normale à la nappe. Une interprétation simple de cette formulation consiste à calculer la dérivée normale à la nappe, au sens des distributions, de la fonction échelon constituée par la discontinuité de potentiel, ce qui fournit une distribution de Dirac d'intensité égale à la discontinuité de potentiel.

Cette distribution est remplacée par une fonction continue décrite par un potentiel de Clebsch, qui permet une représentation de la composante rotationnelle de l'écoulement [31]. La nappe est alors discrétisée par des marqueurs convectés suivant la vitesse locale de l'écoulement.

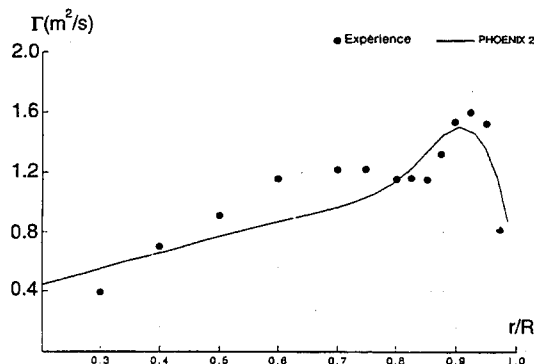


Fig. 15 Répartition de circulation sur le rotor 7 de l'IMFM (calcul PHOENIX 2)

La méthode appliquée au rotor 7 de l'IMFM donne des résultats conformes à l'expérience. Le pic de circulation en extrémité de pale est correctement calculé, mais les valeurs de circulation sur la partie interne de la pale sont moins satisfaisantes, même si le niveau moyen est correct. La Fig. 16 montre la position des nappes calculées par PHOENIX 2. La position expérimentale du tourbillon d'extrémité est également représentée, montrant que ces deux positions diffèrent au plus d'une maille de calcul.

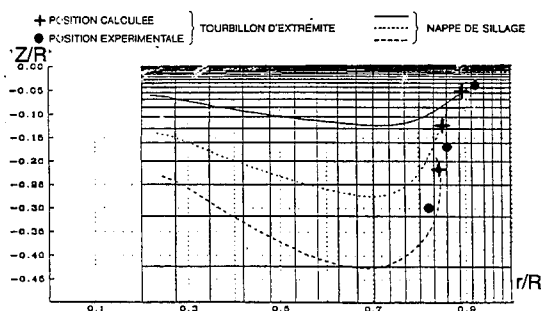


Fig. 16 Comparaison des positions calculées et mesurées du tourbillon d'extrémité (rotor 7 de l'IMFM)

7 LES METHODES D'OPTIMISATION DES ROTORS

7.1 Introduction

L'objectif final du développement de méthodes de calcul aérodynamique est leur application à la définition de formes nouvelles. Les paramètres de définition d'une pale d'hélicoptère sont difficiles à sélectionner, et leur nombre est élevé, rendant ainsi toute étude paramétrique complète illusoire. L'utilisation efficace des méthodes de calcul dans la définition des pales d'hélicoptère ne peut donc se faire que par leur intégration dans un processus d'optimisation numérique.

La complexité du rotor d'hélicoptère rend son calcul par une méthode aérodynamique tridimensionnelle long et coûteux, si bien que l'utilisation de telles méthodes pour la définition de rotors s'est généralement restreinte jusqu'à présent à un balayage paramétrique simple pour définir des géométries d'extrémité de pale [32]. Les méthodes aérodynamiques actuellement utilisables dans un processus d'optimisation de pales d'hélicoptères sont donc nécessairement simples, afin de pouvoir effectuer un nombre important de balayages paramétriques dans un temps raisonnable (à chaque étape de l'étude paramétrique, un calcul de la position d'équilibre de la pale doit en effet être effectué). L'optimisation aérodynamique des rotors d'hélicoptères en est d'ailleurs à ses premiers balbutiements, au contraire de ce qui est appliqué couramment sur les profils [33], [34], et même les voilures d'avion [35], [36]. Un tel travail a été entrepris à l'ONERA dans le cadre de l'opération ORPHEE, pour laquelle le programme de calcul R85 a été couplé au logiciel d'optimisation sous contraintes CONMIN.

7.2 Description de la méthode

Le processus d'optimisation est piloté par le programme CONMIN, qui minimise sous contraintes une fonction objectif par la méthode des directions réalisables, à partir du calcul du gradient de la fonction objectif par rapport aux variables d'optimisation et aux contraintes. Le code R85 fournit le calcul de la fonction objectif et des contraintes, à partir des valeurs des variables d'optimisation transmises par CONMIN. Les calculs de gradient sont effectués par différences finies, ce qui signifie que le nombre de calculs R85 par itération d'optimisation est de l'ordre du nombre de variables d'optimisation, et explique la nécessité d'utiliser un code de calcul de la fonction objectif peu coûteux en CPU.

Les variables d'optimisation aérodynamiques introduites dans le calcul sont les lois d'évolution en envergure de la corde, du vrillage et de la ligne quart de corde au niveau de la mise en flèche en extrémité, les polaires de profils équipant la pale et la répartition en envergure des profils. L'objectif généralement choisi est de minimiser la puissance consommée en vol de croisière rapide ; une maximisation de la portance du rotor peut

également être sélectionnée. Enfin, des contraintes sont imposées sur les efforts de commande du rotor. Des variables faisant également intervenir la dynamique du rotor ont également été introduites dans ce processus d'optimisation pluridisciplinaire [37].

7.3 Exemples d'optimisation

Une première application du programme d'optimisation a consisté en la définition d'un cahier des charges pour des profils minimisant la puissance consommée par le rotor en vol de croisière rapide [38]. Les nouvelles polaires des profils équipant la pale sont obtenues par interpolation dans des fichiers de polaires. Dans ce cas, les variables d'optimisation sont les coefficients d'interpolation des polaires. L'idée sous-jacente à cette optimisation est d'autoriser un coefficient de moment C_{m0} non nul, comme cela a déjà été appliqué sur la pale BERP [39], afin d'obtenir des coefficients de portance maximale C_{zmax} plus élevés et de faire travailler les profils à plus grande finesse. Le processus d'optimisation est initialisé par un rotor proche du rotor 7A, équipé du profil OA312 jusqu'à 85% du rayon et du profil OA309 à partir de 92% du rayon. Les deux profils "internes" et leur position sont optimisés, le profil OA309 étant imposé de 95% du rayon jusqu'à l'extrémité. Les polaires des profils de la pale optimisée correspondent à un profil de 11% d'épaisseur relative, cabreur ($C_{m0}=0,044$), jusqu'à 54% du rayon, et à un profil fin (9%) et piqueur ($C_{m0}=-0,020$) de 59% à 89% du rayon. Il en résulte un affinement, en épaisseur relative, du rotor optimisé par rapport au rotor initial, permettant une diminution de 4,3% de la puissance consommée au point d'optimisation (Fig. 17). Une analyse plus complète des résultats montre que les gains en croisière sont dus à cet affinement des pales ; cette diminution est par contre pénalisante au décrochage, et l'introduction d'un profil fin piqueur, par l'augmentation de sa portance maximale, permet de rattraper cette pénalité. Ceci explique pourquoi le rotor optimisé consomme moins de puissance que le rotor de référence sur pratiquement tout le domaine de vol.

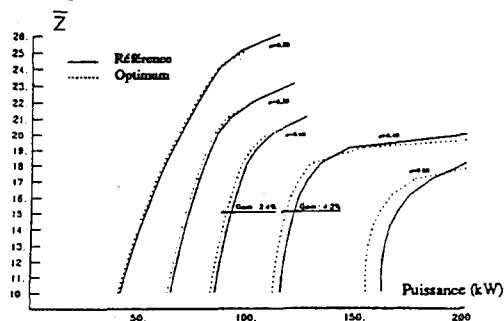


Fig. 17 Comparaison des domaines de vol du rotor initial et du rotor optimisé

Dans une deuxième étape, la forme en plan et le vrillage de la pale ont été optimisés, en conservant les polaires de profils théoriques obtenues auparavant. Cette

optimisation est beaucoup plus difficile que la précédente, car dès que la forme en plan de la pale s'éloigne fortement d'une pale rectangulaire, les couplages aéroélastiques entre les efforts aérodynamiques et la dynamique de la pale peuvent avoir une influence considérable. De plus, la méthode ligne portante est moins précise dans ces configurations complexes, et par conséquent le calcul des gradients par rapport aux variables d'optimisation également. Une définition totalement automatique de la pale par optimisation numérique n'est alors plus possible, et elle doit être complétée par un degré beaucoup plus important d'intervention humaine, pour définir les plages de variation des variables d'optimisation, analyser les résultats, ... La Fig. 18 présente un premier résultat "théorique" issu de ce processus d'optimisation complexe. La corde de la pale est fortement augmentée dans la partie médiane de la pale, afin de concentrer les efforts dans les zones où la finesse des profils est maximale. De même, la flèche d'extrémité permet un meilleur comportement du rotor en croisière rapide. Par contre, le comportement dynamique de la pale doit être examiné avec soin afin de pouvoir bénéficier réellement des gains aérodynamiques apportés par une telle modification de la forme en plan de la pale.

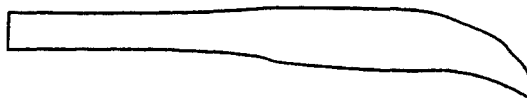


Fig. 18 Première définition d'une forme en plan optimisée de la pale

8 CONCLUSIONS ET PERSPECTIVES

L'ensemble des méthodes de calcul actuellement opérationnelles à la Direction de l'Aérodynamique de l'ONERA pour l'analyse et la définition du rotor principal de l'hélicoptère ont été décrites. Elles vont d'outils d'analyse simples et rapides, mais qui simulent le rotor dans sa globalité, aux méthodes numériques tridimensionnelles beaucoup plus lourdes à mettre en œuvre, qui ne simulent pas complètement le disque rotor et nécessitent donc généralement des données d'entrée issues des premières méthodes ou de l'expérience.

Les méthodes simples sont du type élément de pale. Elles ont généralement été développées initialement par Eurocopter France pour les besoins de leur bureau d'études (R85, METAR), et font l'objet d'une coopération entre l'ONERA et ECF pour leur validation et l'extension de leur domaine de validité. Ainsi, une évolution importante du code METAR a permis de développer la méthode de mise en équilibre du sillage MESIR, applicable à la simulation des interactions pale-tourbillon. Ces méthodes globales permettent une description correcte des performances et des répartitions de charge (aérodynamiques et dynamiques) sur le rotor. Leur coût de calcul généralement modéré les rend utilisables dans un processus de définition automatique de formes par optimisation numérique, même si une telle

application doit être considérée avec prudence pour des pales s'éloignant trop de la forme rectangulaire classique. Néanmoins, ce type de méthode devrait être utilisé de façon courante pendant encore de nombreuses années, en particulier en raison de leur capacité à décrire simultanément l'aérodynamique et la dynamique du rotor et de mettre la pale en équilibre à chaque instant, mais aussi parce qu'elles sont actuellement les seules à pouvoir prévoir les performances du rotor, bien que cette prévision soit fortement dépendante des polaires des profils équipant les pales. Du point de vue purement aérodynamique, les perspectives sérieuses d'amélioration de ces méthodes passent par un couplage avec un code aérodynamique tridimensionnel qui fournirait tout ou partie du torseur aérodynamique (portance, traînée, moment) qui s'exerce sur les pales. Ce travail a d'ores et déjà été entrepris à l'ONERA [11].

Les méthodes tridimensionnelles opérationnelles pour les applications hélicoptères résolvent l'équation du potentiel des vitesses par différences finies/volumes finis, sous sa forme instationnaire pour le rotor en vol d'avancement (code FP3D). L'hypothèse d'écoulement potentiel est généralement suffisante pour le rotor principal d'hélicoptère, car les écoulements supersoniques restent modérés, même pour une configuration de vol à grande vitesse. La principale limitation de ce type de modèle pour le rotor d'hélicoptère est la non représentation des nappes tourbillonnaires, qui ont un effet prépondérant. Elles doivent alors être introduites sous forme de vitesses induites, fournies par un calcul de sillage avec des méthodes de singularités (METAR, MESIR). Une technique de représentation Lagrangienne du sillage dans un calcul potentiel a été développée par Steinhoff et Ramachandran pour le rotor en vol stationnaire, et elle permet de s'affranchir des problèmes de vitesse induite ; les calculs effectués à l'ONERA avec cette méthode (PHOENIX 2) ont montré l'intérêt de cette approche originale ; des premières applications effectuées à l'US Army AFDD ([40], [41]) montrent qu'elle peut s'appliquer également au rotor en vol d'avancement, même pour les configurations difficiles d'interaction pale-tourbillon. Un des efforts importants qui devra être mis en œuvre pour ce type de méthode tridimensionnelle, est le développement de procédures numériques efficaces et précises d'intégration des efforts, afin de pouvoir prévoir les performances du rotor à partir du calcul du champ aérodynamique tridimensionnel autour de la pale. La première application simple du code FP3D avec corrections de couche limite à un rotor non portant en vol d'avancement montre qu'un tel objectif est envisageable dans un futur proche. Bien entendu, et parallèlement à cela, les modèles numériques tridimensionnels utilisés vont évoluer, et les méthodes Euler en développement à l'ONERA ([42], [43]) sont en cours de validation en vue de leur utilisation prochaine dans les applications. Dans un futur plus lointain, une simulation plus réaliste des régions visqueuses devra être intégrée dans ce processus, que ce soit par l'intermédiaire d'un couplage fort fluide parfait-fluide visqueux [44], [45] ou par résolution

directe des équations de Navier-Stokes [46], [47]. Quoiqu'il en soit, un effort très important reste encore à réaliser dans ce domaine, et des progrès réels doivent être accomplis, tant au niveau des algorithmes numériques et de leur efficacité, qu'au niveau des modèles eux-mêmes (en particulier pour la turbulence), afin qu'ils soient utilisables efficacement pour ce type d'application.

Références

- [1] N. Bettschart, D. Gasser. "Analysis of Helicopter Rotor-Fuselage Interaction". *20th European Rotorcraft Forum*. Amsterdam (Pays-Bas) 1994.
- [2] M. Allongue, T. Kryszinski. "Aéroélasticité appliquée aux rotors d'hélicoptères. Validation et application du code R85". *27ème Colloque d'Aérodynamique Appliquée*. AAAF. Marseille (France) 1990.
- [3] G. Arnaud, F. Toulmay, B. Benoit. "Améliorations du modèle aérodynamique du code rotor hélicoptères R85. Validations et applications". *28ème Colloque d'Aérodynamique Appliquée*. AAAF. ISL. Saint-Louis (France) 1991.
- [4] G. Arnaud, P. Beaumier. "Validation of R85/METAR on the Puma RAE flight tests". *18th European Rotorcraft Forum*. Avignon (France) 1992.
- [5] P. Beaumier, E. Berton. "Study of soft-in-torsion blades: ROSOH operation". *18th European Rotorcraft Forum*. Avignon (France) 1992.
- [6] B. Michéa. "Etude des sillages de rotors d'hélicoptères en vol d'avancement et de leur influence sur les performances du rotor (Interaction pale-tourbillon)". *Thèse de Doctorat*. Université de PARIS VI 1992.
- [7] B. Michéa, A. Desopper, M. Costes. "Aerodynamic rotor loads prediction method with free wake for low speed descent flight". *18th European Rotorcraft Forum*. Avignon (France) 1992.
- [8] G. Rahier, P. Spiegel, B. Michéa. "Blade-Vortex Interaction Noise : Prediction and Comparison with Flight and Wind Tunnel Tests". *18th European Rotorcraft Forum*. Avignon (France) 1992.
- [9] M. Costes, H.E. Jones. "Computation of Transonic Potential Flow on Helicopter Rotor Blades". *13th European Rotorcraft Forum*. Arles (France) 1987.
- [10] M. Costes, A. Desopper, P. Ceroni, P. Lafon. "Flow Field Prediction for Helicopter Rotors with Advanced Blade Tip Shapes using CFD Techniques". *2nd International Conference on Basic Rotorcraft Research*. College Park (Maryland) 1988.
- [11] P. Beaumier. "A Full Coupling Procedure Between Rotor Dynamics Code and 3D Unsteady Full Potential Code". *Aeromechanics Specialists Conference*. San Francisco (California) 1994.

- [12] M. Costes, M. Rahaingomanana, A. Desopper. "Weak Coupling Between an Unsteady 3D Full Potential Code and an Unsteady Turbulent Boundary Layer Code. Application to a Helicopter Rotor in Forward Flight". *30th AIAA Aerospace Sciences Meeting*. Reno (Nevada) 1992.
- [13] P. Beaumier, M. Costes, R. Gavériaux. "Comparison Between FP3D Full Potential Calculations and S1 Modane Wind Tunnel Test Results on Advanced Fully Instrumented Rotors". *19th European Rotorcraft Forum*. Cernobbio (Italie) 1993.
- [14] J. Steinhoff, K. Ramachandran. "Free Wake Analysis of Compressible Rotor Flows". *25th AIAA Aerospace Sciences Meeting*. Reno (Nevada) 1987.
- [15] H. Viviand. "Formes conservatives des équations de la dynamique des gaz". *La Recherche Aéronautique*. Année 1974. (No 1). pp. 65-68.
- [16] P.D. Thomas, C.K. Lombard. "The Geometric Conservation Law-A Link Between Finite-Difference and Finite-Volume Methods of Flow Computation on Moving Grids". *11th AIAA Fluid and Plasma Dynamics Conference*. Seattle (Washington) 1978.
- [17] J.L. Steger, F.X. Caradonna. "A Conservative Implicit Finite-Difference Algorithm for the Unsteady Transonic Full Potential Equation". *13th AIAA Fluid and Plasma Dynamics Conference*. Snowmass (Colorado) 1980.
- [18] J.O. Bridgeman, J.L. Steger, F.X. Caradonna. "A Conservative Finite Difference Algorithm for the Unsteady Transonic Potential Equation in Generalized Coordinates". *9th AIAA Atmospheric Flight Mechanics Conference*. San Diego (California) 1982.
- [19] R.C. Strawn, F.X. Caradonna. "Numerical Modeling of Rotor Flows with a Conservative Form of the Full-Potential Equation". *24th AIAA Aerospace Sciences Meeting*. Reno (Nevada) 1986.
- [20] B. Engquist, S. Osher. "Stable and Entropy Satisfying Approximations for Transonic Flow Calculations". *Mathematics of Computation*. Volume 34. (No 149). pp. 45-75. 1980.
- [21] S. Osher, M. Hafez, W. Whitlow Jr. "Entropy Condition Satisfying Approximations for the Full Potential Equation of Transonic Flow". *Mathematics of Computation*. Volume 44. (No 169). pp. 1-29. 1985.
- [22] J. Flores, T.L. Holst, D. Kwak, D. Batiste. "A new Consistent Spatial Differencing Scheme For the Transonic Full-Potential Equation". *21st AIAA Aerospace Sciences Meeting*. Reno (Nevada) 1983.
- [23] W. Whitlow Jr. "Application of a Nonisentropic Full Potential Method to AGARD Standard Airfoils". *26th AIAA Aerospace Sciences Meeting*. Reno (Nevada) 1988.
- [24] J.O. Bridgeman, R.C. Strawn, F.X. Caradonna, C.S. Chen. "Advanced Rotor Computations with a Corrected Potential Method". *45th Forum of the American Helicopter Society*. Boston (Massachusetts) 1989.
- [25] J. Cousteix, R. Houdeville. "Turbulent Boundary Layer Calculations in Unsteady Flows". *Présenté à "Numerical Methods in Applied Fluid Dynamics"*. University of Reading (England) 1978.
- [26] A.J. Landgrebe. "An Analytical Method For Predicting Rotor Wake Geometry". *AIAA Meeting*. Atlanta (Georgia) 1969.
- [27] J.D. Kocurek, J.L. Tangler. "A Prescribed Wake Lifting Surface Hover Performance Analysis". *32nd Forum of the American Helicopter Society*. Washington DC 1976.
- [28] M. Nsi Mba, D. Favier, C. Maresca, P. Crespi. "Helicopter Rotor Wake Investigation using a Laser Doppler Anemometry Technique". *Proceedings of the 4th International Symposium on Applications of Laser Anemometry to Fluid Mechanics (ISALA)*. Lisbonne (Portugal) 1988.
- [29] J. Steinhoff, K. Ramachandran. "Free Wake Analysis of Compressible Rotor Flow Fields in Hover". *12th European Rotorcraft Forum*. Garmish-Partenkirchen (Allemagne) 1986.
- [30] K. Ramachandran. "Free Wake Analysis of Helicopter Rotor Blades in Hover Using a Finite Volume Technique". *Ph. D. Thesis*. University of Tennessee. Knoxville (Tennessee) 1987.
- [31] H. Lamb. *Hydrodynamics*. Publié par : Cambridge University Press. pp 248-249.
- [32] A. Vuillet, M. Allongue, J.J. Philippe, A. Desopper. "Performance and Aerodynamic Development of the Super Puma Mk2 Main Rotor with New SPP8 Blade Tip Design". *15th European Rotorcraft Forum*. Amsterdam (Pays-Bas) 1989.
- [33] J. Reneaux, J.J. Thibert. "The Use of Numerical Optimization for Airfoil Design". *3rd AIAA Applied Aerodynamics Conference*. Colorado Springs (Colorado) 1985.
- [34] H. Bézard. "Rotor Blade Airfoil Design by Numerical Optimization and Unsteady Calculations". *48th Forum of the American Helicopter Society*. Washington DC 1992.
- [35] D. Destarac, J. Reneaux, D. Gisquet. "Numerical Optimization of Wings in Transonic Flow". *AGARD Conference on "Computational Methods for Aerodynamic Design (Inverse) and Optimization"*. Loen (Norvège) 1989.
- [36] D. Destarac, J. Reneaux. "Numerical Optimization applied to Transport Aircraft Aerodynamics". *La Recherche Aéronautique*. Année 1993. (No 1993-2). pp. 39-55.
- [37] P. Leconte, P. Geoffroy. "Dynamic Optimization of a Rotor Blade". *AHS Aeromechanics Specialists Conference*. San Francisco (California) 1994.
- [38] J. Zibi, G. Defresne, M. Costes. "A Numerical Procedure for Aerodynamic Optimization of Helicopter Rotor Blades". *18th European Rotorcraft Forum*. Avignon (France) 1992.
- [39] F.J. Perry. "Aerodynamics of the Helicopter World Speed Record". *43rd Forum of the American Helicopter Society*. Saint-Louis (Missouri) 1987.
- [40] K. Ramachandran, S. Schlechtriem, F.X. Caradonna, J.S. Steinhoff. "The Application of Vorticity Embedding to the Computation of Advancing Rotor Flows". *49th Forum of the American Helicopter Society*. Saint-Louis (Missouri) 1993.

- [41] J.O. Bridgeman, K. Ramachandran, F.X. Caradonna, D. Pritchard. "A Computational Analysis of Parallel Blade-Vortex Interactions using Vorticity Embedding". *50th Forum of the American Helicopter Society*. Washington D.C. 1994.
- [42] J. Sidès, J.C. Boniface. "Solution of the Compressible Euler Equations for Steady Flows around Helicopter Rotor Blades by an Implicit Space-Centered Method". *17th European Rotorcraft Forum*. Berlin (Allemagne) 1991.
- [43] J.C. Boniface, J. Sidès. "Numerical Simulation of Steady and Unsteady Euler Flows around Multibladed Helicopter Rotors". *19th European Rotorcraft Forum*. Cernobbio (Italie) 1993.
- [44] J.C. Le Balleur, P. Girodroux-Lavigne. "Calculation of Fully Three-Dimensional Separated Flows with an Unsteady Viscous-Inviscid Interaction Method". *5th Symposium on Numerical and Physical Aspects of Aerodynamic Flows*. California State University. Long-Beach (California) 1992.
- [45] J.C. Le Balleur. "Calcul par interaction visqueux-non visqueux des écoulements compressibles fortement décollés aux grandes portances sur profils d'ailes et voilures". *Proceedings AGARD-CP-415, AGARD/FDP Symposium on High-lift Aerodynamics*. Banff (Canada) 1992.
- [46] V. Couaillier, Ph. Veysseyre, A.M. Vuillot. "3D Navier-Stokes Computations in Transonic Compressor Bladings". *10th ISABE*. Nottingham (Grande Bretagne) 1991.
- [47] A.M. Vuillot, V. Couaillier, N. Liamis. "3D Turbomachinery Euler and Navier-Stokes Calculations with a Multidomain Cell-Centered Approach". *29th AIAA/ASME/ASEE Joint Propulsion Conference and Exhibit*. Monterey (California) 1993.

3D EULER CALCULATIONS OF MULTIBLADED ROTORS IN HOVER: INVESTIGATION OF THE WAKE CAPTURING PROPERTIES

J. Raddatz
K. Pahlke

DLR, Institute of Design Aerodynamics
Lilienthalplatz 7
D-38108 Braunschweig
Germany

Summary:

The 3D flowfield of a hovering rotor is calculated solving the Euler equations. Performing a grid refinement study it is demonstrated that an Euler method is able to capture the wake and vortices of a hovering rotor without any wake modelling. Accurate prediction of these rotational flow field phenomena needs fine grids with a high resolution in the complete region of the wake system. Additionally, high accuracy for the treatment of all numerical boundaries, which affect the vortex wake, is required. On the other hand, the investigations have shown that surface airloads are less effected by a more detailed resolution of the wake system.

A second part of the study is concerned with wake capturing properties on block boundaries, especially on inner boundaries of overlapping grids. Overlapping grids are very attractive for the computation of a rotor in lifting forward flight or a rotor-body flowfield in hover. The effect of overlapping grids using the chimera technique is investigated comparing Euler solutions for a hovering rotor on a chimera grid system and on conventional single block and two block calculations. The chimera solution reproduces all flow features. The present implementation shows disadvantages concerning the detailed resolution of the wake system.

Symbols:

c	chord	x, y, z	Cartesian coordinates
c_p	pressure coefficient	γ	ratio of specific heats
$c_p = \frac{p - p_\infty}{\frac{1}{2} \rho_\infty (\omega \cdot r)^2}$		θ	pitching angle
C_T	thrust coefficient	ρ	density
E	total specific energy	σ	solidity of the rotor
F	flux tensor	ψ	azimuth
\vec{G}	vector of source terms	ω	angular velocity
H	total specific enthalpy	Index r	blade fixed coordinate system
M	Mach number		
\vec{n}	unit outward to ∂V		
p	pressure		
\vec{q}	velocity vector		
r	radial position of a rotor section		
\vec{r}	$= (x, y, z)^T$ coordinate vector		
R	rotor radius		
dS	surface element		
t	time		
u, v, w	Cartesian velocity components		
V	control volume		
dV	volume element		
\vec{W}	vector of conservative variables		

1. Introduction

Current methods of predicting the flowfield of an hovering rotor range in complexity from relatively simple boundary integral methods [1] up to more sophisticated computational fluid dynamics (CFD) methods solving the full potential [2], the Euler [3] or the Navier-Stokes equations [4].

Most of these methods are coupled with integral wake models to introduce the influence of the vortex wake, obtaining results of high accuracy for many cases, but always dominated by the wake model [5]. Using a prescribed wake model, the wake has to be specialized for each blade shape, making it difficult to treat blades with arbitrary twist, taper or planform. Also some potential flow methods have been coupled with a free-wake approach,

in which the wake is allowed to convect freely with the flow without constraining its trajectory [6]. These methods are restricted in the treatment of compressibility and transonic effects, which are features of the flow around advanced high speed helicopter rotors.

Other recent methods, including the present one, are using direct techniques for the entire solution process without any wake modelling [7]-[10]. The presented method is based on the Euler equations, which describe the complete inviscid flowfield of a lifting hovering rotor, including the wake and its induced effects. The vortex wake and its effects are captured as part of the solution, provided that the grid contains the whole rotor disc. This feature of the Euler (and Navier-Stokes) equations is of great interest due to the importance of the mutual blade-vortex interactions on the aerodynamics of an hovering rotor and the existing problems using any wake model.

In the present study, the multiblock, multigrid Euler/Navier-Stokes code CEVCATS of DLR Braunschweig (for details see [11]-[13]) is used to perform Euler calculations of the flowfield around hovering rotors. The objective of this study is the investigation of the accuracy of the DLR CEVCATS code concerning the prediction of rotational phenomena in the flowfield like the wake or the tip vortex of the rotor blades. Most previous computations of the hovering rotor problem using Euler or Navier-Stokes methods [7]-[10] have shown good agreements with measurements comparing surface pressures or surface velocities. These results indicate that the Euler equations are able to predict the accurate inviscid surface flow quantities as well as the global flow phenomena of a hovering rotor. The investigations presented in this paper are directed towards the accurate modelling of the complete hover flowfield. Using flow field visualization tools the wake geometry, especially the shape and trajectories of the tip vortices, calculated by the Euler code, are shown. The basic investigations are concerning the effects of grid refinement on the wake geometry, the vortex dissipation and finally on the surface pressures.

A second part of the flow visualization studies are the wake capturing properties on block boundaries. These investigations are also concerned with overlapping grids. The use of overlapping grids is one

possibility to calculate a rotor in lifting forward flight or a rotor-body flowfield in hover. The treatment of overlapping grids, known as chimera technique [14],[15], introduces additional numerical errors in space. These additional spatial errors are investigated performing hover calculations using the chimera technique and comparing these results with those on conventional single-block or multi-block grids.

2. Governing equations

In a blade attached coordinate system rotating with a constant angular velocity, the flowfield around a hovering rotor can be treated as steady. In this reference frame the Euler equations can be formulated in terms of either relative or absolute flow variables. The results presented in this study were obtained using the formulation with absolute flow variables, which is necessary for an accurate formulation of the farfield boundary condition.

The Euler equations in Cartesian coordinates are written in integral form as:

$$\frac{d}{dt} \int_{V_r} \vec{W}_r dV_r + \int_{\partial V_r} \vec{F}_r \cdot \vec{n}_r dS_r + \int_{V_r} \vec{G}_r dV_r = 0$$

\vec{W}_r represents the conserved vector of absolute flow variables, \vec{F}_r the corresponding flux tensor and \vec{G}_r is a source term.

For a hovering rotor rotating around the x-axis with the angular velocity $\vec{\omega} = [\Omega, 0, 0]^T$ these quantities are given by:

$$\vec{W}_r = \begin{bmatrix} \rho \\ \rho u_r \\ \rho v_r \\ \rho w_r \\ \rho \tilde{E}_r \end{bmatrix}, \quad \vec{G}_r = \begin{bmatrix} 0 \\ 0 \\ -\rho \Omega w_r \\ \rho \Omega v_r \\ 0 \end{bmatrix},$$

$$\vec{F}_r = \begin{bmatrix} \rho [\vec{q}_r - (\vec{\omega} \times \vec{r}_r)] \\ \rho u_r [\vec{q}_r - (\vec{\omega} \times \vec{r}_r)] + p \vec{i}_x \\ \rho v_r [\vec{q}_r - (\vec{\omega} \times \vec{r}_r)] + p \vec{i}_y \\ \rho w_r [\vec{q}_r - (\vec{\omega} \times \vec{r}_r)] + p \vec{i}_z \\ \rho \tilde{H}_r [\vec{q}_r - (\vec{\omega} \times \vec{r}_r)] \end{bmatrix}$$

The relative velocity \vec{q}_r is given by:

$$\vec{q}_r = \begin{bmatrix} u_r \\ v_r \\ w_r \end{bmatrix} = \begin{bmatrix} 1 & 0 & 0 \\ 0 & \cos \Omega t & \sin \Omega t \\ 0 & -\sin \Omega t & \cos \Omega t \end{bmatrix} \cdot \begin{bmatrix} u \\ v \\ w \end{bmatrix}$$

This system of equations is closed by:

$$p = (\gamma - 1) \rho \left(\tilde{E}_r - \frac{\vec{q}_r^2 - 2\vec{q}_r \cdot \vec{\omega} \times \vec{r}_r}{2} \right)$$

with $\tilde{E}_r = E_r - \vec{q}_r \cdot (\vec{\omega} \times \vec{r}_r)$

and $\tilde{H}_r = \tilde{E}_r + p/\rho$.

\tilde{H}_r is the so called rothalpy, which is constant in the whole flow field for the case of an adiabatic steady flow in the rotating coordinate system.

3. Grid Generation

Body conforming, single block, computational grids were constructed for hovering rotors, using a grid generator based on an elliptic 3D solver (for details see [17]). Because of the cylindrical nature of the flow of a hovering rotor an O-H topology was chosen with the wraparound O in chordwise direction and the H-type in spanwise direction. This grid topology is suitable for 2-bladed as well as for multi-bladed rotors (see Ref. [5]). The grid is clustered near the leading and trailing edges and near the tip region to resolve the tip vortex.

Due to the symmetry of the flow only a segment of the rotor plane containing one blade has to be regarded. The other blades are taken into account by periodicity conditions in the blade azimuthal direction, which swap the flow information at the front and back boundaries of the cylindrical mesh. Using this grid topology it is obvious to generate grids with identical point distributions on the periodicity planes. Therefore, no interpolation of the flow quantities on the periodicity planes is required.

Figure 1 presents the surface grid and two surrounding O-planes of the 2-bladed model rotor used by Caradonna and Tung. The complete grid shape is shown in Figure 2. For a grid refinement study grids of three different sizes were generated starting with a coarse grid of 57 points in the wrap-around "O", 21 points in the normal and 33 points in the radial direction. The grid was refined in all three

index directions for two times obtaining a fine grid of about 2.4 million points. Figure 3 demonstrates the different grid sizes presenting the grid lines in the rotor disk.

Grids used for investigations on the chimera algorithm have been extracted from conventional one block grids in order to minimize differences in the solutions due to different grid shapes. For details see chapter 4.3.

4. Numerical Aspects

4.1 Spatial and Temporal Discretization

The discretization of space and time is separated following the method of lines (Jameson et al. [11]) using a cell-vertex finite volume formulation for the spatial discretization. The flow quantities \vec{W}_r and

the source term \vec{G}_r are taken to be volume averaged and are located at the nodes of the grid. The finite volume discretization leads to a 2. order central difference scheme on a Cartesian grid with constant grid sizes. If an arbitrary nonuniform grid is used, the accuracy depends on the smoothness of the grid. For the cell-vertex scheme a minimum of 1. order accuracy is guaranteed for arbitrary grids (for details see [13]). In order to avoid spurious oscillations a blend of first and third order dissipative terms is introduced.

An explicit Runge-Kutta time stepping scheme is used with an evaluation of the dissipative fluxes at the first two stages [12]. In order to accelerate the convergence to steady state for hover cases rothalpy damping, implicit residual averaging and a multigrid algorithm have been implemented.

4.2 Boundary Conditions

For the blades, a solid wall condition is used at the surface. This boundary condition zeroes the normal component of the velocity vectors at the surface nodes of the body fitted grid and ensures flow parallel to the wall.

The farfield boundary is treated following the concept of Characteristic Variables for non-reflecting boundary conditions.

At the inboard plane boundary near the axis of rotation, spanwise velocity is set to zero and other flow quantities are extrapolated from the grid points inte-

rior to the boundary. Finally, to take advantage of the symmetry of the flowfield from blade to blade in the hovering configuration, flowfield calculations are performed on one isolated rotor blade using the information from the neighbouring blade through a periodic boundary condition procedure.

4.3 Chimera Algorithm

The basic idea of the chimera scheme is to generate body conforming grids (so called child grids) around different bodies independently and to embed these grids into a background grid (so called father grid). There is no need for common boundaries between the grids, but rather an overlap region is required between a child grid and the father grid to provide the means for matching the solutions across the boundary interfaces. The present chimera scheme has been implemented according to references [14] and [15]. [Figure 4](#) shows a child grid embedded into a father grid for a two bladed rotor. In this test case the father grid is identical to a conventional one block grid with a collective pitch angle of 0° . The child grid consists of the inner part of the conventional grid, generated by skipping the second half of grid points in normal direction. It is rotated around the quarter line corresponding to the collective pitch angle. This procedure is of course not typical for overlapping grids, but it was chosen to eliminate possible differences due to different grid shapes or different clustering.

Since the rotor blade in the child grid is an impermeable body with no flow through it, the points of the father grid that fall within the rotor blade are excluded or blanked from the flow field solution. These blanked out points in the father grid form a "hole" in the father grid. [Figure 5](#) shows a view of a child grid and the hole in the father grid. The boundary of this hole is the first of two interface boundaries, that arise because of the use of the chimera scheme. Data for this hole boundary is supplied from the solution contained on the child grid. The outer boundary of the child grid forms the second interface. Flow values for the dummy layer at this outer boundary are provided from the father grid. In this implementation only flow values are exchanged at the chimera boundaries, which simplifies the algorithm, but yields a non-conservative scheme. As it is shown in [16] this can result in inaccurate solutions for supersonic or hypersonic flows. This

deficiency can be corrected by a chimera boundary treatment with conservative flux interpolation. On the other hand several publications show that non-conservative chimera schemes produce accurate solutions for sub- or transonic flows, when it is assured that no shocks cross the chimera boundaries.

In order to provide the flow values at the grid interfaces it is necessary to use interpolation formulae. Different approaches have been published. Higher order interpolation has the advantage of higher spatial accuracy, but unfortunately it may introduce instabilities into the schemes. Therefore trilinear interpolation using the node points of hexahedrons is used in most implementations. This approach is computationally very efficient but it does not ensure that the interpolated point lies within the hexahedron (especially for skewed cells). For these reasons a trilinear interpolation based on tetrahedrons was chosen for the present work which consumes more cpu-time but guarantees that all interpolation coefficients are positive and less or equal 1. Hence it is necessary to find for each boundary point the tetrahedron which contains the boundary point. This search takes advantage of the fact that structured grids are used [15]. For steady cases the search algorithm is run only once.

The time stepping scheme is changed with regard to a special treatment of the hole points. The algorithm is modified such that the flow values for the hole in the father grid are not updated by the Runge-Kutta scheme nor the implicit residual smoothing nor the rothalpy damping.

The chimera scheme in the present work has not been coupled with the multigrid algorithm.

5. Results

The test cases considered in this study correspond to the experimental model hover test conditions of Caradonna and Tung [18]. The experimental model consists of a 2-bladed rigid rotor with rectangular blades with no twist or taper. The blades are made of NACA 0012 airfoil sections with an aspect ratio of 6. The experimental conditions of the presented results are:

$$\begin{aligned} \text{tip Mach number: } M_{\omega R} &= 0.794, \\ \text{collective pitch: } \theta_c &= 8.0^\circ \end{aligned}$$

5.1 Grid refinement study

Figure 6 shows predicted and experimental pressure coefficients at four different blade sections for the selected test case. The figure compares the experimental data with the solutions conducted on the three grids with different grid sizes. The numerical results show the typical behaviour of a grid refinement study with very small discrepancies between fine and medium grid solutions and some larger differences in the pressure values between medium and coarse grid solutions. These results indicate that the fine grid solution is grid converged. All calculations predict an identical shock position. Larger discrepancies can be recognized in the prediction of the shock wave strength. Due to the lack of grid points the coarse grid solution underpredicts the shock strength. The solutions on the finer grids, which agree quite well, show an overprediction of the shock compared to the measured data. One reason for this is that the current calculations are inviscid. Shock-boundary interactions tend to weaken the shock. An inviscid code cannot model this phenomenon, so some discrepancies in predicted and measured shock wave strength are expected. Overall the Euler calculations are in good agreement with the experimental results on all radial stations.

Calculated and measured thrust coefficients are compared in Figure 7. The discrepancies between measurement and computation are caused mainly by viscous effects.

Main objective of this study is the investigation of the prediction of rotational phenomena in the flow field like the wake or the tip vortex of the rotor blade using an Euler code. The flow field investigations are performed extracting radial 2D slices, which are located nearly perpendicular to the mean flow direction. Plotting vorticity contours (magnitude of the local rotation vectors $=|\vec{\nabla} \times \vec{q}|$) the 2D slices show a good representation of the wake and the tip vortices.

The radial location of the slices presented in this paper are indicated in Figure 8. The figure shows the grid lines in the rotor disk and the six different radial slice positions at the rotor blade and at 20°, 40°, 70°, 100° and 140° behind the blade. The vorticity contours of all 2D slices extracted from the fine grid solution are presented in Figure 9. At the first four slices three separate vortices can clearly be

identified. At the radial position 20° behind the blade e.g., the three indicated vortices have an age of 20°, 200° and 380°. The youngest vortex is represented at the end of the rotor disk by concentrated vorticity iso-lines. The older vortices are located below the rotor disk and have moved closer to the hub. Between the radial slices at 70° and 100° the number of clearly identified vortices is reduced, because two vortices are joined to one large vortex. Further downstream the vorticity contours of all radial slices indicate a vortex structure, which has the correct radial position of an additional vortex, but doesn't change its axial position.

The wake of the rotor blades can also clearly be identified. Certainly the wake diffuses due to numerical dissipation, but it is represented in this figure for an age of about 250°.

The effect of grid refinement on the resolution of rotational flow phenomena is studied in Figure 10. It compares vorticity contours plotted at 70° behind the rotor blade of a fine, a medium and a coarse grid. Additionally the corresponding grid planes are presented. The figure clearly shows the strong effect of the different grid density. Whereas the fine grid solution resolves three strong and separate vortices, there is only one weak vortex represented by the coarse grid calculation. The wake dissipates on the coarse grid already after 70°.

Quantitative measurements were taken for the vortex trajectories and these are compared with predicted values in Figure 11. In this figure, a dashed line represents the experimental data from Ref. [18]. The vortex trajectories computed on different grids were obtained using the results from Figure 9 to locate the centers of vortices graphically. The coordinate values of these vortex centers are obtained at discrete azimuthal angles and then transferred to the plots in Figure 11. The plotting of computed results stops when the vortex centers are impossible to determine graphically. The radial contraction of the tip vortex shows reasonable agreement with the experimental data. After a vortex age of 180° the discrepancies between the calculations on the different grids become larger and the computed vortex trajectories show more contraction than indicated by the experiment. These differences in the contraction of the wake system between Euler calculation and experiment have already been mentioned in other publications, e.g. Ref. [9]. One cause for the discrepancies is proba-

bly the absence of the whirl tower in the calculations.

The vertical descent of the tip vortex, computed on the fine grid, shows excellent agreement with the experimental data. The difference which occurs after a vortex age of 280° is caused by the fusion of two vortices to one large vortex due to large grid cells in axial direction (see Figures 9 and 10). The agreement between medium grid calculation and experiment concerning the vertical descent of the tip vortex is fairly good, while the coarse grid results indicate that the coarse grid is not able to resolve one singular tip vortex.

The results of the grid refinement study show that the prediction of the wake system of a hovering rotor is mainly affected by the grid resolution. On the fine grid e.g., the wake dissipation is caused by a low resolution of the grid in axial direction. On the other hand a detailed resolution of the wake system seems not to be very important to obtain reasonable results on the blade surface. The computations indicate that for a 2-bladed rotor the vortex should be well resolved up to a vortex age of at least 180° . At this point the blade is passing over the vortex from the preceding blade for the first time. This is the location where the vortex trajectory and strength have the most influence on the blade airloads. Beyond this point, airloads on the blade surface are less effected by the vortex location.

5.2 Effect of Boundary Conditions

Improvement of Periodicity Boundary Conditions

Figure 12 shows results of two fine grid calculations. On the top of the figure pressure coefficients at three different blade sections and on the bottom vorticity contours at a radial section 70° behind the rotor blade are shown. The presented calculations use different treatments of the periodicity boundary conditions. The first calculation has been performed using two dummy layers at the periodic boundaries obtaining 2. order accuracy at these boundaries. The second calculation uses only one dummy layer leading at these boundaries to 1. order accuracy. Comparing the surface pressures of both fine grid computations there are no determinable differences. In spite of this the flow field visualizations of the different computations show considerable discrepancies. It is clearly visible that the more accu-

rate treatment of the periodic boundary reduces the numerical dissipation, which is indicated by an improved separation of the tip vortices and an improved representation of the wake.

This investigation has been repeated on the medium grid. The result is presented in Figure 13. Again the differences on the surface pressures are negligible. Compared to the fine grid investigation the discrepancies in the resolution of the wake system between 1. and 2. order boundary treatment are somewhat smaller. This effect is caused by the reduced grid fineness. The medium grid has more inherent dissipation and decreases therefore the effect of accuracy improvement at the periodic boundaries.

Chimera Boundaries

In this section the effect of chimera boundaries using overlapping grids for the selected hover case is presented. Corresponding 2D results have been published in Ref. [19].

Figure 14 compares computational results of a conventional single block, a conventional two block and a chimera two block solution with the experimental data. The single block grid is identical to the medium grid used in previous investigations. In order to have a fair comparison, the conventional two block grid and the chimera grid system are based on the conventional one block grid, generating block boundaries in the blade normal direction. The investigation of the chimera technique has been performed using a simplified Euler code with a cell centered finite volume discretization and without multigrid algorithm. Up to now this code allows only first order treatment at chimera boundaries. Therefore all computations for this investigation have been performed using a boundary treatment of 1. order accuracy at all boundaries.

In comparison with 2D results of Ref. [19], which are not shown here, the 3D calculations presented in Figure 14 show a less good agreement. There are differences between the conventional single and two block computations. These differences, especially the movement of the shock position at the blade sections $r/R = 0.89$ and $r/R = 0.96$, are caused by the first order boundary treatment at the inner block boundaries. The chimera two block computation uses the same boundary treatment at the outer boundaries of the child grid. In addition first order interpolation errors occur at the hole

boundaries of the father grid and at the outer boundaries of the child grid which increases the differences between the conventional single block and the chimera computation.

The effect of chimera boundaries on rotational phenomena in the flow field is demonstrated in Figure 15 showing vorticity contours for the three computations at a radial section 20° behind the rotor blade. The small white gaps in the results for the 1 block and the 2 block calculations are caused by the post-processing method, which is not adapted for a flow solver using a cell centered scheme.

The vorticity contours of all calculations indicate two tip vortices. The 20° old tip vortex is represented at the end of the rotor disc by concentrated vorticity iso-lines. The vortex of the preceding blade has moved below the rotor disc and closer to the hub. Comparing single block and conventional two block results there are only small differences in the representation of the second vortex with an age of 200° . Going from the two block to the chimera calculation both vortices are widened and less sharply resolved. The results for the chimera calculation had to be reconstructed using cells of the father and the child grid. This can be recognized in a slight displacement of the vorticity iso-lines.

It is shown that the current implementation of the chimera technique for overlapping has to be improved concerning the accuracy of the boundary treatment.

6. Conclusion

The flowfield of a hovering rotor is calculated solving the Euler equations formulated in terms of the absolute flow variables in a blade attached coordinate system. The vortex wake and its induced effects are captured as part of the overall numerical solution without specifying any wake structure or position, i.e., without any wake modelling.

Performing a grid refinement study it was demonstrated that the accurate prediction of wake and vortices of a hovering rotor is possible using an Euler code. However, fine grids with a high resolution in the complete region of the wake system are needed. Additionally, high accuracy for the treatment of periodicity boundaries or other boundaries is required. These results indicate that the one

block O-H topology for the grid has to be improved for a better wake resolution with less grid points. It is believed that multiblock grids with an O-H (Euler) or C-H (Navier-Stokes) topology near the rotor blade embedded into one or several H-H grids offer a better strategy to generate grids with a reduced number of grid points and an improved resolution of the wake region. Main difficulties using multiblock grids are a smooth design of the block boundaries and an accurate treatment of the boundary conditions.

The results also show that a detailed resolution of the wake system may not be very important to obtain reasonable results for the surface airloads on hovering rotors. Keeping in mind that Euler calculations don't account for viscous effects the surface data predicted on the medium grid show already a good agreement to the experimental data. Even coarse grid calculations may be acceptable for engineering purposes, as long as only flow quantities on the blade surface are required.

Additionally, investigations were made concerning the effect of different block boundaries on the accurate prediction of surface data and wake capturing properties. Solutions for a hovering rotor using a conventional single block, a conventional two block and a chimera grid were compared. It was shown that it is possible to capture the wake system using an Euler code on a chimera grid system. The chimera solution reproduced all flow features but the vortices are captured less sharply. The flow field results of both multiblock computations again demonstrates the need of 2. order treatment of block boundaries. Further investigations are necessary concerning the additional spatial errors of chimera boundaries, especially for cases with larger differences in father and child grids at the chimera boundaries. In addition with the very promising 2D results of Ref. [19] the presented 3D chimera computations give hope that accurate forward flight solutions using the chimera technique will be possible.

7. Acknowledgement

This work is partly founded by CEC, IMT project AERO-2017/2060 (HELISHAPE).

8. Bibliography

- [1] Caradonna, F.X.; Desopper, A. and Tung, C.: 'Finite Difference Modelling of Rotor Flows Including Wake Effects', Paper 2.7, Eighth European Rotorcraft Forum, Aix-en-Provence, France, Aug. 1982.
- [2] Costes, M.; Desopper, A.; Ceroni, P. and Lafon, P.: 'Flow Field Prediction for Helicopter Rotor with Advanced Blade Tip Shapes using CFD Techniques', 2nd International Conference on Basic Rotorcraft Research, College Park (University of Maryland), Feb. 1988.
- [3] Chang, I.-C. and Tung, C.: 'Euler Solution of the Transonic Flow for a Helicopter Rotor', AIAA Paper 87-0523, Jan. 1987.
- [4] Srinivasan, G.R. and McCroskey, W.J.: 'Navier-Stokes Calculations of Hovering Rotor Flowfields', Journal of Aircraft, Vol. 25, No.10, pp. 865-874, 1988.
- [5] Pahlke, K. and Raddatz, J.: '3D Euler Methods for Multibladed Rotors in Hover and Forward Flight', 19th European Rotorcraft Forum, Paper C20, Cernobbio (Como), Italy, September 1993.
- [6] Zerle, L. and Wagner, S.: 'Development and Validation of a Vortex Lattice Method to Calculate the Flowfield of a Helicopter Rotor Including Free Wake Development', 18th European Rotorcraft Forum, Paper 72, Avignon, France, September 1992.
- [7] Kroll, N.: 'Computation of the Flow Fields of Propellers and Hovering Rotors using Euler Equations', 12th European Rotorcraft Forum, Paper 28, Garmisch-Partenkirchen, Germany, September 1986.
- [8] Boniface, J.C. and Sides, J.: 'Numerical Simulation of Steady and Unsteady Euler Flows around Multibladed Helicopter Rotors', 19th European Rotorcraft Forum, Paper C10, Cernobbio (Como), Italy, September 1993.
- [9] Strawn, R.C. and Barth, T.J.: 'A Finite-Volume Euler Solver for Computing Rotary-Wing Aerodynamics on Unstructured Meshes', presented at the 48th Annual Forum of the American Helicopter Society, Washington, DC, June 1992.
- [10] Srinivasan, G.R.; Baeder, J.D.; Obayashi, S. and McCroskey, W.J.: 'Flowfield of a Lifting Rotor in Hover: A Navier-Stokes Simulation', AIAA Journal, Vol. 30, No.10, October 1992.
- [11] Jameson, A.; Schmidt, W.; Turkel, E.: 'Numerical Solutions of the Euler Equations by Finite Volume Methods Using Runge-Kutta Time Stepping Schemes', AIAA-Paper 81-1259 (1981).
- [12] Kroll, N. and Jain, R. K.: 'Solution of Two-Dimensional Euler Equations - Experience with a Finite Volume Code', DFVLR-FB 87-41, Braunschweig, 1987.
- [13] Rossow, C.-C.: 'Berechnung von Strömungsfeldern durch die Lösung der Euler-Gleichungen mit einer erweiterten Finite-Volumen Diskretisierungsmethode', DLR-FB 89-38, Braunschweig, 1989.
- [14] Benek, J. A.; Buning, P. G.; Steger, J. L.: 'A 3-D Chimera Grid Embedding Technique', AIAA 7th Computational Fluid Dynamics Conference, Cincinnati, Ohio, July 15-17, 1985.
- [15] Dougherty, F. C.: 'Development of a Chimera Grid Scheme with Applications to Unsteady Problems', Ph. D. Thesis, Stanford University, USA, 1985.
- [16] Pärt-Enander, E. and Sjögren, B.: 'Conservative and Non-Conservative Interpolation between Overlapping Grids for Finite Volume Solutions of Hyperbolic Systems', Computers Fluids, Vol. 23, No. 3, pp. 551-574, Pergamon Press, 1994.
- [17] Findling, A. and Herrmann, U.: 'Development of an efficient and robust solver for elliptic grid generation', Proceedings of the Third International Conference on Numerical Grid Generation in Computational Fluid Dynamics and Related Fields, Barcelona, Spain, 1991.
- [18] Caradonna, F. X. and Tung, C.: 'Experimental and Analytical Studies of a Model Helicopter Rotor in Hover', NASA TM-81232, September 1981.
- [19] Pahlke, K. and Raddatz, J.: 'Flexibility Enhancement of Euler codes for Rotor Flows by Chimera Techniques', 20th European Rotorcraft Forum, Paper 34, Amsterdam, The Netherlands, October 4th - 7th, 1994.

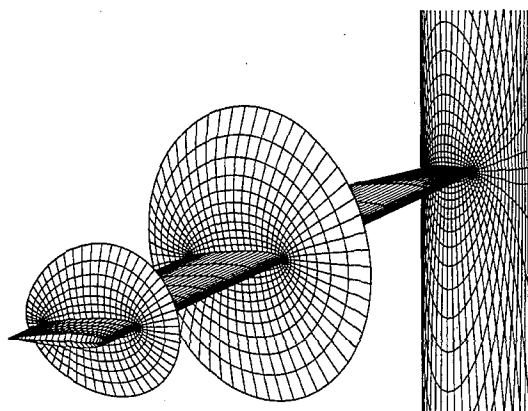


Figure 1: Surface grid

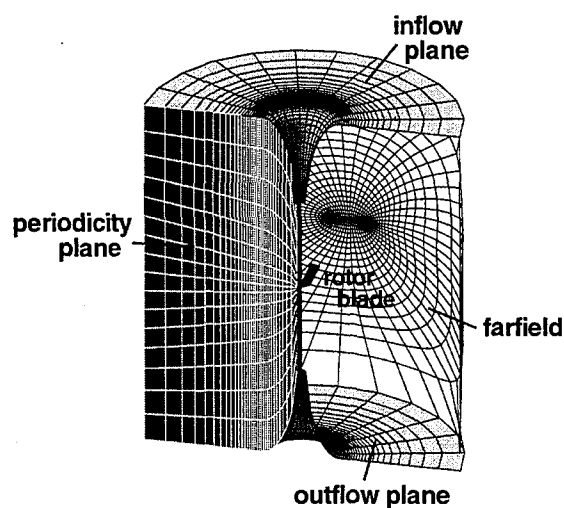


Figure 2: O-H grid around one blade of the 2-bladed Caradonna-Tung rotor

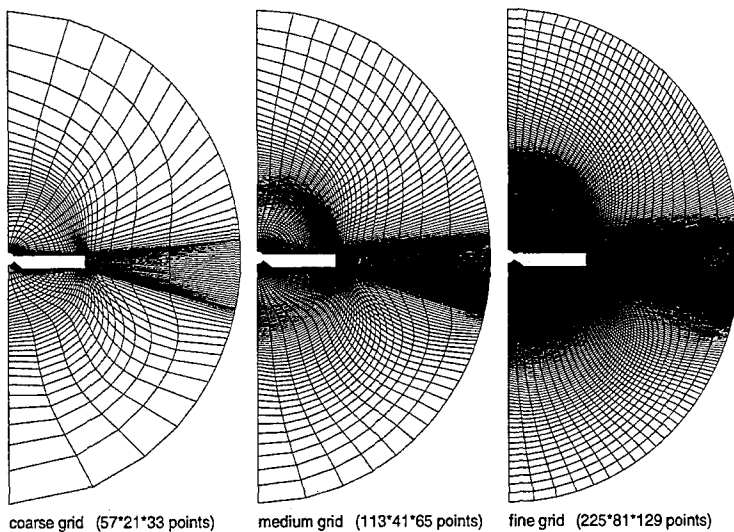


Figure 3: Grid refinement study:
Grid lines in the
rotor disk

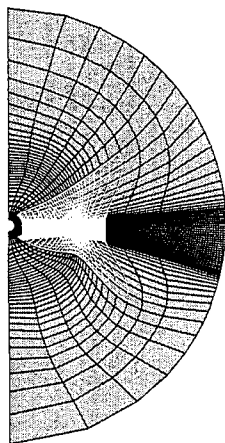


Figure 4: Grid lines in the rotor disk of Chimera Grid:
black lines - father grid
white lines - child grid

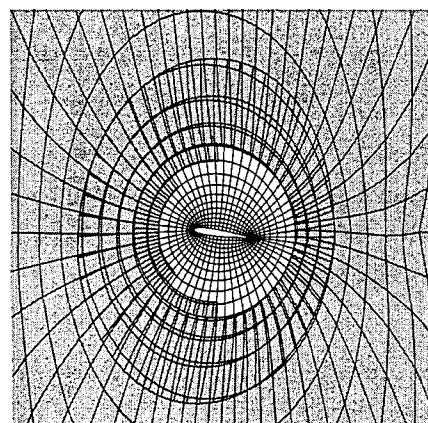


Figure 5: O-type child grid embedded into
O-type father grid
(father grid shaded grey except for the 'hole')

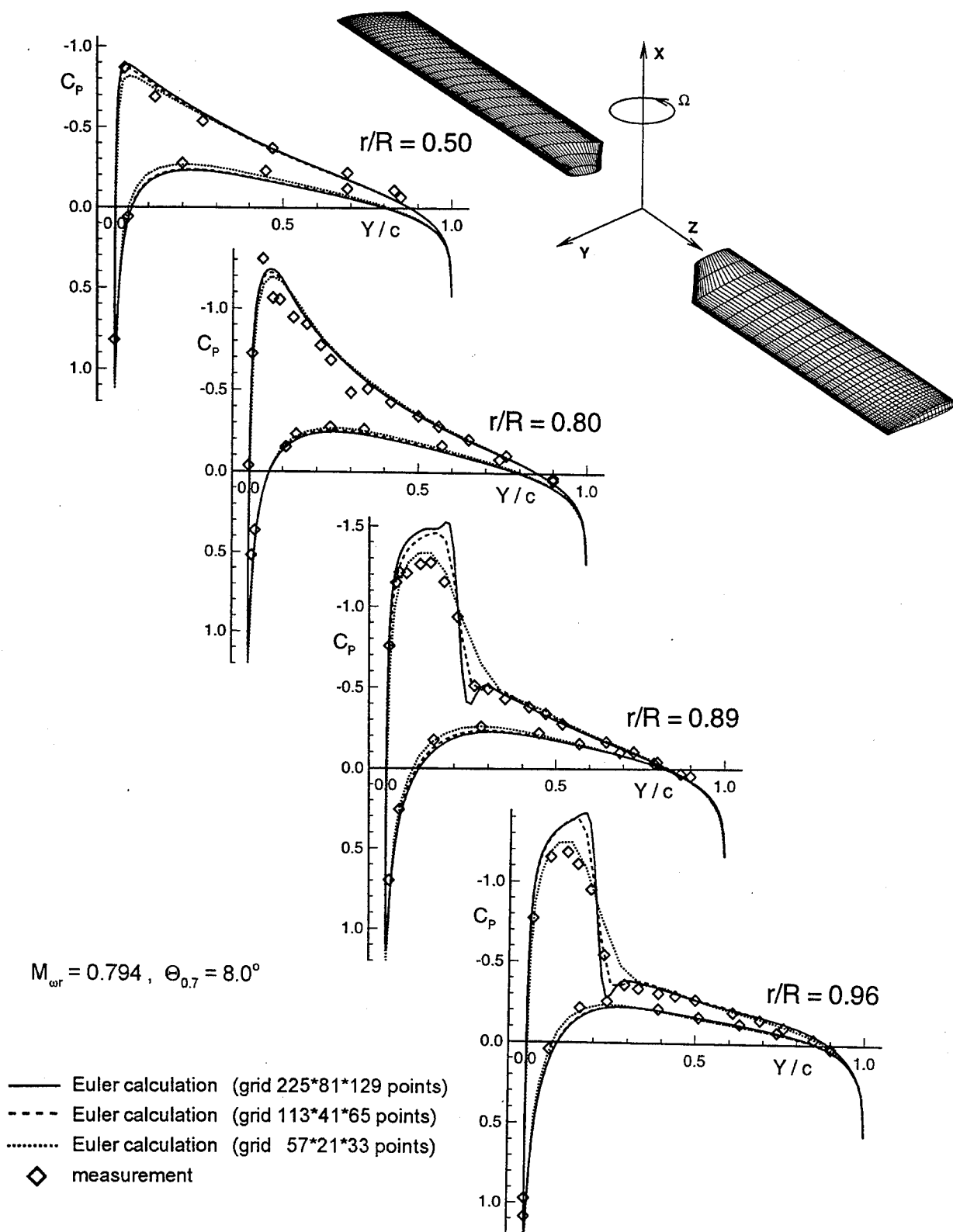


Figure 6: Pressure distributions of 2-bladed Caradonna-Tung model rotor in hover

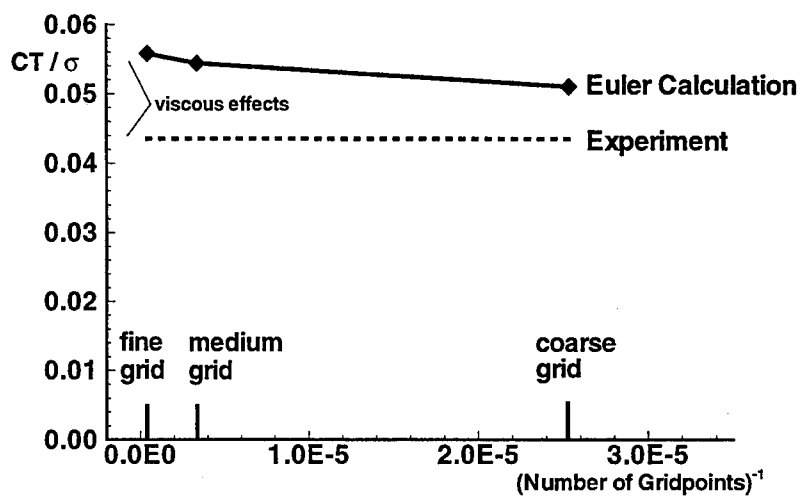


Figure 7: Calculated and measured thrust coefficient of Caradonna Tung rotor in hover
 $\theta_{0.7} = 8^\circ$, $M_{\omega R} = 0.794$

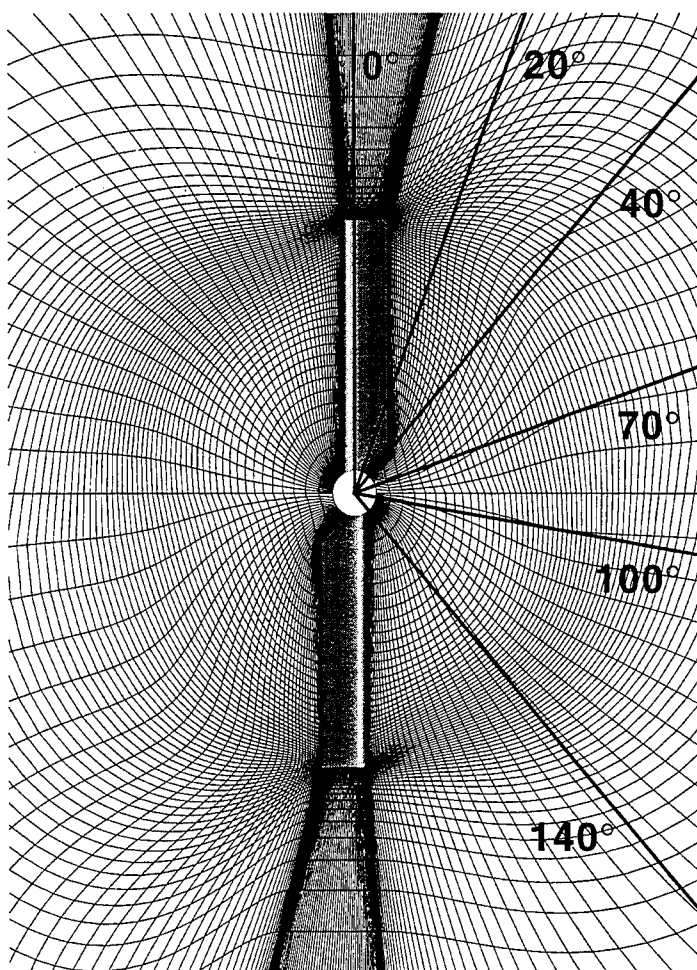


Figure 8: Grid lines in the rotor disk and position of radial slices presented in the following Figures

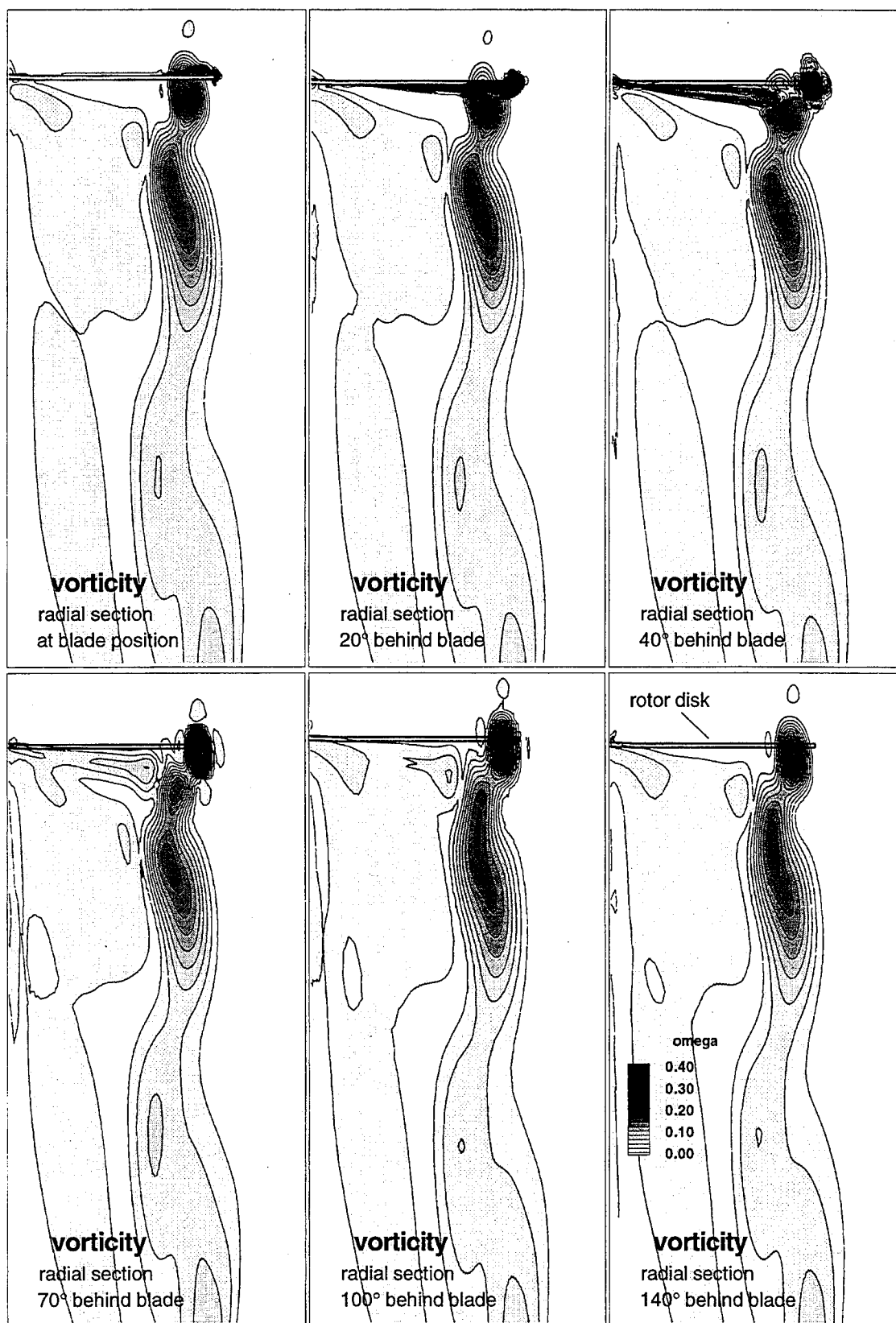


Figure 9: Vorticity contours of Caradonna-Tung model rotor in hover: $\theta_{0.7} = 8^\circ$, $M_{\omega R} = 0.794$
 Calculation on fine grid (225 x 81 x 129 points)

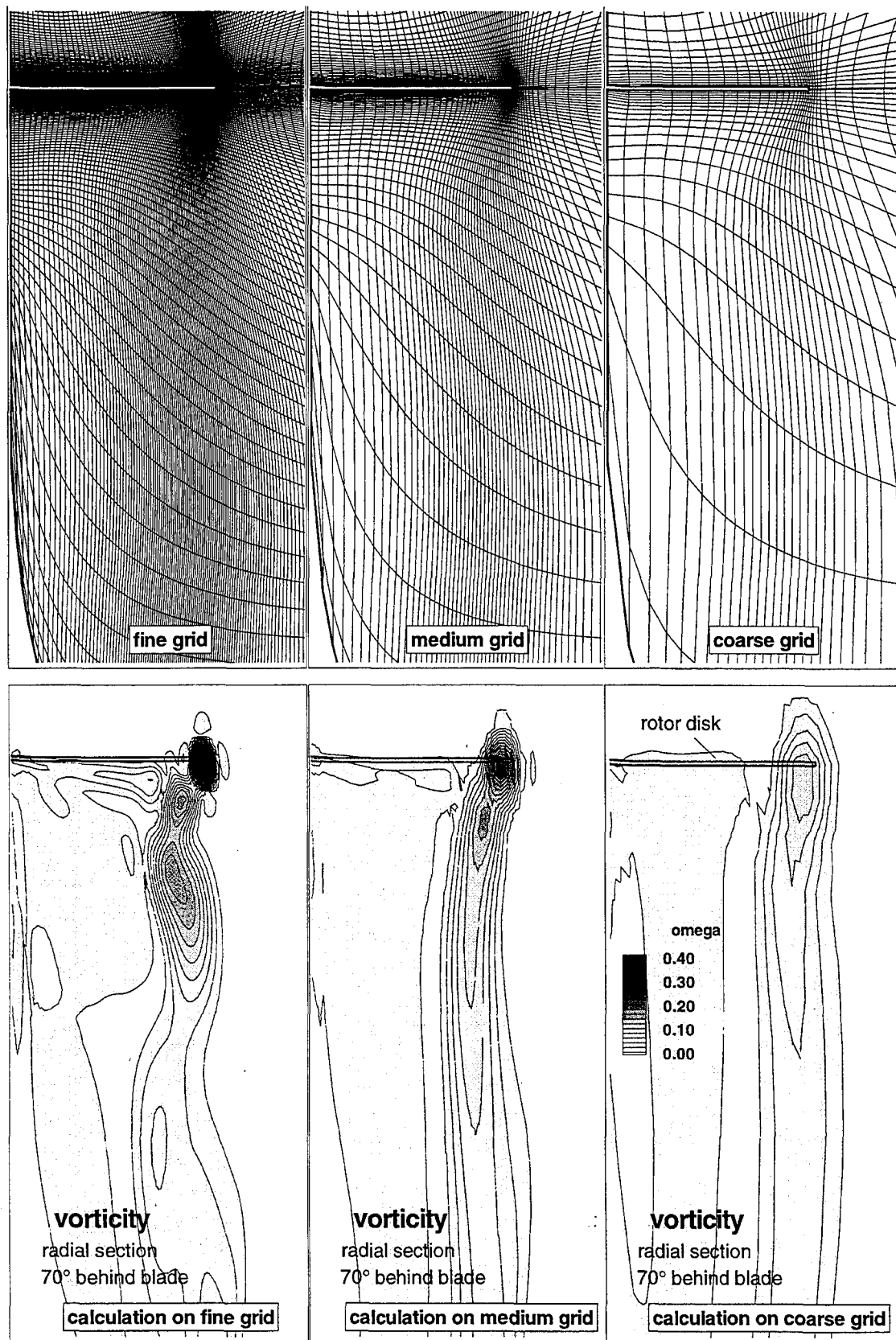


Figure 10: Grid refinement study at a radial position 70° behind the rotor blade,
Caradonna-Tung model rotor in hover: $\theta_{0.7} = 8^\circ$, $M_{\omega R} = 0.794$

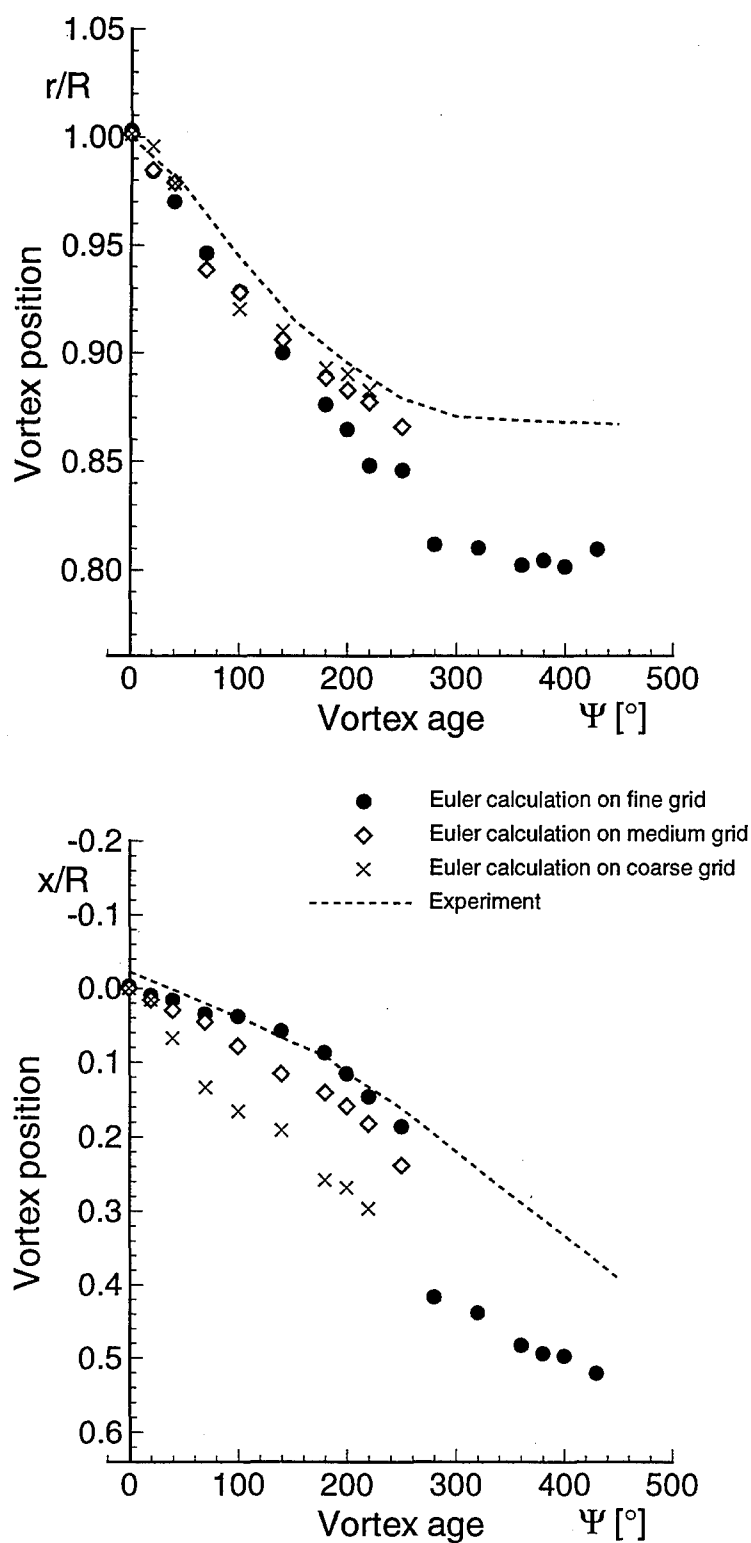
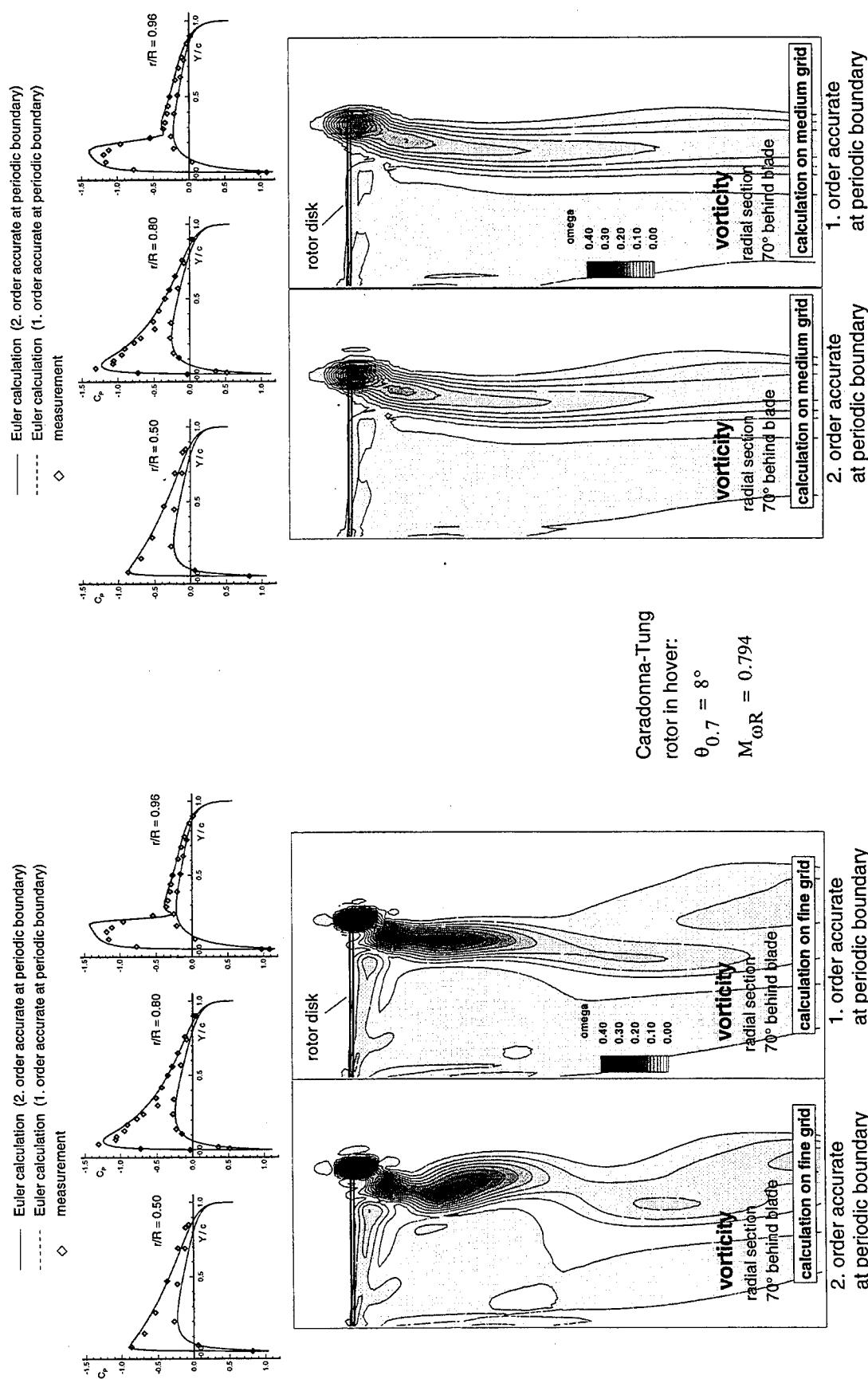


Figure 11: Predicted and experimental vortex trajectories of Caradonna Tung rotor in hover
 $\theta_{0.7} = 8^\circ$, $M_{\omega R} = 0.794$



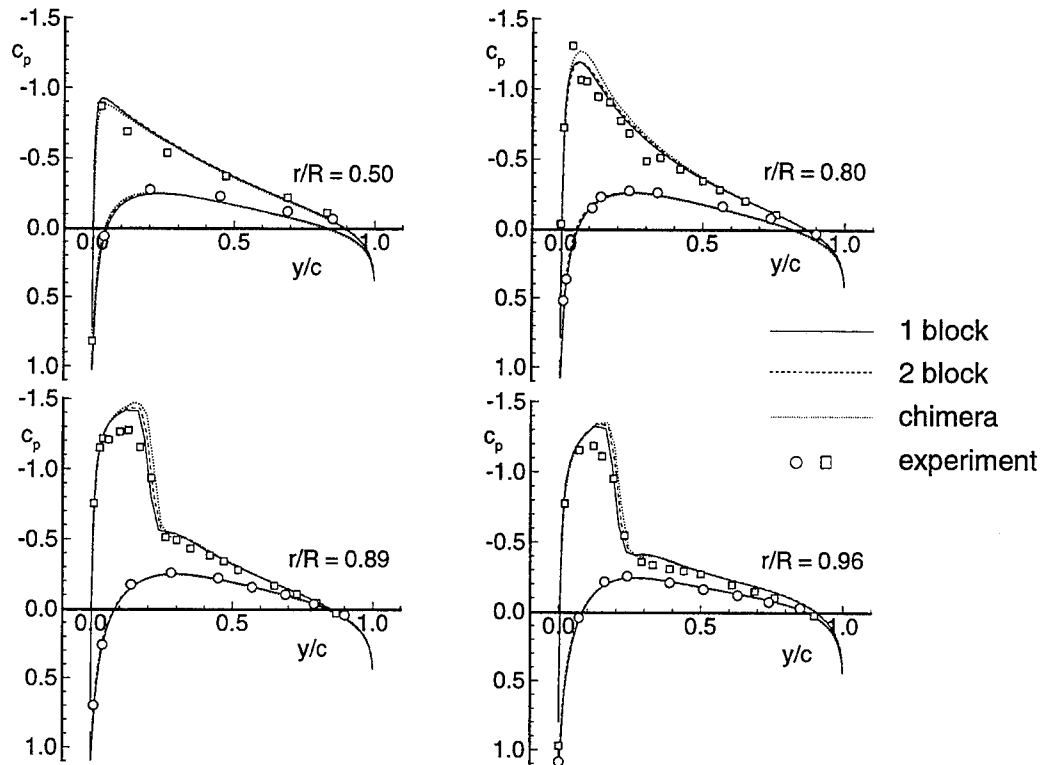


Figure 14: Pressure distributions of 2-bladed Caradonna-Tung rotor in hover: $\theta_{0.7} = 8^\circ, M_{\omega R} = 0.794$

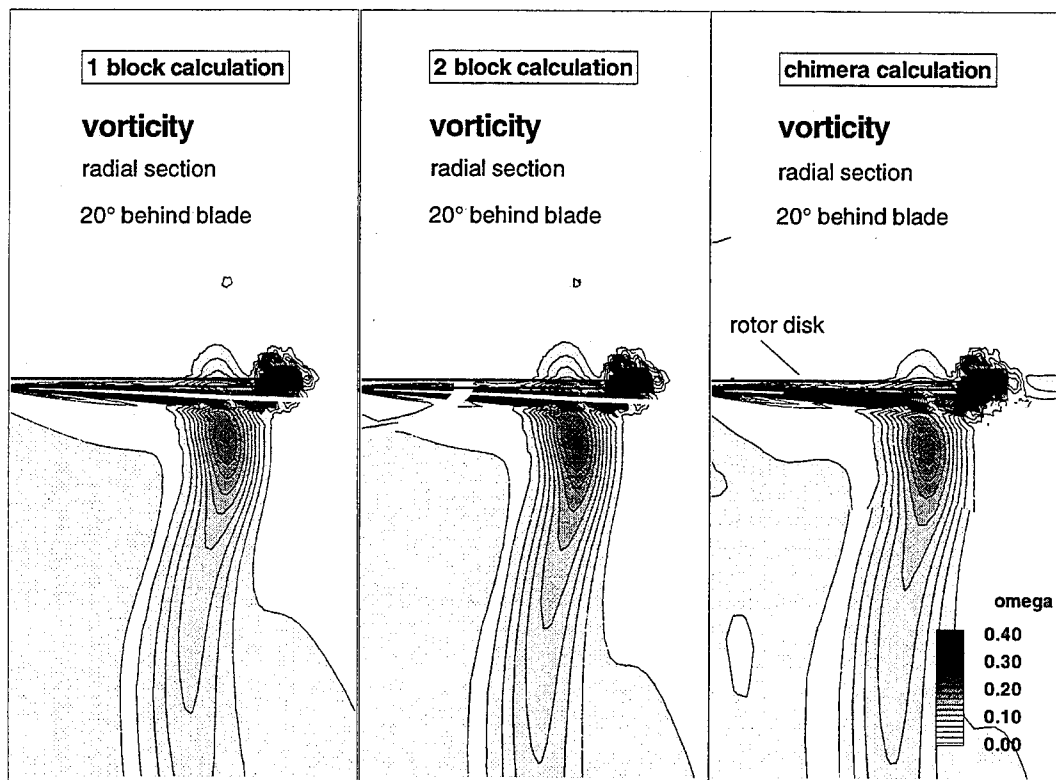


Figure 15: Vorticity contours of 2-bladed Caradonna-Tung rotor in hover: $\theta_{0.7} = 8^\circ, M_{\omega R} = 0.794$, Comparison of 1-block, conventional 2-block and chimera 2-block calculations

FORWARD FLIGHT ROTOR AIRLOADS PREDICTIONS USING A COUPLED NAVIER-STOKES/FULL-POTENTIAL ANALYSIS

C. Berezin
Sikorsky Aircraft Division, UTC
6900 Main St.
PO Box 9729, MS 317A5
Stratford, CT 06497-9129, USA

Prof. L. Sankar
Georgia Institute of Technology
School of Aerospace Engineering
Atlanta, GA 30332-0150, USA

SUMMARY

Unsteady airloads predictions from a hybrid Navier-Stokes/full-potential code for a model UH-60A rotor in forward flight are presented. The code splits the physical domain into a near blade viscous region surrounded by an inviscid potential region. The two regions are coupled through boundary conditions on the interface surface separating them. In addition, the interface surface has been modified to dynamically adjust its position normal to the blade surface depending on the instantaneous distribution of vorticity in the viscous region. This allows roughly a 50 percent reduction of CPU time usage when compared with a standalone Navier-Stokes code. Comparison of the hybrid code surface pressures with the standalone Navier-Stokes results shows good agreement in quadrants one, two, and four. The hybrid code overpredicts the extent of a separated region in the third quadrant which suggests further improvements to the unsteady interface boundary conditions are needed.

1 INTRODUCTION

The aerodynamic loading on a helicopter rotor in forward flight is of great interest to rotor designers. The primary interest is in determining the integrated performance of the rotor and its effect on vehicle speed, range, and payload. Of increasing importance are the effects of the aerodynamic loading on vibration and noise. Accurate and efficient computational methods are desired to assist in the design of high performance, low noise and vibration rotors.

This paper gives results from an ongoing effort to develop a rotor solver which selects a balance between flow physics sophistication and computational efficiency that may be beneficial in the rotor design process. To accurately compute the loading on an advancing rotor over an entire revolution, a solver must be capable of capturing a wide range of physical phenomena. These include transonic effects on the advancing side with shock formation and shock wave/boundary layer interaction, dynamic stall on the retreating side, three-dimensional tip effects with the formation of a trailed tip vortex, and a time varying free stream and cross flow due to rotation. Also, unlike a fixed wing in which the entire wake is convected away at approximately the free stream velocity, the rotor operates in the vicinity of its own wake,

sometimes even intersecting it. Navier-Stokes solver's implicitly capture all of these effects from first principles (Ref. 1-2) but require large amounts of CPU time. Other solvers using reduced governing equation sets such as potential methods (Ref. 3-4) and Euler methods (Ref. 5-7) can capture some of the phenomena at a greatly reduced CPU time requirement, but do not account for some important physical effects such as retreating blade stall.

The code used in this paper reduces the CPU time usage required for unsteady, three-dimensional, viscous rotor solutions. The code is an extension of a fixed-wing/hover code (Ref. 8) called NSFPE that has been extended for forward flight rotor cases (Ref. 9). NSFPE is a tightly coupled solver which uses the Navier-Stokes equations near the blade and in the trailing wake (inner region) to capture viscous effects, and the full potential equation elsewhere (outer region) where viscous effects are negligible. The surface separating the inner and outer regions is called the interface surface. The outer solvers effect on the inner solver, and vice-versa, is handled explicitly as boundary conditions applied at this surface. The code has been applied to a UH-60A forward flight case (Ref. 9). The results compared well with both test data and standalone Navier-Stokes results on the advancing side of the rotor disk while reducing the CPU time required by 44 percent. Results are presented in this paper for the retreating side. Also, the normal location of the interface surface, which was fixed by the user in the previous papers, has been modified to automatically adjust depending on the instantaneous viscous flow solution. This feature removes the need for the user to specify the interface location a priori while allowing for further CPU time reductions when compared with the fixed interface surface method.

The computational method used by NSFPE is described below followed by the results for the UH-60A. Finally, some concluding remarks point to the direction in which further developments will be headed.

2 COMPUTATIONAL METHOD

NSFPE is built on the premise that a viscous solver is only needed in regions where viscous effects are not negligible and an inviscid solver may be used elsewhere. This premise may be exploited to reduce CPU time by using the viscous solver only where it is necessary and

using the much less computationally expensive inviscid solver everywhere else. It would behoove the analyst to have as large an inviscid region as possible as the ratio of inviscid grid points to viscous grid points determines to a large extent the CPU usage. A balance must be obtained, however, because too small a viscous region will have an adverse affect on solution accuracy.

In NSFPE, the physical domain of interest is divided into two adjacent regions. The viscous inner region surrounds the blade and contains the viscous wake and is in turn surrounded by the inviscid outer region. A schematic of the physical domain is shown in Fig. 1. The grid is composed of a series of two-dimensional algebraically generated C-grids stacked in the spanwise direction. The interface surface is defined as the surface separating the two regions and is depicted by the constant ζ grid surface labeled k_{match} . The Reynolds-averaged Navier-Stokes equations are solved in the inner region while the full-potential equation governs the flow in the outer region. Both region's solution procedures are non-iterative and are time accurate which allows for unsteady flow solutions. The solver is tightly coupled in that both inner and outer solvers are passed through once each time step (or iteration for steady or quasi-steady runs) with the influence of one region on the other handled by boundary conditions applied at the interface surface. The inviscid effect on the viscous region is currently lagged by one time step because the inviscid region does not change as quickly as the viscous region. The solver is capable of predicting fully 3-D, unsteady, viscous flow solutions including separation and stall, if present.

Brief descriptions of the Navier-Stokes and full-potential solvers are next followed by the treatment of the rotor far-wake and aeroelastic effects. Finally, the interface boundary conditions are described. The Navier-Stokes solver is similar to the rotor code of Ref. 1 while parts of the full-potential solver were based on Ref. 3.

2.1 Navier-Stokes Formulation

The Reynolds averaged Navier-Stokes equations may be written as

$$q_t + F_x + G_y + H_z = R_x + S_y + T_z \quad (1)$$

where q is a vector of conserved variables, F , G , and H are the convective flux vectors and R , S , and T are the viscous flux vectors. To ease application of the surface boundary conditions for arbitrary bodies the equations are transformed to a body fitted coordinate system (τ, ξ, η, ζ) and (1) becomes

$$q_\tau + F_\xi + G_\eta + H_\zeta = R_\xi + S_\eta + H_\zeta \quad (2)$$

where q , F , G , etc. are related to q , F , G , etc. through the metrics of the transformation.

Equations (2) must be numerically integrated in time starting from an initial guess for q . Boundary conditions are the no-slip condition and zero temperature and pressure gradient at the body surface and undisturbed flow at the far

field boundaries. The boundary conditions at the interface surface will be discussed later.

The equations are integrated in time using a first order accurate in time Euler scheme with central differences spatially for second order accuracy in space. Equations (2) become after discretization

$$\Delta q^{n+1}/\Delta t + \delta_\xi F^{n+1} + \delta_\eta G^* + \delta_\zeta H^{n+1} = (\delta_\xi R + \delta_\eta S + \delta_\zeta T)^n \quad (3)$$

The viscous terms are evaluated explicitly at the old time level n and appear on the RHS. The spanwise flux derivative $\delta_\eta G^*$ is evaluated semi-implicitly using information at both time levels n and $n+1$, using $n+1$ values as soon as they become available.

Since equations (3) contain the terms F and H , which are non-linear in q , they must be linearized in order to solve for q . This is done using a Taylor series expansion as follows:

$$F^{n+1} \approx F^n + A \Delta q^n$$

where $\Delta q^n = q^{n+1} - q^n$ and A is a 5x5 flux Jacobian matrix. This linearization is done similarly for H .

The linearized equations may be written as

$$[I + \Delta t(\delta_\xi A + \delta_\zeta B)] \Delta q^n = R^{n,n+1}$$

where R is the residual. This matrix equation is block pentadiagonal and is expensive to solve. This equation is therefore approximately factored to yield

$$[I + \Delta t \delta_\xi A][I + \Delta t \delta_\zeta B] \Delta q^n = R^{n,n+1} \quad (4)$$

The matrices A and B may be diagonalized as suggested in Ref. 10 to reduce (4) to two tridiagonal inversions which may be solved efficiently using the Thomas algorithm.

The solver incorporates fourth order explicit artificial damping along with second order implicit damping to reduce wiggles in regions of large gradients of flow variables. Further information on this solver appears in Ref. 1.

2.2 Full-Potential Formulation

The 3-D unsteady compressible potential flow may be written in generalized curvilinear coordinates as

$$\left(\frac{\rho}{J}\right)_\tau + \left(\frac{\rho U}{J}\right)_\xi + \left(\frac{\rho V}{J}\right)_\eta + \left(\frac{\rho W}{J}\right)_\zeta = 0 \quad (5)$$

where ρ is the density, and U , V , and W are the contravariant velocities. Using the isentropic gas law and the energy equation, equation (5) may be written (Ref. 3) as the following second order hyperbolic partial differential equation for ϕ :

$$\frac{\rho}{a^2 J} (\phi_{\tau\tau} + U\phi_{\zeta\tau} + V\phi_{\eta\tau} + W\phi_{\xi\tau}) =$$

$$\left(\frac{\rho U}{J}\right)_{\xi} + \left(\frac{\rho V}{J}\right)_{\eta} + \left(\frac{\rho W}{J}\right)_{\zeta} \quad (6)$$

The time derivatives and the mixed time and space derivatives on the LHS of equation (6) are discretized using first order accurate finite difference formulas while the spatial derivatives on the RHS are evaluated using second order accurate central differences.

Because this equation is hyperbolic, it may be advanced in time using a stable marching scheme, for a given initial description of the velocity potential ϕ and its derivative ϕ_{τ} . When the above discretizations are employed, at each time step a system of linear equations result for the quantity $\Delta\phi = \phi^{n+1} - \phi^n$. This equation may formally be written in the form:

$$[M] \{\Delta\phi\} = \{R\} \quad (7)$$

The coefficient matrix and the right hand side R are known quantities, computed at the time level 'n'. The matrix M is a sparse matrix with twenty seven diagonals, reflecting the fact that a node (i,j,k) is linked to its 26 neighbors, $(i-1,j,k)$ etc. On nearly orthogonal grids such as the one used in the present work, only diagonals coupling (i,j,k) to its six neighbors $(i+1,j,k)$, $(i-1,j,k)$, $(i,j+1,k)$, $(i,j-1,k)$, $(i,j,k+1)$ and $(i,j,k-1)$ are non zero. In the ADI scheme used here, the seven-diagonal matrix M was approximately factored into three tridiagonal matrices resulting in the following system:

$$[M_1][M_2][M_3] \{\Delta\phi\} = \{R\} \quad (8)$$

Each of the above three matrices are easily invertible using the Thomas algorithm. The main diagonal terms of the matrices include contributions from each of the three directions as a result of factoring the matrix instead of factoring the equation in operator form. This results in a matrix that is more diagonally dominant than some other possible factorizations, which allows for a stable solution using larger time steps.

2.3 Wake and Trim Effects

In order to accurately predict the airloads on an advancing rotor blade, the rotor trim state must be computed and the effects of the far wake must be included. The trim and wake effects are accounted for in NSFPE through the use of "partial" angles-of-attack as suggested in Ref. 11. These angles are obtained from an external comprehensive rotor code which includes a blade aeroelastic model, a trim state solver, and a vortex lattice wake model. Each spanwise C-grid in NSFPE is rotated by the appropriate partial angle. These angles described the local angle-of-attack at each spanwise station including the effects of elastic deflections, control positions, and far wake induced velocities. The term far wake here is used to describe any of the vortex wake structure which

lies outside the NSFPE physical domain depicted in Fig. 1. All partial angles used in this paper were generated using the RDYNE comprehensive rotor code (Ref. 12).

2.4 Interface Boundary Conditions

The interface surface, denoted as k_{match} in Fig. 1, is simultaneously the outer boundary for the Navier-Stokes region and the inner boundary for the full-potential region. As such, boundary conditions must be specified on this surface for each region. They must be specified in such a way that the solution varies smoothly across the interface.

At each time step, information is exchanged between the inner and outer regions. Both governing equations are solved at $k=k_{match}$ with the Navier-Stokes outer boundary at $k=k_{match}+1$ and the full-potential inner boundary at $k=k_{match}-1$. The Navier-Stokes solver is called first with the $k=k_{match}+1$ boundary data obtained from the previous time steps' full-potential solution. The q vector at the outer boundary is determined by differentiation of the velocity potential and by employing the isentropic relations. Next, the full-potential region is solved using data at the $k=k_{match}-1$ boundary from the current time step Navier-Stokes solution. The velocity potential at $k=k_{match}-1$ is obtained from the known Navier-Stokes mass flux through this boundary.

To maximize the CPU time savings, the interface surface should be located as close to the blade as possible, thereby decreasing the size of the Navier-Stokes region. A user cannot be expected to know this position with a great deal of certainty for any case in general. In addition, if this surface position is fixed in time, it must be far enough from the blade so that the viscous, rotational flow remains within the Navier-Stokes region over the entire rotor disk. This means one must be conservative in selecting its position, conservatism which will drive up the CPU time requirements.

This problem has been eliminated by allowing NSFPE to automatically adjust the interface surface as a function of azimuth (time). The potential region does not allow transport of vorticity and entropy. One of these flow parameters may be examined to determine the extent of the viscous, rotational flow in the Navier-Stokes region. For this paper, vorticity was chosen. A typical plot of vorticity magnitude versus normal distance from the blade, for an attached flow, is depicted in Fig. 2. It is large at the blade surface and then quickly approaches zero. The inviscid, irrotational potential region should extend down to a point where the vorticity is virtually zero. An efficient scheme to determine this extent is depicted in Fig. 3. The vortical solution on a reference plane which is located a specified distance, or safety margin, below the interface surface is examined. If the maximum vorticity on this reference plane falls within the range of two cutoff vorticity magnitudes, ω_{COH} (vorticity high cutoff) and ω_{COL} (vorticity low cutoff), the interface surface stays put. If the maximum vorticity is less than ω_{COL} the surface moves closer to the blade. If it is greater than ω_{COH} , the surface moves away from the blade. The cutoff vorticity magnitudes are

defined as fractions of the maximum vorticity on the blade surface. The use of the safety factor here insures that the flow field in the vicinity of the interface surface is potential.

When the interface surface moves, the appropriate solution must be reconstructed "downstream" of its motion. For example, if it moves up, the Navier-Stokes conserved variable vector must be computed from the potential solution. This may be done as before by differentiation of the velocity potential and application of the isentropic energy equation. If the surface moves down, the potential solution may be reconstructed by numerical integration of the Navier-Stokes velocities along a constant i, j line.

The advantages of the adjustable interface are twofold. Firstly, it eliminates the need for a user to select its location. For a quasi-steady case, the user simply guesses its location, the program will adjust it until it reaches its proper position. Secondly, for unsteady cases, it allows the surface to be close to the blade at azimuths where the vortical region is confined near the blade and it moves it farther from the blade when the vortical region grows. Typically, the vortical region is small on the advancing side and grows in size on the retreating side of the rotor disk. The adjustable interface will tend to maximize the computational efficiency of the code.

3 RESULTS

The following results are given for a UH-60A model scale rotor operating at an advance ratio of 0.3 with $C_L/\sigma=0.09$. The blade is swept by 20 degrees starting at 92 percent radius. A description of the rotor appears in Ref. 13.

The computational grid density was $101 \times 19 \times 41$ points in the streamwise, spanwise, and normal directions, respectively. The grid density, adequate for lift convergence but not drag convergence, is acceptable for testing the boundary conditions at the interface surface. Fig. 4 depicts a subset of the grid in which the extent of the Navier-Stokes region is shown for $k_{\text{match}}=21$.

NSFPE has been previously demonstrated on the advancing side using a fixed interface surface for the same rotor and operating condition and the results are contained in Ref. 9. k_{match} was set at 21 which is approximately 25% of a chord away from the blade surface. The results from Ref. 9 showed the NSFPE predictions to be very close to standalone Navier-Stokes result. The standalone Navier-Stokes code used was called NAV3D and its formulation is the same as the Navier-Stokes formulation in NSFPE. Some discrepancies appeared in the NSFPE predictions near the tip in the second quadrant due to false disturbances at the interface. These advancing side results are now used to validate the dynamic interface surface. The code automatically moved the interface surface from $k=21$ to $k=17$, or approximately 15% of a chord away from the blade. This location was maintained over the entire advancing side as the flow remained attached and the blade pitch was relatively low. Pressure coefficient comparisons from the first and second quadrants for the non-dimensional radial locations 0.775 and 0.945

are shown in Fig. 5. The results are in good agreement. Whereas the fixed interface code of Ref. 9 used 44% less CPU time than NAV3D, the adjustable interface used 53% less time without a degradation of solution accuracy.

For this paper, the solution has been computed for an entire rotor revolution. The interface surface location on the retreating side varied from a high of $k=20$ in the third quadrant down to $k=17$ at the end of the fourth quadrant. Over an entire revolution, NSFPE required slightly less than 50% of the computer time used by NAV3D, as compared with the 44% reduction using a fixed interface at $k_{\text{match}}=21$ in Ref. 9.

A comparison of blade thrust coefficient between NSFPE and NAV3D appears in Fig. 6. The discrepancies on the advancing side were discussed above and the differences appear exaggerated here due to the use of hover tip speed in the non-dimensionalization.

The differences on the retreating side are compressed, however, and the comparison shows large differences near $\psi=270$ degrees. An examination of the flow fields gives some insight into the cause of the differences. Due to the increasing blade pitch, both codes show a recirculation zone on the upper surface of the blade which appears in the third quadrant. Fig. 7 shows velocity vector fields for both codes at $\psi=210$ degrees and a radial location of 0.74 percent. NSFPE shows a slightly larger recirculation bubble than NAV3D. At $\psi=240$ degrees, NSFPE vastly overpredicts the extent of the separated region when compared with NAV3D and its location appears upstream of the NAV3D prediction (Fig. 8). It is believed that these differences are due to the Navier-Stokes boundary condition computation at the interface surface. Plots of C_p versus normal coordinate index on the blade upper surface are shown in Fig. 9. The symbols appearing in the NSFPE flow field of Fig. 8 on a constant ξ -line show the spatial location corresponding to the plots. What is immediately apparent are the oscillations originating at the interface surface and extending into the Navier-Stokes region. These oscillations alter the pressure field along the interface which in turn affects the location and extent of the recirculating region, as this region is most sensitive to the surrounding pressure field.

These oscillations may be due to non-physical reflections occurring at the interface in the Navier-Stokes region. Further evidence of reflections at the interface is apparent upon examination of the quasi-steady convergence history for the Navier-Stokes region at an azimuth of zero degrees (Fig. 10). While the residual drops smoothly for NAV3D, the NSFPE residual shows an oscillatory behavior indicative of reflections at the boundaries. Determining the boundary conditions at the interface using a method which addresses the domains of influence of propagating waves through the use of one-sided differencing may reduce the oscillations and improve solution accuracy.

In the fourth quadrant, the agreement between NSFPE and NAV3D improves as seen by the pressure coefficient comparisons in Fig. 11. At $\psi=300$ degrees, NAV3D shows a small

recirculating region in the tip area that is not seen by NSFPE but at $\psi=330$ degrees the results are very close.

4 CONCLUDING REMARKS

A tightly coupled Navier-Stokes/full-potential rotor analysis (NSFPE) has been utilized over an entire revolution for a model UH-60A rotor in forward flight. The results have been compared with a standalone Navier-Stokes (NAV3D) solution. An automatically adjustable interface surface which improves computational efficiency and reduces required user input has also been demonstrated. The results show good agreement between the two codes except over a portion of the retreating side where non-physical reflections at the interface surface cause problems in the NSFPE solution. Non-reflecting boundary conditions are currently being implemented to alleviate this problem. Over a full rotor revolution, the hybrid code NSFPE used slightly less than 50% of the CPU time used by NAV3D.

5 ACKNOWLEDGMENTS

The standalone Navier-Stokes predictions were performed using the Cray C90 of the Numerical Aerodynamic Simulation Program at the NASA Ames Research Center.

6 REFERENCES

1. Wake, B.E., "Solution Procedures for the Navier-Stokes Equations Applied to Rotors," Ph.D. Dissertation, Georgia Institute of Technology, April 1987.
2. Srinivasan, G.R. and McCroskey, W.J., "Navier-Stokes Calculations of Hovering Rotor Flowfields," *Journal of Aircraft*, Vol. 24, No. 4, 1987, pp. 231-238.
3. Sankar, L.N. and Prichard, D., "Solution of Transonic Flow Past Rotor Blades Using the Conservative Full Potential Equation," *Aerodynamics Conference*, Colorado Springs, Colorado, October 14-16, 1985.
4. Strawn, R.C. and Tung, C., "Prediction of Unsteady Transonic Rotor Loads with a Full-Potential Rotor Code," 43rd Annual Forum of the American Helicopter Society, St. Louis, Missouri, May 18-20, 1987.
5. Wake, B.E., Sankar, L.N., and Lekoudis, S.G., "Computation of Rotor Blade Flows Using the Euler Equations," *AIAA Paper 85-5010*.
6. Agarwal, R.K. and Deese, J.E., "An Euler Solver for Calculating the Flowfield of a Helicopter Rotor in Hover and Forward Flight," *AIAA 19th Fluid Dynamics, Plasma Dynamics, and Laser Conference*, June 1987.
7. Chang, I-C., "Unsteady Euler Solution of Transonic Helicopter Rotor Flow," *AHS Specialists Meeting on Aerodynamics and Aeroacoustics*, February 1987.
8. Sankar, L.N., Bharadvaj, B.K., and Tsung, F. L., "A Three-Dimensional Navier-Stokes/Full-Potential Coupled Analysis for Viscous Transonic Flow," *AIAA 10th Computational Fluid Dynamics Conference*, Honolulu, Hawaii, June 24-27, 1991.
9. Berezin, C.R., and Sankar, L.N., "An Improved Navier-Stokes/Full-Potential Coupled Analysis for Rotors," 32nd Aerospace Sciences Meeting and Exhibit, Reno, NV, January 1994.
10. Pulliam, T.H. and Chaussee, D.S., "A Diagonal Form of an Implicit Approximate-Factorization Algorithm," *Journal of Computational Physics*, Vol. 39, p.347, 1981.
11. Tung, C., Caradonna, F.X., Boxwell, D.A., and Johnson, W.R., "The Prediction of Transonic Flows on Advancing Rotors," 40th Annual Forum of the American Helicopter Society, Arlington, Va. May 16-18, 1984.
12. Sopher, R. and Hallock, D.W., "Time-History Analysis for Rotorcraft Dynamics Based on a Component Approach," *Journal of the American Helicopter Society*, Vol. 31, (1), January 1986.
13. Lorber, P.F., "Aerodynamic Results of a Pressure-Instrumented Model Rotor Test at the DNW," *Journal of the American Helicopter Society*, Vol. 36, (4), October 1991.

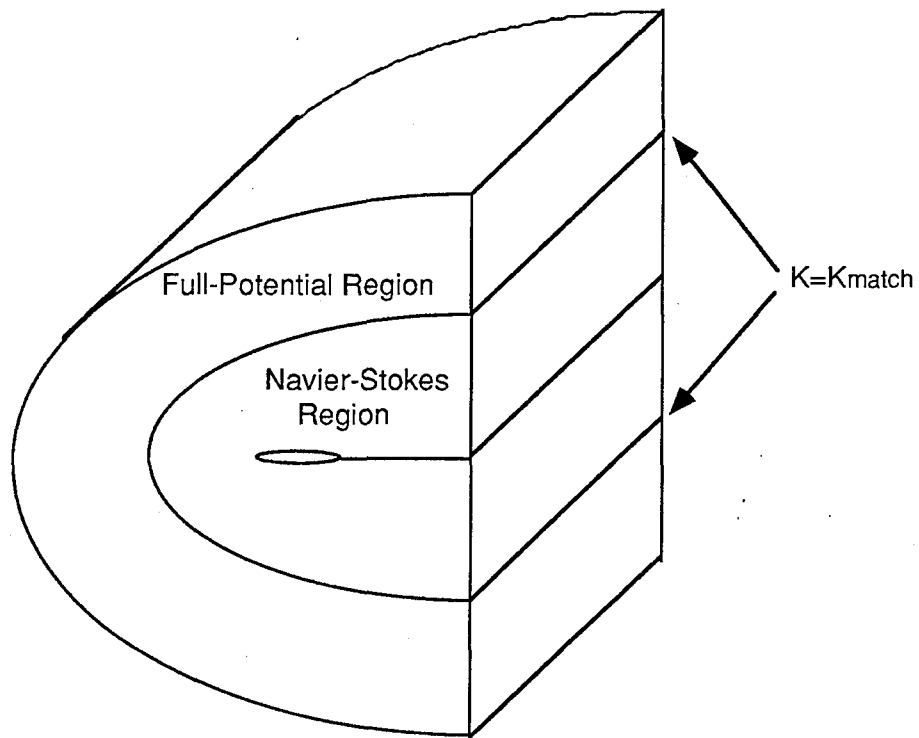


Fig. 1 - NSFPE Physical Domain Schematic

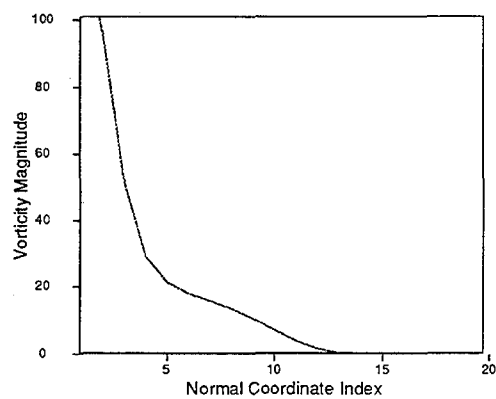


Fig. 2 - Vorticity Magnitude Normal to Blade

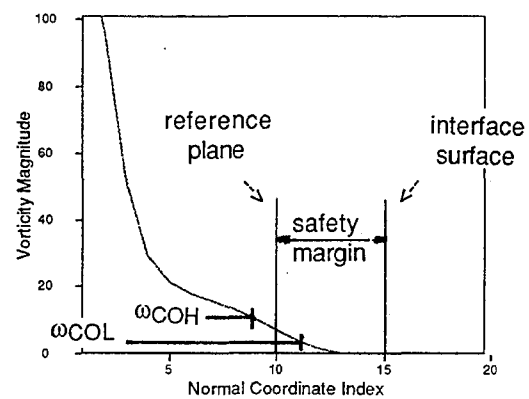


Fig. 3 - Adjustable Interface Surface Logic

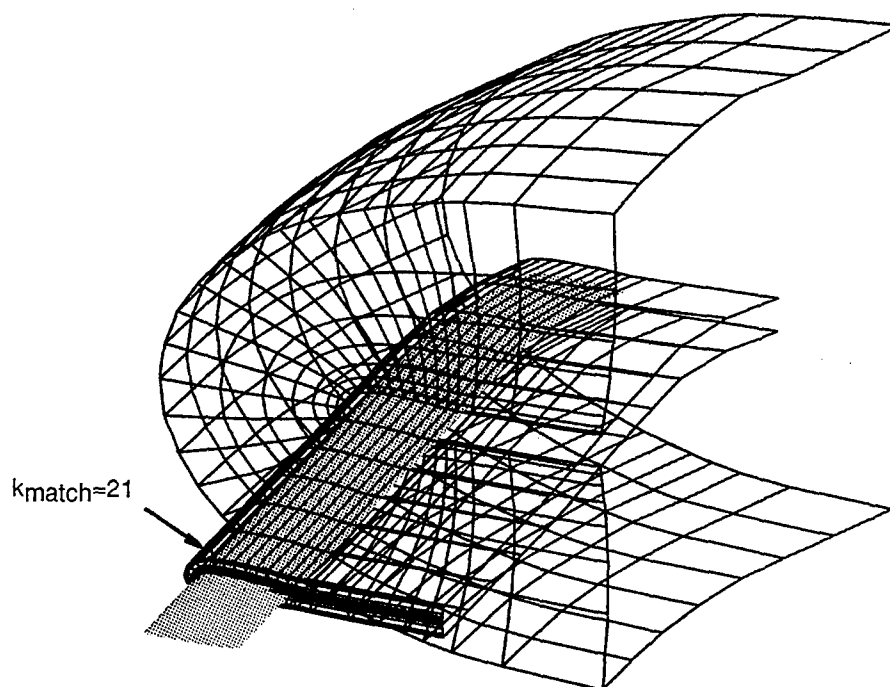
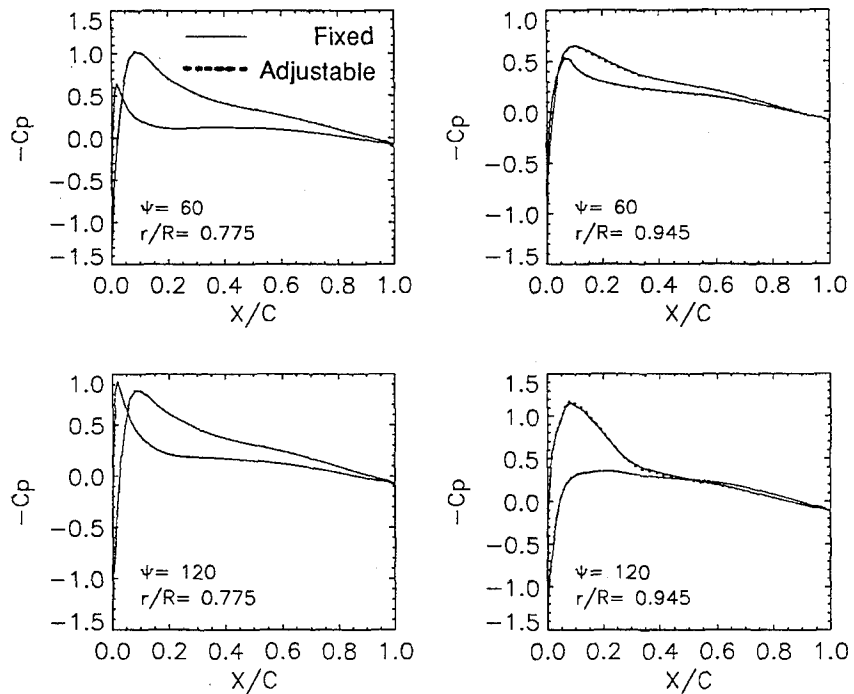


Fig. 4 - Sample Grid Showing Interface Surface

Fig. 5 - Cp Comparisons on Advancing Side
(NSFPE fixed interface vs. NSFPE adjustable interface)

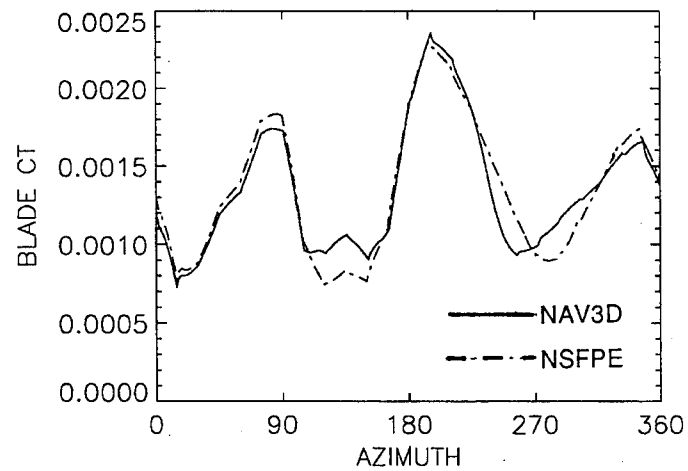


Fig. 6 - Blade Thrust Coefficient Comparison, NSFPE vs NAV3D

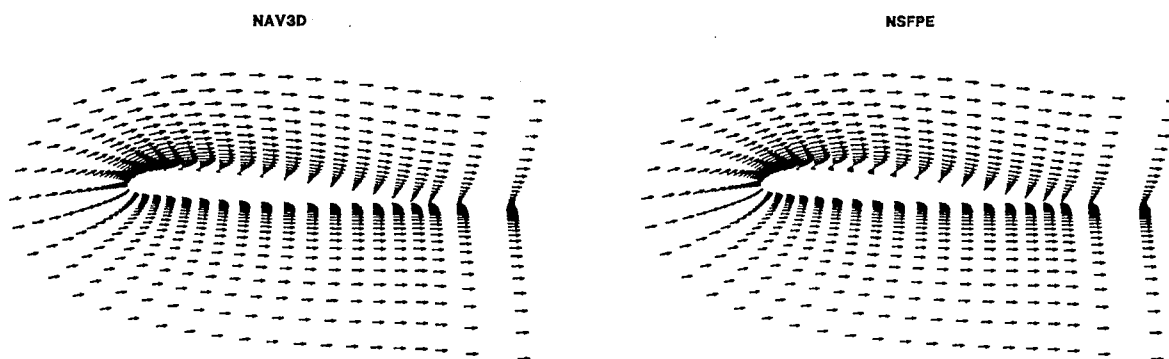


Fig. 7 - Velocity Vectors at $r/R=0.74$, $y=210$ degrees

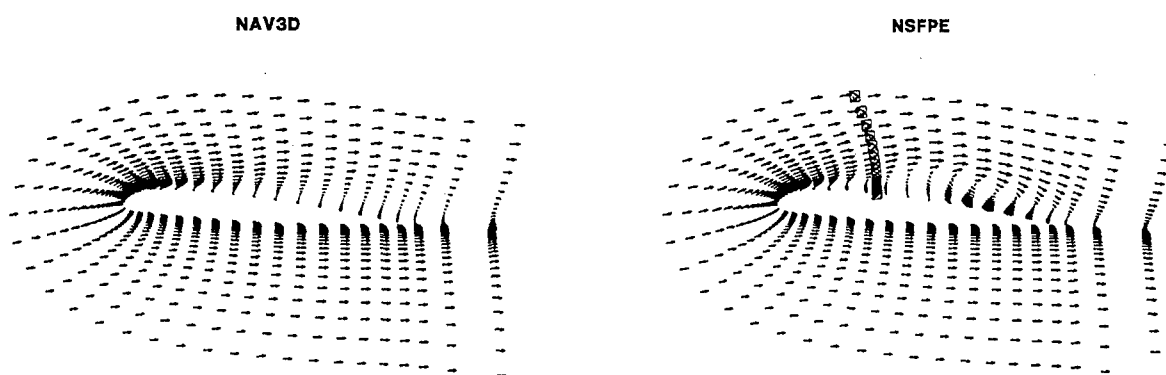


Fig. 8 - Velocity Vectors at $r/R=0.74$, $\psi=240$ degrees

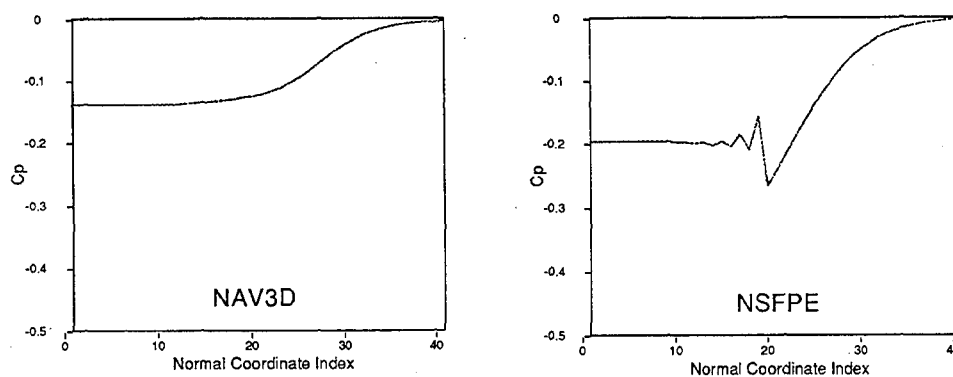


Fig. 9 - C_p Normal to Blade, $k_{\text{match}}=20$, $\psi=240$ degrees

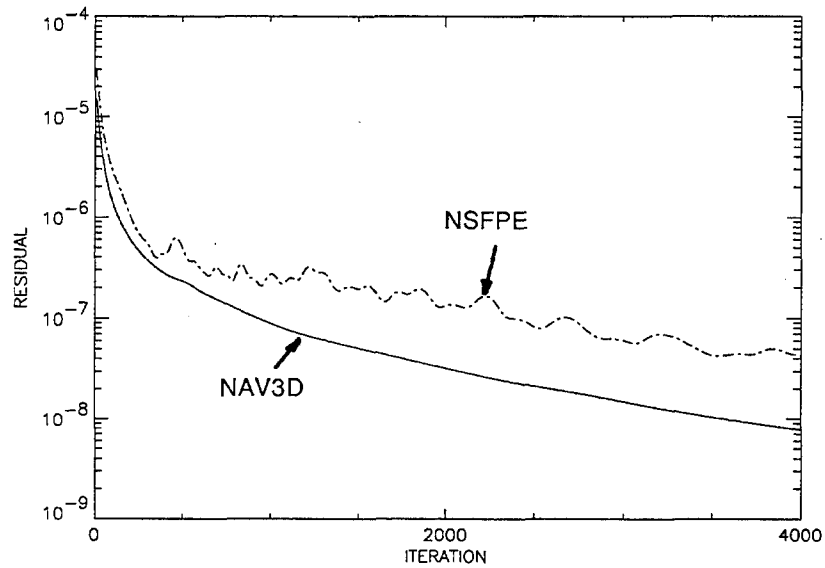


Fig. 10 - Quasi-Steady Convergence History, Navier-Stokes Region, $\psi=0$ degrees

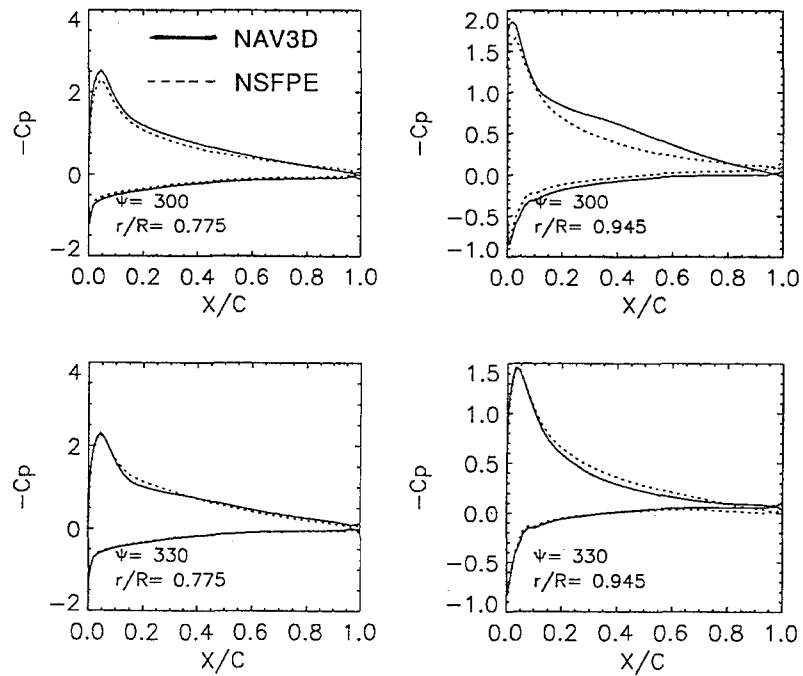


Fig. 11 - C_p Comparisons on Retreating Side, NSFPE vs NAV3D

Computational Fluid Dynamics Development and Validation at Bell Helicopter

J. C. Narramore
Principal Engineer
Bell Helicopter Textron, Inc.
P. O. Box 482
Fort Worth, Texas, USA 76101

SUMMARY

An overview of the development of the Computational Fluid Dynamics (CFD) methodology at Bell Helicopter Textron is given. As new technologies have been developed their functionality has been assessed by their ability to reproduce wind tunnel measurements in a timely manner. Examples of some of these correlation study results are provided.

LIST OF SYMBOLS

ALPHA	Angle of attack (degrees)
C_L	Coefficient of lift
C_M	Coefficient of moment about the quarter chord
C_T	Coefficient of thrust
M	Mach number
q	Dynamic pressure
q_t	Computed speed distribution
q_s	Target speed distribution
α	Angle of attack (degrees)
ΔQ^2	Residual of $q_s^2 - q_t^2$
ΔS	Change in aerodynamic surface ordinate value

1. INTRODUCTION

In order to improve our ability to predict aerodynamic performance and airloads, Bell Helicopter Textron, Inc. has pursued several approaches including wind tunnel testing, empirical methods, analytical methods, and computational fluid dynamic methods. Recently, the development of computational methods for aerodynamic design and analysis of rotorcraft vehicles has increased our ability to predict aerodynamic performance and airloads. The goal of constantly improving productivity of the computational design process has led to the development of many new methods and changes in the aerodynamic design process. As these methods were being developed, validation of the results was carried out by comparing the computational results to wind tunnel test data. As methods became credible they were linked to aerodynamic information systems so that effective use of the codes and the data generated could be achieved. Using this information systems

approach has allowed multiple computational aerodynamic approaches to be used during design and has assimilated wind tunnel test data for the correlation studies.

Developments in high-speed computers have also had an impact on the time required to perform aerodynamic design. Interactive graphic workstations have allowed a new approach to the design of aerodynamic components and the development of grids for complex modeling. Supercomputers have allowed solutions to problems that heretofore would have taken too long to be practical.

Development of a computational fluid dynamics (CFD) methodology at Bell Helicopter Textron, Inc. was initiated in the early 1970's with two-dimensional (2-D) airfoil analysis and design methods. In 1987, the first evaluations of full potential rotor codes were carried out. By 1991, the use of Navier-Stokes methods for some rotorcraft problems had become practical. In this paper, a discussion of the development of computational aerodynamic design methods at Bell will be discussed. Emphasis will be placed on the improvements in productivity and the validation of these methods with wind tunnel data. Advances in airfoil, rotor, wing, and fuselage methods from the initial potential flow methods to full Navier-Stokes methods will be discussed.

2. AIRFOIL DESIGN AND ANALYSIS

Airfoil design has progressed from submitting batch jobs and looking at tabulated results to interactive graphic methods that allow modifications of the control parameters as the solution is progressing. What in 1973 would require one year to complete is now completed in two days because of these improvements in productivity for airfoil design.

An airfoil designer is given the task of producing the best section that will satisfy a set of performance and structural requirements. These requirements may include aerodynamic specifications, such as low drag at specified lift values, high drag divergence Mach numbers, favorable pitching moment, high maximum lift, and gentle stall characteristics. Geometric specifications may

include maximum thickness, nose radius, trailing edge thickness, and thickness distribution for structural and manufacturing considerations.

Inverse airfoil design methods are advantageous, since the pressure distribution which determines the boundary layer development and lift/moment distribution on the section is input. Therefore, the performance is specified and the coordinates that will produce that performance are determined. If geometric constraints are critical, inverse design methods can be used to determine the best aerodynamic configuration within the constraints. Since inverse conformal methods are extremely fast (Ref. 1), these design methods are instantaneous on a typical graphic workstation. As soon as an increment in a parameter is selected, the result appears on the screen. An example of a subsonic airfoil design case in which the geometric constraints are critical is given in Fig. 1. In this case, an aerodynamic fairing was to be designed around the boxed region with a chord length that was limited as is shown. The inverse design method allows an aerodynamic shape to be generated efficiently that satisfies the geometric constraints

while providing good performance characteristics. This interactive method on a graphic workstation greatly improves productivity for subsonic airfoil design.

Recent developments in workstation technology have produced machines that are capable of producing solutions for two-dimensional compressible Navier-Stokes problems. Fig. 2a shows the screen for a two-dimensional interactive airfoil design method that was developed at Bell. In this figure the target pressure distribution and the starting airfoil and its pressure are shown. Using this methodology the designer has control of the solution as the airfoil is being produced. The designer may decide to change the desired pressure distribution or change the run step size, for example. This methodology leads to a very interactive transonic airfoil design process. Fig. 2b shows the resulting airfoil and pressure distribution compared to the target pressure that is the result of the design procedure started in Fig. 2a. This process is possible because of the development of an advanced inverse airfoil design technology. This method is applied to both full potential and

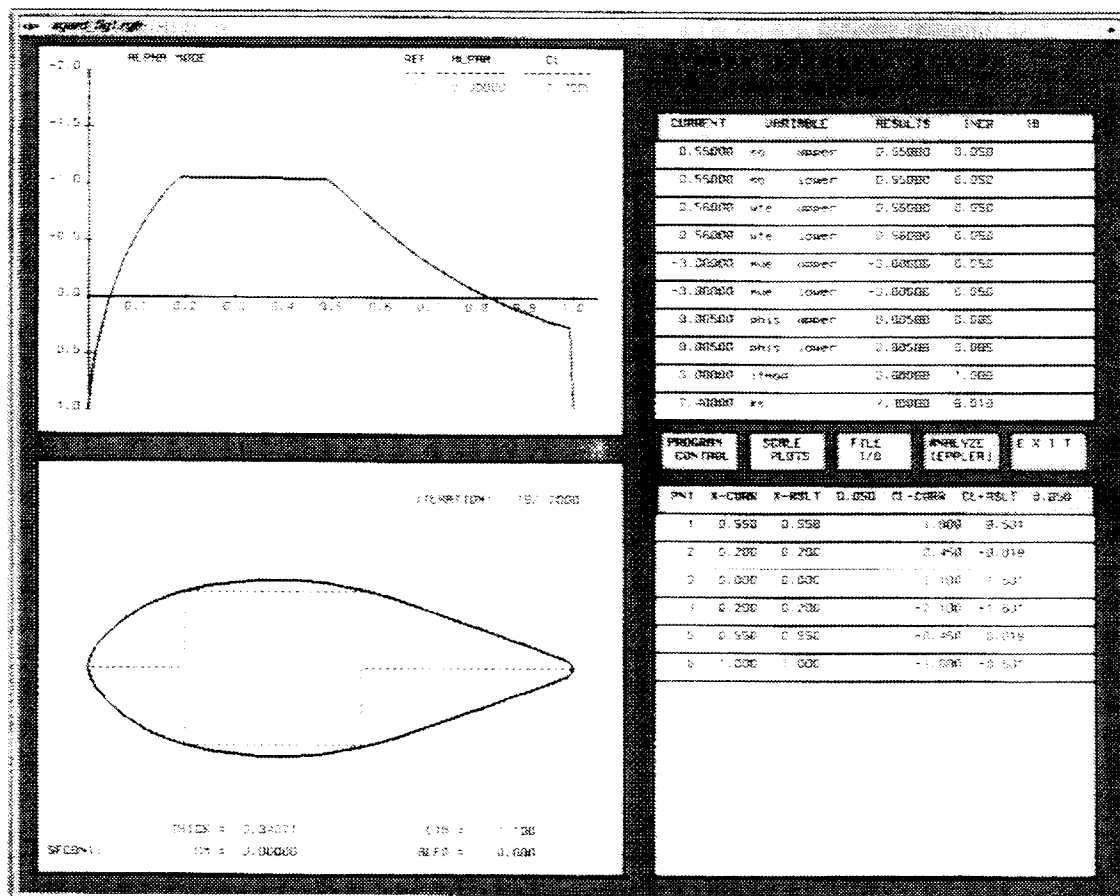
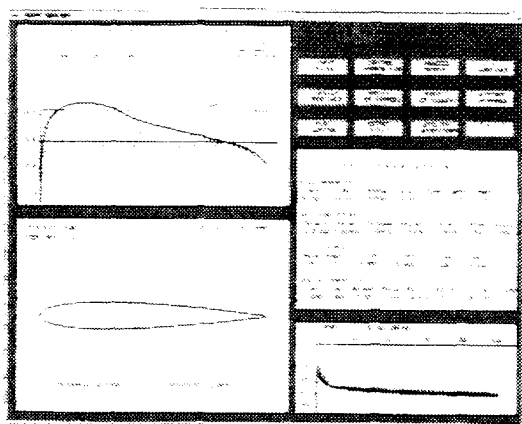
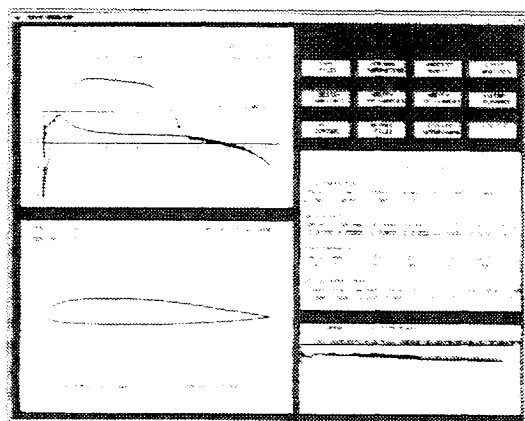


Fig. 1. Subsonic inverse conformal mapping.



4H339B

Fig. 2a. Transonic inverse method: starting airfoil.

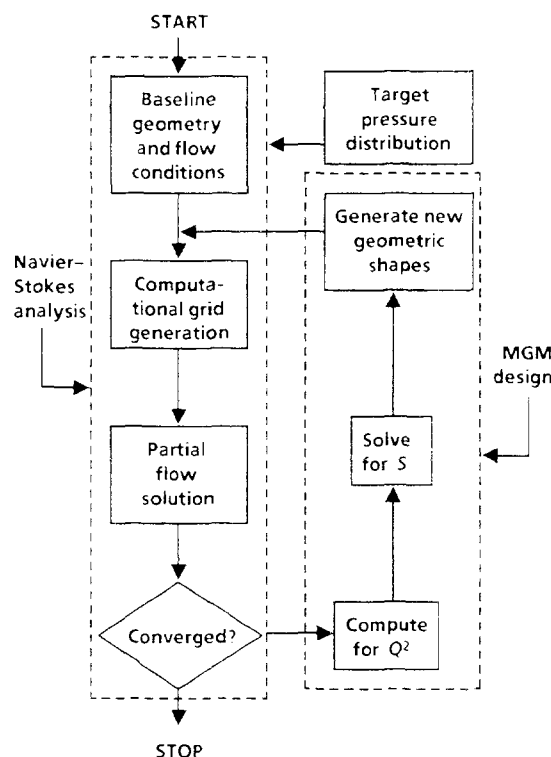


4H340B

Fig. 2b. Transonic inverse method: resulting airfoil.

Navier-Stokes algorithms. The Navier-Stokes inverse airfoil design procedure (Ref. 2) is depicted in Fig. 3. For this Modified Garabedian/McFadden (MGM) method, the airfoil with the desired airfoil pressure distribution is produced as the Navier-Stokes solver converges, which makes it very amenable to an interactive design process. The method is efficient in that it does not significantly increase the computational effort required to obtain an airfoil design above that normally required to use the Navier-Stokes code in analysis mode for a given airfoil.

Fig. 4 shows a comparison of the lift curve of an airfoil that was designed, using these inverse design techniques, to the pretest computations for that section. The pretest data was generated by using a potential flow analysis codes with boundary layer at angles of attack (α) up to 8 degrees and a Navier-Stokes solution at angles of attack above 8 degrees. This figure indicates that a

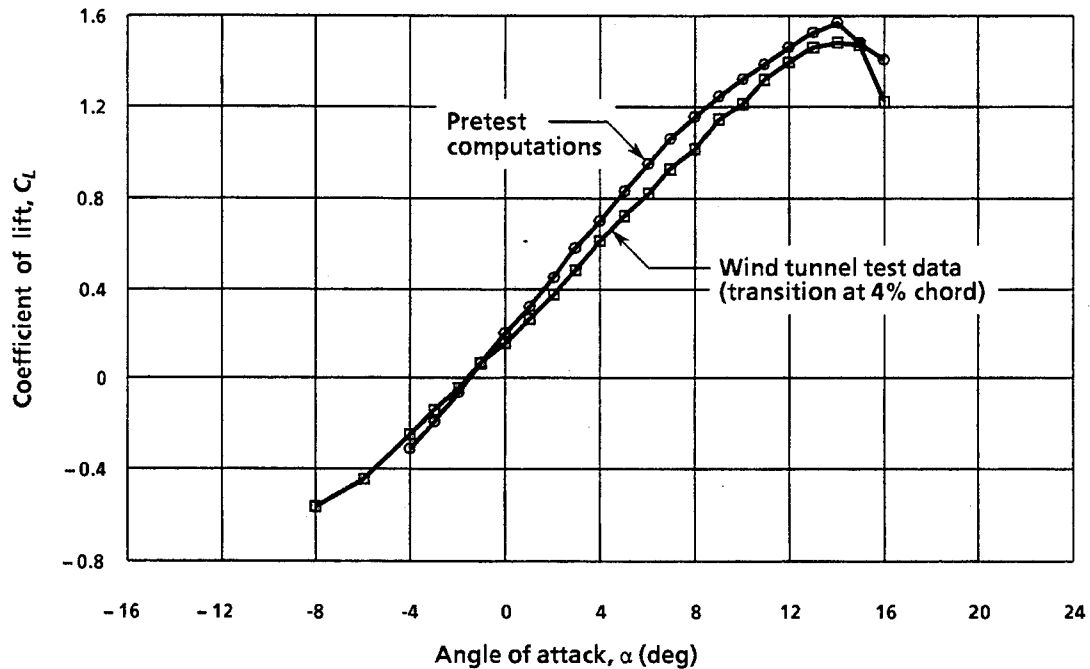


4H341

Fig. 3. MGM code is a unique airfoil design method based on Navier-Stokes equations.

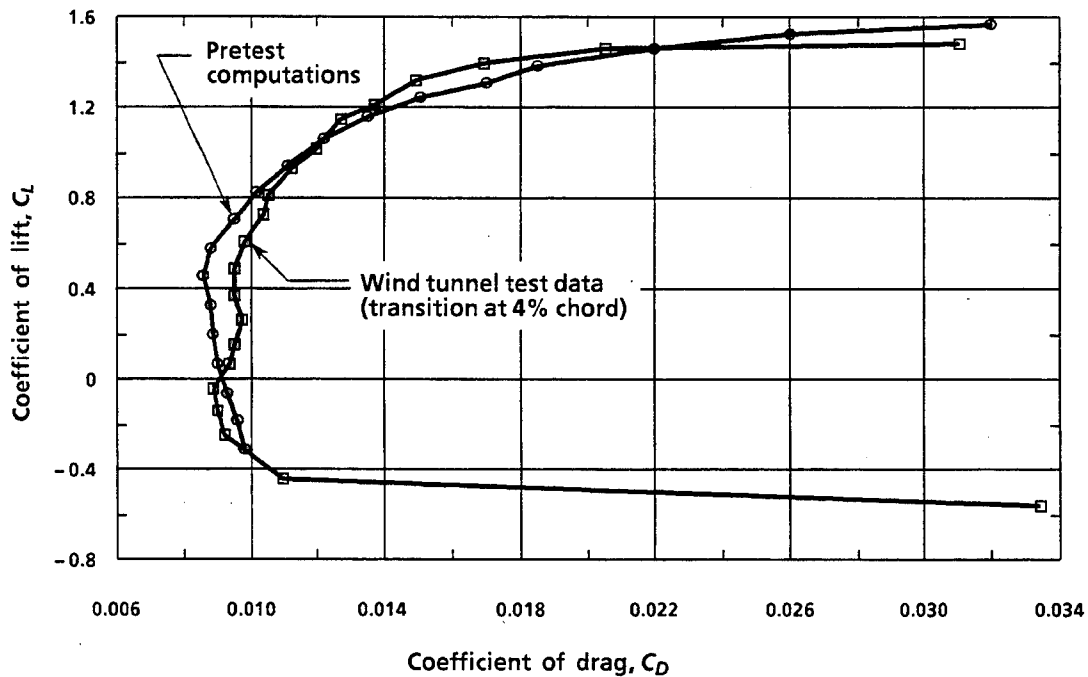
combination of codes that are of different levels of complexity can be used effectively in airfoil evaluations.

At low angles of attack where flow separation does not exist, the potential flow analysis with boundary layer is acceptable for lift computation. At high angles of attack where flow separation exists and potential flow analysis methods break down, Navier-Stokes solutions provide results that correlate well with wind tunnel test data. The maximum lift that was computed by the Navier-Stokes method was within 6% of the measured value. In Fig. 5 the state of the art of computing the drag level is indicated. Pretest computations were made with roughness included to model production rotor drag levels. Fig. 5 shows that the pretest drag level compares well with the measured drag level with transition fixed at 4% chord. At a lift coefficient (C_L) of 0.4, the pretest computed drag level was within 7.5% of the measured drag level. Aerodynamic center, which is a function of the lift and moment curve slopes, is generally difficult to predict. Fig. 6 gives a comparison of the moment coefficient as a function of angle of attack at a Mach number (M) of 0.6 from wind tunnel data and a full potential method. It shows that the trend is correct for this airfoil and that the computed aerodynamic center is



4H342

Fig. 4. Both potential flow and Navier-Stokes methods are required for good correlation.



4H343

Fig. 5. Drag levels with transition fixed were predicted prior to the wind tunnel test.

within 4% of the measured value. For this case, with present Navier-Stokes methods that do not compute a transition location, the correlation is not improved. These validations of the pretest predictions allow for confident use of these computational methods during the design of new airfoils

for application on helicopters and tiltrotor aircraft. Correlation results indicate that at the present time computational results can be used to determine the best airfoil configuration, but that wind tunnel test data is still required to assess the final performance characteristics.

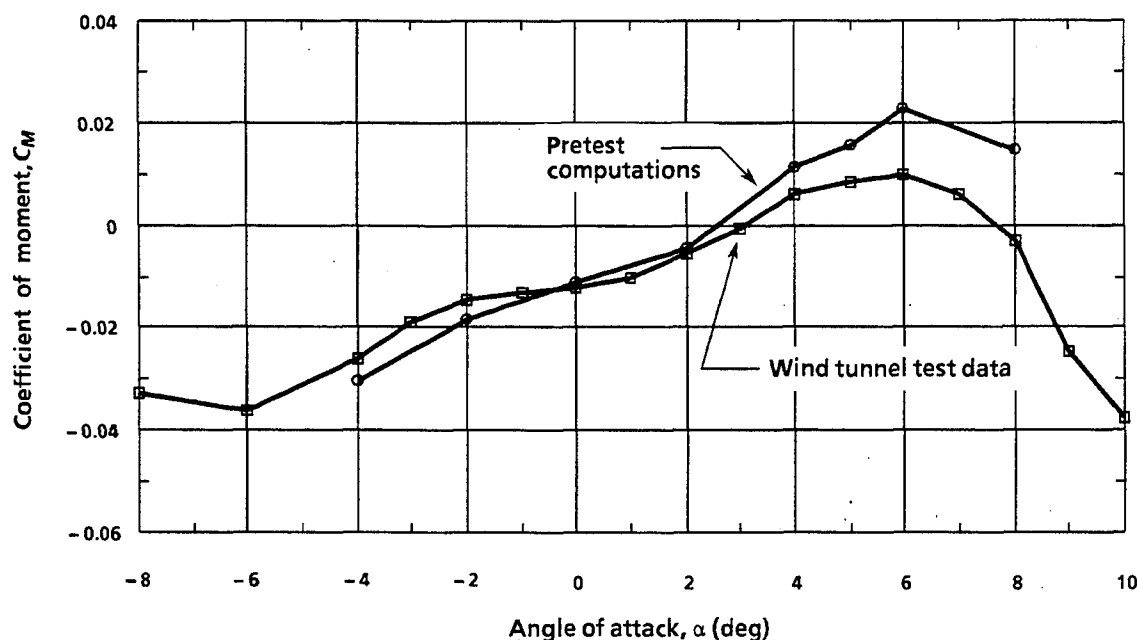


Fig. 6. Moment values are dependent upon transition location and correlate well for this case.

3. 3-D PANEL METHODS

Although 3-D panels methods are not effective for the evaluation of drag and the detailed analysis of flow separation, they have become a standard tool in the determination of aerodynamic load distributions that are used as input to structural analysis codes. At Bell, our approach is to use the same distribution of node points for both the NASTRAN skin panel model and the VSAERO aerodynamic analysis model. In this procedure, methods have been developed that convert the information found on the GRID and QUAD4 data cards for NASTRAN input to a VSAERO input deck. The cards establish the node locations and panel numbers for each panel in the surface grid. Then the critical airload cases are run using VSAERO to produce pressure distributions. These pressure distributions are evaluated and the total load and moment computed. The VSAERO pressure distributions are mapped back to the stress groups by creating PLOAD2 data for the NASTRAN deck. PLOAD2 cards represent the surface pressure input for the NASTRAN deck. Therefore, the pressure distribution that is computed by VSAERO is used directly by the NASTRAN analysis. This provides very high fidelity aerodynamic load distributions to the stress groups.

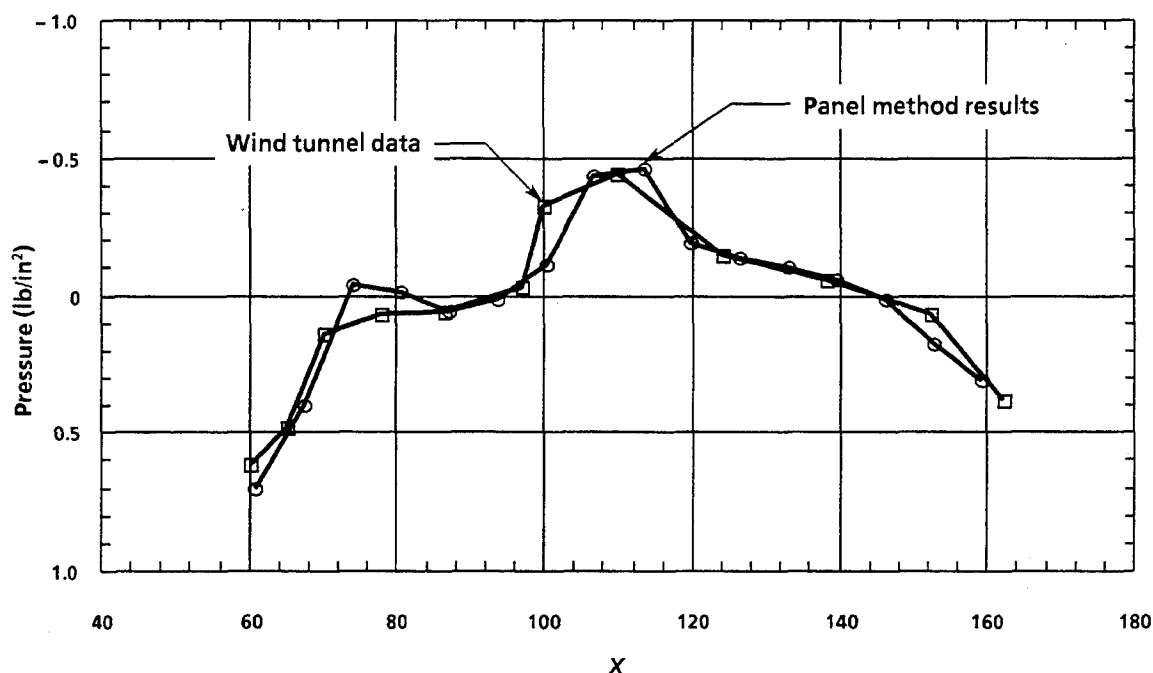
In order to evaluate VSAERO results, frequent correlation with wind tunnel and flight test data is carried out. Fig. 7 shows a comparison of the pressure distribution along the upper centerline of the AH-1S canopy from wind tunnel test data and a

3-D panel method. It shows that, even though this canopy has relatively flat surfaces with sharp breaks, the 3-D panel solution compares very well with the measured pressures. In Fig. 8 the side force as a function of sideslip angle obtained by integrating the pressures from the wind tunnel test is compared to the 3-D panel method results at the same conditions. It should be noted that for this case no wake stitching was performed on the canopy. Since separation is indicated from the corners, separated wake stitching might have improved the results. Fig. 8 indicates that the trend in side force as a function of slideslip angle is somewhat lower than the measured values for this model. This correlation information is then factored into the results that are transferred to the NASTRAN models. Typically some correlation is performed for every different configuration that is evaluated using VSAERO. Therefore, any discrepancies that are not modeled by this singularity method can be accounted for during the development of the airload distributions.

4. 3-D COMPUTATIONAL FLUID DYNAMICS

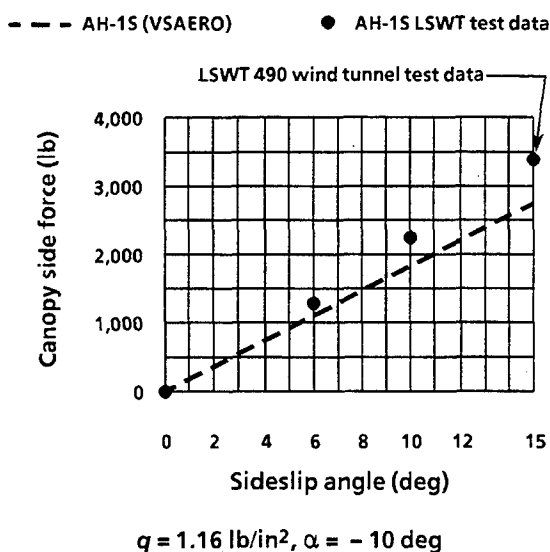
4.1 Initial Studies

Bell Helicopter initially used computational fluid dynamics in the area of airfoil design and analysis as has been described above. Therefore, it was a logical step to extend this to rotor blade analysis. The initial rotor studies were carried out using transonic full potential codes that were modified to



4H345

Fig. 7. Correlation with wind tunnel measurements confirms pressure computation capability.



4H346

Fig. 8. Correlation with wind tunnel measurements confirms load computation capability.

include the rotation terms. These code results provided insight into compressibility effects near the tip of the blade and were applied during the aerodynamic design phase to the development of several tip shapes (Ref. 3). In each of these studies there was also a desire to determine parameters such as drag, flow separation, and accurate forces that can only be achieved if the viscous terms are included in the algorithm formulation.

A decision was made at Bell to concentrate on Navier-Stokes algorithms for use in our rotorcraft problems. Three areas of concentration have led to several successes in the use of Navier-Stokes methods including rotor studies, fuselage studies, and component studies.

4.2 Rotor Studies

In order to validate the Navier-Stokes approach, several rotor studies have been accomplished. Initially, nonrotating blade tip studies were carried out. For the first cases, comparisons were made to wind tunnel test results that were being carried out on several different blade tips. Surface flow visualization, balance forces, and hot wire anemometry data were taken during this test. As the surface flow visualization results were accumulated, questions arose as to the explanation of the surface flow streaks at high angles of attack. At these conditions, streaks indicated flow in unusual directions with no flow separation at some blade locations even at very high angles of attack. At 18 degrees angle of attack on the hyperbolic tip shape the flow was characterized by having separation inboard, no separation near the start of the tip, and an outboard flow that culminates in a separation line near the leading edge of the swept tip. With just the data provided by the wind tunnel test, it was difficult to explain why the surface flow had this characteristic. After the testing was complete, this case was chosen as a difficult case for correlation with a Navier-Stokes results (Ref. 4). The ARC3D code was used as the flow solver on

an $O-O$ grid that was generated around the hyperbolic tip blade shape. Rakes confined to the first grid line off of the surface reproduced the measured surface flow anomalies and confirmed that the flow was not separated near the start of the tip. As is shown in Fig. 9, the stall pattern observed on the blade was replicated by the computational method. When the wakes were allowed to travel off of the surface, the flow phenomenon could be easily observed. The rake lines indicated that a wide tip vortex was forming near the leading edge of the swept tip region that is pulling the surface flow outboard to be entrained by the vortex. Inboard of the start of the swept tip the flow is not entrained and therefore the separation bubble is created. Fig. 10 gives three views of the computational solution results.

For a rotating blade, a Navier-Stokes solver was used to compute the flow near stall of a highly twisted hovering rotor blade (Ref. 5). This study was undertaken since blade element methods that rely on two-dimensional airfoil data tables do not compute high enough lift at the high thrust levels.

Therefore, a Navier-Stokes method was used to gain physical insight into rotor blade characteristics of a blade that had been tested at high thrust levels.

Fig. 11 shows a comparison of the Navier-Stokes code results to the experimental data for thrust coefficient as a function of blade collective pitch angle. It shows that the Navier-Stokes code can produce thrust as a function of blade collective pitch angle that compares well to measured results. The difference in measured and computed thrust values is approximately 6% of measured thrust. It should be noted that the inflow angle as a function of radial station from a lifting surface code (Ref. 6) was used as input to the Navier-Stokes code to produce these results. In fact, some of the difference between the Navier-Stokes results and the measured data is likely to be due to the inaccuracy of the wake model used to set the effective angle-of-attack distribution.

The lift coefficient distribution from the Navier-Stokes solution is compared to a distribution

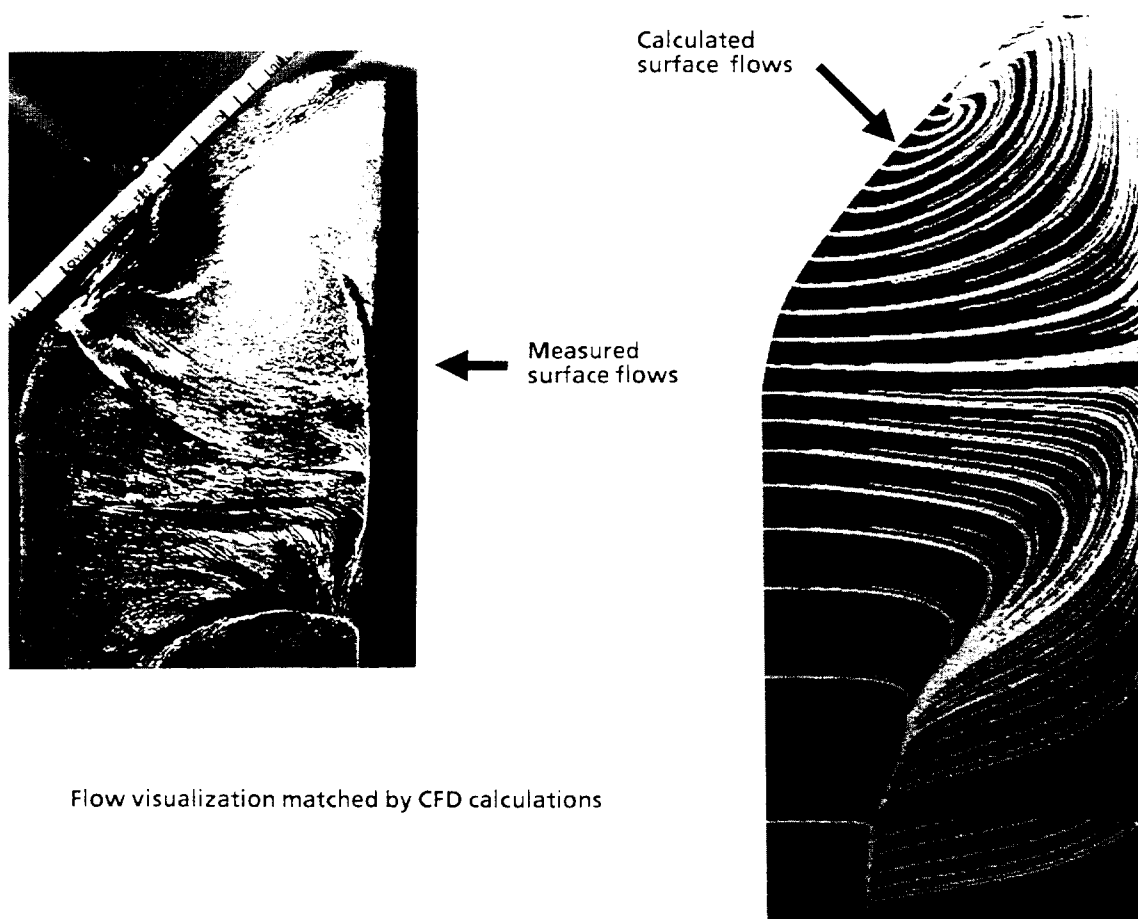
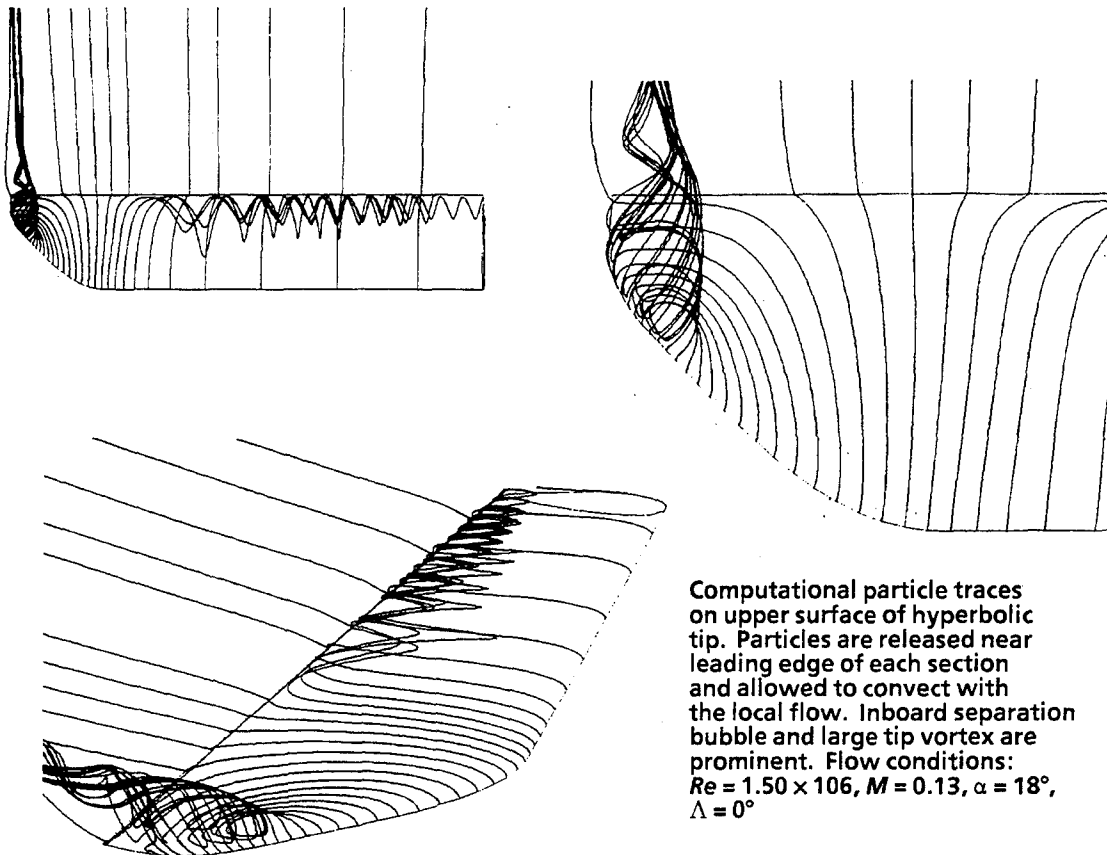


Fig. 9. Navier-Stokes computed flow patterns correlate with wind tunnel results.



4H348

Fig. 10. Navier-Stokes results were used to interpret wind tunnel flow patterns.

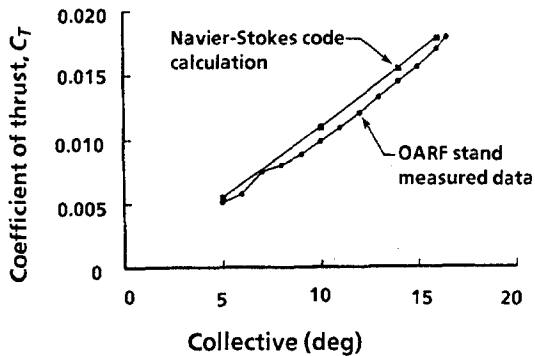


Fig. 11. Comparison of computed and measured thrust coefficient for a tiltrotor.

computed using a lifting surface method (Ref. 6) for a total thrust coefficient (C_T) of 0.0155 in Fig. 12. It indicates that the Navier-Stokes method is predicting a much higher lift coefficient in the inboard region compared to the lifting surface method results at an equivalent thrust level. This difference in the inboard lift coefficient has been observed experimentally by other investigators (Refs. 7, 8, 9). It has been attributed to spanwise flow velocities that effectively thin the boundary

layer separation region on the blade surface in the inboard region (Ref. 8). However, the Navier-Stokes results that were produced during this study indicate that the three-dimensionality of the flow allows the flow to remain attached to higher angles of attack. No outward radial flow velocities were observed in the inboard region of the blade.

Tip speed = 755.00 ft/s

$C_T = 0.0155$

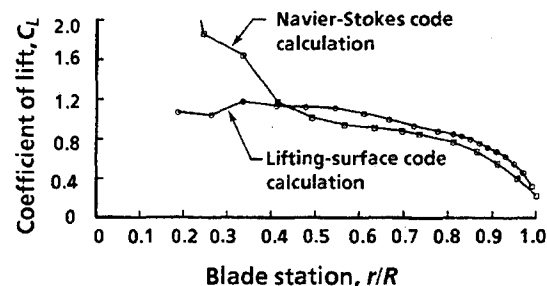
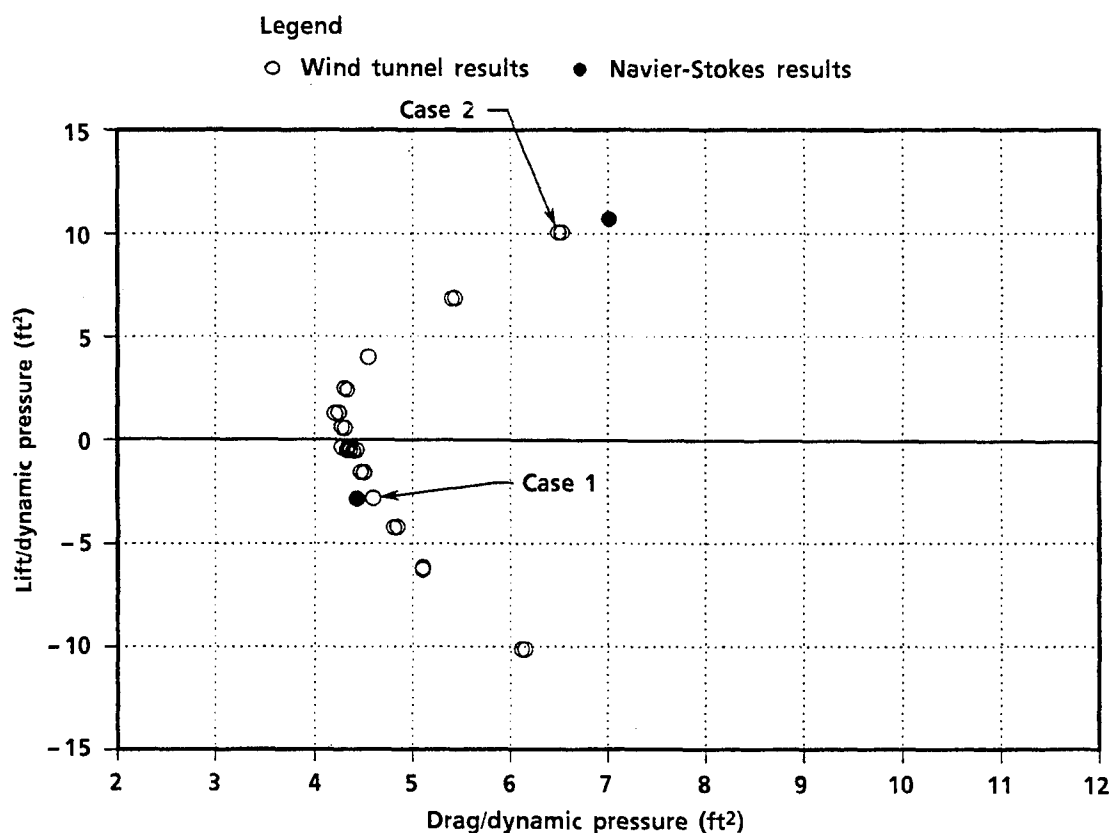


Fig. 12. Navier-Stokes predicts attached flow inboard.

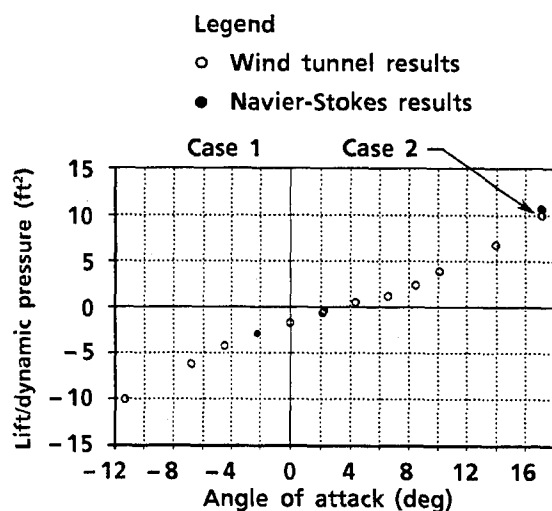
4.3 Fuselage Studies

Navier-Stokes methods have been used successfully to determine the flow about and forces on



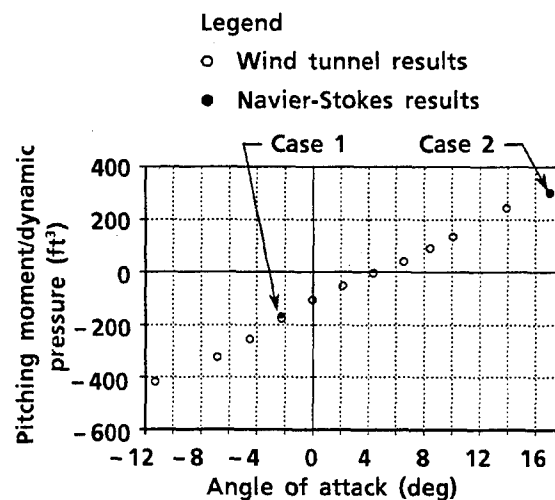
4H351

Fig. 13. Navier-Stokes drag correlates well with test data.



4H352

Fig. 14. Navier-Stokes lift correlates well with test data.



4H353

Fig. 15. Navier-Stokes moment correlates well with test data.

rotorcraft fuselage shapes. The first rotorcraft fuselage study that was conducted correlated Navier-Stokes computations for the lift, drag, pitching moment, and pressures to wind tunnel measurements on the M214ST. During this study, grid configuration and resolution studies were carried out for low and high angles of attack. In

addition, a high yaw case was also correlated to the test data. The best correlation was obtained from runs using a *C-O* grid topology. Figs. 13, 14, and 15 show the drag, lift, and pitching moment comparisons between wind tunnel test data and Navier-Stokes results using the *C-O* grid for the M214ST fuselage shape (Ref. 10). The difference

between the measured drag and the computed drag is only 4% at an angle of attack of -2.28 deg (CASE 1) and 1.7% at an angle of attack of 17.04 deg (CASE 2). The computed lift was within 6.5% of the measured lift for the CASE 2 conditions, as is shown in Fig. 14. In Fig. 15 the pitching moment comparison is given. It shows that the computed pitching moment was within 7.3% of the measured values. These results indicate that good agreement was achieved for all forces including the drag on this fuselage shape.

More recent fuselage studies have also indicated that drag increments due to shape changes on a typical helicopter fuselage can be accurately modeled using Navier-Stokes methods. In 1970, a wind tunnel test was conducted in which the UH-1H single engine helicopter configuration was built up to the M212 twin engine helicopter configuration (Ref. 11). This change requires an increase in the size of the cowl and changes the afterbody shape which resulted in a drag increase for the fuselage. A calculation was made using the methodology developed in the M214ST correlation study to determine if the drag increment measured in this wind tunnel test for these bluff aft body shapes could be predicted. Since the wind tunnel model had a solid cowl with no flow

through the inlet and exhaust regions, that configuration was modeled in the Navier-Stokes solution. However, it is relatively easy to add a mass flow boundary condition to the Navier-Stokes solution that will allow the modeling of inlet and exhaust flows.

A comparison of computed and measured drag versus angle of attack for the UH-1H fuselage configuration is given in Fig. 16. In this case the fuselage-alone drag computed in the Navier-Stokes solution is compared to the measured drag for the fuselage with landing gear. As can be seen, the shape of the computed fuselage-alone drag polar shows the same trend versus angle of attack as the measured data for the fuselage with the landing gear added. The difference between these results can be attributed to the landing gear drag. In Fig. 17 the computed increment in drag as a function of angle of attack is compared to the measured increment when changing from a UH-1H fuselage to an M212 fuselage. The measured data indicated that the increment in drag between the two configurations was reduced as the angle of attack is increased. This is probably because as the angle of attack is increased, the flow about the cowl becomes less of the drag of the body (since it is in the wake of the fuselage). Fig. 17 shows that

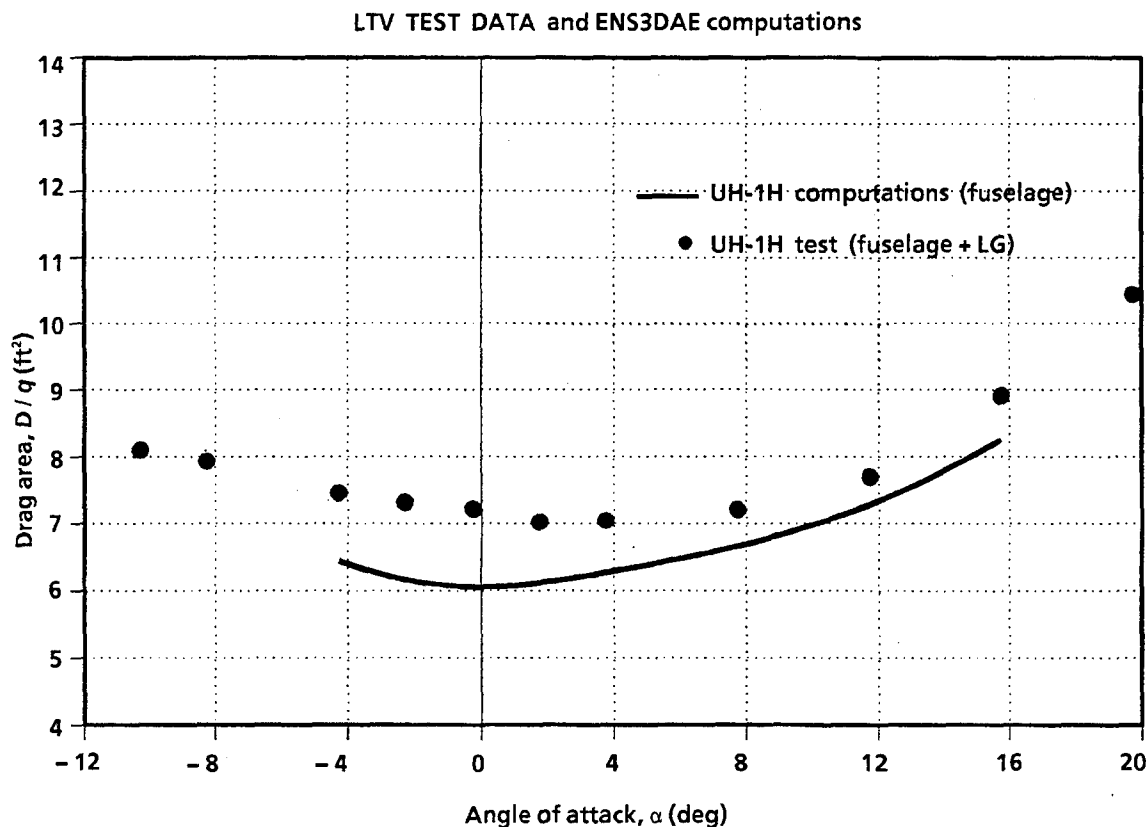
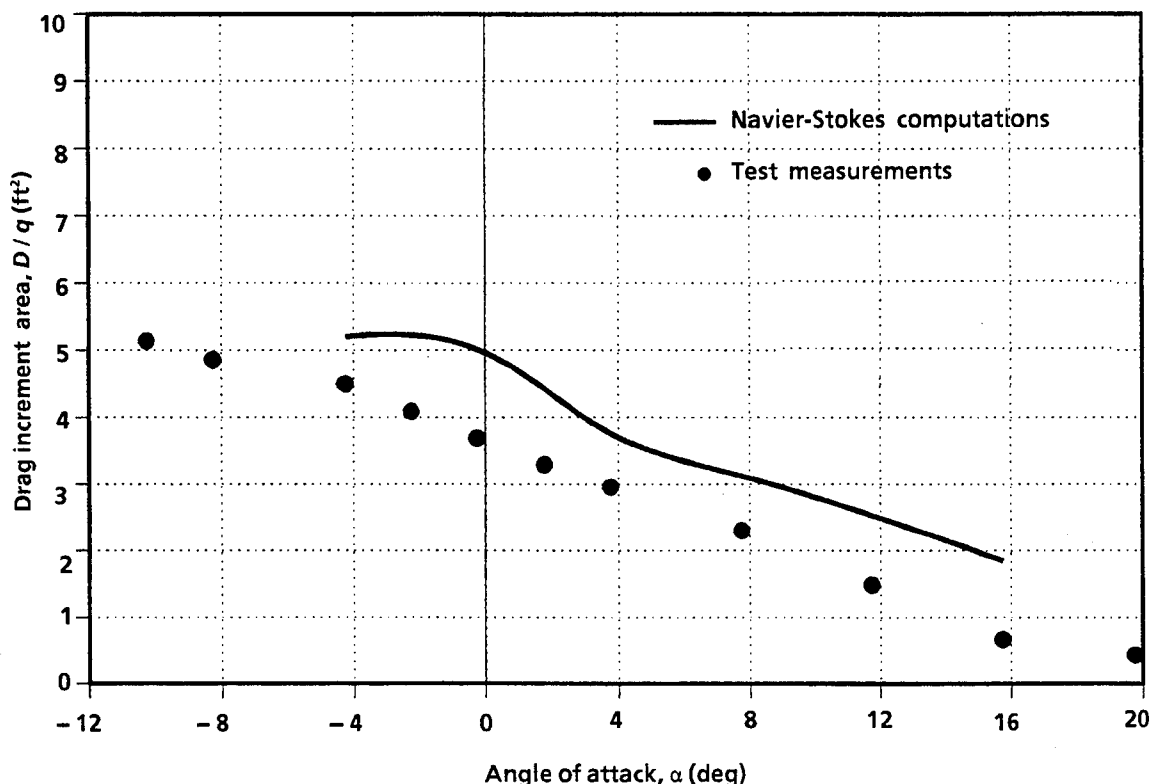


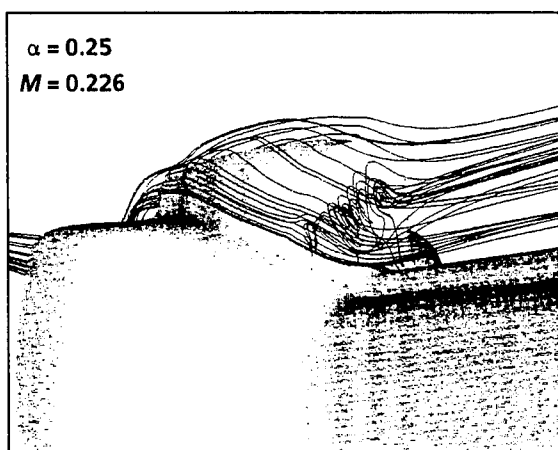
Fig. 16. Fuselage drag trends.

LTV TEST DATA and ENS3DAE computations



4H355

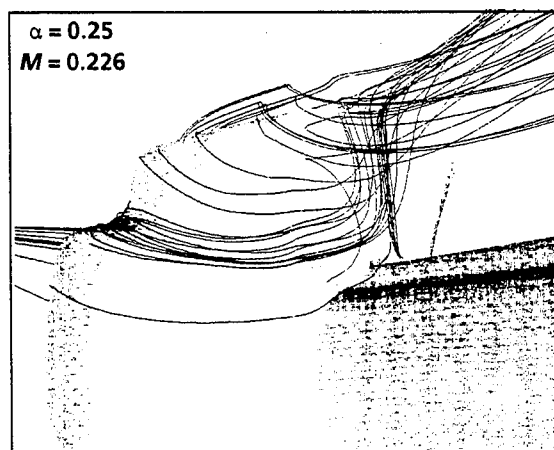
Fig. 17. Fuselage drag increment correlates.



4H356

Fig. 18. Wind tunnel model for UH-1H did not model exhaust.

the Navier-Stokes method predicts the correct trend in the drag increment as a function of angle of attack. Therefore, it is able to determine the subtle flow differences between these two configurations as a function of angle of attack. Since these bodies have bluff steps at the cowl afterbody that produce large regions of separated flow, these results are very encouraging. Fig. 18 shows the separation pattern computed aft of the engine cowl region of the UH-1H fuselage wind tunnel model.



4H357

Fig. 19. Separation pattern is different for M212 cowl.

Particles are caught up in the separation bubble aft of the flat surface and are swirled into a tornado-like shape. This separation pattern is significantly different from the one produced by the M212 cowl modification that is shown in Fig. 19.

4.4 Current Studies

At the present time these methods are being applied to more complex configurations including tiltrotor aircraft and unmanned vehicles. In

addition, new methods are being evaluated for application to detailed rotorcraft problems like advanced tips, details of wing fences, and details of blade tip vortex roll-up. These newer methods are being developed at NASA Ames Research Center and include Navier-Stokes codes such as OVERFLOW (Ref. 12), INS3D (Ref. 13), and UNS2D (Ref. 14), and grid development methods such as PEGSUS (Ref. 15), UI-HYPGEN (Ref. 16), Collar Grid Tools (Ref. 17), and GDCF (Ref. 18). These methods allow complex configurations to be modeled and will represent the next generation of CFD solutions.

5. CONCLUDING REMARKS

As a result of constant improvement in methods and computer capabilities, computational fluid dynamics has become a standard part of the aerodynamic design process at Bell Helicopter. This has been accomplished due to the successful correlation of these computational methods to wind tunnel results.

6. ACKNOWLEDGEMENTS

The author would like to offer a special thanks to the National Aerodynamic Simulator (NAS) Project and to the Army/NASA Joint Rotorcraft CFD Group (RFC) at NASA Ames Research Center for providing computer resources used in some of these studies.

I also wish to thank Jim McCroskey of NASA Ames, Joe Vadyak of Lockheed, and Don Axley of Bell Helicopter Textron, Inc. for their technical assistance during the preparation of material that is used in this paper.

Particular appreciation is expressed to Tom Wood and Jing Yen for valuable discussions in the preparation of this paper and Chuck Gatlin and John Hedric who finalized the graphics and layout.

7. REFERENCES

1. Narramore, J. C., "The Use of Small Computers in a Subsonic Airfoil Design Application," NACA CP 2046, 1978, Volume II, Paper 6.
2. Malone, J. B., Narramore, J. C., and Sankar, L. N., "An Efficient Airfoil Design Method Using the Navier-Stokes Equations," *AIAA Journal of Aircraft*, Vol. 28, No. 3, March 1991, pp. 216-224.
3. Scott, M. T., Sigl, D., and Strawn, R. C., "Computational and Experimental Evaluation of Helicopter Rotor Tips for High-Speed Flight," *AIAA Journal of Aircraft*, Vol. 28, No. 6, June 1991, pp. 403-409.
4. Scott, Matthew, and Narramore, J. C., "Navier-Stokes Correlation of a Swept Helicopter Rotor Tip at High Alpha," AIAA 91-1752, presented at the AIAA 22nd Fluid Dynamics, Plasma Dynamics, and Lasers Conference, Honolulu, Hawaii, June 24-26, 1991.
5. Narramore, J. C., and Vermeland, R., "Navier-Stokes Calculations of Inboard Stall Delay," *AIAA Journal of Aircraft*, Vol. 29, No. 1, Jan-Feb 1992, pp. 73-78.
6. Kocurek, J. D., Berkowitz, L. F., and Harris, F. D., "Hover Performance at Bell Helicopter Textron," AHS Paper 80-3, Presented at the 36th Annual National Forum of the AHS, May 1980.
7. Harris, F. D., "Preliminary Study of Radial Flow Effects on Rotor Blades," *Journal of the American Helicopter Society*, Volume 11, No. 3, 1966.
8. Milborrow, D. J., "Changes in Aerofoil Characteristics Due to Radial Flow on Rotating Blades," British Wind Energy Association, 7th Annual Workshop, Oxford, England, March 1985.
9. Schlichting, H., *Boundary-Layer Theory*, 7th Ed, McGraw-Hill Book Company, New York, 1979, pp. 694-696.
10. Narramore, J. C., and Brand, A. G., "Navier-Stokes Correlations to Fuselage Wind Tunnel Test Data," presented at the 48th Annual Forum of the American Helicopter Society, Washington, DC, June 3-5, 1992.
11. Narramore, J. C., "Navier-Stokes Computations of Fuselage Drag Increments," presented at the 1994 AHS Aeromechanics Specialists Conference, San Francisco, California, January 19-21, 1994.
12. Buning, P., Chan, W., Renze, K., Sondak, K., Chiu, I., and Slotnick, J., "OVERFLOW Users Manual Version 1.6ah," July 1993.
13. Rogers, S. E., and Kwak, D., "Steady and Unsteady Solutions of the Incompressible Navier-Stokes Equations," *AIAA Journal of Aircraft*, Vol. 29, No. 4, April 1991, pp. 603-610.
14. Stremel, P. M., "Calculation of Flow about Two-Dimensional Bodies by Means of the Velocity-Vorticity Formulation on a Staggered Grid," AIAA Paper 91-0600, presented at AIAA 29th Aerospace Sciences Meeting, Reno, NV, January 1991.

15. Suhs, N. E., and Tramel, R. E., "PEGSUS 4.0 Users Manual," Arnold Engineering Development Center, AEDC-TR-91-8, June 1991.
16. Chiu, I. T., "UI User's Manual (Version 1.2)," NASA Ames Research Center, Moffett Field, CA, March 1992.
17. Parks, S. J., Buning, P. G., Steger, J. L., and Chan, W. M., "Collar Grids for Intersecting Geometric Components Within the Chimera Overlapped Grid Scheme," AIAA Paper 91-1587, June 1991.
18. McCann, K., and Meakin, R., "GDCF: An Interactive Approach to Domain Connectivity Among Systems of Overset Grids," 11th AIAA Computational Fluid Dynamics Conference Proceedings, pp. 1039-1040, July 1993.

Cost Efficient Calculation of Compressible Potential Flow Around a Helicopter Rotor Including Free Vortex Sheet by a Field Panel Method

A. Röttgermann
S. Wagner

Institut für Aerodynamik und Gasdynamik
Universität Stuttgart
Pfaffenwaldring 21
D-70550 Stuttgart
GERMANY

1 SUMMARY

To consider compressible transonic effects a vortex lattice method for the computation of the rotor flow is coupled with a field panel method. For this purpose Cartesian grids are used which are not adapted to the contour and only discretise the domain of the nonlinear flow. The basis of this procedure is the separation of the full potential equation into the Laplacian operator and the nonlinear terms. The developed program ROFPM is validated at several test cases of the CARADONNA rotor.

List of symbols

a	local speed of sound
c_p	pressure coefficient
B, \hat{B}	Influence coefficient matrices of potential and velocity components of the single-layer potential
C, \hat{C}	Influence coefficient matrices of the double-layer potential
C^w, \hat{C}^w	matrices of the wake double-layer potential of the vortex sheets
\hat{D}	Influence coefficient matrix of velocity components of field sources
N, N_w	number of blade and wake panels
M	number of field panels
R	radius of the rotor blade
T	artificial viscosity
α, ω	relaxation parameters AF-scheme
μ	singularity strength of double-layer potential
μ_w	doublet strength of wake panels
Φ, ϕ	velocity potential, perturbation potential
$\sigma, \bar{\sigma}$	field source strength
τ	singularity strength of single-layer potential
Θ_c	collective pitch
\vec{r}	radial distance from the rotor center of rotation
$\vec{\Omega}$	rotational speed
\vec{V}	velocity vector (u, v, w)
\mathcal{R}	vector of right hand sides

$(.)^{BF, BW}$	influence blade on field, blade on wake
$(.)^{FF}$	influence field on field
$(.)^{WF, WW}$	influence wake on field, wake on wake

2 INTRODUCTION

Based on the idea of Oswatitsch [1] to describe transonic flows by using integral equations, different methods for airfoils [2, 3], wings [4, 5] and rotors [6] have been developed. A boundary element method computes the linear terms; the nonlinear terms are determined through a field grid, which discretises the outer domain of the contour. An iterative procedure couples the two methods.

At our institute, the blade-vortex interference and the start-up procedure of a helicopter rotor [7] have been computed by vortex lattice methods for some time. The boundary element procedure solves the Laplace equation and thus is restricted to incompressible flows. The presented program ROFPM combines the fast and flexible panel method with a field panel method which registers the transonic nonlinear effects at the blade tip.

In order to save computation time and storage capacity it was taken care that with our method the field grids are as small and simple as possible.

3 THEORETICAL BACKGROUND

3.1 Boundary element method

The compressibility of an isentropic stationary fluid is described by the full potential equation:

$$\left(1 - \frac{u^2}{a^2}\right) \Phi_{xx} + \left(1 - \frac{v^2}{a^2}\right) \Phi_{yy} + \left(1 - \frac{w^2}{a^2}\right) \Phi_{zz} - \frac{2uv}{a^2} \Phi_{xy} - \frac{2vw}{a^2} \Phi_{yz} - \frac{2wu}{a^2} \Phi_{zx} = 0. \quad (1)$$

Dividing the potential equation into the Laplacian operator and the remaining nonlinear terms yields the Poisson equation

$$\nabla^2 \Phi = \sigma, \quad (2)$$

with the abbreviation σ for the nonlinear terms.

$$\begin{aligned} \sigma = & \frac{u^2}{a^2} \Phi_{xx} + \frac{v^2}{a^2} \Phi_{yy} + \frac{w^2}{a^2} \Phi_{zz} \\ & + \frac{2uv}{a^2} \Phi_{xy} + \frac{2vw}{a^2} \Phi_{yz} + \frac{2wu}{a^2} \Phi_{zx} \end{aligned} \quad (3)$$

The local speed of sound is given by

$$a^2 = a_\infty^2 + \frac{\kappa - 1}{2} (|\vec{V}_\infty|^2 - |\nabla \Phi|^2).$$

Green's third identity transforms the differential equation (2) into an integral equation for the perturbation potential ($\Phi = \phi + \phi_\infty$):

$$\begin{aligned} \phi = & -\frac{1}{4\pi} \iint_S \frac{1}{r} \frac{\partial \phi}{\partial n} dS + \frac{1}{4\pi} \iint_S \phi \frac{\partial}{\partial n} \left(\frac{1}{r} \right) dS \\ & - \frac{1}{4\pi} \iiint_V \frac{1}{r} \nabla^2 \phi dV. \end{aligned} \quad (4)$$

3.1.1 Boundary conditions

In order to solve the integral equation (4) the potential values at the contour surface S and at the outer borders of the domain V have to be prescribed. Furthermore, at the outer border the far-field boundary condition is valid:

$$\lim_{r \rightarrow \infty} \Phi = \lim_{r \rightarrow \infty} (\phi + \phi_\infty) = \phi_\infty.$$

At the contour either the normal derivative of the potential or a potential value is determined:

$$\text{NEUMANN:} \quad \vec{n} \nabla \phi = \frac{\partial \phi}{\partial n} = v_n, \quad (5a)$$

$$\text{DIRICHLET:} \quad \phi = \bar{\phi}. \quad (5b)$$

If for the NEUMANN problem the derivative in normal direction of equation (4) is formed

$$\begin{aligned} -\frac{1}{2} \vec{n} (\nabla \phi_a - \nabla \phi_i) + \vec{n} \frac{1}{4\pi} \nabla \iint_S \left\{ -\frac{1}{r} \vec{n} (\nabla \phi_a - \nabla \phi_i) \right. \\ \left. + (\phi_a - \phi_i) \vec{n} \nabla \left(\frac{1}{r} \right) \right\} dS = v_n \end{aligned}$$

and the terms

$$\begin{aligned} \tau &:= -\vec{n} (\nabla \phi_a - \nabla \phi_i) = -\vec{n} \nabla [\phi], \\ \mu &:= -(\phi_a - \phi_i) = -[\phi], \end{aligned}$$

are interpreted as singularity strengths of a single- and double-layer potential, a Fredholm integral equation of the second kind is yielded for the unknown strengths τ and μ . For lifting bodies, the resulting vortex sheets are modelled as thin surfaces \mathcal{W} . Since the wake is a stream surface per definition, the jump of the normal component over the vortex sheet disappears.

$$\vec{n} \cdot (\nabla \Phi_u - \nabla \Phi_l) = 0$$

The jump in potential between the upper and lower side is interpreted as doublet strength.

$$\mu_W := -(\Phi_u - \Phi_l) \quad (6)$$

The integral equation is solved by a collocation method. The surface is divided into rectangular panels; the collocation points are located at the centroids of the elements. To avoid that fluid can penetrate the body, the kinematic boundary condition is required:

$$\vec{n} \nabla \Phi = 0.$$

Thus, the integral equation for the NEUMANN problem is written as:

$$\begin{aligned} \frac{1}{2} \tau_P + \frac{1}{4\pi} \vec{n} \nabla \iint_S \tau \frac{1}{r} dS - \frac{1}{4\pi} \vec{n} \nabla \iint_S \mu \vec{n} \nabla \left(\frac{1}{r} \right) dS \\ - \vec{n} \nabla \iint_W \mu_W \vec{n} \nabla \left(\frac{1}{r} \right) d\mathcal{W} = -\vec{n} \nabla \phi_\infty. \end{aligned}$$

For the internal DIRICHLET boundary condition forcing the perturbation potential inside the body to zero ($\phi_i = 0$) the definitions

$$\tau := -\vec{n} \nabla \phi, \quad (7a)$$

$$\mu := -\phi, \quad (7b)$$

results with a Fredholm integral equation of the second kind for the unknown doublet strength μ :

$$\begin{aligned} \frac{1}{2} \mu_P + \frac{1}{4\pi} \iint_S \tau \frac{1}{r} dS - \frac{1}{4\pi} \iint_S \mu \vec{n} \nabla \left(\frac{1}{r} \right) dS \\ + \iint_W \mu_W \vec{n} \cdot \nabla \left(\frac{1}{r} \right) d\mathcal{W} = 0. \end{aligned}$$

The kinematic flow condition determines the source strength τ from equation (7a):

$$\tau = \vec{n} \cdot (\vec{V}_S + \nabla \phi_\infty).$$

\vec{V}_S is the local velocity of the surface.

3.1.2 Discretisation of the integral equations

In order to simplify the notation, the integral kernels for the NEUMANN problem are defined as

$$B_{ki} = -\vec{n}_k \nabla \iint_{S_i} \left(\frac{1}{r_{ki}} \right) dS_i,$$

$$C_{ki} = \vec{n}_k \nabla \iint_{S_i} \vec{n}_i \nabla \left(\frac{1}{r_{ki}} \right) dS_i,$$

$$C_{kj}^W = \vec{n}_k \nabla \iint_{\mathcal{W}_j} \vec{n}_j \nabla \left(\frac{1}{r_{kj}} \right) d\mathcal{W}_j,$$

and the kernels of the integrals of the DIRICHLET problem are described as

$$B_{ki} = -\iint_{S_i} \left(\frac{1}{r_{ki}} \right) dS_i,$$

$$C_{ki} = \iint_{S_i} \vec{n}_i \nabla \left(\frac{1}{r_{ki}} \right) dS_i,$$

$$C_{kj}^W = \iint_{W_j} \vec{n}_j \nabla \left(\frac{1}{r_{kj}} \right) dW_j.$$

The aerodynamic influence coefficient matrices B , C , and C^W represent the normal components of the velocity influences with the Neumann problem. The matrix elements at the Dirichlet problem reflect the unit influences of the velocity potential.

If all known values are put to the right hand side the discretised equations for all control points $k = 1, \dots, N$ can be written as:

$$\text{NEUMANN: } \sum_{i=1}^N \tau_i B_{ki} + \sum_{i=1}^N \mu_i C_{ki} = R_k,$$

$$\text{DIRICHLET: } \sum_{i=1}^N \mu_i C_{ki} = R_k.$$

The vector of the right hand sides is given by:

$$\text{NEUMANN: } R_k = -\vec{n}_k \cdot \vec{V}_{\infty,k} - \sum_{j=1}^{N_W} \mu_{W_j} C_{kj}^W,$$

$$\text{DIRICHLET: } R_k = -\sum_{i=1}^N \tau_i B_{ki} - \sum_{j=1}^{N_W} \mu_{W_j} C_{kj}^W.$$

3.2 Development of the free vortex sheets

The free vortex sheets of the rotor blades are described through a vortex lattice method. The doublet panels with constant strength μ are equivalent to a vortex ring with the circulation $\Gamma \equiv \mu$, the influence of which on a point P is determined with the Biot-Savart law. In order to simulate the chronological structure of the wake development, an iterative procedure is used modifying the right hand sides.

$$\text{NEUMANN: } R_k(t) = -\vec{n}_k(t) \cdot \left(\vec{V}_{\infty,k}(t) + \vec{\Omega}(t) \times \vec{r}_k(t) + \sum_{j=1}^{N_W} \mu_{W_j} \vec{C}_{kj}^W \right)$$

$$\text{DIRICHLET: } R_k(t) = -\frac{1}{4\pi} \sum_{i=1}^N \left[\vec{n}_k(t) \cdot \left(\vec{V}_{\infty,k}(t) + \vec{\Omega}(t) \times \vec{r}_k(t) \right) B_{ki} - \sum_{j=1}^{N_W} \mu_{W_j} C_{kj}^W \right]$$

As start-up solution ($t = 0$) the system of equations is solved without wake ($N_W = 0$). The strengths of the arising vortex rings are formed according to the Kutta condition $\gamma_{TE} = 0$ from the differences of the doublet strengths of the trailing edge panels:

$$\text{NEUMANN: } \mu_W = \mu_{TE_u} - \mu_{TE_l},$$

$$\text{DIRICHLET: } \mu_W = \mu_{TE_u} - \mu_{TE_l} - \frac{1}{4\pi} (\phi_{\infty TE_u} - \phi_{\infty TE_l}).$$

The new corner points of the wake panels \vec{r}_l ($l = 1, \dots, N_W$) result from the induced velocities of the blade panels \vec{V}_l^{BW} , the vortex layers \vec{V}_l^{WW} , the on-flow velocity and the rotational speed $\vec{\Omega}$ (Figure 1).

$$\vec{r}_l(t + \Delta t) = \vec{r}_l(t) + \left(\vec{V}_{\infty,l}(t) + \vec{\Omega}(t) \times \vec{r}_l(t) + \vec{V}_l^{BW}(t) + \vec{V}_l^{WW}(t) \right) \cdot \Delta t$$

with

$$\vec{V}_l^{BW}(t) = \sum_{i=1}^N \tau_i(t) \hat{B}_{li} + \sum_{i=1}^N \mu_i(t) \hat{C}_{li},$$

$$\vec{V}_l^{WW}(t) = \sum_{j=1}^{N_W(t)} \mu_{W_j} \hat{C}_{lj}^W.$$

The elements of the matrices

$$\hat{B}_{li} = -\nabla_p \iint_{S_i} \left(\frac{1}{r_{li}} \right) dS_i,$$

$$\hat{C}_{li} = -\nabla_p \iint_{S_i} \vec{n}_i \nabla \left(\frac{1}{r_{li}} \right) dS_i,$$

$$\hat{C}_{lj}^W = -\nabla_p \iint_{W_j} \vec{n}_j \nabla \left(\frac{1}{r_{lj}} \right) dW_j,$$

that determine the influence of the rotor on the wake depend on the geometry of the vortex sheets and have to be recalculated at each time-step.

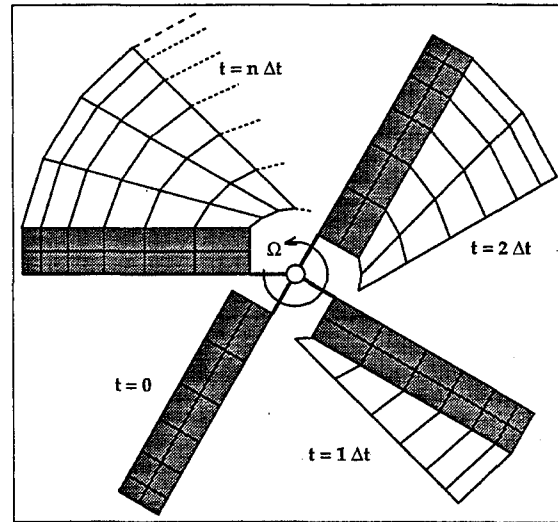


Figure 1: Development of wake structure

The incompressible rotor computation was terminated after two rotations ($\Delta t \cong 15^\circ$) since the doublet distribution on the blades was steady. In order to judge the quality of the wake geometry, the axial component z/R and the radial component r/R of the tip vortex trajectories are shown in Figure 2. The results of the vortex lattice method are compared

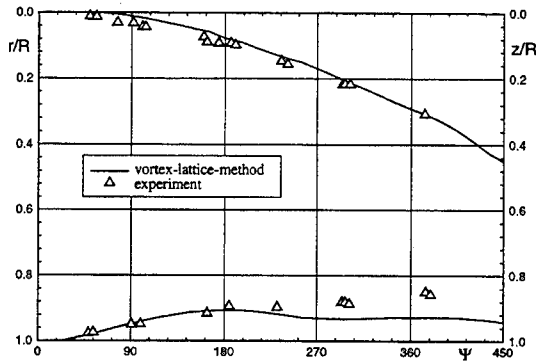


Figure 2: Axial and radial components of the vortex trajectories of CARADONNA rotor ($\Theta_c = 8^\circ$)

to the values measured by Caradonna & Tung [8]. The computed settlement of the vortex sheets corresponds to the measurements, whereas the radial position of the tip vortex corresponds only for $\Psi \leq 180^\circ$ to the experimental data. Afterwards the influence of the start-up vortex ring becomes evident with a radius bigger than the rotor radius and thus again enlarging the vortex layers. If the wake iteration is continued the start-up vortex ring floats further and the constriction of the tip vortices improves also for $\Psi > 180^\circ$.

3.3 Field panel method

The nonlinear character of the differential equation is concentrated in the volume integral from equation (4). This integral describes the compressibility influence of the flow. The singularity strength σ is interpreted as spatial source distribution (equations (2) and (4)).

3.3.1 Boundary conditions and field grid

The perturbation potential is divided into the components from the panel method ϕ^P and the field procedure ϕ^F :

$$\phi = \phi^P + \phi^F. \quad (12)$$

The boundary element method satisfies the kinematic boundary conditions on the body, the far-field boundary condition is satisfied implicitly by the singularities.

Condition $\nabla^2 \phi^F = \sigma - \nabla^2 \phi^P$ is the only explicit demand on the field, thus the grid geometry is insignificant for the solution of the problem. A Cartesian field grid can be used that may penetrate the contour arbitrarily. The field source strengths σ decay rapidly away from the surface due to the $1/r$ -singularity. Thus, the computational grid can be limited to the nonlinear part of the flow and remains very small (Figures 6 and 8).

3.3.2 Iterative procedure

The nonlinear differential equation (2) is solved by an iterative procedure.

Firstly in iteration step $n = 1$ the Laplace equation is solved by the panel method. The kinematic flow condition $\vec{n} \nabla \phi = -\vec{n} \nabla \phi_\infty$ together with equation (12) yield

$$\vec{n} \nabla (\phi^P + \phi^F) = -\vec{n} \nabla \phi_\infty.$$

Consequently, the potential $\phi^{P,n}$ in the iteration step n is determined from:

$$\vec{n} \nabla \phi^{P,n} = -\vec{n} \nabla \phi_\infty - \vec{n} \nabla \phi^{F,n-1}. \quad (13)$$

The field does not provide a contribution to the perturbation potential in the first iteration step $n = 1$, i.e. $\phi^{F,n=0} = 0$. From the linear equation a solution for the singularity strengths of the body is determined. The perturbation potential ϕ^P results from the surface singularities. The velocity potential Φ consists of

$$\Phi^n = \phi^{P,n} + \phi^{F,n-1} + \phi_\infty^n.$$

The distribution of the field source strength σ is a function of potential Φ so that the values of σ in iteration step n are determined from the values of the perturbation potential ϕ^P of the same iteration step and from ϕ^F of the preceding step.

$$\sigma^n = \sigma(\phi^{P,n}, \phi^{F,n-1}, \phi_\infty^n)$$

When the perturbation potential ϕ^P and the field sources σ are known, a new solution for the perturbation potential due to the field ϕ^F has to be computed.

$$\nabla^2 \phi^{F,n} = \sigma^n - \nabla^2 \phi^{P,n}$$

Field potential ϕ^F modifies the boundary condition in the following iteration step (13).

Thus, the contribution of the field to the total potential is determined independently from the boundary element method and iteratively coupled with the panel method. The iteration process is continued until the convergence criterion

$$\max_i |\sigma_i^n - \sigma_i^{n-1}| \leq \varepsilon_\sigma$$

is satisfied. Typically the convergence criterion is $\varepsilon_\sigma = 0.01 \dots 0.1$.

3.3.3 Discretisation of the field

The influence of the field sources is registered in both boundary value problems by the induced velocities. The influence coefficients of a field element i on a point k for the velocities in the three spatial directions are computed analytically.

$$\hat{D}_{ki} = \begin{pmatrix} D_{ki}^x \\ D_{ki}^y \\ D_{ki}^z \end{pmatrix} = \frac{1}{4\pi} \iiint_{V_i} \nabla_p \left(\frac{1}{r_{ki}} \right) dV_i$$

The total velocity at a field control point k in the iteration step n results from:

$$\vec{V}_k^{F,n} = \vec{V}_{\infty,k}^n + \vec{\Omega}^n \times \vec{r}_k^n + \vec{V}_k^{BF,n} + \vec{V}_k^{WF,n} + \vec{V}_k^{FF,n-1},$$

with

$$\begin{aligned}\vec{V}_k^{BF} &= \sum_{i=1}^N \tau_i \hat{B}_{ki} + \sum_{i=1}^N \mu_i \hat{C}_{ki}, \\ \vec{V}_k^{WF} &= \sum_{j=1}^{N_W} \mu_{Wj} \hat{C}_{kj}^W, \\ \vec{V}_k^{FF} &= \sum_{i=1}^M \sigma_i \hat{D}_{ki}.\end{aligned}$$

The derivatives of the velocity components determine the strengths σ of the field sources according to equation (3). The velocity derivatives are approximated by first order accurate central difference operators. If the difference stencil crosses the contour (Figure 3) the single- and double-layer distributions cause a velocity jump over the body surface. The ve-

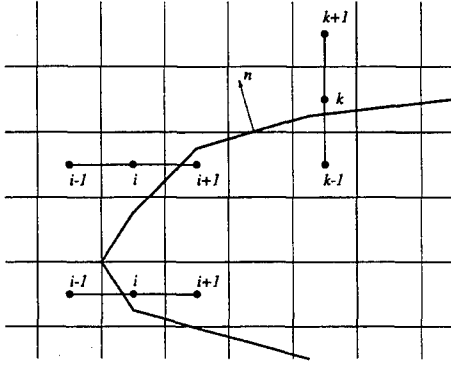


Figure 3: Grid stencil and contour

locity jumps arise from:

$$\begin{pmatrix} \Delta u \\ \Delta v \\ \Delta w \end{pmatrix} = 4\pi \begin{pmatrix} n_x & t_{1x} & t_{2x} \\ n_y & t_{1y} & t_{2y} \\ n_z & t_{1z} & t_{2z} \end{pmatrix} \begin{pmatrix} \tau \\ \delta\mu/\delta t_1 \\ \delta\mu/\delta t_2 \end{pmatrix}.$$

From that the jump terms are derived as

$$\begin{pmatrix} [u_x] & [v_x] & [w_x] \\ [u_y] & [v_y] & [w_y] \\ [u_z] & [v_z] & [w_z] \end{pmatrix} = \begin{pmatrix} \text{sign}(n_x) \\ \text{sign}(n_y) \\ \text{sign}(n_z) \end{pmatrix} \cdot \begin{pmatrix} \Delta u \\ \Delta v \\ \Delta w \end{pmatrix}^T,$$

which corrects the central differential operators.

$$u_x = \frac{u_{i+1,j,k} - u_{i-1,j,k} - [u_x]}{x_{i+1,j,k} - x_{i-1,j,k}}$$

The other derivatives arise analogously.

3.3.4 Artificial viscosity

The mixed character of the differential equation is taken into account by backward differences at supersonic points. In order to consider the correct domain of dependence, the *rotated difference scheme* by Jameson is adopted.

The difference of the centred difference approximation and the upwind formulae for subsonic and supersonic flow introduce an artificial viscosity maintaining computational stability. In order to simplify the computation scheme only central difference operators are used.

It follows that under a rotated difference scheme the artificial viscosity T introduced at supersonic points is

$$T = \left(1 - \frac{q^2}{a^2}\right) \frac{a^2}{q^2} \left[\frac{u}{q} \sigma_x \Delta x + \frac{v}{q} \sigma_y \Delta y + \frac{w}{q} \sigma_z \Delta z \right],$$

which is explicitly added to the field source strength σ :

$$\bar{\sigma}_{i,j,k} = \sigma_{i,j,k} + T_{i,j,k}.$$

The modified field source strength $\bar{\sigma}$ replaces the strength σ in all formulas. The artificial viscosity can stabilise the solution as long as the Mach numbers in front of the shock are $Ma_1 < 1.3$, at higher velocities the flow can no longer be considered as isentropic. The full potential equation is not suitable for flows with strong compression shocks.

3.4 Reduction of computational costs

3.4.1 Computation time and storage requirement

Integral equation procedures can compute boundary values very efficiently but they need a lot of computational time and storage for calculating velocities in the outer domain \mathcal{V} . Most of the cpu-time in a single iteration step is spent for the determination of the velocities \vec{V}^{FF} , \vec{V}^{BF} , and \vec{V}^{FB} .

The velocities at the field control point induced by the field panels are obtained from an AF-scheme:

$$\begin{aligned} & \left(-\alpha B \frac{\bar{\delta}_y}{\Delta y} - \alpha C \frac{\bar{\delta}_z}{\Delta z} - A \frac{\delta_{xx}}{\Delta x^2} \right) \left(\alpha + \frac{\bar{\delta}_y}{\Delta y} \right) \\ & \left(\alpha + \frac{\bar{\delta}_z}{\Delta z} \right) (\phi_{i,j,k}^{n+1} - \phi_{i,j,k}^n) = \alpha^2 \omega \mathcal{L} \phi_{i,j,k}^n. \end{aligned}$$

The residual can be written as

$$\mathcal{L} \phi = \left(A \frac{\delta_{xx}}{\Delta x^2} + B \frac{\delta_{yy}}{\Delta y^2} + C \frac{\delta_{zz}}{\Delta z^2} \right) \phi - \bar{\sigma}.$$

For convenience we write

$$\begin{aligned} A &= 1 - \frac{u^2}{a^2}, & B &= 1 - \frac{v^2}{a^2}, & C &= 1 - \frac{w^2}{a^2}, \\ D &= -\frac{2uv}{a^2}, & E &= -\frac{2vw}{a^2}, & F &= -\frac{2wu}{a^2}. \end{aligned}$$

To calculate potential values inside the field grid, the values of ϕ^F have to be specified at the outer boundaries of the computational grid. The influence coefficient D_{ki} is approximated by the fundamental solution of a point source to reduce computational time:

$$\phi_k^F = \sum_{i=1}^{M^*} \sigma_i D_{ki} \quad \text{with} \quad D_{ki} = -\frac{1}{4\pi r_{ki}}.$$

Since the values of D decay very rapidly with increasing distance from the collocation points, it is sufficient to consider only the neighbour cells M^* to determine the induced velocities at the boundaries. Using the AF3-scheme the computational time can be reduced to 33% of the reference value, see Figure 4.

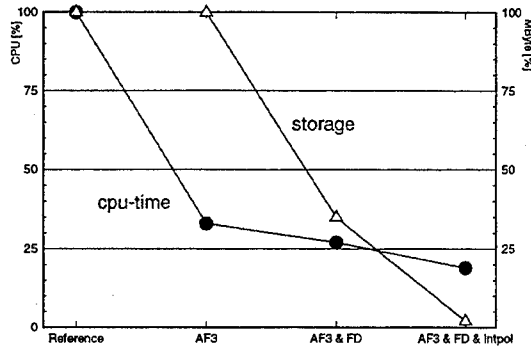


Figure 4: Reduction of cpu-time and storage

The velocities \vec{V}^{BF} are calculated by a finite-difference-method of the Laplacian equation. Potential values ϕ^{BF} are specified at the outer edges of the grid and around the contour. When the potential values are known at all field points the velocity components are obtained by centred difference approximation:

$$\vec{V}^{BF} = -\nabla\phi^{BF}.$$

The storage requirement reduces to 35% of the reference case, because the matrices B, C for the influences of the body on the field points are no longer necessary. This iterative procedure accelerates the calculation of \vec{V}^{BF} , so that the total cpu-time is reduced to 27% of the reference case.

The velocity potential ϕ^F and the velocity field \vec{V}^{FF} are continuous inside the whole field grid. The velocities \vec{V}^{FB} induced by the field can be obtained by a trilinear interpolation of the velocities $\vec{V}^{FF} = -\nabla\phi^F$, saving the determination of the influences of the field on the blade control points. Thus, the computational time could be reduced to 19% of the reference calculation.

The boundary element method was solved by the panel clustering technique of Hackbusch & Nowak [9] and Sauter [10]. According to the choice of the approximation parameters of this method 40 up to 70 % of the cpu-time to determine the AIC-matrix of the blades could be saved.

3.4.2 The subroutine FPM

The incompressible panel methods used in the industry will be extended to handle compressible flow including weak shocks only if the effort is small. For

this purpose a subroutine was developed, which can be easily combined with any existing panel method, see Figure 5. The subroutine calculates additional velocities \vec{V}^{FB} at the collocation points representing the compressible effects and returns these values to the calling program unit.

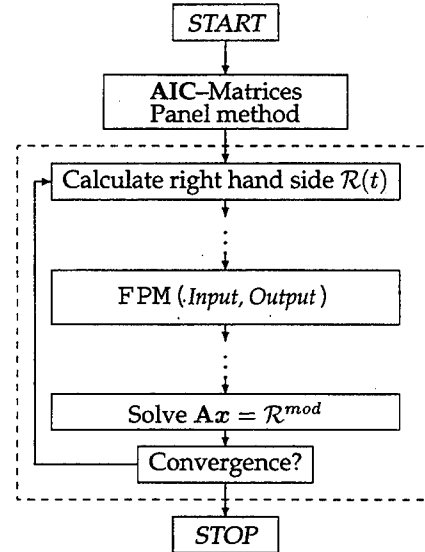


Figure 5: Combination of the subroutine FPM with a panel method

With this subroutine FPM compressible effects of bodies, wings and rotors including free vortex sheets can be simulated.

4 NUMERICAL RESULTS

To validate the program ROFPM several test cases of the model rotor of Caradonna & Tung [8] were calculated. The CARADONNA rotor consists of two untwisted and untapered blades with NACA 0012-sections (aspect ratio $\Lambda = 6$). Both blades are discretised into $N = 360$ surface panels with 12 strips of 30 panels each in chordwise direction. The panel edges are located at 16.7, 33.3, 45, 55, 64.2, 71.8, 77.5, 82.5, 87.2, 90.8, 94.5 and 97.5 % of the blade radius. The Cartesian field grid shown in Figure 6 contains 24 cells in chordwise direction, 14 cells in spanwise direction and 16 elements in the direction of the rotor axis ($M = 5376$ field cells). The field grid may penetrate the contour at an arbitrary position.

Due to the collective pitch, areas of nonlinear flow are expected to appear on the upper side of the blades. Therefore the grid is shifted upwards ($z_{min}/c = -0.25, z_{max}/c = 0.65$). The boundaries of the field grid are located 0.1 chord lengths in front of the leading edge and behind the trailing edge ($x_{min}/c = -0.1, x_{max}/c = 1.1$). The spatial field is restricted to a relatively small area at the tip of the blade ($y_{min}/c = 4.0, y_{max}/c = 6.3$) where the compressible effects occur.

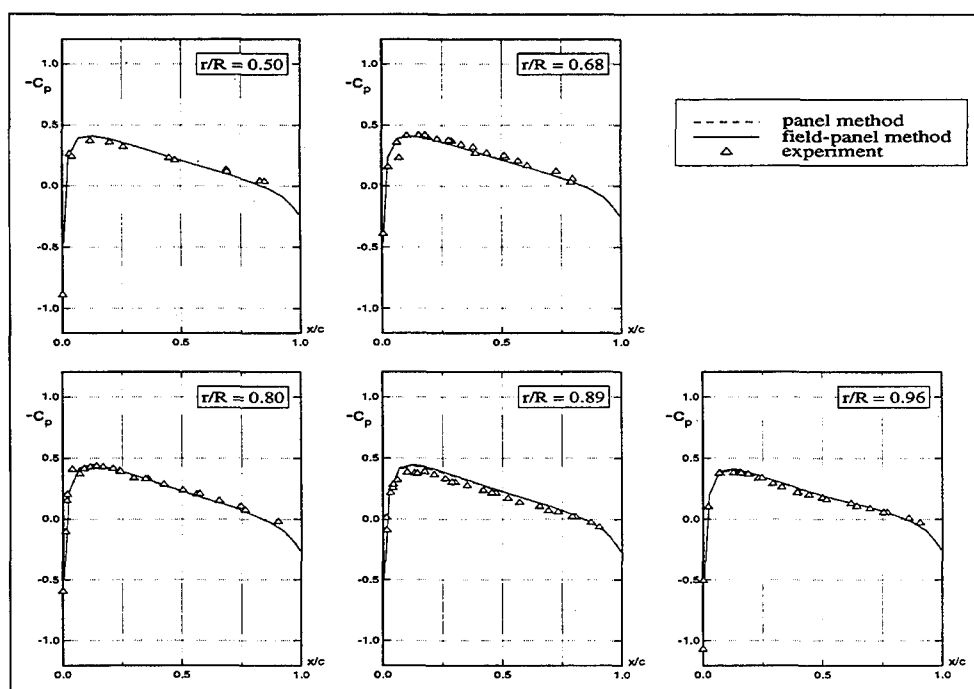


Figure 7: c_p -distribution for $\Theta_c = 0^\circ$, $Ma_{tip} = 0.52$

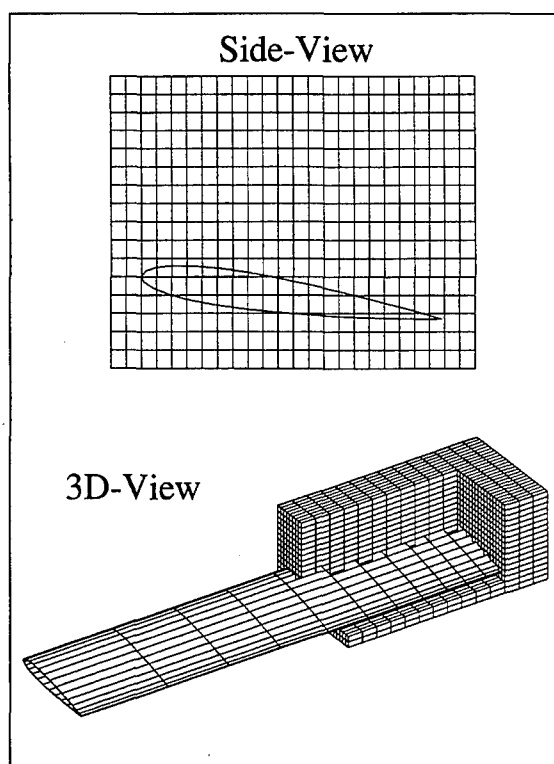


Figure 6: Field grid at the tip of the blade
($24 \times 14 \times 16$ Cells, $-0.1/1.1$; $4.0/6.3$; $-0.25/0.65$)

The first test case is a nonlifting hovering rotor with a tip Mach number $Ma_{tip} = 0.52$ and a collective pitch setting of $\Theta_c = 0^\circ$. Because of the absence of

a vortex sheet the VLM-method reaches the steady solution in the first iteration step. The field panel method needs three more iterations to fulfill the convergence criterion $\varepsilon_\sigma = 0.01$. For this case the IBM workstation RISC/6000-320 runs 15 minutes to obtain the compressible solution.

The calculated pressure distributions at the radial locations $r/R = 0.50, 0.68, 0.80, 0.89$ and 0.96 are compared with the experiment in Figure 7. For this small tip Mach number the solution of the boundary element method and the field panel method are almost identical and match with the experimental data [8].

All other cases handle lifting rotors in hover.

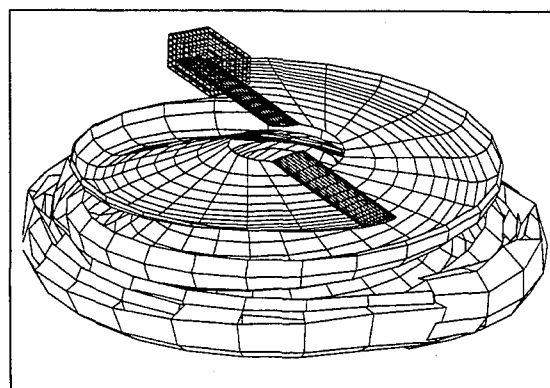


Figure 8: Vortex sheets of CARADONNA rotor ($\Theta_c = 8^\circ$)

Figure 8 shows the vortex sheets emanating from

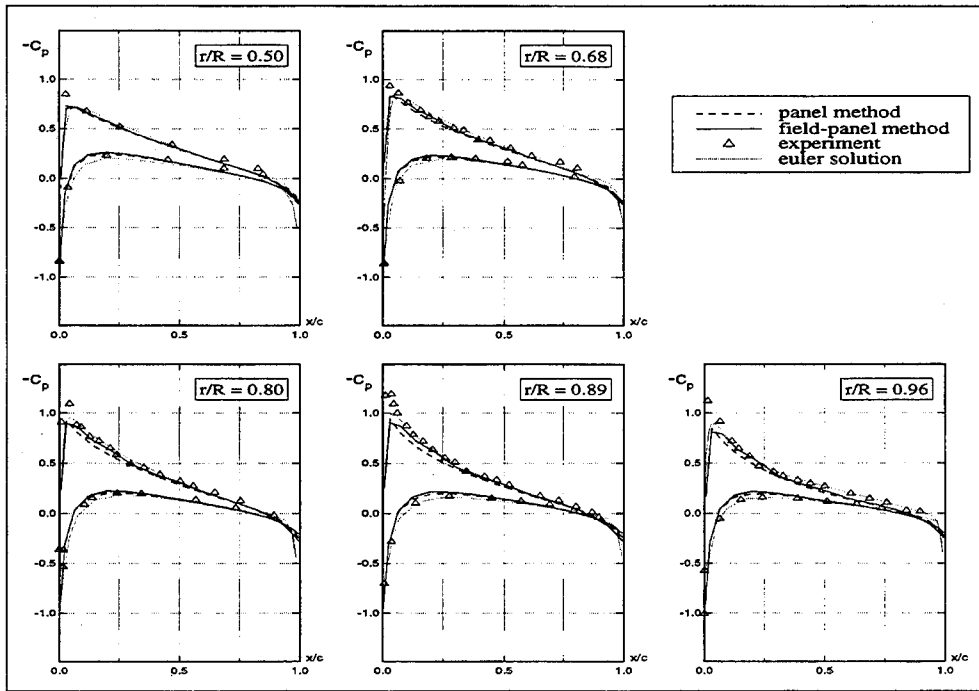


Figure 9: c_p -distribution for $\Theta_c = 8^\circ$, $Ma_{tip} = 0.439$

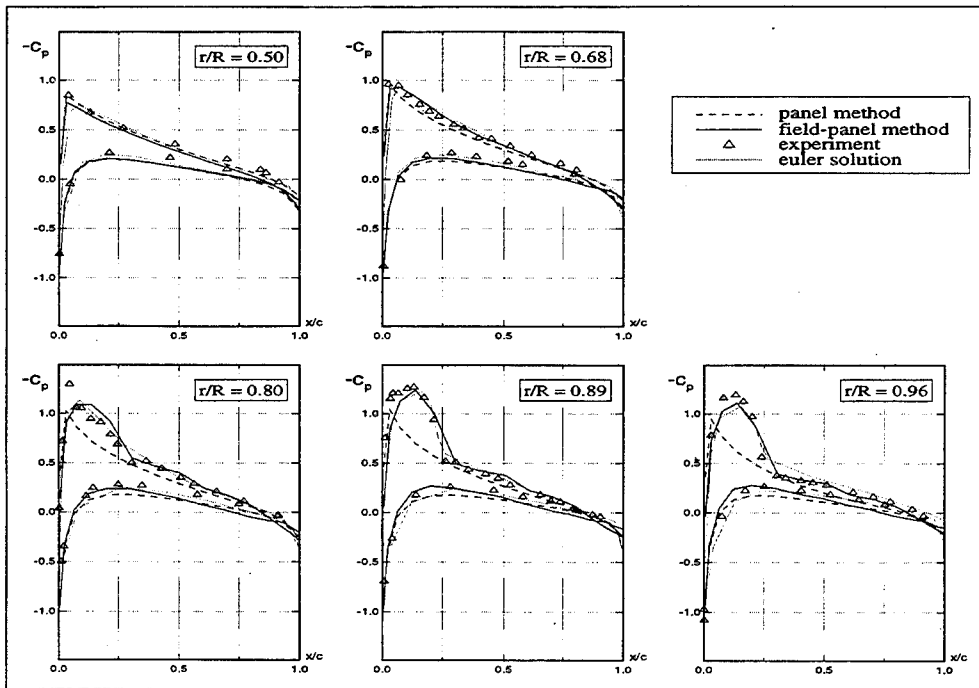


Figure 10: c_p -distribution for $\Theta_c = 8^\circ$, $Ma_{tip} = 0.794$

the trailing edges of the blades for a collective pitch $\Theta_c = 8^\circ$. The vortex sheets are calculated by the incompressible vortex lattice method ROVLM [7], see section 3.2.

The results for the lifting subsonic case ($Ma_{tip} = 0.439$, $\Theta_c = 8^\circ$) are compared with the experi-

mental data and the Euler solution of Krämer [11] in Figure 9. The final result of the linear panel method was used as the first solution of the field panel method. The c_p -distribution obtained with the program ROFPM agrees with the solution of the Euler method; both methods underestimate the suc-

tion peak of the measured data. A reason could be that the discretisation of the leading edge region is too coarse to resolve the pressure gradient. Non-neglectable compressible effects occur only outwards $r/R \approx 0.70$. The incompressible solution is corrected by the field panel method, as can be seen for the last three radial positions in Figure 9.

To show that the field panel method allows to predict transonic flow, the CARADONNA rotor was calculated for the collective pitch $\Theta_c = 8^\circ$ and the tip Mach number $Ma_{tip} = 0.794$. Near the tip of the blades supersonic regions with shock waves appear (Figure 10). The results of ROFPM are in good agreement with the measured data. In particular, the magnitude and the location of the shock agree with reference [8]. The convergence history is shown in Figure 11. The program needs 90 minutes cpu-time for 18 cycles of the compressible iteration procedure. Adding the cpu-time to determine the wake structure, we need 135 minutes, corresponding to 5% of the computational time for the Euler solution [11] on the same machine.

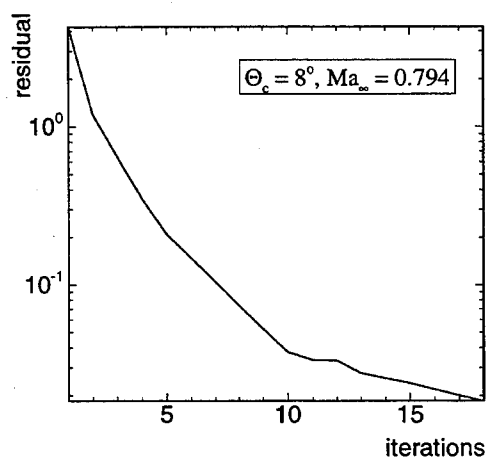


Figure 11: Convergence history ($\Theta_c = 8^\circ$, $Ma_{tip} = 0.794$)

5 CONCLUSION

The program ROFPM describes the blade-vortex-interference of a helicopter rotor with its free vortex sheets. By combining the vortex lattice method with a field panel method, the program can be extended to calculate compressible transonic flow. This combination has several advantages over usual field methods.

- The field panel method uses a Cartesian grid which needs not to be surface fitted, thus avoiding the major task of grid generation.
- The boundary conditions are fulfilled by the panel method alone so that the grid is used only

to calculate the source strengths. In practical cases the field source strengths, which represent the compressibility, decay away from the contour so that the computational grids can be restricted to small regions, where the nonlinear effects cannot be neglected.

- From a theoretical point of view the full potential equation can be divided into a linear boundary element method and a field panel method considering the compressible effects. Therefore, almost every existing linear panel method can be used together with the subroutine FPM.
- The integral equation method can be combined with other finite-difference methods to reduce computational time and storage requirement.

For the future, it is intended to extend the program ROFPM to unsteady flow and to handle rotor-fuselage interference.

6 ACKNOWLEDGEMENT

This work was supported by the Deutsche Forschungsgemeinschaft (DFG Wa424/8).

7 REFERENCES

- [1] K. Oswatitsch. *Die Geschwindigkeitsverteilung bei lokalen Überschallgebieten an flachen Profilen*. ZAMM, 30(1/2):17–24, 1950.
- [2] Larry L. Erickson und Shawn M. Strande. *A Theoretical Basis for Extending Surface-Paneling Methods to Transonic Flows*. AIAA Journal, 23(12):1860–1867, March 1985.
- [3] B. Oskam. *Transonic Panel Method for the Full Potential Equation Applied to Multicomponent Airfoils*. AIAA Journal, 23(9):1327–1334, September 1985.
- [4] Hong Hu. *Study of Integral Equation Methods for Transonic Flow Calculations*. Engineering Analysis with Boundary Elements, 11:101–107, 1993.
- [5] P.M. Sinclair. *A Three-Dimensional Field-Integral Method for the Calculation of Transonic Flow on Complex Configurations — Theory and Preliminary Results*. Aeronautical Journal, 92:235–241, June/July 1988.
- [6] Luigi Morino und Kadin Tseng. *A General Theory of Unsteady Compressible Potential Flows with Applications to Aeroplanes and Rotors*. In P. K. Banerjee und L. Morino, editors, *Boundary Element Methods in Nonlinear Fluid Dynamics*, chapter 6, pages 183–245. Elsevier Applied Science, London and New York, 1990.

- [7] A. Röttgermann, R. Behr, Ch. Schöttl und S. Wagner. *Calculation of Blade-Vortex Interaction of Rotary Wings in Incompressible Flow by an Unsteady Vortex-Lattice Method Including Free Wake Analysis*. In Hackbusch W., editor, *Notes on Numerical Fluid Mechanics*, pages 153 – 166, Braunschweig, 1991. Vieweg Verlag.
- [8] F.X. Caradonna und C. Tung. *Experimental and Analytical Studies of a Model Helicopter Rotor in Hover*. *Sixth European Rotorcraft and Powered Lift Aircraft Forum*, 25:25-1 – 25-19, September 1980.
- [9] W. Hackbusch und Z.P. Nowak. *On the Fast Matrix Multiplication in the Boundary Element Method by Panel Clustering*. *Numerische Mathematik*, 54:463 – 491, 1989.
- [10] St. Sauter. *Der Aufwand der Panel-Clustering-Methode für Integralgleichungen*. Institutsbericht 9115, Institut für Informatik und Praktische Mathematik, Universität Kiel, November 1991.
- [11] Ewald Krämer. *Theoretische Untersuchungen der stationären Rotorblattumströmung mit Hilfe eines Euler-Verfahrens*. Dissertation, Universität der Bundeswehr, Institut für Luftfahrttechnik und Leichtbau, München, Neubiberg, April 1991. Forschungsberichte VDI, Reihe 7: Strömungsmechanik Nr. 197.

EVALUATION DE MODELES AERODYNAMIQUES ET DYNAMIQUES DES ROTORS D'HELICOPTERES PAR CONFRONTATION A L'EXPERIENCE.

J. BESSONE et D. PETOT

ONERA

29, av. de la Division Leclerc - BP 72
92322 CHATILLON CEDEX - FRANCE

1. RESUME

Cet article présente le code de recherches "ROTOR" développé à l'ONERA et appliqué à l'étude aéroélastique des rotors d'hélicoptères, puis s'attache à des confrontations de ROTOR avec l'expérience.

Le noyau central du code calcule les équations de Lagrange associées au rotor. Tout autour apparaissent différents modules: méthodes de résolution, modèles dynamiques et aérodynamiques, formulations de vitesses induites. La structure du rotor est considérée comme une succession de transformations de base et l'originalité de ROTOR réside dans l'écriture directe et automatique des équations sous forme matricielle.

La confrontation de ROTOR avec l'expérience a tout d'abord montré la nécessité d'une modélisation très réaliste du sillage tourbillonnaire. Localement, le modèle de décrochage dynamique ONERA explicite très bien le phénomène de décrochage, améliore sensiblement les calculs, mais ne permet pas toujours d'atteindre les portances expérimentales. L'introduction dans ROTOR de la correction semi-empirique de Houwink réduit le déficit de portance dans la zone des forts décrochages. De plus, lors de résultats préliminaires, le modèle de Hopf fait apparaître les phénomènes oscillatoires de la portance observés expérimentalement dans cette zone. Mais l'utilisation d'extrémités de pale non rectangulaires va demander, pour le calcul des efforts aérodynamiques locaux et des déformées de pale, une analyse plus fine des effets tridimensionnels d'extrémité que seule une aérodynamique de type CFD semble pouvoir estimer correctement.

2. DEFINITION DES NOTATIONS

Ω : Vitesse de rotation du rotor

α_q : Angle d'inclinaison du mât rotor

θ_0 : Angle de pas collectif

θ_c : Angle de pas cyclique latéral

θ_s : Angle de pas cyclique longitudinal

C_T/σ : Coefficient de portance réduite

μ : paramètre d'avancement

δ : Angle de braquage de tab

M: Nombre de Mach

$\beta_0, \beta_c, \beta_s$: Angle de battement cyclique

K_p : Coefficient de pression

C_z : Coefficient de portance

C_x : Coefficient de traînée

C_m : Coefficient de moment aérodynamique

3. INTRODUCTION

La complexité des phénomènes en jeu dans le fonctionnement d'un rotor d'hélicoptère requiert aujourd'hui un outil informatique le plus modulaire possible, offrant le choix et l'interaction aisée parmi différents modèles aérodynamiques ou dynamiques.

Ainsi, l'ONERA a réuni dans le code de recherche ROTOR, un ensemble de modules numériques et de modèles mathématiques existants, dans le but d'évaluer leurs possibilités dans l'amélioration des prédictions de charges aérodynamiques, de stabilité aéroélastique et des performances du rotor.

L'exposé est constitué de deux parties. La première présente le code ROTOR ainsi que les hypothèses utilisées dans les calculs. La seconde confronte résultats de calculs et mesures d'essais en soufflerie réalisés en collaboration avec EUROCOPTER FRANCE.

4. DESCRIPTION DU CODE ROTOR

4.1 Structure générale

L'intérêt de ROTOR est de s'adapter à un large éventail de structures et de fournir des équations facilement exportables pour un couplage avec un problème extérieur. Ainsi, l'écriture des équations de Lagrange associées à la structure [20], noyau central du code, est séparée, de manière très distincte, des différents modules de traitement inhérents au problème posé.

Ceux-ci peuvent être distingués en quatre types:

4.1.1 Modules dynamiques

La première approche utilisée dans ROTOR, pour l'obtention des modes de pale, est un calcul par éléments finis en prenant pour hypothèse principale la linéarité en déformation et en modélisant la pale comme une poutre simple. Les éléments constituant la tête rotor sont alors

considérés comme indéformables et reliés à la pale par des articulations de battement, traînée et pas.

Mais l'utilisation de têtes rotor sans articulation implique maintenant la prise en compte dans la dynamique de termes de déformation fortement non linéaires. Un nouveau module de calcul de la base modale par éléments finis incluant ces termes non linéaires a été réalisé [14] [25]. Un couplage préliminaire avec ROTOR a été effectué.

4.1.2 Modules de vitesses induites

Deux types de champ de vitesses induites à travers le disque rotor sont accessibles: la formulation classique Meijer-Drees ainsi que le couplage de ROTOR avec un modèle de sillage tourbillonnaire appelé METAR [13] [17] et développé par Eurocopter France.

4.1.3 Modules aérodynamiques

Différents phénomènes aérodynamiques apparaissent lorsque la pale effectue un tour rotor. Ainsi, en secteur pale avançante et en extrémité, elle traverse une zone transsonique et subit des ondes de chocs. Par la suite, en pale reculante et en pied, elle est soumise au phénomène de décrochage dynamique.

Ces problèmes liés à de fortes variations de vitesse de vent et d'incidence vues par la pale sont spécifiques au domaine de la voilure tournante et ont très vite limité l'utilisation d'une aérodynamique bidimensionnelle purement quasi-stationnaire. Il est alors apparu nécessaire d'introduire des modélisations plus complexes. L'ONERA a ainsi développé, au cours des dernières années, un premier modèle de décrochage dynamique [7] appelé "modèle de décrochage dynamique ONERA", une version plus élaborée basée sur le concept de bifurcation de Hopf [22] appelée "modèle de Hopf" et une aérodynamique tridimensionnelle de type "Computational Fluid Dynamics" appelée "FP3D" [8] [21] [23], afin d'apporter des solutions aux phénomènes précités.

4.1.4 Modules de résolution

Différentes méthodes de résolution du système d'équations sont accessibles: couplage itératif [6], théorie de Floquet, "solveur" mathématique,...

Elles permettent, dans le cas d'un vol stationnaire ou avançant, la recherche de la stabilité ou de la réponse forcée périodique du rotor. De plus, une résolution par intégration temporelle des équations a été développée. Elle donne, par exemple la réponse des différentes pales lors d'un vol en manoeuvre.

4.2 Ecriture des équations

Une des originalités du code ROTOR réside dans l'écriture automatique et directe sous forme matricielle des équations associées à la structure.

En effet, le rotor est défini en figure 1 comme une chaîne de transformations se succédant les unes aux autres du repère galiléen jusqu'à la tête rotor et se subdivisant en "n" chaînes de la tête rotor jusqu'aux "n" pales.

Ces transformations peuvent être des rotations ou des translations, de type "constante" ou "degré de liberté" et dépendantes ou non du temps. Des groupements spéciaux de transformations, avec plusieurs degrés de liberté, peuvent être envisagés.

Des pales de forme quelconque sont ensuite encastrées en bout de chaînes. Elles sont définies par leur représentation modale dans une base constituée des "m" premiers modes encastrés et non-tournants. Cette base est calculée par un code éléments finis.

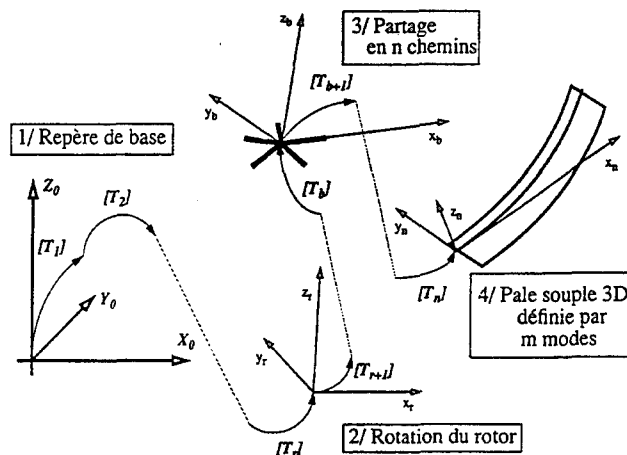


Figure 1 - Définition de la structure par une chaîne de transformations.

La cinématique du rotor est donc parfaitement définie par le produit des matrices de transformations. Le traitement automatique du fichier de données permet alors, par l'ajout ou l'inversion instantanée de telle ou telle articulation, une grande souplesse dans la définition de n'importe quelle type classique de structure.

Par la suite, les équations de Lagrange sont obtenues par linéarisation des déplacements jusqu'au second ordre autour d'une position de fonctionnement et ce pour chaque azimut.

Le système d'équations est alors prêt à être traité par les différents modules de résolution.

5. CONFRONTATION A L'EXPERIENCE

5.1 Base expérimentale:

Deux campagnes de mesures sont à la base des études qui vont être présentées. Elles possèdent des finalités très distinctes et concernent, par voie de conséquence, des rotors aux comportements aérodynamiques très différents.

Dans toutes les confrontations, calculs et essais, imposent les valeurs de la portance et de la force propulsive et répondent à une loi de battement particulière telle que $\beta_s = 0$ et $\beta_c = -\theta_s$.

5.1.1 Rotor ROSOH (S2 Chalais-Meudon)

La campagne d'essais ROSOH a été effectuée à la soufflerie ONERA S2 de Chalais-Meudon [18].

Ce rotor, très peu réaliste, a pour but l'étude de la torsion de pale. Pour ce faire, il possède trois pales rectangulaires souples en torsion dont la fréquence de torsion se situe à 2.5Ω . Ceci a pour conséquence un allongement très faible de 6.5. Cette caractéristique est à souligner car elle est non négligeable et a pour effet d'accentuer certains phénomènes aérodynamiques explicités par la suite.

Les pales possèdent des tabs à angle de braquage δ ajustable sur une bonne partie de leur envergure. Ceci permet le pilotage du moment et la validation concrète de la partie dynamique du code ROTOR.

De plus, les pales sont équipées de jauges extensiométriques (en 25 sections) et de capteurs de pression répartis le long de la corde (en 4 sections).

Les jauges extensiométriques donnent accès aux déformées de battement, traînée et torsion par l'utilisation de la méthode "Strain Pattern Analysis" [19]. L'intégration des coefficients de pression K_p fournissent, quand à eux, les efforts aérodynamiques locaux, portance et moment, appliqués au quart-avant de la pale.

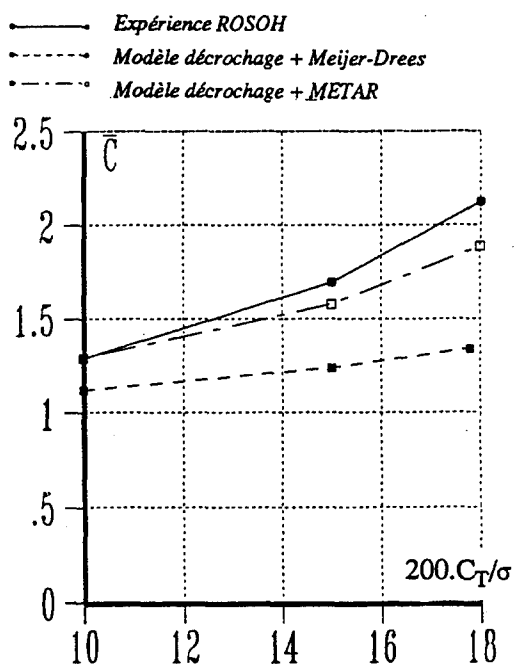


Figure 2 - Puissance C en fonction de la portance $C_T \sigma$ à paramètre d'avancement μ , braquage de tab δ et M, Ω, R fixés.

5.1.2 Rotor 7a MODANE

Cette campagne d'essais a été réalisée dans la soufflerie ONERA S1 de Modane [19] [21].

Le rotor utilisé est classique et conçu pour l'étude des hélicoptères d'une façon aussi proche que possible des rotors réels. Il possède quatre pales à extrémité rec-

tangulaire. Elles sont équipées elles aussi de jauges extensiométriques (en 25 sections) et de capteurs de pression répartis le long de la corde (en 5 sections).

Une partie de ces essais est constituée de cas de vol très fortement chargés, avec diminution de la vitesse de rotation du rotor. Ceci sert de base de données pour l'étude plus spécifique du décrochage.

5.2 Apport du sillage tourbillonnaire METAR

La prise en compte d'une modélisation plus réaliste du champ de vitesse induite a conduit au couplage du code ROTOR avec le modèle de sillage tourbillonnaire METAR. Un bilan de l'apport de ce modèle au sein de ROTOR peut être maintenant présenté.

Le couplage ROTOR / METAR est tel que l'équilibre du disque rotor vis à vis du champ de vitesses induites est obtenu en pale rigide. Une fois l'équilibre atteint, un calcul en pale souple est effectué.

Les calculs exposés ci-après utilisent comme aérodynamique le modèle de décrochage dynamique ONE-RA.

5.2.1 Rotor ROSOH

Les effets induits par le couplage METAR / ROTOR sur le calcul des performances sont spectaculaires. Ainsi, sur la figure 2, la puissance calculée avec une vitesse induite du type Meijer-Drees est systématiquement et fortement sous estimée. L'écart avec l'expérience varie de 15% à plus de 30%. Le couplage ROTOR / METAR permet alors une assez bonne adéquation avec la puissance mesurée (de 0% à 10% environ pour les cas de vol extrêmes).

Sur le plan local, l'intérêt de METAR par rapport à la modélisation Meijer-Drees est tout d'abord la prise en compte de la chute de la portance en extrémité de pale. Ceci explique la bonne adéquation avec l'expérience constatée en figure 3 pour la section à 95% de l'envergure.

METAR provoque, en pale reculante et en pied de pale, une augmentation sensible de l'incidence aérodynamique visible sur la section à 50% de l'envergure. Cette augmentation, associée au retard au décrochage du modèle ONERA, permet d'atteindre les niveaux de portance très importants mesurés lors de l'expérience ($C_z > 2$).

De manière générale, METAR réduit en pale avançante le déphasage avec l'expérience et améliore le niveau de portance. Cependant, l'amplitude des moments aérodynamiques demeure pratiquement inchangée.

Ces résultats mettent ainsi en évidence l'importance des phénomènes aérodynamiques vis à vis de pales de faible allongement. L'introduction d'une modélisation de sillage tourbillonnaire est alors nécessaire, même si elle implique un temps de calcul beaucoup plus pénalisant.

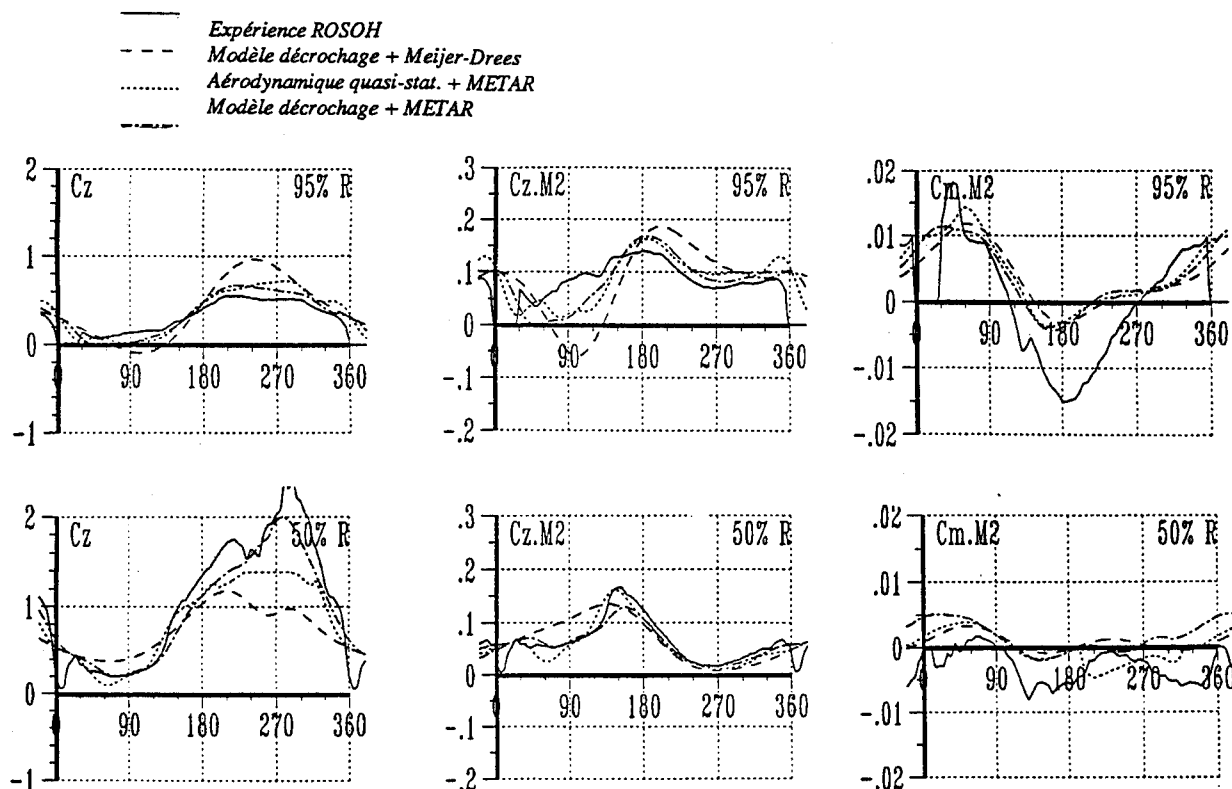


Figure 3 - Coefficient de portance (C_z), portance ($C_z \cdot M^2$) et moment ($C_m \cdot M^2$) pour différentes sections en envergure.

5.2.2 Rotor MODANE

Dans le cas de l'expérience MODANE, les effets dus à l'introduction de METAR sont moins sensibles.

Malgré tout, à faible vitesse ($\mu=0.3$), METAR fait apparaître en extrémité de pale sur la figure 4 les effets induits par les tourbillons provenant des pales précédentes. La formulation Meijer-Drees, beaucoup plus générale car issue de la théorie disque porteur, ne permet pas d'explicitier ces phénomènes.

En revanche, à forte vitesse ($\mu>0.3$), l'ensemble des calculs ont montré une influence moindre de l'introduction de METAR sur le calcul des efforts locaux. Cependant, des variations non négligeables dans le calcul des performances ont été constatées. Par exemple, METAR induit systématiquement une augmentation de puissance de l'ordre de 7%.

5.3 Etude du décrochage dynamique

5.3.1 Modèle de décrochage dynamique ONERA

L'aérodynamique instationnaire décrochée utilisée ici est le modèle de décrochage dynamique ONERA [7].

Son originalité est décomposer chaque coefficient aérodynamique C_z , C_m ou C_x en deux parties. La première caractérise le comportement linéaire instationnaire du coefficient et la seconde apporte la correction instationnaire nécessaire due au décrochage.

— Expérience MODANE
 - - - Modèle décrochage + Meijer-Drees
 Modèle décrochage + METAR

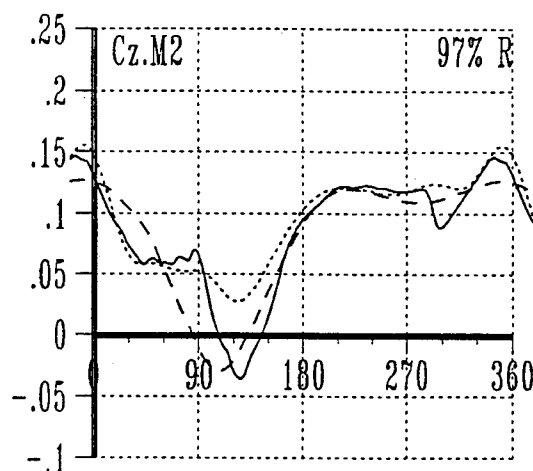


Figure 4 - Portance $C_z \cdot M^2$ à 97% de l'envergure pour un cas de vol $C_T \sigma = 0.075$, $\mu = 0.3$ et $MwR = 0.646$.

Ainsi, la modélisation finale est constituée d'un système linéaire d'équations différentielles du premier et

du second ordre, chacune d'entre elles régissant une partie du phénomène.

De plus, les coefficients des équations qui dépendent de la variable ΔC_z représentant l'écart au décrochage entre les valeurs quasi-stationnaire et linéaire du C_z , ont un caractère assez général et conviennent pour un grand nombre de profils de pale. Ceci facilite d'autant plus l'utilisation du modèle.

5.3.2 Confrontation avec l'expérience ROSOH

Sur la figure 3, l'effet instationnaire du modèle permet, en pale avançante, un recalage de la phase des efforts aérodynamiques calculés par rapport à l'expérience. Dans cette zone, le modèle offre une meilleure évaluation du niveau de portance.

Cependant, les amplitudes de la portance et du moment restent sous estimés en secteur pale avançante, notamment en extrémité de pale. Ceci est lié à des effets aérodynamiques tridimensionnels, non pris en compte par ce modèle de décrochage purement bidimensionnel.

Il est à noter que les chutes de portance et de moment constatées en extrémité de pale dans la zone 0° à 30° semblent être attribuées à l'interaction de la pale et d'un tourbillon généré par le volumineux capot entourant le haut de la tête rotor et convecté vers l'arrière.

5.3.3 Confrontation avec l'expérience MODANE

Le modèle de décrochage dynamique apporte, dans les cas de configurations fortement décrochées, une nette amélioration de la prédiction des efforts aérodynamiques locaux.

De manière générale, et comme le montrent les courbes de la figure 5 représentant portance et moment aérodynamique pour le cas de vol $\mu = 0,3$ et $C_T/\sigma = 0,145$, le retard au décrochage est bien pris en compte par le modèle. Les très fortes valeurs de C_z ($C_z > 2$) rencontrés expérimentalement en pale reculante sont retrouvées par le calcul.

De plus, comme souligné pour l'expérience ROSOH, l'introduction de METAR associée au modèle améliore sensiblement la prévision de la portance en secteur avançant dans la partie courante de la pale.

Malheureusement, après intégration totale de ces efforts sur l'ensemble du disque rotor, on note encore un déficit global de portance obligeant l'utilisateur du code à effectuer des calculs "à commandes imposées" et non pas "à efforts imposés".

De plus, les oscillations de la portance constatées dans la partie fortement décrochée ne sont pas explicitées par le modèle.

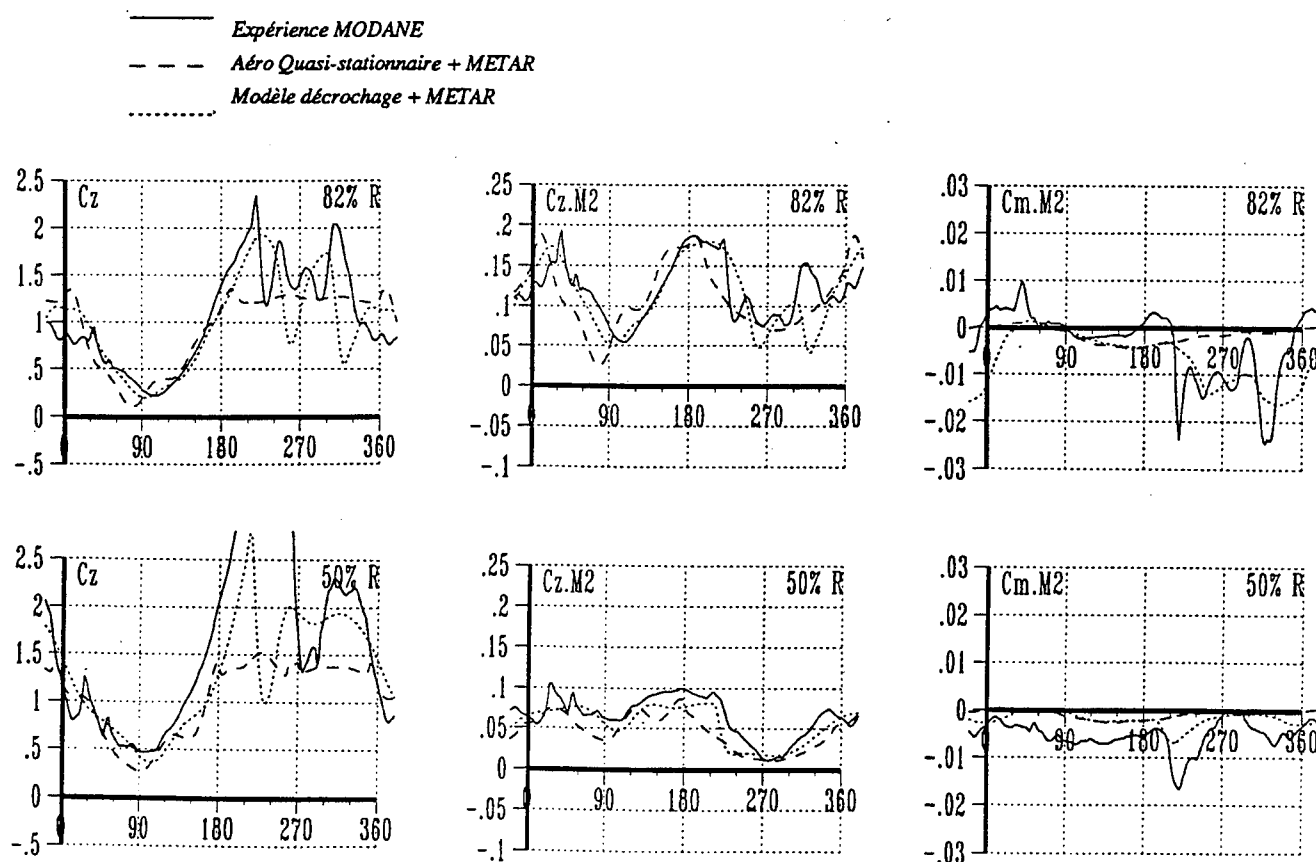


Figure 5.- Coefficient C_z , Portance $C_z \cdot M^2$ et moment $C_m \cdot M^2$ pour les sections à 50% et 82% de l'envergure.

5.3.4 Correction de polaire tournante

Une tentative pour résoudre le problème du niveau de portance dans la zone des forts décrochages est l'introduction dans ROTOR d'une correction semi-empirique appelée "correction de polaire tournante". Celle-ci est issue de la théorie de Houwink [16] et met en évidence les effets de la rotation de la pale sur le niveau de portance.

Ainsi, le principe général de cette correction est d'ajouter aux coefficients aérodynamiques C_z et C_m , dans la partie décrochée de la polaire aérodynamique du profil de pale considéré, un terme correctif de portance ΔC_z proportionnel au rapport corde sur rayon (c/r).

L'effet de cette correction apparaît en figure 6 où le déficit de portance en pale reculante est alors nettement réduit.

Si l'effet correctif local est faible au point de sembler parfois noyé au milieu des oscillations expérimentales, il n'est cependant pas négligeable d'un point de vue global. Ainsi, les polaires rotoriques associées aux calculs des performances du rotor sont améliorées dans la partie fortement décrochée comme le montre la figure 7 d'une évolution à $\mu=0.4$ et $MQR=0.45$. Mais la correction reste abusive autour de $C_T/\sigma = 0.125$.

Cette correction semi-empirique qui se veut universelle nécessite d'autres confrontations avec l'expérience avant d'être systématiquement employée.

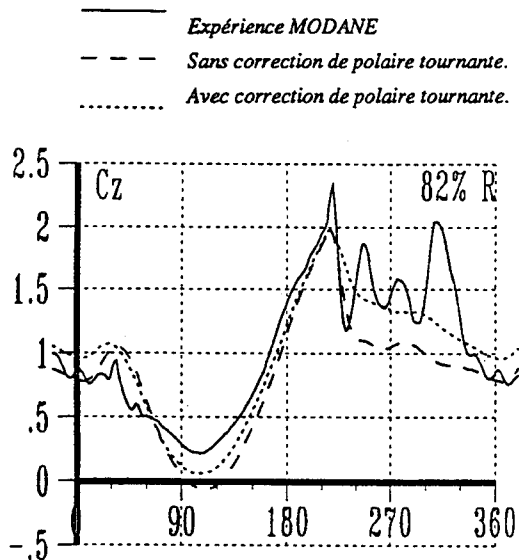


Figure 6 - Coefficient de portance C_z pour une section à 82% de l'envergure, $C_T/\sigma = 0.146$, $\mu=0.3$ et $MQR=0.45$.

5.3.5 Modèle de HOPF

Le modèle dit "de Hopf", développé lui aussi à l'ONERA [22], a pour but d'améliorer les résultats du modèle dit "de décrochage dynamique ONERA". Il conserve l'intérêt d'un modèle bidimensionnel qui, par rapport à une aérodynamique de type CFD par exemple, offre une réelle facilité d'emploi ainsi qu'un coût réduit en temps de calcul.

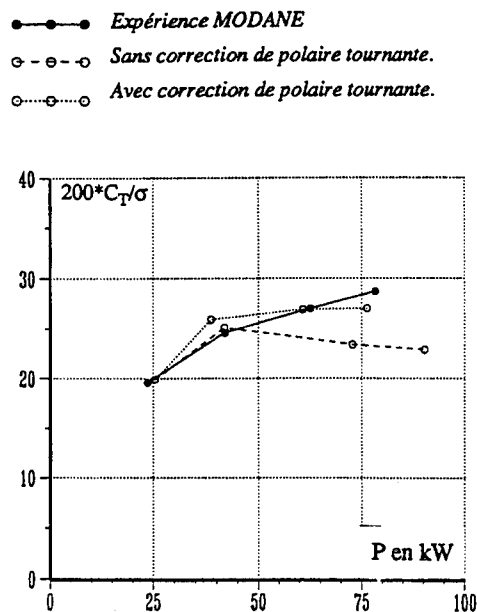


Figure 7 - Puissance P fonction de la portance $200 \cdot C_T/\sigma$ pour une évolution à $\mu=0.4$ et $MQR=0.45$

De même que le précédent, ce modèle considère les coefficients aérodynamiques comme étant la somme de deux termes. Cependant, dans ce cas, la première partie apporte la composante stationnaire du coefficient et est centrée sur la polaire quasi-stationnaire et non purement linéaire du profil de la pale, la seconde introduit une composante oscillatoire représentant la partie instationnaire du coefficient. Ceci conduit à un système non-linéaire d'équations différentielles du premier et second ordre à coefficients constants. Ces coefficients dépendent du profil de pale considéré.

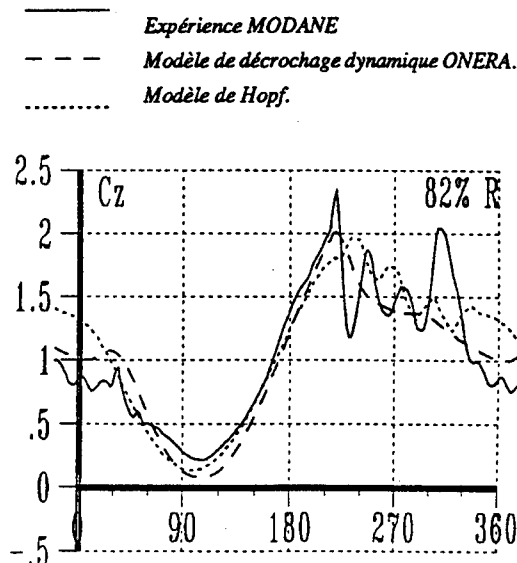


Figure 8 - Coefficient de Portance C_z pour une section à 82% de l'envergure, $C_T/\sigma = 0.146$, $\mu=0.3$ et $MQR=0.45$.

Ce modèle est en cours d'implémentation au sein de ROTOR. Le couplage préliminaire a été réalisé uniquement pour le coefficient de portance C_z . L'aérodynamique considérée pour les calculs de la traînée et du moment aérodynamique est alors quasi-stationnaire.

La figure 8 montre l'apport du modèle de Hopf dans ROTOR. Les niveaux de portance calculés sont sensiblement les mêmes que pour le modèle ONERA. En revanche, le modèle de Hopf fait apparaître les oscillations de fréquence importante apparaissant sur la courbe expérimentale dans la partie décrochée.

5.4 Apport d'une aérodynamique de type CFD

Des insuffisances de calculs subsistent cependant localement en pale avançante et en extrémité. Elles sont liées à des phénomènes aérodynamiques tridimensionnels non pris en compte par les modèles bidimensionnels ou les différentes corrections. Par exemple, l'amplitude du moment est fortement sous-estimée quand l'écoulement est transsonique.

De manière à quantifier les effets aérodynamiques tridimensionnels intervenants en extrémité de pale, un couplage entre le code ROTOR et un code aérodynamique de type CFD a été réalisé. Cette aérodynamique tridimensionnelle a été développée à l'ONERA sous le nom de FP3D.

Le code FP3D résout l'équation tridimensionnelle instationnaire du potentiel des vitesses. Le flux est considéré par hypothèse comme irrotationnel, isentropique et non visqueux pour les rayons supérieurs à 50% de l'envergure. Une aérodynamique quasi-stationnaire est appliquée aux rayons inférieurs.

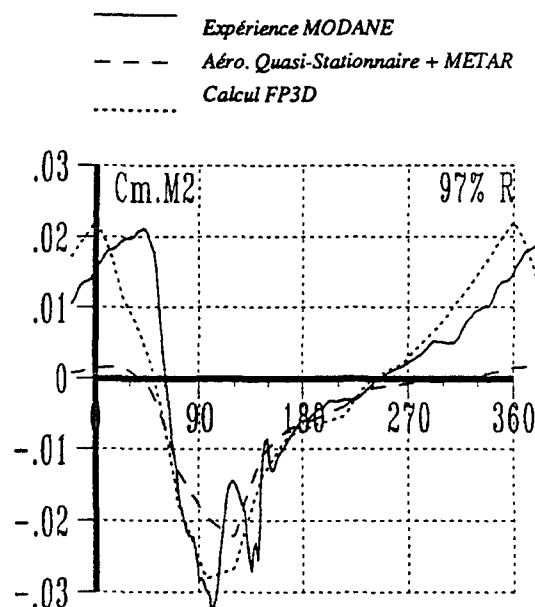


Figure 9 - Calcul FP3D du moment aérodynamique en extrémité de pale. Cas MODANE $C_T/\sigma=0.075$, $\mu = 0,45$.

Un premier couplage ROTOR / FP3D, pour le cas MODANE $C_T/\sigma=0.075$, $\mu=0.45$, offre en figure 9, une

excellente corrélation avec l'expérience du calcul du moment aérodynamique en extrémité de pale. C'est en effet le premier calcul relatif à la campagne MODANE qui fait apparaître un moment positif entre 270° et 60° . La convergence du calcul s'effectue en seulement cinq itérations FP3D, ce qui représente un point positif au vu du coût très important en temps de calcul.

5.5 Etude de la torsion des pales

Cette étude s'est essentiellement appliquée au rotor ROSOH qui offre la possibilité de piloter le moment aérodynamique par l'intermédiaire des tabs d'angle variable.

Cependant, la confrontation des calculs ROTOR avec l'expérience MODANE a montré aussi toute l'importance du calcul de la torsion pour des pales dites "rigides en torsion".

5.5.1 Expérience ROSOH

La confrontation avec l'expérience a montré que le modèle dynamique utilisé était raisonnablement bon pour cette application et a permis de quantifier les différents effets aérodynamiques.

Ainsi, il est, dans ce cas, nécessaire d'introduire des termes correctifs d'amortissement dans l'ensemble des calculs du moment, l'aérodynamique purement quasi-stationnaire n'étant pas suffisante. En effet, lors de vols rapides ($\mu \geq 0,4$) et chargés ($C_T/\sigma=0.075$), le mode de torsion devient fortement excité et faiblement amorti. Des problèmes d'oscillations et de divergence de calcul apparaissent alors.

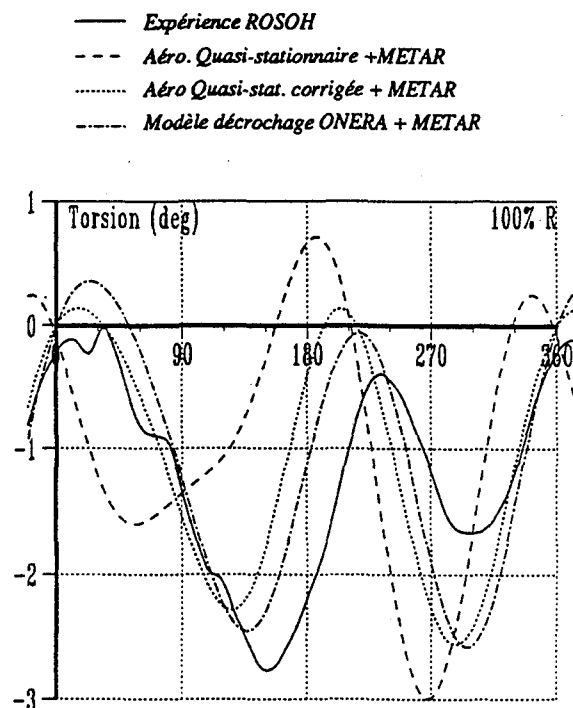


Figure 10 - Angle de torsion en extrémité de pale ROSOH

L'importance des phénomènes aérodynamiques apparaît ainsi tout naturellement dans le tracé de l'angle de torsion en extrémité de pale. Pour le cas de vol $\mu=0.4$, $C_T/\sigma=0.075$ et $\delta = 0^\circ$ de la figure 10, les oscillations excessives du mode de torsion prévues par les calculs disparaissent dès l'introduction, dans l'aérodynamique purement quasi-stationnaire, des termes correctifs d'amortissement.

On améliore les résultats, toujours en figure 10, en prenant en compte le modèle instationnaire ONERA qui se présente comme l'équation de THEODERSEN, mais comporte des termes correctifs en Mach (issus de calculs de WAGNER). Le modèle complet introduit un effet supplémentaire par l'intermédiaire du C_z . La corrélation avec l'expérience est alors excellente en pale avançante, pas encore parfaite dans la partie reculante.

Des calculs réalisés par ECF, incluant des termes non-linéaires de mécanique de pale, ont montré eux aussi d'excellentes oscillations de la déformée en torsion.

5.5.2 Expérience MODANE

Ces pales sont considérées comme assez "raides en torsion" puisque la fréquence du premier mode de torsion est telle que $f=6.5\Omega$. Pourtant, on constate expérimentalement des angles de déformation en torsion en extrémité non négligeables de près de 3° d'amplitude.

Les calculs présentés en figure 11 explicitent assez bien les conclusions du paragraphe 5.3.6 relatives au calcul du moment aérodynamique.

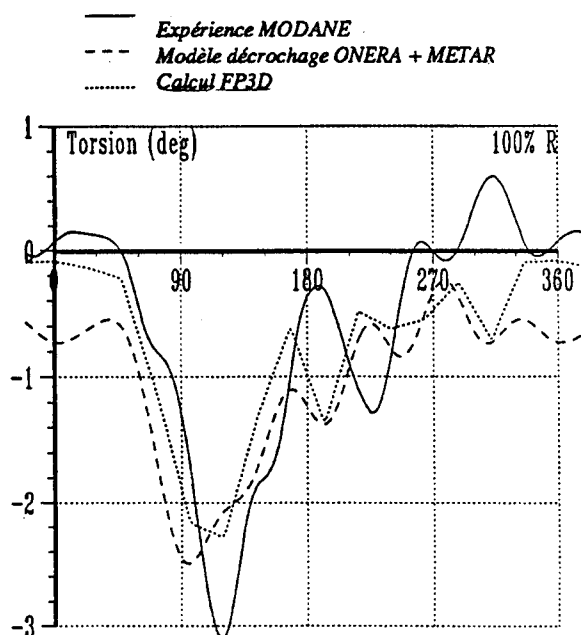


Figure 11 - Angle de torsion en extrémité de pale MODANE

En effet, la modélisation des effets aérodynamiques tridimensionnels en extrémité de pale semble déterminante dans la prédiction des efforts aérodynamiques et par suite des déformations. Le déficit d'amplitude en moment, constaté précédemment dans les calculs utilisant

METAR et le modèle de décrochage dynamique, explique la sous estimation de la torsion en secteur avançant.

Le couplage ROTOR / FP3D apporte dans cette zone une corrélation excellente avec l'expérience.

6. CONCLUSIONS

Tout d'abord, les deux campagnes d'essais relatives à cet article constituent de remarquables bases de données.

De plus, le code de recherche ROTOR est maintenant validé dans un grand nombre de domaines. Opérationnel depuis peu, il nécessite encore des améliorations et des développements pour être tout à fait compétitif.

Il a cependant montré l'intérêt de l'utilisation des modèles de décrochage dynamique ONERA et de HOPF.

De même, il a fait apparaître les grandes insuffisances actuelles des calculs aérodynamiques bidimensionnels en extrémité de pale. Le couplage avec une aérodynamique 3D de type CFD permet de combler ces lacunes. Mais, ce type d'aérodynamique reste encore très onéreux en temps de calcul.

La grande modularité du code ainsi que sa facilité d'utilisation apparaissent donc essentielles dans la validation de nouveaux modèles aérodynamiques et dynamiques développés à l'ONERA.

Le système reste ouvert à de nombreux développements: introduction d'une mécanique non-linéaire, couplage rotor / fuselage, calculs d'optimisation vibratoire de rotors, etc...

7. REFERENCES

- [1] Dat R., Meurzec J.L., *Sur les Calculs de Flottement par la Méthode dite du "Balayage en Fréquence Réduite"*, La Recherche Aéronautique n°133, Novembre 69.
- [2] Costes J.J., Nicolas J., Petot D., *"Etude de la stabilité d'une maquette de convertible"*, La Recherche Aéronautique n°6, 11/1982.
- [3] Petot D., Besson J.M., *"Comportement dynamique d'un prop-fan"*, Symposium on Aerodynamics and Acoustics of Propellers, AGARD FDP, Toronto, 10/1984.
- [4] Costes J.J., Cafarelli I., Tourjansky N., *"Theoretical and Experimental Study of a Model Rotor"*, 16th European Rotorcraft Forum, Garmisch Partenkirchen, 09/1986.
- [5] Sharpe D.L., *An Experimental Investigation of the Flap-Lag-Torsion Aerodynamic Stability of a Small Scale Hingeless Helicopter Rotor in Hover* - NASA TP 2546, 1986.
- [6] Tran C.T., Desopper A., *"An Iteration Technique Coupling 3-D Transonic Perturbation Aerodynamic Theory and Rotor Dynamics in Forward Flight"*, 14th European Rotorcraft Forum, Milano, Italy, 09/1987.

- [7] Petot D., *"Differential Equation Modelling of Dynamic Stall"*, ONERA, La Recherche Aéronautique n5, 1989.
- [8] Bezard H., Costes M., *"An improved Method for the computation of Unsteady Transonic Potential Flow. Application for Airfoil and Blade Performance Prediction."*, 15th European Rotorcraft Forum, Amsterdam, 09/1989.
- [9] Costes JJ, Petot D., *"Forces Aérodynamiques couplées dues au décrochage instantané sur une aile de grand allongement oscillant à grande amplitude"*, AGARD SMP, Sorrento, 04/1990.
- [10] Costes JJ., Cafarelli I., Tourjansky N., *Theoretical and Experimental Study of a Model Rotor*, 16th European Rotorcraft Forum, Glasgow, 1990.
- [11] Costes JJ., *"Unsteady Three-dimensional Stall on a Rectangular Wing"*, 12th European Rotorcraft Forum, Glasgow, 09/1990
- [12] Bousman W., *Rotorcraft Aeromechanical Stability - Methodology Assessment: Phase 2 Workshop* - NASA TM 102272, 1990.
- [13] Arnaud G., Toulmay F., Benoit B., *"Améliorations du modèle aérodynamique du code rotor hélicoptères R85 - Validation et applications"*, 28ème Colloque d'Aérodynamique Appliquée, AAAF, ISL, France, 1991.
- [14] Laulusa A., *"Theoretical and Experimental Investigation of the Large Deflection of Beams"*, International Specialists' Meeting on Rotorcraft Basic Research, Atlanta, 03/1991.
- [15] Polacsek C., Lafon P., *"High Speed Impulsive Noise and Aerodynamic Results for Rectangular and Swept Rotor Blade Tip in SI Wind Tunnel"*, 17th European Rotorcraft Forum, Berlin, 09/1991
- [16] Houwink R., Piers W.J., *"Sectional Prediction of 3D Effects for Separated Flow on Rotating Blades"*, 18th European Rotorcraft Forum, Avignon, France, 09/1992.
- [17] Arnaud G., Beaumier P., *"Validation of R85 / METAR on the PUMA RAE Flight Tests"*, 18th European Rotorcraft Forum, Avignon, France, 09/1992.
- [18] Beaumier P., Berton E., *"Study of Soft-in-Torsion Blades : ROSOH Operation"*, 18th European Rotorcraft Forum, Avignon, France, 09/1992.
- [19] Széchenyi E., Tourjansky N., *"The Measurement of Blade Deflections"*, 18th European Rotorcraft Forum, Avignon, France, 09/1992.
- [20] Petot D., Bessone J., *"Numerical Calculation of Helicopter Equations and Comparison with Experiment"*, 18th European Rotorcraft Forum, Avignon, France, 09/1992.
- [21] Beaumier P., Costes M., Gaveriaux R. *"Comparison between FP3D Full Potential Calculations and SI Modane Wind Tunnel Test Results on Advanced Fully Instrumented Rotors"*, 18th European Rotorcraft Forum, Avignon, France, 09/1992.
- [22] Truong K.V., *"Modèle de décrochage 2-D basé sur la notion de bifurcation de Hopf"*, La Recherche Aéronautique n4, 08/1993.
- [23] Beaumier P., *"A coupling procedure between a rotor Dynamics Code and a 3D Unsteady Full Potential Code"*, AHS, Aeromechanics Specialists Conference, San Francisco, 01/1994.
- [24] Holton A., Petot D., Beroul F., Walker W.R., *"An Anglo-French Rotor Blade Stability Workshop, Using Different Prediction Methods and Results"*, American Helicopter Society 50th Annual Forum, Washington DC, May 94.
- [25] Laulusa A., *"La caractérisation mécanique non-linéaire des pales"*, La Recherche Aéronautique, 1994.

Rotorcraft System Identification - An Overview of AGARD FVP Working Group 18 -

by

Peter G. Hamel

Jürgen Kaletka

Institut für Flugmechanik

Deutsche Forschungsanstalt für

Luft- und Raumfahrt e.V., (DLR)

38108 Braunschweig, Germany

1. SUMMARY

The AGARD FVP Panel, which for the last 20 years has sponsored activities in the field of flight vehicle system identification, decided in 1987 to set up the FVP Working Group 18, tasked with exploring and reporting on the topic of Rotorcraft System Identification. Using flight test data bases from three different helicopters, specialists from research organisations and industry applied their individual evaluation techniques for data quality checking and for the identification and verification of flight-mechanical models. The accomplishments of the Working Group are documented in the Final Report. This paper gives a broad overview on the basic identification methodology and the practical approaches. Representative results are given to illustrate the main identification steps: Specific flight test maneuvers and required measurements, definition of appropriate model structures, application of identification methods, and verification of the results. The Working Group mainly concentrated on the determination of 6 DOF rigid body models. Based on the experience gained in the Group, higher order models have recently been identified. Therefore, the paper also addresses the advances and gives an example for the application of the obtained models.

2. INTRODUCTION AND OVERVIEW

The rotorcraft dynamic response behaviour (output) due to pilot control or gust disturbance effects (input) is described by the interaction of inertial and aerodynamic forces as well as elastomechanic and control forces acting on the rotor and airframe. The relative interactions and interferences between these forces and their effects on the rotorcraft dynamic response vary with flight states and configurations. The prediction of aeromechanical forces and loads of the rotor system and its wake interferences with the empennage and tail rotor require wind-tunnel and flight test validation experiments [1]. Because of aerodynamic scale effects, wind-tunnel model deficiencies, and constrained 'free flight' capabilities certain limitations in the quality and applicability of rotorcraft wind-tunnel model data have always to be envisaged. Therefore, flight tests are necessary to isolate limitations and assess uncertainties from prediction techniques of rotorcraft aeromechanics. Here, a key tool for rotorcraft flight/ground test correlation is provided by system identification, which in its most general form can be defined as the deduction of system characteristics from measured free-flight data. For flight mechanical applications, the aircraft dynamics are modeled by a set of differential equations describing the forces and moments in terms of accelerations, state and control variables. Parameter identification is then the process of comparing and

minimizing the differences between the calculated model response due to measured control inputs and the corresponding measured aircraft response by iteratively adjusting the model coefficients. In this sense, aircraft system identification implies the determination of physically defined aerodynamic and flight mechanics parameters from flight data. Usually, this is an off-line procedure as some skill and iteration are needed to select appropriate data, develop a suitable model structure, identify the coefficients and, finally, verify the results. It explains, why system identification still is often seen in the research area. However, for fixed wing aircraft it is more and more routinely applied, where the majority of experience has been with the estimation of stability and control derivatives for obtaining mostly linearized rigid body equations of motion involving six degrees of freedom (DOF) [2]. A recently increased application spectrum of such in-flight estimated and validated mathematical models is the provision of extremely accurate models required for Level D flight simulators [3 - 5].

Unlike the flight dynamics of most fixed wing aircraft, the dynamics of rotary wing aircraft are characteristically those of high order systems. The large number of degrees of freedom associated with the coupled rotor-body dynamics leads to a high number of unknowns to be estimated, making it rather difficult to successfully apply system identification. A conventional 6 DOF model may be adequate for some handling qualities evaluations, whereas a 12 DOF model structure is about the minimum required for simulation validation or flight control system design. Due to this highly complex dynamic behaviour of rotorcraft, long term interdisciplinary scientific knowledge combined with practical research expertise is needed to use identification and mathematical modelling tools in a most efficient way. It is the main reason that these techniques are mainly concentrated in research organisations [6]. Therefore it was felt to be necessary to establish an improved contact between research institutions and industry. One efficient way of developing this knowledge and providing the research expertise is by using the combined strengths and complementary facilities of the relevant NATO nations in a collaborative programme. This is an area ideally suited to the mission of the **Advisory Group for Aerospace Research and Development (AGARD)**. It was deemed appropriate for the AGARD Flight Vehicle Integration Panel (FVP, formerly: Flight Mechanics Panel, FMP), which for the last twenty years has supported activities in the field of flight vehicle system identification [7-9] to sponsor the Working Group (WG) 18 and, based on the findings of the WG, the Lecture Series LS 178, both on

Rotorcraft System Identification. Main emphasis was placed on bringing together a wide range of research specialists and industry representatives, tasked with exploring and reporting on the topic of rotorcraft system identification. In detail, the Working Group Members were:

From universities: Prof. J. de Leeuw (Toronto), Prof. D. Murray-Smith (Glasgow), Prof. D. Schrage (Georgia Institute of Technology).

From research organizations: Dr. P. Hamel (chairman) and J. Kaletka (both DLR), C. Hofman (NLR), B. Gimonet (CERT/ONERA), Dr. G. Padfield (DRA), Dr. M. Tischler (AFDD, US Army).

From industry: Dr. D. Banerjee (MDHC), A.M. Dequin (ECF), K. Kampa (ECD), A. Russo (Agusta).

3. REVIEW OF AGARD FVP Working Group 18

'Rotorcraft System Identification'

The two principle objectives of the Working Group were 1) to evaluate the strengths and weaknesses of the different approaches and to develop guidelines for the application of identification techniques to be used more routinely in design and development, and 2) to define an integrated and coordinated methodology for application of system identification based on the strengths of each method. These objectives have been pursued in a time frame of about three years (1988-1990), by exercising the full range of available individual system identification approaches, using flight test data provided by WG Members as a common data base from three significantly different helicopter types (Figure 1):

- The attack helicopter MDHC AH-64 (Apache) (provided by MDHC).
- The medium size transport helicopter ECF SA-330 (PUMA) (provided by DRA).
- The small transport helicopter ECD BO 105 (provided by DLR).

The flight test data quality was extensively investigated to detect and correct data errors and to ensure that only reliable data were used for further evaluation. For the identification the WG Members applied their individual approaches. The obtained results were compared and discussed in detail to demonstrate the present state of the art and to provide an overview and expertise to industry for

- better understanding the underlying scientific, technical and operational methodologies involved in rotorcraft identification.
- increased utilization of this modern flight test tool.

A detailed documentation and discussion of the flight test data bases, identification methodologies, obtained results, and potential application areas are given in the WG Final Report and the Lecture Series publication [10,11]. This paper is mainly based on the activities and accomplishments of the Working Group but can only give a few selected and representative examples. In addition, recent advances in rotorcraft system identification are also addressed to present an actual state of the art.

4. PRINCIPLE OF SYSTEM IDENTIFICATION

The general approach used in aircraft system identification is depicted in Figure 2. In flight tests, specifically designed control input signals are used to excite the aircraft modes of interest. Both control inputs and air-

craft response are measured and recorded. The data quality is checked by applying data compatibility and state reconstruction techniques. The identification techniques can be divided into methods working in the time or in the frequency domain. Consequently, the measured data are evaluated in the format of time histories or they are transferred into the frequency domain by FFT or Chirp-Z transformations. For the identification step, the aircraft mathematical model is formulated by a set of differential equations or transfer functions. Based on the differences between the model response due to the measured control inputs and the real aircraft response, the unknown model coefficients are adjusted to obtain a better agreement. Usually the estimation is an iterative process. From the principal approach it is obvious that the identification framework can be divided into three major parts:

- **Instrumentation and filters** which cover the entire flight data acquisition process including adequate instrumentation and data recording.
- **Flight test techniques** which are related to selected rotorcraft maneuvering procedures in order to optimize control inputs.
- **Analysis of flight test data** which includes the definition of the mathematical model structure of the rotorcraft, data quality assessment, and the identification of the unknowns.

Corresponding to these strongly interdependent topics, main emphasis has to be placed on four important aspects of the art and science of system identification:

- The **Maneuver** of the helicopter due to control inputs must provide as much information as possible about the dynamic characteristics of the aircraft. It implies the development of appropriate input signals, optimized in their spectral composition, but still flyable by the pilot.
- Highly reliable **Measurements** are indispensable as system identification always is based on the input/output relationship of the vehicle motion. Measurement inaccuracies, that cannot be corrected or compensated, lead to biased estimation results.
- The definition of the **Model** structure is a key element. Depending on the intended purpose, often high order rotorcraft models are needed and a practical compromise between high bandwidth model accuracy, efforts for flight testing, measurement, and data processing, and system identifiability must be found.
- Suitable identification **Methods** are required for both, data quality analysis and parameter identification. Here, various techniques of different complexity and performance, working in the time or frequency domain are available.

These '**Quad-M**'-requirements must carefully be investigated from a physical standpoint in order to define and execute a successful experiment for system identification.

In the following, the paper will concentrate on a detailed discussion of each of the four **M**, Maneuvers, Measurements, Models, and Methods.

5. MANEUVERS FOR SYSTEM IDENTIFICATION

Independently from the actually applied technique, sys-

tem identification approaches always rely on the information content about the system under test provided by the amplitude and phase relationship between the measured control inputs and the resulting measured system response. Therefore, the test input is one of the major factors influencing the accuracy with which the model parameters can be determined. Generally, it should at least meet the following requirements: all helicopter modes within the frequency range of interest must properly be excited; the flight test duration must be long enough to provide sufficient low frequency information; when linear models are estimated, the aircraft response should stay within small perturbations assumptions from trim; no or only minor additional pilot inputs are allowed, e.g. for keeping the response small. Further, it is often desired that the input can be flown by the pilot.

There are a few standard input signals, which are widely applied for aircraft system identification: Doublet, 3211, and frequency sweep. They were also used in the WG 18 data base. As example, Figure 3 presents the input shapes for the longitudinal control and the resulting pitch and roll rate responses:

Doublet control inputs can be considered as classical input signal for aircraft flight testing in general. In the case of highly coupled high order helicopter models it is generally regarded as having limited value due to its small bandwidth.

The multi-step 3211 input signal has become standard in system identification. The numbers used in the designation refer to the relative time intervals between control reversals. As it excites a wide frequency band within a short time period, it is also suited for moderately unstable systems. Typically, the input signal lasts for about 7 seconds, then the controls are kept constant until the pilot retrimms the aircraft. For rotorcraft identification the signal was slightly modified by intermediate steps to increase the higher frequency content.

Frequency sweeps are increasingly used in recent years. Starting with a sinusoidal signal of the lowest frequency of interest, the frequency is progressively increased up to its maximum and then the aircraft is returned to trim. Typically, this broad-band input signal lasts for about 50 seconds.

Depending on availability in the individual data base, the Working Group used

- for BO 105: 3211 and the frequency sweeps for identification and doublets for verification
- for AH 64: doublets for identification and sign converted doublets for verification.
- for PUMA: 3211 signals for identification and sign converted 3211 for verification.

In the Working Group only forward speed flight conditions at 80 (BO 105, PUMA) and 130 (AH 64) knots were considered. Here, the control inputs and flight tests could be conducted without major problems. However, some general tendencies became obvious:

- Pilot flown control inputs are preferable in comparison to electronically generated inputs for two main reasons: 1) Too large deviations from trim can easily be avoided. 2) In contrast to SAS systems, any correcting or stabilizing pilot inputs in form of small steps or pulses do not cause output/input correlations,

which can render the identification impossible.

- It is often difficult to use existing data bases for identification. Dedicated flight testing is necessary, where emphasis can be placed on the specific needs associated with these techniques (e.g. same trim flight condition, proper excitation, small perturbations, record length, calm air, etc.)
- Repeat of tests is advisable to provide redundant data for the evaluation.

From the WG data bases, only the BO 105 data base was produced for system identification purposes and all data were generated within one well controlled flight test program. It was provided by a research institution experienced in system identification work.

A problem area not addressed by the Working Group are system identification maneuvers at flight conditions, where the aircraft is unstable. For example, the BO 105 in and near hover flight condition has a time to double amplitude of the unstable phugoid mode of about 3.4 seconds. Here, recent flight tests showed, that conventional flight testing for identification was not possible and significant additional control inputs were needed to keep the aircraft response within acceptable amplitude responses. As they were sporadically given, correlation effects could be avoided. Engaged SAS systems, however, with continuous feedback of states to the controls can cause severe identification problems due to data correlation, generally experienced in so called 'closed loop identification'. In the Working Group this effect was seen in the AH 64 frequency sweeps. They were flown open loop for the primary and closed loop for the off-axes, which precluded identification of the off-axis response.

For several applications, like high bandwidth control system design, it is required that the identified models accurately describe the high frequency characteristics. Consequently, the control inputs must also contain higher frequency excitation to provide sufficient information in the flight test data. However, the excitation of the lower frequency rotor modes and structural coupling modes must be avoided, as it can severely damage the helicopter. In particular, when automatically generated inputs are applied or when pilots are not experienced in flight tests for system identification, the flight test engineer must be aware of this danger. In recent years, such problems have occurred particularly with frequency sweeps flown with large amplitude responses in the higher frequency range.

6. MEASUREMENTS AND DATA ANALYSIS

Measurements needed for the identification are defined by the measurement and control vector of the selected model. Only for equation error techniques the state variables are also required. In addition, measurements characterising the flight condition are desirable. For the identification of 6 DOF rigid body models, as used in the Working Group, a standard set of variables to be measured was defined:

- controls.
- translational information for all three axes (horizontal, lateral, vertical): airspeed, linear accelerations.
- rotational information for all three axes: rates, roll and pitch attitudes, heading.

- optional: rotational accelerations (often derived by numerical differentiation of the rates).

These measurements are usually available in modern instrumentation systems. All three WG data bases easily provided this minimum set of data required for identification and gave also additional data, like rotor RPM, engine torque, or a second set of accelerometers at the pilot position, and others. All three helicopters were mainly equipped with individual sensors, but there is no specific preference in comparison to inertial system packages. However, a detailed knowledge about sensor characteristics and data processing is indispensable, which is often difficult to obtain for commercially available instrumentation systems. From this point of view, some advantages can be seen in the use of individual sensors, which also provide more redundancies in the measurements.

A high measurement accuracy is the dominant requirement for system identification. The now available transducers generally provide this accuracy and are appropriate. However, emphasis should be placed on four aspects: 1) the measuring range should be adapted to the test to obtain a high resolution. 2) cross axis sensitivity and sensor misalignment must be minimized, 3) signal (analogue) filtering must exactly be known as phase shifts deteriorate identification results, and 4) a careful calibration of all components is absolutely necessary.

It was seen that most variables needed for the 6 DOF model identification can accurately be measured using standard sensors like accelerometers, gyros, potentiometers or synchros. However, air data measurement still is major problem area. Data obtained from noseboom-mounted pressure sensors and vanes (AH 64 and PUMA) may be acceptable at higher speed but cannot be used for low speed and hover. An air data system designed for helicopters (BO 105) covers the full flight regime. Its accuracy may be acceptable for operational use but for identification purposes it is critical. Therefore, most WG Members used reconstructed speed components, calculated from linear acceleration and attitude measurements. In conclusion, airspeed measurement remains to be problematic.

An area not addressed in the Working Group is the measurement of rotor blade motions. Meanwhile, successful identifications of higher order models with rotor DOF have been published [12], where strain gauge measurements from the blades were evaluated to derive tip path plane variables. The results are promising and indicate that a suitable measurement accuracy of the rotor flapping dynamics can be obtained for a reliable identification of higher order models.

As system identification usually is an off-line process and conducted after completion of flight testing, it is of utmost importance to check and insure the data quality. Here, dedicated flight tests conducted right before and during the actual flight tests should be evaluated immediately to detect any errors as soon as possible. Such checks range from visual data inspection to complex data kinematic compatibility analyses. In the Working Group most Members applied specifically developed techniques

based on extended Kalman filter state reconstruction or they applied the nonlinear Maximum Likelihood identification methods. A comparison of the obtained results proved the applicability of these techniques and their high potential to detect data errors and provide correction values for biases and calibration factors of the measurements or to reconstruct unusable data variables at all.

Based on the experiences made in the Working Group, it is highly recommended to carefully check the measurement quality. All possible attempts should be made during flight testing to isolate and correct errors. Here, even less complex techniques like least squares methods are helpful, followed by a more detailed data analysis, removal of errors, and data reconstruction before beginning the identification.

7. MATHEMATICAL MODELS

Selection of model structure is a critical step in system identification, which will greatly affect both the degree of difficulty in extracting the unknown parameters and the utility of the identified model in its intended application. Following the present state of the art in system identification, the Working Group concentrated on the identification of parametric fully coupled 6 DOF linear derivative models, which are considered as appropriate for the description of the rigid body dynamics for the low and mid frequency range and applicable e.g. for flying qualities evaluations. They are formulated by the state equations characterizing the system dynamics:

$$\dot{x} = Ax + Bu$$

and the measurement equations, which give the relationship between measured data and model responses to be matched by the identification technique:

$$y = Cx + Du$$

with

state vector $x = [u, v, w, p, q, r, \phi, \theta]^T$
 control vector $u = [\text{long stick, lateral stick, collective, pedal}]^T$

and a representative measurement vector
 $y = [u, v, w, p, q, r, \phi, \theta, a_x, a_y, a_z]^T$
 (can be modified)

Such models have their justification as, usually, the eigenvalues associated to blade dynamics are sufficiently higher than the rigid body modes. But it was well understood that use of 6 DOF is a major restriction and that for a more realistic and broader bandwidth representation at least main rotor state variables associated with blade flapping are needed, which adds a significant amount of complexity to measurement requirements, model formulation, and identification. By the end of the Working Group time period, first approaches to determine higher order models were made. They will be addressed later in the paper in the chapter on recent advances.

Usually, linear models based on small perturbation assumptions are used for the identification. They are only valid for the considered flight condition. Although some identification techniques can be applied to fully nonlinear

model formulations, the preference to linear models has two main reasons: 1) Most tools for further system characterization, like stability analysis, and for intended applications, like control system design, require linearized differential equations. 2) Because of the high complexity of the helicopter model it is difficult to specify those nonlinear terms that have a significant effect on the system response and can accurately be identified. An often used compromise is a model formulation with linear aerodynamics and nonlinear kinematic and gravity terms. It significantly helps to reduce prediction errors, when the identified models are applied to calculate higher amplitude maneuvers.

Present standard for system rotorcraft identification is the formulation of system dynamics in the format of flight mechanical derivative models, which represent a global description of the helicopter behaviour. There are two additional different approaches to rotorcraft modelling: generic analytical models and information obtained from wind-tunnel testing.

7.1 Generic analytical models

Based on theory or experimental data generic models calculate the forces and moments acting on individual helicopter components, like main and tail rotor blades, fuselage, engine, etc. The obtained results are evaluated depending on the intended purpose. In example, for helicopter motion simulation the forces and moments are introduced into the equations of motions to obtain time history responses due to control inputs. Various of these simulation computer codes are in use. They differ in application (real time/non real time) and sophistication, mainly depending on the complexity of rotor inflow calculation and rotor blade motion resolution. Comparisons of simulation results to flight measurements usually show good agreements for the on-axis responses. Major problem area is the prediction of cross couplings between pitch and roll motions, which can have even wrong sign.

7.2 Rotorcraft wind-tunnel testing

For fixed-wing aircraft, wind-tunnel testing has become standard and is extensively used to determine and optimize aerodynamic characteristics. However, except for fuselage tests, rotorcraft wind-tunnel tests are still rare [1], mainly for three reasons: 1) rotor tests have to be conducted with rotating blades, which requires a test rig with a rotor drive system, precise control of the rotor states, measurement of high frequency blade variables in the rotating system, data transfer to the fixed system and real time high sampling data recording, evaluation, and monitoring. 2) Because of wind-tunnel size, usually model rotors are tested. Then, rotor scaling must provide both aerodynamic and dynamic similarity. It is only approximately possible, when relatively large model rotors are used and, consequently, larger wind-tunnels are needed. 3) Because of scaling effects, model blades must be manufactured with extremely high accuracy. From these requirements, it is obvious that in comparison to fixed-wing aircraft, wind-tunnel testing of rotorcraft is significantly more complex and expensive. In addition, wind-tunnel tests usually only provide information about steady state characteristics. Simulated 'free' flights, as sometimes conducted for airplane models to obtain information about the dynamics, cannot be accomplished with

helicopter models. Therefore, often helicopters are still designed without wind-tunnel measurements and then tested and modified during the flight test phase.

7.3 Cross-fertilization of modelling approaches

The three approaches, analytical modelling, wind-tunnel model measurements, and flight test evaluation by system identification are well established and have reached maturity. Each of these techniques has its strengths and weaknesses. An efficient way to combine the individual strengths for a general model improvement is not yet developed. Analytical simulation uses wind-tunnel results, but confidence levels are not given and the transferability from model to real size helicopter characteristics is not exactly known. System identification certainly provides the most accurate model, but the formulation in derivative format is too global for the extraction of more detailed information, as needed for analytical model improvement. Comparisons of all three approaches applied to the same helicopter type are very rare. Here, a more problem oriented research is needed to define a practical approach for rotorcraft model improvement, which combines the benefits of the individual approaches. In the Working Group it was tried to stimulate this topic by a contribution for simulation validation.

8. SYSTEM IDENTIFICATION METHODS

System identification techniques can be divided into methods working in the time domain or in the frequency domain. Both approaches were extensively used in the Working Group. The individual techniques are described in more detail in the Working Group Final Report [10]. All techniques have in common, that a 'best' set of unknown parameters is determined by minimizing a given cost function. Depending on the assumptions for the cost function formulation, the minimum search ranges from easily applicable analytically derived closed solutions up to complex iterative solution algorithms. Main difference is the ability of the techniques to handle noisy data, where two sources of noise are considered: process (or state) and measurement noise. Estimation of all unknowns and both noise characteristics leads to very sophisticated methods and is computationally tedious. As mostly done, the Working Group assumed flight tests to be flown in calm air with negligible process noise. Then, the general form of the cost function is given by:

$$J(\xi) = \sum e^T R^{-1} e$$

It is minimized by adjusting the unknown parameters ξ . Differences between the individual techniques are principally characterised by the definition of the error e and the weighting matrix R .

8.1 Time-Domain Approaches

In the last decades, the majority of aircraft identification work is based on the Maximum Likelihood technique accounting for measurement but neglecting process noise, like it was also used by some WG Members. Strictly, this is a so called *output error method* with:

$$e(t) = y(t)_{\text{meas}} - y(t)_{\text{model}}$$

$$R = \frac{1}{N} \sum [y(t)_{\text{meas}} - y(t)_{\text{mod}}] [y(t)_{\text{meas}} - y(t)_{\text{mod}}]^T$$

Here, R is the measurement error noise matrix. To obtain the minimum of the cost function $J(\xi)$ with respect to the unknowns ξ , all first derivatives $\delta J/\delta \xi$ have to be zero. This leads to a set of nonlinear equations that can only be solved iteratively with the main steps: 1. calculation of the cost function J , 2. determination of R , 3. update of the unknowns ξ by minimizing J with respect to the unknowns ξ , 4. calculation of new y . In addition to the parameter estimates, the technique also provides uncertainty levels (standard deviations) for the estimates. The parameters to be determined are primarily the system coefficients (derivatives) but in addition, so called bias terms have to be estimated to compensate effects due to variable zero offsets and drifts. These biases can drastically increase the total number of parameters to be determined and complicate the identification.

For aircraft identification the Maximum Likelihood approach is mostly used as it has several desirable statistical properties. In addition, it allows the identification of non-linear models, where the nonlinearities can be formulated using actual state variables. Often applied approximations, like use of pseudo controls, are not necessary.

Another technique, also used in the Working Group, is based on the assumption of 'perfect' measurements of states and controls. Then, the state variables are formally treated as (pseudo) controls and the individual equations of motion can be identified separately by minimizing the equation error. With:

$$\dot{x} = Ax_{meas} + Bu$$

$$y = \dot{x} + e$$

$$e = y - Ax_{meas} - Bu = y + \xi X$$

$$J(\xi) = \sum e^2$$

it follows

$$\xi = (X^T X)^{-1} y$$

which is the closed, non-iterative solution for the equation error technique. It is a fast and easily applicable method. However, it requires extremely accurate data and therefore high emphasis is placed on data pre-processing.

8.2 Frequency-Domain Approaches

Frequency-domain approaches have some unique characteristics which make them attractive for rotorcraft identification. In particular, they allow concentration on selected frequency ranges, are insensitive to system instabilities, and do not require estimation of biases. In the WG, two approaches were used which, since then, have been increasingly and successfully applied: A Maximum Likelihood technique and a method based on transfer function evaluations.

For the frequency-domain Maximum Likelihood approach measurements are represented in the format of Fourier Transforms and model, cost function, and covariance matrix are formulated and determined in the frequency domain:

$$j\omega x(\omega) = Ax(\omega) + Bu(\omega)$$

$$y(\omega) = Cx(\omega) + Du(\omega)$$

$$e(\omega) = y(\omega)_{meas} - y(\omega)_{model}$$

$$J(\xi, \omega) = \sum e(\omega)^T R(\omega)^{-1} e(\omega)$$

$$R(\omega) = \frac{1}{N} \sum [y(\omega)_{meas} - y(\omega)_{mod}] [y(\omega)_{meas} - y(\omega)_{mod}]^T$$

Comparisons between flight test data and model response are made in frequency-domain formats (e.g. Bode plots) or, after re-transformation, in form of time histories.

In a different approach, a specified group of conditioned transfer functions $T(\omega)_{measured}$ is first derived from the flight test data. Here major emphasis is placed on high accuracy over a wide frequency range. In a second step, the model transfer functions are formulated as:

$$T(\omega)_{mod} = (C(I-A)^{-1}B + D)e^{s\omega}$$

The error and cost function are then

$$e(\omega) = T(\omega)_{meas} - T(\omega)_{model}$$

$$J(\xi, \omega) = \sum e(\omega)^T W(\omega) e(\omega)$$

where the weighting matrix W is based on the coherence of each frequency point to emphasize the most accurate data. For the comparison to flight test data, usually frequency responses are used. Time histories are generated by driving the identified model with the measured control inputs.

8.3 Verification of results

The verification of the identified model is the final key step in the identification process, which assesses the predictive quality of the extracted model. Flight test data not used during the identification are selected to ensure that the model is not tuned to specific data records or input shapes. It is desirable to conduct the verification with data from the same flight conditions but with other control inputs. In the Working Group, not all data bases allowed this ideal situation due to lack of data. But as example, BO 105 identification results were generated from flights with multistep 3211 or frequency sweep inputs. Then, for verification, data with doublet control inputs for each control were used: The previously identified model was driven with the measured control variables and the obtained response was compared to the measured helicopter response. When a satisfying agreement is obtained the identification is completed and the identified model is made available for the intended application. Usually it is provided in form of model coefficients and their standard deviations.

9. REPRESENTATIVE WG RESULTS

The Working Group has evaluated data bases from three different helicopters, AH 64, BO 105, and PUMA (Figure 1). The obtained results are presented and discussed in the Final Report and the AGARD Lecture Series [10,11]. For this chapter, some of the BO 105 results

were selected to give a representative insight into the model accuracy that can be expected from system identification.

9.1 Identification

After data processing and reliability checking, three suitable data sets were selected. Each of them consisted of four different runs with single control pilot inputs.

- 1) Data runs with 3211 input signals were used for identifications in the time-domain as well as the frequency-domain identification based on Fourier transforms.
- 2) Frequency sweep data were used for the frequency-domain identification based on transfer functions.
- 3) Data obtained from doublet control inputs were applied for the verification of the identified models.

The Working Group Members applied their individual identification techniques:

AFDD: The frequency domain method first evaluates frequency sweeps to generate transfer functions, which are then used to identified linear state space models.

CERT, DLR, NAE: Time domain Maximum Likelihood methods were applied. The individual approaches are slightly different from each other. Main differences refer to the treatment the nonlinear gravity terms, like $g \cdot \sin \theta$: CERT identified fully linearized models, NAE used so called 'pseudo control' or 'forcing function' approach where the nonlinear terms are calculated from measurements and treated as known additional control inputs, DLR identified nonlinear models.

Glasgow University: Linear state space models were identified from Fourier transforms in the frequency domain.

NLR: A time-domain equation error technique based on least squares was applied to determine linear models. Only 6 DOF rigid body models were identified. Most Members developed their model structures by first isolating variables that have practically no influences on the aircraft response. They were assumed to be zero. In consequence, from totally 60 possible derivatives the number of actually identified parameters varied from 58 (NAE) to only 30 (University of Glasgow). A further important difference was the inclusion of equivalent time delays to approximate rotor dynamic effects. Here, either the time delays were neglected, set to values suggested by DLR, or individually identified.

From the identification results, Figure 4 demonstrates the good agreement between the measured data and the model response for four different data runs (jointly evaluated as concatenated runs). It confirms that the basic model structure with 6 DOF can correctly represent the helicopter dynamics. Similar results were generated by all WG Members. A full list of the associated identified parameters and their variances is provided in the WG Final Report. Some of the major identified derivatives are given in Table 1. Comparisons showed significant differences even for some of the more important derivatives. The discrepancies were investigated in more detail and could mostly be related to the above mentioned differences in the approaches. As example, it was experienced that the identification of pitch and roll damping for the BO 105 is very sensitive to both time delays and correlation with control derivatives. In general, it was seen that results obtained from the frequency-domain approaches and the Maximum Likelihood time-domain techniques are relatively close, when time delays

are included. The associated eigenvalues are provided in Table 2. It is seen that the oscillatory modes (phugoid and dutch roll) and the lower frequency aperiodic modes (pitch and spiral) agree satisfactorily. Larger differences occurred for the roll and higher frequency pitch modes, which are directly related to the damping derivative differences.

9.2 Verification

The verification of the identified models assesses the predictive quality of the extracted model. It is based on flight data different from those used in the identification. The identified model is kept constant and its response due to the measured control inputs is calculated and compared to the measured response variables. Figure 5 gives the pitch and roll rate results obtained from flight tests with doublet control inputs. Generally, it is seen that all identified models predict the correct tendency of the aircraft response in both on- and off-axis variables. A closer comparison shows a good agreement for the long term (low frequency) response, whereas some larger differences are seen for the time history segments, where the control input was given. Here, some models are more damped or the coupling is less accurate. The fact however, that none of the models can fully reach the maximum peak amplitude of the rates demonstrates that 6 DOF models cannot describe the higher frequency range completely. In this sense, the models generated by the Working Group can be considered as the best possible solution for rigid body model formulations. Further improvements require an extension of the model order by additional degrees of freedom that provide a more realistic characterisation of the rotor dynamics than the equivalent time delay approach. But although the comparisons of the individual results revealed larger differences, all identified models can be considered as accurate in comparison to other approaches. To demonstrate the system identification potential, Figure 6 compares measured time histories to the responses of both, identification and analytical simulation results. It also reveals the fundamental simulation problem: the prediction of cross coupling, which often has the wrong sign. Here, the improvement of simulation codes has become a major challenge [13].

10. RECENT ADVANCES: IDENTIFICATION OF EXTENDED MODELS

The Working Group mainly concentrated on the identification of 6 DOF models. They are useful for various applications, where less accuracy in the high frequency range (from about 2 Hz for the BO 105) can be tolerated. However, for applications like high bandwidth control-system design higher order models with rotor DOF may be required. This subject was addressed in the WG but it was beyond the scope of the Group to work with such models. Meanwhile, successful identification of extended models were conducted by previous Members of the Working Group. It was particularly emphasised by AFDD and DLR, who need more suitable models for the control system design of their In-Flight Simulators BO 105 ATTheS (DLR) and UH60 RASCAL (AFDD). Both are presently applying a model structure, where, in addition to the 6 DOF of the rigid body, the rotor tip path plane is represented by second order differential equations for coning, longitudinal and lateral flapping [14,15]. For hover flight condition, first approaches to include an

inflow DOF were made.

10.1 Representative Results

The basic approach for extending the 6 DOF model is illustrated in Figure 7. The state vector of the rigid body motion is extended by rotor motion variables. Such a model considers 9 DOF and is of 14th order. In comparison to a 6 DOF model, it is more appropriate for helicopters as it includes a physically realistic representation of the dynamics of the most important and dominant helicopter component: the main rotor. In consequence, the rather crude approximation of rotor dynamics by equivalent time delays is no longer needed. Based on BO 105 identification results, Figure 8 compares the eigenvalues of both identified models, the conventional 6 DOF and the extended 9 DOF model. It illustrates that low frequency rotorcraft eigenvalues (phugoid, spiral, Dutch roll, and pitch) are the same for both models, whereas the higher frequency behaviour is characterised by the more refined description of the 9 DOF model. The obtained improvement in the model quality is demonstrated in Figure 9, which compares the roll axis time history responses for both models to the measured data. It is seen that only the 9 DOF model can match the amplitude peaks of the roll acceleration data. These data segments, where the control input is reversed, reveal the model higher frequency behaviour. The model differences become even more obvious, when the results are compared in the frequency domain format as it is demonstrated in Figure 10 for the roll rate response due to lateral stick inputs. The above presented results were obtained from BO 105 flight data. However, their general validity is supported by results generated by AFDD for a different helicopter, a NASA/Army UH-60 [15]. Figure 11 gives frequency responses for the pitch rate (on-axis) and roll rate (off-axis) responses due to longitudinal control inputs. It compares measured UH 60 flight data to both, an identified extended model with rotor DOF and a 6 DOF model. Again, it is seen that the conventional 6 DOF model only agrees for the lower frequency range and that a higher order model is needed to accurately represent the rotorcraft high bandwidth dynamics.

10.2 Application of extended models

At DLR and AFDD the identified higher order models are presently needed for the control-system design of the In-Flight Simulators ATTHes and RASCAL. The general concept for an explicit model following control system and the role of system identification is illustrated in Figure 12. The objective is to make the basic (host) helicopter follow an explicitly defined command model. The commanded model response due to pilot inputs is calculated and fed to the controllers. Here, the feedforward controller is defined as the inverse model of the host aircraft, compensating the host aircraft dynamics. In consequence, the aircraft behaves like the prescribed command model, e.g. like a different helicopter to be simulated. The feedback system mainly corrects for external disturbances. The performance of the control system highly depends on the accuracy of the host aircraft model used for the feedforward controller. First attempts to use 6 DOF models for the BO 105 ATTHes failed mainly for two reasons: 1) 6 DOF models *without* equivalent time delays to account for rotor dynamics are too inaccurate. 2) models *with* equivalent time delays

cannot be applied as the inverted model requires 'time lead', which is unrealistic for real time processes. To eliminate the time delay problems and also to generate rotorcraft models that are accurate within a wide frequency range and in particular at higher frequencies, extended models with rotor DOF were applied for the feedforward controller. Since then, numerous flight tests with various command models and different objectives have confirmed the validity of the control system design for the ATTHes In-Flight Simulator and the high accuracy of its feedforward controller [15].

To illustrate the significant improvement in model following fidelity, Figure 13 compares the frequency responses for measured roll rate to model roll rate for two different cases: 1) an identified conventional 6 DOF rigid body model was used to define the flight control system, and 2) an identified extended model with rotor DOF was applied for the flight control system design. For a perfect simulation, the frequency response should have a magnitude relationship of one and a phase angle of zero for a broad frequency range. It is obvious that only the control system based on the model with rotor dynamics is close to this ideal situation, with increasing (phase) deviations for higher frequencies. The major question for a quality assessment is, if the flight control systems performance is meeting the objectives for its intended application. Therefore, boundaries of so called 'unnoticeable dynamics' are also shown in Figure 13. They were derived for fixed wing aircraft and characterize the limits, where pilots will not notice simulation deficiencies [16]. It is seen that the ATTHes frequency response, based on the extended model, lies within these boundaries. As also good pilot ratings for the simulation where given, it confirms the definition of the boundaries and seems to indicate that they can also be used as a more general quality criterion for high bandwidth flight control systems [17].

10.3 Example for In-Flight Simulation Quality

To explore to potential of simulating the dynamics of different helicopters, a mathematical model of the Westland Lynx helicopter, provided by DRA, was used as a command model for the ATTHes In-Flight Simulator. Various flight tests with Lynx experienced pilots were conducted. They rated the simulation as to be representative for the Lynx for both tested configuration, with SCAS engaged and disengaged.

As example, Figure 14 gives the time histories for a simulated turn maneuver for the Lynx helicopter configuration with SCAS engaged. As control variables the 'Lynx pilot' stick inputs are given together with the BO 105 actuator motions that are needed to make the BO 105 respond like a Lynx helicopter. In particular it should be noted, how the lateral control illustrates the typical different characteristics of the two helicopters: Lynx is an attitude command, BO 105 a rate command system. The simulation fidelity is demonstrated by the good agreement of the model and flight attitude angles.

11. CONCLUSIONS AND RECOMMENDATIONS

The AGARD FVP Working Group 18 on *Rotorcraft System Identification* evaluated flight test data bases from three different helicopters (AH-64, BO-105, SA 330).

The available individual techniques were applied for data processing, data quality and suitability checking, and extraction of flight-mechanical mathematical models and their verification. In addition, examples for potential application areas for system identification were outlined, particularly with respect to industry needs. The WG accomplishments are fully documented in the Final Report [10]. Some of the major *conclusions* are:

- 1) Flight tests must meet specific identification requirements mainly with respect to control inputs and response information content, accurate trim and small perturbation responses, and repeated tests for data redundancy.
- 2) Data accuracy is the main prerequisite for a successful identification. Therefore, a strong emphasis has to be placed on data quality checking, detection and correction of errors, and careful data processing. Techniques for consistency analysis used in the WG ranged from Least Squares to extended Kalman Filter methods. It was seen that modern, correctly calibrated sensors easily provide the required accuracy except for velocity measurements, which are still problematic, especially in the low speed regime.
- 3) The obtained identification and verification results clearly showed the influence of flight test maneuvers and data quality on the identified parameters. As the BO 105 flight tests were defined by the WG and specially flown for identification purposes, the data represent a unique flight data base and a sound basis for the evaluation. The 3211 and frequency sweep control inputs confirmed to be adequate excitation signals.
- 4) The individual identification methods and their potential were characterized. In general, it can be stated that advanced methods, like Maximum Likelihood, are well suited for rotorcraft identification.
- 5) The Working Group mainly concentrated on the determination of classical 6 DOF rigid body models. The identification of higher order models was beyond the scope of the WG time period. However, based on the WG accomplishments, recent advances have shown that such models with rotor DOF can accurately be identified. They are required for more demanding applications, like high bandwidth control system design and high fidelity simulators. In this paper an example for the successful use of extended models for the development of in-flight simulators was given.

Based on the discussions and the accomplishments of the Working Group, the main *recommendations* for future applications and improvements of system identification approaches are:

- 1) Identification techniques have reached maturity levels that make them a powerful tool to support industry projects. Increased use by industry can contribute significantly to cost and risk reduction during the rotorcraft development phase.
- 2) The expertise of system identification development and application is mostly concentrated in research organisations. For an efficient use of this knowledge together with the design experience in industry, common teams can be established to obtain full advantages from identification applications.
- 3) To date, most of the rotorcraft identification has been related to flight conditions in the medium speed range

and to small amplitude maneuvers. The WG has demonstrated the challenge involved with such maneuvers, yet they can be considered as relatively easy compared to other maneuvers in the flight envelope, like hover or turn maneuvers, and higher amplitude responses with strong nonlinear effects. Research activities need to spread into these more complex areas so that possible new problems can be faced and appropriate solutions can be derived.

4) As system identification extracts the rotorcraft characteristics from flight data of the existing aircraft, it is an ideal tool to generate a 'true' mathematical description of the vehicle dynamics. However, the presently used derivative models are a too global representation of the aircraft. Methods to combine the advantages of system identification together with the advantages of other modelling approaches, like generic simulation or wind-tunnel measurements, still have to be found. It is a major research challenge to develop ideas and guidelines for combining these approaches and provide a powerful tool for accurately modelling the characteristics of a helicopter from its design phase through the flight testing phase until the final production.

12. REFERENCES

- [1] Hamel, P.G. et al., "Rotorcraft Model Testing at DNW - Experience and Perspective", Ten years of testing at DNW (1980-1990) Colloquium, 16 October 1990, Nordostpolder, NL
- [2] Iliff, K.W., "Parameter Estimation Analysis for Flight Vehicles", Journal of Guidance, Control, and Dynamics, Vol.12, No.5, 1989
- [3] Jategaonkar, R.V. et al., "Identification of C-160 Simulator Base from Flight Test Data", 10th IFAC Symposium on System Identification, Copenhagen, Denmark, 1994
- [4] Mulder, J.A. et al., "Determination of the Mathematical Model for the New Dutch Government Civil Aviation Flying School Flight Simulator", 18th Annual Symposium of the Society of Flight Test Engineers, Amsterdam, Netherlands, 1987
- [5] Baillie, S.W. et al., "The Flight Test and Data Analysis Program for the Development of a Boeing/de Havilland Dash 8 Simulator Model", 80th Symposium of the AGARD Flight Mechanics Panel on Flight Testing, Crete, Greece, 1992
- [6] Padfield, G.D. (editor), "Application of System Identification in Rotorcraft Flight Dynamics", Vertica Special Edition, Vol.13, No 3, 1989
- [7] Anon., Methods for Aircraft State and Parameter Identification, AGARD CP-172, May 1975
- [8] Hamel, P.G. (editor), Parameter Identification, AGARD LS-104, 1979
- [9] Maine, R.E., Iliff, K.W., "Identification of Dynamic Systems", AGARD AG-300, 1985
- [10] Hamel, P.G. (editor), Rotorcraft System Identification, AGARD AR-280, 1991
- [11] Hamel, P.G. (editor), Rotorcraft System Identification, AGARD LS-178, 1991
- [12] Fu, K.-H., Kaletka, J., "Frequency-Domain Identification of BO 105 Derivative Models with Rotor Degrees of Freedom", Journal of American Helicopter Society, January 1993
- [13] Prouty, R.W., "The Case of the Cross-Coupling Mystery", Rotor & Wing, June 1994
- [14] Fletcher, J.W., "Identification of UH-60 Stability

- Derivative Models in Hover from Flight Test Data", 49th Annual Forum of the American Helicopter Society, May 1993
- [15] von Grönungen, W. et al., "A High Bandwidth Control System for a Helicopter In-Flight Simulator", International Journal of Control, Vol. 59, 1994
- [16] Anderson, M.R., "Robustness Evaluation of a Flexible Aircraft Control System", AIAA Journal of Guidance, Control, and Dynamics, May-June 1993
- [17] Hanke, D.H., Rosenau, G., "Hermes Training Aircraft, Volume 2: Technical Specifications", DLR-IB-111-89/17-2, 1989

	AFDD	CERT	DLR	Glasgow Uni	NAE	NLR
	Frequency Domain	ML (linear)	ML (nonlinear)	ML Frequ. Domain	ML (linear)	LS Equation Error
Derivative	Value (Std.Dev.)	Value (Std.Dev.)	Value (Std.Dev.)	Value (Std.Dev.)	Value (Std.Dev.)	Value (Std.Dev.)
X_u	- 0.0385 (.004)	- 0.058 (.002)	- 0.059 (.001)	- 0.032 (.004)	- 0.050 (.010)	- 0.050 (.001)
Y_v	- 0.221 (.011)	- 0.177 (.003)	- 0.170 (.003)	- 0.131 (.055)	- 0.279 (.005)	- 0.064 (.003)
Z_w	- 1.187 (.056)	- 1.171 (.012)	- 0.998 (.007)	- 0.791 (.018)	- 1.106 (.013)	- 0.875 (.006)
L_p	- 8.779 (.641)	- 2.693 (.056)	- 8.501 (.110)	- 4.470 (.392)	- 7.048 (.201)	- 1.995 (.114)
L_q	3.182 (.624)	1.558 (.090)	3.037 (.125)	0.0 *	4.454 (.222)	0.558 (.171)
M_p	- 0.998 (.066)	- 0.491 (.015)	- 0.419 (.038)	- 1.367 (.032)	- 1.414 (.066)	- 0.878 (.062)
M_q	- 4.493 (.235)	- 2.26 (.025)	- 3.496 (.047)	- 2.217 (.009)	- 2.992 (.074)	- 1.441 (.093)
N_r	- 1.070 (.061)	- 1.116 (.013)	- 0.858 (.007)	- 0.756 (.064)	- 1.017 (.023)	- 0.699 (.035)
$Z_{\delta \text{ col}}$	- 0.388 (.020)	- 0.273 (.003)	- 0.349 (.002)	- 0.259 (.021)	- 0.337 (.005)	- 0.242 (.003)
$L_{\delta \text{ lon}}$	0.073 (.006)	- 0.0028 (.002)	0.024 (.003)	0.0 *	- 0.005 (.004)	0.0301 (.005)
$L_{\delta \text{ lat}}$	0.179 (.014)	0.0551 (.001)	0.185 (.002)	0.0764 (.010)	0.1361 (.004)	0.0534 (.003)
$M_{\delta \text{ lon}}$	0.098 (.004)	0.050 (.002)	0.093 (.001)	0.0565 (.002)	0.0787 (.002)	0.054 (.003)
$M_{\delta \text{ lat}}$	0.00 *	- 0.0003 (.0003)	- 0.009 (.0008)	0.00 *	0.0106 (.0013)	0.005 (.0013)
$N_{\delta \text{ ped}}$	0.057 (.003)	0.043 (.001)	0.049 (.001)	0.443 (.002)	0.484 (.001)	0.044 (.001)
$\tau_{\delta \text{ col}}$	0.168 (.0056)	0.0	0.040	0.102	0.040	0.040
$\tau_{\delta \text{ lon}}$	0.113 (.006)	0.0	0.100	0.044	0.100	0.080
$\tau_{\delta \text{ lat}}$	0.062 (.006)	0.0	0.060	0.074	0.060	0.060
$\tau_{\delta \text{ ped}}$	0.044 (.006)	0.0	0.040	0.0	0.040	0.040

* Eliminated from model structure

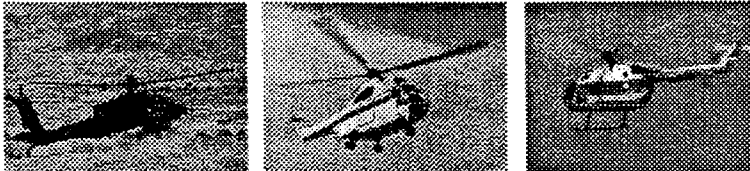
Table 1. Comparison of selected BO 105 derivatives identified by the Working Group Members

Motion	AFDD	CERT	DLR	Glasgow Uni	NAE	NLR
	Frequ. Domain	ML (linear)	ML (nonlinear)	ML Frequ. Domain	ML (linear)	LS Equation Error
Phugoid	[-0.36, 0.30]	[-0.17, 0.32]	[-0.15, 0.33]	[-0.010, 0.35]	[-0.014, 0.33]	[-0.07, 0.33]
Dutch Roll	[+0.22, 2.60]	[+0.13, 2.51]	[+0.14, 2.50]	[+0.16, 2.27]	[+0.13, 2.58]	[+0.17, 2.17]
Roll	(8.32)	[+0.99, 2.89]	(8.49)	(5.12)	(8.47)	(2.38)
Pitch	(6.04)	--	(4.36)	(1.98)	(4.38)	(1.37)
Pitch	(0.49)	(0.66)	(0.60)	(0.64)	(0.63)	(0.71)
Spiral	(0.03)	(-0.05)	(0.02)	(-0.007)	(0.03)	(0.04)

Shorthand notation:

$[\zeta, \omega_n]$ implies $s^2 + 2\zeta\omega_n s + \omega_n^2$, ζ = damping, ω_n = undamped natural frequency (rad/sec)
 $(1/T)$ implies $(s + 1/T)$, (rad/sec)

Table 2. Comparison of BO 105 eigenvalues identified by the Working Group Members



	AH-64	SA-330	BO 105
Role	attack	medium transport	small transport
Mass [kg]	6640	5800	2200
Roll Inertia [kg m^2]	8300	9640	1430
Main Rotor	articulated	articulated	hingeless
Main Rotor Diameter [m]	14.63	15.09	9.83
Hinge Offset [%]	3.8	3.8	15.2 (equiv.)
RPM [1/min]	289	265	424

Figure 1. Helicopters evaluated in the FVP Working Group WG 18

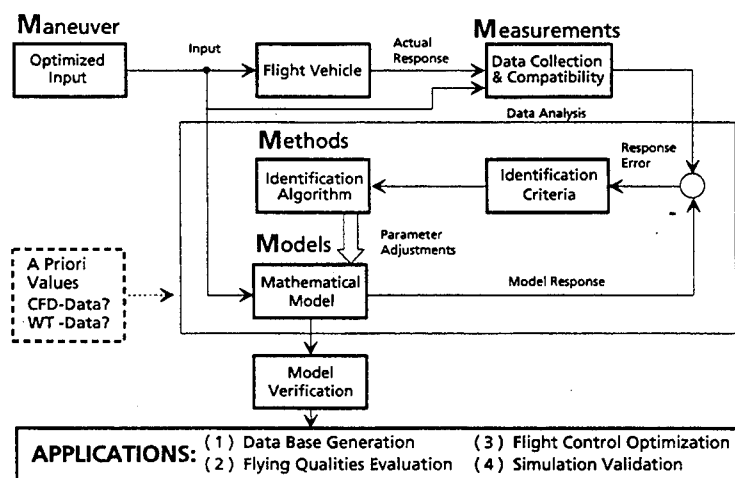


Figure 2. The "Quad M" basics of rotorcraft system identification

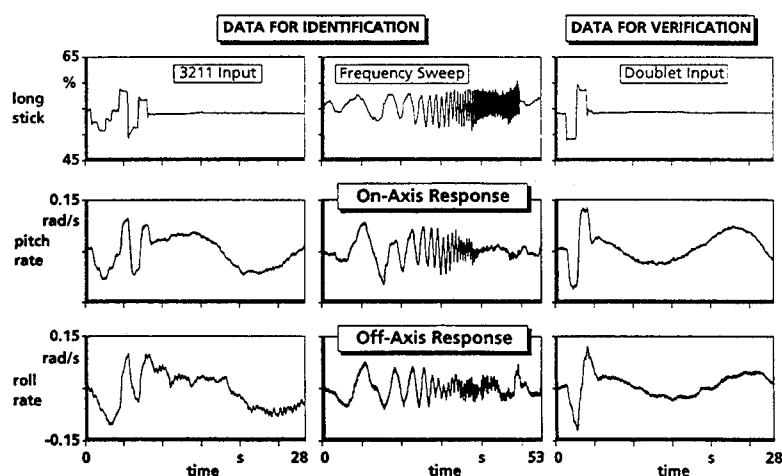


Figure 3. Control inputs for system identification and rate responses (from BO 105 data base)

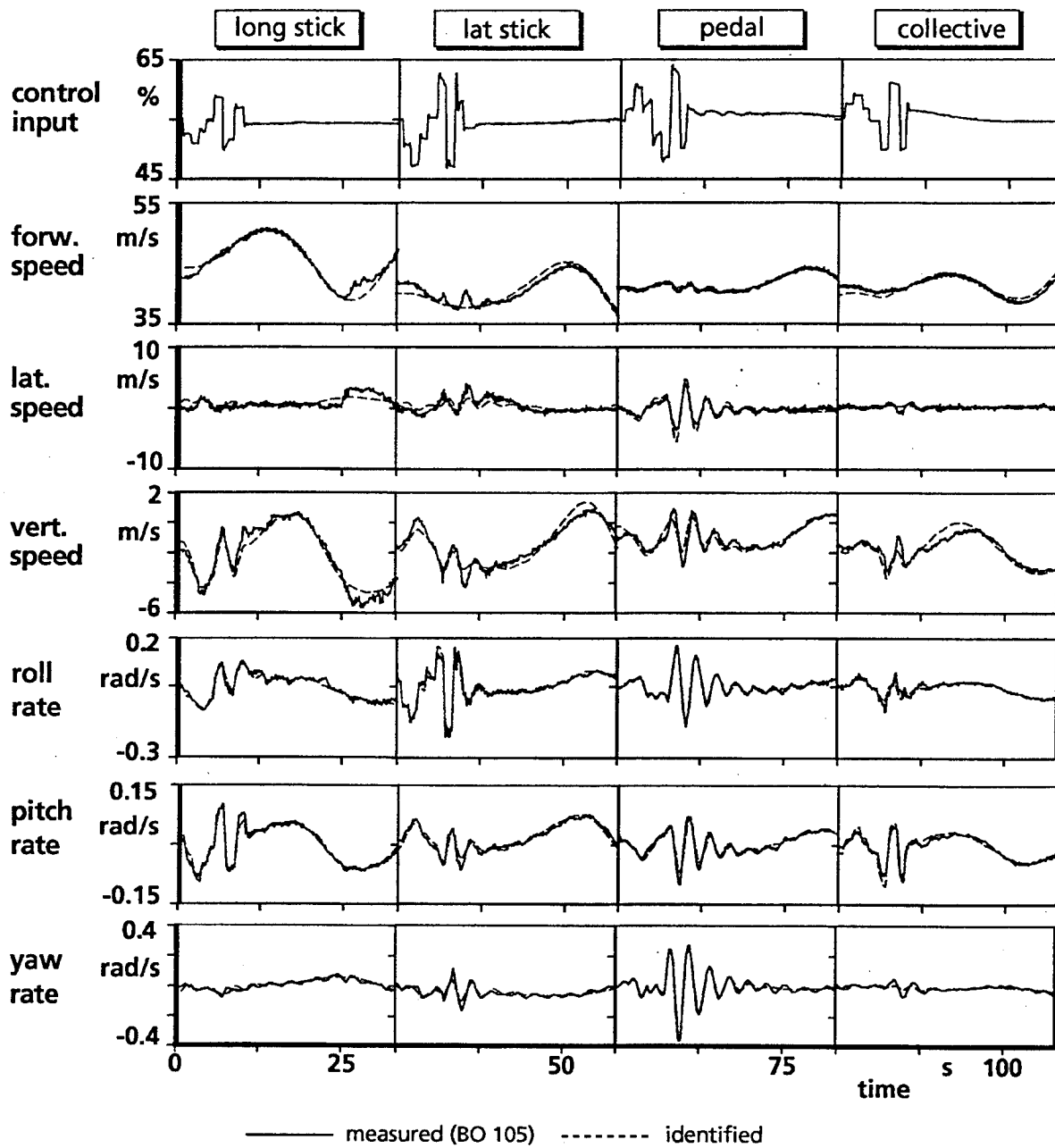


Figure 4. Representative identification result: Comparison of BO 105 flight test data to the response of the identified model

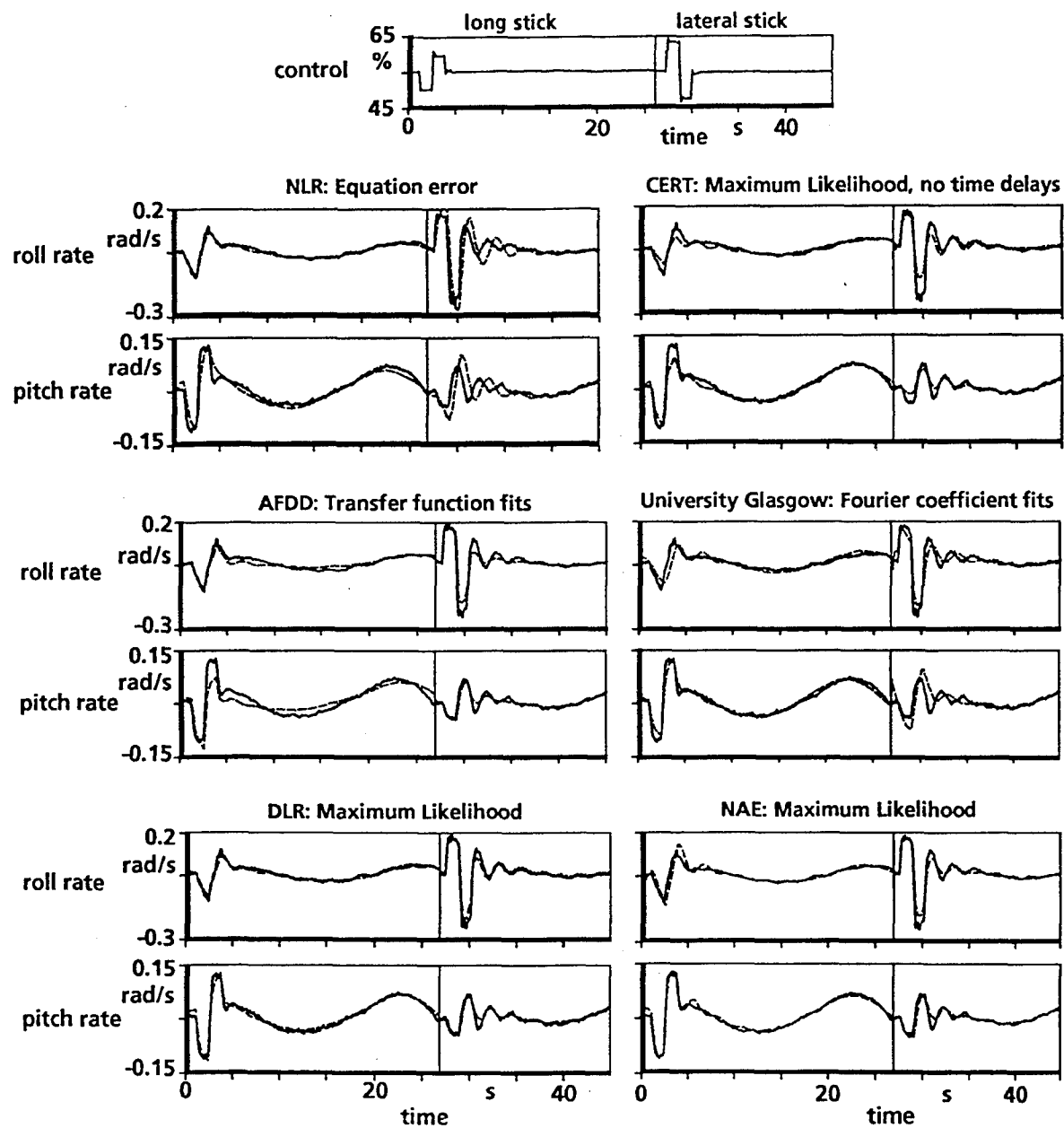


Figure 5. Verification results: Comparison of BO 105 flight test data to the predicted response of the identified model

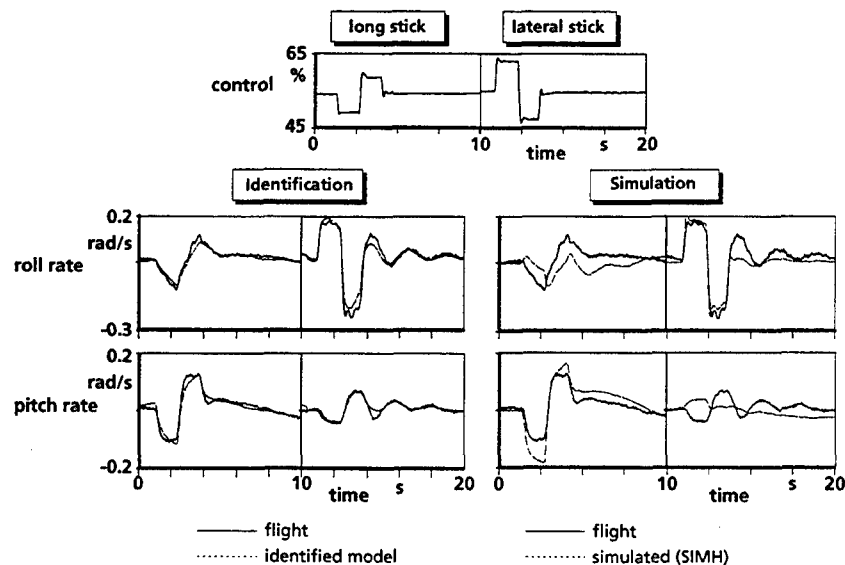


Figure 6. Comparison of the BO 105 flight test data to the response obtained from the identified model and analytical simulation

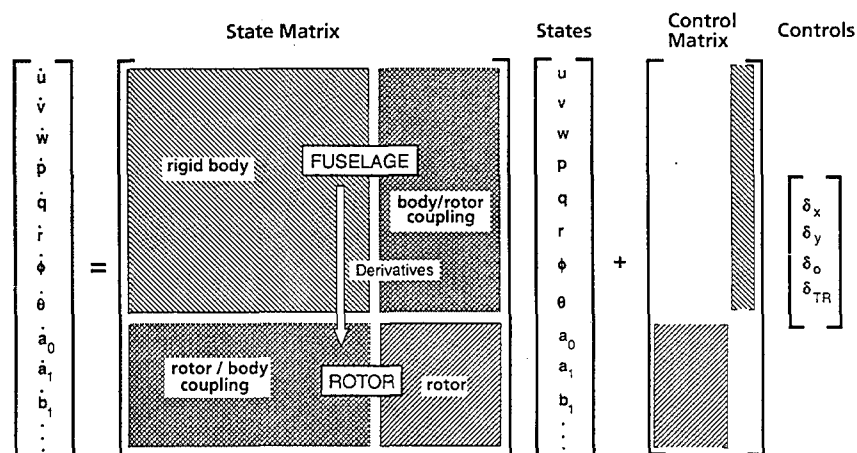


Figure 7. Principle of extended model structure

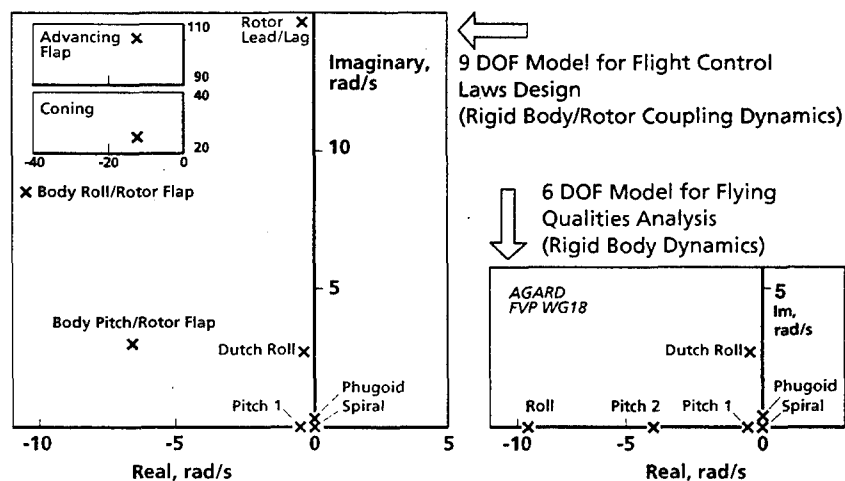


Figure 8. Comparison of poles from two different identified models: a conventional 6 DOF rigid body model and a 9 DOF extended model with 2nd order longitudinal and lateral rotor flapping and coning DOF

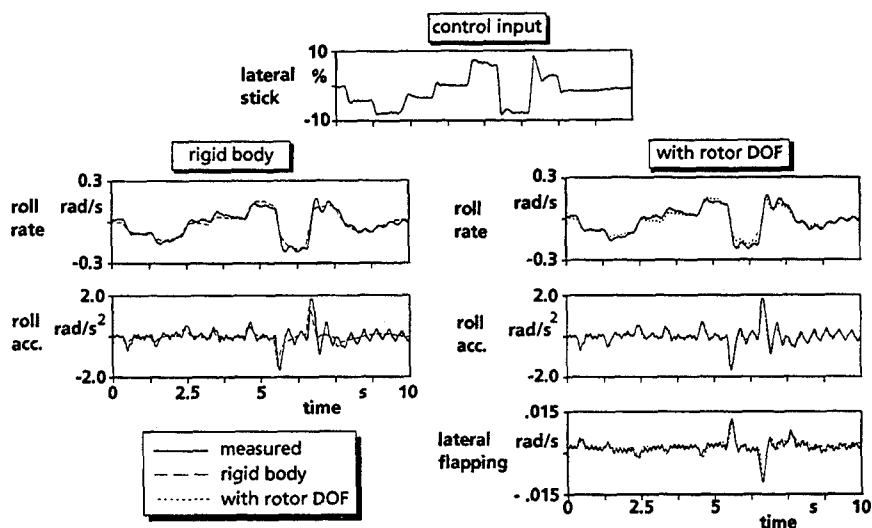


Figure 9. Comparison of flight test data to 6 DOF rigid body and 9 DOF extended model time history responses (BO 105)

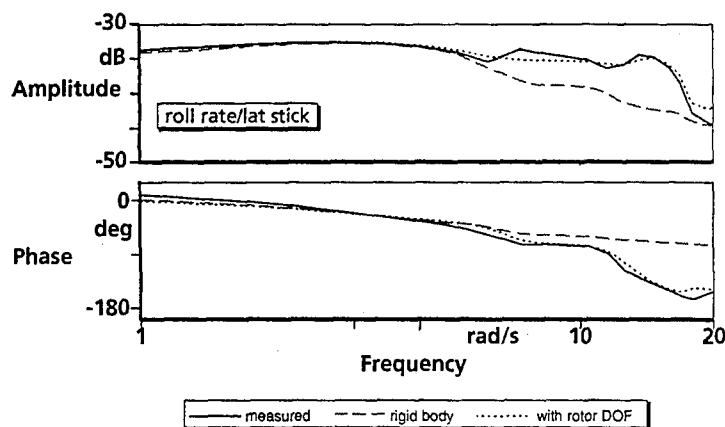


Figure 10. Comparison of BO 105 frequency responses from flight test data, a 6 DOF rigid body model, and a 9 DOF extended model

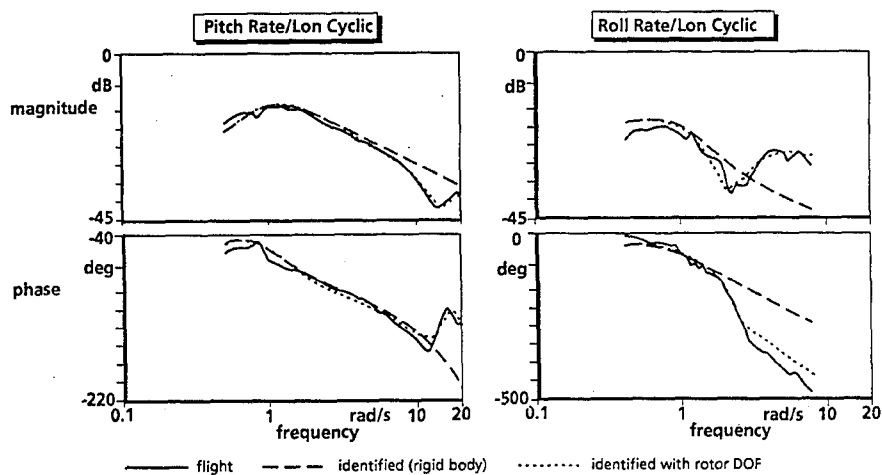


Figure 11. Comparison of UH-60 frequency responses from flight test data, a 6 DOF rigid body model, and a 9 DOF extended model

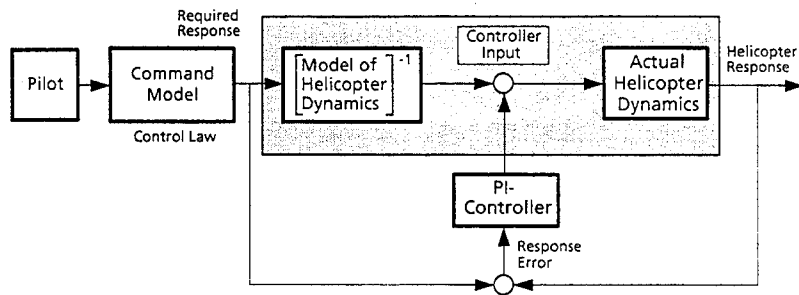


Figure 12. Principle of explicit model-following control system for in-flight simulation

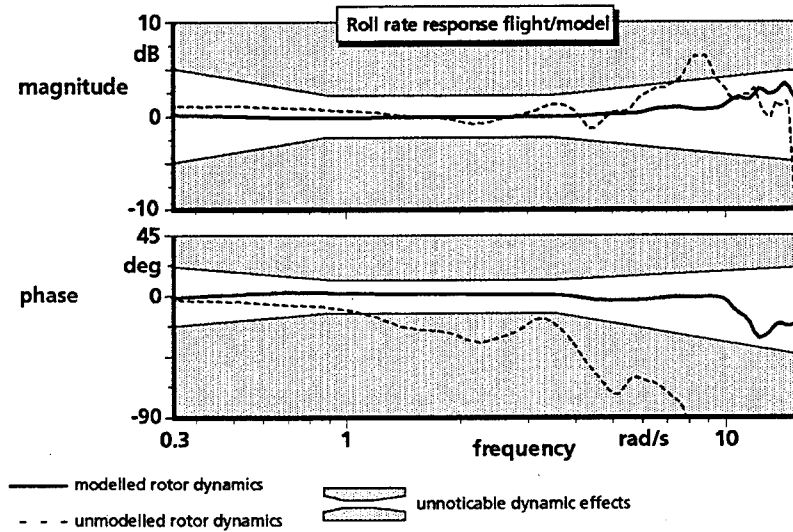


Figure 13. Effect of unmodelled rotor dynamics on the in-flight simulation fidelity of the fly-by-wire BO 105 ATHeS

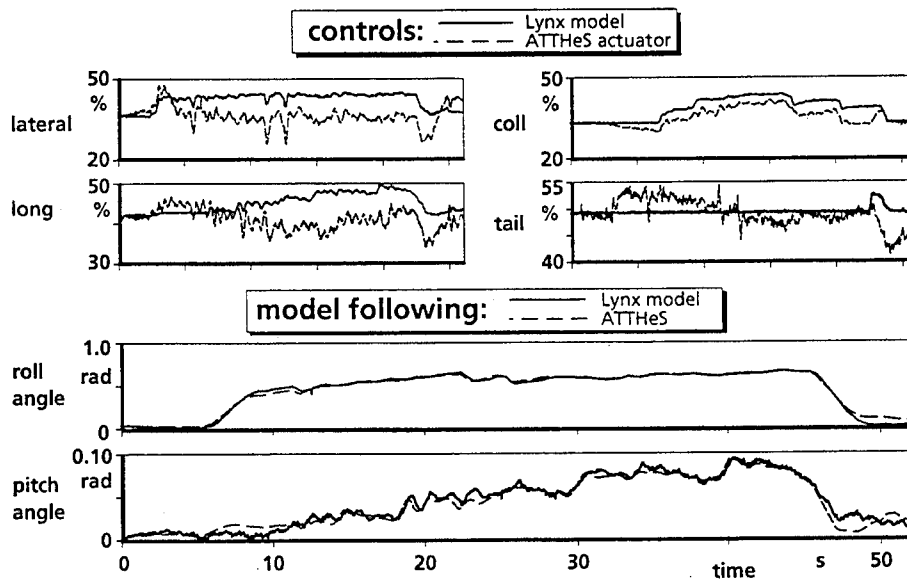


Figure 14. In-flight simulation of Lynx helicopter with BO 105 ATHeS

Effect of Individual Blade Control on Noise Radiation

S. M. Swanson
NASA Ames Research Center
Moffett Field, CA 94035-1000, USA

S. A. Jacklin
NASA Ames Research Center
Moffett Field, CA 94035-1000, USA

G. Niesl
Eurocopter Deutschland GmbH
81663 München, GERMANY

A. Blaas
ZF Luftfahrttechnik GmbH
Kassel-Calden, 34379 Calden, GERMANY

R. Kube
DLR, Lilienthalplatz 7
D-38022 Braunschweig, GERMANY

Abstract

In a joint research programme of NASA Ames Research Center, ZF Luftfahrttechnik, the German Aerospace Research Establishment (DLR), and EUROCOPTER Deutschland, a wind tunnel test was performed to evaluate the effects of Individual Blade Control (IBC) on rotor noise. This test was conducted in the 40x80 ft wind tunnel at NASA Ames Research Center, utilizing a full scale MBB-BO 105 four-bladed rotor system. Three microphones were installed for determination of the radiated noise, two of them on a moveable traverse below the advancing blade side and one in a fixed location below the retreating side.

Acoustic results are presented for flight conditions with Blade-Vortex-Interaction (BVI) noise radiation. High noise level reductions were measured for single harmonic control inputs. In addition to the single harmonic inputs, multi-harmonic inputs were evaluated by superimposing 2/rev to 6/rev harmonics. For the first time the efficiency of sharp wavelets (60 deg and 90 deg width) on acoustic noise were measured. In order to achieve an adequate wavelet shape at the blade tip, corrections were made to account for the blade torsional behaviour.

In parallel with the acoustic measurements, vibratory loads were measured during the BVI flight condition to correlate the effects of IBC on noise and vibrations. It is shown how noise levels and vibrations are affected by specific IBC control inputs. In addition, correlations are made between noise levels and acoustic time histories with IBC phase and amplitude variations. For one IBC input mode with high noise reducing efficiency, a sweep of the movable microphone traverse below the advancing side shows the effect on BVI noise directivity.

1. Introduction

Extremely annoying noise is radiated by a helicopter if the blade tip vortex collides with a following blade. The so-called Blade-Vortex-Interaction (BVI)

noise is primarily radiated during landing approach, when the helicopter is descending into its own rotor wake. Depending on the helicopter design and the actual weight, BVI noise may be generated over a large region of descent flight conditions. Prediction tools capable of designing a helicopter that does not generate BVI noise are currently not available and as such, secondary methods must be used to reduce BVI noise. By a higher harmonic control of the blade pitch, it is possible to modify the miss-distance between the tip vortex and the blade, the vortex strength, or the blade pitch at the position of blade vortex collision in a way that BVI does not occur or is at least reduced in intensity.

First experiments of the noise reduction by a Higher Harmonic blade pitch Control (HHC) have been conducted with actuators in the non-rotating system under the rotor swashplate^{1,2,3,4,5,6}. The shortcoming of HHC in the fixed system is that the pitch angle of one blade cannot be changed without changing the blade pitch of the other blades. Therefore, in case of the 4-bladed rotor, only 3/rev, 4/rev, and 5/rev input modes are possible. This limitation is overcome by introduction of actuators in the rotating system.



Figure 1: Installation of the BO 105 Rotor in the 40x80 ft. Wind Tunnel

presented at the AGARD Aeroacoustic Conference, Oct. 1994, Berlin

For the Individual Blade Control (IBC) system, the conventional blade pitch links are replaced by servo-hydraulic actuators. The actuators, developed by ZF Luftfahrttechnik (former Henschel Flugzeugwerke) were flight tested in 1990 and 1991 on a BO 105 helicopter⁷. The control authority of this system was limited only up to about 0.5 deg due to safety reasons. Although the initial flight tests indicated vibration and noise reductions, the limited thrust and speed of the test aircraft combined with the low authority of the actuators prevented an exploration of the full potential of the IBC system.

Consequently, a new system with higher control authority and with increased frequency response was tested at the National Full Scale Aerodynamic Complex (NFAC) 40- by 80-Foot Wind Tunnel at NASA Ames Research Center. The test was conducted within an international programme between NASA-Ames Research Center, US Army Aeroflightdynamics Directorate, ZF Luftfahrttechnik, the German Aerospace Research Establishment (DLR) and EUROCOPTER DEUTSCHLAND. The programme was supported by the German MOD. A full scale BO 105 rotor system was installed on the NASA/U.S. Army Rotor Test Apparatus which was modified with an IBC system. The primary objectives of the IBC testing were to evaluate the capabilities of such a system to suppress Blade-Vortex-Interaction (BVI) noise, increase rotor performance, and to reduce rotor oscillatory loads and rotor vibrations. This paper presents noise measurement results and analysed acoustic data derived from the IBC wind tunnel entry in spring 1993. A detailed description of the test and the results on rotor performance, loads, and vibrations are given in Reference 8.

2. Test Description

2.1 BO 105 Test Rotor in the Wind Tunnel

A four-bladed BO 105 hingeless main rotor was tested in the 40x80 ft. Wind Tunnel of the NASA Ames Research Center. Figure 1 shows the installation of the rotor in the test section. Table 1 contains the main geometric parameters of the BO 105 rotor design.

Type	Hingeless
Radius	4.90 m
Number of blades	4
Blade chord length	0.27 m
Linear blade twist	-8 deg
Precone	-2.5 deg
Solidity	0.07
Airfoil	NACA 23012

Table 1: BO 105 Rotor Design Characteristics

The rotor was driven by the RTA, a specially designed test rig for operating full scale rotors in the wind tunnels of the NFAC. The rotor performance and the load data were acquired using the static/dynamic rotor balance. The capabilities of the RTA are discussed in more detail in References 8 and 9.

2.2 IBC System

The Individual Blade Control System was installed by replacing the four conventional rotating pitch links between swashplate and rotor blade with servo-hydraulic actuators. These actuators, designed and manufactured by ZF Luftfahrttechnik, apply high frequency control inputs at the blade root in the rotating frame. Commanded and measured actuator strokes are compared separately by two independent systems, consisting of two LVDTs per actuator, twofold signal conditioning, and two computers. A conventional rotor swashplate was used to input collective and cyclic commands required to fly the rotor in the desired condition. The general arrangement of the IBC system on the RTA is shown in Figure 2. Figure 3 shows the IBC actuator installed in the rotor control system.

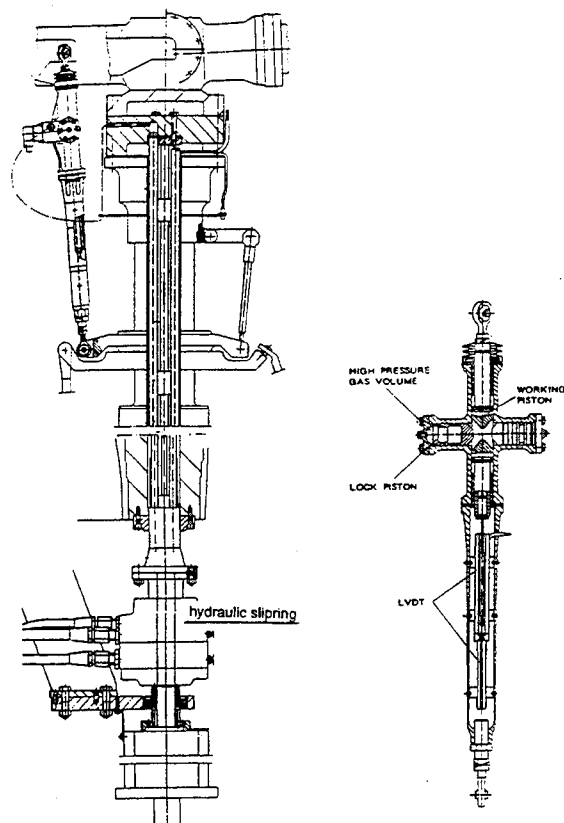


Figure 2: Cross Section of the BO 105 Rotor Hub with the IBC System and the IBC Actuator

The hydraulic power and the control signals are transmitted via slipping devices from the non-rotating to the rotating system and then through the rotor shaft to the hub. The actuators have a stroke of ± 9 mm which results in a maximum blade pitch variation of ± 3 deg at 2/rev input mode. With a frequency response up to 84 Hz, rotor harmonic frequencies up to the 12th harmonic may be excited. For this full-scale test, safety limitations restricted actuator amplitudes to 1.5 deg. Due to structural hardware limitations, only the 2nd through 6th harmonic were available as single frequency inputs and to be summed as multi-harmonic inputs.

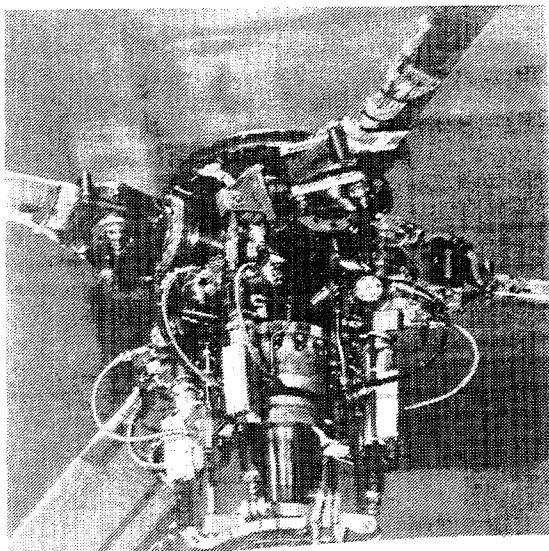


Figure 3: Rotor Hub with IBC Actuators Installed

3. Acoustic Measurement and Analysis

3.1 Test condition

The BVI noise reduction tests were conducted in a simulated flight condition which corresponded to a glide path angle of 6 deg (Table 2). The effective rotor angle-of-attack was determined from flight tests of a BO 105 helicopter ($\alpha_s = 3.9$ deg). Corrected to the wind tunnel test conditions, the resulting geometric shaft angle was 2.9 deg.

Rotor rotational speed	425 RPM
Blade loading C_T/σ	0.070
Helical Tip Mach Number M_{Tip}	0.640
Advance ratio	0.151
Tunnel speed	64 kts
Rotor shaft angle α_s	3.9 deg

Table 2: Nominal Rotor Test Condition for BVI Noise Reduction

During the test, the rotor speed was adjusted to maintain a constant μ and M_{Tip} , by conventional rotor controls set to minimum 1/rev flapping. For safety reasons, no changes in the rotor trim condition were made after the IBC system was activated. To evaluate the effect of these trim offsets on the acoustic measurements, one case was examined with retrimming of the rotor after IBC input. There were no discernible effects found in the trimmed and untrimmed conditions. For the acoustic data presented in this paper, no corrections were applied to account for these trim differences.

3.2 Acoustic Data Acquisition

Figure 4 shows a view of the wind tunnel test section with the microphone locations. The test section is covered by a half foot thick acoustic absorption foam shielded by a perforated metal layer. The thickness of the foam is not sufficient to provide a low cut-off frequency. However, the reflection test and the background noise measurements indicated adequate conditions for the frequency range where BVI noise occurs.

Two microphones (no. 1 and 2) were mounted on the Acoustic Survey Apparatus (ASA) below the advancing blade side of the rotor and one (no. 3) was installed below the retreating side. The ASA is a travelling system that allows for longitudinal movement of the microphones from 8.7 m before to -2.5 m behind the rotor axis.

The data acquisition with the moveable traverse was a very time consuming process. Therefore, the advancing side noise data were measured at a single microphone location with the traverse at the park position (see Fig. 4). This position contained the largest peak-to-peak values for the primary BVI event encountered in the baseline case during the simulated descent flight case. Only for those IBC input conditions which showed high noise reduction were sweeps with the microphone traverse system made in order to identify changes in the noise radiation directivity.

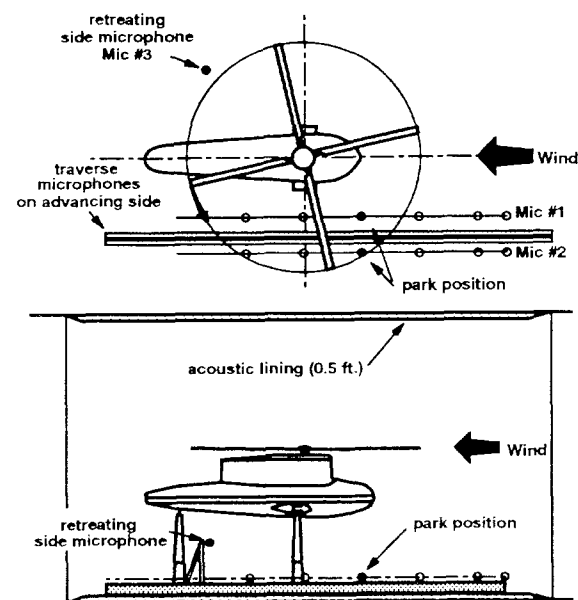


Figure 4: Positions of the Microphones and the Traverse System

The conditioned and amplified microphone signals were recorded onto digital tape at a sample rate of 80,000 samples per second for a measurement time of 30 sec. The data were digitized at a rate of 2048 samples/sec, triggered off the 1/rev signal. Averaged time histories were generated for 40 rotor revolutions, band-pass filtered to emphasize the BVI noise frequency spectra were averaged in the

frequency domain with a bandwidth of 1.7 Hz. The acoustic energy of the band-pass filtered data was used to determine the band limited sound pressure level (BL-SPL), which was used as a comparative index for the different IBC inputs. The frequency limits of the band pass filtering were selected to a range where the BVI noise dominates the frequency spectrum.

Figure 5 shows a spectrum of the advancing blade side BVI noise for the BO 105 rotor without IBC input. Below 150 Hz, the blade loading noise dominates with the majority of the energy in the first and second blade passage frequencies. Between 150 Hz and 1500 Hz, the harmonic noise due to BVI is clearly evident with amplitudes of 10 to 20 dB above the broadband noise. Above 1500 Hz, the BVI noise becomes obscured by the wind tunnel broadband noise. If sound pressure time histories are considered (Figure 6), the band pass filtering removes the blade loading contribution with only minimized effects on the BVI waveform.

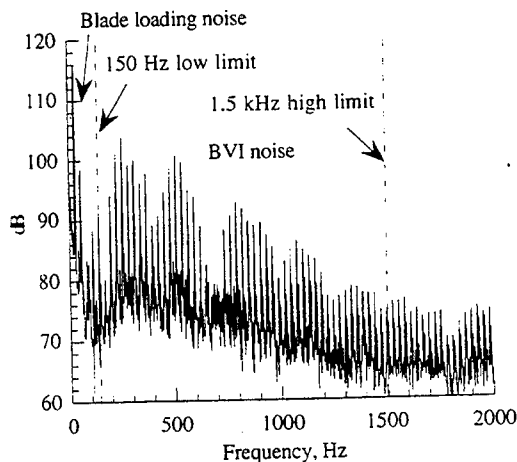


Figure 5: Frequency spectrum of the BO 105 rotor during BVI noise condition¹⁰ (Mic. 1, park position, nominal rotor condition, no IBC)

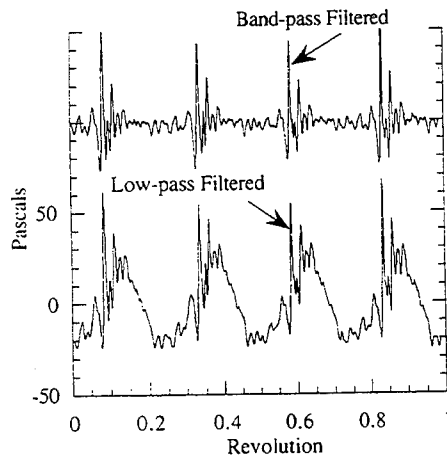


Figure 6: Comparison of band-pass and low-pass time histories for a BO 105 rotor during BVI noise condition¹⁰ (Mic. 1, park position, nominal rotor condition, no IBC)

3.3 Blade Pitch Analysis

With higher harmonic inputs made at the blade root, it is important that the desired higher harmonic function is obtained also along the blade. Prior to the test, it was detected from CAMRAD/JA calculation that the blade torsional behaviour would alter the IBC input magnitude and phase from the blade root to the tip. As the BVI noise is generated at the outer regions of the blade, the resulting blade pitch function on blade tip must be analysed. In order to measure the blade pitch at the tip region, two miniature accelerometers were installed at the blade tip on the leading and the trailing edges. From the accelerometer signals, the magnitude and phase shifts for transforming the input function were determined. The analysis was done for a horizontal flight condition with 43 kt speed, because here a comprehensive data set of all single harmonic input modes was available prior to the acoustic tests. The results are summarized in Table 3. All noise measurement results presented in this paper are referred to azimuth positions corrected to the blade tip.

IBC input mode	Magnitude Amplification $A_i = A / A_0$	Phase Difference ξ_i	Azimuth Phase Shift ψ_i
		deg	deg
2/rev	0.60	-20	-10
3/rev	0.50	-39	-13
4/rev	0.58	-132	-33
5/rev	0.21	-210	-42
6/rev	0.15	-204	-34

Table 3: Blade Torsional Behaviour; Magnitude and Phase Shifts from Blade Root to Blade Tip

4. Single Frequency Input Functions

Single frequency inputs are sine functions whose frequencies are N times the fundamental rotor rotational frequency. The blade pitch curve over azimuth is achieved by superposition of the conventional collective and cyclic rotor control and the higher harmonic blade pitch signal (Figure 7). The blade pitch input of the IBC actuators with single frequencies is determined by the function

$$\Theta_c = A_0 \cos(i \cdot \psi - \varphi_c) \quad (1)$$

where i stands for the single frequency mode, ψ is the rotor azimuth angle, φ_c is the IBC phase angle and A_0 the IBC amplitude.

The function is shifted by 90 deg for each blade, which insures that all blades are affected by IBC in the same way over the entire rotor azimuth, and therefore, the blade dynamics over the entire disc. There are three different effects which may explain the efficiency of higher harmonic control inputs to BVI noise (Figure 8):

- (1) Reduction of the blade pitch angle at the position where blade vortex collision happens.

- (2) Reduction of the vortex strength at the position where the tip vortex is generated.
- (3) Increase of the miss-distance between vortex and blade.

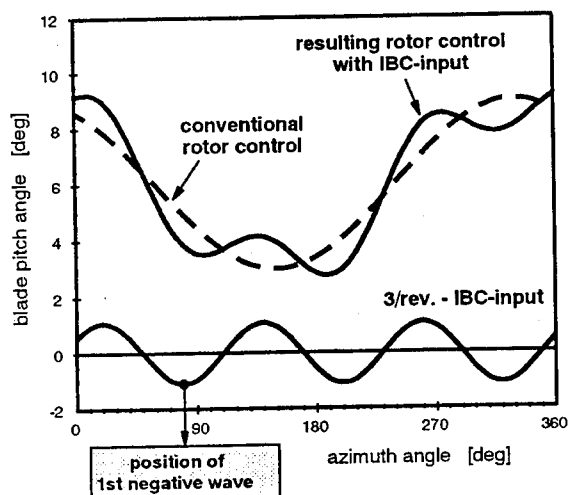


Figure 7: Blade Root Pitch Angle Versus Rotor Azimuth for Conventional Rotor control and a 3/rev Higher Harmonic Signal

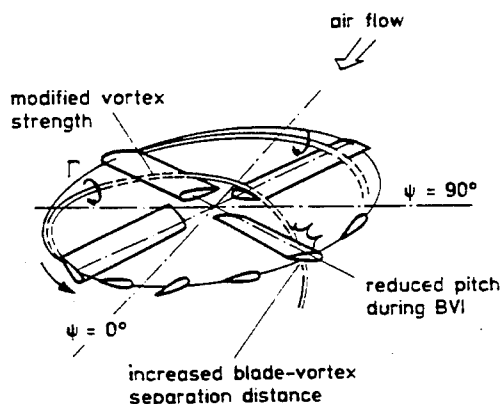


Figure 8: Noise Reduction Mechanism by Higher Harmonic Rotor Control⁵

All three effects are connected to the azimuth region in the rotor disc where the tip vortex is generated and where it moves towards the following blade. During an experiment in the DNW¹¹, the azimuth position of the BVI noise generation was measured for different descent flight conditions. Figure 9 shows measured BVI locations (from the DNW test) for a flight condition similar to the 6 deg descent flight condition chosen for the study. The noise is radiated from about 60 deg azimuth position. Consequently, the corresponding tip vortex is then generated at 120 deg azimuth. On these two positions, the highest noise reductions of IBC inputs are expected.

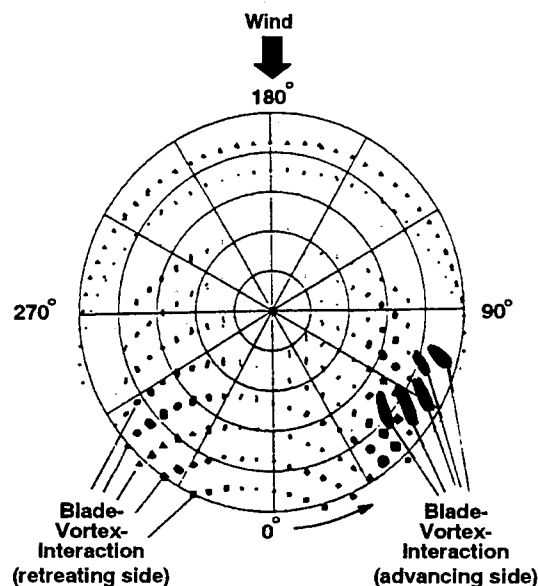


Figure 9: Measured BVI Locations in the rotor disc at 4 deg tip path plane¹¹.

Furthermore, effects number 1 and 2 are presuming a reduction of the blade pitch. Therefore, the most promising kind of analysing the noise versus IBC input is to relate the noise results to the position of the negative wave ψ_{neg} (see Figure 7) on the advancing blade side between 20 deg and 160 deg azimuth position. The pitch angle curve on blade tip is given by the equation

$$\Theta_{C,Tip} = A_i \cdot A_0 \cdot \cos(i \cdot \psi - \varphi_C - \xi_i) \quad (1)$$

where i stands for the single frequency mode, A_i represents the amplification from the root to the tip and ξ_i is the phase shift. It is quite evident, that amplitude and phase of the IBC input are very important for efficient noise reduction, since the strongest BVI is located within a limited azimuth range.

4.1 Acoustic Measurement Results

Figure 10 shows the effects of IBC on the BL-SPL metric for phase sweeps of the 2/rev (Fig. 10a), 3/rev (Fig. 10b), and 6/rev input functions (Fig. 10c). Note that these are for microphone 1 at the park position (see Figure 4). The azimuth regions around 55 deg and 125 deg are marked with shaded bars to emphasize those areas of vortex interaction and generation, respectively. For the 2/rev and 3/rev harmonics, the largest reductions in the BL-SPL were obtained with the negative wave for ψ_{neg} (corrected to blade tip) positioned around these two azimuth regions. If the negative wave was in the region between 60 deg and 120 deg, the BL-SPL increased to a level higher than the non-IBC baseline value.

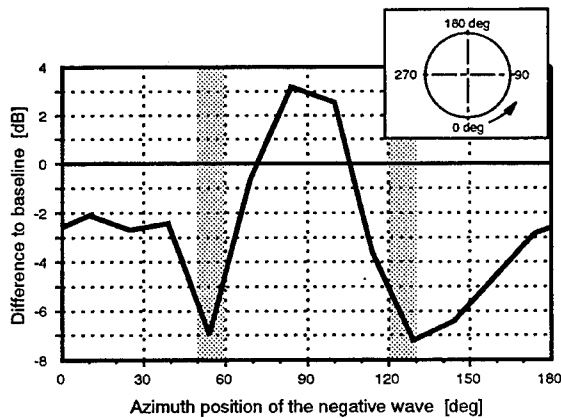


Figure 10a: 2/rev IBC input

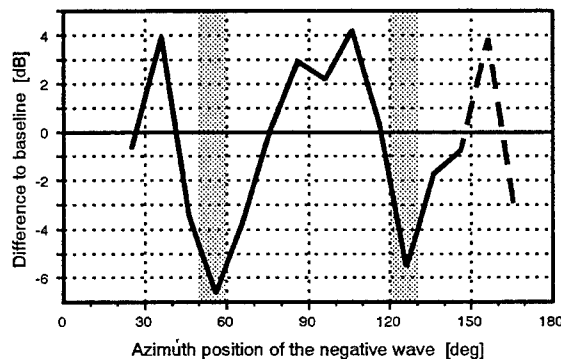


Figure 10b: 3/rev IBC input

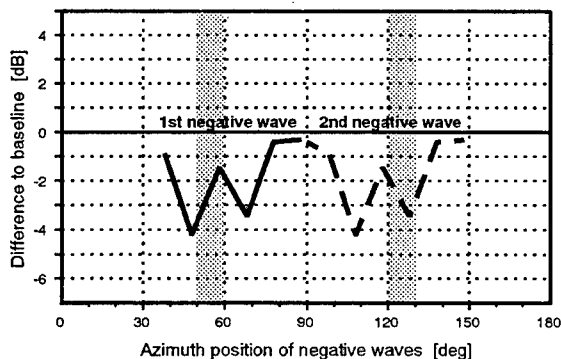


Figure 10c: 6/rev IBC input

Figure 10: Variation in BL-SPL for 2-, 3- and 6/rev IBC Input Function Versus the Position of the Maximum Negative Amplitude on the Advancing Blade Side Corrected to the Tip (Microphone 1, nominal rotor condition, 1 deg IBC Amplitude)

A similar behaviour occurred for the 6/rev input function where a reduction was observed for 50 deg and 130 deg. However, there are two further noise reduction peaks. The 6/rev sinus function is so small, that if one negative wave is at 50 deg azimuth, a second negative wave is within the region from 60 deg to 120 deg which always caused an increase of BVI noise with 2/rev and 3/rev IBC inputs. Therefore, the efficiency of the 6/rev input is reduced compared to

lower harmonic input functions. This is also the case at 6/rev if a negative wave is positioned at 130 deg azimuth.

An analysis of the pressure time histories for a 3/rev IBC input at the positions of highest noise reduction (55 deg and 125 deg azimuth) is presented in Figure 11. Both input functions show an elimination of the primary BVI events encountered in the baseline case.

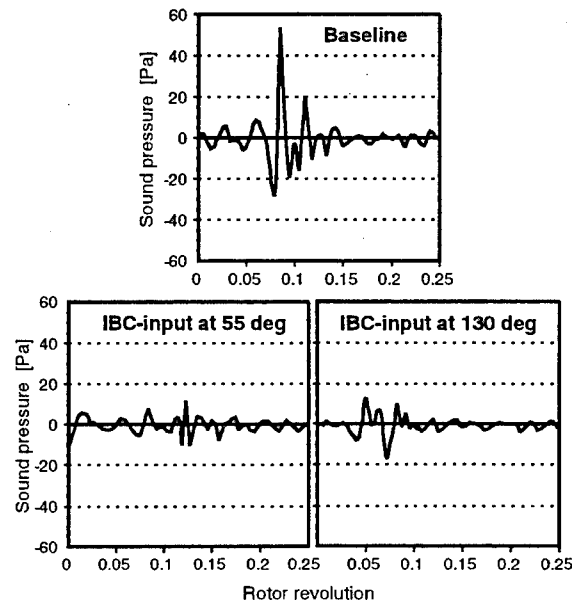


Figure 11: Acoustic Pressure Time Histories for Baseline and 3/rev IBC input (microphone 1 at park position, nominal rotor conditions)

In addition to being a function of IBC phase, the BVI noise is also affected by the input amplitude. As an initial look at the effects of amplitude, an amplitude sweep was conducted for the 2/rev harmonic from 0.4 deg to 1.2 deg with an IBC phase at 130 deg azimuth. The data in Figure 12 show that even with only 0.4 deg amplitude, a considerable reduction can be achieved. Larger noise reductions are seen for 0.8 deg amplitude, whereas for 1.2 deg only smaller additional reductions were measured. For a 2/rev input, large actuator inputs are not necessary to achieve sufficient BVI reduction. This is of special importance, if an additional amplitude angle is necessary at other harmonic inputs (e.g. 3/rev or 4/rev) in order to get improvement of other rotor characteristics (e.g. vibration reduction). It should be noted that this amplitude sweep was completed at only one IBC phase angle and may have different results if another phase angle were considered, for example at the azimuth position of BVI occurrence (55 deg azimuth).

For all IBC cases which show high noise reduction, the two microphones on the advancing blade side were traversed in a horizontal plane below the rotor. The contour plots in Figure 13 show a comparison of the noise directivity of the baseline case with the IBC input

at 130 deg azimuth. In front of the rotor axis, where intensive BVI noise is radiated, noise reductions up to 7 dB can be seen. No reduction was measured in downward direction below the rotor hub. A shift of the BVI noise region, which indicates that the BVI noise is not really reduced but only changed in directivity, could not be observed.

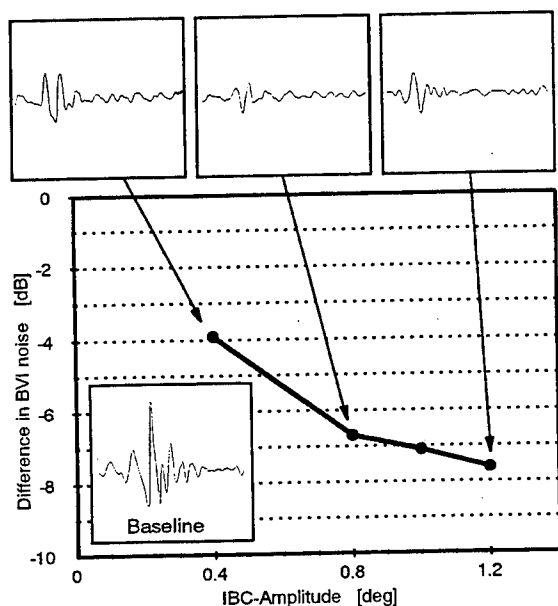


Figure 12: Noise Reduction and Sound Pressure Time Histories versus the IBC Blade Pitch Amplitude (2/rev IBC input, negative wave at 130 deg azimuth)

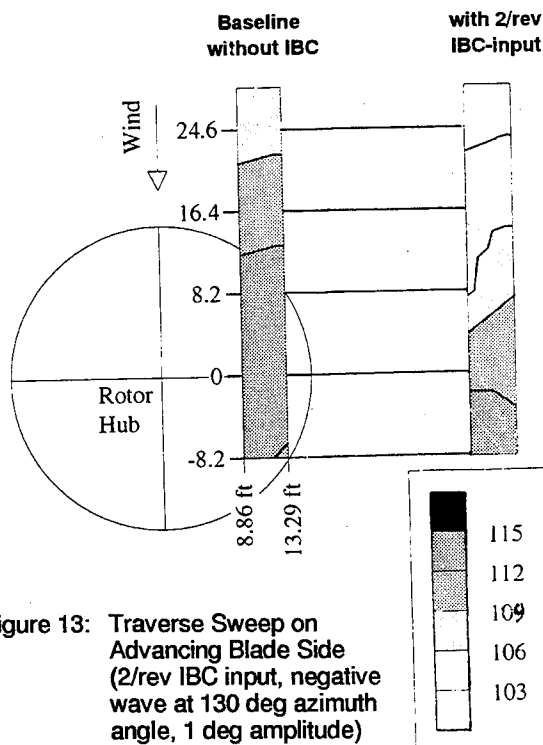


Figure 13: Traverse Sweep on Advancing Blade Side (2/rev IBC input, negative wave at 130 deg azimuth angle, 1 deg amplitude)

4.2 Reduction of Retreating Side BVI

Regarding Figure 9, BVI noise on the retreating side is generated in the region between 300 deg and 330 deg rotor azimuth. Results for noise reduction with 2/rev IBC input on the retreating side are shown in Figure 14. Hereby, the noise reduction is shown versus the rotor azimuth position of the negative wave on the retreating side between 180 deg and 360 deg. IBC inputs lead to a high noise reduction of about 7 dB at 220 deg azimuth angle. That is the region where the tip vortex for retreating side BVI is generated. However, at the azimuth position where BVI occurs, no noise reduction but a noise increase is obtained with IBC input.

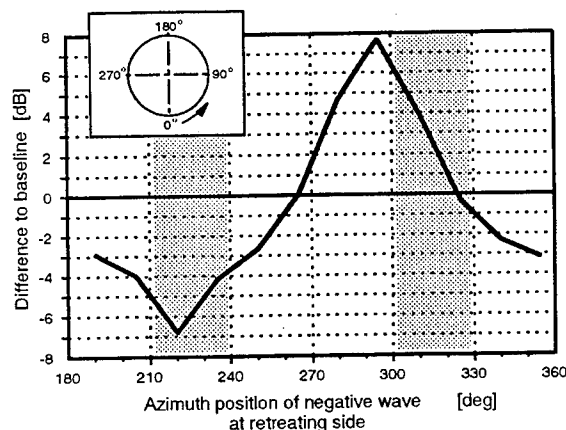


Figure 14: Reduction of Retreating Side BVI noise (2/rev IBC input)

If the IBC phases for the best noise reduction on advancing blade side are considered (Figure 10a), the input function with a negative wave at 130 deg azimuth position has a corresponding negative wave on the retreating side at 310 deg. The very successful IBC input on the advancing side leads to a noise increase on the retreating side. In contrast to the second phase angle with a noise reduction on the advancing side at 55 deg azimuth the corresponding negative wave on the retreating side at 235 deg also shows a reduction of the retreating side BVI noise.

4.3 Comparison with HHC Noise Measurements

Figure 15 shows a comparison between the full-scale IBC noise measurements and the small-scale HHC noise measurements acquired at the DNW⁵. As the actuators in the DNW test were arranged in the non-rotating system, only the 3/rev inputs can be compared. The microphone locations on the traverse system of the full-scale test were designed to match the earlier DNW test increased to account for the model scale differences. Additionally, wind tunnel corrections were applied to account for the closed test section of the NASA full-scale test and the open test section of the DNW wind tunnel. Finally, the blade torsional behaviour of the DNW model scale rotor was determined to adjust the phase input to the blade tip.

A similar noise reduction behaviour can be observed for both tests. The two azimuth positions where noise reductions occurred for the DNW test, 60 deg and 120 deg, were slightly different than the two positions indicated in the full-scale test. Although both tests were conducted starting from the same helicopter flight procedure, the resulting flight condition in the wind tunnels were not exactly the same for the NASA Ames test and the DNW test which is probable caused by different wind tunnel corrections. If the flight condition changes, measurements of the BVI noise characteristics¹¹ have shown that the BVI region also shifts.

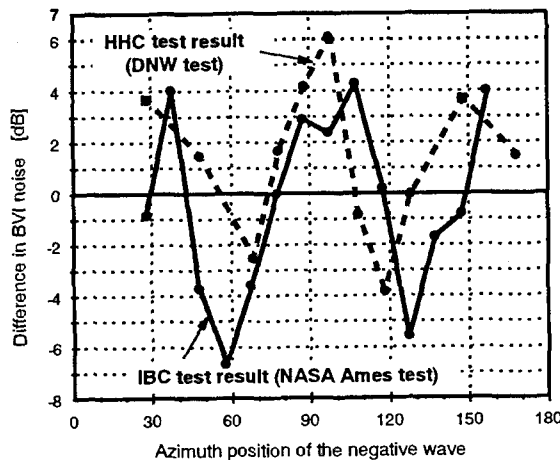


Figure 15: Comparison of the NASA Ames IBC tests with DNW HHC tests (input mode 3/rev with 1 deg amplitude, both tests aiming at a 6 deg descent flight condition at 33 m/s speed)

5. Multi-harmonic Input Functions

A major advantage of the IBC system is seen in the capability to introduce combinations of harmonics starting at the 2/rev input mode. Special blade pitch functions can be formed by Fourier synthesis. One idea was to generate a pulse which changes the blade pitch only over a small azimuth range whereas the blade pitch over the rest of the rotor disc is not affected. The Fourier coefficient were determined for a pulse with an azimuth width of 60 deg. This 60 deg pulse shows a large overshoot due to a limitation on the number of harmonics available. With respect to the good results obtained by 2/rev single frequency input, another pulse was defined with a 90 deg azimuth width. This pulse would be similar to a half wave of the 2/rev single harmonic, with only little overshoot in the remaining 270 deg. Both pulses are shown in Figure 16 compared to a second harmonic single frequency input.

Figure 17 shows the noise reduction for the 60 deg pulse as a function of the azimuth position of the pulse. Note that there is no correlation with the vortex generation location nor the BVI location discussed earlier. This was expected due to the effects of the blade torsional behaviour on the blade tip described in Chapter 3.3.

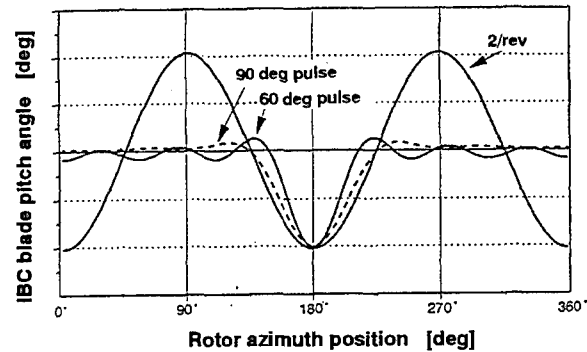


Figure 16: Definition of Multi-harmonic Input Functions (pulse at blade root or wavelet at blade tip) Compared to a 2/rev Single Frequency Input Function

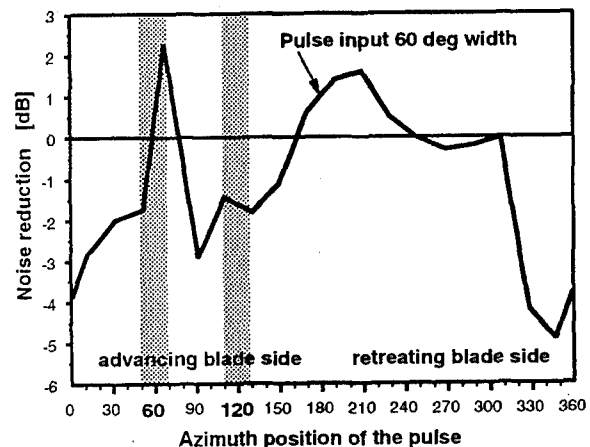


Figure 17: Noise Results by Input of a Pulse at Blade Root

The noise results of the pulse input are more clear if the pitch angle on the blade tip is regarded. The highest noise reduction was obtained for a pulse input at 350 deg azimuth angle: The corresponding blade pitch curves of root and tip analysed from the blade tip accelerometers are shown in Figure 18. The pulse function contains two negative pitch motions in 1st and 2nd quadrants of the rotor disc. This was shown for the single-harmonic input to generate a reduction of BVI noise. If a pulse at 70 deg azimuth is considered (Figure 19), the blade pitch motion contains a decrease in the pitch mainly around 90 deg azimuth range. This was found for the single frequency inputs to lead to an increase in the BVI noise (Figure 10).

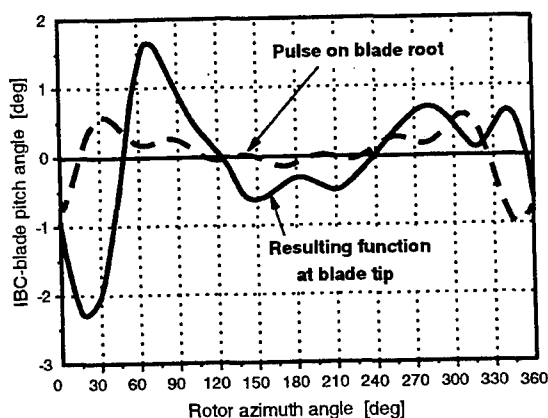


Figure 18: Blade Pitch Curve at Blade Root and Blade Tip for a Pulse Input at 350 deg azimuth angle

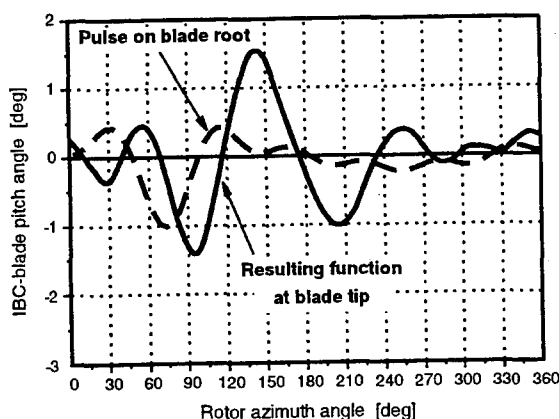


Figure 19: Blade Pitch Curve at Blade Root and Blade Tip for a Pulse Input at 70 deg azimuth angle

Following the idea to correlate all input functions to the outer region of the blade where BVI is generated, the multi-harmonic input at the blade root was modified in a way to get a pulse function at the blade tip. This input, which then was called a "Wavelet", is shown in principle in Figure 20. The dynamic behaviour of the blade is taken into account as derived from the blade tip accelerometers (see Chapter 3.3).

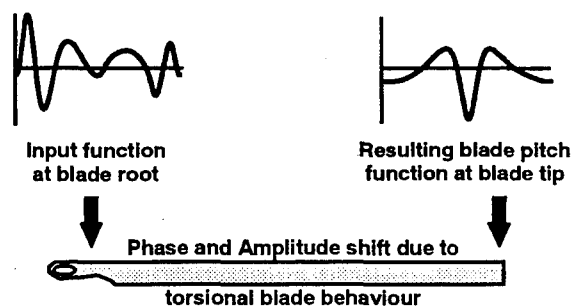


Figure 20: Definition of the Input Function at Blade Root Including the Phase Shift to Blade Tip

The effects of the IBC wavelet input on the BL-SPL for microphone 1 are summarized in Figure 21. It shows results for the 60 deg width and the 90 deg width. Noise reductions were found in the 1st and the 2nd rotor quadrant which corresponds well with the results of the single frequency inputs. However, the reductions were not as high as expected and additional reduction occurred at other azimuth positions. Further study on the wavelet inputs through examination of the blade tip accelerometers helps to explain the low success of the wavelets (Figure 22). It can be seen that the desired wavelet is not transferred to the tip as expected. The negative peak is nearly at the correct azimuth positions, but there are high overshoots and peaks at other azimuth positions which indicate that the blade torsional behaviour is much more complex. The overshoots are probably caused by inter-harmonic coupling: Recent analyses showed, that by introduction of one harmonic input, the neighbour harmonics are also excited at the blade tip.

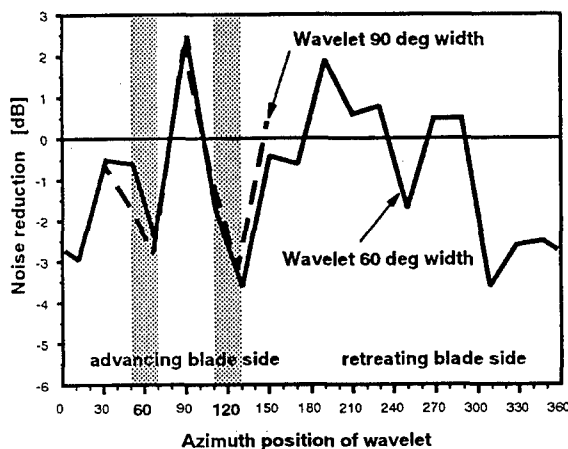


Figure 21: Noise Results by Input of a Wavelet at Blade Tip

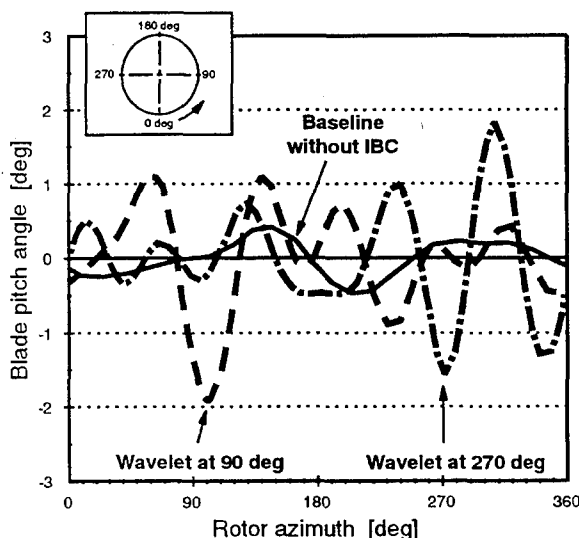


Figure 22: Analysed Blade Pitch Curves at Blade tip

6. Flight Condition Variation

Up to now, the data presented has been for one flight condition, selected because of its high BVI noise. The effect of a change in the flight condition was also simulated by tilting the rotor tip path plane. Two different IBC inputs were tested with variations in the tip path plane angle. These were a 2/rev input with the negative wave at 55 deg and a 2/rev input with the negative wave at 130 deg. Both inputs showed high noise level reductions at the initial tip path plane setting of 2.9 deg, which corresponds to a BO 105 descent flight with 6 deg glide path angle.

The difference between the baseline case and the 2/rev IBC condition for a variation in the descent flight path is presented in Figure 23. If the rotor control and the IBC control conditions are maintained, the IBC input may have a negative effect on noise emission: At 5.5 deg tip path plane, a negative blade pitch input at 130 deg azimuth increases the noise by 4.5 dB.

It is assumed that the wake field is changed in a way which may reduce the miss-distance between blade and wake. High BVI noise is then generated in a flight condition which normally shows lower BVI. The theory is supported by sound pressure time histories, presented in Figure 24. At 3 deg tip path plane, strong BVI noise peaks are generated in the baseline case which are significantly reduced by the IBC system. At 5.5 deg tip path plane, lower BVI noise can be seen in the baseline case. However, with IBC input at 130 deg, the BVI peaks increase strongly.

The measurements of the tip path plane variations clearly show the need for a closed loop control system in order to guarantee an optimum noise reduction during alternating flight conditions.

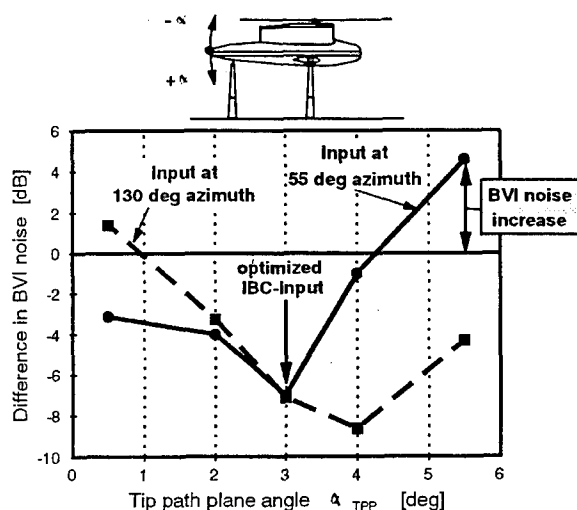


Figure 23: Noise Radiation Versus Tip Path Plane Angle with two Fixed IBC Settings (1 deg Amplitude, Microphone 1 at Park Position)

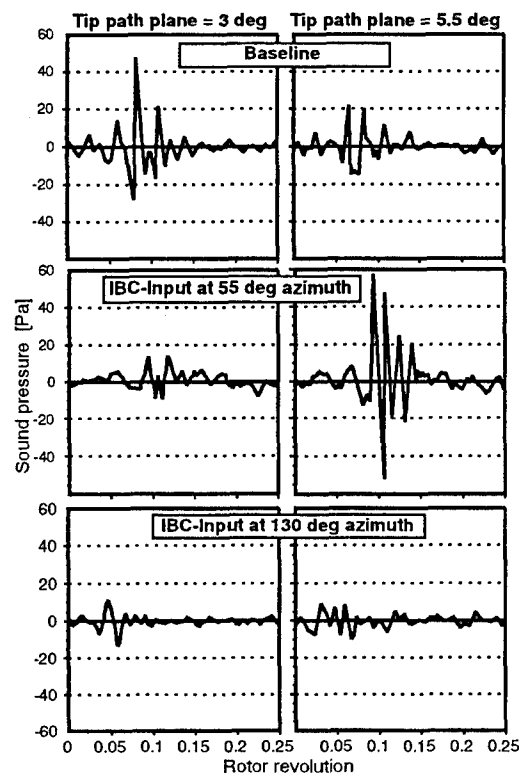


Figure 24: Pressure Time Histories with and without IBC for two flight conditions and two different IBC input Phases (IBC Amplitude 1 deg, Microphone 1 at Park Position)

7. Noise Results of IBC Flight Tests

A similar IBC system, designed and manufactured by ZF Luftfahrttechnik was flight tested in 1990 and 1991 on a BO 105 helicopter. It represented the first flying four-bladed helicopter with the blades individually controlled. For safety reasons, the control authority, the flight velocity, and the loading factor were limited during the test. In addition, the harmonic modes were limited from 2/rev to 5/rev in order to reduce the number of free control parameters.

The flight tests aiming for noise reduction were performed by applying only a 5/rev control. Based on the DNW wind tunnel tests⁵, the 5/rev mode was very promising as it showed a smooth behaviour. During the flight test, the helicopter performed a descent flight with a velocity of 33 m/s and a glide path angle of 6 deg over a ground microphone. This was the same flight condition as the nominal IBC condition in the wind tunnel, except that in the wind tunnel, the controls were trimmed for zero hub moment. Due to the necessary repeats of the flights in order to get an average noise level, the small number of test points required a considerable long test time, especially if compared with the IBC wind tunnel test.

Figure 25 shows the noise radiation presented in the same way as the IBC wind tunnel test results. The highest noise reduction are obtained at an azimuth of about 120 deg. It can be noted that a small noise increase was measured at 100 deg. The shape of the noise radiation versus IBC input confirms the behaviour measured in the wind tunnel test, where noise reductions occurred for a negative wave of the IBC input in the 60 deg and 120 deg regions. The noise radiation time history is presented in Figure 26. The BVI noise was reduced by about 4 dBA during flyover. The successful reduction of noise impulsiveness can be seen from the change in the signal pattern of the sound pressure time histories.

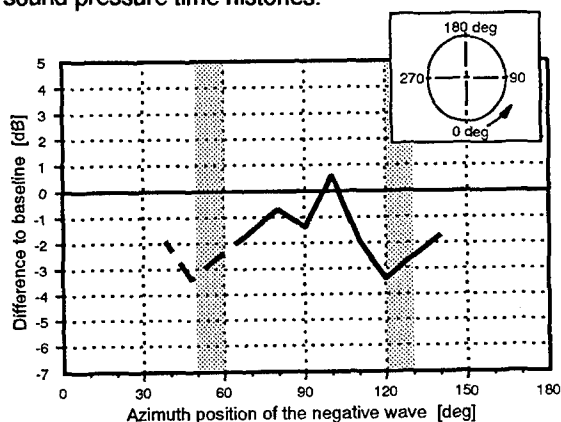


Figure 25: Noise Measurement Results of a Flight Test with IBC on a BO 105 Helicopter (Input mode 5/rev, 0.5 deg amplitude, centerline microphone)

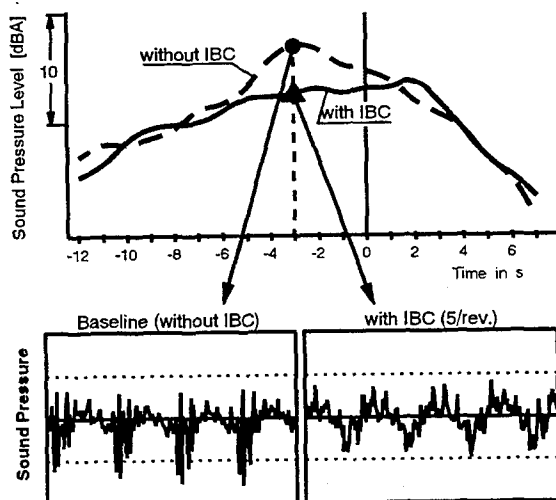


Figure 26: Flyover Noise Time Histories of a BO 105 with and without IBC control (Input mode 5/rev, 0.5 deg amplitude, negative blade pitch at 120 deg azimuth, centerline microphone)

8. Effect of IBC Input on Noise and Vibrations

Although not in the scope of this paper, the question of the combined effect on noise and vibration with IBC should be broached. First measurements of noise and vibrations with higher-harmonic control^{4,5,6} indicated that noise reduction is related to a vibration increase and vice versa.

The effect of a 2/rev IBC input versus the azimuth angle of the negative wave on BVI noise emission and vibratory loads is shown in Figures 27 and 28 for the low speed 6 deg descent flight condition. On positions where high noise reductions were observed, vibratory loads are at least in the same level as the baseline. Some components like the rolling moment and the lateral force even increase significantly. On the other side, vibrations are lower if the negative IBC input is positioned on an azimuth region where BVI noise is increased.

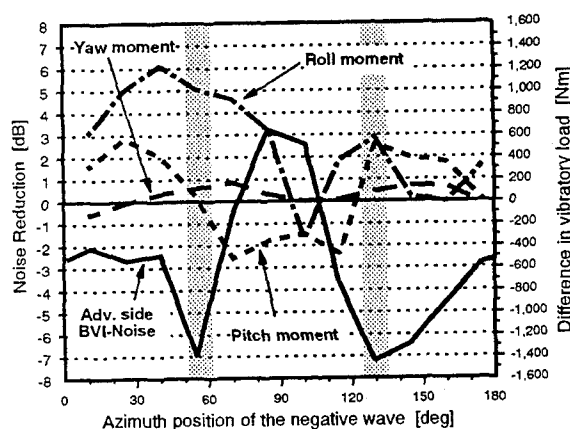


Figure 27: Effect of an IBC 2/rev Input (1 deg Amplitude) on Noise and Vibratory Rotor Moments (Mic. 1 at Park Position)

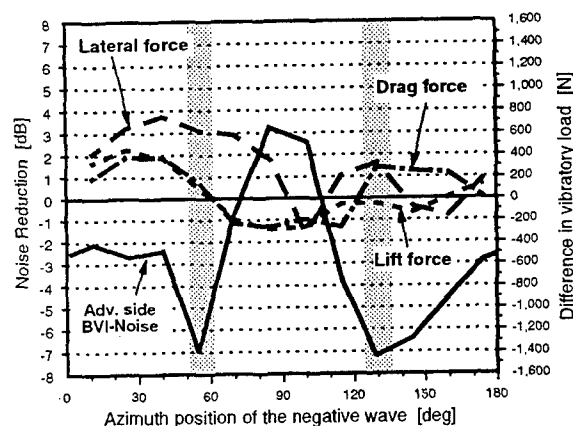


Figure 28: Effect of an IBC 2/rev Input (1 deg Amplitude) on Noise and Vibratory Rotor Forces (Mic. 1 at Park Position)

The situation is even worse if a 3/rev input mode with 1 deg amplitude is considered. Here, the IBC amplitude is higher than necessary for a vibration reduction. High compensations of vibratory loads are obtained with 0.25 deg to 0.5 deg amplitude. At 1 deg amplitude all vibratory forces and moments are increased compared to the baseline case.

The unfavourable behaviour of BVI noise and vibrations with higher harmonic control leads to the concept of multiharmonic input functions, where some single harmonic functions are addressed for vibrations and others for noise reduction. In principle, the feasibility of multiharmonic inputs were confirmed during the HHC test in the DNW. However, as IBC offers more modes compared to HHC in the non-rotating system, the combined noise and vibration reduction is expected to be more efficient.

Conclusions

Rotor control systems, offering Individual Blade Control capabilities are the most promising technology to modify and improve future rotor systems. Active rotor control technology is the only chance to influence directly the rotor characteristics over a wide range of flight conditions. It can be adapted for special flight requirements such as reduced noise, improved rotor performance, or increased ride comfort.

The individual blade control has been proved to be very effective for BVI noise reduction. Noise reductions up to 7 dB were measured by different single frequency input modes. The measurements proved at least two of the effects which were thought to be responsible for the noise reduction: The reduction of the blade pitch at the tip vortex generation region and at the rotor disc section of blade-vortex interaction. Due to the complex dynamic behaviour of the blades, a wavelet generated at the blade tip was not as effective as expected.

First test with flight condition variation indicated the need for a fast closed loop control system which is able to control the phase with respect to BVI noise generation region. In view of the current knowledge, a control concept at least for the advancing side BVI noise reduction will be based on the identification of the azimuth region in the rotor disc where the BVI noise is generated. This may be done by appropriate filtered sensor signals (for example blade pressures).

At an optimum IBC control setting for BVI noise reduction, some of the vibratory loads are increased. However, for an application of the IBC technology on the helicopter, it is necessary to achieve the BVI noise reduction without severe penalties in ride comfort. Therefore, an additional effort is necessary to investigate multi-harmonic inputs in order to address both noise and vibration reduction.

Acknowledgement

The authors thank Mr. Earl Booth of NASA Langley Research Center and Mr. Dietrich Teves from EUROCOPTER DEUTSCHLAND for their helpful advices and their help in the analysis of the acoustic and vibratory data.

References

- /1/ Wood, E.R., Powers, R.W., Cline, J.H., Hammond, C.E., "On Development and Flight Testing a Higher Harmonic Control System", *Journal of the American Helicopter Society*, Volume 30, No. 1, January 1985
- /2/ Lehmann, G., "The Effect of Higher Harmonic Control (HHC) on a Four-Bladed Hingeless Model Rotor", *Vertica*, Vol. 9, No. 3, 1985
- /3/ Brooks, F.T., Booth, E.R., Jolly, J.R., Yeager, W.T., Wilbur, M.L., "Reduction of Blade-Vortex Interaction Noise Through Higher Harmonic Pitch Control", *Vertiflite*, January 1990
- /4/ Splettstößer W.R., Lehmann G., van der Wall B., "Higher Harmonic Control of a Helicopter Rotor to Reduces Blade-Vortex-Interaction Noise", 15th European Rotorcraft Forum, Sept. 1989
- /5/ Splettstößer, W.R., Schultz, K.J., Kube, R., Brooks, T.F., Booth, jr. E.R., Niesl, G.H. and Streby, O., "BVI Impulsive Noise Reduction by Higher Harmonic Pitch Control: Results of a Scaled Model Rotor Experiment in the DNW", Seventeenth European Rotorcraft Forum, Berlin, Germany, 1991
- /6/ Kube R., Achache M., Niesl G., Splettstößer W., "A Closed Loop Controller for BVI Impulsive Noise Reduction by Higher Harmonic Control.", pres. at the American Helicopter Society 48th Annual Forum, Washington D.C. 1992
- /7/ Richter, P., Eisbrecher, H.-D., Klöppel, V., "Design and First Tests of Individual Blade Control Actuators", 16th European Rotorcraft Forum, Glasgow, 1990
- /8/ Jacklin S.A., Nguyen K., Blaas A. and Richter P., "Full-Scale Wind Tunnel Test of a Helicopter Individual Blade Control (IBC) System", *American Helicopter Society 50th Annual Forum*, Washington D.C., May 1994.
- /9/ Norman T.R., Cooper C.R., Fredrickson C.A., Herter J.R., "Full Scale Wind Tunnel Evaluation of the Sikorsky Five-Bladed Bearingless Main Rotor", pres. at the American Helicopter Society 49th Annual Forum, St. Louis, 1993
- /10/ Swanson S.M., Jacklin A.J., Blaas A., Kube R., Niesl G., "Individual Blade Control Effects on Blade-Vortex Interaction Noise", pres. at the American Helicopter Society 50th Annual Forum, Washington D.C., May 1994
- /11/ Splettstößer W.R., Schultz K.J., Martin R.M., "Rotor Blade-Vortex Interaction Noise Source Identification and Correlation with Rotor Wake Prediction", *AIAA 11th Aeroacoustic Conference*, AIAA-87-2744, Oct. 1987

A STUDY OF BLADE-VORTEX INTERACTION AEROACOUSTICS UTILIZING AN INDEPENDENTLY GENERATED VORTEX

C. Kitaplioglu* and F.X. Caradonna+
NASA Ames Research Center
Moffett Field, California 94035
USA

Abstract

This paper presents results from an experimental study of rotor blade-vortex interaction (BVI) aerodynamics and acoustics. The experiment utilized an externally generated vortex interacting with a two-bladed rotor operating at zero thrust to minimize the influence of the rotor's own wake. The rotor blades were instrumented with a total of 60 absolute pressure transducers at three spanwise and ten chordwise stations on both the upper and lower surfaces. Acoustic data were obtained with fixed near-field microphones as well as a movable array of far-field microphones. The test was carried out in the acoustically treated test section of the NASA Ames 80- by 120-Foot Wind Tunnel. Several parameters which influence BVI, such as vortex-rotor separation distance, vortex strength, and vortex sense (swirl direction), as well as rotor tip Mach number and advance ratio, were varied. Simultaneous measurements were obtained of blade surface pressure distributions, near-field acoustics, and far-field acoustics during the vortex-blade encounters.

Nomenclature

c	blade chord
R	rotor radius
α_v	vortex generator angle of attack
z_v	vortex location relative to rotor plane
x, y, z	coordinate system centered on the rotor hub
ψ	azimuth angle measured positive in direction of rotation; $\psi=0$ is downstream
ϕ	elevation angle measured positive down from rotor plane
μ	rotor advance ratio
M_{tip}	hover tip Mach number
$C_p = (p - p_s)/0.5 \rho V_\infty^2$	pressure coefficient
ρ	density
V_∞	tunnel free stream velocity
p	pressure
p_s	static pressure
$L_p = 20 \log_{10}(p/p_{ref})$	Sound Pressure Level (dB)
p_{ref}	reference pressure (2×10^{-5} Pascals, unless otherwise noted)
χ_{bvi}	BVI pressure increment
Π_{bvi}	BVI acoustic amplitude

* Aerospace Engineer, NASA Ames Research Center

+ Staff Scientist, U.S. Army ATCOM Aeroflightdynamics Directorate

Presented at the AGARD Fluid Dynamics Panel Symposium on Aerodynamics and Aeroacoustics of Rotorcraft, Berlin, Germany, October 10-14, 1994.

Introduction

The interaction of a rotor with one or more of its tip vortices can occur in many forms and is a topic of considerable interest. Such interactions are a primary source of rotor vibratory loading. When the rotor blade and the tip vortex are very close and nearly parallel to each other the interaction is particularly strong (though of short duration) and is a major source of rotorcraft noise. This type of interaction is usually referred to as a parallel "BVI" (Blade-Vortex Interaction) and is the subject of this experimental investigation.

A large number of aerodynamic and acoustic computational codes (Refs. 1-5), embodying a wide range of physical models of BVI, have been developed. The aerodynamic models range from two-dimensional, ideal-flow, "vortex-cloud" methods employing conformal mapping solutions to 3-D, compressible Euler/Navier-Stokes CFD methods - with the middle-ground being held by 3-D full-potential CFD methods. Acoustic prediction methods are of two types; the acoustic analogy methods and the more recent Kirchhoff methods. CFD is also used for acoustics but cannot practically be extended to the far-field that acoustics is ultimately concerned with. Nevertheless, CFD has great potential for providing input for Kirchhoff methods. The choice between these methods is dependent on the extent to which flow-field non-linearity dominates the solution. Therefore the near-field aerodynamics is of critical importance both for determining the essential physics and the type of acoustic method that must be used. It is crucially important that we develop combined aeroacoustic computational methods in which we have high confidence. Such confidence requires validation using the simplest possible tests. Until the present, however, all BVI aeroacoustic tests have involved the use of full rotor models operating at typical flight conditions. The complexities of typical rotor flows (with wake geometries whose strength and locations with respect to the blade are difficult to determine) are considerable. We have taken a different approach by performing an experiment which, rather than operating a rotor under typical flight conditions generating BVI, creates a situation that closely resembles the simplified geometry found in the most basic CFD codes. In effect, rather than refining the model to account for real world complexities, we have attempted to refine the experiment to reflect the simplest possible computational model of BVI. If the codes cannot do a good job of correlating with a simplified experiment, there is little reason to expect good correlation with real flight data with all of its complications.

This paper describes the wind tunnel experiment designed to investigate the fundamentals of BVI aeroacoustics and presents some representative blade pressure and far-field acoustic data.

Description of Experiment

The objective of the test was to experimentally simulate the aerodynamics and acoustics of parallel (2-D), unsteady BVI. The main point of the experiment was to set up a situation that matched, as closely as possible, the simplified model of a rotor blade undergoing an unsteady, parallel interaction with a vortex. Figure 1, taken from Ref. 1, illustrates this simple 2-D BVI model. To provide independent control of the interaction parameters, the vortex was generated separately by a wing tip, placed upstream of the rotor and set at an angle of attack. The rotor was operated at zero thrust to minimize the influence of the rotor's own wake/tip-vortex system. The relative positions of the rotor and wing ensure parallelism of the interaction. Figures 2 and 3 illustrate the experimental arrangement in the acoustically treated test section of the NASA Ames 80- by 120-Foot Wind Tunnel. Two similar experiments were previously performed by Caradonna (Refs. 6-8); however, that work focused on the aerodynamic aspects of the problem and did not include acoustic measurements because the wind tunnel had acoustically reflective walls. The present experiment extends that work to include acoustic studies.

The major parameters that influence parallel, unsteady BVI are vortex strength and sense (determined by the vortex generator angle of attack, α_v), vortex-blade separation distance (z_v), rotor advance ratio (μ), and hover tip Mach number (M_{tip}). These were all independently controlled.

A small-scale (7-foot diameter), two-bladed, teetering rotor was used. The blades are untwisted and have a rectangular planform with NACA 0012 airfoil sections of 6-inch chord. The blade Reynolds number was of the order of 10^6 .

The blade surface pressure distribution was measured with a chordwise and spanwise array of 60 absolute pressure transducers (Fig. 4). Two sets of acoustic measurements were made (Figs. 5-6). Two microphones in the near-field of the interaction provided information on the detailed evolution of the acoustic field and can serve to validate "mid-field" calculations of computational aeroacoustics and Kirchhoff methods. A movable array of microphones was used to obtain a limited (due to time constraints) survey of the acoustic far-field.

An extensive set of data for a combination of BVI parameters (Table 1) were obtained. A more detailed description of the experiment and the data acquisition and processing procedures are presented in Ref. 9.

Results

This section presents a detailed discussion of the unsteady features of blade pressures during the BVI encounter. The dependence of the acoustic field, as well as the corresponding blade surface pressures, on various parameters of BVI will be discussed. Some representative cases of BVI will be presented.

Blade pressures

Figure 7 shows a typical set of pressure-time histories on the upper and lower surfaces of the rotor blade during a nominally head-on (zero miss distance) BVI condition (the vortex generator is set to a position that was determined in previous flow visualization runs). Data are shown for a full revolution, at $0.876R$ for a hover tip Mach number of 0.712 and advance ratio of 0.197. The vortex generator was set to an incidence, α_v , of $+12^\circ$. It is seen that the flow environment of this rotor is quite dynamic, in spite of the near-zero collective pitch. The upper surface of the rotor blade at the 90° azimuth position exhibits a weak shock, indicative of supercritical flow. Examination of the data at lower Mach numbers (not shown) reveals that the sharp pressure increase disappears, evidence that this is indeed a shock. There is also a weak BVI interaction that occurs near this point ($\psi=90^\circ$). Evidently the external vortex is inducing enough blade lift variation for the rotor to have a self generated BVI. However, the most prominent single feature is the parallel BVI event at an azimuth of 180° .

It is useful to view the pressure-time histories in terms of the events at the leading edge. Figure 8 shows the time history of the upper and lower surface transducers closest to the leading edge for nominal miss distances of 0.0 and -0.4 chords ($0.876R$, hover tip Mach number of 0.712, advance ratio of 0.197 and $\alpha_v=-12^\circ$). The usefulness of the leading edge transducers is that they usually behave similarly to the other transducers - but in a more sensitive manner - and the differential pressure is a good indicator of the lift history. Figure 8 shows that while the differential pressure is generally not large, except at the BVI, neither is it negligible or particularly smooth. In Fig. 7 we noted the presence of a weak vortex interaction at 90° azimuth. In Fig. 8 (where the vortex sense is reversed) we see weak vortex interactions at both 90° and 270° . It is

significant that there is considerable reduction in the leading edge pressure variations when the vortex moves from 0.0 to 0.4 chords away from the blade. Note that the primary difference in the BVI occurs at-or-before the point where the sign of the differential pressure reverses. This is the early stage of the BVI where the vortex is near the blade leading edge. The latter stage of the BVI is not greatly effected by the proximity change. These proximity-induced changes are very localized effects as the pressure variations show almost no effect of the vortex movement except near $\psi = 180^\circ$, where the early stages of BVI occurs. Nevertheless, the externally generated vortex does have a global effect on the rotor behavior through its effect on the trim state. The rotor is trimmed to zero flapping in order to consistently locate the blade and vortex with respect to each other. The control inputs required for this trim generate a varying rotor lift together with a wake and the previously noted rotor-wake interactions. The influence of the trim state of the rotor on the details of the BVI time history is not fully understood at present. This is illustrated by noting the effect of reversing the sign of the externally generated vortex. We expect that reversing the sign of the vortex should merely cause the upper and lower surface pressures to reverse places. It is seen in Fig. 9 that this is not what occurs. Figure 9 shows the upper and lower surface pressure variations corresponding to Fig. 8b, but with a reversal of vortex sign. It is seen that there are considerable differences between the pressure-time histories between Figs. 9 and 8b. These differences are most prominent at the BVI event, where the magnitude of the early stage differential pressures are greatly reduced, while the latter stage magnitudes are greatly increased. It has been proposed (Ref. 10) that this asymmetry of the differential pressure with respect to vortex sign is due to an innate asymmetry of the vortex. This is not unlikely, since the vortex is only 4 chords old at the time of the interaction. In addition, prominent kinks in the leading-edge pressure traces only occur for positive α_v - indicative of the passage of the feeding wake sheet. However, an alternate explanation is that the rotor collective is non-zero. (The collective was set for zero lift and the magnitude of the collective never exceeded about 0.25° .) It is interesting that all the differential pressures indicate a negative lift at 0° azimuth. This may be indicative of a collective offset. However, the important point is that the BVI is a strictly local phenomena. The significance of a possible collective offset is that the rotor incidence would not be precisely known at the time of the BVI, which implies extra complication in computational modeling of the flow.

We will now discuss the salient details of the BVI. Figure 10 shows the time histories of Fig. 7 on a greatly expanded scale (from about 175° to 210°). Several propagative and convective events are discernible in these data. When the vortex reaches the blade leading edge the upper surface pressures begin an abrupt increase (with the leading edge having the largest pressure variation, this variation decreasing strongly with distance from the leading edge - events with opposite sign occur on the bottom surface). The fact that these particular events occur almost simultaneously from leading to trailing edge is indicative of a very rapid propagative event - downstream from leading to trailing edge - whose propagation speed is the sum of the local speed-of-sound and the local flow velocity. The effect of this first BVI wave appears to be the establishment of a fairly steady pressure level that persists for some duration. The time of persistence is greatest near the leading-edge and is a nearly linear function of distance from the leading edge. During this persistence interval, several occurrences are seen to move downstream at a slower speed that is of the order of the mean flow velocity. For this particular interaction this slower event is only seen on the bottom surface. These events are associated with the chordwise passage of the vortex and vortex-generated flow features. (The fact that convective events are not seen equally on both surfaces suggests that the vortex miss distance may not be exactly zero.) These two occurrences were previously noted in the earlier tests that were conducted in the Army 7- by 10-Foot Wind Tunnel (Refs. 6-8). However, the present data also show an additional propagative event not seen in the earlier tests. At about the time the previously mentioned convective events approach the trailing edge a new wave appears - propagating upstream from the trailing edge. This wave has a fairly broad width and moves upstream slowly (at the speed of sound minus the convection speed). This wave probably results from the trailing-edge Kutta condition asserting itself, either in response to the passing vortex or to the original BVI wave, and propagating that information upstream. This secondary or "Kutta wave" occurs at the same time and has opposite sign on the top and bottom surfaces. Because the sign is opposite, we believe that this latter wave is primarily a response to the convective wave rather than to the vortex itself. The inviscid effect of a vortex at a sharp edge is an expansion on both sides. This wave is weak (compared to the initial BVI pulse) and was not seen in previous testing - possibly due to flow unsteadiness. Similar upstream waves emanating from the trailing edge were recently observed by Obermeier and Schurmann (Ref. 11) in high-speed interferometric studies conducted in a shock tube.

The effect of the BVI on the chordwise pressure distribution is shown in Fig. 11 for the same BVI event shown in Fig. 10. Figure 11a shows the chordwise pressure distribution at an azimuth of about 176° , which is shortly before the impact of the vortex on the leading edge. At this point the lift is still quite small but beginning to rise rapidly. Figure 11b ($\psi = 181^\circ$) shows the pressure distribution near the moment of impact of the vortex center on the leading edge. At this point the lift is a maximum and begins to drop rapidly. Figure 11c ($\psi = 184^\circ$) shows the pressure distribution only 3 degrees later. At this point the lift is zero and dropping. The lift continues to drop until $\psi = 188^\circ$ (Fig. 11d); the entire shape of the pressure distribution is distorted resulting in a significant differential pressure in the trailing-edge region. This trailing edge loading results in a sharp moment pulse and blade "ringing" that was clearly seen in the root torsion strain gages. This point closely corresponds to the point at which the upstream-moving wave commences. After this point we see the re-establishment of circulatory lift and the differential pressure reduces, as does the total lift. Figures 11e and 11f show the evolution of the chordwise pressure distribution as the "Kutta wave" propagates upstream. This last point ($\psi = 207^\circ$) constitutes the termination of the BVI event. We can define the BVI event as that period beginning when the vortex passes the leading edge and ending when the resulting Kutta wave passes the leading edge. These are two easily identifiable events during which time the blade turns about 30 degrees of azimuth, which is about 3 chords of travel at this radial station. The vortex is not close to the blade in the latter stages of the interaction, and this explains the previously-noted lack of sensitivity of these phases of the interaction to miss-distance.

The most prominent feature of the BVI event is the rapid pressure jump which occurs at the leading edge. Since the pressure varies from a distinct peak (which occurs when the vortex is at the leading edge) to a subsequent well-defined "plateau", the magnitude of this change (shown in Fig. 12 for the bottom surface and for several vortex generator angles-of-attack) provides a convenient characterization of the BVI strength. We have summed the absolute values of these pressure coefficient jumps for the upper and lower surfaces, here termed the "BVI pressure increment or χ_{bvi} ", as a simple measure of the BVI. Figure 13 plots χ_{bvi} as a function of nominal vortex miss distance for vortices of opposite sign. It is seen that for a vortex generator incidence angle of $+12^\circ$ χ_{bvi} peaks at a miss distance of about $0.125c$, in contrast to the $\alpha_v = -12^\circ$ case which peaks at a miss distance of $z_v = 0$ chord.

Figure 14 is the acoustic field measured by one of the far-field microphones corresponding to the blade pressures of Fig. 7, and is typical of the BVI acoustic data obtained during the test. As indicated on the figure, the change in acoustic pressure from the peak of the initial rise to the minimum peak is a convenient measure of the BVI acoustic event, which is herein referred to as the "BVI acoustic amplitude, Π_{bvi} ". Π_{bvi} is plotted as a function of nominal vortex miss distance in Fig. 15. Consistent with Fig. 13 for blade pressures, it is seen that for a vortex generator incidence angle of $+12^\circ$, Π_{bvi} appears to peak at a miss distance of approximately 0.125c, in contrast to the $\alpha_v = -12^\circ$ case which peaks at a miss distance of $z_v = 0$ chord.

These observations lead us to believe that the nominal vortex location ($\alpha_v = +12^\circ$) is probably in error by about 0.1c (for unknown reasons that could include errors in the vortex generator position gage or the blade flap gage). For a vortex generator setting of -12° there was no apparent anomaly in the vortex location readout. In addition, the maximum χ_{bvi} for $\alpha_v = -12^\circ$ is greater than that for $\alpha_v = +12^\circ$ (by about 10%). Similarly, the maximum Π_{bvi} for $\alpha_v = -12^\circ$ is greater than that for $\alpha_v = +12^\circ$ (by about 25%). The microphones show much greater sensitivity to vortex sign than the leading edge surface pressures.

These observations probably indicate that the magnitude of the lift of the vortex generator - and hence of the vortex strength - is not the same for the two different incidence angle settings. However, it is most significant that the proximity trend is very similar for the two opposite vortex signs. This indicates that, while there may indeed be some asymmetry of the vortex or a collective offset, there is an essential symmetry to the interaction. The ability to accurately predict the detailed features of the blade pressures during BVI presents a challenge to the analysts.

Acoustics

Far-field and near-field acoustic data are presented and discussed for four representative cases of BVI for which the tip Mach number and advance ratio are fixed at $M_{tip} = 0.712$ and $\mu = 0.196$, respectively. The four cases are for interaction occurring with vortices of opposite sense (swirl direction), obtained by setting the vortex generator wing at $+12^\circ$ and -12° angle of incidence, and for head-on interaction with the

vortex, as well as with the vortex 0.25 blade chord below the blade. These four cases are illustrated in Fig. 16.

Figure 17 shows the acoustic pressure measured by far-field microphones 2-5 (Fig. 5) for the four cases of Fig. 16. These data were obtained with the microphone traverse positioned at 90° relative to the rotor hub (i.e. directly to the retreating side of the hub). Immediately noticeable is the relative phasing of the pulses due to the differences in source-to-microphone distances. Several secondary pulses, which we attribute to tunnel floor reflections (Ref. 9) are also evident. There is a reversal in the sign of the acoustic pressure pulse corresponding to the reversal in the swirl direction of the vortex. No major directivity changes are evident over the range of elevation angles spanned by these microphones. Geometry limitations did not allow positioning microphones at larger elevation angles to better corroborate acoustic field directivity.

There is a noticeable change in the shape of the BVI pulses between head-on interaction and when the vortex is below the blade. The pulse shapes for the head-on cases (Cases I and II) display a sharper rise to a higher peak which is followed by an equally sharp drop. Prior to reaching ambient level, however, the pulse abruptly widens. The $z_v = -0.25$ -chord cases (Cases III and IV), on the other hand, display a more symmetric pulse shape with a more gradual rise than for head-on impact.

As expected, the acoustic pulse amplitudes are much larger for the direct impact cases (Cases I and II) than when the vortex is below the blade (Cases III and IV). In addition, for head-on interaction, the pulse amplitude for the $\alpha_v = -12^\circ$ case (Case I) is significantly larger than the $\alpha_v = +12^\circ$ case (Case II). This is not the case when the vortex is below the blade.

Figure 18 shows the corresponding near-field microphone (Fig. 6) data for the four cases of Fig. 16. Microphone 7 was closer to the blade, at its 180° azimuth position, but at a larger directivity angle than microphone 6. Fig. 18 exhibits several interesting features.

First to be noted is the change in pulse shape with vortex swirl direction. The $\alpha_v = +12^\circ$ cases (Cases II and IV) contain a low amplitude feature at the leading edge reminiscent of thickness noise. This is not seen in the $\alpha_v = -12^\circ$ cases (Cases I and III), most likely because, while the BVI pulse has reversed in amplitude with a reversal in vortex swirl, the thickness noise remains unchanged. Their superposition results in the observed pulse shapes. This is more

pronounced for microphone 7 than for microphone 6, most likely because of the directionality of this mechanism. The presence of this feature may be the result of the specific operating state of the rotor near the 180° azimuth position.

Another interesting feature to note is the relative amplitudes of the two near-field microphones. Whereas for $\alpha_v = -12^\circ$ (Cases I and III) the amplitude for microphone 6 is the same or smaller than that for microphone 7, as would be expected since microphone 6 is at a greater distance, for $\alpha_v = +12^\circ$ (Cases II and IV) microphone 6 exhibits a larger acoustic pulse amplitude. There is also a noticeable difference in the pulsewidths for the two microphones in all cases. These are most likely the result of the complex wave components and their interactions in the near-field.

Summary

This paper presented the results from an experimental study of parallel Blade-Vortex Interaction. A nominally non-lifting rotor was operated in close proximity to the tip-vortex generated by an upstream wing - thus simulating a very simple parallel BVI. Simultaneous rotor blade surface pressure and near- and far-field acoustic data were obtained for a range of vortex miss distances, rotor speeds and vortex strengths. It was found that the rotor, though nominally non-lifting, actually generates a non-negligible wake of its own and that the behavior of this wake, in response to the external vortex, is not simple or well understood. Many detailed features in both the blade pressure and acoustic data were identified and discussed. These include the presence of a downstream, and a much weaker upstream, wave on the blade surface. However, the primary BVI event is prominent and quite localized with no obvious coupling to other rotor events. It is possible to define simple interaction parameters (both in the surface pressures and acoustic signals) that characterize the BVI and give well-defined trends for the BVI behavior as a function of operational quantities, especially the miss-distance. These parameters indicate and provide a measure of possible miss-distance errors, thus guiding the choices of geometry variations that will have to be made in future computations. Study of the leading-edge surface pressure variations indicates a prominent load asymmetry behavior with respect to vortex sign. There is a corresponding asymmetry in the resulting acoustic field. There are several potential explanations of this asymmetry, of which the simplest is the possible presence of a collective offset. Future computations, may

require some variation in the blade incidence in order to better define the effects of such an offset. In spite of such recognized complications, the test reveals detailed features of the BVI, the computational duplication of which, will provide a definitive verification of our understanding of BVI-induced loading and acoustics.

Acknowledgments

The authors wish to acknowledge the assistance of Judy Gallman and Casey Burley in the analysis and interpretation of the experimental results.

References

1. George, A.R. and Chang, S.B., "Noise Due to Transonic Blade-Vortex Interactions," American Helicopter Society 39th Annual Forum, St. Louis, MO, May 1983.
2. Brentner, K.S., "Prediction of Helicopter Rotor Discrete Frequency Noise," NASA TM 87721, Oct. 1986.
3. Gallman, J.M., "The Validation and Application of a Rotor Acoustic Prediction Computer Program," Army Science Conference, Durham, NC, June, 1990.
4. Xue, Y. and Lyrantzis, A.S., "The Use of a Rotating Kirchhoff Formulation for 3-D Transonic BVI Far-Field Noise," American Helicopter Society 49th Annual Forum, St. Louis, MO, May 1993.
5. Baeder, J.D., "The Computation and Analysis of Acoustic Waves In Transonic Airfoil-Vortex Interactions," Ph. D. Thesis, Stanford University, Sept. 1989.
6. Caradonna, F.X., Laub, G.H., and Tung, C., "An Experimental Investigation of the Parallel Blade-Vortex Interaction," 10th European Rotorcraft Forum, The Hague, Netherlands, Sept. 1984.
7. Caradonna, F.X., Lautenschlager, J.L., and Silva, M.J., "An Experimental Study of Rotor-Vortex Interactions," AIAA Paper No. 88-0045, AIAA 26th Aerospace Sciences Meeting, Reno, NV, Jan. 1988.
8. Caradonna, F.X., Strawn, R.C., Bridgeman, J.O., "An Experimental and Computational Study of Rotor-Vortex Interactions," 14th European Rotorcraft Forum, Milano, Italy, Sept. 1988.
9. Kitaplioglu, C. and Caradonna, F.X., "Aerodynamics and Acoustics of Blade-Vortex

Interaction Using an Independently Generated Vortex," American Helicopter Society Aeromechanics Specialists Conference, San Francisco, California, Jan. 1994.

10. Bridgeman, J.O., Ramachandran, K., Caradonna, F.X., and Prichard, D., "The Application of Vorticity Embedding to Parallel Blade-Vortex Interactions," AIAA Paper No. 94-

1919, 12th AIAA Applied Aerodynamics Conference, Colorado Springs, CO, June 20-23, 1994.

11. Obermeier, F. and Schurman, O., "Experimental Investigation on 2D Blade-Vortex-Interaction Noise," AIAA Paper No. 93-4334, 15th AIAA Aeroacoustics Conference, Long Beach, CA, Oct. 25-27, 1993.

TABLE 1 - TEST MATRIX

Mtip	μ	α_v
0.7	0.2	-12°, +12°, +6°
0.6	0.1	-12°, +12°
	0.15	-12°, +12°
	0.2	-12°, +12°, +6°
0.5	0.2	+12°
0.4	0.2	-12°, +12°
0.25	0.2	-12°, +12°

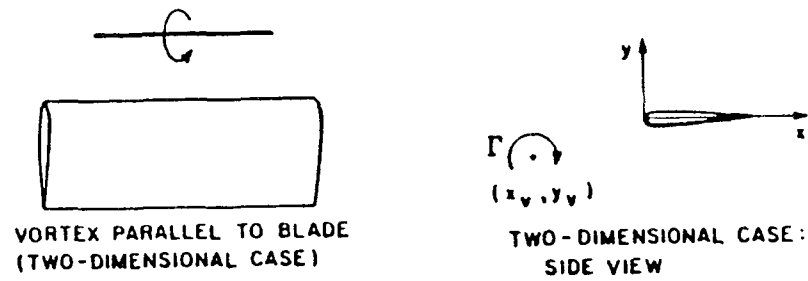


Figure 1. Analytical model of parallel blade-vortex interaction



Figure 2. BVI experiment in the NASA Ames 80- by 120-Foot Wind Tunnel

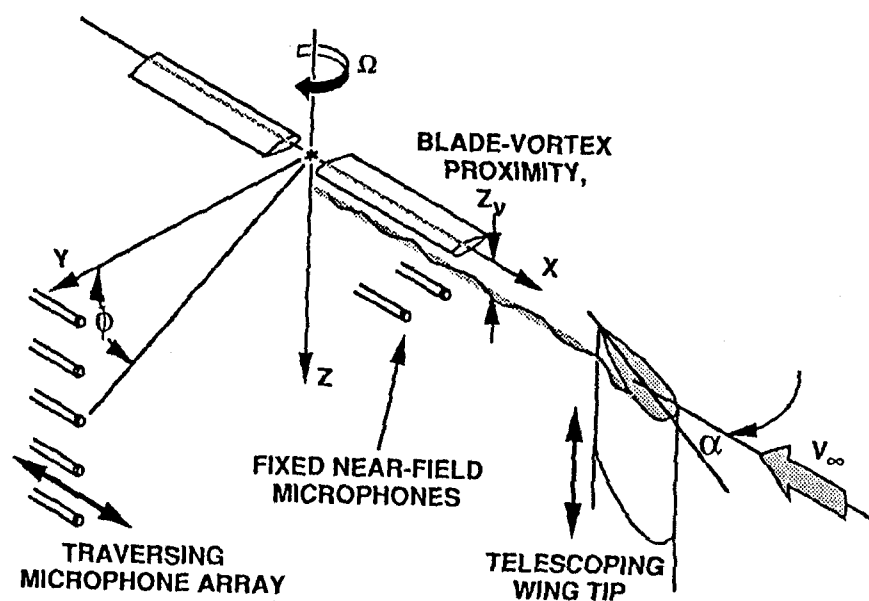


Figure 3. Sketch of BVI test set-up and definition of parameters

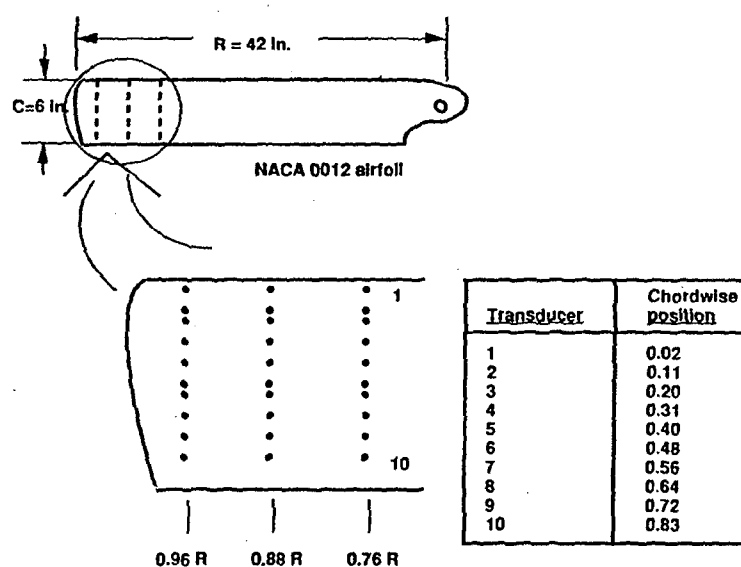


Figure 4. Blade pressure transducer locations (not to scale).
Identical locations for upper and lower surfaces.

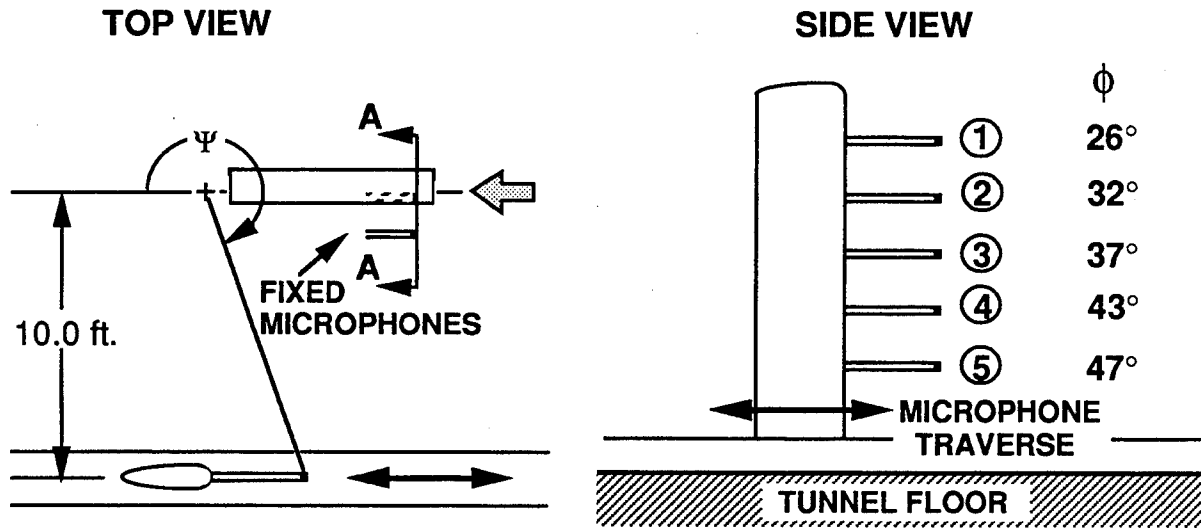


Figure 5. Far field microphone positions (not to scale). Elevation angles are relative to the rotor plane.

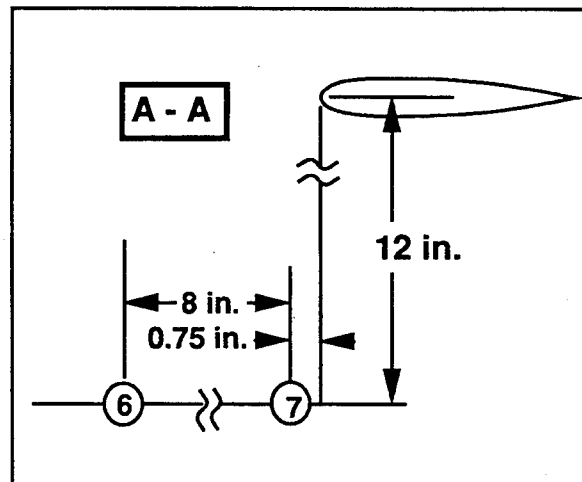
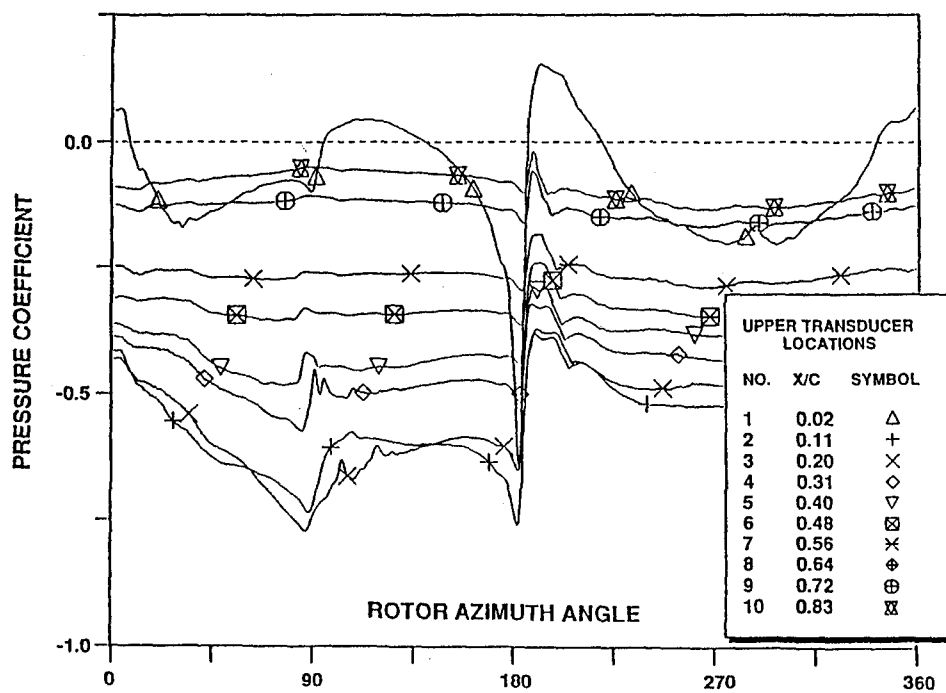
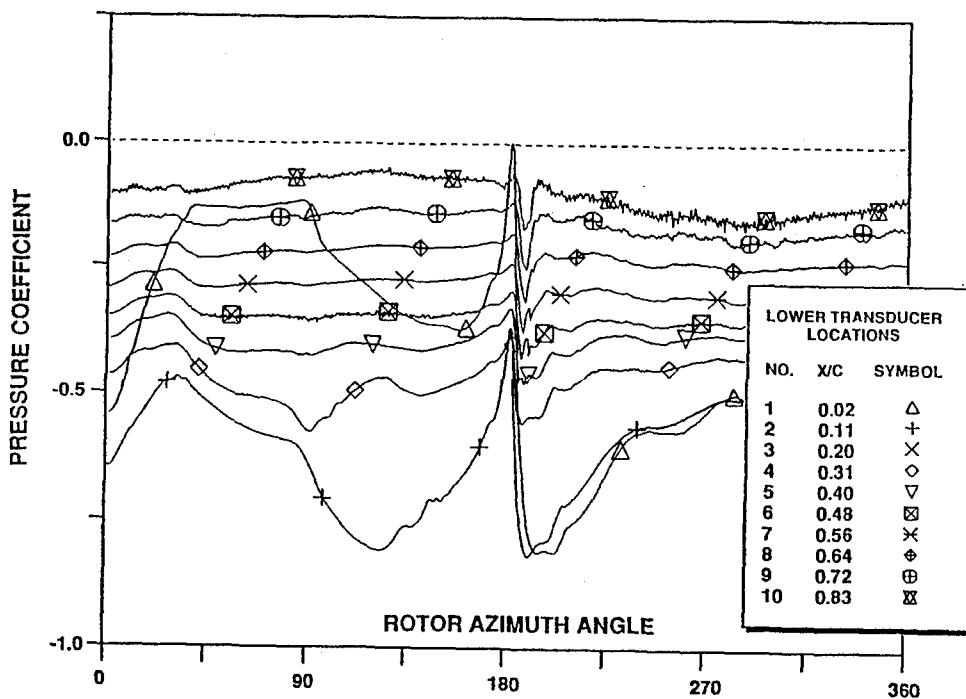


Figure 6. Near-field microphone positions (not to scale)



(a) Upper surface



(b) Lower surface

Figure 7. Blade pressure variations induced by parallel BVI. $M_{tip} = 0.71$, $\mu = 0.2$, $\alpha_v = +12^\circ$, $z_v = 0$, $r/R = 0.88$.

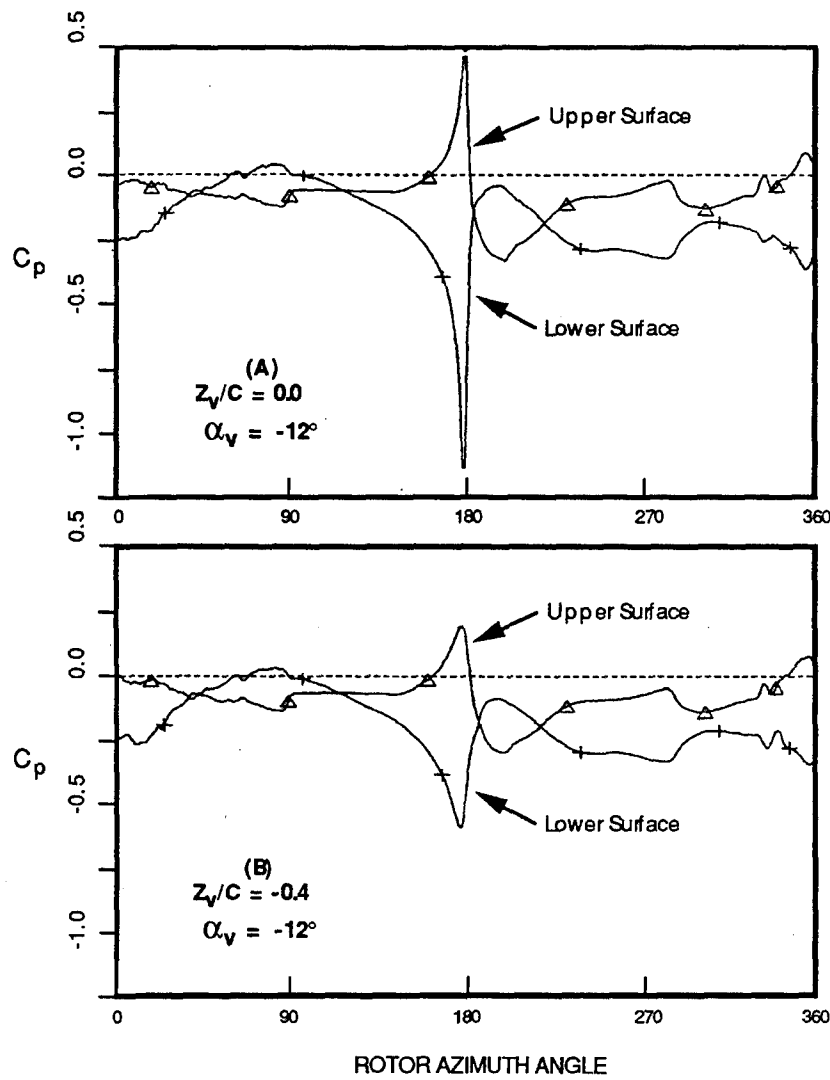


Figure 8. Leading edge pressure variations induced by parallel BVI. $M_{tip} = 0.71$, $\mu = 0.2$, $\alpha_v = -12^\circ$, $r/R = 0.88$, $x/c = 0.02$.

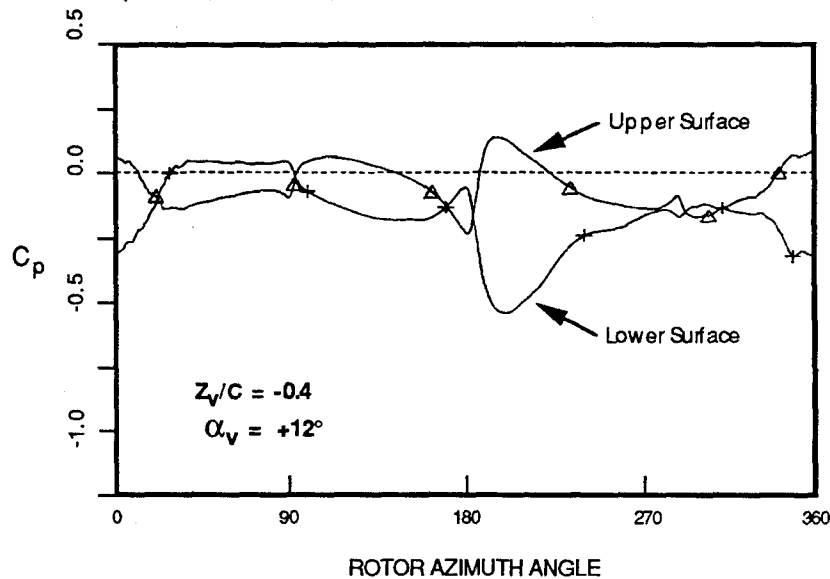
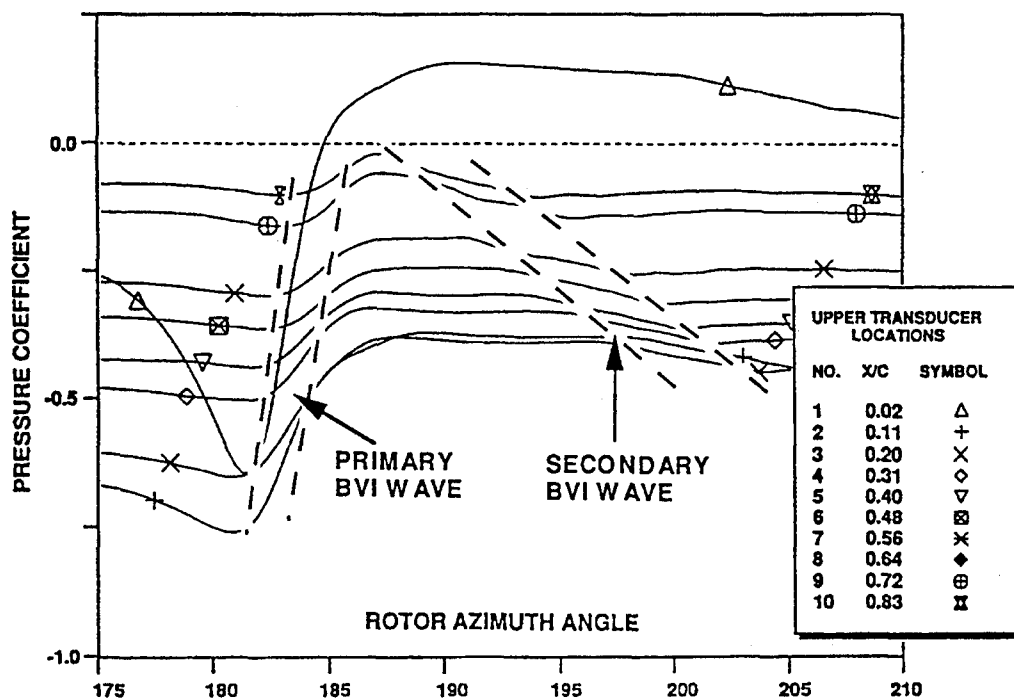
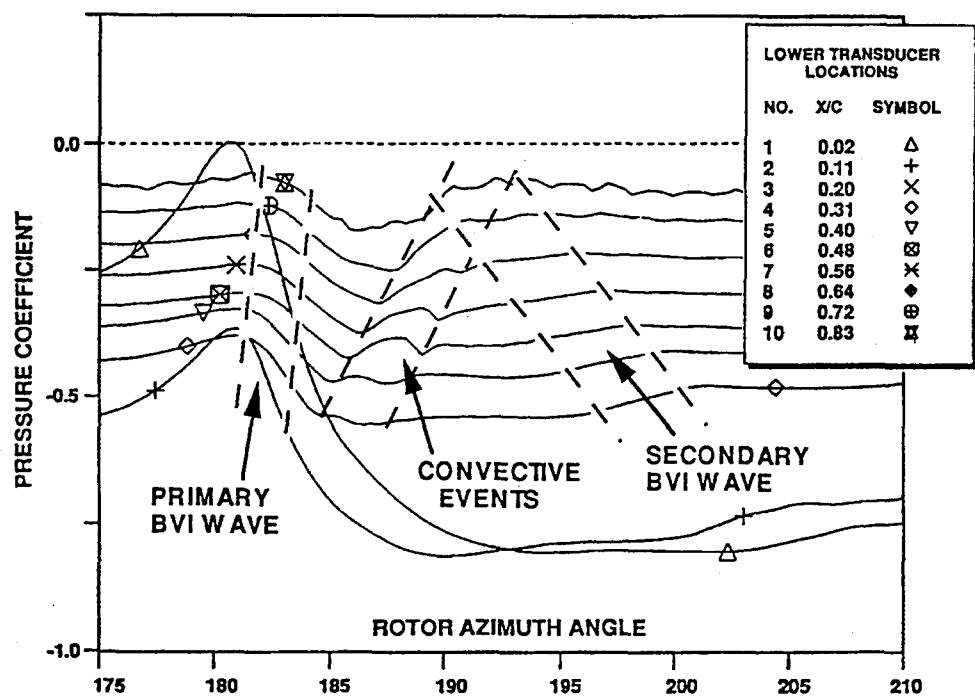


Figure 9. Leading edge pressure variations induced by parallel BVI. $M_{tip} = 0.71$, $\mu = 0.2$, $\alpha_v = +12^\circ$, $r/R = 0.88$, $x/c = 0.02$.



(a) Upper surface



(b) Lower surface

Figure 10. Blade pressure variations induced by parallel BVI. Expanded azimuth scale.
 $M_{tip} = 0.71$, $\mu = 0.2$, $\alpha_v = +12^\circ$, $z_v = 0$, $r/R = 0.88$.

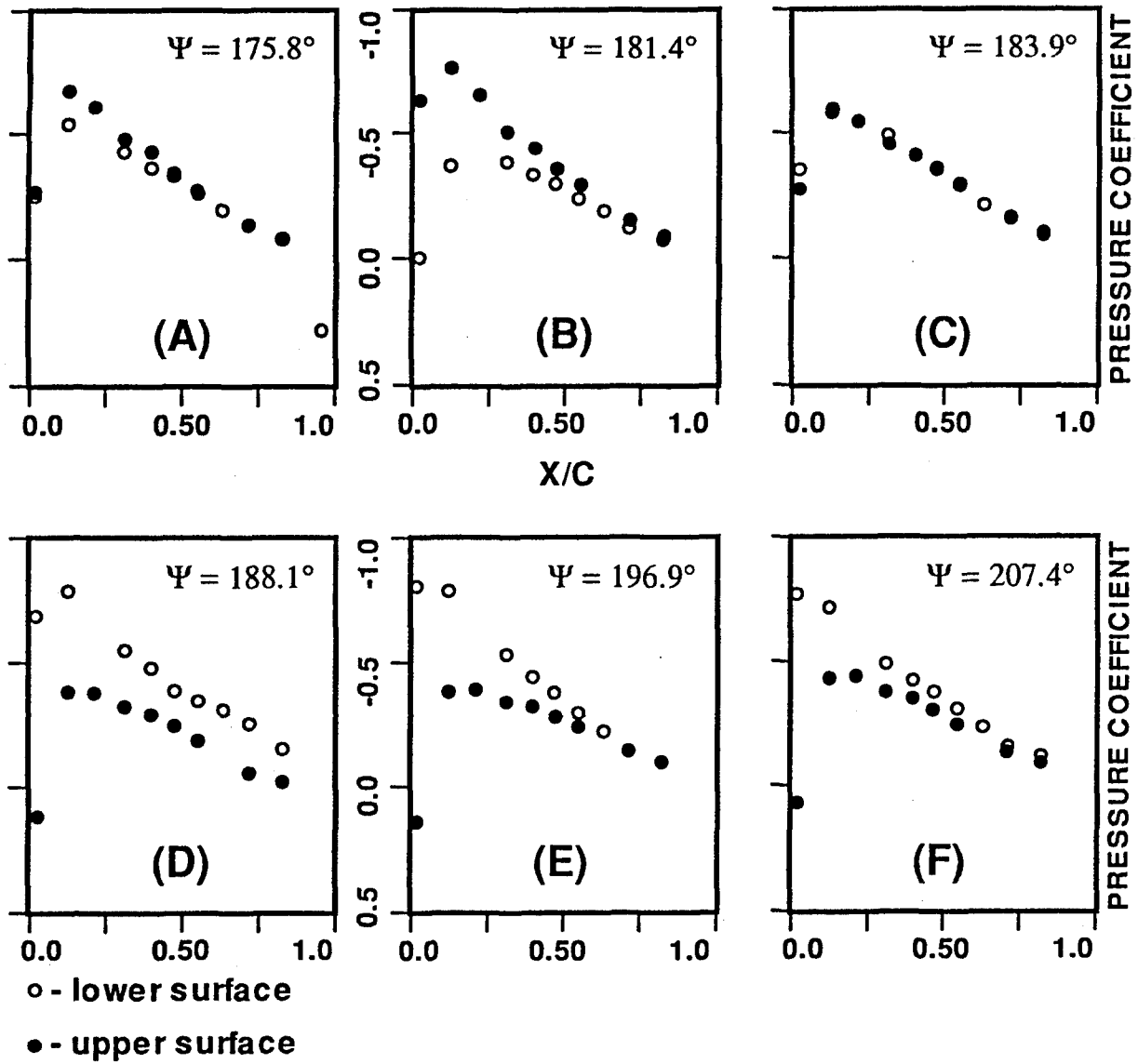


Figure 11. The effect of a parallel BVI on the rotor chordwise pressure distribution.
 $M_{tip} = 0.71$, $\mu = 0.2$, $\alpha_v = +12^\circ$, $z_v = 0$, $r/R = 0.88$.

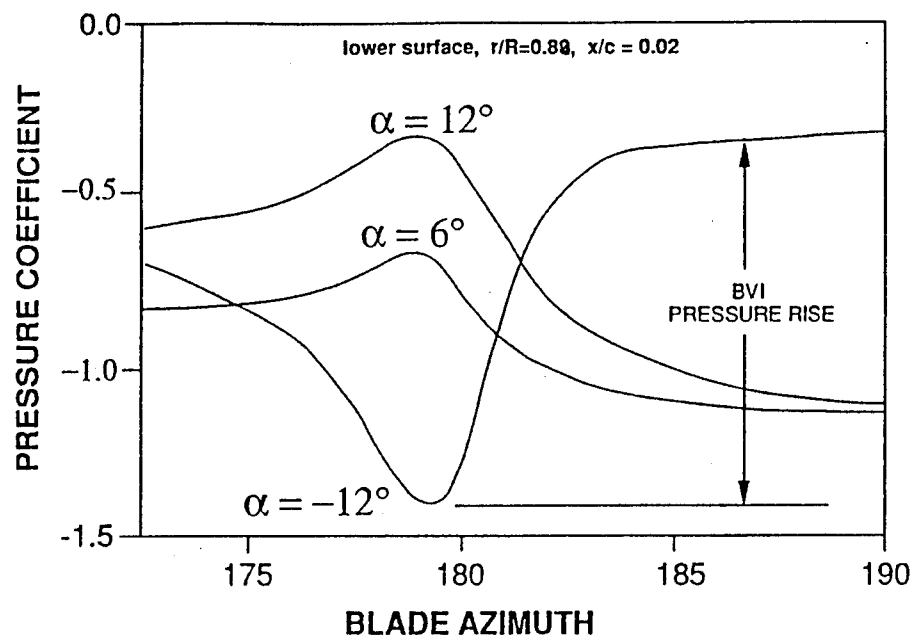


Figure 12. The effect of vortex strength and sense on BVI surface pressure variations.
 $M_{tip} = 0.7$, $\mu = 0.2$, $z_v = 0$.

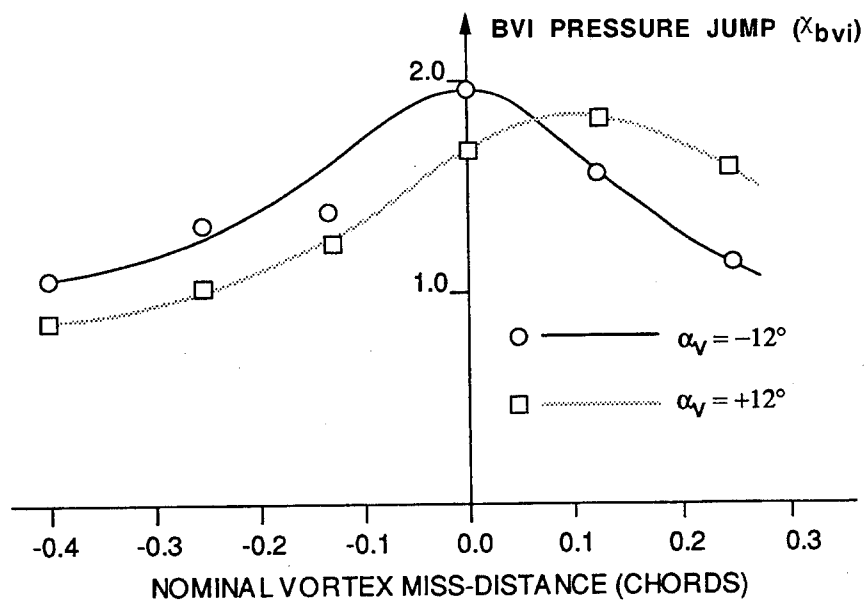


Figure 13. The effect of vortex proximity on the BVI pressure jump. $M_{tip} = 0.7$, $\mu = 0.2$.

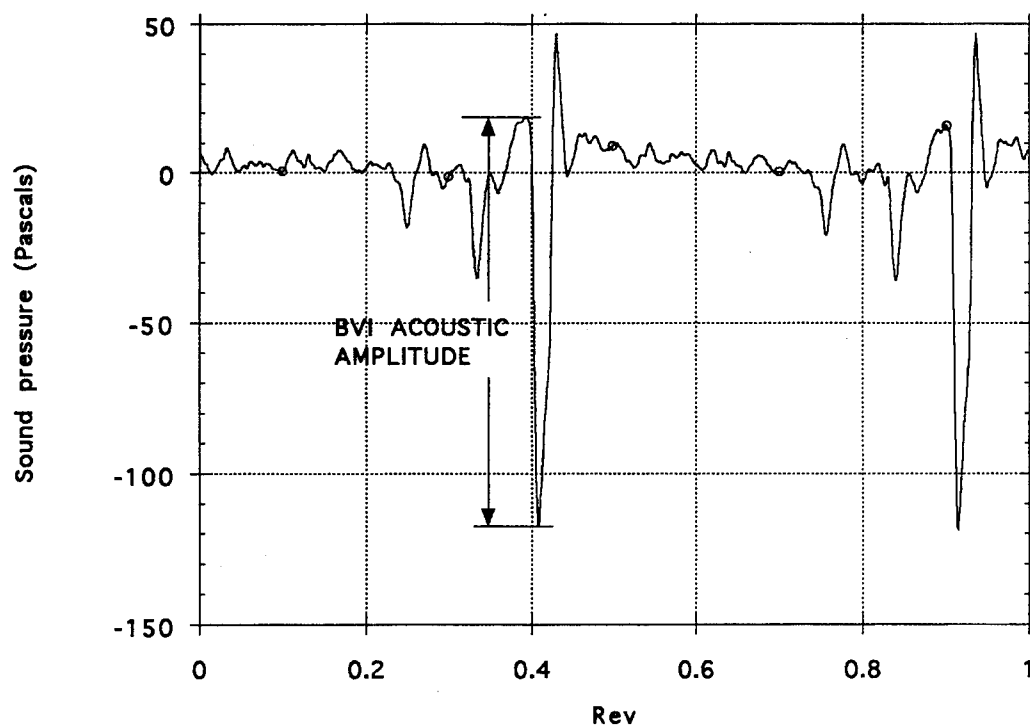


Figure 14. Typical far-field acoustic time history for parallel BVI.

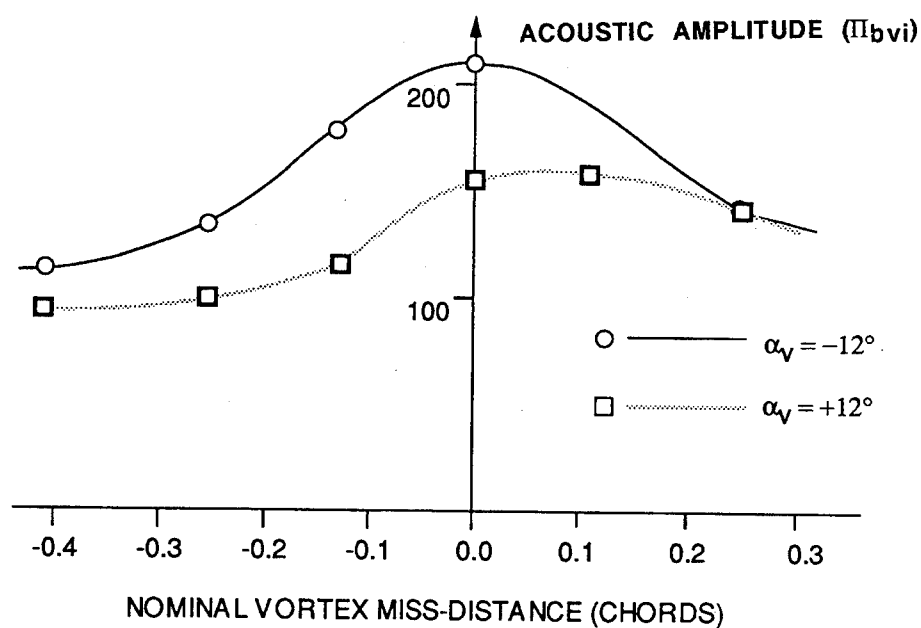


Figure 15. The effect of vortex proximity on the BVI acoustic amplitude.
 $M_{tip} = 0.7$, $\mu = 0.2$.


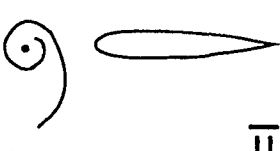
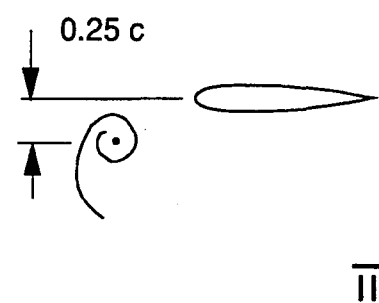
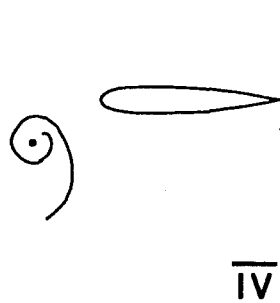
	$\alpha_V = -12^\circ$	$\alpha_V = +12^\circ$
$z_V = 0$	 I	 II
$z_V = -0.25$	 III	 IV

Figure 16. Four BVI configurations

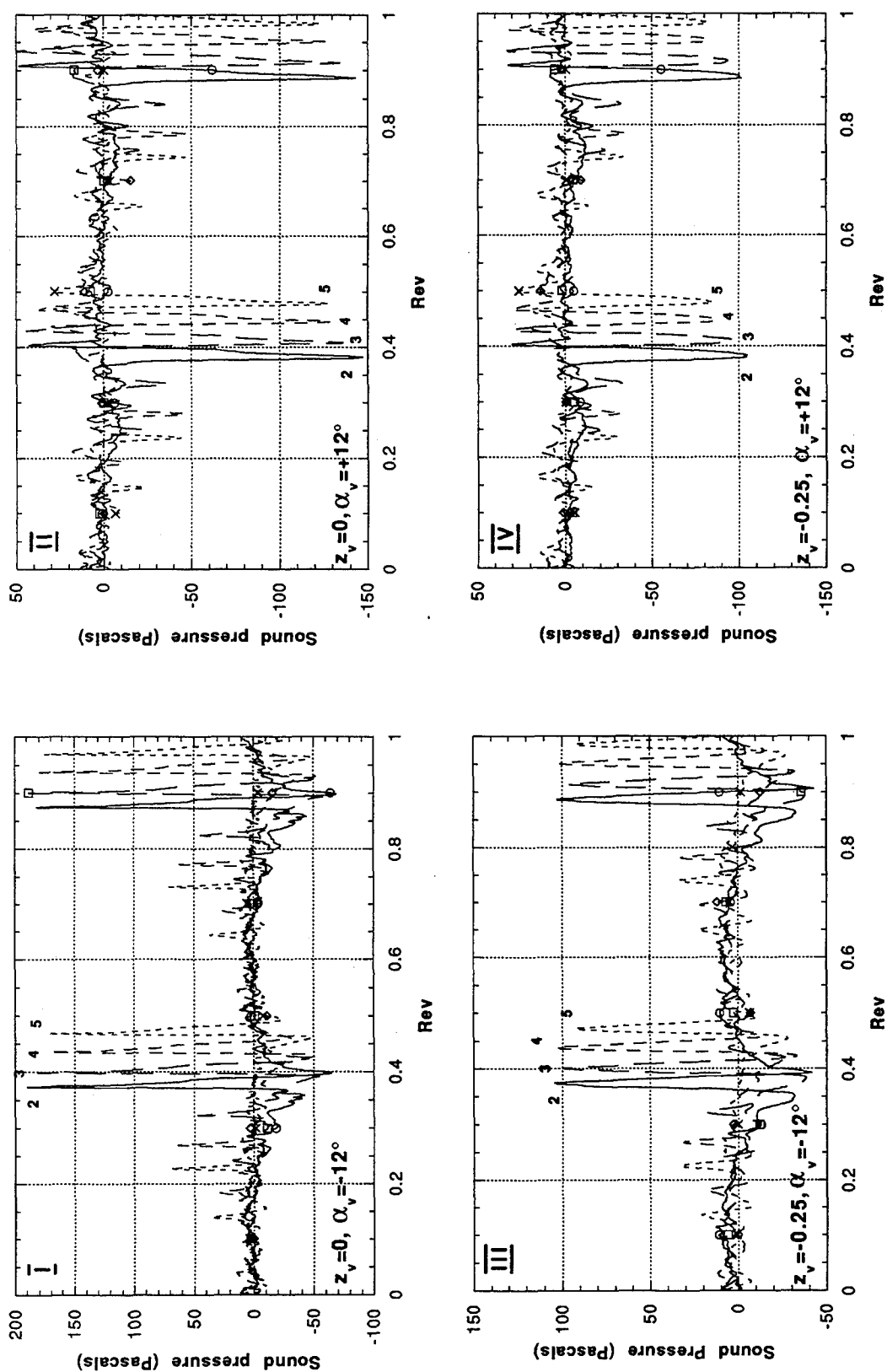


Figure 17. Far-field acoustic pressures. $M_{tip} = 0.71$, $\mu = 0.2$.

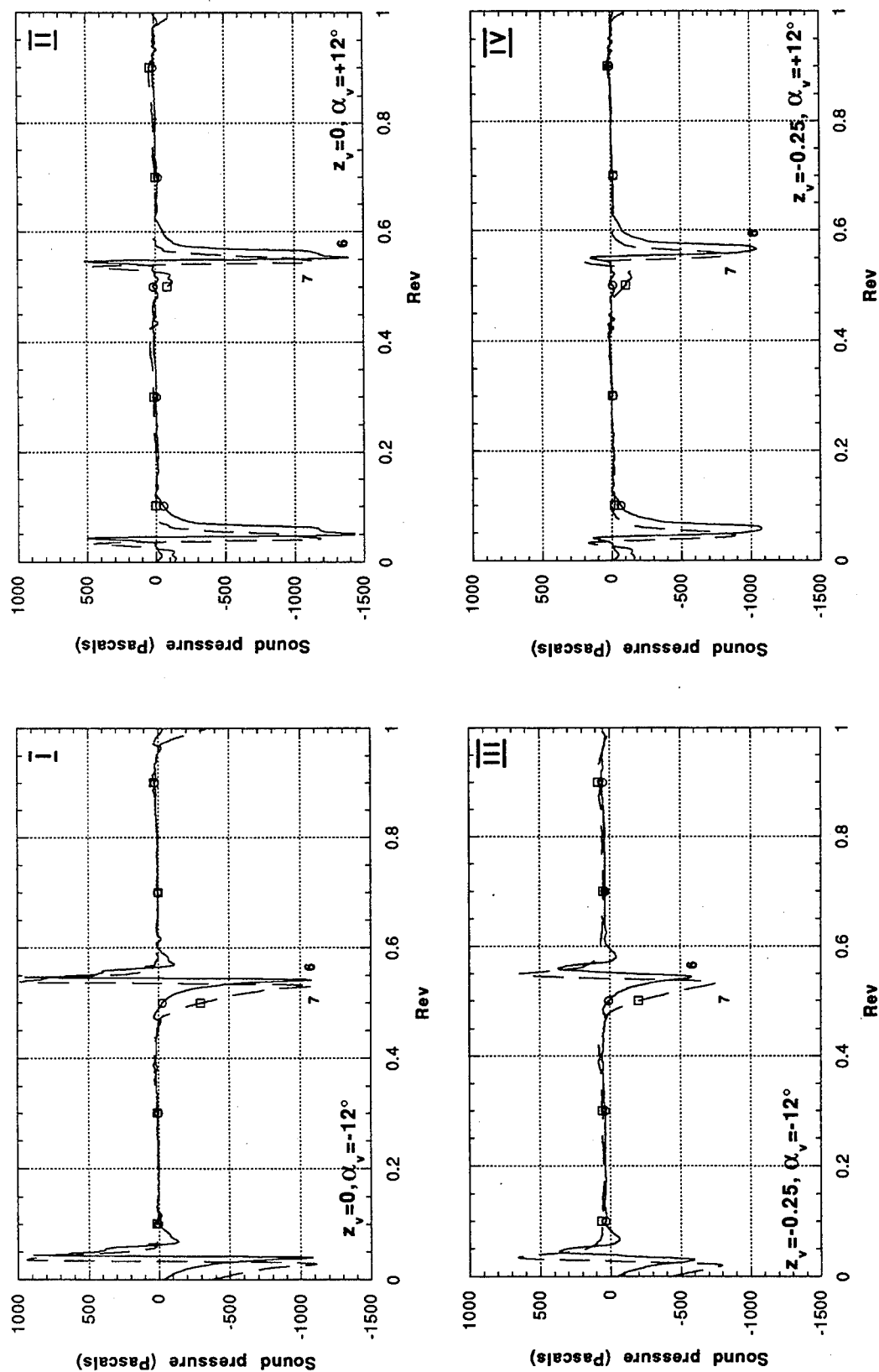


Figure 18. Near-field acoustic pressures. $M_{tip} = 0.71, \mu = 0.2$.

External Noise of Single Rotor Helicopters

V.F. Samokhin,

Aerodynamic Division,
Central Aero-Hydrodynamic Institute (TsAGI),
Moscow, Russia.

M.G. Rozhdestvensky,

Aerodynamic Division,
M.L. Mil Moscow Helicopter Plant, Design Bureau,
2, Socolnichesky Val
Moscow 107113, Russia.

SUMMARY

Intensity, acoustical radiation spectrum, as well as single-rotor external noise level are analysed in the paper based on the experimental data obtained from testing actual helicopters. The helicopter acoustical far-field is shown to be a superposition of the main and tail rotor fields. The external noise spectrum measured on the ground contains discrete and broadband components. Discrete component frequencies are multiples of the main and tail rotor passage frequencies and fall within the frequency ranges 20-160 Hz and 100-500 Hz respectively. Continuous spectrum radiation can be seen within the whole sound frequency range, but the maximum intensity is registered at 500-3,000 Hz frequencies.

It has been found out that the intensity of the helicopter acoustical radiation in the direction corresponding to the maximum external noise level and the power required by the main and tail rotors change according to the same law. The helicopter acoustical field is asymmetric relative to the vertical plane running through the longitudinal axis of the aircraft.

The helicopter external noise level measured in PNdb has been found to be defined by the tail rotor acoustical radiation with a discrete frequency spectrum within 100-500 Hz and the continuous spectrum radiation within 500-3,000 Hz.

The tail rotor configuration is shown to affect the helicopter acoustic response. Experimental studies of the external noise produced by the same helicopter first equipped with a tail rotor with symmetrical layout of the blades and then with an X-shaped tail rotor have allowed to establish that its tail rotor is the dominating source of the helicopter broadband noise. The X-shaped tail rotor has allowed to reduce the helicopter noise by 3-5 PNdb in level flight.

LIST OF SYMBOLS

f	frequency
Δf	frequency range
M_{90}	advancing blade tip Mach number

External noise level of all the civil helicopters under development is restricted to the limiting values, established by international [1] and national [2] standards. In order to implement these regulations in practice the acoustic characteristics of helicopter prototype are under control through all the design stages and operational tests. In this connection the analysis of helicopter noise sources and evaluation of the methods of acoustic emission intensity reduction are very topical. This paper presents the major results of acoustic studies on multi-bladed (more than three main rotor blades) single rotor helicopters, which are being produced and operated in Russia.

Study of helicopter aerodynamic noise sources has started in the sixties and was based on the results of investigations of propeller noise and vortex noise of a fan [3,4]. Basic mechanisms of helicopter main rotor (MR) noise generation have been defined in the very early papers on this topic [5]. A large number of experimental and theoretical studies, carried out in the seventies and eighties and partly presented in the reviews [6 & 7], was devoted to investigation of

specific components of two-bladed main and tail rotor (TR) noise with continuous and discrete sound pressure spectrum frequencies. Some results of external noise study of a helicopter with multi-bladed main rotor are examined in the monograph [8].

Far-field helicopter acoustic field is a superposition of the main and tail rotor acoustic fields and acoustic fields of the engine, gearboxes and transmission. In the general sound pressure spectrum, measured on the ground, there are components of noise emission with discrete, and broadband spectrums (Fig.1). Pure tones are divisible to the main and tail rotor blade passing frequencies and are located in 20-160 Hz (MR) and 100-500 Hz (TR) frequency ranges. Broadband frequency spectrum radiation is displayed through all noise frequency range, but the greatest intensity is registered in 500-3,000 Hz range. Fig.1 shows two typical helicopter noise spectrums, measured under the helicopter flight path at the moment of maximum perceived noise level on the ground ($\tau = \tau_{PNLTM}$). Upper plot corresponds to a mean sound pressure spectrum in the narrow frequency bands ($\Delta f = 12.5$ Hz) of the Mi-28 helicopter with production-type tail rotor. The lower one shows instantaneous narrow band sound pressure spectrum ($\Delta f = 12.5$ Hz) obtained through a frequency scale expansion method for 0-1,000 Hz range. It has been done for one of the measures of initial spectrum shown on the upper plot. One can see from the plots presented that helicopter acoustic emission, measured by a ground microphone in 1,000-3,000 Hz frequency range, doesn't contain any discrete components which level would exceed the level of continuous spectrum components emission. Continuous spectrum emission dominates in the frequency range above 600 Hz.

Acoustic emission power level estimation for single rotor helicopters is presented on Fig.2 for flyover of the Mi-24 and Mi-28 helicopters, as an

example. In the physical sense these data are very approximate because they were calculated under the assumption that the general acoustic field is symmetrical relative to helicopter longitudinal axis. However, as these data were obtained basing on the measurements of sound pressure spectrum under helicopter flyover path, they give a correct qualitative picture of the influence of flight speed on the amount of acoustic energy emitted towards the ground. As results from the data presented on Fig.2, the main rotor blade passing frequency emission dominates in the general helicopter acoustic emission power at the 10-1,000 Hz frequency range, compared to the portion of broadband emission in each of the one third of octave frequency bands. With the flight speed increase and corresponding increase of the advancing MR blade Mach number (M_{90}), the comparative importance of the main rotor first harmonics emission also increases. The function of general acoustic power level versus Mach number is not a monotone one. When the Mach number M_{90} is below 0.78, the general level of harmonic acoustic power reduces with the flight speed increase; when the Mach number exceeds 0.78 ($M > 0.78$) the energy of harmonic acoustic emission starts to grow sharply. Such variation of acoustic emission level is not observed for broadband emission component at low (250 Hz) and high (1,000-2,000 Hz) frequencies. In this case energy emission increases proportionally with Mach number increase with the exponent index of about 6. On the whole, variation of general acoustic power level and harmonic components power level concur with the variations of required mechanical power of the main rotor. The analysis of various acoustic emission components directivity diagrams shows that the sharp increase of harmonic emission power level together with flight speed is caused by the growth of harmonic emission intensity in the main rotor disc plane, which results from the display of

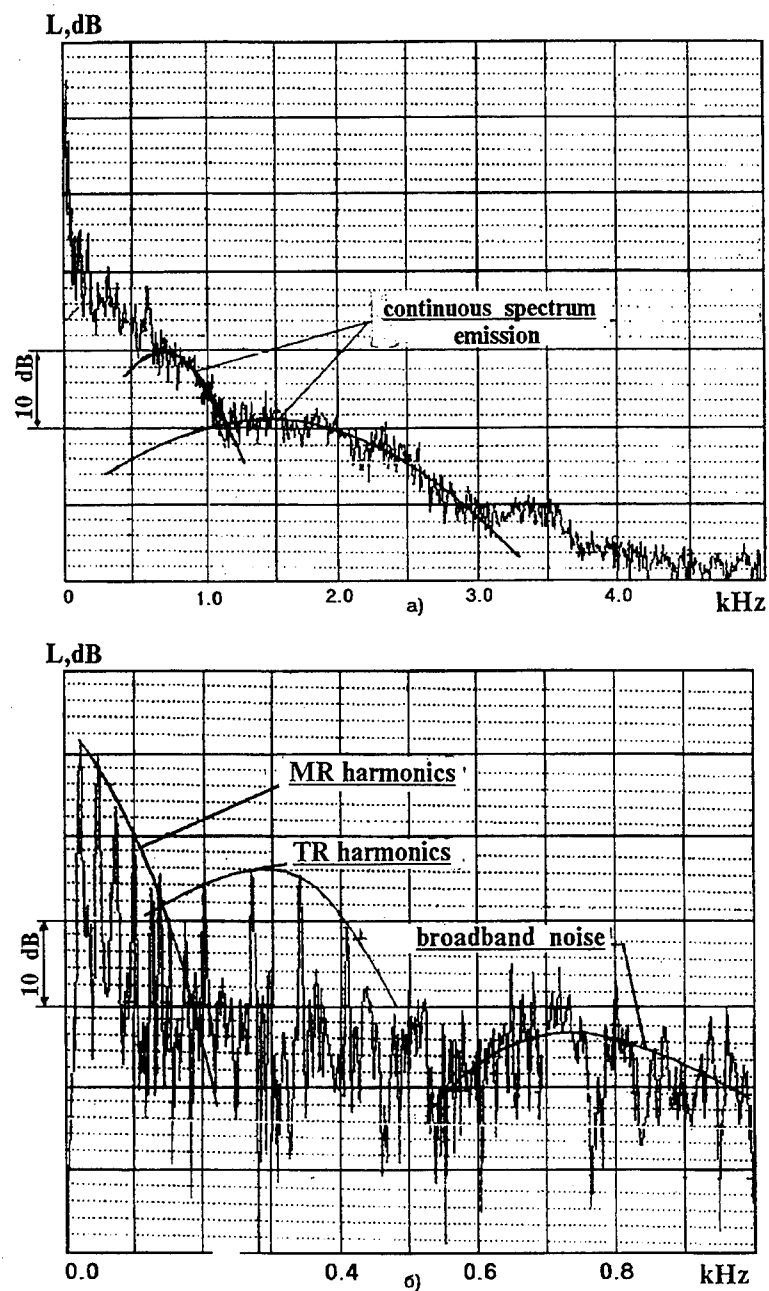


Fig.1. Narrow band sound pressure spectrum of the MI-28 helicopter external noise ($H=150\text{m}$, $\bar{V}=0.325$ $\tau=\tau_{\text{PNLTM}}$)
 a) Averaged spectrum
 b) Instantaneous spectrum with frequency scale expansion ($\Delta f = 12.5 \text{ Hz}$)

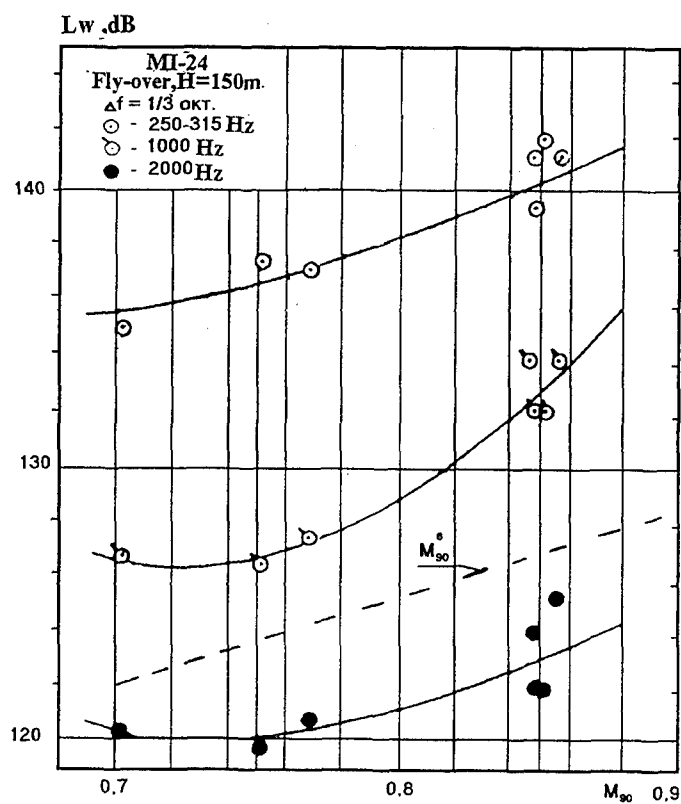
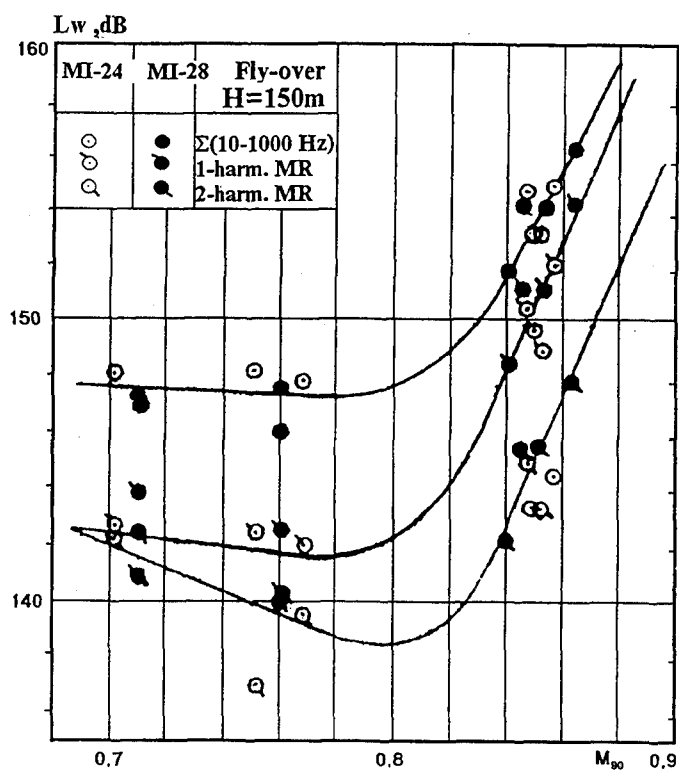


Fig.2. Harmonics and broadband components
emission power level of the main and tail
rotors in the one-third of octave frequency band

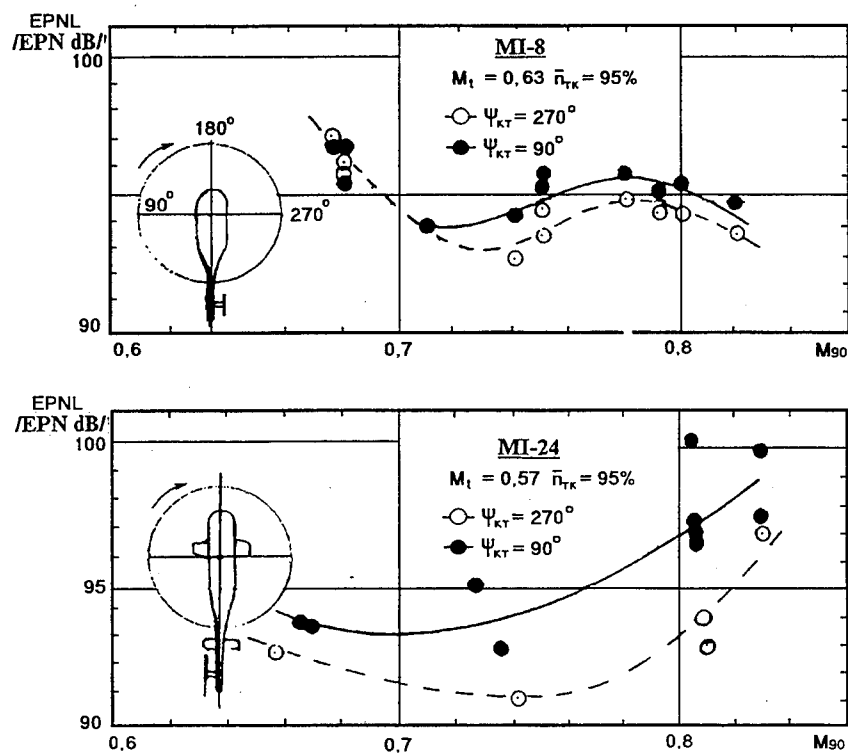


Fig 3. Single rotor helicopter noise level measured on the ground on the sides of flight path ($\psi_{kt}=90^\circ$ Measured point on the side of MR advancing blade)

compressibility effects on the rotor blades. Shockwave effects result in generation of impulsive noise radiation at high helicopter flight speed [9].

Real helicopter flight tests have shown that helicopter acoustic fields are not spatially symmetrical neither during hover, nor in horizontal flight. In hover and vertical flight conditions this asymmetry is caused by the asymmetry of tail rotor position, partial shielding of tail rotor noise radiation by the tail boom and superposition of acoustic fields of the two rotors (MR and TR), rotating in perpendicular planes. In horizontal flight conditions (Fig.3) the asymmetry is explained by the same factors, however the major effect is due to asymmetry of acoustic field of each rotor, relative to its rotation plane. Fig.3 shows the values of EPNL measured on both sides of helicopter flight path, 150 meters away from the ground track.

Harmonic acoustic emission source can be easily identified by harmonic frequency, which correspond either to the main or tail rotor blade passing frequency or to the typical frequency of engine compressor or turbine. The case of broadband component is somewhat more complicated, though often [8] that is the very one component, determining the value of Effective Perceived Noise Level (EPNL) on the ground. Both rotors (MR and TR) or a turbulent wake behind the helicopter can be the possible sources of such an emission. In order to identify the broadband frequency spectrum noise source, dominating in the helicopter external noise radiation, the flyover noise level of the Mi-28 helicopter has been measured. The aircraft versions had two different tail rotors. The initial production one had three blades in the same rotation plane. The modified one had four blades installed in pairs in two parallel planes. Angular displacement of one pair against the other pair, located in the parallel plane, was 36 degrees. Both production and modified tail rotors had the same diameter and tip speed. Comparison of one third of octave

sound pressure spectrums of the helicopter with different types of tail rotors (Fig.4) shows that a tail rotor is responsible for helicopter acoustic emission spectrum in a wide frequency range i.e. 150- 3,000 Hz.

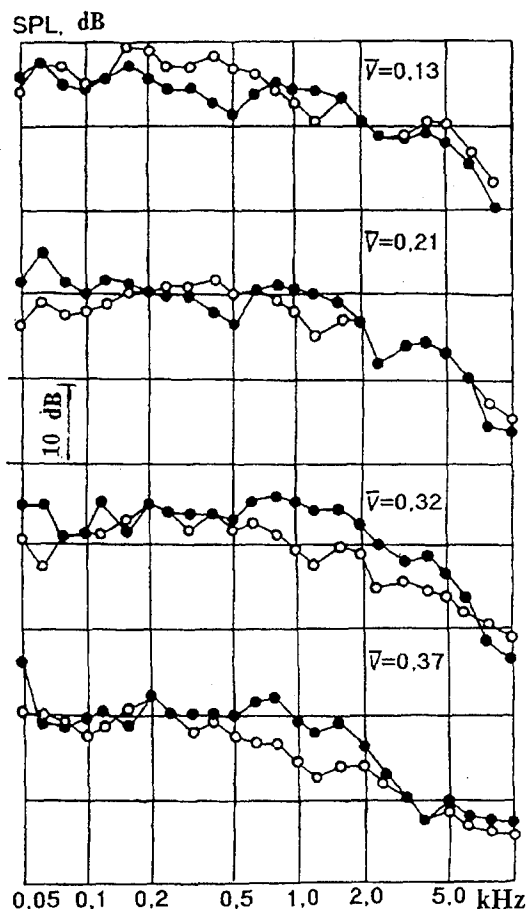


Fig.4. Sound pressure level spectrum in the one- third of octave frequency band for the helicopter with production type (●) and X-shape (○) tail rotor
($H=1000\text{m}$, $\tau=\tau_{PNLTM}$)

The change of tail rotor design changes the levels of sound pressure spectral components. One can notice that the level of broadband noise depends on the flight speed. When the flight speed changes from low ($\bar{V} = V/\omega R = 0.13-0.21$) to high ($\bar{V} = 0.35-0.37$) speed conditions, sound pressure in the 600- 2,000 Hz frequency range increases: by 10 dB for the helicopter with production TR and only by 3dB for the

helicopter with the modified TR. At the same time, the sound pressure levels in the given frequency range for the aircraft with the modified tail rotor remain 10dB lower, compared to the aircraft with the production TR. External noise level of the helicopter, heard on the ground, is reduced by 3-5 TPNdB.

In the narrow band sound pressure spectrums ($\Delta f = 1.25$ Hz), obtained for the frequency range of 0-500 Hz (Fig.5), tail rotor harmonics are found in all the considered sound emission directions: from 7 degrees to the flight direction up to 94 degrees. The first harmonic frequency of the tail rotor noise, taking into account the Doppler effect, is about 36 Hz, which correspond to two-bladed tail rotor emission at the given r.p.m. Thus, the X-shape four-bladed tail rotor generates harmonic emission in the frequency range, like a two-bladed tail rotor does; in the time range it emits like two two-bladed rotors with fixed relative position in the rotor disc.

Tail rotor harmonic emission fills a relatively narrow range in the general helicopter noise spectrum and in the frequency range above 600-800 Hz the helicopter noise emission spectrum becomes broadband for all the directions of noise radiation.

Thus, the tail rotor is one of the main sources of broadband noise, noticeably influencing upon the helicopter noise perceived on the ground. During the tests performed, the production and modified tail rotor's operational conditions were equal. Therefore, the reduction of broadband emission intensity of the modified TR, obtained in tests, in comparison with the production TR, can be resulted from the pressure pulsation intensity reduction, due to specific design features of the modified tail rotor.

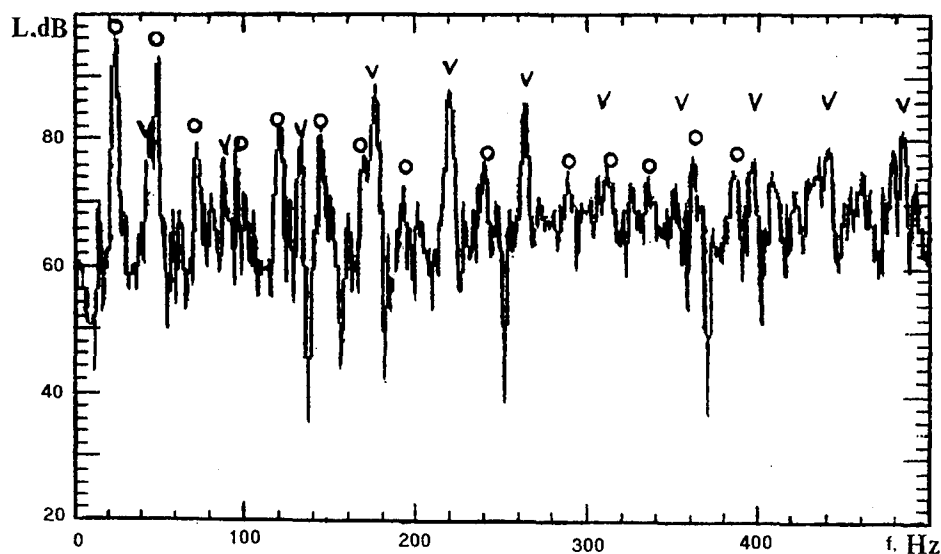


Fig.5. Acoustic emission spectrum of the MI-28 helicopter with X-shape tail rotor ($\bar{V}=0.324$ $H=100m$ $\varphi=34^\circ$)
(o - MR harmonics v - TR harmonics)

REFERENCES

1. Международные стандарты и рекомендуемая практика. Охрана окружающей среды.

Приложение 16 к Конвенции о международной гражданской авиации. Том 1, Авиационный шум. ИКАО, 3-е издание, 1993 г.

2. Вертолеты гражданской авиации. Допустимые уровни шума и методы определения уровней шума. Государственный стандарт, ГОСТ 24647-91.

3. Л.Я.Гутин. О звуковом поле вращающегося винта. ЖТФ, т.6, вып.5, 1936 г.

4. Е.Я.Юдин. О вихревом шуме вращающихся стержней. ЖТФ, т.14, вып.9, 1944, 561-567.

5. M.V. Lowson, J.B. Ollerhead. A theoretical study of helicopter rotor noise.

J.of Sound and Vibration, 1969, 9(2), pp 197-222.

6. T.F.Brooks, R.H.Schlinker. Progress in rotor broadband noise research. Vertica, v.7, N4, 1987, pp 287-307.

7. J.W.Leverton. Twenty-five years of rotorcraft aeroacoustics: historical prospective and important issues.

J.of Sound and Vibration, 1989, 133(2), pp 261-287.

8. А.Г.Мухин, В.Ф.Самохин, Р.А.Шипов и др. Авиационная акустика. Методы расчета шума самолетов и вертолетов на местности. М., Машиностроение, 1986 г.

9. F.H. Schmitz, Y.H.Yu. Helicopter impulsive noise: theoretical and experimental status. J.of Sound and Vibration, 109(3), 1986, pp 361-422.

IN FLIGHT RESEARCH WITH INSTRUMENTED MAIN AND TAIL ROTOR BLADES USING THE DRA BEDFORD AEROMECHANICS RESEARCH LYNX HELICOPTER

P.C. Tarttelin & Lt Cdr A. W. Martyn, RN
Flight Dynamics and Simulation Department
Defence Research Agency
Bedford MK41 6AE
United Kingdom

SUMMARY

This paper serves to inform the reader about in flight research at DRA Bedford on the DRA's Aeromechanics Lynx Control and Agility Testbed (ALYCAT) using instrumented main and tail rotor blades. The paper describes the instrumentation, data analysis techniques and flight test programmes, with the initial results from recent trials using instrumented main rotor blades on ALYCAT presented for the first time, and results from the earlier trials using an instrumented tail rotor blade presented in more detail.

MAIN ROTOR BLADE TRIALS

1 INTRODUCTION

The LYNX Research Instrumented Blades Programme (LYNXRIBs) programme is one of flight tests and data analysis aimed at the production of an accurate database of results to be used primarily for mathematical model validation. The work is in support of the development of a real time aeroelastic model for flying qualities and flight control purposes.

The blade instrumentation and development of analysis software has been a natural progression of the Puma General Purpose Research Instrumented Blade (GPRIB) programme^{1,2}, from which much was learned about both instrumentation and analysis techniques.

The new Lynx blade instrumentation was completed in March 1992, and the first phase of the flight trials programme was completed in May this year.

2 INSTRUMENTATION

The instrumentation to obtain the required data is situated on two standard Lynx metal main rotor blades, known as the Pressure Instrumented Blade (PIB) and the Strain Gauged Blade (SGB). The data from the PIB is used to obtain blade incidence and load data³, while the SGB is used to obtain data from which to synthesize blade displacements^{4,5}. In addition, the airframe and controls are also instrumented to provide body motion, control position and relative velocity data⁶.

The PIB instrumentation, shown in figure 1 consists of 3 main groups of pressure sensors: a leading edge array, a trailing edge array and two chordlines. The leading edge array, consisting of sensors mounted on the surface of the blade at 2% chord within a thin fairing (figure 2 and listed in table 1) are used for incidence derivation, whilst the trailing edge array, consisting of sensors mounted on the blade surface at 98% chord (figure 3 - radial positions are as for the leading edge array) are for detection of trailing edge separation⁷. The

two chordlines at 85% and 98% radius consist of sensors distributed around the blade section (figure 4) within a fairing which extends from 80% radius to the tip (figure 1); these are used for validation of the Indicator Method³, used to derive blade incidence and load.

In addition, a tip pitot sensor is mounted within the tip cap to provide an additional method of relative velocity and sideslip calculation and in flight information.

The distribution of sensors was based on experience with the Puma; they have been grouped to obtain information along the whole radius, but particularly in the region where most activity is expected, ie. the outboard 25% of rotor radius. The 85% chordline enables capture of data over a significant Mach number range without significant tip effects, whilst that at 98% shows such effects clearly.

The SGB instrumentation (figure 5) consists of a radial array of strain gauge bridges (positions listed in table 2); at each position is situated a bridge responsive primarily to each of flatwise, edgewise, and torsional motion. The strain gauge responses are synthesized with those obtained for a set of non-rotating calibration modes, to obtain modal proportions used in turn to obtain the blade displacements from those of the same calibration modes through Strain Pattern Analysis (SPA)⁵.

3 ANALYSIS SOFTWARE

The Research Instrumented Blade Analysis (RIBAN) package was developed for the GPRIB programme, and includes the Indicator Method and SPA. Most of the programs have undergone significant changes so as to operate with either LYNXRIBs or GPRIB data.

The package consists of three main stages:

- (i) Preparation - the desired timeslice of data is processed to produce local blade velocities, displacements (through SPA) and pressure coefficients.
- (ii) The local pressure coefficients and Mach numbers are processed to produce normal load and moment coefficients and incidence (Indicator Method).
- (iii) The local incidence is combined with the local velocity and displacement data to derive the components of local incidence, including downwash.

The major differences between the Puma and Lynx analyses are:

- (i) There are no articulated blade data for the Lynx; it has

a semi-rigid rotor head and thus all blade flap and lag displacements result from elastic motion.

- (ii) The Lynx blade has a linear variation in section with radius; RAE9618, RAE9615 and RAE9617 are the defined sections at 15.6%, 85% and 100% radius respectively. A separate aerodynamic look-up table for the Lynx is therefore necessary.
- (iii) A review of SPA has highlighted some required improvements to the method; these improvements are included in a new version of the program specifically for the Lynx data.

The two major areas of work undertaken specifically for Lynx data are described below:

3.1 Aerodynamic look-up tables

Aerodynamic look-up tables for the RAE9617 and RAE9615 sections have been produced from data measured for RAE(F) by ARA⁷; the data for RAE9615 is shown in figure 6. Together, they only cover two specific blade radial stations, and although interpolation could provide tables for intermediate stations, this would still only provide data at, and outboard of 85% radius. Further tables have been constructed from data calculated using the BVGK program⁸ at DRA(B); correlation with the measured data has indicated that interpolation between calculated data for 35% and 98% radius (the inner- and outermost radial positions) does provide satisfactory look-up table data for all the radial positions.

3.2 SPA enhancements

The lack of rigid blade flap and lag motion on the Lynx main rotor means that the SPA process forms a very important part of the RIBAN analysis. Improvements to SPA resulting from an independent study conducted at Bristol University have been incorporated into a Lynx version of the SPA software. Delays in the flight programme enabled this study to also include the simulation of alternative methods of performing the SPA calibration of the SGB (including error analysis). The results of this study indicate that there will be much improved confidence in the use of this method of obtaining blade displacements.

SPA calibration of the SGB was performed at DRA(B) by the Dynamics and Control Research Group, Engineering Department, University of Manchester in February 1994.

4 FLIGHT PROGRAMME

4.1 Flight conditions

The flight conditions required for the model validation consist of steady flight, manoeuvring flight and control inputs.

The steady flight conditions are:

- (i) hover;
- (ii) straight and level;
- (iii) level turn;
- (iv) climb and descent;

over the range $0.06 < T_e < 0.12$ and $0.6 < M_t < 0.7$ (thrust coefficient/solidity and mean tip Mach number respectively),

though not all T_e values are available over the full range of M_t . The range of values which can be covered are indicated in figure 7; the relevant limits of applicability for the Lynx Mk7 at DRA (B) are indicated and are also outlined in table 3. The method of achieving these conditions is outlined in reference 6. Figure 7 indicates how the method was performed, but a program on a portable computer carried on the aircraft was used to aid rapid calculation of the conditions. About half of the required test points were completed up to May 1994.

The manoeuvring flights contain open loop flight conditions as in the following:

- (i) low speed transition manoeuvres;
- (ii) in ground effect (IGE) level flight;
- (iii) transient turns;
- (iv) roll and pitch oscillations in hover;
- (v) roll reversals;
- (vi) transient pitches.

The control input part of the flight tests is designed to provide closed loop data to cover a range of response frequencies (input frequencies up to 4 Hz), using the following:

- (i) step inputs;
- (ii) doublet inputs;
- (iii) 3211 inputs;
- (iv) frequency sweeps.

These types of control inputs (the first 3 of which are used in any of the three controls) have been used extensively in the past for model validation and system identification; their past use at DRA(B) is described in references 9 and 10. The collective step inputs performed in May 1994.

4.2 Flight database

A database has been set up to store all kneepad flight test point data, and statistical data calculated from the outputs of the on-board data acquisition system. This enables a user to rapidly recall flights already performed for specific test conditions for his analysis, thus maximising the value of the originally recorded data. It is anticipated that all such data from the LYNXRIBs programme will be input in this way.

5 INITIAL RESULTS

Examples of some initial results are given in figures 8 and 9. The examples chosen are those which best indicate the type of information previously unavailable from the Puma research programmes. Figure 8 shows chordline plots of pressure coefficient, C_p , from both flight test and the ARA wind tunnel tests used by the Indicator Method, for identical aerofoil sections, at the 85% radius position, and similarly in figure 9 for 98% radius. In addition to the chordline plots, the normal force coefficient C_N and moment coefficient C_m , integrated from these C_p distributions are also displayed for the rotor revolution in question; the azimuth position relating to the chordline plots is indicated by a vertical line.

The two sets of pressure coefficients are related by matched Mach number and 2% chord C_p value; the similarity of the

two distributions then gives some indication as to the validity of the Indicator Method.

The 85% radius distributions show generally good agreement; it should be noted however, that as indicated from oscillatory aerofoil tests, some differences from predicted unsteady effects are expected. At 98% radius some differences occur; there is a reduction in C_N , (the so-called 'tip loss'). This is represented by a loss in C_p difference between the upper and lower surfaces towards the rear of the section. Relative forward loading in these conditions is to be expected, but the results show it to be almost entirely a reduction of loading at the rear of the section with only a marginal increase at the front of the section.

The analysis of these data is in its early stages, but it is already becoming apparent that there are some interesting features to be observed, the importance of which, in a handling qualities modelling context, are yet to be ascertained.

TAIL ROTOR BLADE TRIALS

6 INTRODUCTION

The characteristics of the helicopter models used for flight simulation typically fail to replicate the major non-linearities evident in helicopter yaw handling and control in low speed flight. The symmetrical yaw pedal margin plot generated using the DRA HELISTAB program, as described by Padfield¹¹, compared with the very asymmetric margin observed during flight trials with ALYCAT, figure 10 and figure 11, demonstrate the magnitude of the problem.

This failing is not unique to HELISTAB and, in the main, is due to a universal lack of understanding of the many interactional mechanisms that affect helicopter tail rotor performance. Consequently, there is a dearth of information on how to model the effects of these interactions in the simulator. One of the aims of the DRA tail rotor strategic research programme was therefore to provide data that would lead to an improved understanding of these mechanisms. The factors affecting tail rotor performance could then be modelled in a manner compatible with the constraints of real time simulation.

Two flight trials were carried out, one with a Puma¹², the other with ALYCAT¹³. This paper represents the outcome of the initial analysis of the ALYCAT data and discusses mechanisms and the features observed.

7 INSTRUMENTATION AND DATA ANALYSIS

The instrumented tail rotor designed and manufactured for ALYCAT was fitted with arrays of leading edge and trailing edge pressure sensors for use with the Indicator Method of blade loading estimation³. This method has been successfully employed by the DRA for main rotor research and has been fully described by Brotherhood and Riley¹⁴ and Brotherhood³. The design and manufacture of the blade and the subsequent conduct of the flight trial has already been reported on by Ellin¹⁵.

The bulk of the data analyzed to date has been that recorded in the hover and during constant velocity sidestep manoeuvres. Approximately 300 of the 1270 test conditions recorded have so far been inspected. The data has proved to be of a contemporary high quality, free from excessive drop-outs and noise, easily justifying the time taken in setting up the instrumentation prior to the trial.

Even in a steady flight condition, the tail rotor flow field varies from revolution to revolution. In order to develop a detailed understanding of the factors affecting the tail rotor it is necessary to analyze the data from many revolutions for each test condition. With so much data to study, a semi-automated analysis routine was created to produce a standard set of 7 plots from each test case, summarising the information contained therein. These plots did not contain sufficient information for the interaction mechanisms to be determined, but allowed the low speed flight envelope to be divided up into regions where similar features in the data had been noted, figure 12.

Both frequency and time domain techniques were employed. Study of the signal from each leading edge pressure sensor for each flight condition revealed differences in the data. It was found that the relative proportions of the main rotor frequency content of the leading edge pressure data varied with flight condition, thus allowing the regions shown in figure 12 to be identified. Examinations of the data in the time domain using statistical techniques complemented this process. Only when specific flight conditions were selected for in-depth analysis to determine the interaction mechanisms was a revolution-by-revolution study of the data made. This time dependency in some aspects of the interactions made dynamic graphics a most useful tool. The animation technique employed was as discussed in Ellin¹⁵.

The detailed mechanisms determined for the main/tail rotor interactions will be described in the next section.

8 INTERACTIONS

8.1 Variations in Tail Rotor Loading Distributions in Hover

Generally, the presence of a main rotor interactive effect on the tail rotor can be detected by inspection of the blade leading edge pressure sensors' signal frequency content. Analysis of the data reveals frequencies of 1R or, more commonly, 4R and their interference frequencies with the tail rotor $nT \pm 4R$ (where R and T are the main and tail rotor rotational frequencies respectively). An exception to this general rule occurs in and around the hover. In these conditions, even though the main rotor wake does not cut across the tail rotor, it passes close enough to the disc leading edge to distort the tail rotor blade tip vortices nearest to the main rotor wake so that they lie outboard of the tip of the following blade. The resultant gap in the otherwise axisymmetric ring of high leading edge pressure coefficient, C_p , and thus high blade loading is shown in figure 13. Negative C_p is conventionally plotted as its increase results in a rise in blade incidence and loading. The tail rotor pressures are not affected by any cyclical variation in the main rotor

wake in this condition, hence the lack of main rotor frequencies. This interaction is discussed by Brocklehurst¹⁶ where a likely mechanism is described.

8.2 Variation in Tail Rotor Loading Distribution in Low Speed Forward Flight

When the aircraft is moving forward at low speed, the tail rotor can become partially or even totally immersed in the main rotor wake. Figure 14 is similar to figure 13 but shows the tail rotor in 30 knots forward flight. The loading peak shown in figure 13 is missing at the rear of the disk as the tail rotor blade trailing tip vortices are left behind by the aircraft motion. The track of the successive main rotor blade trailing tip vortices is also shown; the effect of their interaction with the tail rotor changing as they cross the tail rotor disc. Outboard, within the loading peak region, the main rotor vortices cause a local reduction in the C_p value as shown at the indicated position in figure 15.

Inboard the main rotor vortices cause a local peak followed by a trough in the C_p value as shown in figures 16 and 17. The trough is not always apparent.

Close examination of this interaction effect, especially with the data animated on video, has revealed a discontinuity in the timings of the passage of the effect of the main rotor vortices as shown in figure 18.

The two solid lines on the figure indicate the apparent timing of the passage of the main rotor blade trailing tip vortices. The main rotor vortices pass over the inboard tail rotor leading edge sensors midway between the passage of the peak and the trough and this is taken into account in the figure by the solid line between the 2 dotted ones. The effect of this 'phase shift' is to delay the appearance of the interactional feature in the tip loading peak region until after it has appeared further inboard. It is hypothesized that 2 different interactional mechanisms are employed, one covering the interaction between the main rotor tip vortex and the tail rotor tip vortex and the other between the main rotor tip vortex and the tail rotor blade vortex sheet. The shift shown is approximately 15.5 degrees of main rotor rotation.

Although the two interactions described have a noticeable effect on the tail rotor C_p distribution, their overall effect on the tail rotor thrust is small. It is considered that there would be little to be gained from any attempt to reduce their effect still further. The relative magnitude of the overall tail rotor loading variation should be considered when deciding whether to include the effects of these interactions in a computer model. On a simple model of tail rotor thrust they could perhaps be ignored.

8.2.1 The Interaction Between a Main Rotor Blade Trailing Tip Vortex and a Tail Rotor Blade Trailing Tip Vortex in Forward Flight

The interaction mechanisms described in this section take place in flight conditions where the tip vortices trailed from the main rotor blades are cut by the tail rotor blades. For there to be an effect on the tail rotor loading distribution this intersection must take place when the tail rotor blade in

question is at an azimuth angle where the loading peak is evident. This will limit the visible effect of this interaction to the front of the tail rotor disc.

Assuming that the wakes from the main rotor and the tail rotor were independent and that each had no effect upon the other, the blade trailing tip vortex systems from the two rotors could be drawn as skewed helices. To add complication, the shape of each element on the helices trailed from a rotor would be distorted by the wake contraction and the influence of all the other vortex elements in that rotor's wake. The relative geometry of the main rotor and tail rotor dictates that the helical wake systems from the two rotors will intermesh orthogonally. As the external influences on both wake systems are the same at any given point, the separation between a vortex trailed from a main rotor blade and one from a tail rotor blade will remain constant. The separation between a main rotor vortex element and a tail rotor vortex element will therefore be dependant on the location of that main rotor vortex element when the tail rotor vortex element was formed. A tail rotor blade trailing tip vortex is formed by the rolling up of the vortex sheet shed from the blade outboard of the point of maximum circulation. This roll up process is complete by the time that the blade tip has travelled one rotor radius (ie 60 degrees of blade rotation)¹⁷, and the main rotor blade trailing tip vortex will have been present at its final location whilst this roll up was taking place. The separation distance between successive main rotor and tail rotor vortices will be different because of the non-integer gearing ratio between the rotors.

Contrary to the assumption made at the beginning of the last paragraph, the two wake systems are not independent and each main rotor vortex element will induce motion in each tail rotor vortex element and vice versa. The velocities induced will depend on the strengths of the vortices and the distance between them. Figure 19 shows a sketch of the tip of a tail rotor blade with the trailing tip vortex rolling up behind it. The tail rotor blade is about to cut a main rotor blade trailing tip vortex. That main rotor vortex can induce large variations in the local chordwise velocity at the blade, possibly affecting the point of maximum circulation on the blade and thus subsequently the strength and location of the tip vortex. The vortex sheet shed by the blade may be distorted by the velocities induced by the main rotor vortex. This would affect the roll up process which would again change the properties of the tail rotor tip vortex. Once the roll up process has been completed the two vortices would continue to interact.

The strength of the loading peak near the tip of the blade is most significantly affected by the location of the tip vortex trailed from the preceding blade. If that tip vortex has a discontinuity produced by the interaction just described, then a reduction in the loading peak on the next blade would follow.

For such an effect to be recorded on the instrumented tail rotor blade, the main rotor blade trailing tip vortex would have had to interact with the tip vortex trailed from the preceding tail rotor blade. This will affect the timing of the interactional feature noted in the data effectively delaying it

by 90 degrees of tail rotor rotation. This agrees with the phase shift noted on figure 18.

The reduction in loading peak will not be limited to the passage of one tail rotor blade. The reduction in the loading peak on one blade will reduce the strength of the tip vortex trailed behind that blade and thus affect the loading peak on the next, though to a lesser extent. Therefore, although the loading peak will be rapidly reduced by the interaction, it will return to its original value at a slower rate.

8.3 Interaction Between the Main Rotor Wake and the Tail Rotor in Quartering Flight

Of all the main/tail rotor interactions examined in this study, that occurring in quartering flight and described in this section has the most significant effect on tail rotor performance. In this context, 'quartering flight' describes the flight condition when the sideslip angle is such that the tail rotor is affected by the wake from the edge of the main rotor disc as depicted in figure 20. In forward flight the tail rotor will be in the centre of the main rotor wake and, where they affect the tail rotor, will cut each main rotor blade trailing tip vortex in sequence as they are trailed from the rear of the disc. In quartering flight, ie. sideslip angles of between 45 and 70 degrees depending on the aircraft configuration, the main rotor wake effect on the tail rotor can be much more significant as the tail rotor may be immersed in one of the two 'wing tip' vortices trailed from edges of the main rotor disc. The distortion of the main rotor wake caused by the formation of these wing tip vortices is well documented by Heyson & Katzoff¹⁸ and Brocklehurst¹⁶.

The wing tip vortex is formed from a number of main rotor blade trailing tip vortices rotating round each other. In forward flight the velocity field of each of these trailing vortices will also be rotating such that motion below the vortex centreline will be directed outwards, away from the aircraft centreline as shown in figure 21. The wing tip vortex will therefore constitute a significant velocity field all rotating in this direction. Once the aircraft develops a sideslip angle the wing tip vortices maintain their position with respect to the aircraft's track which will no longer be aligned with the axis of the helicopter. As mentioned above, with a sideslip angle of 45 to 70 degrees the helicopter's tail rotor may end up tracking along one of these vortices. If the tail rotor rotates top blade forward and the centre of the wing tip vortex passes through the centre of the tail rotor disc as in figure 22, then the tail rotor blades will be rotating within a mass of air that already has a component moving in the same direction. The flow field over the blades will therefore be reduced. The resultant reduction in dynamic head means that an increased tail rotor blade pitch is required to produce the necessary thrust. This increased pitch requirement is reflected in the helicopter transmission and control system by a reduction in pedal margin. The situation is the same whether the tail rotor is affected by the wing tip vortex from either the advancing or retreating side of the main rotor disc (areas 3 & 4 on figure 12). The only difference that exists between the two is that when the tail rotor is affected by the vortex from the retreating side of the main rotor, the tail rotor is off-loaded to some extent by the weathercocking action of the

fuselage and the change in tail rotor inflow due to the sideways motion. The yaw control margin is therefore greater than with the same relative wind from the other side of the nose and its reduction proportionally smaller. When the centre of the tail rotor disc is displaced from the vortex centreline as depicted in figure 23, that part of the tail rotor disc between the vortex centreline and the axis of rotation will experience an increase in dynamic head.

With a tail rotor that rotates top blade aft the effect of the wing tip vortex on the yaw control margin is reversed.

It could be expected that the tail rotor would be closer to the start than the end of the wing tip vortex roll up process. The velocity fields round the main rotor vortices would therefore show a marked cyclical variation at the blade passing frequency which would be detected by the tail rotor pressure sensors. Even if the roll-up was well established this frequency would still be evident if the rolled-up vortices retained their identities. As the effect of the main rotor wake on the tail rotor is stronger in this flight condition than in forward flight it would be reasonable to expect that the main rotor induced frequency content would be stronger too. This has not been found to be the case; in fact the tail rotor pressure sensors display a distinct lack of main rotor frequency content in the areas of the flight envelope where pedal margin was reduced. This would suggest that the individual main rotor blade vortex cores had merged into one single larger core whose associated velocity field would display a significant reduced cyclical content. This vortex merging had been noted during research carried out into wake minimisation techniques for large transport aircraft by Rossow¹⁹. In that reference it was found that the major criterion determining whether the two vortex cores merged or not was the ratio of the distance between centre lines and the cores' diameters. If merging of this nature has occurred it would suggest that the roll-up process was approaching completion. The relative strength of the flow field round the merged vortex compared with its individual elements requires further investigation as does its longevity.

8.4 Main Rotor Frequency Content on Tail Rotor Signals in Rearward Flight

In flight with a rearward component of aircraft translational velocity out of ground effect (OGE) the tail rotor cannot be immersed in the main rotor wake. The same is not the case for flight in ground effect (IGE) where the roll-up of the ground vortex will have a significant effect on the tail rotor performance²⁰. It is therefore surprising to find significant main rotor frequencies in the Lynx tail rotor pressure data. Two different forms of this interaction were found, one in figure 12 region 5 where the main rotor blade passing frequency, 4R, was dominant and the other in region 6 where the main rotor rotational frequency, R, took its place. Although other mechanisms such as acoustic feedback and the interaction of the main rotor blades with the tail rotor far wake were considered, the most likely cause of this effect was considered to be the main rotor forcing the fuselage, which, in turn, caused the tail rotor blades to flap giving rise to small changes in loading. The fact that all 7 sensors along the length of the blade appear to be equally affected would tend

to rule out a direct aerodynamic interaction which would affect one part of the blade more than the remainder. The effect of this interaction would be to impart a small additional yawing moment to the fuselage in the same direction as the movement of the tail ie. yaw or sway, that give the input to the tail rotor.

9 CONCLUSIONS

9.1 Main Rotor Instrumented Blade Programme

The preparation and initial use of an instrumented blade set and the associated analysis software has been described. The programme for the capture of a database of flight data for validation of a new mathematical model for handling qualities purposes has also been outlined, and some initial results from the Pressure Instrumented Blade presented. The analysis of such data is ongoing, and is already presenting some interesting features, the effects of which will be incorporated into the aforementioned model to improve its predictive capabilities.

9.2 Tail Rotor Instrumented Blade Programme

A series of flight trials has been conducted with the DRA's ALYCAT Lynx research helicopter to provide a better understanding of the effects influencing tail rotor performance and yaw control. From the data analysis carried out to date the following conclusions can be drawn:

(i) Six distinct mechanisms of main rotor/tail rotor interaction have been noted in the low speed envelope, the most significant of which have been examined in detail.

(ii) In quartering flight, the tail rotor can be immersed in the roll-up of the main rotor blade tip vortices trailed from the edge of the disk. For a tail rotor rotating top-blade-forward, this results in a large net reduction in the dynamic head at the blade giving rise to a reduction in control margin. This is the most significant interaction influencing the tail rotor.

(iii) Close to the hover, the main rotor wake passes just forward of the leading edge of the tail rotor disc distorting the tail rotor trailing vortex wake. This results in a localised reduction in tail rotor loading.

(iv) In forward flight the loading peak, evident at the blade tip in the hover, is missing at the rear of the disc as the trailing tail rotor tip vortices are left behind by aircraft motion.

(v) In rearwards flight the tail rotor can experience small loading variations at main rotor induced frequencies possibly due to main rotor wake effects on the fuselage causing sideways movement of the tail rotor gearbox and hub.

Acknowledgement

The authors would like to acknowledge the fact that the ALYCAT tail rotor instrumented blade trials and analysis was conducted by Lt Cdr A.D.S. Ellin, RN. The results presented in this paper are also presented in more detail in reference 21.

REFERENCES

- 1 M.J.Riley et al., "Estimation of rotor blade incidence and blade deformation from the measurement of pressures and strains in flight", Paper presented at the 14th European Rotorcraft Forum, September 1988.
- 2 P.C.Tarttelin., "Rotor loadings in hover - correlation of theory and experiment", Paper presented at the 15th European Rotorcraft Forum, September 1989.
- 3 P.Brotherhood., "The determination of helicopter blade local normal force coefficient, incidence and stall boundaries from flight measurements of leading and trailing edge pressures", DRA TM FS 1044, May 1993.
- 4 C.J.W.Hassal., "Development and initial application of a technique to measure vibration mode shapes of a rotating blade", RAE TR 77064, 1977.
- 5 A.R.Walker., "Experimental determination of rotating helicopter blade deformations using Strain Pattern Analysis", RAE TM MAT STR 1108, 1988.
- 6 P.C.Tarttelin., "Rotor aeromechanics research with the RAE research Lynx - the experimental facility and test programme", Paper presented at the 16th European Rotorcraft Forum, September 1990.
- 7 C.P.Sugrue., "Aerodynamic look-up tables for Lynx rotor blade analysis", DRA Flight Systems Dept. Working Paper WP(93) 057, June 1993.
- 8 M.R.Collyer., "An extension to the method of Garabedian and Korn for the calculation of transonic flow past an aerofoil to include the effects of boundary layer and wake", RAE TR 77104, 1977.
- 9 S.S.Houston and P.C.Tarttelin., "Theoretical and experimental correlation of helicopter aeromechanics in hover", RAE TM FM 20, 1989.
- 10 S.S.Houston and R.I.Horton., "The identification of reduced order models of helicopter behaviour for handling qualities studies", RAE TM FS(B) 682, 1987.
- 11 Dr G.D.Padfield., "A theoretical model of helicopter flight mechanics for application to piloted simulation", RAE TR 81048, 1981.
- 12 S.F.Baldwin and C.S.Handley., "Flight tests to explore tail rotor limitations in the low speed envelope", Paper presented at the 14th European Rotorcraft Forum, Milan, 1988.
- 13 A.D.S.Ellin and C.D.Brown., "RAE Bedford tail rotor aerodynamic flight research programme - Lynx AH Mk5 trial conduct", Paper presented at the SEFTE Conference on Helicopter Flight Test Techniques, Patuxent River, 1991.

- 14 P.Brotherhood and M.J.Riley., "Flight experiments on aerodynamic features affecting helicopter blade design", Vertica, 1978, Vol 2.
- 15 A.D.S.Ellin., "Flight measurements illustrating key features of tail rotor loading distribution", Paper presented at the Royal Aeronautical society Conference on Helicopter Yaw Control concepts, London, 1990.
- 16 A.Brocklehurst., "Main rotor/tail rotor interactions near hover", Westland Helicopters Ltd RM 535, 1989.
- 17 I.A.Simons et al., "The movement, structure and breakdown of trailing vortices from a rotor blade", ARC 28 993, 1967.
- 18 H.H.Heyson and S.Katzoff., "Induced velocities near a lifting rotor with nonuniform disk loading", NACA Report 1319, 1957.
- 19 V.J.Rossow., "Convective merging of vortex cores in lift-generated wakes", Journal of Aircraft, 1977 Vol 14, No. 3.
- 20 W.Wiesner and G. Kohler., "Tail rotor performance in the presence of main rotor, ground, and winds", Journal of the American Helicopter Society, 1974, Vol 19, No. 3.
- 21 A.D.S.Ellin., "An inflight investigation of Lynx AH Mk5 main rotor/tail rotor interactions", Paper presented at the 19th European Rotorcraft Forum, Italy 1993.

Station	%R
1	35
2	40
3	45
4	50
5	55
6	60
7	65
8	70
9	72
10	75
11	78
12	81
13	83
14	85
15	87
16	89
17	91
18	93
19	96
20	98

Table 1

PIB leading and trailing edge pressure sensor radial positions.

Station	%R
1	3.2
2	5.0
3	6.8
4	14.2
5	17.0
6	19.6
7	25.0
8	31.0
9	41.0
10	48.0
11	64.0
12	74.0
13	85.0
14	96.0

Table 2

SGB strain gauge radial positions.

Item	Minimum	Maximum
Mass (kg)	3704	4763
Altitude (ft)	0	12000
rpm	302	347

Table 3

Lynx ZD559 mass, altitude and rpm limits.

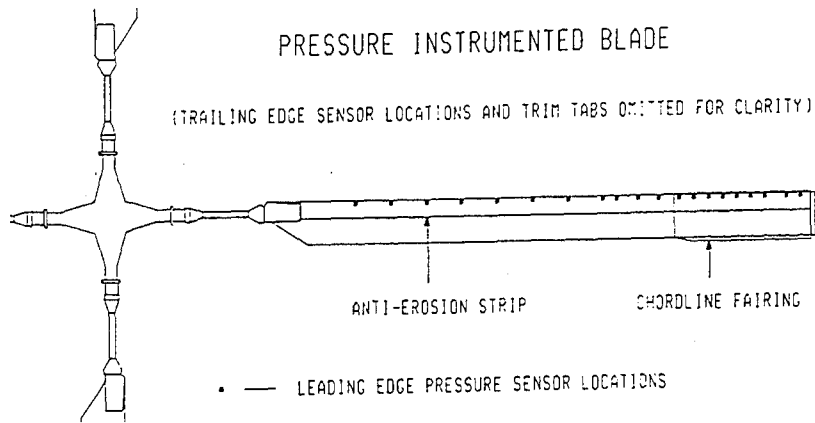


Fig 1 PIB layout

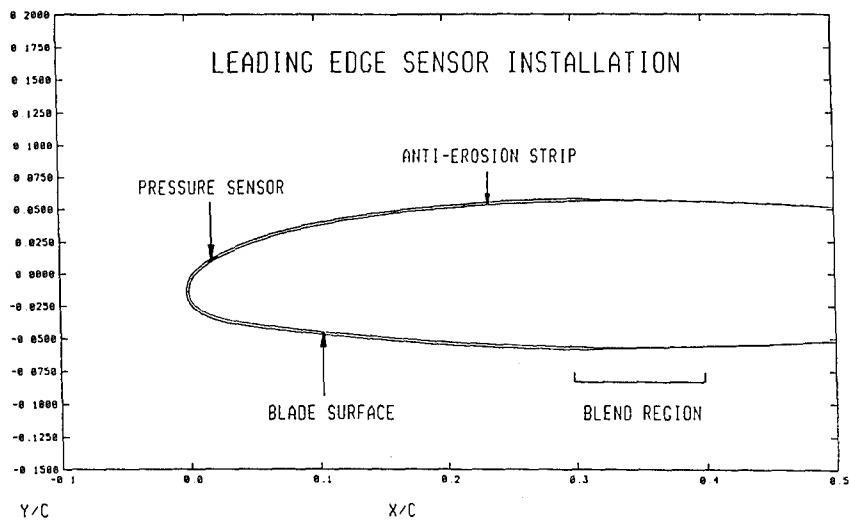


Fig 2 Leading edge sensor installation

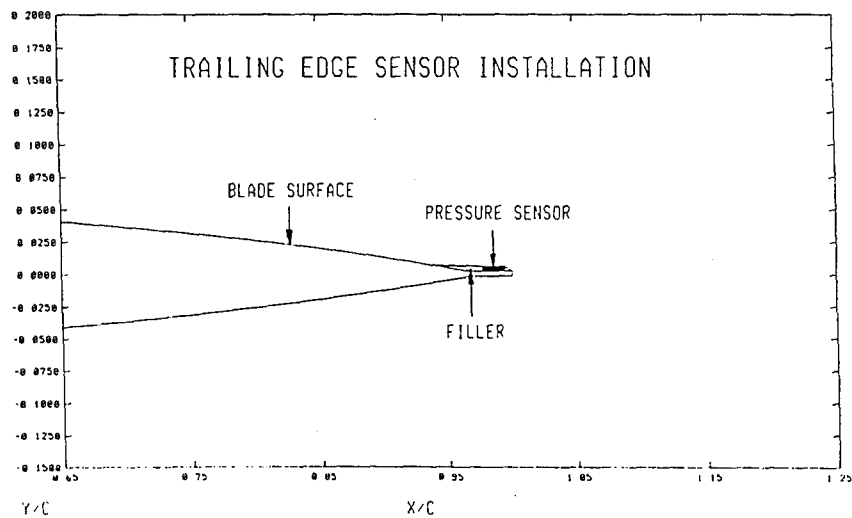


Fig 3 Trailing edge sensor installation

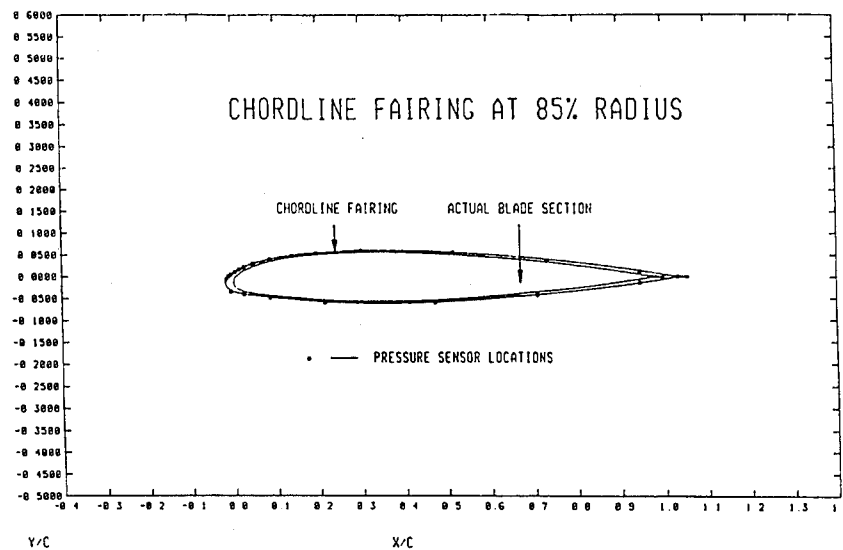


Fig 4 Chordline installation

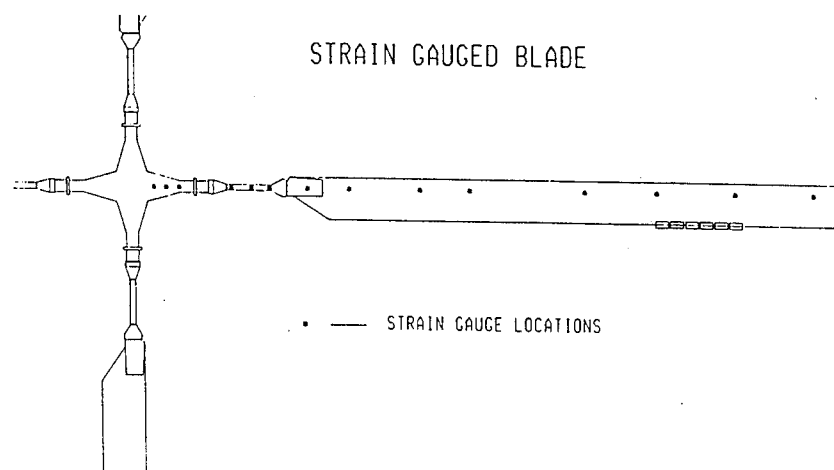
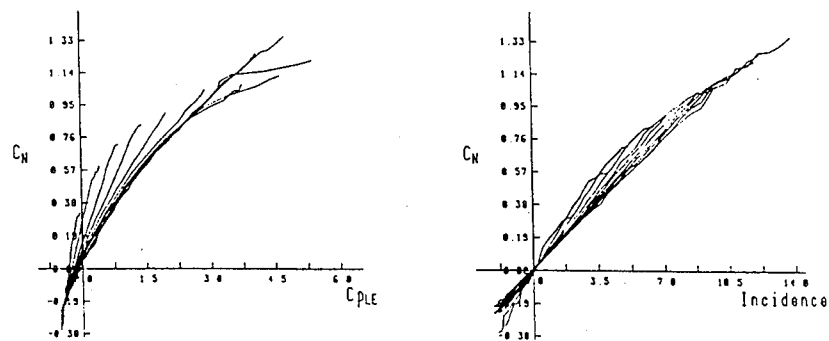


Fig 5 SGB layout



Look-up table data for the RAE 9615 section

Fig 6 RAE 9615 look-up table

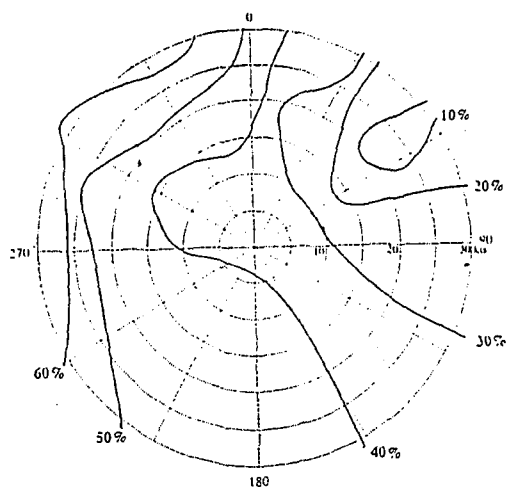


Fig 10 Lynx AH Mk5 Flight Trial Pedal Margin Plot

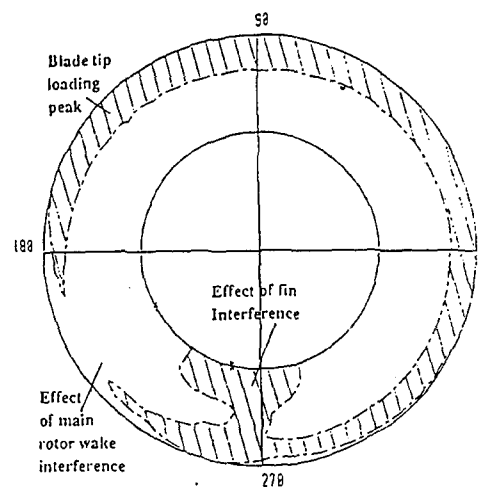
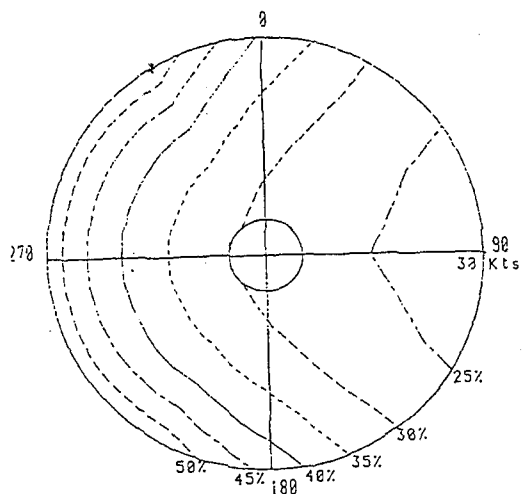
Fig 13 Regions of high C_p for one revolution of the tail rotor (hover).

Fig 11 Lynx AH Mk5 HELISTAB Pedal Margin Plot

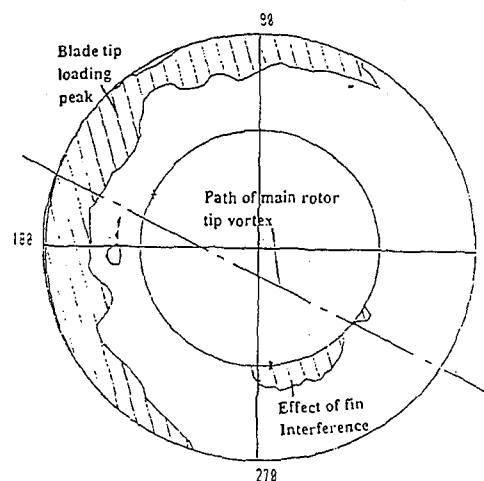
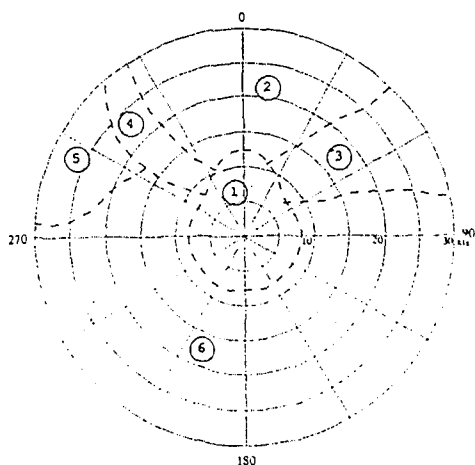
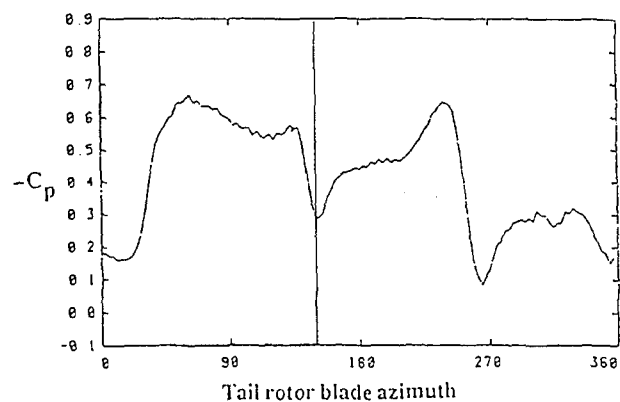
Fig 14 Regions of high C_p for one revolution of the tail rotor (Fwd Flight).

Fig 12 Regions of Main/Tail Interactions.

Fig 15 Localised reduction in C_p caused by main rotor tail rotor interaction.

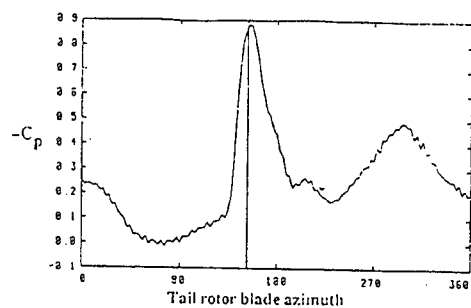


Fig 16 Localised increase in C_p due to velocity induced by a vortex opposing blade rotation.

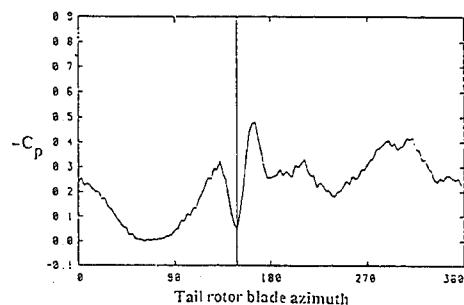


Fig 17 Localised reduction in C_p due to velocity induced by a vortex being with blade rotation.

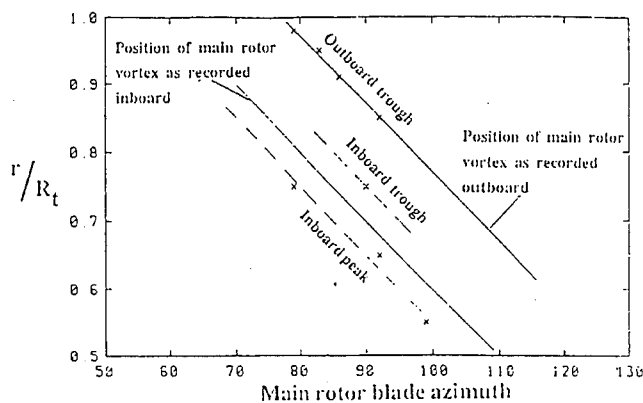


Fig 18 Position of main rotor tail rotor vortex interference effect.

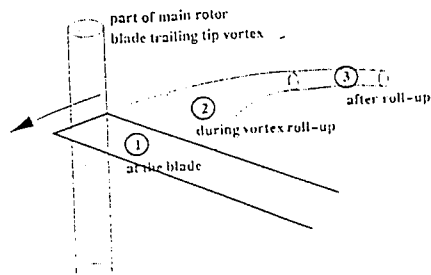


Fig 19 Sketch of main rotor blade vortex tip vortex interaction.

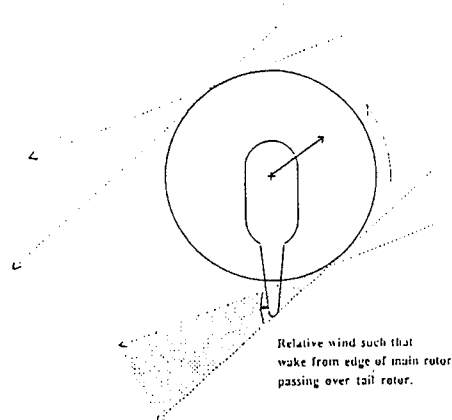


Fig 20 Definition of quartering flight.

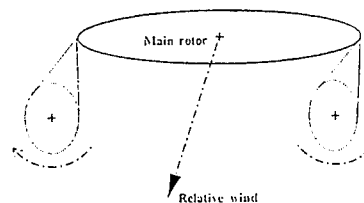


Fig 21 Direction of rotation of 'wing tip' vortices.

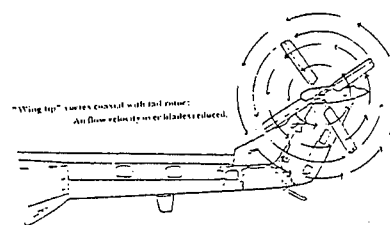


Fig 22 'Wing tip' vortex and tail rotor.

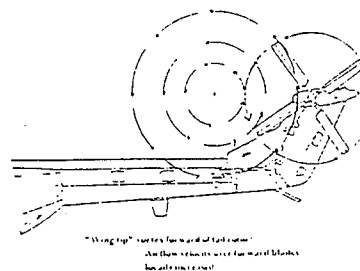


Fig 23 Wing tip vortex forward of tail rotor.

FLOW FIELD INVESTIGATION OF A ROTATING HELICOPTER ROTOR BLADE BY THREE-COMPONENT LASER-DOPPLER-VELOCIMETRY

U. Seelhorst¹, B.M.J. Beesten², K.A. Bütetisch¹

¹ Institute for Fluid Mechanics

DLR German Aerospace Research Establishment

D-37073 Göttingen, Germany

² Department of Aerospace Engineering

RWTH Aachen University of Technology

D-52056 Aachen, Germany

SUMMARY

The measurement of three dimensional local flow vectors of a blade tip vortex at positions near the helicopter rotor plane were performed with a three component laser-Doppler-velocimeter (3D LDV). A 'position monitoring system' synchronized to the blade rotation gave access to blade motion parameters like lead-lag and pitching at the desired radial position of the blade. Mainly results concerning the structure of blade tip vortices were obtained. The measurements of a vortex generated at hover condition showed the correctness of 'time history' data acquisition, e.g. taking data during the time interval when one particular blade is passing the location of the measuring volume of the LDV.

Vortex structure measurements at two different blade tips, a regular square tip for reference and a non-planar tip called winglet, were carried out. First of all the influence of the winglets on vortex structure and blade vortex interaction (BVI) has been investigated. Then in addition to the vortex parameters like vortex/blade miss distance, vortex core size, axial velocity deficit, vortex strength, and vorticity distribution with respect to the spatial orientation of the vortex axis, results on 3D-vorticity distribution and the temporal vortex roll up for the different blade tip vortices have been obtained.

NOMENCLATURE

c	chord length
c_T	rotor thrust coefficient
l	convection length
n	rotor rotational speed
r	radial position
t	time
u, v, w	velocity components
x, y, z	spatial coordinates
BVI	blade vortex interaction
DLR	German Aerospace Research Establishment
FFT	Fast Fourier transformation
ILR	RWTH Aachen, Dept. of Aerospace Engineering
LDV	Laser-Doppler-velocimeter
RWTH	Aachen University of Technology

R	rotor radius
U_0	wind tunnel velocity
V_{convect}	convection velocity
β	rotor tilt angle
ϑ_{coll}	collective pitch
ϑ_{cycl}	cyclic pitch
μ	advance ratio
ω	vorticity
$\omega_x, \omega_y, \omega_z$	vorticity components
Γ	circulation
Ω	rotor frequency
Ψ	azimuth angle
Ψ_0	trigger azimuth angle

1 INTRODUCTION

Measurements of vortex structures behind fixed wings have been performed for many years. For this purpose many different measuring techniques can be applied, e.g. hot wire, pressure probes, interferometry, and LDV. Measurements of vortex structures within the plane of a rotating helicopter rotor, can only be performed by non intrusive measurement techniques. LDV is one of the promising tools which can be used. The feasibility of such flow field measurements has been shown recently [1,2]. For the special application of LDV on the flow field of a rotating helicopter model rotor, especially in the case of large scale model rotors in the large scale wind tunnel DNW, a new high performance three component laser-Doppler velocimeter was developed in the Institute for Fluid Mechanics of the DLR Göttingen.

Two different modes of data acquisition are possible for the investigation of the time dependent flow field of the rotating rotor [3]. The 'strobe technique' yields the flow field attributed to the blades for well known reference angles of the rotor. Data, obtained by 'time history technique', represent the time depending change of the flow field produced by the rotating blade during a well known time interval at one space fixed measurement position within the flow field.

As the first technique is rather time consuming the second is more attractive but boundary conditions for the equivalence of the results of the modes have to be determined. This has been done in the course of a co-operative programme between DLR and RWTH, set up to investigate vortex structures behind

rotor blades. Tests were performed on a helicopter model at hover condition in order to study the procedure how to obtain the data correctly. Then measurements were carried out in Aachen for rotor blades with different tips operated at forward flight condition.

As BVI noise is governed by the induced velocities of tip vortices, the noise level depends on blade vortex miss distance, vortex strength, and vortex structure. The use of non-planar blade tips is one possibility to influence the vortex structure. Therefore, the influence of a non-planar blade (winglet) on vortex structure in comparison to a regular square blade has been investigated.

It should be mentioned that the flow field of a helicopter at forward flight condition is highly unsteady and an instantaneous local velocity value would be meaningless. Due to its periodicity it is possible to sample data over several rotor revolutions. Hence a time averaged result can be obtained if the measurements are triggered accurately referenced to a fixed blade position. It is obvious that precise temporal blade position data are necessary which have to be acquired simultaneously to the velocity data.

This paper describes how these flow field measurements on rotating helicopter blades in hover flight condition and with different blade tip shapes in forward flight condition have been performed. The envisaged flow field quantities need derivatives of the velocity data a high quality of the measured data is required. In particular this is true if the vortex core structure has to be resolved

2 EXPERIMENTAL SET UP

2.1 Test facilities

The tests in hover flight conditions were performed at DLR Göttingen using a four-bladed helicopter model rotor equipped with NACA 0015 airfoils.

Investigations of differences in vortex structure due to different blade tip shapes were performed in the open test section of the ILR Aachen low-speed wind tunnel. A four-bladed model rotor with a diameter of 1.02 m was driven by a 65 KW engine. The rotor was fully articulated and had flapping hinges. Fig. 1 and Fig. 2 show the test set ups including the LDV system.

2.2 Blade geometries

Two different blade tip geometries were tested. As a reference a planar blade was used which has a rectangular shape and is based on an untwisted NACA 0015 airfoil. The second blade tested was a blade with a twisted winglet which was designed in Aachen [4,5]. It has a swept-back tip for better high speed characteristics. The nose is extended in forward direction to improve lift characteristics when retreating and to avoid additional pitching moments caused by the sweep. The non-planarity, defined as the distance between the blade tip and the rotor plane, has a value of about 0.65 chord lengths. Twisting starts at a radius of 91% and reaches 7° at the tip. This generates extra bound circulation at the tip region and pushes the vortex further downward.

Both blades are built in carbon/glass-fibre-composites and have NACA 0015 airfoil sections of 0.054 m main chord length. As a result the four-bladed rotor has a solidity of about 0.135.

2.3 LDV system

For investigations of the complex flow field of blade tip vortices within the plane of a rotating helicopter rotor, LDV as a non intrusive measuring technique has to be applied. As the flow field of a helicopter rotor is highly 3-dimensional, the measurement of the 3D flow vector is necessary for the complete description of the exact structure of the vortex. This can be accomplished by a three component laser-Doppler-velocimeter (3D LDV). The special specifications for a 3D LDV required for the investigation of such problems has been included in the LDV development at the Institute for Fluid Mechanics of the DLR [6]. Fig. 3 shows the schematic set up of the 3D LDV. As the same 3D LDV should also to be used in the open test section of the DNW, a large working distance had to be established and the operation in back scatter, off-axis mode was chosen.

A 6 Watt Argon-Ion Laser is used as light source. The three most intensive laser lines at 476.5 nm (violet), 488 nm (blue) and 514.5 nm (green) respectively are utilised to distinguish the different velocity components in the LDV system. Each of the laser beams is divided into two beams with almost equal intensity (Dantec transmitter box, type 60X41), one of them is superimposed with a Bragg shift of 40 MHz in order to correctly determine the direction of the flow vector. The laser beams are coupled into single mode glass fibres and with 6 individual transmitting optics (Dantec, type 41X171) they are launched into the common probe volume at a distance of 5 m. At that position the probe volume had a diameter of about 0.25 mm. The use of single mode glass fibre ensures a Gaussian beam shape of the laser beams, because only the TEM_{00} mode can propagate through the fibres.

The individual laser beam pairs are arranged in that way that the velocity component perpendicular to the horizontal LDV plane was probed by the green laser light. The projections of the axial velocity component, inclined against the centre line of the undisturbed flow direction by an angle of 85° and -85° respectively, were probed by the violet and blue light.

The velocities, obtained in the LDV fixed coordinate system, have to be transformed in a wind tunnel fixed coordinate system. For good resolution of the cross velocity component v , the angle between the optical axes is chosen to about 30° .

Particles, necessarily introduced into the flow, consist of dispersed oil, having a maximum size lower than $1 \mu\text{m}$. They are small enough to follow the flow correctly [7]. To minimize disturbances occurring from injecting the particles into the flow by a tube, they are introduced far up-stream of the test section in the settling chamber.

Because of low light scattering intensity when operating the LDV in backward scatter mode, the receiving optics of the LDV system require a large aperture to collect enough scattered light to achieve a sufficient high signal quality. As the working distance of the LDV is flexible, two different receiving optics can be integrated into the system. One with an aperture of 350 mm and a flexible working distance from 3 m to 5 m, the other one with an aperture of 500 mm and a fixed working distance of 5m. In this particular case the 350 mm optics were used to collect the scattered light of the green, violet, and blue laser beams, containing the information of all the three individual velocity components, and is coupled into a multi mode glass fibre. The light was fed to a prism to separate the light of different wavelengths and subsequently to

convert the light intensities into electrical signals by photo multiplier tubes.

2.4 Data acquisition

Data acquisition is performed for each component using a fast Fourier based Doppler burst processor (Aerometrics, DSA 3220). The velocity data obtained are stored together with the information of the time of arrival.

Based on the assumption of a periodic flow field due to the rotor revolution, conditional sampling is used to get information on the flow field with respect to the azimuth angle of the blade. A trigger signal from the rotor axis could be shifted with a time delay to an appropriate azimuthal position of the rotor blade with an accuracy of 0.3%. At this position the clock of the data acquisition system was set to zero. Data acquisition was started now for a time window corresponding to a preselected azimuthal window or the time interval needed for the portion of the flow to pass through the probe volume. Usually data were acquired just within an azimuthal window which is only a part of the whole rotor revolution.

Converting 'time history' information into spatial information can be done in two different ways. The transformation of the 'time history' information to the corresponding azimuth angle is done with the simple equation:

$$(1) \quad \Psi = \Psi_0 + (360 \cdot n \cdot t)$$

No assumption has to be made concerning convection velocities, because equation (1) only uses the rotational speed of the rotor for the transformation. Calculation of distances from azimuth angle is easily done with the help of the radius of the rotor.

To transfer the 'time history' information into a spatial information of the flow, the convection velocity of the flow around the vortical structure has to be known:

$$(2) \quad l = V_{\text{convection}} \cdot t$$

The accuracy of the flow field determination in the 'time history' mode may be affected by local deviations from a constant convection velocity. As an approach the convection velocity was assumed to be the vector sum of the free stream velocity and the rotor induced down wash velocity. In reality there may be a change within the time interval in particular in the vicinity of the vortex core.

On the other hand the possible inaccuracy has to be accepted, because the data acquisition in 'time history' mode reduces the total measurement time drastically.

2.5 Position monitoring

As the blade position changes under flight condition in relation to the non-operating rotor, the position of the rotor blade has to be acquired simultaneously to the velocity data acquisition. This is done for each revolution of the one blade selected to be tested at the azimuth angle

Ψ_0 , where the trigger signal from the rotor axis starts the LDV measurements. The position monitoring system, developed at the Institute for Fluid Mechanics of the DLR [8], is used for this purpose. With this system it is possible to obtain the motion of the blade with an accuracy of 0.1 mm. Thus the exact position of the LDV probe volume relative to the rotor blade can be determined.

3 TEST PARAMETERS

3.1 Hover case

First of all, in order to examine the accuracy of vortex structure determination in the 'time history' mode, measurements were performed on a model rotor in hover flight condition. The collective angle was set to $\vartheta_{\text{coll}} = 15.0^\circ$, to create a strong tip vortex. Rotor speed was selected to $n = 1300$ rpm.

The coordinate system for this test case is shown in figure 4. The origin of the coordinate system is defined for an azimuth angle of the blade of $\Psi = 180^\circ$ and is located at the blade tip trailing edge for the x- and y-direction and one chord below the rotor plane for the z-direction. The location of the LDV probe volume is adjusted to the origin of the coordinate system. The choice of the measurement positions in z-direction had to take into account that the formation of the vortex was completed before the down washed vortex entered the LDV probe volume. For different positions in x-direction ($\Delta x = 2.5$ mm) 'time history' measurements were performed with a time window of 11.5 ms, corresponding to an azimuth angle covered by the blade of $\Delta \Psi = 90^\circ$.

3.2 BVI case

Before discussing the measurement positions for the BVI case, the coordinate systems used shall be introduced. In contrast to the set up for the hover case, the rotor plane is rotated by 90° . As shown in Fig. 5 the positive x-direction is equivalent to the flow direction of the wind tunnel (against flight direction) and y points down wash direction.

Due to the limited wind tunnel occupation time, only one flight condition for the two different blades could be investigated. The advance ratio was selected to $m = 0.2$ as a medium speed flight where BVI occurs. To get strong tip vortices the collective angle was set to $\vartheta_{\text{coll}} = 10.0^\circ$ which results in a highly loaded rotor with $c_T = 0.008$. Cyclic angle was set to $\vartheta_{\text{cycl}} = 3.5^\circ$ to trim the rotor. The shaft angle has been $\beta = -3.0^\circ$. Rotor speed was selected to $n = 1500$ rpm.

Measurements were performed in two planes perpendicular to the rotor plane. Fig. 10 shows their locations. Plane I was selected to determine the undisturbed vortex structure of the tip vortices of both blades. It is placed at an azimuth angle of $\Psi = 0^\circ$ and the wind tunnel velocity moves the vortex away from the rotor. A second reason led to this choice. The LDV probe volume had to be traversed in y-direction while the x-variation resulted from 'time history' measurements. As already pointed out the 'time history' data can be converted into the space related data by taking into account the wind tunnel convection velocity. The advantage of this method can be seen in the fact that the measuring time is reduced by more than 95%. The location of the LDV probe volume for the measurements on the undisturbed vortex at $\Psi = 0^\circ$ was shifted 50 mm in x-direction outboard the rotor plane. At this point, at different positions in y-direction 3D-LDV measurements were performed in an azimuthal window of $\Delta \Psi = 60^\circ$ corresponding to a time interval of 6.6 ms. During this time the tip vortex generated at $\Psi = 0^\circ$ passes through the LDV probe volume driven by the wind tunnel velocity and the down wash convection velocity. Subsequently the time dependent velocity data at the measurement station I (0° azimuth angle) have to be converted into the velocity data in the space fixed coordinate system by equation (2).

Measurements in plane II were performed to investigate the vortex roll up and the BVI characteristics of the different

blades. Here a coarse grid of 6 x 11 points in y- and z-direction was chosen with about 50 time interval steps derived from 'time history' results. It has to be noted that the coarse grid reduces the accuracy of the results.

The origin of the coordinate system with respect to the y- and z-direction is again at the blade tip trailing edge with the blade at an azimuth angle of $\Psi = 0^\circ$.

Data acquisition started when the blade was located at an azimuth angle of $\Psi = 85^\circ$ and stopped at a blade azimuth angle of $\Psi = 108^\circ$. This corresponds to a distance of one chord length in front and two chord lengths behind the blade. The azimuthal window was divided into 50 intervals which led to a azimuthal resolution of better than 0.5° . The total number of grid points around the blade is then represented by a cube of 50 by 11 by 6 points. Again the data acquisition in the 'time history' mode reduced the total measuring time by 98%. For the measurements at location II (90° azimuth angle) the time dependent data was transformed to space fixed coordinate data by equation (1).

4 DATA EVALUATION

The calculation of the radial circulation distribution is accomplished by equation (3)

$$(3) \quad \Gamma = \oint v ds$$

where different closed boxes around the vortex centre with different sizes have been chosen in order to study the dependence of resulting circulation on integration path.

The determination of the single components of the vorticity ($\omega_x, \omega_y, \omega_z$) is performed by calculating:

$$(4) \quad \omega_i = \frac{1}{2} \text{rot}(\vec{u}_i)$$

for the centre of a rectangle with data points on each corner. The definition of the orientation of the vorticity components is illustrated in Fig. 5.

5 RESULTS

5.1 Hover case

From all the flow field data obtained in 'time history' data acquisition mode, also velocity profiles for various fixed azimuth angles corresponding to the 'strobe technique' can be selected. In contrast to the velocity profiles in z-direction, obtained from the transformation of the 'time history' data, the velocity profiles in x-direction are not affected by changing drift velocities. They are directly related to spatial coordinates, where the probe volume of the LDV was placed during the measurement.

For a circular vortex, the expected velocity profile of the axial velocity U versus z coordinate should be the same as the normal velocity W versus the x coordinate.

The flow field of the measured blade tip vortex in the x-z-plane is illustrated in Fig. 6. The transformation of 'time history' data is performed by the assumption of a constant down wash velocity of $W_{\text{ind}} = 7 \text{ m/s}$. In order to obtain the velocity field of the undisturbed vortex, the induced down wash velocity W_{ind} has to be subtracted from the measured normal velocity component W. As this leads to a circular vortex, the assumption of a constant induced down wash velocity $W_{\text{ind}} = 7 \text{ m/s}$ is correct.

Fig 8a and b depict the velocity profiles through the vortex core in x- and z-direction. The profiles show identical behaviour. The determined vortex core diameters, defined as the distance between the velocity maxima, are identical. In both cases a value of 10 mm is obtained, corresponding to 18.5% chord length. This finding also indicates, that the assumptions made are correct, namely that the induced down wash velocity is $W_{\text{ind}} = 7 \text{ m/s}$, the roll up process of the vortex has been completed, and any change of the vortex structure within the short measuring time was negligible.

No significant cross velocity component V can be seen in the data. This indicates that the orientation of the x-z-plane where data have been taken is perpendicular to the vortex axis.

From all those results the conclusion can be drawn that 'time history' measurements for flow field investigation are sufficiently accurate if the convective velocity is known.

The calculated vorticity map using equation (4) is shown in Fig. 7. A clear maximum can be detected at the centre of the vortex. As vorticity is a differential value, the absolute value depends on the spatial resolution of the flow field, e.g. the number of the grid points.

Due to the measurement grid, only for 12 closed boxes with different distances to the vortex centre the circulation could be calculated. The radial circulation profile is shown in Fig. 9. The behaviour of this profile is identical to that of a Hamel-Oseen vortex characterized by a constant increase of the circulation within the vortex core region and a constant circulation in the outer region.

5.2 BVI case

A detailed discussion of all aspects of the forward flight results will be found in [9].

Here merely those results will be presented which are related to the problem of data acquisition and evaluation.

The positions of the vortex structure measurements are shown in Fig. 11. A first coarse grid with 20 mm intervals has been refined in the region of the vortex core. A minimum interval size of 2.5 mm in the central part of the grid has been realized with 14 grid points in y-direction.

The vector plots in Fig. 12 depict the vortex locations and their extents. Unfortunately no data in the centre of the vortices are available to measure the exact vortex parameters as for example core diameters or maximum tangential velocities. In Fig. 13 those results of the tangential velocities closest to the vortex centre are presented.

From these data the vortex core diameter of the reference tip vortex has been determined to be 17.8% of the blade chord length or 1.88% of the rotor radius. The corresponding result for the winglet vortex is 22.4% of the chord length. The inexact measurement location underestimates the vortex core diameter of the reference tip. For comparing the difference between both blades more information can be obtained from vorticity plots.

Fig. 14 shows that the reference blade vortex is significantly more concentrated than the winglet vortex. The maximum vorticity is found to be 5190 s^{-1} for the reference blade and 4180 s^{-1} for the winglet case. The difference is expected to be even larger in most flight conditions, because during these tests the collective angle was held constant for both blade types although winglets are known to produce more lift per

collective pitch [5]. Consistently, the circulation of the reference vortex was found to be lower ($0.786 \text{ m}^2/\text{s}$) than that of the winglet ($0.846 \text{ m}^2/\text{s}$). Comparing both vorticity contours it can be recognized that the winglet vortex shows two centres of vorticity and is far away from being rotary symmetric. The two centres are explained by a double vortex that occurs with downward pointing winglets [10].

Comparing the axial velocities as presented in Fig. 15 it was found that the velocity deficit in the centre of the reference vortex is much greater than in the winglet case. This indicates that the winglet vortex is less stable [11].

At 85° azimuthal position of the rotor blade, the change of blade altitude relative to the rotor plane is recorded by the position monitoring system. For the reference blade an average displacement of 6.8 mm in y-direction was detected at a radial position of 0.95. The displacement of the winglet blade at the same radial location was only 0.8 mm in y-direction. These displacements are taken into account for all the calculations of vortex positions relative to the rotor plane.

Fig. 16 shows the measurement position in the y-z-plane for the reference and winglet blade with the expected locations of the created blade tip vortex and the 90° old tip vortex of the preceding blade.

Fig. 17a shows the development of the maximum vorticity for the reference and winglet blade tip vortices. For the reference blade the total maximum vorticity is 20% higher than for the winglet vortex and also the maximum is reached earlier. This can clearly be seen from the gradient ($d\omega_x/dt$) of the vortex strength for the two different vortices (Fig. 17b). For the winglet vortex dissipation starts later than for the reference blade vortex. The dissipation rates for both vortices are almost equal.

In addition to the vorticity the axial velocity component in the vortex centre is an indication for the stability of a vortex [11]. The temporal development of the axial velocity at the position of the maximum vorticity is depicted in Fig. 18. It indicates a very stable vortex for the reference blade and a weaker one for the winglet.

From the data also the position of vortex roll up can be derived. Assuming the position of the maximum vorticity to be the vortex centre, the distance of the vortex centre relative to the rotor plane is obtained. For the reference blade the position of vortex generation is found to be 4 mm above the rotor plane. For the winglet blade the location of vortex generation is 30 mm below the rotor plane at 70% of the winglet depth. The increase of blade vortex miss distance by using winglets has been known from flow visualisation experiments, but the LDV data yield more accurate values.

Further the geometry where interaction takes place is of interest. To investigate the interaction geometry of the preceding blade tip vortex with the blade at 90° azimuth, the x-component of the vorticity component, ω_x , is a good indication. First, the distance of the preceding blade vortex relative to the blade at 90° azimuth can be extracted from the data. For the reference blade (Fig. 19a) the location of the maximum vorticity of -2300 s^{-1} is 10 mm above the rotor blade and at a radial position of 0.95. In the y-z-plane directly after the blade passage (Fig. 19d), the vorticity maximum has decreased to -1500 s^{-1} and is located 3 mm above the blade and at the radial position of 0.91 of the rotor radius. The vorticity contours of the preceding winglet blade tip vortex in front of the blade

show a weak maximum of -700 s^{-1} at 0.91 of the radial position (Fig. 20a). The position is 10 mm below the rotor plane. After interaction with the rotor blade no significant vorticity can be detected (Fig. 20d).

Regarding the three dimensional vorticity distribution explanations for the loss of the vorticity ω_x for the reference blade are found. In addition to the decrease of ω_x from -2300 s^{-1} to -1500 s^{-1} in the y-z-plane behind the blade, there is an increase in the y- and z-component of the vorticity to $\omega_y = 750 \text{ s}^{-1}$ and $\omega_z = -1450 \text{ s}^{-1}$ (Fig. 19b, c, e, f). The total amount of vorticity has still a strength of -2200 s^{-1} . The orientation of the vortex axis after the interaction with the blade has experienced a change of about 45° in the x-z-plane. An equivalent vortex deformation by BVI has been found by flow visualisation earlier [12]. Due to the weakness of the 90° old winglet tip vortex and the larger distance to the blade, no significant vorticity components are left after the interaction with the blade (Fig. 20b, c, e, f).

In addition to the vorticity, the bound circulation can be calculated from the data set. For the six different radial positions the circulation is calculated around the wing along a rectangular box oriented in x- and z-direction. The results are shown in Fig. 21. The circulation profile of the reference blade (Fig. 21a) shows a local minimum at $r/C = 0.7$. This local minimum is created by the blade vortex interaction at this location. The occurrence of a strong gradient with different sign in the circulation profile leads to a so called secondary vortex [10]. For the circulation profile of the winglet blade (Fig. 18b) only a weak gradient in the circulation profile at $r/C=0.7$ can be observed.

6 CONCLUSIONS

Tests have been performed to measure the vortex structure of a rotor in hover and forward flight condition. The measurement of the local flow vectors at positions within the plane of rotation of the helicopter rotor can only be performed with a non intrusive measuring technique. Therefore, a large three component laser-Doppler-velocimeter, designed for application in large wind tunnels like the DNW, was used for this purpose.

A 'position monitoring system' gave access to blade motion parameter (lead-lag motion, pitching, and angle of incidence) at selected radial positions of the blade, where LDV measurements had been performed. This was necessary to determine the actual distance of the LDV probe volume in relation to the blade surface for the time averaged displacement of the blade during the test as well as for the unsteady motion of the blade during the passage of the measurement position.

Most of the tests were run with a 1.02 m rotor equipped with NACA 0015 airfoils with square tips or so called winglets (non-planar blade tips, designed in Aachen) in the wind tunnel of the RWTH Aachen.

Measurements were performed in two planes perpendicular to the rotor plane, one at an azimuth angle $\Psi = 0^\circ$, the other at $\Psi = 90^\circ$.

Velocity vector plots gave first information about position and the extent of the vortices. Velocity distributions were used to obtain vortex data like core diameter and maximum tangential velocities. The vortex core diameter of the square tip was determined as 17.8% of blade chord length or 1.88% of the rotor radius, which is larger than often expected.

All data were compared for both blades to determine the influence of winglets on vortex structure and vortex roll up.

Analyzing the flow field, vortex movements have also been investigated. The increase of blade vortex miss distance by using winglets have been determined exacter than from flow visualization experiments. The vorticity contours at different moments show the vortex roll up and vortex ageing. Many results indicate a surprisingly high amount of 'out of plane' vorticity ω_y and ω_z . These components were created by vortex deformation during BVI. The square tip shows a very fast roll up of the vortex. The maximum vorticity was reached after a further rotation of the blade of about 5° . The subsequent decrease of maximum vorticity due to ageing was moderate. The winglet vortex rolled up significantly slower, its maximum vorticity was found to be 20% less than in the case of the reference blade. The vortex ageing seems to be the same compared to the reference blade.

REFERENCES

- [1] A.J. Landgrebe, B.V. Johnson, Measurement of Model Helicopter Rotor Flow Velocities with a Laser Doppler Velocimeter, *Journal of American Helicopter Society*, Vol 19, no. 3, July 1974
- [2] J.C. Biggers, K.L. Orloff, Laser Velocimeter Measurements of the Helicopter Rotor-Induced Flow Field, *Journal of American Helicopter Society*, Vol 20, no. 1, July 1975
- [3] J.P. Sullivan, An Experimental Investigation of Vortex Rings and Helicopter Rotor Wakes Using a Laser Doppler Velocimeter, *MIT AD - 778768*, June 1973
- [4] S.H.G. Müller, Winglets on rotor blades in forward flight - a theoretical and experimental investigation, *Vertica*, Vol.14, No.1, 1990
- [5] B.M.J. Beesten, Influence of non-planar blade tips on rotor performance, *Forum Proceedings of the 18th European Rotorcraft Forum*, Paper No.73, Avignon, France, Sept. 1992
- [6] U. Seelhorst, K.A. Bütetisch, K.H. Sauerland, Three component Laser-Doppler-Velocimeter development for large wind tunnels, *ICIASF '93 Record*, pp. 33.1-33.7, 1993
- [7] P. Thomas, On the influence of Basset history force on the motion of a particle through a fluid, *Phys. Fluid A4 (9)*, September 1992, pp. 2090-2093
- [8] H. Grauer-Carstensen, A Versatile Model Position Monitoring System, *Rev. Sci. Instrum.* 65, 1994
- [9] B.M.J. Beesten, U. Seelhorst, Vortex Structure Investigation by LDV for two Rotor Blade Tips in Forward Flight, *Forum Proceedings of the 20th European Rotorcraft Forum*, Paper No. 13, Amsterdam, Netherlands, Oct. 1994
- [10] R.H.G. Müller, Special vortices at a helicopter rotor blade, *Journal of the American Helicopter Society*, Vol.35, No.4, Oct. 1990
- [11] S. Leibovich, Vortex stability and breakdown: Survey and extension, *AIAA 1983*, Vol. 22, No. 9, pp 1192-1206
- [12] B.M.J. Beesten, On the Influence of Blade Vortex-Interactions on Vortex Structure, *Forum Proceedings of the 16th European Rotorcraft Forum*, Paper No. II.10.3, Glasgow, Scotland, Sept. 1990



Fig. 1 Test set up for investigations of the flow field in the plane of a rotating helicopter rotor using 3D LDV.

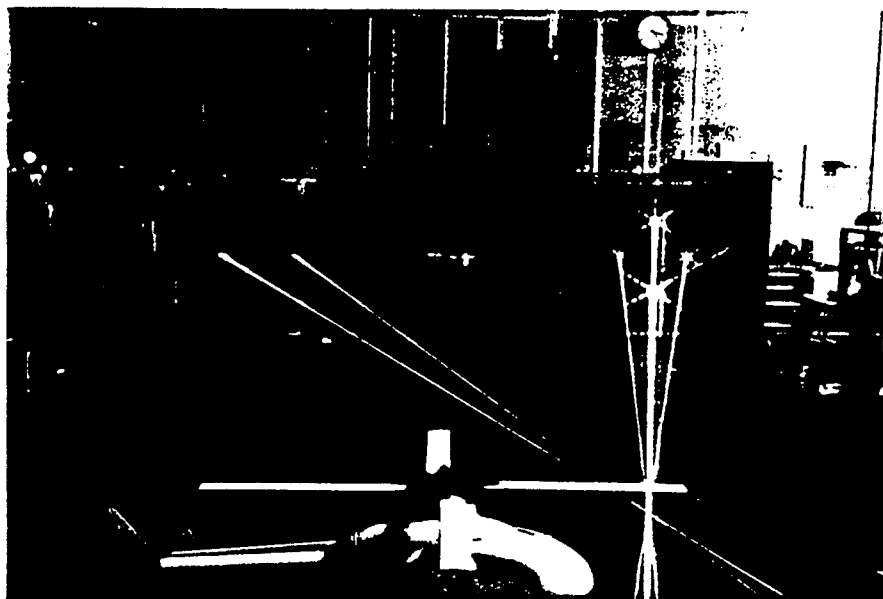


Fig. 2 Test set-up for LDV flow field investigations. Hover flight condition

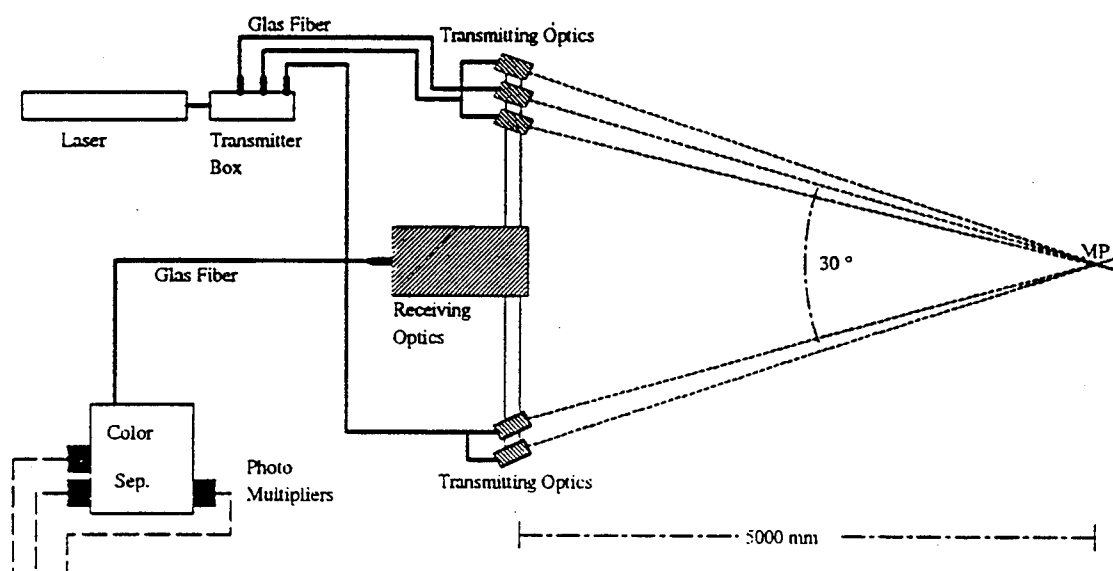


Fig. 3D LDV system of the DLR with 5m working distance

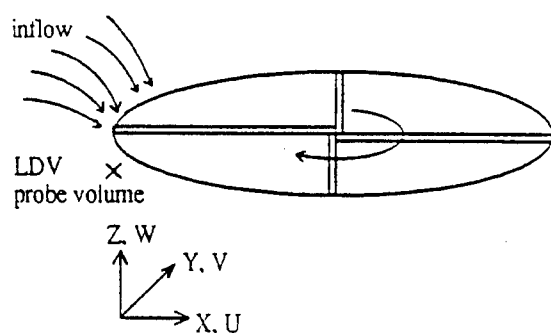


Fig. 4 Co-ordinate system for hover flight condition

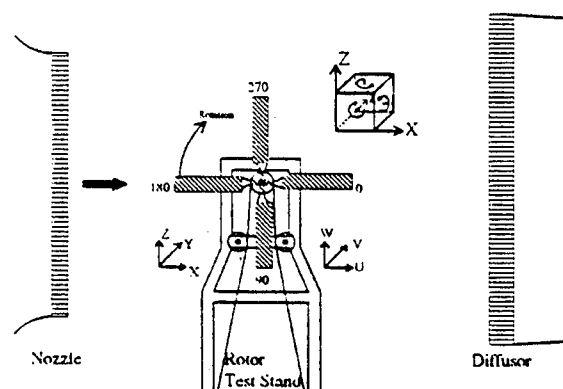


Fig. 5 Co-ordinate systems for forward flight condition

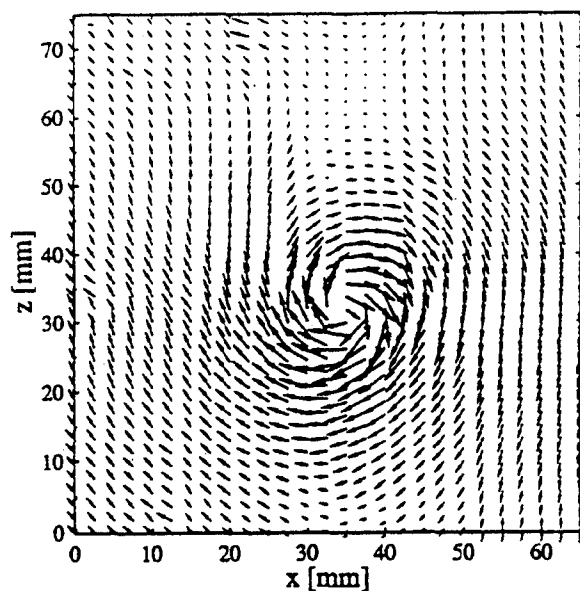


Fig. 6 Velocity map in x-z plane for hover condition.

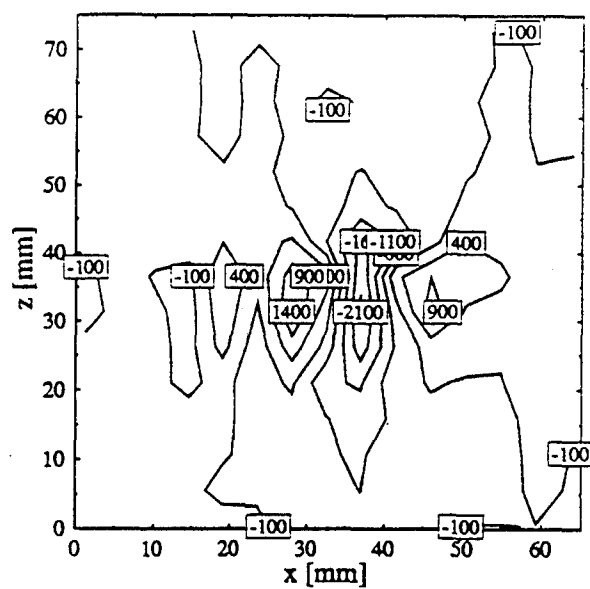


Fig. 7 Vorticity map for hover condition.

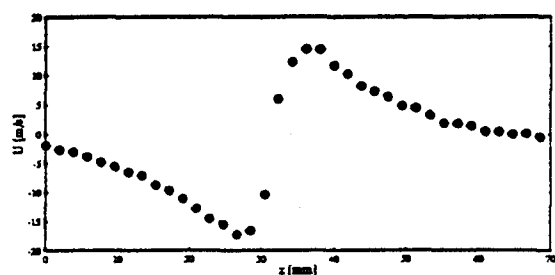


Fig. 8a.b Velocity profiles through vortex center for hover condition.

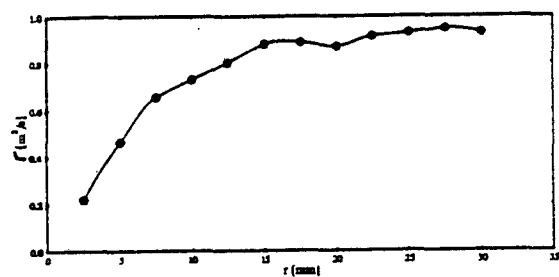
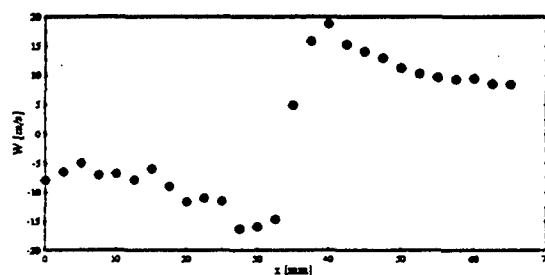


Fig. 9 Circulation profile for hover conditions

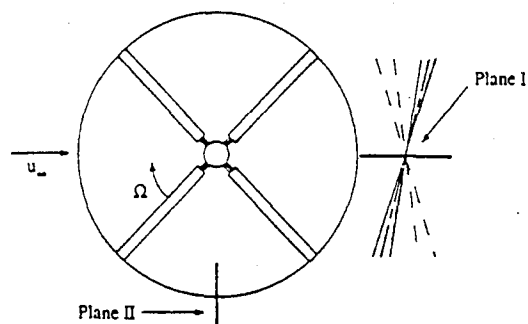
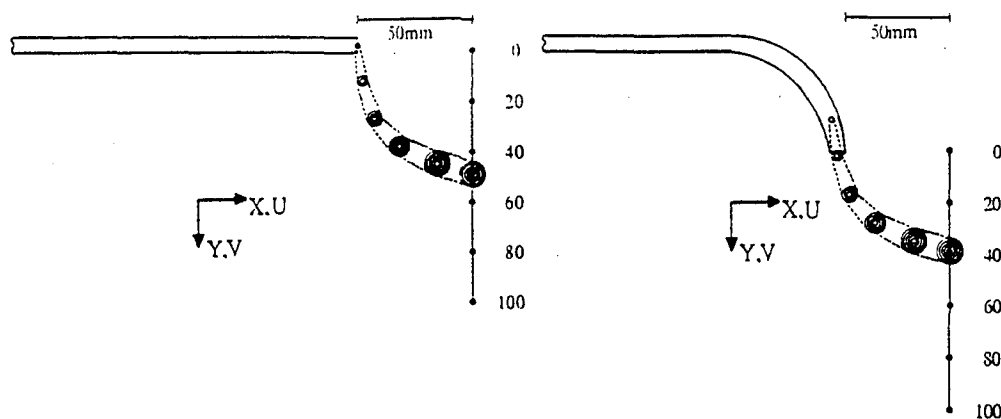
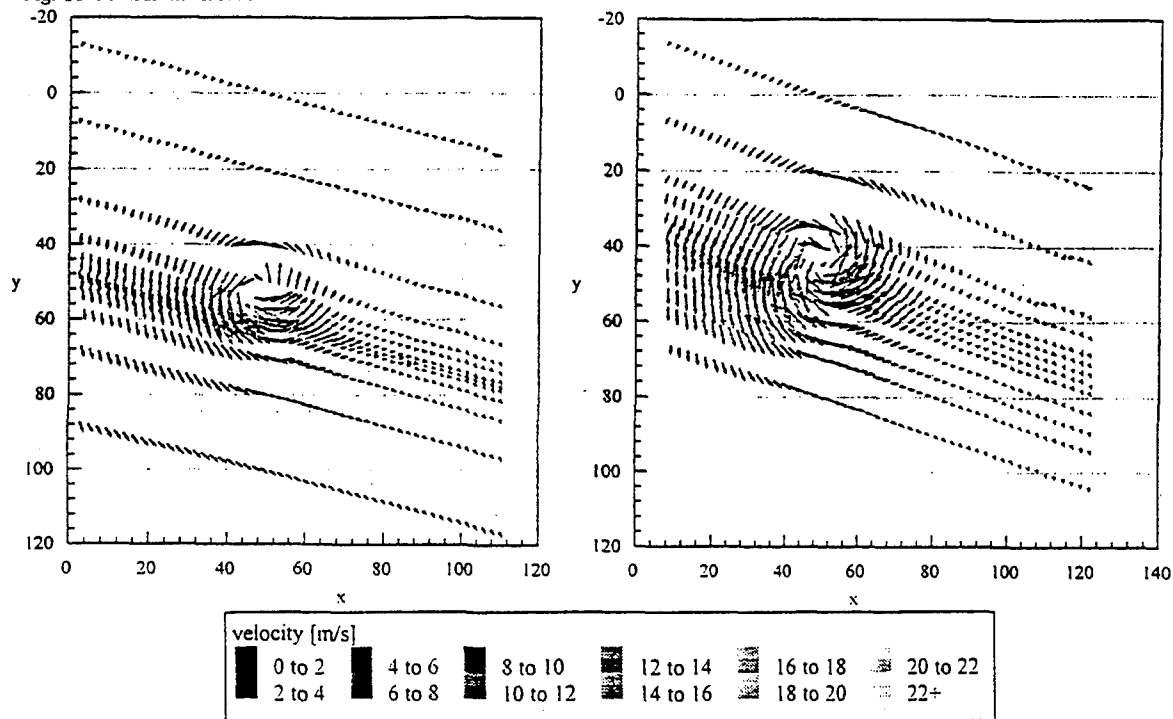


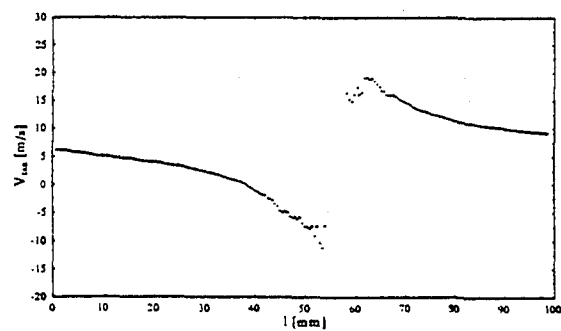
Fig. 10 Measurement locations for forward flight

Fig. 11 Measurement stations for $\Psi = 0^\circ$ 

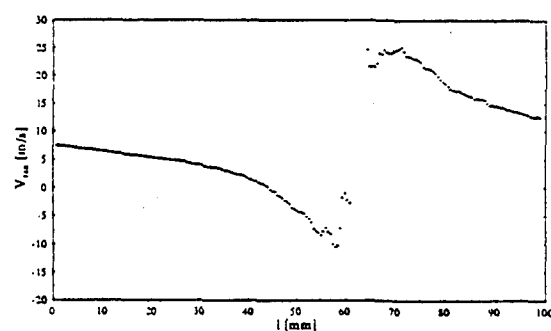
reference blade

winglet blade

Fig. 12 Velocity vector plots



reference blade



winglet blade

Fig. 13 Tangential velocities through the vortex center.

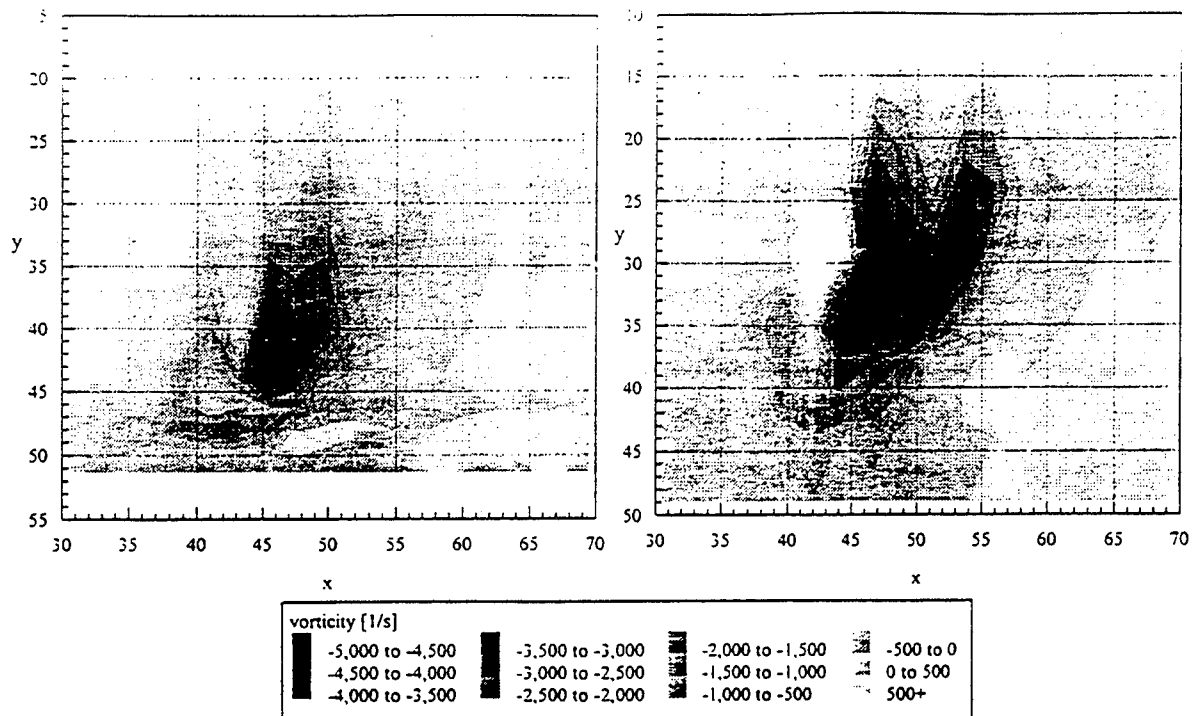
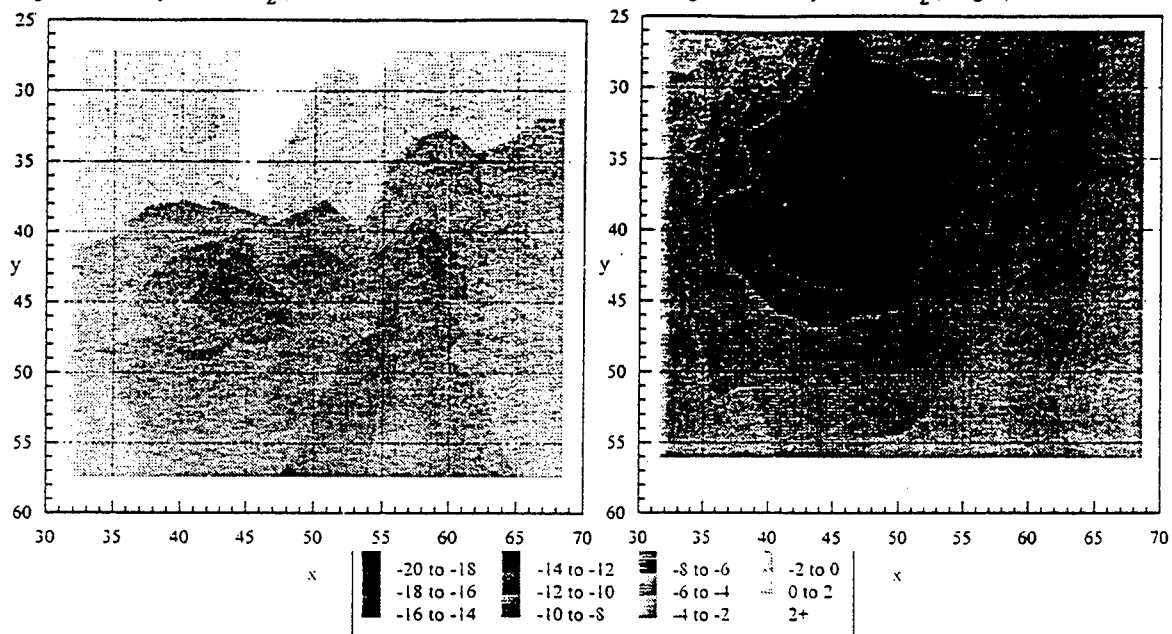
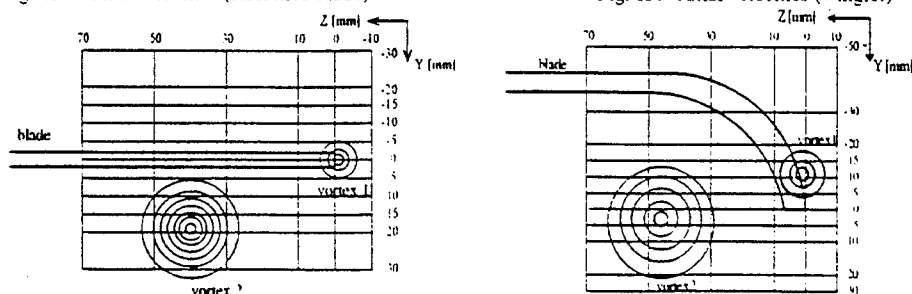
Fig. 14a Vorticity contours ω_z (reference blade)Fig. 14b Vorticity contours ω_z (winglet)

Fig. 15a Axial velocities (reference blade)

Fig. 15b Axial velocities (winglet)

Fig. 16 Measurement grid at $\Psi=90^\circ$

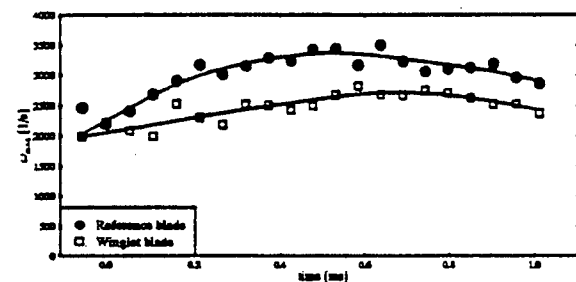
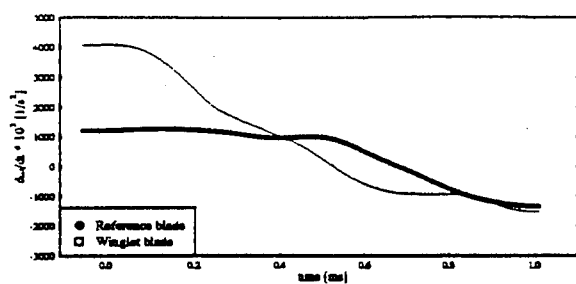
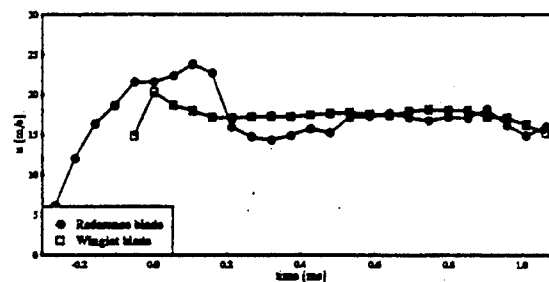
Fig. 17 Development of maximum vorticity ω_x 

Fig. 18 Development of axial velocity

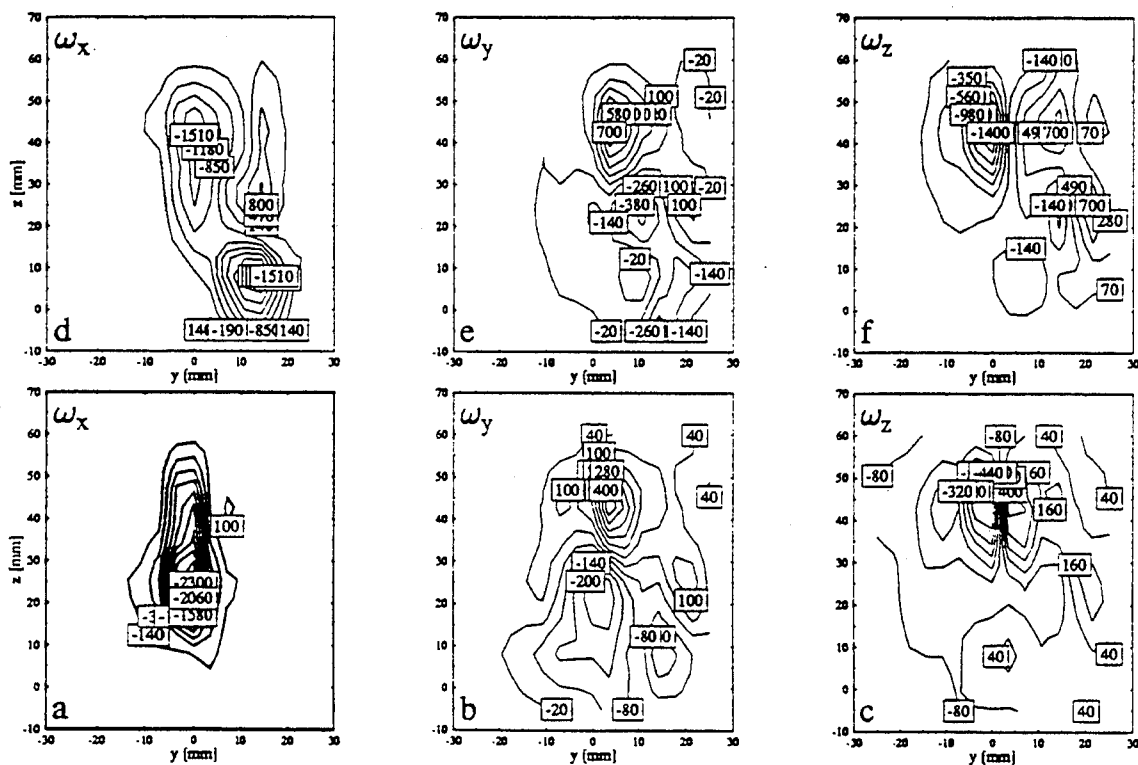


Fig. 19 3D vorticity contours (reference vortex)

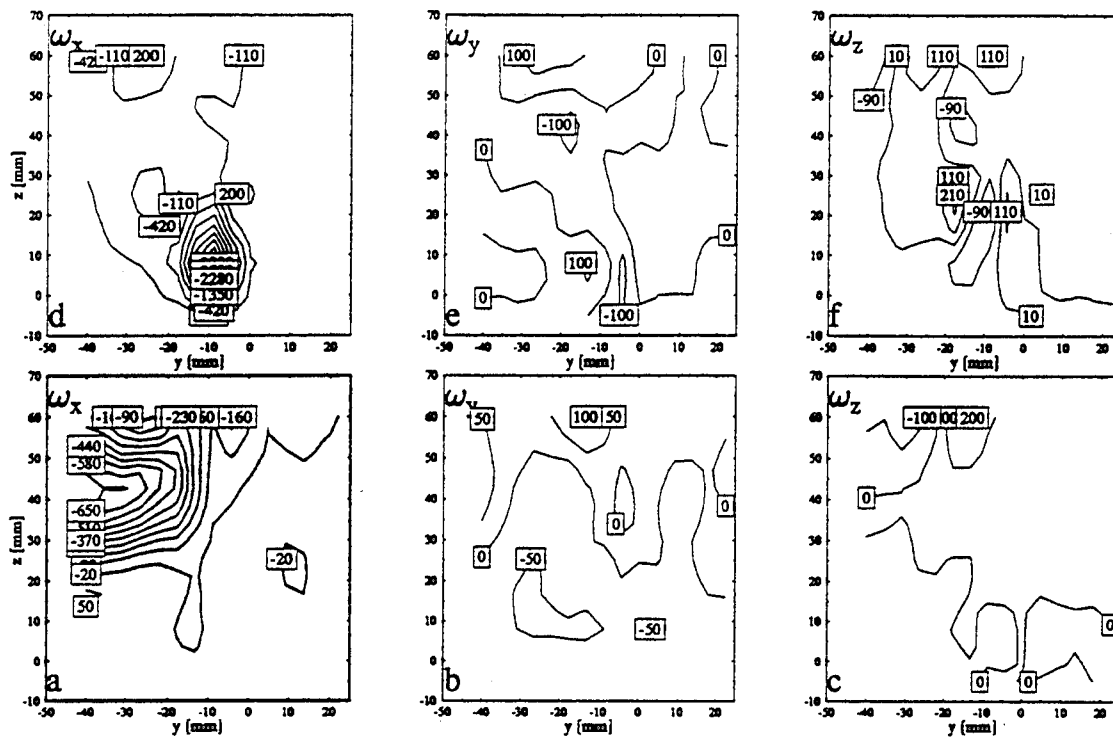


Fig. 20 3D vorticity contours (winglet vortex)

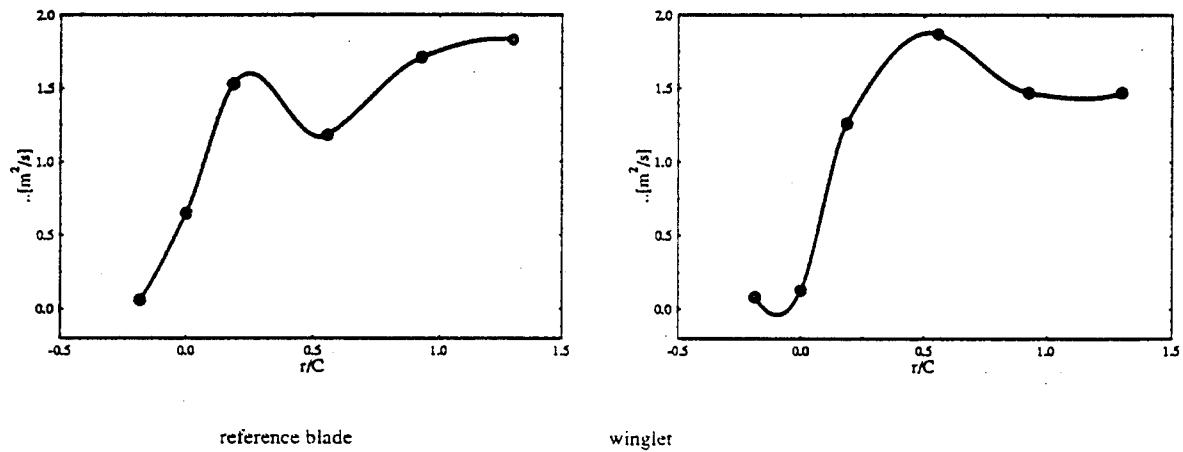


Fig. 21 Bound circulation distribution

DETERMINATION DES CHARGES AERODYNAMIQUES DU ROTOR EN VOL STATIONNAIRE, A L'AIDE D'UNE TECHNIQUE DE VELOCIMETRIE LASER.

E. BERTON
D. FAVIER
C. MARESCA
M. NSI MBA

Institut de Mécanique des Fluides, Université d'Aix-Marseille II, UM 34 du CNRS,
Les Souffleries de Luminy, 163 avenue de Luminy, 13009 Marseille, France.

RESUME

L'étude de la répartition des charges aérodynamiques sur un rotor d'hélicoptère opérant en vol stationnaire, est abordée, dans le présent papier, au moyen d'une nouvelle technique d'exploration par vélocimétrie laser, couplée à une méthode de détermination basée sur les Equations de bilan de quantité de Mouvement et de Kutta (KME méthode). L'efficacité de cette méthode est évaluée pour différentes configurations paramétriques du vol stationnaire.

NOMENCLATURE

b	nombre de pales (b=2 ou 4)
c	corde des profils, (c=0.05 m)
C_T	coefficient de portance du rotor
C_Q	coefficient de puissance du rotor
Γ	circulation le long de l'envergure, (m^2/s)
θ	pas général à $r/R=0.75$, (deg)
θ_v	vrillage de la pale, (deg)
r	distance radiale, (m)
R	rayon du rotor, ($R=0.75$ m)
R_o	rayon du pied de pale ($R_o=0.22R$)
σ	solidité du rotor ($\sigma=bc/\pi R$)
T, Q	traction et couple du rotor, (N, N.m)
u, l	extrados et intrados de la section de la pale
V, W	vitesse tangentielle et radiale
V_e	vitesse d'extrémité de pale, ($V_e=107$ m/s)
ω, Ω	vitesse de rotation, ($\omega=143$ rad/s)
ψ, Ψ_p	azimut de la pale, (deg)

1. INTRODUCTION

La connaissance de la répartition de charges le long de l'envergure de pales en rotation joue un rôle primordial dans le calcul et l'optimisation des performances aérodynamiques des rotors. L'étude du champ aérodynamique d'un rotor en vol stationnaire, est abordée ici, au moyen d'une nouvelle technique d'exploration de l'écoulement par vélocimétrie laser couplée à une méthode de post-traitement, fondée sur les équations de Kutta et de bilan de quantité de mouvement (KME méthode), permettant de corréler les mesures de vitesses autour des pales aux coefficients de charges globales et locales pour une section donnée en envergure.

2. MOYEN D'ESSAIS ET TECHNIQUE DE MESURE

Dans la configuration de vol stationnaire, simulée dans le hall d'essais de la soufflerie S1-Luminy de l'IMFM, les rotors maquettes ($2R = 1,50$ m) sont maintenus à 2,90 m au-dessus du sol par l'intermédiaire d'un ensemble mât-

bati, situé sur une plate-forme anti-vibratile. Les différents rotors faisant l'objet de cette étude sont numérotés de 4 à 7 sur la Figure 1. Ils possèdent tous un vrillage linéaire ($-8,3^\circ$) et sont constitués de profils OA209 suivant l'envergure [1 à 4]. Ces rotors diffèrent seulement par la géométrie d'extrémité de pale : une extrémité en flèche pour le rotor 4, une extrémité en effilée pour le rotor 5, une extrémité parabolique pour le rotor 6 et une extrémité rectangulaire pour le rotor 7 pris comme référence dans le cadre de cette étude. Les conditions paramétriques testées sont les suivantes : rayon du moyeu $R_0 = 0,22R$; vitesse de rotation $\omega = 143$ rd/s ; nombre de pales $b = 2$ ou 4.

Les mesures de performances de traction et de couple sont effectuées à l'aide d'une balance à 6 composantes. Dans le cadre de la présente étude, une nouvelle technique d'exploration du champ d'écoulement au voisinage de la pale a été développée, au moyen d'un vélocimètre laser à fibres optiques et à grande distance focale (2 m). Cette technique permet la mesure du champ des vitesses à la traversée du plan de rotation des pales. La mesure peut aussi être réalisée en un point fixe (U ou L) [3], situé à une certaine distance axiale de l'extrados ou de l'intrados de la section de pale considérée, et conduit à déterminer les composantes de vitesse axiale W et tangentielle V en fonction de l'azimut Ψ de rotation. L'évolution radiale des vitesses tangentielles et axiales mesurées autour de la pale, est alors obtenue par la translation de la partie optique du système de vélocimétrie laser, parallèlement à l'envergure de pale, depuis l'extrémité jusqu'au moyeu. Enfin, il est à noter que l'ensemble des profils de vitesse tangentielle mesurés autour de la pale permettra également de déduire [3], après intégration, la distribution de circulation correspondante $\Gamma = \Gamma(r)$.

3. METHODE DU BILAN DE QUANTITE DE MOUVEMENT

L'application de la méthode du bilan de quantité de mouvement [5, 6] est effectuée sur une surface de contrôle $S = \Sigma_a + \Sigma_w + \Sigma$ entourant la pale à une section r/R donnée (voir équation (1) et Figure 2).

$$-\oint_S \vec{dF}_{ext} ds = \oint_S (\rho \vec{q} \cdot \vec{n}) \cdot \vec{q} ds \quad (1)$$

En désignant par Σ_a , Σ_w les contours entourant le profil de la pale, le sillage issu de la pale, et par Σ le contour rectangulaire extérieur à la section de pale, et en tenant compte : d'une part, de la condition de non glissement sur la surface du profil ($\vec{q} \cdot \vec{n} = 0$); et d'autre part, de l'égalité des pressions sur chacune des frontières du

sillage du profil, l'équation de quantité de mouvement prend la forme particulière donnée par l'équation (2).

$$-\oint_{\Sigma} d\vec{F}_{ext} \cdot \vec{n} \, ds = \oint_{\Sigma} P \cdot \vec{n} \, ds + \oint_{\Sigma} (\rho \vec{q} \cdot \vec{n}) \cdot \vec{q} \, ds \quad (2)$$

En raison du caractère axisymétrique de l'écoulement en vol stationnaire, il est en outre possible de choisir un contour Σ spécifique (voir Figure 3), de longueur d'arc $2\pi/b$. La périodicité de l'écoulement implique alors l'égalité des pressions ($P = P'$) et des champs de vitesses ($V = V'$; $W = W'$) le long des branches latérales AB et DC du contour. L'équation de quantité de mouvement projetée sur l'axe Y permet ainsi d'atteindre la composante élémentaire de la force qui s'applique sur le profil suivant l'axe Y, soit dF_y :

$$-dF_y = \rho r \int_0^{2\pi/b} [W_1 V_1 - W_u V_u] d\psi \quad (3)$$

Tandis que l'application de la relation de Kutta, au contour Σ conduit à la composante verticale de la force, soit dF_z :

$$-dF_z = \rho \Omega r^2 \int_0^{2\pi/b} [V_1 - V_u] d\psi \quad (4)$$

Enfin, les coefficients globaux de traction et de puissance résultent de l'intégration de ces forces élémentaires le long de l'envergure de pale.

$$\Omega C = b \int_{r_a}^{r_b} dF_y (\Omega r) \, dr ; C_Q = \frac{\Omega C}{\rho \pi R^2 V_e^3} \quad (5)$$

$$T = b \int_{r_a}^{r_b} dF_z \, dr ; C_T = \frac{T}{\rho \pi R^2 V_e^2} \quad (6)$$

La théorie des éléments de pale est alors appliquée pour déterminer l'angle induit θ_i et l'angle d'attaque α du profil. Les coefficients de charges locales C_L et C_D sont ensuite déduits de θ_i et des forces élémentaires dF_y et dF_z de la manière suivante :

$$dL = dF_z \cos \theta_i + dF_y \sin \theta_i$$

$$C_L = \frac{dL}{\frac{1}{2} \rho [(\Omega r - V_i)^2 + W_i^2] \cdot c} \quad (7)$$

$$dD = dF_y \cos \theta_i - dF_z \sin \theta_i$$

$$C_D = \frac{dD}{\frac{1}{2} \rho [(\Omega r - V_i)^2 + W_i^2] \cdot c} \quad (8)$$

4. RESULTATS

4.1. Optimisation du Contour d'Intégration

L'application de la méthode KME a montré tout l'intérêt de la sélection adéquate des dimensions géométriques du contour fermé Σ entourant la section de pale, dans la détermination de la distribution de circulation et des charges globales et locales au cours de la rotation. La sélection de la longueur égale à $2\pi/b$ se justifie par rapport aux des conditions de périodicité de l'écoulement

en vol stationnaire et aux simplifications qu'elles apportent.

Afin d'optimiser l'épaisseur Z_Σ sur un rotor quelconque, le champ des vitesses tangentielles et axiales (V , W) est tout d'abord mesuré en fonction de Ψ ($0 \leq \Psi \leq 2\pi/b$) le long de différentes lignes situées au voisinage de l'extrados et de l'intrados du profil situé à une abscisse radiale donnée $r/R = \text{cste}$. Les lignes d'exploration situées sur l'extrados ($Z_\Sigma < 0$) et sur l'intrados ($Z_\Sigma > 0$) se répartissent de façon symétrique par rapport à la ligne passant par le quart-avant du profil, qui est choisie comme origine de référence ($Z_\Sigma = 0$) (Figure 4). Le maillage qui résulte de ces lignes intrados et extrados, est alors utilisé pour définir différents contours d'épaisseur $2Z_\Sigma$ croissante, qui correspondent aux valeurs suivantes de Z_Σ exprimées en centimètres : $Z_\Sigma = \pm 0,5; \pm 1; \pm 2; \pm 2,5; \pm 3; \pm 5; \pm 10$.

A partir des champs de vitesses (V , W) mesurés, les équations du bilan de quantité de mouvement et de Kutta conduisent à analyser l'évolution des charges élémentaires dF_y et dF_z en fonction de Z_Σ . Les résultats de la Figure 5 (cas de la section $r/R = 0,70$ du rotor 7 à $b = 2$ et $\theta = 10^\circ$), montrent que les forces dF_y et dF_z conservent une valeur pratiquement constante tant que l'épaisseur du contour $|Z_\Sigma| \leq 2,5$ cm (soit environ la moitié de la corde).

4.2. Détermination des Charges globales du Rotor

Dans le cas du rotor 7, $b = 4$, $\theta = 10^\circ$, et pour $Z_\Sigma = 1,5$ cm, la Figure 6a donne l'évolution correspondante de la force élémentaire dF_y en fonction de l'abscisse radiale en envergure de pale. La force dF_y a été déduite de l'intégration des profils de vitesses tangentielles et axiales mesurés sur l'intrados et l'extrados de la pale. L'évolution de la force élémentaire dF_y suivant l'envergure de pale permet d'obtenir après intégration, le coefficient de puissance C_Q qui est alors comparé à celui mesuré par la balance. La différence entre le C_Q déduit de l'application du bilan de quantité de mouvement et le C_Q mesuré par la balance 6-composantes est de l'ordre de 2 %.

De la même façon, la Figure 6b donne l'évolution de la force élémentaire dF_z le long de l'envergure. Les résultats montrent que le coefficient de traction C_T déduit de l'intégration de dF_z en fonction de r/R est très proche de celui mesuré par la balance 6-composantes (la différence est ici de l'ordre de 1 %).

La Figure 7 concerne le résultat de l'application de la méthode KME au cas du rotor 4 (possédant un extrémité de pale en flèche), $b = 4$, $\theta = 10^\circ$. Comme dans le cas du rotor 7, le coefficient de puissance C_Q déduit des mesures de vitesses autour de la pale est très proche du coefficient de puissance déterminé par la balance à 6 composantes. La différence est ici de l'ordre de 2% entre les deux valeurs. Des conclusions analogues sont obtenues en ce qui concerne le coefficient de traction C_T , comme le montre la Figure 7b. Dans ce cas, le C_T déduit des

mesures de vitesses autour de la pale est égal à 0.00802 tandis que le coefficient de traction mesuré par la balance à 6 composantes est égal à 0.00797.

4.3. Détermination des Charges Locales Sur la Pale

Comme le montre la Figure 8, les récents développements apportés à la technique de velocimétrie laser à fibres optiques et à grande distance focale, ont permis de réaliser la mesure du champ de vitesse à la traversée du plan de rotation et au voisinage immédiat de la pale. La Figure 8 est typique d'un champ des vitesses induites mesurées autour de la pale, à $r/R = 0.75$ et représente la composition des vitesses tangentielles V et axiales W mesurées par la technique de velocimétrie laser. Sur cette Figure apparaît clairement l'influence du passage de la pale sur le champ de vitesse et notamment le déficit de vitesse caractérisant le sillage à une section donnée.

Cette possibilité de "scanner" l'écoulement autour du profil en rotation, en différentes sections de l'envergure, a ainsi ouvert un champ d'investigation particulièrement riche, qui a notamment permis la reconstitution des lignes de courant (voir Figure 9) et la détermination de l'angle d'incidence α et de l'angle induit θ_i en une section donnée de la pale. Comme l'a montré le paragraphe 3, la connaissance de l'angle θ_i est primordiale pour atteindre les coefficients de charges locales C_L et C_D à partir des forces élémentaires dF_y et dF_z .

La Figure 10 donne la comparaison entre les coefficients (C_L , C_D) déduits de polaires 2D obtenues en écoulement uniforme, avec les mêmes coefficients de portance et de traînée déduits des mesures de vitesses et de l'application de la méthode KME. Un bon recoupement sur les distributions des coefficients de portance et de traînée déduites des deux méthodes, a été obtenu le long de l'envergure de pale.

5. CONCLUSIONS

Les récents développements apportés à la technique de velocimétrie laser à fibres optiques et à grande distance focale, ont permis de réaliser la mesure du champ de vitesse à la traversée du plan de rotation et au voisinage immédiat de la pale. Cette possibilité de "scanner" l'écoulement autour du profil en rotation, en différentes sections de l'envergure, a ainsi ouvert un champ d'investigation particulièrement riche, qui a notamment permis l'élaboration et la validation d'une nouvelle méthode de détermination des charges aérodynamiques de la pale du rotor en vol stationnaire.

Cette nouvelle méthode a été validée sur des rotors à extrémités rectangulaires et évolutives. Dans tous les cas, les valeurs de C_T et C_Q obtenues par la méthode KME recoupent bien les valeurs expérimentales globales fournies par une balance rotative à 6 composantes. En ce qui concerne la détermination des charges locales, les coefficients (C_L , C_D) obtenus, par la méthode KME couplée avec la théorie des éléments de pale, ont été comparés avec les coefficients (C_L , C_D) déduits des

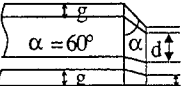
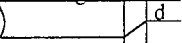
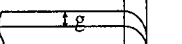
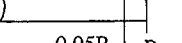
tables 2D. Les distributions des coefficients de portance et de traînée, déduites des deux procédures précédemment citées apparaissent également en bon accord le long de l'envergure de pale.

REMERCIEMENTS

Les auteurs souhaitent remercier la Direction des Recherches Etudes et Techniques (DGA) pour le soutien financier apporté dans le cadre de cette étude et relatif aux contrats N° 90/169 et N° 92/061.

REFERENCES

1. FAVIER, D., MARESCA, C., BERTON, E. and PLANTIN DE HUGUES, P. : "Investigation of the Tip Shape Influence on the Flowfield Around Hovering Rotor Blades", A.I.A.A., 22nd Fluid Dynamics, Plasma Dynamics and Laser Conference, Honolulu, June 1991.
2. FAVIER, D., MARESCA, C., BERTON, E. and PLANTIN DE HUGUES, P. : "Investigation of the Flowfield Around Rotor Blade Tips in Hover", COBEM, 11th Brazilian Congress of Mechanical Engineering, Sao Paulo, December 1991.
3. BERTON, E. : "Contribution à l'Etude de l'Écoulement Induit Autour et dans le Sillage de Surfaces Portantes en Rotation. Application au Rotor d'Hélicoptère en Vol Stationnaire.", Thèse de Doctorat, Université d'Aix-Marseille II, I.M.2., I.M.F.M., Septembre 1992.
4. NSI MBA, M., FAVIER, D., MARESCA, C., CRESPI, P. : "Helicopter rotor wake investigation using a laser doppler velocimeter technique", I.S.A.L.A., Proceedings of fourth International Symposium on Application of L.D.A. to Fluid Mechanics, Lisbon, July 1988.
5. SILVA, M., FAVIER, D., RAMOS, J., NSI MBA, M. and BERTON, E. : "An experimental investigation of the drag mechanisms of a helicopter rotor in hovering flight", Proceedings of 19th European Rotorcraft, Vol. 1, Paper n° 18, Cernobbio, September 1993.
6. RAMOS, J., NSI MBA, M., BERTON, E., FAVIER, D. and SILVA, M. : "A laser velocimetric investigation of the airloads and performance of a model helicopter rotor in hover", A.H.S., Proceedings of the Specialist Conference of the American Helicopter Society on Aeromechanics of Helicopters rotors, Vol. 1, Paper n° 8.1, San Francisco, January 1994.

N° des Rotors	Vrillage	Forme en plan	Profil
4	-8,3°		OA209
5	-8,3°		OA209
6	-8,3°		OA209
7	-8,3°		OA209

$$\frac{a}{c} = 0.15$$

$$\frac{d}{c} = 0.25$$

$$\frac{g}{c} = 0.6$$

Fig. 1. Définition des rotors.

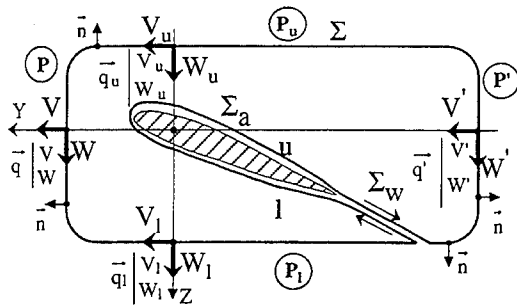
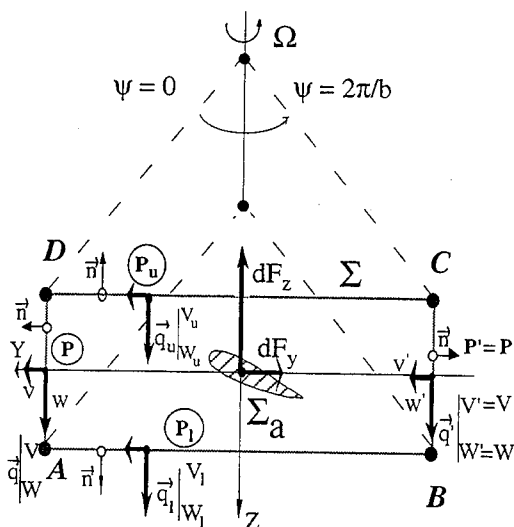
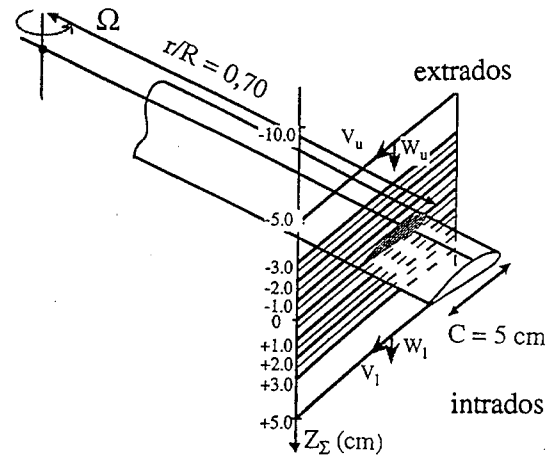
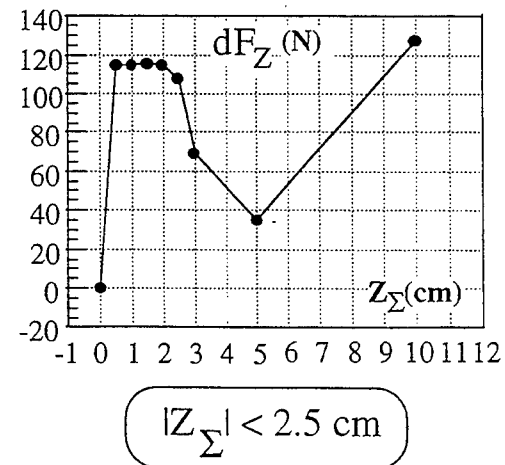
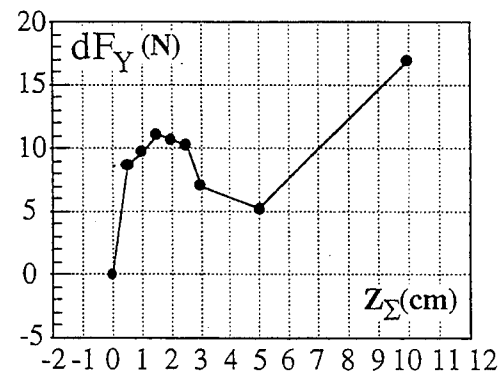


Fig. 2. Contour général d'intégration.

Fig. 3. Contour de longueur $2\pi/b$.Fig. 4. Selection du contour d'intégration Z_Σ .Fig. 5. Influence du contour d'intégration Z_Σ .

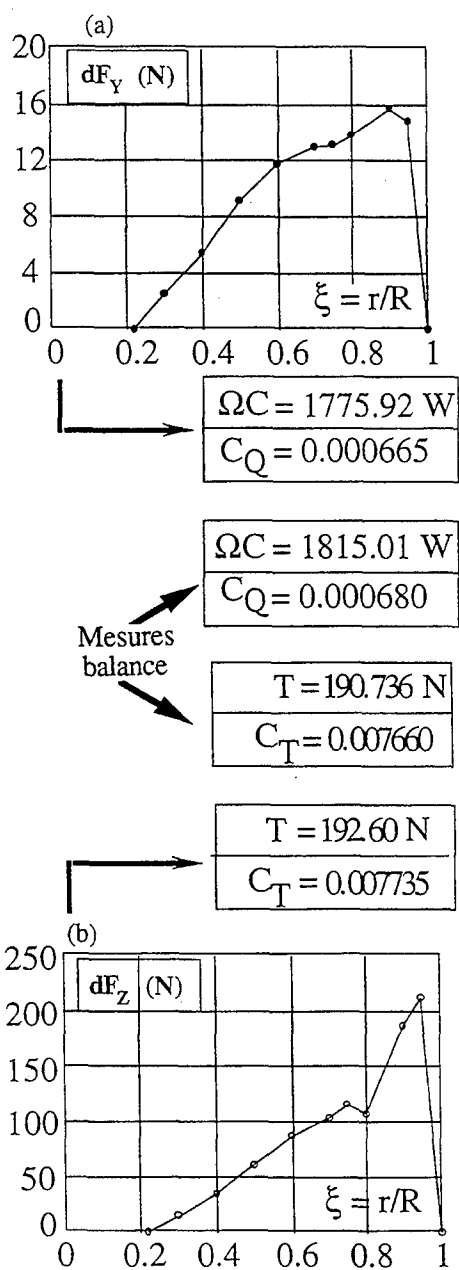


Fig. 6. Evolution des forces élémentaires en envergure (rotor 7, $b = 4$, $\theta = 10^\circ$).

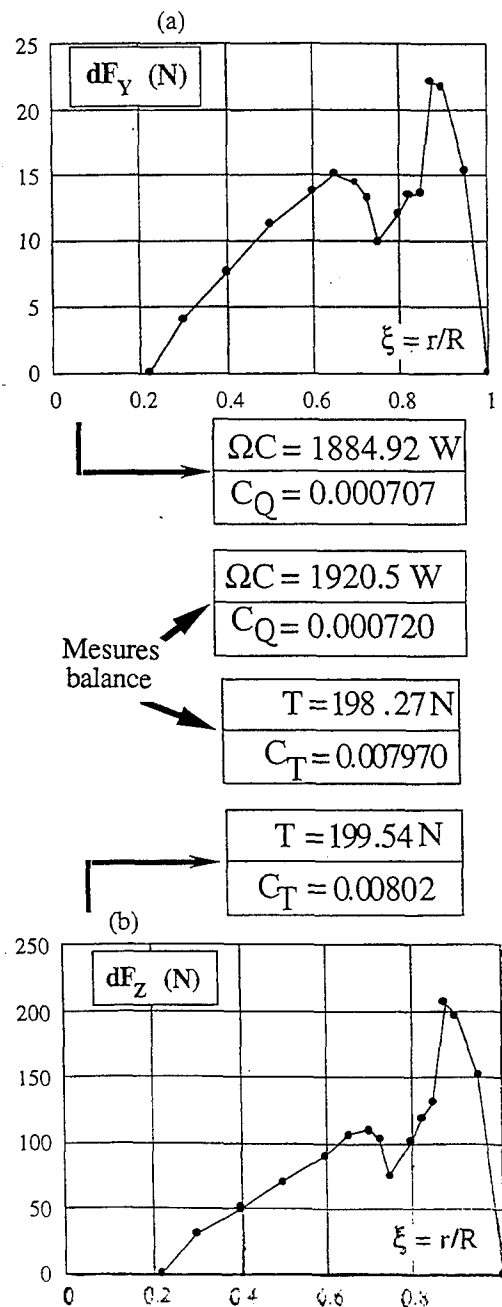


Fig. 7. Evolution des forces élémentaires en envergure (rotor 4, $b = 4$, $\theta = 10^\circ$).

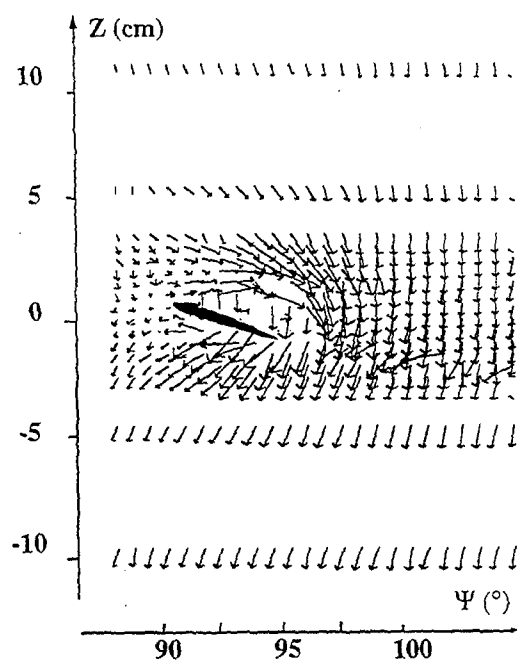


Fig. 8. Champ des vitesses induites, $r/R = 0,75$ (rotor 7, $b = 4$, $\theta = 10^\circ$).

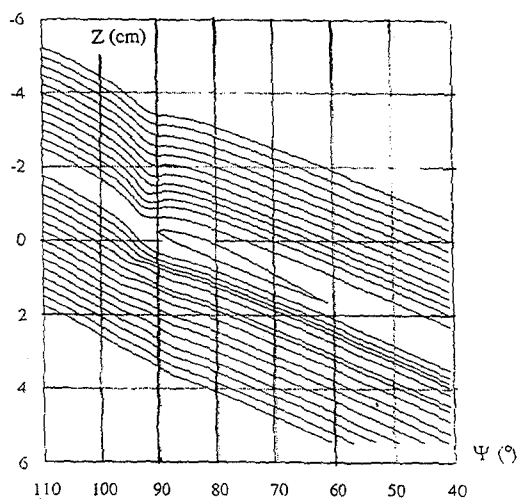


Fig. 9. Lignes de courant autour de la section de pale, $r/R = 0,75$ (rotor 7, $b = 4$, $\theta = 10^\circ$).

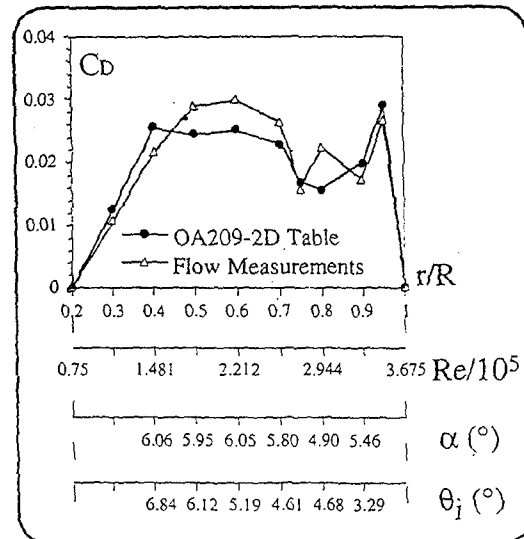
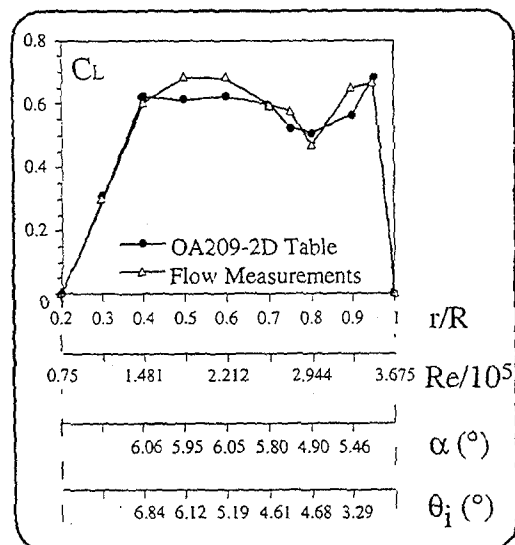


Fig. 10. Comparaison sur les coefficients locaux (C_L , C_D) en envergure (rotor 7, $b = 4$, $\theta = 10^\circ$).

INITIAL RESULTS FROM THE HIGHER HARMONIC CONTROL AEROACOUSTIC ROTOR TEST (HART) IN THE GERMAN-DUTCH WIND TUNNEL

R. Kube, W.R. Splettstoesser, W. Wagner, U. Seelhorst
DLR D-38022 Braunschweig, GERMANY

Y.H. Yu
AFDD Ames Research Center, Moffett Field, CA 94035, USA

A. Boutier, F. Micheli
ONERA, B.P. 72, F-92322 Châtillon, FRANCE

E. Mercker
DNW, Emmeloord, The NETHERLANDS

ABSTRACT

Within a four nation research project jointly conducted by AFDD, NASA, ONERA, DLR and DNW the HHC effects on BVI noise and vibrations were investigated. The project had the objective to gain a physical understanding of the involved mechanisms and comprised theoretical as well as experimental studies. The latter ones were performed in the German Dutch Wind Tunnel (DNW) and had the overall goal to provide information about all relevant parameters. For that purpose, different measurement techniques like laser light sheet, laser doppler velocimetry as well as acoustic and non-intrusive blade deflection measurements were applied to a highly instrumented hingeless model rotor. All of these techniques were employed at different rotor conditions for different HHC settings, thus yielding a very comprehensive data base. It gives a physical insight in the mechanisms involved in BVI noise and vibration reduction by higher harmonic control and forms the basis for an improved understanding and modeling of these complex phenomena.

1. INTRODUCTION

The helicopter is the most popular representative of VTOL aircrafts and is well established both within the military and the civil market. Due to its excellent hover and low speed flight capabilities it is well suited for missions requiring take off and landing in areas inaccessible by other vehicles. However, these hover and low speed flight capabilities are accompanied by a number of disadvantages, such as high internal and external noise levels. The latter one is very intense during maneuver flight as well as landing approach, where the rotor blades interact with the tip vortices shed by the preceding blades. This phenomenon known as Blade-Vortex Interaction (BVI) noise makes the helicopter at certain flight conditions highly annoying and detectable even when it is still far away from the observer.

Therefore extensive theoretical [1-3] and experimental [4,5] studies have been conducted in order to understand the generating and reducing mechanisms of this pulse type noise. It was shown that the BVI noise intensity depends strongly on the vortex strength as well as on the blade-vortex missdistance, parameters which can be influenced by superposing a higher harmonic blade pitch angle to the conventional one. This Higher Harmonic Control (HHC) technique therefore is well suited to reduce the BVI noise level and thus was applied to scaled model rotors in different wind tunnel tests [6,7]. The results showed that, at optimum adjustment of the HHC parameters, the noise emissions of the rotor can in fact be reduced by more than 5dB. However, since these investigations used only a small number of stationary microphones, it could not be clarified whether the results were affected by directivity changes.

A three nation test campaign conducted in the German-Dutch Wind Tunnel [8,9] with a movable inflow microphone array, however, allowed measurements of the BVI noise directivity pattern over a large plane below the rotor and concluded the directivity changes unaffected reduction of the BVI noise level. Although the data evaluation confirmed the results of the earlier tests [6,7] a conclusive explanation of the HHC effects on the BVI noise and vibration level was not possible.

A better insight in the mechanisms of BVI noise and vibration reduction by higher harmonic control was expected from the HHC Aeroacoustic Rotor Test (HART) program which was jointly conducted by US Army, NASA, ONERA, DLR and DNW. The objective of this research program was to improve the physical understanding and modelling of the HHC effects on BVI noise and vibration generation by means of theoretical as well as experimental studies.

In a first step, comprehensive rotor aerodynamic, dynamic and acoustic codes were used to predict the noise radiation without and with HHC [10]. The results were

correlated with data from previous wind tunnel tests, demonstrating that simultaneous aerodynamic blade pressure and acoustic data together with detailed information on the blade-vortex interaction geometry, blade tip vortex strength and core size are essential requirements to establish a complete validation.

The experimental studies performed within this research program, therefore, comprised simultaneous measurements of the aerodynamic pressures on the blade surface and acoustic pressures within a large plane underneath the rotor. Furthermore non-intrusive flow visualization and flow field measurement techniques as well as an interferometric method to determine the blade deformation were applied. The resulting comprehensive data base forms the basis for an explanation of the BVI noise and vibration reduction capability by means of higher harmonic control and with that an improvement of the prediction codes.

2. BLADE VORTEX INTERACTION NOISE AND HIGHER HARMONIC CONTROL

BVI noise occurs in flight conditions where the rotor operates close to or in its own wake. It originates from a parallel interaction of the tip vortices from preceeding blades with the following blades which leads to an impulsive change of the blade loading. Considering for example a 2D-model of a vortex which passes close to a blade element, the vortex represents a velocity disturbance with a velocity profile as shown in fig. 1. The higher the circulation Γ of the vortex, the steeper the velocity gradient passing through the vortex core.

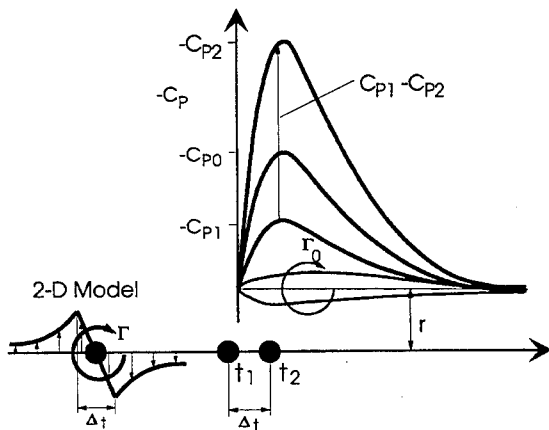


Fig. 1 Mechanism of BVI Noise Generation

The blade element has a circulation Γ_0 and thus generates a lift with a pressure distribution $-c_{p0}$ when the vortex is far away ($t=t_0$). At $t=t_1$ the first part of the vortex

passes the leading edge of the blade element and reduces the lift by generating a pressure distribution $-c_{p1}$. Moving downstream, the vortex becomes completely located below the blade element at $t=t_2$, thus leading to an increased lift with a pressure distribution $-c_{p2}$. Since the time interval Δt between t_1 and t_2 is very short, the pressure distribution changes very abruptly from $-c_{p1}$ to $-c_{p2}$, thus causing a pulse-type noise with the intensity directly proportional to the inverse blade-vortex miss-distance r squared, the vortex circulation Γ and the bound circulation Γ_0 .

These parameters can be affected with a higher harmonic blade pitch angle, superimposed to the conventional one and generated by means of suited electro-hydraulic actuators below or above the swashplate, for instance. Although these actuators have to work very precisely even at high frequencies, they can be realized using inexpensive, standard servovalves combined with high speed closed loop actuator controllers. In case of an implementation below the swashplate of a four bladed rotor, for example, these HHC actuators allow a generation of a 3-, 4- and 5/rev blade pitch angle with an arbitrary phase shift relative to the rotor azimuth (fig. 2). It can specifically be directed to affect the blade-vortex missdistance, the vortex circulation and the bound circulation at the blade-vortex encounters and with that to reduce the BVI noise.

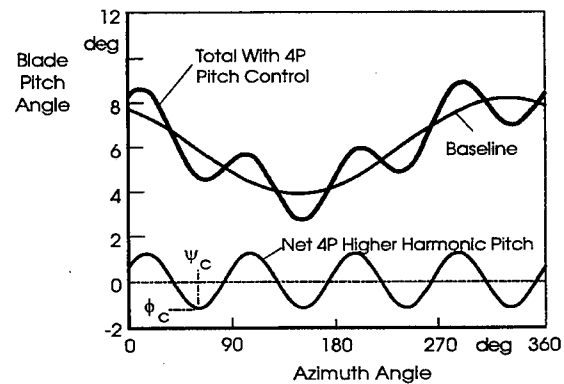


Fig. 2 Higher Harmonic Blade Pitch Angle

3. HART TEST OBJECTIVE AND TEST PLAN

The objective of the HART wind tunnel test was to improve the physical understanding of the mechanisms involved in BVI noise and vibration reduction by higher harmonic control [11]. For that purpose, the complete set of relevant parameters had to be investigated by means of suitable measurement techniques. Requiring a relative large and complex test setup, in general, these

Test Phase	Investigated Parameters
Aeroacoustic Tests	Blade Surface Pressure Noise Emissions
Flow Visualization	Vortex Trajectories, Blade-Vortex Missdistance
Laser Doppler Velocimetry	Vortex Circulation Strength, Vortex Core Size
Videographic and Projected Grid Tests	Blade Deflection, Blade Attitude

Fig. 3 HART Wind Tunnel Test Phases

techniques had to be applied sequentially within separate test phases (fig. 3). The first one, denoted with "Aeroacoustic Tests", aimed on simultaneous measurements of blade pressure and BVI noise radiation. It was followed by "Flow Visualization Tests" using Laser Light Sheet (LLS) techniques to determine the vortex trajectories and blade-vortex missdistances. These results formed the basis for the "Laser Doppler Velocimetry (LDV) Measurements", conducted with the objective to determine the vortex circulation strength and vortex core size. Finally, the test plan comprised "Blade Deflection and Blade Attitude Measurements" using both a projected grid and a videographic method.

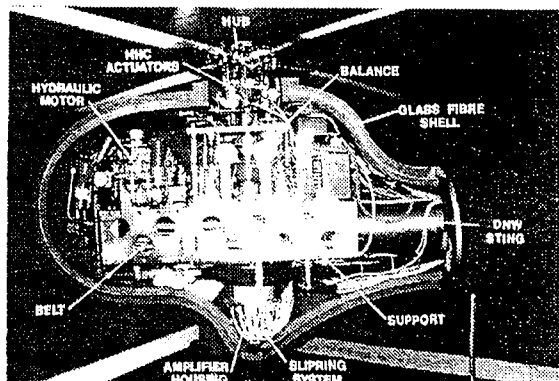


Fig. 4 DLR Rotor Test Rig ROTEST II

4. EXPERIMENTAL SYSTEM

4.1 Rotor and Aeroacoustic Setup

The HART wind tunnel test was conducted with the DLR rotor test rig ROTEST II (fig. 4), a modified version of the former DLR rotor test stand. It essentially consists of a support mounted balance, measuring both the static and dynamic rotor forces and moments. Besi-

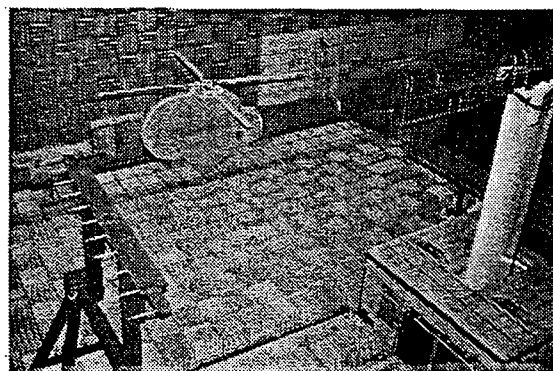


Fig. 5 DLR Rotor Test Rig in DNW

des this balance, a hydraulic motor is mounted on the support, driving the rotor via a flexible belt. Balance, motor and support are housed inside a glass fibre shell covered with open-cell foam in order to insulate the drive system noise on the one hand and to minimize the reflections of the rotor noise on the other hand. The rotor is controlled by three electro-hydraulic actuators below the swashplate which have a high cut-off frequency and therefore feature HHC capabilities. They have an authority of 3° and are transputer controlled thus allowing an easy and time-efficient variation of the HHC amplitude and phase shift.

For the HART wind tunnel test the test rig was attached to the DNW sting mechanism in the open jet test section and equipped with a Mach-scaled model of the hingeless BO105 main rotor (fig. 5). The model had a radius of 2 m and an operational speed of 1040 rpm giving a first blade passage frequency of 70 Hz. The blades were highly instrumented with 124 pressure transducers and 32 strain gauges implemented on one of them (fig. 6). Like all other signals of the rotating frame, the outputs of these sensors were fed through the shaft to a miniature amplifier assembly where they were properly conditioned and transmitted to the fixed frame via a slipring system (fig. 4).

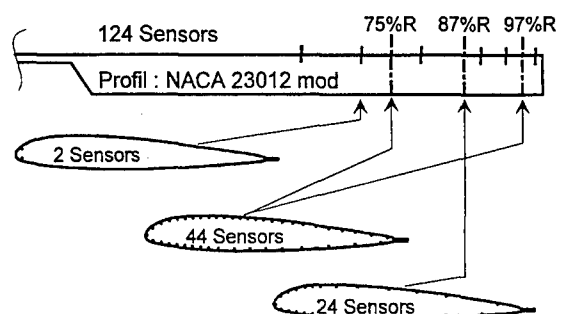


Fig. 6 Pressure Sensor Distribution

The noise emissions of the rotor were measured by means of fourteen microphones, eleven movable and three stationary ones. Whereas one stationary microphone was implemented 1.1 m below the hub at the fuselage, the remaining two were attached at the wind tunnel nozzle within the rotor plane. The eleven movable microphones were mounted on a traversing system which was also covered with open-cell foam in order to avoid rotor noise reflections (fig. 5). In combination with the sound absorptive test rig lining this acoustical treatment of the microphone traverse made it possible to maintain the excellent anechoic properties of the DNW open jet test section, a prerequisite for high quality acoustic data.

The acquisition of the acoustic data was performed by means of a transputer based system being able to sample all microphone signals simultaneously (fig. 7). It was automatically enabled at 17 pre-selected streamwise microphone array positions and was triggered by a 2048/rev blade position reference signal. For each streamwise position 30 rotor revolutions were sampled while the microphone array continued moving slowly with a velocity of 45 mm/s from 4 m downstream to 4 m upstream of the rotor hub.

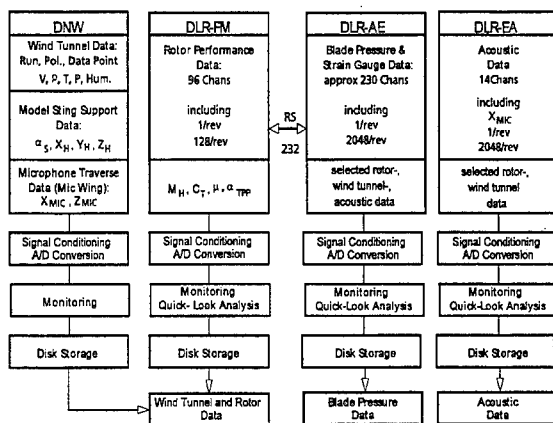


Fig. 7 HART Data Acquisition Systems

A similar system was used for acquisition of the blade pressure and strain gauge data, however with a larger capacity of 240 channels (fig. 7). Each of these channels was triggered with a 2048/rev blade position reference signal, yielding a useful frequency range of 18 kHz. For each rotor condition and HHC setting 64 revolutions were sampled immediately before a microphone traverse run.

Shortly before the acquisition of blade pressure and strain gauge data, the rotor data were measured over a period of 32 revolutions (fig. 7). Triggered by a blade

position reference signal of 128/rev, 96 sensor signals were sampled and evaluated up to a frequency of 210 Hz. This was done after the DNW system had acquired the wind tunnel data which were merged with the digitized sensor signals of the rotor test rig to a common data base (fig. 7).

4.2 Flow Visualization Setup

The aeroacoustic measurements were followed by flow visualization tests using a continuous single laser light sheet, a triggerable fast motion video camera, a stroboscopic light source and an oil smoke generator [12]. The tests aimed on a visualization of the tip vortices, the tip vortex trajectories and especially the blade-vortex missdistance at rotor azimuth positions important for BVI noise. For that purpose oil smoke was injected upstream the rotor by means of a remotely controlled generator located at the wind tunnel nozzle (fig. 8). Moving downstream the oil aerosols hit a light sheet which was emitted by an optical package connected via glass fibre cable to a 5W argon-ion laser. The optical package was mounted on top of the inflow traversing system and had the capability to rotate around its vertical axis, thus allowing to erect the laser light sheet at any azimuth position with any angle to a particular blade. Crossing the light sheet, the oil aerosols scattered the high intensity laser light, which was recorded by a fast motion video camera. Triggered by a 512/rev signal of the rotor test rig, it generated a video picture during a very short time interval thus allowing to work with a non-strobed, continuously emitted laser light sheet.

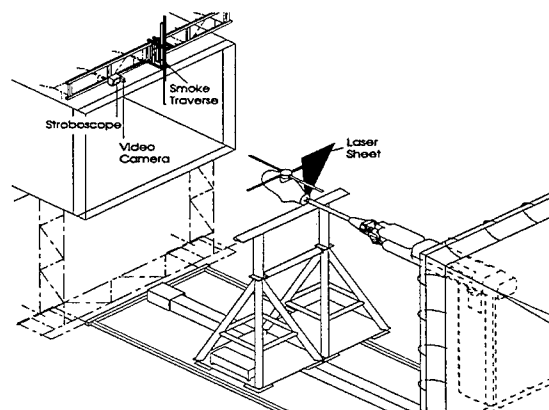


Fig. 8 Flow Visualization Test Setup

Besides a visualization of the tip vortices another objective of the LLS tests was to determine the distance of the tip vortices with respect to a passing rotor blade at a given azimuthal angle. Therefore it was necessary to visualize the vortex and the respective blade simultane-

ously, a requirement which was accomplished by means of a powerful stroboscopic light source. It was installed outside the jet in the proximity of the video camera (fig. 8) and, like this, was also synchronized with the rotor azimuth by means of a 512/rev signal. Since the duration of the strobe length was about 6 times shorter than the time-frame needed to generate the video picture, an outshining of the laser light image by the strobe light was avoided, thus allowing a simultaneous visualization of both, the vortex and the respective rotor blade.

In order to quantify the distance between both, a reference grid of known dimensions was placed in the plane of the light sheet after the wind and the rotor had stopped and was recorded with the same video camera for a few seconds. Later on, this video recording was digitized and overlayed on the original video picture, thus allowing to quantify the blade-vortex missdistance.

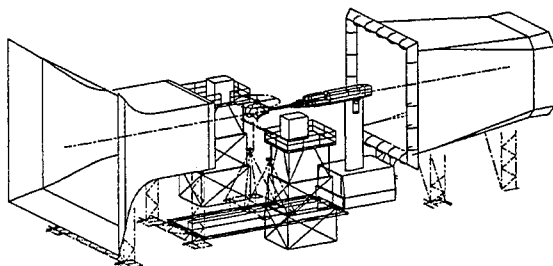


Fig. 9 Sketch of LDV Test Setup

4.3 Laser-Doppler Velocimetry Setup

The objective of the LDV measurements was to determine the strength and core size of the vortices interacting with the rotor blades at 48° and 298° , respectively.

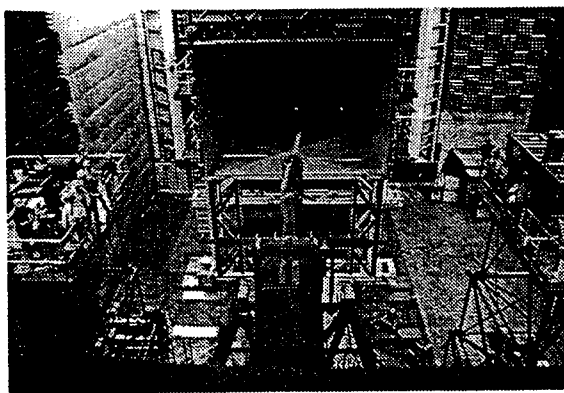


Fig. 10 LDV Towers and Rotor Test Rig

This was done by means of two systems, simultaneously operated by DLR and ONERA. While DLR cared for the blade vortex interaction at the advancing side, ONERA concentrated on the one of the retreating side (fig. 9). Both LDV systems, which were located at platforms of 9m height (fig. 10), had a working distance of 5 m and 3D capability.

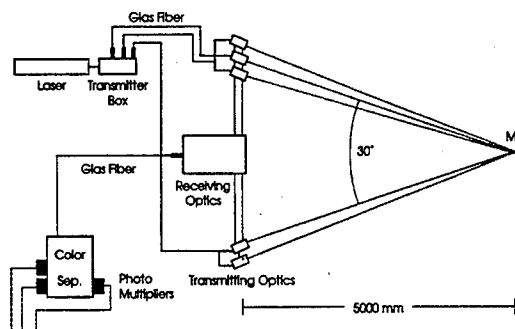


Fig. 11 LDV System of DLR

The LDV system of DLR (fig. 11) operated in back scatter, off-axis mode and used a 6 Watt argon-ion laser as light source [13]. The three most intensive laser lines (476.5nm, 488 nm and 514.5 nm) were utilised to distinguish the different velocity components. Each of the laser beams was divided into two individual beams with similar intensity, one superimposed with a Bragg shift of 40 Mhz, to determine also the direction of the flow vector for this component. The laser beams were coupled into single mode glass fibres and launched into the probe volume via individual transmitting optics. For good resolution of the third velocity component, the angle between the optical axes was set to 30° . The effective size of the probe volume was about 0.25 mm in diameter and 1mm in length. Dispersed oil particles induced into the flow had a size lower than $1\ \mu\text{m}$ and therefore were small enough to follow the flow in the correct manner. As receiving device a single concave mirror was used, collecting the scattered light of all three lines and feeding it into a multi mode glass fibre for being colour separated by a prism system.

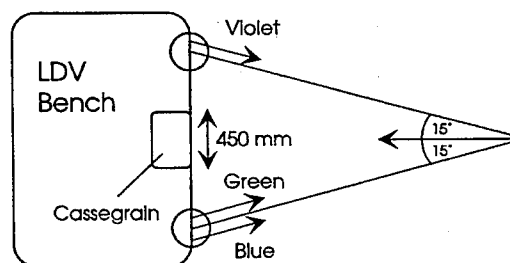


Fig. 12 LDV System of ONERA

The LDV system of ONERA (fig. 12) used a 10 Watts all lines argon laser to create the green 514.5nm- and blue 488nm-components [14] whereas for the violet 476.5nm-component another argon laser, emitting 2 Watts on this line, was used. Green and blue components were issued from a beam dividing system using dichroic plates and mirrors, Cassegrain x5 beam expander and 5 m focal length optics 200 mm in diameter, whereas the violet laser beam was divided into two equal intensity beams which were coupled to 20 m long monomode optical fibers, beam expanders and focussing optics. All three components were equipped with a pair of Bragg cells in order to induce a fringe movement at a 5 Mhz frequency and were arranged at an angle of $\pm 15^\circ$ within and $\pm 45^\circ$ relative to the horizontal plane (fig. 13). With this architecture equal beam intensities of 300 mW to 400 mW at the probe volume and a symmetry of the components relative to the main flow could be achieved, thus ensuring a high accuracy and an optimal velocity measurement domain. The light scattered by $0.5 \mu\text{m}$ particles of incense smoke, injected 50 m up stream into the flow, was collected by a Cassegrain telescope 450 mm in diameter before it was separated by dichroic plates and interferential filters.

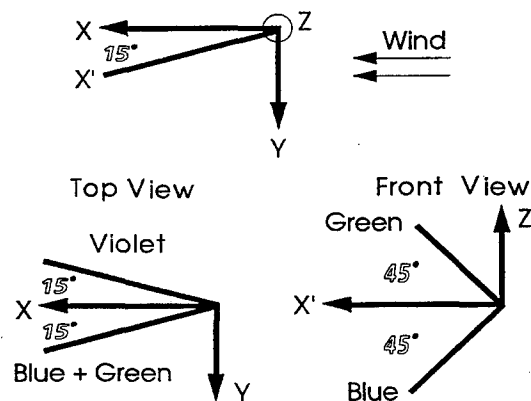


Fig. 13 Geometry of ONERA LDV Components

4.4 Blade-Deflection Measurement Setup

In order to complete the set of investigated BVI noise and vibration relevant parameters, blade deflection measurements based on different techniques were performed at the end of the HART wind tunnel entry. The first ones aiming on a determination of the blade tip position and orientation at azimuthal angles important for BVI noise were conducted in parallel to the LDV measurements. Again two systems, independently operated by DLR and ONERA, were used. Both worked with a CCD camera, differed, however, in the principle of measurement.

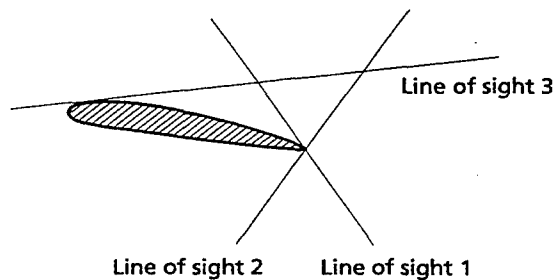


Fig. 14 DLR Blade Deflection Measurement

In case of the DLR system, the blade contours at $r/R=0.87$ were recorded against a background, illuminated by flashlights [13]. From the resulting picture, the blade position and angle of incidence was evaluated by means of a computer program which fixed the trailing edge of the blade image with two lines of sight and then moved the tip contour image towards the third one (fig. 14). The accuracy was with 0.01° and 0.35 mm in the same order of magnitude as the one of the ONERA TART (Target Attitude in Real Time) system which recorded at each rotation of the same blade the image of two retroreflecting circular tapes, stuck at the blade tip and illuminated by means of a stroboscope. The barycentres of the two spots were transmitted via a specific interface to a PC, displaying the angle of incidence as well as the position of the blade tip with respect to the rotor hub in real time.

The deflection of the complete blade finally was measured by means of the so called Projected Grid Method (PGM) developed by DNW. It is based on the fact that a grid, which is projected on the surface of a structure from a certain direction and recorded from a different direction, changes its image when the structure is deformed or displaced. By comparing the image corresponding to the non-deformed and non-displaced state with the one corresponding to the deformed and deflected, the relative deformation and displacement of the structure can be determined.

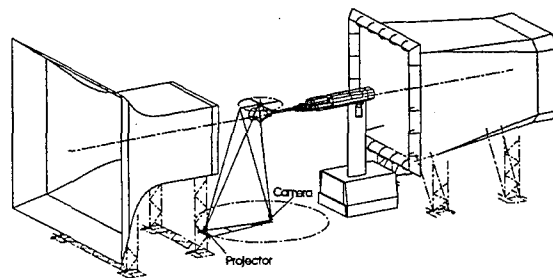


Fig. 15 PGM Test Setup

For the HART wind tunnel test the grid was projected in the darkened test section perpendicular to the leading edge of the dull white painted blades, leading to a parallel shift of the grid pattern in case of a vertical blade displacement and a skewed shift of the grid lines in case of blade torsion. The projection was performed from a specially constructed bench installed underneath the rotor on the test section floor with the center of rotation vertically aligned to the rotor center. The bench was equipped with the grid projector and a high resolving CCD camera and could be rotated over 360° (fig. 15). Once adjusted at a preselected fixed position, the arrangement made it possible, to record the grid pattern at a certain rotor azimuth position by triggering the video camera adequately.

5. HART TEST MATRIX

Although the measurement techniques used for the HART wind tunnel tests were very time consuming, they were applied at different rotor conditions. Most of them represented a descent flight with a variation of the glide path angle from -3° to $+12^\circ$ and an advance ratio of $0.114 \leq \mu \leq 0.275$ corresponding to a wind tunnel velocity range of $25\text{m/s} \leq v \leq 60\text{m/s}$ (fig.16).

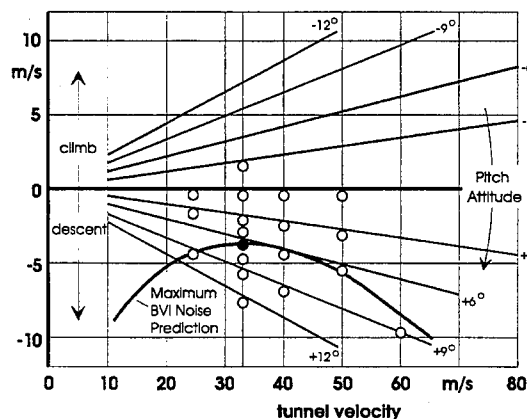


Fig. 16 HART Test Conditions

The nominal test condition was a simulated landing approach at an advance ratio of 0.15 and a glide path angle of 6° corresponding to a wind tunnel velocity of 33m/s and a shaft angle α_s of 5.3° . At this condition a systematic phase shift variation was performed during the aeroacoustic measurements for 3-, 4- and 5/rev HHC showing that for an amplitude of 0.8° a 3/rev blade pitch angle is the most effective one, both with respect to BVI noise and vibrations. The following tests at different shaft angles and advance ratios therefore concentrated on this HHC frequency with a phase shift variation only within a limited interval, interesting from the physical point of view. The LLS, LDV and blade deflection

measurements finally were conducted exclusively for phase shift values leading either to a minimum BVI noise or vibration level, thereby focussing on reasonable rotor azimuth positions, for example the ones where most intense blade-vortex interactions occurred.

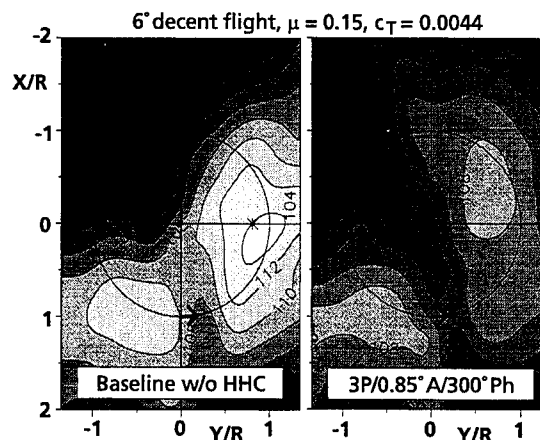


Fig. 17 BVI Noise Pattern Below the Rotor

6. INITIAL TEST RESULTS

6.1 Aeroacoustic Results

According to the HART test objective to investigate the complete set of BVI noise and vibration relevant parameters, a very comprehensive data base was generated. Its initial evaluation showed that a higher harmonic blade pitch angle has quite an influence on the noise emission of a helicopter rotor. Fig. 17 shows the noise pattern underneath the rotor as measured by the movable inflow microphone array and also shows that the maximum BVI noise level occurring at 90° rotor azimuth approximately could be reduced by more than 6 dB.

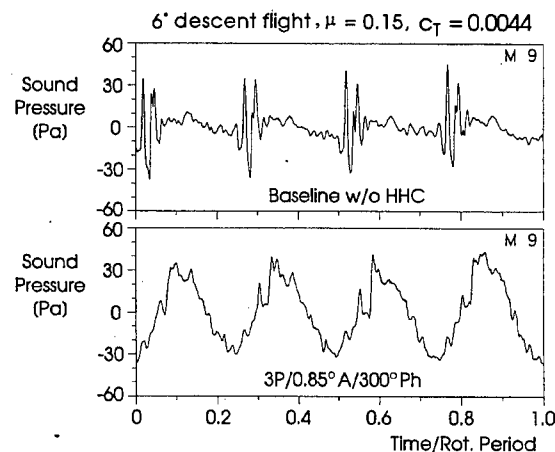


Fig. 18 Sound Pressure Time Histories

The sound pressure time history measured at this location reveals, in case without HHC, strong pressure pulses each one being related to a blade-vortex interaction (fig. 18). They are distinctly reduced when higher harmonic control is enabled with a proper amplitude and phase shift. Even though low frequency loading noise is seen increased in this case the corresponding frequencies are not important on a subjective, for example, A-weighted noise scale.

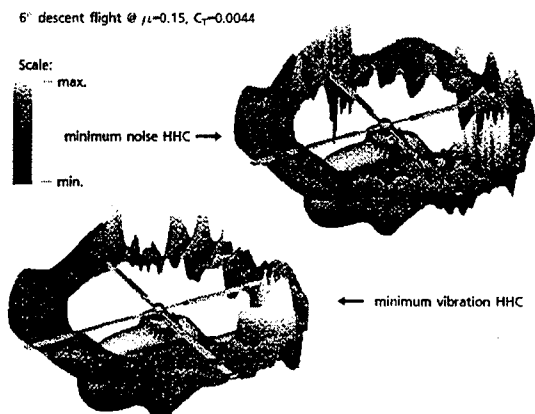


Fig. 19 Leading Edge Pressure Distribution

An overall characteristics of the BVI noise reducing mechanisms in case of higher harmonic control could be derived from the blade pressure data. It was found that strong pressure fluctuations occur between 40° and 70°

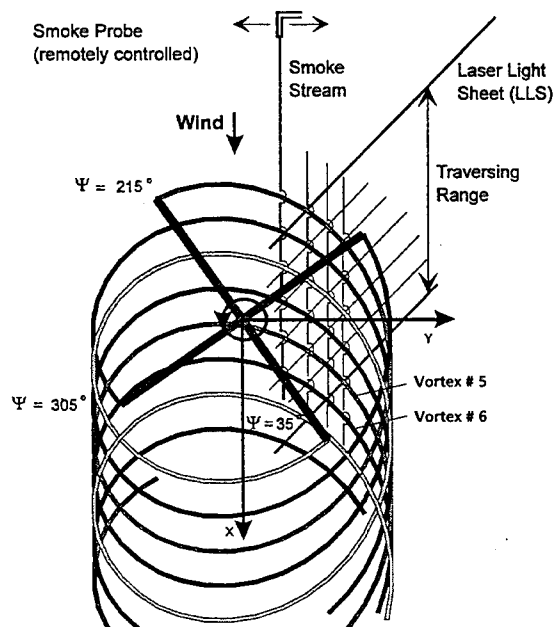


Fig. 20 Application of Laser Light Sheet Technique

rotor azimuth when HHC is not applied and that the parallel blade-vortex interactions of the baseline case are nearly smoothed out by a 3/rev blade pitch angle of 0.8° amplitude and 300° phase shift (fig. 19). However, strong pressure fluctuations occur more upstream at approximately 100° rotor azimuth, but not simultaneously at all radial stations. Obviously, a higher harmonic blade pitch angle makes it possible to substitute the BVI noise generating parallel blade-vortex interactions with non-parallel and therefore non-BVI noise intense ones.

6.2 Flow Visualization Results

Due to the fact that vortex trajectories can only be visualized when smoke is inserted continuously to the flow at the rotating blade tips, the laser light sheet, used for the flow visualization tests, was positioned at different locations under different directions of orientation. Adjusting the remotely controlled smoke probe properly, the tip vortices in the respective cross sections could be visualized (fig. 20).

The corresponding vortex lines, constructed from successive laser cross sections, are shown in fig. 21 exem-

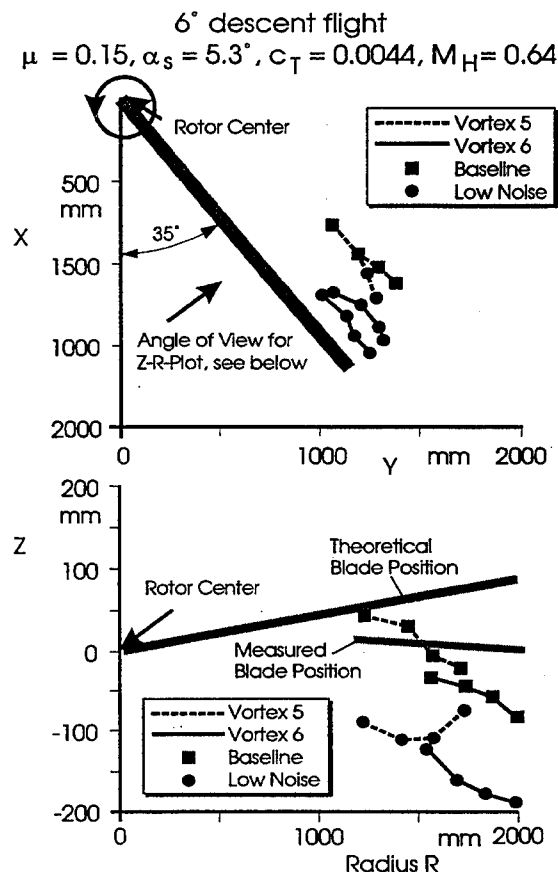


Fig. 21 Vortex Trajectories Determined by LLS

plarily for the baseline and minimum noise HHC case and a rotor azimuth of 35° . The figure shows the increased blade-vortex missdistance occurring in minimum noise case, thus demonstrating, that parallel blade-vortex interactions are, in fact, avoided when a higher harmonic blade pitch angle is superposed with a proper amplitude and phase shift to the conventional one.

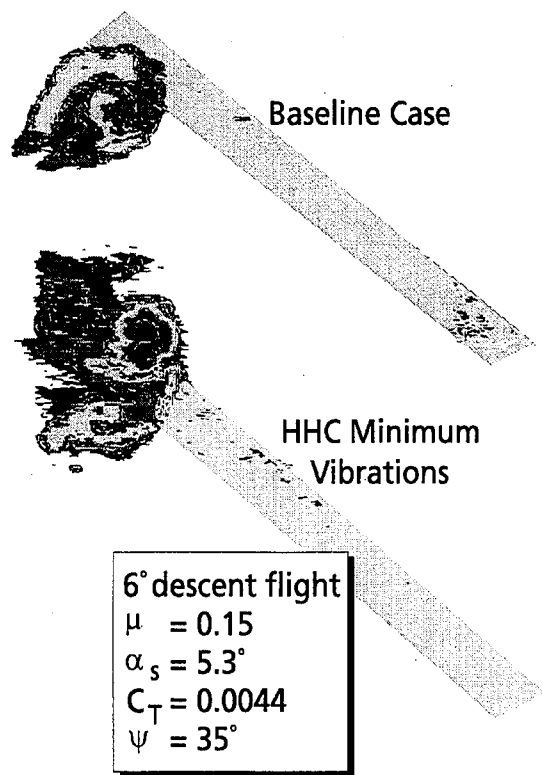


Fig. 22 HHC Effect on Vortex Structure

Besides these results, the LLS measurements provided also informations about the vortex structure and how it is affected by HHC. For example, fig. 22 illustrates that the single, concentrated vortex of the baseline case, occurring within the proximity of 35° rotor azimuth, is converted to a counterrotating double vortex when HHC with minimum vibration control settings is applied.

6.3 Laser-Doppler Velocimetry Results

The strategy of the LDV measurements was to record the velocity time history for a fixed spatial position before the probe volume was moved in vertical direction to another position. The corresponding coordinates as well as their upper and lower limits were based on the flow visualization results, thus making sure, that the vortex is located within the scanned area. For each spa-

tial position, the velocity recording was performed for a number of rotor revolutions and the mean value was determined besides additional statistical parameters. Finally, a mean velocity map was established in form of a vector plot, as shown in fig. 23. It clearly points out the double vortex already detected during the LLS measurements at the advancing side when higher harmonic control was adjusted for minimum vibrations.

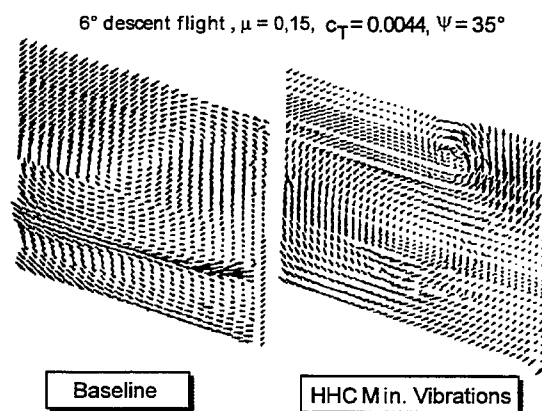


Fig. 23 Velocity Vector Plot

By post-processing of the data included in the mean velocity maps, additional parameters like vortex strength and vortex core size can be calculated. Fig. 24 shows for example the vorticity distribution occurring at the re-treating side for the baseline case and for a case with

6° descent flight, $\mu = 0.15$, $C_T = 0.0044$, $\psi = 300^\circ$

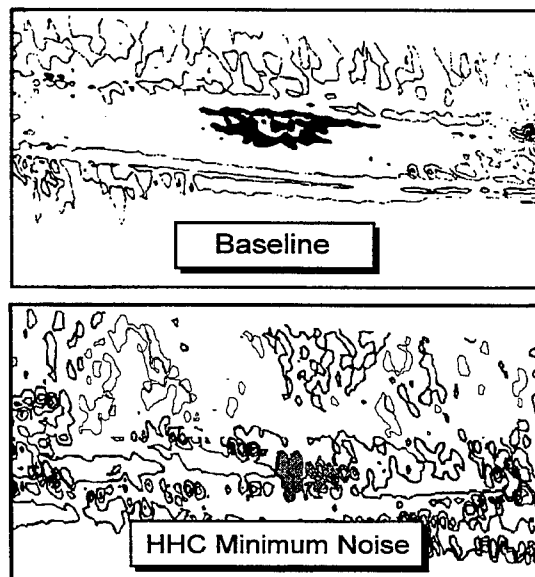


Fig. 24 Vorticity Map

minimum BVI noise HHC settings. It makes clear that a higher harmonic blade pitch angle has a strong influence on the vorticity distribution of the tip vortex which nearly vanishes in minimum BVI noise HHC case.

6.4 Blade Deflection Measurement Results

The results of the blade deflection measurements at different rotor azimuth positions in baseline case and with HHC activated, complete the set of parameters relevant for BVI noise and vibrations. Depending on the measurement techniques applied, the results provide informations either of the absolute deflection at the blade tip or the relative deflection along the blade span. The latter ones resulting from the projected grid method are shown in fig. 25 for the rotor blade at azimuthal angles of 60° and 130° , i.e. at rotor azimuth positions where parallel blade-vortex interactions occur and where the respective vortex is generated. The curves represent the blade bending line relative to the one occurring in baseline case and make clear that the blade is deflected upwards at 60° and downwards at 130° when HHC is adjusted for minimum BVI noise. The opposite trend can be recognized when HHC is adjusted for a minimum vibration level. In this case, the blade is deflected more downwards at 60° , which obviously leads to a closer interaction with the tip vortices passing through the rotor plane at this location thereby generating increased BVI noise levels.

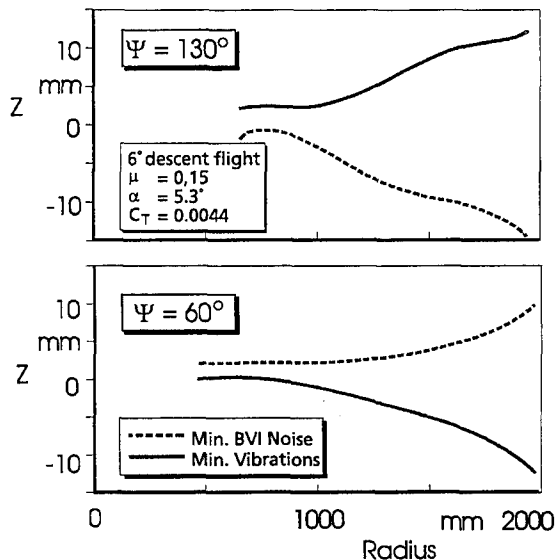


Fig. 25 Elastic Blade Flap Deflection

The elastic blade twist for the same azimuth positions and the same HHC settings is shown in fig. 26. The results, again referenced to the baseline case, demonstrate that an HHC adjustment optimal for BVI noise reduction leads to an increased blade angle of incidence

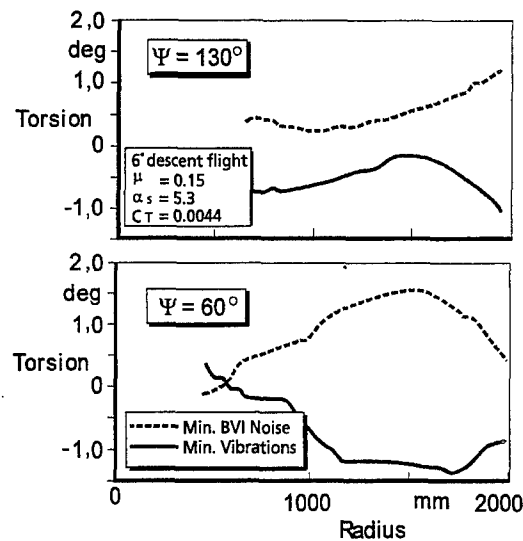


Fig. 26 Elastic Blade Twist

at both 60° and 130° . These results, which are supported by the ones of the videographic methods applied in parallel to the LDV measurements, indicate, that the prime parameter for BVI noise reduction by higher harmonic control is the blade-vortex missdistance.

Concluding Remarks

Due to the manifold measurement techniques applied during the HART wind tunnel test, a comprehensive data base was generated, providing information about all BVI noise and vibration relevant parameters. This data base confirmed that a higher harmonic blade pitch angle is able to reduce the BVI noise level by more than 5 dB. In this case, the strong loading fluctuations in the first quadrant of the rotor disc in descent flight conditions are nearly smoothed out, leading to the conclusion, that the parallel blade-vortex interactions are largely reduced. In fact, the position and orientation of the vortex lines with respect to the blade is modified by a higher harmonic blade pitch angle, which can be derived from the flow visualization results. In addition, the non-intrusive optical methods show that the blade is bended up at the blade-vortex encounters and bended down at the position of vortex generation in minimum noise HHC case. The results of the modified vortex position and orientation found out during the flow visualization measurements indicate that the most important parameter for BVI noise reduction by higher harmonic control seems to be the blade-vortex missdistance. Obviously, this parameter is mainly determined by the tip vortex trajectories whereas the effect of the elastic blade bending and torsion on the reduction of the BVI noise and vibration level by higher harmonic control has still to be investigated in more detail.

References

- [1] Spiegel, P.; Rahier, G.; Michea, B. "BVI Noise: Prediction and Comparison with Flight and Wind Tunnel Tests" pres. at the 18th European Rotorcraft Forum, Avignon, France, 1992
- [2] Open, C.M.; Patrick, M.J. "Directionality of Blade-Vortex Interaction Noise" pres. at the 19th European Rotorcraft Forum, Cernobbio (Como), Italy 1993
- [3] Hassan, A.A.; Charles, B.D.; Tadghighi, H.; Burley, C. "A Consistent Approach for Modeling the Aero-dynamics of Self-Generated Rotor Blade-Vortex Interactions" pres. at the 49th Annual Forum of the American Helicopter Society, St. Louis, Missouri, 1993
- [4] Horner, M.B.; Saliveras, E.; Galbraith, R.A.McD. "An Experimental Investigation of the Oblique Blade-Vortex Interaction" pres. at the 17th European Rotorcraft Forum, Berlin, Germany, 1991
- [5] Beesten, B.M.J. "On the Influence of Blade-Vortex-Interactions on Vortex Structures" pres. at the 16th European Rotorcraft Forum, Glasgow, Scotland, 1990
- [6] Brooks, T.F.; Booth, E.R. "Rotor Blade-Vortex Interaction Noise Reduction and Vibration Using Higher Harmonic Control" pres. at the 16th European Rotorcraft Forum, Glasgow, Scotland, 1990
- [7] Spletstoesser, W.R.; Lehmann, G.; van der Wall, B. "Initial Results of a Model Rotor Higher Harmonic Control (HHC) Wind Tunnel Experiment on BVI Impulsive Noise Reduction" pres. at the 15th European Rotorcraft Forum, Amsterdam, The Netherlands, 1989
- [8] Spletstoesser, W.R.; Schultz, K.-J.; Kube, R.; Brooks, T.F.; Booth, E.R.; Niesl, G.; Streby, O. "BVI Impulsive Noise Reduction by Higher Harmonic Pitch Control: Results of a Scaled Model Rotorexperiment in the DNW" pres. at the 17th European Rotorcraft Forum, Berlin, Germany, 1991
- [9] Brooks, T.F.; Booth, E.R.; Boyd, D.D.; Spletstoesser, W.R.; Schultz, K.-J.; Kube, R.; Niesl, G.; Streby, O. "HHC Study in the DNW to Reduce BVI Noise - An Analysis" pres. at the AHS/RAeS International Technical Specialists Meeting for Rotorcraft Acoustics and Fluid Dynamics, Philadelphia, PA, 1991
- [10] Beaumier, P. et al "Aerodynamic and Acoustic Effects of Higher Harmonic Control on Helicopter Rotor Blade-Vortex Interaction: Predictions and Preliminary Validation" pres. at the 75th AGARD Fluid Dynamics Panel Symposium on Aerodynamics and Aeroacoustics of Rotorcraft, Berlin, Germany, 1994
- [11] Yu, Y.H. et al "HHC Aeroacoustic Rotor Test at the DNW - The joint German/French/US Project -" pres. at the 20th European Rotorcraft Forum, Amsterdam, The Netherlands, 1994
- [12] Mercker, E.; Pengel, K. "Flow Visualization of Helicopter Blade Tip Vortices - A Qualitative Technique to Determine the Trajectory and the Position of the Tip Vortex Pattern of a Model Rotor" pres. at the 18th European Rotorcraft Forum, Avignon, France, 1992
- [13] Seelhorst, U.; Bütefisch, K.A.; Sauerland, K.H. "Three Component Laser-Doppler-Velocimeter Development for Large Wind Tunnel" in ICIASF '93 Record, pp. 33.1 - 33.7, 1993
- [14] Boutier, A.; Lefèvre, J.; Soulevant, D.; Dunand, F. "2D Laser Velocimetry Near Helicopter Blades in DNW (NLR)" in ICIASF '93 Record, pp. 32.1-32.8, 1993

EFFECT OF HIGHER HARMONIC CONTROL ON HELICOPTER ROTOR BLADE-VORTEX INTERACTION NOISE: PREDICTION AND INITIAL VALIDATION

P. Beaumier, J. Prieur, G. Rahier, P. Spiegel, A. Demargne
Office National d'Etudes et de Recherches Aéronautiques
BP 72 - 92322 Châtillon Cedex - FRANCE.

C. Tung, J.M. Gallman, Y. H. Yu,
Aeroflightdynamics Directorate
Ames Research Center, Moffett Field, CA, USA.

R. Kube, B. G. Van der Wall, K. J. Schultz, W. R. Splettstoesser
DLR - Braunschweig, GERMANY.

T. F. Brooks, C. L. Burley, D. D. Boyd, Jr*
NASA Langley Research Center, Hampton, VA, USA
*Lockheed Engineering and Science Company.

ABSTRACT

The paper presents a status of theoretical tools of AFDD, DLR, NASA and ONERA for prediction of the effect of HHC on helicopter main rotor BVI noise. Aeroacoustic predictions from the four research centers, concerning a wind tunnel simulation of a typical descent flight case without and with HHC are presented and compared. The results include blade deformation, geometry of interacting vortices, sectional loads and noise. Acoustic predictions are compared to experimental data. An analysis of the results provides a first insight of the mechanisms by which HHC may affect BVI noise.

1 INTRODUCTION

Noise reduction is presently a key issue for the development of the civil market of helicopters. Among all helicopter rotor noise sources, blade-vortex interactions (BVI) in descent flight, between the rotor and its own wake, are the main sources of nuisance for people living near heliports.

The development of accurate BVI noise predictions based on a correct understanding of noise generation mechanisms has become a major objective for helicopter research. It is essential for the design of quiet rotor geometries as well as for noise control using active means, such as Higher Harmonic Control (HHC), individual blade control, trailing edge flaps...

Acoustic codes based on the integration of the Ffowcs Williams-Hawkins equation (FW-H) [1] with either local blade pressures or sectional loads as input data [2-7] have been developed. The

calculations performed, starting from experimental inputs [4, 8], tend to show that acoustic codes provide good predictions when aerodynamic input data are accurate. The BVI noise prediction problem is then that of correctly predicting blade pressures or sectional loads during blade vortex interactions.

Since BVI events are highly impulsive and acoustics is sensitive to the time derivative of local loads, very accurate predictions of the unsteady fluctuations of these quantities associated to BVI are required. This requirement first implies a precise prediction of the kinematics and of the elastic deformations of the blades in torsion, flap and lag. This is a necessary condition to a correct calculation of local loads which govern the emission of vortices by the blade. Second, it implies a good prediction of the strength and geometry of these vortices at the occurrence of interactions: roll up of the blade vortex sheet which may result in more than a single tip vortex, vortex trajectory with respect to the blade, core size. Third, a suitable aerodynamic modelling is needed to calculate the unsteady loading response of the blade to oncoming vortices, particularly for close blade vortex interactions.

Extensive aerodynamic code developments or improvements are still in progress in order to provide acoustic codes with accurate input data [9-15]. A number of aeroacoustic rotor tests have been carried out to constitute experimental data bases which have been used to validate the theoretical effort. Several of these studies [16-17] were performed with the purpose of demonstrating the effectiveness of HHC for noise reduction. However,

although acoustic data have been gathered, only a very few information on the rotor wake geometry and corresponding blade pressures have been obtained. Furthermore, the mechanisms by which BVI noise is affected by HHC are far from being clearly defined and quantified.

For these reasons, an intensive Higher Harmonic Control Aeroacoustic Rotor Test (HART) program was jointly conducted by Aeroflight Dynamics Directorate (AFDD), DLR, NASA Langley and ONERA. A BVI aeroacoustic test of a highly instrumented BO 105 model rotor in the DNW without and with HHC with measurements of blade position and deformation as well as measurements of the wake geometry by means of Laser Light Sheet (LLS) and Laser Doppler Velocimetry (LDV) was recently performed [18]. In parallel, theoretical models were developed or improved. A first step of this theoretical work was to calculate the BVI noise of rigid rotor blades for simple monocyclic pitch and to compare these results with existing rotor noise data. This work was reported in [15]. A second step was to calculate HHC. The present paper addresses that effort using data for a hingeless rotor operated with HHC which is a non instrumented version of the HART rotor.

The paper presents the status of the prediction tools of AFDD, DLR, NASA and ONERA at the date of May 1994. Aeroacoustic predictions from the four research centers concerning a wind tunnel simulation of a 6° descent flight case are presented and compared. The results include blade position and attitude, blade deformation, location and orientation of interacting vortices, sectional loads and acoustics without HHC and for three different values of the HHC phase. Acoustic predictions are compared to experimental data [17] and discussed.

2 AERODYNAMIC AND ACOUSTIC THEORETICAL PREDICTION METHODS

AFDD, DLR, NASA Langley, and ONERA have independently developed aerodynamic and acoustic prediction tools using different approaches. Each of the codes used to derive the results presented hereafter are briefly described.

2.1 AFDD prediction method

Blade vortex interaction noise is predicted at AFDD in a three stage process. The prediction process starts with the calculation of the rotor wake geometry, the partial inflow angles and the blade motion. This is accomplished by CAMRAD/JA which is a comprehensive analytical model of rotor aerodynamics and dynamics by Johnson Aeronautics [19]. FPR, a full potential rotor flow solver, incorporates the wake geometry and partial inflow angles in the computation of the aerodynamic surface pressures [20-22,9]. The final step in the process is the prediction of the far-field acoustic pressure. RAPP, a rotor acoustic prediction program based on the Ffowcs Williams and Hawkings equation, calculates the acoustic pressure using the FPR computed surface pressures [5].

The rotor aerodynamic analysis in CAMRAD/JA is based on lifting line theory with separate models for the blade and wake that are coupled by the induced velocity and the bound circulation. The blade model, based on 2-D airfoil tables, consists of unsteady, compressible, viscous flow about an infinite aspect-ratio wing. The blade model includes corrections for yawed flow, three dimensional and unsteady effects. A lifting-surface correction is included for the first-order lifting-line theory blade-vortex interactions. The wake model consists of an incompressible vortex wake from a lifting-line with distorted wake geometry (free wake). The inboard trailed and shed vorticity is modeled using vortex sheets. The law of Biot and Savart is used to calculate the rotor wake induced velocity. The circulation in the wake is determined by the radial and azimuthal variation of the bound circulation. The trim analysis in CAMRAD/JA involves solving for the trim variables (rotor control input and aircraft Euler angles) from the algebraic equations obtained by setting the thrust, tip-path plane angle, etc. to target values. The periodic rotor motion and airframe vibration are obtained by solving differential equations of motion. The CAMRAD/JA computed wake geometry and inflow angles are used in FPR to solve for the aerodynamic surface pressures. Since the computational domain of FPR will include some of the wake geometry, CAMRAD/JA calculates the partial angle-of-attack, obtained by excluding the wake inside the computational domain when evaluating the non-uniform induced velocity [19]. The partial angles include the effects of HHC, when it is applied i.e. elastic deformation and changes in inflow.

FPR solves the 3-D, unsteady, full potential equation for transonic flow with the density function determined by the Bernoulli equation. This rotor code, in strong conservation form, is based on the fixed-wing code of Bridgeman et al [20]. Discrete vortices are introduced into the finite-difference computations using a velocity decomposition method. The total velocity field is the sum of the gradient of the potential and the known vortex velocity. The potential equation is solved using half-point differencing formulas. First-order backward differencing is used in time and second-order differencing is used in space Ref. [21, 22, 9]. The time step for the solution corresponds to 0.125 degrees rotor azimuth, or about 64 time steps per chord at the rotor tip. The reason for this relatively small time step is to capture the BVI events that happen in a very short period of time. The velocities associated with the discrete vortices are determined using the law of Biot and Savart as described by Scully in [23]. The vortex is defined as a series of straight line segments with the strength varying linearly along each segment. An algebraic model is used for the solid body rotation of the vortex core.

A simple, yet accurate rotor acoustic prediction program (RAPP) utilizes the FW-H equation in a form well suited to incorporate blade surface

pressures from computational codes such as FPR. The volume integral that models the noise produced by a non-linear flow field (from the knowledge of the Lighthill stress tensor) is not included in the computation performed by RAPP. It is assumed in the current work that the blade vortex interactions do not result in strong shocks and that the contribution to noise from this non-linear flow field term is negligible.

RAPP uses the acoustic lifting line method to model the blade surface loading. The acoustic lifting line is the quarter chord of the acoustic planform and consists of the locations of the contributing sources. These source locations are found by solving the retarded time equation [24]. In this formulation, the force terms in the FW-H equation are modelled as chordwise compact sources distributed spanwise along the quarter chord of the acoustic planform. Note that the term «acoustic lifting line» refers to the location of the contributing sources, not to the method of determining the aerodynamics. The aerodynamic sectional coefficients that describe the source strengths are calculated by FPR and contain information over the whole chord. This technique works well as long as there is sufficient azimuthal resolution of the sectional lift and drag input.

2.2 DLR prediction method

DLR applies the S4 rotor simulation code to predict the spanwise blade loading provided as input to the acoustic code AKUROT.

The S4 code is based on three main modules, which all together are controlled by the rotor trim algorithm. Its purpose is mainly of flight mechanic nature, especially prediction of HHC on rotor dynamics. Due to basically arbitrary stepsize, it is also suited for noise predictions. The main modules of S4 comprise:

Aerodynamic model

This is a lifting line method based on the algorithm of U. Leiss [25]. It consists of an analytical math model to describe the 2D steady airfoil behavior over all ranges of Mach number and angle of attack that a helicopter rotor blade airfoil experiences. Because of the analytical functions, this algorithm can also be used for calculation of unsteady aerodynamics, based on the arbitrary motion theory. For this purpose, the velocities at the airfoil section are split into their origin: 1) those from blade motion are handled with the Wagner function, 2) those from the wake far field are handled like a gust problem using the Küssner function. With this method, an effective angle of attack and an effective stall angle are calculated, leading to unsteady aerodynamic coefficients, and including dynamic stall.

Wake model

A prescribed, distorted wake geometry is used as described by T. Beddoes [26]. This applies for the near wake (mostly the first 15 deg. behind a blade) as well as for the tip vortex. The modelling of a second vortex trailed inboard of the tip is possible.

Within the simulation, only a set of pre-calculated influence coefficients is used in combination with the actual circulation distribution to calculate the induced velocities. Offline of the simulation, additional deflections of the blade motion are introduced to generate new influence coefficients and to rerun the simulation with these.

Aeroelastic model

For blade dynamics, uncoupled flap, lead-lag and torsional modes are used. Coupling exists in form of Coriolis forces and the aerodynamic forces. The mode deflections and the aerodynamic forces are used by the force summation method to get the rotating hub forces and moments and then these are transformed into the nonrotating system. Time integration is done by a Runge-Kutta 4th order scheme.

Trim algorithm

Thrust, pitch and roll moment are normally used to trim the rotor to the desired condition, holding the shaft angle constant, by varying the basic rotor control angles. Additionally, a HHC controller can be implemented.

Output

The output consists of a variety of rotor data time histories. Basically there are the nonrotating forces and moments, additionally all blade degrees of freedom and all aerodynamic values at the blade elements. For purpose of noise prediction, the output stepsize is 2 degrees in azimuth and 20 radial stations along the blade. The matrix of lift distribution is used as input for the acoustic calculation.

For acoustic calculation, the DLR uses the acoustic code AKUROT. This code was developed in 1987 [4] and first validated with experimental data from the 1982 AH1-OLS-model rotor tests in the DNW. The code is based on the FW-H equation (Farassat formulation 1) and includes thickness noise term, loading noise term and also an approximated quadrupole noise term. The calculation is performed in the time domain. For the HART predictions at low speed conditions, only the linear thickness and loading terms are used and, in this case, the code is similar to several other acoustic codes like WOPWOP [28], RAPP [5], PARIS [6] or ROTAC [7].

The input data for the loading term are provided by the S4-rotor simulation code described before. Because the S4 code is a lifting line code, only loading data for one chordwise station (quarter chord line) are available, for 20 radial stations and 180 azimuthal stations. To obtain a smoother result, the loading data were interpolated to get inputs for 1024 azimuthal and 20x8 radial stations before performing the acoustic calculation.

2.3 Langley prediction method

The prediction of highly impulsive noise sources requires high resolution blade loads in both space and time. At Langley, several methods for

computing these airloads have been under development. Predictions used in the present paper is primarily from the HIRES rotor noise code. This uses a modified and enhanced version of CAMRAD [19], designated as CAMRAD.Mod1, and the relatively fast high-resolution post-processing blade loads code, HIRES. The HIRES code in its preliminary form was applied in an earlier, more global analysis [12] of data from the same HHC/BVI test that is examined in this report. The other prediction method, with which some of the present non-HHC data is compared, is a CFD approach. This uses a comprehensive rotor code (either CAMRAD, CAMRAD.Mod1, or CAMRAD/JA) and the full-potential CFD code FPRBVI in post-processing. Both approaches use the rotor acoustic code WOPWOP.

For the present problem, both of the prediction methods start with a 10 degree azimuthal resolution (low resolution) determination of the rotor wake and blade motion using CAMRAD.Mod1. The enhancements of CAMRAD.Mod1 which were employed here include HHC input capability and the use of an optional Beddoes [27] indicial unsteady aerodynamic modelling, as an alternate to using the existing Johnson aerodynamic model in CAMRAD. The rotor blade dynamics coding has not been altered, but the dynamics are indirectly affected through the choice of the aerodynamic forcing function (Beddoes model). In Mod1, the wake details are still determined by the Scully free-wake subroutine which is iterated with the aerodynamic calculations in the trim loop. Wind tunnel and fuselage flow effects are accounted for by (1) making mean «flight» adjustments in tip-path-plane angle and velocity and (2) linearly superpositioning calculated velocity and wake distortions and then iterating with the trim loop. The wind tunnel and fuselage corrections required for these calculations are obtained using Langley codes which were recently developed.

For the cases presented, the rotor was trimmed to the measured value of the thrust coefficient C_T/σ and zero 1 per rev. moment. The input values for rpm, density, and temperature were those measured in the test. The trimmed rotor condition and wake geometry from CAMRAD.Mod1 are used as input to both HIRES and FPRBVI to compute the high resolution blade loads.

The HIRES code computes loads at 1 degree azimuth steps and 75 radial stations. These high temporal (azimuthal) resolution blade loads are obtained by recomputing the influence coefficients and the interpolated wake geometry at every 1 degree azimuth. The Beddoes indicial aerodynamic modelling is valid for arbitrarily small temporal steps and impulsive loading. HIRES uses a subroutine to smooth the straight line segmented wake elements of CAMRAD.Mod1. To simulate an incomplete (or intermediate age) vortex roll-up, an optional dual tip vortex core model, was employed with an inner core radius of 0.3 c, containing 70 percent of the circulation, and an

outer core radius of 3.3 c, containing the remaining 30 percent.

The FPRBVI code is a version of FPR(V2.1) [22] which has been modified to include, all wake elements (both advancing and retreating sides) for a given distance downstream of the rotor. The code accounts for blade sweep, taper, and finite aspect-ratio, along with compressibility effects, including possible generation of shocks about the blade. The FPRBVI calculations presented were made with a stacked O-grid size of 80x36x24 in the chordwise, spanwise, and normal directions, respectively. The computational domain extends from 50% to 120% radius, and approximately $\pm 0.28R$ in the streamwise and vertical directions. The computations used eight time steps per degree with 60 degrees of time (azimuth) overlap aft of the rotor to ensure periodicity. The BVI modelling was accomplished with the surface transpiration option in FPRBVI and the tip vortex wake was interpolated to 2 degrees resolution and smoothed in time and space prior to input into FPRBVI. FPRBVI modelled the tip vortex core using a dual-core model identical to that employed in the HIRES code.

The rotor acoustic prediction code WOPWOP [28] implements the acoustic formulation 1A of Farassat. This non-compact formulation is a time-domain representation of the FW-H equation excluding the volume source or «quadrupole» term for subsonic flow. The inputs to WOPWOP include the physical characteristics such as blade shape as a function of chord and span. The aerodynamic characteristics include the blade loading acting over this blade surface as a function of azimuthal position. For the predictions presented, the loads were input to WOPWOP at every 1 degree of azimuth. The inputs differed in that the calculated sectional loads from HIRES was applied as compact loading at the quarter-chord, whereas FPRBVI specified the pressure distribution over the chord.

2.4 ONERA prediction model

The numerical methods developed at ONERA use five main steps to compute the aeroacoustics of helicopter rotors in low speed descent flight conditions. First, the rotor is trimmed to the correct flight or test condition. Second, the rotor wake is computed. The interacting vortices are then determined in geometry and intensity. In a fourth step, the local blade surface pressures are calculated. Finally, the sound radiation is calculated using an acoustic non-compact formulation with this calculated blade surface pressure distribution as input.

The trim of the rotor is done by R85/METAR [29], initially developed by Eurocopter France. This code computes the dynamic (quasi-steady) response and elastic deformations in torsion, flap and lag by solving the Lagrange equations in which the elastic energy is written using a linear beam model. The unknowns are written as a linear combination of eigenmodes (6 in the present calculation) computed

in a rotating frame. The aerodynamic model is based on a lifting line method: the aerodynamic coefficients C_l , C_m and C_d are directly read in 2D airfoil tables. Then, they are corrected for Reynolds influence and some linear unsteady effects (Theodorsen theory) are added for the C_m coefficient. In METAR calculation, the rotor wake is described by vortex lattices, the geometry of which is prescribed depending on the trim of the rotor. The Biot and Savart formulation is used to calculate the induced velocities on the lifting line. A coupling between the R85 and the METAR code is made until convergence on the induced velocities. For the cases presented, the rotor was trimmed to the measured value of C_l/σ and to following values of the 1st harmonic flapping $\beta_{1c} = 0.09$, $\beta_{1s} = 0.38$. Wind tunnel corrections of the rotor shaft angle were also used (see below).

The rotor prescribed wake geometry obtained by R85/METAR is then distorted by using a free wake model: MESIR [30]. In this code, a lifting line method is also used and the blade motion is given as an input by R85/METAR. MESIR initially assumed that the blades were rigid ([15]); a new version of this code has been developed in order to take into account the blade deformations (torsion and flapping), calculated by R85/METAR too.

In a third step, MENTHE («Modelling of the Roll up of the Vortex Sheet of a Helicopter Rotor», unpublished) identifies the portions of the MESIR predicted vortex sheet the intensity of which is sufficient to result in a roll up. These rolled sheet regions constitute the interacting vortices. Their intensities and locations are computed starting from the characteristics of the MESIR wake and provided as inputs to the aerodynamic code ARHIS for calculation of the blade-vortex interaction. MENTHE also provides ARHIS with the influence of the remaining part of the MESIR wake in the form of quarter chord induced velocities. This modelling of the roll up of vortices has been found necessary because interaction vortices do not generally coincide (in location and intensity) with grid lines of the MESIR wake.

The fourth step is the prediction of the blade pressure by the ARHIS code. ARHIS is based on a 2D-singularity method and predicts unsteady flows in incompressible and non-viscous fluids [31]. The 3D problem is solved by a 2D-by-slices calculation. The 2D calculation conditions are chosen to simulate as close as possible the real 3D aerodynamics in each section and at each azimuth. The effect of finite blade span are introduced through an elliptic-type correction of the pressure coefficients. Subsonic compressibility effects are taken into account by use of Prandtl-Glauert corrections associated with a local thickening of the blade profile. In the case of strong interaction, the vortex is modelled as a cloud of elementary vortices in order to take into account its deformation. The viscous core radius of the vortex is calculated using a law derived from experimental results with its intensity and age at the occurrence

of interactions, as main parameters. For the present calculations, the viscous core radius is about 0.1 chord for advancing blade side interactions and 0.15 chord for retreating blade side interactions. The azimuthal step depends on the impulsivity of the interactions. It may be less than 0.1° .

The noise radiation is computed by the PARIS code [6]. PARIS is based on the FW-H equation and uses a time domain formulation. It predicts the loading and thickness noise. The loading noise is computed starting from the pressure distribution provided by ARHIS.

An efficient spanwise interpolation method has been implemented in PARIS in order to minimize the amount of airload data required for BVI noise predictions. This interpolation identifies the BVI impulsive events on the signatures generated by each individual blade section and deals with their phase and amplitude. This method, used with aerodynamic inputs from 11 blade sections provides the same result as a prediction using airload data from 30 sections, without interpolation. Thus, aerodynamic and acoustic CPU time are reduced by a factor of 3. Furthermore, a subroutine allows to correlate the peaks of a BVI noise signature to the corresponding source locations on the rotor disk. It can be used to identify the noisiest interactions.

3 THEORETICAL PREDICTIONS AND CORRELATION WITH EXPERIMENTAL DATA

3.1 Experimental set up and selected test cases

The calculations presented hereafter refer to the test campaign [17] in DNW 6x8 m open test section.

Model rotor

The model rotor is a 40% dynamically scaled model of a hingeless BO105 main rotor. The blades were not pressure-instrumented. The rotor characteristics are the following:

- 4 blades
- radius: $R = 2$ m
- chord length: $c = 121$ mm
- rectangular planform
- linear twist: -8° (root to tip)
- zero hub/blade precone angle
- modified NACA 23012 airfoil
- nominal rotor operating speed = 1050 rpm (blade passage frequency bpf of 70 Hz).

Acoustic set up and processing

We recall that the in-flow acoustic instrumentation of DNW consists in an eleven-microphone array mounted on a traversing system. As the traverse system was slowly moving, acquisitions were selected each 0.5 m in the flow direction from 4 m upstream to 4 m downstream of the rotor hub. Acoustic results were thus provided on an array of $(17 \times 11) = 187$ microphone locations in a plane $(8 \text{ m} \times 5.4 \text{ m})$ situated at 2.3 m (1.2 R) underneath the rotor (Fig. 1).

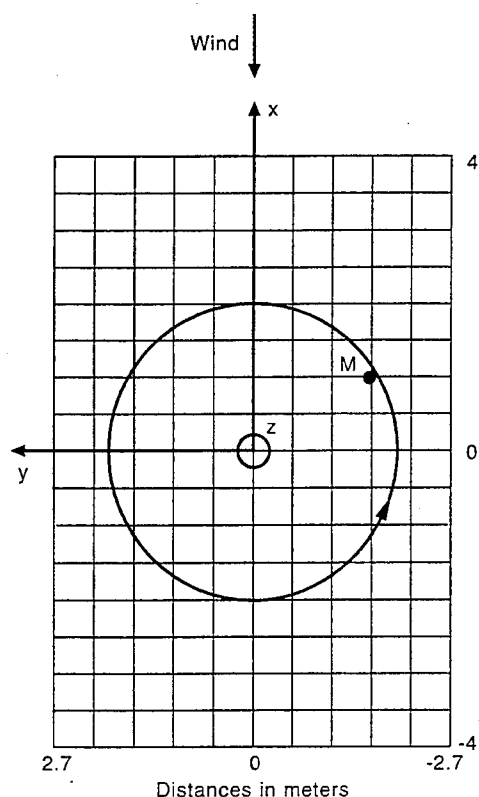


Fig. 1 - Top view of the rotor plane showing the acoustic measurement (and prediction) grid.

To estimate the BVI impulsive noise content, the experimental (as well as theoretical) noise contour plots have been derived from acoustic signals filtered in a 6th to 40th bpf frequency band. In order to characterize discrete frequency noise (the only noise component addressed here), the experimental time signatures were processed in synchronization with the rotation of the rotor shaft. Each experimental signature presented in this paper correspond to an ensemble average of elementary signals. The experimental noise contour plots refer to the spectrum of the averaged signatures.

Selected test cases

Four tests cases have been selected, one with conventional cyclic pitch (baseline case) representative of a typical full scale descent flight of a BO 105 helicopter and 3 cases with 4/rev. higher harmonic pitch control, only differing in the setting of the HHC phase.

- advance ratio: $\mu = 0.15$
- rotating tip Mach number: $M_H = 0.641$
- rotor tip path angle referenced to tunnel streamwise axis and corrected for open jet wind tunnel effects: $\alpha = 3.8^\circ$
- thrust coefficient: $C_T/\sigma = 0.044$
- rotor operated at zero hub moment.

HHC parameters are:

	Amplitude ($^\circ$)	phase ($^\circ$)
Baseline (Run 139)	0	0
Low BVI (Run 175)	1.2°	34
Single BVI (Run 178)	1.2°	124
Mult. BVI (Run 182)	1.2°	244

The HHC phase ϕ is related to the HHC component of the pitch θ_{HHC} and the blade azimuth ψ as follows:

$$\theta_{HHC} = 1.2^\circ \cos(4\psi - \phi)$$

Run 175 corresponds to a typical low BVI noise case. Runs 178 and 182 both correspond to increased BVI noise with respect to the baseline case: Run 178 with a pronounced single blade-vortex interaction on the advancing side, Run 182 with typical multiple interactions.

3.2 Theory-experiment correlation

Blade attitude

A correct prediction of the blade attitude (especially at the tip) is important for the simulation of BVI because it has direct consequences on the vortex strength and on the position of the vortex relative to the blade.

Blade pitch

The elastic tip pitch is plotted versus azimuth in Fig. 2 for the four selected test case.

The mean value of the torsional deformation is found negative (nose down deformations) by all the partners and varies from -0.5° (for DLR) to -2° (for ONERA). For the baseline case, the time dependence of the torsion is weak so that the different predictions only differ by the torsion mean value. The order of magnitude of these differences (from -0.5 to -2°) looks important. However, these differences are partly compensated by the collective pitch θ_0 in the trim loop (for every calculation, the trim is done on total C_T/σ). For the three cases with HHC (Fig. 2), the torsional response is dominated by its 4/rev. component. This is not very surprising since the eigen frequency of the 1st torsional mode of the blade is 3.6/rev. which is very close to the 4/rev. frequency of the HHC. However, large discrepancies are found between the different calculations, not only in peak-to-peak amplitude (which varies from 5° for AFDD to 9° for DLR) but also in phase. If the phase of AFDD calculations is taken as a reference, it can be seen that the DLR prediction is very slightly in advance of phase, the Langley one is 11° in advance of phase and the ONERA prediction is 7° in lag of phase: this means that there may be more than 15° phase difference between all the calculations!

Tip deflection

The mean value of the predicted blade tip deflection (Fig. 3) is about 6 cm. The ONERA calculation is systematically different from the others because of a 1/rev. dominant deflection which does not appear in AFDD, Langley or DLR analysis. This 1/rev. component is a consequence of the trim conditions used by ONERA (see Section 2.4), it disappears when a «0 hub moments» condition is

used. Every partner predicts an increase in amplitude of the 4/rev. component with HHC (just as for torsion). The same differences as above in the phase response between the different analyses are found.

Wake geometry

The analysis of wake geometries near the azimuth of interaction ($\psi = 50^\circ$) is a crucial point. Theoretical results are presented for the baseline and single BVI case on Fig. 4. Note that only tip

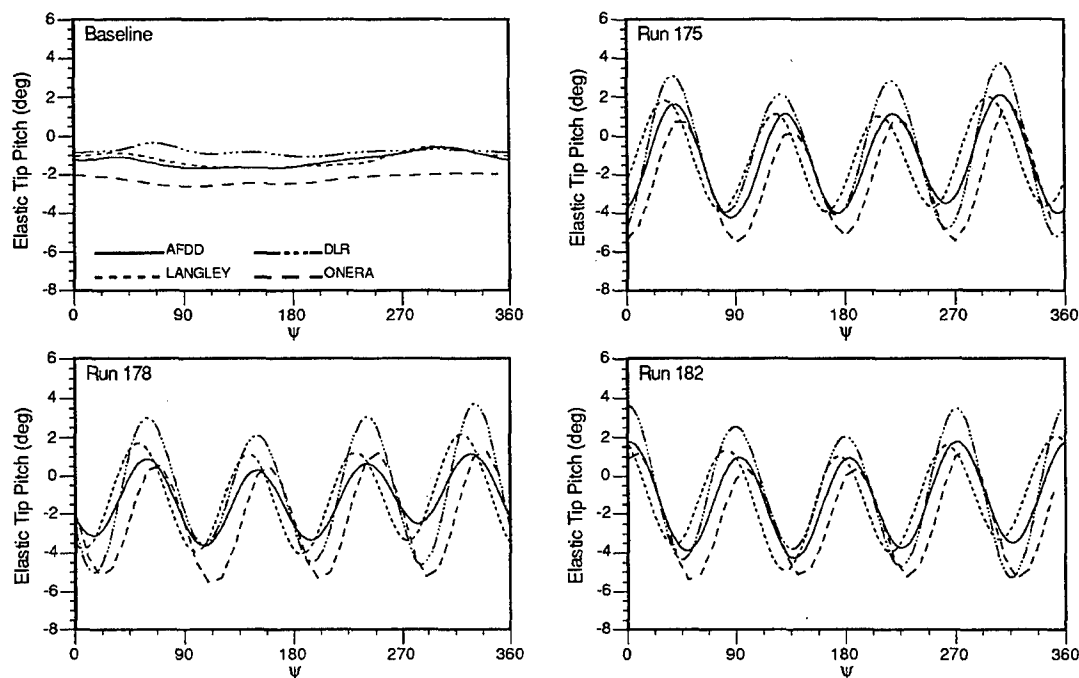


Fig. 2 - Elastic pitch angle at the blade tip as a function of azimuth (theory).

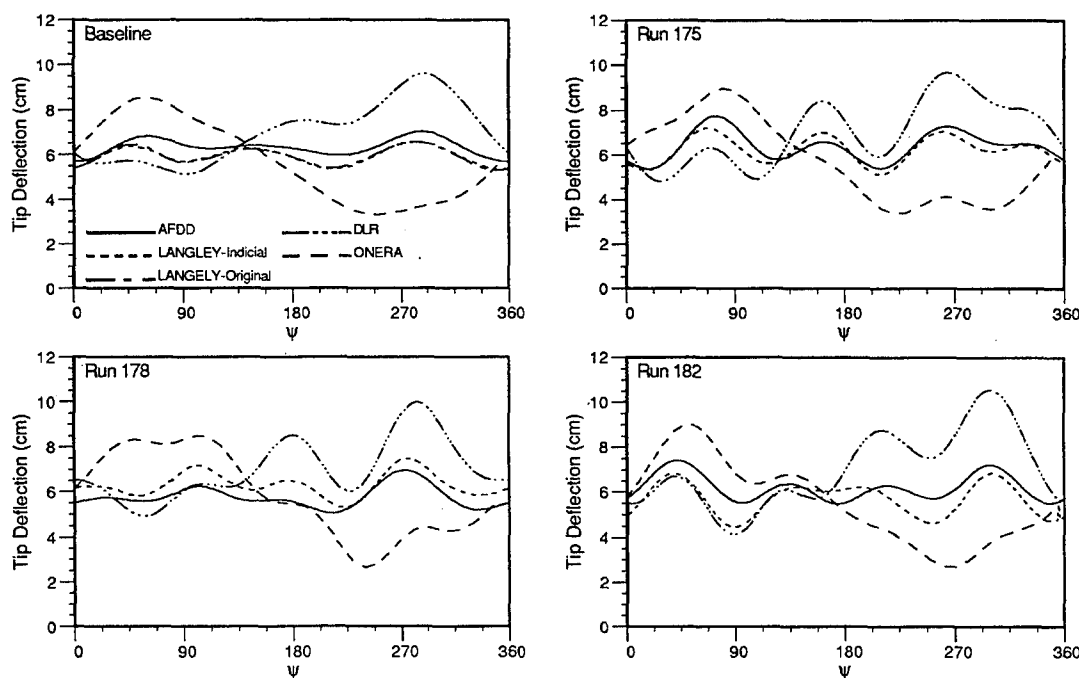


Fig. 3 - Blade tip deflection as a function of azimuth (theory).

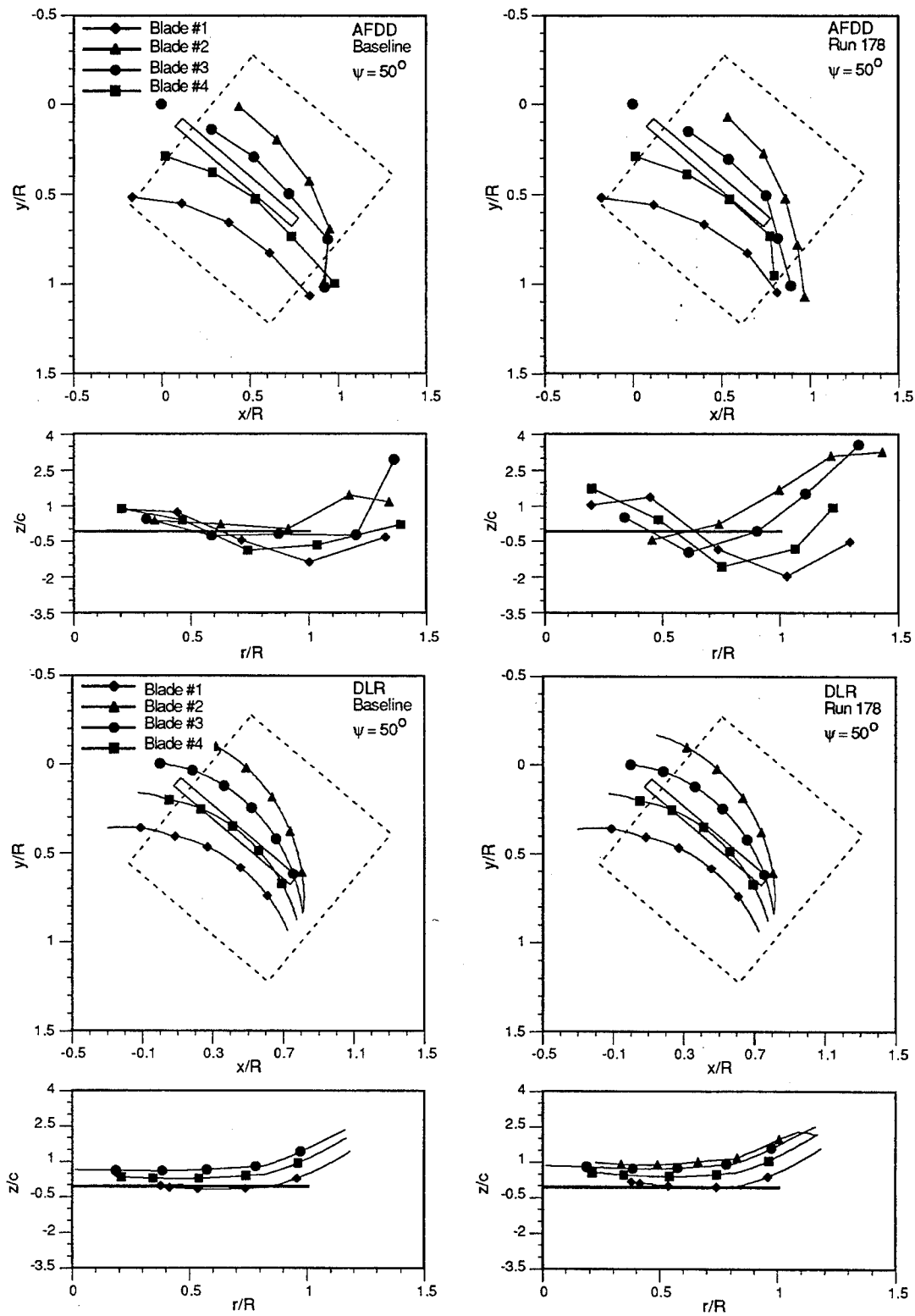


Fig. 4 - Geometry of blade vortex interaction at azimuth $\psi = 50^\circ$ (theory).

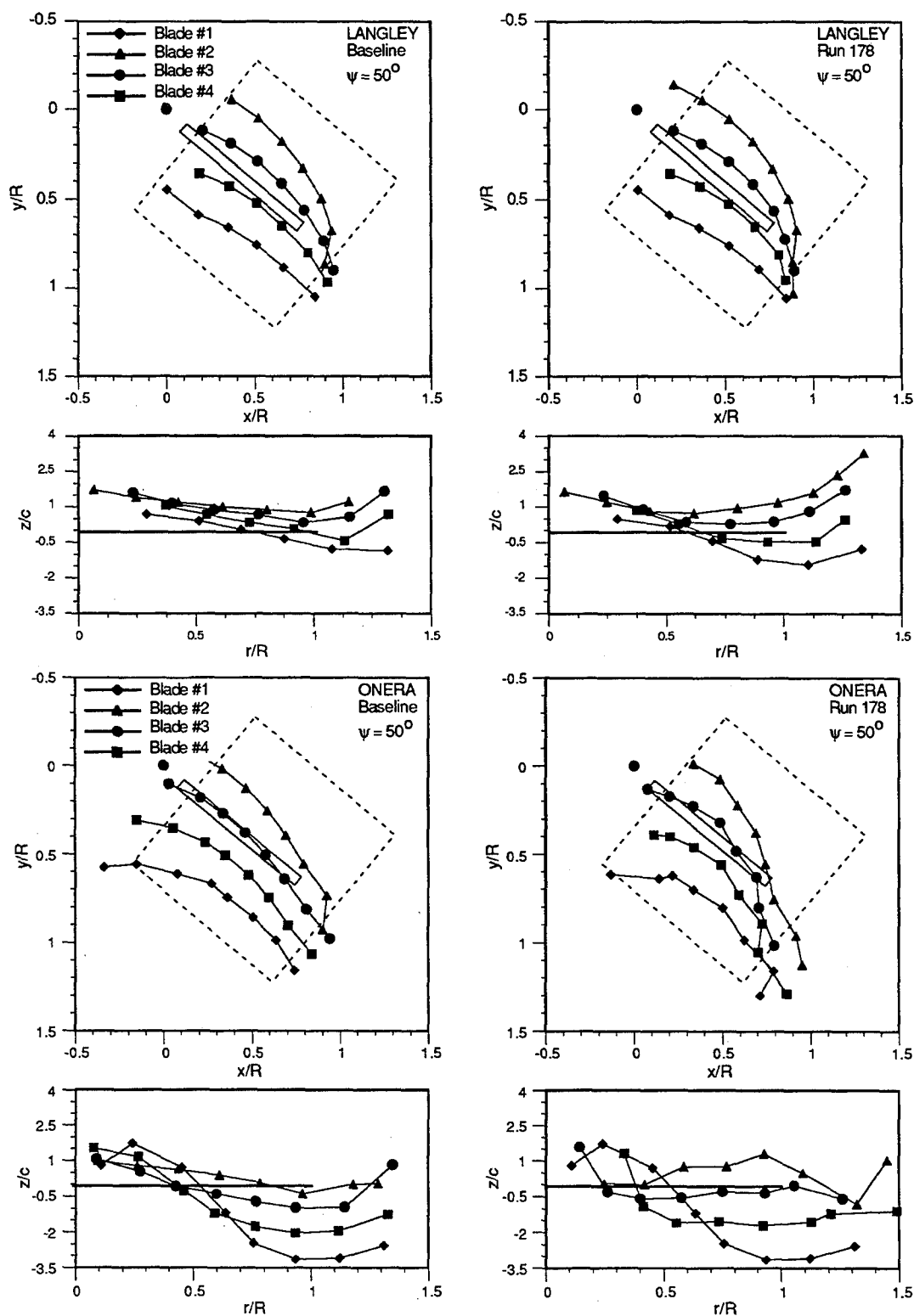


Fig. 4 - (continued)

vortices which are dominant and are the source of the main BVI events for these two cases are shown. Vertical blade-vortex miss-distances refer to the deformed blade except for AFDD where it refers to the tip path plane.

The wake geometries calculated by Langley and AFDD are very similar because they use basically the same free wake code included in CAMRAD. However some discrepancies can be seen, particularly on the side view representing the miss distance between the vortices and the blade. The ONERA wake geometry looks different, both on the top view and on the side view. For instance, the vortex emitted by Blade 3 has already been in interaction at the blade tip at $\psi = 50$ deg in the ONERA analysis whereas it has not yet interacted in AFDD or Langley calculations. These differences in the location of interactions are a bit surprising since the location of interactions mainly depends on the vortex convection velocity which is the same free stream velocity in all the calculations. The DLR geometry strongly differs from the others because they use a prescribed wake model which is probably not accurate enough for such a low advance ratio ($\mu = 0.15$).

Despite all these differences, the three free wake calculations tend to exhibit the same trends for the change in wake geometries from the baseline to the single BVI cases. This change mainly consists in:

- a change in the interaction orientation (top view) which is more oblique near the blade tip in the single BVI case;
- a change in the vortex altitude with respect to the blade (side view). Fig. 3 shows that this increase is not due to differences in the aeroelastic blade motion between both cases, the amplitude of which is weak; it is rather a consequence of the convection of the vortex by the induced flow. The amount of increase depends on the calculation: 0.8c for AFDD, 0.5c for ONERA.

Section loads

A distinction has to be made between the low and high frequency components of the blade loads (Fig. 5). With respect to low frequencies, all the calculations look more or less similar with a dominant 4/rev. component in HHC cases, as a consequence of the torsional response of the blade. Impulsive events (due to BVI), are predicted by every analysis near Azimuth 50-60° on the advancing side and near 300-310° on the retreating side. However, the number and amplitude of the BVI peaks vary very much from one analysis to another.

Acoustic results

Experimental and theoretical noise contour plots (generated using the grid defined in Fig. 1) and typical acoustic time signatures are presented respectively in Figs. 6 and 7.

The rotor signatures refer to Microphone M located 2.4 m underneath the rotor, on the advancing side,

in a region of intense BVI noise (Fig. 1). Differently from the noise contour plots for which the results have been filtered in a 6th to 40th bpf frequency band, the time signatures are unfiltered.

An analysis of Fig. 6 shows that no research center completely succeeds in predicting the correct trends for variation of the acoustic level as a function of HHC phase. Maximum noise directivities on the advancing side from AFDD, Langley and ONERA tend to be in the second quadrant, as in experiment, while they are in the first quadrant for DLR. This shift in directivity is related to the wake prediction. It is certainly due to the fact that DLR uses a prescribed wake model, differently from AFDD, Langley and ONERA which use a free wake analysis.

Calculated acoustic time signatures (Fig. 7) differ qualitatively (with respect to the number of BVI peaks) and quantitatively with more or less agreement with experiment. Note, however that, at least qualitatively, the single BVI peak of Run 178 is rather well predicted.

For the baseline case (Fig. 7a), two kinds of results are presented by Langley both using the same wake calculation (CAMRAD.Mod1 with Beddoes indicial model) but either FPRBVI or HIRE codes to compute the inputs to the acoustic code. The calculation using FPRBVI exhibits some undesirable wiggles while the one using HIRE does not. Wiggles can also be found in AFDD predictions. These might be related to the way by which calculations using both potential codes FPRBVI and FPR are conducted.

Analysis of the results relative to Run 178 (Fig. 7c) is particularly interesting. The low frequency component of the noise is rather well predicted by every partner except ONERA for which it is in lag of phase with respect to experiment. This tendency, also found for other HHC test cases, can be connected to a previously mentioned phase lag in the prediction of torsional deformations. With respect to BVI frequency band, the single peak is rather well predicted by AFDD, Langley and ONERA. The occurrence (in time) of the ONERA peak matches experiment while AFDD and Langley predictions are slightly in lag of phase. This delay corresponds to a delay in predicted occurrences of noisy blade vortex interactions, previously pointed out from the analysis of theoretical wake geometries.

4 DISCUSSION

In addition to the study presented above, some aspects of the BVI modelling are investigated in order to quantify their influence on aeroacoustic predictions in the present section.

4.1 Influence of taking into account the blade flexibility

The first torsional eigenfrequency of the hingeless BO 105 model rotor (3.6/rev.) is very close to the

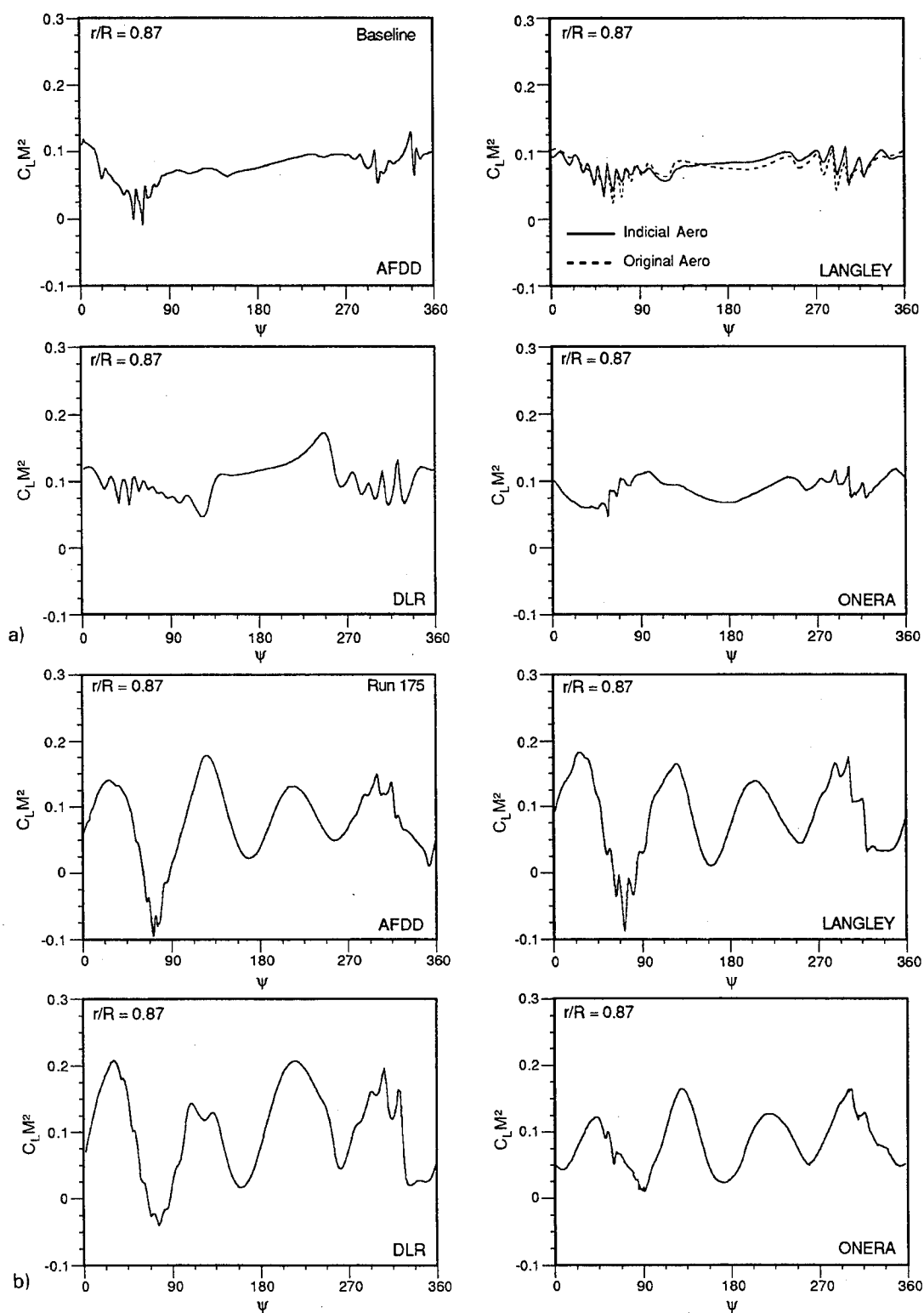


Fig. 5 - Section loads as a function of azimuth (theory).
a) Baseline case, b) Run 175 (low BVI).

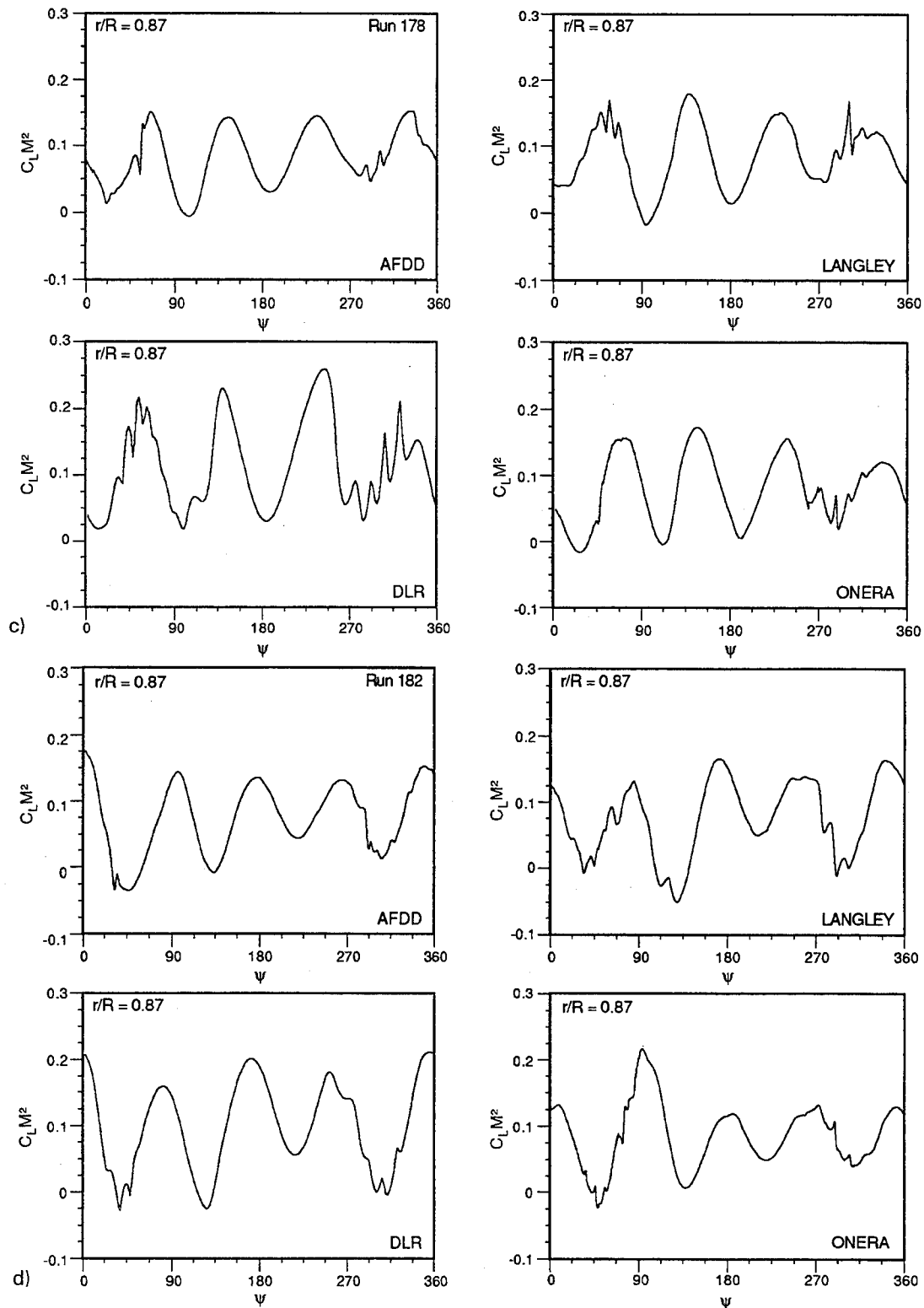


Fig. 5 - Section loads as a function of azimuth (theory).
 c) Run 178 (single BVI), d) Run 182 (mult. BVI).

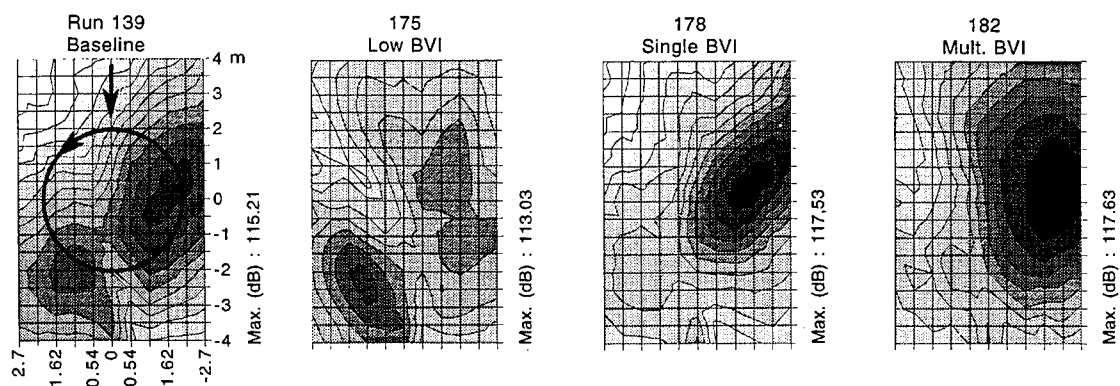


Fig. 6a - Theory/experiment correlation: mid-frequency noise contours (1 dB noise level increment). Experiment [17].

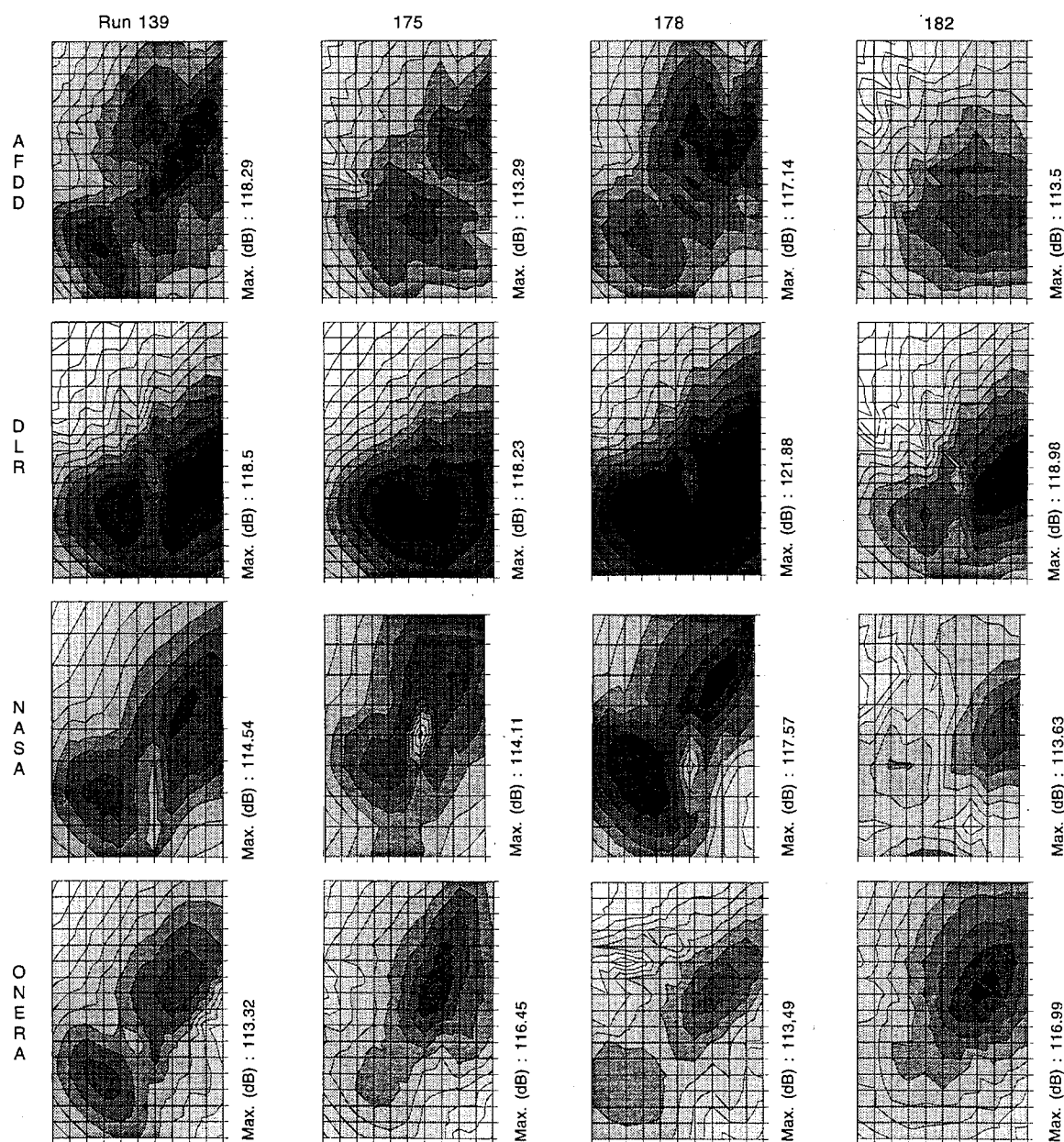


Fig. 6b - Theory/experiment correlation: mid-frequency noise contours (1 dB noise level increment). Theory.

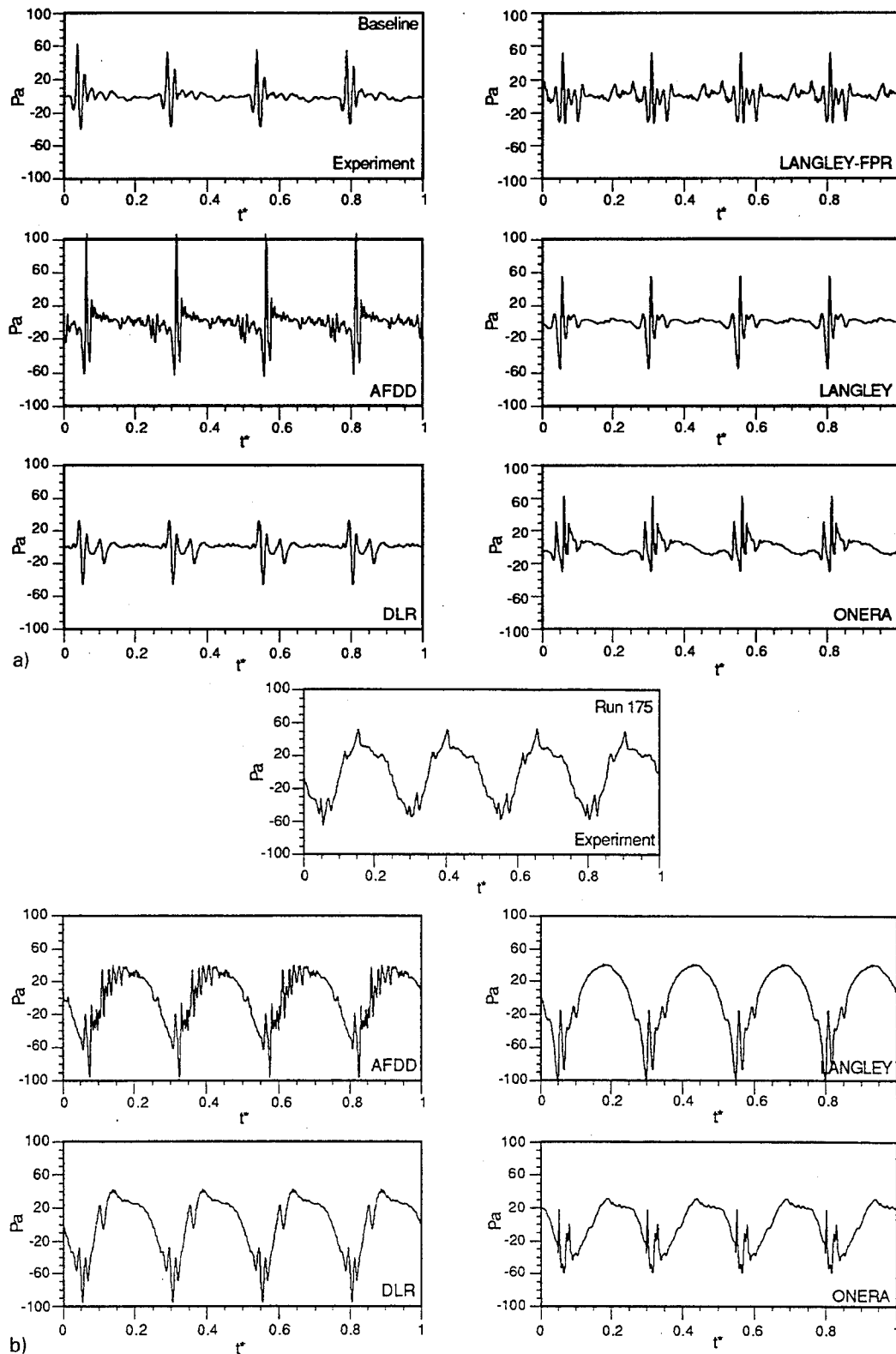


Fig. 7 - Typical acoustic signatures: theory/experiment correlation (t^* =time/rotation period).
a) Baseline, b) Run 175 (low BVI).

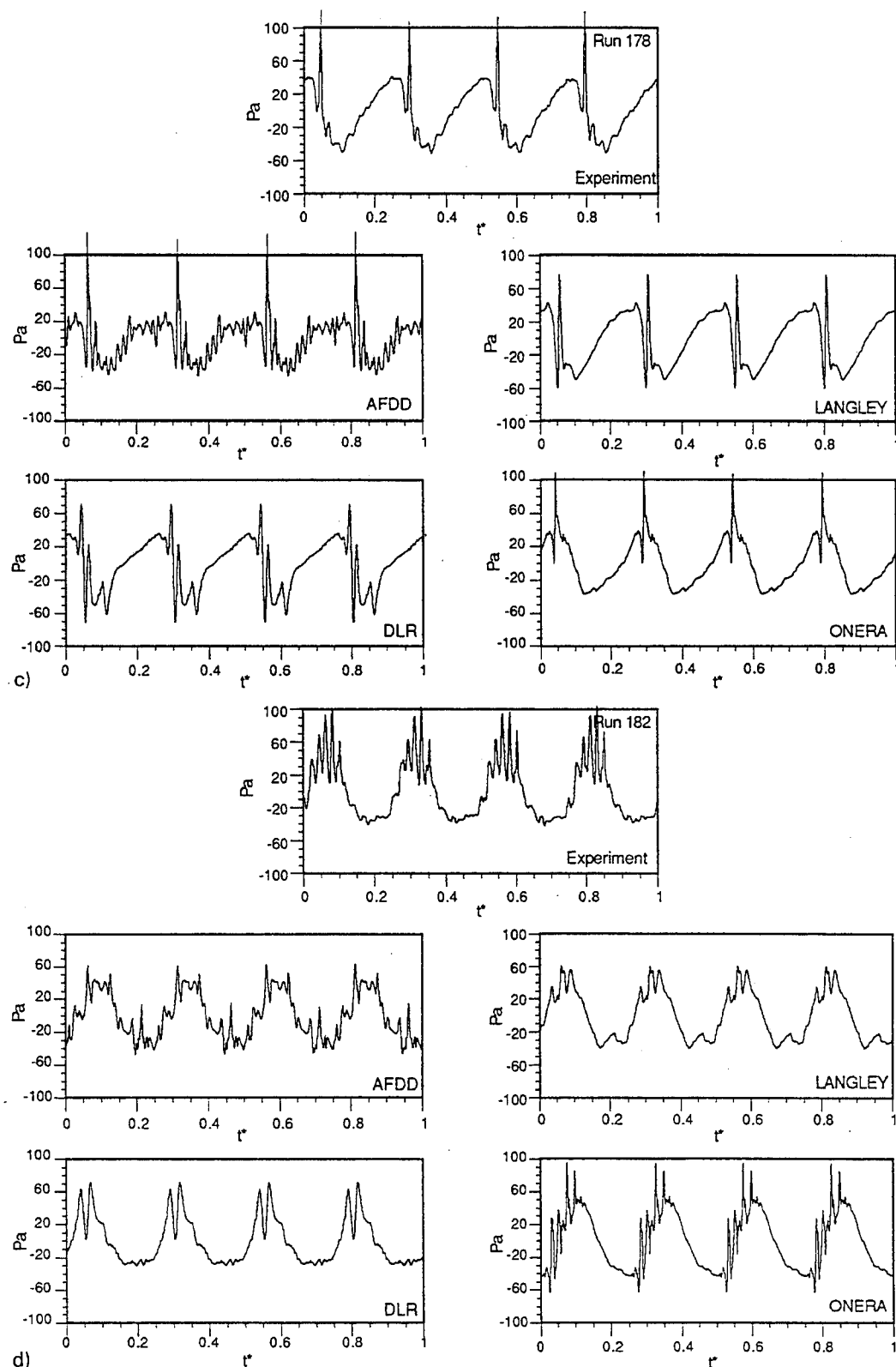


Fig. 7 - Typical acoustic signatures: theory/experiment correlation (t^* =time/rotation period).
c) Run 178 (single BVI), d) Run 182 (mult. BVI).

frequency (4/rev.) of the HHC excitation of the blade pitch. Due to aeroelasticity effects, the question of predicting the combined influences of HHC and blade flexibility on BVI noise is of concern. This subject was first addressed in [12] along with calculations. It is addressed in the present study using theoretical results from ONERA.

Typical acoustic results for the baseline case, from rigid and aeroelastic blade calculations and from experiment, are presented in Fig. 8. The figure refers to an advancing side microphone location close to the maximum of BVI noise, generated about 50-60° blade azimuth. It is seen that the rigid blade model overpredicts noise by a factor of 2. Taking into account the aeroelasticity of the blade provides a better correlation with experiment (though underpredicted by about 30% in terms of peak-to-peak amplitudes).

To understand how the blade flexibility can affect noise, it is necessary to quantify its effect:

- on the strength of the interacting vortices at the time they are emitted,
- on the geometry of BVI at the occurrence of interactions.

According to predictions, for the baseline case, flexibility affects the blade loading mainly in the tip region. Fig. 9a shows that the aeroelastic-blade model tends to predict lower $C_L M^2$ than the «rigid blade model», particularly before 70° and after 100°

in azimuth. Note that in Fig. 9a unlike the other analyses of the paper, $C_L M^2$ is given each 10° by the MESIR code. Since it is known that the two peaks of the noise signatures of Fig. 8 are caused by tip vortices generated in the vicinity of $\psi = 120^\circ$, it is interesting to analyse what happens at this azimuth in terms of predicted circulation Γ . From Fig. 9b, it appears that taking into account flexibility tends to increase Γ in the inner part of the blade and to decrease it near the tip. This is a direct consequence of the torsional deformations (Fig. 10) which are negative at the blade tip (nose down pitching moment) with a mean value of about -2° on the baseline case. ONERA code lower value of the circulation at the tip at $\psi = 120^\circ$ results in a decrease of the strength of the emitted tip vortices in the same proportion. Fig. 11 compares the geometries, with respect to the blade, of the same vortices at the occurrence of interactions (close to Azimuths 50-60°). It appears that the predicted locations of tip vortices in parallel interaction (those responsible for the acoustic peaks of Fig. 8) are much below the blade tip with aeroelastic blades than with rigid blades. This effect, added to the predicted decrease in the strength of these vortices, explains the changes in theoretical noise signatures due to flexibility (Fig. 8).

In the single BVI case, the blade loading is much affected by the blade flexibility (Fig. 12), mostly in terms of the phase of the 4/rev. component of $C_L M^2$: some dramatic changes of the loading can be seen near 60 and 120°. This is also a consequence

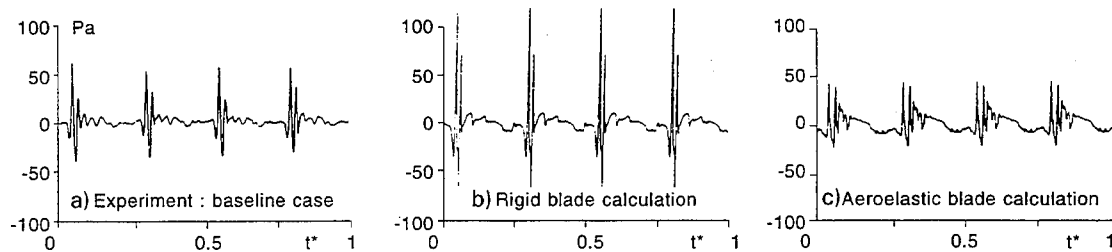


Fig. 8 - Comparison of rigid and aeroelastic blade computations with experiment: acoustic time signatures ($x/R = .25$, $y/R = .81$, $z/R = -1.2$), baseline case.

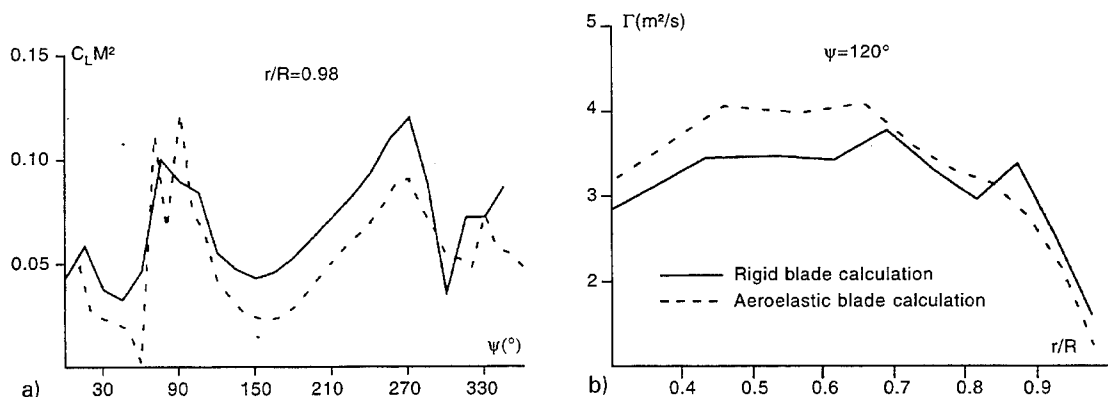


Fig. 9 - Comparison of rigid and aeroelastic blade computations for the baseline case.
a) Section loads, b) Blade circulation at azimuth of interacting vortex generation.

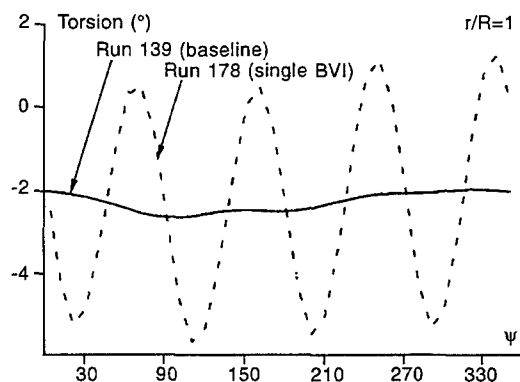


Fig. 10 - Blade torsion response to Higher Harmonic Control (theory).

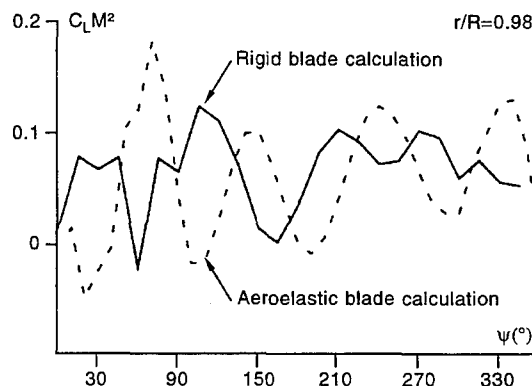


Fig. 12 - Comparison of rigid and aeroelastic blade computations for the single BVI case.

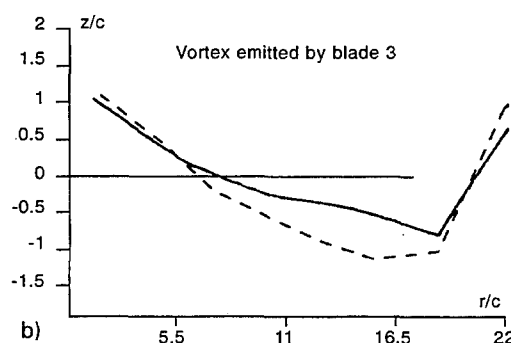
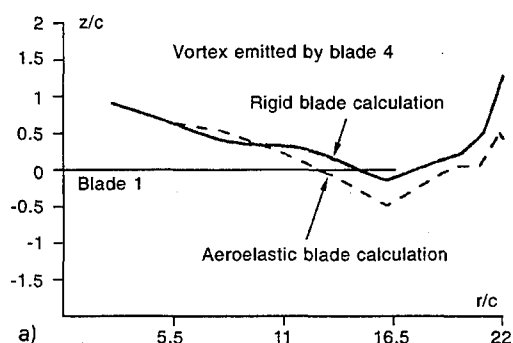


Fig. 11 - Comparison of predicted blade-vortex geometries using rigid and aeroelastic blade models for the baseline case.

of the torsional deformation (Fig. 10), which is dominated by its 4/rev. component. Fig. 13 shows how the aeroelastic-blade model improves the acoustic theory/experiment correlation: the signature of Fig. 13c (aeroelastic blade model) is dominated by a strong single peak, in phase with the experimental one, which was not the case for rigid-blade calculations (Fig. 13b). The low frequency component, well predicted in amplitude is however, in lag of phase with respect to experiment: this question has been previously addressed.

Comparison of Figs. 5a and 9a respectively with Figs. 5c and 12 shows the important influence of HHC on the azimuthal and radial evolution of the blade loading which modifies the trajectory of the vortex over the rotor disk and the resultant blade vortex geometry. Particularly, this, more than the aeroelastic deflection of the blade tip, affects the blade vortex miss-distance (as mentioned in Section 3.2).

4.2 Wind tunnel and fuselage corrections

Wind tunnel wall corrections were computed using a method developed by Brooks which is consistent with Heyson methodology [32], but is based on vortical rather than dipole modelling. This theory predicts the wall corrections as a function of position relative to the nozzle exit. Corrections may be computed at single locations (such as at the hub)

or at many locations to determine the variation over the tunnel test section. This variation can be seen in Fig. 14 for the rotor «flight» conditions considered in this paper. The corrections are plotted in terms of contours of the flow angle between V_x (parallel to tunnel velocity) and V_z (induced velocity due to wind tunnel test section flow boundary effects) at spatial locations over a horizontal plane which includes the rotor disk. The mean value of the corrections over the rotor disk is -1.12° , which is significant. The correction to be performed is subtract 1.12° from the geometrical rotor tip path plane angle in all the calculations.

The fuselage flow field corrections are determined by a potential flow panel method. The fuselage correction contour over the rotor disk is shown in Fig. 15. The 1990 DNW test fuselage and hub are modelled. It is seen that the flow angles are quite high immediately forward and aft of the hub region. The flow goes over the hub unimpeded; but the BVI geometry is affected. However, in traditionally strong BVI regions, the flow curvature angles are seen to be small. For this fuselage/hub geometry, the average over the disk is $+0.16^\circ$.

The basic correction approach is to sum the mean values of the fuselage and the wind tunnel corrections, that is $+0.16^\circ - 1.12^\circ = -0.96^\circ$, and add this to the tunnel-referenced tip path plane

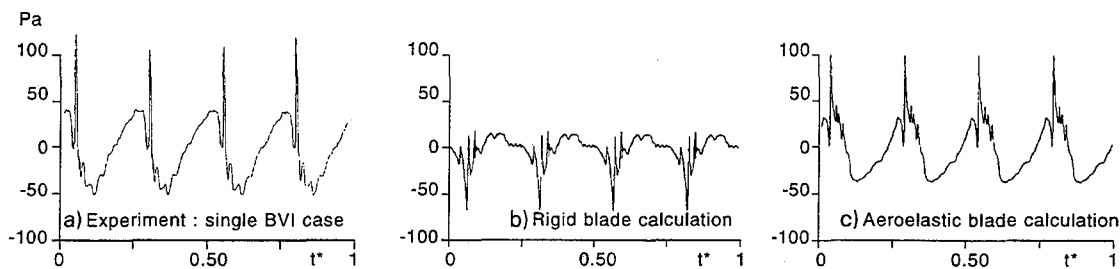


Fig. 13 - Comparison of rigid and aeroelastic blade computations with experiment: acoustic time signatures, single BVI case.

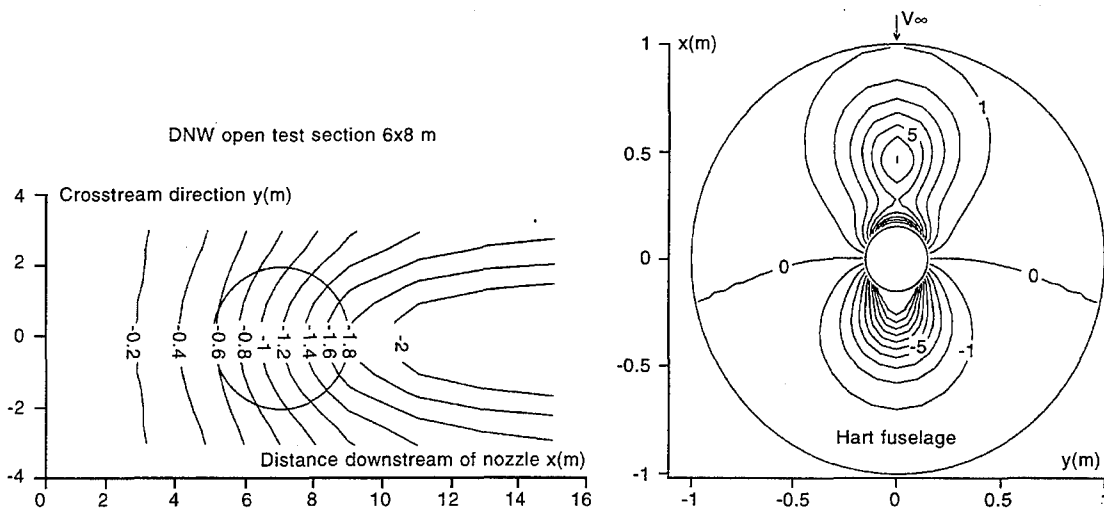


Fig. 14 - Local wind tunnel corrections for the reported test cases: vertical deviation (degree) of the flow velocity due to the wind tunnel.

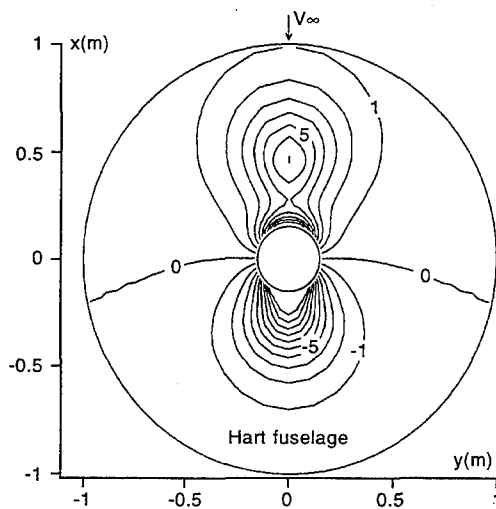


Fig. 15 - Local fuselage corrections: vertical deviation (degree) of the flow velocity due to the fuselage.

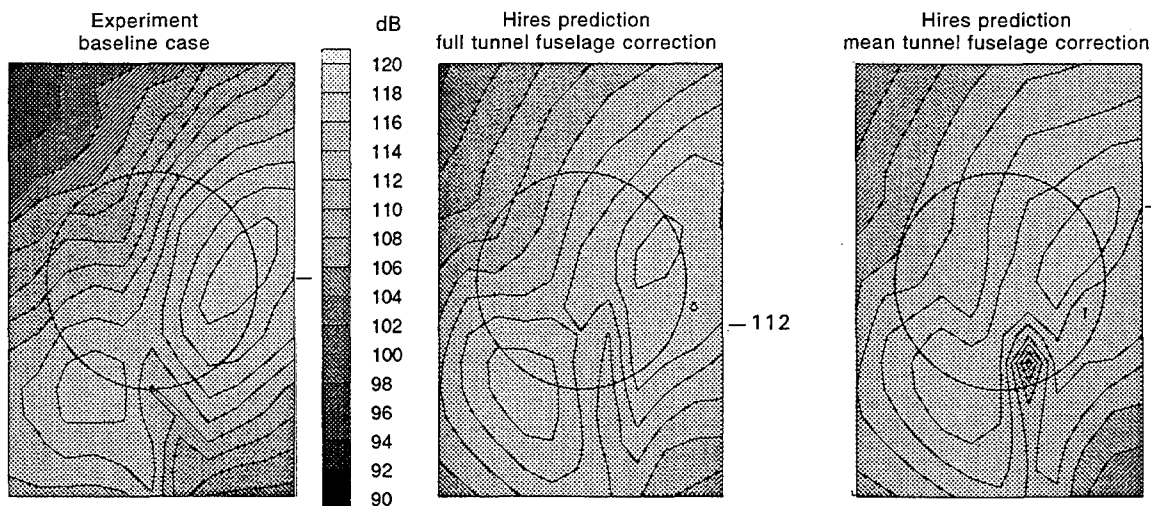


Fig. 16 - Effect of wind tunnel and fuselage corrections on noise predictions

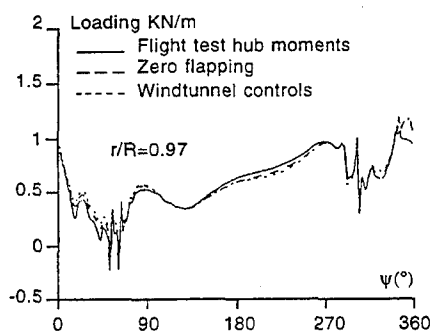


Fig. 17 - Influence of rotor trim conditions on predicted blade loads.

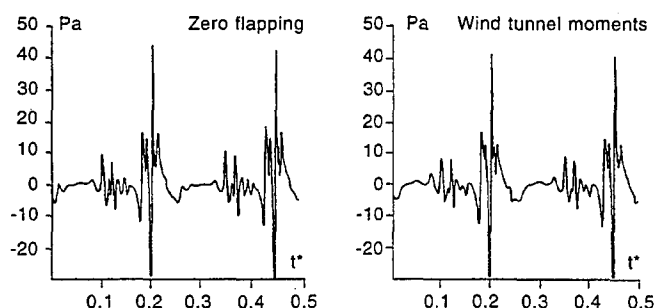


Fig. 18 - Influence of rotor trim conditions on predicted acoustic time signatures.

angle. Langley takes the additional step to incorporate flow and wake distortions into performance code trim loop and in the noise calculations. Fig. 16 illustrates the difference obtained with the two methods on the baseline case. The predicted levels for this case are different by 1 to 2 dB by using the full tunnel + fuselage correction instead of the «simple» mean tunnel fuselage correction. This and other comparisons show that the simplest approach does capture the primary BVI noise directional effects.

4.3 Influence of the rotor trim

The degree of equivalence of wind tunnel and full scale flight measurements is an issue that has recently been addressed by several studies [33], [34]. One of the differences between wind tunnel and flight tests results comes from the rotor trim. The question is: how do the differences in trim conditions affect aeroacoustics? This is an important question because wind tunnel or flight tests are not always performed in the same conditions: sometimes «zero flapping», sometimes «zero hub-moments» (no pitching, no roll moment at the hub) or even some other trim condition. A parametric study, done by AFDD, led to the conclusion that BVI was almost not affected by the trim conditions (at least those tested). For instance, the blade loading (Fig. 17) using the «zero flapping» control law is very similar to the one with the wind tunnel control law. Correspondingly, the calculated acoustic pressure time histories (Fig. 18) are almost identical. The only parameter affected by the trim is the flapping deformation or moment.

5 CONCLUSION

Theoretical tools need improvement for reliable prediction of the effect of the HHC phase setting on BVI noise. To do this, the present analysis shows that, because of the high dependence of acoustics on the calculated wake geometry, an accurate aeroelastic blade and free wake analysis is necessary.

At this time, it is premature to propose, from pure theoretical studies, a complete explanation of the

mechanisms by which HHC may affect BVI noise. However, the discussion of the baseline and HHC cases shows that the predicted effects of HHC on blade vortex miss-distances at the occurrences of interactions is a consequence more of the differences in convection of the vortices by the induced flow than aeroelastic blade tip deflection.

The next step of the HART Program will be to compare theory to experimental results obtained in DNW in June 1994: not only acoustic data but aerodynamics (surface blade pressures), blade deformations and wake geometries. This experimental data base will provide, thanks to LLS and LDV measurements, crucial information on the rotor wake (vortex strength, trajectory with respect to the blade, vortex core size). It should help improving prediction codes and understanding the effect of HHC on BVI noise.

REFERENCES

- [1] - Ffowcs Williams, J.E., and Hawkins, D.L., «Sound Generation by Turbulence and Surfaces in Arbitrary Motion», Philosophical Transactions of the Royal Society of London, Series A, Vol. 264, May 1969, pp. 321-342.
- [2] - Nakamura, Y., «Prediction of Blade-Vortex Interaction Noise from Measured Blade Pressure», 7th European Rotorcraft Forum, Paper 32, Garmisch-Partenkirchen, Germany, September 8-11, 1981.
- [3] - Farassat, F., and Succi, G.P., «Prediction of Helicopter Rotor Discrete Frequency Noise», Vertica, Vol. 7, 1983, pp. 307-320.
- [4] - Schultz, K.J., and Spletstoesser, W.R., «Prediction of Helicopter Rotor Impulsive Noise using Measured Blade Pressures», 43rd Annual Forum of the AHS, Saint-Louis, Mi, May 18-20, 1987.
- [5] - Gallman, J.M., «The Validation and Application of a Rotor Acoustic Prediction Computer Program», Army Science Conference, Durham, NC, June 12-15, 1990.

- [6] - Spiegel, P., and Rahier, G., «Theoretical Study and Prediction of BVI Noise Including Close Interaction», AHS Technical Specialists Meeting for Rotorcraft Acoustics and Rotor Fluid Dynamics, Philadelphia, Pa, October 15-17, 1991.
- [7] - Schaffar, M., Haertig, J., and Gnemmi, P., «Computation of the BVI Noise for the BO 105 Model Rotor in Forward Flight and Comparison with Wind Tunnel Tests», 47th Annual Forum of the AHS, Phoenix, Az, May 6-8, 1991.
- [8] - Visintainer, J.A., Burley, C.L., Marcolini, M.A., and Liu, R.S., «Acoustic Predictions using Measured Pressures from a Model Rotor in the DNW», 47th Annual Forum of the AHS, Phoenix, Az, May 6-8, 1991.
- [9] - Caradonna, F.X., and Strawn, R.C., «An Experimental and Computational Study of Rotor-Vortex Interaction», *Vertica*, Vol. 12, 4, 1988, pp. 314-324.
- [10] - Hassan, A., Tung, C., and Sankar, L.N., «An Assessment of Full Potential and Euler Solutions for Self-Generated Rotor Blade-Vortex Interaction», 46th Annual Forum of the AHS, Washington, D.C., May 21-23, 1990.
- [11] - Van Der Wall, B., «An Analytical Model of Unsteady Profile Aerodynamics and its Application to a Rotor Simulation Program», 15th European Rotorcraft Forum, Amsterdam, Netherlands, September, 1990.
- [12] - Brooks, T.F., Booth, E.R., Jr., Spletstoesser, W.R., Schultz, K.J., Kube, R., Niesl, G., and Streby, O., «HHC Study in the DNW to Reduce BVI Noise - An Analysis» AHS Technical Specialists Meeting on Rotorcraft Acoustics and Rotor Fluid Dynamics, Philadelphia, Pa, October 15-17, 1991.
- [13] - Pike, A.C., «Validation of High Frequency Airload Calculations using Full Scale Flight Test Acoustic Data», AHS Technical Specialists Meeting on Rotorcraft Acoustics and Rotor Fluid Dynamics, Philadelphia, Pa, October 15-17, 1991.
- [14] - Spiegel, P., Rahier, G., and Michéa B., «Blade-Vortex Interaction Noise: Prediction and Comparison with Flight and Wind Tunnel Tests», 18th European Rotorcraft Forum, Avignon, France, September 15-18, 1992.
- [15] - Yung, H. Yu., Tung, C., Gallman, J.M., Spletstoesser, W.R., Schultz, K.J., Van Der Wall, B., Spiegel, P., Rahier, G., Michéa, B., and Costes, M., «Aerodynamics and Acoustics of Rotor Blade-Vortex Interactions: Analysis Capability and its Validation», 15th AIAA Aeroacoustics Conference, Long Beach, Ca, October 25-27, 1993.
- [16] - Brooks, T.F., and Booth, E.R., «Rotor Blade-Vortex Interaction Noise Reduction and Vibration using Higher Harmonic Control», 16th European Rotorcraft Forum, Glasgow, U.K., September 18-20, 1990.
- [17] - Spletstoesser, W.R., Schultz, K.J., Kube, R., Brooks, T.F., Booth, E.R., Jr., Niesl, G., and Streby, O., «BVI Impulsive Noise Reduction by Higher Harmonic Pitch Control: Results of a Scaled Model Rotor Experiment in the DNW», 17th European Rotorcraft Forum, Berlin, Germany, September 24-27, 1991.
- [18] - Kube, R., Spletstoesser, W.R., Wagner, W., Seelhorst, U., Yu, Y.H., Boutier, A., and Mercker, E., «Initial Results from the Higher Harmonic Control Aeroacoustic Rotor Test (HART) in the German-Dutch Wind Tunnel», 75th AGARD Fluid Dynamics Panel Meeting and Symposium on Aerodynamics and Aeroacoustics of Rotorcraft, Berlin, Germany, October 10-14, 1994.
- [19] - Johnson, W., «CAMRAD/JA A Comprehensive Analytical Model of Rotorcraft Aerodynamics and Dynamics», Johnson Aeronautics, Palo Alto, Ca, 1988.
- [20] - Bridgeman, J.O., Steger, J.L. and Caradonna, F.X., «A Conservative Finite-Difference Algorithm for the Unsteady Transonic Potential Equation in Generalized Coordinates». AIAA 82-1388, AIAA 9th Atmospheric Flight Mechanics Conference, San Diego, Ca, August 9-11, 1982.
- [21] - Strawn, R., and Tung, C., «The Predictions of Transonic Loading on Advancing Helicopter Rotors», NASA TM 88 238, US AVSCOM TM 886-A-1, April 1986.
- [22] - Strawn, R.C., and Caradonna, F.X., «Conservative Full-Potential Model for Unsteady Transonic Rotor Flows», *AIAA Journal*, Vol. 25, 2, February 1987, pp. 193.
- [23] - Scully, M.P., «Computation of Helicopter Rotor Wake Geometry and its Influence on Rotor Harmonic Airloads», Massachusetts, Institute of Technology, ASRL TR 178-1, March 1975.
- [24] - Wells, V.L., «Analysis of the Acoustic Planform Method for Rotor Noise Prediction», *AIAA Journal*, Vol. 26, 5, May 1988, pp. 522-523.
- [25] - Leiss, U., «A Consistent Mathematical Model to Simulate Steady and Unsteady Rotor Blade Aerodynamics», 10th European Rotorcraft Forum, The Hague, Netherlands, August 28-31, 1984.
- [26] - Beddoes, T.S., «A Wake Model for High Resolution Airloads», US Army/AHS International Conference on Rotorcraft Basic Research, Research Triangle Park, NC, February 1985.
- [27] - Beddoes, T.S., «Two and three Dimensional Indicial Methods for Rotor Dynamic Airloads», AHS National Specialists Meeting on Rotorcraft Dynamics, November 1989.

- [28] - Brentner, K.S., «Prediction of Helicopter Rotor Discrete Frequency Noise for three Scale Models», 25th AIAA Aerospace Sciences Meeting, AIAA Aerospace Sciences Meeting, AIAA 87-0252, Reno, Nv, January 12-15, 1987.
- [29] - Arnaud, G., and Beaumier, P., «Validation of R85/METAR on the Puma RAE Flight Tests», 18th European Rotorcraft Forum, Avignon, France, September 15-18, 1992.
- [30] - Michéa, B., Desopper, A., and Costes, M., «Aerodynamic Rotor Loads Prediction Method with Free Wake for Low Speed Descent Flight», 18th European Rotorcraft Forum, Avignon, France, September 15-18, 1992.
- [31] - Rahier, G., and Spiegel, P., «Bruit d'Interaction Pale-Tourbillon d'un Rotor Principal d'Hélicoptère», Journal d'Acoustique, Vol. 5, 1992, pp. 171-180.
- [32] - Heyson, H.H., «Use of Superposition in Digital Computers to Obtain Wind Tunnel Interference Factors for Arbitrary Configurations, with Particular Reference to V/STOL Models», NASA TR R-302, 1969.
- [33] - Signor, D.B., Watts, M.E., Hernandez, F.J., and Felker, F.F., «Blade-Vortex Interaction Noise: a Comparison of In-Flight Full Scale and Small Scale Measurements», AHS Aeromechanics Specialists Conference, San Francisco, Ca, January 19-21, 1994.
- [34] - Peterson, R.L., and Maier, T., «Correlation of Wind Tunnel and Flight Test Results of a Full-Scale Hingeless Rotor», AHS Aeromechanics Specialists Conference, San Francisco, Ca, January 19-21, 1994.

Calculation of High-Speed Noise from Helicopter Rotor Using Different Descriptions of Quadrupole Source

S. Ianniello and E. De Bernardis
Aeroacoustics Branch
C.I.R.A., Italian Aerospace Research Center
via Maiorise
81043 Capua
Italy

SUMMARY

The problem of quadrupole noise prediction is addressed and treated through the acoustic analogy approach, comparing different solution forms for the FW-H equation including the nonlinear source term. In particular, results obtained using the volume integration of the quadrupole source are presented. A comparison is established with results from a set of acoustic Euler calculations; a comparative analysis of the computing time is conducted, and methods to reduce the computational effort requested by the volume integration are proposed. Then, a particular description of quadrupole source term is introduced, giving rise to some surface integrals. Their role is investigated in order to assess how they affect the quadrupole noise calculation.

LIST OF SYMBOLS

c_0	speed of sound in undisturbed air
D	rotor diameter
d	distance of the observer from rotor hub
M_r	Mach number in the source-observer direction
M_{tip}	rotor blade tip Mach number
\hat{n}_i	unit normal vector to the blade surface
p_Q	acoustic pressure from quadrupole source term
R	rotor radius
r	source-observer distance
\hat{r}_i	unit vector in the source-observer direction
T_{ij}	Lighthill stress tensor
u_i	fluid velocity
δ_{ij}	Kronecker delta
ρ	local air density
γ	specific heat ratio c_p/c_v of air

1. INTRODUCTION

Although a great deal of theoretical and computational work has been carried out over the last few years, a reliable evaluation of noise from helicopter rotors with blade tip speed in the high transonic range is still far to be achieved. Prediction technology has been growing up considerably through the research effort of mathematicians and aeroacousticians: several theoretical formulations have been developed and implemented in computer codes. Nevertheless, both theoretical and numerical tools cannot be considered at an ultimate definition stage, and the task of providing effective prediction codes for calculating the sound field of helicopters has not yet been accomplished.

Among the methods used in the prediction of noise from moving bodies, those based on the Ffowcs Williams-Hawkings (FW-H) equation [1] represent perhaps the most instructive example in order to realize how the en-

hancement of theoretical formulations may affect the capabilities of computational tools. A number of computer codes have been developed over the last twenty years, following approaches based on the solution of the FW-H equation: time and frequency domain formulations have been exploited to find suitable expressions for the acoustic pressure field.

Accurate results can be easily achieved as far as linear sources are dominant: in fact, thickness noise can be estimated based on the description of blade geometry and motion, and loading noise only requires the pressure distribution on the blade surface. Generally, these data are somehow available, although problems may arise when strong blade-vortex interaction occurs, which causes highly unsteady airload. Predictions based on surface data prove to be quite good up to moderate tip Mach number. As the tip speed increases, effects of the flow field around the blade become more and more important: at tip Mach number in the transonic range, no prediction can be reasonably compared to experimental results if quadrupole source effects are neglected in the numerical calculation: in fact, thickness noise and quadrupole noise have the same order of magnitude in this case. Two major concerns toward the use of the FW-H equation for quadrupole noise calculation are related to the huge amount of data to be treated: an accurate description of the flow field around the blade is needed and, once this is available, a volume integration is requested, leading to large computer cost.

Aim of this paper is to present some recent numerical results obtained in the prediction of quadrupole noise, comparing different solution methods. Thus, section 2 is devoted to a brief introduction of the nonlinear term and the explanation of the main problems connected to its numerical evaluation; then the *momentum thickness* approximation is introduced and applied to two different test cases (section 3). The results obtained from the volume integration and their comparison with analogous calculations performed through an Euler code are presented in section 4; an analysis of the requested CPU time is then developed, to compare the two different computational approaches. Finally, section 5 is devoted to an alternate formulation. Some surface contributions arise in this formula: their role is investigated to assess the impact on the numerical evaluation of quadrupole noise.

2. QUADRUPOLE SOURCE TERM

Since the late '70s numerical calculations have confirmed the importance of quadrupole noise contribution to the acoustic pressure field at tip Mach numbers around 0.8 [2,3,4]; experimental results at increasing tip speed show

that the resulting acoustic pressure waveforms have a progressively higher peak value and exhibit an asymmetric shape, in contrast with numerical predictions based on the linear terms only. Thus, the research interest moved to the nonlinear term in the Ffowcs Williams-Hawkins equation, which is expressed by:

$$\tilde{Q} = \frac{\partial^2}{\partial x_i \partial x_j} [T_{ij} H(f)] \quad (1)$$

where $T_{ij} = \rho u_i u_j + P_{ij} - c_0^2 \rho \delta_{ij}$ represents the Lighthill stress tensor. Here, ρ is the local air density, u_i is the velocity of the air flow, and P_{ij} the compressive stress tensor ($P_{ij} = p \delta_{ij} - \Sigma_{ij}$, with Σ_{ij} the viscous stress tensor). The Heaviside function $H(f)$ points out that the source term is nonzero only when $f > 0$, that is outside the surface $f = 0$, which represents the blade. Applying a standard Green function approach, the source term (1) gives rise to an integral expression, where the double space derivative is usually transformed into a double time derivative; thus, the quadrupole noise term takes the form:

$$\begin{aligned} 4\pi p'_Q(\mathbf{x}, t) = & \frac{1}{c_0^2} \frac{\partial^2}{\partial t^2} \iiint_{f>0} \left[\frac{T_{ij} \hat{r}_j \hat{r}_i}{r|1-M_r|} \right]_{\tau^*} dV \\ & + \frac{1}{c_0} \frac{\partial}{\partial t} \iiint_{f>0} \left[\frac{3T_{ij} \hat{r}_j \hat{r}_i - T_{ii}}{r^2|1-M_r|} \right]_{\tau^*} dV \\ & + \iiint_{f>0} \left[\frac{3T_{ij} \hat{r}_j \hat{r}_i - T_{ii}}{r^3|1-M_r|} \right]_{\tau^*} dV \quad (2) \end{aligned}$$

The volume integrals in equation (2) extend, in principle, to the whole space surrounding the blade; the integration is performed using a frame of reference fixed to the moving blade (considered as a rigid body); the factor $|1-M_r|$ appearing in the above formula, accounts for the change of reference from the air-fixed to the blade-fixed frame, and $M_r = M_i \hat{r}_i$ is the local Mach number of the blade-fixed frame of reference in the source-observer direction. The subscript τ^* means that all the quantities within square brackets in the integrals have to be evaluated, for every source point, at the proper retarded time.

The main difficulty in the numerical evaluation of expression (2) arises from the volume integration and the corresponding requirement for an accurate description and treatment of the flow field surrounding the blade. The calculation of a three-dimensional velocity field around the blade is a very difficult task, especially for the Mach number range where the quadrupole contribution is important. Furthermore, when this aerodynamic input is somehow available, the computational tool has to deal with a huge set of data, leading to heavy computational burden. The task of improving the accuracy of quadrupole noise prediction, while maintaining acceptable computer cost, is still a research challenge.

3. MOMENTUM THICKNESS APPROXIMATION

Different approximations have been implemented in aeroacoustic codes in the attempt of turning the volume integration into a sequence of simpler operations. The method proposed by Yu, Caradonna and Schmitz [3] is based on the assumptions of an isentropic and quasi-steady flow and allows the analysis of only in-plane and far-field observer positions. For these microphone locations the source points placed on any line perpendicular to the blade surface can be assumed to have the same emission time of the corresponding point on the blade;

the squared magnitude of the perturbation velocity is then integrated along such direction, to obtain the so-called *momentum thickness* distribution along every blade section contour. This quantity is used to estimate the surface distribution of quadrupole source strength, which eventually allows the evaluation of the acoustic pressure through an integral extending to the blade surface:

$$\begin{aligned} 4\pi p'_Q(\mathbf{x}, t) = & \frac{\partial^2}{\partial t^2} \iint_S \left\{ \left[\int_n \left(\frac{u}{u_0} \right)^2 dn \right] \right. \\ & \left. \left[\rho \left(1 + \frac{\gamma-1}{2} M_0^2 \right) \frac{M_0^2}{r|1-M_r|} \right] \right\}_{\tau^*} dS \quad (3) \end{aligned}$$

where M_0 is the local blade Mach number. Starting with equation (3), a further simplifying assumption was adopted by Schultz and Spletstoesser [5]: based on numerical results, they related the unknown momentum thickness distribution to the maximum streamwise perturbation velocity, exploiting the empirical expression:

$$\int_n \left(\frac{u}{u_0} \right)^2 dn \approx A C \left(\frac{u_{\max}}{u_0} \right)^3 \quad (4)$$

where C is the blade section chord and A a parameter depending on the tip Mach number. Figures 1 and 2 show the acoustic pressure time histories (sum of thickness and quadrupole contributions) at tip Mach numbers of 0.8 and 0.9, where the quadrupole noise has been calculated through equations (3) and (4).

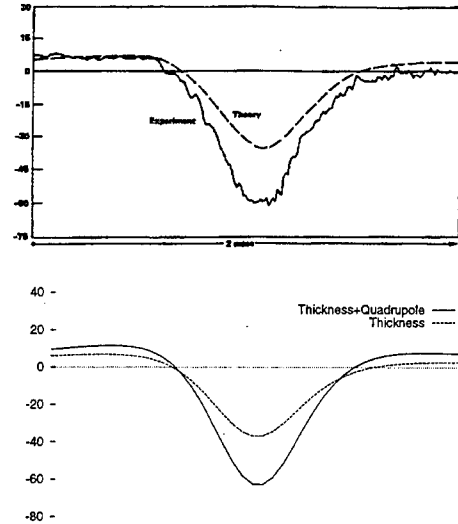


Figure 1 - Comparison between predicted acoustic signatures and experimental pressure time histories, for in-plane observer position, with $d/D = 1.5$ and tip Mach number of 0.80. The quadrupole source term has been evaluated through the "momentum thickness" approximation. The top figure is reprinted from [2] and the notation "Theory" refers to a simple thickness noise calculation.

The agreement with experimental data (reported at the top of the figures, and published in [2]) is quite satisfactory, especially at the tip Mach number 0.8 (figure 1), where the symmetric pattern of the resulting signature and the negative peak pressure are well-predicted. As the rotational speed increases, the appearance of stronger shock

waves and their delocalization outside the blade tip, significantly affect the shape of the acoustic signature, while the peak value increases dramatically. In these conditions, the approximation based on the *momentum thickness* is no longer able to describe the complex phenomena taking place in the flow field; at the tip Mach number 0.9, in spite of a fairly good agreement between the peak values of the calculated waveform and the experimental data, the predicted acoustic pressure signature still results in a symmetric pattern, while the experimental wave exhibits the characteristic *sawtooth* shape, due to the strong shock.

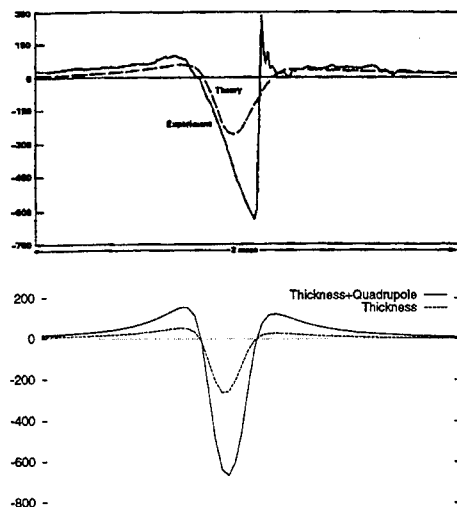


Figure 2 - At a tip Mach number of 0.90, although the predicted peak pressure is in good agreement with the experimental data, the shapes of the two signatures look very different: the approximation is unable to describe the phenomena related to the presence of strong shock waves in the flow field around the blade tip.

4. THE VOLUME INTEGRATION

4.1. Helicopter noise prediction using FW-H equation

The application of the acoustic analogy approach for the prediction of quadrupole noise from helicopters has often been regarded as an elegant exercise of little practical interest. The method is strongly dependent on the quality of aerodynamic data, and is usually considered too expensive from a computational point of view. Over the last few years the use of alternative computational techniques, as the Kirchhoff's approach, or the direct use of aerodynamic codes for observer locations placed in the far field (Computational Aeroacoustics), has provided very encouraging results in the evaluation of the high-speed impulsive noise [6,7,8]. However, the acoustic analogy is the only approach to allow a schematic partitioning of the resulting noise signature: a definite relationship exists between the integral terms appearing in the solution of the FW-H equation and the different noise generating mechanisms related to the presence of the body in the flow field. In this frame, the attempt to perform acoustic calculations through the FW-H equation seems to be very important, especially at a research stage. Furthermore, we will try to prove that the computational effort for a complete volume integration in the space surrounding the blade is definitely comparable to the computer time requested, for the same test case, by an Euler solver.

A computer program for calculation of helicopter rotor noise (HERNOP), based on the solution of FW-H equation, has been developed at C.I.R.A. within the Brite/Euram project HELINOISE [9]. HERNOP code includes a module for the evaluation of high-speed impulsive noise, using the volume integration of quadrupole source. At the present stage, this module enables the calculation of quadrupole noise only for hovering rotor, and source points at subsonic speed (*i.e.*, involving single emission time). Further developments are expected from C.I.R.A. effort in the frame of the IMT project HELISHAPE: major enhancements include the extension to forward flight and the capability of determining multiple emission times for source points at supersonic speed.

An accurate description of the flow around the blade is requested by the above aeroacoustic code. Aerodynamic data are currently provided by UTAH code, a computer program developed at the Rotorcraft Aerodynamics group of CIRA [10]. This is based on a non-conservative full-potential formulation and calculates the fluid velocity and density fields in a prescribed volume around the body: then, the Lighthill stress tensor field can be calculated, as requested by the acoustic code. A very fine grid (denoted as Q-grid) is adopted by UTAH code for aerodynamic calculations aimed at providing input data to HERNOP code (which exploits the same grid): the Q-grid includes approximately 30000 source points, and may extend off the blade tip up to 30% of blade span (a sketch of the grid is shown in figure 3); the maximum chordwise size is of $3.14C$, and 15 different layers are usually considered, in the normal direction, around the blade (giving a maximum size of $5.7C$ in Z -direction) to provide high spatial resolution on the fluid velocity field.

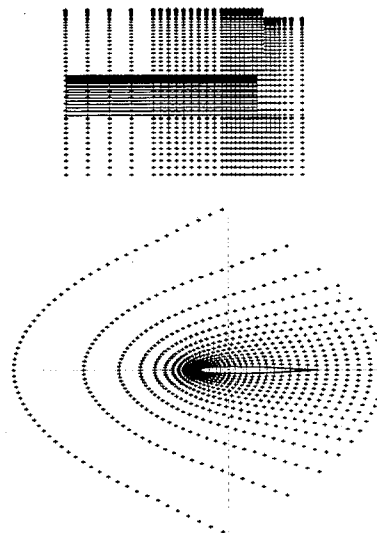


Figure 3 - Planform and side views of UTAH Q-grid.

4.2. Capabilities and limits of the volume integration

In order to show the current state of the volume integration routine, some numerical results are shown in figures 4 to 6. Here, a comparison is proposed between pressure waveforms from HERNOP code and acoustic results obtained by Baeder, Gallmann and Yu [6], using an Euler code. Test cases refer to a UH-1H nonlifting, hovering rotor at tip Mach numbers varying between 0.60 and 0.90;

microphone position is in the rotor plane, at $3.09R$ from rotor hub, R being the tip radius of the rotor blade.

Results from HERNOP code are reported on the right, with the decomposition of the noise signature into thickness (dotted line) and quadrupole contributions; the pressure time histories on the left are those calculated with the Euler solver, extending the computational grid in order to include the far-field microphone location. The markers represent experimental data (when available), while the dashed line is the thickness noise: this is calculated with a different tool, since the Euler solution does not allow to distinguish the different contributions to the overall acoustic pressure signature.

Figure 4 refers to tip Mach numbers of 0.60 and 0.70: in these cases the quadrupole source term contribution is very small, as it clearly appears from the solution of the FW-H equation obtained from HERNOP.

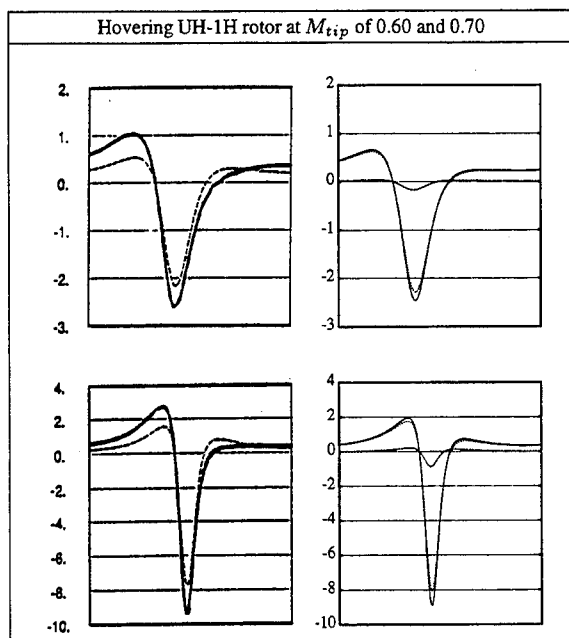


Figure 4 - Comparison between acoustic pressure signatures obtained with an Euler code (left) and the solution of the FW-H equation (right), for a hovering rotor at M_{tip} of 0.60 and 0.70 (top to bottom).

At tip Mach numbers between 0.80 and 0.88 (figure 5, top to bottom), the quadrupole contribution significantly increases. Up to a M_{tip} of 0.85 satisfactory results are still obtained: the shape of the predicted signatures, as well as the calculated peak pressures, are in good agreement with the experimental data. At M_{tip} of 0.88 the experimental signature starts losing its symmetry, and the Euler solution does perfectly follow this trend. Here, the FW-H solution is slightly affected by a loss of information due to the restriction of the off-blade portion of the grid, including only points at subsonic speed.

At larger tip Mach numbers (figure 6, $M_{tip} = 0.90$), the input data provided by the aerodynamic code does not contain the contribution from the region across the sonic cylinder: this is crucial to determine the shape and peak value of the acoustic waveform. In fact, as the tip Mach number increases, the blade tip approaches the sonic cylinder. Thus, at points across this critical area the

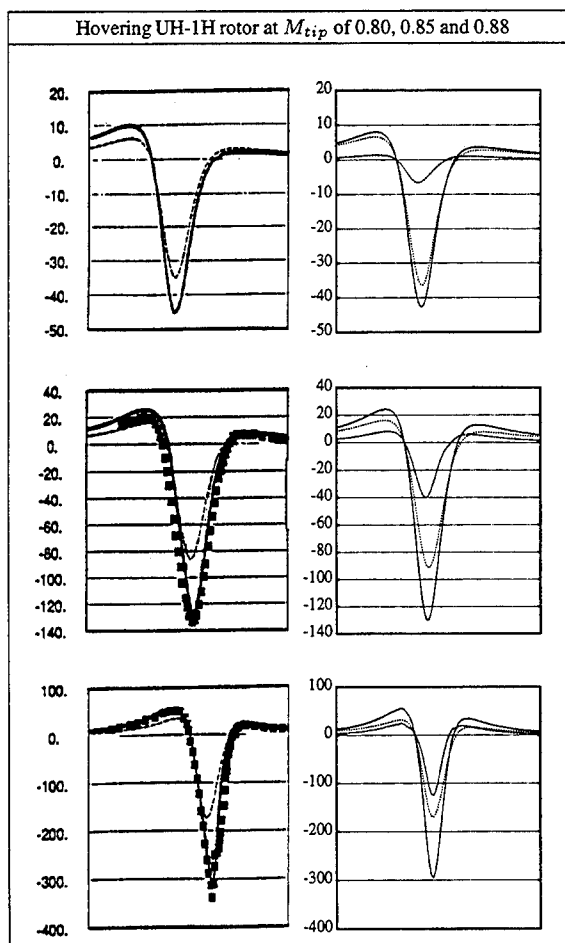


Figure 5 - For $M_{tip} \geq 0.80$, the quadrupole noise contribution becomes significant. Even at the highest M_{tip} , the results from the FW-H equation and the Euler code are both in good agreement with the experimental data.

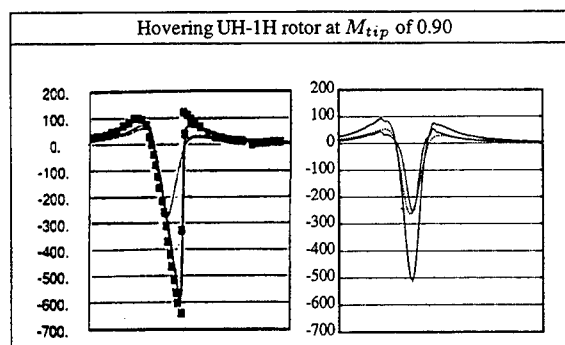


Figure 6 - At $M_{tip} = 0.90$, the aerodynamic data lose accuracy, and the experimental peak pressure is significantly underestimated by the numerical prediction based on the volume integral of quadrupole source.

source strength is still quite large, and the vicinity of the condition of sonic speed in the radiation direction (represented by M_r approaching 1 in the integral expression of the acoustic pressure) gives rise to important contributions to the global quadrupole effect. The volume integral of quadrupole noise is strongly affected by the poor description of the source strength, and the solution of the

FW-H equation can no longer provide a realistic prediction, while the results of Euler calculation still exhibits a satisfactory agreement with the experimental signature.

4.3. An assessment of computational cost

The main problem in the application of the acoustic analogy approach for the quadrupole noise prediction is related to the CPU time requested by the volume integration. Each of the hovering test cases presented in this paper has requested approximately 12 hours on a CONVEX C3860 System, equipped with 6 processors; this is a large computing time, compared to the 80 minutes of CPU required on a CRAY-YMP for the Euler solutions to converge [6]. The comparison between the computational speed of these two computer systems is strongly affected by the use of single or double precision and the adoption of particular optimization procedures in the compilation processes. In general, CRAY-YMP may be considered to be four times faster than CONVEX 3860 System, whose computational speed is even reduced to a half by the adoption of double precision! On the other hand, all the volume integration results have been obtained with very heavy runs, using the fine Q-grid, 1024 time steps per revolution period, and always adopting double precision for numerical calculations.

To achieve a reduction of computational cost, an analysis of different computational domains is proposed, along with a comparison between the corresponding numerical predictions for the quadrupole noise. In table 1 the results from five different UTAH grids are reported, with the comparison between the requested CPU time and the predicted peak values for the noise signatures. The corresponding pressure waveforms are shown in figure 7.

Grid	X	Y	Z	Peak Value (Pa)	CPU Time (s)
A	32	15	7	-27.652	2420.8
B	39	17	9	-28.818	4310.9
C	47	17	9	-35.773	4628.7
D	47	23	11	-38.809	8691.8
Q	63	31	15	-39.026	20960.7

Table 1 - Comparison between different UTAH grids for quadrupole noise prediction. All the results have been obtained with a 512 time steps run, on the CONVEX C3860.

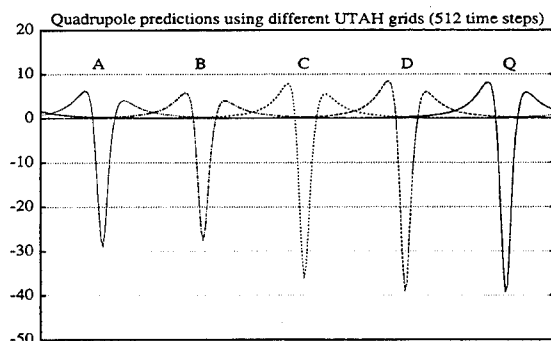


Figure 7 - Quadrupole noise signatures obtained using the different numerical grids described in table 1.

The result from D-grid is very interesting: the predicted peak value exhibits a difference of 0.55% compared to the Q-grid prediction and has been obtained with 2.45 CPU hours, with a reduction of about 60% on computational

effort. Note the difference between the C-grid and D-grid results, which points out the importance of Y (spanwise) stations in the achievement of a reliable prediction.

A further, possible reduction of CPU time may be obtained by decreasing the number of time steps requested to reach an accurate solution; the aim is achieved by taking time derivatives inside the integrals in equation (2). This manipulation splits up the first two terms into 16 and 4 terms, respectively, allowing a decomposition of quadrupole noise into three different components. These are shown in figure 8 for the test case at $M_{tip} = 0.85$. Thus, the quadrupole source term can be seen as the sum of a far-field component (depending on the $1/r$ factor), a near-field component (depending on $1/r^2$) and a very near field component, which depends on $1/r^3$ and may be generally neglected.

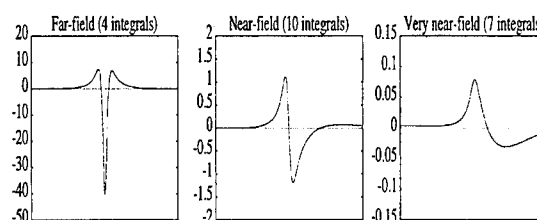


Figure 8 - The far-field (sum of 4 integrals), near-field (10 integrals) and "very" near-field (7 integrals) components of quadrupole source term, obtained with the Q-grid and 1024 time steps.

Still referring to the test case at tip Mach number of 0.85, figure 9 shows the comparison between numerical results obtained using the two different integral expressions. The K-code includes all the derivatives inside the integrals: compared to the S-code, whose solution requested 1024 time steps, a good prediction for the resulting pressure signature is already achieved through the 256 time steps run, obtaining a further remarkable reduction (approximately 30%) of the computing time.

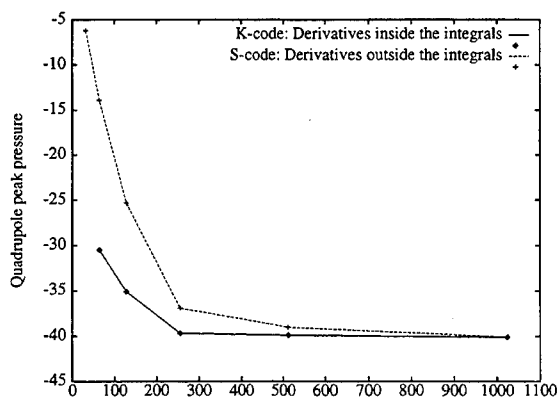


Figure 9 - Predicted peak pressure versus number of time steps is plotted for the two different forms of volume integration. Taking time derivatives inside the integrals, a good prediction of quadrupole noise is achieved with only 256 time steps.

In conclusion, by suitably choosing the numerical grid, and taking derivatives inside the integrals, a satisfactory quadrupole noise prediction can be achieved with about

150 minutes on the CONVEX 3860, (using double precision); thus, from the point of view of the computational effort requested, the volume integration seems to be definitely comparable to the Euler calculation.

5. QUADRUPOLE FROM SURFACE TERMS

The numerical results obtained through the volume integration have shown how the prediction of quadrupole noise may be pursued through the acoustic analogy approach, provided that a set of good quality aerodynamic data is available. We have also proved that the CPU time requested for the calculation may be considerably reduced, to become comparable to the computational effort required by an acoustic Euler calculation; furthermore, our volume integration code has not been particularly optimized, so that a further reduction on computing time may probably be achieved.

Anyhow, the possible extraction of some surface integrals from the volume terms certainly represents a promising way to perform a less expensive calculation of quadrupole noise. In this context, an effective description of quadrupole source term has been proposed by Farassat in 1987 [11]. Exploiting the concept of derivative of generalized functions, and considering as surfaces of discontinuity in the flow field both the shock surface and the blade surface, Farassat decomposes the nonlinear term into four different contributions, each relating to a particular noise generating mechanism. Thus, the original volume integrals are turned into the sum of the so-called *pure* (volume) quadrupole term (that usually treated in the Lighthill's jet noise theory), and some surface integrals: this should allow a remarkable reduction of CPU time. Several papers have been published on this subject, mostly investigating the role and the importance of the different terms [12]; in particular, the so called *blade* and *wake surface* terms are recognized to be negligible compared to the *shock noise*, especially, for high tip speed blades [13].

However, attention must be paid to these surface integrals, since their numerical evaluation may lead to unexpected results. Farassat and Brentner [14] have calculated the blade surface sources contribution for a hovering rotor, finding unacceptably large values of the acoustic pressure for a viscous fluid flow. This has been explained through the role of volume term and its own contribution inside the boundary layer, where the high velocity gradients partially cancel and moderate the surface sources effects. Such a balancing has also been verified for an incompressible, two-dimensional flow over a circular cylinder, where the knowledge of the exact solution allows a direct comparison between the different contributions. On the other hand, this seems to happen even if an inviscid fluid model is considered, with a slip condition enforced on the blade surface: in this case, the volume term does not include any boundary layer contribution. Starting with the expression (1), the nonlinear term has been rewritten in the following form:

$$\begin{aligned} \bar{Q} = & \frac{\partial^2 T_{ij}}{\partial x_i \partial x_j} H(f) + 2 \frac{\partial}{\partial x_i} \{T_{ij} \hat{n}_j \delta(f)\} \\ & - T_{ij} \frac{\partial \hat{n}_i}{\partial x_j} \delta(f) - T_{nn} \delta'(f) \end{aligned} \quad (5)$$

where $\delta(f)$ is the Dirac delta function, and denotes the surface source terms giving rise to the surface integrals.

Up to now every attempt to numerically solve the FW-H equation with the quadrupole source term written in the above form has led us to deal with very large contributions from the surface terms, though considering — for the evaluation of T_{ij} upon the blade surface — an inviscid flow model. Actually, the manipulation of equation (5) is very complex, due, in particular, to the appearance of the $\partial \hat{n}_i / \partial x_j$ tensor, and the derivative of a delta function; thus, the large resulting signatures may arise from computational errors caused by some geometric formulas implemented in the code. However, any attempt to extract from expression (1) surface integrals requires a particular attention, because these terms may individually be very far from the expected results. To show this particular aspect of the surface integrals, let us consider an irrotational flow; thus, the quadrupole source term may be written as follows:

$$\begin{aligned} \bar{Q} = & \frac{1}{2} \frac{\partial^2}{\partial x_i^2} [\rho u^2 H(f)] - \frac{\partial}{\partial x_i} \left[\frac{u^2}{2} \frac{\partial \rho}{\partial x_i} H(f) \right] \\ & - \frac{\partial}{\partial x_i} \left[u_i \frac{\partial \rho}{\partial t} H(f) \right] \\ & + \frac{\partial}{\partial x_i} [\rho u_i v_n \delta(f)] - \frac{1}{2} \frac{\partial}{\partial x_i} [\rho u^2 \hat{n}_i \delta(f)] \end{aligned} \quad (6)$$

The examples reported in figures 10 and 11 refer to the hovering UH-1H rotor at tip Mach number of 0.80. The numerical evaluation of the two surface integrals $p_{Q_{s_1}}$ and $p_{Q_{s_2}}$ (coming from the last two terms in the right-hand side of equation (6)) is shown in figure 10, where they are separately compared to the overall quadrupole noise (calculated with the volume integration, and already shown in figure 5). Note that each surface integral gives a contribution of the same order of magnitude of the overall quadrupole pressure p'_Q .

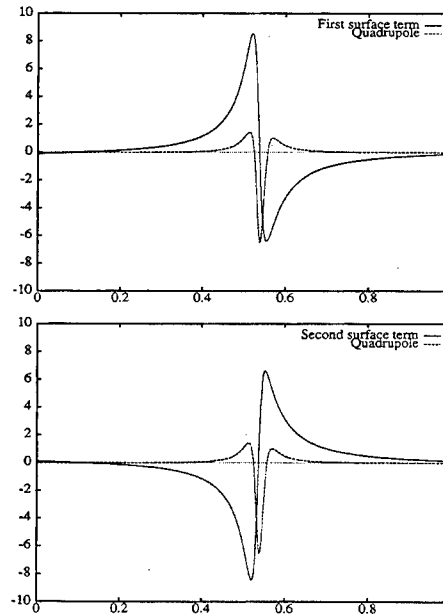


Figure 10 - Although an inviscid flow model is used, the two surface contributions from equation (6) are very large compared to the acoustic pressure p'_Q .

In figure 11, the sum of $p_{Q_{s_1}}$ and $p_{Q_{s_2}}$ is plotted, and a comparison with the overall quadrupole noise signal.

ture is established: the total surface contribution exhibits a positive peak value, which contrasts the negative peak pressure of the overall quadrupole signature; then, the surface terms do not provide the expected effect of allowing a "partial" quadrupole noise prediction.

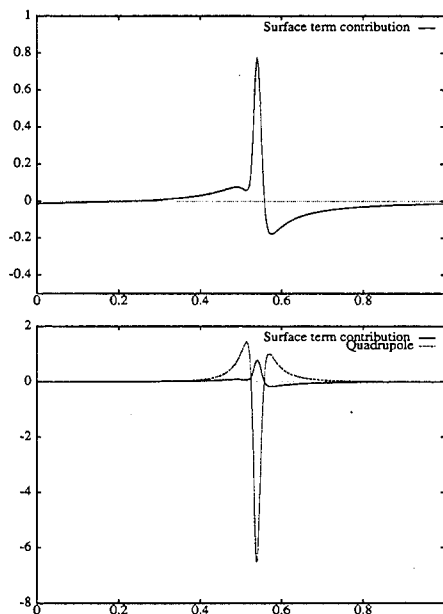


Figure 11 - Top picture shows the sum of terms p_{QS_1} and p_{QS_2} , which exhibits a pattern contrasting that of the overall quadrupole noise (comparison in the bottom picture).

6. CONCLUSIONS

Different numerical techniques for the evaluation of quadrupole noise have been presented in this paper. The solution of the FW-H equation has been pursued through a three-dimensional integration in a prescribed volume around the body. Exploiting the aerodynamic data from a full-potential code, excellent results have been obtained, up to a tip Mach number of 0.88, for a nonlifting, hovering rotor and an in-plane microphone location. A comprehensive analysis of computational effort and a comparison with the CPU time requested by an Euler solver, have encouraged the attempt to use the acoustic analogy approach as a tool for helicopter high-speed impulsive noise prediction. A particular description of the nonlinear term has also been implemented, showing an unexpected behaviour of some surface terms extracted from the volume integrals. On the ground of these numerical results, an accurate analysis is being conducted, concerning the opportunity to develop the surface integration method for quadrupole noise prediction.

REFERENCES

1. Ffowcs Williams, J.E. and Hawkins, D.L., "Sound Generation by Turbulence and Surfaces in Arbitrary Motion", *Philosophical Transactions of the Royal Society*, A264, 1969, pp 321-342.
2. Boxwell, D.A., Yu, Y.H. and Schmitz, F.H., "Hovering Impulsive Noise: Some measured and Calculated Results", *Vertica*, 3, 1978, pp 35-45.
3. Yu, Y.H., Caradonna, F.X. and Schmitz, F.H., "The Influence of the Transonic Flow Field on High-Speed Helicopter Impulsive Noise", *Proceedings of the 4th European Rotorcraft and Powered Lift Aircraft Forum*, Stresa, Italy, 1978, Paper 58.
4. Schmitz, F.H. and Yu, Y.H., "Transonic Rotor Noise — Theoretical and Experimental Comparisons", *Proceedings of the 4th European Rotorcraft and Powered Lift Aircraft Forum*, Bristol, United Kingdom, 1980.
5. Schultz, K.J. and Spletstoesser, W.R., "Prediction of Helicopter Rotor Impulsive Noise Using Measured Blade Pressures", *Proceedings of the 43rd Annual Forum & Technology Display of the American Helicopter Society*, St. Louis, Missouri, 1988.
6. Baeder, J.D., Gallman, J.M. and Yu, Y.H., "A computational Study of the Aeroacoustics of Rotors in Hover", *Proceedings of the 49th Annual Forum of the American Helicopter Society*, St. Louis, Missouri, 1993.
7. Prieur, J., Costes, M. and Baeder, J.D., "Aerodynamic and Acoustic calculations of Transonic Non-lifting Hovering Rotors", *Proceedings of the International Technical Specialists Meeting on Rotorcraft Acoustics and Fluid Dynamics*, Philadelphia, Pennsylvania, 1991.
8. Srinivasan, G.R. and Baeder, J.D., "Recent Advances in Euler and Navier-Stokes Methods for Calculating Helicopter Rotor Aerodynamics and Acoustics", *Proceedings of the 4th International Symposium on Computational Fluid Dynamics*, Davis, California, 1991.
9. Ianniello, S., "C.I.R.A. Effort within the Brite/Euram Project Helicopter and Tilt-Rotor Aircraft Exterior Noise Research (HELINOISE) — Part I: Theoretical and Computational Work", *CIRA TR-94-0023*, 1994.
10. Pagano, A., "UTAH Unsteady Transonic Aerodynamics of Helicopters — Calcoli per pale non portanti", *CIRA DILC-EST-TR-278*, 1993.
11. Farassat, F., "Quadrupole Source in Prediction of the Noise of Rotating Blades — A New Source Description", *AIAA Paper 87-2675*, 1987.
12. Farassat, F. and Myers, M.K., "An Analysis of the Quadrupole Noise Source of High Speed Rotating Blades", in Lee, D., Cakmak, A. and Vichnevetsky, R. (eds.), "Computational Acoustics" (Vol. 2), Amsterdam, The Netherlands, Elsevier Science Publishers, 1990 (ISBN 0 444 88721 0), pp 227-240.
13. Farassat, F., Lee, Y.J., Tadghighi, H. and Holz, R., "High-Speed Helicopter Noise — Shock Waves as a Potent Source of Sound", *Proceedings of the International Technical Specialists Meeting on Rotorcraft Acoustics and Fluid Dynamics*, Philadelphia, Pennsylvania, 1991.
14. Farassat, F. and Brentner, K.S., "The Influence of Quadrupole Sources in the Boundary Layer and Wake of a Blade on Helicopter Rotor Noise", *Proceedings of the International Technical Specialists Meeting on Rotorcraft Acoustics and Fluid Dynamics*, Philadelphia, Pennsylvania, 1991.

A BOUNDARY INTEGRAL METHOD FOR UNIFIED TRANSONIC AERODYNAMIC AND AEROACOUSTIC ANALYSIS OF HOVERING ROTORS

M. Gennaretti, U. Iemma and L. Morino

Terza Università di Roma

Dipartimento di Meccanica e Automatica

via C. Segre 2, 00146 Rome

Italy

1. SUMMARY

The subject of this paper is the unified aerodynamic and aeroacoustic analysis of transonic hovering rotors.

The aerodynamic/aeroacoustic problem is stated in terms of the velocity potential, whereas the solution is determined by applying a shock-capturing boundary integral formulation. Particular emphasis is given to the analysis of the non-linear terms in the equation for the velocity potential, whose contribution cannot be neglected for the transonic flow case analysis. Their contribution is expressed in a conservative form.

Starting from the solution for the potential, the Bernoulli theorem is used to determine both the pressure distribution on the body surface (aerodynamic solution) and the acoustic pressure in the field (aeroacoustic solution).

Numerical results are presented in order to show the capability of the methodology in determining both the aerodynamic and aeroacoustic solutions for transonic rotor configurations.

2. INTRODUCTION

In this work we present some recent developments of a boundary integral methodology for the unified analysis of aerodynamics and aeroacoustics of potential, transonic flows. Specifically, we outline a full-potential, shock-capturing boundary integral formulation that has been obtained as an extension of the direct integral formulation introduced by Morino [1] and extended with his collaborators to transonic aerodynamics and aeroacoustics, with applications to rotors [2-11]. The solution for the velocity potential function is given in terms of a boundary integral representation extended over the body and wake surfaces which, for transonic flows, includes also a field integral in the fluid region surrounding the body portion

where nonlinear terms are relevant (*e.g.*, blade tips for hovering rotors). This approach is adopted here because, in comparison with CFD techniques, it allows an easier and more computationally efficient analysis of transonic flows around rotors, especially for complex configurations, such as a free-wake analysis of a helicopter rotor in the presence of the fuselage.

Boundary integral equations have been the first successful approach for the analysis of transonic aerodynamics. Indeed, the pioneering works of Oswatitsch [12] of 1950 and Spreiter and Alskne [13] of 1955, for steady, two-dimensional, transonic flows, precede the 1971 finite-difference work of Murman and Cole [14], which is considered a milestone in the development of numerical techniques for the solution of transonic flows.

Further boundary-integral-equation approaches are investigated by Nixon [15, 16] who presents a small perturbation scheme for the solution of unsteady two-dimensional and steady three-dimensional flows, and Piers and Sloof [17], who apply a shock capturing integral formulation to the TSP model. Tseng and Morino [2] present the first transonic result obtained from the formulation of Morino [1], based on a nonconservative TSP approach. A non-conservative formulation for the full-potential equation has been presented by Sinclair [18, 19] and applied to two-dimensional and three-dimensional configurations, respectively. In contrast to Tseng and Morino [2], where the field sources are due exclusively to nonlinear terms, in Sinclair [18, 19] the field sources include all the compressibility terms (linear and nonlinear). This implies that the differential operator for the boundary integral formulation of Tseng and Morino [2] is that of the wave equation, whereas for Sinclair [18, 19] is the Laplacian.

Applying a TSP formulation similar to that used by Tseng and Morino [2], Iemma, Mastroddi, Morino, and Pecora [6], present the first validation for three-dimensional unsteady flows, whereas the extension to the full-potential analysis for fixed wings is considered in Morino and Iemma [9]. Preliminary results for the simulation of transonic flows around helicopter rotors in hover are presented in Iemma, Gennaretti and Morino [10].

As in Refs. [4], [5], and [7] for subsonic flows, we adopt a unified aerodynamic/aeroacoustic approach for the analysis of hovering transonic rotor. Once the potential solution has been found on the body surface, on the wake surface, and in the fluid region where the non-linear terms cannot be neglected, it is possible to evaluate the potential everywhere in the field (by using the integral representation) and hence, by means of the Bernoulli theorem, the pressure distribution. This approach to aeroacoustics is considerably different from those commonly used, that are based either on the Kirchhoff equation or on the application of the Ffowcs Williams and Hawkings equation [20], and determine the acoustic field from previous knowledge of aerodynamic data. A review of the development of the classical boundary integral formulations for aeroacoustics is not attempted here; an extensive presentation of several aeroacoustic formulations is given in Farassat and Myers [21].

This paper is divided in six Sections. In the next Section the differential formulation for full-potential flows is presented, whereas in Section 4 we derive the boundary integral formulation used to obtain the numerical results described in Section 5. Concluding remarks are presented in Section 6. Gennaretti has been primarily responsible for the extension of the original formulation of Morino [1] to the aerodynamics and aeroacoustics of rotors in subsonic flows, Iemma for the extension of the formulation to transonic flows, in particular for the development of the transonic algorithm. The numerical implementation has been jointly performed by Gennaretti and Iemma.

3. FULL-POTENTIAL FLOWS

We consider compressible, irrotational, isentropic flows of ideal gases. For such type of flows, the fluid velocity \mathbf{v} is expressed in terms of the scalar potential ϕ by $\mathbf{v} = \nabla\phi$, and the governing equations are the continuity equation,

$$\frac{\partial \rho}{\partial t} + \nabla \cdot (\rho \mathbf{v}) = 0 \quad (1)$$

the Bernoulli theorem,

$$\frac{\partial \phi}{\partial t} + \frac{1}{2} v^2 + h = h_\infty \quad (2)$$

(where h is the enthalpy), and the isentropic law for ideal gases $h/\rho^{\gamma-1} = \text{constant}$. As shown in [3], combining the above equations, isolating the linear terms, and moving all the non-linear terms to the right hand side of the equation, in a frame of reference fixed with the undisturbed flow (air frame of reference), one obtains the following form for the non-linear equation of the velocity potential

$$\nabla^2 \phi - \frac{1}{a_\infty^2} \frac{\partial^2 \phi}{\partial t^2} = \sigma \quad (3)$$

where $a_\infty^2 = (\gamma - 1)h_\infty = \gamma p_\infty / \rho_\infty$ is the speed of sound in the undisturbed flow, whereas σ denotes all the non-linear terms, and is given by

$$\begin{aligned} \sigma &= \nabla \cdot \left[\left(1 - \frac{\rho}{\rho_\infty} \right) \nabla \phi \right] + \frac{\partial}{\partial t} \left(1 - \frac{\rho}{\rho_\infty} - \frac{1}{a_\infty^2} \frac{\partial \phi}{\partial t} \right) \\ &= \nabla \cdot \tilde{\mathbf{b}} + \frac{\partial \tilde{b}}{\partial t} \end{aligned} \quad (4)$$

where $\rho/\rho_\infty = [1 - (\dot{\phi} + v^2/2)/h_\infty]^{1/(\gamma-1)}$.

The above differential formulation is completed by the following boundary conditions. We assume that the body surface S_B is impermeable, i.e., $(\mathbf{v} - \mathbf{v}_B) \cdot \mathbf{n} = 0$, where \mathbf{v}_B is the velocity of the point \mathbf{x} on the surface of the body S_B . Furthermore, we assume that the flow is at rest in points located far from the moving body, i.e., $\mathbf{v} = 0$ at infinity. In terms of the velocity potential, the above boundary conditions are given by

$$\frac{\partial \phi}{\partial n} = \mathbf{v}_B \cdot \mathbf{n} \quad \text{for } \mathbf{x} \in S_B \quad (5)$$

and

$$\phi = 0 \quad \text{at infinity} \quad (6)$$

In addition, we need a boundary condition on the wake (see [3] or [22] for details). The wake is a surface of discontinuity for the velocity potential. It may be shown that the principles of conservation of mass and momentum yield that S_W is not crossed by fluid particles ($\mathbf{v} \cdot \mathbf{n} = \mathbf{v}_W \cdot \mathbf{n}$, where \mathbf{v}_W is the velocity of the point on the surface of the wake S_W) and pressure is continuous across it ($\Delta p = 0$). In terms of the velocity potential, the first condition yields

$$\Delta \left(\frac{\partial \phi}{\partial n} \right) = 0 \quad (7)$$

whereas from the second one, using Bernoulli's theorem, one obtains

$$\frac{D_W (\Delta \phi)}{Dt} = 0 \quad (8)$$

where $D_W/Dt = \partial/\partial t + \mathbf{v}_W \cdot \nabla$, with \mathbf{v}_W representing the velocity of a point \mathbf{x}_W of the wake (*i.e.*, by definition, the average of the velocity on the two sides of the wake). Equation (8) states that $\Delta\phi$ is constant in time following a wake point and equal to the value it had when \mathbf{x}_W left the trailing edge. This value is obtained from $\Delta\phi$ on the body, in correspondence of the trailing edge (trailing edge condition).¹

4. INTEGRAL FORMULATION

For the sake of clarity and simplicity, in this Section we limit the discussion of the boundary integral formulation to the case of an isolated rigid surface in arbitrary motion as introduced by Gennaretti [4]. This is adequate when the wake surface is fixed with respect to the body as in the cases of interest here, *i.e.*, helicopter rotors in hover and propellers in axial flow (the extension to the presence of multiple bodies, necessary when the wake is not rigidly connected to the rotor, is presented in [7], whereas the general formulation for deforming surfaces is presented by Gennaretti [8]). In order to accomplish this, it is convenient to consider two different spaces: the air space (*i.e.*, the space rigidly connected with the undisturbed air) and the body space (*i.e.*, the space rigidly connected with the body). Let the transformation relating ξ to \mathbf{x} be given by²

$$\xi = \hat{\xi}(\mathbf{x}, t) = \xi_0(t) + \mathbf{R}(t)\mathbf{x} \quad (9)$$

where $\mathbf{R}(t)$ is rigid-body-rotation isomorphism relating the two spaces, whereas ξ_0 is the image of the point $\mathbf{x} = 0$. Note that Eq. (9) implies, for any $f = f[\hat{\xi}(\mathbf{x}, t), t]$,

$$\frac{\partial f}{\partial t} = \frac{\partial f}{\partial t} \Big|_{\xi=\text{const.}} + \mathbf{v}_x \cdot \nabla f \quad (10)$$

where $\partial/\partial t$ denotes the time derivative in the body space, ∇f denotes the gradient of f also in the body space, whereas \mathbf{v}_x denotes the body-space vector of the velocity of a body-space point \mathbf{x} relative to the air space; for hovering rotors with $\mathbf{x} = 0$ representing the hub, \mathbf{v}_x is related to \mathbf{v}_x (air-space vector of the velocity of \mathbf{x} relative to the air space) by

$$\mathbf{v}_x = \frac{\partial}{\partial t} \hat{\xi}(\mathbf{x}, t) = \mathbf{R}\mathbf{v}_x \quad (11)$$

¹For a detailed discussion of this issue see [32].

²In this section, the vectors in the body space are denoted with Latin boldface letters, whereas those in the air space are denoted with Greek boldface letters. In particular, ξ denotes the position vector in the air space, whereas \mathbf{x} denotes the position vector in the body space.

The equation for the velocity potential in the body space is given by

$$\nabla^2 \phi - \frac{1}{a_\infty^2} \frac{d_B^2 \phi}{dt^2} = \sigma \quad \mathbf{x} \in \mathcal{V} \quad (12)$$

where

$$\frac{d_B}{dt} = \frac{\partial}{\partial t} \Big|_{\xi=\text{const.}} = \frac{\partial}{\partial t} - \mathbf{v}_x \cdot \nabla \quad (13)$$

denotes the body-space time derivative following a fixed point of the air space, whereas \mathcal{V} denotes the volume where the flow is potential (*i.e.*, the whole space minus the solid volume and an infinitesimal volume that includes the wake surface). This volume is assumed to be time independent in the body space.

The fundamental solution of the operator on the left side of Eq. (12) satisfies the equation

$$\nabla^2 G - \frac{1}{a_\infty^2} \frac{d_B^2 G}{dt^2} = \delta(\mathbf{x} - \mathbf{x}_*) \delta(t - t_*), \quad \mathbf{x} \in \mathcal{V} \quad (14)$$

with boundary condition $G(\infty, t) = 0$ and initial conditions $G(\mathbf{x}, 0) = \dot{G}(\mathbf{x}, 0) = 0$. For the cases of subsonic and transonic flows considered here, G has the expression (see [22])

$$G(\mathbf{x}, \mathbf{x}_*, t, t_*) = \frac{-1}{4\pi\hat{\rho}} \delta(t - t_* + \theta) \quad (15)$$

where θ (that represents the time required for a signal to propagate from \mathbf{x} to \mathbf{x}_*) satisfies the equation $a_\infty \theta = \|\hat{\xi}(\mathbf{x}, t_*) - \hat{\xi}(\mathbf{x}_*, t_*)\|$. In addition, $\hat{\rho} = [\varrho]1 + \varrho \cdot \mathbf{v}_x/a_\infty \varrho$, where $\varrho = \hat{\xi}(\mathbf{x}, t) - \hat{\xi}(\mathbf{x}_*, t_*)$ and $\varrho = \|\varrho\|$, whereas $[\dots]^\theta$ denotes evaluation at time $t = t_* - \theta$.

Multiplying Eqs. (12) and (14) by G and ϕ respectively, subtracting, using Eq. (13), integrating with respect to time, and taking into account the initial conditions on ϕ and G , one obtains

$$\begin{aligned} \phi(\mathbf{x}_*, t_*) = & - \int_0^\infty \iiint_{\mathcal{V}} \nabla \cdot (G \nabla \phi - \phi \nabla G) d\mathcal{V} dt \\ & - \frac{1}{a_\infty^2} \int_0^\infty \iiint_{\mathcal{V}} \mathbf{v}_x \cdot \nabla \left(G \frac{d_B \phi}{dt} - \phi \frac{d_B G}{dt} \right) d\mathcal{V} dt \\ & + \int_0^\infty \iiint_{\mathcal{V}} G \sigma d\mathcal{V} dt \end{aligned} \quad (16)$$

Next, note that for any f and \mathbf{w} , $\nabla \cdot (f\mathbf{w}) = f\nabla \cdot \mathbf{w} + \nabla f \cdot \mathbf{w}$, and that $\nabla \cdot \mathbf{v}_x = 0$ (since the body space moves in rigid-body motion). Then, applying Gauss' theorem, as well as the conditions at infinity for ϕ and G , Eq. (16) reduces to

$$\phi(\mathbf{x}_*, t_*) = \int_0^\infty \iint_S \left(G \frac{\partial \phi}{\partial n} - \phi \frac{\partial G}{\partial n} \right) dS dt$$

$$\begin{aligned}
& + \frac{1}{a_\infty^2} \int_0^\infty \iint_S \left(G \frac{d_B \phi}{dt} - \phi \frac{d_B G}{dt} \right) \mathbf{v}_x \cdot \mathbf{n} dS dt \\
& + \int_0^\infty \iiint_V G \sigma dV dt
\end{aligned} \quad (17)$$

where S is the boundary of V and \mathbf{n} is its inwardly directed unit normal.

Next, using Eq. (15), integrating with respect to time, and setting $\hat{G} = -1/4\pi\hat{\rho}$, one finally obtains the following boundary integral representation, in the body frame of reference, for the velocity potential ϕ , for a body in arbitrary rigid motion

$$\begin{aligned}
\phi(\mathbf{x}_*, t_*) &= \iint_S \left[\hat{G} \frac{\partial \phi}{\partial \tilde{n}} - \frac{\partial \hat{G}}{\partial \tilde{n}} \phi \right]^\theta dS \\
&+ \iint_S \left[\frac{\partial \phi}{\partial t} \hat{G} \left(\frac{\partial \theta}{\partial \tilde{n}} + \frac{2}{a_\infty^2} \mathbf{v}_x \cdot \mathbf{n} \right) \right]^\theta dS \\
&- \frac{1}{a_\infty^2} \iint_S \left[\hat{G} \phi \frac{\partial}{\partial t} (\mathbf{v}_x \cdot \mathbf{n} \mathbf{v}_x \cdot \nabla \theta - \mathbf{v}_x \cdot \mathbf{n}) \right]^\theta dS \\
&+ \iiint_V [\hat{G} \sigma]^\theta dV
\end{aligned} \quad (18)$$

where

$$\frac{\partial}{\partial \tilde{n}} = \frac{\partial}{\partial n} - \frac{1}{a_\infty^2} \mathbf{v}_x \cdot \mathbf{n} \mathbf{v}_x \cdot \nabla \quad (19)$$

For the cases of interest here, *i.e.*, hovering rotors and propellers with fixed wake, the third integral on the right hand side is identically zero. In addition, all the results presented here are for steady-state flows (in the body frame of reference). In this case the integral representation for the potential assumes the following simpler expression

$$\begin{aligned}
\phi(\mathbf{x}_*, t_*) &= \iint_S \left(\hat{G} \frac{\partial \phi}{\partial \tilde{n}} - \frac{\partial \hat{G}}{\partial \tilde{n}} \phi \right) dS \\
&+ \iiint_V \hat{G} \sigma dV
\end{aligned} \quad (20)$$

Consider first the case $\sigma = 0$ (subsonic flows). If \mathbf{x}_* is in V , Eq. (20) is an integral representation for $\phi(\mathbf{x}_*, t_*)$ in terms of ϕ and $\partial\phi/\partial\tilde{n}$ on S . On the other hand, if \mathbf{x}_* is on S , Eq. (20) represents a compatibility condition between ϕ and $\partial\phi/\partial\tilde{n}$ for any function ϕ satisfying Eq. (12).

In the case of non-lifting bodies, we identify S with the surface of the body, S_B . Then, $\partial\phi/\partial n$ is known from the boundary condition, and the compatibility condition yields an integral equation which may be used to obtain the values of ϕ on S from those of $\partial\phi/\partial n$. After discretization (see later) one obtains a system of linear algebraic equations. For the case

of lifting bodies, an explicit treatment of the wake is required. Consider an isolated rotor in hover or an isolated propeller in axial flow and identify S in Eq. (20) with a surface S_{BW} surrounding body and wake. Letting the portion of S_{BW} that surrounds the wake approach S_W , we obtain a contribution on the wake surface that is related only to $\Delta\phi$ (as $\Delta(\partial\phi/\partial n) = 0$ on S_W , see Eq. (7)); $\Delta\phi$ is obtained from Eq. (8).

For transonic flow cases, the non-linear term cannot be neglected and the formulation is modified accordingly. The solution is obtained through a pseudo time-marching technique based on Eq. (18).

It should be emphasized that, once the potential is known on S , Eq. (20) with \mathbf{x}_* in the field yields the value of ϕ anywhere in the field. Therefore, we evaluate the aeroacoustic field, *i.e.*, the pressure in the field around the body, by using the solution for the potential in the Bernoulli theorem.

For numerical purposes, the above formulation is applied by discretizing both body and wake surfaces into quadrilateral elements, and dividing the involved fluid region into volume elements. Referring the reader to Ref. [4] for details on the numerical implementation of the surface terms, here we outline the field term contribution. Applying a zeroth-order discretization, the discretized version of the non-linear term is given by

$$\iiint_V \sigma \hat{G} \Big|_{\mathbf{x}_*=\mathbf{x}_k} dV \approx \sum_q \hat{H}_{kq} (\overline{\nabla \cdot \mathbf{b}})_q \quad (21)$$

where $\hat{H}_{kq} = \iiint_{V_q} \hat{G}_k dV$, with $\hat{G}_k = \hat{G}|_{\mathbf{x}_*=\mathbf{x}_k}$, whereas $\mathbf{b} = \tilde{\mathbf{b}} - \hat{\mathbf{b}} \mathbf{v}_x$, and $(\overline{\nabla \cdot \mathbf{b}})_q$ denotes the mean value inside the volume element V_q of the term $\nabla \cdot \mathbf{b}$. Next, in order to avoid the evaluation of the divergence operator, we perform the following convenient transformation

$$\begin{aligned}
(\overline{\nabla \cdot \mathbf{b}})_q &= \frac{1}{V_q} \iiint_{V_q} \nabla \cdot \mathbf{b} dV \\
&= \frac{1}{V_q} \iint_{\partial V_q} \mathbf{b} \cdot \mathbf{n} dS
\end{aligned} \quad (22)$$

where \mathbf{n} is the outwardly directed unit normal to the surface ∂V_q .

This approach yields a very efficient computational algorithm and appears to be more convenient, particularly for the analysis of three-dimensional flows around wings and rotors, with respect to other numerical formulations used by the authors (in which an integration by part was used to avoid the evaluation of $\nabla \cdot \mathbf{b}$, see [10]).

5. NUMERICAL RESULTS

In this Section some numerical applications of the formulation described above are discussed. Results for steady-state aerodynamics in the transonic regime are presented first, and validated by comparison with existing CFD methods. These results concern two- and three-dimensional flows around both fixed wings and rotors. After the assessment of the integral aerodynamics, aeroacoustic applications are presented. The acoustic signal generated by a subsonic propeller and a hovering rotor in transonic conditions are evaluated using the present integral formulation, and compared with the results obtained by the Ffowcs Williams and Hawkins formulation, as well as with experimental data.

5.1 Fixed-wing aerodynamics

The present non-linear aerodynamic formulation has been widely validated in the past in both subcritical and supercritical problems [11]. In the present paper, in order to show the shock capturing property of the method with respect to other CFD approaches (finite volumes, finite differences, finite elements methods), a brief review of the most significant results is given. Figure 1 depicts the pressure distribution over the surface of a circular cylinder at $M_\infty = 0.5$. Such a flow involves a strong shock wave and is frequently used as a test for the assessment of transonic simulations. Results from the present method are compared with those from a finite-volume full-potential conservative formulation [23]. Two different mesh sizes are

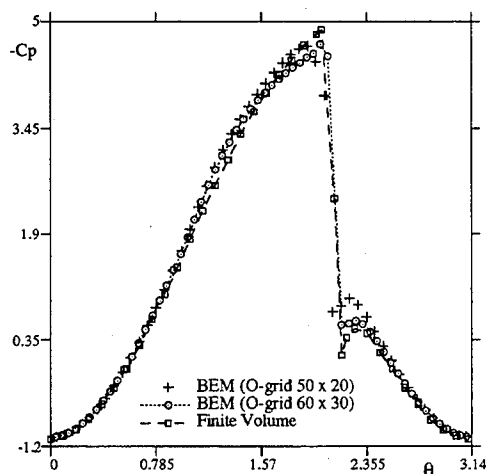


Figure 1: Pressure coefficient over a circular cylinder with $M_\infty = 0.5$.

used for the integral approach. The comparison with the reference result is satisfactory in terms of both

strength and position of the shock. Note that the computed shock appears as an actual pressure discontinuity confined within one single grid element, whereas in the finite-volume solution it is smeared over three volumes. Figure 2 deals with the convergence history of the iterative non-linear procedure. The rate of convergence is extremely fast, even in the presence of a strong shock. The converged solution around the cylinder is achieved in about 10 pseudo-time steps (as mentioned before, steady solutions are obtained through a pseudo-time marching technique).

In Figure 3 the flow about a NACA 0012 airfoil at $M_\infty = 0.82$ and $\alpha = 0^\circ$ is analyzed. The pressure distribution is compared with full-potential finite-volume results by Jameson [24]. The result obtained with a finite-volume solution of the Euler equation is also included [25]. Such a comparison is meaningful since the entropy jump induced by the shock is negligible in the present case (weak shock), and therefore Euler and full-potential solutions are comparable (the two models are equivalent when the flow remains isentropic). The comparison shows a very good agreement between the present solution and the two CFD methods considered. The shock determined by the integral solution is confined within one single element, and its strength is well predicted. However, a slight difference in the shock position with respect to the full-potential finite-volume solution may be observed. As we will see later, this behaviour occurs for certain

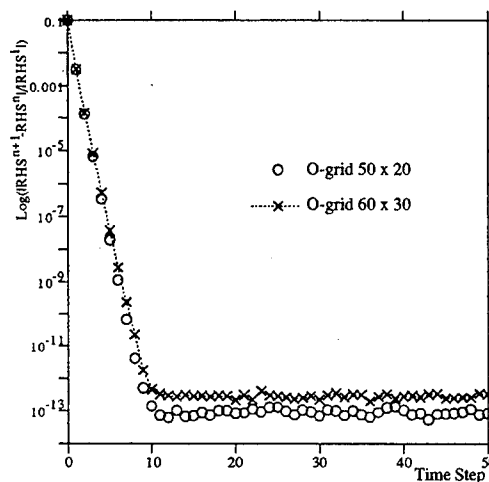


Figure 2: Time history of the residual for the solution over a circular cylinder with $M_\infty = 0.5$.

configurations and is currently under investigation. It may be due to the simple geometry used in the definition of the computational grid around the body surface (note that the result in Fig. 3 has been obtained by a H-type field grid, whereas the result in Fig. 1,

where the shock position is well predicted, has been obtained by a regular O-type field grid). Figure 4

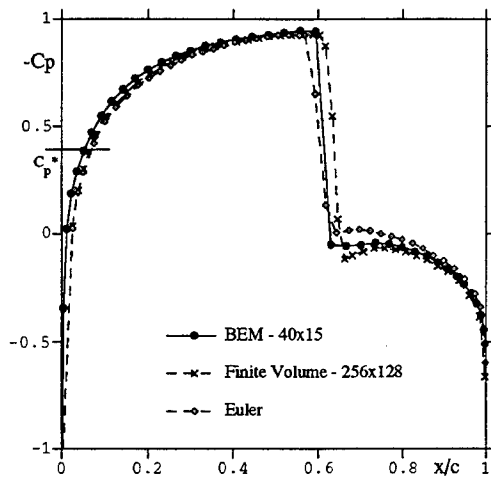


Figure 3: Pressure coefficient over a non-lifting NACA 0012 airfoil with $M_\infty = 0.82$.

deals with a transonic three-dimensional flow around an isolated rectangular wing with a 6% circular arc section. The aspect ratio is 4, $M_\infty = 0.857$, and $\alpha = 1.5^\circ$. The pressure distribution at the root sec-

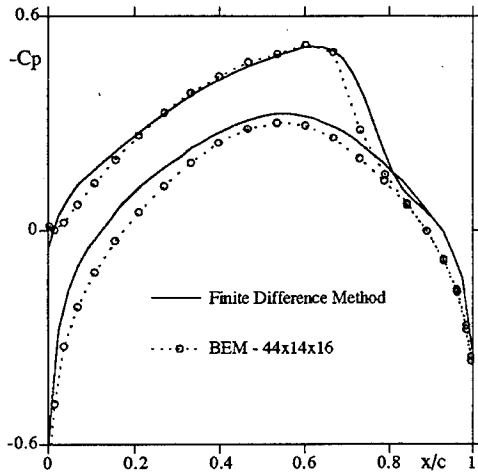


Figure 4: Pressure coefficient over the root section of a rectangular wing with 6% biconvex section, $AR = 4$, $M_\infty = 0.857$, and $\alpha = 1.5^\circ$.

tion is compared with the result of a finite-difference simulation [26]. The behaviour of the present solution is satisfactory, even if the calculated shock position is slightly different from that in the reference result. Such a discrepancy is similar to that discussed for the result in Fig. 3.

5.2 Rotary-wing aerodynamics

In order to validate the presented integral formulation for the analysis of transonic flows around rotary wings, the non-lifting UH-1H hovering rotor with $M_{TIP} = 0.88$ has been considered. In Fig. 5

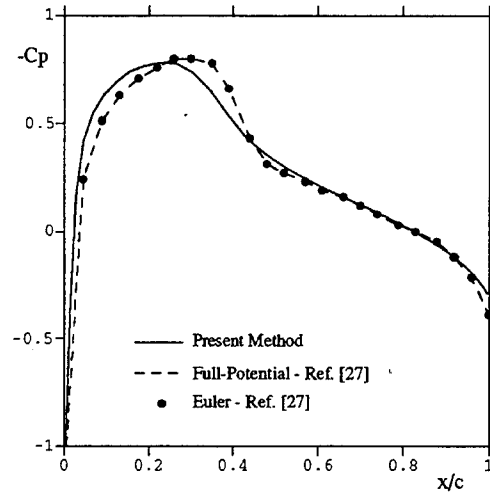


Figure 5: Non-lifting UH-1H rotor in hover. Chordwise pressure distribution at the blade section $r/R = 0.89$ for $M_{TIP} = 0.88$.

the computed pressure distribution at blade section $r/R = 0.89$ is compared with CFD full-potential and Euler solutions presented in [27]. The agreement is acceptable, but the computed shock position is again located upstream with respect to that in the reference results. The same comparison is shown in Fig. 6 for

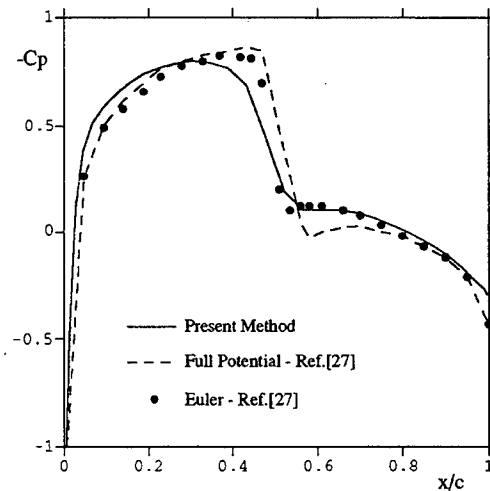


Figure 6: Non-lifting UH-1H rotor in hover. Chordwise pressure distribution at the blade section $r/R = 0.95$ for $M_{TIP} = 0.88$.

the blade section at $r/R = 0.95$. In this case the discrepancy in shock strength and position is even larger. For such a configuration our full-potential result appears to be closer to the CFD Euler one rather than to the CFD full-potential one. Probably, the error induced by the rude geometry field grid becomes larger and larger as the analyzed flow configurations become more complex. Thus, the slight discrepancy in Fig. 3 for the NACA 0012 airfoil, turns out to be the more severe difference in Fig. 6 for the UH-1H hovering rotor. Therefore, in order to enhance the accuracy of the transonic rotor flow results in the vicinity of the shock, a more refined field grid geometry appears to be necessary.

5.2 Rotary-wing aeroacoustics

Next, some acoustic results obtained by the present unified aerodynamic/aeroacoustic integral formulation will be presented.

First, we consider a propeller in subsonic flow. This concerns a problem examined experimentally by Magliozzi [28] and computationally by Farassat and Succi [29] (to which the reader is referred for the details of the blade geometry). It consists of a

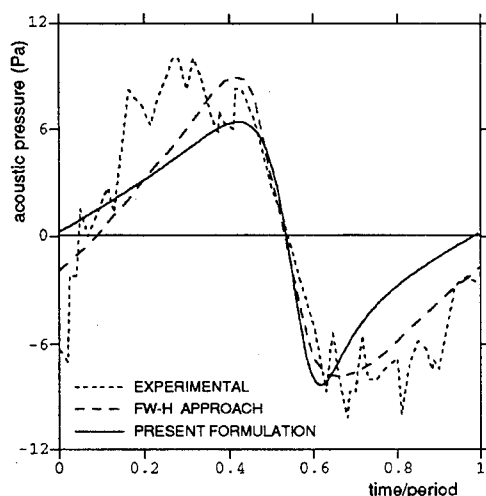


Figure 7: Calculated and measured acoustic signatures for the general aviation propeller, $M_{TIP} = 0.71$, in-plane observer.

three-bladed propeller, having radius $R = 1.295m$ and non-linear twist. The considered tip Mach number is $M_{TIP} = 0.71$, corresponding to a rotational speed of 1,760rpm. Figure 7 presents the aeroacoustic pressure in the plane of the rotor, at a distance of 7.28m from the axis of the rotor. The comparison is performed among the available experimental data,

the numerical solution obtained by Farassat and Succi [29] using the Ffowcs Williams and Hawkings formulation, and the numerical results predicted using our unified aerodynamic/aeroacoustic formulation. The same comparison is presented in Figure 8, where the acoustic signal is referred to an observer placed 3.05m behind the propeller plane at a distance of 7.28m from the axis. For both cases, the two numerical simulations agree quite well and give a satisfactory prediction of the measured acoustic pressure. Then, aeroa-

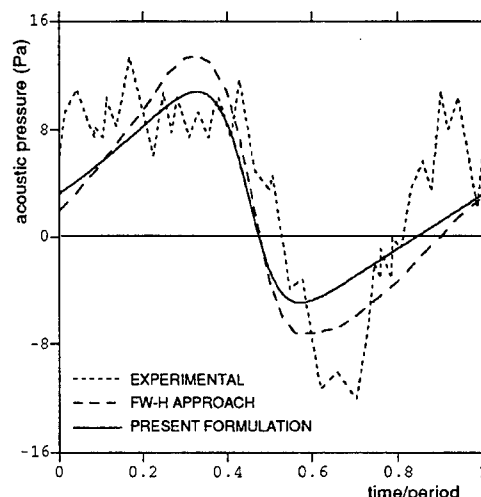


Figure 8: Calculated and measured acoustic signatures for the general aviation propeller, $M_{TIP} = 0.71$, aft observer.

coustic results concerning the transonic, non-lifting UH-1H hovering rotor are discussed. Figure 9 depicts the acoustic pressure computed by our methodology for an in-plane-observer located at a distance $d = 3.09R$ from the rotor, with $M_{TIP} = 0.85$. For the same test case, Fig. 10 shows the numerical results obtained by a Ffowcs Williams and Hawkings formulation [30] based on CFD aerodynamic data, whereas Fig. 11 shows experimental and numerical results presented in Ref. [31]. All of the acoustic results are in a very good agreement, even if the noise components are different. In our case, the acoustic signal may be decomposed into a body source contribution (first term on the right side in Eq. (20)), and a field source contribution, being the body doublet contribution negligible for non-lifting cases. On the other hand, the acoustic solution based on the Ffowcs Williams and Hawkings equation is typically decomposed into a thickness and a quadrupole noise (loading noise is not present for non-lifting cases), but the relationship between the two sets of components is not a simple matter to determine, and in general they have to be different.

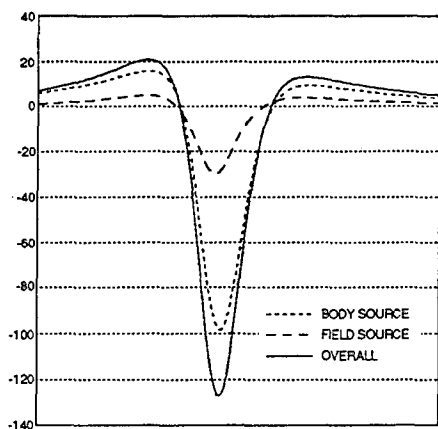


Figure 9: Calculated acoustic signatures for the UH-1H non-lifting hovering rotor. $M_{TIP} = .85$. Present formulation.

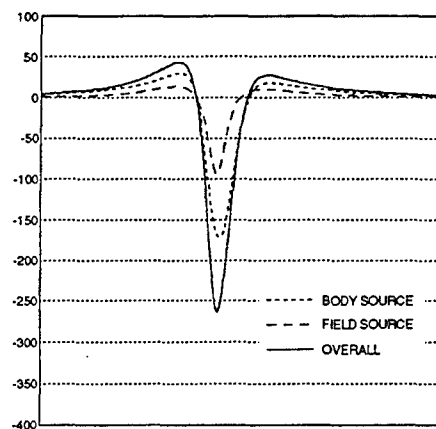


Figure 12: Calculated acoustic signatures for the UH-1H non-lifting hovering rotor. $M_{TIP} = .88$. Present formulation.

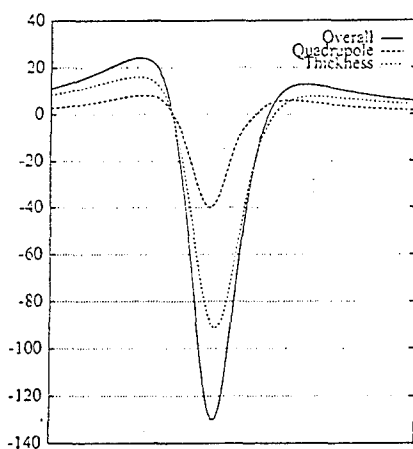


Figure 10: Calculated acoustic signatures for the UH-1H non-lifting hovering rotor. $M_{TIP} = .85$. From [30].

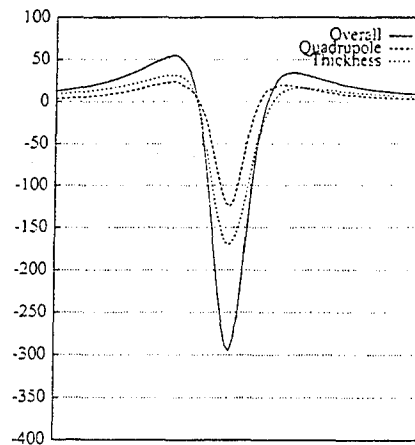


Figure 13: Calculated acoustic signatures for the UH-1H non-lifting hovering rotor. $M_{TIP} = .88$. From [30].

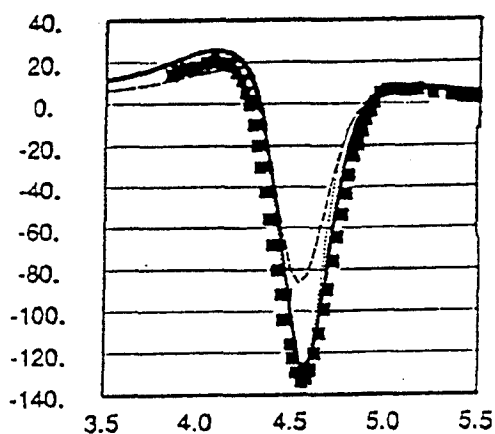


Figure 11: Calculated acoustic signatures for the UH-1H non-lifting hovering rotor. $M_{TIP} = .85$. From [31].

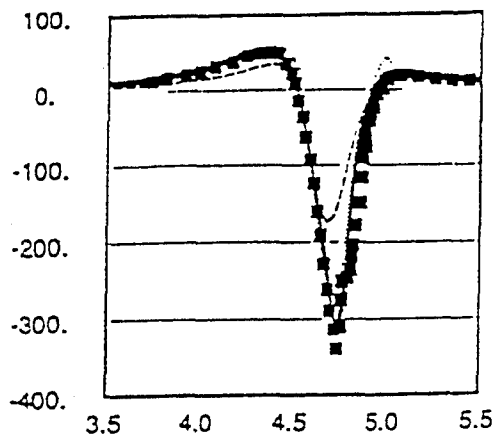


Figure 14: Calculated acoustic signatures for the UH-1H non-lifting hovering rotor. $M_{TIP} = .88$. From [31].

The same set of results is shown in Figs. 12, 13 and 14 for $M_{TIP} = 0.88$. Also in this case, a satisfactory agreement among the three types of results may be observed, even if the source field term in our methodology appears to be slightly under-predicted (probably, this is due to the same reasons mentioned above in the discussion about accuracy in prediction of shock strength and position).

6. CONCLUDING REMARKS

A boundary element method for the unified aerodynamic and aeroacoustic shock-capturing transonic full-potential analysis of rotors has been presented. The formulation described is valid for isolated rigid bodies in arbitrary motion.

Numerical results concerning two-dimensional and lifting fixed wing configurations have been presented in order to demonstrate the good accuracy of the obtained solution, with respect to existing full-potential numerical results based on widely used CFD methodologies.

Non-lifting hovering rotor cases have also been investigated. The aeroacoustic solution appears to be in good agreement both with existing numerical results based on the solution of the Ffowcs Williams and Hawkings equation and with experimental data. The aerodynamic solution calculated is comparable with existing CFD results, but further investigation is required in order to enhance the accuracy of the solution in the vicinity of the shock.

In order to improve both accuracy and efficiency of the computational algorithm, future work includes development of the presently used zeroth-order numerical discretization to a third-order one.

REFERENCES

1. Morino, L., "A General Theory of Unsteady Compressible Potential Aerodynamics", NASA CR 2464, 1974.
2. Tseng, K. and Morino, L., "Nonlinear Green's Function Method for Unsteady Transonic Flows", in Nixon, D. (ed), "Transonic Aerodynamics", Progress in Aeronautics and Astronautics, 81, 1982.
3. Morino, L. and Tseng, K., "A General Theory of Unsteady Compressible Potential Flows with Applications to Aeroplanes and Rotors", in Banerjee, P. K. and Morino, L. (eds.), "Nonlinear Problems of Fluid Dynamics", Developments in Boundary Element Methods, 6, Elsevier Applied Science Publishers, Barking, UK, 1990.
4. Gennaretti, M., "Metodo delle Equazioni Integrali al Contorno per Analisi Aerodinamica e Aeroacustica di Rotori in Flussi Potenziali", Compressibili, Non Stazionari, Tesi di Laurea, (Aeronautical Engineering), University of Rome La Sapienza, Rome, Italy (in Italian), 1989.
5. Gennaretti, M. and Morino, L., "A Unified Approach for Aerodynamics and Aeroacoustics of Rotors in Compressible Potential Flows", in Anigeri, B.S. and Tseng, K. (eds.), "Boundary Element Methods in Engineering", Springer-Verlag, 1990.
6. Iemma, U., Mastroddi, F., Morino, L. and Pecora, M., "A Boundary Integral Formulation for Unsteady Transonic Potential Flows", AGARD Specialists Meeting on Transonic Unsteady Aerodynamics and Aeroelasticity Proceedings, San Diego, CA, 1991.
7. Morino, L. and Gennaretti, M., "Toward an Integration of Aerodynamics and Aeroacoustics of Rotors", DGLR/AIAA Paper 92-02-003, DGLR/AIAA 14th Aeroacoustic Conference, Aachen, Germany, 1992.
8. Gennaretti, M., "Una Formulazione Integrale di Contorno per la Trattazione Unificata di Flussi Aeronautici Viscosi e Potenziali", Tesi di Dottorato di Ricerca, Università di Roma "La Sapienza", Rome, Italy, 1993. (in Italian)
9. Morino, L. and Iemma, U., "Boundary Integral Equations and Conservative Dissipation Schemes for Full Potential Transonic Flows, Computational Mechanics", 13, 1993, pp 90-99.
10. Iemma, U., Gennaretti, M. and Morino, L., "Boundary Element Method for Unified Transonic Aerodynamic and Aeroacoustic Analyses of Rotors", XIX European Rotorcraft Forum Proceedings, Cernobbio, Italy, 1993.
11. Iemma, U., "Metodi Integrali in Aerodinamica Transonica", Tesi di Dottorato di Ricerca, Università di Roma "La Sapienza", Rome, Italy, 1994. (in Italian)
12. Oswatitsch, K., "Die Geschwindigkeitsverteilung ab Symmetrische Profilen beim auftreten lokaler Überschallgebiete", Acta Physica Austriaca, 4, 1950, pp 228-271.

13. Spreiter, J. R. and Alksne, A. Y., "Theoretical Prediction of Pressure Distribution on Non-Lifting Airfoils at High Subsonic Speeds", NACA R 1217, 1955.
14. Murman, E.M. and Cole, J.D., "Calculation of Plane Steady Transonic Flows", AIAA Journal, 9, 1971.
15. Nixon, D., "Transonic Flow Around Symmetric Airfoil at Zero Incidence", Journal of Aircraft, 11, 1974, pp 122-124.
16. Nixon, D., "Calculation of Unsteady Transonic Flows Using the Integral Equation Method", AIAA Journal, 16, 9, 1978, pp 976-983.
17. Piers, W.J. and Sloof, J.W., "Calculation of transonic flow by means of a shock-capturing field panel method", AIAA Paper 79-1459, 1979.
18. Sinclair, P. M., "An Exact Integral (Field Panel) Method for the Calculation of Two-Dimensional Transonic Potential Flow around Complex Configurations", Aeronautical Journal, Paper No. 1394, 1986 pp 976-983.
19. Sinclair, P. M., "A Three-Dimensional Field Integral Method for the Calculation of Transonic Flow on Complex Configurations - Theory and Preliminary Results", Aeronautical Journal, Paper No. 1482, 1988, pp 235-241.
20. Ffowcs Williams, J. E. and Hawkins, D. L., "Sound Generated by Turbulence and Surfaces in Arbitrary Motion", Philosophical Transactions of the Royal Society of London, A264, 1969, pp 321-342.
21. Farassat, F. and Myers, M.K., "Extension of Kirchhoff's Formula to Radiation from Moving Surfaces", NASA TM 89149, 1987.
22. Morino, L. and Gennaretti, M., "Boundary Integral Equation Methods for Aerodynamics", in Atluri, S.N., "Computational Nonlinear Mechanics in Aerospace Engineering", AIAA Progress in Aeronautics and Astronautics, 146, AIAA, Washington, DC, 1992, pp 235-241.
23. Salas, M.D., "Recent Developments in Transonic Euler Flow over a Circular Cylinder", NASA TM 83282, 1982.
24. Jameson, A., "Transonic Potential Flow Calculation Using Conservation Form", AIAA Second Computational Fluid Dynamic Proceedings, 1975, pp 148-161.
25. Hirsch, C., "Numerical Computation of Internal and External Flows", 2, J. Wiley & Sons, New York, 1966.
26. Steger, J.L. and Caradonna, F.X., "A Conservative Finite Difference Algorithm for the Unsteady Transonic Full-Potential Equation", NASA TM 81211, 1980.
27. Prieur, J., Costes, M. and Baeder, J.D., "Aerodynamic and Acoustic Calculations of Transonic Nonlifting Hovering Rotors", International Technical Specialists Meeting on Rotorcraft and Rotor Fluid Dynamics, Philadelphia, Penn., 1993.
28. Magliozzi, D., "The Influence of Forward Flight on Propeller Noise", NASA CR 145105, 1977.
29. Farassat, F. and Succi, G. P., "A Review of Propeller Noise Prediction Technology with Emphasis on Two Current Methods for Time Domain Calculation", Journal of Sound and Vibration, 71, 1980, pp 399-419.
30. Ianniello, S. and De Bernardis, "Calculation of High Speed Noise From Helicopter Rotors Using Different Description of Quadrupole Source", Proceedings of AGARD Symposium on Aerodynamics and Aeroacoustics of Rotorcraft, Berlin, Germany, 1994.
31. Baeder, J.D., Gallman, J.M. and Yu, Y.H., "A Computational Study of the Aeroacoustics of Rotors in Hover", American Helicopter Society 49th Annual Forum, St. Louis, Missouri, 1993.
32. Morino, L., "Boundary Integral Equations in Aerodynamics", Appl. Mech. Rev., 36, 8, 1994, pp 445-466.

ACKNOWLEDGEMENTS

This work was partially supported through a contract from AGUSTA ELI S.p.A. to the Terza Università di Roma, and through postdoctoral fellowships to Dr. M. Gennaretti and Dr. U. Iemma.

Aeroacoustic Calculation of Helicopter Rotors at DLR

K.-J. Schultz, D. Lohmann, J.A. Lieser, K.D. Pahlke

DLR Institute of Design Aerodynamics
Lilienthalplatz 7
D-38108 Braunschweig, GERMANY

Summary

The rotor noise level is one of the main design parameters for future rotorcrafts. This fact requires accurate aeroacoustic prediction tools. The two most annoying contributors to rotor noise radiation are blade vortex interaction impulsive noise (BVI) and highspeed compressibility impulsive noise (HI). At DLR great effort is concentrated on these two impulsive noise phenomena. The paper presents examples of: 1) the prediction of lowspeed BVI impulsive noise using aerodynamic input from a quasisteady formulation of the panel method LBS and the linear terms of the FWH-equation for acoustic calculation and 2) the prediction of highspeed hover and forward flight impulsive noise using transonic aerodynamic input from a 3D-EULER code and the FWH-equation including the nonlinear quadrupole term for the acoustic calculation. The calculated results are compared with experimental data from the AH-1/OLS (UH-1H) model tests in DNW, 1982, and from the HELINOISE test (BO 105 model in DNW). The prediction of lowspeed BVI noise is highly dependent on the used wake model for the blade pressure calculation, while the acoustic calculation is quite straightforward. The comparison of experimental data with calculated acoustic results using blade pressure input from the LBS code in connection with Beddoes wake model shows satisfactory agreement. In the highspeed case the perturbation velocity field solution of the EULER code provides the input for the quadrupole volume integral in the FWH-equation. Four different solutions to solve the quadrupole term are presented for the hover case: volume integration, two kinds of pre-integration in blade normal direction and an approximation using the blade surface values. In comparison with experimental data the different calculated results for the hover case show that the expensive volume integration provides the best solution, but the approximated approaches are also satisfactory. For the highspeed forward flight case the quadrupole approach with pre-integration has been selected and quite successfully applied.

List of Symbols

c	speed of sound
c_p	pressure coefficient
c_T	thrust coefficient

l_r	force on the fluid per unit area in observer direction
M	Mach number
M_r	Mach number in source-observer direction
p	pressure
r	source-observer distance
T_{ij}	Lighthill tensor
u_{ij}	perturbation velocity
U	free stream velocity
v_n	blade normal velocity disturbance
α_{tp}	tip path plane angle
γ	specific heat ratio
μ	advance ratio
σ	source strength
ϕ	velocity potential
Ψ	rotor azimuth angle

1. Introduction

Rotor aeroacoustic has become an important research field due to noise reduction requirements for both civil rotorcraft as well as military rotorcraft. Meanwhile the most annoying contributors to helicopter noise are wellknown:

1. Blade vortex interaction impulsive noise, occurring at descent flight conditions and radiating mainly to the ground. (Disturbing noise around heliports!)
2. Highspeed impulsive noise which is caused by the transonic flow field with shock delocalization on the advancing blade tip and radiating mainly in forward inplane direction. (Detectibility over long distances!)

Thus the rotor noise level is one of the main design parameters for the next generation of rotorcraft and this requires accurate aeroacoustic prediction tools. Several national as well as international joined research programs were established to reduce rotor impulsive noise radiation with participation of national research centers and helicopter industry, in the past mainly in the US but presently also in the EU (for example HELINOISE, ERATO, HELISHAPE, HART).

In the past intensive experimental research efforts have been carried out by rotor model wind tunnel tests and helicopter flight tests to improve the physical understanding of

rotor aerodynamics, acoustics and dynamics and thus to validate and improve the aerodynamic and acoustic codes for prediction of rotor noise. Especially tests with simultaneously measured blade pressures and radiated noise were successful (Ref 1,2). But it was found that more information about rotor aerodynamic and dynamic is necessary. Therefore tests with additional simultaneous measurements (rotor wake geometry, blade tip deflection etc.) were performed (Ref 3).

In parallel to the experimental research the development of aerodynamic and acoustic codes to predict rotor noise has been forced. Three different aeroacoustic approaches have been established during the last years. Up to now the application of Lighthills acoustic analogy method represented in the Ffowcs-William/Hawkings (FWH)-equation (Ref 4) and especially for rotor acoustics in Farassats formula 1 and 1A (Ref 5,6) has been the most usual approach (Ref 7-17). In this case aerodynamic input data like the rotor blade surface pressures and the perturbation velocity field around the blade are required. These aerodynamic data can be supplied from experiment, or better from reliable aerodynamic predictions. Recently a second method was applied using a Kirchhoff formulation for acoustic radiation with aerodynamic input data calculated at the so-called sonic cylinder (Ref 18,19). For both approaches accurate aerodynamic calculation is the first and most important step to accurately predict the radiated noise.

A third method is the so-called computational acoustics, the direct calculation of rotor noise based on the EULER-equation or other CFD field methods (Ref 20).

At DLR Braunschweig applications of the direct EULER-method are planned for the near future and the application of the Kirchhoff-method is in development. At present rotor noise calculations are performed only with the FWH method. Results from different aerodynamic codes or results from blade pressure measurements are used as input for the DLR acoustic code AKUROT.

For the calculation of rotor aerodynamics 3 different approaches were used at DLR up to now:

- a) Rotor simulation code (lifting line method, but including rotor dynamic, Ref 21).
- b) Panel methods, especially, LBS (Lifting Body Surface method with prescribed wake model, Ref 22,23) and an other newly developed unsteady code with free wake modelling and offline aeroelastic coupling (Ref 24).
- c) 3-D-EULER-method (including transonic conditions, Ref 25).

The presented paper is a combination of originally two separately proposed papers and will be therefore concentrated on two special topics:

1) Low speed blade vortex interaction (BVI) impulsive noise using the LBS code for aerodynamics and the linear terms of the FWH-equation for acoustics.

2) Highspeed impulsive noise (HI) using the DLR-3D-EULER code for the transonic aerodynamics and the FWH equation including different approaches to solve the nonlinear Quadrupole volume integral term for acoustics.

2. Low speed BVI impulsive noise prediction

2.1 Governing acoustic equation and prediction scheme

For acoustic calculation the DLR uses the acoustic code AKUROT. This code was developed in 1987 (Ref. 11,12) and first validated with experimental data from the OLS-AH1-model rotor tests in the DNW, 1982 (Ref. 1,2). The code is based on the Ffowcs William/Hawkings equation (Farassat formulation 1) and includes the thickness noise term, the loading noise term and also an approximated quadrupole noise term. The calculation is performed in the time domain.

For predictions at low speed conditions only the linear thickness and loading terms are used and in this case the code is similar to several other acoustic codes like „WOP-WOP“ from NASA Langley, „ROTAC“ from ISL, „RAPP“ from NASA Ames, „HERNOP“ from C.I.R.A. or „PARIS“ from ONERA, all using Farassats formulation 1 or 1a.

Farassats formulation 1 is written:

$$4\pi p(x, t) = \frac{1}{c} \frac{\partial}{\partial t} \iint_S \left[\frac{p v_n c + l_r}{r(1 - M_r)} \right]_{ret} dS \quad (1)$$

$$+ \iint_S \left[\frac{l_r}{r^2(1 - M_r)} \right]_{ret} dS$$

The sound pressure p at the observer time t on an observer position x depends on two integrals, radiating from the source location at the retarded time. The first one includes the thickness noise part with the velocity disturbance normal to the blade surface v_n as important parameter and the loading noise part with the force on the fluid per unit area in the observer direction l_r as important parameter. M_r is the source Mach-number component in observer direction and r is the observer-source distance. The second integral is the loading nearfield term which can be neglected for farfield predictions.

Details of the prediction scheme and the numerical approach can be found in Ref. 11,12.

2.2 Aerodynamic input (LBS code)

In the present paper a Lifting Body Surface (LBS) method for propellers based on linear potential theory with extensions for compressible and unsteady flows is used for rotors in lifting forward flight. There are two main reasons for this approach. Firstly, the method is very fast, it is validated for propellers and it was successfully applied as a

design method for fans (Ref 22) and rotors (Ref. 23). Secondly, it is compatible to the acoustic methods of Farassat type one (Ref 11,12) used at DLR, because the structure of computer codes and the mathematical background is very similar. The aerodynamic and the acoustic method are both boundary integral methods. The integrals are similar and the same surface meshes can be used.

The LBS-method is based on the isentropic potential flow model. With the second Green's identity the volume integral over a three-dimensional domain is expressed by surface integrals over panels located on the surface of the body. The advantage of such a boundary element method is, that even in three dimensional flows the number of algebraic equations to be solved is moderate. The method yields the pressure on the body surface, which is sufficient for calculating low speed noise for descend flight.

The governing equation for aerodynamics can be derived by integrating the FWH equation with respect to time and considering the complete time history of the sources (Ref 22):

$$4\pi\phi(x, t) = \iint_S \left[\frac{\sigma}{r(1-M_r)} \right]_{\text{ret}} dS \quad (2)$$

$$+ \int_{-\infty}^t \iiint_S \frac{\partial}{\partial n} \left[\frac{\Delta p/\rho}{r(1-M_r)} \right]_{\text{ret}} dS dt$$

For the calculation of rotors compressibility and unsteadiness have to be taken into account. In the present method the distances between emission point and receiving point are transformed similar to the Prandtl-Glauert-Goethert rule using Lorentz contraction.

Because of the use of acceleration potential the wake is described by means of paths of singularities instead of vortices.

The loading term is divided into a part corresponding to the bound vortex and a second part corresponding to the free vortices which represents the wake. The surface integration of dipoles in the wake integral is replaced by an integration along the path of the singularities by use of acceleration potential. There are no singularities in the wake since the wake is free of forces and the acceleration potential is continuous through the wake.

Since the nonlinear interaction between rotor and wake is very important in case of the descending helicopter a linear model for propellers was replaced by the model of Beddoes (Ref 26) for the description of the path of the singularities. This leads to a better weighting of the BVI peaks compared to experiments.

Detailed description of the aerodynamic method and the prediction scheme can be found in Ref 23.

2.3 Results for the AH-1/OLS model rotor

The first forward flight calculations were done for the AH-1/OLS rotor which has rectangular linear twisted

blades with a slightly modified NACA 0012 profile. The descend flight case 3017, which is a typical BVI case, was chosen (Ref 2). In the experiment the number of pressure sensors in chord direction was low. Therefore, no lift coefficients were calculated from experimental pressure measurements and the time history of pressure on 3 percent chord line at four radial locations is directly compared with experiments in figure 1. It should be mentioned, that

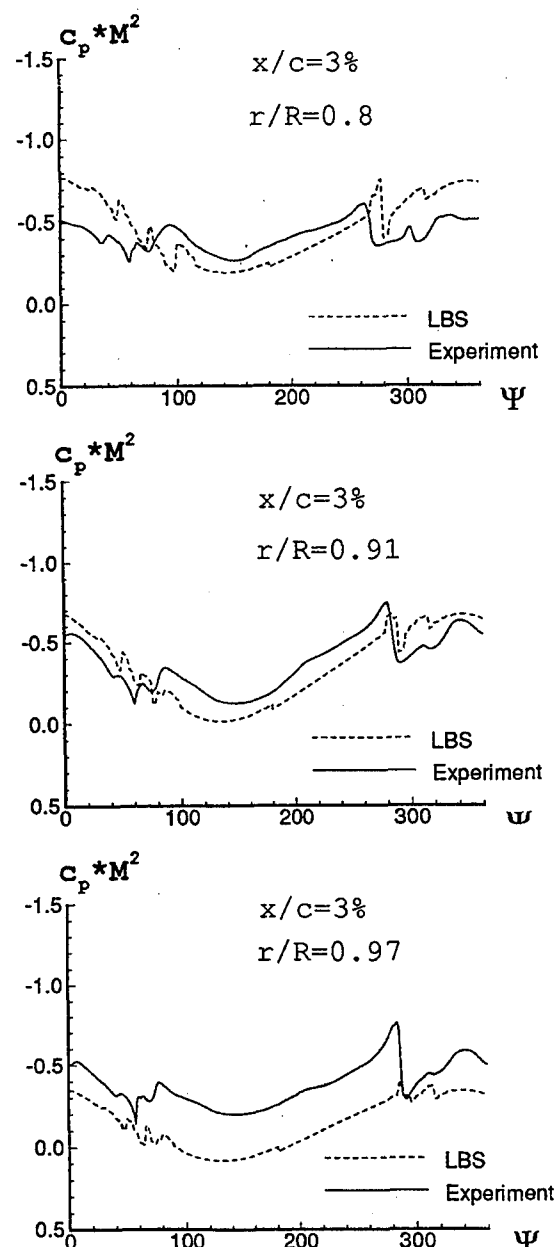


Fig. 1: Comparison of calculated and measured chordwise pressure coefficient distribution for the AH-1/OLS model rotor in lifting forward flight, descent with BVI, $\mu = .164$, $M_{tip} = 0.664$, $\alpha_{TPP} = 1.0$ deg, $c_T = .0054$

due to the resolution with eight panels on the upper side the suction peak in the region around three percent chord is difficult to resolve. Linear interpolation between nearest points were used. But the time gradients due to BVI especially in the region around sixty degrees which are important for the acoustic pressure in flight direction are similar to the experimental ones. The resolution in time was two degrees.

Figures 3 a-h show the acoustic signatures in comparison to the experiments. The microphone positions are shown in figure 2. The peak to peak values are predicted too small for some microphone positions. This may be caused by the not exactly corresponding calculated blade pressure time histories with the measured ones, especially in the 1th and 4th quadrant, where advancing side and retreating side BVI occur, but may also be caused by the missing quadrupole term in the acoustic calculation.

The directivity characteristics of BVI impulsive noise are represented well. The calculated peaks are at the correct position in time for all different microphone positions.

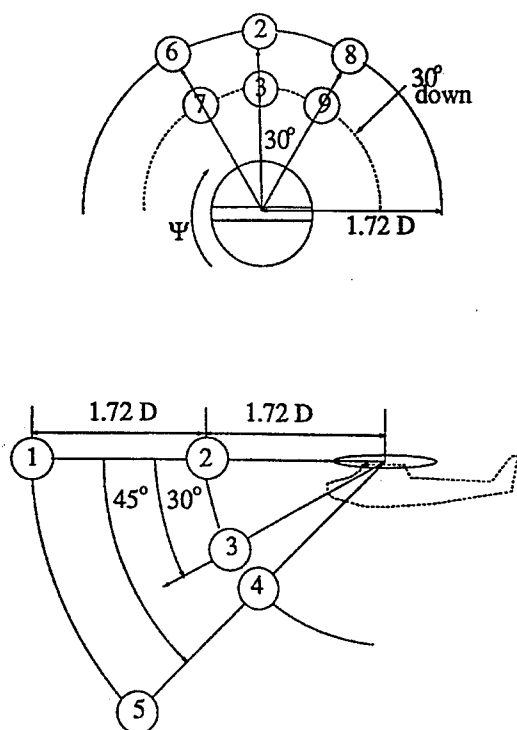


Fig. 2: Microphone positions

2.4 Results for the BO 105 model rotor

The LBS method was also applied to calculate the noise radiation for a BVI condition of the BO 105 model rotor tested in the DNW (HELINOISE). The BO 105 rotor is a hingeless rotor and the dynamic behaviour of the blade which was not taken in to account here is more important compared to the rigid one.

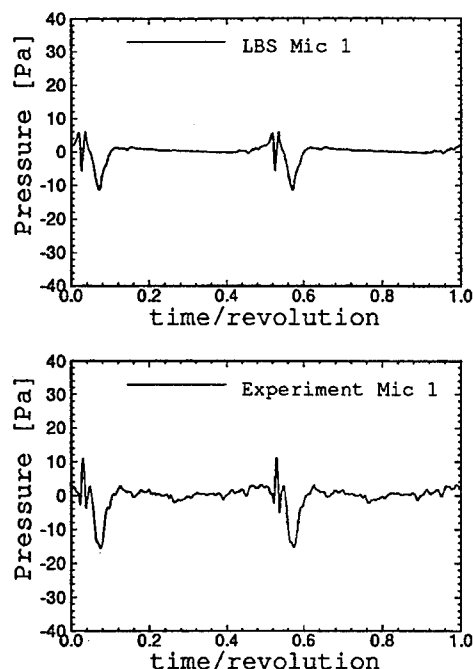


Fig. 3 a: Comparison of calculated and measured chord-wise pressure coefficient distribution for the AH-1/OLS model rotor in lifting forward flight, descent with BVI, $\mu = .164$, $M_{tip} = 0.664$, $\alpha_{TPP} = 1.0$ deg, $c_T = .0054$ microphone position 1 of Figure 2

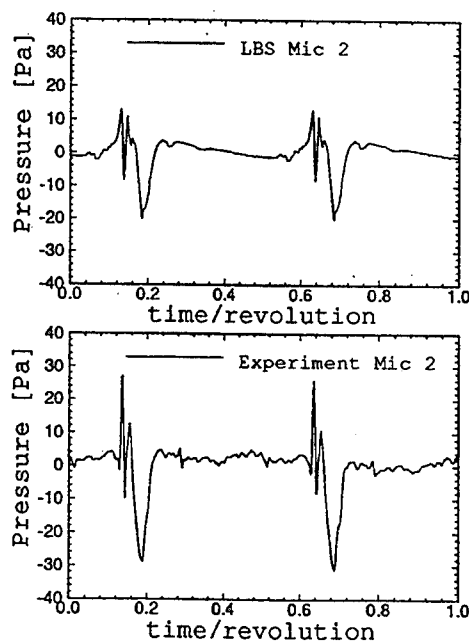


Fig 3 b:, microphone position 2 of Figure 2

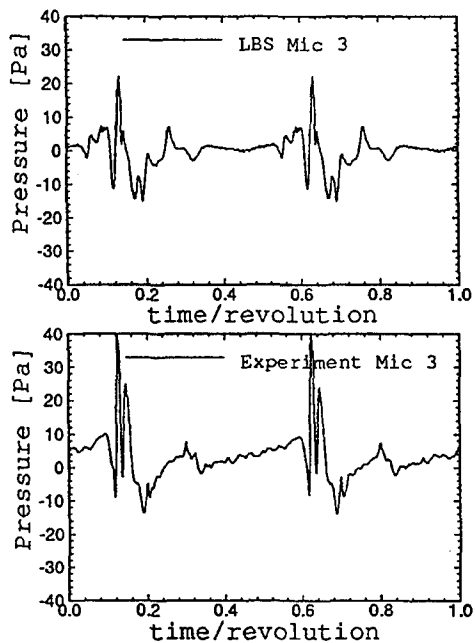


Fig. 3 c: , microphone position 3 of Figure 2

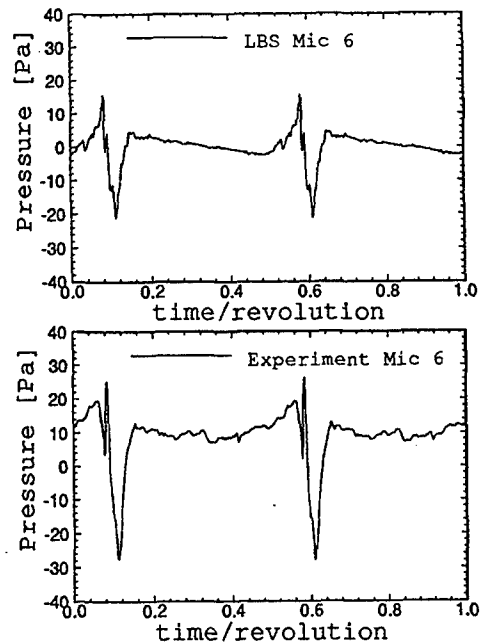


Fig. 3 e: microphone position 6 of Figure 2

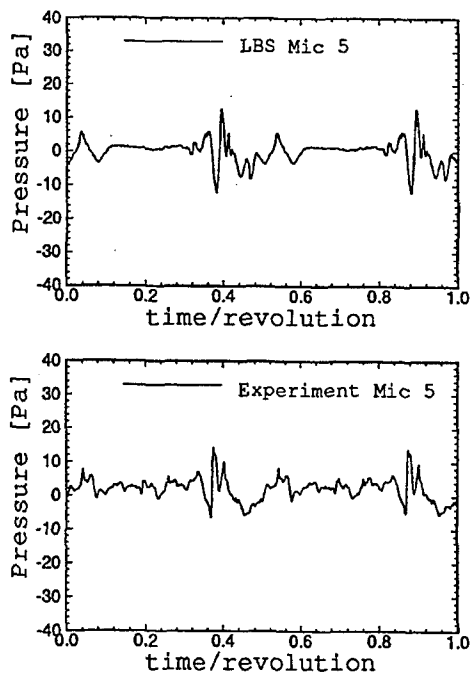


Fig. 3 d: , microphone position 5 of Figure 2

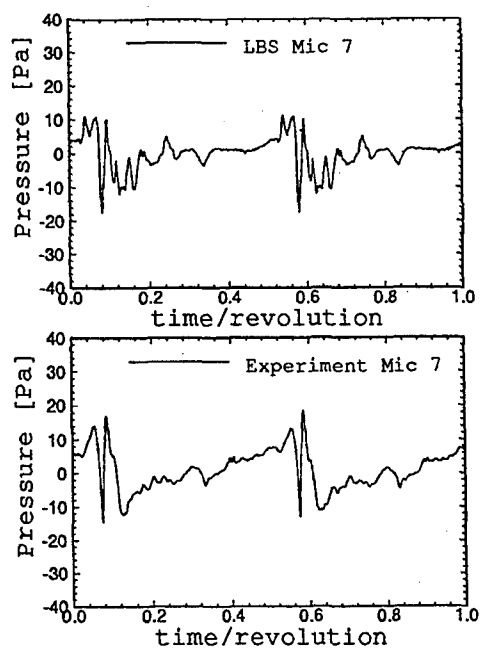


Fig. 3 f: , microphone position 7 of Figure 2

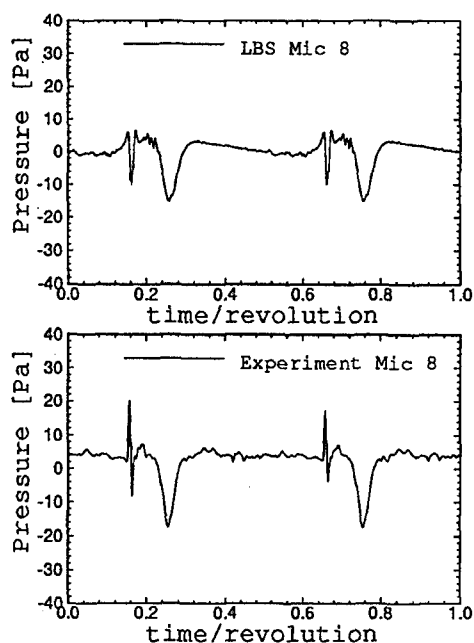


Fig. 3 e: , microphone position 8 of Figure 2

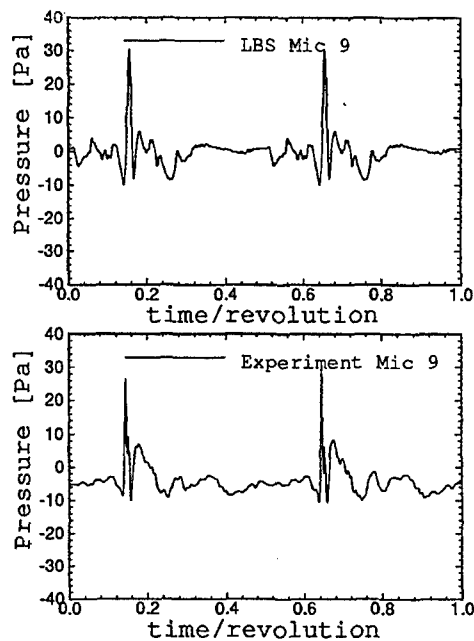


Fig.3 h: , microphone position 9 of Figure 2

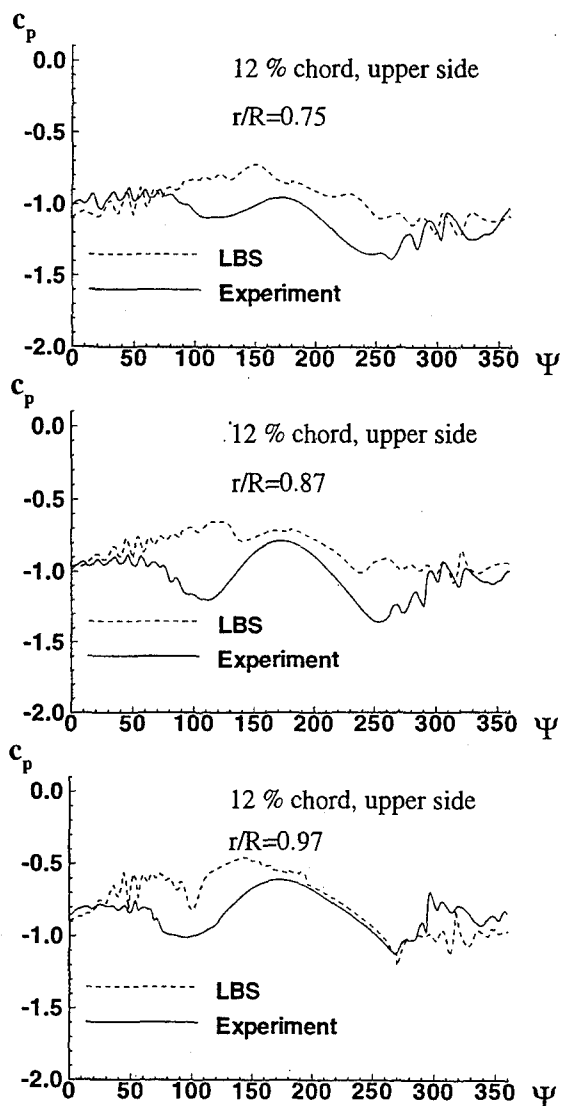


Fig. 4: Calculated unsteady c_p - distribution vs. azimuth compared with experimental BO 105 model rotor data for 3 radial stations and for a chordwise position of 12 % chord on the upper side

Figure 4 shows the unsteady c_p distribution for 3 radial stations ($r/R=.75$, $.86$ and $.96$) and a chordwise station near the leading edge (12 % chord) on the upper side. The BVI-caused peaks on the advancing and on the retreating side are quite well predicted as can be seen from the comparison with experimental data.

Figure 5 shows the acoustic result using this aerodynamic

input for the loading term of the FWH-equation. Figure 5a shows a comparison of the calculated sound pressure time history of a selected microphone position near the advancing side maximum radiation direction with experiment. The agreement of the signal shapes is quite satisfactory, but it should be noted that the agreement may be not as good in other radiation directions. The comparison of the experimental and calculated noise field underneath the rotor, presented as mid-frequency level contours (figure 5b), shows similarity in level and in the directivity characteristic. The advancing side as well as the retreating side BVI maxima are quite well predicted.

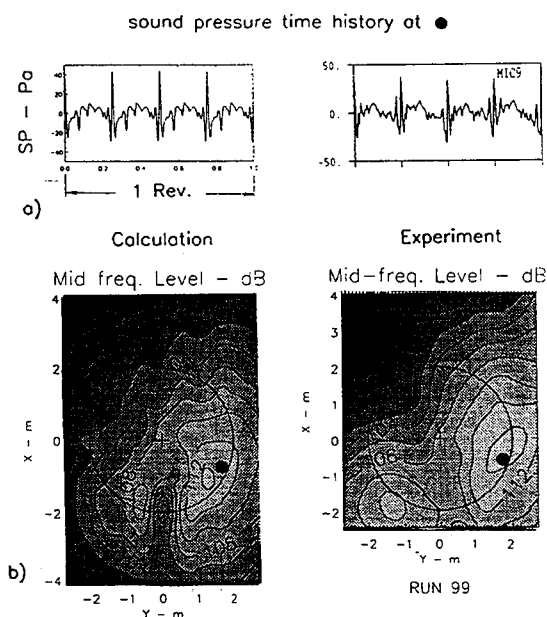


Fig. 5: Calculated mid-frequency level contours and sound pressure time histories for a selected position near the maximum radiation compared with experimental data from HELINOISE test (Ref 3)

3. Highspeed impulsive noise prediction

Recently both the Kirchhoff method and the computational acoustics are often applied for highspeed (hover) noise radiation prediction. The present paper shows that also the FWH method including the quadrupole term can provide sufficient results for both the highspeed hover case as well as the highspeed forward flight case, supposing that the perturbation velocity field around the blade is well predicted with aerodynamic field methods like the 3D-EULER methods.

3.1 Governing acoustic equation and prediction scheme

The acoustic calculation of the linear terms of the FWH equation (thickness and loading noise) is the same as for lowspeed cases and has been described before. For high-speed cases with blade tip Mach numbers of about .9 the quadrupole term of the FWH equation becomes most im-

portant and has to be included.

The quadrupole noise term is represented by a volume integrale equation, here written after transformation of the space derivatives into time derivatives:

$$4\pi p_Q(x, t) = \frac{1}{c^2} \frac{\partial^2}{\partial t^2} \left(\iiint_V \left[\frac{T_{ij} r_j r_i}{r(1-M_r)} \right]_{ret} dV \right) \quad (3)$$

$$+ \frac{1}{c} \frac{\partial}{\partial t} \left(\iiint_V \left[\frac{3T_{ij} r_j r_i - T_{ii}}{r^2(1-M_r)} \right]_{ret} dV \right)$$

$$+ \left(\iiint_V \left[\frac{3T_{ij} r_j r_i - T_{ii}}{r^3(1-M_r)} \right]_{ret} dV \right)$$

This nonlinear volume integral equation is very complex and the solution requires immense computational power. A first approximation is the use of only the first integral, the second time derivative, most important for the farfield radiation. The second term is only in the order of about 1% of the first term as test calculations have shown. The third term is a nearfield term and can also be neglected.

The governing Lighthill tensor T_{ij} is written:

$$T_{ij} = \rho u_i u_j + p_{ij} - c^2 \rho \delta_{ij} \quad (4)$$

The mean part of the Lighthill tensor is $\rho u_i u_j$. As a further approximation it is assumed that the perturbation velocity field near the blade (about 1-2 chordlength) is the most efficient contributor. The integration is then performed only for this near-blade volume. Furthermore it is assumed that the component parallel to the blade surface (or even parallel to the chord in the nonlifting hover case) is most important. The radial component can be neglected because the component in observer direction is zero when the maximum Mach number in observer direction is reached. Considering only the in-plane radiation the vertical component of the perturbation velocity acts also vertical to the source-observer direction and can be neglected. In this case the first part of the Lighthill tensor is simply:

$$\rho u_i u_j = \rho u^2 \quad (5)$$

This approximation was introduced by Yu, Caradonna and Schmitz (Ref. 27). Also their approximation for the rest of the Lighthill tensor is applied:

$$p_{ij} - c^2 \rho \delta_{ij} = \frac{\gamma - 1}{2} \rho M^2 u^2 \quad (6)$$

Thus the quadrupole noise can be written:

$$4\pi p_Q(x, t) = \quad (7)$$

$$\frac{\partial^2}{\partial t^2} \left(\iiint_V \left[\frac{\rho M^2}{r(1-M_r)} \left(1 + \frac{\gamma - 1}{2} M^2 \right) \left(\frac{u_r}{U} \right)^2 \right]_{ret} dV \right)$$

To solve this approximated quadrupole equation four different approaches were used and compared for the hover case.

1. Volume integration of the quadrupole intensity
2. Pre-integration of the quadrupole intensity in blade normal direction using the original grid system.
3. Pre-integration after coordinate transformation.
4. Approximation using the quadrupole intensity on the blade surface.

The first method is solving the volume integral, that means calculations for each finite volume element in an appropriate range around the rotor blade. An aerodynamic field solution can be used directly in the applied grid system.

The second and third method are using an approach first applied by Yu, Caradonna, Schmitz (Ref 27). The perturbation velocity-square is integrated in the direction normal to the blade (normal to the rotor plane) before performing the acoustic far-field prediction providing a special quadrupole intensity value assumed to act parallel to the blade (parallel to the rotor plane). In this way the quadrupole term is approximated by a surface integral similar to the loading term:

$$4\pi p_Q(x, t) = \quad (8)$$

$$\frac{\partial^2}{\partial t^2} \left(\iint_S \left[\frac{\rho M^2}{r(1-M_r)} \left(1 + \frac{Y-1}{2} M^2 \right) \int_n \left(\frac{u_r}{U} \right)^2 dn \right] dS \right)_{ret}$$

The fourth approach is using a further approximation similar to that presented by Schultz und Spletstoeser (Ref. 11,12) and tested by Ianniello et al (Ref 17). This approximation supposes a relationship between the blade surface perturbation velocity (or blade surface pressure via Bernoulli equation) and the quadrupole intensity (the integral in normal direction). Thus a blade surface solution from panel methods (or measured blade surface pressures) can be used to predict the highspeed quadrupole noise.

The available 3D-EULER field solution allows an improved investigation of this approximation, the direct comparison of the surface and the integrated quadrupole intensity. The relationship:

$$A = \int \left(\frac{u}{U} \right)^2 dn / \left(\frac{u}{U} \right)^2_{Surface} \quad (9)$$

can be estimated and used for an approximated quadrupole calculation:

$$4\pi p_Q(x, t) = \quad (10)$$

$$\frac{\partial^2}{\partial t^2} \left(\iint_S \left[\frac{\rho M^2}{r(1-M_r)} \left(1 + \frac{Y-1}{2} M^2 \right) A \left(\frac{u_r}{U} \right)^2_{Surface} \right] dS \right)_{ret}$$

3.1.1 Governing aerodynamic equation and prediction scheme(3D-EULER code)

The DLR 3D Euler code for rotor flows solves the Euler equations transformed into a moving coordinate system fixed to the rotor blade which is assumed to be rigid. The discretization of space and time in the governing equations is separated following the method of lines (Jameson et al., - Ref 28) using a finite volume formulation for the spatial discretization. The flow quantities are taken to be volume averaged. The finite volume discretization reduces to a second-order central difference scheme on a Cartesian grid with constant grid sizes. If an arbitrary nonuniform grid is used, the accuracy of this scheme depends on the smoothness of the grid. In order to avoid spurious oscillations a blend of first and third order dissipative terms is introduced. An explicit Runge-Kutta time stepping scheme is used with an evaluation of the dissipative fluxes at the first two stages.

In Euler-computations on grids containing the whole rotor disc the wake is part of the solution. Consequently no wake model is used for hover cases. Up to now the code is not able to handle several blades in relative motion, which is necessary for the lifting forward flight case. Therefore the flow around only one blade is calculated using the wake model according to Beddoes (fixed wake, Ref 26,21) providing the downwash and the wake effects of the whole rotor. This wake model provides a field of induced velocities normal to the tip path plane which are used to change the solid body boundary condition in the Euler code.

In order to accelerate the convergence to steady state for hover cases rothalpy damping, implicit residual averaging (Ref 29) and a multigrid algorithm have been implemented. The technique of implicit residual averaging has been adapted to time-accurate calculations for forward flight cases.

Body conforming, single block, computational grids were constructed for multibladed hovering rotors, using a grid generator based on an elliptic 3D solver. Because of the cylindrical nature of the flow of a hovering rotor an O-H topology was chosen with the wraparound O in chordwise direction and the H-type in spanwise direction.

Due to the symmetry of the flow only a segment of the rotor plane containing one blade has to be regarded. The other blades are taken into account by periodicity conditions in the blade azimuthal direction, which swaps the flow information at the front and back boundaries of the cylindrical mesh. On account of this grid topology it is obvious to generate grids with identical point distributions on the periodicity planes. Therefore, no interpolation of the flow quantities on the periodicity planes is required. Grids used for forward flight calculations are constructed quite similar but with a far field of cylindrical shape.

More details about the method, also numerical aspects of the algorithms and the grid generation are described in

Ref 25.

3.2 3D-EULER hover results

For validation purpose the UH1H twisted model rotor in non-lifting hover (Ref 1, 15) was calculated with the 3D-EULER code for the critical tip Mach number of .9. Because of the twist upper and lower side are slightly different and have to be considered separately.

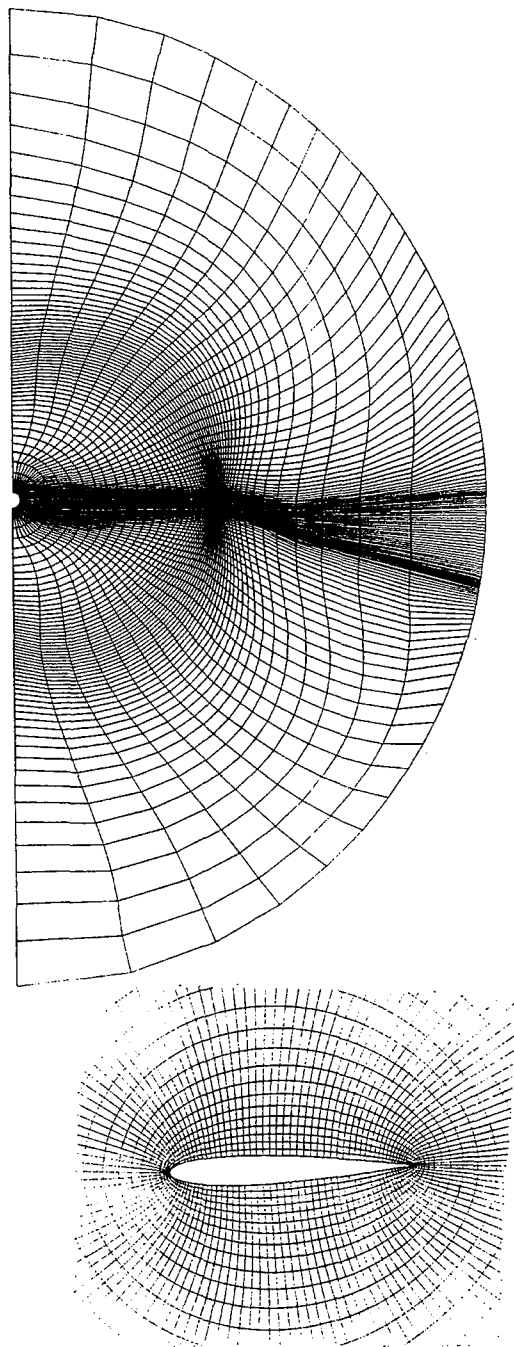


Fig. 6: O-H-grid system used for 3D-EULER calculation of a highspeed hover case

Figure 6 shows the applied O-H-grid system. This grid system is not optimized for acoustic calculations, but the chordwise resolution was refined from originally 65 to 129 grid points, and the radial grid was curved beyond the blade tip in order to improve the resolution of the delocalized shock. Since the O-grid system is not optimal for the pre-integration in normal direction for calculating the quadrupole noise a coordinate transformation is necessary. Furthermore near the sonic cylinder at about 111% radius the resolution is not refined enough for the direct acoustic evaluation. Therefore the radial grid can not be directly used and a simple interpolation has to be applied.

Figure 7 shows the chordwise c_p -distribution for a radial station of 95% and a tip Mach number of .9, obtained with the original 65-grid and the refined 129-grid. For the acoustic calculation it is very important to accurately calculate the shock behaviour in the transonic flow regime. This figure demonstrates the improvement in the shock resolution due to the refined grid.

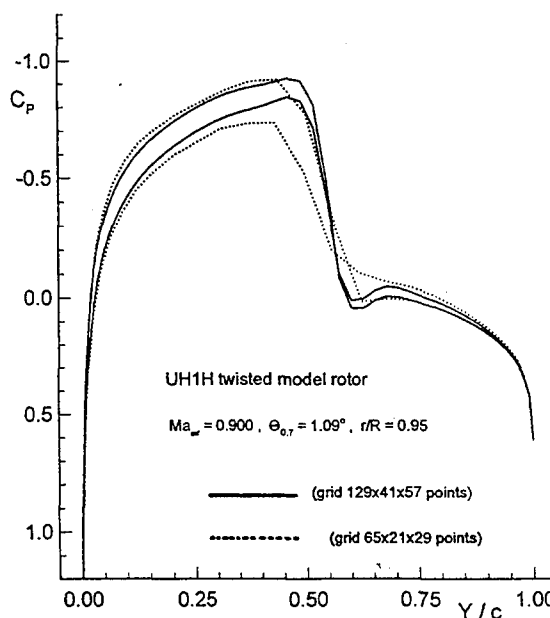


Fig. 7: Comparison of the chordwise c_p -distribution for calculations with a) 129 chordwise grid points, b) 65 chordwise grid point

3.2.1 Quadrupole intensity

The further investigation concentrates on the field solution of the perturbation velocity component parallel to the blade. In figure 8 the chordwise and chord-normal distribution of the quadrupole parameter u^2/U^2 is shown for different radial stations. The comparison demonstrates that almost up to the sonic cylinder the perturbation is concentrated in the chord regime and also about one chord in the normal direction. Only near and beyond the sonic cylinder the perturbation is more extended in chordwise direction as well as in blade normal direction.

Figure 9 compares the integrated quadrupole intensity field for the upper side and for a tip Mach number of .9. using the original O-grid system and after transformation to

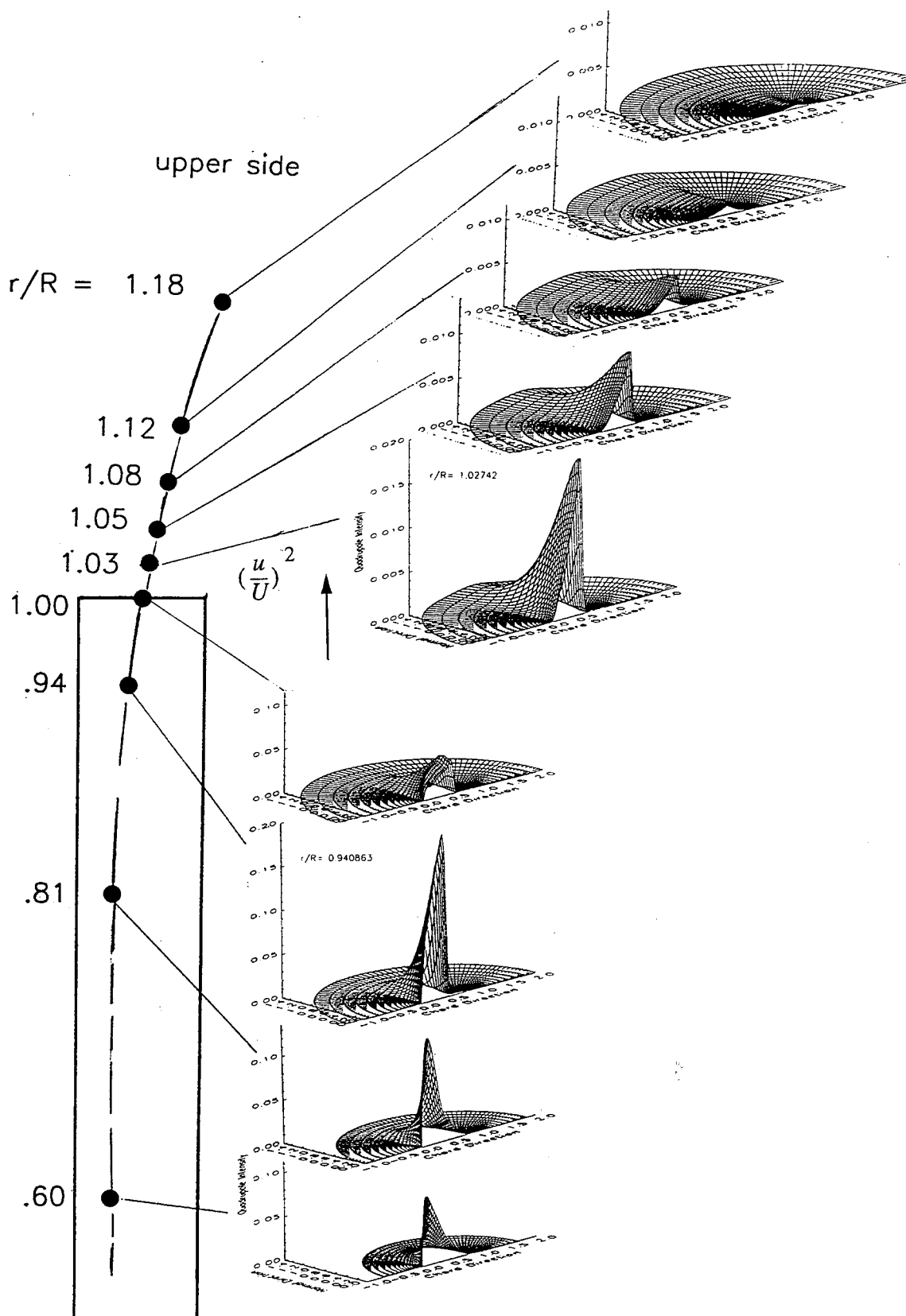


Fig. 8: Quadrupole intensity distribution in chordwise and blade-normal direction for different radial stations (UH-1H model rotor in hover with $Mt=9$)

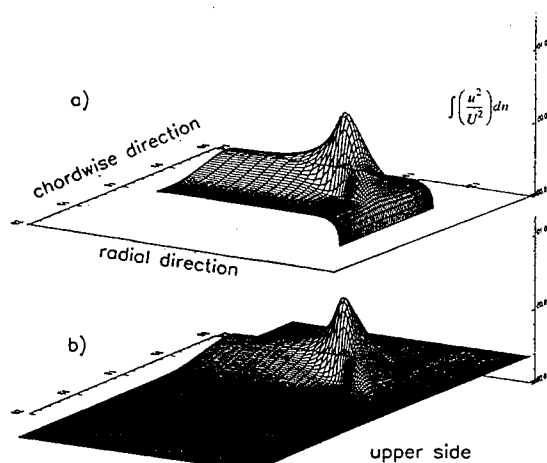


Fig. 9: Pre-integrated quadrupole intensity in chordwise and radial direction, a) integrated along the original normal grid line, b) integration after coordinate transformation in chord-normal direction

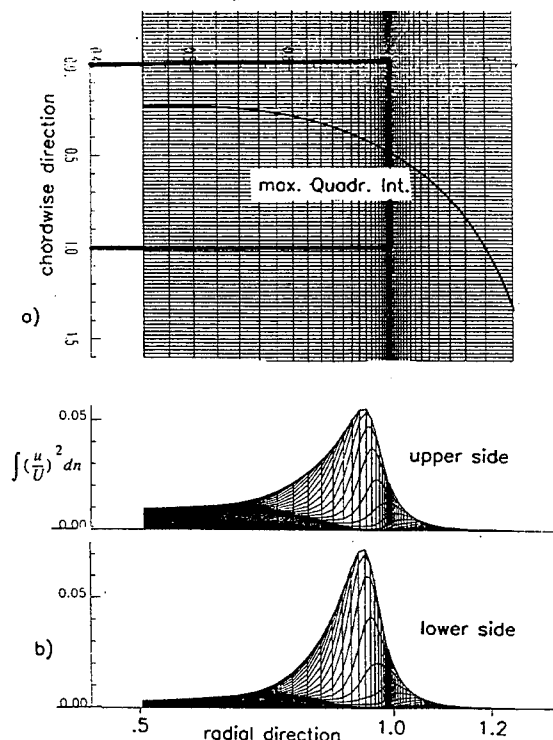


Fig. 10: Chordwise (azimuthal) slope of the max. quadrupole intensity vs. radius (a) and radial distribution of the pre-integrated quadrupole intensity for $M_t = .9$, upper and lower side (b)

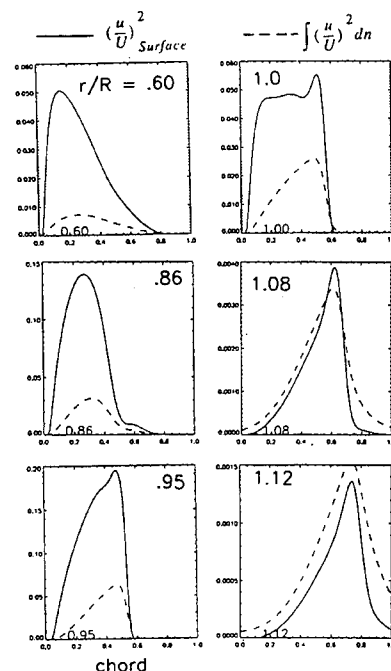


Fig. 11: Comparison of the chordwise surface- and pre-integrated quadrupole intensity for different radial stations

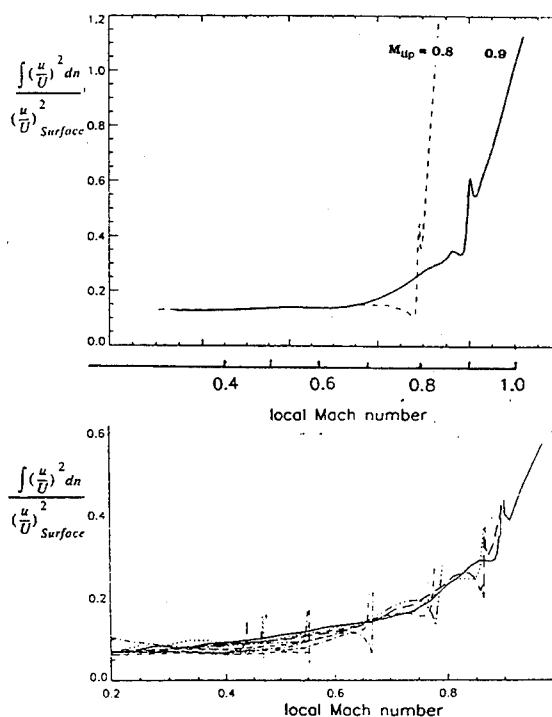


Fig. 12: Relationship between the pre-integrated quadrupole intensity maximum and the surface maximum dependent on the local Mach number, a) hover with $M_t = .8$ and $.9$, b) highspeed forward flight on advancing side (different tip Mach numbers and pitch angles)

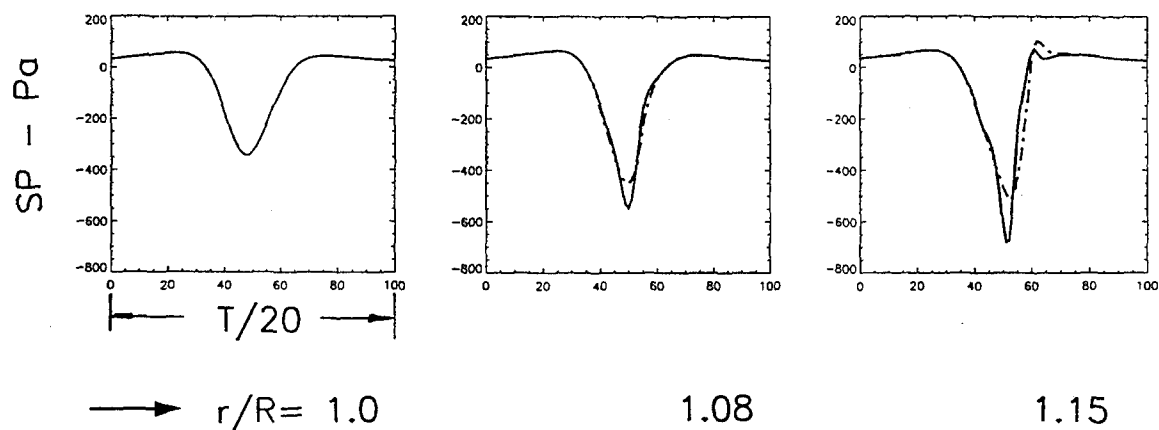


Fig. 13: In-plane noise signatures (1.6 rotor diameter distance), calculated with volume integration and with pre-integration in the original grid system.

a) up to $r/R=1.0$ ($M=.9$), b) up to $r/R=1.08$ ($M=.973$) and c) up to $r/R=1.15$ ($M=1.04$)

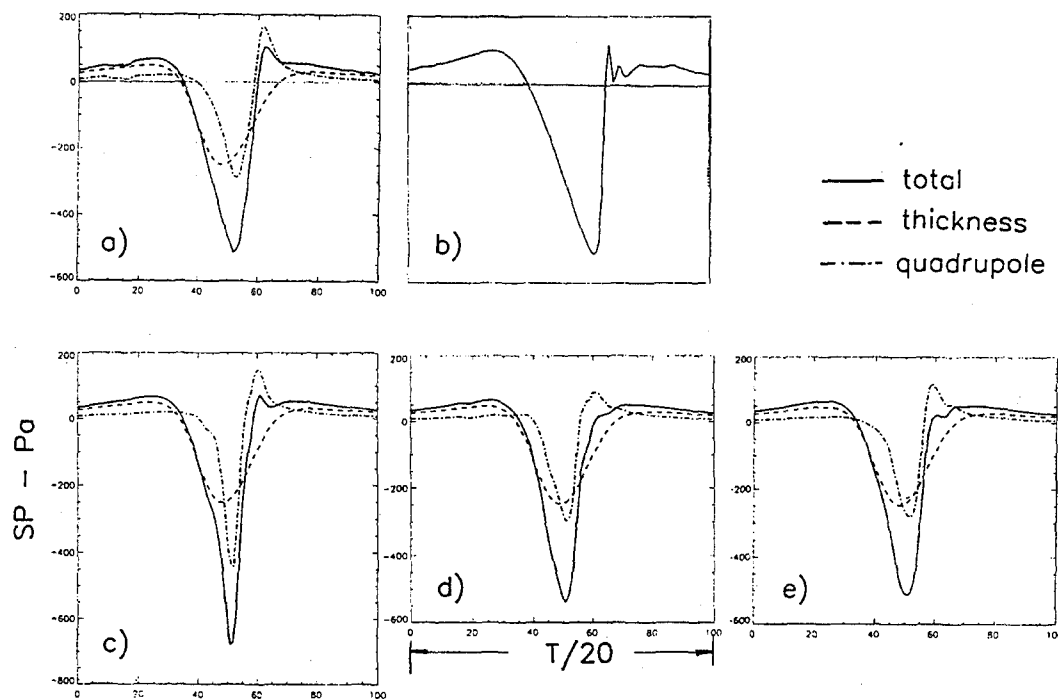


Fig. 14: In-plane sound pressure signatures compared with experiment (twisted UH1H blade, $M_t=.9$) for different quadrupole approaches:

- a) Volume integration
- b) Experiment
- c) Pre-integration in the original grid system
- d) Pre-integration after coordinate transformation
- e) Approximation using the surface values

obtain chordwise equally spaced finite volume elements covering a range of -0.5 up to 2.5 chord-length. In the first case the complete perturbation field is placed on the blade surface and the curved extension beyond the tip.

The radial distribution of the integrated quadrupole intensity is shown in [figure 10b](#) for upper and lower side and for the tip Mach number of $.9$. The envelopes show the maximum values along blade span. In the top-view (the surface grid itself) the radial slope of the maximum quadrupole intensity is drawn in.

3.2.2 Quadrupole approximation

[Figure 11](#) shows the comparison of the chordwise surface and integrated quadrupole intensity for different radial stations and a tip Mach number of $.9$. The comparison shows that the curve shapes are quite similar without the region near the blade tip and near the sonic cylinder. Here the integrated quadrupole intensity is more extended in both chordwise directions compared to the surface value.

[Figure 12a](#) shows the relationship factor A for the chordwise maximum dependent on the local blade Mach number for hover with tip Mach numbers of $.8$ and $.9$. This factor is supposed to be dependent on the local Mach number, the blade pitch (c_p) and the blade tip shape (3D effect). The figure shows a strong 3D-effect at the blade tip but in the range below $r/R=.95$ the curve is quite steady. To show the influence of pitch and Mach number in more detail in [figure 12b](#) this factors are plotted vs. local Mach number for different pitch angles and different tip Mach numbers as obtained from forward flight results on different azimuthal stations. Neglecting the tip effect and averaging the different curves for different pitch angles an approximated dependence only from the local Mach number may be expressed in an empirical formula.

Such formula should be only applied up to the radial position of about 95%. In addition the slope of the quadrupole intensity beyond this position has to be used as can be seen in [figure 10b](#) and the azimuthal shift of the maximum as to observe in [figure 10a](#). It should be noted that in Ref 17, where this approximation was applied at least the required chordwise and thus azimuthal delay of the quadrupole intensity has not been considered. Therefore the unsymmetrical acoustic wave form was not calculated.

3.2.3 Comparison of noise prediction results

Noise predictions for the highspeed hover case were performed using the four different approaches to calculate the quadrupole term as described before.

For all of the described approaches it is very important to be careful with the numerical procedure near the sonic cylinder. The radial and chordwise steps have to be sufficiently small in this regime in order to get smooth integral results, because every numerical unsteadiness would be considerably intensified after the second derivative. Furthermore the observer time steps at maximum source-observer Mach number have to be small enough to get sufficiently small retarded time increments. The retarded time difference for a given observer time difference could be too large to catch the maximum source-observer Mach number. Often different results are caused more by differences in the numerical discretization as by different aerodynamic inputs.

The importance of the sonic cylinder region for the acoustic result is demonstrated in [figure 13](#), where noise signatures are compared, obtained with volume integration and with pre-integration in the original grid system: a) for

calculation up to the blade tip ($r/R=1.0$), b) calculation up to $r/R=1.08$ (before the sonic cylinder) and c) up to $r/R=1.15$ (beyond the sonic cylinder). The tip Mach number is $.9$, (thus the sonic cylinder at $r/R=1.11$) and the observer position is inplane at a distance of $1.6 R$. The comparison shows that up to the blade tip the results of the different approaches are nearly identical. This is also valid for the other approaches. Including the sonic cylinder regime the results are quite different. With the pre-integration, using the original grid system the amplitude is much higher because the quadrupole intensity is concentrated on one chord-length. The radial contributions to the total result increase up to the sonic cylinder, but with integrating beyond the sonic cylinder the results are not further significantly increased.

[Figure 14](#) shows a comparison of the different numerical results with experimental data (Ref. 1,15). The volume integral solution is quite similar to the experiment in amplitude and wave form, but the „saw tooth“-shape is not so strong predicted as measured., the increasing flank is not so steep. Obviously the shock behaviour is not exact enough reproduced. The EULER-grid system as well as the acoustic code resolution have to be improved. The results with pre-integration before and after coordinate transformation are quite different. The chordwise distribution of the integrated quadrupole intensity is more realistic after coordinate transformation and the result is similar to that for the volume integration. Even the result with application of the surface value approximation is almost as good as the volume integration result, only the signal shape is slightly smaller due to concentration in one chord-length. But it should be noted that this result is obtained with the input values directly coming from the EULER solution. Normally for a new rotor blade with improved design the necessary input data are unknown and the application of the approximation may be questionable.

3.3 Application to high-speed forward flight

In forward flight the blade pressures and the perturbation velocity field are highly unsteady because of the required cyclic pitch to balance the lift at different velocities on the blade. The aerodynamic field solution has to be solved for a lot of azimuthal stations (for example 3200/rev using EULER code). This amount of data raises the computational expense rapidly. However, the Euler code has been applied to get the field solution for a highspeed flight condition which can be compared with experimental results from the AH-1/OLS-model rotor test in DNW (Ref. 1). The forward speed is about 80 m/s and the advancing tip-Mach number is $.893$.

[Figure 15](#) shows calculated lower and upper side chordwise blade pressure coefficient distributions for different azimuthal stations compared with experimental results. The agreement is quite good and thus the calculated results are worthwhile to calculate the radiated noise. This is also to be observed from [figure 16](#) where the azimuthal distribution of $c_p \cdot M^2$ is compared with experimental data for a radial station of about 95% and different chordwise positions. The comparison shows that some details of the unsteady behaviour (obviously coming from BVI) are missing in the calculated results, but in general they agree.

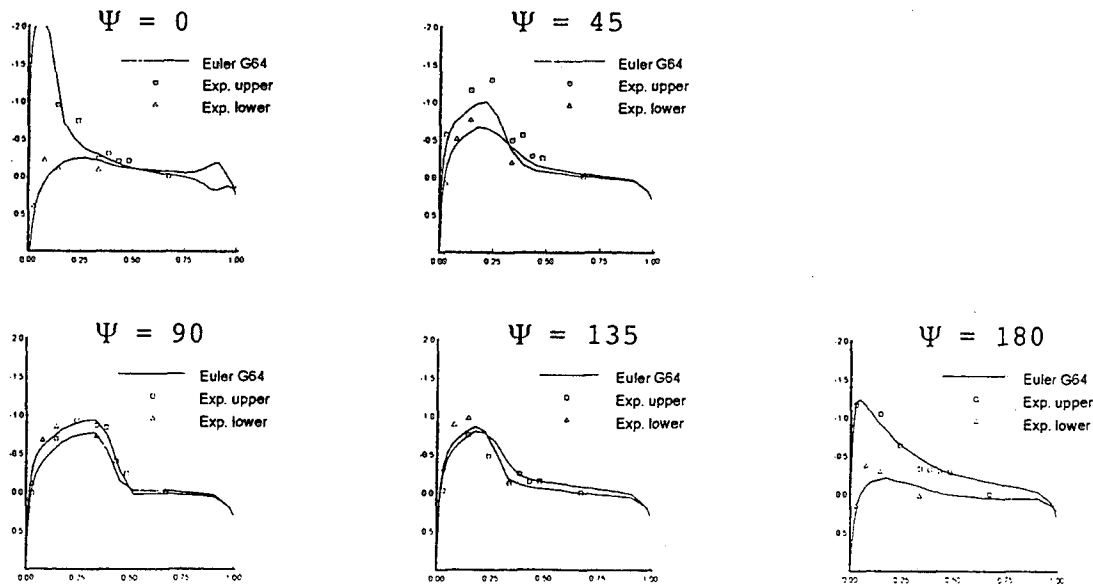
Ah1/OLS Run 9006 $r/R=0.955$ $Mu=0.345$ 

Fig. 15: Calculated chordwise c_p - distribution for different azimuthal stations for a highspeed forward flight case (AH-1/OLS rotor model, $\mu = .345$) at the radial position of $r/R=0.955$ compared with experiment

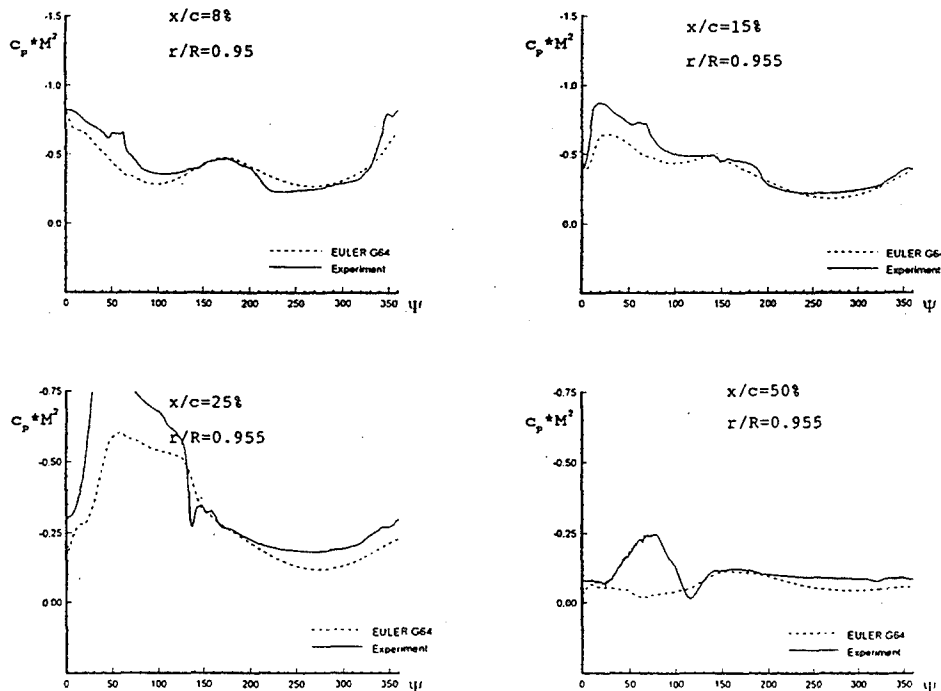


Fig. 16: Calculated azimuthal $c_p * M^2$ distribution for a radial position of $r/R=0.955$ and different chordwise stations compared with experiment. upper side, conditions as for Fig. 15.

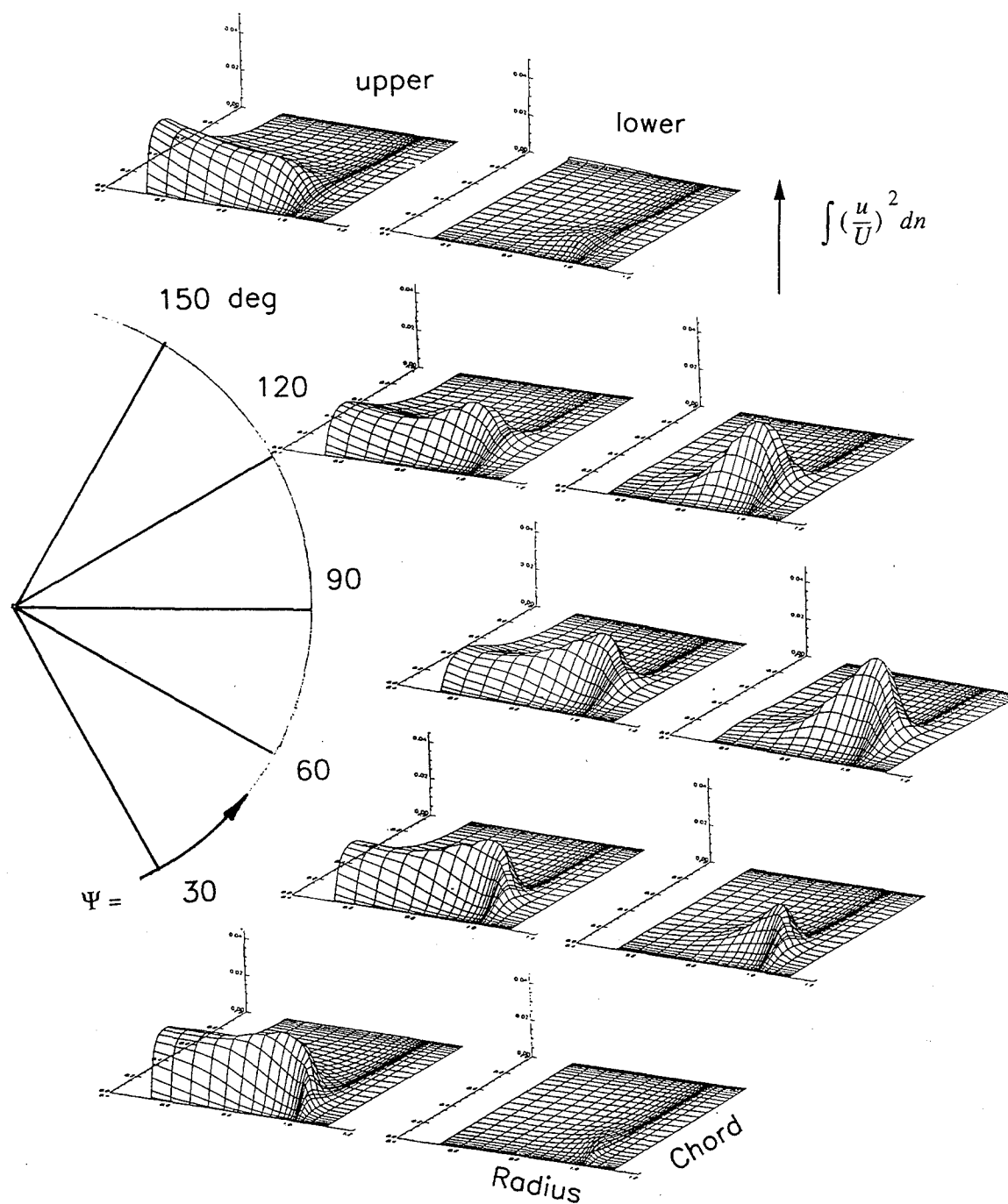


Fig 17: Spanwise and chordwise distribution of the pre-integrated quadrupole intensity for different azimuthal stations, upper and lower side, conditions as for Fig. 15

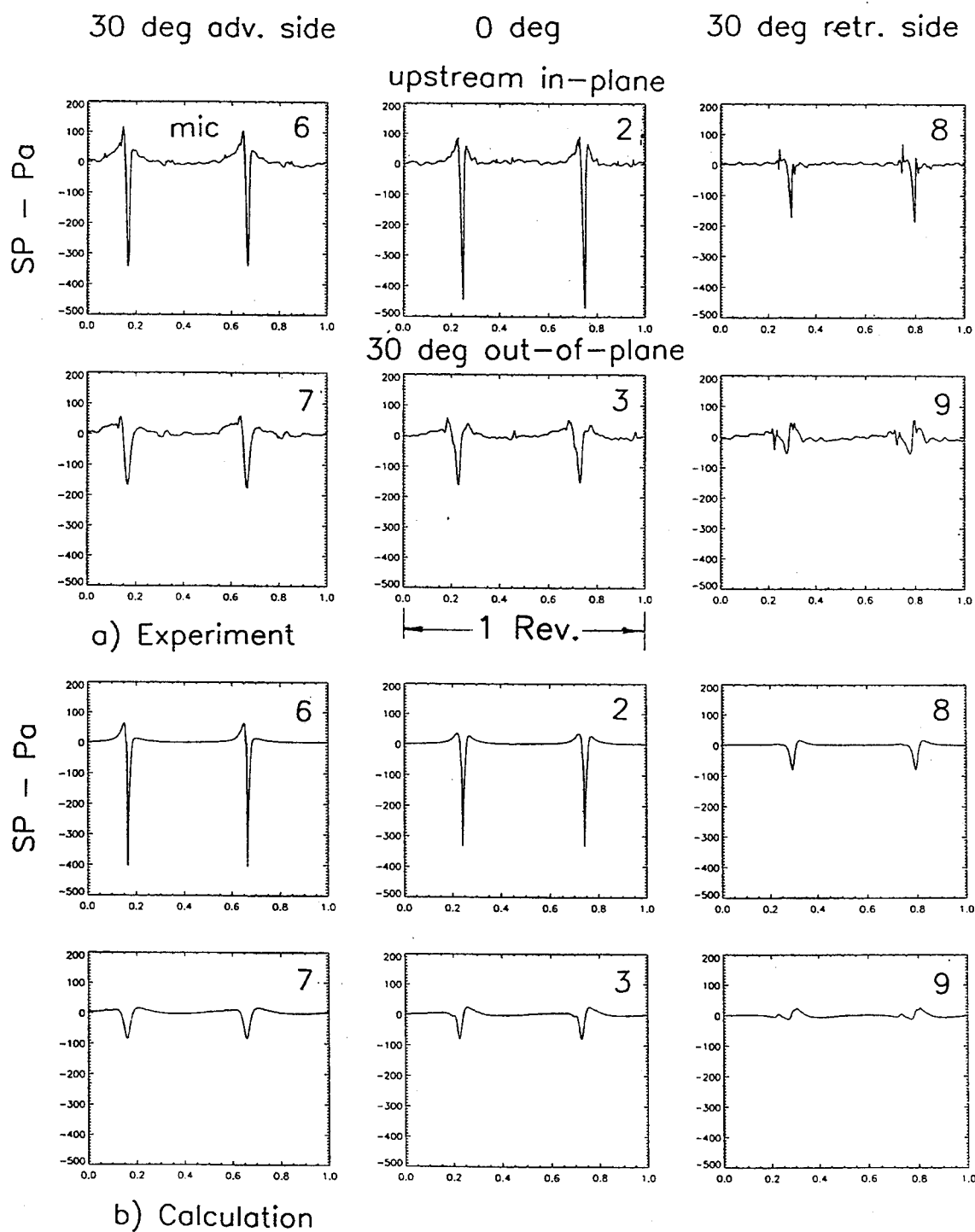


Fig. 18: Comparison of calculated and measured sound pressure time histories for different microphone positions, conditions as for Fig. 18, microphone positions as in Fig. 2.

ment is acceptable. The results are obtained with a chord-wise resolution of 65 points instead of 129 as used for the hover calculations. This was found to be sufficient because the advancing tip Mach number is below .9 and thus the shock is less significant.

The comparison of different approaches to solve the quadrupole term for the hover case has shown that the pre-integration after a coordinate transformation may be a good compromise. Therefore for the highspeed noise prediction this method has been applied to reduce the computational effort.

Because the calculated unsteadiness is relatively weak the coordinate transformation as well as the pre-integration of the quadrupole intensity in normal direction was performed only for 12 azimuthal stations (every 30 degrees). The unsteady behaviour between the 12 stations has been transferred from the unsteady blade surface pressure solution.

Figure 17 compares the integrated quadrupole intensity on upper and lower side for different azimuthal stations on the important advancing side. At about 90 degree azimuth the quadrupole intensity distribution is similar to that for the hover case with $M_t = .9$

Figure 18 shows the calculated highspeed impulsive noise compared with experimental data. The in-plane radiation as well as the 30 degree-out-of-plane radiation to the advancing and retreating side and in direct upstream direction is shown. For the in-plane results the agreement is quite good, especially upstream and to the advancing side. In-plane the quadrupole term is dominating and the unsteady loading term with small BVI content as seen in the experimental data is of second order. Out-of-plane the calculated acoustic amplitudes are underpredicted compared with experiment. This is probably caused more by the underpredicted unsteadiness in the calculated blade pressures for the loading term which is dominating in out-of-plane radiation directions as by an unaccuracy in the quadrupole term which is of second order in out-of-plane directions.

It is planned to calculate a highspeed forward flight case from the HELINOISE experiment with a BO 105 rotor model. A first EULER calculation assuming rigid blades and the comparison of the result with experimental data has shown that for a hingeless rotor without knowledge of the exact dynamic rotor behaviour the result is not sufficient and at this status not worthwhile to present. For example the experimental blade pressure data show in the 2th quadrant of the azimuthal distribution strong negative lift near the blade tip which has not been calculated. But at a later date the exact rotor dynamic (blade motion) will be provided from experiment and can be included in the EULER calculation. With this information the aerodynamic and consequently the acoustic results may be considerably improved.

4. Concluding Remarks

For low-speed BVI noise prediction using the linear thickness and loading terms of the FWH-equation the aerodynamic input is provided by the LBS-code, which is a singularity method for rotors in lifting forward flight and includes also thickness and loading. Compressibility for unsteady subsonic flow is included with restriction to linear theory. The loading term is calculated with the aid of the acceleration potential. The term is divided in two parts. One is similar to the source integral and the other is calculated by line integration along the paths of the singularities which are described by Beddoes prescribed wake model.

Looking at the details of the aerodynamic results discrepancies are still present. This is due to the wake model, the discretization and linearisation (angle of attacks, compressibility). Nevertheless the overall acoustic results are fairly good compared to experiment. The directivity characteristics and the BVI wave form are quite satisfactory represented.

For highspeed hover and forward flight acoustic calculation the transonic 3D perturbation field solution calculated with a 3D-EULER code has been used as input for the nonlinear quadrupole term of the FWH-equation which has been calculated in addition to the linear terms of the FWH-equation. The flowfield of a hovering rotor is calculated solving the EULER equation formulated in terms of the absolute flow variables in a blade attached coordinate system. The flowfield of a rotor in forward flight has been calculated with a time-accurate 3D EULER method using the Beddoes wake model.

Four different approaches to solve the quadrupole volume integral are compared for the hover case.

1. Solving the volume integral
2. Pre-integration normal to the blade in the original EULER-grid system.
3. Pre-integration normal to the chord after coordinate transformation.
4. Approximation using the surface quadrupole intensity and a relationship between this surface value and the pre-integrated quadrupole intensity.

Comparing the different results with experimental data it is validated that the expensive volume integral solution provides the best result. The amplitude is quite well predicted, but the resolution of the „saw-tooth“ noise signal shape should be improved by refined discretisation in the EULER calculation as well as in the acoustic calculation. With the approximations, especially with pre-integration after coordinate transformation the results are also quite satisfactory.

For the highspeed forward flight case the pre-integration after coordinate transformation was applied to reduce the computer effort. The comparison with experiment shows good agreement in inplane radiation direction, but less agreement in out-of-plane direction. This is mainly caused

by an underprediction of the unsteady loading contribution.

References

1. Boxwell, D.A., Schmitz, F.H., Spletstoesser, W.R. and Schultz, K.-J. : Model Helicopter Rotor High-speed Impulsive Noise: Measured Acoustics and Blade Pressures, 9th European Rotorcraft Forum, 1983, Stresa, Italy
2. Spletstoesser, W.R. , Schultz, K.-J., Bockswell, D.A. and Schmitz, F.H.: Helicopter Model Rotor Blade Vortex Interaction Impulsive Noise : Scalability and Parametric Variations, 10th European Rotorcraft Forum, The Hague, The Netherlands, 1984
3. Spletstoesser, W.R., Junker, B., Schultz, K.J., Wagner, W., Weitemeyer, W., Protosaltis, A. and Fertis, D.: The HELINOISE Aeroacoustic Rotor Test in the DNW- Test Documentation and Representative Results, DLR-Mitt. 93-09
4. Ffowcs Williams, J.E. and Hawkings, D.L.: Sound Generated by Turbulence and Surfaces in Arbitrary Motion, Philos. Trans. R.Roc London, Ser. A, Vol.264, pp. 321-342, 8 May, 1969
5. Farassat, F.: Theory of Noise Generation from Moving Bodies with an Application to Helicopter Rotors, NASA TR R-451, Dec. 1975
6. Brentner, K.: Prediction of Helicopter Rotor Discrete Frequency noise, NASA TM 87721, 1986
7. Schaffar, M., Haertig, J. and Gnemmy, P.: Computation of BVI Noise for the BO 105-Model Rotor in Forward Flight and Comparison with Wind Tunnel Tests, 47th AHS-Forum, Phoenix,
8. Spiegel, P., Rahier, P. and Michea, B.: Blade Vortex Interaction Noise: Prediction and comparison with Flight and Wind Tunnel Tests, 18th European Rotorcraft Forum, Avignon, France, 1992
9. Yu, Y.H., Tung, C., Gallmann, J., Spletstoesser, W.R., Schultz, K.J., van der Wall, B. Spiegel, P., Rahier, G., Michea, B. and Costes, M.: Aerodynamics and Acoustics of Rotor Blade-Vortex Interactions: Analysis Capability and its Variation, 15th AIAA aeroacoustics Conference, Long Beach, CA, 1993
10. Burley, C.L., and Tadghighi, H.: Importance of High Accuracy Blade Motion and Ailoads Prediction for Acoustic Analysis, 50th Annual Forum Proceedings, Vol. I, pp 25-44, Washington, DC, May 1994
11. Schultz, K.J., and Spletstoesser, W.R.: Prediction of Helicopter Rotor Impulsive Noise Using Measured Blade Pressures, 43th AHS Forum, St. Louis, Missouri, May 1987
12. Schultz, K.J. and Spletstoesser, W.R.: Measured and Predicted Impulsive Noise Directivity Characteristics, 13th European Rotorcraft Forum, Arles, France, September 1987
13. Prieur, J.: Calculation of Transonic Rotor Noise Using a Frequency-Domain Formulation, AIAA Paper 86-1901
14. Prieur, J., Costes, M. and Baeder, J.D.: Aerodynamic and Acoustic Calculation of Transonic Nonlifting Hovering Rotors, AHS Technical Specialists Meeting on Rotorcraft Acoustics, Philadelphia, 1991
15. Boxwell, D.A., Yu, Y.H. and Schmitz, F.H.: Hovering Impulsive Noise: Some Measured and Calculated Results, Vertica, Vol 3, pp 35-45
16. Schmitz, F.H. and Yu, Y.H.: Transonic Rotor Noise - Theoretical and Experimental Comparisons, 6th European Rotorcraft Forum, Bristol, 1980
17. Ianniello, S., Guy, G., Gennaretti, M. and de Bernardis, E: Validation of a New Code for the Prediction of Noise generated by Helicopter Rotors, 19th European Rotorcraft Forum, Cernobbio (Como), Italy, Sept 1993
18. Yu, Y.H., Lee, S. and Isom, M.P.: Rotor Highspeed Noise Prediction with a Combined CFD-Kirchhoff Method, 50th Annual Forum Proceedings, Vol. I, pp 103-113, Washington, DC, May 1993
19. Lyrantzis, A., Kilaras, M. and Xue, Y.: Transonic 3_D BVI Noise Using a Rotating Kirchhoff Formulation for Advanced Rotors, 50th Annual Forum Proceedings, Vol. I, pp 115-127, Washington, DC, May 1993
20. Baeder, J.D.: Euler Solutions to Nonlinear Acoustics of Non-Lifting Hovering Rotor Blades, 16th European Rotorcraft Forum, Glasgow, Scotland, Sept. 1990
21. Van der Wall, B.: An Analytical Model of Unsteady Profile Aerodynamics and its Application to a Rotor Simulation Program, 16th European Rotorcraft Forum, Amsterdam, The Netherlands, Sept. 1989
22. Lohmann, D. : Prediction of Ducted Fan Aeroacoustics with a Lifting Surface Method, DGLR/AIAA 14th Aeroacoustics Conference, Aachen, Germany, May 1992
23. Lieser, J.A., Lohmann, D. and Schultz, K.J.: Prediction of Rotor Aeroacoustics in Forward Flight by a Lifting Surface Method, 50th Annual Forum Pro-

- ceedings, Vol. I, pp 45-60, Washington,DC, May 1993
24. Ahmed, S.,and Vidjaja, V.: Unsteady Panel Method Calculation of Pressure Distribution on BO 105 Model Rotor Blades and Validation with DNW Test Data, 50th Annual Forum Proceedings, Vol. II,pp1211-1231, Washington,DC, May 1993
 25. Pahlke, K. and Raddatz, J.: 3D Euler Methods for Multibladed Rotors in Hover and Forward Flight, Paper No. C20, 19th European Rotorcraft Forum, Cernobbio(Como), Italy, September 1993
 26. Beddoes, T.: A Wake Model for High Resolution Ailoads, Int. Conf. on Rotorcraft Basic Research, Research Triangle Park,NC, 1985
 27. Yu, Y.H., Caradonna, F. X. and Schmitz, F.H.: The Influence of the Transonic Flow Field on High-Speed Helicopter Impulsive Noise, Paper 58, 4th European Rotorcraft and Powered Lift Aircraft Forum, Stresa, Italy, September 1978
 28. Jameson, A.; Schmidt, W.; Turkel, E. Numerical Solutions of the Euler Equations by Finite Volume Methods Using Runge-Kutta Time Stepping Schemes. AIAA-Paper 81-1259 (1981).
 29. Kroll, N. Berechnung von Strömungsfeldern um Propeller und Rotoren im Schwebeflug durch die Lösung der Euler-Gleichungen. DLR-FB 89-37.

Prévision du bruit externe des hélicoptères: les méthodes numériques vues par un industriel

Predicting Helicopter External Noise: Numerical Methods As Conceived by an Industrialist

François TOULMAY, Danielle FALCHERO, Gilles ARNAUD
EUROCOPTER, Département Aéromécanique
Aéroport de Marseille-Provence
B.P. 13, 13725-Marignane — Cedex
FRANCE

Résumé: les méthodes examinées concernent le bruit rotationnel des rotors, le bruit impulsif d'interaction pale/tourbillon, le bruit à grande vitesse, le bruit large-bande des rotors, les différents types de bruit de fenestron, et le bruit des turbomachines. Un bilan des points forts et des lacunes, illustré par des corrélations avec l'expérience, est établi en se plaçant du point de vue de l'hélicoptériste, c.à.d. en fonction des possibilités de prévision de la chaîne complète incluant le calcul des charges aérodynamiques instationnaires. De ce point de vue, le bruit de fenestron au point fixe et le bruit rotationnel des rotors sont prévus de façon satisfaisante, mais le calcul des charges en cas d'interaction n'a pas encore toute la précision requise. Les recherches concernant le bruit grande vitesse se poursuivent, et celles concernant le bruit large-bande nécessitent d'être reprises. Pour les turbomachines, l'hélicoptériste ne dispose d'aucune alternative à l'approche purement expérimentale.

Abstract: This paper investigates the methods used for rotor rotational noise, impulsive noise from blade/vortex interaction, high speed noise, rotor broadband noise, the various types of fenestron noise, and noise from the turboshaft engines. From the helicopter manufacturer's standpoint i.e. with respect to the prediction capability of the full chain of codes, including unsteady airloads calculation, an analysis of strengths and deficiencies is made and illustrated with experimental correlations. From this point of view, the fenestron in hovering flight and the rotational noise of rotors are both satisfactorily predicted, but in the event of interactions, the load calculation does not offer the full desired accuracy. Research regarding high speed noise is in progress and that regarding broadband noise must be resumed. As regards turboengines, there is no alternative to the experimental approach for the helicopter manufacturer.

Besoins de l'industrie et contexte scientifique

Depuis les premiers modèles produits en série, l'hélicoptère a conservé l'image d'un appareil remarquable à la fois par son aptitude au vol vertical et son agilité, mais aussi par son bruit si caractéristique et si peu harmonieux qu'il a pu être comparé à celui d'un hachoir ("chopper") ou d'une machine à battre. Malgré les évolutions techniques ayant conduit à un abaissement considérable du niveau sonore, telles que le remplacement des moteurs à piston par des turbomachines, ou les profils de pale optimisés en régime transonique, malgré l'entrée en vigueur d'une réglementation internationale contraignant les constructeurs à concevoir des hélicoptères moins bruyants (début des années 80), cette image négative persiste dans l'esprit du public. Sans doute la longévité des hélicoptères anciens et bruyants encore en service y contribue-t-elle, de même que la banalisation progressive de ce véhicule qui ne bénéficie plus beaucoup de l'attrait propre aux innovations aéronautiques.

Aussi, après avoir tiré parti des réductions de bruit résultant de la maturation naturelle du concept hélicoptère, les constructeurs s'engagent à présent dans une conception orientée spécifiquement par le souci de discrétion sonore, en acceptant délibérément une progression plus modeste voire une stagnation des performances. Le but est autant d'anticiper un éventuel durcissement de la norme internationale OACI (et du règlement FAA pour le marché américain) que de satisfaire à de multiples règlements opérationnels locaux qui tendent aujourd'hui à limiter très sévèrement les opérations et à rendre peu rentable l'exploitation des hélicoptères pour le transport civil dans de nombreuses zones d'importance économique cruciale.

Ainsi Eurocopter s'est fixé pour objectif de concevoir tous ses nouveaux modèles pour un niveau de bruit inférieur de 6 à 8 décibels à la norme OACI, alors que les modèles de la gamme précédente se situent déjà, pour la plupart, à un niveau très honorable de 3 à 5 dB sous cette norme. Il s'agit donc de diviser par un facteur deux la puissance acoustique émise ou, pour le moins, d'obtenir un résultat équivalent sur la perception auditive.

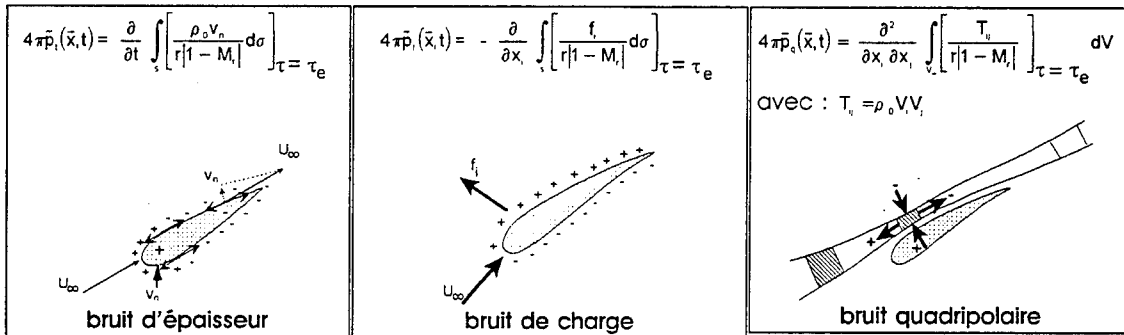


Figure 1: sources de bruit d'après la formulation FW-H

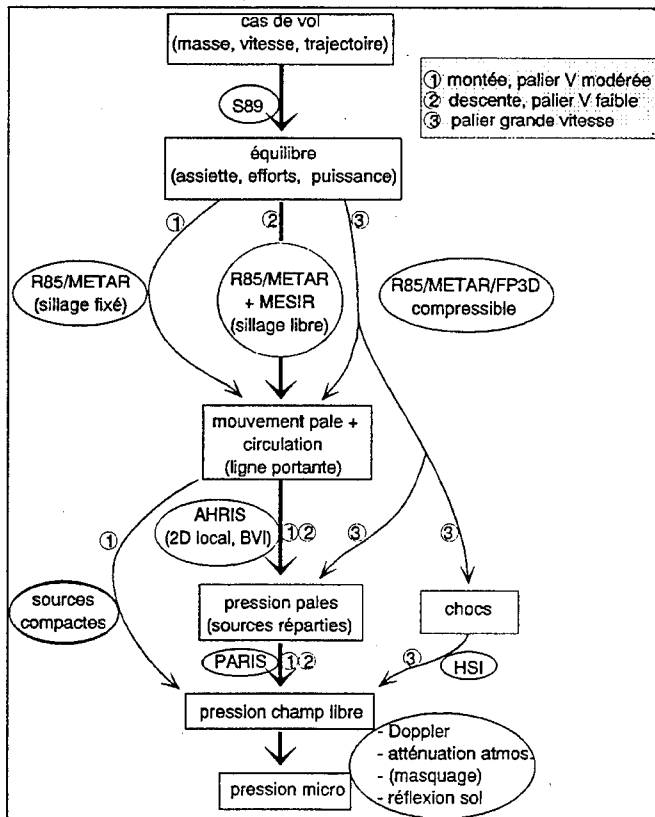


Figure 2: chaîne de calcul du bruit de rotor

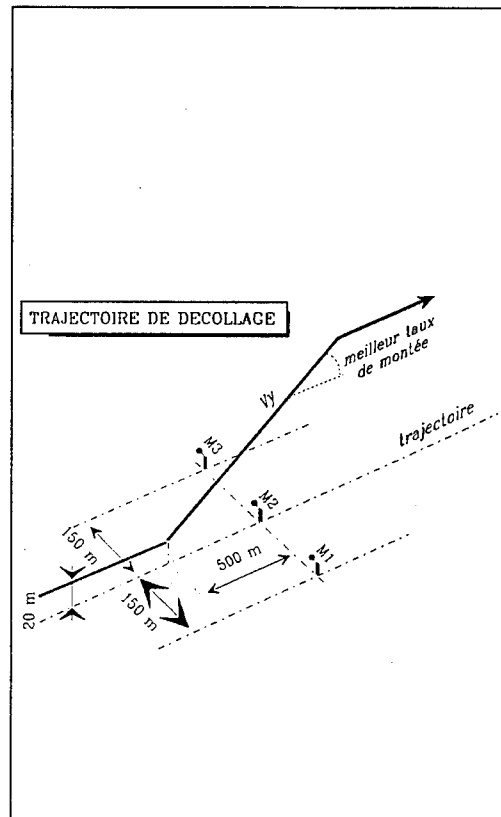


Figure 3: trajectoire de montée type OACI

Un tel résultat ne peut être obtenu sans conséquences inacceptables que grâce à une connaissance approfondie des mécanismes de génération et de propagation du bruit, et grâce à des outils de calcul permettant une prévision fine des phénomènes en jeu. L'application de règles simples du genre: "réduire la vitesse périphérique de 10%" risque en effet d'aboutir à des résultats acoustiques décevants, et de conduire à des appareils à la charge utile réduite et aux qualités de vol dégradées. Si la limitation de la vitesse périphérique fait certainement partie des moyens à employer pour atteindre l'objectif de discrétion, il doit s'accompagner d'un effort général concernant notamment la conception aérodynamique des rotors et l'installation motrice.

Fort heureusement, l'aéroacoustique est une branche jeune de la mécanique des fluides qui a bénéficié d'avancées théoriques spectaculaires depuis moins de 25 ans, le point de départ étant marqué, pour les voilures tournantes, par la publication de l'article des anglais Ffowcs Williams et Hawkins (réf. 3) en 1969. Utilisant les progrès accomplis parallèlement par l'aérodynamique, des méthodes numériques de prévision du bruit des rotors ont été mises au point et validées avec succès par différents organismes de recherche, notamment par la NASA et l'US Army aux USA (voir la synthèse récente de Brentner et Farassat, réf.40).

En France, l'ONERA et Eurocopter ont coopéré afin de mettre en place progressivement une chaîne de calcul complète du bruit rotor, intégrant la mécanique du vol hélicoptère, le calcul des charges aérodynamiques locales, la génération de bruit, la propagation atmosphérique et le post-traitement des spectres et des signaux acoustiques. Des travaux analogues concernant les fenestrons ont été menés avec l'Ecole Centrale de Lyon, tandis que les recherches concernant le bruit des turbomachines sont effectuées en liaison avec l'industriel Turboméca.

Même si de nombreux éléments manquent encore pour simuler complètement un hélicoptère, l'utilisation des outils existants permet dès à présent d'optimiser la conception des appareils du point de vue acoustique tout en préservant les performances de mission et l'efficacité économique du véhicule.

Sources de bruit

Pour un hélicoptère classique à turbines, les sources de bruit à considérer sont: les pales des rotors principaux et anticouple, et le(s) turbomoteur(s). Pour certains appareils de fabrication Eurocopter, le rotor anticouple classique est remplacé par un rotor caréné de faible diamètre appelé fenestron, qui génère également du bruit, mais par des mécanismes un peu différents, ce qui nécessite une modélisation adaptée. Etant donné les vitesses modérées atteintes par les hélicoptères, les bruits aérodynamiques produits par le fuselage et ses

appendices fixes s'avèrent négligeables par rapport à celui des parties tournantes.

Rotors

La modélisation du bruit des rotors fait appel à la théorie de l'analogie aéroacoustique due à Lighthill (réf.1). Elle permet, grâce à une habile manipulation des équations de Navier-Stokes, de traiter la propagation des ondes dans un champ aérodynamique quelconque comme si elle s'effectuait dans l'air au repos, le champ aérodynamique n'apparaissant dans l'équation linéaire de propagation que comme un terme source d'étendue spatiale limitée. Les travaux ultérieurs de Ffowcs Williams et Hawkins (FW-H, réf.3) ont conduit à remodeler l'équation de Lighthill de façon à exprimer plus commodément le terme source lorsque le champ aérodynamique est créé par des surfaces aérodynamiques imperméables de forme quelconque et subissant des mouvements arbitraires. La pression acoustique observée en un point extérieur à ces surfaces s'exprime alors comme la somme de trois termes intégraux (figure 1):

1. un terme dit monopolaire, qui ne dépend que de la vitesse de déplacement des surfaces, dans le sens de la normale. Quand les surfaces en question sont définies à partir de profils d'aile, ce terme prend le nom de bruit d'épaisseur et il est directement lié au volume de l'aile en déplacement
2. un terme dit dipolaire, qui ne dépend que de la répartition de charge sur les surfaces (pression et contrainte de cisaillement visqueux). Pour cette raison, il est également appelé bruit de charge
3. un terme dit quadripolaire, où interviennent les dérivées du tenseur de Lighthill et qui nécessite l'intégration sur tout volume du fluide où règnent de forts gradients de vitesse (cisaillements visqueux, chocs).

L'évaluation du bruit quadripolaire soulève des difficultés considérables car il suppose une connaissance complète de l'écoulement dans les couches limites et sillages (problème de modélisation de la turbulence) et autour des chocs, si chocs il y a dans le cas considéré. Le bruit de charge est souvent calculé en négligeant les contraintes visqueuses, de sorte que la pression à la paroi calculée par une méthode de potentiel relativement simple peut convenir pour l'évaluer, sous réserve d'une précision spatio-temporelle adéquate. Quant au bruit d'épaisseur, il peut être évalué facilement à partir du moment où la forme et le mouvement de pale sont connus avec précision.

Bruit rotationnel

En théorie, le bruit rotationnel englobe tous les types de bruit déterministes et périodiques dont le spectre se compose uniquement de raies de fréquences multiples

de la fréquence de rotation. Le langage courant, plus limitatif, regroupe sous le nom de bruit rotationnel l'ensemble formé par le bruit d'épaisseur et par le bruit de charge uniquement dans les basses fréquences c.à.d. celui produit par la composante stationnaire de la portance et par ses fluctuations lentes au cours d'un tour rotor (premiers harmoniques du spectre de Fourier). Compte-tenu de la faible vitesse de rotation d'un rotor principal, de l'ordre de 3 à 6 tours par seconde, et du faible nombre de pales (2 à 5), le bruit rotationnel tombe dans les fréquences les plus basses audibles par l'oreille humaine. Il est cependant important de savoir bien le calculer car l'énergie en jeu est importante, et les basses fréquences se propagent bien à grande distance, avec très peu d'absorption par l'atmosphère. Même faiblement perçu par l'oreille, c'est bien le bruit rotationnel du rotor principal qui confère à l'hélicoptère sa signature acoustique si particulière.

Pour le rotor arrière anticouple classique, les fréquences sont plus élevées à cause du faible diamètre, et son bruit est donc particulièrement gênant: sa sonorité est comparable à celle d'une hélice propulsive, mais avec un niveau heureusement plus faible grâce à sa charge au disque réduite. Le cas particulier du fenestron, qui relève de méthodes distinctes, sera traité plus loin.

La figure 2 montre la chaîne de calcul utilisée pour l'évaluation du bruit des rotors, qu'il s'agisse d'un rotor principal ou bien d'un rotor arrière classique. La première étape utilisant le code de simulation S89 consiste à simuler l'équilibre de l'appareil sur sa trajectoire afin de connaître les angles d'incidence et de dérapage, ainsi que efforts globaux s'appliquant aux différents rotors. A ce stade, il n'est pas nécessaire de connaître tous les détails de l'écoulement aérodynamique autour des pales, et l'on utilise généralement un modèle de vitesses induites simple tel que celui de Meijer-Drees. La puissance demandée au(x) moteur(s) est également calculée lors de cette simulation.

L'étape suivante consiste à évaluer, pour chacun des rotors, la répartition de la charge aérodynamique le long d'une pale, et ses variations au cours d'un tour. On suppose bien sûr que toutes les pales d'un même rotor se comportent de façon identique, et que les charges sont périodiques puisque l'on ne s'intéresse qu'aux cas de vol stabilisé. L'outil utilisé est le code de calcul rotor R85 (réf. 5, 6, 9), basé sur la méthode des éléments de pale et la théorie de la ligne portante. Les mouvements de la pale, y compris ses déformations élastiques, sont calculés de façon couplée avec les efforts aérodynamiques. Le sillage des pales est discrétisé par un réseau de tourbillons, et les vitesses induites par ce sillage sur les pales sont obtenues par la loi de Biot et Savart (sillage incompressible). Si l'on ne s'intéresse qu'au bruit rotationnel, ou si le cas de vol considéré ne donne pas lieu à des interactions tourbillonnaires trop intenses (vol de montée, ou vol en palier à vitesse modérée), la géométrie du sillage est prescrite en négligeant ses déformations (modèle

cycloidal) ou bien en utilisant un modèle de déformation empirique inspiré par les travaux de Landgrebe: sillage de type METAR (réf. 35, 7, 8, 9).

La répartition de la portance dans le sens de la corde, entre le bord d'attaque et le bord de fuite, peut-être évaluée de plusieurs façons: le code AHRIS (d'origine ONERA) effectue un calcul tranche par tranche de la pale, par une méthode 2D incompressible dans lequel les gros tourbillons les plus proches de la pale sont modélisés par des nuages de micro-tourbillons et convectés librement tout en se déformant (réf. 13). Pour les cas à vitesse élevée, une autre méthode consiste à coupler au calcul R85 un code 3D utilisant une formulation du type potentiel complet des vitesses (réf. 20), prenant donc en compte la compressibilité. Ce calcul couplé R85/FP3D, utilisé à l'ONERA, simule le sillage tourbillonnaire par une modification des conditions aux parois, ce qui constitue une approximation suffisante pour les cas de grande vitesse où le sillage passe loin sous les pales. Enfin, pour l'évaluation du seul bruit rotationnel, donc limité aux basses fréquences, on peut, en première approximation, se dispenser des calculs précédents en faisant l'hypothèse des sources compactes dans le sens de la corde (portance concentrée au quart avant des profils).

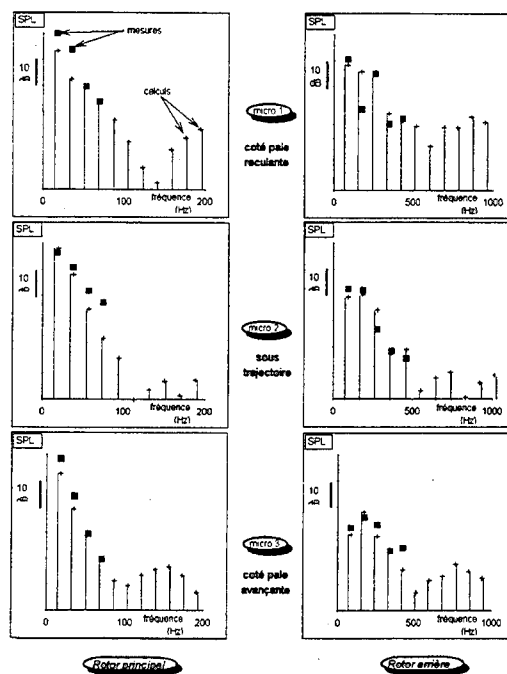


Figure 4: spectres des rotors du Super-Puma MK2 en vol de montée

L'étape suivante effectuée grâce au code PARIS (origine ONERA, réf. 13) consiste à intégrer le bruit monopolaire et dipolaire dans le domaine temporel à partir du mouvement des pales et des charges ainsi déterminées. Le point d'écoute étant supposé se déplacer à la même vitesse que le centre rotor, le signal de pression est périodique: il suffit de calculer le signal produit par une seule pale au cours d'un tour, puis d'y ajouter le même signal déphasé pour les autres pales de façon à reconstituer le bruit produit par le rotor complet. Ce calcul acoustique peut être répété pour de nombreux points régulièrement espacés sur la trajectoire, et pour une ou plusieurs positions de microphone.

Les figures 3 et 4 montrent l'application de la méthodologie décrite ci-dessus au rotor principal du Super-Puma AS332 Mark 2, pour un vol de montée de type certification OACI. Les spectres mesurés ont été obtenus par une analyse en bandes étroites autour de l'instant de bruit maximal (PNLT maximal) pour chacun des microphones. Le microphone n°1 est situé du côté de la pale reculante, le n°2 à la verticale sous la trajectoire, et le n°3 du côté de la pale avançante. Pour le rotor principal, fig. 4 à gauche, les quatre premiers harmoniques seulement ont pu être extraits avec précision du spectre mesuré. Le spectre calculé a été obtenu par un calcul aérodynamique du type sillage prescrit METAR, suivi d'un calcul de type AHRIS (sources réparties). Le résultat du calcul PARIS est corrigé de l'effet Doppler, de l'absorption atmosphérique, et de la réflexion au sol. On voit que le niveau des raies calculées est en général égal ou un peu inférieur à celui des raies mesurées, avec l'écart le plus important pour l'harmonique 4 du microphone n°2.

La figure 4 à droite montre une comparaison analogue pour le rotor arrière, et cela pour le même cas de vol. On constate ici une concordance plutôt meilleure que pour le rotor principal, avec notamment une estimation satisfaisante de l'importance relative des 5 premiers harmoniques sur les microphones n°2 et 3. En moyenne, le niveau des raies est bien prévu.

Dans ces comparaisons, il convient bien sûr de ne pas attribuer systématiquement tous les écarts au calcul en conservant à l'esprit l'inévitable dispersion des mesures: l'appareil en vol subit continuellement des perturbations et des corrections de pilotage, alors que le calcul fait l'hypothèse d'un vol parfaitement stabilisé. De plus, il faut rappeler qu'il s'agit d'un calcul totalement prédictif, c.à.d. basé uniquement sur la connaissance des caractéristiques de l'appareil, et sa trajectoire, sans possibilité d'ajustement au niveau des charges aérodynamiques sur les pales puisque celles-ci n'ont pas été mesurées.

Dans ce contexte, on peut considérer les résultats ci-dessus concernant le bruit rotationnel comme très satisfaisants.

Bruit d'interaction BVI

Lorsque l'appareil effectue une descente à vitesse modérée pour préparer son atterrissage, le disque rotor fonctionne avec un angle d'incidence légèrement positif, le souffle rotor repousse les tourbillons émis par les extrémités des pales, de sorte que ceux-ci passent pratiquement dans le plan de rotation et viennent couper la trajectoire des pales suivantes. Le bruit créé par les charges rapidement variables prend alors un caractère impulsif très caractéristique.

La figure 5a montre le lieu de toutes les interactions possibles d'une pale pour un rotor quadripale dans un cas typique de descente. Les chiffres indiquent le numéro de la pale ayant émis le tourbillon, la pale interactionnée étant la n°1 par convention (numéros croissants par ordre de passage dans une direction fixe). Ces interactions sont d'autant plus nombreuses que la vitesse est faible, et que le nombre de pales est plus grand. Mais toutes ces interactions possibles ne se traduisent pas par du bruit impulsif, car plusieurs conditions doivent se trouver réunies pour qu'un tel bruit soit perçu.

La première condition est que le tourbillon concerné se trouve sur la trajectoire de la pale ou à proximité immédiate, ce qui ne se produit que pour des combinaisons précises de vitesse et de taux de descente. La figure 5b montre une cartographie partielle de la charge aérodynamique sur le disque rotor dans le premier quadrant (secteur arrière, coté avançant). On voit que des fluctuations importantes de la portance se produisent en extrémité de pale dans trois secteurs différents: vers les azimuts 10°, puis 60 à 70°, et enfin vers 90 à 100°.

Une deuxième condition déterminant le bruit impulsif est que les ondes de pression émises par les différentes sections de la pale soient en concordance en phase. De façon schématisée (figure 6), on peut considérer l'interaction aérodynamique comme une source acoustique se déplaçant le long du tourbillon, lequel est quasiment immobile dans la masse d'air. Suivant la vitesse instantanée de la pale et l'angle formé entre la pale et le tourbillon, la vitesse de déplacement de la source peut être soit subsonique, soit supersonique. Si cette vitesse est subsonique (fig. 6a), il n'y a concordance de phase dans aucune direction d'écoute, et le bruit ne présente pas de caractère impulsif: la plupart des interactions possibles de la figure 5a se trouvent dans ce cas. Si la vitesse de l'interaction est supersonique (fig. 6b), alors on peut tracer un cône de Mach - ou du moins un petit tronçon de cône, car l'interaction apparaît et disparaît très vite. Dans le plan du rotor, il existe donc deux directions privilégiées de propagation vers lesquelles sont envoyées périodiquement des bouffées de bruit impulsif.

Ces directions de propagation du bruit impulsif, lorsqu'elles existent, sont reportées sur la figure 5c en fonction de l'azimut de la pale interactionnée. On constate que la propagation du bruit impulsif ne peut se produire que pour les interactions situés dans une plage d'azimut comprise entre 40° et 70°, ou bien entre

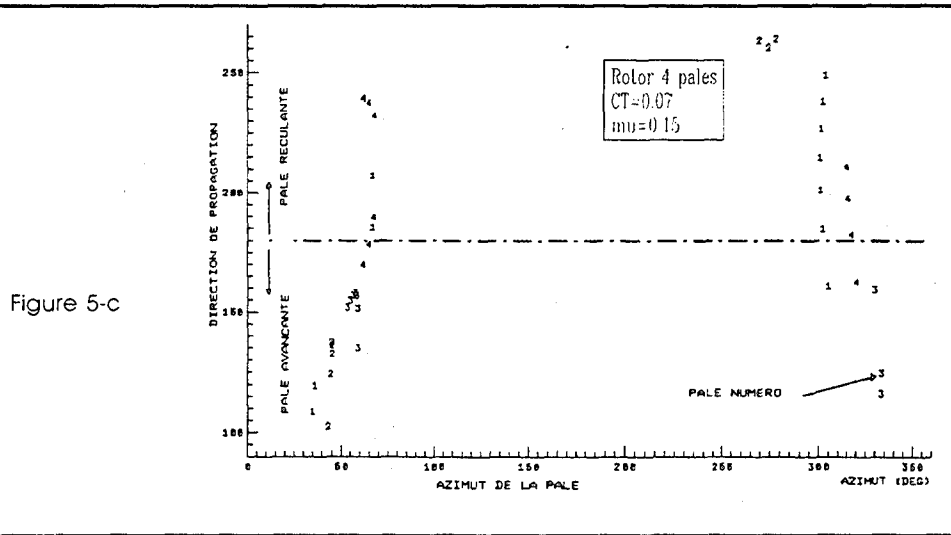
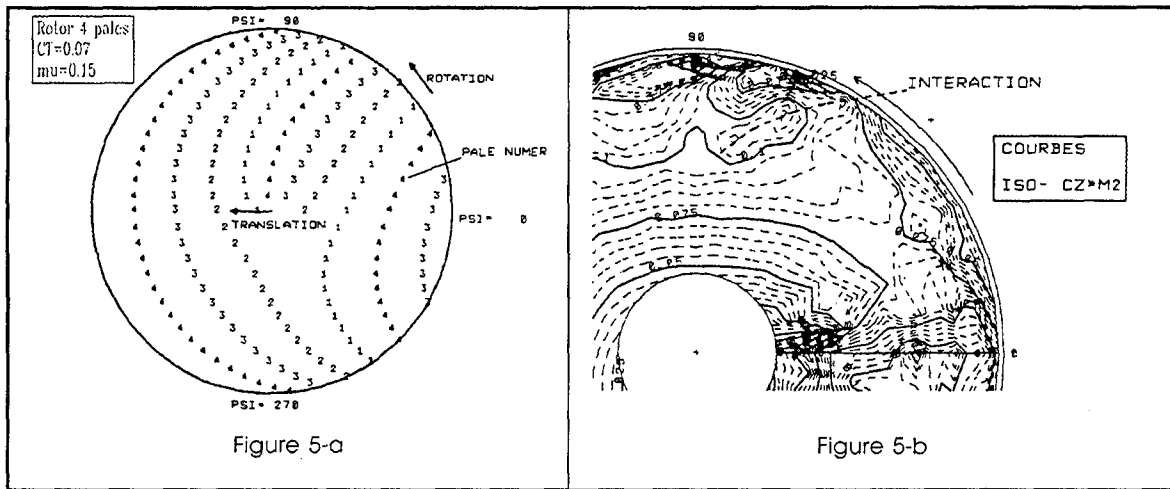


Figure 5: interactions BVI pour un rotor quadripale en descente,
(a) localisation, (b) charges, (c) propagation

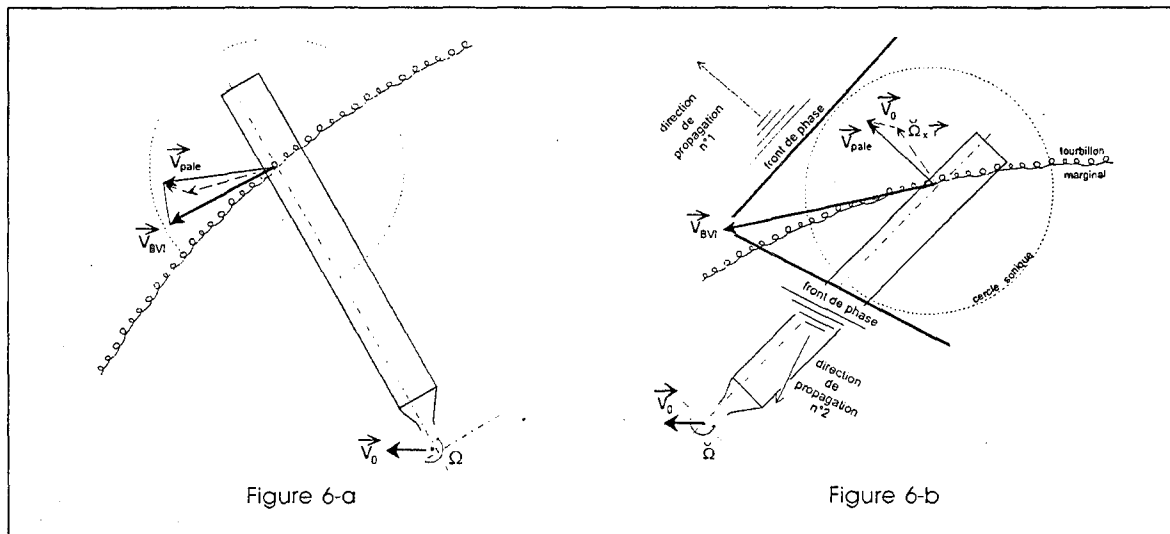


Figure 6: types d'interactions BVI, (a) non propagatives, (b) propagatives

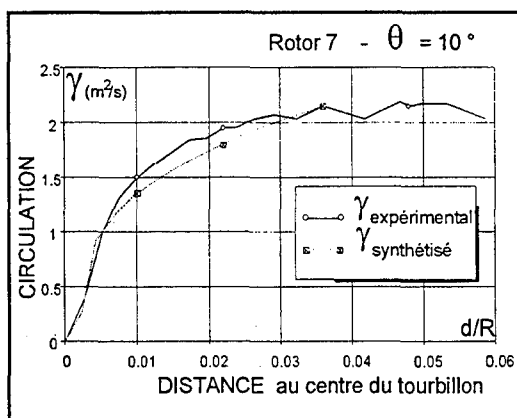


Figure 7: Répartition de circulation dans le tourbillon issu d'une pale rectangulaire (réf. 15)

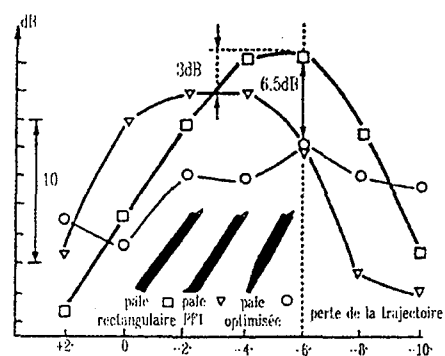


Figure 8: Bruit BV1 en descente, mesuré en soufflerie pour trois types de pales

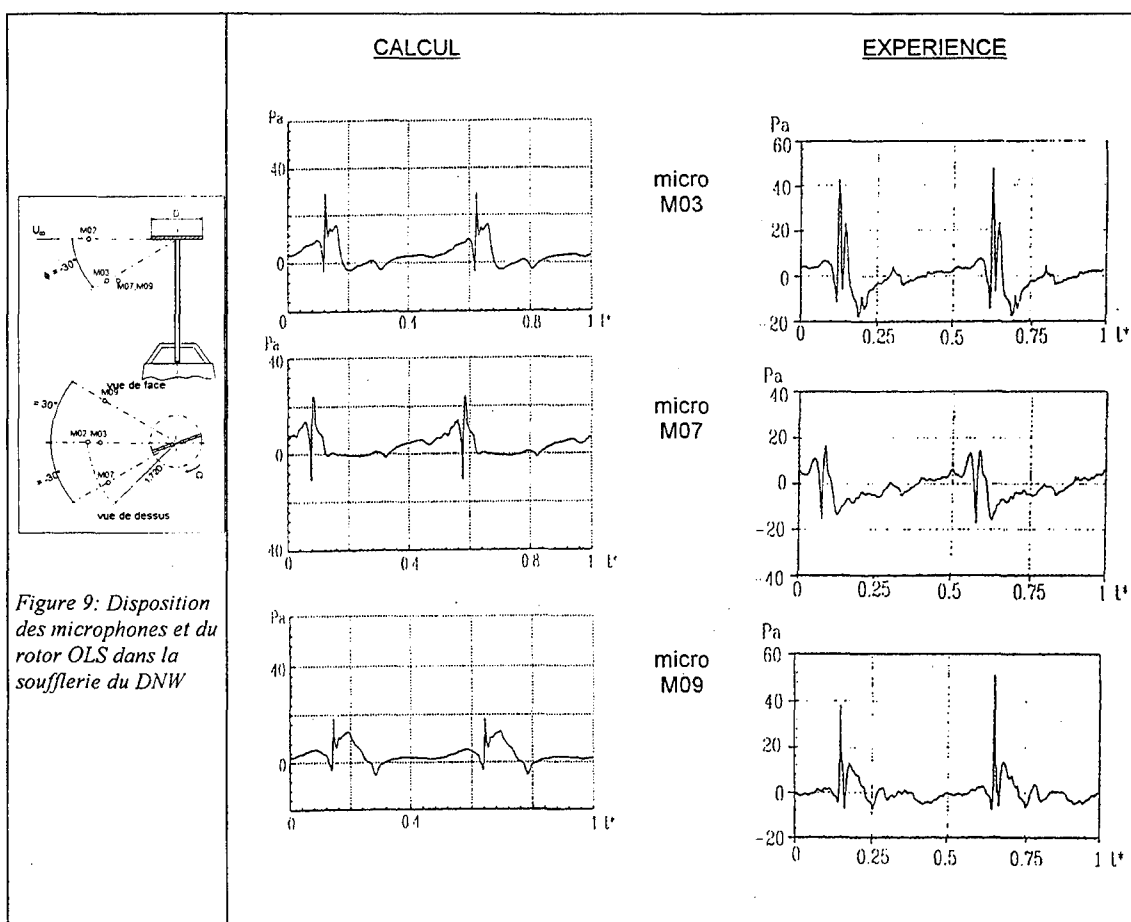


Figure 10: Signatures calculées et mesurées sur une configuration de descente

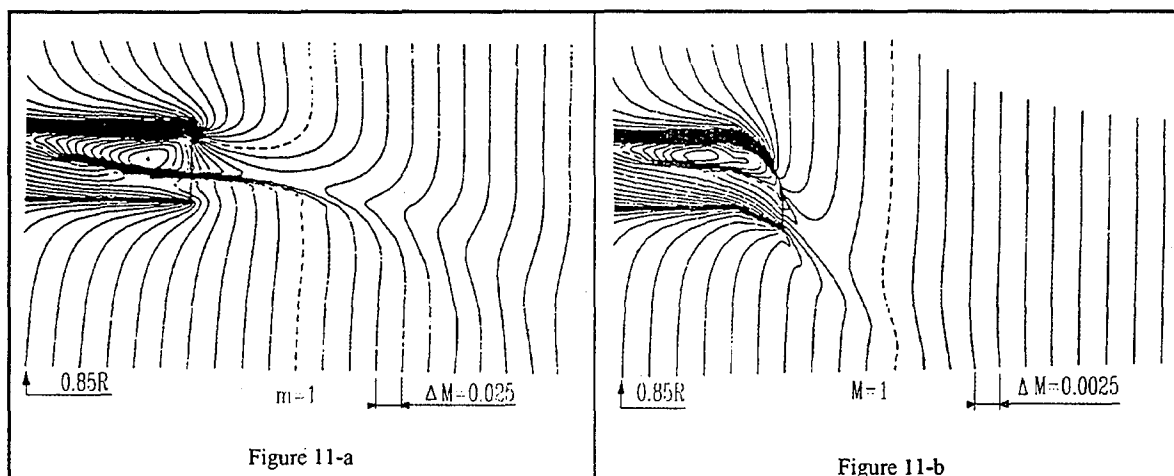


Figure 11: cartes de nombre de Mach, (a) pale rectangulaire, (b) extrémité de type PF2 (réf. 19)

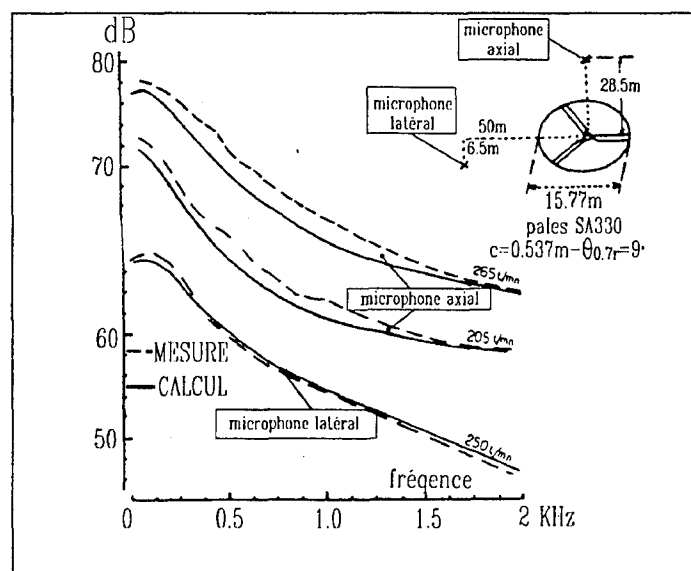


Figure 12: validation du modèle de bruit large-bande sur rotor au banc

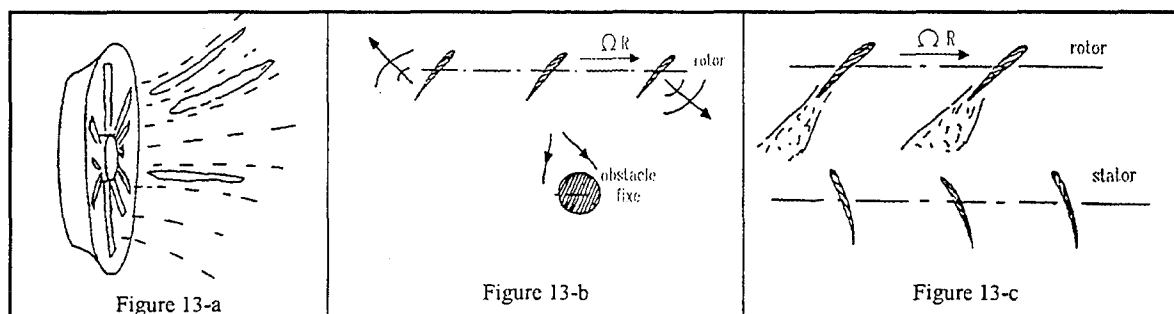


Figure 13: mécanismes de génération du bruit fenestron, (a) ingestion de turbulence, (b) charge du rotor due à un obstacle, (c) interaction du stator par le sillage du rotor

280° et 330°. Les plus gênantes sont celles qui se propagent vers l'avant de l'appareil, dans une direction proche de la trajectoire car elles sont alors perçues de façon répétitive et prolongée par un observateur au sol. Dans le cas étudié ici, seules les interactions provenant de la pale 1 (après environ 3/4 de tour) et de la pale 4 (après environ un tour) peuvent créer une gêne importante. Cependant, quelque soit le nombre de pales et la vitesse, les interactions qui sont propagatives se produisent toujours dans les mêmes plages d'azimut pour la pale interactionnée.

Pour quantifier le phénomène, il est essentiel de bien prévoir les variations de portance, donc de connaître avec précision la trajectoire des tourbillons, notamment la distance minimale entre pale et tourbillon au moment de l'interaction: on remplace alors le modèle de sillage prescrit METAR par le modèle de sillage libre MESIR (ONERA, réf. 11, 12, 13) dérivé du précédent par la mise en équilibre des tourbillons. Un autre code de sillage en équilibre avec calcul acoustique associé a également été développé à l'Institut Saint-Louis (réf. 36, 37). L'équilibrage du sillage, toujours très long et coûteux malgré l'utilisation des supercalculateurs, s'avère cependant indispensable pour prédire le bruit impulsif de type BVI.

Le diamètre du tourbillon et sa structure fine joue aussi un rôle essentiel dans l'intensité du phénomène: toutes choses égales par ailleurs, l'interaction sera d'autant plus brève et intense que le noyau du tourbillon sera de plus faible diamètre. La théorie de Betz (réf. 14) fournit certaines relations entre d'une part, la répartition radiale de vitesse dans le noyau tourbillonnaire et d'autre part, la répartition de circulation sur la pale à l'instant de son émission. Quelques études ont été consacrées à cet aspect du problème, en particulier celles effectuées par l'IMFM qui ont donné lieu à de nombreuses mesures pour différentes formes de pale. La figure 7 montre un exemple de telles mesures (réf. 15).

A Eurocopter, l'influence de la forme de pale sur la structure du tourbillon et sur le bruit BVI a fait l'objet d'essais en soufflerie anéchoïque, avec des résultats favorables notamment pour une pale effilée comportant une loi de vrillage particulière (figure 8, réf. 26, 16).

Les essais du rotor bipale AH1-OLS consistent un bon test pour toute la chaîne de calcul du bruit BVI. La figure 9 montre la disposition des microphones dans la soufflerie du DNW. Sur la figure 10, les signatures acoustiques calculées d'après les charges déterminées par l'ONERA (calcul MESIR, réf. 12), sont comparées aux signatures mesurées: recoupement satisfaisant pour le microphone n°7 situé du côté de pale avançante, mais les pics d'impulsivité sont sous-estimés pour les micros n° 3 et 9. Ces résultats ont été améliorés par l'ONERA avec les versions plus récentes des codes.

Si l'on rapproche ces résultats des très bonnes corrélations obtenues sur le même rotor par Schultz et

Spellstoesser (réf. 17) en utilisant les pressions mesurées sur les pales comme données du calcul acoustique, on peut conclure que le calcul des charges aérodynamiques constitue le maillon le plus faible de la chaîne de calcul. Mais pour un industriel qui utilise le calcul de façon prédictive afin de réduire le coût des essais, c'est la validité de l'ensemble de la méthode, incluant le calcul des charges, qui doit être évaluée.

Bruit grande vitesse

Les bruits mono- et dipolaire vont toujours croissant avec le nombre de Mach de l'hélicoptère, cependant on réserve l'appellation de bruit grande vitesse au bruit impulsif caractéristique qui apparaît au delà d'un certain seuil de Mach: il est généré par les ondes de choc prenant naissance en extrémité de pale en position avançante et les sources acoustiques correspondantes sont de type quadripolaire. Il a été démontré que le bruit grande vitesse ne devient propagatif que lorsque la poche supersonique à l'extrados s'étend au delà de l'extrémité de pale jusqu'au cercle fictif où le Mach d'entraînement atteint l'unité (cercle sonique): le rotor fonctionnant alors en régime de "délocalisation des chocs" (réf. 17).

En théorie, la prévision du bruit grande vitesse relève encore de la formulation de FW-H mais les difficultés pratiques sont très importantes: les sources quadripolaires se trouvent concentrées au voisinage des chocs, avec des non linéarités et de forts gradients dans l'espace et le temps que la résolution des calculs actuels ne permet pas d'approcher de façon satisfaisante. D'autres approches sont à l'étude, en particulier des formulations de type Kirchhoff où l'on utilise une surface cylindrique fictive englobant le rotor et toutes les non-linéarités de l'écoulement: un calcul arodynamique 3D particulièrement précis est alors utilisé pour déterminer les conditions aux limites sur cette surface. Des premiers résultats prometteurs ont été obtenus par l'ONERA avec une telle approche appliquée à un rotor non portant en vol d'avancement.

Du fait de ces difficultés, les méthodes de prévision du bruit grande vitesse restent pour quelques années encore du ressort des laboratoires de recherche. Dans l'industrie, on tente simplement de minimiser ce bruit en exploitant l'effet de certaines formes sur l'étendue et l'intensité des chocs. Toute forme qui permet d'augmenter le Mach de délocalisation peut être considérée a priori comme bénéfique. La figure 11 illustre par exemple l'effet favorable d'une mise en flèche de l'extrémité: pour un même nombre de Mach, on observe une délocalisation des chocs pour l'extrémité droite, délocalisation qui ne se produit plus pour la forme parabolique en flèche de type PF1 définie par l'ONERA (réf. 19, 20).

Bruit large bande

Le bruit rotationnel et les différents types de bruit impulsif examinés ci-dessus sont dits déterministes car ils sont générés par des écoulements aérodynamiques autour des pales parfaitement

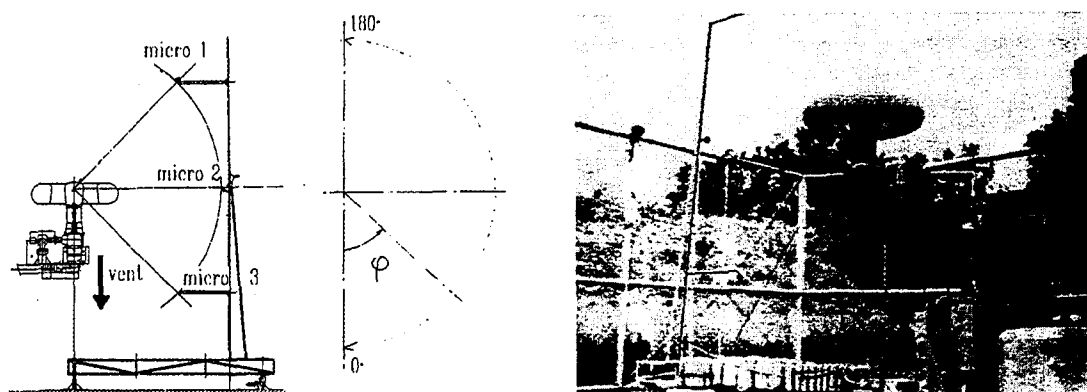


Figure 14: système de mesure de bruit au banc des fenestrons

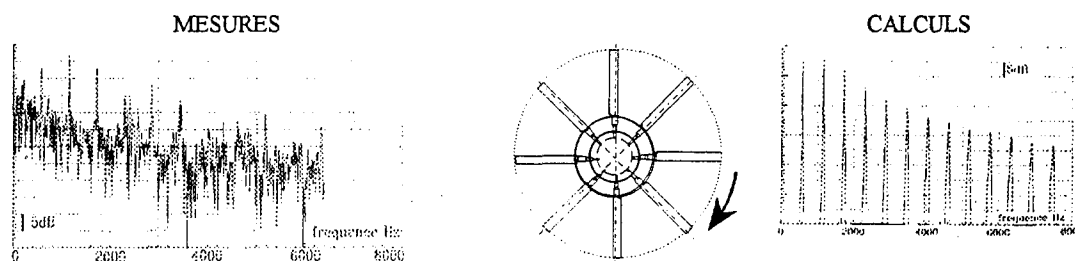


Figure 15: comparaison calcul/essai pour un fenestron non modulé

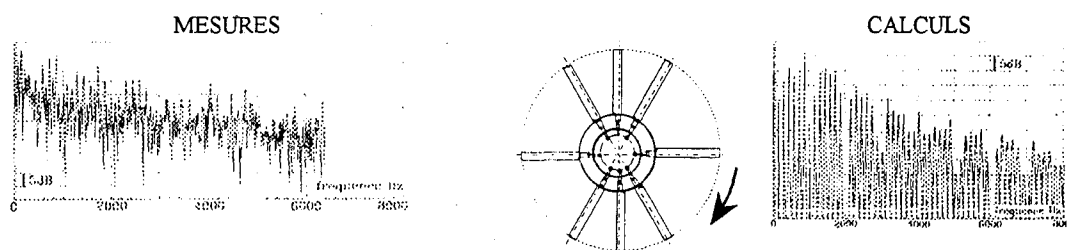


Figure 16: comparaison calcul/essai pour un fenestron à modulation de phase

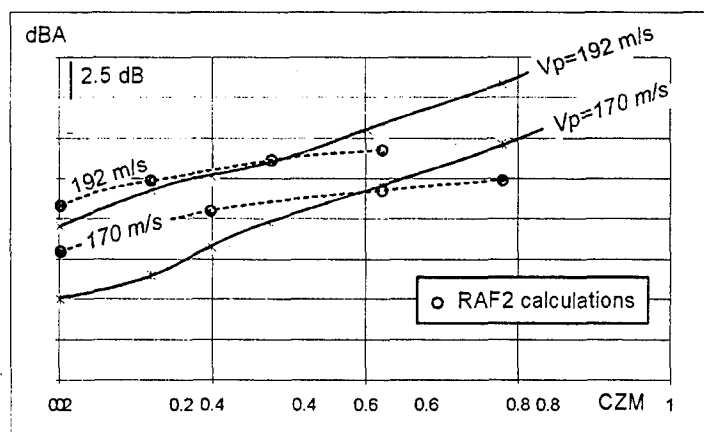


Figure 17: effet de la poussée et du régime sur le niveau de bruit du fenestron

périodiques. Dans le domaine fréquentiel, leur spectre est composé uniquement de raies.

Cependant l'examen des spectres expérimentaux révèle aussi un bruit à large bande issu des rotors qui trouve son origine dans les fluctuations aléatoires de pression à la surface des pales. De multiples phénomènes entrent en jeu: interaction avec la turbulence ingérée par le rotor, interaction avec la nappe tourbillonnaire interne, fluctuations turbulentes dues aux couches limites, effet de culot au bord de fuite, et mécanisme de formation du tourbillon marginal à la confluence des couches limites intrados et extrados. La fréquence centrale du bruit large bande, non corrélée avec la fréquence fondamentale du rotor, varie en permanence en fonction de la vitesse instantanée des profils.

Ce bruit prend d'autant plus d'importance que les bruits d'origine déterministe sont faibles, et c'est généralement en vol stationnaire ou en palier à vitesse modérée que l'on observe la plus forte part de bruit large-bande, atteignant alors un niveau de puissance du même ordre que celui des autres sources.

Plusieurs formules semi-empiriques anciennes permettent l'estimation du niveau et de la répartition spectrale de ce bruit pour une aile ou pour un rotor en translation axiale, notamment celles dues à Fink (réf. 21), à Wright, ou à Davidson & Hargest. Elles sont basées sur l'étude statistique d'un plus ou moins grand nombre de mesures acoustiques mais leur domaine d'application reste assez limité. Eurocopter, ex Aérospatiale DH, a développé depuis de nombreuses années une méthode basée sur l'étude de la similitude des spectres de pression à la paroi (réf. 22). La pale est discrétisée en corde et en envergure en fonction de la longueur de corrélation des fluctuations locales. Les spectres de puissance sont intégrés numériquement en tenant compte de la position du point d'écoute et des mouvements de rotation et de translation de la pale. On peut ainsi traiter des cas de vol très variés sans banque de données spécifique. La validité de cette méthode s'est avérée satisfaisante pour une série d'essais particuliers effectués au banc sur un rotor à pleine échelle (figure 12).

Du fait de l'aboutissement des recherches concernant les bruits rotationnels et impulsifs, l'étude du bruit large-bande, considérée comme plus ardue encore, avait été délaissée ces dernières années. La reprise de ces travaux semble nécessaire car le bruit de type large-bande reprend relativement plus d'importance lorsque les phénomènes impulsifs sont minimisés, notamment dans la recherche de procédures de vol à moindre bruit.

Bruit de fenestron

Le concept de fenestron est apparu en France à la fin des années soixante sur Gazelle, et tend depuis lors à se généraliser sur les appareils légers, essentiellement pour des raisons de sécurité (réf. 23, 24, 25, 26, 27). A

Eurocopter, les efforts de recherche ont d'abord été concentrés sur les aspects technologiques et sur l'amélioration de ses performances (réf. 23, 24). Plus récemment, la réduction de bruit est devenue un objectif majeur dans la conception des fenestrons, et ceci dès le stade de l'avant projet (réf. 26, 28, 29).

L'étude des mécanismes de génération de bruit propres au fenestron a débouché sur un code prévisionnel dénommé RAF, et développé à l'Ecole Centrale de Lyon (réf. 30, 31, 32). Plusieurs campagnes d'essais au banc ont fourni les données nécessaires à sa validation. Les récents essais d'un fenestron préfigurant celui de l'EC135 (réf. 28) ont confirmé les prévisions du code concernant l'influence sur le bruit de paramètres tels que la variation de régime, la position du redresseur, ou la modulation de phase du rotor (espacement non régulier des pales). A ce jour, ce code n'est utilisable que pour les configurations de vol stationnaire, ce qui constitue une aide à la conception déjà très substantielle. Son extension au vol d'avancement dépend en fait des progrès qui seront réalisés en aérodynamique pour la prévision des sillages turbulents (fuselage, rotor principal) et celle des interactions entre la carène et l'écoulement externe.

Les études ont suggéré, et les mesures ont confirmé, que trois mécanismes d'émission sonore dominant dans le bruit d'un fenestron (figure 13):

- l'ingestion de la turbulence atmosphérique qui provoque des fluctuations de charge sur les pales du rotor,
- le bruit des charges stationnaires et périodiques sur le rotor, comprenant notamment les charges impulsives dues à l'interaction avec les obstacles situés en aval (arbre de puissance, bras supports),
- le bruit des charges fluctuantes sur le redresseur (stator), lorsque le fenestron en est équipé. Ces fluctuations résultent du sillage des pales tournantes qui interagissent périodiquement avec les pales fixes.

La figure 14 montre le dispositif expérimental utilisé pour le fenestron.

Pour une configuration sans modulation de phase, c.à.d. avec huit pales régulièrement espacées, le spectre de puissance acoustique mesuré dans le plan de l'arbre de transmission et du côté amont apparaît sur la figure 15. Les harmoniques calculés par le code, de rang 8, 16, 24, ..., 8k, recoupent bien les mesures, surtout si l'on tient compte de la forte directivité propre à cette configuration. La décroissance des harmoniques à haute fréquence est particulièrement bien restituée.

La figure 16 montre une corrélation analogue pour le même rotor au même point de fonctionnement, mais avec une modulation de phase. Le spectre est beaucoup plus dense puisque les harmoniques 2, 4, 6, ..., 2k apparaissent à présent: la disposition des pales conserve en effet une symétrie d'ordre 2 pour des

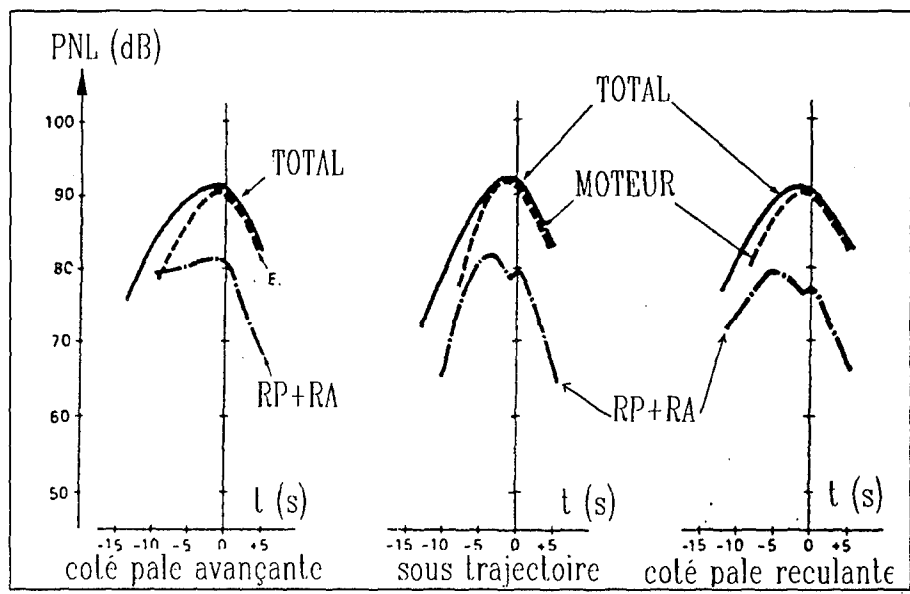


Figure 18: Analyse du bruit mesuré pour un Super-Puma Mark I en montée



Figure 19: banc de mesure acoustique des turbomachines (Sté Turboméca)

raisons d'équilibrage. Les raies émergent moins du niveau moyen, ce qui correspond à l'effet recherché visant à minimiser la gêne auditive des sons purs. Le niveau des raies est prévu de façon assez satisfaisante en général, avec cependant un harmonique 2 sous-estimé.

La figure 17 présente l'évolution du bruit du fenestron sans modulation en fonction du coefficient de portance moyenne des profils Czm et pour plusieurs régimes de rotation. Le microphone est situé à 45° du côté amont de la carène. On constate que le calcul surestime un peu le niveau aux portances faibles et modérées, puis tend à le sous estimer à forte portance. Ceci pourrait révéler une mauvaise estimation des charges aérodynamiques lorsque le décrochage commence à se manifester en extrémité de pale. Par ailleurs, l'effet du régime s'avère un peu sous-estimé.

Cependant il convient de souligner à nouveau que le bruit est calculé sur la base de charges aérodynamiques résultant elles-mêmes d'un calcul, plutôt que sur des charges mesurées. Il est probable que la connaissance des vraies charges améliorerait encore les résultats, mais une telle démarche ne serait pas conforme à une utilisation de type industrielle, qui vise à guider la définition et l'optimisation des appareils en minimisant le nombre et le coût des mesures.

Dans cette optique, on peut considérer que le code RAF remplit correctement son rôle. Les recherches se poursuivent dans le but de pouvoir calculer les charges aérodynamiques fluctuantes en vol de translation, et également, de prendre en compte l'effet de masquage et de diffraction créé par la carène pour les directions proche du plan de rotation.

Bruit des turbomachines

Certains auteurs ont souligné l'importance du bruit des moteurs pour les hélicoptères (réf. 10, 34). Concernant le Super-Puma Mark I, Damongeot (réf. 10) a analysé les enregistrements des vols de certification, et conclut que cette source de bruit domine largement le bruit rotationnel des rotors dans les phase de survol et de montée: figure 18.

Dans la perspective d'un modèle global de bruit hélicoptère, il importe donc de disposer d'un module turbomachine. Cependant la prévision par le calcul du bruit rayonné par tous les organes d'une turbomachine s'avère quasiment impossible par le fait que les nombreuses sources acoustiques sont confinées dans un circuit aérodynamique complexe et comportant des obstacles aux formes variées. Il n'appartient d'ailleurs pas à l'hélicoptériste de tenter une telle modélisation. L'approche utilisée à Eurocopter consiste simplement à transposer en vol les mesures faites au banc acoustique sur une turbomachine déjà développée.

Le motoriste Turboméca, en particulier, s'est équipé d'un banc spécialisé pour les mesures acoustiques

(figure 19) sur lequel il est possible de monter les capotages, l'entrée d'air et la tuyère conformément à l'installation motrice d'un hélicoptère donné. Les microphones sont montés sur un chariot mobile permettant d'explorer le champ sonore dans toutes les directions utiles pour la simulation d'un vol. Les données collectées à différents niveaux de puissance sont analysées par tiers d'octave, corrigées de la réflexion au sol et ramenées aux conditions atmosphériques standardisées.

Pour la simulation d'un vol, les fichiers ainsi constitués sont interpolés en un grand nombre de points de la trajectoire, en fonction du niveau de puissance et de la direction d'observation. Les spectres tiers d'octave sont ensuite décalés de l'effet Doppler, extrapolés en distance et corrigés de l'absorption atmosphérique. Si nécessaire, une réflexion sélective du sol peut être introduite. Le spectre est traité comme celui d'un bruit à large bande, à l'exception d'une ou deux raies de compresseur qui émergent et dont la fréquence est connue précisément. Pour les hélicoptères bimoteurs, on considère que les deux spectres ne sont pas corrélés, et l'on additionne simplement les puissances acoustiques, à moins que l'une ou l'autre des entrées d'air ou des tuyères ne soit masquée par le fuselage. Les spectres successifs, calculés toutes les 0,5 secondes, sont pondérés par les spectres précédents suivant les dispositions de la norme OACI (effet de traînage).

La figure 20a montre les spectres calculés pour le Super Puma Mark II en montée, à l'instant du bruit perçu maximal (PNLTmax): rotor principal seul, rotor arrière seul, moteurs seuls, et bruit total calculé. Le microphone considéré est situé du côté de la pale avançante. On constate que le bruit rotationnel des rotors domine dans les basses fréquences jusqu'à environ 300 Hz. Au delà, c'est le bruit des moteurs qui domine.

La figure 20b compare le bruit total calculé avec celui mesuré pour ce même microphone. Le bilan est le suivant:

- au dessus de 4000 Hz, c.à.d. dans les bandes où le bruit moteur domine, le niveau est surestimé. Un effet de diffraction par le fuselage, non pris en compte par le calcul pourrait expliquer cet écart,
- entre 300 et 4000 Hz, le niveau calculé est trop faible. L'absence du bruit large-bande des rotors dans ce calcul semble responsable du problème,
- entre 70 et 300 Hz, le niveau calculé correspond pour l'essentiel au rotor arrière, et s'avère correct,
- en dessous de 70 Hz, le niveau de certaines bandes laissées vides par le bruit rotationnel du rotor principal est cependant significatif dans le spectre mesuré. L'origine de cette énergie n'est pas élucidée.

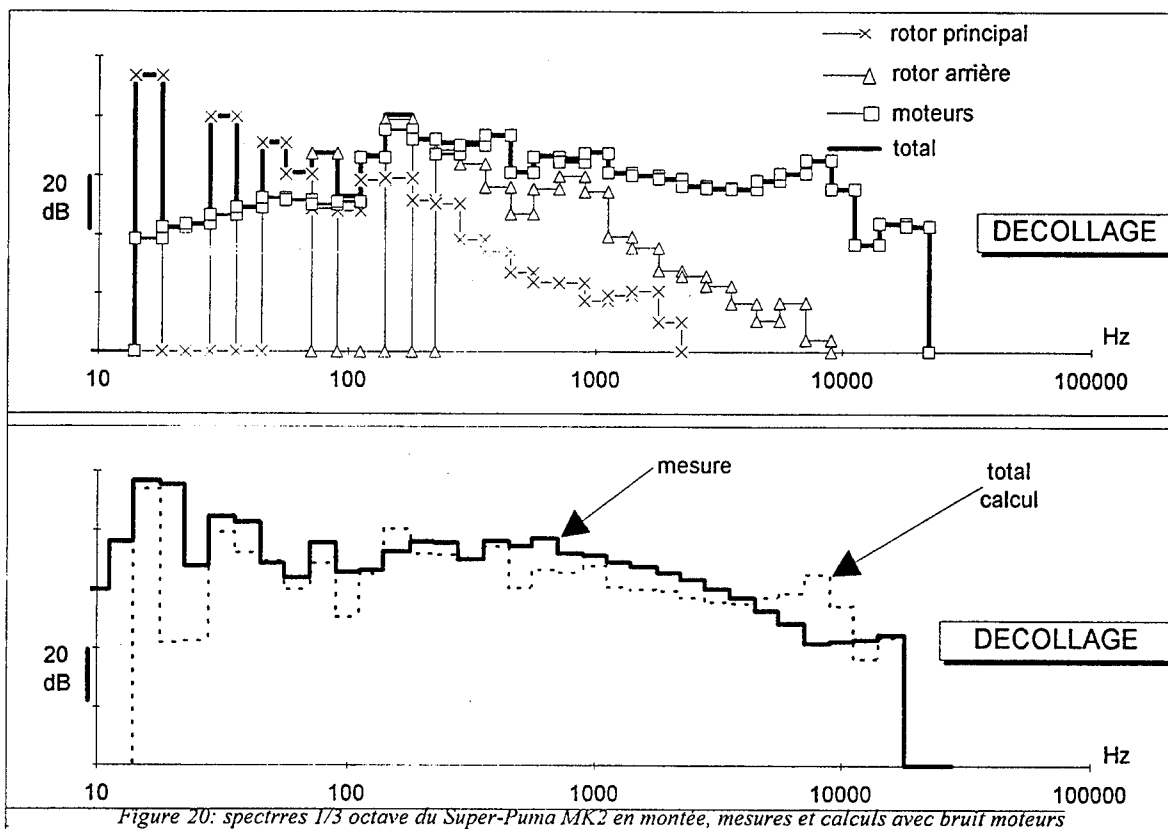


Figure 20: spectres 1/3 octave du Super-Puma MK2 en montée, mesures et calculs avec bruit moteurs

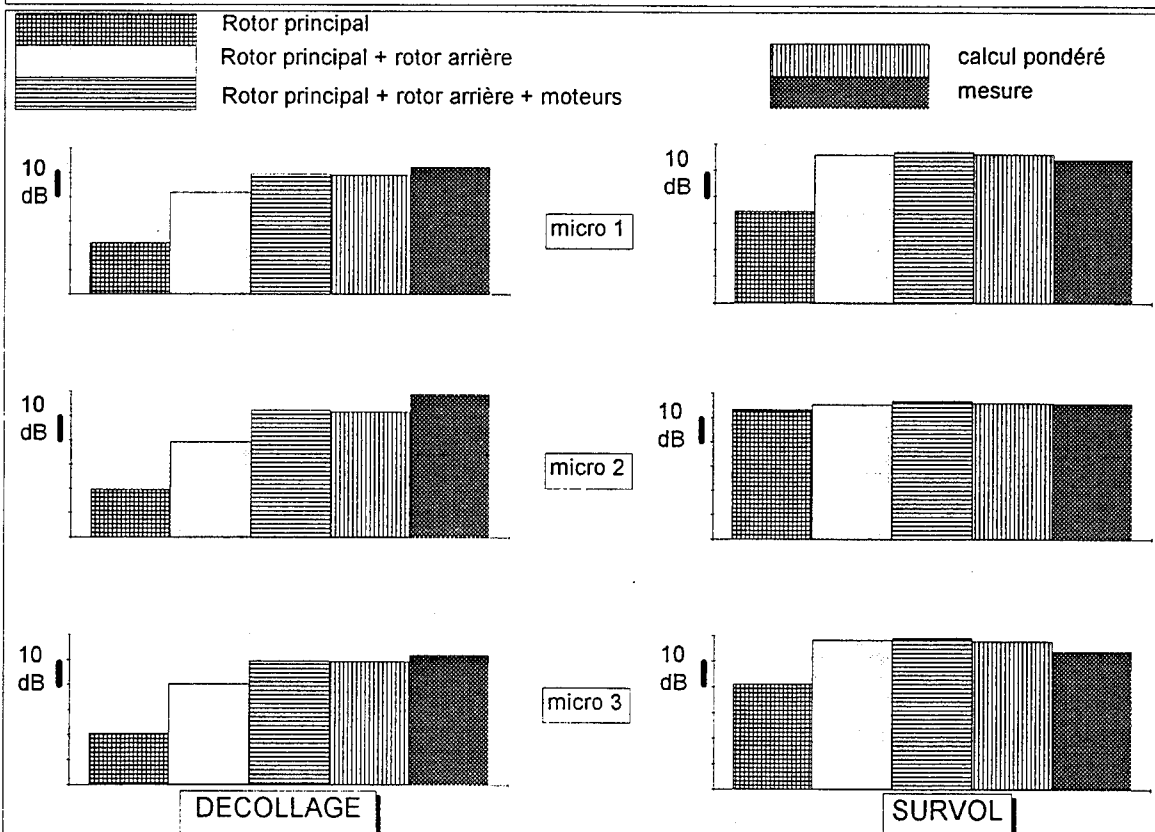


Figure 21: niveaux de bruit perçu en TPNdB à l'instant du PNL maximum mesuré du Super-Puma MK2 (21-a) en montée, (21-b) en survol

Les remarques ci-dessus se vérifient de la même façon sur les autres microphones, situés du côté pale reculante, et sous la trajectoire de l'appareil (non montrés ici).

Gêne auditive

Pour quantifier la gêne auditive provoquée par l'hélicoptère, on exprime le niveau global à un instant donné suivant la méthode du TPNL qui intègre les facteurs physio- et psychoacoustiques: réponse de l'oreille en fréquence et en amplitude, et correction de sons purs: certaines défaillances du calcul peuvent n'avoir alors que peu de conséquences en pratique.

Toujours pour le même cas de montée du Super-Puma Mark II, la figure 21-a montre comment évolue les niveaux sonores des trois microphones, en dB-PNLT c.à.d. avec les corrections de sons purs, lorsqu'on introduit progressivement les sources de bruit dans le calcul: d'abord le rotor principal seul, puis les deux rotors ensemble, enfin les deux rotors et les moteurs. Le niveau suivant reprend toutes les sources, avec la pondération par les spectres des instants précédents.

On constate que le bruit du rotor principal (bruit rotationnel uniquement) se situe à plus de 20 dB sous le niveau global: en l'absence de bruit impulsif, son spectre ne contient que des fréquences très basses, et sa contribution est quasiment négligeable.

Avec le rotor arrière, le niveau se situe encore 8 à 13 dB sous le niveau global. Le calcul prédit donc bien que la troisième composante, le bruit des moteurs, constitue la source dominante lors du passage au PNL maximal, pour la nouvelle version Mark II du Super-Puma comme pour la version antérieure Mark I (fig. 18).

La pondération par les instants précédents, qui sont d'un niveau plus faible, tend à abaisser légèrement le niveau pondéré. Ce niveau pondéré se situe à moins de 3 dB sous le niveau mesuré pour chacun des microphones, ce qui constitue plutôt un bon résultat. Malgré la surestimation du bruit des moteurs à haute fréquence, il manque de l'énergie dans la partie la plus sensible du spectre: probablement la part correspondant au bruit large bande des rotors.

La figure 21-b montre le même type de corrélation pour le cas de survol, calculé avec les mêmes codes. Le bruit total est cette fois un peu surestimé, notamment sur les microphones latéraux. L'analyse détaillée indique que le bruit de charge du rotor arrière est à l'origine de cet écart. La prise en compte des effets de compressibilité sur le calcul aérodynamique devra sans doute être améliorée pour y remédier.

Validation par l'écoute

Pour compléter l'analyse scientifique des spectres et des niveaux, et juger rapidement des forces ou faiblesses des méthodes, il existe un moyen direct: convertir les résultats numériques en signal audio, écouter et comparer aux enregistrements de vol. Ceci nécessite un traitement particulier, d'une part pour les bruits déterministes, et d'autre part pour les bruits large-bande.

Pour les bruits déterministes, les codes délivrent généralement un signal périodique pour une série de points se déplaçant avec le centre du rotor, donc mobiles par rapport au sol. Par une interpolation convenable dans l'espace-temps entre les points successifs de la trajectoire, on restitue le signal pseudo-périodique vu par le microphone fixé au sol, donc mobile par rapport au rotor.

Pour les bruits large-bande, le spectre de puissance est d'abord lissé et rediscrétisé en bandes fines de largeur constante. La phase de chaque bande est tirée au hasard, puis une FFT inverse permet d'obtenir un signal pseudo-périodique qui est ensuite traité de la même façon qu'un bruit déterministe.

L'interpolation assure la dopplérisation du signal, en faisant l'hypothèse d'une source acoustique ponctuelle. Un traitement additionnel permet d'intégrer au passage l'absorption atmosphérique et la réflexion sélective du sol.

Grâce aux auditions effectuées par cette méthode, on a pu vérifier concrètement l'importance du bruit des moteurs, et la difficulté à le restituer complètement.

Conclusions et perspectives

L'utilisation des calculs prévisionnels en milieu industriel a pour but d'anticiper le niveau de bruit d'un hélicoptère en projet, puis de le réduire avec un minimum d'essais. Les cas de validation examinés ici font apparaître les conclusions suivantes:

- le bruit rotationnel est bien maîtrisé, à la fois pour le rotor principal et pour le rotor arrière classique, en l'absence d'interactions: cas de Super-Puma en montée.
- le bruit impulsif d'interaction en descente, de type BVI, reste d'une prévision difficile car les charges aérodynamiques sont extrêmement sensibles aux conditions de vol. Les calculs avec sillage équilibré sont longs, et leur résolution doit être améliorée. La modélisation de la structure du tourbillon doit être raffinée pour les pales à extrémité non rectangulaire.
- la prévision du bruit impulsif à grande vitesse n'a pas atteint une maturité suffisante pour être appliquée dans l'industrie, mais des informations utiles pour le choix des formes de pale et de la

vitesse périphérique sont tirées des calculs tridimensionnels transoniques.

- le bruit large bande des rotors, qui contribue de façon non négligeable au bruit total dans certaines phases de vol, est particulièrement complexe. Sa modélisation peut cependant être abordée par des méthodes semi-empiriques, avec différents niveaux de raffinement. Une réactivation des recherches dans ce domaine est souhaitable.
- le bruit des fenestrons, avec ou sans modulation, est prédictible pour les cas de vol stationnaire, et les travaux se poursuivent pour étendre la méthode au vol d'avancement.
- le bruit des turbomachines, également très complexe, domine souvent dans le bruit total, notamment en montée. Pour l'hélicoptériste, son évaluation se borne à une transposition en vol de mesures faites au banc moteur: il ne s'agit donc pas vraiment d'une approche prévisionnelle.

A mesure que les méthodes atteignent une maturité suffisante, elles sont harmonisées et intégrées dans une chaîne de calcul qui permet des analyses composant par composant, ou bien l'évaluation d'un niveau global pour l'hélicoptère, ou encore l'écoute directe des signaux en simulation de vol. Grâce à ces méthodes, des améliorations acoustiques ont déjà été apportées sur la définition des appareils, avec notamment le fenestron équipant le EC135. Elles sont activement utilisées pour l'optimisation acoustique des appareils futurs, en coopération étroite avec les organismes de recherche, en particulier l'ONERA : programme ERATO pour le rotor principal, programme HELICOPTERE SILENCIEUX concernant l'ensemble du véhicule.

Remerciements

Les auteurs souhaitent remercier les chercheurs de l'ONERA, divisions OA et OP, pour leur contribution majeure à l'avancement des méthodes rotor, M. Roger (Ecole Centrale de Lyon) pour son travail concernant les fenestrons, ainsi que MM. Haertig et Schaffar (Institut Saint-Louis) pour les fructueux échanges qu'ils ont suscité. Les recherches d'Eurocopter-France sont soutenues financièrement par le STPA, la DRET et la DGAC.

Références

- (1) M.J. Lighthill, 1952, *Proceedings of the Royal Society, A221*, 564-587, On sound generated aerodynamically, general theory
- (2) M.W. Lowson, 1965, *Proceedings of the Royal Society, A286*, 559-572, The sound field of singularities in motion
- (3) J.E. Ffowcs Williams and D.L. Hawkins, 1969, *Philosophical Transactions of the Royal Society, A264*, pp 321-342, Sound generated by turbulence and surfaces in arbitrary motion
- (4) F. Farassat, 1975, NASA TR R-451, Theory of noise generation from moving bodies with application to helicopter rotors
- (5) M. Allongue, & T. Kryszinski, 1990, *43rd Annual Forum of the AHS*, Validation of a new general Aérospatiale aeroelastic rotor model through the wind tunnel and flight test data
- (6) M. Allongue, & T. Kryszinski, 1990, *27^{ème} Colloque d'aérodynamique appliquée, AAAF, Marseille*, Aéroélasticité appliquée aux rotors d'hélicoptères - validation et application du code R85
- (7) A. Dehondt, & F. Toulmay, 1990, *Vertica, Vol 14, N°4*, pp 573-585, Influence of fuselage on rotor inflow, performance and trim
- (8) W.B. Bousman, C. Young, N. Gilbert, F. Toulmay, W. Johnson, M.J. Riley, 1989, *15th European Rotorcraft Forum, paper 21*, Correlation of Puma airloads - lifting-line and wake calculations
- (9) G. Arnaud, B. Benoit, & F. Toulmay, 1991, *28^{ème} Colloque AAAF, Saint-Louis (France)*, Améliorations du modèle aérodynamique du code rotor hélicoptères R85 - validations et applications
- (10) A. Damongeot, F. D'Ambra & B. Masure, 1983, *39th Annual Forum of the AHS*, Towards a better understanding of helicopter external noise
- (11) B. Michéa, 1992, *thèse de doctorat de l'université de Paris 6, Mécanique des fluides*, Etude des sillages d'hélicoptère en vol d'avancement et leur influence sur les performances du rotor (Interaction pale-tourbillon)
- (12) B. Michéa, A. Desopper, & M. Costes, 1992, *18th European Rotorcraft Forum*, Aerodynamic rotor loads prediction method with free wake for low speed descent flight
- (13) P. Spiegel, G. Rahier, & B. Michéa, 1992, *18th European Rotorcraft Forum, paper 66*, Prediction of blade-vortex interaction noise: prediction and comparison with flight and wind-tunnel tests
- (14) A. Betz, 1932, *NACA TM 7-13*, Behavior of vortex systems
- (15) P. Plantin de Hugues, 1991, *thèse de doctorat de l'Université d'Aix-Marseille 2*, Etude du système tourbillonnaire généré en extrémité de pale d'un rotor d'hélicoptère en vol stationnaire
- (16) *Brevet français n°88-12188, publié le 23/11/1990*, Pale pour voilure tournante d'aéronef et voilure tournante comportant une telle pale (inventeur: A. Damongeot)

- (17) K.J. Schultz, & W.R. Spletstoesser, 1987, *43th Annual Forum of the AHS*, Prediction of helicopter rotor impulsive noise using measured blade pressures
- (18) Y.H. Yu, F.X. Caradonna and F.H. Schmitz, 1978, *3rd European Rotorcraft Forum*, paper 58, The influence of the transonic flow field on high-speed helicopter impulsive noise
- (19) J. Prieur, P. Lafon, M. Caplot & A. Desopper, 1987, *43rd Annual Forum of the AHS*, Aerodynamics and acoustics of rectangular and swept rotor blade tips
- (20) M. Costes & H.E. Jones, 1987, *13rd European Rotorcraft Forum*, Computation of transonic potential flow on helicopter rotor blades
- (21) M.R. Fink, 1978, *AIAA Journal*, Vol 18, N°10, Minimum on-axis noise for a propeller or helicopter rotor
- (22) A. Damongcot, 1980, *7^{ème} Colloque d'acoustique aéronautique*, Lyon, Bruit large-bande des rotors d'hélicoptères
- (23) R. Mouille, F. d'Ambra, 1986, *39th Annual Forum of the AHS*, The fenestron, a shrouded tail rotor concept for helicopters
- (24) A. Vuillet, & F. Morelli, *AGARD CP-423*, New aerodynamic design of the fenestron for improved performance
- (25) Ph. Roesch, 1990, *Royal Aeronautical Society, Conference on helicopter yaw control concepts*, London, The fenestron anti-torque concept
- (26) J.J. Philippe, & H.J. Marze, 1994, *Nouvelle revue d'Aéronautique et d'Astronautique n°2* (Dunod éd.), L'hélicoptère silencieux, un programme de recherches en cours, une réalité de demain
- (27) M.G. Clemmons, 1992, *48th Annual Forum of the AHS*, Antitorque safety and the RAH-66 fantail
- (28) M. Vialle, & G. Arnaud, 1993, *19th European Rotorcraft Forum*, A new generation of fenestron fan-in-fin tail rotor on EC135
- (29) M. Allongue, 1994, *La Recherche Aérospatiale*, éditeur ONERA, octobre 1994, Les recherches à Eurocopter pour réduire le bruit externe des hélicoptères (english edition also available)
- (30) F. Fournier, 1988, *thèse de doctorat de l'Ecole Centrale de Lyon*, Mise au point d'une méthode de calcul adaptée au bruit des fenestrons d'hélicoptères
- (31) M. Roger, 1994, *Acustica vol. 80*, pp 238-246, Sur l'utilisation d'un modèle de sillages pour le calcul du bruit d'interaction rotor-stator
- (32) M. Roger, 1994, *Acustica vol. 80*, pp 247-259, Contrôle du bruit aérodynamique des machines tournantes axiales par modulation de phase
- (33) P.E. Duncan, & B. Dawson, 1974, *Journal of Sound and Vibration Vol 33(2)*, pp 143-154, Reduction of interaction tones from axial flow fans by suitable design of rotor configuration
- (34) R.D. Janakiram, M.J. Smith, & H. Tadghighi, 1989, *AIAA paper 89-1147*, Importance of engine noise as a source of helicopter external noise
- (35) A.T. Egolf, & A.J. Landgrebe, 1983, *NASA CR-3726 & 3727*, Helicopter rotor wake geometry and its influence in forward flight (2 volumes)
- (36) P. Gnemmi, J. Haertig, Ch. Johé, 1992, *18th European Rotorcraft Forum*, paper 15, Validation of the ROTAC code for the rotor noise prediction
- (37) P. Gnemmi, 1993, *thèse de doctorat de l'Institut Franco-Allemand de recherches de Saint-Louis*, Contribution à la prévision du bruit rayonné par un rotor d'hélicoptère en régime subsonique
- (38) R.A. Golub, & D.S. Weir, 1987, *45rd Annual Forum of the AHS*, The prediction of the noise generating mechanisms of an Aérospatiale 365N-1 Dauphin helicopter
- (39) D.S. Weir, & R.A. Golub, 1989, *AHS specialists' meeting on aerodynamics and aeroacoustics*, The phase II ROTONET System
- (40) K. S. Brentner and F. Farassat, 1994, *Journal of Sound and Vibration*, 170(1), pp 79-96, helicopter noise prediction: the current status and future direction

ANALYSIS OF ROTOR FORCES IN A SHIP AIRWAKE

G. Syms
S.J. Zan

Applied Aerodynamics Laboratory
NRC Institute for Aerospace Research
Montreal Road, Bldg M-2
Ottawa, Ontario K1A 0R6
CANADA

SUMMARY

This paper examines the helicopter/ship dynamic interface by combining both experimental and numerical analyses. The flow field over the flight deck of a frigate model was mapped experimentally in a wind tunnel using both stationary and flying hot-film sensors. Using the velocity time-histories measured in the wind tunnel, a numerical representation of the airwake which shares the same spectral characteristics was generated. A blade-element model of the main rotor of a helicopter was then "flown" in this numerical airwake to determine the steady and unsteady loads acting on the rotor. The results of a set of test simulations indicate: 1) that an increase in unsteady rotor loads occurs when spatial cross-correlation functions are included in the generation of the numerical flow field; 2) that the fluctuating vertical velocity has a greater effect on the unsteady rotor loads than the fluctuating horizontal velocity; 3) that the spectra of unsteady forces and moments show similar broadband and resonant behaviour at different free-stream velocities.

LIST OF SYMBOLS

(x, y, z)	non-dimensional coordinate system
D	spectral matrix of white-noise sources
H	frequency response matrix of linear system
h_{ij}	transfer functions of linear system
n_i	white-noise source at location i
R_{ij}	turbulent velocity correlation tensor for velocity components i and j
S	spectral matrix of measured signal
(u, v, w)	velocity field
(x, y, z)	dimensional coordinate system of ship
w_i	unsteady vertical velocity at location i
*	conjugate transpose

1. INTRODUCTION

Helicopter flight onto and from the decks of non-aviation ships such as frigates can be considerably more difficult than the execution of the same manoeuvre on land. The helicopter is immersed in the unsteady airwake in the lee of the ship superstructure. This airwake contains significant gradients in mean wind speed and direction as well as increased turbulence intensities compared to those of the natural

wind. The mean flow gradients are associated with shear layers that arise due to flow separations from the superstructure. Considering the fact that a typical frigate superstructure is of the same geometric size as a helicopter rotor diameter, it could be expected that the mean flow gradients and unsteady shear layers both will alter the rotor performance, possibly increasing pilot workload. Furthermore the scale of turbulence shed from a superstructure will vary in size with characteristic dimensions less than or equal to the superstructure. Such eddies can also be expected to affect the rotor loads.

Analysis of the helicopter/ship dynamic interface is further complicated by the coupling of the rotor downwash and the airwake. Although sophisticated flight simulators are being developed for the helicopter/ship interface, complete numerical modelling of the coupled problem as part of a real-time simulation is beyond the realm of current capabilities [1]. At present, simulators permit "flight" of a helicopter through a prescribed turbulent flow field based on the premise that the rotor downwash and airwake are uncoupled. Such models provide estimates of rotor forces, which, when integrated with the helicopter equations of motion, can be used to estimate helicopter response in a given flow field.

In this investigation, such a numerical helicopter model is used to predict the steady and unsteady rotor loads arising from immersion of the rotor in the experimentally-determined wake of a generic frigate. The rotor loads are computed using the rotor module of the GENHEL computer code, which was acquired from the United States Naval Air Warfare Center through The Technical Cooperation Program (TTCP), Technical Panel HTP-6.

The goals of the investigation were: (a) to make detailed flow measurements in a wind tunnel of the airwake in the vicinity of a scale model of a generic frigate (obtaining both single-point and multi-point data); (b) to perform a parametric study to assess the degree of rotor detailing required in the numerical model; (c) to calculate mean and unsteady forces produced by a rotor in a suitably-scaled airwake based on the results of (a). Items (a) and (c) are discussed in this paper.

2. EXPERIMENTAL DETAILS

The wind tunnel measurements were carried out in the IAR 0.9m low-speed wind tunnel. A model of the lowest 50 meters of the atmospheric boundary layer was incorporated using the spire technique [2]. This model includes the correct variation of velocity with height, the correct variation of turbulence intensities with height, and reasonable representations of the length scales of turbulence in the boundary layer. For this experiment, the goal was to attain a wind tunnel flow simulation appropriate to a ship travelling at 10 knots into a headwind of 48 knots at 10 metres above sea level. Comparisons of the measured quantities with values expected in the atmosphere for rough sea conditions [3] are shown in Figures 1a and 1b. The mean profiles are in good agreement, although the turbulence intensities are slightly too large in the wind tunnel. This is not considered a serious problem since the development of the airwake would not be affected by small changes in intensity. In Figure 1, the $z = 0$ plane corresponds to sea level, whereas in all subsequent discussion the $z = 0$ plane corresponds to the flight deck.

A three-view drawing of the ship is presented in Figure 2. The geometric scaling of the wind tunnel model is 1:300. The frigate model has a superstructure loosely based on the Canadian Patrol Frigate. The Reynolds number of the experiment, based on the ship beam of 38.1 mm, is about 15×10^3 , in excess of the minimum of 11×10^3 recommended in [4]. The flight deck is clearly evident at the stern, and the bull's-eye thereon is the origin of the coordinate system used throughout the report.

The ship-model airwake was measured using TSI cross hot-film anemometers. A quartic function was used to describe the relationship between the cooling velocity and the probe output voltage.

Characteristics of the airwake were determined in three separate phases. In the first phase, the mean and root-mean-square (rms) values of u , v and w were determined over the region (Fig. 3):

$$\chi = -3/2, -2/2, -1/2 \dots 7/2;$$

$$v = 0, -1/8, -2/8 \dots -8/8;$$

$$\zeta = 4/6, 5/6, 6/6 \dots 12/6.$$

The region was surveyed twice; the second time with the probe axis rolled 90° from its orientation during the first survey, in order to measure the third orthogonal velocity component. Because the model was tested at zero yaw, measurements were made on the port side of the model only. Symmetry relationships were invoked to establish the flow on the starboard

side of the ship. These measurements, were made at a sample rate of 100 Hz per channel for 10.24 seconds.

In the second phase, measurements were made with a "flying" cross hot-film probe which can correctly obtain flow velocities in a reversing flow but is less effective elsewhere. The flying probe was used because it was recognized that some of the first-phase measurements would be made in a reversing flow, in which case a stationary probe produces misleading results. Only u -component data were obtained from the flying probe because v and w were too small to be resolved accurately. These flying-probe measurements were made over a region somewhat larger than the size of the separation bubble behind the hangar. In this way, a finite volume existed for which data were acquired with both the stationary and flying probes. By carefully examining both sets of data, it was possible to ascertain the boundaries of reversing flow and thus resolve the flow structure of the entire airwake. The details are described in [5].

In the third phase, measurements of cross-spectra and cross-correlations between various points in the flow were made by the simultaneous acquisition of data from two stationary cross-film probes. Only the streamwise and vertical velocity components were measured in this phase as it was thought that the unsteady rotor forces would be most influenced by these flow components. These data were acquired at a height of 9 meters above the deck, which corresponds to the "high hover" position. The locations of the measurement points in this plane are indicated in Figure 4. Measurements were made using a sample-and-hold A/D converter, so that no appreciable time lags would result in the data collected from different films. Such time lags would make accurate determination of cross-spectra and cross-correlations impossible. Data were collected at a sample rate of 2 kHz per channel for 15.36 seconds with a probe spacing of 15 mm, and for 20.48 seconds with a probe spacing of 30 mm. Because of the difficulty in obtaining flow-correlation characteristics at a point directly downstream of a reference point, the stencil of points used for the measurements was a regular grid rotated 45° with respect to the ship axis system. Again, advantage was taken of the symmetry of the geometry in establishing flow-correlation properties.

The data were reduced to full-scale values for presentation. The physics of bluff-body incompressible flow allows the experimenter to choose any two of the length, velocity and time scalings. The geometric scale was fixed at 1:300, the velocity scaling was chosen to be 1:6 and thus the time scaling defaults to 1:50.

The data presented are time-averaged values of the three velocity components and the turbulence intensities of the three velocity components. The turbulence intensities are defined as the standard deviation of the relevant component divided by the time-averaged value of the streamwise velocity at the same location. The velocity time histories recorded in the wind tunnel contain information on the statistical and probabilistic nature of the airwake. The experimental data indicated that the airwake velocities could be considered to be Gaussian.

3. NUMERICAL MODELLING

A. Numerical Airwake

Having collected the wind tunnel data, the next task is to use that data to create a numerical representation of the measured flow field through which the rotor will be "flown".

To numerically generate the unsteady velocity field, a set of independent white-noise sources $n_i(t)$ are filtered through a constant-parameter linear system $h_{ij}(t)$,

$$w_i(t) = \sum_{j=1}^N \int_0^T h_{ij}(\tau) n_j(t-\tau) d\tau$$

$$i = 1..N \quad (1)$$

where N is the number of points in the flow field and T is the maximum lag interval used in computing the correlations. Note that the unsteadiness of only one velocity component is recreated (either w or u), although the algorithm developed below is directly expandable to include all three components if suitable experimental data exist.

If the spectral functions of the white-noise sources, $n_i(t)$, are described by a constant diagonal matrix D , and a matrix S contains the auto- and cross-spectral density functions of the two-point correlation measurements, then the relation

$$D^{-1}S = H^*H \quad (2)$$

can be written, where S and D are known and H is as yet unknown. Equation (2) is an underdetermined system for the elements of H . If, however, it is assumed that H is lower triangular, then $D^{-1}S$ can be decomposed and written as a matrix multiplied by its conjugate transpose [6]. Having found H , it can be transformed into the time domain, thus generating the necessary transfer functions for

equation (1).

The linear system $h_{ij}(t)$, constructed from the spectral matrix H , will create a numerical velocity field with the same statistical properties as the measured airwake. Although no attempt is made to recreate the probabilistic properties of the experimental data, comparison of the probability density and cumulative distribution functions for the numerical and experimental velocity fields shows similar Gaussian behaviour.

The spectral matrix S contains the auto-spectral density functions for all the measured points along the diagonal. Off the diagonal are the cross-spectral density functions of the various pairs of points. An extremely large amount of data would be required to fill the entire matrix accurately. The experiment established the cross-correlation only between a given point and a collection of its neighbours. The stencil of neighbours was the same for all points in the plane and its application to one of the measurement locations is represented by the shaded circles of Figure 4. The remaining cross-correlations were set equal to zero. In the numerical model, this implies that the flow correlation lengths are less than a rotor radius. Spectra were calculated by first computing the appropriate correlation functions and then transforming them into the frequency domain. It is believed that a reasonable compromise was reached between the accuracy of the spectral matrix S and the amount of time required to gather the experimental data required to generate S .

In the language of statistical theory of turbulence, the above algorithm generates an unsteady flow field by computing an approximation to the three-dimensional second-order correlation tensor R_{ij} [7]. The current method treats only one of the diagonal terms since only one velocity component is computed, but as mentioned previously, all three components can be included and an approximation to the full tensor would result. Unlike other methods of simulating turbulence [8, 9], the current one does not require the assumptions of isotropy, homogeneity or a frozen flow field. The last assumption is unnecessary since the measured time histories provide information on the temporal effects on the correlation tensor. The dependence of the tensor on spatial location and separation (i.e. non-homogeneity and anisotropy respectively) is maintained through the discretization of the plane of high hover and the stencil of the two-point measurements. In summary, the presented method increases the accuracy of the numerical turbulent flow field by using the experimental data to generate the correlation tensor's spatial and temporal

dependence.

B. Computation of Rotor Forces and Moments

The numerical airwake computed in the previous section is used as input to the rotor simulation. The rotor simulated is that of a UH60A Black Hawk helicopter manufactured by Sikorsky Aircraft. The rotor module has been extracted from the full GENHEL code. This module computes the forces and moments on the main rotor given a prescribed helicopter centre of gravity motion, engine setting, control inputs and wind field. Adjustment of the control settings affecting the trim of the helicopter was limited to modifying only the collective pitch. Its value was adjusted so that the mean rotor thrust was approximately equal to the weight of the helicopter when the rotor was placed in the unsteady airwake at high hover. This set of control settings was used for all the simulations presented in this paper.

The rotor model used is derived from a blade-element analysis [10]. Of particular importance with respect to this simulation are the blade-element velocities from which the aerodynamic and inertial loads of the rotor are computed. The numerical airwake provides an increment to the three orthogonal components of the mean airspeed at the centre of gravity which is taken to be 30.9 m/s (or 101 ft/s) - the velocity the rotor would experience in the earth's boundary layer at a position equivalent to high hover. The mean flow field in the airwake is bi-linearly interpolated in the plane of measurement to the various blade-element locations. In addition, the time-varying velocities at the blade-element locations are computed first by generating them at the experimental measurement points using the convolution integrals of equation (1) and then interpolating them in time and space. The effect of the airwake has thus been included in the calculation of the blade-element velocities generating the rotor forces and moments in the presence of an unsteady airwake.

4. **THE AIRWAKE - RESULTS AND DISCUSSION**

A. Airwake Mean Velocities

Figure 5 presents the variation in the mean streamwise velocity component for several planes above the flight deck. The data presented have been converted to prototype scale. The boundary between the stationary-probe data and flying-probe data corresponds approximately to the boundary of the region for which reversing flow was detected. Inside the boundary,

reversing flow exists and thus only the flying-probe data is valid. The agreement across the boundary is excellent. It is evident that for lateral locations more than one beam away from the ship centreline, the ship has little effect on the flow field for the zero degree yaw case, in agreement with other IAR data [11]. Figure 5 indicates that the time-averaged u -component of the velocity is always in the direction of the free-stream. Measurements were not made close enough to the deck to detect the sign change in the mean value of the u -component.

The stationary probe was also capable of resolving the vertical and lateral velocities in the airwake. These velocity magnitudes were an order of magnitude smaller than those of the streamwise component [5]. Similar results were obtained by the Aeronautical Research Laboratory, Australia, examining full-scale measurements on an FFG-7 Frigate for a wind angle of 0 degrees [12]. For both the lateral and vertical velocity components, the largest magnitudes were found on the boundary between the regions where the stationary- and flying-probe data were valid. Thus the possibility exists that the largest lateral and vertical components of velocity exist within the region of reversing flow and thus were not determined; however, it is unlikely that the magnitudes are significantly greater than those that were measured.

B. Airwake Turbulence Intensities

Measurements of the streamwise turbulence indicated that the region of increased turbulence over that in the natural wind is contained, approximately, directly above the flight deck, extending vertically about one hangar height above the top of the hangar. Upstream of the bull's eye and below the top of the hangar, the mean speeds are approaching zero and the streamwise intensities approach 300% [5].

Measurements of the lateral turbulence indicated that the airwake intensities are comparable in magnitude to the streamwise intensities in regions where the stationary-probe data is valid [5]. This observation, supported by the measurements of [4], makes the airwake distinct from the natural wind, wherein the streamwise intensities are generally double those of the lateral and vertical winds. It was not possible to resolve the lateral or vertical velocity components within the region of reversing flow, so intensities were not determined in this region. However, considering the fact that the streamwise and lateral intensities are of similar magnitude away from reversing flow, it would not be unexpected to find similar lateral turbulence intensity magnitudes in the reversing flow, i.e.

up to several hundred percent based on a local mean velocity.

The variation in vertical turbulence intensities over the flight deck is also presented in Figure 5. The intensities are again normalized on the local mean streamwise velocity. The highest levels of intensity are found closer to the deck. Unfortunately, the highest levels occur in the reversing flow region, where measurements could not be made with confidence. Since the vertical intensities are of the same magnitude as the streamwise and lateral intensities, magnitudes of several hundred percent could again be expected upstream of the bull's eye ($x = 0$) for heights below the top of the hangar.

Spectra of the measured and computed vertical velocities determined at high hover directly above the centre of the flight deck are presented in Figure 6. The spectra are presented at prototype scale. At the higher frequencies, the spectra have a slope of $-5/3$, consistent with all turbulence spectra in the inertial subrange.

5. ROTOR SIMULATION - RESULTS AND DISCUSSIONS

A. Numerical Airwake

The first step in the simulation of the rotor in the airwake was the generation of a numerical representation of the experimentally measured flow field. This involved creating and decomposing the spectral matrix S .

The matrix S consists of the auto-spectral density functions along the diagonal and the measured cross-spectral density functions off the diagonal. When the experimental spectra were combined in S , scatter in the magnitudes of the spectral estimates at low frequencies formed a matrix which was not always positive-definite and thus could not always be decomposed. In each spectra, the low frequencies are the least accurate because of the limited amount of averaging done at the long lag intervals when computing the autocorrelation. A filter thus had to be applied at the low frequencies to ensure positive-definiteness. The effect of this filter on the velocity spectra can be seen in Figure 6. The agreement between the spectra is quite good throughout the frequency range of interest with a deterioration due to the filter evident at the low frequencies. Longer experimental time histories and/or a more accurate method of computing the elements of the matrix should eliminate the need to use a filter.

B. Rotor Forces and Moments

Having obtained a numerical representation of the airwake of a frigate, the numerical helicopter rotor can be "flown" through it. The simulations produce time histories of the unsteady rotor forces and moments which can then be analyzed in the time or frequency domain.

Using the stationary hot-film measurements, steady rotor loads can be computed over a larger domain than simply a plane at high hover. To this end, the rotor was placed in various horizontal planes (with the rotor hub remaining over the origin on the flight deck) to determine the effect of elevation on the mean rotor forces and moments. Figure 7 shows this effect on the Z-force (the vertical force in body axes) and the rolling moment. The solid line shows the response of the rotor to the steady airwake while the dashed line shows the response without the airwake but still including the vertical variation of free-stream velocity in the atmospheric boundary layer. (It must be remembered that the control settings were not modified between simulations.) It can be seen that as the rotor rises out of the airwake, its response approaches that in the free-stream. This trend is relatively smooth due to the fact that these horizontal planes lie above the fluctuating shear layer separating from the hangar deck.

The numerical representation of the airwake includes the spatial variation of three components of the mean flow field in the plane of high hover as well as the temporal variation of one velocity component. Four test cases were run which systematically varied specific flow-field characteristics to examine their effect on the rotor. Three test cases were run with the w velocity component being computed as unsteady since it was believed that this component would have the greatest influence on the rotor [13]. The fourth test case was run with an unsteady u -component instead to examine that assumption.

Of the three test cases run with a fluctuating w -component, one was run with the full spectral matrix S decomposed into its associated frequency response functions. The next case had all the off-diagonal terms in S set to zero to isolate the rotor's response to the auto-spectra. In the final w case, the measured velocity field was scaled by a factor of $2/3$ to decrease the free-stream velocity to 20.6 m/s while maintaining the same turbulence intensities and cross-spectral information and using the full matrix.

The results from these four simulations can be found in Table 1 and Figure 8. Table 1 contains the means and standard deviations of all the

Force (N)	W Unsteady (Full Matrix)		W Unsteady (Diagonal Matrix)		U Unsteady		W Unsteady (20.6 m/s)	
	Mean	Std Dev	Mean	Std Dev	Mean	Std Dev	Mean	Std Dev
X	2082	211	2075	154	2076	80	2771	154
Y	-1477	137	-1479	116	-1470	39	-1179	88
Z	-59820	2710	-59744	1863	-59594	646	-54625	1748
Moment (N.m)								
Roll	-6880	1058	-6905	873	-6891	216	-5348	764
Pitch	22951	1515	22960	1149	22841	671	17095	965
Yaw	24557	574	24644	418	25200	193	25867	314

Table 1: Mean and Standard Deviation of Rotor Forces and Moments for Various Test Cases

rotor forces and moments for each case. Again, it must be noted that the collective pitch was the only control input set before all the test cases were run. Notably then, the cyclic pitch was not altered from a nominal trim setting in free-stream conditions. These results show that the omission of the off-diagonal terms reduces in magnitude the unsteady response of the rotor while maintaining the mean forces and moments. A reduction of the standard deviations but not the means also occurs when the u -component is made to fluctuate instead of the w -component. This supports the belief previously stated that the w -component is more important in these rotor simulations. Finally, the effect of decreasing the free-stream velocity simply decreases the mean and standard deviation of the forces and moments.

The unsteady response of the rotor for the four test cases can be examined in the frequency domain. Figure 8 contains the auto-spectral density functions of the Z-force and rolling moment. Information on the other forces and moments can be found in [5]. The rotor responds to the turbulent velocity field in a resonant manner at four different frequencies: 5.2, 17.3, 34.5 and 48.6 Hz. The fact that these frequencies are unchanged when the free-stream velocity is altered indicates that these are structural modes.

6. CONCLUSIONS

This paper has described a combined experimental and numerical approach to determining the steady and unsteady loads produced by a rotor in a ship airwake. The airwake, which was numerically generated based

on experimental data, was input into a numerical model of a flying rotor. The mutual interaction between the spinning rotor and the flow field was not modelled. The following conclusions are drawn from this investigation.

- 1) Turbulence intensities of several hundred percent are present in the reversing flow region behind the hangar and above the flight deck. The intensities are roughly equivalent for all three velocity components.
- 2) The incorporation of airwake cross-spectral information into the turbulence modelling leads to increased rotor responses over those determined in the absence of cross-spectral information.
- 3) The fluctuating vertical component of velocity has a greater effect on the unsteady rotor loads than does the fluctuating streamwise component of velocity.
- 4) If the free-stream wind speed is reduced, the mean and unsteady rotor loads are reduced in magnitude, although the shape of the spectra remain essentially unchanged.

7. REFERENCES

- [1] Clement, W.F., Gorder, P.J. and Jewell, W.F. "Development of a Real-Time Simulation of a Ship-Correlated Airwake Model Interfaced with a Rotorcraft Dynamic Model", AIAA/AHS Flight Simulation Technologies Conference, August 1992. AIAA-92-4149-CP.

- [2] Irwin, H.P.A.H. "Design and Use of Spires for Natural Wind Simulation" NRC-NAE-LTR-LA-233, 1979.
- [3] Cook, N.J. "The Designer's Guide to Wind Loading of Building Structures - Part 1", Butterworths, London, 1985.
- [4] Healey, J.V. "Establishing a Database for Flight in the Wakes of Structures", Journal of Aircraft, vol. 29, no. 4, pp. 559-564, Jul-Aug 1992.
- [5] Zan, S.J. and Syms, G. "Numerical Prediction of Rotor Forces in an Experimentally-Determined Ship Airwake" NRC-IAR-LTR-AA-15, To be published.
- [6] Dodds, C.J. and Robson, J.D., "Partial Coherence in Multivariate Random Processes", Journal of Sound and Vibration, 42(2) 1975.
- [7] Hinze, J.O. "Turbulence", McGraw Hill, New York, Second Edition, 1975.
- [8] Etkin, B. "Dynamics of Atmospheric Flight", John Wiley & Sons, Toronto, 1972.
- [9] Robinson, P.A. and Reid, L.D. "Modelling of Turbulence and Downbursts for Flight Simulators", Journal of Aircraft, Volume 27, Number 8, August 1990.
- [10] Howlett, J.J., "UH-60A BLACK HAWK Engineering Simulation Program: Volume 1 Mathematical Model" NASA Contractor Report 166309, 1981.
- [11] Zan, S.J. and Garry, E.A. "Wind Tunnel Measurements of the Airwake Behind a Model of a Generic Frigate", NRC-IAR-LTR-AA-13, June 1994.
- [12] Gilbert, N. Aeronautical and Maritime Research Laboratories, Melbourne, Personal Communication, 1993.
- [13] Funk Jr, J.D. Naval Air Warfare Center, Personal Communication, 1993.

8. ACKNOWLEDGEMENTS

This work was funded in part by the Institute for Aerospace Research of the National Research Council of Canada (IAR/NRC) and in part by the Department of National Defence (DND FE 220792 NRC 05). The authors would like to acknowledge the efforts of Ms. Hui Cai in designing the flying-probe mechanism and of Ms. Stephanie Lavigne in producing the coloured representations of the flow field.

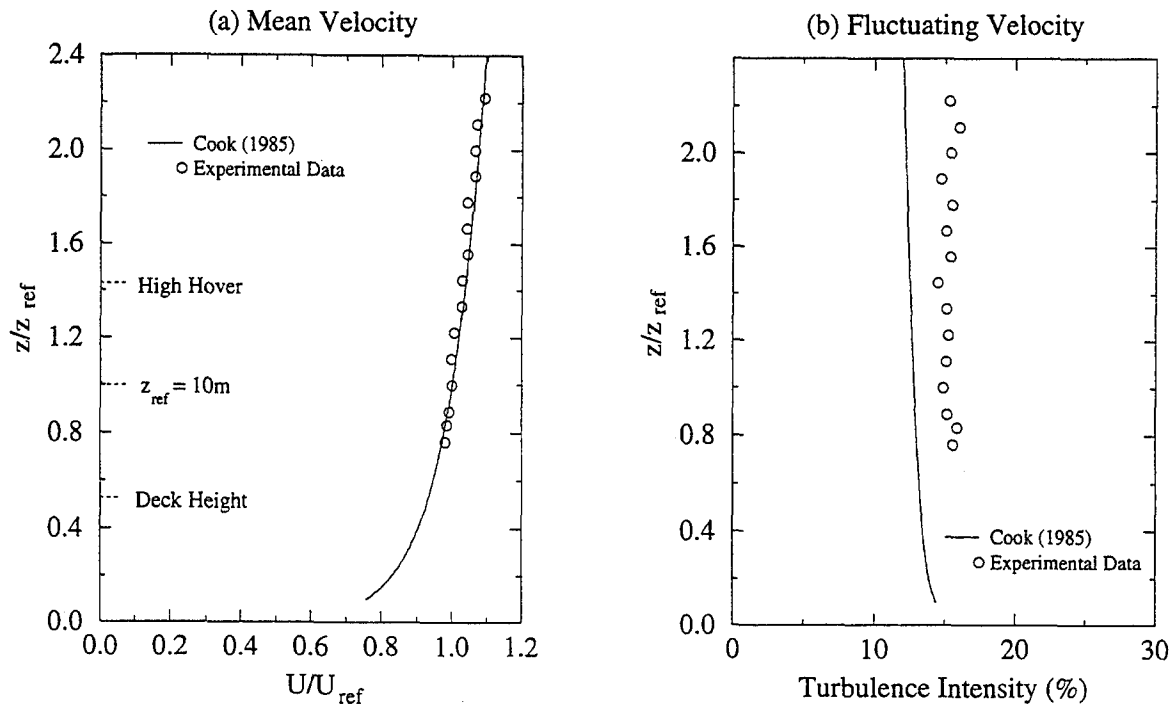


Figure 1: Characteristics of Wind Simulation

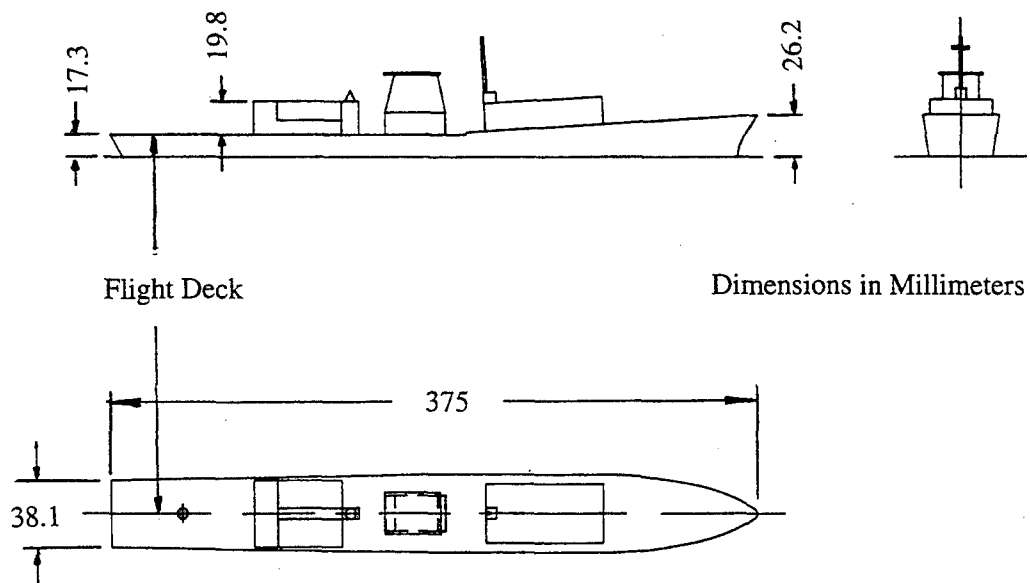


Figure 2: Generic Frigate Model

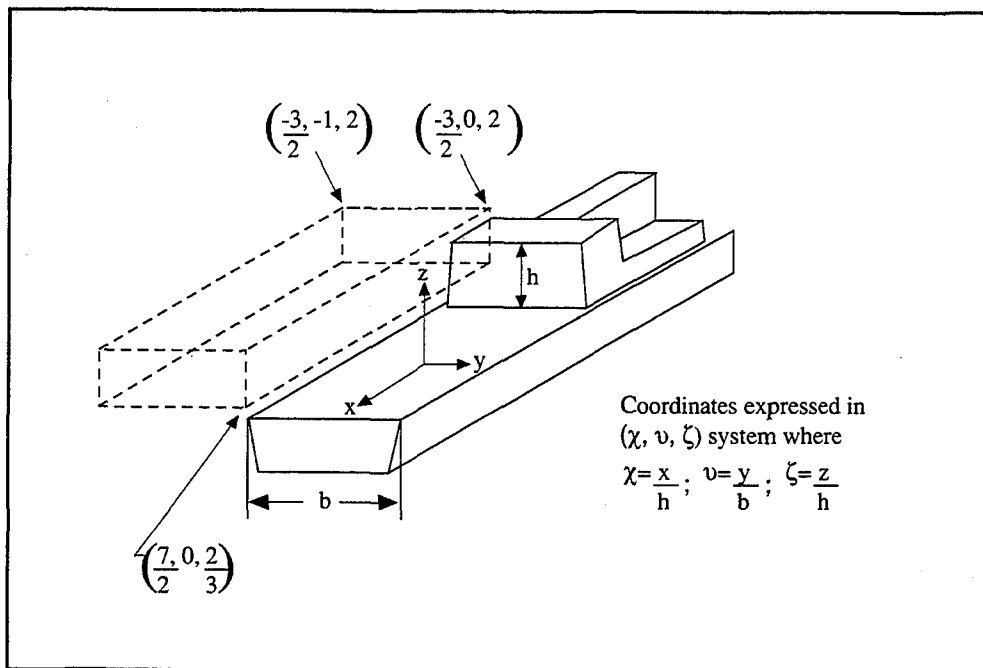


Figure 3: Measurement Volume for Data Acquired with the Fixed Probe

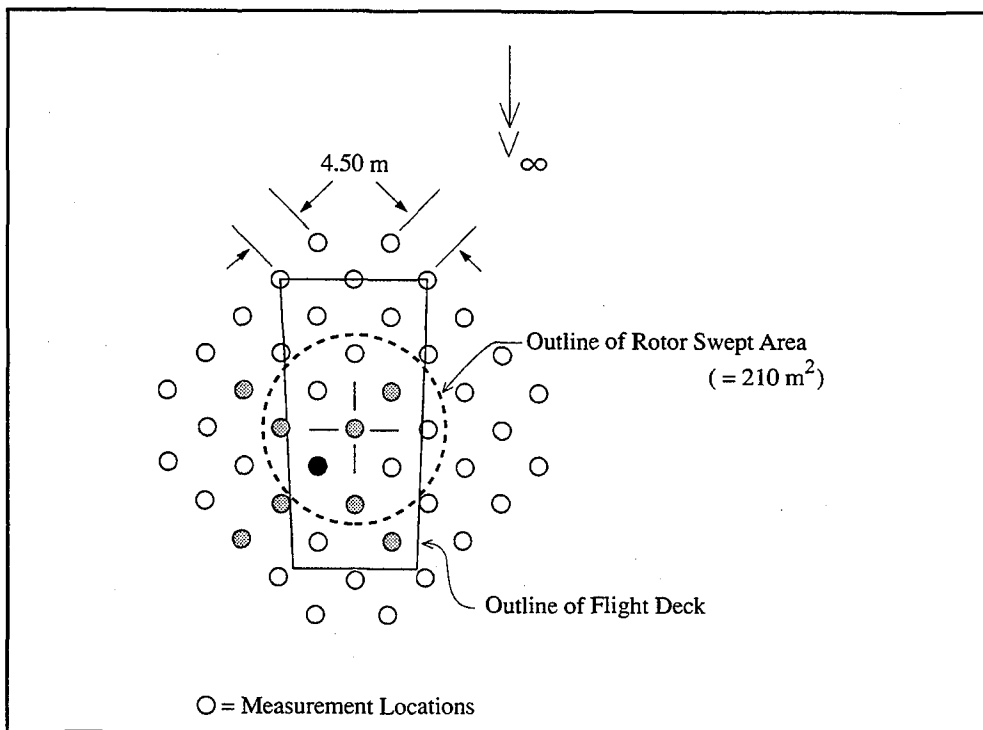


Figure 4: Measurement Locations for Two-Point Correlation Evaluations at High Hover

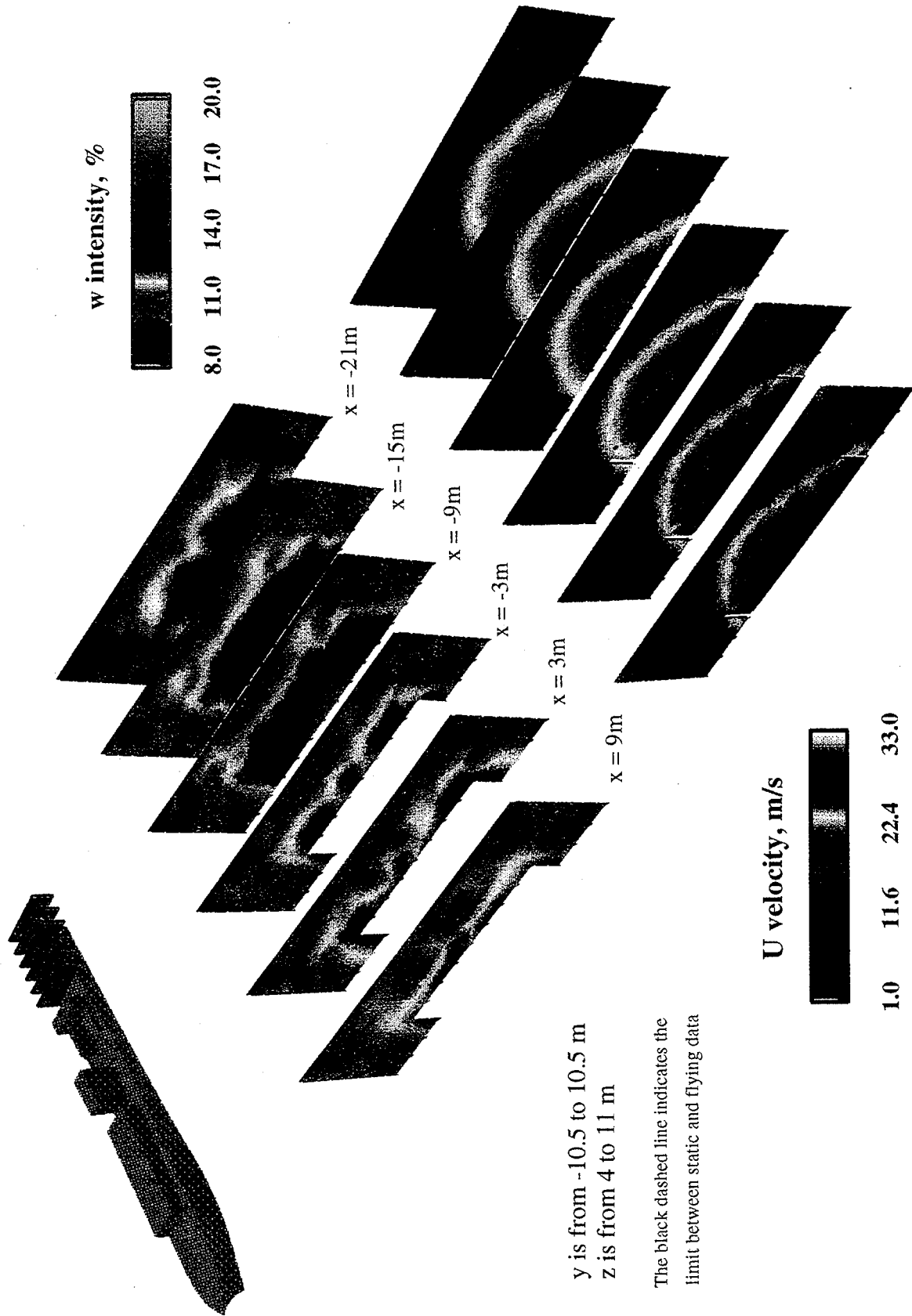


Figure 5: Effect of Streamwise Location on Variation of U Velocity and w Intensity in YZ Planes

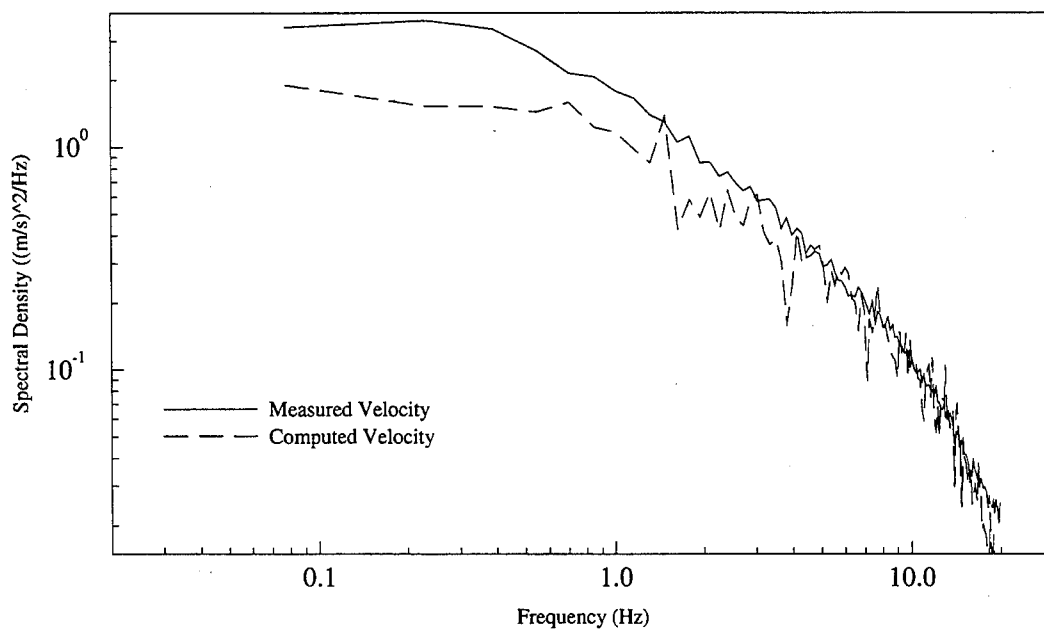


Figure 6: Autospectral Density Function of Vertical Velocity at Centre of Rotor Plane

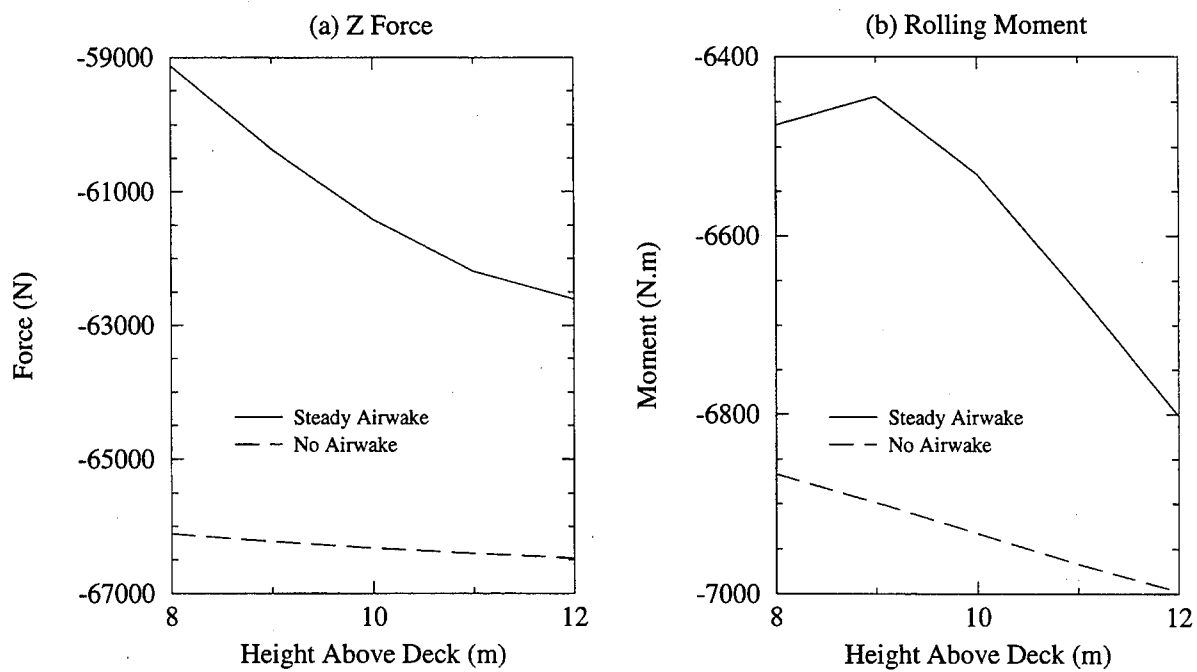


Figure 7: Variation of Rotor Loads with Height Above Deck

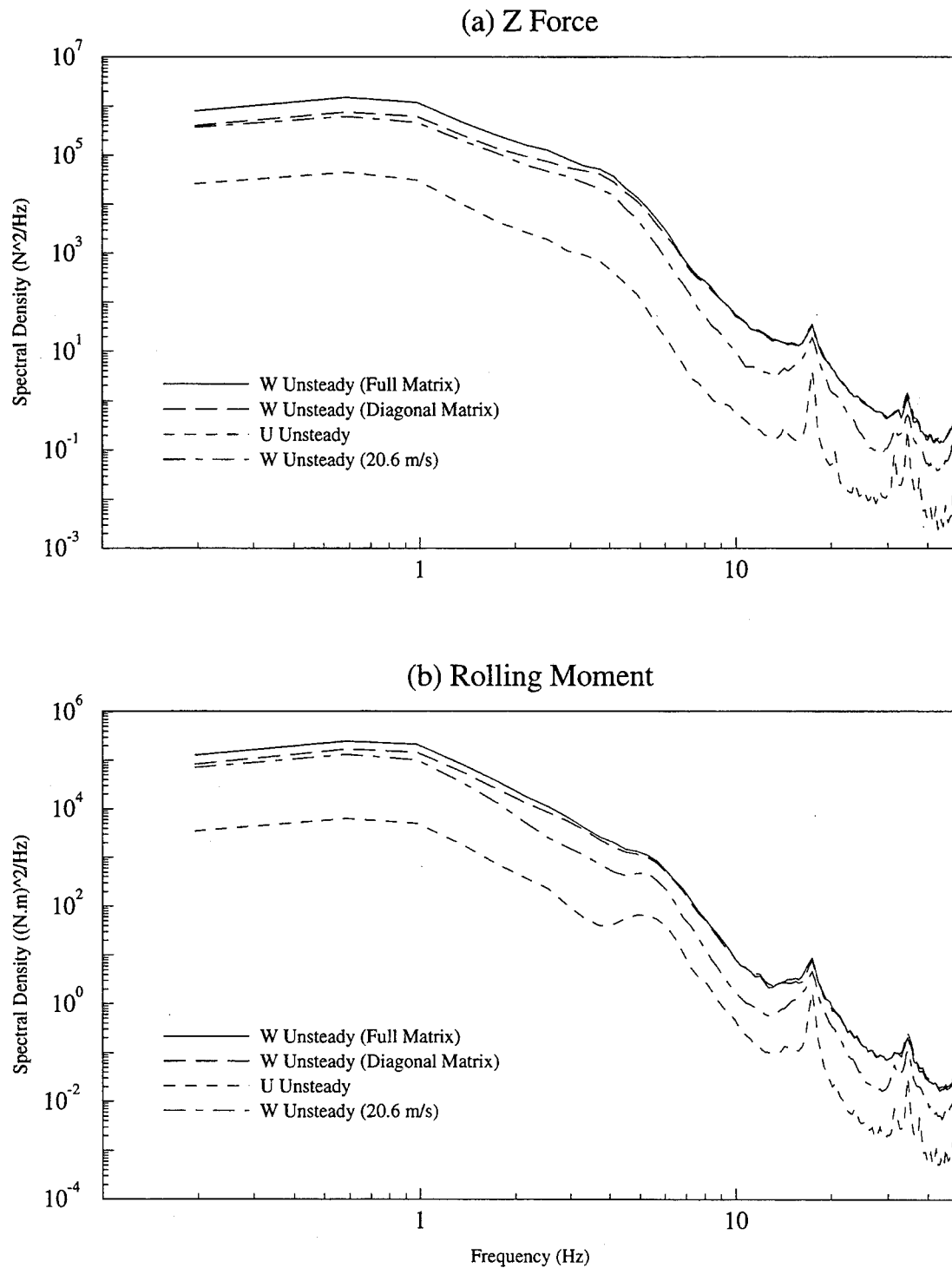


Figure 8: Autospectral Density Function of Rotor Loads
for various Test Conditions

A THEORETICAL AND EXPERIMENTAL INVESTIGATION INTO THE ROTOR BLADE AEROELASTIC BEHAVIOUR OF A SHIPBORNE HELICOPTER DURING ROTOR ENGAGEMENT AND BRAKING

S. J. Newman.

Lecturer in Helicopter Engineering
Department of Aeronautics and Astronautics
University of Southampton
Southampton. SO17 1BJ, UK

Summary

Under normal operating flight procedures, a helicopter main rotor revolves at a strictly controlled speed. The centrifugal forces generated keep balance with the aerodynamic loads with the result that the rotor blade motion, in particular the blade flapping, is maintained under control. To reach the normal rotational speeds the rotor must of course pass through lower speeds, both during acceleration and deceleration, and during these periods the blades can fall prey to the phenomenon of blade sailing. With this, not inconsiderable aerodynamic loads can be generated when the helicopter is operating in high winds and with the reduced centrifugal forces because of the lower rotor speeds, the blade flapping motion can build up to dangerously large deflections.

Operation off the flight deck of a ship is a common example of the type of atmospheric problem capable of generating blade sailing. To predict this behaviour, theoretical models have been developed. However, the necessary justification of the predictions will involve experimental testing since the potential severity of the blade motion requires that this verification must be undertaken at model scale. To this end, two wind tunnel testing programs have been performed, with the intention of analysing the airflow patterns over a ship's deck and secondly to operate a rotor under the severe wind conditions which could be reasonably expected to occur. The results of these two avenues of work have been combined with the theoretical model to produce a consistent set of results.

1 Introduction

During its life, a helicopter is required to operate in adverse weather conditions which are particularly relevant to the shipborne variant. Perched on the flight deck of a ship and subjected to the high wind speeds found in the open sea, the helicopter rotor is subjected to periods of intense aerodynamic forcing, the effects of which are exacerbated by the influence of the ship itself via the hull and superstructure. Amongst the various difficulties posed to the helicopter main rotor blades, one occurs whilst the rotor is turning at low rotational speeds during engagement or disengagement, with appropriate prevailing wind conditions.

The rotor blades will move out of the plane of rotation via the flapping hinge to such an extent that contact with either the fuselage or the ship's deck is possible and, in such cases, the ground and flight crews are placed in significant danger. The blade motion out of the plane of rotation, due to the flapping hinges or flexures, which form part of the rotor hub, allows the rotor disc plane to be controlled by the pilot through cyclic pitch. At normal operating rotor speeds blade flapping motion is severely limited by the considerable centrifugal forces experienced which balance the high aerodynamic lift forces and therefore keep the blade flapping in check. At low rotor speeds, however, the centrifugal forces and hence the large restoring moments on the rotor blades are much reduced. In relatively calm conditions this does not pose a problem since the aerodynamic loads are similarly reduced. However, high winds generate appreciable aerodynamic loads on the blades and can build up to such a degree that the

reduced centrifugal loads can no longer keep a close restraint on the blades in flap and large excursions are now possible giving rise to the so called phenomenon of blade sailing.

The investigation of this potentially violent blade behaviour has been the subject of an extended piece of work of which the latest stage involved the testing of a helicopter/ship model in a wind tunnel with a mapping of the flowfield over the ship's deck using a Laser Doppler Anemometer (LDA). This experimental work was necessary for two reasons. Firstly, the use of a wind tunnel and helicopter model permits a tight control to be exercised over the aerodynamic conditions and secondly, since blade sailing is a violent aeroelastic phenomenon it has the potential to inflict considerable damage to the aircraft itself, but more importantly can cause fatalities to the operating personnel. Such tragic events have occurred in the past and so investigative work must be achieved by a model test.

Earlier wind tunnel tests, reference 1, were conducted on a 1/120th scale model of a Rover Class Royal Fleet Auxiliary vessel to observe the flow characteristics around the flight deck area. *(This choice of vessel was necessary because of earlier comparative full scale testing at sea for which this was the only available type.)* The results of this experiment showed that winds from a direction of 90° to the ship's centre line (*abeam*) provided the most critical conditions since a significant upward component on the windward side was generated. Theoretical calculations indicated that this was particularly important in triggering blade sailing.

To investigate further and provide a comparison with the theory, wind tunnel tests were conducted. A proprietary helicopter model was suitably modified and installed on a wooden structure built to represent the ship's flight deck and the vertical sides of the ship's hull. The ship structure was scaled to the situation of a Westland Lynx sized airframe operating from a Rover Class Royal Fleet Auxiliary. The helicopter rotor was of a two bladed teetering type which was used for the first set of tests.

Further testing was conducted with one blade having been replaced by a counterbalance weight. This allows the rotor blade to behave individually and not be influenced by the opposite blade of the teetering rotor pair. Because of space limitations on the paper, only the two bladed test results are presented.

The results of these experiments showed good agreement with theory for the more windward deck locations of the helicopter, but those results for positions towards the leeward deck edge were totally different in character. The reasons were found to lie in the nature of the flow developed over the ship caused by the separation off the windward deck edge (See Figure 1). To further investigate this matter, tests in a different wind tunnel were undertaken and a full three component laser doppler anemometer traverse was performed over the ship model.

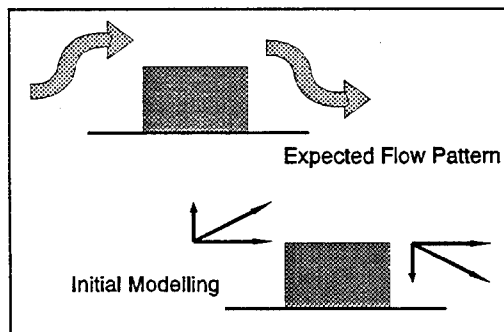


Figure 1 - Initial Modelling of Flow over Ship

3 - Theoretical Model

The rotor blade is assumed to be rigid in flap. With the rotor model under test this is a reasonable assumption, but at full scale this will not be the case. The flapping equations of motion for the rotor blade pair, or blade/counterbalance weight were derived. The rotor speed was used as an input to the method and the solution of the equations of motion gives the blade flapping behaviour as a time history. The aerodynamic conditions experienced by a rotor blade under high wind/low rotor speed conditions makes a closed form solution

impossible. The angles of attack vary enormously and take sections of the blade in and out of stall. For these reasons a numerical solution was adopted. Fourth order Runge Kutta was employed to integrate the equations of motion.

An empirical aerodynamic specification (reference 2) was used for the lift coefficient variation with incidence. The amplitude of rotor flapping expected meant that contact with either of the mechanical flapping limits was certain to occur. In such an event the theoretical method held the blade on the respective stop until the blade moved away into free flapping motion. The numerical method continued until a stop was again encountered whereupon the process was repeated. No allowance for a bouncing effect was made. The violence of the blade impacts on the stops did indicate that a bounce could occur, however, the subsequent agreement between the theory and experiments showed that any bouncing did not materially affect the results. The aerodynamic loads on the blade(s) held them securely against the stops and any bouncing which may have occurred was rapidly arrested.

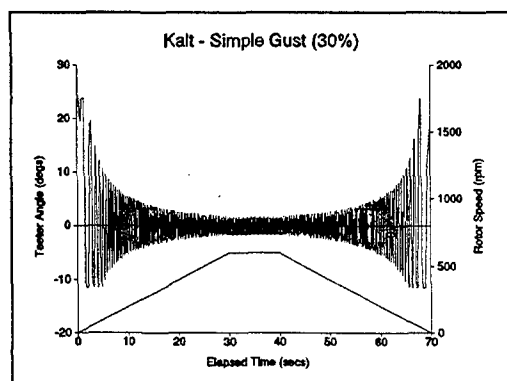


Figure 2 - Rotor Blade Flapping Behaviour using Simple Flow Model

A typical type of prediction is shown in Figure 2. This shows the blade flapping behaviour and rotor speed variation against time. The data used for the incident wind is shown diagrammatically in Figure 1. The top diagram shows what was considered to be a reasonable but simple

approximation to the flow. This is broken down into a wind with horizontal component directly across the deck with a vertical component superimposed upwards on the windward deck edge and downward on the leeward edge, with a linear variation across the deck width. The horizontal component was determined by the appropriate wind speed and the vertical component was taken to be 30% of the horizontal component. This value was chosen from the data obtained in reference 1. The concentration of large flapping excursions at low rotor speed is readily apparent.

4 - Helicopter Rotor Rig Wind Tunnel Tests

Previous work on the flow over a ship's flight deck showed that the most severe case occurred when the wind direction was directly abeam. On this basis the wind tunnel test model was of a ship's flight deck aligned at right angles to the incident wind direction. This required its placement across the wind tunnel section, as shown in Figure 3.

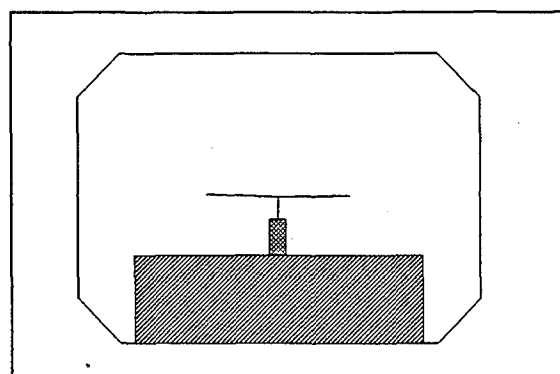


Figure 3 - Installation in Wind Tunnel

In order to give a sensible size to the model and to avoid wall interference, the settling chamber of one of the Department's wind tunnels was used. The rotor model was selected to be a modified kit, (Kalt Cyclone), where the ratio of the height of the rotor hub to rotor radius was close to that of the Westland Lynx aircraft. Seeing as the Rover Class R.F.A. vessel had been used before, it was selected to be that used in the tests. Using the Kalt Cyclone as a scaled down Lynx, the deck dimensions were

established and constructed out of wood. The helicopter model was assembled, omitting the tail boom and rotor, and mounted on an aluminium plate. This was designed to fit into a slot cut into the flight deck of the ship model. This allowed the rotor to be positioned across the flight deck. In this way the effect of windward/leeward deck locations could be observed. The model was then clamped to the deck and wooden blanking panels used to cover the open spaces of the slot. Five deck locations (A to E) were used from windward (A) to deck centre (C) and leeward (E). B and D are one quarter and three quarters of the deck width, respectively, from windward.

Power for the helicopter model is normally supplied by a proprietary glow plug model engine. This is of no use for accurate testing since the power characteristics are not suitable, and the exhaust carries a considerable amount of castor oil which would have severely affected the instrumentation. A small electric motor was fitted to the rotor underneath the aluminium plate and connected to the rotor shaft via the normal spur gears fitted to the model by a steel shaft. The placement of the motor allowed a slip ring assembly to be installed within the helicopter body. Thus when the model was clamped to the deck, the only part above the deck level was the helicopter itself, thereby keeping the flow interference by the fuselage to only appropriate components. The arrangement is shown in Figure 4.

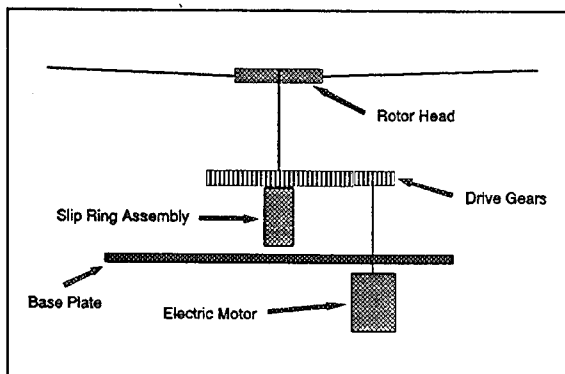


Figure 4 - Schematic View of Rotor Model

The rotor speed variation was controlled by an

electronic unit which allowed for a linear ramp up of rotor speed from rest, a period of constant rotor speed, finishing with a linear ramp down to rest. This behaviour is completely determined by the three time periods and the maximum rotor speed. These values were selected on the control box and the complete sequence was then automatic. This method was chosen for reasons of repeatability.

The blade position was measured by a potentiometer placed on the central part of the hub with the wiper in contact with the blade cuff. An identical dummy potentiometer was fitted to the other side of the hub to avoid the spring load on the wiper to bias the blade flapping. A long throw potentiometer is fitted to the blade control spider, or rotating star, to monitor the blade pitch angle. The tests described here did not use any variation in blade pitch throughout the programme. The blade pitch was set to nominally zero rotor thrust, which is consistent with operational practice. The blades are untwisted but the aerofoil section has camber and so was set using an estimate of the no lift angle.

The maximum rotor speed was set at 600 rpm and a wind tunnel speed of 5 m/s was used for the results as described here. If advance ratio is used as a basis for scaling the relative speeds of rotor and wind tunnel, this corresponds to a Lynx experiencing a wind of 47 knots which is close to the usual quoted figure of 50 knots.

The data from the rig was as follows:-

- (a) Rotor Speed
- (b) Blade Flap Angle
- (c) Blade Pitch Angle
- (d) Azimuth Marker

All four signals were recorded, with a timebase on a RACAL Store 4 tape recorder. These were later processed using the ASYST computer software package.

5 - Ship Flow Wind Tunnel Tests

As will be described in the results section, the

typical result of a simple wind model as described in Figure 2 was shown to be adequate for deck locations near to the windward half of the deck area, but totally inadequate for those toward the leeward deck edge. It was therefore concluded that the simple wind approximation was not sufficient and a separate set of wind tunnel tests was necessary to determine quantitatively the wind variation when interacting with the ship's hull. The work described in reference 1 used a triple hot wire anemometer which possessed a cone of acceptance where any wind direction outside of this cone could not be relied upon and the processing software rejected them. For wind directions from abeam to astern, the amount of rejected data samples was not a problem, however, winds from the bow direction produced a very high proportion of rejected points that these conditions were abandoned. This acceptance cone could not be tolerated for the proposed tests and so use of a three component laser doppler anemometer was planned. This required testing in the working section of the Department's largest wind tunnel. The ship model used for the previous tests was not suitable for this since blockage in excess of 50% would have occurred which would have completely obscured the results. Consequently a smaller scale (2.8:1) ship model was constructed. A result of a traverse is shown in Figure 5 and the differences with Figure 1 are apparent.

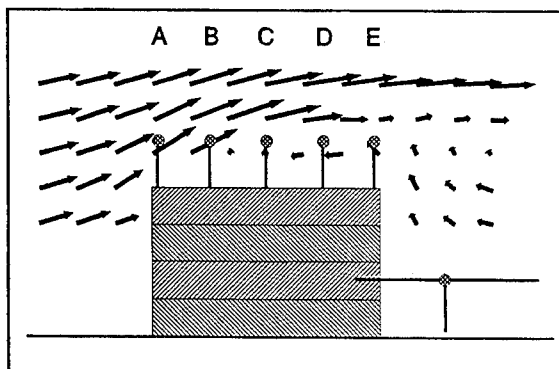


Figure 5 - LDA Flow Patterns over Ship

The results of this data was then used as an input to the theoretical method.

6 - Results

The set of flapping time histories shown in figures 6 to 10 show two distinct types of behaviour.

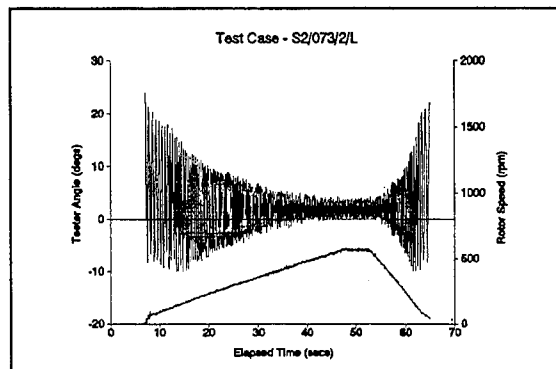


Figure 6 - Blade Behaviour, Position A

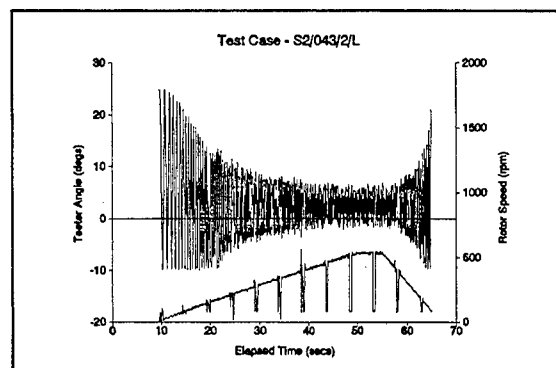


Figure 7 - Blade Behaviour, Position B

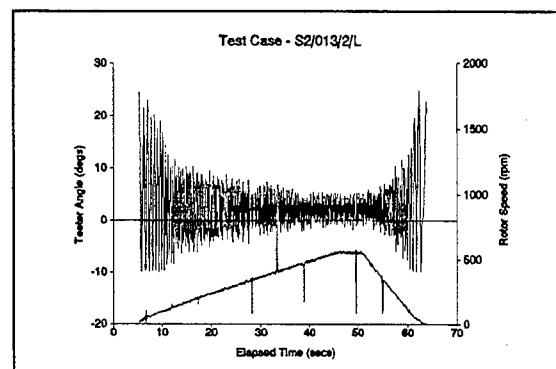


Figure 8 - Blade Behaviour, Position C

(A long run up time was selected since it would be the most prone to blade sailing.) The results of equivalent long run down times are shown in Figures 11 to 15 and are seen to be similar in behaviour. Deck locations A to C show a

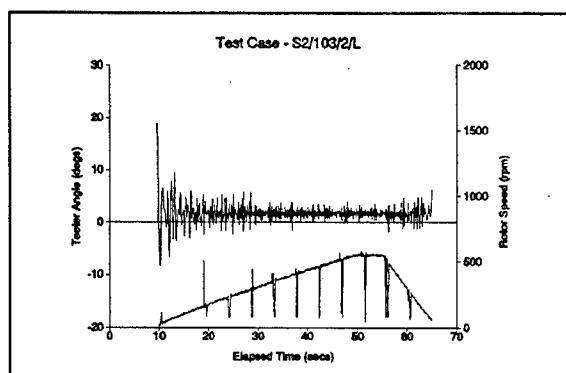


Figure 9 - Blade Behaviour, Position D

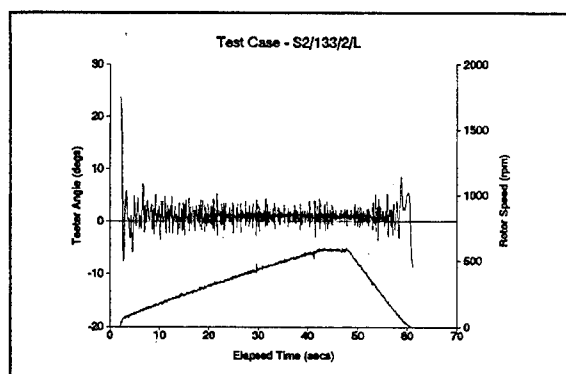


Figure 10 - Blade Behaviour, Position E

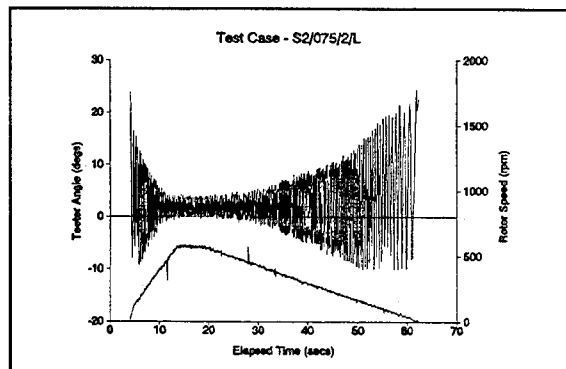


Figure 11 - Blade Behaviour Position A

reasonable agreement with the type of behaviour predicted by the simple wind model. Seeing as these three cases are to windward, this shows that the wind behaviour around the windward deck edge is as initially predicted. However, the positions D and E are completely different. Observation of the rotor blade motion during the

tests indicated that windward locations produced a rotor disc which was steady at the maximum rotor speed but which suffered from excessive blade sailing behaviour at the lower rotor speeds.

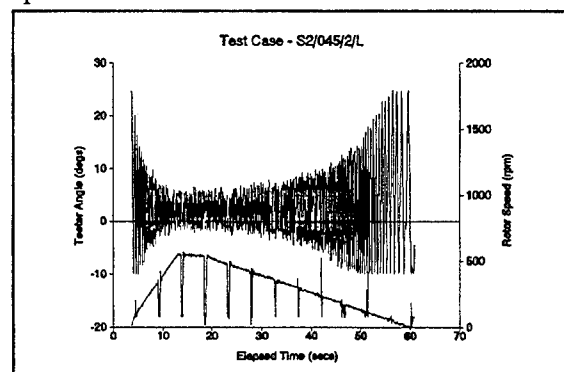


Figure 12 - Blade Behaviour Position B

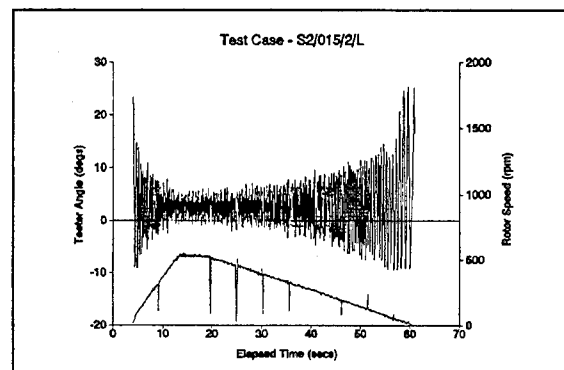


Figure 13 - Blade Behaviour Position C

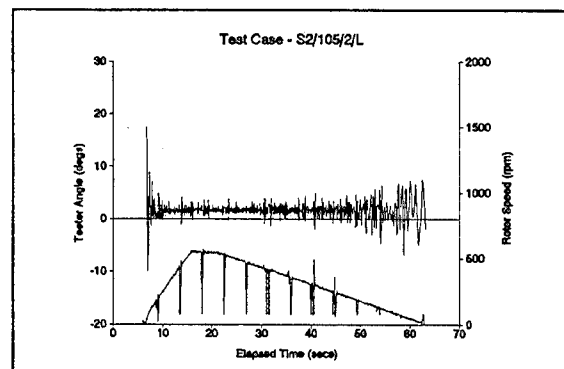


Figure 14 - Blade Behaviour Position D

The leeward deck locations gave a behaviour which was relatively benign at low rotor speeds but an unsteady rotor disc behaviour was seen at the higher rotor speeds which manifested itself as a constant twitching of the disc. This

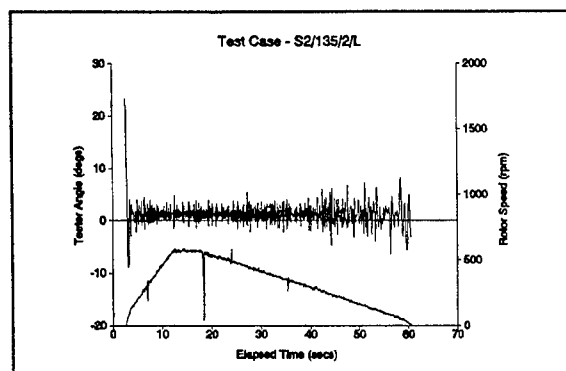


Figure 15 - Blade Behaviour Position E

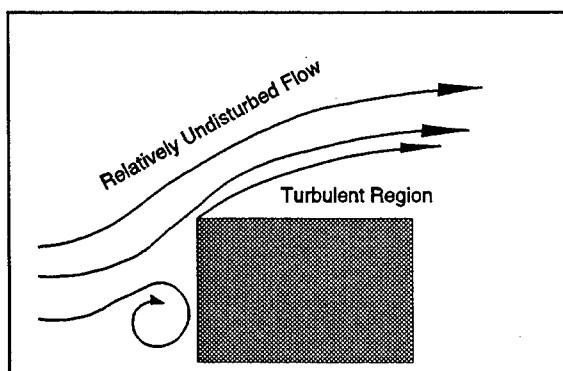


Figure 16 - Schematic of Flow over Ship

appeared to indicate that the relatively clean air surrounding the windward deck edge controlled the first three positions A to C and drove the blade sailing behaviour, whilst the leeward positions were dominated by a turbulent airstream which did not trigger excessive blade motion but did not allow the rotor disc to settle. Figure 16 shows a schematic diagram of the behaviour experienced with these tests. They were obtained by a search with a wool tuft for the boundary between relatively smooth incident air and the region of turbulence caused by the flow separation off the windward deck edge and its subsequent recirculation. Having determined the overall situation, a closer look at the detailed behaviour showed that position B proved the worst for blade sailing whilst position D was the most gentle. It was anticipated that position A would be the worst and position E the best, so these results were at first a surprise.

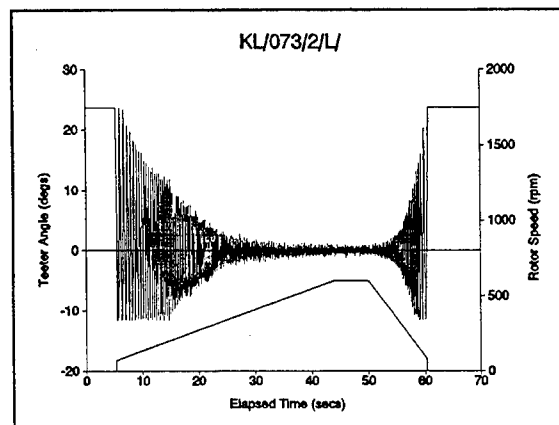


Figure 17 - Theoretical Blade Behaviour, Position A

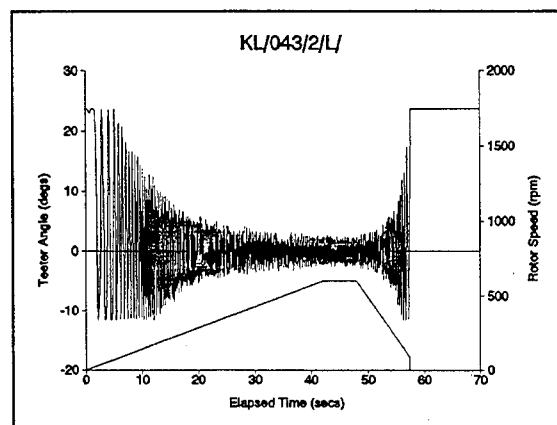


Figure 18 - Theoretical Blade Behaviour, Position B

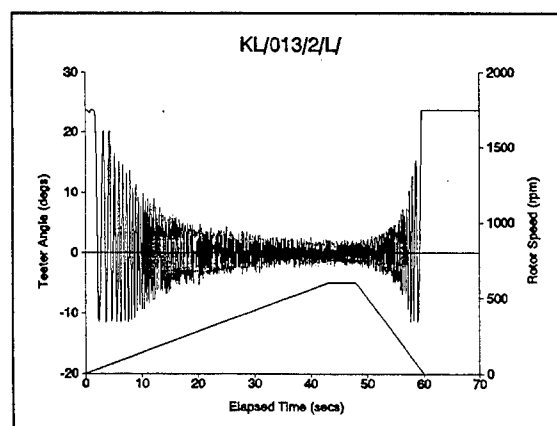


Figure 19 - Theoretical Blade Behaviour, Position C

When the results of the LDA tests were analysed, as shown in Figure 5 the reasons for

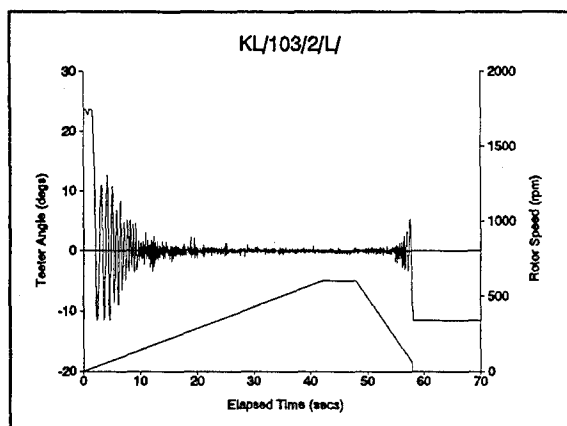


Figure 20 - Theoretical Blade Behaviour, Position D

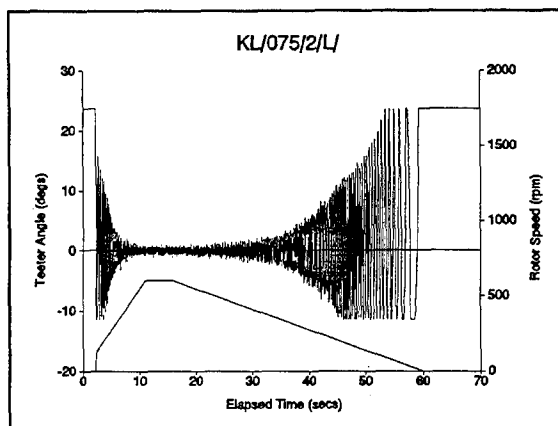


Figure 22 - Theoretical Blade Behaviour, Position A

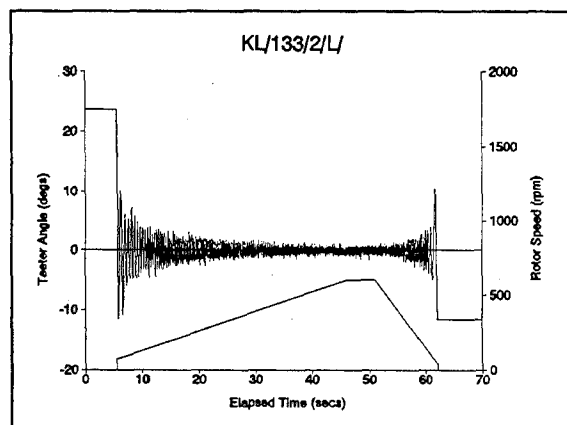


Figure 21 - Theoretical Blade Behaviour, Position E

the differing character of the blade sailing were soon apparent. Included on the figure is a diagram of the rotor size and height. Further development of the theoretical model is under way to use this data in place of the simple wind model. The results are shown in Figures 17 to 26. These results can be seen to compare with the experimental test data to a close degree.

The most obvious difference is in the flapping amplitude during the central constant rotor speed time period. The test data shows a higher amount of flapping, particularly with deck locations A to C.

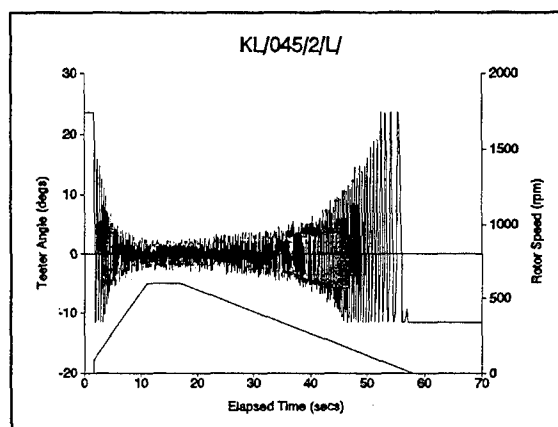


Figure 23 - Theoretical Blade Behaviour, Position B

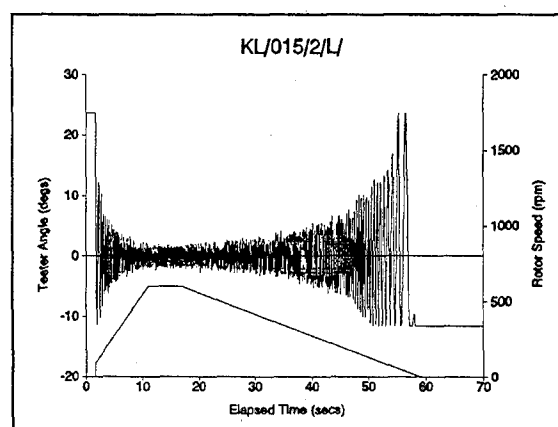


Figure 24 - Theoretical Blade Behaviour, Position C

The theoretical results were obtained assuming zero cyclic pitch. The difference in flapping

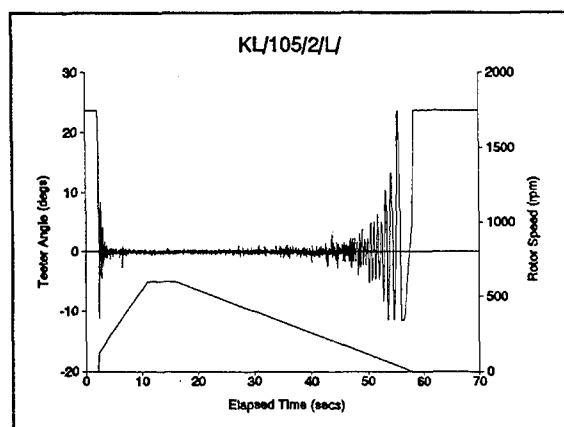


Figure 25 - Theoretical Blade Behaviour, Position D

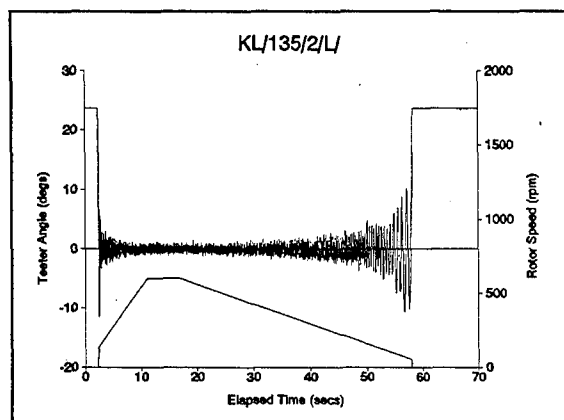


Figure 26 - Theoretical Blade Behaviour, Position E

could be attributed to application of between 1° or 2° . A helicopter model is not designed specifically for research work and so there tends to be an amount of backlash in the control system. The blade pitch sensor was used to check that the cyclic pitch was zero, however, the backlash could have allowed a small amount of cyclic pitch to be present when the rotor spun. A second consideration could be the size of the grid used to obtain the flow data over the ship's deck. Figure 5 shows the flow pattern around the deck and the influence of the recirculating region. The flow must reach stagnation at the deck surface and so the linear

interpolation used for points below the bottom row of points may not reflect the true nature of the flow because of too coarse a grid in this important region. A second test using the LDA is being undertaken to increase the number of data points in the region of the deck surface to enable the interpolation to be more precise. Additionally, an improved seeding arrangement is to be used to give a higher number of samples for the LDA system.

7 - Conclusions

The initial conclusion of the research is that blade sailing does exist. This is an odd statement to make as the phenomenon is well known, and feared, by helicopter pilots worldwide. The fact is that detailed literature surveys have so far produced virtually no evidence of extensive research on the subject. Having acknowledged its existence, the mechanisms of its generation can be examined. The simple wind model has shown that the important driving force is the vertical wind component and its variation over the rotor disc. The maximum blade flapping amplitudes occur at rotor speeds of approximately 10% to 15% of the normal operating value. The rotor tests have shown that a simple wind model is not sufficient for realistic prediction of blade behaviour, particularly in the sense of greatly differing characteristics when the rotor is to windward or to leeward. The cause of this behaviour was determined by the LDA wind tunnel tests which showed the extent and character of the separation of the wind off the windward deck edge and the recirculation region towards the leeward deck edge. The most severe blade sailing was found to occur at the deck location B which is one quarter of a deck width from the windward edge.

Figure 5 shows the flow patterns and the rotor hub centre positions. Position B can be seen to lie almost exactly on the boundary of the recirculation region. In this way the blade is entirely within the turbulent region or in comparatively undisturbed air. The most benign behaviour was found at position D where, on reference to Figure 5, can be seen to place virtually the entire rotor disc within the

turbulent region with little vertical wind component. This explains the rotor blade behaviour seen during the tests. Positions A and C have the rotor disc spanning the turbulence boundary but without the exact 50/50 split found with position B. Position E, when compared with position D, also has the rotor disc lying within the turbulent air but as can be seen with Figure 5, the influence of the recirculation of the air downstream of the ship's hull causes an increase in the blade flapping behaviour.

Having explained the rotor rig behaviour with the observed flow patterns surrounding the ship, the test data from the LDA wind tunnel experiments must be used as input data to the theoretical model. When this is done the agreement with the rotor tests are seen to be very encouraging. The agreement is not perfect but the differences can be explained and further work is being undertaken to address these matters. The research described in this paper has concerned itself with a rigid rotor blade behaviour. In reality the blades will undergo a degree of elastic bending. Discussion of this matter is beyond the scope of this paper but previous work, see references 3 and 4, has examined blade bending and very importantly the interaction of the blades with the rotor hub flapping restraints (droop stop, or anti flap assembly). The methods of both pieces of work are based on the same principles, and the research conducted using a rigid blade, and described in this paper, allows confidence to be obtained in the overall method.

As a final comment, the tests described in this paper have been concerned with an abeam wind. This was seen to be the potentially worst case. Recent conversations with navy pilots have indicated that blade sailing can occur with winds coming from the forward quarter and tend to be insidious in character. Its occurrence tends to be a surprise in that the rotor acceleration or deceleration can be seen to proceed with no apparent problems when a shift in the wind flow over the deck will trigger the blades to sail. This indicates that the effect of the wind flow over the deck is of great importance, not only from the obvious point of view of generating the

aerodynamic loads to cause the blade behaviour but also the potential to suddenly change its character. Further consideration of its unsteady nature must therefore be undertaken.

8 - Acknowledgements

The author would like to thank the following for their help and support during the various phases of this research. Firstly to Ron Walker and Dick Davies of DRA Farnborough for being patient and supportive and, above all, for allowing me to pick their brains as technical monitors. I offer to Jeff Baldwin, Ian McKnight, John Mason and Geoff Thomas my grateful thanks for their help in conducting the wind tunnel tests and reducing the test data.

The research was sponsored by a contract from DRA.

Any opinions expressed in this paper are those of the author.

9 - References

1. Hurst. D. W. and Newman. S. J., "Wind tunnel measurements of ship induced turbulence and the prediction of helicopter rotor blade response.", *Vertica* 12(3) 1988 p267-278.
2. Beddoes. T. S., "An analytical model for trailing edge stall", RP 637, Westland Helicopters Ltd., April 1981.
3. Newman. S. J., "A theoretical model for predicting the blade sailing behaviour of a semi rigid rotor helicopter.", *Vertica* 1990 14(4), p531-544.
4. Newman. S. J., "The application of a theoretical blade sailing model to predict the behaviour of articulated helicopter rotors.", *Journal of The Royal Aeronautical Society* June/July 1992 Vol 96 No.956 p233-239.

THE ROLE AND STATUS OF EULER SOLVERS IN IMPULSIVE ROTOR NOISE COMPUTATIONS

James D. Baeder
Assistant Professor
Aerospace Engineering Department
University of Maryland
College Park, Maryland 20742 USA

SUMMARY

Several recent applications (in the last five years) of Euler solvers in the computation of impulsive noise from rotor blades emphasize their emerging role in complementing other methods and experimental work.

In the area of high-speed impulsive noise the use of Euler solvers as research tools has become fairly mature with very favorable comparisons with experimental data, especially in hover. The grid sizes and resulting computational times are reasonable when compared to those required for accurate surface aerodynamics alone. Furthermore, Euler solvers have provided a rich database with the resolution and accuracy needed for input to Kirchhoff and acoustic analogy methods for predicting the far-field noise. On the other hand, the application of Euler solvers to calculate blade-vortex interaction noise is still far from mature. The computational resources required for accurate calculations away from the blade are much larger than for high-speed impulsive noise. Current calculations help improve the basic understanding of the phenomena involved, but to date no comparisons with experiment have been made. Fortunately, the use of coupled Euler solver/Kirchhoff methods seems to offer promise for a robust and efficient technique for predicting both high-speed impulsive noise and blade-vortex interaction noise.

Finally, a simple model problem of an isolated vortex interacting with an arbitrarily prescribed pitching airfoil demonstrates the feasibility of using Euler solvers to examine noise reduction techniques. The use of simple aerodynamic quasi-static theory and the computed lift time history as feedback to determine the required pitching motion appears sufficient to significantly dampen the unsteady loading and subsequent acoustics by an order of magnitude within a few blade passages.

1. INTRODUCTION

Noise can severely restrict rotorcraft usage in both civilian and military operations. When it occurs, impulsive noise is unquestionably the loudest and the most annoying source of noise. It is annoying because the ear is particularly sensitive to pressure changes that occur over a very short period of time (high frequency). Impulsive noise can be broken down into two areas: high-speed impulsive noise (HSI), and blade-vortex interaction noise (BVI). Furthermore, the investigation of impulsive noise can be broken down into three areas: (1) basic understanding of the physical phenomena, (2) the prediction and comparison with experiment and other methods, and (3) noise reduction techniques.

1.1 High-Speed Impulsive Noise

High-speed impulsive noise is caused by compressibility effects. As the advancing tip Mach number of the rotor increases, the flowfield becomes nonlinear with the formation of supersonic pockets in the tip region of the rotor blade. If the tip Mach number is large enough, the phenomenon known as delocalization may occur, wherein the supersonic pocket on the blade extends out to the far-field beyond the rotor¹. In this case the noise becomes much more impulsive in nature and focused in a narrow region. Since the influence of lift on HSI noise is secondary one does not need to be concerned with trying to accurately model the details of the wake, currently one of the most difficult areas in rotorcraft aeroacoustic predictions.

HSI noise usually occurs in forward flight. However, its characteristics may be duplicated in hover by increasing the rotational speed to match the advancing tip Mach number. Both cases result in a similar relationship between peak acoustic pressure and tip Mach number². Because of unsteady effects in forward flight, HSI noise is usually first studied in hover.

Initial attempts to model HSI noise only incorporated the linear term (monopole) from the Lighthill³ acoustic analogy approach of Ffowcs Williams and Hawkins⁴. The poor agreements with experiment caused several investigators to incorporate nonlinear (quadrupole) terms with the strength of the terms determined from small disturbance aerodynamic calculations of the flow-field in the vicinity of the blade tip⁵⁻⁶. This improved the correlation with experimental data, but only up until just below the point of delocalization. The next improvement in HSI noise prediction occurred when the results from a full potential equation solver were used as input to a nonlinear Kirchhoff method⁷⁻⁹. The application of Euler solvers to HSI noise computations will be discussed in detail later in the paper.

1.2 Blade-Vortex Interaction Noise

As a vortex passes by a rotor blade it induces a time varying vertical velocity that changes the local angle of attack. This causes a fluctuation in pressure in the leading edge region, resulting in the propagation of blade-vortex interaction noise. BVI noise is dominant in low-speed descending forward flight, when the vortices shed during the passage of previous blades interact closely with succeeding blades. This self-induced interaction is very difficult to model, since it requires an accurate computation of the unsteady three-dimensional aerodynamics (with possible transonics) as well as of the precise positions and strengths of the curved vortices. Fortunately, the physics of the problem can be

modeled with the interaction of a single isolated prescribed line vortex interacting with a rotor blade.

Initial attempts to investigate BVI noise further simplified the problem by looking at a single vortex interacting with an airfoil. This 2-D model problem was investigated using various methods for computing the unsteady surface pressures. A linear acoustic analogy approach was coupled with an incompressible Euler method to predict noise in the far-field¹⁰. The small disturbance equations were used to directly compute the mid-field¹¹⁻¹² as well as coupled to a Kirchhoff method to predict the far-field noise¹³. Direct Euler computations were also performed and indicated that the small disturbance equations did not correctly propagate the acoustic waves¹⁴. Unfortunately, no good experimental acoustic data exists for the 2-D case.

At the same time, researchers had developed procedures for predicting the 3-D self-generated BVI case using simple aerodynamic and wake models, coupled with acoustic propagation using the linear terms (monopole and dipole) of the acoustic analogy approach¹⁵. Since then, several researchers have started to examine the coupling of comprehensive codes with full potential solvers and linear acoustic analogy codes¹⁶. This results in slightly better agreement with experiment, although still only qualitatively. In order to remove the uncertainties of wake prediction several researchers started examining the 3-D model problem of an isolated blade-vortex interaction. A full potential solver with linear acoustic analogy propagation¹⁷ was used in preparation for an experiment in the 80'x120' wind tunnel at Ames. More recently researchers started examining the inclusion of initial nonlinear propagation effects for the 3-D model problem. A full potential code was coupled to a linear Kirchhoff method for the 3-D interaction in hover¹⁸. The application of an Euler code to directly compute the initial nonlinear formation and propagation of the acoustics for the 3-D model problem in forward flight will be discussed later in the paper.

1.3 Impulsive Noise Reduction

Most of the preceding work has focused on the basic understanding of impulsive noise and its prediction. However, as important as accurate predictions of impulsive noise are the ultimate goal is to be able to reduce the impulsive noise generated by the rotor blades.

Noise reduction techniques can be broken down into two areas: passive and active. Most experimental and computational work has been concentrated in examining passive means of noise reduction such as reshaping the blade tip planform and/or airfoils or reducing the tip speed. Other methods for impulsive noise reduction are: flapping to enlarge the interaction distance, a trailing edge flap, suction/blowing in the leading edge region, higher harmonic control and individual blade control.

Unfortunately, due to the importance of compressibility for accurately modeling the unsteady effects and the phasing inherent in impulsive noise, incompressible methods are not very well suited for examining noise reduction techniques. An example of the application of Euler solvers to investigate

a novel method for noise reduction will be discussed later in the paper.

2. NUMERICAL SOLUTION PROCEDURES

This section contains a brief summary of three methods that can utilize Euler solvers to investigate the impulsive noise of rotor blades.

2.1 Computational Fluid Dynamics

Most CFD methods can be constructed to satisfy the acoustic equations of propagation as well as to calculate the transonic flow field in the vicinity of the rotor blade. Therefore, the use of a purely CFD method has been proposed for many years. However, such methods were thought to be impractical, with an accurate solution requiring too large of computer resources. However, Baeder¹⁹ demonstrated the feasibility of using a unified CFD method to simultaneously calculate the aerodynamics and acoustics of a nonlifting rotor blade in hover. The numerical solution procedure of CFD requires the determination of the proper set of governing equations, numerical algorithm, and computational grid.

Governing Equations. The choice of governing equations affects the computational time and the level of physics modeled. The aerodynamic flow about rotor blades has been solved over a wide range of governing equations, from lifting-line to Navier-Stokes. Fortunately, viscous effects are minimal for noise in hover and thus the Euler equations are able to capture all of the important features. The Euler equations are preferable to simpler governing equations because of the strong shocks that accompany HSI noise and may occur during BVI noise formation.

Numerical Algorithm. The Euler equations can be solved using various numerical algorithms. Srinivasan and Baeder²⁰ used a structured finite-difference code, TURNS (Transonic Unsteady Rotor Navier-Stokes), to investigate HSI noise in both hover and forward flight. The same code has been used to examine the initial formation and propagation of 3-D BVI noise²¹. Strawn et al²² used an unstructured finite-difference code to investigate HSI noise in hover. The results were similar to those of Baeder et al²³. Results from the TURNS code are shown in this paper; the code can be run in Euler mode by setting a switch that causes the viscous terms to be neglected. Roe upwind-biasing with high-order MUSCL-type limiting on the right-hand-side provides accuracy, while an LU-SGS implicit operator on the left-hand-side is computationally efficient as well as robust. The details of the algorithm are described by Srinivasan et al²⁴.

For the blade-vortex interaction cases, the vortex is preserved in the solution through the use of a nonlinear perturbation technique²⁵. An isolated vortex in freestream is a solution to the Euler equations. Thus, the known or prescribed flow can be subtracted from the Euler solution of an isolated vortex interacting with the rotor blade. This reduces the smearing of the vortex and allows for an accurate representation of the effects of the vortex even in regions where the grid is very coarse.

Computational Grid. Computational grids for calculating the aerodynamics of rotor blades have tended to be highly clustered in the vicinity of the rotor blade surface, with a coarse distribution of points away from the blade. Although acceptable for aerodynamic calculations, this is not acceptable for acoustic calculations. It was determined in the hover study of HSI noise that the largest gradients occur in the azimuthal direction¹⁹. Furthermore, the high frequency noise is confined to a small region of the total flow field. Thus, the clustering of the points away from the rotor only along the region near the linear characteristic curve drastically reduces the number of grid points, while maintaining an accurate solution. Unfortunately, BVI noise is not as well confined since it will also propagate outward in a circular pattern. Therefore, for BVI problems the grid is stretched in the direction normal to the blade surface to maintain a fine spacing for several chords away from the blade surface²¹.

Three-dimensional grids are constructed from a series of two-dimensional hyperbolic C-grids. Each spanwise section is bent and stacked such that away from the immediate vicinity of the blade surface they lie at a constant radial distance from the rotational axis. Furthermore, each section is rotated in the azimuthal direction to maintain the fine clustering in the vicinity of the linear characteristic curve. The amount of rotation can vary with vertical distance from the plane of rotation. The front and back portion of each of the sections may be modified to allow for a simplified simulation of multiple blades in hover.

Figure 1 shows the portion of a sample grid lying in the plane of the rotor (only every other grid line is shown). The grid extends outward to over four rotor radii. The sweeping of the grid outside of the sonic cylinder is clearly evident. Because this grid is for a two-bladed rotor, the grid covers a 180 degrees of azimuth. Figure 2 shows the portions of a sample grid lying at two radial stations (every grid line is shown). At the sonic cylinder there is no sweeping back of the grid in the azimuthal direction; however, the section at slightly over three rotor radii demonstrates the variation in sweep with vertical distance and how the clustering of points is swept rearward.

2.2 Euler Solvers Coupled with Kirchhoff

Although various formulations have been developed to allow for arbitrary motion of the Kirchhoff surface²⁶, the surface can be chosen to be stationary for a rotor in hover and simply translating in forward flight. An alternative is to have the Kirchhoff surface rotate with the rotor blade. Then the elements of the Kirchhoff surface can correspond to those of the CFD grid and no interpolation from the CFD mesh to a Kirchhoff mesh is needed. However, a rotating formulation is more complex than a nonrotating formulation, especially if the surface rotates supersonically.

A nonlinear formulation is not needed if the Kirchhoff surface is chosen to include the nonlinear flow field. Therefore, the classical stationary Kirchhoff formulation is sufficient for studying the noise from hovering rotors if the surface is placed sufficiently far enough from the rotor surface such that nonlinear effects are minimal, but close enough such that the

input data is not suspect. The classical Kirchhoff formulation for a stationary surface, S , can be written as:

$$p(\mathbf{x}, t) = \frac{1}{4\pi} \int_S \left[\frac{\cos\theta}{r^2} p - \frac{1}{r} p_n + \frac{\cos\theta}{cr} p_\tau \right] dS$$

where p is the acoustic pressure; (\mathbf{x}, t) are the space and time variables for the observer location; (\mathbf{y}, τ) are the space and time variables for the surface source location; θ is the angle between the normal vector on the surface, \mathbf{n} (pointing out), and the radiation direction, \mathbf{r} ; r is the distance between the observer and surface source locations; and c is the speed of sound. All of the quantities within the integral are evaluated at the retarded (emission or source) time.

Therefore, for the hovering results shown later, the Kirchhoff surface is chosen to be a stationary cylinder with a radius that corresponds to one of the grid spanwise radial stations. However, the CFD solution is obtained as a steady solution in the frame of the rotor. The first step is to interpolate the pressure and its normal and time derivatives onto a cylindrical mesh that rotates with the rotor blade. The spacing in the azimuthal direction is constant while the spacing in the vertical direction is arbitrary. Since the radial location of the Kirchhoff surface corresponds to one of the grid spanwise radial stations the pressure on that C-grid is interpolated onto the constant azimuthal mesh. The normal pressure on the cylindrical mesh is obtained by performing a similar interpolation on the grid station just interior to the Kirchhoff surface and performing a first-order one-sided difference. If the flow is delocalized it is necessary to improve the accuracy of the derivative by performing the interpolation on a weighted average of the grid stations located at and just interior to the Kirchhoff surface. Since the rotor is in hover and the azimuthal spacing is constant, time derivatives on the cylindrical mesh are obtained using a simple second-order central difference. The second step is to perform the surface integration over the stationary Kirchhoff surface for a fixed observer. The stationary Kirchhoff surface corresponds exactly to the rotating cylindrical mesh at a retarded time equal to zero. At other times the pressure and its derivatives on the stationary Kirchhoff surface must be interpolated in the azimuthal direction from the cylindrical mesh using the retarded time. A simple linear interpolation is employed. The repetition of this process provides pressure time histories at various observer locations²³.

The formulation is slightly more complex in forward flight and requires much greater storage and CPU time since the CFD data is unsteady and more interpolation is required²⁷.

2.3 Euler Solvers Coupled to Acoustic Analogy

The Ffowcs Williams and Hawkins (FW-H) equation considers helicopter noise to be broken down into three components: (1) the thickness noise generated by the displacement of fluid as the blade rotates, (2) the loading noise generated by distributed aerodynamic forces on the blade surface and (3) the nonlinear noise generated by the Lighthill stress. The acoustic analogy approach models thickness and loading noise by integrating monopole and dipole sources over the surface of the blade and models the nonlinear noise by

integrating quadrupole sources over the whole volume of the fluid domain. The quadrupole term needs to be included to fully account for high-speed impulsive noise. However, the difficulty and expense of calculating the volume integral has limited its application; the inclusion of the nonlinear term for unsteady calculations appears to not be feasible. This has motivated some work for trying to simplify the volume integral²⁸. The FW-H equations may be solved in either the time-domain or frequency domain.

The strength and distribution of the monopole sources are purely geometric. Thus, the thickness noise calculations do not require input from an aerodynamic code. The Euler solver can supply the strength and distribution of the loading dipoles on the blade surface as well as the quadrupoles off of the blade surface^{23,29}.

3. DYNAMICALLY TWISTING ROTOR BLADE

The feasibility of dramatic noise reduction using smart materials to dynamically twist a rotor blade in response to a blade-vortex interaction is demonstrated by utilizing an Euler solver to look at the simple model problem of an isolated vortex interacting with an arbitrarily prescribed pitching airfoil. An Euler solver is preferred because of the transonic effects that may accompany BVI noise. Advanced passive designs, such as higher harmonic control and advanced planform and airfoil shapes, are limited by compromises and are unable to adapt to a changing flowfield.

3.1 Concept

The concept for a dynamically twisting rotor, shown in figure 3, is to embed spanwise sensors that indicate the spanwise loading time history. Simple linear theory is then used to predict the twisting motion required to offset the previously measured fluctuating loads. The dynamic twist is applied using piezo-ceramic actuators. The application of feedback each blade passage reduces the fluctuating loads and resulting acoustics to low levels within a few blade passages. In addition, the incorporation of feedback allows the twisting motion to adapt to the flowfield as it slowly changes with time. The advantage of such a method is that no information concerning the wake geometry or vortex strengths are required, only the measured surface aerodynamics as a result of the interactions. Furthermore, the noise is attacked at the source of generation.

3.2 Model Problem

In order to test this concept, the TURNS code is used to simulate the nonlinear, compressible aerodynamics of an isolated vortex interacting with an arbitrarily pitching airfoil as shown in figure 4. First, the lift time history is calculated for the baseline case with no pitching motion. Quasi-steady aerodynamics is used to determine the relationship between the measured lift and the pitching motion that would be required to offset it:

$$C_l = \frac{2\pi}{\beta} \left[\alpha + \frac{b}{V} \dot{\alpha} \right]$$

where α is the angle of attack; b is the semi-chord; V is the freestream velocity; β is the Prandtl-Glauert correction; and C_l is the sectional lift coefficient. Thus, given the lift time history, $C_l(t)$, the pitching motion, $\alpha(t)$, can be determined by applying a simple backward difference of the pitching rate term in time. The airfoil-vortex interaction is then recalculated using this prescribed pitching motion. The continued application of feedback gradually reduces the fluctuating loads, vibrations, and acoustics. In this simulation the CFD code acts as the sensor and the actuator is assumed to have no amplitude or bandwidth limitations.

4. RESULTS AND DISCUSSION

This section contains representative results and some discussion.

4.1 HSI Noise in Hover

Results in this section are displayed for a 1/7th scale model of a modified UH-1H main rotor with two straight untwisted blades of constant chord with NACA 0012 airfoil sections and an aspect ratio of 13.7. This rectangular blade was used by both Boxwell et al³⁰ and Purcell⁸ for experiments performed in the U. S. Army Aeroflightdynamic Directorate's anechoic chamber. The high-speed impulsive noise in the plane of rotation for this rotor blade has been examined using several different Euler codes, either directly or coupled with acoustic propagation codes^{18-19,22-23,28-29,31-32}. Similar results have been obtained for more complex geometries^{19,23}, over a range of tip Mach numbers^{19,23,32}, and also out of the plane of rotation²³.

The high-speed impulsive noise of this model rotor in hover is calculated with the collective angle of the rotors set to zero degrees in order to minimize the effects of lift. The TURNS code is run in Euler mode on grids that consist of 133 points in the wrap-around direction with 97 points on the blade surface, 45 points in the spanwise direction with 17 points on the blade surface and 31 points in the normal direction. Figure 5 shows pressure contours in the plane of the rotor for the UH-1H rotor blade, without twist, at a tip Mach number of 0.90. The disturbance is seen to lie in a small region in the vicinity of the linear characteristic curve. Figure 6 shows a comparison with experiment of the pressure time histories in the plane of the rotor at the sonic cylinder and 3.09 rotor radii. The agreement with experiment is excellent. This agreement with experiment is maintained all the way up to a tip Mach number of one³².

Figure 7 shows the comparison of the same data from experiment, direct Euler results, Euler coupled with a Kirchhoff code, linear thickness noise, and Euler coupled with linear acoustic analogy. Since the Kirchhoff surface is located at a cylinder of 1.277 rotor radii, it includes the nonlinear region of the flowfield, and the agreement with experiment and the direct Euler calculation is excellent. Even for cases where the flowfield is strongly delocalized it appears that the contributions from Lighthill stress in the region more than one or two chords outside of the sonic cylinder is negligible. The placing of the Kirchhoff surface at approximately 1.25 rotor radii is optimal for including the

important nonlinearities while minimizing cost. As a result, minimal additional computational resources are needed to compute the complete aeroacoustic flowfield as opposed to just the aerodynamic flowfield. The disagreement of the linear acoustic analogy results with experiment indicates the importance of off-blade nonlinear effects. Although this disagreement diminishes with decreasing tip Mach number and as one leaves the plane of rotation, some disagreement between linear and nonlinear predictions is still seen for tip Mach numbers as low as 0.6 and 20 degrees out of the plane of rotation²³.

If a nonlinear acoustic analogy method is used by including the quadrupole terms in the flowfield²⁹, the agreement with experiment is very good as shown in figure 8. The improvement when compared to results from transonic small disturbance is due to a more accurate prediction of the shock geometry as well as its strength³³.

4.2 HSI Noise in Forward Flight

Results in this section are displayed for the OLS rotor blade of an AH-1 helicopter. The maximum thickness of the airfoil cross-section is 9.71 percent of chord and the aspect ratio of the blade is 9.22. Acoustic data has been obtained for full-scale OLS blades in flight test by the in-flight technique developed by the U. S. Army Aeroflightdynamics Directorate³⁴ and for a 1/7th scale model of the rotor in the open-jet anechoic test section of the Deutsch-Niederlaendischer Windkanal (DNW)³⁵. The high-speed impulsive noise in the plane of rotation for this rotor blade has been examined using the TURNS code both directly³² and coupled to a Kirchhoff code²⁷.

Once again, to minimize the effects of lift, the high-speed impulsive noise in forward flight is calculated for a modified OLS blade, without twist, at a collective angle of zero degrees and without cyclical pitch. The TURNS code is run in Euler mode for a hover tip Mach number of 0.664 and an advance ratio of 0.258 (advancing tip Mach number of 0.837) on a grid that consists of 97 points in the wrap-around direction with 75 points on the blade surface, 55 points in the spanwise direction with 19 points on the blade surface and 31 points in the normal direction. A supersonic pocket begins to form around $\Psi = 70^\circ$ and reaches its greatest extent around $\Psi = 105^\circ$. However, the supersonic pocket does not extend off of the blade tip³². By $\Psi = 135^\circ$ the shock has disappeared. Figure 9 shows the pressure time histories at three positions in the plane of the rotor at 3.44 rotor radii. The agreement with experiment is excellent. The predicted negative peak pressure of 66 Pa directly upstream of the center of rotation compares with a linear theory prediction of only 45 Pa²⁸.

Since the solution is obtained at every point in the computational domain detailed contour plots can be obtained. In figure 10 contour plots of the log10 of the absolute value of the negative peak pressure are plotted in the plane of the rotor. The dark thick solid line on the advancing side represents a peak negative pressure of 100 Pa. The maximum of this pressure peak clearly occurs upstream of the advancing side of the rotor disc, dropping off fairly sharply to the sides of the rotor.

When the advancing tip Mach number is increased to 0.896 the flow is much more nonlinear. The supersonic pocket begins to form around $\Psi = 50^\circ$, reaches its greatest extent around $\Psi = 105^\circ$ and disappears around $\Psi = 160^\circ$. The supersonic pocket extends off of the blade tip, but the computations never show the flow to be delocalized. As a result the agreement with experiment is less satisfactory³². Although the simplification of no twist and no pitching motion might explain some of the discrepancies, it is also possible that excessive numerical smearing may occur as the Euler code propagates the disturbance to the far-field. In comparison with the flow in hover, the flow is now unsteady and the grid is not always exactly aligned with the shock at all times. Thus, additional improvements in time accuracy and high-order uniform spatial accuracy should be investigated. More recently, Strawn and Biswas²⁷ coupled TURNS with a translating Kirchhoff code with slightly improved results in the far-field.

4.3 BVI Noise of Isolated Vortex Interaction

The rotor modeled is the NACA 0012 rotor with a rectangular planform and an aspect ratio of 7.125 and no twist used in the experiments of Caradonna et al. Initially the pressure instrumented rotor was tested in the Army AFDD 7x10 wind tunnel to measure the aerodynamics of the interaction³⁶. Recently, the same rotor was tested in the Ames 80x120 wind tunnel with microphones placed on the retreating blade side in order to simultaneously measure the aeroacoustics³⁷. A schematic of the test is shown in figure 11. The particular test conditions used in this sample result are a hover tip Mach number of 0.713 and an advance ratio of 0.197. The rotor is run at zero degrees collective. Thus, the blade generates zero thrust in the absence of the vortex. The vortex has a strength of 1.218 (non-dimensionalized with the free-stream velocity and the chord of the rotor) and passes a quarter chord below the plane of the rotor at a blade azimuth of 180 degrees. The vortex was generated by a wing placed directly upstream of the center of rotation: resulting in the parallel interaction at a blade azimuth of 180 degrees.

The blade-vortex interaction noise from the interaction of an isolated vortex with a rotor blade in forward flight is calculated using the above numerical procedure to determine the feasibility of such a method for directly calculating the initial nonlinear formation and propagation of BVI noise. The grid consists of 169x45x57 points with 121x23 points on the blade surface. A time step of 0.2 degrees is used along with 4 newton-type subiterations. Two calculations are performed: the aerodynamic and acoustic field around the isolated rotor without the vortex interaction and with the vortex interaction.

The calculated surface pressures are in good agreement with available experimental data. The lift on the 3-D rotor blade-vortex interaction is less than for 2-D airfoil interactions with the same dimensionless parameters. This is due to 3-D tip loss effects as well as to the reduction in the interaction due to the resulting tip vortex. The finite span seems to cause a faster rise in the lift during the vortex interaction and a faster relaxation of the flowfield after the vortex encounter²¹.

Pressure Contours Inboard of tip. The pressure disturbance contours at the 88% of span location are shown in figure 12 for a blade azimuthal location of 185° . At this location the vortex is located approximately one-quarter chord under the three-quarter chord of the rotor section. The first plot shows the instantaneous pressure disturbance: $(p-p_\infty)/p_\infty$. This will be called the total pressure disturbance. The second plot shows the pressure disturbance due to thickness noise and any high-speed impulsive (for the same case but without the vortex interaction): $(p_{w/o \text{ vortex}}-p_\infty)/p_\infty$. This will be called the thickness pressure disturbance. The last plot shows the difference between these two cases and thus highlights the noise due to the fluctuating lift: $(p-p_{w/o \text{ vortex}})/p_\infty$. This will be called the lift pressure disturbance.

It is not surprising that the effect of the vortex interaction is more clearly seen in the bottom plot, since it removes the effects of the blade thickness. Note that in all of these plots the contour intervals are 0.0005 of the free stream pressure. Strong pulses have just left the upper and lower leading edge surfaces and started to propagate outward. The acoustic pulse is somewhat anti-symmetric with respect to the airfoil mean chord line. The pressure pulse from the upper surface consists of a compression-expansion-compression wave. The initial expansion wave is very steep. The pressure pulse from the lower surface consists of an expansion-compression-expansion wave. The peak pulses appear to occur approximately 45° degrees above and below the plane of the vortex.

Figure 13 plots the lift pressure disturbance contours at the same radial location for three later times: blade azimuths of 190° , 195° and 200° . The pressure disturbance is clearly seen to be propagating outward with its center at the vortex core. Since the plots are fixed with respect to the blade, the vortex core is visible in these plots as the disturbance that is slowly convecting away from the blade trailing edge. By the time that the blade reaches 200° , the acoustic wave has started to reach the coarser portion of the grid and is starting to become distorted and attenuated. The contour intervals seem to indicate that the strength of the acoustic pulse is starting to fall like $1/R$, as it should in the far-field. In addition to the pulse that originated at the leading edge, and additional pulse is seen to originate near the trailing edge of the rotor as the vortex passes underneath. However, this wave is much weaker than the first wave.

Pressure Contours Outboard of tip. The pressure disturbance contours at a radial location of $r/R = 1.125$ are shown in figure 14 for a blade azimuthal location of 185° . Again the three plots show the total pressure disturbance, the pressure disturbance due to the thickness of the blade, and the lift pressure disturbance. Note that in these plots the contour interval is reduced to 0.00025 of the free stream pressure, half of that used in the earlier contour plots. At this radial location the noise due to the thickness of the blade is much smaller. The pressure disturbance due to the vortex interaction is clearly visible. Since the radial location is almost one chord past the tip of the rotor, it is not surprising that the lift pressure disturbance has not propagated out as far from the vortex core as it did for the inboard location.

Figure 15 plots the lift pressure disturbance contours at the same $r/R = 1.125$ radial location for three later times: blade azimuths of 190° , 195° and 200° . As the pressure disturbance propagates outward from the vortex it actually increases in strength. This is due to the increase in contribution from the more inboard part of the blade. The pulse that originated near the trailing edge of the rotor blade seems to be much weaker at this radial station.

A preliminary examination of the data further outboard²¹ seems to indicate that a Kirchhoff surface could be used at approximately 1.25 rotor radii from the center of rotation. However, additional grid points and/or improved CFD algorithms are most likely needed to provide an accurate solution at this surface for input to a Kirchhoff code. Confidence in the quantitative prediction of the noise from an isolated BVI awaits a detailed comparison with experiment.

4.4 Noise Reduction

In order to test the concept of a dynamically twisting rotor blade for BVI noise reduction, baseline cases for a NACA0012 airfoil interacting with a vortex of non-dimensional strength of 0.2 are computed using a two-dimensional version of the TURNS code. The vortex core size is 0.05 chords and it passes 0.26 chords underneath the airfoil. The grid consists of 133×31 points with 97 points on the airfoil surface. A non-dimensional time step of 0.025 is used along with 3 newton-type subiterations. The vortex passes underneath the airfoil quarter-chord when $X_v = 0.0$. Two cases are examined: subsonic ($M_\infty = 0.5$) and transonic ($M_\infty = 0.8$). The lift time histories for both cases are shown in figure 16. The lift time histories are similar except for the delayed positive peak for the transonic case, due to the strong compressibility effects and shock motion.

The resulting pitching motion calculated for two applications of feedback are shown for the subsonic case in figure 17. The maximum pitching angle is only on the order of one to two degrees. However, the pitching motion is very fast. The resulting lift time histories for the two applications of feedback are shown in figure 18. After the first application of a pitching motion the fluctuating lift is greatly reduced. The second application of a refined pitching motion further reduces the fluctuating lift to a level one-fifth of the original with no pitching motion. The time derivative of the lift time history, plotted in figure 19, will be approximately proportional to the far-field noise for a compact source. This figure demonstrates that the BVI noise will be reduced by almost an order of magnitude (or 20dB) after just two blade passages. For the transonic case the pitching motion is very similar to that for the subsonic case. However, the simple quasi-static aerodynamics is not as effective of a controller for the transonic case. However, the time derivative of the lift time history is still reduced by almost a factor of two, as shown in figure 20.

The penalty to be paid for the decreased fluctuating loads and flapping vibrations is the increased moments as shown in figures 21 and 22. The change in the pitching moments are due to the large pitching rates mentioned previously. This is not as dramatic for the transonic case due to the decreased shock motion.

These figures illustrate the suitability of Euler solvers to explore noise reduction methods. Further work needs to be done to improve the aerodynamic feedback model and to investigate the flowfield off of the airfoil surface. Also, aeroelastic effects and the effects of possible limitations of the actuator amplitude and bandwidth have been ignored. Overall though, the possibility for large reductions in BVI noise seems to warrant such future work.

5. CONCLUSIONS

This work summarizes the application of Euler solvers to impulsive rotor noise computations. With special attention to numerical solution procedures it has been demonstrated that Euler solvers can play an important role in computational aeroacoustics. Direct Euler computations compare favorably with experiment, where available. Furthermore, the detail of information available is much greater than that which can be obtained experimentally. As a consequence, the Euler solutions form a rich numerical database that can be used as input to Kirchhoff and acoustic analogy methods to test the simpler and more computationally efficient propagation methods. In particular, the coupling of Euler solutions to Kirchhoff methods seems the most practical approach to accurate predictions in the far-field.

HSI noise calculations (especially in hover) are very mature, while BVI calculations are much less mature. Work should be done to improve the time and spatial accuracy and efficiency of the unsteady HSI and BVI calculations. Confidence in the quantitative prediction of the noise from an isolated BVI awaits a detailed comparison with experiment.

Euler solvers are useful tools for performing assessments of noise reduction techniques, especially when compressibility effects are crucial. The preliminary results for a dynamically pitching airfoil show significant noise reduction within a few blade revolutions, even for cases with very large transonic pockets. Further analytical/computational work should be performed in this area. Eventually, experimental work should be initiated to validate and refine the concept.

6. ACKNOWLEDGEMENTS

The research on high-speed impulsive noise was supported by the U. S. Army Aeroflightdynamics Directorate while the author was a civil servant at the laboratory. The research on blade-vortex interaction noise is supported by NASA Ames under Contract NAG2898, with Cahit Kitaplioglu as Contract Monitor. The research on active noise control is supported by the U.S. Army Research Office under Contract DAAL03-92-G-0121, with Gary Anderson as Contract Monitor.

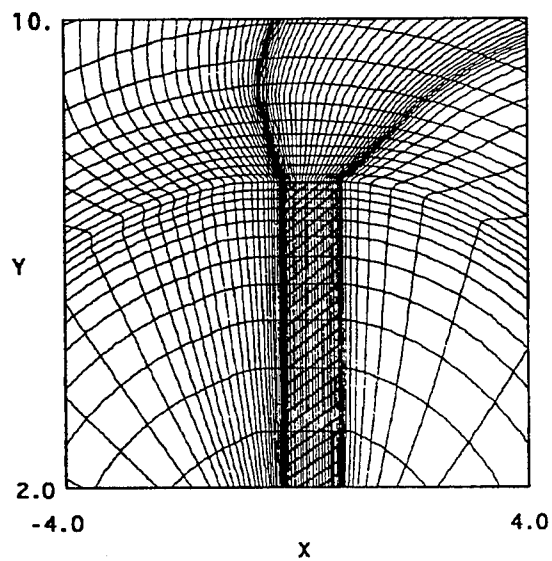
Supercomputer time were provided by the Numerical Aerodynamics Simulation Facility and the Central Computing Facility located at NASA Ames. Workstation time was provided by the Center for Rotorcraft Education and Research at the University of Maryland, funded by the U.S. Army Research Office under Contract DAAL03-88-C-0002, with Thomas L. Doligalski as Contract Monitor.

The author would especially like to thank Vasudev Parameswaran and Marc Amerigo for their assistance in the research on active noise control.

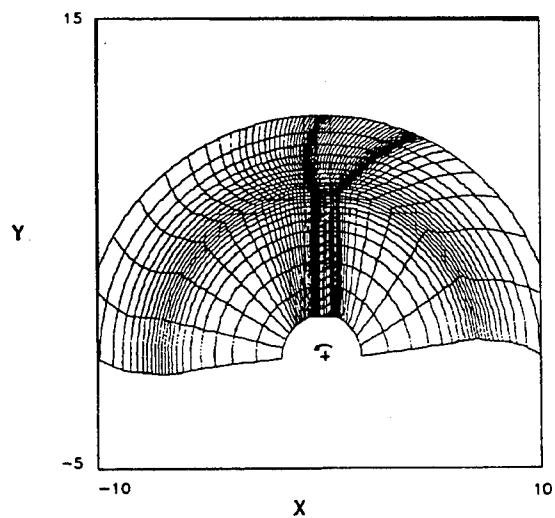
REFERENCES

1. Yu, Y. H., Caradonna, F. X., and Schmitz, F. H., "The Influence of the Transonic Flow Field on High-Speed Helicopter Impulsive Noise," Paper No. 58, 4th European Rotorcraft Forum, Italy, 1978.
2. Schmitz, F. H. and Yu, Y. H., "Helicopter Impulsive Noise: Theoretical and Experimental Status," NASA TM 84390 and USAAVRADCOM TR 83-A-2, November 1983.
3. Lighthill, M. J., "On Sound Generated Aerodynamically," Philosophical Transactions of the Royal Society, A564, 1952.
4. Ffowcs Williams, J. E. and Hawkins, D. L., "Sound Generated by Turbulence and Surfaces in Arbitrary Motion," Philosophical Transactions of the Royal Society, A264, 1969.
5. Schmitz, F. H. and Yu, Y. H., "Transonic Rotor Noise - Theoretical and Experimental Comparisons," Vertica, Vol. 5, 1982, pp. 55-57.
6. Prieur, J., "Calculation of Transonic Rotor Noise Using a Frequency Domain Formulation," AIAA Journal, Vol. 26, No. 2, Feb. 1988.
7. Isom, M. and Purcell, T. W., "Geometrical Acoustics and Transonic Sound," AIAA 87-2748, AIAA 11th Aeroacoustics Conference, Sunnyvale, California, 1987.
8. Purcell, T. W., "CFD and Transonic Helicopter Sound," Paper No. 2, 14th European Rotorcraft Forum, Milan, Italy, 1988.
9. Purcell, T. W., "A Prediction of High-Speed Rotor Noise," AIAA 89-1130, AIAA 12th Aeroacoustics Conference, San Antonio, Texas, 1989.
10. Hardin, J. C. and Mason, J. P., "A New Look at Sound Generation by Blade/Vortex Interaction," Paper No. 2, Winter Annual Meeting of the ASME, New Orleans, Louisiana, 1984.
11. George, A. R. and Chang, S. B., "Noise due to Transonic Blade-Vortex Interactions," 39th Annual Forum of the American Helicopter Society, St. Louis, Missouri, 1983.
12. Baeder, J. D., McCroskey, W. J., and Srinivasan, G. R., "Acoustic Propagation Using Computational Fluid Dynamics," 42nd Annual Forum of the American Helicopter Society, Washington, D. C., 1986.
13. Lyrantzis, A. S., and George, A. R., "Far-Field Noise of Transonic Blade-Vortex Interactions," Journal of the American Helicopter Society, Vol. 34, No. 3, July 1989.
14. Baeder, J. D., "The Computation and Analysis of Acoustic Waves in Transonic Airfoil-Vortex

- Interactions", Ph.D. Dissertation, Stanford University, Sept. 1989.
15. Brentner, K. S., and Farassat, F., "Helicopter Noise Prediction: The Current Status and Future Direction," AIAA 14th Aeroacoustics Conference, Aachen, Germany, May, 1992.
 16. Tadghighi, H., Hassan, A. A., and Charles, B., "Prediction of Blade-Vortex Interaction Noise Using Airloads Generated by a Finite-Difference Technique," Journal of the American Helicopter Society, Vol. 37, No. 4, Oct. 1992.
 17. Gallman, J. M., "Parametric Computational Study of Isolated Blade-Vortex Interaction Noise," AIAA Journal, Vol. 32, No. 2, February 1994.
 18. Xu, Y. and Lyrintzis, A. S., "Rotating Kirchhoff Method for Three-Dimensional Transonic Blade-Vortex Interaction Hover Noise," AIAA Journal, Vol. 32, No. 7, July 1994.
 19. Baeder, J. D., "Euler Solutions to Nonlinear Acoustics of Non-lifting Hovering Rotor Blades," Paper No. II.3.3, 16th European Rotorcraft Forum, Glasgow, Scotland, 1990.
 20. Srinivasan, G. R. and Baeder, J.D., "TURNS: A Free-Wake Euler/Navier-Stokes Numerical Method for Helicopter Rotors," AIAA Journal, Vol. 31, No. 5, May 1993.
 21. Baeder, J.D., and Srinivasan, G.R., "Computational Aeroacoustic Study of Isolated Blade-Vortex Interaction Noise," American Helicopter Society Aeromechanics Specialists Meeting, San Francisco, CA, Jan. 1994.
 22. Strawn, R. C., Garceau, M., and Biswas, R., "Unstructured Adaptive Mesh Computations of Rotorcraft High-Speed Impulsive Noise," AIAA 93-4359, AIAA 15th Aeroacoustics Conference, Long Beach, CA, Oct. 1993.
 23. Baeder, J. D., Gallman, J. M., and Yu, Y. H., "A Computational Study of the Aeroacoustics of Rotors in Hover," 49th Annual Forum of the American Helicopter Society, St. Louis, Missouri, May 1993.
 24. Srinivasan, G. R., Baeder, J. D., Obayashi, S., and McCroskey, W. J., "Flowfield of a Lifting Rotor in Hover: A Navier-Stokes Simulation," AIAA Journal, Vol. 30, No. 10, Oct. 1992.
 25. Buning, P. G., and Steger, J. L., "Solution of the two-dimensional Euler equations with generalized coordinate transformation using flux-vector splitting," AIAA Paper 82-0971, 1982.
 26. Farassat, F., and Myers, M. K., "Extension of Kirchhoff's Formula to Radiation from Moving Surfaces," Journal of Sound and Vibration, Vol. 123, No. 3, 1988.
 27. Strawn, R. C., and Biswas, R., "Computation of Helicopter Rotor Acoustics in Forward Flight," 19th Army Science Conference, Orlando, Florida, June 1994.
 28. Tadghighi, H., Holz, R., Farassat, F., and Lee, Y.-J., "Development of a Shock Noise Prediction Code for High-Speed Helicopters - The Subsonically Moving Shock," 47th Annual Forum of the American Helicopter Society, Phoenix, Arizona, May 1991.
 29. Prieur, J., Costes, M., and Baeder, J. D., "Aerodynamic and Acoustic Calculations of Transonic Nonlifting Hovering Rotors," International Technical Specialists Meeting on Rotorcraft and Rotor Fluid Dynamics, Philadelphia, Pennsylvania, Oct. 1991.
 30. Boxwell, D. A., Yu, Y. H., and Schmitz, F. H., "Hovering Impulsive Noise: Some Measured and Calculated Results," NASA CP-2052, 1978, and Vertica, Vol. 3, No. 1, 1979.
 31. Rho, O. and Kim, Y. S., "An Analysis on High Speed Impulsive Noise of Transonic Helicopter Rotor," 48th Annual Forum of the American Helicopter Society, Washington, D. C., 1992.
 32. Baeder, J. D., "Euler Solutions to Nonlinear Acoustics of Non-lifting Rotor Blades," International Technical Specialists Meeting on Rotorcraft and Rotor Fluid Dynamics, Philadelphia, Pennsylvania, 1991.
 33. Prieur, J., "Importance of an Accurate Prediction of the Shock Curvature for High-Speed Rotor Noise Calculation," Journal of the American Helicopter Society, Vol. 37, No. 1, Jan. 1992.
 34. Schmitz, F. H., and Boxwell, D. A., "In-Flight Far-Field Measurement of Helicopter Impulsive Noise," Journal of the American Helicopter Society, Vol. 21, No. 4, Oct. 1976.
 35. Boxwell, D. A., Schmitz, F. H., Splettstoesser, W. R., and Schultz, K. J., "Model Helicopter Rotor High Speed Impulsive Noise - Measured Acoustics and Blade Pressures," Paper No. 17, 9th European Rotorcraft Forum, Stresa, Italy, 1983.
 36. Caradonna, F. X., Strawn, R. C., and Bridgeman, J. O., "An Experimental and Computational Study of Rotor-Vortex Interactions," Vertica, Vol. 12, No. 4, 1988.
 37. Kitaplioglu, C., Caradonna, F. X., "Aerodynamics and Acoustics of Blade-Vortex Interaction Using an Independently Generated Vortex," American Helicopter Society Aeromechanics Specialists Meeting, San Francisco, Jan. 1994.

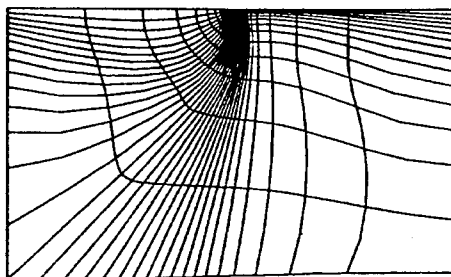


a) Close-Up.



b) Far-Away.

Fig 1. Grid in the plane of the rotor (every other line shown).



a) Sonic Cylinder.

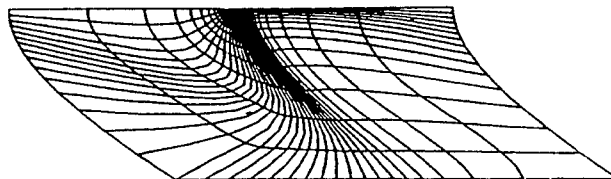
b) $r/R=3.09$.

Fig 2. Grid in the cylindrical plane perpendicular to the plane of rotor (every other line shown).

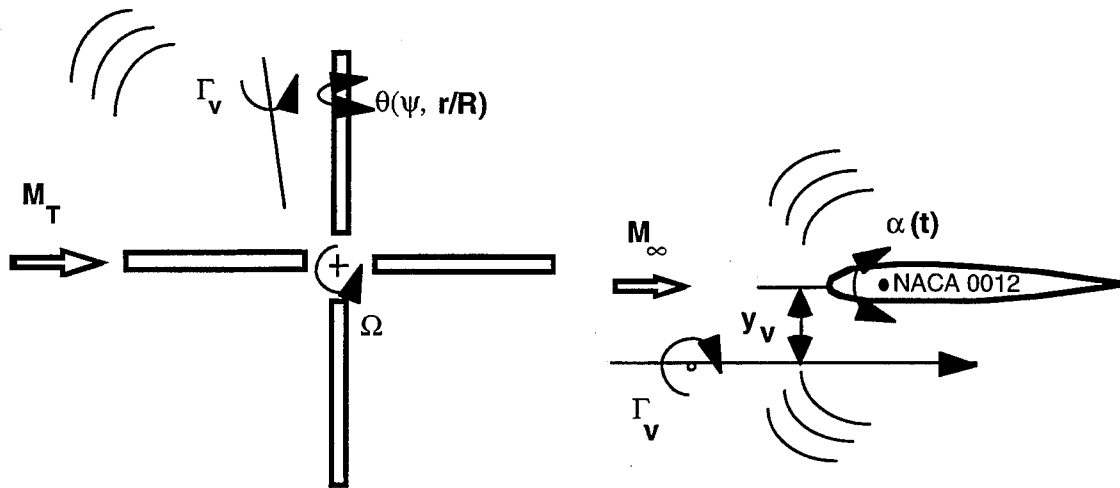


Fig 3. Schematic of a dynamically twisting rotor blade. Fig 4. Schematic of an isolated vortex interacting with an arbitrarily prescribed pitching airfoil.

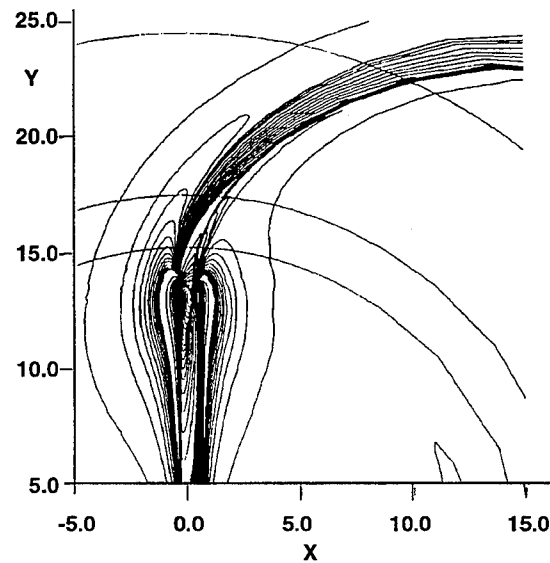
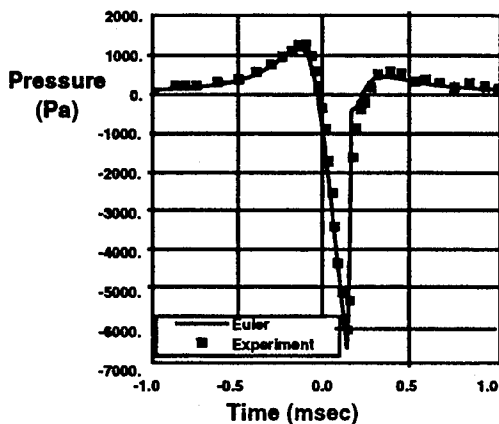
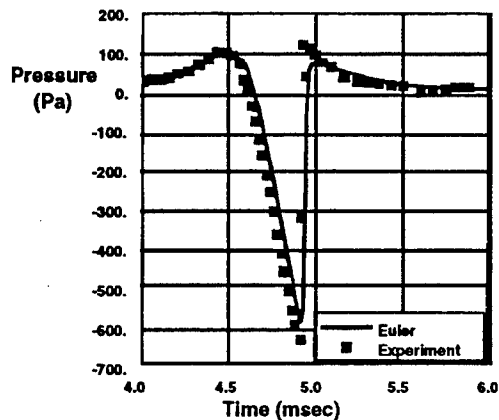


Fig 5. Pressure contours in the plane of the rotor at $M_H = 0.90$ for untwisted UH-1H using TURNS code (contour interval = 2500 Pascal near the blade, 200 Pascal away from the blade) (Ref. 23).



a) Sonic Cylinder



b) 3.09 Rotor Radii

Fig 6. Comparison of Euler solution with experiment of pressure time histories in the plane of the rotor at $M_H = 0.90$ for untwisted UH-1H (Ref. 23).

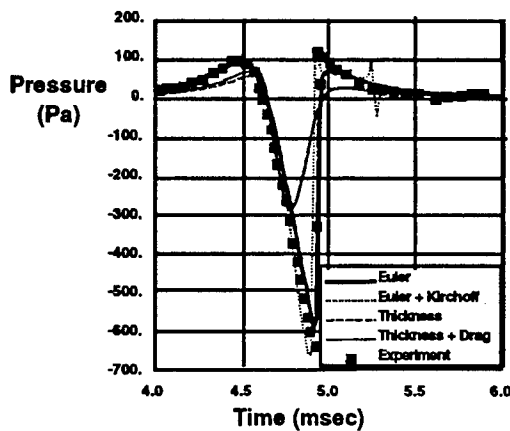


Fig 7. Comparison of the predicted pressure time histories in the plane of the rotor at 3.09 rotor radii for untwisted UH-1H for three methods at $M_H = 0.90$ (Ref. 23).

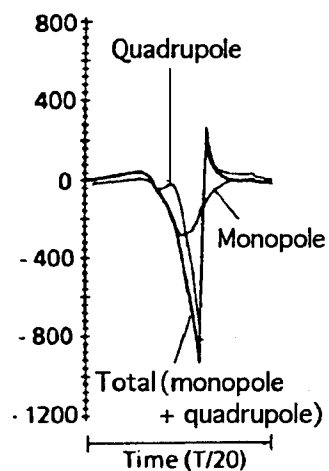


Fig 8. Time history in-plane at $r/R = 3.09$ for an untwisted UH-1H blade in hover, $M_{TIP} = 0.90$ calculated using Euler inputs to nonlinear acoustic analogy code (Ref. 29).

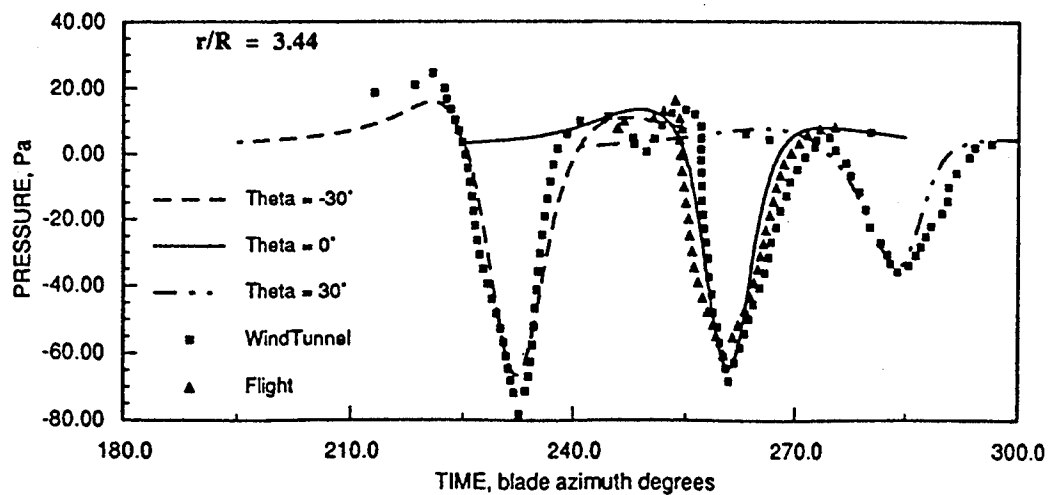


Fig 9. Comparison with experiment of pressure time histories in-plane at $r/R = 3.44$ for an untwisted OLS blade in forward flight, $M_{AT} = 0.837$ (Ref. 32).

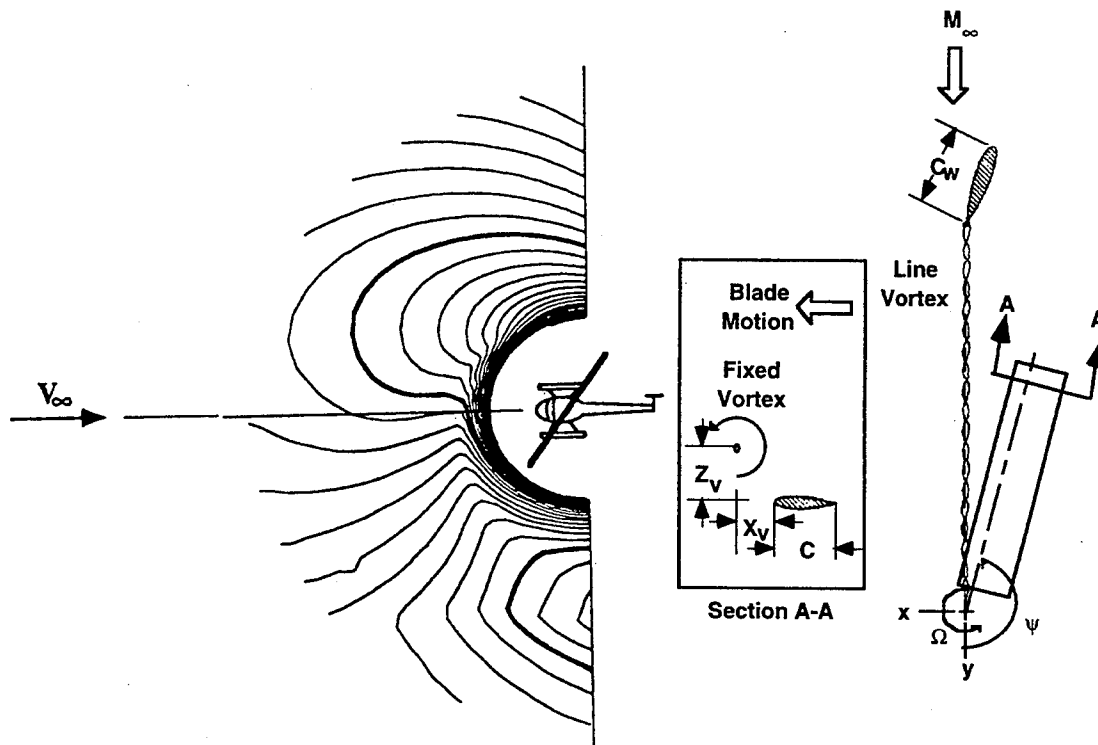
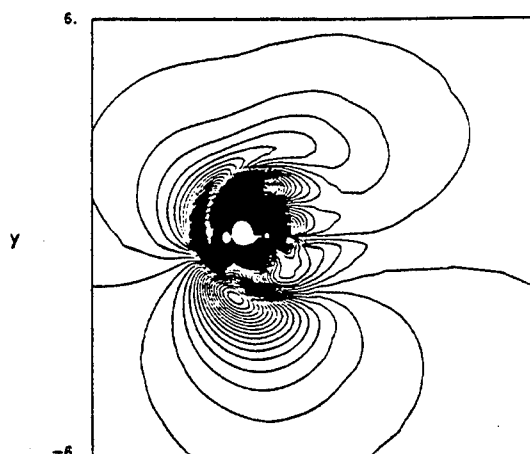
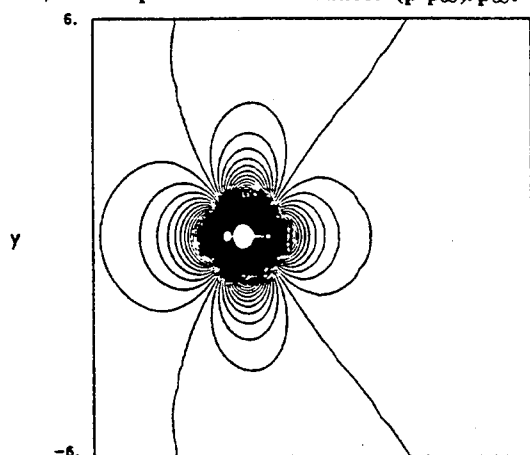


Fig 10. $\text{Log}_{10}(\text{Pressure})$ contours in the plane of the rotor for an untwisted OLS blade in forward flight, $M_{AT} = 0.837$ (Ref. 32).

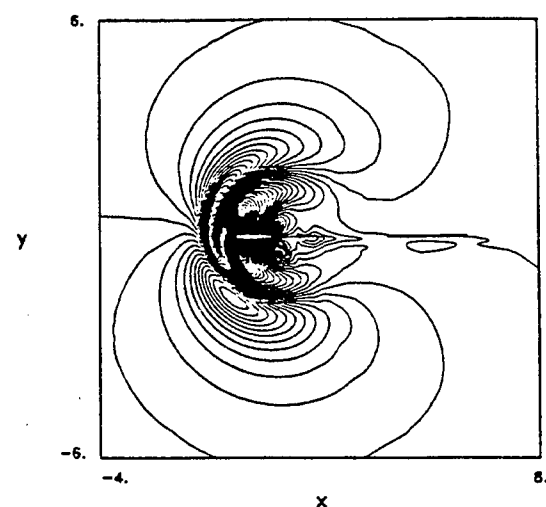
Fig 11. Schematic of an advancing rotor blade passing a line vortex in a wind-tunnel experiment.



a) Total pressure disturbance: $(p-p_{\infty})/p_{\infty}$.

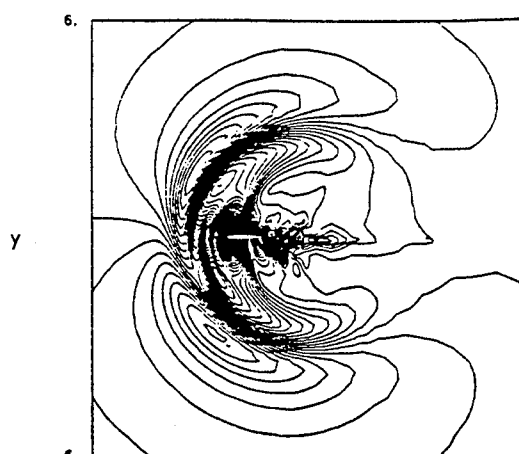


b) Thickness pressure dist.: $(p_{w/o \text{ vortex}} - p_{\infty})/p_{\infty}$.

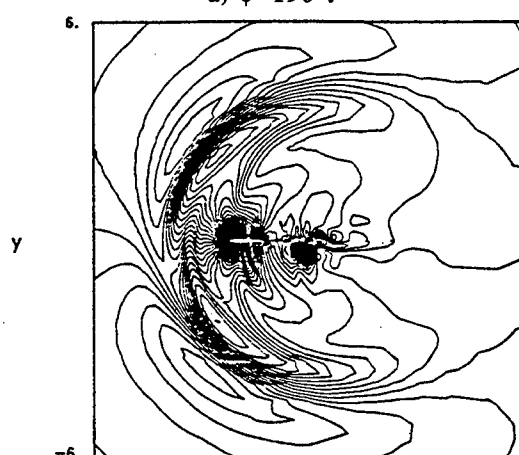


c) Lift pressure disturbance: $(p - p_{w/o \text{ vortex}})/p_{\infty}$.

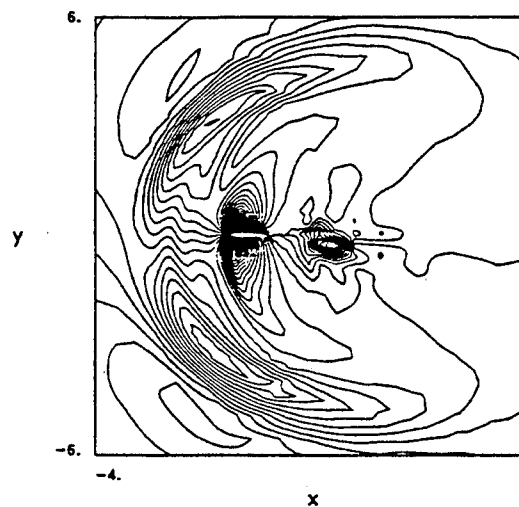
Fig 12. Pressure disturbance contours at 88% span and $\psi=185^\circ$.



a) $\psi=190^\circ$.

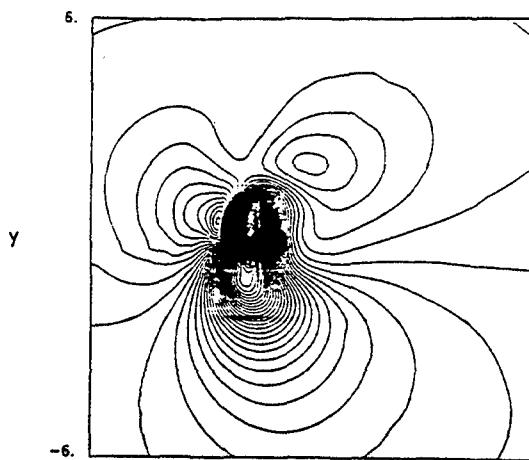


b) $\psi=195^\circ$.

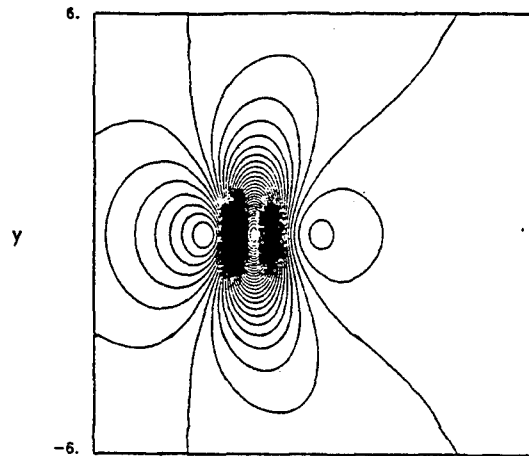


c) $\psi=200^\circ$.

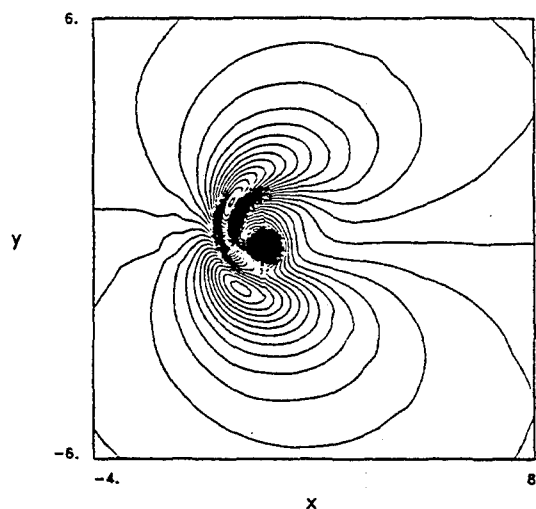
Fig 13. Lift pressure disturbance contours at 88% span.



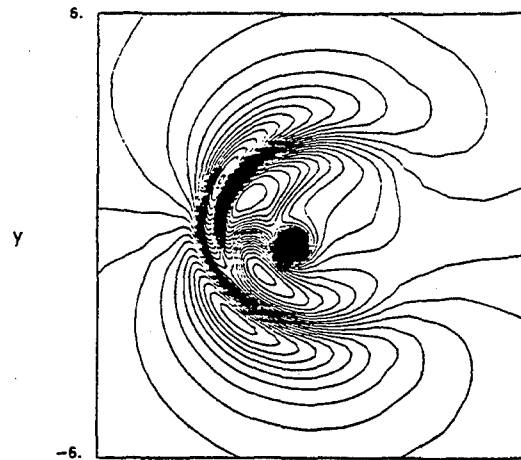
a) Total pressure disturbance: $(p-p_\infty)/p_\infty$.



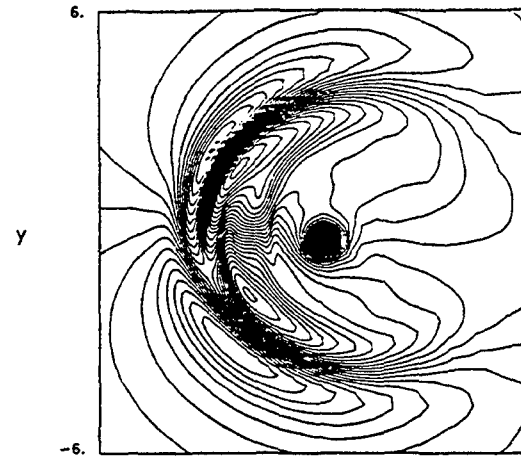
b) Thickness pressure dist.: $(p_{w/o \text{ vortex}} - p_\infty)/p_\infty$.



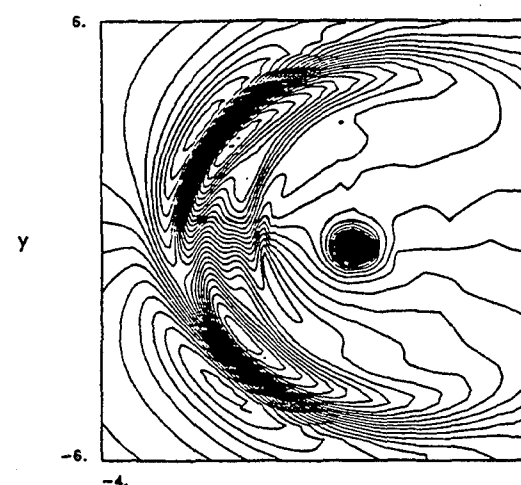
c) Lift pressure disturbance: $(p - p_{w/o \text{ vortex}})/p_\infty$.



a) $\psi=190^\circ$.



b) $\psi=195^\circ$.



c) $\psi=200^\circ$.

Fig 14. Pressure disturbance contours at Fig 15. Lift pressure disturbance contours at $r/R=1.125$ and $\psi=185^\circ$

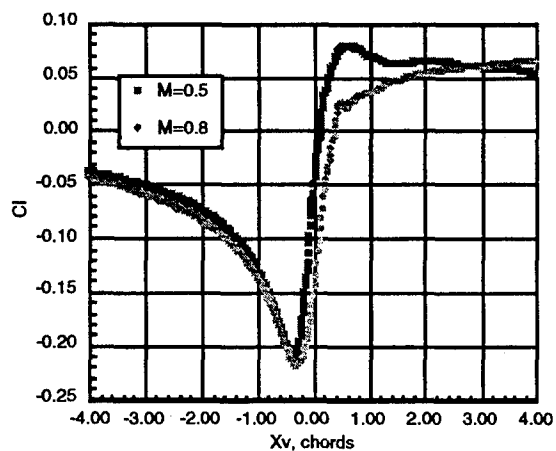


Fig 16. Lift time history, baseline cases.

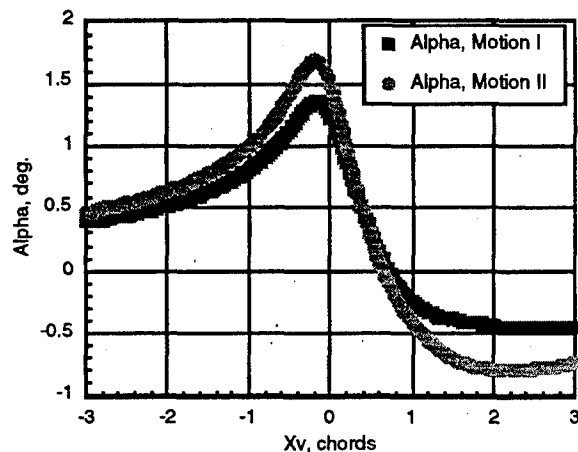


Fig 17. Pitching motion, subsonic case.

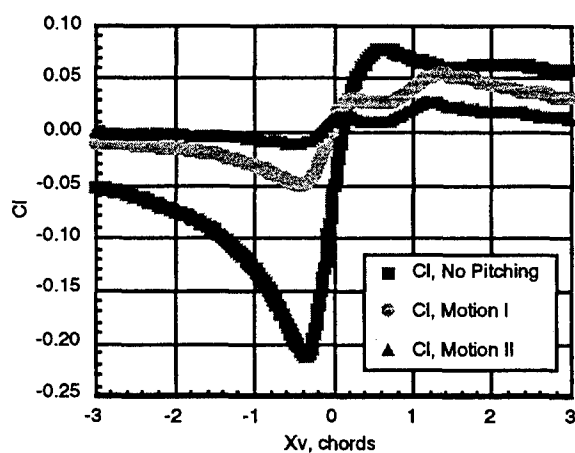


Fig 18. Lift time histories with and without pitching motion, subsonic case.

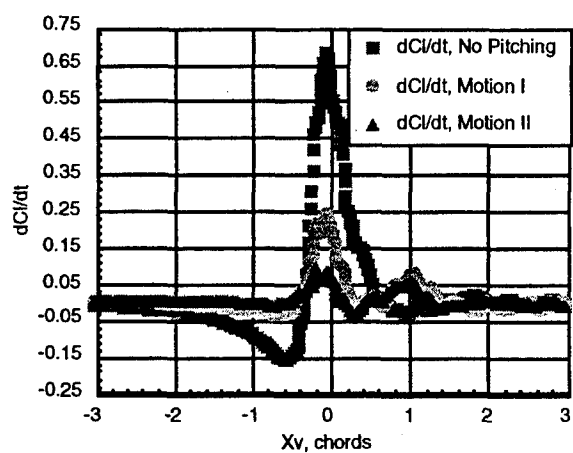


Fig 19. Time derivative of lift time histories with and without pitching motion, subsonic case.

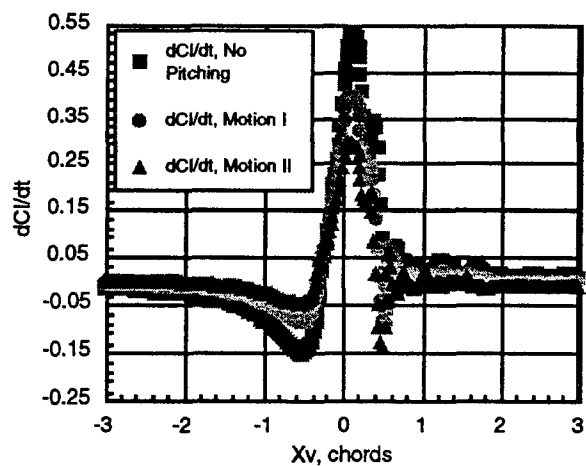


Fig 20. Time derivative of lift time histories with and without pitching motion, transonic case.

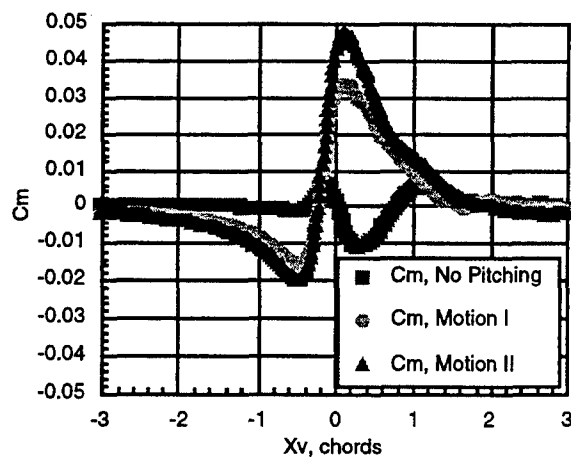


Fig 21. Pitching moment time histories with and without pitching motion, subsonic case.

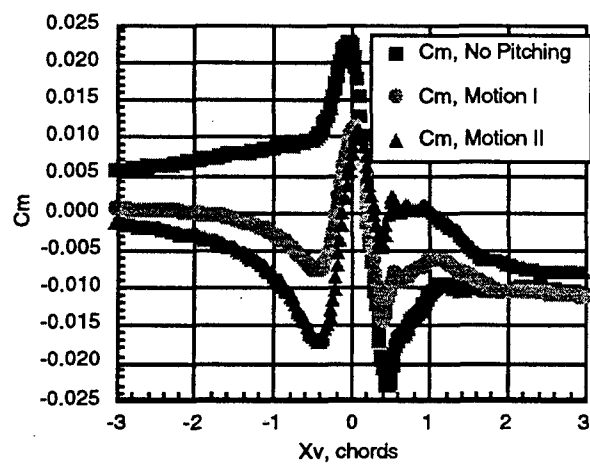


Fig 22. Pitching moment time histories with and without pitching motion, transonic case.

THE USE OF KIRCHHOFF'S METHOD IN ROTORCRAFT AEROACOUSTICS

Anastasios S. Lyrintzis

Associate Professor
School of Aeronautics and Astronautics
Purdue University
West Lafayette, IN 47907-1282, USA

1. ABSTRACT

A comprehensive review of the use of Kirchhoff's method in rotorcraft aeroacoustics is given. Kirchhoff's integral formulation allows radiating sound to be evaluated based on quantities on an arbitrary control surface S if the wave equation is assumed outside. The control surface S is assumed to include all the nonlinear flow effects and noise sources. Thus only surface integrals are needed for the calculation of the far-field sound. A numerical CFD method can be used for the evaluation of the flow-field solution in the near-field and thus on surface S . Kirchhoff's integral formulation has been extended to an arbitrary, moving, deformable piecewise-continuous surface. The available Kirchhoff formulations are reviewed and various rotorcraft aeroacoustic applications are given. The relative merits of Kirchhoff's method are also discussed.

2. INTRODUCTION

Flow-generated sound has been familiar to man for centuries. However, very little study of the mechanisms governing these sounds was done until after World War II. In recent years the increasing use of helicopter and the projected use of tilt-rotor aircraft have drawn attention to the noise that they generate.

Noise is now becoming a serious concern early in the design process rather than a problem to be corrected during the production stages, since in order to comply with FAA rules, aircraft manufacturers must have very good estimates of the detailed noise characteristics of the proposed aircraft. If rotorcrafts are to be considered as widely accepted, mature military and civilian vehicles, the new generation has to be quieter than its predecessors. A recent review of the current status and the future direction of helicopter noise and tilt-rotor aircraft noise is given by Brentner and Farassat [1] and George et al. [2], respectively. Among the several types of helicopter and tilt rotor aircraft noise, impulsive noise is the loudest and the most annoying. There are two kinds of impulsive noise: blade-vortex interaction noise (BVI), and high-speed impulsive noise (HSI).

Both theoretical and experimental studies are being conducted to understand the basic noise mechanisms. Flight-test or wind-tunnel test programs can be used, but in either case difficulties are encountered such as high expense, safety risks, and atmospheric variability, as well as reflection problems for wind tunnel tests. As the available computational power increases numerical techniques are becoming more and more appealing. Although complete noise models have not yet been developed, numerical simulations with a proper model are increasingly being employed for the prediction of aerodynamic noise because they are low cost and efficient. This research has led to the emergence of a new field: Computational Aeroacoustics (CAA). A recent review of the status of CAA is given by Hardin and Hussaini [3].

Presented at the AGARD 75th Fluid Dynamics Panel Meeting and Symposium on Aerodynamics and Aeroacoustics of Rotorcraft, Berlin, Germany, Oct. 1994.

CAA is concerned with the prediction of the aerodynamic sound source and the transmission of the generated sound starting from the time-dependent governing equations. The full, time-dependent, compressible Navier-Stokes equations describe these phenomena. Although recent advances in Computational Fluid Dynamics (CFD) and in computer technology have made first-principles CAA plausible, direct extension of current CFD technology to CAA requires addressing several technical difficulties in the prediction of both the sound generation and its transmission.

Once the sound source is predicted, several approaches can be used to describe its propagation. The obvious strategy is to extend the computational domain for the full, nonlinear Navier-Stokes equations far enough to include the location where the sound is to be calculated. However, if the objective is to calculate the far-field sound, this direct approach requires prohibitive computer storage and leads to unrealistic CPU times. The best solution seems to be the separation of the computation into two domains, one describing the nonlinear generation of sound, and the other describing the linear propagation of sound.

There are several alternatives to describing the sound propagation once the source has been identified, the first of which is the acoustic analogy. In this method the governing Navier-Stokes equations (assumed to be valid in the source region) are rearranged to be in wave-type form (i.e. acoustic analogy, Lighthill [4], Ffowcs Williams, Hawkings [5]). The far-field sound pressure is then given in terms of a volume integral over the domain containing the sound source, especially when quadrupole sources are present. However, the volume integrals required lead to computational problems.

Another method is to use a CFD near-field solution plus a linearized Euler's equation. This method starts from the numerical calculation of the nonlinear near- and mid-field while the far-field is found from a linearized Euler solution. This method seems to have very good potential, however the solution still has to be found in the far-field numerically. Far-field mesh spacing, diffusion and dispersion errors have to be adequately resolved. This method has not yet been used in rotorcraft aeroacoustics and will not be discussed further here.

The final alternative is Kirchhoff's method, that is a nonlinear CFD solution plus Kirchhoff's integral for the far-field. A Kirchhoff's integral formulation allows the radiating sound to be evaluated based on

quantities on an arbitrary control surface S , when the linear wave equation is assumed valid outside the control surface. Thus only surface integrals are needed and the dimension of the problem is reduced by one (compared to acoustic analogy). The control surface S is assumed to include all the nonlinear flow effects and noise sources. A numerical CFD method can be used for the evaluation of the flow-field solution in the near-field and on control surface S . The method has been extended for an arbitrary moving deformable surface (e. g. Farassat and Myers [6]) and to include some nonlinear effects [7, 8]. A numerical method can be used for the evaluation of the flow-field solution in the near field and on surface S . The method has been used for 2-D BVI noise [9-12], 3-D BVI noise [13, 14] and HSI noise [15-20]. The above method can also be used in other acoustic problems, such as propeller noise, fan noise, jet noise, etc. A recent review of the uses of Kirchhoff's method in aeroacoustics can be found in reference [21].

In this paper we are going to discuss briefly the various methods of analysis for rotorcraft aeroacoustics, i.e. full flow field CFD solution, acoustic analogy and Kirchhoff's method. Then the application of the Kirchhoff formulations for various rotorcraft acoustic applications will be reviewed. The relative merits of Kirchhoff's method versus other methods will also be discussed.

3. METHODS OF COMPUTATIONAL AEROACOUSTIC ROTORCRAFT ANALYSIS

Sound can be considered as the propagating part of the entire flow-field. In a few cases the radiated sound can be found by solving the entire flow field. In most cases of practical interest one cannot find a full numerical solution everywhere in the flow because of diffusion and dispersion errors caused by increasing mesh size in the far-field. In addition, the acoustic fluctuations are usually quite small (about three to five orders of magnitude less than the flow fluctuations). Thus, it is often advantageous, or even necessary, to develop ways of determining the far-field noise from near-field solutions. To do so the computation is separated into two domains, one describing the nonlinear generation of sound, the other describing the linear propagation of sound.

The main approaches used to find the far-field noise can be classified as follows:

1) *Full Flow-Field CFD*: This is a calculation of the full nonlinear flow field using CFD including far-

field waves. However, since the dissipation and the dispersion properties of traditional CFD numerical schemes tend to damp the acoustic oscillations or sometimes generate artificial disturbances, high-order of accuracy schemes and grid refinement strategies are employed. An example of an application of CFD techniques for the calculation of radiating waves from transonic blade-vortex interactions (BVI) is given by Baeder et al. [22, 23]. The high-speed impulsive (HSI) noise was also investigated by Baeder et al. [24-26, 17] using the same technique. Various levels of approximation (i. e. small disturbance, Euler and Navier Stokes equations) were used. However, in order to numerically resolve the details of the acoustic three-dimensional far-field, a very fine mesh should be used, which makes these computations somewhat impractical, even with today's powerful supercomputers. Furthermore, because the acoustic fluctuations are usually quite small, the use of a nonlinear equation (e. g. Euler, Navier Stokes) could result in errors (Stoker and Smith, [27]).

2) *Acoustic Analogy*: This is a nonlinear near-field CFD calculation plus the application of an integral equation (e. g. Lighthill, [4]) for the far-field. In the acoustic analogy, the governing Navier-Stokes equations are rearranged to be in wave-type form. The far-field sound pressure is then given in terms of a volume integral using second derivatives over the domain containing the sound source. It should be noted that the sound sources (in the absence of solid bodies) are quadrupoles due to turbulence and/or shock waves including refraction and diffraction of the sound field. In the presence of solid bodies more terms representing monopoles (e. g. expanding sphere) and dipoles (i. e. unsteady force) should be added to Lighthill's formula to construct the Ffowcs-Williams Hawkins equation (Ffowcs-Williams and Hawkins, [5]). All integrals are evaluated in the retarded (emission) time. The monopole and dipole terms are easy to evaluate, because they are surface integrals over the body surface. The nonlinear near- and mid-field can be evaluated using CFD techniques. Experimental data can also be used when available. The far-field is found from a linear Green's function formulation evaluated in terms of surface and volume integrals over the retarded time transformations of the near- and mid-field flow and body surfaces. WOPWOP [28] and RAPP [29] are production codes based on acoustic analogy (Farassat's formulation 1A [30]) and are widely used by NASA and the U. S. rotorcraft industry. The major difficulty with the acoustic analogy is the evaluation of the quadrupole term which requires a volume integral evaluation. In transonic flow there are substantial difficulties in including the nonlinear quadrupole term (which requires second derivatives) in the volume integrals, especially around moving shock

surfaces. Thus, many investigators (e. g. Tadghighi et al., [31]) use near-field data only on the blade surface, a method that cannot be used in the transonic cases, since the effects of shocks are not accounted for. Near-field data can be evaluated either from experiments, or from CFD computations. However, Baeder et al. [17] showed that for HSI noise this method is not accurate for tip Mach numbers as low as 0.7. Farassat and Tadghighi [32] have tried to simplify the formulation of the shock related noise and apply it in some special cases (e. g. Tadghighi et al., [33]). However, we feel that there are still substantial difficulties preventing the wide use of their formulation. Many examples of the applications of acoustic analogy in helicopter aeroacoustics are given by Brenner and Farassat [1].

3) *Kirchhoff Method: CFD Near-field Plus Kirchhoff Integral Formulation*. This is a calculation of the nonlinear near- and mid-field using CFD techniques with the far-field solutions found from a linear Kirchhoff formulation evaluated on a control surface S surrounding the nonlinear-field. The control surface S is assumed to include all the nonlinear flow effects and noise sources. The full nonlinear equations are solved in the first region (near-field), using CFD techniques, and a surface integral of the solution over the control surface gives enough information for the analytical calculation in the second region (far-field). This method provides an adequate matching between the aerodynamic nonlinear near-field and the acoustic linear far-field. The advantage of the method is that the surface integrals and the first derivatives needed can be easily evaluated from the near-field numerical data; full diffraction and focusing effects are included while eliminating the propagation of the reactive near-field. The method is simple and accurate as it accounts for the nonlinear shock-related noise in the far-field and is the method that we go on to investigate further in this paper.

4. KIRCHHOFF'S METHOD

4.1 Introduction

Kirchhoff's method is an innovative approach to noise problems which takes advantage of the mathematical similarities between the aeroacoustic and electrodynamic equations. The considerable body of theoretical knowledge regarding electrodynamic field solutions can be utilized to arrive at the solution of difficult noise problems.

Kirchhoff's formula was first published in 1882 although primarily used in the theory of diffraction of light and in other electromagnetic problems, it has

also many applications in studies of acoustic wave propagation (e. g. Pierce, [34]). The classical Kirchhoff formulation is limited to a stationary surface. Morgans [35] derived a Kirchhoff formula for a moving surface (i. e. the interior region of an expanding sphere) using the Green's function approach. However, his analysis was lengthy and complicated. There has been some disagreement about the correctness of Morgans' final result. Ffowcs Williams and Hawkins [5] and Hawkins [36] claim that there is an "error" in the final formula, whereas Farassat and Myers [6, 37] claim that there is only an "ambiguity" in the final result and it is clear from the derivation that Morgans was very much aware of the details that caused it. Munro [38] also agrees that Morgans' formula is correct.

Khromov [39] presented another extended Kirchhoff formulation. He converted the wave equation into a Laplace equation by introducing an imaginary part for the time variable. However, this novel approach is counter-intuitive and led to an error early in the derivation as pointed out by Ffowcs Williams and Hawkins [3] and shown by Farassat and Myers [37].

Generalized functions can also be used for the derivation of an extended Kirchhoff formulation. A field function is defined to be identical to the real flow quantity outside a control surface S and zero inside. The discontinuities of the field function across the control surface S are taken as acoustic sources, represented by generalized functions. Ffowcs Williams and Hawkins [5] derived an extended Kirchhoff formulation for sound generation from a vibrating surface in arbitrary motion. However, in their formulation the partial derivatives were taken with respect to the observation coordinates and time and that is difficult to use in numerical computations. Farassat and Myers [6] derived an extended Kirchhoff formulation for a moving, deformable, piecewise smooth surface. The same partial derivatives were taken with respect to the source coordinates and time. Thus their formulation is easier to use in numerical computations and their relatively simple derivation shows the power of generalized function analysis.

Morino and his co-workers have also developed various extended Kirchhoff formulations. Morino [40-43] derived an extended Kirchhoff's formulation for the special case when control surface S moves in uniform translation with respect to the undisturbed air. He used the Green's function approach. The method is suitable for airplane aerodynamics and became the basis of direct panel methods which are widely used for the evaluation of aerodynamic loads in aircraft design. Subsequently, the more general term "boundary-element method" was introduced a term that covers

panel and lifting surface methods depending on the representation of the surface of the body. The method was extended to a rotating surface (e. g. helicopter rotor) by Morino et al. [44] and finally to surface moving in an arbitrary motion Morino et al. [45-46]. Their formulation is based on the velocity potential Φ , but this is not a limitation, since pressure p can be found using Bernoulli's theorem. It should be noted that Morino's formulations were derived with aerodynamic applications in mind. However, they can be used in rotorcraft aeroacoustics, as well (e. g. Lyrintzis and George [10], Xue and Lyrintzis, [13]).

In the remaining parts of the paper, we are going to show some typical Kirchhoff formulations and discuss some rotorcraft aeroacoustic applications.

4.2 Theoretical Development of Typical Kirchhoff Formulations

In all subsequent formulations we will make the assumption of a rigid (i. e. not deformable) surface S , for simplicity. We will attempt to unify the nomenclature so the formulations will be easier to compare. It should be noted that there is a sign difference in the definition of distance r between Morino and Tseng [46] and Farassat and Myers [6] that causes a sign difference in their final formulas. The reader is referred to the original references for the exact formulations, detailed assumptions and derivations.

4.2.1 Stationary Surface

A Kirchhoff's surface S (Figure 1) is assumed to enclose all the nonlinear effects and sound sources. Outside this surface the acoustic flow field is linear and is governed by the wave equation. Let Φ be a quantity satisfying the wave equation (i. e. pressure, (disturbance) velocity potential) in the exterior of surface S :

$$\frac{1}{c^2} \frac{\partial^2 \Phi}{\partial t^2} - \nabla^2 \Phi = 0 \quad (1)$$

Φ and its first derivatives (i. e. $\partial\Phi/\partial t$, $\partial\Phi/\partial n$) should be continuous outside surface S .

c is the speed of sound at ambient conditions.

In Morino's formulation, a Green's function approach is used to derive a representation for the solution of the convective wave equation in terms of the surface pressure and its derivatives. The Green function is a solution of the equation

$$\nabla^2 G - \frac{1}{c^2} \left(\frac{\partial}{\partial t} \right)^2 G = \delta(x-x', y-y', z-z', t-\tau) \quad (2)$$

where δ is the Dirac delta function. The observer location is $\mathbf{x}=(x, y, z, t)$ and $\mathbf{y}=(x', y', z', \tau)$ is the

source. (Superscript ' is used to denote the source position.) G must satisfy the causality condition for hyperbolic equations:

$$G = \frac{\partial G}{\partial t} = 0 \text{ for } t < \tau'. \quad (3)$$

The solution for the above equation for the subsonic case is given by

$$G = - \frac{\delta(\tau' - t + \tau)}{4\pi r} \quad (4)$$

where τ' is the retarded (emission) time and τ is the time delay (r/c) between emission and detection

$$\tau' = t - \tau = t - \frac{r}{c} \quad (5)$$

The classical Kirchhoff formulation for a stationary control surface S (figure 1) can be written as (e. g. Pierce, [33])

$$4\pi\Phi(x,t) = \int_S \left[\frac{\Phi}{r^2} \frac{\partial r}{\partial n} - \frac{1}{r} \frac{\partial \Phi}{\partial n} + \frac{1}{c r} \frac{\partial r}{\partial n} \frac{\partial \Phi}{\partial \tau} \right]_{\tau} dS \quad (6)$$

where:

$[\]_{\tau}$ denotes evaluation in the retarded (emission) time, e. g. $[\Phi]_{\tau} = \Phi(y, t - r/c)$

(x, t) and (y, τ') are the space-time variables of the observer and the source (surface), respectively, r is the distance between observer and source: $r = |x - y|$;

it should be noted that $\cos \theta = \partial r / \partial n$ where θ is the angle between the normal vector on the surface n (pointing out) and the radiation direction $r = x - y$.

Equation (6) is an integral representation of Φ at points exterior to S in terms of information prescribed on the control surface S . It can be used for the computation of noise at an arbitrary point, if the solution is known on surface S . The numerical simulations can provide Φ and its normal and time derivative. It should be noted that the first term has an $1/r^2$ dependence with distance r and it is not significant in the far-field. Furthermore, for the observer on or inside the surface, Φ equals zero. In fact, if the observer is on the surface, equation (1) is an integral equation for Φ on S . This is the basis of modern boundary-element methods (e. g. Morino, [40, 41]). This also shows that Φ , $\partial\Phi/\partial\tau$, and $\partial\Phi/\partial n$ are not independent on the surface S .

4.2.2 Uniformly Subsonically Moving Surface

Now the outside flow is governed by the convective wave equation

$$\nabla^2 \Phi - \frac{1}{c^2} \left(\frac{\partial}{\partial t} + U_{\infty} \frac{\partial}{\partial x} \right)^2 \Phi = 0 \quad (7)$$

where U_{∞} is the uniform velocity of the control surface S . If U_{∞} is zero, the above equation reduces to the simple wave equation. If U_{∞} is a subsonic speed, the solution for the Green's function becomes:

$$G = - \frac{\delta(\tau' - t + \tau)}{4\pi r_0} \quad (8)$$

where subscript o denotes evaluation at the Prandtl-Glauret transformation:

$$x_0 = x, \quad y_0 = \beta y, \quad z_0 = \beta z. \quad (9)$$

Thus the distance between the observer and the surface point in Prandtl-Glauret coordinates is

$$r_0 = \{(x - x_0)^2 + \beta^2 [(y - y_0)^2 + (z - z_0)^2]\}^{1/2} \quad (10)$$

The time delay τ is still uniquely defined for this case. The physical meaning of the time delay τ can be explained using figure 2. O is the observation point and P is the source point. P_0 is the source point at the time of the emission. The time delay now becomes:

$$\tau = \frac{[r_0 - M_{\infty}(x - x_0)]}{c \beta^2} \quad (11)$$

where M_{∞} is the free stream Mach number and:

$$\beta = (1 - M_{\infty}^2)^{1/2} \quad (12)$$

After some algebra, Φ can be expressed in terms of surface integrals (see Morino [42], equation 3.15):

$$4\pi\Phi(x,t) = \int_{S_0} \left[\frac{\Phi}{r_0^2} \frac{\partial r_0}{\partial n_0} - \frac{1}{r_0} \frac{\partial \Phi}{\partial n_0} + \frac{1}{c r_0 \beta^2} \frac{\partial \Phi}{\partial \tau} \left(\frac{\partial r_0}{\partial n_0} - M_{\infty} \frac{\partial x_0}{\partial n_0} \right) \right]_{\tau} dS_0 \quad (13)$$

where subscript o denotes the transformed variable, (e. g. \mathbf{n}_o is the outward pointing vector normal to the surface S_o) and all the values are calculated at the retarded time. It can be easily checked that equation (13) reduces to equation (6) when U_∞ is zero. The formulation can be readily extended to a uniformly supersonically moving surface (Morino [42]). In this case there are two retarded times and subscript t in equation (6) denotes contribution from both.

4.2.3 Arbitrarily Moving Kirchhoff Surface

The formulation for an arbitrary, subsonically-moving, rigid Kirchhoff's surface (e. g. Farassat and Myers, [6]) can be written as:

$$4\pi\Phi(\mathbf{x},t) = \int_S \left[\frac{\partial\tau/\partial n}{r^2(1-M_r)} \Phi - \frac{1}{r(1-M_r)} \left(\frac{\partial\Phi}{\partial n} + \frac{M_n}{c} \frac{\partial\Phi}{\partial\tau} \right) + \frac{1}{c(1-M_r)} \frac{\partial}{\partial\tau} \left(\frac{\partial\tau/\partial n - M_n}{r(1-M_r)} \Phi \right) \right] dS \quad (14)$$

where \mathbf{y} and \mathbf{r} are now a functions of time: $\mathbf{y}(\tau)$, $\mathbf{r}(\tau)$, M_r is the Mach number in the direction of wave propagation from the source to the observer: $M_r = \mathbf{v} \cdot \mathbf{r} / r c$ (\mathbf{v} is the local source-surface velocity $\mathbf{v} = \partial\mathbf{y}/\partial\tau$), M_n is the local normal Mach number on S : v_n/c . (v_n is the local normal velocity of S with respect to the undisturbed medium). All the quantities are also evaluated for the retarded (emission) time which now is the root τ' of the equation

$$\tau - t + r(\tau)/c = 0 \quad (15)$$

This equation has a single root for the subsonic case. Note that for the steady surface: $\tau' = t - r/c$. For complicated motions, equation (15) has to be solved numerically (e. g. Newton-Raphson technique). The normal and the time derivatives of Φ , i. e. $\partial\Phi/\partial\tau$, and $\partial\Phi/\partial n$, are taken with respect to source coordinates and time which makes the formula easy to apply in computations.

It should be noted that the time derivative in the last term of equation (14) can be evaluated analytically, so equation (15) can be written as:

$$4\pi\Phi(\mathbf{x},t) = \int_S \left[\frac{E_1}{r(1-M_r)} + \frac{\Phi E_2}{r^2(1-M_r)} \right] dS \quad (16)$$

where

$$E_1 = (M_n^2 - 1) \frac{\partial\Phi}{\partial n} + M_n \mathbf{M}_t \cdot \nabla' \Phi - \frac{M_n}{c} \dot{\Phi} + \frac{1}{c(1-M_r)} [(\dot{n}_r - \dot{M}_n - \dot{n}_M) \Phi + \left(\frac{\partial\tau}{\partial n} - M_n \right) \dot{\Phi}] + \frac{1}{c(1-M_r)^2} \left[\dot{M}_r \left(\frac{\partial\tau}{\partial n} - M_n \right) \Phi \right] \quad (17)$$

$$E_2 = \frac{1-M^2}{(1-M_r)^2} \left(\frac{\partial\tau}{\partial n} - M_n \right) \quad (18)$$

Here the dot over M and n denotes derivative with respect to source time. In addition:

$$\begin{aligned} \dot{M}_r &= \dot{\mathbf{M}} \cdot \hat{\mathbf{r}}, & \dot{n}_r &= \dot{\mathbf{n}} \cdot \hat{\mathbf{r}}, & \dot{M}_n &= \dot{\mathbf{M}} \cdot \mathbf{n}, \\ \dot{n}_M &= \dot{\mathbf{n}} \cdot \mathbf{M}, & \dot{\mathbf{n}} &= \boldsymbol{\omega} \times \mathbf{n} \end{aligned}$$

where: $\hat{\mathbf{r}} = \mathbf{r}/r$, ∇' is the surface gradient operator, and $\boldsymbol{\omega}$ is the angular velocity of surface S (S is assumed rigid).

The simplified expression for E_2 was given by Myers and Hausmann [47]. In the original paper of Farassat and Myers [6] a more complicated formula for E_2 is given. Simplified expressions for E_1 and E_2 for a rigid surface in uniform rectilinear motion were given by Myers and Hausmann [48].

The above formulation is valid when the observer is stationary and the surface is moving at an arbitrary subsonic speed. However, for the case of an advancing rotating blade the observer is usually moving with the free flow speed (e. g. helicopter rotor in a wind tunnel with a free stream not equal to zero). The formulation can be adjusted for this case by allowing the observer to move with the free stream instead of being stationary in the equation (15) of the retarded time. In fact for the case of a uniformly moving surface, we started from equation (16) and derived Morino's formula (equation 13) for a uniformly moving surface and moving observer at the same speed.

In Farassat's formulation the Kirchhoff surface is assumed to be moving subsonically. Extension to supersonically-moving surfaces can be made, but the analysis becomes lengthy and complicated and the complete form of the formulation has not yet been published, but it is now developed (Farassat and Myers, [49]).

Morino's formulation for an arbitrarily moving surface (e.g., Morino and Tseng [46]) can be written as

$$4\pi\Phi(y_*, \tau_*) = \int_S \left[\left(-\frac{\partial}{\partial n} \left(\frac{1}{r(1-M_T)} \right) \Phi - \frac{1}{r(1-M_T)} \frac{\partial \Phi}{\partial n} \right. \right. \\ \left. \left. + \frac{1}{(1-M_T)} \frac{\partial \Phi}{\partial \tau} \left(\frac{\partial \tau'}{\partial n} - \frac{v_n}{c^2} \right) \right] dS \quad (19)$$

$$\text{where:} \quad \frac{\partial}{\partial n} = \frac{\partial}{\partial n} - \frac{v_n}{c^2} \mathbf{v} \cdot \nabla' \quad (20)$$

$$\frac{\partial}{\partial n} = -\mathbf{n} \cdot \nabla - \frac{v_n}{c^2} \frac{d}{dt} \quad (21)$$

Superscript ' is used to denote the source point and τ' is still the solution of the retarded time equation (15).

Note that in equation (19) the solution is evaluated for the source (surface) coordinates, that means that the observer is moving with the same velocity as the surface, whereas in equation (16) the observer is stationary. The formulation of equation (16) could be more useful for the noise in cases of a fixed observer and a moving source. However, the formulation of equation (19) could be used for a comparison check of Kirchhoff's formulation with a CFD solution, since in both techniques rotating coordinates are usually used. Equation (19) will also reduce to equation (13) for a uniformly moving surface and to equation (6) for a stationary surface. It should be noted that Morino's formulation (equation 19) can be easily extended to supersonically moving surfaces (Morino and Tseng, [46]) by just summing the values at all the retarded times τ' , whereas Farassat's formulation (equation 16) can not be easily extended. The two formulations are mathematically equivalent. This is easy to see for the case of a uniformly moving surface.

Isom et al. [6-7] developed a nonlinear Kirchhoff formulation (Isom's formulation) for some special cases (i. e. stationary surface at the sonic cylinder, high frequency approximation and observer on the rotation plane). They have included in their formulation some nonlinear effects using the transonic small disturbance equation. The nonlinear effects are generally accounted for with a volume integral (e. g. Morino and Tseng, [46]). However, they showed that for the above special cases the nonlinear effects can be reduced to a surface integral.

4.3 Applications and Numerical Techniques

Kirchhoff's formula has been extensively used in light diffraction and other electromagnetic problems, aerodynamic problems, i. e. boundary-elements (e. g. Morino and Tseng [46]), as well as in problems of wave propagation in acoustics (e. g. Pierce [34]). Kirchhoff's integral formulation has been used extensively for the prediction of acoustic radiation in terms of quantities on boundary surfaces (the Kirchhoff control surface coincides with the body). Kirchhoff's method has also been used for the computation of acoustic scattering from rigid bodies

However, we feel the main power of Kirchhoff's formulation is to extend near-field aeroacoustic calculations to the far-field for nonlinear problems (e. g. transonic flow). The nonlinear aerodynamic near-field can be evaluated using CFD techniques. This idea of matching between a nonlinear aerodynamic near-field and a linear acoustic far-field was first proposed by Hawkings [50], and has been used by several investigators in various problems. The separation of the problem into linear and nonlinear regions allows the use of the most appropriate numerical methodology for each. We have been referring to this technique as the "Kirchhoff method."

The use of Kirchhoff's method is based on Kirchhoff formulations (e. g. eqs 6, 13, 16, 19). The values of the pressure (or velocity potential) and its normal and time derivatives on an arbitrary surface S are enough to give the far-field radiation at any external point. The surface S is assumed to enclose all the nonlinear flow effects and noise sources. Pressure (or velocity potential) and its derivatives are numerically calculated from an aerodynamic near-field code. Since it is assumed that the linear wave equation is valid outside this control surface S , this surface must be chosen large enough to include the region of nonlinear behavior. However, the accuracy of the numerical solution is limited to the region immediately surrounding the near-field, because of the usual increase of mesh spacing with distance. Thus, since the size of S is limited by the accuracy in the numerical solution for the mid-field, a judicious choice of S is required for the effectiveness of the Kirchhoff method. For example, Patrick et al. [51] recommend that the deviation of the velocity at S from its average value should not be allowed to be more than 5%. Xue and Lyrantzis [52] relate the size of the Kirchhoff surface for transonic blade-vortex interactions to the transonic similarity parameter for a given vortex strength. However, the more accurate procedure seems to be the testing the wave propagation of the CFD solution for a ray of points in order to find the appropriate linear region and place the Kirchhoff

surface there (e. g. references [9-10]). The results should be independent of the placement of the Kirchhoff surface, as long as the surface stays in the linear region. Another idea, not tested yet, is to substitute directly into the right-hand side of the integral Kirchhoff equation and measure the difference between the predicted (i. e. the left-hand side of the equation) and the actual value. If the difference is low we are in the linear region.

By making calculations with different surfaces, it was found by Lyrantzis and George [53] that the tip surface or cylinder base contributions of the Kirchhoff surface have only a small effect in most cases. The effect of mesh size, wave thickness, numerical or analytical (when available) derivatives was also studied by Lyrantzis [54] and Lyrantzis and George [53]. They used some simple analytical cases to evaluate the effects of the above factors. It should be noted that sometimes a finer CFD mesh is needed to resolve details such as the high frequency content of the solution on the Kirchhoff surface S before the numerical evaluation of the surface integral. Some simple analytical cases to demonstrate the effectiveness of Kirchhoff's formulation were also performed by Myers and Hausmann [48] and Jaeger and Korkan [55]. Finally, Meadows and Atkins [56] tested the use of Kirchhoff's method in the evaluation of the noise due to an oscillating sphere. They examined the effect of the order of integration for the surface integrals and the number of points per period and per wavelength in the retarded time.

5. ROTORCRAFT AEROACOUSTICS APPLICATIONS

The Kirchhoff method for a uniformly moving surface was used in two-dimensional transonic blade-vortex interactions (BVI) to extend the numerically calculated nonlinear aerodynamic BVI results to the linear acoustic far-field (references [9-11]). Typical results from this application are shown in figure 3; in this figure the CFD solution for a two dimensional transonic BVI case is compared to the Kirchhoff solution while the unsteady transonic small disturbance code VTRAN2 is used for the CFD calculations for a point $P (-0.35, -0.186, 0)$ just outside the Kirchhoff surface, upstream and beneath the blade, for a NACA 64A006 airfoil, Mach number $M = 0.822$, vortex strength $C_{1v} = 0.4$, $(C_{1v} = 2\Gamma/U_\infty c)$, where Γ is the vortex strength, U_∞ is the free stream velocity and c is the vortex strength) y_0 (vortex miss distance) $= -0.5$, $x_s = 0.25, 1.25$, $y_s = \pm 1.8$, $z_s = 8$ (all distances are in chords). The vortex moves at constant speed U_∞ (fixed vortex path). The initial vortex position is $x_0 = -9.51$ chords and the free stream

velocity is one (arbitrary units) so the vortex passes below the airfoil leading edge at time $T = 9.51$. The agreement between the CFD and the Kirchhoff method results is excellent. The Kirchhoff method was used to test ideas for BVI noise reduction (Xue and Lyrantzis, [12]).

Kirchhoff's method has been applied to hover High-Speed Impulsive (HSI) noise. Baeder et al. [17] and Strawn et al. [18] used a stationary Kirchhoff surface that encloses the entire rotor. The state-of-the-art Transonic Unsteady Rotor Navier Stokes (TURN) code [57, 58] was used for the near-field CFD calculations. An unstructured grid was used by Strawn et al. [18]. Kirchhoff's method predicted the HSI hover noise very well using about half the CPU of the straight CFD calculation. The results are also compared with a linear (i. e. monopole plus dipole sources) acoustic analogy method (RAPP code [29]). The acoustic analogy results were inaccurate for tip Mach numbers higher than 0.7, because of the omission of quadrupole sources. Figure 4 shows some typical acoustic HSI signals from Baeder et al. [17] at a distance of 3.09 rotor radii and compares with experiments by Purcell [59]. Results from Strawn et al. [18] are similar. The method was recently extended to an advancing rotor HSI noise by Strawn and Biswas [20]. It should be noted that, detailed CFD information out to the stationary Kirchhoff cylinder is necessary as an input. In addition, the aerodynamic input, which is usually in rotating blade coordinates, has to be transformed to stationary coordinates, a process that introduces some errors. Since the cylinder surface is not included, the method seems to be well suited for HSI noise calculations where the main signal is on the rotor plane. However, the application of this method for BVI noise, where noise radiation occurs also in downward directions and detailed CFD information is needed near the blade, is doubtful.

Isom et al. [7], and Purcell [59, 60] used a modified Kirchhoff method which also included some nonlinear effects for a stationary surface, to calculate high-speed compressibility noise for the hover case. Results (not shown here) show good agreement with experimental data. However, the method has several limitations, and the results do not show any distinct advantage over the simple linear Kirchhoff method.

Another Kirchhoff method used in helicopter rotor noise is the rotating Kirchhoff method (i. e. the surface rotates with the blade). The method was used for three-dimensional transonic BVI's for a hovering rotor by Xue and Lyrantzis [13]. The near-field was calculated using the Full Potential Rotor (FPR) code. The rotating Kirchhoff formulation allows the Kirchhoff surface to rotate with the blade; thus a smaller cylinder

surface around the blade can be used. No transformation of data is needed because the CFD input is also rotating. Since more detailed information is utilized for the accurate prediction of the far-field noise this method is more efficient. We feel that the rotating Kirchhoff formulation is needed for the BVI problem, since the details of the flow around the airfoil caused by the vortex are important in determining the far-field noise.

Typical results (pressure vs rotor azimuthal angle Ψ) are shown in figure 5, where the CFD solution is compared to the Kirchhoff solution at point $P(x,y,z)=(0.56,9.89,0.705 \text{ chords})$ just outside the Kirchhoff surface. A rotating formulation is used for the Kirchhoff method and the FPR is used for the CFD calculations. It should be noted that both solutions are in the rotating (i. e. blade fixed) coordinate system (i. e. Morino's formulation, equation 19). The Kirchhoff control surface coincides with the grid lines, $L=11$ is used in this case. The results are almost the same. The small errors are probably due to the relatively coarse mesh used in the FPR calculations. The rotating Kirchhoff method (Farassat's formulation) compares very well with experimental results [59], as shown in figure 6, where results from Purcell [59] (Isom's formulation [8]) are also included. FPR is used in both cases. A 1/7 scale model of a UH-1H rotor was used experimentally; results are shown for $M=0.88$ and 0.90 at a distance $R=3$ radii. It should be noted that a more detailed grid resolution near the rotor tip was used in reference [59]. However, the coarser method used in the rotating Kirchhoff method yields satisfactory results.

The rotating Kirchhoff method was extended for an advancing rotor (Lyrintzis et al. [14]) and was applied to HSI noise (Lyrintzis et al. [19]). Typical results for an advancing BVI case are shown in figure 7, where also some experimental results are shown (Kitaplioglu and Caradonna [61]). The Mach number is 0.6 and the advance ratio is 0.2 . The comparison with experimental results is very good.

A slight drawback of the rotating Kirchhoff method is that the rotating speed of the tip of the rotating surface needs to remain subsonic, because Farassat's formulation is currently limited to subsonically moving surfaces. An extension to supersonically moving surfaces is needed. This imposes limits to the position of the tip of the rotating Kirchhoff surface in very high Mach number cases (e. g. $M=0.92-0.95$ for hover). However, Farassat and Myers [49] are currently extending the formulation to supersonically moving surfaces. We expect that this extension will be employed in the rotating Kirchhoff formulation in the near future.

6. CONCLUDING REMARKS

Kirchhoff's method consists of the calculation of the nonlinear near- and mid-field usually numerically with the far-field solutions found from a linear (or nonlinear) Kirchhoff formulation evaluated on a surface S surrounding the nonlinear-field. The surface S is assumed to include all the nonlinear flow effects and noise sources. The separation of the problem into linear and nonlinear regions allows the use of the most appropriate numerical methodology for each. The advantage of this method is that the surface integrals and the first derivatives needed can be evaluated more easily than the volume integrals and the second derivatives needed for the evaluation of the quadrupole terms when acoustic analogy is used. All near-field complicated nonlinear effects that are necessary for far-field accurate acoustic prediction. The method is simple and accurate and accounts for the nonlinear quadrupole noise in the far-field. Full diffraction and focusing effects are included while eliminating the propagation of the reactive near-field. Some results indicative of the uses of Kirchhoff's method were shown here, but the reader is referred to the original references for further details.

The use of Kirchhoff's method in rotorcraft aeroacoustics has increased substantially the last 5-10 years, because of the development of reliable CFD methods that can be used for the evaluation of the near-field. A simple set of portable Kirchhoff subroutines can be developed to calculate the far-field noise from inputs supplied by any aerodynamic near/mid-field code. Some issues that need to be addressed before the wide-spread application of Kirchhoff subroutines are the determination of proper Kirchhoff surface placement, the choice of an adequate grid. Finally, the subroutines should be extended to handle supersonically moving surfaces. However, as these subroutines develop and become mature, Kirchhoff's method may very well replace the Acoustic Analogy method used today for acoustic problems when nonlinear quadrupole terms are present.

7. ACKNOWLEDGMENTS

The author wishes to acknowledge the support of the University of Minnesota Supercomputer Institute (MSI) and Cray Research Inc.

8. REFERENCES

1. Brentner, K. S., and Farassat, F., "Helicopter Noise Prediction: The Current Status and Future Direction," *Journal of Sound and Vibration*, Vol. 170(1), Feb. 1994, pp. 79-96.
2. George, A. R., Coffen, C. D., and Ringler, T. D., "Advances in Tilt Rotor Noise Prediction," *Proceedings of the 14th DGLR/AIAA Aeroacoustics Conference*, Aachen, Germany, May 1992, pp. 510-531.
3. Hardin, J. C., Hussaini, M. Y., *Computational Aeroacoustics*, Springer-Verlag, New York, 1993.
4. Lighthill, M. J., 1952, "On Sound Generated Aerodynamically I General Theory," *Proceedings of The Royal Society*, London, Vol. 221A, 1952, pp. 564-587.
5. Ffowcs Williams, and Hawkins, D. L., 1969, "Sound Generation BY Turbulence And Surfaces in Arbitrary Motion," *Philosophical Transactions of The Royal Society*, London, Vol. 264A, pp. 321-342.
6. Farassat, F., and Myers, M. K., "Extension of Kirchhoff's Formula to Radiation from Moving Surfaces," *Journal of Sound and Vibration*, Vol. 123, No. 3, June 1988, pp.451-460.
7. Purcell, T. W., Strawn, R. C., and Yu, Y. H., 1987, "Prediction of High-Speed Rotor Noise With a Kirchhoff Formula," *Proceedings of the American Helicopter Society National Specialists' Meeting on Aerodynamics and Aeroacoustics*, Arlington, TX.
8. Isom, M. P., Purcell, T. W., Strawn, R. C., "Geometrical Acoustics and Transonic Sound," AIAA paper 87-2748, AIAA 11th Aeroacoustics Conference, Sunnyvale, CA, 1987.
9. George, A. R., and Lyrantzis, A. S., "Acoustics of Transonic Blade-Vortex Interactions," *AIAA Journal*, Vol. 26, No. 7, July 1988, pp. 769-776.
10. Lyrantzis, A. S., and George, A. R., "Far-Field Noise of Transonic Blade-Vortex Interactions," *American Helicopter Society Journal*, Vol. 34, No.3, July 1989, pp.30-39.
11. Lyrantzis, A. S., and Xue, Y., "A Study of the Noise Mechanisms of Transonic Blade-Vortex Interactions," *AIAA Journal*, Vol. 29, No. 10, Oct. 1991, pp. 1562-1572.
12. Xue, Y., and Lyrantzis, A. S., "Transonic Blade-Vortex Interactions: Noise Reduction Techniques," *AIAA Journal of Aircraft* Vol. 30, No. 3, May-June 1993, pp. 408-411.
13. Xue, Y., and Lyrantzis, A. S., "Rotating Kirchhoff Formulation for 3-D Transonic BVI Noise for a Hovering Rotor," *AIAA Journal* Vol. 32, No. 2, July 1994, pp. 1350-1359.
14. Lyrantzis, A. S., Kilaras, M., and Xue, Y., "Transonic 3-D BVI Noise Using a Rotating Kirchhoff Formulation for Advancing Rotors" *Proceedings of the AHS 50th Annual Forum*, Vol. I, Washington, DC, May 1994, pp. 115-127.
15. Purcell, T. W., 1988, "CFD and Transonic Helicopter Sound," Paper No. 2, 14th European Rotorcraft Forum.
16. Purcell, T. W., "A Prediction of High-Speed Rotor Noise," AIAA 89-1130, AIAA 12th Aeroacoustics Conference, San Antonio, TX, Apr. 1989.
17. Baeder, J. D., Gallman, J. M., and Yu, Y. H., "A Computational Study of the Aeroacoustics of Rotors in Hover" *Proceedings of the 49th Annual Forum of the American Helicopter Society*, St. Louis, MO, May 1993, Vol. I, pp. 55-71.
18. Strawn, R., Garceau M., and Biswas R., "Unstructured Adaptive Mesh Computations of Rotorcraft High-Speed Impulsive Noise" AIAA paper 93-4359, presented at the 15th AIAA Aeroacoustics Conference, Long Beach, CA, Oct. 1993.
19. Lyrantzis, A. S., Xue, Y., and Kilaras, M. S., "A Prediction of High-Speed Rotor Noise Using a Rotating Kirchhoff Formulation", AIAA paper 94-0463, AIAA 32nd Aerospace Science Meeting, Reno, Nevada, Jan. 1994.
20. Strawn, R. C., Biswas, R., "Computation of Helicopter Rotor Acoustics in Forward Flight," Presented at the 19th Army Science Conference, June, Orlando, FL., Jul. 1994
21. Lyrantzis, A. S. "The Use of Kirchhoff Method in Aeroacoustics," *ASME Journal of Fluids Engineering*, Vol. 116, No. 4, Dec. 1994.

22. Baeder, J. D., McCroskey, W. J., and Srinivasan, G. R., "Acoustic Propagation Using Computational Fluid Dynamics," *Proceedings of the 42nd Annual Forum of the American Helicopter Society*, Washington, DC, June, 1986, Vol. 1, pp. 551-562.
23. Baeder, J. D., "Computation of Non-Linear Acoustics in Two-Dimensional Blade-Vortex Interactions," Paper No. 1-1, 13th European Rotorcraft Forum, Arles, France, Sept. 1987.
24. Baeder, J. D., "Euler Solutions to Nonlinear Acoustics of Non-Lifting Hovering Rotor Blades," 16th European Rotorcraft Forum, Glasgow, Scotland, Sept. 1990.
25. Baeder, J. D., "Euler Solutions to Nonlinear Acoustics of Non-Lifting Rotor Blades," *Proceedings of AHS/RAeS International Technical Specialists meeting on Rotorcraft Acoustics and Rotor Fluid Dynamics*, Philadelphia, PA, Oct. 1991.
26. Srinivasan, G. R., and Baeder J. D., "Recent Advances in Euler and Navier-Stokes Methods for Calculating Helicopter Rotor Aerodynamics and Acoustics," 4th International Symposium on Computational Fluid Mechanics, Sept. 1991.
27. Stoker, R. W., and Smith, M. J., "An Evaluation of Finite Volume Direct Simulation and Perturbation Methods in CAA Applications," AIAA 93-0152, AIAA 31st Aerospace Science Meeting, Reno, NV, Jan. 1993.
28. Brentner, K. S., "Prediction of Helicopter Rotor Discrete Frequency Noise," NASA TM-87721, Oct. 1986.
29. Gallman, J. M., "The Validation and Application of a Rotor Acoustic Prediction Computer Program," *Proceedings of the Army Science Conference*, Durham, North Carolina, 1990.
30. Farassat, F., "Theory of Noise Generation From Moving Bodies With Application to Helicopter Rotors," NASA TR-R-451, 1975.
31. Tadghighi, H., Hassan, A. A., and Charles, B., "Prediction of Blade-Vortex Interaction Noise Using Airloads Generated by a Finite-Difference Technique," *American Helicopter Society Journal*, Vol. 37, No. 4, Oct. 1992, pp. 38-47.
32. Farassat, F., and Tadghighi, H., "Can Shock Waves on Helicopter Rotors Generate Noise? A Study of the Quadrupole Source," *Proceedings of the 46th Annual Forum of the American Helicopter Society*, Washington DC, May, 1990, Vol. 1, pp. 323-346.
33. Tadghighi, H., Holz, R., Farassat, F., and Lee Y-J, 1991, "Development of Shock Noise Prediction Code for High-Speed Helicopters - The Subsonically Moving Shock" *Proceedings of the 47th Annual Forum of The American Helicopter Society*, Phoenix, AZ, May, 1991, pp. 773-789.
34. Pierce, A. D., "Acoustics: An Introduction to Its Physical Principles And Applications", McGraw-Hill, New York, 1981.
35. Morgans, R. P., "The Kirchhoff Formula Extended to a Moving Surface," *Philosophical Magazine*, 9, s.7, No. 55, 1930, pp. 141-161.
36. Hawkings, D. L., "Comments on the Extension of Kirchhoff's Formula to Radiation From Moving Surfaces," *Journal of Sound and Vibration*, Vol. 132, 1989, No. 1, p. 160.
37. Farassat, F., and Myers, M. K., Author's Replay to "Comments on the Extension of Kirchhoff's Formula to Radiation From Moving Surfaces," *Journal of Sound and Vibration*, Vol. 132, No. 3, 1989, p. 511.
38. Munro, D. H., "The Production of Sound by Moving Objects," Ph.D. Dissertation, Massachusetts Institute of Technology, 1980.
39. Khromov, V. A., "Generalization of Kirchhoff's Theorem For The Case of a Surface Moving in an Arbitrary Way," *Soviet Physics - Acoustics*, Vol. 9, 1963, pp. 68-71.
40. Morino, L., "Unsteady Compressible Potential Flow Around Lifting Bodies: General Theory," AIAA paper No. 73-196, 1973.
41. Morino, L., "A General Theory of Unsteady Compressible Potential Aerodynamics," NASA Contractor Report CR-2464, Dec. 1974.
42. Morino, L., "Steady, Oscillatory, and Unsteady Subsonic and Supersonic Aerodynamics - Production Version 1.1 (SOUSSA-P, 1.1), Vol. 1, Theoretical Manual," NASA Contractor Report CR-159130, 1980.

43. Morino, L., "Mathematical Foundations of Integral Methods," in *Computational Methods in Potential Aerodynamics*, Ed. L. Morino, Computational Mechanics Publications, Southampton, UK, 1985.
44. Morino, L., Freedman, M. I., Deutsch, D. J., and Sipcic, S. R., "An Integral Equation Method for Compressible Potential Flows in an Arbitrary Frame of Reference," in *Computational Methods in Potential Aerodynamics*, Ed. L. Morino, Computational Mechanics Publications, Southampton, UK, 1985.
45. Morino, L., Bharadvaj, B. K., Freedman, M. I., and Tseng, K., "BEM For Wave Equation With Boundary in Arbitrary Motion And Applications to Compressible Potential Aerodynamics of Aeroplanes and Helicopters" in *Advanced Boundary Element Methods*, Ed. T. A. Cruse, Springer-Verlag, New York, 1988.
46. Morino, L., and Tseng, K., "A General Theory of Unsteady Compressible Potential Flows with Applications to Airplanes and Rotors" in *Developments in Boundary Element Methods*, Vol. 6, Banerjee, P. K., and Morino L. eds, Elsevier Applied Science Publisher, Barking, UK, 1990, pp. 183-245.
47. Myers, M. K., and Hausmann, J. S., "On the Application of the Kirchhoff Formula for Moving Surfaces," *Journal of Sound and Vibration*, Vol. 139, 1990, pp. 174-178.
48. Myers, M. K., and Hausmann, J. S., "Computation of Acoustic Scattering from a Moving Rigid Surface," *Journal of the Acoustical Society of America*, Vol. 91(5), 1992, pp. 2594-2605.
49. Farassat, F. and Myers, M. K., "Kirchhoff Formula for Supersonic Surfaces" to be presented at the ASME 115th Winter Annual Meeting, Chicago, IL, Nov. 1994.
50. Hawkings, D. L., "Noise Generation by Transonic Open Rotors," Westland Research Paper 599, 1979.
51. Patrick, S. M., Davis, C. M., and Atassi H., "Acoustic Radiation from a Lifting Airfoil in Nonuniform Subsonic Flows" in *Computational Aero- and Hydro-Acoustics*, FED Vol. 147, eds: Mankbadi, R., R., Lyrantzis, A. S., Baysal, O., Povinelli, L. A., and Hussaini, M. Y., pp. 41-46, ASME Fluids Engineering Conference, Washington, DC, June 1993.
52. Xue, Y., and Lyrantzis, A. S., "Noise Reduction for Transonic Blade-Vortex Interactions," *Proceedings of AHS/RAeS International Technical Specialists meeting on Rotorcraft Acoustics and Rotor Fluid Dynamics*, Philadelphia, PA, Oct. 1991.
53. Lyrantzis, A. S., "Transonic Blade-Vortex Interactions," Ph.D. Dissertation, Sibley School of Mechanical and Aerospace Engineering, Cornell University, Ithaca, NY, Jan. 1988.
54. Lyrantzis, A. S., and George, A. R., "The Use of Kirchhoff Method in Acoustics," *AIAA Journal*, Vol. 27, No. 10, Oct. 1989, pp. 1451-1453.
55. Jaeger, S., and Korkan, K. D., "On the Prediction of Far-Field Computational Aeroacoustics of Advanced Propellers," AIAA paper 90-3996, AIAA 13th Aeroacoustics Conference, Oct. 1990.
56. Meadows, K., and Atkins, H. L., "Evaluation of a Hybrid Kirchhoff-CFD Approach for Computational Aeroacoustics," presented at the 14th IMACS World Congress, Atlanta, GA, July 1994.
57. Srinivasan, G. R., Baeder, J. D., Obayashi, S., and McCroskey, W. J., "Flowfield of a Lifting Rotor in Hover - A Navier-Stokes Simulation," *AIAA Journal*, Vol. 30, No. 10, October 1992, pp. 2371-2378.
58. Srinivasan, G. R., and Baeder, J. D., "TURNS: A Free-Wake Euler/Navier-Stokes Numerical Method for Helicopter Rotors," *AIAA Journal*, Vol. 31, No. 5, May 1993, pp. 959-962.
59. Purcell, T. W., "CFD and Transonic Helicopter Sound," Paper No. 2, 14th European Rotorcraft Forum, Sept. 1988.
60. Purcell, T. W., "A Prediction of High-Speed Rotor Noise," AIAA 89-1130, AIAA 12th Aeroacoustics Conference, San Antonio, TX, 1989.
61. Kitaplioglu, C., and Caradonna, F., "Aerodynamics and Acoustics of Blade-Vortex Interaction Using an Independently Generated Vortex," AHS Specialists' Aeromechanics Conference, Jan. 1994.

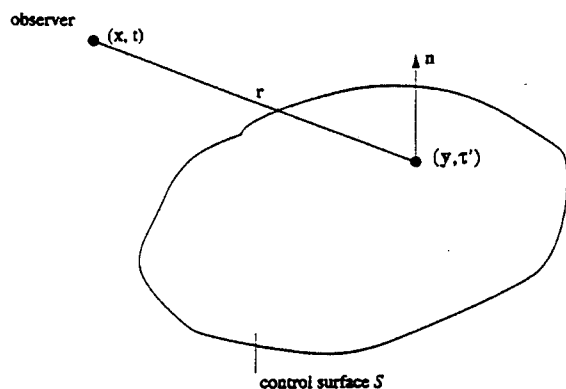


Fig. 1 Kirchhoff's surface S and notation

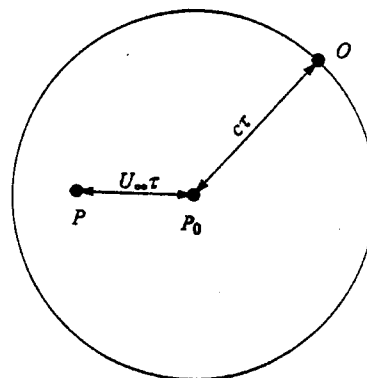
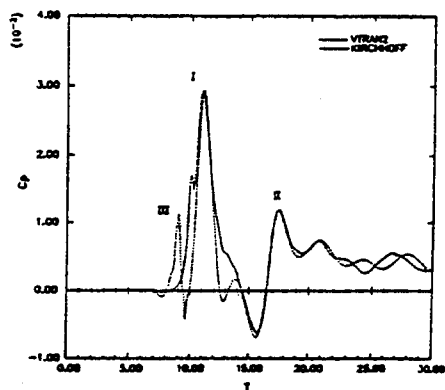
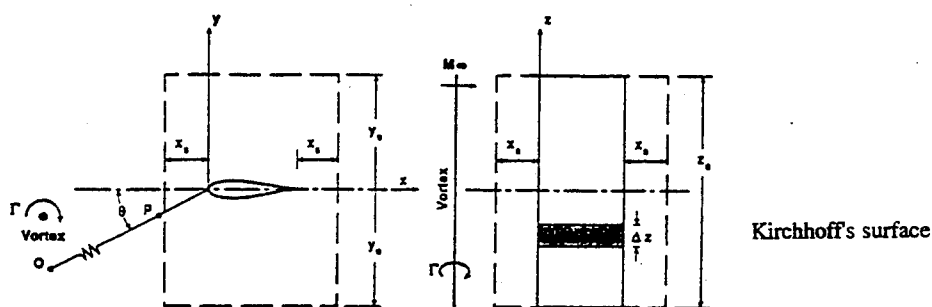
Fig. 2 Effect of retarded time τ for a source (point P) moving with a constant subsonic speed U_∞ .

Fig. 3 CFD and Kirchhoff's method results for 2-D BVI at point P (-0.35, -0.186, 0); NACA 64A006, Mach number $M = 0.822$, vortex strength $C_{IV} = 0.4$, ($C_{IV} = 2\Gamma/U_\infty c$, where Γ is the vortex strength, U_∞ is the free stream velocity and c is the vortex strength), y_0 (vortex miss distance) = -0.5, $x_s = 0.25, 1.25$, $y_s = \pm 1.8$, $z_s = 8$ (all distances are in chords), fixed vortex path (from George and Lyrintzis [9]).

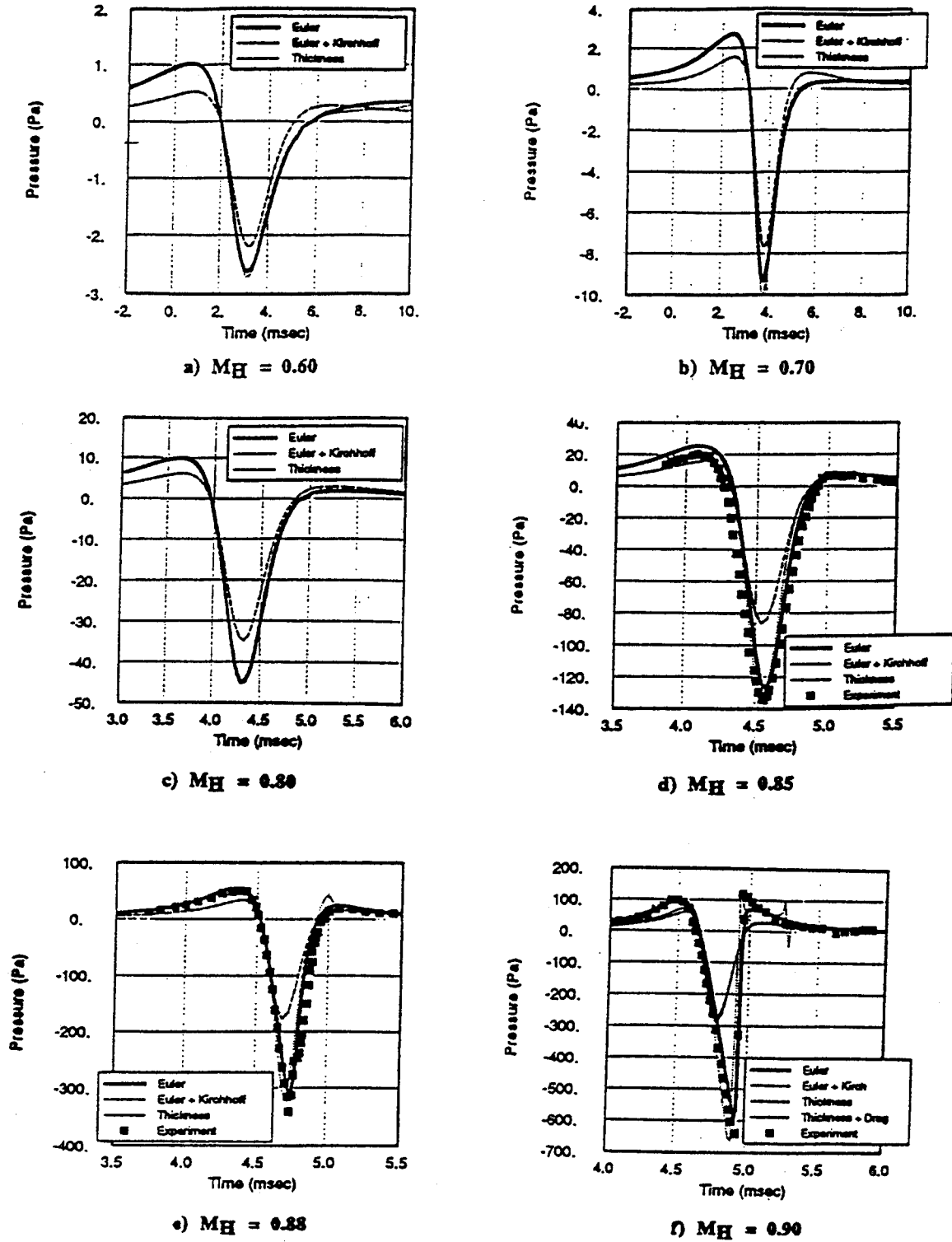


Fig. 4 Comparison of the predicted pressure time histories in the plane of the rotor at 3.09 rotor radii for untwisted UH-1H for three methods at various tip Mach numbers (from Baeder et al., [17]).

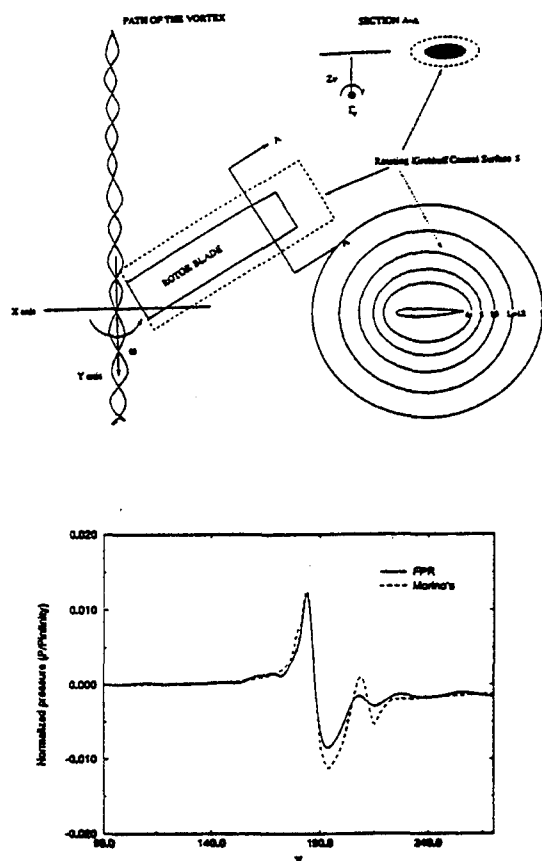


Fig. 5 CFD and Kirchhoff's method results for 3-D BVI at point P (0.56,9.89,0.705 chords) on L=11; Mach number $M=0.75$, vortex strength $\Gamma_v = \Gamma/Mc = 0.2$, vortex miss distance $Z_v = 0.26$, (from Xue and Lyrantzis, [13]).

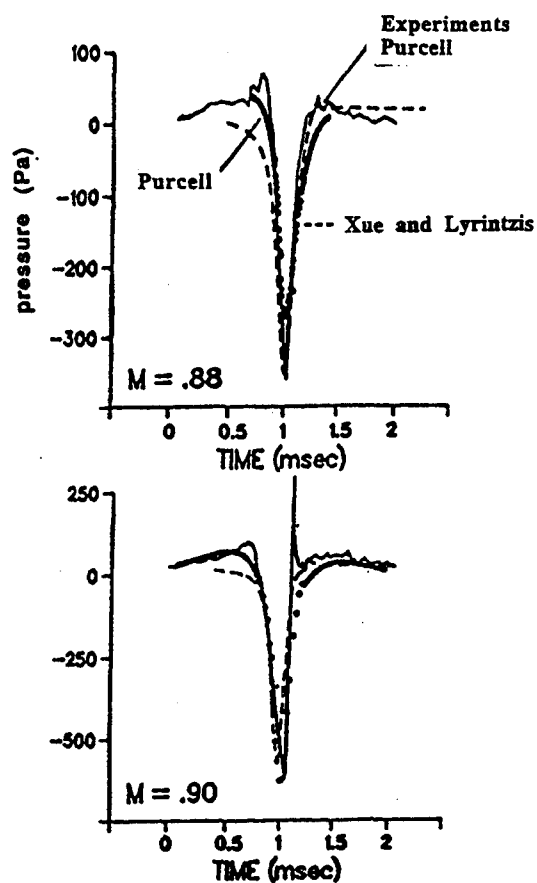


Fig. 6 HSI acoustic pressure predictions for Mach numbers, $M=0.88$, 0.90 , distance $R=3$ radii. Experiments and computations from Purcell [59] are also shown, (from Xue and Lyrantzis [13]).

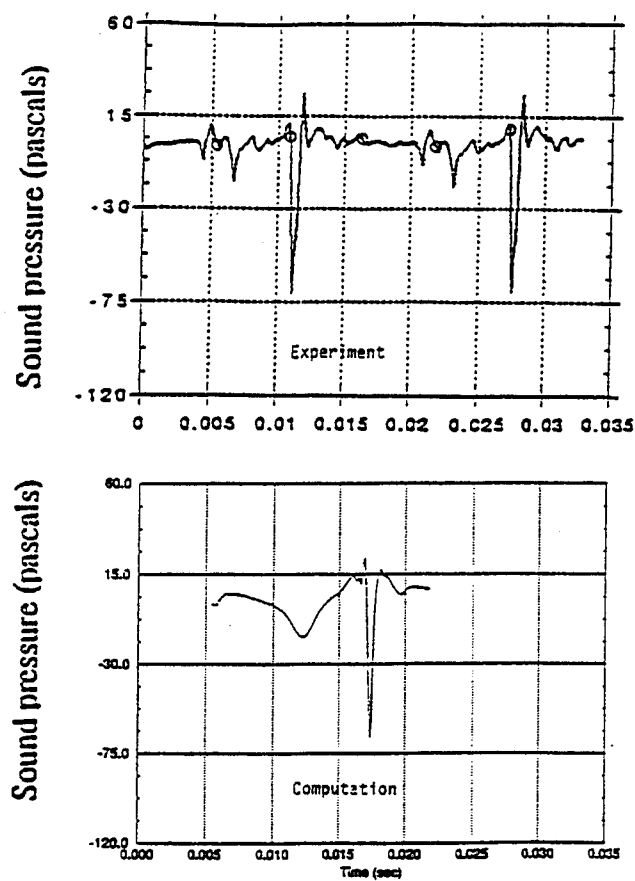


Fig. 7 BVI acoustic noise predictions for an advancing rotor: $M=0.6$, $\mu=0.2$, $\Gamma_v=0.1$. Experimental results from Kitaplioglu and Caradonna [61] are also shown.

Acoustic Design of Rotor Blades Using a Genetic Algorithm

V. L. Wells*, A. Y. Han†, and W. A. Crossley†

Department of Mechanical and Aerospace Engineering
Arizona State University, Box 876106
Tempe, AZ USA 85287-6106

ABSTRACT

A genetic algorithm coupled with a simplified acoustic analysis was used to generate low-noise rotor blade designs. The model includes thickness, steady loading and blade-vortex interaction noise estimates. The paper presents solutions for several variations in the fitness function, including thickness noise only, loading noise only, and combinations of the noise types. Preliminary results indicate that the analysis provides reasonable assessments of the noise produced, and that genetic algorithm successfully searches for "good" designs. The results show that, for a given required thrust coefficient, proper blade design can noticeably reduce the noise produced at some expense to the power requirements.

1 INTRODUCTION

Conceptual design of rotor systems often relies on partially qualitative decisions made by members of a design team to determine important design features. Selection of airfoil section(s) represents one example of this type of design decision-making. Such choices naturally reflect the bias, experience, and personal preferences of the designer and the design team. Other decisions made by designers are based on complicated analytical models for the aerodynamics, dynamics, weight, and performance of the rotor blades. Some optimization procedure, usually numerical or graphical, provides a basis for the final blade design. This design process can be characterized as complex, somewhat arbitrary, and very time-consuming.

These designers, who make the final decisions regarding the geometry and operating parameters of a rotor system, rarely have experience or training in the field of acoustics, nor is acoustic calculation, other than the observation of a few "rules of thumb," generally included in the analytical evaluation performed during the conceptual design process. Consequently, one of the more important attributes of a rotor system—its noise signature—tends to receive little or no attention during the phase of design which can affect it the most. It seems apparent,

then, that a need exists for a tool which can not only provide a logical means for making design decisions, but which can also easily incorporate multi-objective and highly-complex goal functions (such as low-noise and low-weight). The genetic algorithm (GA) may provide a basis for the development of such a design tool.

Computer scientists developed genetic algorithms in the mid-1960's as a programming technique for constructing computer programs[1]. The methodology gradually found its way into other fields, particularly as an optimization tool. Applications of GA have only recently appeared in aerospace engineering problems[2]. Significant among the advantages of GA is the ability to combine discrete, integer, and continuous variables in a single optimization problem[3]. Thus, the selection of airfoil section (a discrete variable) or number of blades (an integer variable), can be handled by the GA-based optimization as easily as the choice of disk loading (a continuous variable). Because the genetic algorithm is not calculus-based, it can be used as a global optimizer of highly-non-smooth and discontinuous functions. The more widely-used numerical optimization procedures cannot readily handle non-continuous variables or functions because of their reliance on the computation of numerical derivatives.

Genetic algorithms appear to have great potential for application to rotorcraft design problems, especially in their ability to incorporate discrete, integer, and continuous variables. The paper discusses the design of a rotor system using a GA-based design code to find an optimal selection of the following characteristics: airfoil section, blade planform (including taper and twist), disk loading, tip speed, solidity, and number of blades. The "optimal" rotor is defined as that producing the lowest sound pressure level as measured during a descent maneuver. A thrust constraint is imposed on the rotor system, but the value of power required is unrestricted. In this way, the exercise clearly shows the trade-off between power and low noise levels.

2 GENETIC ALGORITHMS

Genetic algorithms mimic the patterns of natural selection and reproduction characteristic of biological

*Associate Professor

†Graduate Student

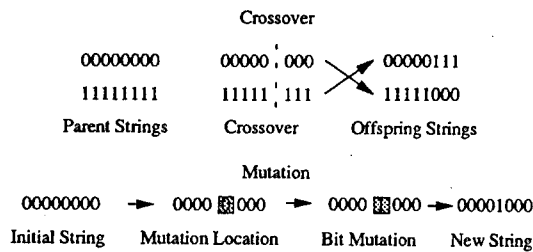


Figure 1: Crossover and Mutation Operators

populations. This concept of "survival of the fittest" as an optimization algorithm originated in work presented by Holland[4] and has since been expanded by Goldberg[5] and others. The methodology has developed into an accepted search and optimization technique. Design variables form the "genes" of a given design and are mapped into binary strings. These strings are then concatenated to form the "chromosome" for a combination of variables which represent an individual design point.

An initial generation is created by randomly placing "1"s and "0"s along the chromosome for a given number of individuals. The values of the design variables in each of these individuals is decoded from the binary string through a set of mapping relationships. From these values, a fitness is assigned to each individual. This fitness is analogous to the objective function value in a numerical optimization problem. Individual chromosomes with high fitness value are more likely to survive and be used as parents for subsequent generations. The search procedure used in GA follows a structured probabilistic information exchange among the members of the population of design points. The reproduction process includes crossover, where a "child" design inherits traits from both of its parent designs, and mutation, where a bit in the chromosome string is changed, thereby introducing a trait not seen in either parent. Figure 1 illustrates the crossover and mutation operators on a simple chromosome string.

Many current efforts in engineering design employ numerical optimization to improve upon the results of standard design processes. The genetic algorithm does not replace these numerical methods. Instead, it provides a tool for searching a larger and more difficult design space than is easily handled by the calculus-based procedures. GA can be used as a global optimizer of highly non-smooth and discontinuous functions because it does not require gradient evaluations and has no requirement for functional continuity. For a highly complex and multi-modal design space, GA provides a rapid search in the direction of the global optimum.

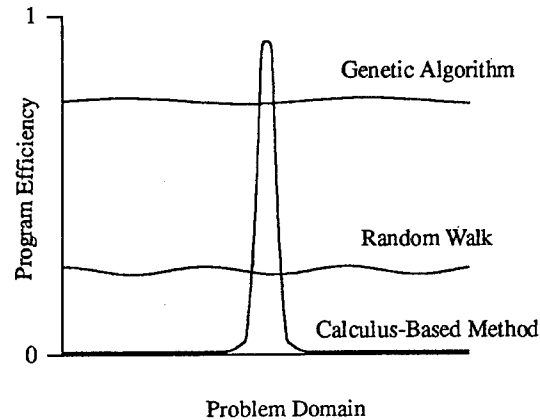


Figure 2: Program Efficiency vs Problem Domain

Because genetic algorithms do not compute gradients, they do not complete a search at a local optimum. In fact, the GA has no way of determining the optimality of a given design, and, therefore, a GA search cannot guarantee optimum fitness. In addition, GA can be prone to *premature convergence*[5] where the population has become uniform in character, but it lacks near-optimum individuals. Premature convergence can result when a problem statement is difficult for the genetic algorithm to approach (GA hard[5]) or from sampling error, especially in the initial randomly-generated population. As described above, however, a genetic algorithm can search a large region and will move the population in the direction of the global optimum. The technique, then, is appropriate in conceptual design where the design space is large and contains several types of variables. Once the search region is narrowed, a calculus-based method can usually select an optimal combination of the continuous design variables. Figure 2 shows the relative efficiency of the GA and the calculus-based method in finding the global optimum of a function versus the domain size and complexity.

3 GENETIC ALGORITHMS IN THE DESIGN OF LOW-NOISE ROTOR SYSTEMS

The design process involves both a means for analyzing a candidate design and a method for choosing the best of those candidates. In the case presented here, the analysis component consists of a prediction of the noise level of a rotor system based on the known design variables. The genetic algorithm, on the other hand, performs the crossover and mutation operations and selects the individuals (or rotor systems) which will serve as parents to the next generation with no actual knowledge of the design variables themselves. For the most part, the procedures

operate in isolation, with the GA routine requiring only knowledge of the fitness of each individual in a generation, and the fitness evaluation knowing only the selected values for the design variables.

3.1 Acoustic Fitness

In the conceptual design phase, the analysis tools used must provide realistic values for the performance of a given system. On the other hand, because many potential design points must be considered, the level of detail used in evaluating performance cannot be too high simply because of time considerations. Consequently, a compromise is made in determining the fitness of a given individual in the design point population.

Predicting the thickness noise requires knowledge of the rotor blade planform (including twist), airfoil section, and tip Mach number. Loading noise prediction, including that derived from BVI, demands a description of the complete, time-dependent loading distribution on the rotor blades. Modern practice in rotor noise prediction includes a wake analysis followed by an aerodynamics calculation, usually with the aid of a CFD tool. Results from the aerodynamic loading prediction are used as input to a noise prediction code. Several authors have shown fairly good results using this method, including Gallman[6] and Spiegel, *et. al.*[7].

Though the quality of the data resulting from the above methodology may be quite good, that benefit occurs only at the expense of time. A prediction method which is useful for conceptual design applications cannot take hours of computer time to run since thousands of design points must be analyzed within a reasonable time span. Thus, a compromise philosophy was followed in developing the fitness evaluation procedure for the low-noise rotor blade. The analysis utilizes a combination of "exact" and approximate techniques in an attempt to obtain reasonable, though not completely accurate, noise and performance levels. The reduced level of accuracy is tolerable at the initial stages of the design as long as the relative noise levels among various rotor designs are correctly predicted.

A code developed by the authors predicts the acoustic signature of the rotor system. The code, based on an acoustic analogy formulation, has been tested extensively and used previously to study the noise produced by helicopter rotors and propellers of various planforms and under many operating conditions[8, 9]. The method predicts both loading and thickness noise in hover and in helicopter or propeller forward flight for observers either on the ground (flyover condition) or traveling with the vehicle. The code can handle both high-speed impulsive and blade-vortex interaction noise predictions, but blade loading input must be provided.

A blade element method based on the suggestions

of Prouty[10] is used to determine power, thrust, and the spanwise load distribution over the rotor blade. A panel method due to Kuethe and Chow[11], which utilizes panels with linearly distributed vortices, determines the chordwise loading distribution for the lift coefficient predicted by the blade element code and the specified airfoil. As such, the current loading distribution is limited to incompressible flow, although the power calculation does take into account an increase in profile drag and lift-curve slope due to compressibility.

The blade element/panel code calculations provide the pressure input for the steady loading noise prediction. As discussed above, computing pressures for input to a blade-vortex interaction noise calculation requires many hours of computer time, so that a simpler approximation to the BVI noise prediction is considered appropriate to this application. A method developed by Hardin[12],[13] and based on the theory of Howe[14], was adapted for the purpose of determining the relative noise produced by blade-vortex interaction.

3.1.1 BVI-Noise Prediction

The inhomogeneous wave equation with source terms is generally "solved" using Green's theorem to write the solution in terms of integrals over the surface containing the sources. The solution method makes use of the free-space Green's function which appears in the aforementioned integrals. Howe[14] produced a solution for the noise field in the vicinity of a semi-infinite flat plate by developing a Green's function appropriate to the geometry and conditions of the problem. Such a methodology is useful since the resulting solution does not involve integrals over the bounding surface (in this case, the flat plate). Hardin adapted Howe's method for finding an alternate Green's function to determining that which applies in the region surrounding an airfoil. Thus, in the case of an airfoil interacting with a vortex, no integral over the airfoil surface itself is required. In order to compute the noise field, only the strength of the vortex and its motion (including its position relative to the airfoil), and a simplified solution for flow about the airfoil, are required.

Hardin's method is, strictly speaking, limited to cases where the Mach number of the interaction between the airfoil and the vortex is low. A typical BVI event in forward flight descent occurs at a Mach number of approximately 0.6. The method is considered to be adequate for computations in this Mach number range. The method assumes that the most prominent interactions are essentially two-dimensional. This assumption ensures that the calculated pressure is a conservative estimate of the actual, since it has been shown that parallel interactions produce the highest acoustic pressure levels.

The fitness evaluation routine considers a dimensionless form of the acoustic pressure given by Hardin[12]. The pressure, nondimensionalized by $\rho_0 c^2$, where ρ_0 is the ambient density and c is the speed of sound, is given as

$$p(x, t) = -\frac{\Gamma \Gamma_0 M_{tip} M_0}{8\pi^2} M_0 \frac{x_2}{x} \frac{c_{tip} c_0 \ell}{x r^2} \times \left[\sin(2\theta - \theta_0) - \frac{\Gamma_0 c_0}{2\pi r} \cos \theta \right], \quad (1)$$

where all variables in the above expression are dimensionless. The $(\cdot)_0$ subscripts refer to the position on the rotor blade at which the BVI occurs—at the suggestion of Hardin, this evaluation uses the 75% radius. Thus, Γ_0 is the circulation about the airfoil at .75R, whereas Γ represents the circulation strength of the vortex with which the blade interacts. x (magnitude x) is the location of the observer, and r (magnitude r) is the vortex location, both relative to the rotor airfoil. The angle, θ , is the angle of the vortex with respect to the rotor airfoil, and θ_0 is the pitch of the rotor blade. The quantity, ℓ , refers to the dimensionless (with respect to rotor radius) length of rotor over which the interaction takes place. The acoustic pressure produced by the blade-vortex interaction also depends on the chord lengths, c_0 and c_{tip} , and the Mach numbers, M_0 and M_{tip} . Some of the parameters in the above equation, such as the Mach numbers and the chords, are either design variables directly, or they are easily calculated from them. The other parameters, such as vortex strength and location, must be estimated from the design variables. Clearly, the tip vortex strength depends on the circulation strength near the rotor blade tip, and Γ is assigned the value of the circulation at the 95% rotor radius. The miss distance, r , depends on the trajectory of the vortex once it is shed. This is estimated using the average induced velocity at the rotor plane which, in turn, is a function of the rotor thrust coefficient.

The current version of the BVI fitness calculation uses an adaptation of the terms in Hardin's equation to account for the effect of core size on the blade-vortex interaction noise. According to Gallman[6], a reasonable estimate for the vortex core size is 20% of the rotor blade tip chord. The effect of the core is introduced through a variation in the circulation strength as a function of the distance from the center of the vortex. Letting Γ_c represent the total circulation strength of the trailing tip vortex, the strength at some distance from the center is estimated as

$$\Gamma = \begin{cases} \Gamma_c \left(\frac{r}{r_c}\right)^2 & \text{if } r < r_c \\ \Gamma_c & \text{if } r \geq r_c \end{cases}$$

where r_c is the core radius.

In addition to providing the acoustic pressure at a given observer location and time, Hardin's model

gives a methodology for computing the vortex motion once it is under the influence of the rotor blade. In order to utilize this procedure, it is assumed that the major interaction occurs at an azimuthal angle of 45°, and that the interaction begins when the rotor passes through 0°. Of course, the exact interaction location depends strongly on the advance ratio and the number of blades. However, a precise determination of the location requires substantial computation time, and virtually all of the strongest interactions occur near the 45° azimuthal angle.

3.2 Fitness Function

The actual fitness of an individual is determined through the value of an objective function which can be described by

$$f = A_1 N_s + A_2 N_{BVI} + \sum_i C_i (\max[0, g_i(x)])$$

In the above equation, N_s and N_{BVI} represent the measures of noise produced by the steady thickness and loading, and by the blade-vortex interactions, respectively. A_1 and A_2 are coefficients chosen to weight the noise sources appropriately. The third term represents a penalty function which is used to ensure, for example, that the rotor is not stalled or that it meets any imposed constraints.

3.3 Genetic Algorithm Methodology

The genetic algorithm-based design code utilizes the three basic operators—selection, crossover and mutation. The code is customized for the current application with variations on these operators and with “higher order” operators which alter the performance of the basic genetic algorithm and help to avoid premature convergence (as described above).

A tournament selection method chooses individuals which will contribute to succeeding generations. In this approach, two individuals are selected without replacement from the current population. These individuals are evaluated for fitness, and that with the better fitness of the two survives for the crossover step. A second pair is evaluated in the same manner, and the superior individual from that pair is “mated” with the better of the original two. The process continues until the new generation is filled. Unlike more traditional roulette-wheel or rank-order selection methods[5], tournament selection compares two individuals at a time rather than comparing the relative fitness of one individual against the entire population. This avoids problems with fitness scaling which can lead to premature convergence. Figure 3 outlines the tournament selection process. As an additional hedge against premature convergence, the code can use an “elitist” tournament selection in which the best individual from the current genera-

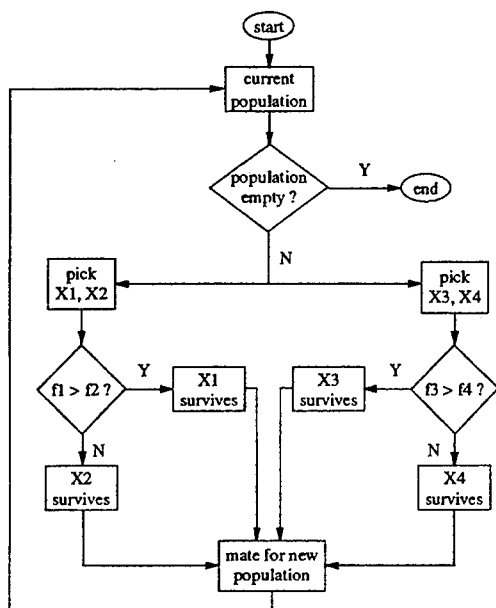


Figure 3: Tournament Selection Process

tion is retained and it replaces the least fit member of the next generation.

The design code can employ a further scheme to stall the onset of premature convergence. When no improvement in the best individual is noted after five generations, a G-bit improvement[5] method, a gradient-like bitwise improvement approach, is used. For the current best individual in the population, the G-bit improvement routine varies one bit at a time in the string. The single bit change producing the best fitness string is entered into the population, replacing the worst member of the current generation. The G-bit improvement, in effect, forces a mutation on the best individual in order to introduce new string patterns into the population.

To use the genetic algorithm, the seven design variables are coded into binary strings. The variable list contains one discrete variable—the airfoil section—and one integer variable—the number of blades. Table 1 shows the mapping between these variables and their binary strings. The other variables, blade twist, blade taper, solidity, rotor tip speed, and disk loading, are continuous, with the resolution of the binary string determining the level of continuity in these quantities. Table 2 illustrates the mapping between the continuous variables and their binary strings. Better resolution of the continuous variables could be obtained by increasing the string length for each variable. However, even with the current total string length of 27 bits, a total design space of 2^{27} , or 134,000,000 different individuals

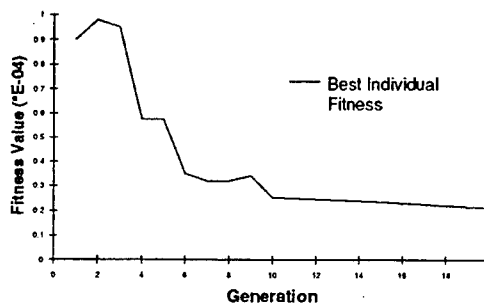


Figure 4: Convergence History for Thickness Noise Fitness

are represented.

4 RESULTS

This section presents several sets of results for differing objective functions. The tabulated results in this section show the best individual in each generation as the genetic algorithm progresses. The values of the seven design parameters as well as the power required to hover are given for each best individual.

4.1 Low Thickness Noise Rotor System

The initial results were calculated for a fitness function which accounted only for thickness noise. In order to conserve computation time, the simple GA code was used, which does not incorporate the G-bit improvement or the elitist tournament selection schemes. Table 3 shows the evolution of the rotor system through twenty generations. The population contained 40 individuals. Note that, fairly substantial changes occur in the design through the first few generations, and, for the most part, only minor changes take place subsequently. This is typical of most optimization procedures, and of genetic algorithms in particular. Figure 4 shows the fitness value of the best individual in a generation as a function of the generation number. In this particular case, the fitness value does not decrease monotonically as the number of generations increases. This is not unusual since the simple GA does not guarantee that the children of a given set of parents will necessarily be superior to the parents.

The fitness function contains the sum of the maximum negative peak pressure and a penalty function which, helps to eliminate stalled rotor blades from the viable set of solutions. If the program detects that a section of the blade is stalled, it computes a term whose value increases with the severity of the stall. If more than one section is stalled, a similar term is added to the first, so that this penalty term is a measure of how much stall occurs and how

Airfoil Section	Binary String	Number of Blades	Binary String
NACA 0012	000	2	000
NACA 0015	001	3	001
NACA 23012	010	4	010
NACA 23015	011	5	011
NACA 63A012	100		
NACA 63A015	101		

Table 1: Discrete and Integer Design Variable-to-Binary String Mapping

Variable (units)	Minimum Value	Maximum Value	Resolution	String Length
Solidity	0.050	0.125	0.005	4 bits
Linear Twist (degrees)	- 15	-7	1	3 bits
Tip Speed (ft/sec)	625	780	5	5 bits
Disk Loading (lb/ft ²)	3.0	18.5	.5	5 bits
Blade Taper Ratio	0.2	0.9	0.1	3 bits

Table 2: Continuous Design Variable-to-Binary String Mapping Parameters

Gener- ation	Airfoil	# Blades	Solidity	Twist (degrees)	Tip Speed (ft/sec)	Disk Loading (lb/ft ²)	Taper	Power (HP)
1	0012	4	.070	-12	685	3.5	.6	1859
2	0012	4	.070	-12	685	3.5	.9	1913
3	0012	5	.115	-9	655	7.0	.4	2873
4	0015	5	.065	-10	645	3.5	.6	3607
5	0015	5	.065	-10	645	3.5	.6	3607
6	0012	5	.065	-10	645	3.5	.6	2016
7	0012	5	.065	-10	645	3.5	.4	1969
8	0012	5	.065	-10	645	3.5	.4	1969
9	0012	5	.065	-15	645	3.5	.6	2103
10	0012	5	.065	-8	625	3.5	.4	2142
11	0012	5	.065	-10	625	3.5	.4	2131
12	0012	5	.065	-10	625	3.5	.4	2131
13	0012	5	.065	-15	625	3.5	.4	2167
14	0012	5	.065	-15	625	3.5	.4	2167
15	0012	5	.065	-15	625	3.5	.4	2167
16	0012	5	.065	-8	625	3.5	.2	2121
17	0012	5	.065	-8	625	3.5	.2	2121
18	0012	5	.065	-10	625	3.5	.2	2083
19	0012	5	.060	-10	625	3.5	.4	2404
20	0012	5	.060	-10	625	3.5	.4	2404

Table 3: Evolution of Low Thickness Noise Rotor System

severely each section stalls. Therefore, it is possible and likely that the code will allow some small amount of stall on the rotor blade as long as the noise produced by such a blade is lower than an unstalled one. If, however, the stall progresses to more than one or two sections, or if a section reaches an angle well above its stall angle, the selection procedure will likely not choose that individual since the penalty will indicate that it cannot meet the requirement to lift the necessary weight. This phenomenon can occur, for example, in the case of highly tapered blades. The thickness-noise fitness function will tend to favor blades with a large amount of taper. However, in order to lift the helicopter, those blades will have to operate at high lift coefficient (and, thus, high angle) where the blade chord is reduced. The code chooses an individual with a taper ratio of 0.4 rather than the minimum of 0.2 because the higher angles required on the more highly-tapered blade result in large penalty terms for stall.

The table shows that the genetic algorithm reaches a solution which is consistent with an intuitive assessment of the design variables and their effect on the thickness noise. It chooses the thinnest airfoil available, the NACA 0012, and the largest number of blades. The solidity is low, keeping the amount of area low, and the twist is moderate so that the collective angle is kept reasonable (thereby reducing the effective thickness of the rotor). The lowest possible tip speed is also chosen. Disk loading does not have a major effect on the thickness noise, but low disk loading will keep the thrust coefficient low so that the collective angle can remain moderate. Figure 5 shows an illustration of the rotor with the lowest thickness noise after 20 generations. Notice that the lowest noise solution does not correspond to the lowest power rotor, although some of the noise reduction alterations do have a beneficial effect on the power required as well.

4.2 Low Loading Noise Rotor System

Table 4 shows several generations in the evolution of a rotor system intended to minimize the steady loading noise. Again, the population consists of 40 individuals, and the schemes for preventing the occurrence of premature convergence are not utilized in the current algorithm. Since this noise component depends largely on the amplitude of the pressure distributed on the rotor blade, the algorithm tends to choose designs which minimize pressure peaks. This can be seen in the choice of high solidity, in order to distribute the load, and low disk loading, which maintains low thrust coefficient. In addition to the pressure, the loading noise depends on the integrated area of the rotor weighted for velocity. Thus, the chosen designs have fairly high taper and the lowest possible tip speeds, a trend also seen for the thickness noise. Figure 6 illustrates the characteristics

of the rotor with the lowest loading noise after 20 generations.

4.3 Rotor System with Low Thickness and Loading Noise

Because of the choice for the location of the observer—in front of and below the rotor plane—the loading noise dominates a signature made up of a sum of the two steady components. Thus, a solution for low thickness plus loading noise should follow the trends indicated in the solution for only loading noise. Figure 7 shows the rotor with the lowest combination of thickness and loading noise after 15 generations of evolution. Notably, it does not look the same as the solution for low loading noise. This illustrates an important characteristic of the genetic algorithm. Since the algorithm does not use derivatives, it has no way to determine whether or not a certain individual is, in fact, optimal. It can only tend towards optimality by choosing the best individuals from a given population. As long as the solution has evolved over enough generations, the algorithm will always choose a good design, though it may not be the best design in the entire design space.

The chosen solution for the combined thickness and loading noise has higher solidity and less taper than the best solution for loading noise alone. The genetic algorithm trades off the increased area near the rotor tip (less taper) for decreased blade loading (higher solidity) and, thus, lower loading source strength.

4.4 Low-Noise Rotor System

The final case studied includes the thickness, loading and blade-vortex interaction noise components in the fitness function. The coefficients in the objective function were chosen to make the BVI and the steady loading terms approximately equal for a nominal case. Table 5 shows the evolution history for several generations. This case was terminated after 15 generations because of excess CPU time requirements, though the population continued to evolve. Nevertheless, the results indicate that the genetic algorithm is driving the population towards one of lower-noise rotors. One noticeable difference between the current result and those discussed previously is that the suggested tip speed is higher. This may be due to the fact that the higher tip velocity will allow the rotor blade sections to operate at lower lift coefficients, thereby reducing the strength of the trailing tip vortex. However, the solution should be allowed to evolve further before any real conclusions can be drawn about the resulting rotor design.

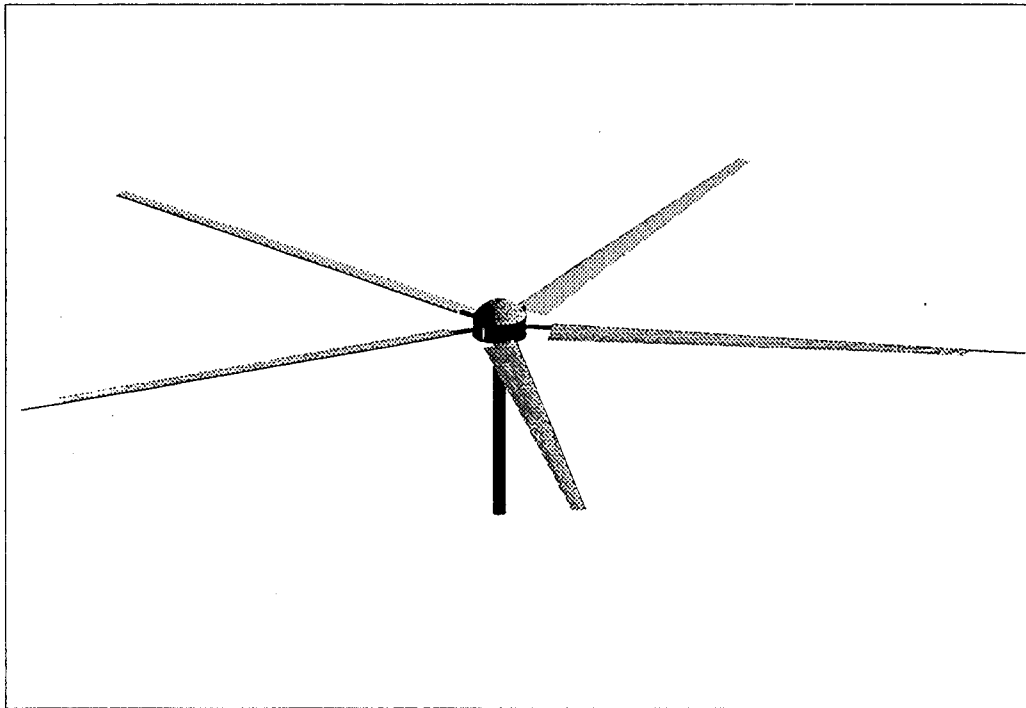


Figure 5: Solution for Low Thickness Noise Rotor after 20 Generations

Gener- ation	Airfoil	# Blades	Solidity	Twist (degrees)	Tip Speed (ft/sec)	Disk Loading (lb/ft ²)	Taper	Power (HP)
1	0015	5	.105	-8	625	5.5	.5	4819
2	23012	5	.105	-14	650	4.5	.5	1828
5	0015	5	.115	-15	685	3.0	.9	1969
10	23012	5	.115	-15	625	3.0	.5	1811
15	0012	5	.115	-15	625	3.0	.4	1811
20	0012	5	.115	-15	625	3.0	.4	1811

Table 4: Evolution of Low Loading Noise Rotor System

Gener- ation	Airfoil	# Blades	Solidity	Twist (degrees)	Tip Speed (ft/sec)	Disk Loading (lb/ft ²)	Taper	Power (HP)
1	0012	4	.115	-11	700	3.0	.4	2126
2	0012	5	.110	-11	700	3.0	.4	2074
5	0012	5	.120	-13	665	3.0	.8	2061
10	0012	5	.120	-15	680	3.0	.8	2146
15	0012	5	.120	-15	670	3.0	.8	2096

Table 5: Evolution of Low Total Noise Rotor System

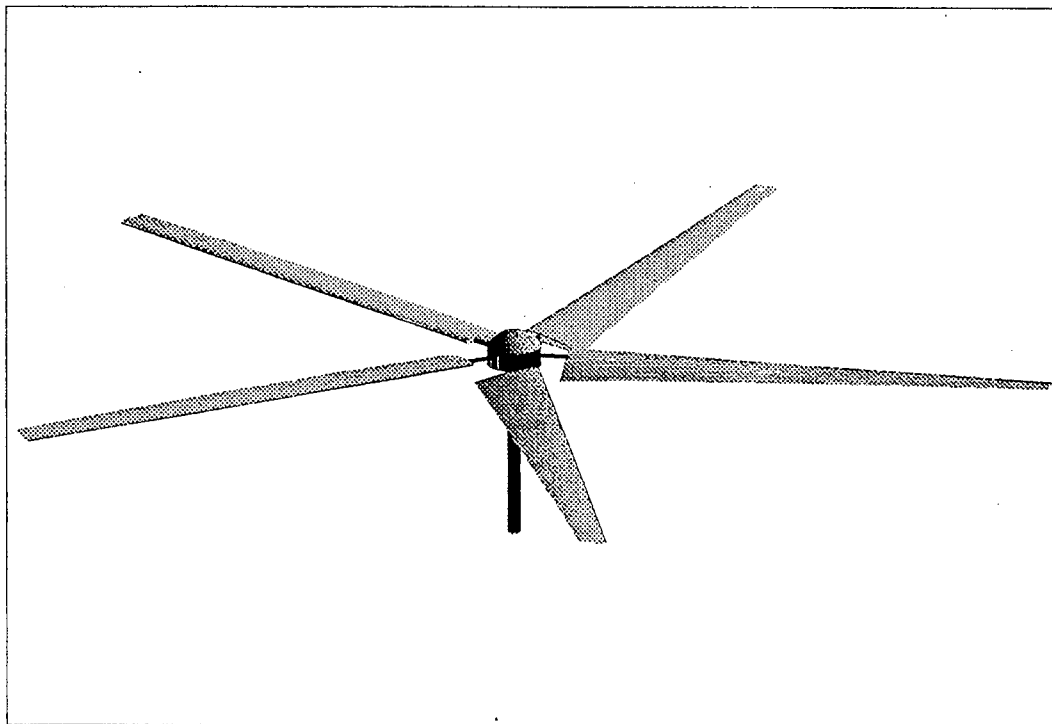


Figure 6: Solution for Low Loading Noise Rotor after 20 Generations

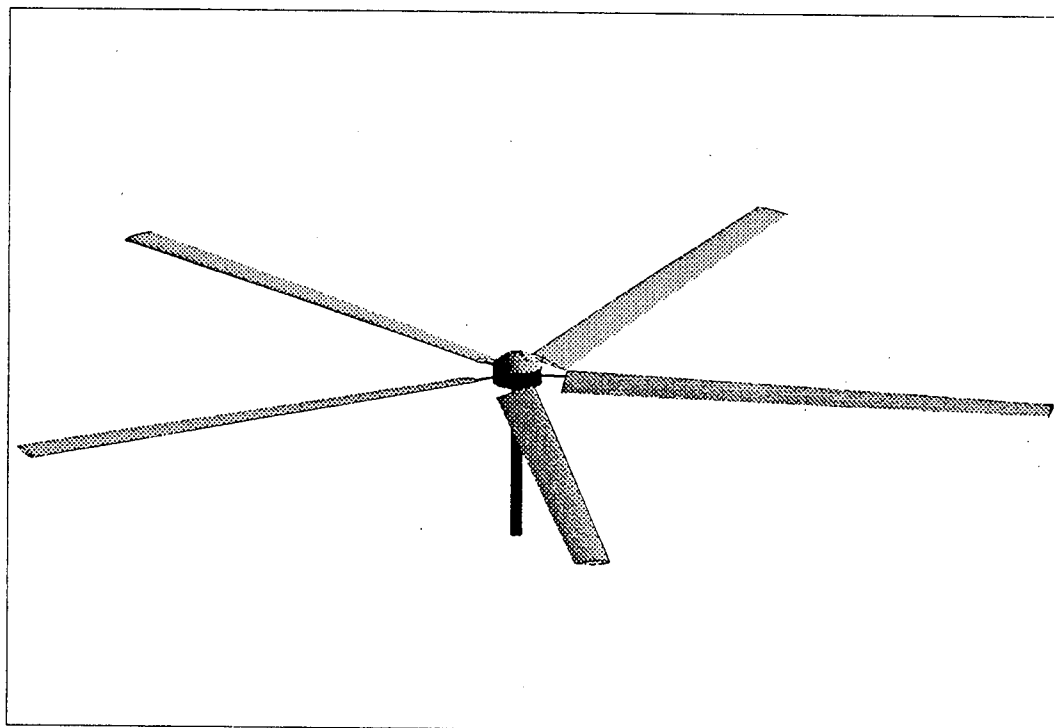


Figure 7: Solution for Low Loading and Thickness Noise Rotor after 15 Generations

5 CONCLUSIONS

The paper illustrates the feasibility of utilizing a relatively new methodology for the design of a low-noise rotor system. The genetic algorithm method can incorporate discrete, integer, and continuous variables into one optimal design procedure, and it, therefore, seems particularly appropriate for use in the selection of rotor design and operational parameters. The paper presents solutions for the design of rotors with lowered acoustic signatures, and, examines the trade-offs required in order to achieve a low-noise design.

The results provide several low-noise rotor blade solutions. Though none of these is guaranteed to be optimal in the sense that it represents the very lowest-noise rotor in the design space, all of them are "good" solutions. In general, the lowest noise solution is not the lowest power solution, although the noise-lowering trends in some of the design variables decrease the power required to hover as well. If it is desired to design a low-noise and low-power rotor, the fitness function can be defined to include a power term with an appropriate coefficient. In this way, the genetic algorithm is well-suited to handle multi-objective design problems. The results presented here indicate that the method will easily incorporate low noise as part of a multi-objective fitness function in the design of rotor systems.

ACKNOWLEDGEMENTS

This research has been sponsored by NASA Ames Research Center under Grant Number GR NAG 2882. Mr. Crossley's participation is sponsored by McDonnell Douglas Helicopter Systems.

References

- [1] J. H. Holland, "Genetic algorithms," *Scientific American*, pp. 66-72, July 1992.
- [2] K. KrishnaKumar, "Genetic algorithms—a robust optimization tool," *AIAA 93-0315*, January 1993.
- [3] C.-Y. Lin and P. Hajela, "Genetic algorithms in optimization problems with discrete and integer design variables," *Engineering Optimization*, vol. 19, pp. 309-327, 1992.
- [4] J. H. Holland, *Adaptation in Natural and Artificial Systems*. MIT Press, 1992.
- [5] D. E. Goldberg, *Genetic Algorithms in Search, Optimization and Machine Learning*. Addison Wesley, 1989.
- [6] J. M. Gallman, C. Tung, Y. H. Yu, and S. L. Low, "Prediction of blade-vortex interaction noise with applications to higher harmonic control," *AIAA-93-4331*, 1993.
- [7] P. Spiegel and G. Rahier, "Theoretical study and prediction of bvi noise including close interactions," in *Proceedings of the International Technical Specialists Meeting on Rotorcraft Acoustics and Rotor Fluid Dynamics*, American Helicopter Society and Royal Aeronautical Society, October 1991.
- [8] V. L. Wells, "Acoustic waveform singularities from supersonic rotating surface sources," *AIAA Journal*, vol. 29, pp. 387-394, March 1991.
- [9] V. L. Wells and A. Han, "Geometrical and numerical considerations in computing advanced-propeller noise," *Journal of Aircraft*, vol. 30, pp. 365-371, May-June 1993.
- [10] R. W. Prouty, *Helicopter Performance, Stability and Control*. PWS Engineering, 1990.
- [11] A. M. Kuethe and C.-Y. Chow, *Foundations of Aerodynamics*. John Wiley & Sons, 1986.
- [12] J. C. Hardin and S. L. Lamkin, "Concepts for reduction of blade/vortex interaction noise," *Journal of Aircraft*, vol. 24, pp. 120-125, February 1987.
- [13] J. C. Hardin and J. P. Mason, "A new look at sound generation by blade/vortex interaction," *Transactions of the ASME—Journal of Vibration, Acoustics, Stress, and Reliability in Design*, vol. 107, pp. 224-228, April 1985.
- [14] M. S. Howe, "Contributions to the theory of aerodynamic sound with application to excess jet noise and the theory of the flute," *Journal of Fluid Mechanics*, vol. 71, pp. 625-673, 1975.

GENERAL DISCUSSION

Dr. W.J. McCroskey, NASA AMES, USA

We come now to the final session of this symposium. An important part of this Symposium and something that is incorporated into many AGARD activities, but is rather unique to AGARD, is the way that we finish off our Symposia. AGARD often commissions an expert in the field who serves as what we call the Technical Evaluator, to summarize the Conference in its total context and to write a report that is either included in the Conference Proceedings or in a separate document published shortly thereafter. This helps a lot to stimulate an extended general discussion. We try to keep the coffee breaks as long and open as possible, because that is where a lot of good discussion occurs. We also think it is very important to have a session at the end for people to raise questions or points that may be on their mind, maybe stimulated by the Technical Evaluator's opening summary; but in any case, to put the total meeting in somewhat better context. This helps us see the global forest and not just the trees.

The plan for this is that first we will have some remarks by the Technical Evaluator, whom I will introduce in just a moment. Following his presentation we will entertain brief questions just for clarification, or some questions about something he has said, but in general, hold your comments and questions until the general discussion later. After Mr. Dadone has finished his remarks, there will be short presentations by two other persons who are invited Commentators, and I will introduce them in due course. Following that will be the open discussion that I have already talked about. I will say now, and I will remind you again later, that in this open discussion, all of the remarks are being recorded and will be transcribed to be included in the Conference Proceedings. That is another very special thing that AGARD does. Therefore, it is very important that when you do pose a question or a comment, to use the microphone. Obviously, it won't be possible for someone in Brussels next month to transcribe your remarks, if it didn't get recorded by means of the microphone. Secondly, you must identify yourself, so that in the transcription, we will know from whom came these erudite remarks. However, you don't have to be timid about what you say, because you will have a chance to edit the final transcription.

Hopefully, these opening administrative details have given everyone time to come and take his seat. I would like to say a few words in introduction of our Technical Evaluator, Mr. Leo Dadone from the Boeing Helicopter Company. He was educated at the University of Pennsylvania in the U.S., taking B.S. and M.S. degrees there in 1964 and 1966 in Mechanical Engineering. He has been at Boeing Helicopter since completion of his studies at the University of Pennsylvania. I am sure that many of you know him personally or through his publications in Helicopter Aeromechanics.

Mr. Dadone, Boeing Helicopter Company, USA

Thank you, Jim. First of all I must thank Dr. Korner and Dr. McCroskey and all the members of the Program Committee for the

opportunity to attend this Symposium and to share with you some of my thoughts. I also must congratulate all the authors and all the Session chairmen for a tremendous job. We covered a lot of territory in these three days. I am going to take the opportunity now to review what we have accomplished and put it in the context of what the rotorcraft industry needs.

There are several basic questions from the manufacturers' point of view. The first is, "what are the significant trends in rotorcraft aeromechanics?". And then, "are we after the right problems"? And particularly when the Universities and Laboratories are involved, "do we have a good mix of research?". Clearly, no matter how hard-nosed we can be in industry, we need methods and concepts to use in the near term to solve our design problems, but we cannot ignore the fact that the Universities and Laboratories must carry out advanced research, which may or may not bear fruit, or may not bear fruit in the near term. And finally, "what are the priorities?". Well, as far as the rotorcraft industry is concerned, I am not totally sure of the priorities, it depends with whom you talk, but certainly our biggest concern today is that we need to make the rotorcraft quiet. And of course, rotorcraft (helicopters, tilt-rotors and so on), do not operate like airplanes, and they do shake. The fact is that we have to suppress vibration, and that is very costly. And, we have to lower the cost of building, buying and maintaining rotorcraft. Finally, and this is a challenge, we need to reduce the design cycle time. This is where analysis is necessary. All of this advanced research becomes really useful only if it can be used in reducing design cycle time.

I will try to give some answers to these questions, and I suspect that in the subsequent discussion, we will talk again about these questions. Maybe together we will come to a consensus whether or not this meeting has addressed these issues properly.

During the opening remarks, Dr. Korner reminisced a little bit about the last time there was a Symposium addressing rotorcraft, and he was thinking of the 1982 meeting in London, where we talked about airloads and airload prediction methods. He commented, quite rightly, that many things have happened since then. Since 1982, CFD became not just a subject of academic interest; it became a tool that we all either use or try to use. Computers suddenly are playing a very big role in what we do, and that role is expanding rapidly. We do have all sorts of computer gurus around, which we surely need to sort things out. And we have had several major tests since 1982, wind tunnel tests including the DNW series of wind tunnel tests, and flight tests like the BO-105, the SA 330 and the UH 60. We also had some major joint programs between the U.S. and the European Community. We have new test hardware. We have built new rotor test stands, new blades, with emphasis on heavily instrumented blades, new measurement techniques - it is mind boggling to me to see how well, and in how much detail, we can measure the flow field of a rotor. Modeling the flow field of a rotor is a terribly difficult problem. The airplane people have it easy compared to us. Capturing the details of the rotor wake and of what happens in the vicinity of the blade is very difficult. There has been a great deal of improvement in acoustics methods, both in terms of prediction, and in terms of

measurement. But that is not all that happened. This Symposium did not address it, but to some of us, it is as though there is a giant standing behind the door: tilt-rotors. The tilt-rotor is this creation between a helicopter and an airplane. In fact, at least two of us here, Bell and Boeing, have built and are flying right now the V22. We have great hopes of seeing the V22 into production, and then have civil tilt-rotor derivatives and so on. Almost all that was done with helicopters will be of benefit to tilt rotors. So, everything that we have done in conjunction with this Symposium and over the last ten years will be applicable to the tilt-rotor. And much more will be needed that is tilt-rotor specific. If the tilt-rotor will, in fact, happen, by the time we meet again, in ten years or so, we will have 80% of the meeting devoted to tilt-rotor problems.

Another relevant development are remotely piloted vehicles. This is an interesting area in itself, and there are helicopter and tilt-rotor applications for it.

Finally, the big worldwide development is that all of a sudden the world has changed, and as a proof of this we have our colleagues from Russia with us. Three weeks ago I was at the first Forum of the Russian Helicopter Society. There is a wealth of information, talent and experience to be found in Russia.

The one dark side today, and it affects us (and of course this is not the forum to discuss it, but we cannot ignore it) is the world economy. The economy has put a damper on a lot of our research, but I hope that, for everybody's sake, the situation will improve soon.

We spent three days here, and we covered Dynamic Stall, (experimental and analytical aspects of it), Wind Turbines, Aerodynamic Prediction Methods, Experimental Investigations, Acoustic Predictions and Interference. Particularly after this last paper, I would have made a separate category of optimization. There were thirty-four papers, of which two were invited. Eleven were survey papers. The two invited papers gave us a clear update about the specific subjects they were covering. I ran some quick statistics, and I am not going to bore you with the bulk of it, but seventeen of the papers dealt with CFD or had a significant CFD ingredient. Twelve of the papers addressed test programs in the wind tunnel tests and flight tests. Of course, they are extremely important, and they go hand-in-hand with CFD, because CFD remains a gleam in somebody's eye until you can validate it. And there were twelve papers which dealt with noise.

At this point I will go through a few comments about the various subjects. First of all, I want to say a couple of words about the invited papers. We had three invited papers, but much to our regret Professor Tischenko could not make it. He was going to give the overview of Russian helicopter work. I can assure you it would have been a tremendously interesting presentation, but we will have other chances. Jack Landgrebe gave the opening paper, and he addressed the status of CFD. He gave us a very good summary of where we stand. Sometimes it was a little bit sobering, but that is certainly the way to go. Dr. Hamel's paper presented the findings of the Flight Vehicle Panel's Working Group 18, and that dealt with rotorcraft

system identification. Not surprisingly, he concluded that today's methods permit the correlation of wind tunnel, flight test analysis, CFD, etc., on a rudimentary level only. He suggested that we still have a lot to do, but we are gathering a lot of data and a lot of experience, and hopefully, the correlation with test evidence is not going to be rudimentary for very long. In fact, as he pointed out, we need to model accurately the complete helicopter characteristics from the design stage all the way through production and flight test.

Let us go now through the actual subjects. CFD, as I stated, was dealt with in seventeen of the papers. These papers dealt with every aspect of CFD from Navier-Stokes, to the Euler codes, and the potential flow codes. We talked about many applications, and I cannot stress enough how important these are. We applied CFD to rotor blades, and to blade tips, and we looked at transonic flow effects. Of course, very importantly, we looked at acoustics. An interesting novelty was the fact that we started again looking at windmills, and in the context of CFD, and there is a lot to be learned from that. The big bright hope that we still have (and that as of this Symposium hasn't been completely fulfilled), is to be able to use CFD to model rotor wakes. It turns out that the CFD modeling of rotor wakes still holds a great promise, but the CFD wakes dissipate too soon, or they do not quite capture all the features that we want. But they are very, very important, because at present we model the rotor wakes almost exclusively by vortex element methods. Of course, our "rotor wakes" are a little bit a figment of our imagination, and they can best be described as a "fit" through the truth. Only when CFD will extract the wake from the flow field will we be able to truly correlate with test data. CFD has been used on fuselages. And CFD is the only chance we have of dealing with BVI noise explicitly. We saw some papers on dynamic stall. Again, CFD demonstrated great potential, and it showed to us how complex the phenomenon of dynamic stall really is. Transition and turbulence modeling remain to be resolved. CFD has been very revealing of some flow details, but we cannot throw away our wind tunnel models yet.

I was very intrigued by the variable camber paper, by the way, as far as CFD applications are concerned. Particularly because it dealt with leading edge camber. We often think of trailing edge camber changes as being the only viable approach, but it may be that dynamic stall delay by leading edge camber could lead to useful rotor blade devices. We certainly see a great potential for variable camber as the next step beyond higher harmonic control and individual blade control (IBC). A more elegant way of implementing IBC, as actually suggested in this paper, would be to modify the blade locally and not to try to pitch the whole blade at some high frequency. Another thing that the survey papers repeatedly brought up, is the coupling between the comprehensive codes and CFD. This is still not a completely mature approach, but it is yielding results, and it is really up to the users not to wait for perfection and to extract whatever information can be gotten with the methods as they are. We cannot rely on CFD by itself, because rotor CFD, as it stands now, cannot trim the rotor to the correct forces. CFD is also not equipped to handle blade dynamic motions and blade elastic deflections. Maybe ten years from now we will have finite element structural models coupled with CFD, but that is still a long way off.

And again, we need the comprehensive codes because of their vortex element wake models, because the CFD wake modeling is not sufficiently accurate and robust. Of course, the coupling of CFD with comprehensive rotor analysis codes is the key to rotor noise predictions. In order to predict BVI noise, you have to know exactly what your blade is doing, you have to know exactly where the wake is, and where the vortices are concentrated. In fact, you may be dealing with partially rolled-up vortices, not just the concentrated vortices that we draw for convenience.

Many problems remain with CFD. Turbulent modeling is one, and it was addressed in more than one of the papers. Much more will have to be done, and that is not just for rotorcraft. Even in fixed wing aircraft, turbulence modeling is a problem. Our favorite conclusion is that we need more work to make CFD work. But it works! It just doesn't work as well as we would like it to. In fact, Jim Narramore, from Bell, showed us how well one can help to solve practical problems with CFD.

I also noticed, which is a sign of the times, concern with cost effectiveness. Costs is more and more of an issue, and I think that this will come up during the discussion. It is true that we need codes that are accurate and robust. But we have to meet our designers' requirements even if we cannot afford a CRAY or a supercomputer. One more observation about CFD. An interesting question was brought up by Wayne Johnson early in the meeting. He was asking, "can we quantify, from the users end, how accurate we need to be?" What can I say? As accurate as possible. Although more often than not, the question is not just accuracy, it is whether CFD can do it at all. We have our CFD specialists, and sometimes, when we assign a problem to them, they say that it can be done, and then come back six weeks later and say that it didn't work. It is not their fault, it is just that they were treading on uncharted territory. In the middle of the CFD session, I complained about the fact that even in some relatively small things we haven't quite worked out all the details. I will bring up again that, given the incidence angle, all CFD codes appear to be unable to predict the correct lift. Maybe it is a matter of how you grid the trailing edge, or something else, but the truth is that the CFD codes do not predict the lift correctly. In fact, two or three papers showed data which confirmed that CFD consistently overpredicts the lift. Now when you try to couple CFD with a comprehensive rotor analysis code, which is based on airfoil tables, which is real data, you have a big mismatch, and a lot of people ignore it. I do not think that we can. If you do not have the right lift, you will not get the right induced power, and you will not get the right BVI.

I do not want to discourage fundamental research. We are interested in the most accurate representation possible of the physics. There is no question about it. So, advanced research must continue. Even if it is not useful to industry in the very near term, in the very long term it probably will be. Now, the one complaint that we have had in industry, and which is generally ignored by the CFD community, is that the biggest stumbling block to us is grid generation. We devote a lot of time to making the CFD solutions faster. We use parallel computers, and massively parallel computers. But then when

we have a complicated flow problem, it takes us six months to set up the grid. At that point, whether it takes one, two or three days to run the solution, it is no longer terribly important. Although, once we have the grid, obviously we want the answers right away. Grid generation is a big issue as far as the useability of CFD.

We had a couple of papers which addressed the combination of viscous and inviscid grids. That is very promising. From the industry point of view, my biggest wish would be an adaptive grid. There hasn't been much talk about adaptive grids at this symposium, but adaptive grids could be the solution to capturing the real details of the flow field while making CFD useable to the industry.

Dynamic stall - it is a big subject. A lot is going on, and we are hoping to eventually predict it by CFD. Very interesting to me was the paper dealing with low Reynolds number data over the full Mach number range. For all these years we have been running model scale wind tunnel tests and making predictions and carrying out calculations with full scale airfoils, as far as stall delay is concerned. When we run a model rotor test we have to make some significant assumptions to be able to correlate with the full scale rotor test data. Until now, I haven't seen any unsteady data at model rotor Reynolds numbers, and at the right Mach numbers, so that this test is very interesting. We had an entry from the Russians, and I am sure that Russia is going to be a tremendous resource to us in the future.

Windmills - until now, we were helping the windmill people. Some of us have been involved in windmill programs over the years. We witness a change now, where the windmill people can help us. There were interesting papers on stall, and on the CFD modeling of root end effects. That is a tilt-rotor problem. A lot of useful experience will probably come from the windmills. Even some of the wake modeling, as for instance the vortex particle method. I think that we should look at windmills very carefully. As far as comprehensive rotor analysis codes, we all have them, and we all use them in more or less similar ways. So, it is useful to share our experiences, and we will just have to read each others papers very carefully and call on each other for questions.

What is real exciting to me is the progress in the test area. I would miss my flight if I had to talk about all the test developments. Almost suddenly, the combination of new instrumentation (blade pressures, blade strain gauges, advanced balances, dynamic balances) and all the flow field measurement techniques, have given us a chance for an unprecedented insight into what is happening. What is even more exciting is that we have that level of sophistication being applied to helicopters. We have seen many new flight test programs, and incidentally, conditions like manoeuvres, transition, etc., you really cannot address in a wind tunnel, so the new flight test programs have a tremendous role in furthering our knowledge. We have been all really working by rules of thumb, but now we will be able to quantify what the real differences are between stall at high thrust and high speed and stall during manoeuvres. So, I am just thrilled with the quality and quantity of the data that has been presented. Now that we have a

tremendous amount of data, I just hope that we will take the time to document it, and will not lose it somewhere. Sometimes large bodies of data become unavailable, for practical purposes, within a few years.

The last topic was acoustics. Again, we had the HART program, which addressed both vibration and acoustics. Between the HART program, with the higher harmonic control, and the individual blade control test, an impressive amount of important experimental evidence was acquired. I did raise the question earlier whether the HART program can be extended to more advanced blades. I hope so. In fact, whether individual blade control or higher harmonic control are really viable, because they are somewhat complex, the lessons learned could lead us to the use of smart-structure materials and localized blade actuation - blades changes such as flaps and leading edge camber. We should be able to do the equivalent of individual blade control or higher harmonic control with devices which are much smaller, much simpler, much less complicated mechanically and which are on the blades and not in the control system. So, there is a lot to be done in this area. Very good surveys of what has been done were presented in several papers.

A lot of work has been done in high speed impulsive noise, and it is very important. I am not qualified to discuss the details of how all these integrations are carried out, but in industry we are ready and eager to use whatever tools you gentlemen can provide to us. We are not proud about it. In the absence of better tools, we all employ some mix of analysis, CFD and test evidence. For now, in the balance, we still have to test. In the future, I hope, in acoustics, as in other areas, we will be able to rely less and less on test. That is where analysis may actually pay off.

This morning's session again dealt with acoustics. I was glad to hear Dr. Baeder say that he considered impulsive noise prediction a mature technology. I will have to talk to him again. And of course, we were all very interested in the paper on genetic algorithm applications to the design of low noise rotors.

One final word. I was very intrigued by the interference papers. They addressed a very important aspect of interference which I do not automatically associate with the aerodynamic interference effects we normally study. When I think of interference, as an aerodynamicist, I think of what the rotor does to the fuselage, or the fuselage does to the rotor, and the rotor does to the wing, and so on. Here we are dealing with the operational environment. I must admit that there have been occasions when we were asked what we knew about the blade strikes at low speeds, and we did not know much about the subject. But there are a few experts, and I am very grateful that these papers were presented. Approaching ships from the air through their turbulent wake is also something that we have dealt with. It has been an important subject and it will continue to be important in the future since the Navy is a big customer of ours.

I think that this about wraps up my impressions about the papers. I will be glad to answer any questions, or continue later within the general discussion.

Dr. W.J. McCroskey

Thank you very much. If someone has a particular question for clarification that they would like to raise at this point while he is on the podium, otherwise, I would like to defer comments and questions of a more general or more extended nature to the general discussion period which will follow shortly. Thank you very much.

I am sure you can appreciate how difficult it is to sit there and try to absorb all this stuff and then you have a break of 25 minutes or so for coffee, and then you are supposed to get back up and tell everyone what they have really been hearing during the last four days. Thanks very much for those comments, and we will look forward to the written report that goes with this.

We also decided to include in this discussion a couple of leading experts from the Continent, who would be invited as commentators, because I am sure they have some perspectives that would be useful for us to hear. The first is Jean Jacques Philippe from ONERA, where he is a coordinator for rotorcraft. He was educated at Ecole Centrale de Lille and has been at ONERA since 1969, and he is certainly known to all the rotorcraft community. Also, this should be a treat for the Fluid Dynamics Panel members who have not met him or seen him in action before.

J.-J. Philippe, ONERA

Thank you very much, Jim, for your invitation to this attractive symposium. Ladies and gentlemen, the comments I will make at this symposium will be mainly dedicated to the aerodynamic research work, while Dr. Heller will talk about research in aeroacoustics.

First, I would like to recall that good aerodynamic tools are mandatory to predict correctly rotor performance, noise and vibrations, but we must not forget that rotorcraft aerodynamics and aeroacoustics are quite complex, and a lot of phenomena still have to be well understood and well predicted. Moreover, multidisciplinary research is required to solve the problems related to helicopters.

I will start with research on dynamic stall. You know that the dynamic stall appearing on retreating blades is a real limitation for higher helicopter performance. It is a true challenge to be able to predict correctly such a rotor configuration and the consequences on power, blade stresses, control loads and vibrations. CFD codes are requested, but semi-empirical models are mandatory, for inclusion in performance, noise and vibration codes..

This specialist meeting has obviously demonstrated that good progress has been made at the level of 2D configurations, but mainly for airfoils oscillating in pitch. It is a first step, but it is not sufficient. We need to take into account the variable Mach numbers that a rotor blade section meets in forward flight. This variable Mach number is a parameter that is far from negligible. For the 3D aspects of the problem, we have learned from wind-turbine researchers - it's useful for helicopter specialists, but insufficient for predicting correctly the 3D unsteady behavior on helicopter rotor blades.

Theoretically, the 3D Navier-Stokes codes will solve the problem in the future, but when? and at what cost? In my opinion, an intermediate step could be the development and use of strong coupling techniques between inviscid and viscous flow codes. However, to help industry today (industry people always want a fast response to their problems), I think that we have to continue to develop semi-empirical models including rotation and 3D effects. Models such as those developed by MIL in Russia or by ONERA in France, are very useful for the design of efficient rotors and for the prediction of their limitations. However, we have not to forget to introduce these aerodynamic models in aeroelastic codes to take into account the large blade deformations that occur in such configurations.

Let us continue with 3D CFD codes for helicopters. The flows on rotor blades in forward flight are obviously 3D and unsteady. Consequently, we need 3D and unsteady CFD codes for improved predictions of such complex flows, even for non-separated flows, for a better understanding of the flows on the blades, for pressure distribution, local lift, moment and drag computations and hopefully, in the future, for accurate power reduction. It's also necessary to recall that the knowledge of blade pressures is mandatory for accurate evaluations of rotor noise.

The papers presented during this symposium have demonstrated that in the USA and in Europe a large amount of effort has gone into the development of CFD codes. CFD codes are more and more used, not only at research level, but also by industry for aerodynamic and aeroacoustic purposes. However, for rotors, work remains to be done for Euler codes and obviously, for Navier-Stokes codes which are still far from operational. The challenge for the aerodynamicists is to prove that they are able to calculate from CFD codes the power required by the rotor, with an acceptable computer time. Hover is probably the most important and difficult configuration and the one to be solved first. In my opinion, a good job can also be done by using Full Potential and Euler codes, on the condition they are coupled to boundary layer codes. This solution could be sufficient if we have no separated flows or no dynamic stall configuration.

We also need to couple these CFD codes with aeroelastic codes, because rigid blades do not exist in reality. Large deformations in torsion may exist for the blades, as proved by numerous experiments. Even, at low speed, for BVI configurations, we have the proof that deformation computation is necessary, when, for example, the rotor is operating with HHC. For the fuselages, CFD codes and more specifically Navier-Stokes codes are mandatory for good predictions of fuselage drag. The paper given by Bell during this symposium has provided a good example of the usefulness of such Navier-Stokes codes to assist in the design of low drag fuselages. However, the accuracy of the present Navier-Stokes codes needs to be improved to have access to reliable drag estimations. For the present time, the prediction of fuselage drag remains a true challenge.

I will add some comments on experimental studies. Experimental investigations with detailed reliable measurements are of prime importance for a good knowledge and understanding of the physics, but also for a detailed validation of the aerodynamic and aeroacoustic

prediction tools. Local pressures and stresses on the rotor blades, velocities around the rotor and in its wake, acoustic pressures in the far field are some of the typical measurements we absolutely need. However, some of the measurements are difficult to carry out in a rotor environment and progress remains to be made in the experimental field, for example, by improving the accuracy of measurements. We need good and detailed measurements in wind tunnels but also in flight.

During this symposium, excellent papers have been presented, mainly concerning wind-tunnel tests, with the acquisition of excellent detailed aerodynamic and aeroacoustic data base. HART tests with cooperation between the United States, Germany and France is the best example of the numerous data which are required in order to validate correctly the aerodynamic and aeroacoustic codes for rotors.

For the future, we have not only to continue to run highly instrumented tests for rotors and fuselages, but also for complete powered models. We also have to prove to industry that wind-tunnel tests simulate very accurately the phenomena observed in flight, that these tests help improve helicopter design and can be used to avoid numerous problems they meet during the development phase of a helicopter, or alternatively, to find a fast solution to solve these problems. We also need flight tests with well instrumented rotors and fuselage, and detailed comparisons between flight tests and wind-tunnel tests for the same aircraft.

I will add that, for fuselage research, the use of pressurized wind tunnels could be interesting to study Reynolds number effects; they will enable the validation of CFD viscous codes as far as this important parameter is concerned.

Thank you for your attention, and now, Dr. Heller will comment on the aeroacoustic papers of this symposium.

Dr. W.J. McCroskey

Thank you very much, Mr. Philippe for your comments and perception on what has been presented here and what has to be done. The second commentator is Dr. Hanno Heller from the Design Institute for Aerodynamics at DLR, where he has been since the mid-1970's. He received his doctorate at the Technical University in Berlin and worked with BBN Industries in the U.S. before joining DLR. He is also well known in the rotorcraft community and should also be a delightful new experience for the rest of the Panel members.

Dr. H. Heller, Institute of Design Aerodynamics, Germany

Ladies and Gentlemen, it is a great pleasure for me to make a few comments regarding the aeroacoustics part of our very successful Conference. The very fact that this Symposium is actually the fourth major conference dealing with helicopters, one way or another, during this year, seems to be an indication of the importance of the area we are involved in; the aerodynamics of rotors, the aeroelastics, the aeromechanics and last but not least, the aeroacoustics. In talking about helicopter noise, I think it is appropriate to put this into a somewhat larger context, and in so doing, I thought I would very briefly discuss the overall situation as regards helicopter noise. I

would like to draw your attention on the actual interdependence of research and briefly mention the four conferences this year and what the key issues dealt with were at these conferences. Of course, our present Conference will get most of the attention, and then perhaps to end that, I can make a few comments on where I think the research should go into.

The overall situation, as we all know, is that the helicopters are still too noisy inside and out. There is, in the densely populated European area, an increasing sensitivity towards aircraft noise, and helicopter noise in particular. If one talks about interior noise, the passenger is expecting levels that are comparable to those in commercial jet aircraft. City center heliports are a very difficult issue and not welcomed. A very important area is noise legislation. As we all know, noise limits are set by aviation authorities on a national basis and on an international basis the ICAO working groups work in this area. There are many who think that the noise limits are too stringent. Without going into that subject, I would just like to show the current noise limits as established by ICAO in Annex 16, Chapter 8, to indicate that a large number of helicopter types are already way below the noise limits. Without evaluating this fact, I would just like to draw your attention to it. Some people, manufacturers and operators, for example, think that the noise certifications are really done for unrealistic flight conditions, and this in particular, seems to refer to the approach condition where there is a fixed 6 degree descent angle at V_y . Whereas, in reality a helicopter pilot may make a landing approach at an initially higher angle then gradually decrease that angle and also decrease the speed. The question is whether we address the right problem when we talk about the BVI. Now BVI, as we all well know (and we have had close to half of the papers in acoustics dealing with that particular subject) occurs at certain combinations of flight speeds and descent angles, but each and every helicopter may have its own approach path which may run something like this, perhaps, or a helicopter may have particular critical combinations of descent speeds and flight angles, and if the helicopter pilot is given information on where this would be for his helicopter, then he could probably avoid strong BVI altogether. The question is whether we address the right problem in spending so much effort in understanding BVI noise. The answer, of course, being that this is almost unavoidable. No matter what you do, one way or another you are going to hit this very critical flight regime. Noise certification definitely is too costly, it costs several hundred thousand dollars to noise certificate a helicopter. Therefore, the ICAO noise group is working towards defining cheaper, still accurate noise certification procedures, especially for the lighter, and hence cheaper, helicopters. The areas that are of most interest to us are the noise prediction and the noise reduction aspects. Prediction, as you all know, is very important. It is important for both the manufacturer and the operator. Noise reduction is just as much of importance.

So, where does research come in? This I would like to illustrate with a vu-graph which I hopefully have here showing the interdependence of research. The manufacturer, as we have heard today and the past few days, needs noise reduction technology. If he wants to design a helicopter (and the tendency is towards faster

helicopters), he might have to use blades that very soon reach the critical regime where shocks appear and even delocalize. Hence, the manufacturer needs to know what are the critical blade configurations in order to avoid such adverse aerodynamic effects. He also, of course, needs accurate prediction codes. It is important for the manufacturer to know where his future helicopter lies with respect to the noise limits. It is of little consolation if he can predict its noise only within a margin of 3 or 4 dB, because then he would have to put a large acoustic safety margin into the design of a new helicopter. The other group of people interested in research results are the operators, and in this context, I just want to mention the "fly neighborly" program. The heliports insist on quiet takeoff and approaches. And finally, the noise legislator needs research inputs to define realistic noise limits that are technologically and environmentally and economically viable. He must develop just noise certifications that are close to what the general public can tolerate and be economically viable to the operator, and he must strive for simplified procedures. Last but not least, the passenger and the land user are the ones that want to have quiet helicopters inside and out.

As I mentioned, there have been four major conferences this year dealing with helicopter noise (and probably some have actually attended all of these): there was the NASA Aeromechanics Specialists' Conference in January of this year at the Ames Research Center; then the 50th AHS Forum in Washington in May; last week we had the 20th European Rotorcraft Forum in Amsterdam and today, of course, we "celebrate" the 75th FDP Symposium on Rotorcraft Acoustics here in Berlin.

Within these four conferences there were about thirty-five papers which addressed aeroacoustics one way or another. Here the key issues were in the area of noise prediction, emphasizing Lighthill's acoustic analogy approach with Kirchhoff formulations emerging as a very viable tool and some computational concepts to directly predict the aeroacoustics, with emphasis on the blade vortex interaction process. Of course, the need is also for high speed impulsive noise prediction capabilities (blade tip Mach numbers exceeding 0.9). Then there were a number of papers treating experimental aspects, where experiments were used either for theory validation, or to investigate the physics of the flow phenomena, or for the development of technological concepts leading to noise reduction. Of course, many of these experiments dealt with all four of these aspects.

As far as noise forecast is concerned, there are a number of approaches to predict the rotor noise (employing rotor geometric and dynamics data) in flight operation conditions and eventually arrive at the far field noise. The most common is Lighthill's acoustic analogy approach, which relates the noise to three source terms: the monopole, dipole, and quadrupole which in turn, are related to thickness-, loading-, and high-speed-noise. The art, of course, is to determine these three source terms. The monopole term is quite easy to evaluate from blade geometrical information. The dipole or the loading noise term, needs input from linearized potential flow methods such as the lifting line, the lifting surface or more sophisticatedly, the unsteady panel method, which provide - and that

is what we would like to have - not only the section lift, but also the unsteady pressures on the blade surface. There are also possibilities to determine the perturbation velocities around the blade which one needs to determine the quadrupole term. These are the established methods to arrive at the loading noise. Euler codes and full potential methods can be employed to determine the pressures on the blade surface again to be used, say, in conjunction with the Lighthill acoustic analogy to determine the loading noise part, or they can be used, in terms of perturbation velocities, to determine the quadrupole term. This information on perturbation velocities can be used in Kirchhoff formulations as mentioned earlier, to predict the noise. Finally, there are the computational aeroacoustic methods which are based on CFD and attempt to directly determine both the acoustics and the aerodynamics without recourse to an analogy.

If we now look at the specific acoustics papers of our Conference, it turns out that four of them dealt with experiments and the last eight with prediction. Of the experimental papers three treated BVI noise reduction one way or another. The first paper by Niesl and co-authors used a test set-up in the NASA Ames 40 x 80 foot anechoically treated tunnel to implement individual blade control and this is probably the way to go rather than using higher harmonic blade control. Describing a more generic experiment, Kitaplioglu and his co-authors used an artificially generated vortex to impinge on a two blade rotor; with such kind of very basic experiment, I think, the computational procedures can be very well validated. The report by Rozhdestvensky from Russia tells us quite interestingly that tail rotors can be a dominant source and that by using x-shaped tail rotors a lot of noise reduction could be attained. The tail rotor acoustics is in fact an area where we have to increase our research effort.

The most complex and comprehensive rotor aeroacoustics test I think ever conducted as reported by Kube and co-authors, occurred in the context of the HART project, where the U.S. Army, ONERA, DLR and DNW joined forces. Here an instrumented main rotor model was employed which had been already used in the earlier HELINOISE project (that was financed by the European Community) and also prior to this particular test there had been some higher harmonic control tests without instrumented blades and the combination of these two research projects then eventually led to the very complex HART test where not only blade pressures and acoustics were simultaneously measured, but also flow visualization was used to investigate the vortex core size, the blade-vortex miss distance and several other important parameters. Let me mention one of the "aesthetically appealing" results, which illustrates that by employing higher harmonic control, one can, in the first quadrant (where normally the BVI would occur), "straighten" things out and achieve a noise reduction of about 5 dB.

Regarding the papers dealing with the theoretical aspects, I would like to mention the work of Ianniello and Bernardis who in order to predict the high speed noise solved the Ffowcs Williams and Hawkins equation with a three dimensional integration in a prescribed volume around the blade. They used aerodynamic data from a full potential code and were able to predict the noise up to blade tip Mach numbers of 0.88. Schultz and his co-authors dealt with the prediction

schemes used at DLR, both for BVI and for high speed impulsive noise. BVI is predicted by using the acoustic analogy technique, and for the high speed case, the aerodynamic results from the Euler codes were taken as inputs. Different solutions for the volume integral were employed with success.

Toulmay and his co-authors indicated that from the industry's point of view the prediction schemes were not yet accurate enough. While it is possible to predict thickness-, loading- and rotational noise reasonably well, he feels that high speed impulsive noise is not predicted yet as well as BVI noise is. In his work, ONERA CFD input is frequently used. Baeder in his paper this morning introduced the Euler method as a computational aeroacoustics tool and he used it to demonstrate the noise reduction potential of dynamically twisting a rotor blade in response to a BVI, promising some 12 dB noise reduction. Lyrantzis, in addressing the Kirchhoff approach showed that with the development of reliable CFD methods to predict the near field aerodynamics, the far-field noise can be computed from input supplied from any of these aerodynamic codes. The last paper this morning by Professor Wells on Genetic Algorithms was sort of an evolutionary type of approach to the helicopter noise problem. We were quite impressed with that paper.

So, this brings us to the question of where research should go. In the area of noise prediction, the efforts will be on the highly sophisticated full-potential Euler methods which are important for validation calculations and they should be extended towards lifting high-speed forward flight with correct wake simulation and inclusion of blade dynamic properties. The slightly less complex schemes are the linearized potential flow methods and they are very good for parametric studies. Again the problem here is to include the blade dynamic properties. One needs the high azimuthal resolution for the wake, and one should try to improve the quadrupole term estimation again.

As a side remark, I would like to draw your attention to a paper that Professor Lowson of Bristol University last year presented at the ERF in Cernobbio where he statistically looked at noise certification data and surprisingly enough he was able, taking very basic parameters of a helicopter, to predict noise certification levels within, I recall, plus or minus 2 or 3 dB.

Experimental efforts play a vital role as we have heard today and during the last few days with the availability of excellent wind tunnels such as the DNW, the French CEPRA 19, the Bedford transonic tunnel, the S1 Modane and the Ames facility, all of which have some acoustic treatment. They can all be used to good avail. We will see the application of ever more sophisticated testing techniques. Among these are: blade-mounted sensors in the determination of blade pressures, sophisticated microphone arrays, laser doppler velocimetry (LDV) for vortex strength, particle image velocimetry (PIV) for velocity distributions, the laser light sheet (LLS) technique to determine vortex miss distance and the projected grid method to determine the blade deflection.

As Monsieur Philippe also emphasized, flight tests are important to

complement the wind tunnel tests. It is important to do these flight tests also with instrumented blades, in particular, to understand the reasons for wind tunnel and full-scale flight test differences which could have numerous reasons. Finally, in the area of noise reduction, where are the visionary approaches? I think we have heard about some of them in the Conference, such as employment of advanced blade geometries, active blade control methods (such as IBC or HHC) or rather than using these rather "crude" control mechanisms for a blade to let "smart structures" directly control blade twist or camber. Porous blades, tip blowing, tip suction, tip vanes, all sorts of things I believe will be developed and tested in the next few years. Operationally, one could think of variable rpm especially for approach flights. I think the 75th AGARD FDP Symposium on the Aerodynamics and Acoustics of Rotorcraft has been a very successful Conference. It has set the stage for years to come in terms of future aeroacoustics research.

Dr. W.J. McCroskey

Thank you Dr. Heller. We will now have a session of some 15 or 20 minutes of open discussion and comments from the audience. I want to remind you again we encourage your participation. It is absolutely essential to use the microphone and to identify yourself, but don't be too shy about the exact words you use because you will have a chance to edit the transcription. Would anyone like to make a general comment or a question about the meeting or about any of the comments of our three presenters here in this session?

Mr. F. Toulmay, Eurocopter, France

Just a short comment about Mr. Heller's presentation. He presented the direct, Computational Fluid Dynamic simulation for high-speed noise as an alternative to the Kirchhoff formulation. But as an industry representative, I cannot fully agree with this approach, because I cannot imagine to make a direct simulation of the noise, at a distance of 10 or 20 rotor diameters. I would like it as a means to calculate inputs for the Kirchhoff calculation, not as an alternative, isn't it right? Do you agree?

Dr. Heller

Kirchhoff is, of course, not an alternative method to the direct computation of noise with the help of CFD, but rather one of several approaches with aerodynamic input to calculate the acoustics. An appropriate aerodynamic input to Kirchhoff (as well as other analogy approaches) is, for example, the one obtained from CFD-methods, such as Euler, Navier-Stokes, Singularity methods, etc.

Dr. G. Meier, DLR, Germany

I think that we have learned a lot in this Conference about inviscid unsteady aerodynamics and also aeroacoustics problems, but I see in the background as important questions and matters for the future, the coupling with mechanical structures. The problems of aeroelasticity have not been tackled so much here in the Conference, but I think they are very important, especially in connection with higher and intelligent types of control of blades.

Another point I would like to make with respect to viscous interaction. Many of the basic understandings of aeroacoustics is

possible without taking into account the viscous interaction of the flow. But considering that we have a transitional type of flow in the helicopter rotor and different effects with respect to the boundary layer and also with respect to the transonic behavior of the flow, I think it is of high importance to take into account also problems of boundary layer transition and of shock boundary layer interaction. For scientific work, we have a lot of problems in this field to do.

Dr. W.J. McCroskey

Is there some feeling in the audience about either the importance of or the difficulties in coupling these more sophisticated codes, which seems to be the trend, to the structural dynamics, and later incorporating them into comprehensive codes. This is an issue that we debate from time to time in the U.S. and in our laboratory. We would be interested to know if some of the participants here at the Conference feel that progress is going as well as can be expected within current budgets, or is this an area that perhaps should receive more emphasis at the expense of something else.

Dr. H. Korner, DLR, Germany

I will say something to this and also a response to what M. Toulmay, from Aerospatiale said. I also have difficulties in believing that full CFD to computational acoustics will very soon lead to results which really can be used in the short term in industry. However, I think that the Kirchhoff approach and also other approaches based on Euler will come up very soon here. You must not forget that we have skilled scientists who are able to speed up our codes, to find new acceleration techniques and furthermore, you must also see that the development of the computer side is very fast. I would like to draw your attention also to parallel computers. I think that also in the very near future we will be able to use these methods in this area. As to the connection with structures method, I think that this also should be done, especially the coupling between aerodynamics and structural problems. These are very important things. It is necessary for mathematicians and applied, structural people and aerodynamicists to develop fast solvers, and I am sure that within some years we will be able to do this. The fixed wing people are a bit ahead of us, but this is quite natural, because they don't have such a difficult problem as we have.

J. Landgrebe, United Technologies Research Center, USA

Jim, I'll try to respond to your question wearing the hats of both a researcher and someone who is connected directly to industry. Our research organization (UTRC) is tied directly to Sikorsky, so we get involved with the aeroelastic as well as the aerodynamic side of helicopter technology. I think for most rotors and most applications, the aeroelastic side is ahead of the aerodynamic side. There are exceptions that I will mention in a moment. For those cases where we can predict the aeroelastics quite adequately if we have the airloads, such as for the more conventional rotors, the question really comes to the computer time and the computer size. If we had an accurate CFD airloads solution, we could couple the codes together (couple it with the dynamic and aeroelastic simulation) and get the answer. The problem is that you have to iterate between the two. When you tell the dynamicist that you've got an airload

solution from a Navier-Stokes code, he'll get the dynamics and the aeroelastics for you. When you come back and tell him that you have to re-run your Navier-Stokes code again, which is going to take another two days and that's not the final solution - that is where the problem is. So, it gets to a question of whether or not you do this iteratively or you try to couple right into the code in a less iterative manner, the structures and the dynamics. That is where a lot of attention has to be paid right now as to how to couple more internally.

The other side of the problem is that we know that we have inaccuracies in the CFD codes. There are still problems to be solved. So, the dynamicist says that until you solve those problems, they don't want to see you. Why put in all of the fancy aeroelastics and couplings when the accuracy of the aerodynamics is not sufficient to warrant it. When we get into fancy tip designs and concepts with active control and different complex configurations, the aeroelastics are going to become more complex as well. We are compounding the problem. I agree with what was said earlier. I think a lot of attention has to be paid to this coupling and the best way to do it. That is, how to do it efficiently and how to improve, not just the aerodynamic codes, but also the aeroelastic codes, when it comes to very complex configurations. Just to give you examples, when you start thinking of soft torsional blades for aeroelastic compliance for active control, whether it be dynamic twist or just a soft tip, or when you start thinking of exotic or fancy plan forms for the tip, whether it be a BERP tip or a swept-taper-anhedral tip, the aeroelastics become quite complicated as well.

Mr. J.-J. Philippe, ONERA, France

For me, for the future, coming back to your question about the coupling with aeroelasticity codes, it seems for me to say that we know for sure that the blades are flexible. The torsion effect is the main parameter which drives the loads and the power. Also the deformation of the blade is very important to have exactly the good condition of functioning of the airfoil during its rotation. Perhaps before waiting for Navier-Stokes, which will solve the entire problem, we can do a good job with just coupling inviscid code and the boundary layer codes. Hopefully, a lot of configurations of helicopters are without stall and without strong shocks, and so the main parameters for me are to have fair pitching moment prediction coming from CFD codes. It seems mandatory to couple inviscid codes with boundary layer codes in the first step while waiting for more sophisticated codes.

Dr. W.J. McCroskey

Maybe I will pursue this just a little more toward closure. I think in the rotor community the resources are declining and issues that we really face are ones like where to concentrate our effort, and necessarily as a by-product, what to let go. That dichotomy then takes many forms, but one that is relevant here is the following: on the one hand, it will be so long before the Euler/Navier-Stokes can be sufficiently coupled to a structural code, and at the present time you can't trim it, even if you have it coupled. So, why not eliminate that direction altogether and use these codes to help as alternatives to wind tunnels, i.e., help to better understand the

complex flows and help to produce empirical models that can be coupled to the structural dynamics. The other side of the argument is why should we keep using computer resources, and using more sophisticated codes, if they are going to make the unrealistic assumption of rigid blades with a known and prescribed motion. So, that is the range of debate. I haven't heard here explicit recommendations that we drop the work on the more sophisticated codes. Particularly in the BVI, it was pointed out that it is essential to have a better aerodynamic flow field prediction than can be obtained from lifting line methods. But perhaps there are some who feel that the entire effort on the Euler/Navier-Stokes and more advanced codes is misspent. That could be.

Are there areas that people in the audience feel really do deserve heavier emphasis and/or other areas that they feel really should be deferred in this era of what I would call a less-than-zero-sum game?

Dr. H. Korner, DLR, Germany

I think the last presentation we had this morning was very interesting, and I think that especially this topic of advanced design and optimization is a very important thing which has to be addressed a bit more in the future. We have learned in the past to design airfoils for fixed wings, we are able to do this. Where are the inverse methods for helicopter blade and rotor design, based on more complex methods than they are at the moment? Where is the coupling of this or other sorts of methods with optimization methods? This is something I am missing, I would like to see more of it.

Professor C. Ciray, Middle East Technical University, Turkey

I would like to put a question to the audience where we have so many distinguished experts on the subject. What would the experts like to see us create as a technical meeting in the future as the AGARD Fluid Dynamics Panel? For example, Mr. Dadone was much impressed in a Conference about Key Rotor Problems. Would, for example, an "aerodynamics of transition from vertical to horizontal flight", be of interest? If there are other ideas or other subjects, I think, they would help us to guide to create a technical meeting or meetings on these lines.

Mr. Fillipone, Technical University of Denmark

I would like to point out something about the genetic optimization, because I am doing something like that myself, but not on BVI. From the experience I have gained so far I can say that the interest in this method relies on a cheap flow solver. In fact, we need thousands of iterations, because the GA actually does not search in the one direction, but in several directions. Then, we could use the genetic algorithm for optimizing nearly everything, because this is a non-convex optimization. So, the question is that we need something which is cheap, so that we can afford as many iterations as we need. The GA has another advantage: it doesn't care if the flow solver is accurate enough or not. It just needs to know if it is consistent. If it mostly overestimates or underestimates the performance, whether the GA always climbs, so in the end what we need to know is whether the final solution is better than the previous one or not. The cost of the optimization depends, of course, on the number of parameters.

The larger the number of parameters, the larger is the binary string. The larger the binary string, the larger the search space and slower the rate of convergence. Therefore it would be more appropriate to do some kind of hierarchic optimization: choose a set of parameters, optimize those and then go to other parameters.

Dr. Baeder

Regarding the use of the different experimental and computational methods to carry the genetic algorithm concepts, it seems like we need a good mixture of all these different methods. We shouldn't all be concentrating on just one of the aspects, and at times shouldn't be covering all of them. However, we do need perturbations to occur where we start to look into these things, because from time to time, what was once impractical, becomes practical. We can see different things from the different methods. Regarding the comment earlier about the use of direct CFD for doing acoustic calculations, I would say use that appropriately. Just like you wouldn't perform a big wind tunnel test for every configuration, but you use that to get some empirical knowledge. In the same way, you use the big CFD codes to gain additional knowledge that you can use empirically for the simpler methods.

I was quite impressed with the paper from DLR. It now looks that if you have the CFD solution, you could use a very simple estimate for the quadrapole. As long as you are accurate about where you place it, a good prediction could be provided in the far field. If we didn't keep on branching out and looking at these different areas, we would miss something.

Dr. N. Kroll, DLR, Germany

As I am coming from a research organization, I would like to put the question to the helicopter industry. Do we need, besides all these high sophisticated CFD methods for rotors, do we need also some research on Navier-Stokes codes for fuselage or is it done by using some commercial software packages like "FIRE" or whatever they call it?

Dr. W.J. McCroskey

It is hard to cut off a discussion when you ask for questions or additional comments, but if anyone has a quick response to that, I'll entertain it, otherwise I'll take it in the spirit of a challenge to those of us who may be involved in planning as well as conducting research. Is there any quick response?

Mr. L. Dadone

Jim Narramore should be answering this question. Bell has used, fairly successfully, Navier-Stokes codes to analyze fuselages and to reduce the drag of fuselages. I guess the limitation is that when you have very gentle gradients which precipitate separation, then it is tricky. The whole difficulty is in the turbulence modeling, as mentioned before. In the case of helicopters, you cannot just eliminate separation, often enough you have to live with it. So, you have to try to minimize the regions of separation without actually making them go away as you do in airplanes. Then you have unsteady solutions and you have, in fact, turbulence modeling being the real

obstacle. I don't know if that answers your question, but we are interested, and we are pursuing it. Further research is necessary to make these tools really useful to us. Otherwise, we have to go back to wind tunnel tests.

Dr. W.J. McCroskey

I think it is time to bring this part of our Conference to a close. In absolute terms, our total overrun of some twelve minutes out of a four day conference is a small percentage error, but in the things that really matter to our Chairman, we have cut 80% of the time that was allocated to him for closing remarks. I am sure that he is very anxious for this session to close. I would like to thank the Technical Evaluator and the invited Commentators for the effort that they put in coming and doing this. Thank you, the audience, for your participation, your comments and questions. With that, the technical part of this meeting is closed. I pass the microphone to our Chairman, Mr. Christian Dujarric.

M. Christian Dujarric, ASE-Programme HERMES, France

Thank you for cutting down my time for a speech. I will not need a long time. Ladies and Gentlemen, we have had four interesting days of presentations on aerodynamics and aeroacoustics for rotors. I must now close this Symposium which has been a success, not only in the quality of the presentations but also in the quality of the participants. For the Fluid Dynamics Panel, I would like to thank the two Co-Chairmen of the Program Committee, Dr. Horst Korner and Dr. Jim McCroskey. I would also like to thank the Program Committee, Prof. Decuypere, Dr. Chan, Ing. Gen. Bernard Monnerie, Professor Sabetta, Dr. Steketee, Dr. Luis Calavera, Prof. Ciray, Dr. Clarkson, Prof. Saric and Mr. Lou Williams. I would also like to thank the Technical Evaluator for this meeting, Dr. Dadone, who has done a remarkable job in his summary and his constructive evaluation of our work. Thanks to Mr. Philippe and Dr. Heller for their prepared comments which complemented and reinforced the technical evaluation of Dr. Dadone. Our thanks also to all the authors who presented their work, and particularly, the invited commentators, Mr. Landgrebe, who has presented an interesting panorama of activities in the U. S., Professor Hamel, who has presented to us the point of view of the Flight Vehicle Integration Panel, Monsieur Petot, who has contributed to our Symposium for SMP.

I would also like to thank our Russian participants, Dr. Rozhdestvensky and Mr. Boulanovsky, who have given us the latest information from their country. We regret that Professor Tischenko was not able to attend to present the prediction methods used in Russia regarding aerodynamics on helicopter rotors.

I would also like to thank all the participants for the discussion that has just taken place. I am sure that this discussion will bring new progress and new applications for the helicopter. The high quality of the scientific work must not allow us to forget the remarkable organizational work which made it possible to hold this Symposium. I would like to particularly thank our sponsors, IBM, DLR, NEC, Eurocopter Germany, and also I would like to personally thank the local organizer, Dr. Karl Kienappel to whom we are grateful

for the excellent arrangements for this Symposium. Dr. Karl Kienappel was assisted in these arrangements by Madame Strempel and Madame Wiegand, and I know that these people have devoted a lot of time to allow us to have had such good conditions and comfort for our work. Once again, thank you.

I would like to call to your attention the difficult work accomplished by our interpreters, which was brilliantly done by: Mrs. Korving, Mrs. Main and Mr. Shearer. Thank you also to the technicians who insured the good functioning of the audiovisual equipment as well as the people who have contributed to the logistics of our Conference, Mr. Berndt, Mr. Gerlach, Mr. Muller, Mr. Schultz, Mr. Orfritz and Mr. Rietz.

May I also thank the secretary for the Panel, Miss Anne-Marie Rivault as well as our Panel Executive, Mr. Jack Molloy for the considerable administrative work done to prepare this meeting. I hope I have not forgotten anyone. Finally, I would like to present the program for 1995. There is a Symposium in the spring on "Aerodynamics of Store Integration and Separation". This will take place in Ankara, Turkey. In autumn, we have planned to organize a Symposium in Spain on "The Progress and Challenges of CFD Methods and Algorithms". We also have two special courses to be held at the von Karman Institute and at NASA, Ames - the first course on "Parallel Computing in CFD". The second course concerns "Capsule Aerothermodynamics".

I thank you for your attention.

REPORT DOCUMENTATION PAGE

1. Recipient's Reference	2. Originator's Reference AGARD-CP-552	3. Further Reference ISBN 92-836-0015-0	4. Security Classification of Document UNCLASSIFIED/ UNLIMITED														
5. Originator Advisory Group for Aerospace Research and Development North Atlantic Treaty Organization 7 rue Ancelle, 92200 Neuilly-sur-Seine, France																	
6. Title AGARD Conference Proceedings No. 552 Aerodynamics and Aeroacoustics of Rotorcraft																	
7. Presented at/sponsored by The 75th Fluid Dynamics Symposium held in Berlin, Germany, 10-13 October 1994																	
8. Author(s)/Editor(s) Various			9. Date August 1995														
10. Author's/Editor's Address Various			11. Pages 508														
12. Distribution Statement There are no restrictions on the distribution of this document. Information about the availability of this and other AGARD unclassified publications is given on the back cover.																	
13. Keywords/Descriptors <table><tr><td>Aerodynamics</td><td>Acoustics</td></tr><tr><td>Helicopters</td><td>Noise (sound)</td></tr><tr><td>Rotary wing aircraft</td><td>Stalling</td></tr><tr><td>Rotors</td><td>Hovering</td></tr><tr><td>Rotary wings</td><td>Wind turbines</td></tr><tr><td>Computational fluid dynamics</td><td>Vortices</td></tr><tr><td>Aeroacoustics</td><td>Predictions</td></tr></table>				Aerodynamics	Acoustics	Helicopters	Noise (sound)	Rotary wing aircraft	Stalling	Rotors	Hovering	Rotary wings	Wind turbines	Computational fluid dynamics	Vortices	Aeroacoustics	Predictions
Aerodynamics	Acoustics																
Helicopters	Noise (sound)																
Rotary wing aircraft	Stalling																
Rotors	Hovering																
Rotary wings	Wind turbines																
Computational fluid dynamics	Vortices																
Aeroacoustics	Predictions																
14. Abstract <p>The papers prepared for the AGARD Fluid Dynamics Panel (FDP) Symposium on "Aerodynamics and Aeroacoustics of Rotorcraft", which was held 10-13 October 1994 in Berlin, Germany are contained in this Report. In addition, a Technical Evaluator's Report aimed at assessing the success of the Symposium in meeting its objectives, and an edited transcript of the General Discussion held at the end of the Symposium are also included.</p> <p>The Symposium brought together scientists in different fields of aerodynamics and aeroacoustics to review and discuss their recent results in the area of rotary-wing aircraft in order to foster future development. The program included 35 papers from North America, Western Europe, and Russia organized in the following technical sessions: Dynamics Stall, Wind Turbines, Aerodynamic 3D Prediction Methods, Experimental Investigations of Helicopter Rotors, Acoustic Prediction Methods, and Interference Problems.</p>																	

AGARD

NATO  OTAN

7 RUE ANCELLE • 92200 NEUILLY-SUR-SEINE

FRANCE

Télécopie (1)47.38.57.99 • Télex 610 176

DIFFUSION DES PUBLICATIONS

AGARD NON CLASSIFIEES

Aucun stock de publications n'a existé à AGARD. A partir de 1993, AGARD détendra un stock limité des publications associées aux cycles de conférences et cours spéciaux ainsi que les AGARDographies et les rapports des groupes de travail, organisés et publiés à partir de 1993 inclus. Les demandes de renseignements doivent être adressées à AGARD par lettre ou par fax à l'adresse indiquée ci-dessus. *Veuillez ne pas téléphoner.* La diffusion initiale de toutes les publications de l'AGARD est effectuée auprès des pays membres de l'OTAN par l'intermédiaire des centres de distribution nationaux indiqués ci-dessous. Des exemplaires supplémentaires peuvent parfois être obtenus auprès de ces centres (à l'exception des Etats-Unis). Si vous souhaitez recevoir toutes les publications de l'AGARD, ou simplement celles qui concernent certains Panels, vous pouvez demander à être inclu sur la liste d'envoi de l'un de ces centres. Les publications de l'AGARD sont en vente auprès des agences indiquées ci-dessous, sous forme de photocopie ou de microfiche.

CENTRES DE DIFFUSION NATIONAUX

ALLEMAGNE

Fachinformationszentrum,
Karlsruhe
D-76344 Eggenstein-Leopoldshafen 2

BELGIQUE

Coordonnateur AGARD-VSL
Etat-major de la Force aérienne
Quartier Reine Elisabeth
Rue d'Evere, 1140 Bruxelles

CANADA

Directeur, Services d'information scientifique
Ministère de la Défense nationale
Ottawa, Ontario K1A 0K2

DANEMARK

Danish Defence Research Establishment
Ryvangs Allé 1
P.O. Box 2715
DK-2100 Copenhagen Ø

ESPAGNE

INTA (AGARD Publications)
Pintor Rosales 34
28008 Madrid

ETATS-UNIS

NASA Headquarters
Code JOB-1
Washington, D.C. 20546

FRANCE

O.N.E.R.A. (Direction)
29, Avenue de la Division Leclerc
92322 Châtillon Cedex

GRECE

Hellenic Air Force
Air War College
Scientific and Technical Library
Dekelia Air Force Base
Dekelia, Athens TGA 1010

ISLANDE

Director of Aviation
c/o Flugrad
Reykjavik

ITALIE

Aeronautica Militare
Ufficio del Delegato Nazionale all'AGARD
Aeroporto Pratica di Mare
00040 Pomezia (Roma)

LUXEMBOURG

Voir Belgique

NORVEGE

Norwegian Defence Research Establishment
Attn: Biblioteket
P.O. Box 25
N-2007 Kjeller

PAYS-BAS

Netherlands Delegation to AGARD
National Aerospace Laboratory NLR
P.O. Box 90502
1006 BM Amsterdam

PORTUGAL

Força Aérea Portuguesa
Centro de Documentação e Informação
Alfragide
2700 Amadora

ROYAUME-UNI

Defence Research Information Centre
Kentigern House
65 Brown Street
Glasgow G2 8EX

TURQUIE

Millî Savunma Başkanlığı (MSB)
ARGE Dairesi Başkanlığı (MSB)
06650 Bakanlıklar-Ankara

Le centre de distribution national des Etats-Unis ne détient PAS de stocks des publications de l'AGARD.

D'éventuelles demandes de photocopies doivent être formulées directement auprès du NASA Center for AeroSpace Information (CASI) à l'adresse ci-dessous. Toute notification de changement d'adresse doit être fait également auprès de CASI.

AGENCES DE VENTE

NASA Center for
AeroSpace Information (CASI)
800 Elkridge Landing Road
Linthicum Heights, MD 21090-2934
Etats-Unis

ESA/Information Retrieval Service
European Space Agency
10, rue Mario Nikis
75015 Paris
France

The British Library
Document Supply Division
Boston Spa, Wetherby
West Yorkshire LS23 7BQ
Royaume-Uni

Les demandes de microfiches ou de photocopies de documents AGARD (y compris les demandes faites auprès du CASI) doivent comporter la dénomination AGARD, ainsi que le numéro de série d'AGARD (par exemple AGARD-AG-315). Des informations analogues, telles que le titre et la date de publication sont souhaitables. Veuillez noter qu'il y a lieu de spécifier AGARD-R-*nnn* et AGARD-AR-*nnn* lors de la commande des rapports AGARD et des rapports consultatifs AGARD respectivement. Des références bibliographiques complètes ainsi que des résumés des publications AGARD figurent dans les journaux suivants:

Scientific and Technical Aerospace Reports (STAR)
publié par la NASA Scientific and Technical
Information Division
NASA Headquarters (JTT)
Washington D.C. 20546
Etats-Unis

Government Reports Announcements and Index (GRA&I)
publié par le National Technical Information Service
Springfield
Virginia 22161
Etats-Unis
(accessible également en mode interactif dans la base de
données bibliographiques en ligne du NTIS, et sur CD-ROM)



Imprimé par le Groupe Communication Canada
45, boul. Sacré-Cœur, Hull (Québec), Canada K1A 0S7

AGARD

NATO  OTAN

7 RUE ANCELLE • 92200 NEUILLY-SUR-SEINE

FRANCE

Telefax (1)47.38.57.99 • Telex 610 176

DISTRIBUTION OF UNCLASSIFIED

AGARD PUBLICATIONS

AGARD holds limited quantities of the publications that accompanied Lecture Series and Special Courses held in 1993 or later, and of AGARDographs and Working Group reports published from 1993 onward. For details, write or send a telefax to the address given above. *Please do not telephone.*

AGARD does not hold stocks of publications that accompanied earlier Lecture Series or Courses or of any other publications. Initial distribution of all AGARD publications is made to NATO nations through the National Distribution Centres listed below. Further copies are sometimes available from these centres (except in the United States). If you have a need to receive all AGARD publications, or just those relating to one or more specific AGARD Panels, they may be willing to include you (or your organisation) on their distribution list. AGARD publications may be purchased from the Sales Agencies listed below, in photocopy or microfiche form.

NATIONAL DISTRIBUTION CENTRES

BELGIUM

Coordonnateur AGARD — VSL
Etat-major de la Force aérienne
Quartier Reine Elisabeth
Rue d'Evere, 1140 Bruxelles

CANADA

Director Scientific Information Services
Dept of National Defence
Ottawa, Ontario K1A 0K2

DENMARK

Danish Defence Research Establishment
Ryvangs Allé 1
P.O. Box 2715
DK-2100 Copenhagen Ø

FRANCE

O.N.E.R.A. (Direction)
29 Avenue de la Division Leclerc
92322 Châtillon Cedex

GERMANY

Fachinformationszentrum
Karlsruhe
D-76344 Eggenstein-Leopoldshafen 2

GREECE

Hellenic Air Force
Air War College
Scientific and Technical Library
Dekelia Air Force Base
Dekelia, Athens TGA 1010

ICELAND

Director of Aviation
c/o Flugrad
Reykjavik

ITALY

Aeronautica Militare
Ufficio del Delegato Nazionale all'AGARD
Aeroporto Pratica di Mare
00040 Pomezia (Roma)

LUXEMBOURG

See Belgium

NETHERLANDS

Netherlands Delegation to AGARD
National Aerospace Laboratory, NLR
P.O. Box 90502
1006 BM Amsterdam

NORWAY

Norwegian Defence Research Establishment
Attn: Biblioteket
P.O. Box 25
N-2007 Kjeller

PORTUGAL

Força Aérea Portuguesa
Centro de Documentação e Informação
Alfragide
2700 Amadora

SPAIN

INTA (AGARD Publications)
Pintor Rosales 34
28008 Madrid

TURKEY

Millî Savunma Başkanlığı (MSB)
ARGE Dairesi Başkanlığı (MSB)
06650 Bakanlıklar-Ankara

UNITED KINGDOM

Defence Research Information Centre
Kentigern House
65 Brown Street
Glasgow G2 8EX

UNITED STATES

NASA Headquarters
Code JOB-1
Washington, D.C. 20546

The United States National Distribution Centre does NOT hold stocks of AGARD publications.

Applications for copies should be made direct to the NASA Center for AeroSpace Information (CASI) at the address below.

Change of address requests should also go to CASI.

SALES AGENCIES

NASA Center for

AeroSpace Information (CASI)
800 Elkridge Landing Road
Linthicum Heights, MD 21090-2934
United States

ESA/Information Retrieval Service

European Space Agency
10, rue Mario Nikis
75015 Paris
France

The British Library

Document Supply Centre
Boston Spa, Wetherby
West Yorkshire LS23 7BQ
United Kingdom

Requests for microfiches or photocopies of AGARD documents (including requests to CASI) should include the word 'AGARD' and the AGARD serial number (for example AGARD-AG-315). Collateral information such as title and publication date is desirable. Note that AGARD Reports and Advisory Reports should be specified as AGARD-R-nnn and AGARD-AR-nnn, respectively. Full bibliographical references and abstracts of AGARD publications are given in the following journals:

Scientific and Technical Aerospace Reports (STAR)
published by NASA Scientific and Technical
Information Division
NASA Headquarters (JTT)
Washington D.C. 20546
United States

Government Reports Announcements and Index (GRA&I)
published by the National Technical Information Service
Springfield
Virginia 22161
United States
(also available online in the NTIS Bibliographic
Database or on CD-ROM)



Printed by Canada Communication Group
45 Sacré-Cœur Blvd., Hull (Québec), Canada K1A 0S7

ISBN 92-836-0015-0